OXFORD TEXTBOOKS IN CLINICAL NEUROLOGY

INCLUDES ACCESS TO
OXFORD
MEDICINE
ONLINE

Oxford Textbook of
Neuroimaging

Edited by
Massimo Filippi

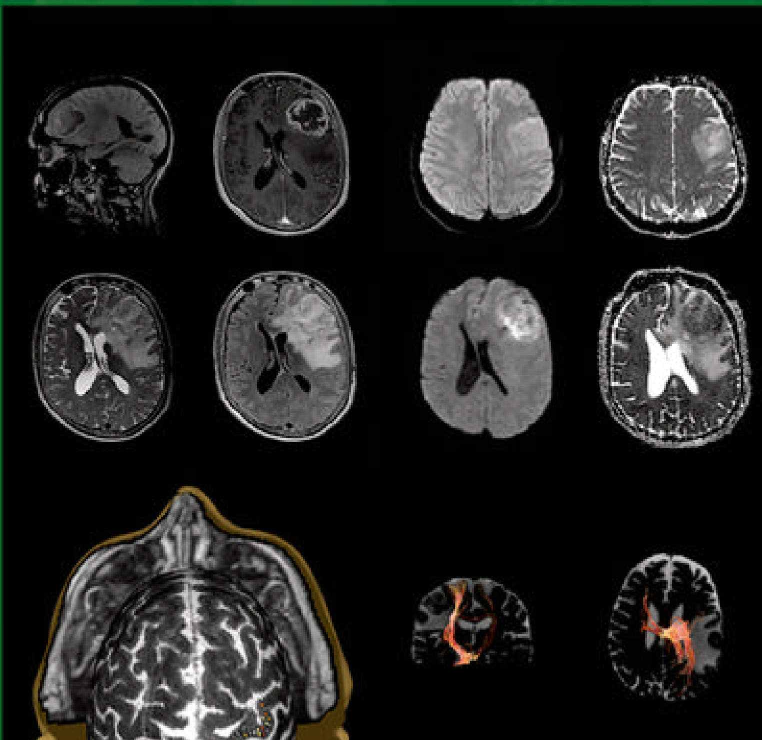

OXFORD

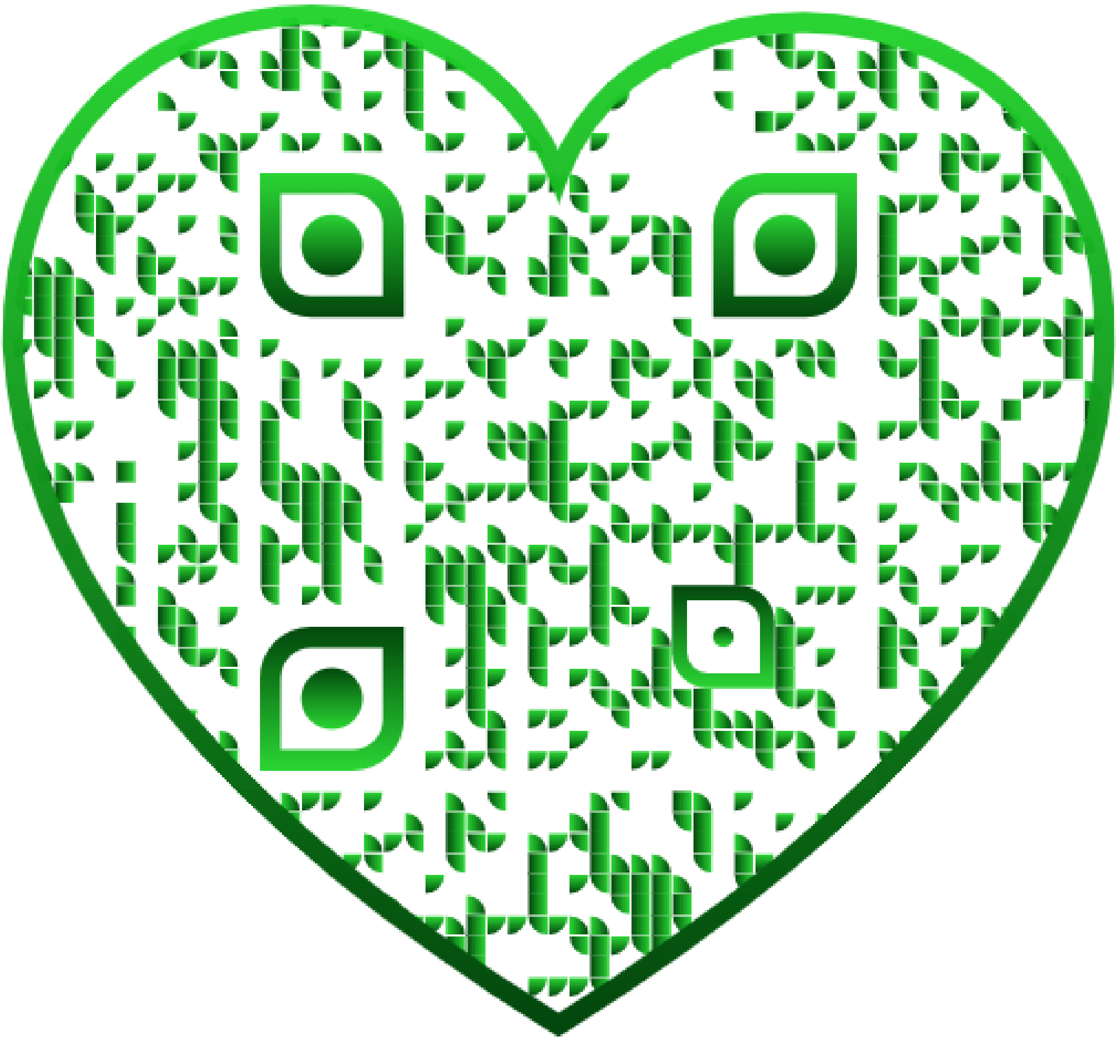

Oxford Textbook of
Neuroimaging

Oxford Textbooks in Clinical Neurology

PUBLISHED

Oxford Textbook of Epilepsy and Epileptic Seizures
Edited by Simon Shorvon, Renzo Guerrini, Mark Cook, and Samden Lhatoo

Oxford Textbook of Vertigo and Imbalance
Edited by Adolfo Bronstein

Oxford Textbook of Movement Disorders
Edited by David Burn

Oxford Textbook of Stroke and Cerebrovascular Disease
Edited by Bo Norrving

Oxford Textbook of Neuromuscular Disorders
Edited by David Hilton-Jones and Martin R. Turner

Oxford Textbook of Neurorehabilitation
Edited by Volker Dietz and Nick Ward

FORTHCOMING

Oxford Textbook of Cognitive Neurology and Dementia
Edited by Masud Husain and Jonathan Schott

Oxford Textbook of Headache Syndromes
Edited by Michel Ferrari, Joost Haan, Andrew Charles, David Dodick, and Fumihiko Sakai

Oxford Textbook of Clinical Neurophysiology
Edited by Kerry Mills

Free personal online access for 12 months

Individual purchasers of this book are also entitled to free personal access to the online edition for 12 months on *Oxford Medicine Online* (www.oxfordmedicine.com). Please refer to the access token card for instructions on token redemption and access.

Online ancillary materials, where available, are noted at the end of the respective chapters in this book. Additionally, *Oxford Medicine Online* allows you to print, save, cite, email, and share content; download high-resolution figures as Microsoft PowerPoint slides; save often-used books, chapters, or searches; annotate; and quickly jump to other chapters or related material on a mobile-optimised platform.

We encourage you to take advantage of these features. If you are interested in ongoing access after the 12-month gift period, please consider an individual subscription or consult with your librarian.

Oxford Textbook of Neuroimaging

Edited by

Massimo Filippi
Neuroimaging Research Unit, and Department of Neurology, Institute of Experimental Neurology, Division of Neuroscience, San Raffaele Scientific Institute, Vita-Salute San Raffaele University, Milan, Italy

Series Editor

Christopher Kennard

OXFORD
UNIVERSITY PRESS

OXFORD
UNIVERSITY PRESS

Great Clarendon Street, Oxford, OX2 6DP,
United Kingdom

Oxford University Press is a department of the University of Oxford.
It furthers the University's objective of excellence in research, scholarship,
and education by publishing worldwide. Oxford is a registered trade mark of
Oxford University Press in the UK and in certain other countries

© Oxford University Press 2015

The moral rights of the authors have been asserted

First Edition published in 2015

Impression: 1

All rights reserved. No part of this publication may be reproduced, stored in a retrieval system, or transmitted, in any form or by any means, without the prior permission in writing of Oxford University Press, or as expressly permitted by law, by licence or under terms agreed with the appropriate reprographics rights organization. Enquiries concerning reproduction outside the scope of the above should be sent to the Rights Department, Oxford University Press, at the address above

You must not circulate this work in any other form
and you must impose this same condition on any acquirer

Published in the United States of America by Oxford University Press
198 Madison Avenue, New York, NY 10016, United States of America

British Library Cataloguing in Publication Data
Data available

Library of Congress Control Number: 2015933911

ISBN 978–0–19–966409–2

Printed in China by
Asia Pacific Offset Ltd.

Oxford University Press makes no representation, express or implied, that the drug dosages in this book are correct. Readers must therefore always check the product information and clinical procedures with the most up-to-date published product information and data sheets provided by the manufacturers and the most recent codes of conduct and safety regulations. The authors and the publishers do not accept responsibility or legal liability for any errors in the text or for the misuse or misapplication of material in this work. Except where otherwise stated, drug dosages and recommendations are for the non-pregnant adult who is not breast-feeding

Links to third party websites are provided by Oxford in good faith and for information only. Oxford disclaims any responsibility for the materials contained in any third party website referenced in this work.

Preface

The last few decades have witnessed extraordinary advances in clinical neurology, with some of the most remarkable achievements related to neuroimaging. Conventional computerized tomography (CT), magnetic resonance (MR), nuclear medicine, and ultrasound techniques are playing an increasingly important role in facilitating diagnosis, prognosis and therapeutic decisions in several neurological conditions. Furthermore, the advent of quantitative MRI techniques, such as magnetization transfer and diffusion tensor imaging, is constantly changing the landscape of the diagnostic work-up of neurological diseases on the basis of objective findings as shown, for instance, in the case of multiple sclerosis, Alzheimer's disease and stroke. The improved and more advanced techniques also offer unique surrogate markers of disease pathophysiology and for monitoring clinical trials of new experimental treatment and individual patient response to therapies available on the market.

The overall scope of this book is to provide a basic overview of the established and latest neuroimaging methodologies, and to illustrate their application to the main diseases of the brain and the spinal cord, in both adult and paediatric patients.

'Central to the effective evaluation of an image is an understanding of the technical aspects of image production', said Bob Grossman, one of the pioneers and most prominent figure in the field, in his *Neuroradiology: The requisites*. The organization of the book is such that the introductory chapters review in detail the fundamentals of available structural and functional neuroimaging techniques, including CT, conventional and advanced MR techniques, single-photon emission CT and positron emission tomography, ultrasound, and image analysis methods. Then, it moves from the basics of imaging techniques to the main applications in the different branches of clinical neurology. The reader will be accompanied to the appropriate interpretation of neuroimaging findings in a systematic way throughout the volume. The chapters on adult neurological disorders start covering the application of neuroimaging in headache, epilepsy, neoplasia, and infectious diseases. Then, the invaluable clinical role of neuroimaging in inflammatory, cerebrovascular, and neurodegenerative diseases is discussed, as well as the challenging issue of spinal cord imaging. The book ends with three chapters on congenital malformations of the brain and skull, and inflammatory and metabolic central nervous system disorders in paediatric patients. Although each chapter stands alone, reference to previous chapters is given to avoid unnecessary overlap.

My hope is that this book will provide a balanced state-of-the-art of neuroimaging for neurologists and radiologists to help guide their reading of imaging findings in patients in everyday clinical practice, to improve their understanding of the pathophysiological basis of neurological conditions and to set up the stage for future research. This book should also prove of interest to students, residents, other young fellows and technologists, who wish to learn more about this rapidly developing area of medicine.

This book would not exist without the outstanding contributions of worldwide recognized experts in the field who generously provided chapters, images, thoughts, and vision to this volume. I hope you will enjoy reading it as much as we enjoyed writing its chapters.

Massimo Filippi
Milan, Italy, May 2015

Contents

Abbreviations *ix*

Contributors *xiii*

SECTION 1
Fundamentals of neuroimaging techniques

1 Computed tomography *3*
Qinghua Hou, Elizabeth Tong, Cong Gao, and Max Wintermark

2 Modern methods for accurate T_1, T_2, and proton density MRI *13*
Sean C. L. Deoni, Sandra M. Meyers, and Shannon H. Kolind

3 Magnetic resonance spectroscopy *27*
Christoph Juchem and Daniel Pelletier

4 Diffusion magnetic resonance imaging *40*
Silvia De Santis

5 Magnetization transfer imaging *50*
Mark A. Horsfield and Mara Cercignani

6 Cerebral perfusion imaging *59*
Linda Knutsson and Birgitte Fuglsang Kjølby

7 Functional magnetic resonance imaging *68*
Ralf Deichmann and Christian Schwarzbauer

8 Principles of brain single-photon emission computed tomography imaging *79*
Yong Du and Habib Zaidi

9 Positron emission tomography *90*
Bart N. M. van Berckel, Adriaan A. Lammertsma, and Ronald Boellaard

10 Ultrasound *97*
Claudio Baracchini

SECTION 2
Clinical applications

11 Headache *117*
Till Sprenger and Peter J. Goadsby

12 Epilepsy and related disorders *124*
Dewi Schrader, Neda Bernasconi, and Andrea Bernasconi

13 Adult neoplasia *139*
Phiroz E. Tarapore, Corinna C. Zygourakis, Soonmee Cha, and Mitchel S. Berger

14 Infections of the nervous system *151*
Kate F. Mahady, Tarek A. Yousry, and H. Rolf Jäger

15 Multiple sclerosis and related disorders *168*
Massimo Filippi, Paolo Preziosa, and Maria A. Rocca

16 Stroke *185*
Franz Fazekas, Stefan Ropele, and Christian Enzinger

17 Neuroimaging in vascular cognitive impairment: Structural and functional imaging in vascular dementia *200*
Lars-Olof Wahlund, Lena Bronge, Irina Savitcheva, and Rimma Axelsson

18 Alzheimer's disease *208*
Massimo Filippi and Federica Agosta

19 Frontotemporal lobar degeneration *224*
Massimo Filippi and Federica Agosta

20 Dementia with Lewy bodies *239*
Michael J. Firbank and John T. O'Brien

21 Movement disorders: Parkinson's disease and atypical parkinsonisms *246*
Massimo Filippi and Federica Agosta

22 Neuroimaging of prion diseases *263*
Eduardo Caverzasi, Leonel Takada, Paolo Vitali, Marina Pan, and Michael D. Geschwind

23 Motor neuron diseases 279
Massimo Filippi and Federica Agosta

24 Cerebellar ataxia and related disorders 295
Mario Mascalchi and Alessandra Vella

25 Spinal cord injury 315
Patrick Freund, Siawoosh Mohammadi, Nikolaus Weiskopf, and Armin Curt

26 Spinal cord diseases 323
Maria A. Rocca, Paolo Preziosa, and Massimo Filippi

27 Traumatic brain injury 335
Matilde Inglese and Elan J. Grossman

28 Neuroimaging in disorders of consciousness 346
Olivier Bodart, Vanessa Charland-Verville, Steven Laureys, and Olivia Gosseries

29 Congenital malformations of the brain and skull 354
Sara Nuñez, Sonia Bermudez, Mónica C. Vargas, Andrés Puerta, and María T. Mantilla

30 Paediatrics: central nervous system inflammatory disorders 370
Leonard H. Verhey and Brenda Banwell

31 Paediatrics: congenital metabolic central nervous system disorders 387
Deborah L. Renaud

32 Central nervous system vasculitis 397
Giulio Zuccoli, Nicolò Pipitone, Caterina Giannini, and Carlo Salvarani

Index 405

Abbreviations

^{1}H-MRS	proton magnetic resonance spectroscopy
2D	two-dimensional
3D	three-dimensional
4D CTA	time-resolved computed tomography angiography
4D	four-dimensional
5-ala	5-aminolevulinic acid
AADC	L-aromatic amino acid decarboxylase
ABD	Adamantiades–Behçet disease
AC	attenuation correction
ACA	anterior cerebral artery
ACC	agenesis of the corpus callosum
ACS	asymptomatic carotid stenosis
AD	Alzheimer's disease
ADC	apparent diffusion coefficient
ADEM	acute disseminated encephalomyelitis
ADP	adenosindiphosphate
ADS	acute demyelinating syndrome
AHA/ASA	American Heart Association/American Stroke Association
AHM	acute hemiplegic migraine
AIC	Akaike's information criterion
AIDS	acquired immunodeficiency syndrome
AIF	arterial input function
ALFF	amplitude of low frequency fluctuations
ALS	amyotrophic lateral sclerosis
AMI	area membranacea inferior
AMN	adrenomyeloneuropathy
AMS	area membranacea superior
ANCA	anti-neutrophil cytoplasmic antibodies
AOA-2	ataxia oculomotor apraxia type 2
aPrD	acquired prion disease
AQP4	aquaporin-4
ARSACS	autosomal recessive spastic ataxia of Charlevoix–Saguenay
ARWMC	age-related white matter changes
ASD	autism spectrum disorders
ASL	arterial spin labelling
ASPECTS	Alberta Stroke Program Early CT Score
AT	ataxia telangectasia
ATP	adenosintriphosphate
BA	basilar artery
BBB	blood–brain barrier
BBBP	blood–brain barrier permeability
BCS	Balo's concentric sclerosis
BMS	benign multiple sclerosis
BOLD	blood oxygenation level dependent
BSE	bovine spongiform encephalopathy
bSSFP	Inversion Recovery Steady-State Free Precession
bvFTD	behavioural variant of frontotemporal dementia
CAA	cerebral amyloid angiopathy
CAD	carotid artery distensibility
CADASIL	cerebral autosomal dominant arteriopathy with subcortical infarcts and leukoencephalopathy
cART	combination antiretroviral therapy
CASL	continuous arterial spin labelling
CBD	corticobasal degeneration
CBF	cerebral blood flow
CBS	corticobasal syndrome
CBV	cerebral blood volume
CC	corpus callosum
CCA	cortical cerebellar atrophy
CCALD	childhood cerebral adrenoleukodystrophy
CCH	coded contrast harmonics
CCM	cerebral cavernous malformations
CCSVI	chronic cerebrospinal venous insufficiency
CCU	contrast-enhanced carotid ultrasonography
CDR	clinical dementia rating
CDR	collimator-detector response
CDRF	collimator-detector response function
CECT	contrast-enhanced computed tomography
CE-MRA	contrast-enhanced MRA
CEST	chemical exchange saturation transfer
CHARMED	composite hindered and restricted model of diffusion
CHESS	chemical shift selective
Cho	choline
CIS	clinically-isolated syndrome
CISS	constructive interference in steady state
CL	cortical lesions
CLIPPERS	chronic lymphocytic inflammation with perivascular pontine enhancement responsive to steroids
CMR_{glu}	cerebral metabolic rate of glucose
CMV	cytomegalovirus
CNR	contrast-to-noise ratio
CNS	central nervous system
CoAA	congophilic amyloid angiopathy

cPACNS	childhood primary angiitis of the central nervous system
Cr	creatine
CRION	chronic relapsing inflammatory optic neuropathy
CRLB	Cramér–Rao lower bounds
CRS-R	Coma Recovery Scale-Revised
CSD	cortical spreading depression
CSF	cerebrospinal fluid
CSI	chemical shift imaging
CST	corticospinal tract
CT	computed tomography
CTA	computed tomography angiography
CVD	cerebrovascular disease
CW	continuous wave
CWD	chronic wasting disease
CWPR	continuous wave power equivalent
DAI	diffuse axonal injury
DAT	dopamine transporter
DBS	deep brain stimulation
DCE-MRI	dynamic contrast-enhanced magnetic resonance imaging
DESPOT1	driven equilibrium single pulse observation of T$_1$
dGEMERIC	delayed gadolinium-enhanced magnetic resonance imaging
DIR	double-inversion recovery
DIS	dissemination in space
DIT	dissemination in time
DKI	diffusional kurtosis imaging
DLBD	dementia with Lewy–Bodies
DM	dura mater
DMN	default mode network
DOC	disorders of consciousness
DOPA	dihydroxyphenylalanine
DSA	digital subtraction angiography
DSC-MRI	dynamic susceptibility contrast magnetic resonance imaging
DT	diffusion tensor
DTBZ	18F-dihydrotetrabenazine
DT-MRI	diffusion tensor magnetic resonance imaging
DTI	diffusion tensor imaging
DVST	dural venous sinus thrombosis
DW	diffusion-weighted
DWI	diffusion-weighted imaging
EA-2	episodic ataxia type 2
EBV	Epstein–Barr virus
ECG	electrocardiogram
EDH	epidural haematomas
EDSS	Expanded Disability Status Scale
EEG	electroencephalography
EES	extravascular extracellular space
EOCA	early onset cerebellar ataxia
EPI	echo planar imaging
EPISTAR	echo planar imaging with signal targeting with alternating frequency
ESR	erythrocyte sedimentation rate
ESSE	effective source scatter estimation
FAIR	flow alternating inversion recovery
FA	fractional anisotropy
FBP	filtered back-projection
FCD	focal cortical dysplasia
fCJD	familial Creutzfeldt–Jacob disease
FDG	[^{18}F]-2-fluoro-2-deoxy-D-glucose
FDR	false discovery rate
FFI	fatal familial insomnia
FLAIR	fluid-attenuated inversion recovery
FMD	flow-mediated vasodilation
fMRI	functional magnetic resonance imaging
FOV	field-of-view
FRDA	Friedreich ataxia
FSE	fast spin echo
FTD	frontotemporal dementia
FTLD	frontotemporal lobar degeneration
FUS	fused in sarcoma
FWE	family-wise error
GA1	glutaric aciduria type I
GABA	γ-aminobutyric acid
GALC	galactocerebrosidase
GCDH	glutaryl-CoA dehydrogenase
GCS	Glasgow Coma Scale
Gd	gadolinium
GFAP	glial fibrillary acidic protein
GLM	general linear model
Gln	glutamine
Glu	glutamate
GM	gray matter
GPC	glycerophosphorylcholine
gPrD	genetic prion disease
GR	read-out gradient
GRASE	gradient and spin echo
GRE	gradient echo
GRF	Gaussian random field
GRN	progranulin gene
GS	slice selection gradient
GSH	glutathione
GSS	Gerstmann–Straüssler–Scheinker disease
HAD	HIV-associated dementia
HAND	HIV-associated neurocognitive disorders
HARDI	high angular resolution diffusion imaging
HCA	hypertensive cerebral angiopathy
HDFET	high-definition focusing emission tomographic scanner
HHV6	human herpes virus 6
HIV	human immunodeficiency virus
HIVE	HIV encephalopathy
hPrD	human prion disease
HRF	haemodynamic response function
HSE	herpes simplex encephalitis
HSP	hereditary spastic paraplegias
HSV	herpes simplex virus
HTLV-1	human T-lymphotrophic virus
ICA	independent component analysis
ICH	intracranial haemorrhage
iCJD	iatrogenic Creutzfeldt–Jacob disease
ICL	intracortical lesion
ICP	intracranial pressure
IFN	interferon
IFOF	inferior fronto-occipital fasciculus
IGE	idiopathic generalized epilepsies

IJV	internal jugular veins
ILF	inferior longitudinal fasciculus
IMT	intima-media thickness
IntCA	internal carotid artery
IP	international panel
IR	inversion recovery
IRIS	immune reconstitution inflammatory syndrome
ISI	inter-stimulus interval
ISIS	image-selected in vivo spectroscopy
IUS	intra-operative ultrasound
IV	intravenous
JE	Japanese encephalitis
Lac	lactate
LASER	localization by adiabatic selective refocusing
LB	Lewy body
LBSL	leukoencephalopathy with brain stem and spinal cord involvement and lactate elevation
LEHR	low-energy high-resolution
LL	Look–Locker
LMN	lower motor neuron
LOR	line of response
MAP	maximum a posteriori
MAPT	microtubule-associated protein tau
MBCC	model-based cross-talk compensation
MCA	middle cerebral artery
MCI	mild cognitive impairment
MCP	middle cerebellar peduncles
MCS	minimally-conscious state
MD	mean diffusivity
MDL	minimum description length
MDR	multidrug-resistant
MEB	muscle–eye–brain
MEG	magnetoencephalography
MELAS	mitochondrial myopathy, encephalopathy, lactic acidosis, and stroke-like episodes
MI	mechanical index
MIBG	metaiodobenzylguanidine
mIns	myo-inositol
MIP	maximum intensity projection images
MK	mean kurtosis
MLC	megalencephalic leukoencephalopathy with subcortical cysts
ML-EM	maximum-likelihood expectation-maximization
MM	macromolecule
MMA	methylmalonic acidaemia
MND	motor neuron disease
MNGIE	mitochondrial neuro-gastrointestinal encephalomyopathy
MOLLI	modified Look–Locker inversion
MPM	multi-parameter mapping
MPRAGE	magnetization-prepared-rapid-acquisition-gradient-echo
MRA	magnetic resonance angiography
MRI	magnetic resonance imaging
MRS	magnetic resonance spectroscopy
MRSI	magnetic resonance spectroscopic imaging
MS	multiple sclerosis
MSA	multi-system atrophy
MSA-P	multiple system atrophy-parkinsonism
MSFC	multiple sclerosis functional composite
MT	magnetization transfer
MT MRI	magnetization transfer magnetic resonance imaging
MTI	magnetization transfer imaging
MTL	medial temporal lobes
MTR	magnetization transfer ratio
MTT	mean transit time
NA	normal-appearing
NAA	N-acetyl aspartate
NAAG	N-acetyl aspartylglutamate
NAWM	normal appearing white matter
NCSE	non-convulsive status epilepticus
NCT	non-contrast head computed tomography
NMO	neuromyelitis optica
NO	nitrous oxide
NP-PACNS	non-progressive primary angiitis of the central nervous system
npRPD	non prion rapidly progressive dementias
NSE	neuron specific enolase
NTD	neural tube defects
OI	opportunistic infections
ON	optic neuritis
ONSD	optic nerve sheath diameter
OS-EM	ordered-subsets expectation-maximization
OVS	outer-volume suppression
PACNS	primary angiitis of the central nervous system
PD4	Parkinson's disease
PAG	peri-aqueductal gray matter
PASL	pulsed arterial spin labelling
PBD	peroxisomal biogenesis defects
PC	phase contrast
PCA	posterior cerebral artery
P-cPACNS	progressive childhood primary angiitis of the central nervous system
PCASL	pseudo-continuous arterial spin labelling
PCho	phosphocholine
PCNSL	primary central nervous system lymphoma
PCNVS	primary central nervous system vasculitis
PCPCS	Pediatric Cerebral Performance Category Scale
PCr	phosphocreatine
PCT	perfusion computed tomography
PDCP	Parkinson's disease cognitive-related network pattern
PDD	Parkinson's disease dementia
PDRP	Parkinson's disease -related covariance pattern
PET	positron emission tomography
PiB	Pittsburgh compound B
PLS	primary lateral sclerosis
PMA	progressive muscular atrophy
PMD	Pelizaeus–Merzbacher disease
PML	progressive multifocal leukoencephalopathy
PMT	photomultiplier tubes
PP	primary progressive
PPA	primary progressive aphasia
PPIX	protoporphyrin IX
PrD	prion disease
PRESS	point resolved spectroscopy
PrET	proton emission tomography
PRF	pulse repetition frequency

PRNP	prion protein
PSF	point spread function
PSP	progressive supranuclear palsy
PSWC	periodic sharp wave complex
PtCA	pontocerebellar atrophy
PVC	partial volume effect compensation
PVE	partial volume effect
PWI	perfusion-weighted imaging
QA	quality assurance
QRAP	quantification of relaxation times and proton density
RBSC	reconstruction-based scatter compensation
RCDP	rhizomelic chondrodysplasia punctata
rCMRGl	regional cerebral metabolic rate of glucose
rCMRO	regional cerebral metabolic rate of oxygen
RCVS	reversible cerebral vasoconstriction syndrome
ReHo	regional homogeneity
RF	radio frequency
RLS	right-to-left shunt
rOEF	regional oxygen extraction fraction
ROI	region-of-interest
RR	relapsing-remitting
RSN	resting-state network
rtPA	recombinant tissue plasminogen activator
SA	spinal atrophy
SAH	subarachnoid haemorrhage
SAOA	sporadic adult onset ataxia
SAR	specific absorption rate
SBP	specific binding potential
SCA	superior cerebellar artery
SCC	spinal cord compression
SCD	subacute combined degeneration
SCI	spinal cord injury
SCIWORA	spinal cord injury without radiographic abnormality
sCJD	sporadic Creutzfeldt–Jacob disease
SCP	superior cerebellar peduncles
ScRF	scatter response function
SDH	subdural haematomas
SDSE	slab-derived scatter estimation
SE	spin echo
SLE	systemic lupus erythematosus
SLF	superior longitudinal fasciculus
SN	substantia nigra
SNR	signal-to-noise ratio
SP	secondary progressive
SPECT	single photon emission computed tomography
SPGR	spoiled gradient recalled
SPIO	super-paramagnetic iron particles of oxide
SPM	statistical parametric mapping
SRF	spatial response function
SS	Sjögren's syndrome
SSPE	subacute sclerosing panencephalitis
STEAM	stimulated echo acquisition mode
STIR	short-tau inversion recovery
SUNCT	short-lasting unilateral neuralgiform headache attacks with conjunctival injection and tearing
SUV	standardized uptake value
SUVr	SUV ratios
SV-cPACNS	small vessel childhood primary angiitis of the central nervous system
SVD	small vessel diseases
SWEDD	subjects with scans without evidence of dopaminergic deficit
SWI	susceptibility-weighted imaging
T1w	T_1-weighted
T2w	T_2-weighted
T2*w	T_2*-weighted
T2*-GRE	T2*-weighted gradient echo
TAC	trigeminal autonomic cephalalgias
TAPIR	T1 mapping with partial inversion recovery
TAR	transactive response
TB	tuberculosis
TBI	traumatic brain injury
TBM	tensor-based morphometry
TBSS	tract-based spatial statistics
TCA	tricarboxylic acid cycle
TCCD	transcranial colour-coded Doppler
tCR	total creatine
TDP	transactive response DNA binding protein
TDP-43	TAR DNA-binding protein 43
TGC	time-gain compensation
TE	echo time
TLE	temporal lobe epilepsy
ThI	thermal index
ThIB	thermal index, bone index
ThIC	thermal index, cranial index
ThIS	thermal index, soft tissue index
TI	inversion time
TIA	transient ischaemic attack
TM	transverse myelitis
TMS	transcranial magnetic stimulation
ToF	time of flight
tPA	tissue plasminogen activator
TR	repetition time
TSE	turbo spin echo
TSI	transient symptoms with infarction
TSPO	translocator protein 18KDa
TTP	time to peak
UMN	upper motor neuron
UNC	uncinate fasciculus
UPSIO	ultra-small particles of iron oxide
UV	ultraviolet
UWS	unresponsive wakefulness syndrome
VaD	vascular dementia
VBM	voxel-based morphometry
VCI	vascular cognitive impairment
vCJD	variant Creutzfeldt–Jacob disease
VMAT2	vesicular monoamine transporter
VOF	venous output function
VRS	Virchow–Robin spaces
VV	vertebral vein
VZV	Varicella zoster virus
WM	white matter
WMH	white matter hyperintensities
WNV	West Nile virus
WWS	Walker–Warburg syndrome
Xe-CT	xenon computed tomography
X-ALD	X-linked adrenoleukodystrophy

Contributors

Federica Agosta, Neuroimaging Research Unit, Institute of Experimental Neurology, Division of Neuroscience, San Raffaele Scientific Institute, Vita-Salute San Raffaele University, Milan, Italy

Rimma Axelsson, Division of Radiology, Department of Clinical Science, Intervention and Technology (CLINTEC), Karolinska Institutet, Stockholm, Sweden

Brenda Banwell, Professor of Neurology and Pediatrics, Children's Hospital of Philadelphia, University of Pennsylvania, Philadelphia, PA, USA

Claudio Baracchini, Department of Neuroscience, University of Padua School of Medicine, Padua, Italy

Bart N. M. van Berckel, Department of Radiology & Nuclear Medicine, VU University Medical Center, HV Amsterdam, The Netherlands

Mitchel S. Berger, Department of Neurological Surgery, University of California, San Francisco, CA, USA

Sonia Bermudez, Neuroradiology Section, Department of Diagnostic Imaging, University El Bosque, Fundación Santa Fe de Bogota University Hospital, Bogotá, D.C., Colombia

Andrea Bernasconi, Professor of Neurology, FRQS National Researcher, Director-Neuroimaging of Epilepsy Laboratory, Montreal Neurological Institute, McGill University, Montreal, QC, Canada

Neda Bernasconi, Neuroimaging of Epilepsy Laboratory, Department of Neurology and McConnell Brain Imaging Center, Montreal Neurological Institute, McGill University, Montreal, QC, Canada

Olivier Bodart, Coma Science group, Cyclotron Research Centre and Neurology Department, University and University Hospital of Liege, Liege, Belgium

Ronald Boellaard, VU University Medical Center, Amsterdam, The Netherlands

Lena Bronge, MRI Dept, Department for Clinical Science, Intervention and Technology, Division of Radiology, Karolinska Institutet, Stockholm, Sweden

Eduardo Caverzasi, Department of Neurology, Memory and Aging Center, University of California, San Francisco, CA, USA

Mara Cercignani, Clinical Imaging Sciences Centre (CISC), Brighton & Sussex Medical School, Brighton, UK

Soonmee Cha, Departments of Radiology and Neurological Surgery, Neuroradiology Section, University of California, San Francisco, CA, USA

Vanessa Charland-Verville, Coma Science group, Cyclotron Research Centre and Neurology Department, University and University Hospital of Liege, Liege, Belgium

Armin Curt, Spinal Cord Injury Center, Balgrist University Hospital, Zürich, Switzerland

Ralf Deichmann, Goethe University Frankfurt, Brain Imaging Center, Frankfurt, Germany

Sean C. L. Deoni, Advanced Baby Imaging Lab, School of Engineering, Brown University, Providence, RI, USA

Silvia De Santis, CUBRIC, School of Psychology, Cardiff University, Cardiff, UK

Yong Du, Department of Radiology, Division of Medical Imaging Physics, Johns Hopkins Medical Institutions, Baltimore, MD, USA

Christian Enzinger, Department of Neurology, Department of Radiology, Division of Neuroradiology, Medical University of Graz, Graz, Austria

Franz Fazekas, Department of Neurology, Medical University of Graz, Graz, Austria

Massimo Filippi, Neuroimaging Research Unit, and Department of Neurology, Institute of Experimental Neurology, Division of Neuroscience, San Raffaele Scientific Institute, Vita-Salute San Raffaele University, Milan, Italy

Michael J. Firbank, Institute of Neuroscience and Newcastle University Institute for Ageing, Newcastle University, Newcastle upon Tyne, UK

Patrick Freund, Spinal Cord Injury Center, Balgrist University Hospital, Zürich, Switzerland; Wellcome Trust Centre for Neuroimaging, UCL Institute of Neurology, UCL, London, UK; Department of Brain Repair and Rehabilitation, UCL Institute of Neurology, UCL, London, UK

Birgitte Fuglsang Kjølby, Center of Functionally Integrative Neuroscience (CFIN), Department of Neuroradiology, Aarhus University Hospital, Aarhus, Denmark

Cong Gao, Guangzhou Medical University, the 2nd Affiliated Hospital, Department of Neurology, Guangzhou, China

Michael D. Geschwind, Department of Neurology, Memory and Aging Center, University of California, San Francisco, CA, USA

Caterina Giannini, Laboratory Medicine & Pathology, Mayo Clinic, Rochester, MN, USA

Peter J. Goadsby, Headache Group-Department of Neurology, University of California, San Francisco, San Francisco, CA USA; NIHR-Wellcome Trust Clinical Research Facility, King's College London, London, UK

Olivia Gosseries, Coma Science group, Cyclotron Research Centre and Neurology Department, University and University Hospital of Liege, Liege, Belgium

Elan J. Grossman, Center for Biomedical Imaging, Department of Radiology, Department of Physiology and Neuroscience, New York University School of Medicine, New York, NY, USA

Mark A. Horsfield, Department of Cardiovascular Sciences, University of Leicester, Leicester Royal Infirmary, Leicester, UK

Qinghua Hou, Guangzhou Medical University, the 2nd Affiliated Hospital, Department of Neurology, Guangzhou, China

Matilde Inglese, Department of Neurology, Radiology and Neuroscience, Mount Sinai School of Medicine, New York, NY, USA

H. Rolf Jäger, Institute of Neurology, University College London, London, UK

Christoph Juchem, Yale University School of Medicine, New Haven, CT, USA

Linda Knutsson, Department of Medical Radiation Physics, Lund University, Lund, Sweden

Shannon H. Kolind, Department of Medicine, University of British Columbia, BC, Canada

Adriaan A. Lammertsma, VU University Medical Center, Amsterdam, The Netherlands

Steven Laureys, Coma Science group, Cyclotron Research Centre and Neurology Department, University and University Hospital of Liege, Liege, Belgium

Kate F. Mahady, Institute of Neurology, University College London, London, UK

María T. Mantilla, Department of Diagnostic Imaging, Clínica Reina Sofia, Organización Sanitas Internacional, Associate Professor of Neuroradiology undergraduated and residency programs, Bogotá, Colombia

Mario Mascalchi, Quantitative and Functional Neuroradiology at Meyer Children and Careggi Hospitals, Florence Italy. 'Mario Serio' Department of Experimental and Clinical Biomedical Sciences, University of Florence, Florence, Italy

Sandra M. Meyers, Department of Physics and Astronomy, University of British Columbia, BC, Canada

Siawoosh Mohammadi, Wellcome Trust Centre for Neuroimaging, UCL Institute of Neurology, UCL, London, UK; Department of Systems Neuroscience, University Medical Center Hamburg, Hamburg, Germany

Sara Nuñez, Neuroradiology Section, Department of Diagnostic Imaging, Clínica Universitaria Colombia

John T. O'Brien, Foundation Professor of Old Age Psychiatry, Department of Psychiatry, University of Cambridge, Cambridge, UK

Marina Pan, Department of Neurology, Pavia State University, Pavia, Italy

Daniel Pelletier, Yale University School of Medicine, New Haven, CT, USA

Nicolò Pipitone, Rheumatology Unit, Department of Internal Medicine, Azienda Ospedaliera ASMN, Istituto di Ricovero e Cura a Carattere Scientifico, Reggio Emilia, Italy

Paolo Preziosa, Neuroimaging Research Unit, and Department of Neurology, Institute of Experimental Neurology, Division of Neuroscience, San Raffaele Scientific Institute, Vita-Salute San Raffaele University, Milan, Italy

Andrés Puerta, Clinica Universitaria Colombia, Organización Sanitas Internacional, Bogotá , Colombia

Deborah L. Renaud, Directior-Neurometabolic Clinic and Leukodystrophy Program, Co-director-Mayo Clinic Peroxisomal Disorders Program, Consultant and Associate Professor, Division of Child and Adolescent Neurology, Departments of Neurology and Pediatrics, Mayo Clinic, Rochester, MN, USA

Maria A. Rocca, Neuroimaging Research Unit, and Department of Neurology, Institute of Experimental Neurology, Division of Neuroscience, San Raffaele Scientific Institute, Vita-Salute San Raffaele University, Milan, Italy

Stefan Ropele, Department of Neurology, Medical University of Graz, Graz, Austria

Carlo Salvarani, Rheumatology Unit, Department of Internal Medicine, Azienda Ospedaliera ASMN, Istituto di Ricovero e Cura a Carattere Scientifico, Reggio Emilia, Italy

Irina Savitcheva, Karolinska University Hospital, Division of nuclear Medicine, Department of Clinical Science, Intervention and Technology (CLINTEC), Karolinska Institutet, Stockholm, Sweden

Dewi Schrader, Department of Neuropediatrics, BC Children's Hospital, University of British Columbia, Vancouver, BC, Canada

Christian Schwarzbauer, Aberdeen Biomedical Imaging Centre, University of Aberdeen, Lilian Sutton Building, Foresterhill, Aberdeen, Scotland, UK

Till Sprenger, Department of Neurology, University Hospital Basel, Basel, Switzerland

Leonel Takada, Cognitive and Behavioral Neurology Unit, Department of Neurology, University of Sao Paulo Medical School, Sao Paolo, Brazil

Phiroz E. Tarapore, Department of Neurological Surgery, University of California, San Francisco, CA, USA

Elizabeth Tong, University of Virginia, Department of Radiology, Neuroradiology Section, Charlottesville, VA, USA

Mónica C. Vargas, Neuroradiology Section, Clínica del Country, Bogotá, D.C., Colombia

Alessandra Vella, Nuclear Medicine Department, Le Scotte Hospital, Siena, Italy

Leonard H. Verhey, Neurosciences & Mental Health, The Hospital for Sick Children, University of Toronto, Toronto, ON, Canada

Paolo Vitali, Brain MRI 3T Mondino Research Center, C. Mondino National Neurological Institute, Pavia, Italy

Lars-Olof Wahlund, Section for clinical geriatrics, NVS Dept, Karolinska Institutet, Karolinska University Hospital, Huddinge, Sweden

Nikolaus Weiskopf, Wellcome Trust Centre for Neuroimaging, UCL Institute of Neurology, UCL, London, UK

Max Wintermark, Stanford University, Department of Radiology, Neuroradiology Section, Stanford, CA, USA

Tarek A. Yousry, Institute of Neurology, University College London, London, UK

Habib Zaidi, Geneva University Hospital, Division of Nuclear Medicine and Molecular Imaging, Geneva, Switzerland

Giulio Zuccoli, Children's Hospital of Pittsburgh at the University of Pittsburgh Medical Center, Pittsburgh, PA, USA

Corinna C. Zygourakis, Department of Neurological Surgery, University of California, San Francisco, CA, USA

SECTION 1

Fundamentals of neuroimaging techniques

CHAPTER 1

Computed tomography

Qinghua Hou, Elizabeth Tong,
Cong Gao, and Max Wintermark

Introduction

Since its first introduction in 1971, computed tomography (CT) has evolved rapidly. With the evolution from fan beam to cone beam, and from axial to helical mode, the increase in the number of detectors (from a single detector array to 256/320 detector arrays), and the advent of dual energy technology, CT now offers very short scan time (even for extensive anatomical coverage), improved spatial and temporal resolution, and reduced patient dose, both in terms of radiation and contrast agent. CT is the imaging modality of choice in the emergency setting. It is fast, its requirements are low, and it is available 24 hours a day, 7 days a week. Modern CT scanners offer volumetric acquisitions, which improve the capability to evaluate intracranial and spinal structures in reconstructed three-dimensional (3D) views. With the development of post-progressing software, CT has expanded its applications beyond the evaluation of structural anatomy to include functional analyses such as perfusion-CT (PCT) to assess cerebral blood supply (Table 1.1).

Despite these technological advances, the basic imaging principle of CT has not been changed and relies on X-ray physics. The radiation dose concerns associated with CT remains, although it has been alleviated by a number of dose-reduction techniques implemented by the imaging manufacturers. Nowadays, the radiation dose of a non-contrast head computed tomography (NCT) ranges from 1.7 to 2.5 mSv [1,2], lower than the background radiation for a person living in Boston for a year (approximately 3 mSv) [3]. The estimated lifetime risk of death from cancer that is attributable to a single NCT is 0.01–0.02% [4]. With the advent of dual-energy CT, the radiation dose associated with CT may be reduced further when contrast-enhanced examination is applied [5].

Computed tomography technology

CT is an imaging technique based on X-rays, a form of electromagnetic radiation with a wavelength range of 0.01–10 nm. X-ray beams can traverse the human body and be used to create an image (they can penetrate, but do no harm), while at the same time the photon energy it carries makes it an ionizing radiation, which can cause harm to living tissue (in proportion to the absorption). CT imaging uses a specific range of wavelengths of X-rays (wavelength below 0.2–0.1 nm) to obtain good penetration and limit the ionizing radiation harm. Unlike conventional X-ray imaging, CT images are not developed directly from the attenuation of projection X-rays. Instead, slices of specific areas of the body are imaged and divided into a matrix of voxels, the intensity of which is calculated from multiple projections from an X-ray source to a panel of detectors, both rotating in the CT gantry. The attenuation value of an individual voxel depends upon its contents and can be quantitatively scored in Hu (Hu; called after the inventor of CT), which ranges from −1000 Hu to +1000 Hu, with water in the middle (Hu = 0), and air (−1000 Hu) and bone (+1000 Hu) at the extremities of the scale. Modern CT scanners can reconstruct axial, sagittal, coronal, oblique, 3D, or even 4-dimensional (4D) images.

Single-slice versus multislice computed tomography scanners

In very early single-slice CT scanners, a single row of detectors were arrayed in a line opposite to the X-ray tube inside the CT gantry. These scanners used a narrow beam of X-rays (pencil width), which was collimated and developed very little scatter when it passed through the human body. With such scanners, one gantry rotation could only sample one slice.

In multislice CT scanners, detectors are arrayed linearly in multiple rows, so that the machine can cover multiple slices in one rotation (up to 320 slices with the most advanced CT technology). Also, a fan beam X-ray is used. The benefits of this geometry are not only limited to obtaining a larger coverage with one single rotation, but can also shorten the scanning time. With multislice CT scanners, the spatial and temporal resolution, and the contrast resolution are also greatly improved.

The latest generation of CT scanners (e.g. 320-dector row CT) uses a cone beam of X-rays with a flat panel detector for capturing the images. Cone-beam CT scanners can produce 3D images with a single rotation of the gantry [6], and also time-resolved CT-angiogram (4D CTA) showing the dynamic progression of the contrast through arteries and veins [7].

Image reconstruction algorithms

For a considerable time, filtered back-projection has dominated the field of CT image reconstruction. Filtered back-projection runs

Table 1.1 Comparison of CT, MRI, and single photon emission tomography (SPECT)/positron emission tomography (PET) imaging

	CT	**MR**	**SPECT/PET**
Spatial resolution	0.5 mm	1 mm	4–6 mm
Scan time	seconds	20–40 minutes	10–15 minutes [22]
Availability	24/7	24/7	Business hours
Contrast	Iodinated-based	Gadolinium-based	Radionuclide tracer
Vascular imaging	CTA and CT-venogram	MRA, contrast-enhanced (CE)-MRA, MRV	Not applicable
Functional imaging	Perfusion and blood–brain barrier permeability evaluation	Perfusion and diffusion, O_2 consumption, and metabolism spectrum analysis, connectivity analysis, etc.	Blood supply and metabolic rates evaluation, blood–brain barrier imaging.
Artefacts	Streak artefact (Fig. 1.1), beam-hardening.	Geometric distortion caused by susceptibility artefacts, chemical-shift artefacts, Gibbs' artefacts	Photon scatter and attenuation
Major limitations	Ionizing radiation, low sensitive to posterior fossa lesions	Longest scan time, metal implant and pace maker contra-indication	Ionizing radiation, limited availability in the emergency setting

the projection images back through the image to obtain a rough approximation of the original object (back-projection), and uses a high-pass filter to eliminate the image blurring caused by such 'back-projection'.

More recently, iterative reconstruction algorithms have been developed, originally to reduce the noise of images. These algorithms consist of a series of sequential reconstructions and corrections—forward- and back-projection reconstruction steps, and comparison of the projection data with the real measured raw data and correction of deviation in projection between each step. The correction is based on the statistical counting of the detected photons in the reconstruction process. The iterative process can be performed in the raw data domain, in the image domain alone, or in both [8,9].

Iterative reconstruction can reduce the radiation dose associated with CT studies by 20–40% without compromising image quality [10–13]. One of the downsides of iterative reconstruction lies in the longer image reconstruction time.

Single-source versus dual-source computed tomography

Dual-energy CT is an emerging CT modality. There are currently two ways used for dual-energy scanning:

1. Two X-ray tubes and two detectors (mounted on a CT gantry with a mechanical offset of 90°) with the two X-ray tubes being operated at different voltages.
2. A single X-ray tube that can rapidly switch its peak voltage and one detector.

Through the simultaneous acquisition of two image series with different kVp (e.g. 40 and 140 kVp), dual-energy CT facilitates material separation. For example, it can be used to generate virtual non-contrast images of the brain from a contrast-enhanced CT; this also allows the removal of bone and calcium from a CTA [14,15].

Computed tomography imaging modalities

NCT

Routine NCT is performed in the axial plane, parallel to the orbitomeatal line, with 2.5-mm thick slices. For cervical spine imaging, 0.625-mm thick slices are obtained, while 1.5-mm thick slices are the standard for imaging the thoracic and lumbar spine.

NCT is used for the initial evaluation of many intracranial and spinal lesions, especially in the acute setting. NCT is the first-line examination for acute traumatic brain injury (TBI) and stroke, since it is especially suited for detecting ischaemia, haemorrhage, and skull fracture.

NCT is less sensitive than magnetic resonance imaging (MRI) for the assessment of posterior fossa and brainstem lesions, due to hard-beam artefacts (Fig. 1.1), and for the diagnosis of conditions such as haemorrhagic or non-haemorrhagic diffuse axonal injury, contusion, early infarction, encephalitis, and brain tumour.

Contrast-enhanced computed tomography

Enhancement after injection of iodinated contrast indicates intravascular enhancement due to an increased permeability of the blood–brain barrier, which leads to a leakage of the contrast material into the interstitium. By analysing the enhancement patterns associated with contrast agent injection, contrast-enhanced computed tomography (CECT) can help differentiate lesions such as vascular malformations, neoplasms, and active inflammation (infectious and non-infectious) [16].

Computed tomography angiography

Computed tomography angiography (CTA) with multiplanar reformatted images, maximum intensity projection images (MIP), and 3D reconstructions of axial source images provide images comparable with, or even superior to, those obtained with digital subtraction angiography (DSA) [17,18]. Unlike time-of-flight magnetic resonance angiography (MRA), CTA is less susceptible to turbulent or slow-flow artefacts. Spatial resolution of CTA is approximately twice that of gadolinium-enhanced MRA [19]. CTA has become

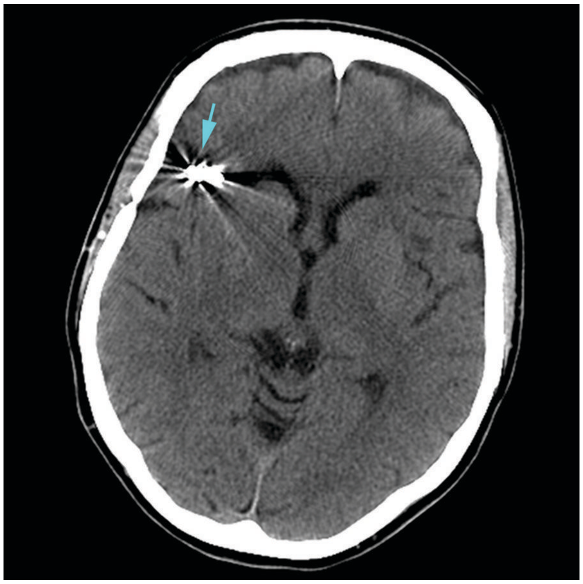

Fig. 1.1 Streak artefact on non-contrast CT caused by intravascular stent (arrow).

the modality of choice to non-invasively assess cervical and intracranial vessels. Dynamic CTA provides dynamic, real-time information, similar to that offered by DSA, which is rarely used for diagnostic purposes.

PCT

PCT evaluates capillary, tissue-level circulation, which is beyond the resolution of traditional anatomic imaging. PCT is most commonly carried out using dynamic sequential scanning of a pre-selected slab of the brain (modern CT scanners offer whole-brain coverage), during the injection of a bolus of iodinated contrast material as it travels through the vasculature. By recording the wash-in and wash-out of the contrast bolus through the cerebral vasculature, several parameters describing the cerebral perfusion, i.e. cerebral blood flow (CBF), cerebral blood volume (CBV), mean transit time (MTT), time to peak (TTP), and blood–brain barrier permeability (BBBP), can be quantitatively evaluated on reconstructed colour maps.

PCT limitations and pitfalls include the following:

1. Complex post-processing and long-lasting experience in interpretation of the images.
2. Due to arterial input function (AIF) delay, vascular stenosis may result in an overestimation of the area of cerebral perfusion abnormality [20]. It is therefore of importance that PCT should be performed and interpreted with concurrent CTA.
3. Although higher than MR perfusion-weighted imaging [21] and SPECT/PET, the resolution of PCT maps is still relatively low. Small infarcts may be missed, and white matter changes can be misdiagnosed.

Common CT features

CT findings are categorized into hyperdense, isodense, and hypodense, depending on their density compared with that of normal brain tissue (approximately 40 Hu). Normal cerebrospinal fluid (CSF) has a density of around 5 Hu. Bone density is greater than 350 Hu, fat density is –100 Hu, and that of air is –1,000 Hu.

CT hyperdensity

Acute intracranial haemorrhages

Acute haemorrhage always appears as a hyperdense area in any region of the brain parenchyma, ventricles, subarachnoid space, or extra-axial space. Over time, intracranial haemorrhages become isodense (in the subacute phase) [23] and hypodense (in the chronic phase) [24]. Of note, low attenuation within an acute haematoma may indicate hyperacute, ongoing bleeding [25].

Vascular clot

An acute thrombus can be detected on NCT as an area of hyperdensity, featuring the 'dense artery sign' in the setting of a M1 occlusion of the middle cerebral artery (MCA) (Fig. 1.2), and the 'dot sign' in the setting of a M2 or M3 occlusion. Venous sinus thrombosis also appears hyperdense on NCT, while featuring a delta sign or triangular lack of contrast filling on post-contrast CT.

Calcifications

Calcifications are very hyperdense. Some calcifications in the brain are within normal limits, e.g. pineal gland calcifications, choroid plexus calcifications, falx calcifications, and basal ganglia calcifications/mineralization. Basal ganglia calcifications (and cerebellar dentate nuclei calcifications) are particularly pronounced in patients with Fahr's disease [26]. Calcifications are also seen in a variety of pathological conditions, e.g. vascular malformations, chronic haematomas, brain infections, brain tumours, and congenital malformations, such as Sturge–Weber syndrome and tuberous sclerosis.

Others

Highly cellular neoplasms, such as lymphomas, can appear as hyperdense.

CT hypodensity

Oedema

Subacute infarcts, infections, and brain tumours alter the permeability of the blood–brain barrier, resulting in vascular leakiness and water extravasation into the interstitial space, or vasogenic oedema. The accumulation of interstitial water decreases the attenuation of brain tissue and features a hypodensity. Likewise, chronic ischaemia causes encephalomalacia and gliosis, which also present as hypodensity on CT.

Hydrocephalus

Hydrocephalus relates to enlarged ventricles. In obstructive hydrocephalus, ventricles upstream of an obstructive lesion are selectively dilated (Fig. 1.3). In communicating hydrocephalus, all ventricles are dilated.

Mass effect

Mass effect refers to the deviation or distortion of normal structures by an abnormal structure or mass, and the swelling accompanying it. Mass effect is typically observed in the case of large intracranial haematomas and brain tumours, as well as in the setting of malignant infarct. Early mass effect is seen as local effacement of sulci. Progressive mass effect results in midline shift, ventricular entrapment, and herniation (Fig. 1.4). Ventricular entrapment typically occurs when there is significant midline shift, the foramen of Monroe is compressed, and the drainage of the lateral ventricles is impaired. There are different types of herniation—subfalcine, uncal, downward transtentorial, upward transtentorial, and tonsillar and transcalvarial herniation types. Severe herniation can cause

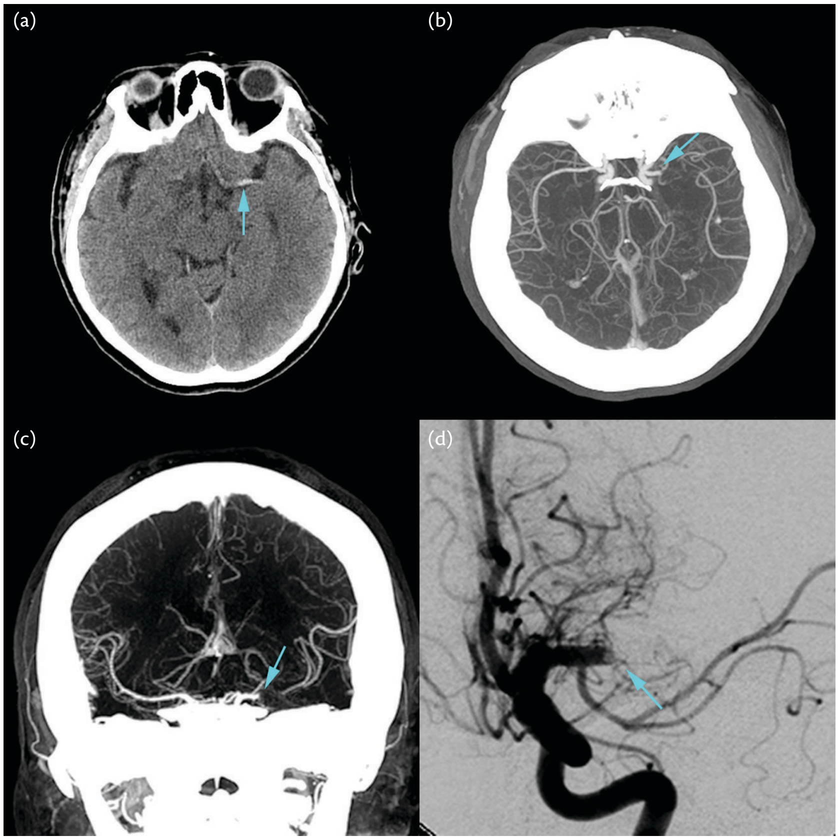

Fig. 1.2 Hyperdense MCA sign caused by an acute intravascular clot. This finding on non-contrast CT (a, arrow) corresponds to a segmental filling defect on CT-angiography (b,c, arrows) and on digital subtraction angiography (d, arrow).

secondary ischaemic lesions, by compression of neighbouring arteries (anterior cerebral artery by subfalcine herniation, posterior cerebral artery by uncal and downward transtentorial herniation), and is lethal without prompt surgical decompression.

CT clinical applications

Ischaemic stroke

NCT is the imaging modality of choice to initially assess patients suspected of acute stroke, despite its limited sensitivity to ischaemia in the first few hours following symptom onset [27]. Sensitivity to acute ischaemia can be improved by setting the window centre level around 30 Hu and narrowing the window width to 8–10 Hu [28]. The role of NCT in the setting of an acute stroke is mainly to rule out the presence of haemorrhage [29] and mimics of stroke, such as infection, inflammation, and neoplasm. Early signs of ischaemic stroke on NCT include sulcal effacement, blurring of cortical gray–white matter differentiation, and in 50% of patients [30] a dense artery sign, as described previously. The Alberta Stroke Program Early CT Score (ASPECTS) quantifies the extent of the ischaemic changes visible on CT and helps to determine whether

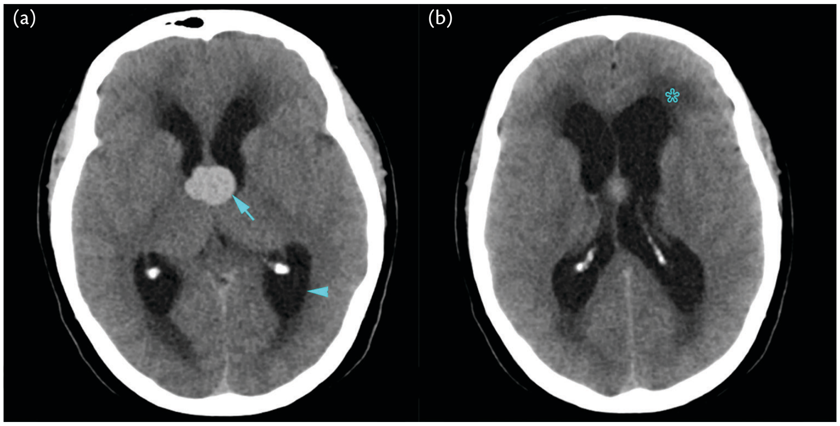

Fig. 1.3 Obstructive hydrocephalus caused by colloid cyst in the foramen of Monroe (arrow). The obstruction led to sequential enlargement of bilateral ventricles (a, arrowhead) and interstitial oedema in periventricular tissues (b, star).

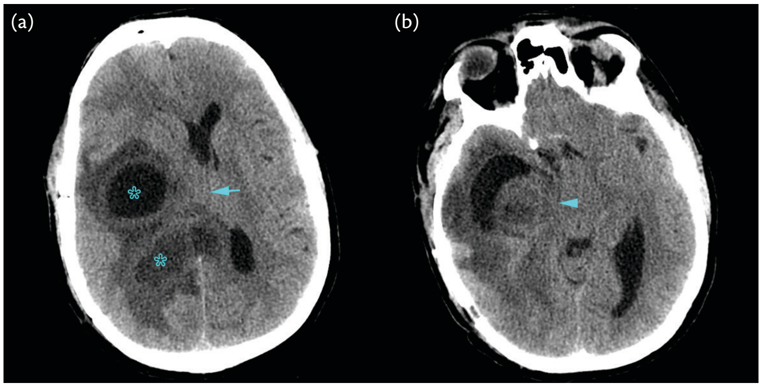

Fig. 1.4 Midline shift and uncal herniation caused by a right insular/temporal abscess. Non-contrast CT clearly demonstrates the mass effect caused by this abscess (a, star) with shift of the midline to the left (a, arrow), entrapment of the temporal horn of the right lateral ventricle, and right uncal herniation (b, arrowhead) compressing the midbrain.

an acute stroke involves more than one-third of the MCA territory. The latter represents a contraindication to the administration of IV tissue plasminogen activator (tPA), together with the presence of haemorrhage on the admission NCT [29]. In the subacute phase of an ischaemic stroke, a typical 'wedge-shaped' hypodensity can be seen on NCT (Fig. 1.5).

CTA is routinely used to detect the exact site of arterial occlusion in stroke patients. Compared with DSA, CTA has a 98.4% sensitivity and 98.1% specificity for detecting proximal intracranial arterial occlusion [23], and an 85% sensitivity and 93% specificity in detecting significant extracranial arterial stenosis [30]. In addition to the luminal evaluation, CTA is capable of evaluating the arterial wall, detecting vasculopathies (for instance, dissection), and characterizing carotid atherosclerotic plaques [31]. Intracranially, CTA source images have increased sensitivity for acute ischaemic changes and can assess the collateral circulation distal to an arterial occlusion. Finally, when the stroke CTA scan extends below the origin of the aortic arch to include the left atrium or the whole heart, CTA can detect the presence of a left atrial or ventricular thrombus.

PCT is increasingly recognized as a diagnostic tool in patients with suspected stroke. Its applications in the setting of stroke include, but are not limited to:

1. Improving the sensitivity and accuracy of stroke diagnosis (in some cases, a lesion on PCT leads to more careful scrutiny and identification of a vascular occlusion that was not evident (Fig. 1.5), particularly in the M2 and more distal MCA branches) [32–35].
2. Excluding stroke mimics [36].
3. Better assessment of the ischaemic core [34] and collateral flow [18].
4. Prediction of haemorrhagic transformation and malignant oedema [37, 38].

Currently, different PCT software use different methods to process the data, and extract the infarct core and penumbra information. Standardization of PCT processing and interpretation is lacking. The use of a relative MTT threshold of 145% of the contralateral values to delineate the total ischaemic area is suggested, and an absolute CBV threshold of 2 mL/100 g to differentiate the infarct core and the penumbra within the total ischaemic area [39].

The safety of the combined use of CTA and PCT in stroke patients has been well documented [40]. Iodinated contrast administration for CTA/PCT does not cause significant renal injury nor does it interfere with the safety and efficacy of the tPA treatment [41].

Intracranial haemorrhage

The AHA/ASA guidelines indicate that either NCT or MRI may be used in the initial diagnostic evaluation of an intracranial haemorrhage (ICH) [42].

The majority of spontaneous ICHs are related to arterial hypertension. Hypertensive ICHs (Fig. 1.6) tend to involve the basal ganglia, thalamus, cerebellum, and brainstem, resulting from the rupture of micro-aneurysms of perforating vessels in these regions. When multiple haematomas are seen, if the haematomas have an irregular shape, or if they occur in unusual locations, secondary ICH should be considered.

Subarachnoid haemorrhage (SAH) occurs in the setting of trauma and of aneurysmal rupture (Fig. 1.7). Sensitivity of NCT to SAH in the first 24 hours is close to 100%. After 48 hours NCT sensitivity decreases to less than 85% [43]. In the presence of a negative NCT after 48 hours, a lumbar puncture is then required to detect xanthochromia.

CTA is used in patients with acute ICH for the purpose of identifying secondary causes of ICH [44]. CTA has a sensitivity and specificity comparable with DSA in terms of detecting intracranial aneurysms [45,46]. CTA presents a number of advantages in terms of surgical planning—CTA data can easily be uploaded to neuronavigation systems [47], and show precisely the relationship of the aneurysm to the skull base [48,49], calvarium, and adjacent veins [50]. CTA is also useful in planning an endovascular intervention.

CTA and CECT can detect the 'spot sign', corresponding to the acute extravasation of contrast in the haematoma (Fig. 1.6). A 'spot sign' is indicative of haematoma expansion [51] and predictive of a poor outcome.

PCT has been used to detect a 'penumbra' surrounding haematomas. The existence of such a penumbra surrounding haematomas is still very much debated [52,53]. In a series of patients who underwent surgical haematoma evacuation, PCT after surgery demonstrated a correction of the perfusion deficit surrounding the haematoma, suggesting that the latter represents reduced oxygen demand of tissue damaged by pressure and clot components [52].

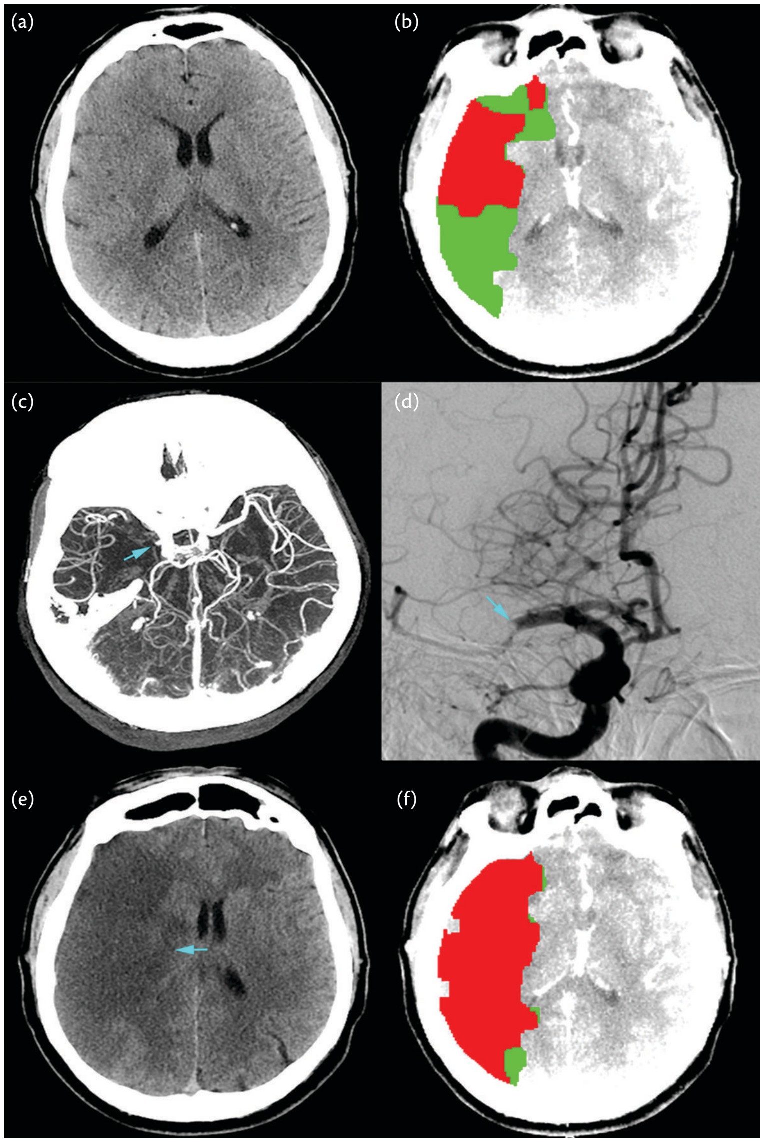

Fig. 1.5 Typical CT imaging workup in a patient suspected of acute ischaemic stroke. (a) NCT shows mild effacement of the right lentiform nucleus. (b) PCT shows the right MCA to be ischaemic, with a mixture of ischaemic core (red) and penumbra (green). (c) CT-angiography demonstrates the right MCA occlusion (arrow) responsible for the ischaemia, later confirmed on digital subtraction angiography (d, arrow). (e,f) Follow-up NCT and PCT demonstrate that, in the absence of early recanalization, the whole ischaemic territory infarcted.

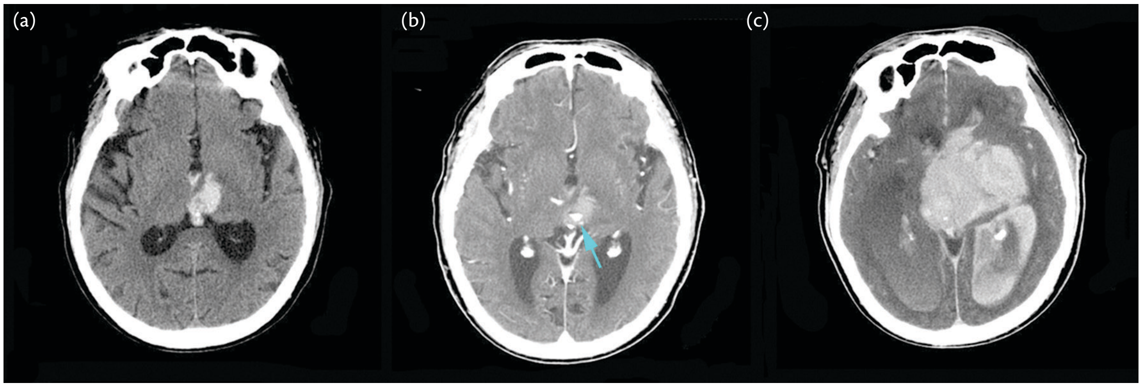

Fig. 1.6 'Spot sign' on contrast-enhanced CT. (a) NCT shows an intraparenchymal haematoma in the left thalamus with extension in the third ventricle. (b) Contrast-enhanced CT shows a 'spot sign' (arrow) within the parenchymal haematoma, indicating active extravasation of contrast. (c) The size of the parenchymal haematoma and the intraventricular extension have progressed significantly, as typically seen when the 'spot sign' is present.

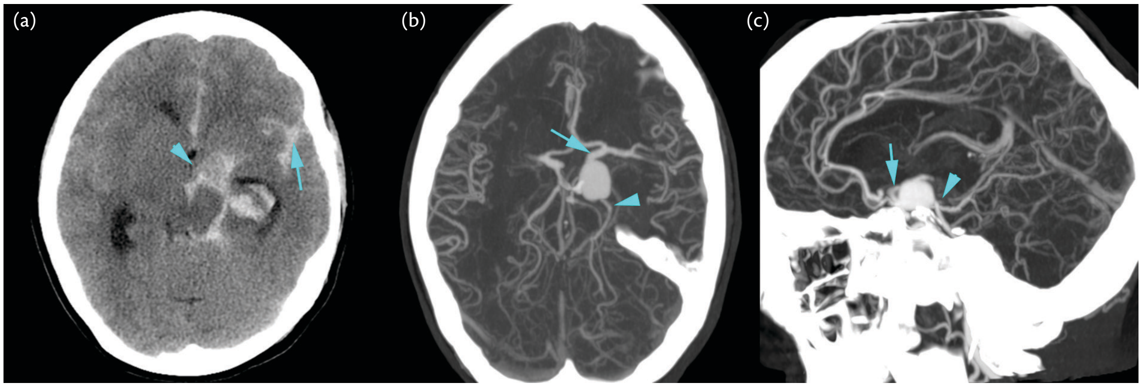

Fig. 1.7 Aneurysmal subarachnoid haemorrhage. (a) NCT demonstrates subarachnoid haemorrhage in the left Sylvian fissure (arrow), the left ambient cistern, and the interhemispheric fissure. A relative hypodensity suggests the presence of an aneurysm in the left posterior communicating artery region (arrowhead), later confirmed on CT-angiography maximal intensity projections (b,c; arrows for suprclinoid internal carotid artery and arrowheads for posterior communicating artery).

PCT is also used to detect vasospasm, one of the complications of subarachnoid haemorrhage that typically occurs 4–7 days following SAH, and it adds prognostic information regarding delayed cerebral ischaemia and poor outcome [54,55].

Another complication of SAH is communicating hydrocephalus, which can be diagnosed early on NCT.

Traumatic brain injury

CT is the imaging modality used to screen trauma patients in the acute phase [56]. Head NCT is indicated in trauma patients with loss of consciousness or post-traumatic amnesia if one or more of the following is present—age greater than 60 years, headache, vomiting, drug or alcohol intoxication, deficits in short-term memory, physical evidence of trauma above the clavicle, Glasgow Coma Scale score less than 15, post-traumatic seizure, focal neurological deficit, or coagulopathy [57].

Skull fractures may be linear, comminuted, or depressed (Fig. 1.8). They are demonstrated as discontinuities with or without displacement on the CT bone windows, and may be associated with extra-intracranial air and/or haemorrhage. Whenever a bone fracture is identified, underlying brain parenchyma should be scrutinized for traumatic injury. Thin-slice CT with multiplanar reformats increases the sensitivity of the technique to subtle skull fractures, e.g. of the temporal bone.

Epidural haematomas (EDHs) are associated with skull fractures, and generally result from a traumatic injury to branches of the middle meningeal artery. An EDH appears on NCT as a lenticular or biconvex blood collection. EDHs can cross dural insertions (falx, tentorium), but do not usually cross suture lines.

Subdural haematomas (SDHs) occur in elderly patients with brain atrophy. They usually occur in the absence of skull fractures. They have a crescentic shape on NCT. SDHs can cross sutures. They do not cross, but extend along dural attachments (falx, tentorium). Acute and subacute SDHs may be subtle and difficult to detect. An appropriate, narrow CT window when reviewing NCT can help, together with a subtle loss of normal brain sulci or the buckling of gray–white matter junction caused by the SDH.

Traumatic SAH is usually more localized than aneurysmal SAH, and generally has its epicentre at the site of the coup. As a result of contrecoup injury, traumatic SAH may also occur contralateral to the side of direct impact [25].

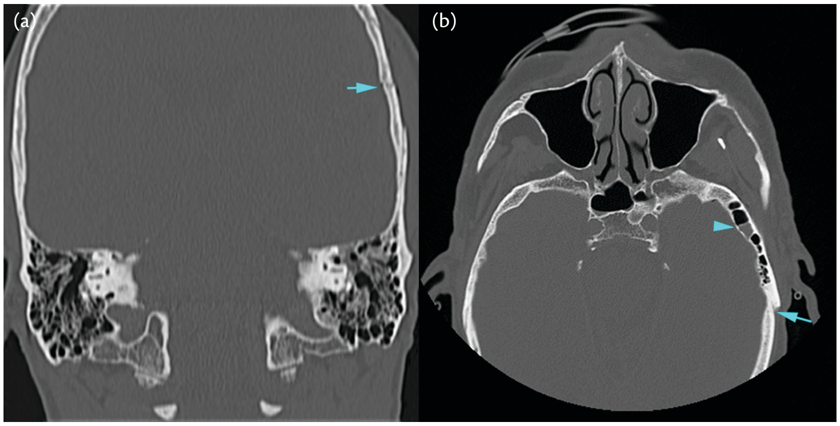

Fig. 1.8 Mildly depressed left frontal and temporal bone fractures. Bone windows of thin non-contrast CT slices in coronal and axial planes demonstrate the discontinuity and mild depression of left frontal and temporal bones (a and b, arrows).

Table 1.2 Rotterdam Classification score

Predictor value	Score
Basal cisterns	
Normal	0
Compressed	1
Absent	2
Midline shift	
No shift or shift <5 mm	0
Shift>5 mm	1
Epidural mass lesion	
Present	0
Absent	1
Intraventricular blood or traumatic SAH	
Absent	0
Present	1

Note: to make the grading numerically consistent with the grading of the motor score of GCS and with Marshall CT classification, the final score is the sum of the scoring items +1.

Modified from Maas, A.I., Hukkelhoven CW, Marshall LF, et al. (2005). Prediction of outcome in traumatic brain injury with computed tomographic characteristics: a comparison between the computed tomographic classification and combinations of computed tomographic predictors. *Neurosurgery*, **57**(6), 1173–82. Copyright (2005), with permission from Lippincott Williams & Wilkins.

Parenchymal contusions on NCT appear as focal low-density areas, except if they are haemorrhagic, in which case they appear as hyperdense. Contusions can be seen deep to a skull fracture or on the opposite side of the brain, as part of a contrecoup injury.

The above CT features of TBI constitute the core of the Rotterdam CT classification (Table 1.2).

Penetrating injuries can damage cervical and intracranial arteries and veins. Skull fractures, especially skull base fractures, can also result in vascular injuries. The latter can be evaluated by CTA (or CT-venogram). CTA can detect traumatic dissection and pseudoaneurysms with high sensitivity.

PCT abnormalities have been reported after TBI. Focal perfusion abnormalities are observed in and around contusions [59], and can be detected before structural abnormalities become apparent. PCT abnormalities might be useful to triage patients with extra-axial blood collections who need aggressive surgical treatment versus those who can be treated conservatively [60]. In TBI patients, baseline PCT hyperaemia is associated to a favourable outcome, while oligaemia is the hallmark of an unfavourable outcome [61]. PCT can provide information about cerebral vascular auto-regulation [60], and therefore can be used as a monitoring tool in TBI patients.

Modern CT with multiplanar reformats is the gold standard for the evaluation of the cervical spine for fractures, and has a sensitivity that is two or three times that of plain films [62]. Also, CT is more accurate than plain films in diagnosing thoracolumbar spine traumatic injuries (Fig. 1.9) [63]. CT can provide indirect signs to suggest ligamentous injury, but when these are suspected MRI is the preferred method of evaluation.

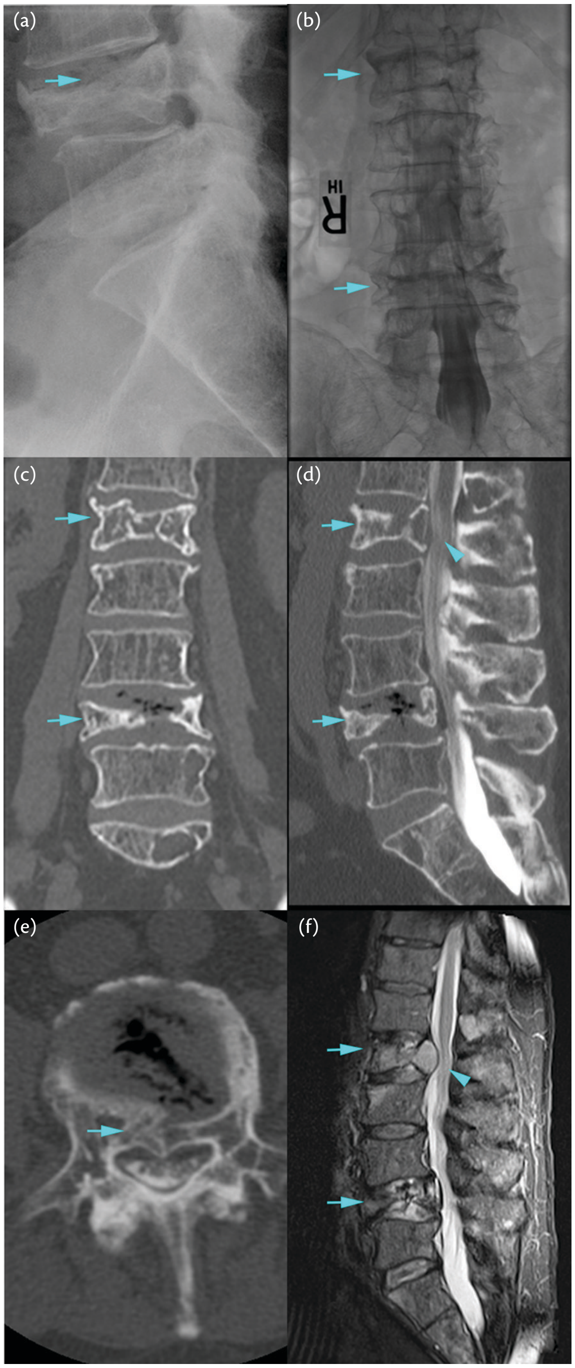

Fig. 1.9 Spine fractures. (a) Lateral plain film and (b) anteroposterior myelogram demonstrate two compression fractures (L1 and L4, arrows) in a severely osteoporotic spine. (c,d,e) CT and (f) MRI allow better characterization of the posterior wall and any compromise of the spinal canal by fracture fragments (arrowheads).

Others

MRI, and not CT, is the standard-of-care for the evaluation of patients with suspected epilepsy, infections, or brain tumours. CT in these patients is only obtained to rule out haemorrhage, hydrocephalus, or mass effect, especially in the emergency setting. CT is usually obtained with contrast in these cases.

Conclusions

CT is the fastest neuroimaging modality and has been established as the first line of examination in the setting of stroke and TBI. With its exquisite spatial resolution and functional capabilities, coupled with new developments, such as whole-brain coverage and dual-energy scanning, CT will remain the test of first choice in the evaluation of neurological disorders in the emergency setting.

References

1. Wintermark M, Maeder P, Verdun FR, et al. (2000). Using 80 kVp versus 120 kVp in perfusion CT measurement of regional cerebral blood flow. *AJNR American Journal of Neuroradiology*, **21**(10), 1881–4.
2. Cohnen M, Wittsack HJ, Assadi S, et al. (2006). Radiation exposure of patients in comprehensive computed tomography of the head in acute stroke. *AJNR American Journal of Neuroradiology*, **27**(8), 1741–5.
3. Konstas AA, Wintermark M, and Lev MH. (2011). CT perfusion imaging in acute stroke. *Neuroimaging Clinics of North America*, **21**(2), 215–38, ix.
4. Berris, T, Gupta, R, and Rehani, MM. (2013). Radiation dose from cone-beam CT in neuroradiology applications. *AJR American Journal of Roentgenology*, **200**(4), 755–61.
5. Postma AA, Hofman PA, Stadler AA, et al. (2012). Dual-energy CT of the brain and intracranial vessels. *AJR American Journal of Roentgenology*, **199**(Suppl. 5), S26–33.
6. Anas EM, Kim JG, Lee SY, et al. (2011). High-quality 3D correction of ring and radiant artifacts in flat panel detector-based cone beam volume CT imaging. *Physics in Medicine and Biology*, **56**(19), 6495–519.
7. Orrison WW, Jr, Snyder KV, Hopkins LN, et al. (2011). Whole-brain dynamic CT angiography and perfusion imaging. *Clinical Radiology*, **66**(6), 566–74.
8. Winklehner A, Karlo C, Puippe G, et al. (2011). Raw data-based iterative reconstruction in body CTA: evaluation of radiation dose saving potential. *European Radiology*, **21**(12), 2521–6.
9. Maass C, Meyer E, and Kachelriess M. (2011). Exact dual energy material decomposition from inconsistent rays (MDIR). *Medical Physics*, **38**(2), 691–700.
10. Ren Q, Dewan SK, Li M, et al. (2012). Comparison of adaptive statistical iterative and filtered back projection reconstruction techniques in brain CT. *European Journal of Radiology*, **81**(10), 2597–601.
11. Korn A, Fenchel M, Bender B, et al. (2012). Iterative reconstruction in head CT: image quality of routine and low-dose protocols in comparison with standard filtered back-projection. *AJNR American Journal of Neuroradiology*, **33**(2), 218–24.
12. Becce F, Ben Salah Y, Verdun FR, et al. (2013). Computed tomography of the cervical spine: comparison of image quality between a standard-dose and a low-dose protocol using filtered back-projection and iterative reconstruction. *Skeletal Radiology*, **42**(7), 937–45.
13. Katsura M, Sato J, Akahane M, et al. (2013). Comparison of pure and hybrid iterative reconstruction techniques with conventional filtered back projection: image quality assessment in the cervicothoracic region. *European Journal of Radiology*, **82**(2), 356–60.
14. Gupta R, Phan CM, Leidecker C, et al. (2010). Evaluation of dual-energy CT for differentiating intracerebral hemorrhage from iodinated contrast material staining. *Radiology*, **257**(1), 205–11.
15. Thomas C, Andreas Korn, Dominik Ketelsen, et al. (2010). Automatic lumen segmentation in calcified plaques: dual-energy CT versus standard reconstructions in comparison with digital subtraction angiography. *AJR American Journal of Roentgenology*, **194**(6), 1590–5.
16. Garg RK, Desai P, Kar M, et al. (2008). Multiple ring enhancing brain lesions on computed tomography: an Indian perspective. *Journal of Neurological Sciences*, **266**(1–2): 92–6.
17. Ledezma CJ, and Wintermark M. (2009). Multimodal CT in stroke imaging: new concepts. *Radiology Clinics of North America*, **47**(1), 109–16.
18. Tan JC, Dillon WP, Liu S, et al. (2007). Systematic comparison of perfusion-CT and CT-angiography in acute stroke patients. *Annals of Neurology*, **61**(6), 533–43.
19. Moore C, Heck D, Beauchamp N, et al. (2003). Detection on CT angiography of an accessory middle cerebral artery simulating a fusiform aneurysm on MR angiography. *AJR American Journal of Roentgenology*, **180**(2), 544–5.
20. Waaijer, A, van der Schaaf IC, Velthuis BK, et al. (2007). Reproducibility of quantitative CT brain perfusion measurements in patients with symptomatic unilateral carotid artery stenosis. *AJNR American Journal of Neuroradiology*, **28**(5), 927–32.
21. Coutts SB, Simon JE, Tomanek AI, et al. (2003). Reliability of assessing percentage of diffusion-perfusion mismatch. *Stroke*, **34**(7), 1681–3.
22. Wintermark M, Sesay M, Barbier E, et al. (2005). Comparative overview of brain perfusion imaging techniques. *Stroke*, **36**(9), e83–99.
23. Lev MH, Farkas J, Rodriguez VR, et al. (2001). CT angiography in the rapid triage of patients with hyperacute stroke to intraarterial thrombolysis: accuracy in the detection of large vessel thrombus. *Journal of Computer Assisted Tomography*, **25**(4), 520–8.
24. Jakubik LD, Cockerham J, Altmann AR, et al. (2003). The ABCs of pediatric laboratory interpretation: understanding the CBC with differential and LFTs. *Pediatric Nursing*, **29**(2), 97–103.
25. Le TH, and Gean AD. (2009). Neuroimaging of traumatic brain injury. *Mount Sinai Journal of Medicine*, **76**(2), 145–62.
26. Ogi S, Fukumitsu N, Tsuchida D, et al. (2002). Imaging of bilateral striopallidodentate calcinosis. *Clinical Nuclear Medicine*, **27**(10), 721–4.
27. Grotta JC, Chiu D, Lu M, et al. (1999). Agreement and variability in the interpretation of early CT changes in stroke patients qualifying for intravenous rtPA therapy. *Stroke*, **30**(8), 1528–33.
28. Lev MH, Farkas J, Gemmete JJ, et al. (1999). Acute stroke: improved nonenhanced CT detection—benefits of soft-copy interpretation by using variable window width and center level settings. *Radiology*, **213**(1), 150–5.
29. Jauch EC, Saver JL, Adams HP Jr, et al. (2013). Guidelines for the early management of patients with acute ischemic stroke: a guideline for healthcare professionals from the American Heart Association/American Stroke Association. *Stroke*, **44**(3), 870–947.
30. Liebeskind DS, Sanossian N, Yong WH, et al. (2011). CT and MRI early vessel signs reflect clot composition in acute stroke. *Stroke*, **42**(5), 1237–43.
31. Kim SJ, Ryoo S, Hwang J, et al. (2012). Characterization of the infarct pattern caused by vulnerable aortic arch atheroma: DWI and multidetector row CT study. *Cerebrovascular Disease*, **33**(6), 549–57.
32. Schramm P, et al. (2004). Comparison of perfusion computed tomography and computed tomography angiography source images with perfusion-weighted imaging and diffusion-weighted imaging in patients with acute stroke of less than 6 hours' duration. *Stroke*, **35**(7), 1652–8.
33. Kloska SP, Schellinger PD, Klotz E, et al. (2004). Acute stroke assessment with CT: do we need multimodal evaluation? *Radiology*, **233**(1), 79–86.
34. Wintermark M, Fischbein NJ, Smith WS, et al. (2005). Accuracy of dynamic perfusion CT with deconvolution in detecting acute hemispheric stroke. *AJNR American Journal of Neuroradiology*, **26**(1), 104–12.
35. Scharf J, Brockmann MA, Daffertshofer M, et al. (2006). Improvement of sensitivity and interrater reliability to detect acute stroke by dynamic perfusion computed tomography and computed tomography angiography. *Journal of Computer Assisted Tomography*, **30**(1), 105–10.
36. Keedy A, Soares B, and Wintermark M. (2012). A pictorial essay of brain perfusion-CT: not every abnormality is a stroke! *Journal of Neuroimaging*, **22**(4), e20–33.
37. Ryoo JW, Na DG, Kim SS, et al. (2004). Malignant middle cerebral artery infarction in hyperacute ischemic stroke: evaluation with multiphasic perfusion computed tomography maps. *Journal of Computer Assisted Tomography*, **28**(1), 55–62.
38. Hom J, Dankbaar JW, Soares BP, et al. (2011). Blood–brain barrier permeability assessed by perfusion CT predicts symptomatic hemorrhagic

transformation and malignant edema in acute ischemic stroke. *AJNR American Journal of Neuroradiology*, **32**(1), 41–8.
39. Wintermark M, Flanders AE, Velthuis B, et al. (2006). Perfusion-CT assessment of infarct core and penumbra: receiver operating characteristic curve analysis in 130 patients suspected of acute hemispheric stroke. *Stroke*, **37**(4), 979–85.
40. Lima FO, Lev MH, Levy RA, et al. (2010). Functional contrast-enhanced CT for evaluation of acute ischemic stroke does not increase the risk of contrast-induced nephropathy. *AJNR American Journal of Neuroradiology*, **31**(5), 817–21.
41. Aulicky P, Mikulík R, Goldemund D, et al. (2010). Safety of performing CT angiography in stroke patients treated with intravenous thrombolysis. *Journal of Neurology, Neurosurgery & Psychiatry*, **81**(7), 783–7.
42. Morgenstern LB, Hemphill JC 3rd, Anderson C, et al. (2010). Guidelines for the management of spontaneous intracerebral hemorrhage: a guideline for healthcare professionals from the American Heart Association/American Stroke Association. *Stroke*, **41**(9), 2108–29.
43. Edlow JA, Malek AM, and Ogilvy CS. (2008). Aneurysmal subarachnoid hemorrhage: update for emergency physicians. *Journal of Emergency Medicine*, **34**(3), 237–51.
44. Delgado Almandoz JE, and Romero JM. (2011). Advanced CT imaging in the evaluation of hemorrhagic stroke. *Neuroimaging Clinics of North America*, **21**(2), 197–213, ix.
45. Delgado Almandoz JE, Schaefer PW, Forero NP, et al. (2009). Diagnostic accuracy and yield of multidetector CT angiography in the evaluation of spontaneous intraparenchymal cerebral hemorrhage. *AJNR American Journal of Neuroradiology*, **30**(6), 1213–21.
46. Yeung R, Ahmad T, Aviv RI, et al. (2009). Comparison of CTA to DSA in determining the etiology of spontaneous ICH. *Canadian Journal of Neurological Sciences*, **36**(2), 176–80.
47. Schmid-Elsaesser R, Muacevic A, Holtmannspötter M, et al. (2003). Neuronavigation based on CT angiography for surgery of intracranial aneurysms: primary experience with unruptured aneurysms. *Minimally Invasive Neurosurgery*, **46**(5), 269–77.
48. Marro B, Galanaud D, Valery CA, et al. (1997). Intracranial aneurysm: inner view and neck identification with CT angiography virtual endoscopy. *Journal of Computer Assisted Tomography*, **21**(4), 587–9.
49. Villablanca JP, Hooshi P, Martin N, et al. (2002). Three-dimensional helical computerized tomography angiography in the diagnosis, characterization, and management of middle cerebral artery aneurysms: comparison with conventional angiography and intraoperative findings. *Journal of Neurosurgery*, **97**(6), 1322–32.
50. Kaminogo M, Hayashi H, Ishimaru H, et al. (2002). Depicting cerebral veins by three-dimensional CT angiography before surgical clipping of aneurysms. *AJNR American Journal of Neuroradiology*, **23**(1), 85–91.
51. Huynh TJ, Demchuk AM, Dowlatshahi D, et al. (2013). Spot sign number is the most important spot sign characteristic for predicting hematoma expansion using first-pass computed tomography angiography: analysis from the PREDICT study. *Stroke*, **44**(4), 972–7.
52. Etminan N, et al. (2012). Perfusion CT in patients with spontaneous lobar intracerebral hemorrhage: effect of surgery on perihemorrhagic perfusion. *Stroke*, **43**(3), 759–63.
53. Herweh, C, Beseoglu K, Turowski B, et al. (2007). Evidence against a perihemorrhagic penumbra provided by perfusion computed tomography. *Stroke*, **38**(11), 2941–7.
54. Killeen RP, Mushlin AI, Johnson CE, et al. (2011). Comparison of CT perfusion and digital subtraction angiography in the evaluation of delayed cerebral ischemia. *Academic Radiology*, **18**(9), 1094–100.
55. Kunze E, Pham M, Raslan F, et al. (2012). Value of Perfusion CT, Transcranial Doppler Sonography, and Neurological Examination to Detect Delayed Vasospasm after Aneurysmal Subarachnoid Hemorrhage. *Radiology Research and Practice*, **2012**, Article ID 231206.
56. Provenzale JM. (2010). *Imaging of traumatic brain injury: a review of the recent medical literature. AJR American Journal of Roentgenology*, **194**(1), 16–19.
57. Jagoda AS, Bazarian JJ, Bruns JJ Jr, et al. (2009). Clinical policy: neuroimaging and decisionmaking in adult mild traumatic brain injury in the acute setting. Journal of Emergency Nursing, **35**(2), e5–40.
58. Maas AI, Hukkelhoven CW, Marshall LF, et al. (2005). Prediction of outcome in traumatic brain injury with computed tomographic characteristics: a comparison between the computed tomographic classification and combinations of computed tomographic predictors. *Neurosurgery*, **57**(6), 1173–82; discussion 1173–82.
59. Wintermark M, van Melle G, Schnyder P, et al. (2004). Admission perfusion CT: prognostic value in patients with severe head trauma. *Radiology*, **232**(1), 211–20.
60. Wintermark M, Chioléro R, van Melle G, et al. (2004). Relationship between brain perfusion computed tomography variables and cerebral perfusion pressure in severe head trauma patients. *Critical Care Medicine*, **32**(7), 1579–87.
61. Metting Z, Rödiger LA, Stewart RE, et al. (2009). Perfusion computed tomography in the acute phase of mild head injury: regional dysfunction and prognostic value. *Annals of Neurology*, **66**(6), 809–16.
62. Diaz JJ, Jr, , Gillman C, Morris JA Jr, et al. (2003). Are five-view plain films of the cervical spine unreliable? A prospective evaluation in blunt trauma patients with altered mental status. *Journal of Trauma*, **55**(4), 658–63; discussion 663–4.
63. Hauser CJ, Visvikis G, Hinrichs C, et al. (2003). Prospective validation of computed tomographic screening of the thoracolumbar spine in trauma. *Journal of Trauma*, **55**(2), 228–34; discussion 234–5.

CHAPTER 2

Modern methods for accurate T_1, T_2, and proton density MRI

Sean C. L. Deoni, Sandra M. Meyers,
and Shannon H. Kolind

Introduction

To date, the majority of clinical and research magnetic resonance imaging (MRI) relies on the acquisition and interpretation of qualitative relaxation time (T_1, T_2, and T_2*) or proton density-weighted images, whose contrast depends on the intrinsic tissue properties (i.e. differences in underlying tissue relaxation times and water content), acquisition approach (i.e. imaging sequence and acquisition parameters), and extraneous hardware factors (such as radio frequency (RF) receiver coil geometry, sensitivity, patient positioning, coil loading, and electronic signal amplifier gains) (Fig. 2.1).

As an example, this can be illustrated mathematically by contrasting the ideal signal equation for an inversion recovery experiment for a given inversion time (TI), repetition time (TR) and echo time (TE):

$$S_{IR} = PD \times (1 - 2\,e^{-TI/T_1} + e^{-TR/T_1})\,e^{-TE/T2^*}, \qquad [1]$$

which assumes uniform coil sensitivity and gain, and perfect and homogeneous 180° inversion and 90° sampling pulses, with a more generalized and realistic expression,

$$S_{IR} = PD \times B_1^- \times \zeta \times (1 - \beta e^{-TI/T_1} + e^{-TR/T_1})\,e^{-TE/T2^*} \sin\left(\frac{\pi}{2} \times B_1^+\right) \qquad [2]$$

In Eqn [2], the effects of the spatial variability in coil sensitivity imperfect inversion pulse efficiency (β), and sampling pulse flip angle inhomogeneity are included, in addition to a factor offset (ζ) that incorporates amplifier gain and image scaling factors, which do not spatially vary. Thus, although the inversion recovery signal and the resultant image contrast can be preferentially 'tuned' to maximally exploit tissue T_1, T_2, T_2*, or proton density differences through the adjustment of acquisition parameters (such as TI, TR, TE, the influence of extraneous and inconsistent hardware factors cannot be completely removed. Furthermore, while the contrast may be preferentially weighted towards individual relaxation processes or proton density, all of these intrinsic parameters will still contribute, even if only subtly, to the acquired signal. This has the effect of diminishing image contrast and potentially obscuring subtle changes.

This complex mixture of signal sources challenges the interpretation of observed contrast, or changes in contrast, since alterations in one parameter can be masked by associated changes in the others. Furthermore, inconsistent patient-related factors (such as B_1^+) make it difficult to directly or *quantitatively* compare signal values between patients, time-points, or imaging centres. Thus, there remain limitations in the utility of conventional qualitative imaging in identifying subtle alterations associated with early disease, monitoring disease progression, or evaluating responses to treatment therapies.

One approach to simplifying data interpretability, while at the same time increasing tissue contrast and longitudinal reproducibility, is direct relaxation time and/or water content quantification, also termed quantitative relaxometry and water content mapping [1]. Calculation of T_1, T_2, and proton density cleanly separates these intrinsic relaxation and proton density properties from each other, as well as from extraneous patient and hardware-related influences. Beyond image quality and consistency [2], quantitative relaxometry has been shown to have clinical relevance in a variety of applications [1,3]. Since the basis of relaxation is molecular motion [4], these parameters are directly influenced by the local tissue microstructure and biochemistry. Characteristics such as tissue density, macromolecule, protein and lipid composition, and paramagnetic atom (e.g. iron) concentration have each been shown to alter the measured relaxation times. Structural or compositional changes, resulting from disease pathology, development, learning, or plasticity, therefore, will likely result in measurable T_1, T_2 and/or proton density changes. For example, the establishment of the lipid rich myelin sheath during early neurodevelopment, along with associated proteins, cholesterol, iron containing oligodendrocytes and glial cells, results in rapid and substantial T_1 and T_2 changes over the first 2 years of life [5,6]. Likewise, the reduced T_1 and T_2 of white matter compared with gray matter primarily derives from the different concentration of myelin [7]. Similarly, differing concentrations of ferritin may underlie the T_1, T_2, and T_2* variations observed between deep gray matter structures [8,9]. T_1 is also strongly influenced by changes in water content, which will be discussed in greater detail later in this chapter.

Beyond developmental changes, pathological processes including oedema, inflammation, tumour infiltration, iron accumulation, and necrosis, alter the local tissue microstructure and biochemistry, and can result in substantial relaxation time changes [5,10–14]. For example, in multiple sclerosis (MS), T_1 and T_2 alterations within

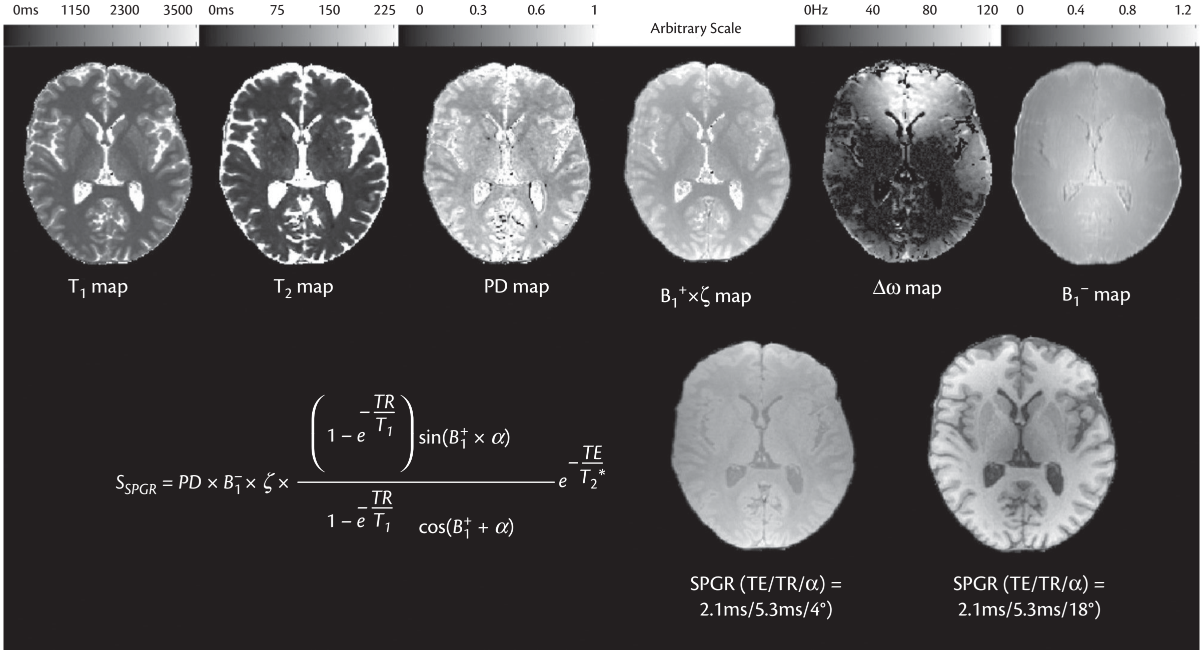
0ms 1150 2300 3500
0ms 75 150 225
0 0.3 0.6 1
Arbitrary Scale
0Hz 40 80 120
0 0.4 0.8 1.2
T_1 map
T_2 map
PD map
$B_1^+ \times \zeta$ map
$\Delta\omega$ map
B_1^- map
$S_{SPGR} = PD \times B_1^- \times \zeta \times \frac{\left(1 - e^{-\frac{TR}{T_1}}\right) \sin(B_1^+ \times \alpha)}{1 - e^{-\frac{TR}{T_1}} \cos(B_1^+ + \alpha)} e^{-\frac{TE}{T_2^*}}$
SPGR (TE/TR/α) = 2.1ms/5.3ms/4°)
SPGR (TE/TR/α) = 2.1ms/5.3ms/18°)

Fig. 2.1 The contrast observed in conventionally acquired T_1, T_2, or proton density-weighted images results from a complex mixture of each of these intrinsic effects, along with other patient-specific and hardware influences, and acquisition type. For example, the T_1-weighted spoiled gradient recalled echo (SPGR) signal is a complex mixture of proton density, T_1, and T_2*, as well as flip angle inhomogeneity (B_1^+), RF coil sensitivity and gain ($B_1^- \times \zeta$). At long TE, off-resonance effects ($\Delta\omega$) will also influence the acquired signal. Through the choice of acquisition parameters (TE, TR, and flip angle, α) the SPGR signal can be preferentially proton density or T_1-weighted.

'normal appearing' white matter are suggestive of tissue disruption unseen on conventional diagnostic MR images [15]. In epilepsy, areas with abnormally increased T_1 and T_2 values may correspond to the seizure focus [16], offering a potential adjunct to electroencephalography (EEG) in localizing seizure foci. In cardiac applications, alterations in T_1 and T_2 may be indicative of myocardial fibrosis, and rapid measurement of T_1 following bolus injection of contrast can permit quantitative evaluation of cardiac output and functioning [17]. Finally, a mainstay of cartilage imaging is delayed gadolinium-enhanced magnetic resonance imaging (dGEMRIC) [18]. Likewise, evaluation of water content has clinical application to pathological conditions involving oedema or inflammation, such as stroke and brain tumours [19].

However, despite the salient advantages of quantitative relaxometry and water content mapping, adoption of these approaches in the research and clinical realms has been slow. This may be due, in part, to the perceived lengthy acquisition times, relatively poor spatial resolution, or limited brain coverage associated with conventional measurement methods. Established 'gold-standard' approaches, such as multiple inversion time inversion recovery (or multiple repetition time saturation recovery), spin echo for T_1, and multiple echo time spin or gradient echo for T_2 and T_2*, respectively, can require acquisition protocols lasting 60 minutes or longer. This clearly places these methods beyond clinical limits. While the use of accelerated read-outs, such as multiple spin echo (termed fast spin echo (FSE) or turbo spin echo (TSE)) or gradient refocused echo planar imaging (EPI), can substantially reduce acquisition times to the order of seconds or minutes, they do so at the expense of reduced maximal spatial resolution, increased echo time (and, therefore, reduced signal-to-noise ratio (SNR)), image degradation with increased acceleration or echo train lengths, and sensitivity to off-resonance effects (main B_0 field inhomogeneities) that can lead to signal drop-outs and geometric distortions.

Diligent and creative work by many research groups over the past decade, however, has led to the development of alternative rapid measurement approaches that afford acquisition times and spatial resolutions on par with more conventional T_1, T_2, and proton density-weighted images. The aim of this chapter is to review these methods and address the potential pitfalls associated with each.

Methods

T_1 mapping

Multislice TI-cycled IR-EPI

The large dynamic range and high intrinsic SNR afforded by the inversion recovery (IR) approach makes it an attractive base from which to develop new techniques. The principal limitation of IR, however, is the requirement that TR be long with respect to T_1 in order for the spin system to relax to near equilibrium, allowing full characterization of the recovery curve. Even with the use of single-shot or segmented EPI read-outs, there can remain significant 'dead-time' following the end of the read-out train and the next inversion preparation pulse. To make more efficient use of this time, Clare and Jezzard [20] proposed a multislice IR-EPI sequence (Fig. 2.2), in which up to 12 two-dimensional (2D) image slices are acquired following each volume-selective 180° inversion preparation pulse, each with an incremented TI. After each subsequent inversion pulse, the ordering of the 2D slices is shifted such that each slice is acquired with a different TI. As a result, after 12 repeats, each of the 12 slices will have been acquired with the same set of 12 different inversion times. For additional slices, e.g. to cover the full brain volume, the whole process may be repeated. Using

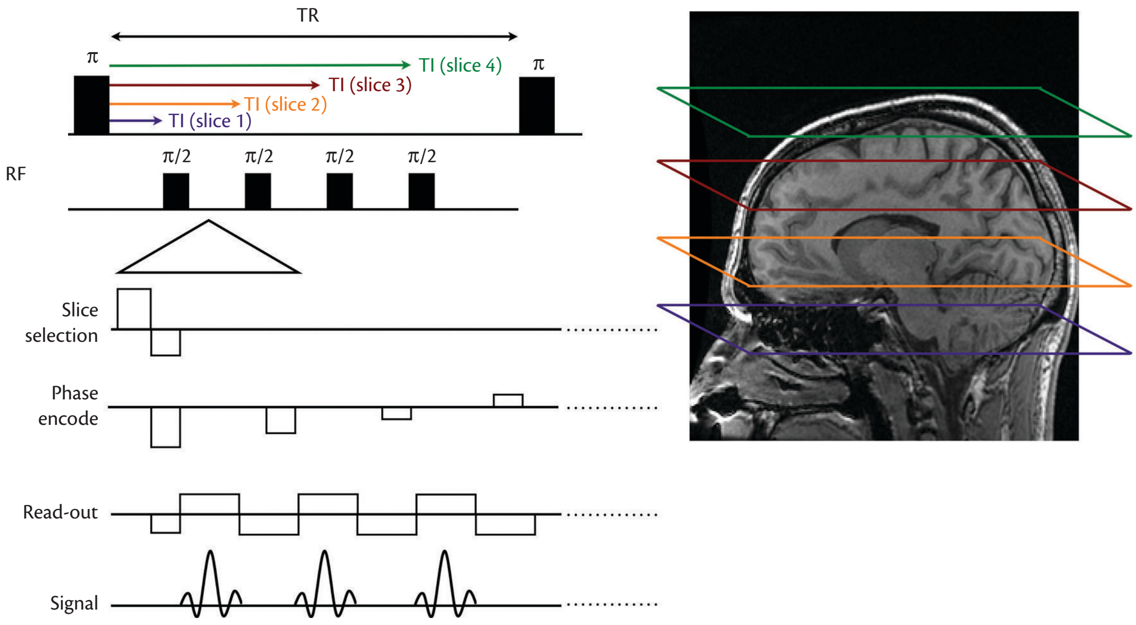

Fig. 2.2 Illustrative pulse sequence diagram for the multislice interleaved IR-EPI T_1 mapping method. After each TR, the ordering of the slices is changed so that after *N* TR intervals, each of the *N* slices will have been acquired with each TI increment.

this approach, 60 slice volumetric T_1 maps can be acquired in less than 3 minutes, representing a substantive improvement over the conventional IR approach.

Since the approach is essentially a time efficient IR experiment, T_1 is calculated from the data using the three-parameter IR signal model given in Eqn [3]. Here, the equilibrium magnetization proportionality constant, ρ, represents a composite of the PD, B_1^-, ζ, sin α, and terms from Eqn [2] and β accounts for imperfect 180° inversion pulses.

$$S_{IR} = \rho \times \left(1 - \beta \mathrm{e}^{-TI/T_1} + \mathrm{e}^{-TR/T_1}\right) \qquad [3]$$

While more efficient than conventional IR, this method's reliance on an EPI read-out imparts potential disadvantages in terms of image quality and artefacts as noted above. Furthermore, the multislice nature of the method also introduces the potential for through-slice dephasing (due to the different slice ordering on each repeat), as well as flow artefacts between adjacent slices.

Look–Locker

Perhaps the most widely used of the rapid T_1 mapping approaches, the method of Look and Locker (Look–Locker (LL)) [21] makes efficient use of the dead-time between successive inversion pulses in the IR sequence to comprehensively and continuously sample the full T_1 recovery curve using a series of small angle (α typically less than 40°) RF pulses separated by a short time delay (τ) (Fig. 2.3). In an imaging setting, each of these samples comprises a k_y line in a different image. Thus, the experiment is repeated *N* times, where *N* is the number of k_y lines in the final map image (i.e. *N* = 128 in a 128 × 128 matrix image). Due to the disturbing effect of the α RF pulses, the magnetization recovers to an effective equilibrium (that differs from the thermal equilibrium) via an *apparent* T_1 relaxation rate ($T_{1,e}$) that is related in a known way to the true T_1. To calculate T_1, the data is fitted to the following general model:

$$S_{LL} = PD\left[A - Be^{\frac{-(TI+(j-1)\tau)}{T1\beta}}\right]\sin \times \mathrm{e}^{\frac{-TE}{T2^*}}, \qquad [4]$$

simplified to,

$$S_{LL} = PD\left[A - Be^{\frac{(TI+(j-1)\tau)}{T_{1,e}}}\right], \qquad [5]$$

where,

$$A = \frac{1 - e^{-\frac{\tau}{T_1}}}{1 - e^{-\frac{\tau}{T_1}}\cos\alpha} \qquad [6]$$

$$-B = \frac{A\left(1 + e^{-\frac{\tau}{T_1}}\right) + \left(1 + e^{-\frac{\tau}{T_I}}\right)}{1 + e^{-\frac{(T_1 + N\tau)}{T_1}}\cos^N \alpha}, \qquad [7]$$

and *j* is the α RF pulse number and *N* is the total number of RF pulses.

Finally, T_1 is calculated from $T_{1,e}$ as

$$T_{1,e} = \frac{T_1}{1 - \frac{T_1}{\tau}\mathrm{In}(\cos\alpha)} \qquad [8]$$

Although the signal model is more complicated, this approach allows rapid T_1 estimation with accuracy comparable with conventional IR. As presented, this approach is inherently 2D in nature. To acquire 3D images, the approach could be repeated for each k_z slice; however, this would require $k_y \times k_z$ repeats, potentially leading to

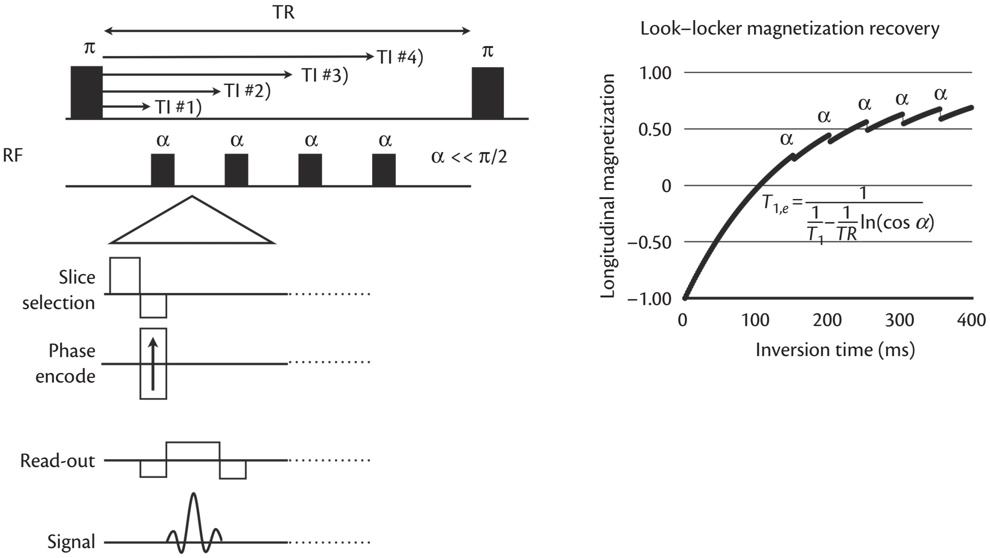
TR
π
TI #4)
π
TI #3)
TI #2)
TI #1)
α
α
α
α
RF
α << π/2
Slice
selection
Phase
encode
Read-out
Signal
Look–locker magnetization recovery
Longitudinal magnetization
1.00
0.50
0
−0.50
−1.00
0
100
200
300
400
Inversion time (ms)
α
α
α
α
α
$T_{1,e} = \frac{1}{\frac{1}{T_1} - \frac{1}{TR}\ln(\cos\alpha)}$

Fig. 2.3 Pulse sequence timing diagram and magnetization recovery curve for the LL T1 measurement technique.

exhaustive scan times, depending on the desired resolution and volume size. To address this, Henderson and colleagues [22] proposed grouping successive α pulse samples into k_y 'blocks'. This effectively reduces the number of repeats by the number of blocked samples, allowing time-efficient, fully 3D acquisitions.

As the acquired signal and effective $T_{1,e}$ are influenced by the sampling RF pulse angle, correct knowledge of this angle is necessary for accurate T_1 estimation (Fig. 2.4). Inhomogeneity in the transmitted flip angle can arise from poorly designed RF pulse profiles, or more intrinsic RF attenuation and tissue dielectric effects. Ideally, the applied RF pulse profile is a boxcar or 'top hat' function, providing the desired flip angle uniformly across the excited volume. Unfortunately, in an effort to minimize pulse and scan time durations, and/or energy deposition, the achieved profile may become more Gaussian in shape, with the transmitted flip angle varying across the excited volume or slice. In 3D acquisitions, this less-than-ideal profile may be tolerable if the anatomy of interest lies within the centre portion of the excited slab, where the flip angle is approximately uniform and of the desired (i.e. 'prescribed') value. For single-slice, or multiple 2D slice applications, however, the measured signal becomes an integrated function of flip angle [23]. In these cases, or when accuracy is required across the full 3D volume, flip angle calibration is necessary.

RF coil geometry and RF attenuation, and dielectric resonance effects also lead to deviations of the intended flip angle throughout the image volume. Asymmetric RF coils have non-uniform RF power profiles, resulting in the flip angle varying with distance from the coil. Dielectric resonance (RF penetration) effects also result in variations in the transmitted flip angle and increase in severity as the main magnetic field strength increases.

Minimization of flip angle-related errors can be achieved through improved RF pulse design [24]; use of B_1 insensitive pulses [25,26]; numerical RF modelling [23]; or calibration of the transmitted flip angle field [27]. Optimized RF pulse design, such as SLR pulses [24], provide idealized excitation profiles, minimizing the fall-off regions at the edges of the slab. If necessary in single-slice applications, the flip angle can be numerically modelled and accounted

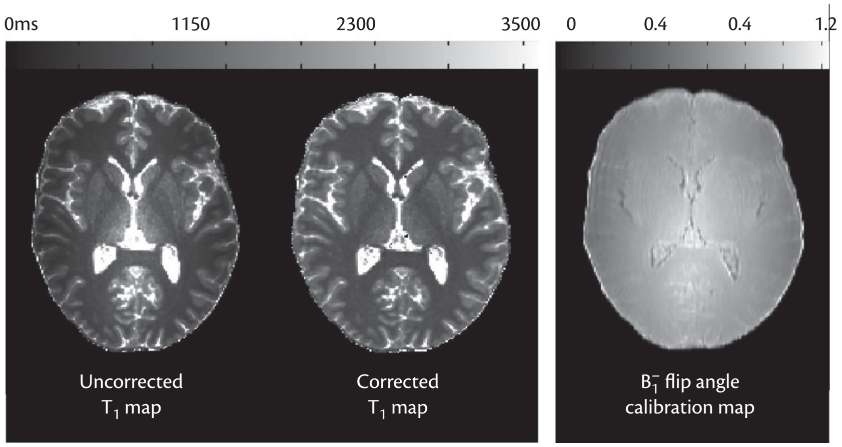
0ms
1150
2300
3500
0
0.4
0.4
1.2
Uncorrected
T_1 map
Corrected
T_1 map
B_1^- flip angle
calibration map

Fig. 2.4 Example of the effect of inaccurate knowledge of the transmitted flip angle on the estimated T_1. In a 3D acquisition, the RF pulse profile tapers off towards the edges of the excited volume, resulting in increasing T_1 errors in this area. Calibration of the flip angle field can help correct or minimize these errors.

for in T_1 measurements [23]. Composite or fast passage adiabatic pulses, which are less sensitive to RF amplitude, offer more uniform flip angles profiles, but require lengthy pulse durations and can have high energy deposition.

In addition to transmitted flip angle considerations, the short inter-sampling pulse delay, τ, may also introduce stimulated-echo artefacts into the acquired signal. For rapid imaging, τ is often much less than T_2 or T_2^*, resulting in coherent transverse magnetization being present before each sampling pulse is applied. Left unchecked, this residual magnetization will introduce additional T_2-weighting into the signal, as well as stimulated echoes [28] that further corrupt the desired T_1-weighted signal. To eliminate residual magnetization, a combination of RF [29] and gradient spoiling [30] is generally used to dephase the transverse magnetization before the application of each RF pulse.

Modified LL for cardiac applications

While quantitative imaging, in particular, dynamic T_1 mapping following bolus contrast injection, has clinical utility in evaluating cardiac function [17], measurement of a moving structure introduces several challenges. In particular, imaging sequences need to be cardiac gated and performed during breath-hold in order to minimize artefacts due to physiological motion. The current standard is an adaption of the LL method, termed modified Look–Locker inversion (MOLLI) recovery [31,32]. In its original single-slice description (Fig. 2.3), the technique utilizes an electrocardiogram (ECG)-triggered selective inversion (180°) pulse, followed by a delay of TI, and then repeated rapid single-slice, single-shot acquisition read-outs interspaced by time τ until the end of the imaging period of the cardiac cycle. Three or more 180° TI read-out blocks are applied with differing TIs, and a delay of 4s or longer between blocks, to allow for complete magnetization recovery. Data acquired from all blocks are then combined and the LL model (Eqns [5] and [8]) is used to estimate T_1. To achieve high spatial resolution, the approach can be combined with parallel acquisition strategies. This sequence can also be extended to 3D by making use of a multislice acquisition and incorporating respirator triggering [33].

As with the conventional LL approach, however, MOLLI is susceptible to flip angle inhomogeneity, as well as more obvious motion, flow and slice misalignment artefacts due to the beating heart.

Variable flip angle spoiled gradient recalled method (driven equilibrium single pulse observation of T1)

Each of the presented methods retains the principle of sampling the recovery of the longitudinal magnetization following an inversion or saturation preparation pulse. However, an alternative approach does away with this central tenet. Through the application of repeated RF pulses with constant inter-pulse delay, TR, and complete spoiling of the transverse magnetization (Fig. 2.5), the spin-system is driven to a dynamic equilibrium that depends on T_1 [34], as:

$$S_{SPGR} = PD\frac{1-e^{-\frac{TR}{T_1}}}{1-e^{-\frac{TR}{T_1}}\cos\alpha}\sin\alpha \times e^{-\frac{TE}{T2^*}} \qquad [9]$$

and simplified to:

$$S_{SPGR} = PD\frac{1-e^{-\frac{TR}{T_1}}}{1-e^{-\frac{TR}{T_1}}\cos\alpha}\sin \qquad [10]$$

The variable flip angle method, also termed driven equilibrium single pulse observation of T_1 (DESPOT1), employs a series of

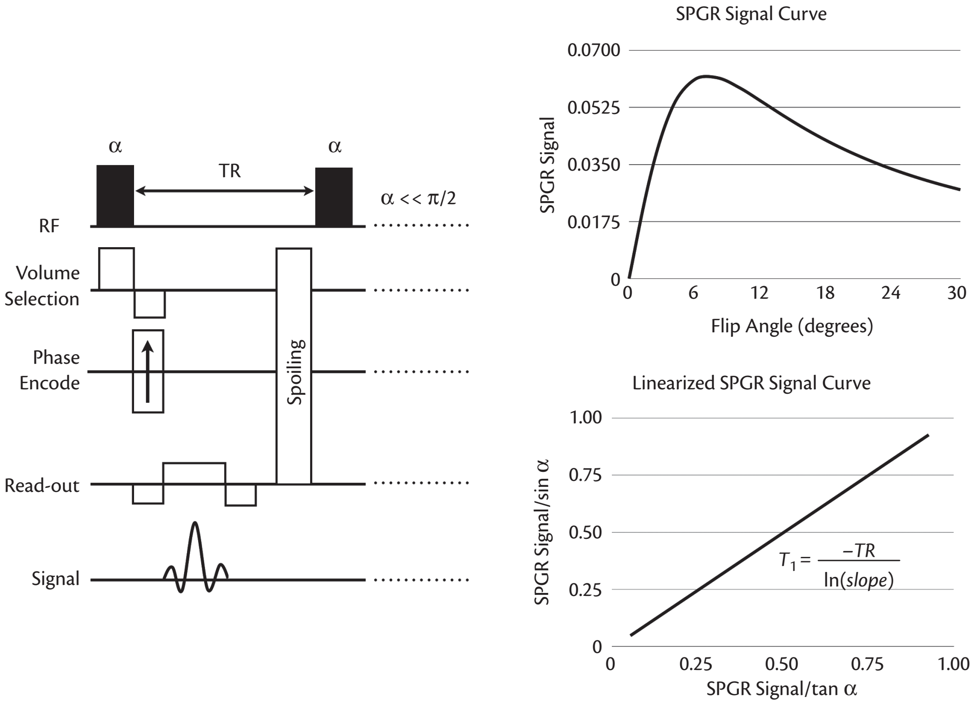

Fig. 2.5 Pulse sequence timing diagram and signal 'recovery' curve (as a function of flip angle) for SPGR and DESPOT1. Also shown is the linearized signal curve that allows T_1 to be calculated from as few as two acquisitions.

spoiled gradient recalled (SPGR) echo or spoiled fast low angle shot (FLASH), acquired at incremented flip angles. The SPGR signal model can then be either explicitly fitted to the acquired data, or Eqn [10] can be linearized as:

$$\frac{S_{SPGR}}{\sin\alpha} = \frac{S_{SPGR}}{\tan\alpha} e^{-\frac{TR}{T_1}} + PD\left(1 - e^{-\frac{TR}{T_1}}\right) \qquad [11]$$

and T_1 can be calculated directly from the slope of the $S_{SPGR}/\sin\alpha$ versus $S_{SPGR}/\tan\alpha$ line. This unconventional linearization has the advantage of allowing T_1 to be calculated from as few as 2 SPGR data points, substantially reducing the acquisition time required by the method. First proposed by Christensen [34], this method has been subsequently refined and optimized by a number of authors [35–40], and is often considered the most efficient method for T_1 measurement.

As with the LL method, however, DESPOT1 requires accurate knowledge of the transmitted flip angle. Furthermore, incomplete spoiling of the transverse magnetization before each RF pulse (using a combination of RF and gradient spoiling) can result in residual coherent transverse magnetization [41,42]. This drives the equilibrium magnetization away from predicted value through the production of stimulated echoes [43], resulting in substantial T_1 inaccuracy.

T_2 mapping

Variable flip angle steady state free precession method (driven equilibrium single pulse observation of T_2)

Conceptually similar to DESPOT1 variable flip angle method for T_1 determination, driven equilibrium single pulse observation of T_2 (DESPOT2) [38,44] makes use of variable flip angle true fast imaging with steady state (TrueFISP) or balanced steady state free precession (SSFP) to derive T_2 values. Unlike SPGR, in which the transverse magnetization is completely spoiled before each RF pulse, allowing only the longitudinal magnetization to reach equilibrium, in balanced SSFP, the transverse magnetization is refocused prior to each RF pulse. By balancing all gradients, such that the net gradient area and moment across each TR is zero, both the longitudinal *and* transverse magnetizations are brought into dynamic equilibrium [28] (Fig. 2.6). The resultant equilibrium magnetization sampled just prior to each RF pulse is, therefore, a complex mixture of T_1, T_2, proton density, off-resonance effects ($\Delta\omega$), and the phase of the RF pulse (θ_{RF}).

$$M_x^- = PD\left(1 - e^{-\frac{TR}{T_1}}\right) e^{-\frac{TR}{T_2}} \sin\alpha \sin\phi / \qquad [12]$$

and

$$M_y^- = PD\left(1 - e^{-\frac{TR}{T_1}}\right) e^{-\frac{TR}{T_2}} \sin\alpha \left(\cos\phi - e^{-\frac{TR}{T_2}}\right) / \qquad [13]$$

where,

$$d = \left(1 - e^{-\frac{TR}{T_1}} \cos\alpha\right)\left(1 - e^{-\frac{TR}{T_2}} \cos\phi\right) - e^{-\frac{TR}{T_2}}\left(e^{-\frac{TR}{T_1}} - \cos\alpha\right)\left(e^{-\frac{TR}{T_2}} - \cos\phi\right), \qquad [14]$$

$$\phi = \theta_{RF} + \Delta\omega TR, \qquad [15]$$

and

$$S_{SSFP} = \sqrt{M_x^{-2} + M_y^{-2}} \qquad [16]$$

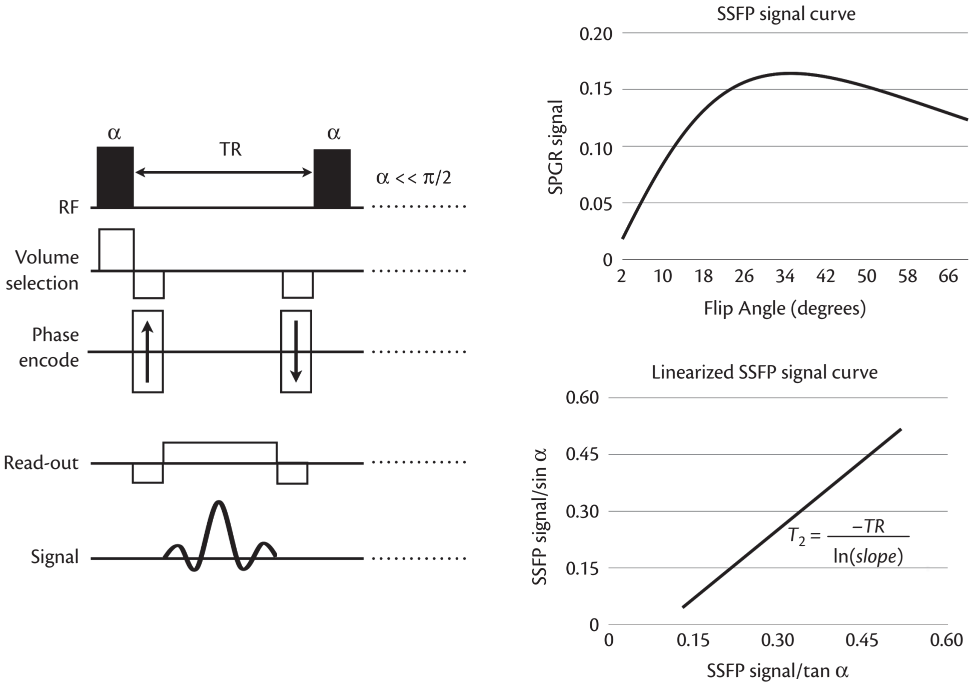

Fig. 2.6 Pulse sequence timing diagram and the raw and linearized signal 'recovery' curves (as a function of flip angle) for balanced SSFP and DESPOT2.

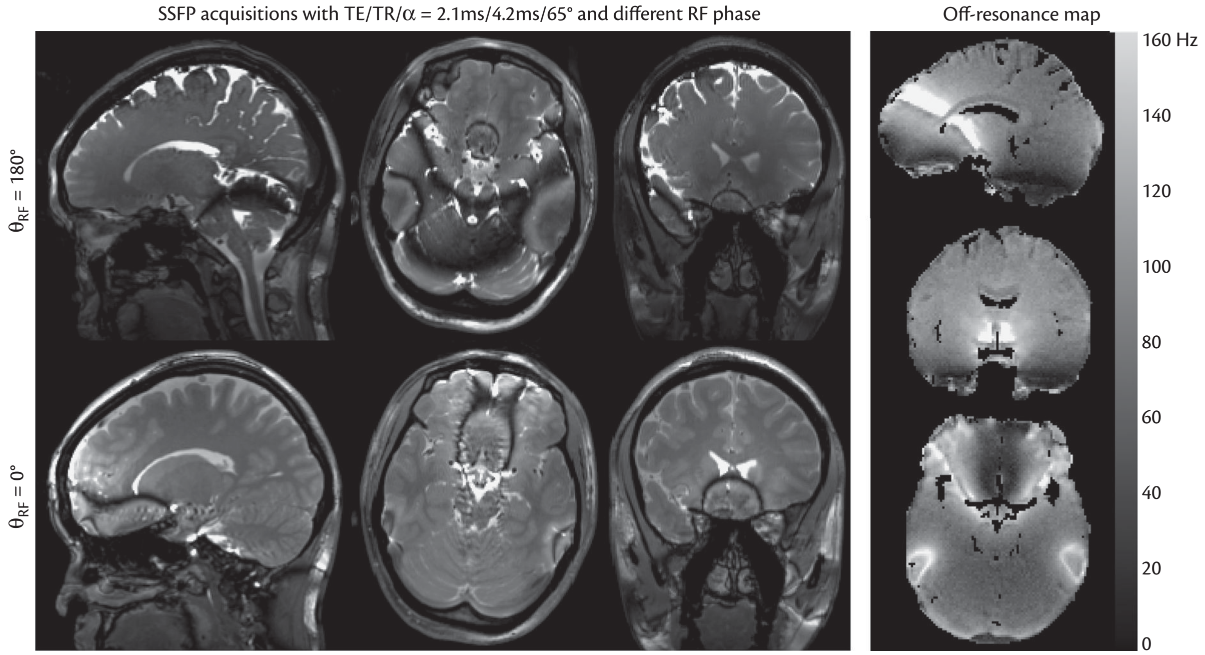

Fig. 2.7 Examples of the off-resonance banding artefact commonly seen in balanced SSFP images. Changing the phase of the RF pulse can spatially shift the artefact. Through acquisition of data with different RF phases, a complete fit to the SSFP signal equations can be performed, allowing calculation of the off-resonance, or B_0-field. This map can subsequently be used to correct SSFP derived T_2 maps.

Under ideal conditions (i.e. $\Delta\omega = 0$), TE = 1/2TR, and $\theta_{RF} = 180°$, Eqn [16] simplifies to:

$$S_{SSFP} = PD\frac{\left(1-e^{-\frac{TR}{T_1}}\right)\sin\alpha}{1-e^{-\frac{TR}{T_1}}e^{-\frac{TR}{T_2}}-\left(e^{-\frac{TR}{T_1}}-e^{-\frac{TR}{T_2}}\right)\cos\alpha}, \qquad [17]$$

which, like Eqn [10], can be recast in the linear Y = mX + B form as

$$\frac{S_{SSFP}}{\sin\alpha} = \left(\frac{e^{-\frac{TR}{T_1}}-e^{-\frac{TR}{T_2}}}{1-e^{-\frac{TR}{T_1}}e^{-\frac{TR}{T_2}}}\right)\frac{S_{SSFP}}{\tan\alpha} = \frac{PD\left(1-e^{-\frac{TR}{T_2}}\right)}{1-e^{-\frac{TR}{T_1}}e^{-\frac{TR}{T_2}}} \qquad [18]$$

Thus, with prior knowledge of T_1, T_2 can be calculated directly from the slope of the $S_{SSFP}/\sin\alpha$ versus $S_{SSFP}/\tan\alpha$ line. Combined with DESPOT1, for example, T_1 and T_2 can be determined from as few as four images [38]. However, it is rarely the case that $\Delta\omega = 0$, i.e. that all spins are perfectly on-resonance. In SSFP images, areas of off-resonance appear as repeating bands of reduced or null signal, and are especially pronounced near tissue–air interfaces, such as the sinuses, base of brain, and inner ear (Fig. 2.7). To correct for these effects, a full non-linear fit to the general signal expression (Eqn [16]) is required [44]. Furthermore, data with differing θ_{RF} patterns are needed in order to shift the banding artefact throughout the image [45]. Beyond off-resonance effects, the dependence of the SSFP signal on flip angle means accurate knowledge of the transmitted flip angle is crucial for accurate T_2 estimation. Thus, as with the rapid T_1 measurement techniques, modelling or calibration of the transmitted flip angle is needed. While these additional calibration steps increase the overall acquisition time, combined whole-brain T_1 and T_2 maps can still be acquired in less than 10 minutes using DESPOT1 and DESPOT2.

More recent exploration of the SSFP signal has introduced an additional confound to DESPOT2, that being the influence of magnetization transfer (MT) effects from off-resonance bound protons [46,47]. This additional signal source can result in the measured signal deviating from the predicted value, with dependence on the RF pulse length and flip angle, leading to T_2 errors. While correction for these effects [48] can minimize T_2 measurement errors, the exploitation of this MT influence can become an active area of research for rapid and efficient MT imaging [49,50].

Multi-echo gradient and spin echo

An alternative high speed T_2 imaging approach is provided by the combined gradient and spin echo sequence (GRASE) [51]. Following an initial preparation pulse, the GRASE sequence (Fig. 2.8) consists of a train of 180° pulses, with an odd number of gradient echoes that sample successive k_y lines placed in-between each 180° pulse pair. By combining spin and gradient echoes, and varying the k_y order, the method can be made less sensitive to main magnetic field inhomogeneities that lead to the image artefacts and signal voids common in gradient echo EPI images, while achieving similar reductions in acquisition time.

Through the acquisition of multiple GRASE images, each with incremented TE, T_2 can be calculated via the conventional spin echo signal equation [52],

$$S_{SE} = \rho\left(1-e^{-\frac{TR}{T_1}}\right)e^{-\frac{TE}{T_2}} \qquad [19]$$

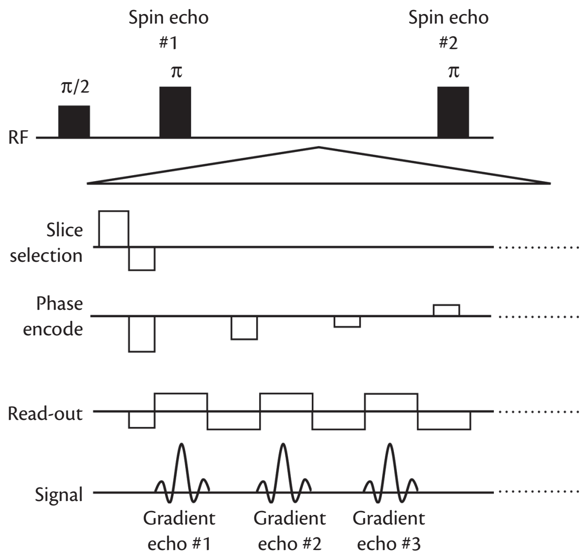

Fig. 2.8 Pulse sequence timing diagram for the combined gradient and spin echo (GRASE) sequence.

Here, T_1 effects can be minimized by making TR substantially longer than T_1 (generally five times longer). More simply, the T_1 term can be included in the ρ term during fitting, with the caveat that this term no longer solely reflects the proton density.

Combined T_1 and T_2 mapping

In a number of applications, it may be useful to acquire not only T_1 or T_2 measurements, but both. As the MR signal from any pulse sequence is inherently a mixture of T_1 and T_2 (or T_2^*) effects, suitable variation of acquisition parameters may enable simultaneous mapping of T_1 and T_2. An indirect approach to simultaneous T_1 and T_2 measurement may be the combination of DESPOT1 with DESPOT2 [38], which can provide both measures with as few as four acquisitions (alongside suitable flip angle calibration and assuming no off-resonance conditions). The mixed contribution of T_1 and T_2 to the balanced steady-state free precession (bSSFP) signal, however, also affords an opportunity for their combined calculation without relying on a set of SPGR acquisitions [53].

Inversion recovery steady-state free precession

One such approach for calculating T_1 and T_2 (as well as PD) using bSSFP involves the pre-application of an adiabatic 180° inversion pulse followed by a bSSFP read-out train that samples the evolution of the magnetization towards a steady-state value [53]. This is analogous to the Look-Locker method, except that the magnetization recovery is sampled using bSSFP in place of SPGR. When the bSSFP inter-pulse delay is short (i.e. $\tau << T_1$ and T_2), the initial and steady-state signal can be expressed as:

$$S_0 = \rho \sin\left(\frac{\alpha}{2}\right), \qquad [20]$$

and

$$S_{ss} = \frac{\rho \sin\alpha}{\left(\frac{T_1}{T_2}+1\right) - \left(\frac{T_1}{T_2}+1\right)\cos\alpha} \qquad [21]$$

The time-course between S_0 and S_{SS} is described by:

$$S(n\,\tau) = S_{SS}\left[1 - INV \times e^{-\frac{n\tau}{T_1^*}}\right], \qquad [22]$$

with:

$$\frac{1}{T_1^*} = \frac{1}{T_1}\cos^2\left(\frac{\alpha}{2}\right) + \frac{1}{T_2}\sin^2\left(\frac{\alpha}{2}\right) \qquad [23]$$

and

$$INV = 1 + \frac{S_0}{S_{ss}} \qquad [24]$$

Thus, from sequential measures during the magnetization evolution from S_0 to S_{SS} can be used to calculate both T_1 and T_2 provided the flip angle is accurately known. The inversion preparation pulse reduces the method's sensitivity to bSSFP off-resonance, however, these effects can increase at higher field strengths (i.e. 3T and above).

Quantification of relaxation times and proton density

Through two modifications to the LL approach, namely replacing the initial inversion preparation pulse with a 90° saturation pulse eliminating any potential delay between the last SPGR sampling pulse and the following inversion preparation, arises an alternative method for calculating T_1, T_2^* and ρ termed quantification of relaxation times and proton density (QRAP) [54].

As with the LL signal, the recovery is parameterized principally by the *effective* $T_{1,e}$ (Eqn [4]). To obtain measures of T_2^*, two SPGR read-outs are acquired at each τ with differing echo times. With knowledge of T_1 and T_2^*, the expected signal at zero TE can be calculated to provide an estimate of ρ.

Fingerprinting

Recently, a novel approach to quantitative imaging has been proposed that differs in concept and design from the techniques described thus far. Rather than explicitly modelling signal recovery, MR 'fingerprinting' instead aims to use a pattern-recognition classifier to determine T_1 and T_2, as well as other quantitative parameters [55]. In this approach, heterogeneous MR data (that is, from different acquisition sequences and/or different acquisition parameters) is acquired. Within each voxel, this set of signals represents a unique signature, or fingerprint. Theoretical signals corresponding to the applied acquisition strategy are then calculated for a wide range of T_1, T_2, T_2^*, ρ, and off-resonance values, creating a reference database of signal models (e.g. the fingerprint library). Correlations are then calculated between the measured signal fingerprint and each reference print in the library to determine the most appropriate match and, therefore, corresponding quantitative values. In preliminary reports, the method shows good reliability even in the presence of motion and other artefacts.

Each of the described approaches affords the ability to acquire whole-brain quantitative T_1 and T_2 maps (Fig. 2.9) with acquisition times comparable with conventionally-acquired weighted images. Cumulatively, the use of quantitative images has seen increasing application in a range of neurological conditions, including cancer [56], epilepsy [16,57,58], multiple sclerosis [3,15,59–60] and others [61]; as well as psychiatric conditions, such as autism

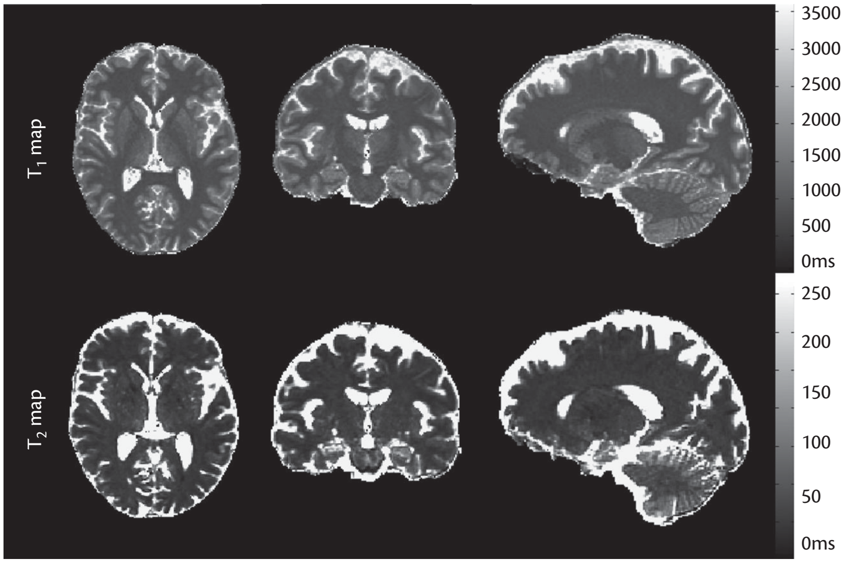

Fig. 2.9 Example tri-plane views of whole-brain (1 × 1 × 1) mm^3 isotropic matched T_1 and T_2 maps acquired at 3T in less than 8 minutes using the DESPOT1 and DESPOT2 techniques (including flip angle field calibration).

spectrum disorders (ASD) [62,63], schizophrenia [64–66], and Alzheimer's disease [67,68]. In addition to these more direct and clinically-focused applications, quantitative relaxometry has also found use in studies of neurodevelopment, brain maturation, and ageing [69–72]. The relative independence of T_1 and T_2 on hardware, scanner manufacturer, and even acquisition parameters, as well as the high intra- and inter-site reliability of relaxometry measures, lends relaxometry to multicentre and longitudinal studies [73]. Such studies are increasingly necessary to accommodate large study populations, or to track disease progression and treatment response.

With *a priori* knowledge of the underlying and intrinsic relaxation parameters, it is also possible to reconstruct conventionally appearing T_1- or T_2-weighted images [74]. Termed 'synthetic imaging,' this approach makes use of calculated T_1 and T_2 maps, substituting these values back into the governing sequence signal equations, and allowing the construction of any arbitrarily-weighted image through the manipulation of chosen acquisition parameters. Exemplified in Fig. 2.10, such synthetic images can closely approximate traditionally acquired images, as well as offer the benefit of removing coil sensitivity profiles [74].

Multiple component relaxation

In the preceding discussion, it was assumed that the relaxation of magnetization within each imaging voxel could be adequately described by a single T_1 and T_2 relaxation constant. However, this assumption ignores the complex geometry and architecture of biological tissue. In tissue such as brain parenchyma, water is highly compartmentalized into anatomical subdomains, each with unique biophysical and biochemical properties. These differing characteristics impart unique T_1, T_2 and T_2^* relaxation properties onto the water protons residing within them. Thus, each anatomical domain has a distinct MR signal signature, with the overall measured signal representing a powder-average of these individual contributions. Furthermore, if the boundaries between these compartments are water permeable, water may readily exchange between them. The end result of this complexity is that signal decay is often ill-described by single T_1 and T_2 values [75].

Multicomponent relaxometry (MCR) analysis (Fig. 2.11) aims to decompose these independent signal contributions for the net measured signal. This approach provides a potential method for investigating sub-voxel tissue microstructure [76–78]. Within brain and spinal cord, MCR analysis of T_2 and, more recently T_1 and , relaxation data has yielded two distinct and reproducible water environments, with one broadly attributed to the less-restricted intra and extra-cellular water; and the other to water trapped within the lipid bilayers of the myelin sheath. The result of MCR analysis can be quantitative measures of these volume fractions, one of which, the myelin water volume fraction, has seen increasing utility in the study of MS and other demyelinating disorders.

While offering insight into sub-voxel tissue microstructure, the presence of multi-component relaxation also introduces a potential confound when performing conventional, 'single-component' relaxation time estimation. Particularly in the case of T_2 mapping, the choice of acquisition parameters (i.e. TE) or sequence design (GRASE echo spacings) can bias the estimated T_2 to either the short- or long-water species.

Water content (or proton density) mapping

Brain tissue is 70–80% water, but this fundamental quantity is often neglected in studies of brain structure and pathology. During development and across lifespan, alterations in brain water content occur [79–82]. Biological tissue undergoes dramatic and sometimes rapid decreases in water content during early maturation, and throughout the first several decades of life, while more gradual decreases in water content occur up until the last decades of life. Many neurological disorders are accompanied by changes in brain water content. For example, MS [83,84], stroke [85], brain tumours [86], and head trauma [87,88] feature changes in water content due to inflammation and/or oedema. Oedema can be hazardous or even lethal due to the associated rise in intracranial pressure [89]. While most brain lesions have increased water content, there is also

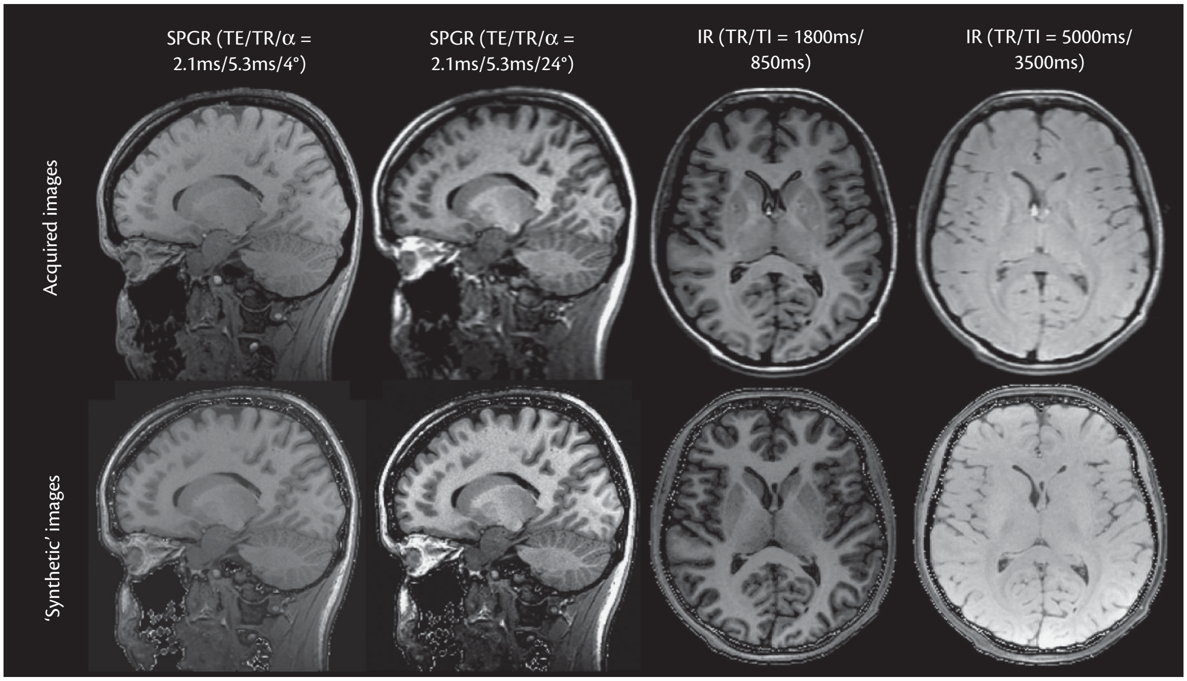
SPGR (TE/TR/α = 2.1ms/5.3ms/4°)
SPGR (TE/TR/α = 2.1ms/5.3ms/24°)
IR (TR/TI = 1800ms/ 850ms)
IR (TR/TI = 5000ms/ 3500ms)
Acquired images
'Synthetic' images

Fig. 2.10 Example comparison of acquired SPGR and IR images versus synthetic images calculated from ***a priori*** acquired T_1 and proton density maps.

evidence that in certain conditions, such as chronic alcoholism [90], the brain can be dehydrated.

Despite the important influence water has on the brain, there is remarkably little literature on the measurement of brain water content *in vivo* and even less on the role of water content in pathology. Since signal in MRI is derived from water, water content can affect many types of contrast and quantitative MR measurements, and is a confounding variable, which is often ignored in these techniques. Accurate measurement of water content could allow changes in microstructure and other variables to be differentiated from changes due to water alone, allowing a more thorough analysis of pathology, and therapies or treatments. Water content measurement is also valuable for spectroscopy, since determining absolute concentrations of metabolites requires calibration to a known standard such as the internal water signal [91].

Accurate water content mapping has proven to be a difficult task, as it generally requires accurate knowledge of the relaxation times, is sensitive to both transmit (B_1^+) and receive (B_1^-) (i.e. main magnetic field and flip angle) inhomogeneity, and relies on normalization to a valid water standard. Using an internal standard such as cerebrospinal fluid (CSF) leads to complications because of flow and long relaxation time that may not be well characterized by the acquisition technique. Using an external water source eliminates artefacts due to flow, and relaxation times can be reduced using doping agents. However, external standards can cause discomfort to the subject, extend the field of view (and thus increase imaging time or voxel size), and require corrections for relaxation effects and temperature differences. They also tend to be situated in regions of especially poor RF homogeneity, making B_1 correction particularly challenging. Water content measurement is even more difficult at higher fields, as B_1 is less uniform and simply using the reciprocity theorem to correct for the receiver coil sensitivity profile does not seem to be as effective [92].

Estimating water content directly from T_1

One popular method for estimating water content uses the linear relationship between $1/T_1$ and the inverse of water content [93–97]. In this model, T_1 in brain is assumed to stem from two different spin populations: 'free water', having a long T_1 relaxation time, and motion restricted 'bound water', said to be loosely hydrogen-bonded to macromolecules and proteins, having a much shorter T_1 [98]. Since the observed longitudinal relaxation is mono-exponential, it is assumed that the resulting total relaxation rate is a weighted average of the two individual compartment relaxation rates, and the spin magnetization exchanges rapidly between these compartments. These assumptions lead to an approximate equation relating water content and T_1: $1/T_1 = A/(\text{water content}) + B$, where A and B are assumed to be constant.

The simplicity of using the inverse of T_1 as a surrogate for water content is attractive, and the linear relationship has been found to hold relatively well in normal brain tissue. However, this technique has some obvious limitations, as T_1 relaxation is also affected by factors other than water content. As was touched on previously, T_1 is influenced by paramagnetic atom (e.g. iron) concentration, the presence of myelin lipids, such as cholesterol, and temperature (to a greater extent than water content). In addition, some studies have found that the simple linear relationship does not hold in the presence of certain pathological processes, such as oedema [99].

Extracting water content from T2* decay

One of the most accurate water content mapping techniques involves rapid collection of T_2^* relaxation data with a multiple echo time gradient echo sequence; Neeb et al. [100,101] introduced this approach using QUTE (Quantitative T_2^* mapping), which is based on a modified EPI read-out scheme that shares similarities with both FLASH and EPI. T_2^* decay data are fitted with a single exponential or 3rd order polynomial, and the acquired curve is used to

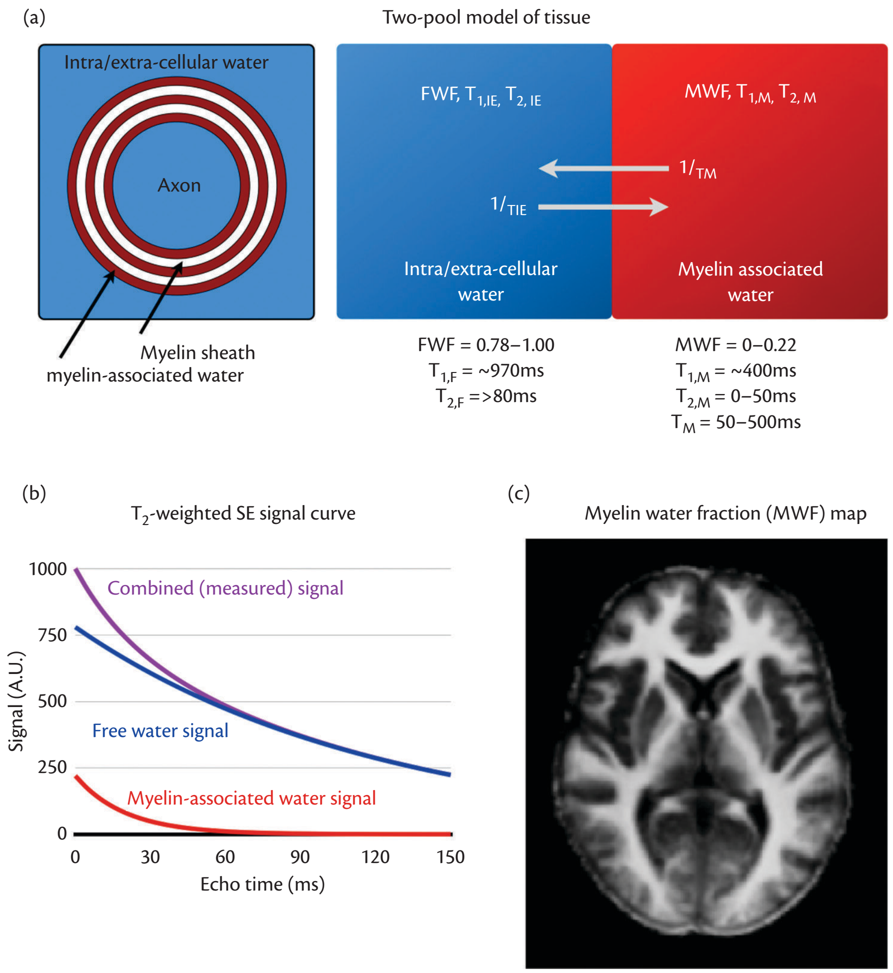
(a)
Two-pool model of tissue
Intra/extra-cellular water
Axon
Myelin sheath
myelin-associated water
FWF, $T_{1,IE}$, $T_{2,IE}$
MWF, $T_{1,M}$, $T_{2,M}$
$1/_{TM}$
$1/_{TIE}$
Intra/extra-cellular water
Myelin associated water
FWF = 0.78–1.00
$T_{1,F}$ = ~970ms
$T_{2,F}$ =>80ms
MWF = 0–0.22
$T_{1,M}$ = ~400ms
$T_{2,M}$ = 0–50ms
T_M = 50–500ms
(b)
T_2-weighted SE signal curve
Combined (measured) signal
Free water signal
Myelin-associated water signal
Signal (A.U.)
1000
750
500
250
0
0
30
60
90
120
150
Echo time (ms)
(c)
Myelin water fraction (MWF) map

Fig. 2.11 *Multicomponent relaxation:* the two-pool model (a) of brain tissue comprises the free intra- and extracellular water (blue), and water trapped between the lipid bilayers of the myelin sheath (red). The measured MR signal contains contributions from each of these water pools (b). MCR aims to reconstruct these individual contributions and quantify the volume of the myelin water pool, termed the myelin water fraction (MWF) (c).

extrapolate the signal to time zero. The signal is then corrected for T_1 saturation effects using T_1 values measured in a separate acquisition (Neeb et al. used an approach termed T1 mapping with partial inversion recovery (TAPIR) [100], which is a variation of the LL method).

B_1 inhomogeneity must also be addressed. Typically B_1^+ variations are corrected using some version of the double angle method [103]. When separate transmit (body) and receive (head) coils are used, B_1^- inhomogeneity can be mapped by comparing images with identical parameters acquired once using the body coil and once using the head coil for reception. The ratio of these images is multiplied by the B_1^+ map to obtain an estimate of B_1^- for the head coil [101].

Finally, corrected proton density is normalized to a reference probe containing pure water placed in the field of view, after correction for temperature differences between the standard and brain [104]. Depending on the choice of T_2^*, T_1, and B_1 mapping techniques, acquisition times for the entire protocol can range from 10 to 20 minutes.

One difficulty with this method is the reliance on accurately fitting the T_2^* decay, which can deviate from mono-exponential behaviour in the presence of magnetic field inhomogeneities or imperfect RF excitation slice profiles. An alternate approach is to employ a very short echo time combined with third order polynomial fitting to extrapolate to time zero. To date, no work using this technique has been published at higher field strength than 1.5T, likely due to the challenges of increased B_1 inhomogeneity. This group has, however, recently introduced a modified gradient echo water content mapping technique, in which the expected correlation between inverse proton density and $1/T_1$ was exploited to correct for residual inhomogeneity at 3T [105].

Variable flip angle techniques

Variable flip angle techniques for T_1 mapping can be extended to quantify proton density [92,106,107]. As defined for equation [3], the multiplication factor ρ is given by

$$\rho = PD \times B_1^- \varsigma \times e^{-\frac{TR}{T_2^*}} \qquad [25]$$

As the other variables in Eqn [25] can be fitted using the approach described in the DESPOT1 section, proton density can be calculated given knowledge of T_2^* and B_1^-. Volz et al. [92,106] estimated T_2^* by acquiring two gradient echo data sets with different echo times. The B_1^- correction implemented by Neeb et al. [101], described earlier, was found to be ineffective at 3T. Instead, a post-processing bias field correction algorithm available in the software SPM can be used, which is based on a probabilistic framework for simultaneous tissue segmentation, registration and correction of a multiplicative bias comprised of low spatial frequencies [108,109].

Corrected proton density was normalized to CSF. The total acquisition time for the water content mapping protocol by Volz et al. is 18 minutes; however, Sabati and Maudsley [107] recently developed an accelerated variant of this technique that covers whole brain in 6.5 minutes.

As this approach is based on the variable flip angle T_1 measurement method, it suffers the same potential pitfalls as described in that section, including requiring accurate knowledge of B_1 inhomogeneities. The bias field correction smooths the signal in the brain based on assumptions of homogeneity in certain tissue classes and, therefore, may not perform well in the presence of brain abnormalities, which accompany many pathologies. Additionally, because the technique was specifically designed to remove signal non-uniformities across the brain, it is questionable whether it would give reliable results in external water standards, which is probably the reason that only CSF has been used for normalization. To address this issue, Volz developed another method for B_1^- inhomogeneity correction based on pseudo-proton density maps produced from the linear relationship between inverse water content and T_1 [106]. B_1^- maps are approximated by dividing proton density by the pseudo-proton density maps. This procedure can be performed in regions of 'normal brain tissue', and B_1^- maps can be extrapolated to other areas of the brain using 3D polynomial fitting; however, it is still limited by its reliance on normal brain tissue values, which may not be present, and the accuracy of extrapolation.

Conclusions

As described, quantitative T_1, T_2, and water content imaging offers a number of advantages over established and conventional-weighted imaging approaches. These advantages include simplicity of analysis and interpretation of identified changes. Recent acquisition techniques coupled with appreciation of, and correction for, relevant sources of error have made the acquisition of whole-brain high spatial resolution quantitative T_1, T_2, and proton density maps a clinically feasible alternative to conventional T_1, T_2, or proton density-weighted imaging. While analysis of these maps is in its infancy, and new techniques will be needed to fully exploit the image contrast and noise characteristics present in quantitative images, inspiration can be drawn from other quantitative imaging techniques, such as proton emission tomography (PET), to glimpse the rich information contained within these data. Furthermore, when combined with alternative MR-based imaging techniques, including diffusion tensor MRI and MR spectroscopy, a more complete picture of brain structure, architecture and metabolism may be formed.

Acknowledgements

This work was supported by the National Institutes of Mental Health (R01 MH087510) and the Milan & Maureen Ilich Foundation.

References

1. Alexander AL, Hurley SA, Samsonov AA, et al. (2011). Characterization of cerebral white matter properties using quantitative magnetic resonance imaging stains. *Brain Connectivity*, **1**, 423–46.
2. Deoni, S.C., Williams SC, Jezzard P, et al. (2008). Standardized structural magnetic resonance imaging in multicentre studies using quantitative T1 and T2 imaging at 1.5T. *NeuroImage*, **40**, 662–71.
3. MacKay AL, Vavasoiur IM, Rauscher A, et al. (2009). MR relaxation in multiple sclerosis. *Neuroimaging Clinics of North America*, **19**, 1–26.
4. Bloembergen N, Purcell EM, and Pound RV. (1948). Relaxation effects in nuclear magnetic resonance absorption. *Physical Review*, **73**, 679–712.
5. Paus T, Collins DL, Evans AC, et al. (2001). Maturation of white matter in the human brain: a review of magnetic resonance studies. *Brain Research Bulletin*, **54**, 255–66.
6. Deoni SC, Dean DC, O'Muircheartaigh J, et al. (2012). Investigating white matter development in infancy and early childhood using myelin water fraction and relaxation time mapping. *NeuroImage*, **63**, 1038–53.
7. Koenig SH, Brown RD, Spiller M, et al. (1990). Relaxometry of brain: why white matter appears bright in MRI. *Magnetic Resonance Medicine*, **14**, 482–95.
8. Gelman N, Ewing JR, Gorell JM, et al. (2001). Interregional variation of longitudinal relaxation rates in human brain at 3.0t: relation to estimated iron and water contents. *Magnetic Resonance in Medicine*, **45**, 71–9.
9. Gelman N, Gorell JM, Barker PB, et al. (1999). MR imaging of the human brain at 3.0T: preliminary report on transverse relaxation rates and relation to estimated iron content. *Radiology*, **210**, 759–67.
10. Damadian RV. (1971) Tumor detection by nuclear magnetic resonance. *Science*, **171**, 1151–3.
11. Naoko S, Sakai O, Ozonoff A, et al. (2009). Relaxo-volumetric multispectral quantitative magnetic resonance imaging of the brain over the human lifespan: global and regional aging patterns. *Magnetic Resonance Imaging*, **27**, 895–906.
12. Williams LA, Gelman N, Picot PA, et al. (2005). Neonatal brain: regional variability of *in vivo* MR imaging relaxation rates at 3.0T—initial experience. *Radiology*, **235**, 595–603.
13. Hoque R, Ledbetter C, Gonzalez-Toledo E, et al. (2007). The role of quantitative neuroimaging indices in the differentiation of ischemia from demyelination: an analytical study with case presentation. *International Review of Neurobiology*, **79**, 491–519.
14. Li Y, Srinivasan R, Ratiney H, et al. (2008). Comparison of T1 and T2 metabolite relaxation times in glioma and normal brain at 3T. *Journal of Magnetic Resonance Imaging*, **28**, 342–50.
15. Stevenson VL, Parker GJM, Barker GJ, et al. (2000). Variations in T1 and T2 relaxation times of normal appearing white matter and lesions in multiple sclerosis. *Journal of Neurological Sciences*, **178**, 81–7.
16. Jackson GD, Connelly A, Duncan JS, et al. (1993). Detection of hippocampal pathology in intractable partial epilepsy: increased sensitivity with qualitative magnetic resonance T2 relaxometry. *Neurology*, **43**, 1793–9.
17. IIes L, Pfluger H, Phrommintikul A, et al. (2008). Evaluation of diffuse myocardial fibrosis in heart failure with cardiac magnetic resonance contrast-enhanced T1 mapping. *Journal of the American College of Cardiology*, **52**, 1574–80.
18. Tiderius CJ, Olsson LE, Leander P, et al. (2003). Delayed gadolinium-enhanced MRI of cartilage (dGEMRIC) in early knee osteoarthritis. *Magnetic Resonance Medicine*, **49**, 488–92.
19. Venkatesan R, Lin W, Gurleyik K, et al. (2000). Absolute measurement of water content using magnetic resonance imaging preliminary findings in an *in vivo* focal ischemic rat model. *Magnetic Resonance Medicine*, **43**, 146–50.
20. Clare S, and Jezzard P. (2001). Rapid T1 mapping using multislice echo planar imaging. *Magnetic Resonance Medicine*, **45**, 630–4.
21. Zhang YT, Yeung HN, Carson PL, et al. (1992). Experimental analysis of T1 imaging using a single-scan multiple-point, inversion-recovery technique. *Magnetic Resonance in Medicine*, **25**, 337–43.
22. Henderson E, McKinnon G, Lee TY, et al. (1999). A fast 3D Look–Locker method for volumetric T1 mapping. *Magnetic Resonance in Medicine*, **17**, 1163–71.

23. Parker GJ, Barker GJ, and Tofts PS. (2001). Accurate multislice gradient echo T1 measurement in the presence of non-ideal RF pulse shape and RF field nonuniformity. *Magnetic Resonance in Medicine*, **45**, 838–45.
24. Pauly P, Le Roux P, Nishimura D, et al. (1991). Parameter relations for the Shinnar-Le Roux selective excitation pulse design algorithm. *IEEE Transactions on Medical Imaging*, **10**, 53–65.
25. Madhuranthakam AJ, Busse RF, Brittain JH, et al. (2008). B1-insensitive fast spin-echo using adiabatic square wave enabling of the echo train (SWEET) excitation. *Magnetic Resonance in Medicine*, **59**, 1386–93.
26. Garwood M, Ugurbil K, Rath AR, et al. (1989). Magnetic resonance imaging with adiabatic pulses using a single surface coil for RF transmission and signal detection. *Magnetic Resonance in Medicine*, **9**, 25–34.
27. Insko EK, and Bolinger L. (1993). Mapping of the radiofrequency field. *Journal of Magnetic Resonance Series A*, **103**, 82–5.
28. Carr HY. (1958). Steady-state free precession in nuclear magnetic resonance. *Physics Review*, **112**, 1693–701.
29. Denolin V, Azizieh C, and Metens T. (2005). New insights into the mechanisms of signal formation in RF-spoiled gradient echo sequences. *Magnetic Resonance in Medicine*, **54**, 937–54.
30. Lin W, and Song HK. (2009). Improved signal spoiling in fast radial gradient echo imaging: applied to accurate T1 mapping and flip angle correction. *Magnetic Resonance in Medicine*, **62**, 1185–94.
31. Messroghli DR, Radjenovic A, Kozerke S, et al. (2004). Modified Look–Locker inversion recovery (MOLLI) for high resolution T1 mapping of the heart. *Magnetic Resonance in Medicine* **52**, 141–6.
32. Messroghli DR, Greiser A, Frohlich M, et al. (2007). Optimization and validation of a fully-integrated pulse sequence for modified Look–Locker inversion recovery (MOLLI) T1 mapping of the heart. *Journal of Magnetic Imaging*, **26**, 1081–6.
33. Gai ND, and Butman JA. (2009). Modulated repetition time Look–Locker (MORTLL): a method for rapid high resolution three-dimensional T1 mapping. *Journal of Magnetic Imaging*, **30**, 640–8.
34. Christensen KA, Grand DM, Schulman EM, et al. (1974). Optimal determination of relaxation times of Fourier transform nuclear magnetic resonance. Determination of spin-lattive relaxation times in chemically polarized species. *Journal of Physical Chemistry*, **78**, 1971–7.
35. Homer J, and Beevers MS. (1985). A re-evaluation of a rapid "new" method for determining NMR spin-lattice relaxation times. *Journal of Magnetic Resonance*, **63**, 287–97.
36. Wang HZ, Riederer SJ, and Lee JN. (1987). Optimizing the precision in T1 relaxation estimation using limited flip angles. *Magnetic Resonance Medicine*, **5**, 399–416.
37. Homer J, and Roberts JK. (1990). Routine evaluation of Mo ratios and T1 values from driven equilibrium NMR spectra. *Journal of Magnetic Resonance*, **87**, 265–72.
38. Deoni SCL, Rutt BK, and Peters TM. (2003). Rapid combined T1 and T2 mapping using gradient recalled acquisition in the steady state. *Magnetic Resonance in Medicine*, **49**, 515–26.
39. Deoni SCL, Peters TM, and Rutt BK. (2004). Determination of optimal angles for variable nutation proton magnetic spin-lattice, T1, and spin-spin, T2, relaxation times measurement. *Magnetic Resonance in Medicine*, **51**, 194–9.
40. Chang LC, Koay CG, Basser PJ, et al. (2008). Linear least-squares method for unbiased estimation of T1 from SPGR signals. *Magnetic Resonance in Medicine*, **60**, 496–501.
41. Denolin V, Azizieh C, and Metens T. (2005). New insights into the mechanisms of signal formation in RF spoiled gradient echo sequences. *Magnetic Resonance in Medicine*, **54**, 937–54.
42. Lin W, and Song HK. (2009). Improved signal spoiling in fast radial gradient echo imaging: applied to accurate T1 mapping and flip angle correction. *Magnetic Resonance in Medicine*, **62**, 1185–94.
43. Preibisch C, and Deichmann R. (2009). Influence of RF Spoiling on the Stability and Accuracy of T1 Mapping Based on Spoiled FLASH with Varying Flip Angles. *Magnetic Resonance in Medicine*, **61**, 125–35.
44. Deoni SC. (2009). Transverse relaxation time (T2) mapping in the brain with off-resonance correction using phase-cycled steady-state free precession. *Journal of Magnetic Resonance Imaging*, **30**, 411–17.
45. Zur Y, Wood ML, and Neuringer LJ. (1990). Motion-insensitive steady-state free precession imaging. *Magnetic Resonance in Medicine*, **16**, 444–59.
46. Gloor M, Scheffler K, and Bieri O. (2008). Quantitative magnetization transfer imaging using balanced SSFP. *Magnetic Resonance in Medicine*, **60**, 691–700.
47. Crooijmans HJ, Gloor M, Bieri O, et al. (2011). Influence of MT effects of T2 quantification with 3D balanced steady-state free precession imaging. *Magnetic Resonance in Medicine*, **65**, 195–201.
48. Crooijmans HJ, Scheffler K, and Bieri O. (2011). Finite RF pulse correction on DESPOT2. *Magnetic Resonance in Medicine*, **65**, 858–62.
49. Bieri O, and Scheffler K. (2007). Optimized balanced steady-state free precession magnetization transfer imaging. *Magnetic Resonance in Medicine*, **58**, 511–18.
50. Garcia M, Gloor M, Radue EW, et al. (2012). Fast high resolution brain imaging with balanced SSFP: interpretation of quantitative magnetization transfer towards simple MTR. *NeuroImage*, **59**, 2020–211.
51. Oshio K, and Feinberg DA. (1991). GRASE (gradient and spin echo) imaging: a novel fast MRI technique. *Magnetic Resonance in Medicine*, **20**, 344–9.
52. Quaia E, Toffanin R, Guglielmi G, et al. (2008). Fast T2 mapping of the patellar articular cartilage with gradient and spin echo magnetic resonance imaging at 1.5T: validation and initial clinical experience in patients with osteoarthritis. *Skeletal Radiology*, **37**, 511–17.
53. Scheffler K, and Hennig J. (2001). T1 quantification with inversion recovery TrueFISP. *Magnetic Resonance in Medicine*, **45**, 720–3.
54. Warntjes JB, Leinhard OD, West J, et al. (2008). Rapid magnetic resonance quantification on the brain: optimization for clinical usage. *Magnetic Resonance in Medicine*, **60**, 320–9.
55. Ma D, Gulani V, Seiberlich N, Lui K, et al. (2013). Magnetic resonance fingerprinting. *Nature*, **495**, 187–92.
56. Pathak AP, Gimi B, Glunde K, et al. (2004). Molecular and functional imaging of cancer: advances in MRI and MRS. *Methods in Enzymology*, **386**, 1–58.
57. Rugg-Gunn FJ, Boulby PA, Symms MR, et al. (2005). Whole-brain T2 mapping demonstrates occult abnormalities in focal epilepsy. *Neurology*, **64**, 318–25.
58. Van Paesschen W, Duncan JS, Stevens JM, et al. (1997). Etiology and early prognosis of newly diagnosed partial seizures in adults: a quantitative hippocampal MRI study. *Neurology*, **49**, 753–7.
59. Manfredonia F, Ciccarelli O, Khaleeli Z, et al. (2007). Normal appearing brain T1 relaxation time predicts disability in early primary progressive multiple sclerosis. *Archives of Neurology*, **64**, 411–15.
60. Ropele S, Strasser-Fuchs S, Augustin M, et al. (2000). A comparison of magnetization transfer ratio, magnetization transfer rate, and the native relaxation time of water protons related to relapsing-remit- ting multiple sclerosis. *AJNR American Journal of Neuroradiology*, **21**, 1885–9.
61. Vymazal J, Righini A, Brooks RA, et al. (1999). T1 and T2 in the brain of healthy subjects, patients with Parkinson disease, and patients with multiple system atrophy: relation to iron content. *Radiology*, **211**, 489–95.
62. Hendry J, DeVito T, Gelman N, et al. (2006). White matter abnormalities in autism detected through transverse relaxation time imaging. *NeuroImage*, **29**, 1049–57.
63. Petropoilos H, Friedman SD, Shaw DWW, et al. (2006). Gray matter abnormalities in autism spectrum disorder revealed by T2 relaxation. *Neurology*, **67**, 632–6.
64. Supprian T, Hofmann E, Warmuth-Metz M, et al. (1997). MRI T2 relaxation times of brain regions in schizophrenic patients and control subjects. *Psychiatry Research: Neuroimaging*, **75**, 173–82.
65. Kalus P, Slotboom J, Gallinat J, et al. (2005). The amygdala in schizophrenia: a trimodal magnetic resonance imaging study. *Neuroscience Letters*, **375**, 151–6.
66. Walerfang M, Wood SJ, Velakoulis D, et al. (2006). Neuropathological, neurogenetic and neuroimaging evidence for white matter pathology in schizophrenia. *Neuroscience & Behavioural Reviews*, **30**, 918–48.
67. Bauer CM, Jara H, and Killioany R. (2010). White brain quantitative T2 MRI across multiple scanners with dual echo FSE: applications to AD, MCI and normal aging. *NeuroImage*, **52**, 508–14.

68. Ramani A, Jensen JH, and Helpern JA. (2006). Quantitative MR imaging in Alzheimer disease. *Radiology*, **241**, 26–44.
69. Hasan KM, Wallmuni IS, Kramer LA, et al. (2010). Human brain atlas-based volumetry and relaxometry: application to healthy development and natural aging. *Magnetic Resonance Medicine*, **64**, 1382–9.
70. Evans AC. (2006). The NIH Study of Normal Brain Development. *NeuroImage*, **30**, 184–202.
71. Deoni SCL, Mercure E, Blasi A, et al. (2011). Mapping infant brain myelination with magnetic resonance imaging. Journal of Neuroscience, **31**, 784–91.
72. Deoni SCL, Dean DC, O'Muircheartaigh J, et al. (2012). Investigating white matter development in infancy and early childhood using myelin water fraction and relaxation time mapping. *NeuroImage*, **15**, 1038–53.
73. Deoni SCL, Williams SCR, Jezzard P, et al. (2008). Standardized structural magnetic resonance imaging in multicentre studies using quantitative T1 and T2 imaging at 1.5T. *NeuroImage*, **40**, 662–71.
74. Deoni SC, Rutt BK, and Peters TM. (2006). Synthetic T1-weighted brain image generation with incorporated coil intensity correction using DESPOT1. *Magnetic Resonance Imaging*, **24**, 1241–8.
75. Whittall KP, MacKay AL, and Li DKB. (1999). Are mono-exponential fits to a few echoes sufficient to determine T2 relaxation for *in vivo* human brain? *Magnetic Resonance Medicine*, **43**, 1255–7.
76. MacKay A, Laule C, Vavasour I, et al. (2006). Insights into brain microstructure from the T2 distribution. *Magnetic Resonance Imaging*, **24**(4), 515–25.
77. Kroeker RM, and Henkelman RM. (1991). Analysis of biological NMR relaxation data with continuous distributions of relaxation times. *Journal of Magnetic Resonance*, **69**, 218–35.
78. Menon RS, Rusinko MS, and Allen PS. (1991). Multiexponential proton relaxation in model cellular systems. *Magnetic Resonance in Medicine*, **20**, 196–213.
79. Iglesias JE, Konukoglu E, Zkic D, et al. (2013). Is synthesizing MRI contrast useful for inter-modality analysis. *Medical Image Computing and Computer-Assisted Intervention*, **16**, 631–8.
80. Chang L, Ernst T, Poland RE, et al. (1996). *In vivo* proton magnetic resonance spectroscopy of the normal aging human brain. *Life Sciences*, **58**, 2049–56.
81. Neeb H, Zilles K, and Shah NJ. (2006). Fully-automated detection of cerebral water content changes: study of age- and gender-related H2O patterns with quantitative MRI. *NeuroImage*, **29**, 910–22.
82. Holland BA, Haas DK, Norman D, et al. (1986). MRI of normal brain maturation. AJNR American Journal of Neuroradiology, **7**, 201–8.
83. Laule C, Vavasour IM, Moore GRW, et al. (2004). Water content and myelin water fraction in multiple sclerosis: a T2 relaxation study. *Journal of Neurology*, **251**, 284–93.
84. Tourtellotte W, and Parker J. (1968). Some spaces and barriers in postmortem multiple sclerosis. *Progress in Brain Research*, **29**, 493–525.
85. Katzman R, Clasen R, Klatzo I, et al. (1977). Report of Joint Committee for Stroke Resources. IV. Brain edema in stroke. *Stroke*, **8**, 512–40.
86. Papadopoulos MC, Saadoun S, Binder DK, et al. (2004). Molecular mechanisms of brain tumor edema. *Neuroscience*, **129**, 1009–18.
87. Tornheim PA, and McLaurin RL. (1981). Acute changes in regional brain water content following experimental closed head injury. *Journal of Neurosurgery*, **55**, 407–13.
88. Unterberg AW, Stover J, Kress B, et al. (2004). Edema and brain trauma. *Neuroscience*, **129**, 1019–27.
89. Kamman RL, Go KG, Brouwer W, et al. (1988). Nuclear magnetic resonance relaxation in experimental brain edema: effects of water concentration, protein concentration, and temperature. *Magnetic Resonance Medicine*, **6**, 265–74.
90. Wiese JG, Shlipak MG, and Browner WS. (2000). The alcohol hangover. *Annals of Internal Medicine*, **132**, 897–902.
91. Christiansen P, Toft PB, Gideon P, et al. (1994). MR-visible water content in human brain: a proton MRS study. *Magnetic Resonance Imaging*, **12**, 1237–44.
92. Volz S, Nöth U, and Deichmann R. (2012). Correction of systematic errors in quantitative proton density mapping. *Magnetic Resonance in Medicine*, 2012; 68: 74–85.
93. Fatouros PP, and Marmarou A. (1999). Use of magnetic resonance imaging for *in vivo* measurements of water content in human brain: method and normal values. *Journal of Neurosurgery*, **90**, 109–15.
94. Fatouros PP, Marmarouk A, Kraft KA, et al. (1991) *In vivo* brain water determination by T1 measurements: effect of total water content, hydration fraction, and field strength. *Magnetic Resonance in Medicine*, **17**, 402–13.
95. Kamman RL, Go KG, and Berendsen HJ. (1990). Proton-nuclear magnetic resonance relaxation times in brain edema. *Advances in Neurology*, **52**, 401–5.
96. Kato H, Kogure K, Ohtomo H, et al. (1986). Characterization of experimental ischemic brain edema utilizing proton nuclear magnetic resonance imaging. *Journal of Cerebral Blood Flow & Metabolism*, **6**, 212–21.
97. Fu Y, Tanaka K, and Nishimura S. (1990). Evaluation of brain edema using magnetic resonance proton relaxation times. *Advances in Neurology*, **52**, 165–76.
98. Fullerton GD, Potter JL, and Dornbluth NC. (1982). NMR relaxation of protons in tissues and other macromolecular water solutions. *Magnetic Resonance Imaging*, **1**, 209–26.
99. Bederson JB, Bartkowski HM, Moon K, et al. (1986). Nuclear magnetic resonance imaging and spectroscopy in experimental brain edema in a rat model. *Journal of Neurosurgery*, **64**, 795–802.
100. Neeb H, Zilles K, and Shah NJ. (2006). A new method for fast quantitative mapping of absolute water content *in vivo*. *NeuroImage*, **31**, 1156–68.
101. Neeb H, Ermer V, Stocker T, et al. (2008). Fast quantitative mapping of absolute water content with full brain coverage. *NeuroImage*, **42**, 1094–109.
102. Shah NJ, Zaitsev M, Steinhoff S, et al. (2001). A new method for fast multi-slice T1 mapping. *NeuroImage*, **14**, 1175–85.
103. Stollberger R, and Wach P. (1996). Imaging of the active B1 field *in vivo*. *Magnetic Resonance in Medicine*, **35**, 246–51.
104. Tofts PS. (2003). *Quantitative MRI of the brain: measuring changes caused by disease*. Chichester: Wiley.
105. Abbas Z, Gras V, Möllenhoff K, et al. (2014). Analysis of proton-density bias corrections based on T1 measurement for robust quantification of water content in the brain at 3 Tesla. *Magnetic Resonance in Medicine*, **72**, 1735–45.
106. Volz S, Nöth U, Jurcoane A, et al. (2012). Quantitative proton density mapping: correcting the receiver sensitivity bias via pseudo proton densities. *NeuroImage*, **63**, 540–52.
107. Sabati M and Maudsley AA. (2013). Fast and high-resolution quantitative mapping of tissue water content with full brain coverage for clinically-driven studies. *Magnetic Resonance in Medicine*, **31**: 1752–9.
108. Ashburner J, and Friston KJ. (2005). Unified segmentation. *NeuroImage*, **26**, 839–51.
109. Weiskopf N, Lutti A, Helms G, et al. (2011). Unified segmentation based correction of R1 brain maps for RF transmit field inhomogeneities (UNICORT). *NeuroImage*, **54**, 2116–24.

CHAPTER 3

Magnetic resonance spectroscopy

Christoph Juchem and Daniel Pelletier

Introduction

The human brain is a highly dynamic and complex chemical environment in which metabolic homeostasis and brain function rely on a sophisticated interplay of a wealth of neurochemicals. The communication between neurons, for instance, involves the release of neurotransmitters and the concomitant energy requirement is reflected by the concentration of related metabolites. Quantitative information on the involved substances is therefore necessary to study these processes and to understand the underlying mechanisms. More importantly, a number of neurological dysfunctions and clinical conditions are reflected by the tissue's neurochemical composition.

Magnetic resonance spectroscopy (MRS) allows the detection and quantification of chemical compounds from localized portions of the living tissue, e.g. the brain, in a non-invasive fashion. It thereby provides a powerful tool to assess key aspects of metabolism, such as glucose utilization, glutamine synthesis rate or tricarboxylic acid cycle (TCA or Krebs cycle) cycle fluxes *in vivo* [1]. In fact, an entire family of MRS methods has been developed to study various aspects of the brain's neuro-energetics and neurotransmitter cycling [2]. In the clinics, the repertoire of measurable compounds, together with the quantitative character of the derived information makes MRS a versatile tool for the identification of clinical conditions, for longitudinal patient monitoring, and for treatment efficacy assessment. The goal of this chapter is to summarize the basic concepts of commonly applied MRS methods, to describe their potential, and to discuss limitations from a clinical perspective.

In vivo MR spectroscopy

Atomic nuclei with a magnetic moment (or 'spin') can exhibit resonance behaviour in a magnetic field. This magnetic resonance effect is governed by the Larmor equation as a simple linear relationship between the magnetic field B perceived by the nucleus and the resultant resonance frequency ω:

$$\omega = -\gamma B$$

The relative scaling, γ, the so-called gyromagnetic ratio, is a nucleus-specific constant. The hydrogen nucleus ^{1}H (i.e. a proton) is the prime example for an MR-sensitive isotope, as ^{1}H resonance signals from hydrogen nuclei bound in tissue water provide the basis for magnetic resonance imaging (MRI) of the human body. When a human subject is placed in the scanner of a given field strength, one could assume that all of the body's ^{1}H nuclei exhibit the same resonance frequency. In reality, however, minute frequency variations are observed, depending on the molecular structure go the atomic nucleus is embedded in. The field variations causing these frequency shifts are based on two different effects—the electronic, i.e. chemical, environment around the atomic nucleus at hand results in a so-called 'chemical shift' and the correlation of different nuclei of the same molecule mediated through their binding electrons is referred to as dipolar or J-coupling. Chemical shift and J-coupling critically rely on the molecules' chemical and geometric composition. As such, their measurement provides a wealth of intramolecular, microscopic information from a relatively simple, 'macroscopic' MRS experiment. Notably, chemical shift and J-coupling effects are the basis for the key role MRS is playing in structural and analytical chemistry. Although chemical shift and J-coupling have been discovered already in the 1950s, it was not until more than 20 years later that MRS was applied to identify and quantify biochemicals in living cells [3] and eventually *in vivo* [4]. With this paradigm shift, the goal was no longer to study the physico-chemical properties of substances, but to use the knowledge on the substance-specific spectroscopic patterns, i.e. their spectroscopic fingerprint, to separate and quantify these substances *in vivo*. The first clinical applications of MRS, such as the identification of metabolites as surrogate markers for neuronal and glial disorders [5], opened the door to the wealth of clinical MRS methods that are available today.

MR spectroscopy allows the non-invasive quantification of neurochemicals that contain MR-sensitive isotopes (e.g. ^{1}H). Hydrogen is prevalent in most metabolites of the human brain and the ^{1}H nucleus is the most relevant isotope for *in vivo* MR spectroscopy. The gyromagnetic ratio of ^{1}H is highest for all stable isotopes and, therefore, its sensitivity in MR experiments is higher than for any other nucleus. Furthermore, the natural abundance of the ^{1}H nucleus is almost 100%. Although a series of brain metabolites can be identified with ^{1}H MRS [6], the number of substances assessable under *in vivo* conditions does not exceed 15–20 [7–9] and is typically well below. Further MR-visible isotopes with biochemical relevance have been shown to provide valuable information on tissue physiology and biochemistry. Phosphorus (^{31}P) MRS, for instance, allows the quantification of key components related to energy metabolism (adenosintriphosphate (ATP), adenosindiphosphate (ADP), and phosphocreatine) and to study, e.g. bioenergetic deficits, in response to disease [10]. MR spectroscopy employing the ^{13}C isotope enables the study of Krebs cycle intermediates and the predictable transfer of infused ^{13}C-label between specific positions of the carbon chains of these intermediates stands out by providing turnover rates and metabolic fluxes [2]. Cellular proliferation is accompanied by alterations in sodium/hydrogen exchange kinetics and sodium content has been linked to tumour growth and malignancy. More specifically, elevated sodium (^{23}Na) concentrations have been found in human brain tumours when mapped with magnetic resonance spectroscopic imaging (MRSI) techniques [11]. Today's clinical MR spectroscopy, however, mostly relies on ^{1}H, whereas other nuclei are predominantly used in basic and preclinical research. The need for custom-made hardware and specialized MRS methods for non-^{1}H MRS might be reasons why these applications have not prevailed yet in clinical practice. This review focuses on the clinical applications of ^{1}H MRS. For a detailed discussion of MRS employing other isotopes, the reader is referred to the literature.

Magnetic resonance spectroscopy methods

Basics of MR spectroscopy

The goal of *in vivo* ^{1}H MRS is to quantify biochemical substances in a non-invasive fashion. In general, the signal amplitudes of an MRS acquisition and the resultant peaks in the reconstructed spectrum, directly scale with the number of resonating nuclei and the substance amount seen by the MRS experiment. As such, spectral peaks and patterns provide a direct measure for the concentration of the metabolite at hand. Water is by far the most prevalent ^{1}H-containing compound in human tissue and therefore contributes the largest part of the MR signal (Fig. 3.1a). Since the water concentration itself is of little clinical relevance, its signal is typically minimized in MRS experiments to better reveal the metabolites-of-interest (Fig. 3.1b).

A prominent limitation of ^{1}H MRS of brain metabolites is the small frequency spread between spectral peaks. This limited spectral dispersion leads to severe spectral overlap of the observed patterns and poses a significant challenge for the identification and separation of the individual compounds. Notably, the problem of spectral overlap is further complicated *in vivo* by limited magnetic field homogeneity and the resultant broadening of spectral lines. Moreover, adequate signal-to-noise ratio (SNR) is particularly relevant when partially overlapping spectral structures are to be disentangled, as is typically the case for ^{1}H MRS. Fortunately, the selection of accessible brain metabolites includes many key players of the brain's neurochemistry (some of which are described in this review). The majority of chemical compounds present in the brain, however, have concentrations well below the detection limit. Dopamine levels in human brain tissue, for instance, are in the micromolar range which precludes the quantification of this important neurotransmitter with MRS methods. Stronger scanner B_0 fields increase the available MR sensitivity and SNR, and can improve the detection limit somewhat [12]. Within an experiment, the attainable SNR can be increased when larger volumes are considered as the available signals scale with the number of covered spins and, therefore the amount of tissue exhibiting a given substance. The concomitant reduction of spatial (and therefore anatomic/functional) specificity, however, is an obvious caveat to this approach. Alternatively, SNR improvements can be obtained by combining the data from various repetitions. As such, SNR gains of the square root of the number of repeats are achieved. In practice, however, the applicability of this approach is limited by the progressively larger time penalty per additional SNR gain. Most MRS applications apply data summation for SNR/sensitivity improvement, but the number of repeats rarely exceeds 128 or 256 averages. Although the approaches discussed can alleviate some of the burdens of low MR sensitivity; in reality, they all have obvious limitations and are not able to fundamentally overcome the millimolar detection limit of ^{1}H MRS.

Chemical shift

Based on the Larmor condition, the resonance frequency of a nucleus is determined by its gyromagnetic ratio and the magnetic field it is exposed to. If the nucleus is not free, but part of a chemical compound, in most cases, a shielding of the external field B_0 by the surrounding electrons is observed. The change of the nucleus' MR frequency due to this screening is termed 'chemical shift' and provides the main concept of MR spectroscopy. The effect of electronic shielding is field dependent and so are the resultant absolute frequency shifts in Hertz. ^{1}H chemical shifts observed *in vivo* are in the order of parts per million (ppm) and typically referenced using internal standards such as the 2.01 ppm methyl singlet of N-acetyl aspartate (NAA). Several ^{1}H down-field resonances (found at higher ppm values) have been reported [13], however, clinical MRS largely relies upon the up-field resonances covering the 1–4 ppm range.

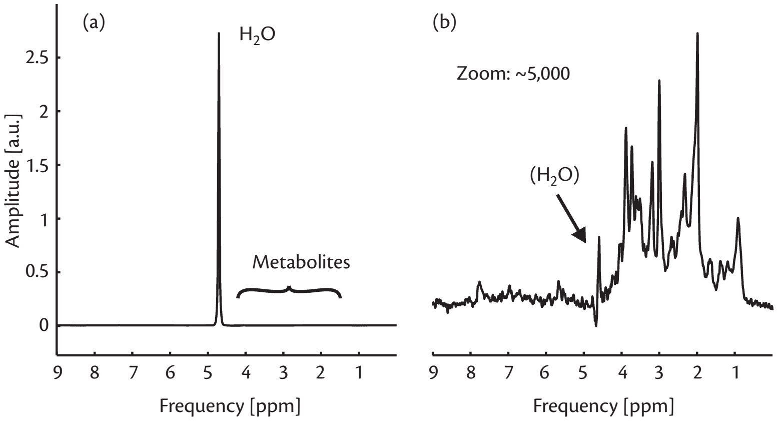

Fig. 3.1 The role of water suppression for *in vivo* ^{1}H MR spectroscopy of the human brain. (a) The water content in human brain tissue largely exceeds the concentrations of other observable substances and dominates the appearance of the spectrum. (b) Suppression of the water signal allows an unobstructed view on the neurochemicals-of-interest.

Scalar coupling

Nuclei in a molecule may not only couple directly, but also indirectly via their chemical bindings. Since the linkage of these nuclear spins is provided by their binding electrons, the interaction has been named J-coupling. If the chemical shift differences of a compound are large compared with its J-coupling constants, the spectrum is considered to be of first order. Spectra, for which the J-couplings and the differences in chemical shift are of the same order of magnitude, are considered second order. While absolute values of the chemical shift depend on the magnetic field strength, J-couplings do not, which leads to a strong field dependence of the overall MR spectrum. Many ^{1}H brain metabolites exhibit J-couplings (glutamate (Glu), glutamine (Gln)). Strong scanner B_0 fields are also advantageous to improve their spectral dispersion and to simplify spectral patterns by the reduction of second order coupling effects.

Quantification of magnetic resonance spectra

The signal of an MRS resonance, corresponding to the area of its spectral peak, is proportional to the abundance of the resonating nucleus and, thereby, allows the quantification of its host compound. If the chemical has more than one resonating nucleus, more than one peak is observed in the spectrum and the concomitant redundancy in information can be used to improve the accuracy of the substance quantification. The metabolite-specific combination of chemical shifts and J-couplings of the neurochemicals gives rise to unique spectral patterns similar to a human finger print. ^{1}H MR spectra acquired from the human brain *in vivo*, however, contain the combined information from all observable metabolites as the sum of their individual spectroscopic patterns (Fig. 3.1), which need to be disentangled to derive the individual metabolite concentrations. The limited spectral dispersion (i.e. the spread of the observed resonance peaks) for ^{1}H MRS [6] and the limited (broad) line widths achievable *in vivo* [14] lead to severe spectral overlap. In practice, the reliable identification of individual metabolites proves difficult despite the principle specificity of their spectral patterns. Different ways have been proposed to assess spectral composites of *in vivo* ^{1}H MR spectra of brain metabolites and to achieve a reliable quantification either in the time (or measurement) domain [15] or, equivalently, in the spectral domain (Fig. 3.2) [16].

Since the experimentally measured spectrum is considered the sum of the individual metabolite contributions, any quantification method aims at reproducing the overall spectrum by an appropriately scaled linear combination of the potential, individual metabolite contributions [17,18]. The necessary scaling corresponds to the metabolite concentrations. Deconvolution and, therefore quantification errors, are typically estimated as Cramér–Rao lower bounds (CRLB), which describe the lowest possible standard deviations of all unbiased model parameter estimates [19]. The analysis requires prior knowledge of the basis spectra, i.e. the specific spectral patterns of the potentially detected metabolites. This information can be derived experimentally by MRS measurements of metabolite solutions or by numerical simulation based on the spectroscopic characteristics of the metabolites, i.e. the chemical shifts, the J-couplings, and the number and type of nuclei. Notably, basis spectra are specific for the MRS experiment at hand, since their appearance relies on the scanner B_0 field strength and details of the MRS experiment, such as radiofrequency (RF) pulses, gradient scheme, or sequence timing. The exact magnitude of the spectral metabolite signals depends on experimental parameters such as RF coil performance, voxel geometry, B_0 field strength, receive channel characteristics, and MR sequence, including the adjustment quality. The overall correction factor to compensate these effects can be expected to be identical for all metabolites. Therefore, if this correction can be derived from a quantitative standard, i.e. if the concentration of at least one of the observed substances is known, it can be applied to all other metabolites to derive absolute tissue concentrations. Mostly, the concentrations from NAA, total creatine (Cr + PCr) or water are used for this purpose as they are easy to detect and quantify, and are known to be reasonably stable under regular physiological conditions [20,21]. Although MRS, in principle, is a quantitative method, the reliability and reproducible quantification of neurochemicals with MRS remains challenging in clinical practice [22]. Potential error sources include methodological and technical aspects, but can also be of physiological or clinical nature. For instance, metabolite relaxation times have been reported to be affected by disease [23] and the use of water as quantitative reference can be prohibitive when its concentration is pathologically altered, e.g. in inflamed tissue of acute multiple sclerosis (MS) lesions.

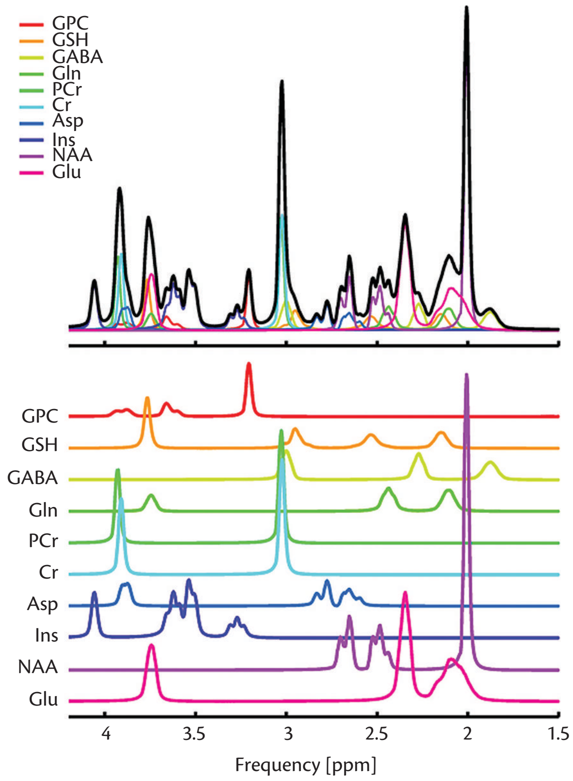

Fig. 3.2 Quantification of ^{1}H MR spectra as linear combination of model spectra (LCModel). (a) *In vivo* ^{1}H spectra consist of a sum of signals from the apparent neurochemical profile. (b) The quantification aims at reproducing the spectrum at hand as a scaled combination of the spectral patterns from individual metabolites. For each substance, the necessary scaling corresponds to the apparent concentration.

Single-voxel spectroscopy

Brain metabolism consists of complex mechanisms not only at the gross anatomical scale, but also with an extensive cellular heterogeneity [24]. It is therefore desirable to derive metabolic information selectively from a specific anatomical, functional, or clinical target area (e.g. a tumour or MS lesion). A variety of pulse sequences has been developed to obtain metabolic information from single, rectangular voxel volumes, so-called single-voxel MRS techniques. They differ mainly by the way the excitation pulses are used (slice-selective versus global) and by the number of acquisitions required to achieve volume selection. In practice, the point resolved spectroscopy (PRESS [25]) and stimulated echo aquisition mode (STEAM [26]) have largely prevailed due to their single-shot character, i.e. full 3-dimensional volume selection is achieved in a single acquisition. Their susceptibility to movement artefacts is inherently lower compared with multishot techniques where several acquisitions need to be combined, e.g. image-selected *in vivo* spectroscopy [ISIS] [27]. The PRESS sequence is based on a double-spin echo experiment consisting of a 90° RF pulse for excitation and two 180° refocusing pulses. Each of the RF pulses is applied in a frequency-selective fashion in the presence of a magnetic field gradient to extract a planar slice (Fig. 3.3).

With the use of orthogonal slice orientations, the voxel volume for MRS is extracted as the intersection of the three slices (Fig. 3.4).

Localization with STEAM relies on the same geometric principle, but three 90° RF pulses are used to obtain the spectroscopic information in form of a stimulated echo. With STEAM, T_2-relaxation is apparent only during part of the MR sequence and echo times as short as 1 ms can be achieved [28], which is considered an advantage over PRESS. However, in recent years, short echo times have also been made available for PRESS and PRESS-like methods under certain conditions [8,29]. On the downside, the theoretically achievable signal for STEAM is only one-half of the spin-echo method PRESS (and can be further reduced [30]). Fully or partially adiabatic versions of PRESS, localization by adiabatic selective refocusing (LASER) [31] and semi-LASER [32], respectively, stand out due to their robustness against RF amplitude variations (e.g. with the use of surface coils) and their improved volume localization [33], albeit at an increase in RF power deposition. In practice, the best technique for the problem at hand depends on study design parameters, such as the targeted metabolites (which define the echo time to be used), together with the technical capabilities of the available MR system, including RF peak power, maximum gradient strength, and gradient slew rate. The reader interested in these methodological details is referred to the literature [30,34].

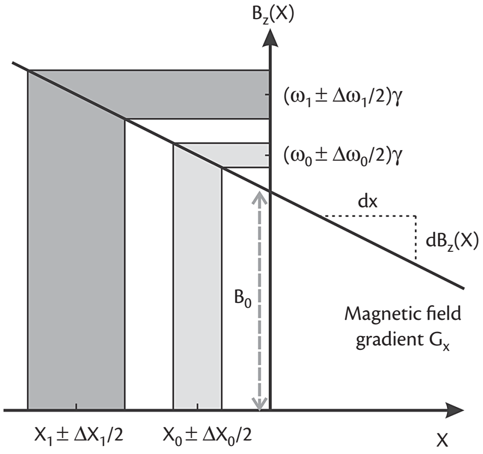
$B_z(X)$
$(\omega_1 \pm \Delta\omega_1/2)\gamma$
$(\omega_0 \pm \Delta\omega_0/2)\gamma$
dx
$dB_z(X)$
B_0
Magnetic field gradient G_x
$X_1 \pm \Delta X_1/2$
$X_0 \pm \Delta X_0/2$
X

Fig. 3.3 Magnetic field gradient: Slice selection and chemical shift displacement. The application of a band-limited radio-frequency pulse in the presence of a linear magnetic field gradient (here G_x) allows the selection of a planar slice, since the Larmor condition is only fulfilled for the spins within this area. Slice position x and slice thickness Δx are hereby defined by the centre frequency of the RF pulse ω and the width of the RF pulse Δω, respectively, relative to the strength of the applied gradient field $G_x = dB_z(x)/dx$.

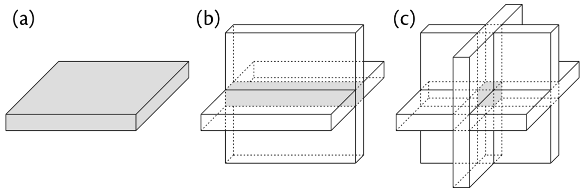

Fig. 3.4 Concept of gradient-based localization for single-voxel MRS methods, such as stimulated echo aquisition mode (STEAM) and point resolved spectroscopy (PRESS). The combination of three slice-selective RF pulses (compare with Fig. 3.3) reduces the sensitive volume to a slice (a), a column (b) and ultimately a voxel (c) as intersection of the three slices. The method allows region-specific MRS, since the acquired spectral signals stem from the selected volume only. Magnetization that it is located outside the selected voxel and, therefore, has not been excited by all three RF pulses is eliminated by additional 'spoiler' gradients (not shown).

Magnetic resonance spectroscopic imaging

Spectroscopic findings need to be put in a meaningful frame of reference for the study of metabolic alterations. This can be achieved, for instance, by statistical comparison of neurochemical information between patient and control cohorts in a group analysis. With this approach, potential intra-subject abnormalities are convoluted with regular inter-subject variability, a problem that does not exist if reference information is provided from the same subject. Such metabolic information from various regions of the same brain can either be achieved by multiple, (subsequent or interleaved) or single-voxel MRS acquisitions, or by MRS in which the volume-of-interest is further subdivided using MRI techniques, known as MRSI (Fig. 3.5).

Two-dimensional (2D) MRSI, for instance, is typically achieved by (pre)selecting a slice-shaped volume with STEAM or PRESS, before the metabolite signals from that slice are mapped by an additional phase-encoding scheme along two spatial dimensions. Data reconstruction then reveals a spatially-resolved array of MR spectra from the considered 2D slice [35,36]. As such, MRSI provides intra-subject reference information (e.g. from neighbouring or contralateral areas) and thereby allows the brain's regional metabolite distribution to be mapped in an unbiased fashion. Notably, pixels can be shifted with MRSI or summed together post-acquisition as long as the region-of-interest (ROI) has been covered, whereas with single-voxel MRS, the ROI has to be chosen for the experiment at hand. The SNR achievable with MRSI shares the same dependency on field-of-view (FOV) and spatial resolution with regular MRI, i.e. it is proportional to the MRSI voxel volume, and increases with the square root of the acquisition time [37]. On the downside, optimal experiment conditions, e.g. with respect to RF pulse power or

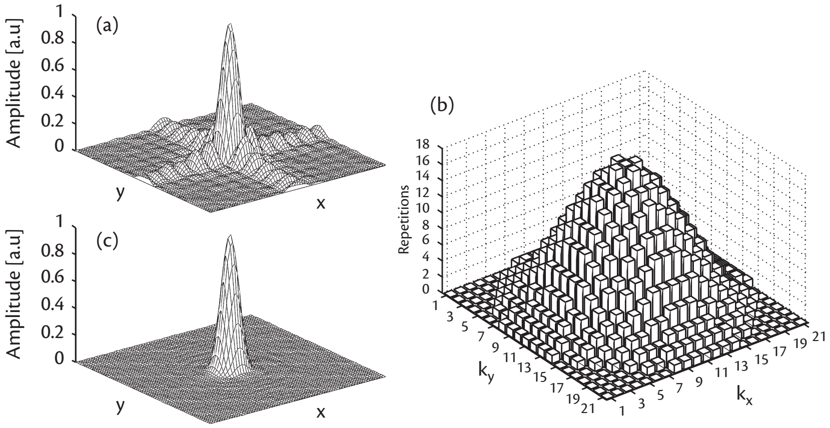

Fig. 3.5 Benefits of acquisition-weighting for spectroscopic MRI. Accurate spatial representation is of paramount importance for meaningful MRSI, however, acquisition time constraints limit the size of k-space encoding schemes that can be obtained *in vivo*. The consequences of limited k-space size and homogenous sampling include significant side bands of the spatial response function (SRF), i.e. spatial misregistration (a). A weighted acquisition scheme that focuses on the central k-space positions by sampling them more often, while (b) can alleviate artificial SRF side bands and provide largely improved spatial accuracy without penalty in experiment sensitivity.

magnetic field homogeneity, are more difficult to achieve over large MRSI volumes compared with single-voxel MRS.

The substitution of one phase encoding direction with an echo planar imaging (EPI) read-out considerably reduces the acquisition time [38,39] and other fast MRSI techniques with different types of EPI gradient wave forms [40,41] or SPIRAL read-out trajectories [42] have been developed. Conventional phase encoding and fast MRSI techniques, however, share the same dependency on the acquired SNR per time [30,41]. In other words, there is no net gain in sensitivity with the use of fast MRSI techniques and more data averaging is required to match the sensitivity of conventional MRSI. As such, fast techniques allow significant scan time reductions if SNR is not limited, but should be avoided otherwise. Higher demands on gradient performance, increased susceptibility to artefacts, and the need for non-standard MR sequences and data analysis with fast MRSI techniques might be reasons why conventional phase encoding remains the method of choice for most clinical MRSI applications.

Water suppression

The largest part of the human body consists of water with contents of at least 2/3 in all types of tissue, except fatty tissue and bone. The exact values are in the range of 50 Mol, but depend on anatomy, sex, age, and health status. In the healthy human brain, water concentrations of 83 and 70% were reported for the gray and white matter, respectively [43]. Concentrations of the detectable brain metabolites are, in contrast, 10^3–10^4 times smaller and, therefore, much harder to detect. A two-step subtraction scheme has been proposed recently to remove water signals from MR spectra by frequency-selective inversion of the metabolite signals in one of the MRS acquisitions [44,45]. The direct suppression of the water signal, however, remains the most widely applied solution to the problem. To this end, differences in the chemical shifts of water and the brain metabolites are used to selectively excite the water resonance by a frequency-selective RF pulse. The water signal is then minimized (i.e. spoiled) by phase-spoiling gradients, while the metabolite signals remain unaffected. This chemical shift selective (CHESS [46]) method for water suppression is typically repeated several times to improve the suppression factor. Since there is no interaction with the metabolite signals with CHESS, water suppression can be performed prior to (and, for STEAM, even during) the MRS acquisition.

Outer volume suppression

MRS relies on the assumption that the observed biochemical information originates from the targeted brain area, i.e. its proper spatial registration. Combinations of slice-selective RF pulses are used with single-voxel MRS methods to define the volume-of-interest. The inevitable sidebands of spatial selection RF pulses, however, cause some excitation of signals from outside the addressed volume. The resultant contributions to the acquired ^{1}H MR spectrum cannot be distinguished from signals of the targeted brain area and, therefore, falsify the quantitative results. The more prominent problem for ^{1}H MRS arises from lipid and fat resonances that originate from the skull at signal strengths 100–1000 times stronger than those of the detectable brain metabolites [24]. Even low amplitude sidebands from the target voxel selection within the brain lead to strong and broad artificial resonances in the 0.9–1.9 ppm range in the obtained spectra [47,48] and strongly hamper the spectrum quantification [24]. If the magnetization from outside the selected volume is actively spoiled before the MRS acquisition, the risk of artificial signal contributions is minimized. The most commonly applied method for outer-volume suppression (OVS) employs a frequency selective RF pulse in the presence of a magnetic field gradient to excite the unwanted magnetization from the spatial slice (outside the ROI) before it is erased by phase spoiling (Fig. 3.6) [49].

Magnetic field homogeneity and shimming

MR spectroscopy, like any other MR method, relies on the Larmor equation (Eqn 1). If the magnetic field varies over the volume-of-interest, e.g. an MRS voxel, a distribution of Larmor frequencies is observed, rather than a single frequency and spectral peaks appear broadened on top of the natural line width. In MRS, line broadening leads to a loss of sensitivity and spectral resolution and, therefore, excellent spatial homogeneity of the magnetic field over the target

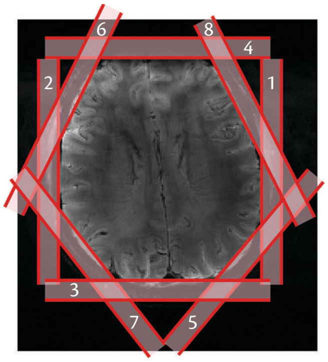

Fig. 3.6 Outer-volume suppression (OVS) for spectroscopic MRI of the human brain. Signals from cranial lipids can be minimized by their selective excitation (compare with Fig. 3.3) followed by phase-spoiling gradients to eliminate them. The oval shape of the skull in an axial section through the human head is hereby typically approximated by a series of planar OVS slices.

volume is essential for optimal results. The placement of a human head in a magnetic field generates magnetic field distortions due to the susceptibility differences between tissue and the surrounding air. Spectral line broadening, based on magnetic field inhomogeneity, cannot be corrected for by post-processing and, therefore, needs to be minimized experimentally before or throughout the MRS experiment. The importance of magnetic field homogeneity for MRS cannot be overstated and various correction (so-called 'shimming') methods have been developed in recent years [50–53]. Their discussion, however, exceeds the scope of this chapter and the interested reader is referred to the literature.

Sequence imperfections and eddy currents

The fast switching of magnetic field gradients is known to induce currents in the conducting structures of its close environment. These so-called 'eddy currents' result in secondary, artificial magnetic fields throughout the scanner bore, which alter the original gradient field spatially and temporally. The field artefacts that originate from eddy currents of the scanner's cold conducting structures can extend over hundreds of milliseconds, and reach into the MRS sequence and acquisition window. The resultant, temporally varying phase modulations lead to spectral baseline artefacts in the MRS spectrum that can easily mask the targeted metabolite signals, thereby rendering the experiment useless. If the phase modulation is known, however, it can be rewound and removed from the data. Therefore, metabolite MRS should always be accompanied by the acquisition of an identical data set without water suppression. The resultant high SNR water signal contains the phase behaviour from the eddy current-induced field terms and can be used to correct the line shape artefacts of the metabolite signals [54]. For a comprehensive review of artefacts and pitfalls associated with MRS/MRSI, the reader is referred to the literature [30,55].

Clinical magnetic resonance spectroscopy

The human brain is a highly heterogeneous system, both histologically and functionally, and neurochemicals have been found to be non-uniformly distributed throughout it. For instance, the concentration of Glu as the major excitatory neurotransmitter in the mammalian brain varies between gray and white brain matter, but also between different brain areas [7,14,56]. Similar differences are observed for most neurochemicals and not even the water concentration can be considered uniform throughout the brain [21]. Metabolite concentrations can be affected by brain function [57–59], age [60,61], the female menstrual cycle [62], or physiological challenges such as hypoglycaemia [63]. Furthermore, considerable inter-subject variability complicates individual influences [64]. The unique ability of MRS to disentangle these effects by quantitative, although non-invasive measurements of the brain's neurochemistry within specific anatomical areas or functional subunits sets MRS aside from other imaging modalities. However, if not accounted for by proper study design and experiment execution, the various dependencies and confounding influences can easily render the obtained MRS results useless, or worse can lead to false interpretations.

Routine clinical MRS primarily aims to assess the health status of patients. Pathological conditions can lead to distinct changes of the metabolic profile and clinical markers have been developed for a clinically meaningful interpretation. As such, MRS methods are used to characterize disease via metabolic alterations, to monitor disease progression and treatment. MRS methods are particularly suitable for the latter, longitudinal applications due to their non-invasiveness and the lack of radiation exposure from methods such as positron emission tomography. While clinical MRS focuses mainly on metabolic irregularities and the brain's pathoneurochemistry, benefits have also been demonstrated for other conditions, e.g. diabetes and prostate cancer.

Metabolites of interest

Ten to twenty neurochemicals are typically accessible with ^{1}H MRS in the human brain, depending on the experimental conditions and the achieved data quality [7,65]. Here, the most relevant neurochemicals for ^{1}H MRS are summarized with respect to their clinical relevance; a more comprehensive description can be found elsewhere [6,30,66].

N-acetylaspartate

NAA is an amino acid that is exclusively found in the central and peripheral nervous system. The concentrations in the brain are the second highest (after Glu) and depend on region, age, and health status [67]. Its' exact physiological function remains unclear [68], but it functions as storage for aspartate, a precursor for N-acetylaspartylglutamate (NAAG) and osmotic functionalities are considered. Due to its exclusive appearance in neurons and axons, and its absence from mature glia cells, NAA can be used as neuronal marker [69]. The higher neuronal density in gray brain matter is reflected by higher amounts of NAA (8–11 mM) compared with white matter (6–9 mM) [55,70]. In pathologies with concomitant degeneration of neurons, a decrease of NAA levels is observed [71,72]. In ^{1}H MR spectroscopy, the methyl group of NAA gives rise to the most prominent peak in *in vivo* brain spectra, located at 2.01 ppm. This singlet peak is commonly used as internal frequency reference as it remains stable under physiological changes of temperature or pH. Furthermore, NAA has been suggested as an internal, quantitative reference, as NAA concentrations remain largely unaffected even under acute metabolic disturbances [70].

Choline-containing compounds

Three choline-containing compounds, i.e. choline (Cho), phosphorylcholine (or phosphocholine, PCho) and glycerophosphorylcholine (GPC), are accessible with ^{1}H MRS and have been found to be uniformly distributed throughout the brain. They are involved in the synthesis and degradation of phospholipids, which are essential for cellular membrane composition. Furthermore, Cho is a precursor for acetylcholine, which acts as a neuromodulator in the brain. The total Cho concentration in the brain is 1–2 mM and interpreted as a measure for cell density and membrane turnover. The methyl groups of the various cholines lead to strong singlet resonances around 3.2 ppm, which are easily identifiable in an MRS spectrum; their separation, however, is not possible *in vivo*.

Myo-inositol

Myo-inositol is a 6-carbon cyclic sugar alcohol with concentrations in the order of 5 mM in the human brain. Inositol is considered a growth factor for mammalian cells, but the exact function of inositol (and its various derivatives) remains poorly understood. Inositol provides a precursor reservoir for second/third messenger substances and thereby links hormone-receptor binding to intracellular activity [73]. Furthermore, it is thought to be involved in the regulation of cell volume and to act as a storage form of glucose, predominantly in glial cells [74]. The detection and quantification of myo-inositol is hampered by the severe spectral overlap with glycine at 3.55 ppm, and with Cho and taurine at 3.27 ppm. Scyllo-inositol, the second most abundant inositol isomer, can be observed since all protons resonate at the identical chemical shift of 3.35 ppm.

Creatine and phosphocreatine

Creatine (Cr) is a non-protein amino acid that is synthesized in kidney, liver, and pancreas. The phosphorylation of creatine to the high energy substrate phosphocreatine (or creatine phosphate, PCr) through creatine kinase provides an energy reservoir that is crucial for keeping ATP levels constant by the conversion of PCr back to Cr. In the brain, Cr and PCr are present in neurons and glial cells. Furthermore, PCr is thought to be a phosphorus buffer, and to act as an energy transporter between the mitochondria and the sites of energy consumption [30]. Two prominent peaks are observed at 3.03 ppm and 3.93 ppm, which can be attributed to the methyl and methylene protons of Cr and PCr. Total creatine (tCr) is the most commonly used internal standard, but cannot be used when its concentration might be affected by pathological processes [75].

Glucose and lactate

Glucose is the main substrate for the neuronal energy metabolism. It is metabolized with oxygen to water and carbon dioxide to replenish the cerebral ATP reservoirs via aerobic TCA cycling or (without oxygen) via anaerobic glycolysis [76,77]. A triggering of the latter by Glu has been suggested as mechanism for the coupling between neuronal activity and energy metabolism [78]. Lactate is the product of anaerobic glycolysis during physiological effort or during pathological conditions [79]. Its concentrations in normally-oxygenated healthy brain tissue are below the detection limit for MRS, but can be elevated if the supply of oxygen is impaired (e.g. due to stroke or brain trauma) or when the energy consumption exceeds regular levels (e.g. in tumours).

Lipids and macromolecules

Multiple lipid and macromolecule (MM) signals are known to contribute to *in vivo* ^{1}H spectra of the brain. These resonances are heavily broadened due to intramolecular, dipolar couplings and, therefore, contribute broad baseline components to the overall spectrum, rather than distinct, sharp peaks or multiplet structures. Notably, the lipid and MM signals originate from the MRS voxel itself and are not the result of imperfect volume selection. Alterations in the brain's MM levels have been reported for clinical conditions [80]. In regular MRS, however, the baseline uncertainties they create are known to reduce the quantification accuracy of the metabolite signals. Therefore, macromolecules should be either minimized experimentally during the MRS acquisition or explicitly measured in a separate experiment and considered in the metabolite analysis [81,82].

Glutamate and glutamine

Glu is a low molecular weight amino acid and the major excitatory neurotransmitter in the mammalian central nervous system [79]. In addition, Glu is part of the TCA and the urea cycles, i.e. it is not exclusively related to neuronal activity. It is present in different cell types, although its concentration is highest in neurons. Gln is derived from Glu by Gln synthetase in the Glu–Gln cycle [79,83] and located in astrocytes. Besides the regulation of glutamatergic neurotransmission, Gln plays a role in ammonia detoxification and as transport form of amino nitrogen [73]. Glu and Gln spectra are complex and strongly field-dependent due to the strong couplings between the ^{1}H nuclei and, furthermore, critically depend on the details of the MR sequence [6,84]. The splitting of Glu ^{1}H into many low amplitude signals and their significant overlap with resonances from other brain metabolites make it hard to quantify despite fairly high concentrations in the brain (9–12 mM [73,85]). MRSI of Glu has been demonstrated at 4 Tesla [86] and specific techniques have been developed for the Glu–Gln separation [87,88]. Improved separation and quantification accuracy of Glu and Gln, however, is the prime benefit of ^{1}H MRS at ≥7 Tesla [14].

γ-Aminobutyric acid

γ-Aminobutyric acid (GABA) is the main inhibitory neurotransmitter in the human brain. It is thought to be synthesized by Glu decarboxylation and, therefore effectively from Gln, but additional synthesis pathways are assumed [89]. GABA is found in the brain and the spinal cord and known to act on (at least) two different receptor types. The detection of GABA with direct ^{1}H MRS is complicated by the multiplet structure of its resonances and significant overlap with signals from other metabolites.

Advanced techniques

Although many neurochemicals can be measured with basic STEAM- and PRESS-based MRS or MRSI, specific techniques have been developed to improve the quantification accuracy of selected metabolites or to access additional ones. The refocusing of an individual J-coupled resonance, for instance, allows its selective inversion, while the rest of the spectrum remains unaffected. The subtraction of two spectra with and without this inversion cancels all but the selected resonance. While a large part of the spectroscopic information is compromised with this so-called J-difference editing, a specific metabolite resonance and, therefore, the metabolite-of-interest itself can be quantified at higher precision. GABA quantification is the prime example for J-difference editing [90] and reliable *in vivo* quantification of GABA has been demonstrated throughout the brain [91,92]. Similarly, glutathione (GSH) and vitamin C (aspartate) quantification has been made possible with this approach [93–95].

A variety of substances with biochemical relevance contain MR-detectable nuclei other than ^{1}H and thereby allow complementary insights into the brain's pathoneurochemistry. MR spectroscopy of substances containing phosphorus (and therefore the MR sensitive isotope ^{31}P) provides access to the brain's energy metabolism and related disorders. ^{13}C MRS has been proven beneficial for the study of clinical conditions such as Alzheimer's disease, Canavan's disease or epilepsy, however, its use remains largely limited to research and ^{13}C MRS only slowly finds its way into the clinical routine [96]. ^{23}Na, ^{19}F, and ^{17}O MRS are less often applied [30]. Especially, the combination of information derived from multinuclear MRS, i.e. MRS employing various isotopes, proves powerful to assess multiple aspects of a disease. Current examples include the combination of ^{1}H and ^{31}P in MS [97], or the study of liver tumours with ^{1}H, ^{31}P, and ^{13}C MRS [98].

Other advanced MRS methods aim at increasing the measurement sensitivity by polarization transfer, spin decoupling or the infusion of enriched substrates, i.e. metabolites that exhibit the considered isotope at concentrations beyond its natural abundance. The infusion of ^{13}C-labelled acetate or glucose, for instance, allows the determination of TCA cycle intermediates (and fluxes) and the Glu/Gln cycling at largely increased sensitivities compared with signals based purely on the low natural abundance of ^{13}C of only 1% [2,99,100]. Similarly, increased spin polarization that exceeds regular values, so-called hyperpolarization, has been used to increase the MRS signal strength and, therefore, its detection sensitivity [101].

Advanced MRS techniques provide powerful and elegant tools for biomedical research. The need for sophisticated methodology and, in many cases, specific hardware, might be the reasons why their application has been mostly limited to research [30].

Clinical applications

Clinical ^{1}H MRS aims to characterize disorders and to benefit patients by providing diagnostic value that is complementary to other modalities. ^{1}H MRS does not measure disease directly, since neurochemical information can only provide an indirect means of a pathological alteration of the tissue's biochemical composition due to disease. Ideally, a metabolic alteration can be identified as marker for a specific disease. The understanding of the underlying processes is desirable, although it is not strictly necessary as long as the marker is unique. In reality, biochemical alterations are rarely disease-specific and combinations thereof are used for improved statistical power and diagnostic reliability. In clinical practice, the usefulness and efficacy of ^{1}H MRS for neurological diagnosis and neurotherapeutic decision-making is key [102].

Tumours

Tissue biopsy with subsequent histopathological grading is the gold standard for brain tumour diagnostics. Multiple repetitions for treatment control, however, are prohibitive and extracting tissue from essential vegetative, cognitive, or motor areas is contraindicated completely. T_1- and T_2-weighted MRI are valuable for the characterization of tumour morphology and the surrounding parenchyma. However, they do not always provide a clear-cut distinction, e.g. between necrotic areas as a result of radiation treatment and recurrences of the tumour. MRS techniques fill this gap through the assessment of regional neurochemistry in a non-invasive fashion. Increased Cho levels are observed in tumours in response to its increased cell density and are thought to represent enhanced cell membrane turnover and cell proliferation, i.e. the ongoing existence of cancerous cells [103–105]. Choline levels can even provide a handle on the differentiation of tumour types based on their variable necrotic fractions [106], a question that can also be addressed via the areas' lipid content. NAA levels are found to be reduced with the displacement of neuronal by tumour cells. The anaerobic fraction of tumour metabolism is represented by significant lactate levels in high-grade tumours, which also show decreases in total Cr. Metabolite ratios (e.g. Cho/NAA, Cho/Cr or NAA/Cr) combine these findings for individual metabolites and have been proven more useful to reliably characterize the tumour at hand with respect to type, necrotic and proliferating regions, its aggressiveness, or the degree of malignancy [107,108]. Similar measures and criteria have been developed for non-brain tumours. The ratio of (total) Cho plus (total) Cr over citrate is applied, for instance, to identify and localize tumour tissue in the prostate [109]. While MRS can improve the sensitivity and specificity for tumour grading or the distinction of recurrent tumours from treatment related metabolic changes, other applications, such as the differentiation of metastasis from high-grade astrocytomas, remains difficult [110].

Multiple sclerosis

Multiple sclerosis is an inflammatory disorder of the central nervous system that causes demyelination and neurodegeneration. ^{1}H MRS allows to assess the concomitant histopathological changes and brain damage from the earliest stage and to monitor disease progression [111]. More specifically, reduced NAA in MS plaques is interpreted as a result of secondary axonal loss, i.e. neuronal injury [71], and thereby provides a measure (and predictor) for clinical disability. Similarly, the observation of lipids is considered a consequence of myelin breakdown and the accumulation of lipid droplets within macrophages [112]. Elevated Cho levels from increased membrane turnover have been associated with myelin degradation and infiltration with inflammatory cells [113]. Further metabolic changes include increased lactate levels as a result of anaerobic metabolism of inflammatory cells and elevations of myo-inositol [114], which indicates a relationship between glial proliferation and functional impairment [22]. Metabolic profiling of MS particularly benefits from additional spatial encoding with MRSI to study neurochemical alterations in white matter lesions, but also in gray matter and normal appearing white matter tissue throughout the brain [22,115]. The NAA/Cr ratio from regions around the corpus callosum proved to be a representative measure for axonal

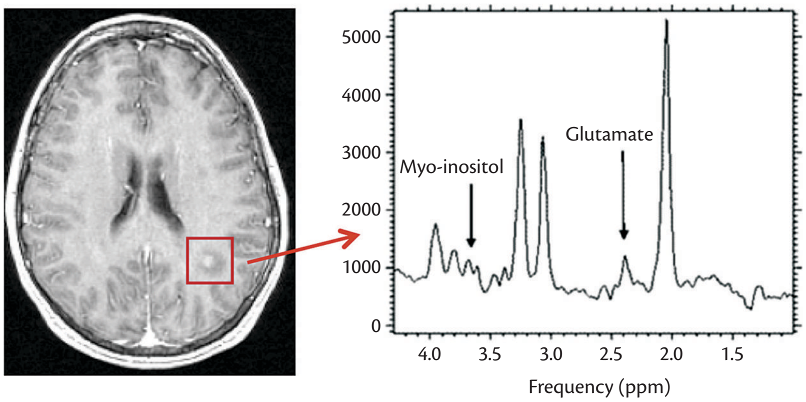

Fig. 3.7 TE-averaged MRS voxel surrounding an acute enhancing MS lesion. In such lesion, Glu and inositol concentrations are increased, by up to 30 and 40% respectively, compared with control white matter.

integrity in the brain of MS patients [115] and has the potential to monitor treatment effects [116]. An excess of Glu concentration using TE-averaged MRS was demonstrated in acute MS lesions (Fig. 3.7) [117].

Alzheimer's and Parkinson's disease

Alzheimer's and Parkinson's diseases are the most common forms of neurodegenerative disorders affecting the central nervous system. The diagnosis can be challenging for clinicians at the early stages of the disease. Decreased NAA and elevated myo-inositol in the mesial temporal and parietal cortex have been consistently reported in subjects with Alzheimer's [118,119]. Interestingly, using automated segmentation and cortical thickness measures from high resolution anatomical MR images combined with single voxel ^{1}H MRS, a group of investigators found a significant increase in sensitivity (97%) and specificity (94%) between subjects with early Alzheimer's, and healthy controls compared with either MR-based measures alone [120]. Similarly, early Parkinson's disease subjects were found to have higher concentrations of GABA in the pons and putamen relative to controls, whereas no metabolites changes were detected in the substantia nigra, suggesting that pathological injury in the lower brainstem areas may precede nigral involvement [121] and MRS may offer a paraclinical tool for disease staging.

Neuropsychiatric disorders

The impact of neuropsychiatric disorders on brain tissue is subtle and cannot be easily characterized with MRI. In fact, global and/or local alterations of the brains' elaborate neurochemistry networks have been identified with several neuropsychiatric disorders. More specifically, significantly reduced GABA and elevated Glu levels have been found in depressed patients [122,123] and the concentrations of both metabolites are known to be affected by alcohol addiction and sobriety [124,125]. Neurotransmitter systems are reportedly involved in neuropsychiatric disorders with Glu and, moreover, GABA being among the key players [126]. Furthermore, the relevance of various combinations of the metabolites NAA, Cho, myo-inositol, Cr, and lactate is known for schizophrenia, bipolar disorder, unipolar major depression, and anxiety disorders [66].

Other clinical conditions

MRS methods are also used in routine neurological practice and for research on traumatic brain injury [127,128], epilepsy [129,130], human immunodeficiency virus (HIV) [131,132], amyotrophic lateral sclerosis [133], and diabetes [134, 135]. The reader is referred to the corresponding chapters in this book and the literature for further details.

Clinical magnetic resonance spectroscopy: quo vadis?

To date, MRS is primarily used in basic clinical research, and for drug development and evaluation of treatment efficacy. The patient pool available to individual researchers or centres is often limited, especially when rare diseases are studied. Small sample sizes suffer from limited statistical power of the results obtained and are prone to miss out relevant aspects. The consideration of the results from multiple sites, such as the investigation of HIV subjects with dementia [136] is considered the appropriate remedy. However, the experimental standardization and coordination of such multicentre studies can be problematic [137,138].

The ideal MRS method for clinical diagnostics should provide a unique surrogate marker for clinical decision-making based on the combination of a fast measurement and a robust data analysis. Although the benefits of MR spectroscopy for clinical research and diagnostics have been demonstrated, the expectations of the impact of MR spectroscopy on clinical practice from 20 years ago have not been fully met. Deviations from the ideal MRS experiment lead to reduced spectral quality, limited quantification accuracy and, therefore, to progressively less reliable metabolic information as the basis for clinical disease management. Limited specificity of MRS with respect to the unique identification of clinical conditions, however, probably poses the main limitation. While confounding effects, e.g. inter-subject variability, age, or menstrual cycle, can be considered by study design in patient populations, the interpretation of neurochemical information from a single subject for clinical diagnostics appears to be far more difficult. MR spectroscopy is mostly used in addition to other modalities to achieve satisfactory, overall diagnostic sensitivity and specificity, when both methods are combined. MRS will only prevail as an independent diagnostic tool when disease-specific markers prove reliable enough as the sole basis for diagnostics and neurotherapeutic decision-making of an individual patient. High field strength scanners, standardized quantification methods, calibration across multiple sites and platforms, and large clinical validation studies are needed to achieve this goal.

References

1 Mason GF, Gruetter R, Rothman DL, et al. (1995). Simultaneous determination of the rates of the TCA cycle, glucose utilization, alpha-ketoglutarate/glutamate exchange, and glutamine synthesis in human brain by NMR. *Journal of Cerebral Blood Flow Metabolism*, **15**(1), 12–25.
2 Rothman DL, De Feyter HM, de Graaf RA, et al. (2011). 13C MRS studies of neuroenergetics and neurotransmitter cycling in humans. *NMR in Biomedicine*, **24**(8), 943–57.
3 Shulman RG, Brown TR, Ugurbil K, et al. (1979). Cellular applications of 31P and 13C nuclear magnetic resonance. *Science*, **205**(4402), 160–6.
4. Bottomley PA, Hart HR, Edelstein WA, et al. (1983). NMR imaging/spectroscopy system to study both anatomy and metabolism. *Lancet*, **2**(8344), 273–4.
5. Gill SS, Small RK, Thomas DG, et al. (1989). Brain metabolites as 1H NMR markers of neuronal and glial disorders. *NMR Biomedicine*, **2**(5–6), 196–200.
6. Govindaraju V, Young K, & Maudsley AA. (2000). Proton NMR chemical shifts and coupling constants for brain metabolites. *NMR in Biomedicine*, **13**(3), 129–53.
7. Emir UE, Auerbach EJ, Van De Moortele PF, et al. (2012). Regional neurochemical profiles in the human brain measured by (1) H MRS at 7 T using local B(1) shimming. *NMR in Biomedicine*, **25**(1), 152–60.
8. Mekle R, Mlynarik V, Gambarota G, et al. (2009). MR spectroscopy of the human brain with enhanced signal intensity at ultrashort echo times on a clinical platform at 3T and 7T. *Magnetic Resonance in Medicine*, **61**(6), 1279–85.
9. Tkac I, Oz G, Adriany G, et al. (2009). In vivo 1H NMR spectroscopy of the human brain at high magnetic fields: metabolite quantification at 4T vs. 7T. *Magnetic Resonance in Medicine*, **62**(4), 868–79.
10. Befroy DE, and Shulman GI. (2011). Magnetic resonance spectroscopy studies of human metabolism. *Diabetes*, **60**(5), 1361–9.
11. Ouwerkerk R, Bleich KB, Gillen JS, et al. (2003). Tissue sodium concentration in human brain tumors as measured with 23Na MR imaging. *Radiology*, **227**(2), 529–37.
12. Ugurbil K, Adriany G, Andersen P, et al. (2003). Ultrahigh field magnetic resonance imaging and spectroscopy. *Magnetic Resonance Imaging*, **21**(10), 1263–81.
13. Rothman DL, Behar KL, Prichard JW, et al. (1997). Homocarnosine and the measurement of neuronal pH in patients with epilepsy. *Magnetic Resonance in Medicine*, **38**(6), 924–9.
14. Tkac I, Andersen P, Adriany G, et al. (2001). In vivo 1H NMR spectroscopy of the human brain at 7 T. *Magnetic Resonance in Medicine*, **46**(3), 451–6.
15. Vanhamme L, Sundin T, Hecke PV, et al. (2001). MR spectroscopy quantitation: a review of time-domain methods. *NMR in Biomedicine*, **14**(4), 233–46.
16. Mierisova S, and Ala-Korpela M. (2001). MR spectroscopy quantitation: a review of frequency domain methods. *NMR in Biomedicine*, **14**(4), 247–59.
17. Provencher SW. (1993). Estimation of metabolite concentrations from localized in vivo proton NMR spectra. *Magnetic Resonance in Medicine*, **30**(6), 672–9.
18. Provencher SW. (2001). Automatic quantitation of localized in vivo 1H spectra with LCModel. *NMR in Biomedicine*, **14**(4), 260–4.
19. Cavassila S, Deval S, Huegen C, et al. (1999). The beneficial influence of prior knowledge on the quantitation of in vivo magnetic resonance spectroscopy signals. *Investigative Radiology*, **34**(3), 242–6.
20. Danielsen ER, & Henriksen O. (1994). Absolute quantitative proton NMR spectroscopy based on the amplitude of the local water suppression pulse. Quantification of brain water and metabolites. *NMR in Biomedicine*, **7**(7), 311–18.
21. Kreis R, Ernst T, & Ross BD. (1993a). Absolute quantitation of water and metabolites in the human brain. II. Metabolite concentrations. *Journal of Magnetic Resonance B*, **102**, 9–19.
22. Chard DT, Griffin CM, McLean MA, et al. (2002). Brain metabolite changes in cortical grey and normal-appearing white matter in clinically early relapsing-remitting multiple sclerosis. *Brain*, **125**(Pt 10), 2342–52.
23. Brief EE, Vavasour IM, Laule C, et al. (2010). Proton MRS of large multiple sclerosis lesions reveals subtle changes in metabolite T(1) and area. *NMR in Biomedicine*, **23**(9), 1033–7.
24. Rothman DL. (1994). *^{1}H NMR studies of human brain metabolism and physiology*. San Diego: Elsevier Science and Technology Books.
25. Bottomley PA. (1984). Selective volume method for performing localized NMR spectroscopy. US patent Office.
26. Frahm J, Merboldt KD, and Hanicke W. (1987). Localized proton spectroscopy using stimulated echos. *Journal of Magnetic Resonance*, **72**, 502–8.
27. Ordidge, R. J, Connelly, A, & Lohman, J. A. B. (1986). Image-selected in vivo spectroscopy (ISIS). A new technique for spatially selective NMR spectroscopy. *Journal of Magnetic Resonance*, *66*, 283–94.
28. Tkac I, Starcuk Z, Choi IY, et al. (1999). In vivo 1H NMR spectroscopy of rat brain at 1 ms echo time. *Magnetic Resonance in Medicine*, **41**(4), 649–56.
29. Zhong K, and Ernst T. (2004). Localized in vivo human 1H MRS at very short echo times. *Magnetic Resonance in Medicine*, **52**(4), 898–901.
30. de Graaf RA. (2008). *In vivo NMR spectroscorpy: principles and techniques*, 2nd edn). London: John Wiley and Sons.
31. Garwood M, and DelaBarre L. (2001). The return of the frequency sweep: designing adiabatic pulses for contemporary NMR. *Journal of Magnetic Resonance*, **153**(2), 155–77.
32. Scheenen TW, Klomp DW, Wijnen JP, et al. (2008). Short echo time 1H-MRSI of the human brain at 3T with minimal chemical shift displacement errors using adiabatic refocusing pulses. *Magnetic Resonance in Medicine*, **59**(1), 1–6.
33. Kaiser LG, Young K, and Matson GB. (2008). Numerical simulations of localized high field 1H MR spectroscopy. *Journal of Magnetic Resonance*, **195**(1), 67–75.
34. Kreis R. (1997). Quantitative localized 1H MR spectroscopy for clinical use. *Progress in NMR Spectroscopy*, **31**, 155–95.
35. Brown TR, Kincaid BM, and Ugurbil K. (1982). NMR chemical shift imaging in three dimensions. *Proceedings of the National Academy of Sciences, USA*, **79**(11), 3523–6.
36. Maudsley AA, Hilal SK, Perman WH, and Simon HE. (1983). Spatially resolved high resolution spectroscopy by 'four-dimensional' NMR. *Journal of Magnetic Resonance*, **51**, 147–52.
37. Macovski A. (1996). Noise in MRI. *Magnetic Resonance in Medicine*, **36**(3), 494–7.
38. Macovski A. (1985). Volumetric NMR imaging with time-varying gradients. *Magnetic Resonance in Medicine*, **2**(1), 29–40.
39. Mansfield P. (1984). Spatial mapping of the chemical shift in NMR. *Magnetic Resonance in Medicine*, **1**(3), 370–86.
40. Adalsteinsson E, Irarrazabal P, Spielman DM, et al. (1995). Three-dimensional spectroscopic imaging with time-varying gradients. *Magnetic Resonance in Medicine*, **33**(4), 461–6.
41. Posse S, Dager SR, Richards TL, et al. (1997). In vivo measurement of regional brain metabolic response to hyperventilation using magnetic resonance: proton echo planar spectroscopic imaging (PEPSI). *Magnetic Resonance in Medicine*, **37**(6), 858–65.
42. Adalsteinsson E, Irarrazabal P, Topp S, et al. (1998). Volumetric spectroscopic imaging with spiral-based k-space trajectories. *Magnetic Resonance in Medicine*, **39**(6), 889–98.
43. McIlwain H. (1985). *Biochemistry and the central nervous system*, 5th edn. Edinburgh: Churchill Livingstone.
44. de Graaf RA, Sacolick LI, and Rothman DL. (2006). Water and metabolite-modulated MR spectroscopy and spectroscopic imaging. Paper presented at the ISMRM, annual meeting, Seattle, 3063.

45. Dreher W, and Leibfritz D. (2005). New method for the simultaneous detection of metabolites and water in localized in vivo 1H nuclear magnetic resonance spectroscopy. *Magnetic Resonance in Medicine*, **54**(1), 190–5.
46. Haase A. (1986). Localization of unaffected spins in NMR imaging and spectroscopy (LOCUS spectroscopy). *Magnetic Resonance in Medicine*, **3**(6), 963–9.
47. Seeger U, Klose U, Lutz O, et al. (1999). Elimination of residual lipid contamination in single volume proton MR spectra of human brain. *Magnetic Resonance Imaging*, **17**(8), 1219–26.
48. Seeger U, Klose U, Mader I, et al. (2003). Parameterized evaluation of macromolecules and lipids in proton MR spectroscopy of brain diseases. *Magnetic Resonance in Medicine*, **49**(1), 19–28.
49. Duyn JH, Gillen J, Sobering G, et al. (1993). Multisection proton MR spectroscopic imaging of the brain. *Radiology*, **188**(1), 277–82.
50. Gruetter R. (1993). Automatic, localized in vivo adjustment of all first- and second-order shim coils. *Magnetic Resonance in Medicine*, **29**(6), 804–11.
51. Juchem C, Nixon TW, Diduch P, et al. (2010). Dynamic shimming of the human brain at 7 Tesla. *Concepts in Magnetic Resonance*, **37B**(3), 116–28.
52. Juchem C, Nixon TW, McIntyre S, et al. (2011). Dynamic multi-coil shimming of the human brain at 7 Tesla. *Journal of Magnetic Resonance*, **212**, 280–8.
53. Shen J, Rothman DL, Hetherington HP, et al. (1999). Linear projection method for automatic slice shimming. *Magnetic Resonance in Medicine*, **42**(6), 1082–8.
54. Klose U. (1990). In vivo proton spectroscopy in presence of eddy currents. *Magnetic Resonance in Medicine*, **14**(1), 26–30.
55. Kreis R. (2004). Issues of spectral quality in clinical 1H-magnetic resonance spectroscopy and a gallery of artifacts. *NMR in Biomedicine*, **17**(6), 361–81.
56. Frahm J, Bruhn H, Gyngell ML, et al. (1989). Localized proton NMR spectroscopy in different regions of the human brain in vivo. Relaxation times and concentrations of cerebral metabolites. *Magnetic Resonance in Medicine*, **11**(1), 47–63.
57. Mangia S, Tkac I, Gruetter R, et al. (2007). Sustained neuronal activation raises oxidative metabolism to a new steady-state level: evidence from 1H NMR spectroscopy in the human visual cortex. *Journal of Cerebral Blood Flow Metabolism*, **27**(5), 1055–63.
58. Mason GF, Sanacora G, de Graaf RA, et al. (2005). Light deprivation lowers brain GABA. Paper presented at the Proceedings of the Society of Biological Psychiatry.
59. Shulman RG, Blamire AM, Rothman DL, et al. (1993). Nuclear magnetic resonance imaging and spectroscopy of human brain function. *Proceedings of the National Academy of Sciences, USA*, **90**(8), 3127–33.
60. Kreis R, Ernst T, and Ross BD. (1993b). Development of the human brain: in vivo quantification of metabolite and water content with proton magnetic resonance spectroscopy. *Magnetic Resonance in Medicine*, **30**(4), 424–37.
61. Pouwels PJW, Brockmann K, Kruse B, et al. (1994). Regional age dependence of human brain metabolites from infancy to adulthood as detected by quantitative localized proton MRS. *Pediatric Research*, **46**(4), 474.
62. Harada M, Kubo H, Nose A, et al. (2010). Measurement of variation in the human cerebral GABA level by in vivo MEGA-editing proton MR spectroscopy using a clinical 3 T instrument and its dependence on brain region and the female menstrual cycle. *Human Brain Mapping*.
63. De Feyter HM, van den Broek NM, Praet SF, et al. (2008). Early or advanced stage type 2 diabetes is not accompanied by in vivo skeletal muscle mitochondrial dysfunction. *European Journal of Endocrinology*, **158**(5), 643–53.
64. Oz G, and Tkac I. (2011). Short-echo, single-shot, full-intensity proton magnetic resonance spectroscopy for neurochemical profiling at 4 T: validation in the cerebellum and brainstem. *Magnetic Resonance in Medicine*, **65**(4), 901–10.
65. Hofmann L, Slotboom J, Jung B, et al. (2002). Quantitative 1H-magnetic resonance spectroscopy of human brain: influence of composition and parameterization of the basis set in linear combination model-fitting. *Magnetic Resonance in Medicine*, **48**(3), 440–53.
66. Maddock RJ, and Buonocore MH. (2012). MR Spectroscopic studies of the brain in psychiatric disorders. *Current Topics in Behavioural Neuroscience*, **11**, 199–251
67. Pouwels PJW, and Frahm J. (1998). Regional metabolite concentrations in human brain as determined by quantitative localized proton MRS. *Magnetic Resonance in Medicine*, **39**(1), 53–60.
68. Birken DL, and Oldendorf WH. (1989). N-acetyl-L-aspartic acid: a literature review of a compound prominent in 1H-NMR spectroscopic studies of brain. *Neuroscience & Biobehavioral Reviews*, **13**(1), 23–31.
69. Simmons ML, Frondoza CG, and Coyle JT. (1991). Immunocytochemical localization of N-acetyl-aspartate with monoclonal antibodies. *Neuroscience*, **45**(1), 37–45.
70. Wang Y, and Li SJ. (1998). Differentiation of metabolic concentrations between gray matter and white matter of human brain by in vivo 1H magnetic resonance spectroscopy. *Magnetic Resonance in Medicine*, **39**(1), 28–33.
71. Arnold DL, Matthews PM, Francis G, et al. (1990). Proton magnetic resonance spectroscopy of human brain in vivo in the evaluation of multiple sclerosis: assessment of the load of disease. *Magnetic Resonance in Medicine*, **14**(1), 154–9.
72. Bruhn H, Frahm J, Gyngell ML, et al. (1989). Cerebral metabolism in man after acute stroke: new observations using localized proton NMR spectroscopy. *Magnetic Resonance in Medicine*, **9**(1), 126–31.
73. Ross BD. (1991). Biochemical considerations in 1H spectroscopy. Glutamate and glutamine; myo-inositol and related metabolites. *NMR in Biomedicine*, **4**(2), 59–63.
74. Fisher SK, Novak JE, and Agranoff BW. (2002). Inositol and higher inositol phosphates in neural tissues: homeostasis, metabolism and functional significance. *Journal of Neurochemistry*, **82**(4), 736–54.
75. Caramanos Z, Narayanan S, and Arnold DL. (2005). 1H-MRS quantification of tNA and tCr in patients with multiple sclerosis: a meta-analytic review. *Brain*, **128**(Pt 11), 2483–506.
76. Buxton RB. (2002). *Introduction to functional magnetic resonance imaging principles and techniques*. Cambridge: Cambridge University Press.
77. Siesjo BK. (1978). *Brain energy metabolism*. New York: Wiley.
78. Magistretti PJ, and Pellerin L. (1999). Cellular mechanisms of brain energy metabolism and their relevance to functional brain imaging. *Philosophical Transactions of the Royal Society, London B, Biological Sciences*, **354**(1387), 1155–63.
79. Rothman DL, Sibson NR, Hyder F, et al. (1999). In vivo nuclear magnetic resonance spectroscopy studies of the relationship between the glutamate-glutamine neurotransmitter cycle and functional neuroenergetics. *Philosophical Transactions of the Royal Society, London B, Biological Sciences*, **354**(1387), 1165–77.
80. Mader I, Seeger U, Weissert R, et al. (2001). Proton MR spectroscopy with metabolite-nulling reveals elevated macromolecules in acute multiple sclerosis. *Brain*, **124**(Pt 5), 953–61.
81. Behar KL, Rothman DL, Spencer DD, et al. (1994). Analysis of macromolecule resonances in 1H NMR spectra of human brain. *Magnetic Resonance in Medicine*, **32**(3), 294–302.
82. Hofmann L, Slotboom J, Boesch C, et al. (2001). Characterization of the macromolecule baseline in localized (1)H-MR spectra of human brain. *Magnetic Resonance in Medicine*, **46**(5), 855–63.
83. Rothstein JD, Martin L, Levey A. I, et al. (1994). Localization of neuronal and glial glutamate transporters. *Neuron*, **13**(3), 713–25.
84. Rothman DL, Hanstock CC, Petroff OA, et al. G. (1992). Localized 1H NMR spectra of glutamate in the human brain. *Magnetic Resonance in Medicine*, **25**(1), 94–106.
85. Ross BD, and Bluml S. (1996). New aspects of brain physiology. *NMR in Biomedicine*, **9**(7), 279–96.
86. Mason GF, Pan JW, Ponder SL, et al. (1994). Detection of brain glutamate and glutamine in spectroscopic images at 4.1 T. *Magnetic Resonance in Medicine*, **32**(1), 142–5.

87. Hurd R, Sailasuta N, Srinivasan R, et al. (2004). Measurement of brain glutamate using TE-averaged PRESS at 3T. *Magnetic Resonance in Medicine*, **51**(3), 435–40.
88. Mayer D, Kim DH, Adalsteinsson E, et al. (2006). Fast CT-PRESS-based spiral chemical shift imaging at 3 Tesla. *Magnetic Resonance in Medicine*, **55**(5), 974–8.
89. Kandel ER, Schwartz JH, and Jessel TM. (1991). *Principles of neuronal science*. New York: McGraw-Hill.
90. Rothman DL, Petroff OA, Behar KL, et al. (1993). Localized 1H NMR measurements of gamma-aminobutyric acid in human brain in vivo. *Proceedings of the National Academy of Sciences, USA*, **90**(12), 5662–6.
91. Morgan PT, Pace-Schott EF, Mason GF, et al. (2012). Cortical GABA levels in primary insomnia. *Sleep*, **35**(6), 807–14.
92. Oz G, Terpstra M, Tkac I, et al. (2006). Proton MRS of the unilateral substantia nigra in the human brain at 4 tesla: detection of high GABA concentrations. *Magnetic Resonance in Medicine*, **55**(2), 296–301.
93. Emir UE, Raatz S, McPherson S, et al. (2011). Noninvasive quantification of ascorbate and glutathione concentration in the elderly human brain. *NMR in Biomedicine*, **24**(7), 888–94.
94. Kaiser LG, Marjanska M, Matson GB, et al. (2010). (1)H MRS detection of glycine residue of reduced glutathione in vivo. *Journal of Magnetic Resonance*, **202**(2), 259–66.
95. Srinivasan R, Ratiney H, Hammond-Rosenbluth KE, et al. (2010). MR spectroscopic imaging of glutathione in the white and gray matter at 7 T with an application to multiple sclerosis. *Magnetic Resonance Imaging*, **28**(2), 163–70.
96. Ross B, Lin A, Harris K, et al. (2003). Clinical experience with 13C MRS in vivo. *NMR Biomedicine*, **16**(6–7), 358–69.
97. Hattingen E, Magerkurth J, Pilatus U, et al. (2011). Combined (1)H and (31)P spectroscopy provides new insights into the pathobiochemistry of brain damage in multiple sclerosis. *NMR in Biomedicine*, **24**(5), 536–46.
98. Ter Voert E, Heijmen L, van Laarhoven H, et al. (2011). In vivo magnetic resonance spectroscopy of liver tumors and metastases. *World Journal of Gastroenterology*, **17**(47), 5133–49.
99. Badar-Goffer RS, Bachelard HS, and Morris PG. (1990). Cerebral metabolism of acetate and glucose studied by 13C-n.m.r. spectroscopy. A technique for investigating metabolic compartmentation in the brain. *Biochemistry Journal*, **266**(1), 133–9.
100. Shen J, Petersen KF, Behar KL, et al. (1999). Determination of the rate of the glutamate/glutamine cycle in the human brain by in vivo 13C NMR. *Proceedings of the National Academy of Sciences, USA*, **96**(14), 8235–40.
101. Kurhanewicz J, Vigneron DB, Brindle K, et al. (2011). Analysis of cancer metabolism by imaging hyperpolarized nuclei: prospects for translation to clinical research. *Neoplasia*, **13**(2), 81–97.
102. Lin A, Ross BD, Harris K, et al. (2005). Efficacy of proton magnetic resonance spectroscopy in neurological diagnosis and neurotherapeutic decision making. *NeuroRx*, **2**(2), 197–214.
103. Gill SS, Thomas DG, Van Bruggen N, et al. (1990). Proton MR spectroscopy of intracranial tumours: in vivo and in vitro studies. *Journal of Computer Assisted Tomography*, **14**(4), 497–504.
104. Herminghaus S, Pilatus U, Moller-Hartmann W, et al. (2002). Increased choline levels coincide with enhanced proliferative activity of human neuroepithelial brain tumors. *NMR in Biomedicine*, **15**(6), 385–92.
105. Howe F.A, Barton SJ, Cudlip SA, et al. (2003). Metabolic profiles of human brain tumors using quantitative in vivo 1H magnetic resonance spectroscopy. *Magnetic Resonance in Medicine*, **49**(2), 223–32.
106. McKnight TR. (2004). Proton magnetic resonance spectroscopic evaluation of brain tumor metabolism. *Seminars in Oncology*, **31**(5), 605–17.
107. Herminghaus S, Dierks T, Pilatus U, et al. (2003). Determination of histopathological tumor grade in neuroepithelial brain tumors by using spectral pattern analysis of in vivo spectroscopic data. *Journal of Neurosurgery*, **98**(1), 74–81.
108. McKnight TR, Lamborn KR, Love TD, et al. (2007). Correlation of magnetic resonance spectroscopic and growth characteristics within Grades II and III gliomas. *Journal of Neurosurgery*, **106**(4), 660–6.
109. Scheenen TW, Klomp DW, Roll SA, et al. (2004). Fast acquisition-weighted three-dimensional proton MR spectroscopic imaging of the human prostate. *Magnetic Resonance in Medicine*, **52**(1), 80–8.
110. Hollingworth W, Medina LS, Lenkinski RE, et al. (2006). A systematic literature review of magnetic resonance spectroscopy for the characterization of brain tumors. *AJNR American Journal of Neuroradiology*, **27**(7), 1404–11.
111. De Stefano N, and Filippi M. (2007). MR spectroscopy in multiple sclerosis. *Journal of Neuroimaging*, **17**(Suppl. 1), 31S–35S.
112. Wolinsky JS, Narayana PA, and Fenstermacher MJ. (1990). Proton magnetic resonance spectroscopy in multiple sclerosis. *Neurology*, **40**(11), 1764–9.
113. Davie CA, Hawkins CP, Barker GJ, et al. (1994). Serial proton magnetic resonance spectroscopy in acute multiple sclerosis lesions. *Brain*, **117**(Pt 1), 49–58.
114. Kirov II, Patil V, Babb JS, et al. (2009). MR spectroscopy indicates diffuse multiple sclerosis activity during remission. *Journal of Neurology, Neurosurgery & Psychiatry*, **80**(12), 1330–6.
115. Pelletier D, Nelson SJ, Grenier D, et al. (2002). 3-D echo planar (1) HMRS imaging in MS: metabolite comparison from supratentorial vs. central brain. *Magnetic Resonance Imaging*, **20**(8), 599–606.
116. Khan O, Shen Y, Bao F, et al. (2008). Long-term study of brain 1H-MRS study in multiple sclerosis: effect of glatiramer acetate therapy on axonal metabolic function and feasibility of long-Term H-MRS monitoring in multiple sclerosis. *Journal of Neuroimaging*, **18**(3), 314–19.
117. Srinivasan R, Sailasuta N, Hurd R, et al. (2005). Evidence of elevated glutamate in multiple sclerosis using magnetic resonance spectroscopy at 3 T. *Brain*, **128**(Pt 5), 1016–25.
118. Jones RS, and Waldman AD. (2004). 1H-MRS evaluation of metabolism in Alzheimer's disease and vascular dementia. *Neurology Research*, **26**(5), 488–95.
119. Soher BJ, Doraiswamy PM, and Charles HC. (2005). A review of 1H MR spectroscopy findings in Alzheimer's disease. *Neuroimaging Clinics of North America*, **15**(4), 847–52, xi.
120. Westman E, Wahlund LO, Foy C, et al. (2010). Magnetic resonance imaging and magnetic resonance spectroscopy for detection of early Alzheimer's disease. *Journal of Alzheimer's Disease*, **26**(Suppl. 3), 307–19.
121. Emir UE, Tuite PJ, and Oz G. (2012). Elevated pontine and putamenal GABA levels in mild-moderate Parkinson disease detected by 7 tesla proton MRS. *PLoS One*, **7**(1), e30918.
122. Sanacora G, Fenton LR, Fasula MK, et al. (2006). Cortical gamma-aminobutyric acid concentrations in depressed patients receiving cognitive behavioral therapy. *Biological Psychiatry*, **59**(3), 284–6.
123. Sanacora G, Gueorguieva R, Epperson CN, et al. (2004). Subtype-specific alterations of gamma-aminobutyric acid and glutamate in patients with major depression. *Archives of General Psychiatry*, **61**(7), 705–13.
124. Mason GF, Petrakis IL, de Graaf RA, et al. (2006). Cortical gamma-aminobutyric acid levels and the recovery from ethanol dependence: preliminary evidence of modification by cigarette smoking. *Biological Psychiatry*, **59**(1), 85–93.
125. Mon A, Durazzo TC, and Meyerhoff DJ. (2012). Glutamate, GABA, and other cortical metabolite concentrations during early abstinence from alcohol and their associations with neurocognitive changes. *Drug & Alcohol* Dependence, **125**(1–2), 27–36.
126. Chang L, Cloak CC, and Ernst T. (2003). Magnetic resonance spectroscopy studies of GABA in neuropsychiatric disorders. *Journal of Clinical Psychiatry*, **64**(Suppl. 3), 7–14.
127. Brooks WM, Friedman SD, and Gasparovic C. (2001). Magnetic resonance spectroscopy in traumatic brain injury. *Journal of Head Trauma Rehabilitation*, **16**(2), 149–64.
128. Marino S, Ciurleo R, Bramanti P, et al. (2011). 1H-MR spectroscopy in traumatic brain injury. *Neurocritical Care*, **14**(1), 127–33.
129. Hajek M, Dezortova M, and Krsek P. (2008). (1)H MR spectroscopy in epilepsy. *European Journal of Radiology*, **67**(2), 258–67.

130. Hammen T, and Stefan H. (2004). [(1)H MR spectroscopy. Methods and applications in diagnosis and assessment of surgical and conservative treatment strategies in epilepsies]. *Nervenarzt*, **75**(10), 970–83.
131. Lentz MR, Kim WK, Lee V, et al. (2009). Changes in MRS neuronal markers and T cell phenotypes observed during early HIV infection. *Neurology*, **72**(17), 1465–72.
132. Mohamed MA, Lentz MR, Lee V, et al. (2010). Factor analysis of proton MR spectroscopic imaging data in HIV infection: metabolite-derived factors help identify infection and dementia. *Radiology*, **254**(2), 577–86.
133. Turner MR, and Modo M. (2010). Advances in the application of MRI to amyotrophic lateral sclerosis. *Expert Opinion in Medicine Diagnosis*, **4**(6), 483–96.
134. Boesch C, Machann J, Vermathen P, et al. (2006). Role of proton MR for the study of muscle lipid metabolism. *NMR in Biomedicine*, **19**(7), 968–88.
135. Machann J, Stefan N, and Schick F. (2008). (1)H MR spectroscopy of skeletal muscle, liver and bone marrow. *European Journal of Radiology*, **67**(2), 275–84.
136. Sacktor N, Skolasky RL, Ernst T, et al. (2005). A multicenter study of two magnetic resonance spectroscopy techniques in individuals with HIV dementia. *Journal of Magnetic Resonance Imaging*, **21**(4), 325–33.
137. Keevil SF, Barbiroli B, Collins DJ, et al. (1995). Quality assessment in in vivo NMR spectroscopy: IV. A multicentre trial of test objects and protocols for performance assessment in clinical NMR spectroscopy. *Magnetic Resonance Imaging*, **13**(1), 139–57.
138. Webb PG, Sailasuta N, Kohler SJ, et al. (1994). Automated single-voxel proton MRS: technical development and multisite verification. *Magnetic Resonance in Medicine*, **31**(4), 365–73.

CHAPTER 4

Diffusion magnetic resonance imaging

Silvia De Santis

Introduction

Diffusion magnetic resonance imaging is a non-invasive imaging technique able to generate in vivo images of the soft tissues, in which the contrast reflects the local diffusion properties of the water molecules and can be tuned to focus on the length scales typical of the relevant cellular structures.

The idea that underpins D-MRI is that it is possible to 'label' water molecules. This label is given to nuclei by manipulating the phase of the transverse magnetization, and the motion is deduced by checking this label after a given time, so that the larger the motion that occurred, the larger the obtained signal attenuation. Importantly, the label is only sensitive to the incoherent, thermally-driven motion, so that a coherent net displacement or flux has no impact on the signal attenuation. For manipulating the phase of the transverse magnetization, magnetic field gradients are turned on twice during the acquisition, according to [1]. The magnitude of the diffusion weighting is quantified by the *b*-value, that takes into account the time elapsed between the two pulses, i.e. the time in which the experiment is sensitive to the molecules' motion, and the gradient strength and duration. The larger the *b*-value, the larger the signal attenuation.

Molecular diffusion is the spontaneous random motion of the molecules that takes place in every fluid whose absolute temperature is higher than zero Kelvin. The molecules are constantly moving due to their thermal energy and this motion is considered random because the trajectories are continuously deviated by collisions with other water molecules (Fig. 4.1a). In complex media like the brain, these trajectories are also influenced by the shape and orientation of the structures the particles are moving in (e.g. axonal membranes, cell bodies, glia, inclusions, and macromolecules; Fig. 4.1b), allowing the extraction of indirect microstructural information, such as cell size and orientation. When analysing diffusion in such media, the diffusivity estimated using D-MRI is referred to as the apparent diffusion coefficient (ADC). 'Apparent' indicates that the collisions happen not only with similar molecules, as it would be in the case of self-diffusion in a glass of water, but also with barriers, where the diffusion coefficient deviates from its self-diffusion value, becoming dependent on the diffusion time.

The pronounced dependence of the diffusion properties on the local orientation of the structures makes D-MRI particularly suitable to investigate orientated structures such as muscles (e.g. the hearth), bone marrow, and especially the central nervous system (CNS), which is currently the tissue most studied using diffusion MRI. One of the main advantages of D-MRI is that it permits calculation of the so-called diffusion anisotropy, i.e. the fact that orientated structures exhibit different diffusion properties in different directions. For example, in axonal bundles, the motion of water molecules is less hindered along the bundle than in the perpendicular direction (Fig. 4.1c), leading to an orientational dependence of the signal loss. The simplest model that accounts for the anisotropy of diffusion in orientated structures is a tensor, a mathematical construct that fully describes molecular diffusion in 3D space. The diffusion tensor is a 3×3 symmetric square matrix, so that it has six unique components: three diagonal elements corresponding to diffusivities along three orthogonal axes and three off-diagonal elements corresponding to the correlation between displacements along those orthogonal axes.

In the diffusion tensor MRI (DT-MRI) framework [2,3], the tensor can be recovered by combining diffusion measurements along at least six non-collinear orientations (plus one scan with no diffusion weighting) and assuming a Gaussian diffusion regime (i.e. the probability of diffusion in a particular direction has a Gaussian shape whose width is proportional to the square root of the diffusion time). From the diffusion tensor, scalar parameters that embody intrinsic features of diffusion can be extracted.

The tensor framework provides an estimation of the direction in which the diffusivity of the fitted tensor is greatest (i.e. the principal eigenvector). Together with the other two mutually orthogonal orientations, i.e. the second and third eigenvectors, it identifies a reference frame where the diffusion tensor is diagonal (the off-diagonal elements are zero).

The information contained in the diffusion tensor is difficult to visualize on a voxel-by-voxel basis. To have a more intuitive idea of what a tensor represents, a convenient way is to plot the associated ellipsoid—a surface representing the distance that a molecule will diffuse to with equal probability from the origin. The principal axes of the ellipsoid are given by the tensor eigenvectors and the lengths are scaled according to the square root of the diffusivities measured along the three eigenvectors. The less mathematically inclined can think about the associated ellipsoid as the profile generated by a drop of ink placed in water. If no obstacles are present, the ink will diffuse in a spherical profile, while if the ink particles are hindered by barriers, diffusion will be eased along the direction orthogonal to the obstacles. Fig. 4.2 shows the diffusion ellipsoid for the three cases shown in Fig. 4.1.

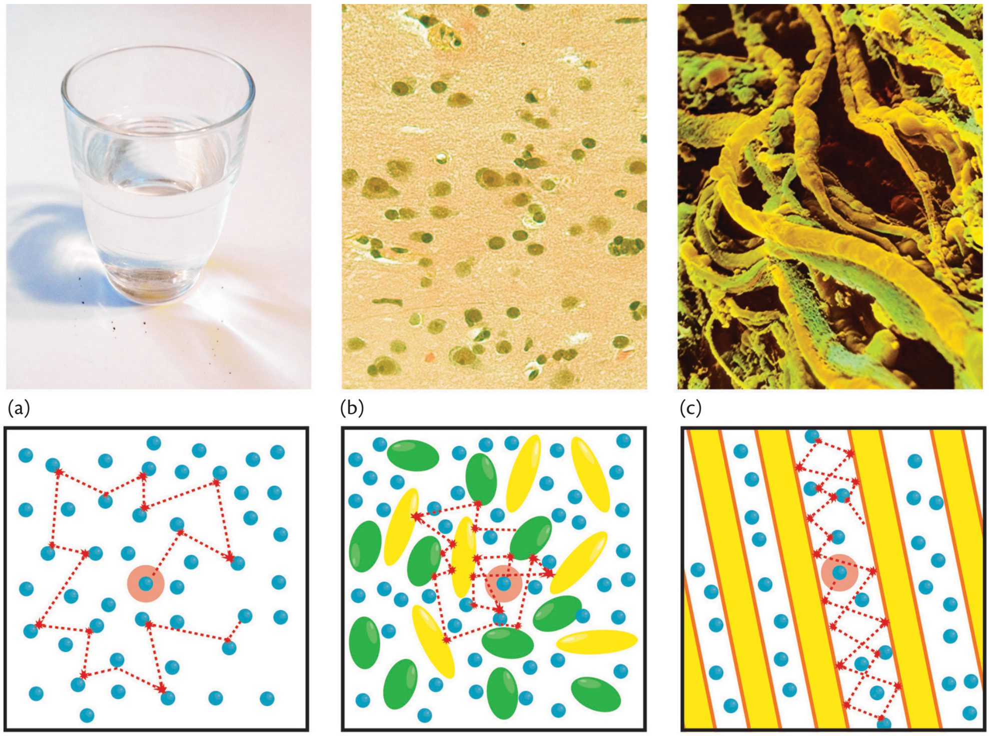

Fig. 4.1 Schematic representation of three different regimes of water diffusion. In a glass of water, water molecules undergo self-diffusion, i.e. they are constantly moving and colliding with other water molecules. Following the path of one of them, one would find that the averaged square distance from the origin is proportional to the elapsed time and that the probability of having diffused a certain length is independent of the direction (a). In complex media, such as the grey matter, collisions happen not only with other solvent particles, but also with barriers, cell membranes, and other macromolecules. The averaged square distance from the origin is still proportional to the elapsed time, but one would find that the particle has diffused a shorter distance than if it was in a glass of water. The probability of having diffused a certain length is still mostly independent of the direction (b). In ordered media, such as white matter, the probability of diffusion is dependent on the direction, since the particle is more likely to move in the direction of the axon major axis than orthogonal to it (c).

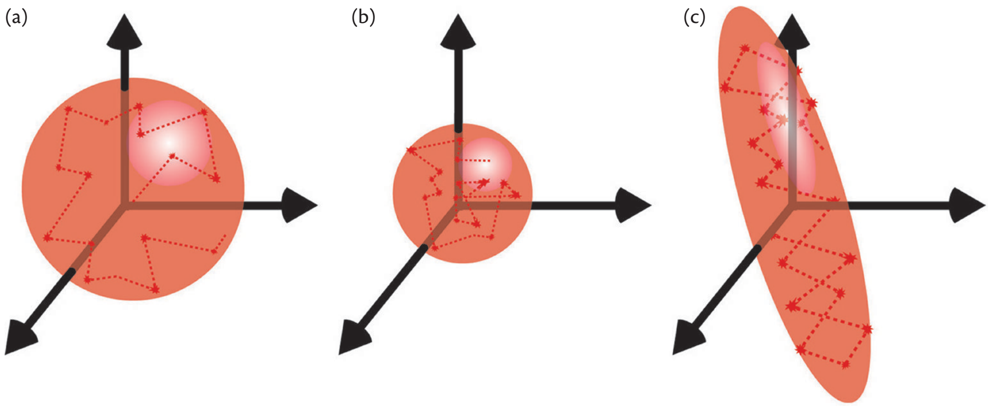

Fig. 4.2 Diffusion ellipsoids for the three cases of Fig. 4.1: isotropic self-diffusion (a), isotropic diffusion (b) and anisotropic diffusion (c) in complex media.

From the tensor, different indices can be extracted, the most popular being the mean diffusivity (MD) and the fractional anisotropy (FA). MD is the mean of the three diffusivities measured along the eigenvectors and is interpreted as the average diffusivity in the voxel (Fig. 4.3a). FA is proportional to the standard deviation of the diffusivities measured along the eigenvectors divided by their root mean squared and quantifies the degree of anisotropy of the media (Fig. 4.3b), scaled so that anisotropic tissues have FA values closer to 1, while isotropic tissues have FA values closer to 0 [4]. In addition, the orientation of the local structures can be measured voxel-wise as the orientation of the principal eigenvector, i.e. the direction of the greatest diffusivity. This is generally displayed using a colour convention, according to which red indicates left-right orientation, green indicates anterior-posterior orientation and blue indicates superior-inferior, weighted by the FA map (Fig. 4.3c) [5].

The orientational content of the diffusion signal has been exploited to gain information about the local fibre pathways architecture, assuming that the direction in which the diffusivity of the

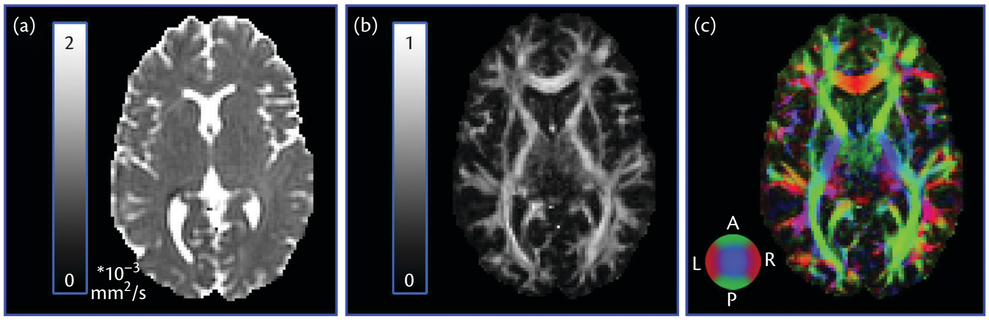

Fig. 4.3 Illustrative images of DT-MRI parametric maps from a healthy volunteer. Mean diffusivity (a), fractional anisotropy (FA, b) and direction of largest diffusivity, weighted by the FA (c).

fitted tensor is greatest coincides with the main fibre orientation. By merging this information in contiguous voxels, axonal tracts can be followed, allowing the delineation of specific white matter pathways. This process is referred as to tractography [6–11].

The widespread popularity that D-MRI, in general, and DT-MRI, in particular, has gained in the last 20 years relies on its non-invasiveness and versatility, currently being widely applied in research, as well as in clinical practice. This chapter focuses on the DT-MRI framework, i.e. the framework that uses the diffusion tensor to model diffusion data. Optimal strategies for acquiring and analysing DT-MRI data are discussed in the subsequent two sections. In the following section, the major advances documenting the clinical utility of DT-MRI are reviewed briefly (for a more detailed review, see [12]). The final section is devoted to those techniques that overcome the diffusion tensor model to provide a better understanding of the biophysics associated with the diffusional dynamics.

How to acquire diffusion data

The first step to be performed before starting a DT-MRI experiment is to ensure that the instrumentation is free from systematic errors that may affect the accuracy in the estimate of the parameters of interest. Such errors can be eliminated by performing a quality assurance (QA) routine. The hardware components most likely to influence accuracy comprise the gradient system—errors in gradient amplitude, direction, and linearity can contribute up to 10% inaccuracy in quantification of apparent diffusivity [13]. Several phantoms for checking FA and fibre orientation estimates have been built ad-hoc over the last few years [14–16], but they are still not widely available. Liquids of known diffusivity can be used to calibrate the absolute gradient power [17–20]. This requires a constant temperature check. Recently, a QA pipeline specific for D-MRI has been introduced [21], the advantage being that it requires an isotropic phantom and that the temperature does not need to be known.

When designing a DT-MRI experiment, the researcher has to choose a number of parameters, striking a good balance between the precision of the results and the experimental time that can be afforded. The most commonly used acquisition scheme is now the twice-refocused spin-echo echo planar imaging (EPI) sequence that is designed to minimize the distortions caused by the rapid switching on and off of the gradients [22] used to label the water molecules [1]. The first step is to choose the geometry to be prescribed, on the basis of the CNS areas of interest, taking into account that more slices mean a longer repetition time and, thus, an increased total experimental time. Pure axial orientation gives the best quality data in terms of ghosts and distortions. For most purposes (tractography above all), it is highly desirable to have isotropic imaging voxels, so that there is no preferential averaging of fibre orientations along a particular axis. Smaller voxels allow for increased definition of anatomical details, but since they also lead to a reduction in the signal-to-noise ratio (SNR), is it important to ensure that the SNR of all scans falls above a given threshold, to avoid hitting the domain where the Rician-distributed data begin to look non-Gaussian [23,24] (at any rate, models exist to account for this). A simple calculation suggests that the SNR in white matter in the non-diffusion weighted image needs to be greater than 20 (for the details, see [25], note 10).

Once the geometry is chosen, the sequence parameters that need to be defined by the user are the *b*-value and the gradient orientations, because the other experimental parameters (echo time, diffusion time and gradient duration) are normally optimized by the scanner to maximize the SNR.

The optimal *b*-value is generally dependent on the parameter of interest whose variance is to be minimized, but it is possible to define a range in which good estimates of the most studied D-MRI parameters can be drawn. It has been shown that the optimal choice of the *b*-value falls for CNS imaging in the range $750<b<1300$ s/mm^2, providing good estimates of MD, FA, and fibre orientations [26–28].

While the *b*-value has only a modest effect on the total experimental time, the number of gradient orientations impacts on the experiment duration. Six is the bare minimum number of unique gradient orientations needed for tensor reconstruction, but when there are no time constraints, more orientations should be acquired, resulting in an overdetermined system that permits a more robust tensor estimation. Jones [29] has shown that unique sampling orientations should be chosen, rather than repeats of the same set of sampling orientations, to maximize the statistical rotational invariance on DTI estimates, i.e. the dependence of the uncertainty in parameters as a function of orientation of the structure with respect to the encoding gradients. Available data suggest that 20 or more unique orientations is ideal to maximize the precision for FA [30], while 30 or more unique orientations are needed for obtaining robust estimates of MD and the principal eigenvector orientation [29]. In addition, the gradient sampling vectors should be distributed in the space as uniformly as possible in order to have an average SNR that is as uniform as possible, irrespective of the fibre orientation. Conturo et al. [31] observed that the optimal arrangement of four vectors (i.e. tetrahedral) also occurs in nature to uniformly balance electrostatic repulsion in chemical *sp*3 hybrid orbitals. This can be extended to any number of gradient orientations, so that a practical way of choosing *n* evenly distributed gradient directions is that of minimizing the total electrostatic repulsion between 2*n* charges on a sphere. A good practice is also to order the gradient directions to be run, so that if the scan is corrupted or terminated before completion, due to subject non-compliance, the most uniform coverage of the sphere is obtained [32,33].

When more gradient orientations are sampled, one should also acquire more than one unweighted image, so that the ratio of measurements made with diffusion weighting to those without should be around 8–10:1 [26]. For a comprehensive approach to optimal strategies for DT-MRI acquisition, see [34].

Accuracy and precision can be compromised by artefacts. The most relevant sources of artefacts in D-MRI are cardiac pulsation, subject motion, and hardware-related artefacts (e.g. eddy current distortions). Brain diffusion measurements can be severely corrupted by cardiac-induced brain motion, involving mainly the brainstem and the periventricular regions [35]. The main effect on the diffusion-weighted images is a signal dropout, which in turn causes artefactual changes in diffusivity and anisotropy [36,37]. That is why it is recommended that diffusion data, if time allows, are acquired with cardiac-gating. Eddy currents cause image distortions, predominantly in the phase-encoding direction [38]. They need to be minimized through proper calibration of the pre-emphasis of the gradients [39] and by choosing diffusion pulse waveforms specifically designed to reduce eddy currents [22]. Diffusion images are also prone to other hardware-related artefacts; for a comprehensive analysis, see [40].

Non-brain D-MRI also has specific recommendations. Applications outside brain are often challenging due to the effect of the surrounding cerebrospinal fluid and lipid, the sensitivity to motion, and the presence of nearby bony structure. Thus, they require careful choices of the experimental set-up, e.g. to compensate the low SNR, low *b*-values are generally used (around $b = 500$ s/mm^2). Methods have been developed to overcome these challenges, e.g. suppression of fat and CSF signal, fast sequences, use of surface coils, and high field MR systems to allow high resolution imaging [41].

How to analyse diffusion data

Once the data have been collected, the first and most important step that must be done is to examine the raw images, checking for unexpected signal dropouts.

Residual eddy current-induced distortions and subject head motion must be corrected. Using affine registration of diffusion-weighted images with respect to the unweighted images is a popular way of addressing both motion and distortion at the same time, but it should be mentioned that slice-by-slice distortion corrections provide better results [42]. The affine registration has 12 degrees of freedom, with translation, rotation, magnification, and shear along each of the logical axes, i.e. *x*, *y*, and *z*. Normalized mutual information has been successfully used as an effective similarity measure for multimodal image registration; in D-MRI, it is preferred since diffusion and non-diffusion-weighted images have very different contrast [43,44]. It is important to rotate the gradient table after the affine registration; failure to do so in the presence of significant head motion can lead to substantial errors in estimates of anisotropy and fibre orientation [45].

There are three widely used approaches to estimate the diffusion tensor from the diffusion-weighted data—ordinary linear least squares, weighted linear least squares [2] and non-linear least squares [46]. The approaches are ordered according to increasing robustness against noise, but also increasing computational time. Linear least square methods involve the log transformation of the diffusion-weighted signal intensities. These approaches are computationally very advantageous, but the consequence of taking the log transformation is that, although the noise in the signal prior to the log transformation is uniform, after the log transformation, the variance in the log-transformed signal becomes a function of the signal itself. In weighted linear least square, the covariance matrix is instead used to account for the noise properties after such transformation. Non-linear least square approaches fit the model to the data directly and should be preferred when computational time is not an issue. It is also worth mentioning an approach recently proposed, known as robust estimation of tensors by outlier rejection (RESTORE) [35]. RESTORE uses iteratively reweighted least-square regression to identify potential outliers and subsequently exclude them, reducing the need for identifying corrupted images by visual inspection.

Tractography algorithms typically fall into two categories—deterministic and probabilistic. Deterministic algorithms account for only one estimate of fibre orientation at each point in space, usually based on the principal eigenvector, and a pathway is reconstructed by moving from one point to another by following its direction, as shown in Fig. 4.4. In probabilistic algorithms, at each point in space, there is a distribution of possible fibre orientations, and pathways are propagated repeatedly through this field, each time drawing a random sample from the distribution of orientations, thus leading to a distribution of possible pathways.

Deterministic algorithms require the user to specify termination criteria for the tracts, in order to constrain the tractography. Generally, tracking is terminated if the front of the tract enters a region where the anisotropy is below a fixed value (in order to prevent the tract reconstruction entering into the GM or CSF) or if the path turns more than a given angle between one step and the next (in order to exclude unfeasible tracts). FA = 0.15 and angles of 30° are common choices. There is, however, no general consensus in the literature as to what this angular threshold should be and depends on the anatomy, step size, and voxel dimensions. For probabilistic tractography instead, the only stopping criterion is the angular deviation between successive steps.

Clinical applications

In the last 20 years, FA has become the most widely used diffusion-based index in neurological research (the number of FA-related publications doubles every 3 years, with more than 3000 papers published so far), its reduction being commonly interpreted as a marker of loss of white matter integrity [47]. Before discussing the clinical applications of DT-MRI, it is useful to understand the origins of FA contrast.

The *b*-value that is typically used for DT-MRI analysis is such that the signal obtained is sensitive to the diffusivity of water *hindered* in the extracellular/extra-axonal space, while the water undergoing slower diffusion (such as the one trapped inside the axons or cells

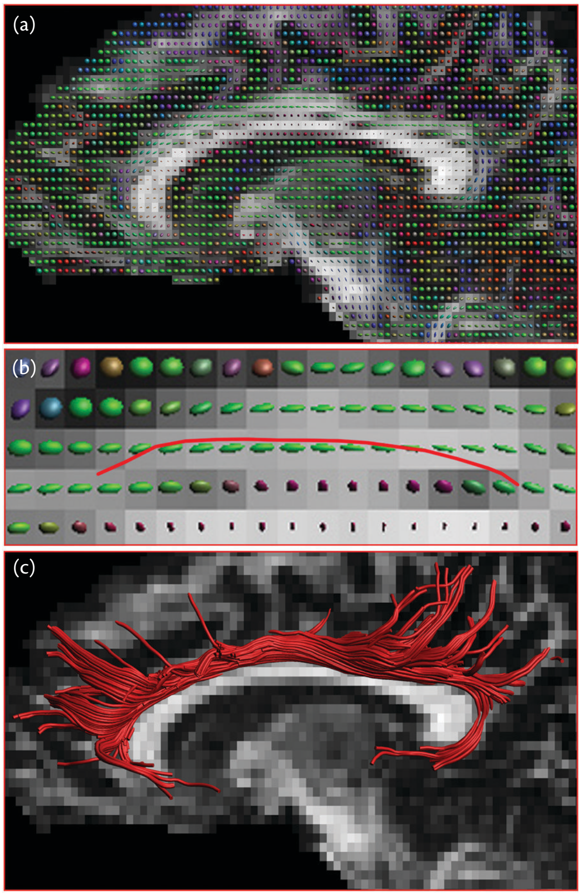

Fig. 4.4 Illustrative examples of deterministic tractography. The principal orientation of the diffusion tensor is used to define voxel-wise the dominant fibre orientation. Generally, an anisotropy threshold is selected, so that only voxels with a non-negligible anisotropy are used to propagate the tract, i.e. with diffusion ellipsoid that are enough 'pointy'. (a) The diffusion ellipsoids are shown for one sagittal slice. (b) The zoom on the central part of the cingulum bundle, which is characterized by high anisotropy and an anteroposterior orientation (green). The red line shows the streamline obtained by connecting up a set of pixels based on their preferred directions. (c) The result of the streamline reconstruction in the whole left cingulum bundle.

that is considered *restricted*) is only negligibly attenuated and thus cannot be measured.

In addition, myelin is not a prerequisite for obtaining diffusion anisotropy in neuronal tissue [48,49], even though it is now well recognized that myelin modulates FA values and thus FA is also sensitive to demyelination/remyelination. FA, however, also depends on a number of other factors, such as the axonal diameter, axonal density, and above all, architectural tissue paradigm [50]. Therefore, the FA contrast cannot be unambiguously assigned to a specific biological state, but it is more a sum of different contributions. A simulation using the CHARMED model [51,52] to create different biological conditions with the same measured FA values is shown in Fig. 4.5. A consequence of this is the fact that DT-MRI indices in general, and FA in particular, are very sensitive with respect to local changes in diffusivity properties, but not specific towards the cause of the observed change.

Brain

Several CNS pathological conditions are associated with significant changes in the diffusion properties of the involved tissue. Multiple sclerosis (MS) brains show significant reductions of FA and an increase of MD in areas where lesions are located, accompanied by a similar, but less marked pattern in areas on normal-appearing white matter [53–57]. Fig. 4.6 shows an example of the abnormalities that can be observed using DT-MRI compared with FLAIR imaging.

Elevation of water content (oedema) of a tissue compartment also modifies its diffusion properties. Two kinds of oedema are considered relevant in neurological research–cytotoxic oedema and vasogenic oedema. In the early 1990s, ADC images proved to be very useful to depict ischaemic strokes in the brain [58,59], by early detection (within a couple of minutes) of the cytotoxic oedema [60]. In the acute phase, the ischaemic lesion is associated with an ADC drop, caused by the increase of the intracellular volume due to cell swelling [61]. For a review on diffusion and perfusion MR imaging of acute ischaemic stroke, see [62,63]. With cell death and damage to the blood–brain barrier, vasogenic oedema occurs, which is characterized by an increased ADC and a marked decrease of FA values [64,65], caused by an increased extracellular volume.

DT-MRI maps (especially colour-coded maps) are widely used to delineate white matter around brain tumours [66–68], where the tumour can either displace or infiltrate the tissue. An example is reported in Fig. 4.7. This is very useful for presurgical planning and post-surgical monitoring. Recently, tractography reconstruction of fibre pathways crossing the area affected by a tumour has become an important tool to further improve neurosurgical planning [69–71].

DT-MRI has been successfully used to investigate the structural basis of normal brain development. The increase of white matter anisotropy during development appears to take place in two steps. The first increase takes place before the histologic appearance of myelin, and is accompanied by an increase in the number of microtubule-associated proteins in axons, a change in axon morphology, and a significant increase of oligodendrocytes [72,73]. The second, more marked increase of anisotropy is associated with the process of myelination that accompanies brain maturation. For a comprehensive review, see [74].

Spinal cord

D-MRI has been also widely applied outside the cerebral WM. Diffusion imaging in the acute phase may be relevant in predicting outcome from spinal cord trauma. Acute cord ischaemia also shows a specific pattern in the measured diffusion indices [75].

Spinal cord MRI is an important diagnostic instrument because focal lesions are common in early MS, and rare in other neurological diseases with non-specific brain lesions [76]. Demyelination affects both WM and GM throughout the spinal cord in MS and are visible as abnormalities in the diffusion indices in lesions [77], as well as in normal-appearing WM and GM [78].

Traumatic, tumorous, ischaemic or inflammatory lesions of the spinal cord, resulting in displacement and deformation of the white matter (WM) tracts, are also successfully displayed using DT-MRI tractography [79].

Optic nerve

Lesions of the optic nerve (optic neuritis, ON), mostly associated with MS, have also been investigated using D-MRI. An increase in ADC in chronic ON (but not in acute ON) was reported by Iwasawa et al. [80]. Diffusion indices were shown to successfully discriminate between affected nerves, and unaffected contralateral and healthy control nerves [81–83, but for a review, see 84]. However, questions about the mechanisms of specific tract vulnerabilities are

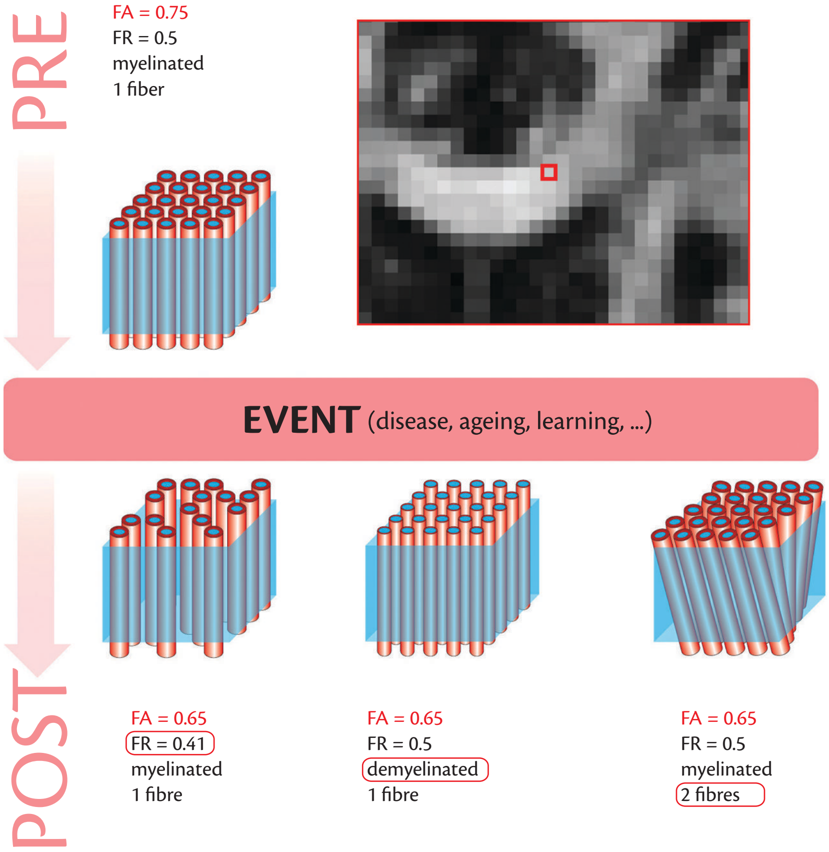
PRE
FA = 0.75
FR = 0.5
myelinated
1 fiber
EVENT (disease, ageing, learning, ...)
POST
FA = 0.65
FR = 0.41
myelinated
1 fibre
FA = 0.65
FR = 0.5
demyelinated
1 fibre
FA = 0.65
FR = 0.5
myelinated
2 fibres

Fig. 4.5 An example of the possible pitfalls in the interpretation of fractional anisotropy (FA) as an index of structural integrity. If two FA measures are collected from the same voxel, for example before and after an event that is supposed to be accompanied by microstructural modifications, a decrease in FA, from 0.75 to 0.65, can be caused by a number of different configurations (reduction in axonal density, demyelination, difference in the architectural paradigm). The values are obtained simulating the signal according to the CHARMED model [49,50].

still open since no correlative MRI–pathological study of the optic nerve exists [76].

Beyond DT-MRI

Despite the popularity that DT-MRI has acquired over the years, there are at least two major issues that dampen the enthusiasm of the research and clinical community—the inadequacy of the tensor model to characterize fibre orientation when there is more than one fibre population within a voxel, and the inadequacy of the Gaussian model to describe the diffusional dynamics when motion is restricted.

The first issue is often addressed experimentally using the high angular resolution diffusion imaging (HARDI) approaches, i.e.

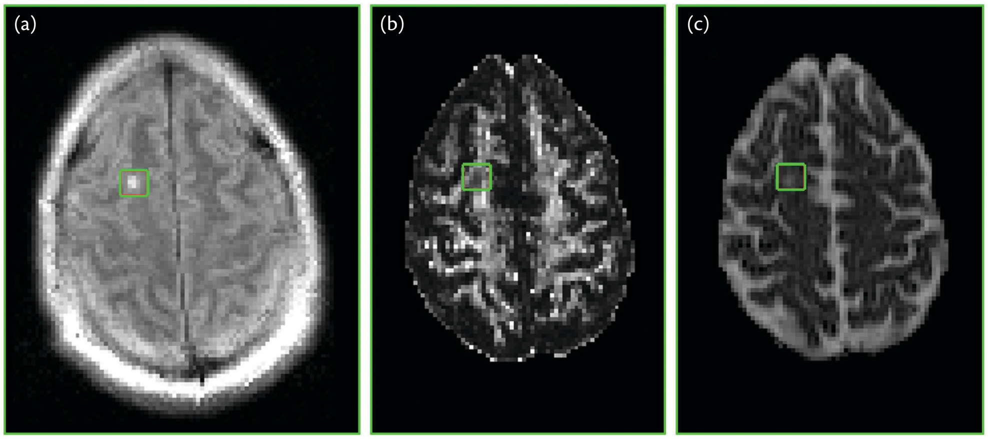

Fig. 4.6 An illustrative example of DT-MRI parametric maps from a patient with multiple sclerosis at disease onset. The FLAIR image (a) shows a hyperintense lesion. Decrease in fractional anisotropy (FA, b) and increased mean diffusivity (MD, c) are observed in the lesioned area using DT-MRI.

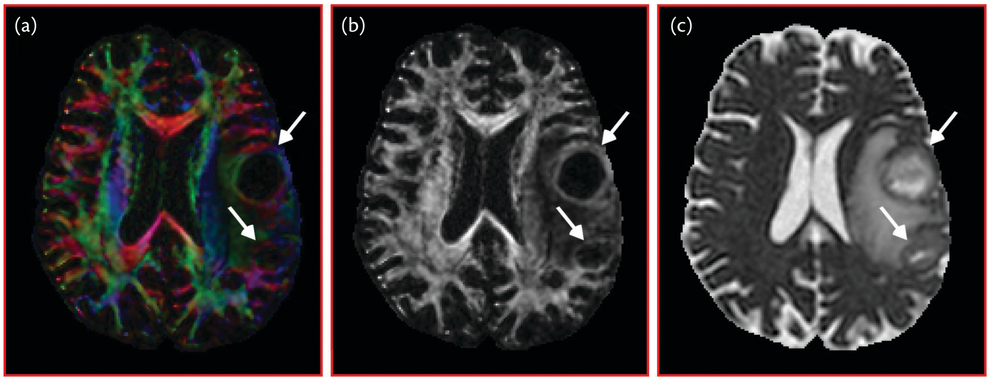

Fig. 4.7 An illustrative example of DT-MRI parametric maps from a patient with a brain tumour. The diffusion colour-coded map (a) and fractional anisotropy (FA) map (b) show hypo-intensity in the tumour area and hyper-intensity in the rim surrounding the tumour, while MD (c) is increased both in the tumour area and in the surrounding oedema.

Courtesy of Dr A. Bizzi.

using a large number of unique gradient orientations to acquire data and search for the *n* different fibre orientations that have generated the measured diffusion pattern. Several model-based and model-free approaches have been proposed to identify fibre orientation: fitting more than one tensor to the data [85], deconvolving the idealized response from a single fibre population to extract the distribution of fibre orientations [86,87], or obtaining the 3D displacement probability profile directly from the data using the mathematical properties of the diffusion signal [88,89]. Fig. 4.8 illustrates the impact of one of these HARDI approaches (the

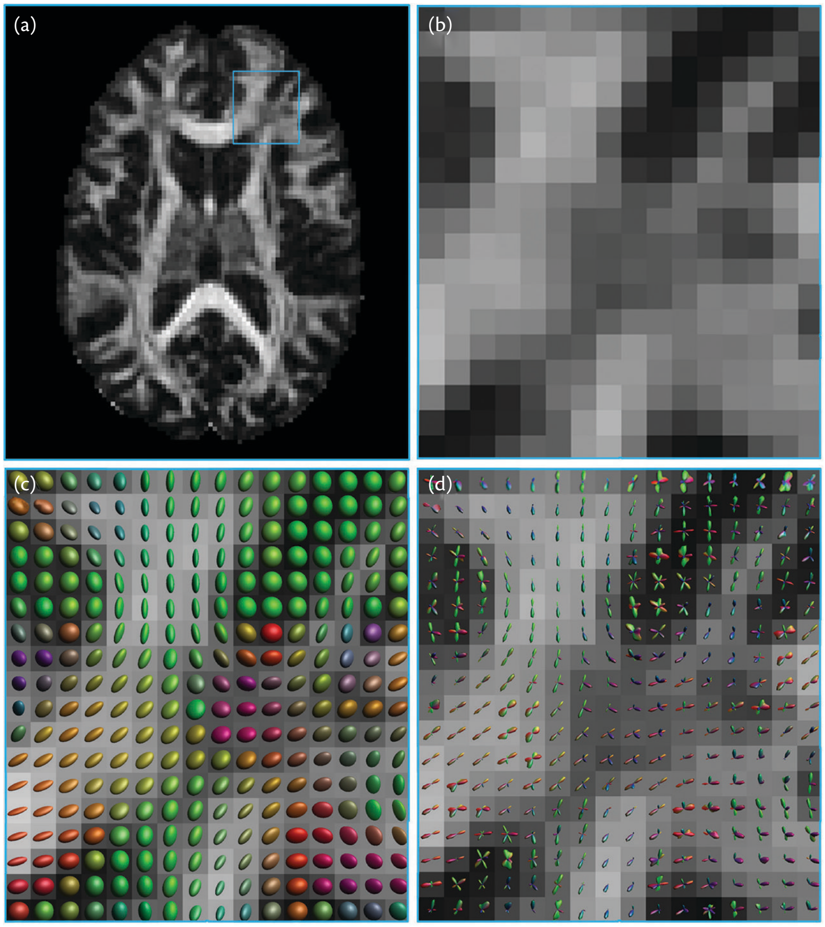

Fig. 4.8 Illustrative images to show the difference between the orientational information extracted from diffusion tensor and from HARDI. (a) An area of reduced fractional anisotropy (FA) is selected and magnified in (b). (c) The diffusion ellipsoids fail identifying the complex fibre orientation, where the genu of the corpus callosum is crossing the superior longitudinal fasciculus, that is instead detected by the HARDI (d).

constrained spherical deconvolution [86]) on the ability to define fibre orientations versus the tensor model. For a detailed review and comparison of these methods, see [90].

The second issue is generally addressed by modelling the signal as arising from different subcompartments, capitalizing on the sensitivity of D-MRI to different length scales of the water displacements and, thus, of cellular structures. To this end, more than one *b*-value is necessary. Initially, a bi-exponential model was introduced to fit the signal [91]. However, the volume fractions of the two water phases obtained using the bi-exponential model do not fit those known to characterize intra- and extracellular water fractions [92]), thus leading to controversial interpretations of the results. A popular approach to overcome this issue is the use of diffusional kurtosis imaging (DKI) [93,94]. In this model, the deviation from Gaussian behaviour is quantified using a convenient dimensionless metric called the excess kurtosis, which is determined from the first three terms of an expansion of the logarithm of the MR signal intensity in powers of *b*. At the moment, DKI proposes parametric maps to be used in combination with DT-MRI conventional outputs. More recently, it has been proposed that this intrinsic non mono-exponential behaviour can be described by a specific non-Gaussian probability density function leading to a stretched-exponential model for the diffusion signal as a function of the *b*-value [95–99].

Hybrid approaches can be particularly useful both for identifying more than one fibre orientation within a given voxel and for accounting for the non-Gaussian behaviour of the signal. For instance, the composite hindered and restricted model of diffusion, or CHARMED [51,52], explains the signal as the contribution of two different pools: a hindered extra-axonal compartment and one or more intra-axonal compartments, whose properties are characterized by a model of restricted diffusion perpendicular to fibre axis within impermeable cylinders. The former is accessible by tuning the *b*-value to focus on the fast-diffusing species, while the latters are accessible by tuning the *b*-value on the slow-diffusing species. This model provides distinct WM-specific parameters, e.g. axonal density, and was recently extended to estimate the axonal diameter [100,101].

As a concluding remark, it is very challenging to define general guidelines for performing non DT-MRI experiments, since the design is specific to the different techniques mentioned. A general recommendation is to go for high *b*-values, given that the angular dependency of signal is more pronounced at higher *b*-values [102–103], but considering that the SNR becomes much lower.

Acknowledgements

The author wishes to thank Professor D. K. Jones for useful discussions and suggestions.

References

1. Stejskal E, and Tanner J. (1965). Spin diffusion measurements: spin echoes in the presence of a time-dependent field gradient. *Journal of Chemical Physics*, **42**, 288–92.
2. Basser PJ, Mattiello J, and LeBihan D. (1994). Estimation of the effective self-diffusion tensor from the NMR spin echo. *Journal of Magnetic Resonance, Series B*, **103**(3), 247–54.
3. Basser PJ. (1995). Inferring microstructural features and the physiological state of tissues from diffusion-weighted images. *NMR in Biomedicine*, **8**(7–8), 333–44.
4. Beaulieu C. (2002). The basis of anisotropic water diffusion in the nervous system—a technical review. *NMR in Biomedicine*, **15**(7–8), 435–55.
5. Pajevic S, and Pierpaoli C. (1999). Color schemes to represent the orientation of anisotropic tissues from diffusion tensor data: application to white matter fiber tract mapping in the human brain. *Magnetic Resonance Medicine*, **42**(3), 526–40.
6. Conturo TE, Lori NF, Cull TS, et al. (1999). Tracking neuronal fiber pathways in the living human brain. *Proceedings of the National Academy of Sciences, USA*, **96**(18), 10422–7.
7. Jones DK, Simmons A, Williams SC, et al. (1999). Non-invasive assessment of axonal fiber connectivity in the human brain via diffusion tensor MRI. *Magnetic Resonance Medicine*, **42**(1), 37–41.
8. Mori S, Crain BJ, Chacko VP, et al. (1999). Three-dimensional tracking of axonal projections in the brain by magnetic resonance imaging. *Annals of Neurology*, **45**(2), 265–9.
9. Basser PJ, Pajevic S, Pierpaoli C, et al. (2000). In vivo fiber tractography using DT-MRI data. *Magnetic Resonance Medicine*, **44**(4), 625–32.
10. Parker GJM, Haroon HA, and Wheeler-Kingshott CAM. (2003). A framework for a streamline-based probabilistic index of connectivity (PICo) using a structural interpretation of MRI diffusion measurements. *Journal of Magnetic Resonance Imaging*, **18**(2), 242–54.
11. Poupon C, Mangin J, Clark CA, et al. (2001). Towards inference of human brain connectivity from MR diffusion tensor data. *Medical Image Analysis*, **5**(1), 1–15.
12. Assaf Y, and Pasternak O. (2008). Diffusion tensor imaging (DTI)-based white matter mapping in brain research: a review. *Journal of Molecular Neuroscience*, **34**(1), 51–61.
13. Conturo TE, McKinstry RC, Aronovitz JA, et al. (1995). Diffusion MRI: precision, accuracy and flow effects. *NMR in Biomedicine*, **8**(7–8), 307–32.
14. von dem Hagen EAH, and Henkelman RM. (2002). Orientational diffusion reflects fiber structure within a voxel. *Magnetic Resonance Medicine*, **48**(3), 454–9.
15. Fieremans E, Deene YD, Delputte S, et al. (2008). The design of anisotropic diffusion phantoms for the validation of diffusion weighted magnetic resonance imaging. *Physics in Medicine and Biology*, **53**(19), 5405–19.
16. Zhou F, Hubbard P, Eichhorn S, et al. (2011). Jet deposition in near-field electrospinning of patterned polycaprolactone and sugar-polycaprolactone core-shell fibres. *Polymer*, **52**, 3603–10.
17. Tofts PS, Lloyd D, Clark CA, et al. (2000). Test liquids for quantitative MRI measurements of self-diffusion coefficient in vivo. *Magnetic Resonance Medicine*, **43**(3), 368–74.
18. Nagy Z, Weiskopf N, Alexander DC, et al. (2007). A method for improving the performance of gradient systems for diffusion-weighted MRI. *Magnetic Resonance Medicine*, **58**(4), 763–8.
19. Spees WM, Song SK, Garbow JR, et al. (2012). Use of ethylene glycol to evaluate gradient performance in gradient-intensive diffusion MR sequences. *Magnetic Resonance Medicine*, **68**(1), 319–24.
20. Wu YC, and Alexander A. (2007). A method for calibrating diffusion gradients in diffusion tensor imaging. *Journal of Computer Assisted Tomography*, **31**, 984–93.
21. De Santis S, Evans CJ, and Jones DK. (2013). RAPID: a Routine Assurance Pipeline for Imaging of Diffusion. *Magnetic Resonance Medicine*, **70**(2), 490–6.
22. Reese TG, Heid O, Weisskoff RM, et al. (2003). Reduction of eddy-current-induced distortion in diffusion MRI using a twice-refocused spin echo. *Magnetic Resonance Medicine*, **49**(1), 177–82.
23. Edelstein WA, Bottomley PA, and Pfeifer LM. (1984). A signal-to-noise calibration procedure for NMR imaging systems. *Medical Physics*, **11**(2), 180–5.
24. Gudbjartsson H, and Patz S. (1995). The Rician distribution of noisy MRI data. *Magnetic Resonance Medicine*, **34**(6), 910–14.
25. Jones DK, and Leemans A. (2011). Diffusion tensor imaging. *Methods in Molecular Biology*, **711**, 127–44.
26. Jones DK, Horsfield MA, and Simmons A. (1999). Optimal strategies for measuring diffusion in anisotropic systems by magnetic resonance imaging. *Magnetic Resonance Medicine*, **42**(3), 515–25.
27. Armitage PA, and Bastin ME. (2001). Utilizing the diffusion-to-noise ratio to optimize magnetic resonance diffusion tensor acquisition

strategies for improving measurements of diffusion anisotropy. *Magnetic Resonance Medicine*, **45**(6), 1056–65.
28. Alexander DC, and Barker GJ. (2005). Optimal imaging parameters for fiber-orientation estimation in diffusion MRI. *NeuroImage*, **27**(2), 357–67.
29. Jones DK. (2004). The effect of gradient sampling schemes on measures derived from diffusion tensor MRI: a Monte Carlo study. *Magnetic Resonance Medicine*, **51**(4), 807–15.
30. Papadakis NG, Murrills CD, Hall LD, et al. (2000). Minimal gradient encoding for robust estimation of diffusion anisotropy. *Magnetic Resonance Imaging*, **18**(6), 671–9.
31. Conturo TE, McKinstry RC, Akbudak E, et al. (1996). Encoding of anisotropic diffusion with tetrahedral gradients: a general mathematical diffusion formalism and experimental results. *Magnetic Resonance Medicine*, **35**(3), 399–412.
32. Cook PA, Symms M, Boulby PA, et al. (2007). Optimal acquisition orders of diffusion-weighted MRI measurements. *Journal of Magnetic Resonance Imaging*, **25**(5), 1051–8.
33. Dubois J, Poupon C, Lethimonnier F, et al. (2006). Optimized diffusion gradient orientation schemes for corrupted clinical DTI data sets. *MAGMA*, **19**(3), 134–43.
34. Jones DK. (2011). In Jones DK. (ed.) *Diffusion MRI: theory, methods and applications*, Section III.15. Oxford: Oxford University Press, Oxford.
35. Chang LC, Jones DK, and Pierpaoli C. (2005). RESTORE: robust estimation of tensors by outlier rejection. *Magnetic Resonance Medicine*, **53**(5), 1088–95.
36. Skare S, and Andersson JL. (2001). On the effects of gating in diffusion imaging of the brain using single shot EPI. *Magnetic Resonance Imaging*, **19**(8), 1125–8.
37. Pierpaoli C, Marenco S, Rohde G, et al. (2003). Analysing the contribution of cardiac pulsation to the variability of quantities derived from the diffusion tensor. In: *Proceedings of the International Society for Magnetic Resonance in Medicine*, 11th Scientific Meeting.
38. Turner R, Lebihan D, Maier J, et al. (1990). Echo-planar imaging of intravoxel incoherent motion. *Radiology*, **177**, 407–14.
39. Papadakis NG, Martin KM, Pickard JD, et al. (2000). Gradient preemphasis calibration in diffusion-weighted echo-planar imaging. *Magnetic Resonance Medicine*, **44**(4), 616–24.
40. Skare ST, and Bammer R. (2011). In Jones DK (ed.), *Diffusion MRI: theory, methods, and applications*, Section III.12. Oxford: Oxford University Press.
41. Barker GJ. (2001). Diffusion-weighted imaging of the spinal cord and optic nerve. *Journal of Neurological Sciences*, **18**(Suppl. 1), S45–9.
42. Jones DK, and Cercignani M. (2010). Twenty-five pitfalls in the analysis of diffusion MRI data. *NMR in Biomedicine*, **23**(7), 803–20
43. Maes F, Collignon A, Vandermeulen D, et al. (1997). Multimodality image registration by maximization of mutual information. *IEEE Transactions in Medicine Imaging*, **16**(2), 187–98.
44. Studholme C, Constable RT, and Duncan JS. (2000). Accurate alignment of functional EPI data to anatomical MRI using a physics-based distortion model. *IEEE Transactions in Medicine Imaging*, **19**(11), 1115–27.
45. Leemans A, and Jones DK. (2009). The B-matrix must be rotated when correcting for subject motion in DTI data. *Magnetic Resonance Medicine*, 2009; **61**(6), 1336–49.
46. Koay CG, Chang LC, Carew JD, et al. (2006). A unifying theoretical and algorithmic framework for least squares methods of estimation in diffusion tensor imaging. *Journal of Magnetic Resonance*, **182**(1), 115–25.
47. Jones DK, Knösche TR, and Turner R. (2012). White matter integrity, fiber count, and other fallacies: the do's and don'ts of diffusion MRI. *NeuroImage*, **73**, 239–54.
48. Beaulieu C, and Allen PS. (1994). Determinants of anisotropic water diffusion in nerves. *Magnetic Resonance Medicine*, **31**(4), 394–400.
49. Wimberger DM, Roberts TP, Barkovich AJ, et al. (1995). Identification of 'premyelination' by diffusion-weighted MRI. *Journal of Computer Assisted Tomography*, **19**(1), 28–33.
50. Pierpaoli C, and Basser PJ. (1996). Toward a quantitative assessment of diffusion anisotropy. *Magnetic Resonance Medicine*, **36**(6), 893–906.
51. Assaf Y, Freidlin RZ, Rohde GK, et al. (2004). New modeling and experimental framework to characterize hindered and restricted water diffusion in brain white matter. *Magnetic Resonance Medicine*, **52**(5), 965–78.
52. Assaf Y, and Basser PJ. (2005). Composite hindered and restricted model of diffusion (CHARMED) MR imaging of the human brain. *NeuroImage*, **27**(1), 48–58.
53. Horsfield MA, Larsson HB, Jones DK, et al. (1998). Diffusion magnetic resonance imaging in multiple sclerosis. *Journal of Neurology, Neurosurgery, & Psychiatry*, **64**(Suppl. 1), S80–S84.
54. Werring DJ, Clark CA, Barker GJ, et al. (1999). Diffusion tensor imaging of lesions and normal-appearing white matter in multiple sclerosis. *Neurology*, **52**(8), 1626–32.
55. Bammer R, Augustin M, Strasser-Fuchs S, et al. (2000). Magnetic resonance diffusion tensor imaging for characterizing diffuse and focal white matter abnormalities in multiple sclerosis. *Magnetic Resonance in Medicine*, **44**(4), 583–91.
56. Filippi M, Cercignani M, Inglese M, et al. (2001). Diffusion tensor magnetic resonance imaging in multiple sclerosis. *Neurology*, **56**(3), 304–11.
57. Ciccarelli O, Werring DJ, Wheeler-Kingshott CA, et al. (2001). Investigation of MS normal-appearing brain using diffusion tensor MRI with clinical correlations. *Neurology*, **56**(7), 926–33.
58. Moseley ME, Kucharczyk J, Mintorovitch J, et al. (1990). Diffusion-weighted MR imaging of acute stroke: correlation with T2-weighted and magnetic susceptibility-enhanced MR imaging in cats. *AJNR American Journal of Neuroradiology*, **11**(3), 423–9.
59. Moseley ME, Mintorovitch J, Cohen Y, et al. (1990). Early detection of ischemic injury: comparison of spectroscopy, diffusion-, T2-, and magnetic susceptibility-weighted MRI in cats. *Acta Neurochirugia*, 51(Suppl.), 207–9.
60. Sevick RJ, Kanda F, Mintorovitch J, et al. (1992). Cytotoxic brain edema: assessment with diffusion-weighted MR imaging. *Radiology*, **185**(3), 687–90.
61. Mintorovitch J, Yang GY, Shimizu H, et al. (1994). Diffusion-weighted magnetic resonance imaging of acute focal cerebral ischemia: comparison of signal intensity with changes in brain water and Na+, K(+)-ATPase activity. *Journal of Cerebral Blood Flow & Metabolism*, **14**(2), 332–6.
62. Harris AD, Coutts SB, and Frayne R (2009). Diffusion and perfusion MR imaging of acute ischemic stroke. *Magnetic Resonance Imaging Clinics of North America*, **17**(2), 291–313.
63. Wu O, Nentwich L, Chutinet A, et al. (2011). In Jones DK. (ed.), *Diffusion MRI: theory, methods, and applications*, Section IV.31. Oxford: Oxford University Press.
64. Zelaya F, Flood N, Chalk JB, et al. (1999). An evaluation of the time dependence of the anisotropy of the water diffusion tensor in acute human ischemia. *Magnetic Resonance Imaging*, **17**(3), 331–48.
65. Beauchamp NJ, Ulug AM, Passe TJ, et al. (1998). MR diffusion imaging in stroke: review and controversies. *Radiographics*, **18**(5), 1269–83; discussion 1283–5.
66. Witwer BP, Moftakhar R, Hasan KM, et al. (2002). Diffusion-tensor imaging of white matter tracts in patients with cerebral neoplasm. *Journal of Neurosurgery*, **97**(3), 568–75.
67. Clark CA, Barrick TR, Murphy MM, et al. (2003). White matter fiber tracking in patients with space-occupying lesions of the brain: a new technique for neurosurgical planning? *NeuroImage*, **20**(3), 1601–8.
68. Field AS. (2011). In Jones DK. (ed.), *Diffusion MRI: theory, methods, and applications*, Section IV.33. Oxford: Oxford University Press.
69. Holodny AI, Schwartz TH, Ollenschleger M, et al. (2001). Tumor involvement of the corticospinal tract: diffusion magnetic resonance tractography with intraoperative correlation. *Journal of Neurosurgery*, **95**(6), 1082.
70. Yu CS, Li KC, Xuan Y, et al. (2005). Diffusion tensor tractography in patients with cerebral tumors: a helpful technique for neurosurgical planning and postoperative assessment. *European Journal of Radiology*, **56**(2), 197–204.

71. Nimsky C, Ganslandt O, Hastreiter P, et al. (2005). Preoperative and intraoperative diffusion tensor imaging-based fiber tracking in glioma surgery. *Neurosurgery*, **56**(1), 130–7; discussion 138.
72. Hüppi PS, Maier SE, Peled S, et al. (1998). Microstructural development of human newborn cerebral white matter assessed in vivo by diffusion tensor magnetic resonance imaging. *Pediatric Research*, **44**(4), 584–90.
73. Neil JJ, Shiran SI, McKinstry RC, et al. (1998). Normal brain in human newborns: apparent diffusion coefficient and diffusion anisotropy measured by using diffusion tensor MR imaging. *Radiology*, **209**(1), 57–66.
74. Hüppi PS, and Dubois J. (2006). Diffusion tensor imaging of brain development. *Seminars in Fetal and Neonatal Medicine*, **11**(6), 489–97.
75. Küker W, Weller M, Klose U, et al. (2004). Diffusion-weighted MRI of spinal cord infarction—high resolution imaging and time course of diffusion abnormality. *Journal of Neurology*, **251**(7):818–24
76. Filippi M, Rocca MA, Barkhof F, et al. (2012). Association between pathological and MRI findings in multiple sclerosis. *Lancet Neurology*, **11**(4), 349–60.
77. Miller DH, Thompson AJ, and Filippi M. (2003). Magnetic resonance studies of abnormalities in the normal appearing white matter and grey matter in multiple sclerosis. *Journal of Neurology*, **250**(12), 1407–19.
78. Hesseltine SM, Law M, Babb J, et al. (2006). Diffusion tensor imaging in multiple sclerosis: Assessment of regional differences in the axial plane within normal-appearing cervical spinal cord. *American Journal of Neuroradiology*, **27**(6), 1189–93.
79. Vargas MI, Delavelle J, Jlassi H, et al. (2008).Clinical applications of diffusion tensor tractography of the spinal cord. *Neuroradiology*, **50**(1), 25–9.
80. Iwasawa T, Matoba H, Ogi A, et al. (1997). Diffusion-weighted imaging of the human optic nerve: a new approach to evaluate optic neuritis in multiple sclerosis. *Magnetic Resonance Medicine*, **38**, 484–91.
81. Kolbe S, Chapman C, Nguyen T, et al. (2009). Optic nerve diffusion changes and atrophy jointly predict visual dysfunction after optic neuritis. *NeuroImage*, **45**(3), 679–86.
82. Naismith RT, Xu J, Tutlam NT, et al. (2010). Radial diffusivity in remote optic neuritis discriminates visual outcomes. *Neurology*, **74**(21), 1702–10.
83. Trip SA, Wheeler-Kingshott C, Jones SJ, et al. (2006). Optic nerve diffusion tensor imaging in optic neuritis. *NeuroImage* **30**, 498–505.
84. Kolappan M, Henderson AP, Jenkins TM, et al. (2009). Assessing structure and function of the afferent visual pathway in multiple sclerosis and associated optic neuritis. *Journal of Neurology*, **256**(3), 305–19.
85. Tuch DS, Reese TG, Wiegell MR, et al. (2002). High angular resolution diffusion imaging reveals intravoxel white matter fiber heterogeneity. *Magnetic Resonance Medicine*, 48(4), 577–82.
86. Tournier JD, Calamante F, Gadian DG, et al. (2004). Direct estimation of the fiber orientation density function from diffusion-weighted MRI data using spherical deconvolution. *NeuroImage*, **23**(3), 1176–85.
87. Tournier JD, Calamante F, and Connelly A. (2007). Robust determination of the fibre orientation distribution in diffusion MRI: non-negativity constrained super-resolved spherical deconvolution. *NeuroImage*, **35**(4), 1459–72.
88. Wedeen VJ, Hagmann P, Tseng WYI, et al. (2005). Mapping complex tissue architecture with diffusion spectrum magnetic resonance imaging. *Magnetic Resonance Medicine*, **54**(6), 1377–86.
89. Tuch DS. (2004). Q-ball imaging. *Magnetic Resonance in Medicine*, **52**(6), 1358–72.
90. Alexander DC. (2005). Multiple-fiber reconstruction algorithms for diffusion MRI. *Annals of the New York Academy of Sciences*, 1064, 113–33.
91. Maier SE, Vajapeyam S, Mamata H, et al. (2004). Biexponential diffusion tensor analysis of human brain diffusion data. *Magnetic Resonance in Medicine*, **51**(2), 321–30.
92. Nicholson C, and Syková E. (1998). Extracellular space structure revealed by diffusion analysis. *Trends in Neuroscience*, **21**(5), 207–15.
93. Jensen JH, Helpern JA, Ramani A, et al. (2005). Diffusional kurtosis imaging: the quantification of non-Gaussian water diffusion by means of magnetic resonance imaging. *Magnetic Resonance in Medicine*, **53**(6), 1432–40.
94. Lu H, Jensen JH, Ramani A, et al. (2006). Three-dimensional characterization of non-Gaussian water diffusion in humans using diffusion kurtosis imaging. *NMR in Biomedicine*, **19**(2), 236–47.
95. Bennett KM, Schmainda KM, Bennett RT, et al. (2003). Characterization of continuously distributed cortical water diffusion rates with a stretched-exponential model. *Magnetic Resonance Medicine*, **50**(4), 727–34.
96. Ozarslan E, Basser PJ, Shepherd TM, et al. (2006). Observation of anomalous diffusion in excised tissue by characterizing the diffusion-time dependence of the MR signal. *Journal of Magnetic Resonance*, **183**(2), 315–23.
97. Hall MG, and Barrick TR. (2008). From diffusion-weighted MRI to anomalous diffusion imaging. *Magnetic Resonance in Medicine*, **59**(3), 447–55.
98. Magin RL, Abdullah O, Baleanu D, et al. (2008). Anomalous diffusion expressed through fractional order differential operators in the Bloch-Torrey equation. *Journal of Magnetic Resonance*, **190**(2), 255–70.
99. De Santis S, Gabrielli A, Bozzali M, et al. (2011). Anisotropic Anomalous Diffusion assessed in the human brain by scalar invariant indices. *Magnetic Resonance in Medicine*, **65**, 1043–52.
100. Barazany D, Basser PJ, and Assaf Y. (2009). In vivo measurement of axon diameter distribution in the corpus callosum of rat brain. *Brain*, **132**(Pt 5), 1210–20.
101. Alexander DC, Hubbard PL, Hall MG, et al. (2010). Orientationally invariant indices of axon diameter and density from diffusion MRI. *NeuroImage*, **52**(4), 1374–89.
102. Alexander AL, Hasan KM, Lazar M, et al. (2001). Analysis of partial volume effects in diffusion-tensor MRI. *Magnetic Resonance Medicine*, **45**(5), 770–80.
103. Akazawa K, Yamada K, Matsushima S, et al. (2010). Optimum b value for resolving crossing fibers: a study with standard clinical b value using 1.5-T MR. *Neuroradiology*, **52**(8), 723–8

CHAPTER 5

Magnetization transfer imaging

Mark A. Horsfield and Mara Cercignani

The magnetization transfer phenomenon

Even in the very earliest days of magnetic resonance imaging (MRI), the physico-chemical properties of tissue were recognized as important contributors to image contrast, and therefore to the diagnostic value of the image [1,2]. The longitudinal (T_1) and transverse (T_2) relaxation times are influenced by the types of chemical and cellular structures that are found in tissue. Standard T_1- and T_2-weighting have formed the basis of contrast in most MR images since the clinical utility of these types of scan was demonstrated by showing abnormal morphology or pathology [3,4].

Standard MRI detects signals only from hydrogen nuclei (protons) that are 'mobile' (contained within a liquid)—if a hydrogen atom is part of a molecule that is large and cannot move about freely, then the signal from that hydrogen atom will decay too quickly to be seen using a clinical MRI scanner. Most MRI pulse sequences have minimum echo times of the order of 2–10 ms, so if the T_2 of the protons is less than a millisecond or so, then those protons cannot be detected directly by MRI. Such protons are found in large molecules (macromolecules), such as large proteins, cell membranes, and myelin. However, the mobile protons are in constant motion, and come into regular and intimate contact with the macromolecular protons; indeed, it is quite possible for a proton in a water molecule to exchange with a proton in a macromolecule when the water momentarily binds to the surface of the macromolecule. Under these conditions, it is easy to see that the spin state (the proton magnetization state, which is measured with MRI) of the mobile protons can exchange with that of the macromolecular protons, and vice versa (Fig. 5.1). This exchange of magnetization, which can be either by direct chemical exchange of the hydrogen atom or by spin-spin interactions, forms the basis of magnetization transfer imaging (MTI).

As shown in Fig. 5.1, the proton T_2 is reflected in the width of the resonance line that is seen in the MR spectrum: protons with a long T_2 have a narrow resonance line, while protons with a short T_2 have a broad resonance line. Using a radio frequency (RF) wave that has a frequency well away from the central narrow resonance line ('off-resonance'), it is possible to excite the macromolecular spins, while leaving the liquid spins largely unaffected. If sufficient off-resonance power is applied, then the macromolecular spins become 'saturated', a state in which the numbers of up-spins and down-spins are equalized, and the net magnetization vector is zero. If some of this saturated magnetization is transferred to the liquid protons by the exchange processes described above, then they, too, can become partially saturated and the signal intensity from the observable liquid protons is reduced; this forms the basis of the MT contrast mechanism (Fig. 5.2) [5].

Magnetization transfer in routine clinical imaging

Magnetization transfer (MT) contrast is generally used to increase the contrast between fluids and other tissues with a high macromolecular content in a number of MRI applications [6]. For example, in musculoskeletal imaging it is used to improve contrast between cartilage and synovial fluid, while in cardiac imaging, it can improve the conspicuity of the blood in white-blood imaging. Of particular note is its use in time-of-flight magnetic resonance angiography, where it is routinely used to increase suppression of the background brain tissue, resulting in striking improvement in small vessel conspicuity [7]. MT is also useful in contrast-enhanced brain MRI, where the background suppression results in increased conspicuity of enhancing lesions [8], which is of proven benefit in detecting acute MS lesions [9].

Measuring magnetization transfer

Acquisition of MT data

Continuous wave

Acquiring MT-weighted images with continuous wave (CW) off-resonance excitation requires MRI hardware that is not normally found on routine imaging machines. The RF energy is applied for a long period (typically of the order of one second) with quite low power, using a second transmitter system [5]. The RF energy is applied just before the image acquisition, and despite the low power, the energy absorbed can be significant because of the long application duration. Continuous wave saturation has now largely fallen out of use in clinical investigations.

Pulsed

Saturation of the macromolecular spins can also be achieved using regular clinical MRI systems without specialized hardware. The off-resonance pulses are applied in the same way as other pulses used as part of the imaging pulse sequence, but are interspersed between the image acquisition and are typically of slightly longer duration (of the order of 10 ms) and have a larger flip angle to create maximum magnetization saturation. The exact form of the RF pulse is not too important, as long as the frequency is sufficiently far away from the main water resonance and there is a smooth excitation profile with no pronounced side lobes so that direct saturation of the liquid pool is minimized.

Acquisition challenges

MRI systems operating at higher field strengths (3.0 T and beyond) are becoming increasingly common in the hospital, and with this

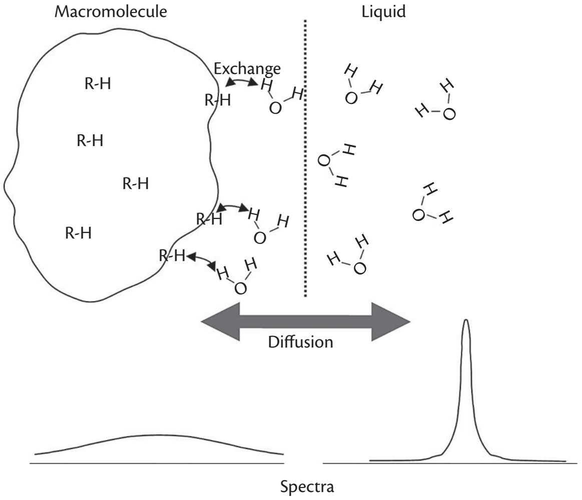

Fig. 5.1 Representation of a macromolecule that has functional groups (R) with bonded hydrogen atoms (H) that are available to exchange with those in water. Macromolecules are relatively immobile, and the nuclei of any hydrogen atoms on them exhibit a short transverse relaxation time T_2, so that their signal is not normally seen in an MR image. The short T_2 is also manifested as a broad resonance line in the MR spectrum. Conversely, liquids move freely and have a long T_2 and narrow resonance line. The spin states are in constant exchange between the macromolecule and the fluid, either by chemical exchange or by spin–spin interactions, so that the state of the magnetization in the macromolecule can influence that in the fluid.

comes a challenge for MT imaging. Although virtually all imaging will benefit from improved signal-to-noise ratio at high field, the power deposited in the patient by RF pulses increases rapidly with resonance frequency. This can be a limiting factor in the design of efficient MT pulse sequences where specific absorption rate (SAR) limits are easily reached, although the problem can mitigated by using pulses with a lower amplitude but longer duration [10].

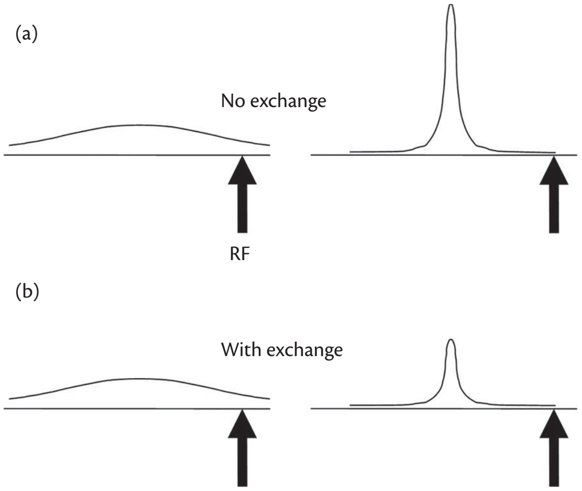

Fig. 5.2 If an off-resonance RF pulse, indicated by the arrow, is applied, it has no effect on the observable fluid spectrum if the fluid protons are not exchanging magnetization with the macromolecular protons (a). However, if there is exchange (b), then the saturated macromolecular magnetization is transferred to the fluid, resulting in a reduction of the amplitude of the observable signal. This is seen as a reduced brightness in the image in regions where the fluid is in intimate contact with macromolecules.

Quantification

One of the benefits of MT imaging is that it is able to probe the properties of protons bound to macromolecules, which are normally MRI-invisible, in a quantitative way. However, the degree of sophistication varies, with simple methods being quick to acquire, and more complex acquisition taking considerable scan time. A compromise needs be made between the time that can be devoted to MT imaging of each patient, and the information about the tissue and pathology that can be extracted.

Simple MT ratio

A simple approach to quantifying the degree of signal loss in an MT-saturated experiment is to calculate the magnetization transfer ratio (MTR). This was introduced by Dousset et al. [11], who computed the MTR as a percentage difference between two images, one acquired with off-resonance saturation (M_s) and one without (M_0):

$$\mathrm{MTR} = \frac{M_0 - M_S}{M_0} \times 100 \cdot$$

An MTR map is obtained by applying this simple formula on a voxel-by-voxel basis, and it is typically expressed in percentage units (pu), although in some cases it is expressed as a fraction. In the brain, both white and gray matter have a positive MTR, whose value depends on the amount of saturation applied, while CSF should have a value close to zero since the saturation pulses should ideally have no effect where there is no macromolecular content (Fig. 5.3).

Two-pool model

The MTR is regarded as a ‘quantitative’ measurement because it provides an index that can be compared between serial scans of the same patient (providing they have been collected using the same scanner and the same pulse sequence) or between populations of subjects, and can be correlated with clinical variables. However, the MTR does not have a direct physical or biological interpretation, since it is the result of a combination of several more fundamental quantities, rather than reflecting a particular one. Specifically, the MTR is dependent on T_1, as well as on the density of macromolecules. In some circumstances (e.g. demyelinating lesions) the increase in T_1 can partially mask the decrease in macromolecular density, resulting in an apparent stability of the MTR. Furthermore, the MTR is highly dependent on the acquisition parameters. The characteristics of the MT-saturating pulse, including the shape, amplitude, duration, and offset frequency, have a major effect on the measured MTR. Similarly, imaging parameters such as the repetition time (TR) and the excitation flip angle can affect the MTR [12].

A more quantitative approach, with the potential to provide measures of pathology more reproducible than the MTR, relies on an analytical description of the two-pool model.

Most of the quantitative MT (QMT) methods available to date are derived from the model proposed by Henkelman *et al.* [13], reproduced in Fig. 5.4. This model was originally developed for a CW irradiation experiment in agar gels, in which RF pulses of several seconds with constant amplitude are used to saturate the macromolecular pool.

In Fig. 5.4, pool ‘A’ represents the liquid pool, and pool ‘B’ represents the macromolecular pool. Each pool can be characterized by its density of spins, M_0^A and M_0^B, respectively. Since M_0^A is constant

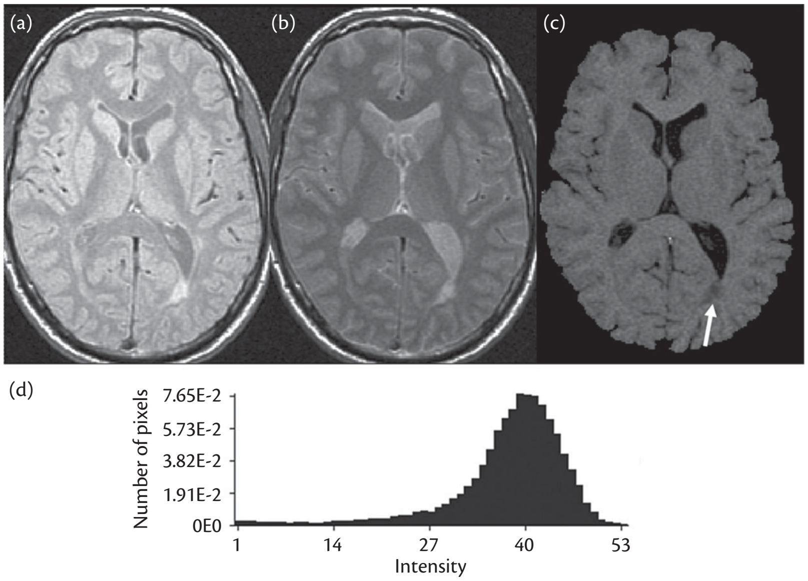

Fig. 5.3 One slice from a multi-slice data set: (a) without MT saturation pulse, (b) with off-resonance saturation pulse applied, (c) calculated MTR image. Note the low MTR value in the MS lesion posterior to the ventricular horn (arrow). (d) MTR histogram for this slice. The most common MTR value (histogram peak position) occurs at around 40 pu.

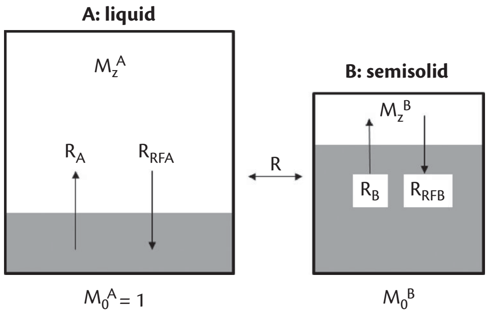

Fig. 5.4 Two-pool model proposed by Henkelman *et al.* [13]. The shaded areas correspond to the saturated spins at a given time. M_0^A and M_0^B are the fully relaxed values of magnetization associated with the two pools. Each pool is characterised by its longitudinal relaxation rates (R_A and R_B), and by its rate of loss of longitudinal magnetization due to the RF irradiation (R_{RFA} and R_{RFB}). The exchange rate between the two pools, R, is assumed to be symmetrical.

Adapted with permission from Henkelman RM, *et al.* (1993). *Magnetic Resonance Medicine*, Copyright 1993, John Wiley Inc.

and $M_0^A >> M_0^B$, it is often assumed to be unity to normalize the experiment. The shaded portion of the boxes in Fig. 5.4 represents the proportion of saturated spins in each pool, while the white area indicates the spins that are in the longitudinal direction, for a given instant of time. The proportion of saturated spins depends on the irradiation history. After the RF irradiation has been turned off, longitudinal relaxation tends to bring the magnetization back to the longitudinal direction, with relaxation rates R_A ($=1/T_1^A$) and R_B ($=1/T_1^B$), respectively. The effect of off-resonance irradiation, however, counteracts longitudinal relaxation and tends to reduce the longitudinal magnetization with rates R_{RFA} and R_{RFB}, respectively. Additionally, the two pools exchange magnetization with a rate constant R. The exchange in each direction is proportional to the relative populations, i.e. the exchange from A to B is characterized by a rate RM_0^B (often referred to as k_f) and the exchange from B to A by a rate RM_0^A.

Based on this model, a system of coupled Bloch equations [13] can be derived, describing the evolution of the system with time, as a function of the saturating amplitude and offset frequency. If the system can be solved for M_z at the time of signal sampling, the resulting signal intensity equation can be fitted to data collected with variable settings of saturating power and offset frequency.

In the CW case, considered by Henkelman *et al.*, the system can be solved analytically in the steady state, where R_{RFA} and R_{RFB} are proportional to the Lorentzian absorption line shape of each pool.

The Z-spectrum and extension to pulsed MT

The theoretical model introduced by Henkelman et al. [13] has been validated in vitro using either solutions that mimic the properties of tissue [13,14] or tissue samples [15,16] under CW irradiation. Measurements are typically obtained at variable saturating power and offset frequency, and normalized by the unsaturated signal intensity. The two-pool model can be fitted directly to the set of ratios M_A/M_0^A.

One of the first validating experiments was performed in agar gels [13], showing an agreement between calculations and measured data to within 1–3% (Fig. 5.5). Data can be plotted against the offset frequency to obtain what is known as a Z-spectrum [17], the shape of which is characteristic of the MT behaviour.

As mentioned in the section on 'Continuous wave', CW irradiation is impractical and generally not available for clinical imaging experiments. For a pulsed MT acquisition, Henkelman's equation must be modified to allow for the short duration of the saturation pulses relative to T_1. In this case, the system Bloch equations can only be solved numerically [18], which is impractical for model fitting. In order to provide a computationally-efficient approach, a number of approximated signal equations for pulsed MT, all based on the original two-pool model, have been developed [19–22]. We summarize the methods originally introduced almost simultaneously by three different groups.

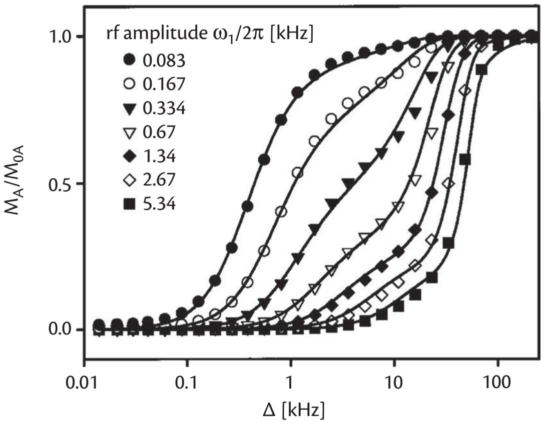

Fig. 5.5 Continuous wave magnetization transfer data from 4% agar gel (symbols) and the fitted two-pool model (solid line) of Henkelman *et al.* [13]. Data are plotted for six different RF amplitudes and 26 offset frequencies.

Reproduced with permission from Henkelman RM, *et al.* (2001). *NMR in Biomedicine*, Copyright 2001, John Wiley Inc.

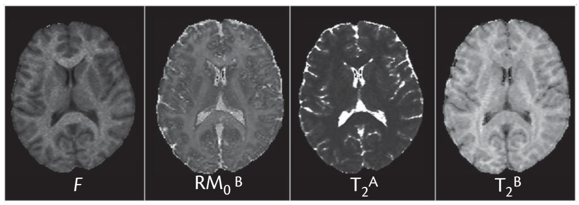

Fig. 5.6 Magnetization transfer parameter maps from a healthy participant, obtained by fitting Sled and Pike's model [20] to a set of 20 images obtained with variable RF amplitudes and offset frequencies. *F* is the relative size of the macromolecular pool (believed to reflect myelination), RM_0^B is the forward exchange rate, T_2^A is the transverse relaxation time of the liquid pool, and T_2^B is the transverse relaxation time of the macromolecular pool.

Ramani et al. used a continuous wave power equivalent approximation (CWPE) [21], where the pulse is simply approximated by CW irradiation with the mean square amplitude that would give the same power over the interval between MT pulses. By means of the CWPE approximation, Henkelman's steady state model can be straightforwardly applied to the *in vivo* MRI case, neglecting the imaging elements of the pulse sequence. Since Ramani's equation does not explicitly model the effects of the excitation pulses and TR, its description of the MT-weighted signal is valid only when the degree of T_1-weighting in the acquisition sequence is minimal [23]. The authors also introduced the macromolecular fraction,

$$f = \frac{M_0^B}{M_0^A + M_0^B}$$

as a proxy for the degree of myelination.

Sled and Pike [20] proposed an elegant approach based on the subdivision of the pulse sequence into a series of periods of free precession, CW irradiation, and instantaneous saturation of the free pool. During each of these periods, the coupled Bloch equations for the system have either an exact or an approximate solution, and these solutions can then be concatenated by imposing the appropriate initial conditions, leading to an expression for the measured signal which is less time-consuming to compute than numerically integrating the full set of differential equations.

The degree of myelination is quantified as the relative size of the macromolecular pool, *F*,

$$F = \frac{M_0^B}{M_0^A}.$$

Parameter maps produced using this approach are shown in Fig. 5.6. A modified version of this model was presented by Portnoy *et al.* [19].

Yarnykh [22] proposed a technique that approximates shaped RF pulses by an effective rectangular pulse, with the same duration as the real pulse (τ_{SAT}), and constant amplitude ω_{1eff}:

$$\omega_{1eff} = \frac{1}{\tau_{SAT}} \int_0^{\tau_{SAT}} \omega_1^2(t)dt.$$

This approach neglects any direct saturation of the liquid pool (thus requiring sufficiently large offset frequency). Following an approach similar to that of Sled and Pike [20], Yarnykh decomposed the sequence into a period of saturation, a delay for spoiling gradients, a read-out period, and a relaxation period.

The solutions (in matrix form) obtained for each period are then concatenated to yield an expression for the magnetization vector immediately before a read-out pulse. Assuming short time intervals and low excitation flip angles, the expression is further simplified using a first order approximation.

It has been shown [19,23] that these three approximations yield consistent results, providing that the experimental conditions comply with the basic assumptions.

Beyond the two-pool model

The two-pool model is a simplistic description of WM characteristics, which neglects the existence of multiple water compartments. Based on the results obtained using quantitative T_2 mapping [24,25], it is known that at least two separate water compartments can be distinguished in the human white matter—intra-/extracellular water and water trapped within the myelin layers. Quantitative T_2 mapping, however, does not account for the exchange of magnetization between proton pools. In summary, these two methods, namely QMT and T_2 mapping, offer two complementary views of white matter characteristics, both of which are limited, since T_2 imaging relies on the fundamental assumptions that water exists in isolated compartments, while the two-pool model for MT neglects the existence of multiple water pools. Combining these views, a more comprehensive model for WM that includes four communicating proton pools can be conceived. The four pools can be identified as myelin solids, myelin water, intra/extracellular water, and non-myelin solids, including most of the basic features of the multicompartment T_2 water model and the two-pool MT model. Such a model has been introduced [26,27], although the number of parameters to be fitted makes it impractical for *in vivo* applications. However, this analytical description can be used to predict the behaviour of T_2 spectra and MT as a function of myelin content, thus helping the interpretation of changes observed with these quantitative MRI methods based on simplified models of white matter [27].

Reduced models

Despite the potential added value of QMT imaging, its clinical applications have been limited so far, due to both the difficulty in the implementation, and the long scan times required for a robust estimation of the parameters of interest. The latter issue can be addressed by the introduction of simplified models, which require a smaller number of parameters to be estimated.

One strategy to decrease the data required is to impose physically meaningful constraints on some of the model parameters, thus reducing the number of quantities to be estimated to a subset. Yarnykh and Yuan [28] used this approach and constrained both T_2^A and T_2^B, based on some experimental observations. First, they noted that the product $T_2^A R_A$ is fairly constant in CNS tissues, despite the variability of T_2^A and R_A taken separately. Secondly, they observed that T_2^B values for the brain, both *in vivo* and *in vitro* [16,29] are fairly constant, typically ranging between 9 and 12 μs, with little difference between white and gray matter. By fixing the ratio $T_2^A R_A$ to 0.055 (at 1.5 T) and T_2^B to 11 μs, they were able to reduce the number of MT sampling points to 4 (plus a T_1-mapping scan).

An alternative approach to simplifying MT models relies on other assumptions. For example, the complexity is greatly reduced if complete saturation of the macromolecular pool is assumed. Then, the forward exchange rate (RM_0^B or k_f) can be expressed as a function of the T_1 measured under saturation (T_{1sat}) and of the MTR:

$$k_f = \frac{\text{MTR}}{T_{1\text{sat}}}\cdot$$

These conditions never hold for *in vivo* experiments, since complete saturation cannot be achieved for safety reasons. Nevertheless, Ropele *et al.* [30] have used this method to estimate k_f (RM_0^B) in conditions of incomplete saturation. Although k_f measured using this methods might be sensitive to biological changes, caution is needed when interpreting results of *in vivo* applications.

Finally, a simple method for obtaining MT-related information is to summarize the MT saturation effects in a single phenomenological parameter (comparable with the MTR), without attempting to assign it a specific biological meaning. As already mentioned, one of the limitations of the MTR is its dependency on T_1. Helms *et al.* [31] proposed a method based on three acquisitions (just one more than needed for a simple MTR computation) to separate the two contributions. The method is a modification of the T_1-quantification approach based on two 3D gradient-echo acquisitions with differing flip angles [32]. From these images, it is straightforward to compute the equilibrium magnetization and T_1. These quantities can then be used to extract the parameter of interest, δ (MT saturation), from a third acquisition, which is an MT-weighted 3D gradient-echo.

The phenomenological term δ is independent of relaxation, and appears to be sensitive to the presence of demyelination [33].

Sources of error

Quantification of the MTR is a relatively straightforward procedure, which essentially depends on the amount of saturation power applied. Thus, the most significant source of error in MT-weighted acquisitions is radiofrequency (B_1) field non-uniformity. Any error in the local B_1 field will be reflected in the estimated MTR, with higher values measured in the anatomical locations where B_1 is stronger. This issue becomes more relevant with QMT. Similarly, any imperfection in the static magnetic field (B_0) will result in a deviation from the nominal value of Δf. B_1 inhomogeneity can be reduced by using the body-coil for transmission, although this solution is unlikely to be sufficient to mitigate the problem at field strengths higher than 1.5 T. Ideally, the B_0 and B_1 fields should be measured at the same time as the MT acquisition, and used to correct the data retrospectively.

When using 2D multi-slice sequences, it is possible to observe an incidental MT effect from the slice selective pulses used [34]. In a multi-slice acquisition, every slice-selective RF pulse is experienced as off-resonance irradiation by the other slices, and thus the amount of incidental MT saturation is related to the number of slices. This effect is likely to be relevant only for pulse sequences that use multiple refocusing pulses, such as rapid acquisition with relaxation enhancement (RARE) [35]. The magnitude of the effect is proportional to the number of RF pulses per unit time, and therefore it increases with the number of slices collected within a TR. Although attempts have been made to derive a simple model to describe this effect as a function of the number of excited slices [36], such a model is likely to be approximate since the frequency offset from resonance varies for each pulse.

Magnetization transfer data analysis methods in neuroimaging

Regional analysis

Region-of-interest (ROI) analysis may be useful for clarifying the degree of tissue damage within individual lesions seen on T_2-weighted scans, or within anatomical regions associated with particular symptoms or function. Here, the normal procedure would be to register a T_2-weighted scan with a calculated MT image, define the outline of the ROIs using the T_2-weighted images, and then transfer these outlines onto the MT images, using the calculated MT parameter value within the ROIs as an index of tissue damage.

Whole-brain analysis

With histogram analysis, a histogram of pixel MT parameter values is formed from the whole of the brain parenchyma; thus, both focal damage and more widespread diffuse tissue damage are reflected in changes to the shape of the histogram, with a general shift towards lower MTR values as the density of macromolecules is reduced with demyelination or axonal loss. However, histograms also have disadvantages: first, insight into the positional origin of changes in the histogram shape is lost. Secondly, cerebral atrophy can lead to an increase in the contamination of the signal from parenchyma by signal from cerebrospinal fluid (CSF). A simple intensity threshold can remove a great deal of the signal from CSF—a typical procedure is to discard the histogram below MTR values of 5–10 pu. This will ameliorate the problem, but partial volume effects mean that it is not possible to set the cut-off to remove the effect of CSF completely. Nevertheless, atrophy is an important factor in the progression of some neurological diseases, such as MS, and this aspect of the MTR histogram can also give insights into the status of patients [37].

Production of an MTR histogram first requires that the brain parenchyma and CSF be separated from other tissue. This segmentation procedure can be accomplished manually by delineating the brain outline, or automatically [38], and will probably be done most successfully using the non-MT image. After CSF removal (as in the preceding paragraph), the histogram can be conveniently divided into bins of 1 pu; this helps smooth out the effects of noise, while preserving the features of the shape of the histogram. The histogram is then normalized so that the sum of all bin values is unity; this removes the effect of brain size on the shape characteristics of the histogram.

Simple, robust statistics can summarize the shape of the histogram, such as the:

1. Location of the histogram peak.
2. Height of the histogram peak.
3. Average MTR.

Pathological damage to tissue in MS will cause a reduction in the density of macromolecules and a general shift towards lower MTR values. Normally, there will be a broadening of the histogram peak, reducing the peak height, although if the pathological damage is uniformly dispersed throughout the brain, an increase in peak height and corresponding narrowing of the peak may also be seen.

Interpretation

Parameter interpretation

Myelin is believed to dominate the MT exchange process in white matter, and therefore changes in the MTR have mainly been interpreted as myelin damage. The interpretation of MT changes in the grey matter is more challenging. The MTR value is proportional to the product $R \cdot F \cdot T_1^A$ [39], and therefore can reflect changes in any of these three parameters. Quantitative MT parameters reflect different properties of the macromolecular pool, and may potentially measure differing pathological substrates.

Most research has focused on demonstrating that F reflects myelin content. A post-mortem study [40] showed that a similar parameter was strongly associated with a histological measure of myelination obtained by assessing light transmittance on stained MS brain slices. The same paper also demonstrated the ability of that parameter to differentiate between demyelinated and remyelinated lesions, as well as between remyelinated lesions and the normal appearing white matter (NAWM). Evidence from animal models of demyelination and axonal loss [41,42], suggests that myelin alone could explain the difference in F measured in gray and white matter. These data also support the hypothesis that axonal loss in the absence of demylination does not affect F [42]. However, there is still some debate about whether the technique truly reflects myelin content *in vivo*.

Among the other MT parameters, T_2^B has received little attention, mainly because it appears relatively stable across conditions (healthy subjects versus patients, WM versus GM, etc.). Recent observations, however, suggest that this parameter might be sensitive to WM fibre orientation [43,44].

Finally, the interpretation of RM_0^B, or k_f, the pseudo-first order forward exchange rate, is uncertain, as the exact mechanisms of MT are still unknown. Based on results obtained in the cortex of patients with Alzheimer's disease, it has been suggested that it might reflect metabolic changes [45].

Clinical findings in the CNS

Multiple sclerosis

Many workers have shown a marked reduction of MTR values in MS lesions that would seem to indicate severe tissue damage [11,46–54]. Post-mortem studies also show a strong correlation between MTR values in MS lesions and the percentage of residual axons and the degree of demyelination [54,55].

Decreased MTR has also been found in the NAWM of MS patients, although the changes are more pronounced adjacent to focal T_2-weighted lesions [56,57]. Changes to the MT values in newly-enhancing MS lesions have been investigated over periods of time ranging from 3 to 36 months [58–64]. On average, MTR drops dramatically when the lesions start to enhance, and can show partial or complete recovery during the following few months. The rapid changes point to oedema and its resolution, or demyelination and remyelination as the most probable pathological mechanisms underlying these short-term MTR changes. However, it seems unlikely that oedema alone is sufficient to explain these findings, since previous studies [11,58] showed that oedema in the absence of demyelination results in only modest MTR reductions. It is intriguing that MTR reductions have also been detected in the NAWM before lesion formation [60,61,65]. Oedema, marked astrocytic proliferation, perivascular inflammation, demyelination, and axonal loss may all account for an increase in the unbound water fraction in the NAWM [54,66–68].

MT-MRI has also been used to assess the global MS brain disease burden with MTR histogram analysis [69]. MS patients typically have lower average MTR, histogram peak height and peak position than normal subjects [69,70].

QMT techniques have shown that the relative size of the macromolecular pool, F, is increased in lesions and NAWM, while the bound water T_2 increased only in lesions [71]. QMT has been used to investigate the pathological substrates of benign MS [72]. In the corticospinal tract, a reduction in the F, without a change in the diffusion fractional anisiotropy was interpreted as evidence of demyelination, but with axonal preservation.

Other white matter disorders

MT-MRI has been used to assess the tissue damage both within visible lesions and in the normal-appearing white matter in several other white matter disorders. Abnormally low MTR is typically seen in T_2 lesions associated with vascular diseases [73,74], human immunodeficiency virus (HIV) encephalitis [47], other infections [75] and systemic autoimmune diseases [76]. Markedly decreased MTR has been seen in lesions from patients with progressive multifocal leukoencephalopathy (PML) [77], central pontine myelinolisis [78], and cerebral autosomal dominant arteriopathy with subcortical infarcts and leukoencephalopathy (CADASIL) [79]. MTR changes in the NAWM have also been noted in some of these diseases [77,80,81], and also in traumatic brain injury [82,83].

The cervical cord has been studied in several white matter disorders using MTR histograms, such as Devic's neuromyelitis optica [84] and CADASIL [85]. It is even possible to study MTR changes in the optic nerve [86], although this remains challenging.

Other CNS disorders

MT-MRI has been used to quantify the extent of brain pathology in patients with other neurological and psychiatric conditions, including Alzheimer's disease (AD), Parkinson's disease (PD), epilepsy, and schizophrenia. In AD, diffuse changes are seen in the cortex and particularly in the temporal lobe GM, and changes correlate with cognitive impairment [87]; in early AD, reduced MTR is also seen in the hippocampus [88,89]. In PD, the location and extent of MTR changes seen in both white matter and subcortical grey matter are related to the symptomatology of the disease [90].

Reduced whole brain MTR histogram peak height has been reported in patients with nocturnal frontal lobe epilepsy, but not in those with idiopathic generalized epilepsy [91]. Reduced MTR values of amygdalae and hippocampi were reported in three of ten patients with temporal lobe epilepsy, but the MTR abnormality was concordant with electroclinical lateralization in only one of these patients [92].

Widespread MTR reductions have been also reported in the frontal and temporal cortex of schizophrenic patients [93], while decreased MTR in the parieto-occipital cortex and the genu of the corpus callosum were associated with the severity of symptoms. Reduced MTR values have also been found in the white matter of the temporal lobes of schizophrenic patients [94].

Chemical exchange saturation transfer

Principle of CEST and its applications

Chemical exchange saturation transfer (CEST), is a relatively novel contrast mechanism that shares some of the principles of MT. The main difference lies in the fact that, while MT contrast is based on magnetization exchange between cellular solid or semisolid protons and water protons, CEST contrast originates from chemical exchange between labile and water protons. These exchangeable solute protons resonate at a frequency different from the bulk water, and therefore CEST-MRI requires a much narrower bandwidth of the RF irradiation in order to be more specific to the resonances of interest, such as -NH and -OH groups. The saturation is subsequently transferred to bulk water. After a few seconds of irradiation, the water signal becomes slightly attenuated. The signal saturation can be visualized as a function of the saturating frequency using a Z-spectrum, in a similar fashion to MT. Since direct saturation of water is unavoidable and results in a symmetric signal reduction around the water resonance frequency, the water resonance is assigned a value of zero, and CEST effects are quantified via the so-called MTR asymmetry analysis [95]:

$$\mathrm{MTR}_{\mathrm{asym}}(\Delta\omega) = \mathrm{MTR}(\Delta\omega) - \mathrm{MTR}(-\Delta\omega) = \frac{S_{\mathrm{sat}}(-\Delta\omega)}{S_0} - \frac{S_{\mathrm{sat}}(\Delta\omega)}{S_0}$$

where Δω is the offset frequency. This analysis is also based on an inherent assumption of symmetry of non-CEST contributions around the water signal, which often is incorrect, especially *in vivo*.

To date, most CEST studies have been carried out *in vitro* [96,97] and in animal models [98,99]. Some *in vivo* human brain applications have been described [100], mainly in tumours.

Conclusion

Magnetization transfer imaging is a fairly well-established form of quantitative MRI. Using quite straightforward methods, if carefully performed, it can produce reliable, semi-quantitative values that are sensitive to CNS pathology. More quantitative methods that probe the underlying tissue changes more directly are still relatively new, and require considerable expertise to implement. Many further in-depth clinical studies are required to link the measures made with the pathology in various CNS disorders.

References

1. Damadian R. (1971). Tumor detection by nuclear magnetic resonance. *Science*, **171**(976), 1151–3.
2. Lauterbur PC. (1973). Image formation by induced local interactions: examples employing nuclear magnetic resonance. *Nature*, **242**(5394), 190–1.
3. Bydder GM, Steiner RE, Young IR, et al. (1982). Clinical NMR imaging of the brain: 140 cases. *AJR American Journal of Roentgenology*, **139**(2), 215–36.
4. Rinck PA, Bielke G, and Meves M. (1984). Modified spin-echo sequence in tumor diagnosis. *Magnetic Resonance in Medicine*, **1**(2), 236.
5. Wolff SD, and Balaban RS. (1989). Magnetization transfer contrast (MTC) and tissue water proton relaxation in vivo. *Magnetic Resonance in Medicine*, **10**(1), 135–44.
6. Balaban RS, and Ceckler TL. (1992). Magnetization transfer contrast in magnetic resonance imaging. *Magnetic Resonance Quarterly*, **33**(2), 773–8.
7. Edelman RR, Ahn SS, Chien D, et al. (1992). Improved time-of-flight MR angiography of the brain with magnetization transfer contrast. *Radiology*, **184**(2), 395–9.
8. Finelli D, Hurst G, Gullapali R, et al. (1994). Improved contrast of enhancing brain lesion on post-gadolinium, T1-weigthed spin-echo images with use of magnetization-transfer. *Radiology*, **190**(2), 553–9.
9. Mehta RC, Pike GB, and Enzmann DR. (1995). Improved detection of enhancing and nonenhancing lesions of multiple sclerosis with magnetization transfer. *American Journal of Neuroradiology*, **16**(9), 1771–8.
10. Cercignani M, Symms MR, Ron MA, et al. (2006). 3D MTR measurement: from 1.5 T to 3.0 T. *NeuroImage*, **31**(1), 181–6.
11. Dousset V, Grossman RI, Ramer KN, et al. (1992). Experimental allergic encephalomyelitis and multiple sclerosis: lesion characterization with magnetization transfer imaging. *Radiology*, **182**(2), 483–91.
12. Finelli DA, and Reed DR. (1998). Flip angle dependence of experimentally determined T1sat and apparent magnetization transfer rate constants. *Journal of Magnetic Resonance Imaging*, **8**(3), 548–53.
13. Henkelman RM, Huang X, Xiang Q-S, et al. (1993). Quantitative interpretation of magnetization transfer. *Magnetic Resonance in Medicine*, **29**(6), 759–66.
14. Morrison C, Stanisz G, and Henkelman RM. (1995). Modeling magnetization transfer for biological-like systems using a semi-solid pool with a super-Lorentzian lineshape and dipolar reservoir. *Journal of Magnetic Resonance, Series B*, **108**(2), 103–13.
15. Quesson B, Thiaudière E, Delalande C, et al. (1997). Magnetization transfer imaging in vivo of the rat brain at 4.7 T: interpretation using a binary spin-bath model with a superlorentzian lineshape. *Magnetic Resonance in Medicine*, **38**(6), 974–80.
16. Morrison C, and Henkelman MR. (1995). A model for magnetization transfer in tissues. *Magnetic Resonance in Medicine*, **33**(4), 475–82.
17. Grad J, Mendelson D, Hyder F, et al. (1991). Applications of nuclear magnetic cross-relaxation spectroscopy to tissues. *Magnetic Resonance in Medicine*, **17**(2), 452–9.
18. Graham SJ, and Henkelman RM. (1999). Pulsed magnetization transfer imaging: evaluation of technique. *Radiology*, **212**(3), 903–10.
19. Portnoy S, and Stanisz GJ. (2007). Modeling pulsed magnetization transfer. *Magnetic Resonance in Medicine*, **58**(1), 144–55.
20. Sled JG, and Pike GB. (2000). Quantitative interpretation of magnetization transfer in spoiled gradient echo MRI sequences. *Journal of Magnetic Resonance*, **145**(1), 24–36.
21. Ramani A, Dalton C, Miller DH, et al. (2002). Precise estimate of fundamental in-vivo MT parameters in human brain in clinically feasible times. *Magnetic Resonance Imaging*, **20**(10), 721–31.

22. Yarnykh VL. (2002). Pulsed Z-spectroscopic imaging of cross-relaxation parameters in tissues for human MRI: theory and clinical applications. *Magnetic Resonance in Medicine*, **47**(5), 929–39.
23. Cercignani M, and Barker GJ. (2008). A comparison between equations describing in vivo MT: the effects of noise and sequence parameters. *Journal of Magnetic Resonance*, **191**(2), 171–83.
24. Laule C, Leung E, Li DK, et al. (2006). Myelin water imaging in multiple sclerosis: quantitative correlations with histopathology. *Multiple Sclerosis*, **12**(6), 747–53.
25. Whittall KP, Mackay AL, Graeb DA, et al. (1997). In vivo measurement ofT2 distributions and water contents in normal human brain. *Magnetic Resonance in Medicine*, **37**(1), 34–43.
26. Levesque I, and Pike G. (2009). Characterizing healthy and diseased white matter using quantitative magnetization transfer and multicomponent T(2) relaxometry: a unified view via a four-pool model. *Magnetic Resonance in Medicine*, **62**(6), 1487–96.
27. Stanisz GJ, Kecojevic A, Bronskill MJ, et al. (1999). Characterizing white matter with magnetization transfer and T-2. *Magnetic Resonance in Medicine*, **42**, 1128–36.
28. Yarnykh VL, and Yuan C. (2004). Cross-relaxation imaging reveals detailed anatomy of white matter fiber tracts in the human brain. *NeuroImage*, **23**(1), 409–24.
29. Sled JG, Levesque I, Santos AC, et al. (2004). Regional variations in normal brain shown by quantitative magnetization transfer imaging. *Magnetic Resonance in Medicine*, **51**(2), 299–303.
30. Ropele S, Stollberger R, Hartung H, et al. (2000). Estimation of magnetization transfer rates from PACE experiments with pulsed RF saturation. *Journal of Magnetic Resonance Imaging*, **12**, 749–56.
31. Helms G, Dathe H, Kallenberg K, et al. (2008). High-resolution maps of magnetization transfer with inherent correction for RF inhomogeneity and T1 relaxation obtained from 3D FLASH MRI. *Magnetic Resonance in Medicine*, **60**(6), 1396–407.
32. Venkatesan R, Lin W, and Haacke EM. (1998). Accurate determination of spin-density andT1 in the presence of RF-field inhomogeneities and flip-angle miscalibration. *Magnetic Resonance in Medicine*, **40**(4), 592–602.
33. Draganski B, Ashburner J, Hutton C, et al. (2011). Regional specificity of MRI contrast parameter changes in normal ageing revealed by voxel-based quantification (VBQ). *NeuroImage*, **55**(4), 1423–34.
34. Dixon WT, Engels H, Castillo M, et al. (1990). Incidental magnetization transfer contrast in standard multislice imaging. *Magnetic Resonance Imaging*, **8**(4), 417–22.
35. Melki PS, and Mulkern RV. (1992). Magnetization transfer effects in multislice RARE sequences. *Magnetic Resonance in Medicine*, **24**(1), 189–95.
36. Santyr GE. (1993). Magnetization transfer effects in multislice MR imaging. *Magnetic Resonance Imaging*, **11**(4), 521–32.
37. Kalkers NF, Hintzen RQ, Van Waesberghe JH, et al. (2001). Magnetization transfer histogram parameters reflect all dimensions of MS pathology, including atrophy. *Journal of the Neurological Sciences*, **184**(2), 155–62.
38. Horsfield MA, Rovaris M, Rocca MA, et al. (2003). Whole-brain atrophy in multiple sclerosis measured by two segmentation processes from various MRI sequences. *Journal of the Neurological Sciences*, **216**(1), 169–77.
39. Henkelman RM, Stanisz GJ, and Graham SJ. (2001). Magnetization transfer in MRI: a review. *NMR in Biomedicine*, **14**(2), 57–64.
40. Schmierer K, Tozer DJ, Scaravilli F, et al. (2007). Quantitative magnetization transfer imaging in postmortem multiple sclerosis brain. *Journal of Magnetic Resonance Imaging*, **26**(1), 41–51.
41. Ou X, Sun S-W, Liang H-F, et al. (2009). The MT pool size ratio and the DTI radial diffusivity may reflect the myelination in shiverer and control mice. *NMR in Biomedicine*, **22**(5), 480–7.
42. Ou X, Sun S-W, Liang H-F, et al. (2009). Quantitative magnetization transfer measured pool-size ratio reflects optic nerve myelin content in ex vivo mice. *Magnetic Resonance in Medicine*, **61**(2), 364–71.
43. Cercignani M, Symms MR, Schmierer K, et al. (2005). Three-dimensional quantitative magnetisation transfer imaging of the human brain. *NeuroImage*, **27**(2), 436–41.
44. Muller D, Pampel A, and Moller H. (2010). Orientation dependence of magnetization transfer in human white matter. Paper presented at the International Society for Magnetic Resonance in Medicine (ISMRM), 18th Scientific Meeting, Stockholm, Sweden.
45. Giulietti G, Bozzali M, Figura V, et al. (2012). Quantitative magnetization transfer provides information complementary to grey matter atrophy in Alzheimer's disease brains. *NeuroImage*, **59**(2), 1114–22.
46. Dousset V, Brochet B, Vital A, et al. (1995). Lysolecithin-induced demyelination in primates—preliminary in-vivo study with MR and magnetization-transfer. *American Journal of Neuroradiology*, **16**(2), 225–31.
47. Dousset V, Armand JP, Huot P, et al. (1997). Magnetization transfer imaging in AIDS-related brain diseases. *Neuroimaging Clinics of North America*, **7**(3), 447–60.
48. Brenner RE, Munro PMG, Williams SCR, et al. (1993). The proton NMR spectrum in acute EAE: the significance of the change in the Cho:Cr ratio. *Magnetic Resonance in Medicine*, **29**(6), 737–45.
49. Lexa F, Grossman R, and Rosenquist A. (1994). MR of Wallerian degeneration in the feline visual system—characterization by magnetization transfer rate with histopathologic correlation. *American Journal of Neuroradiology*, **15**(2), 201–12.
50. Loevner LA, Grossman RI, McGowan JC, et al. (1995). Characterization of multiple sclerosis plaques with T1-weighted MR and quantitative magnetization transfer. *American Journal of Neuroradiology*, **16**(7), 1473–9.
51. Thorpe JW, Barker GJ, Jones SJ, et al. (1995). Magnetisation transfer ratios and transverse magnetisation decay curves in optic neuritis: correlation with clinical findings and electrophysiology. *Journal of Neurology, Neurosurgery & Psychiatry*, **59**(5), 487–92.
52. Kimura H, Meaney DF, McGowan JC, et al. (1996). Magnetization transfer imaging of diffuse axonal injury following experimental brain injury in the pig: characterization by magnetization transfer ratio with histopathologic correlation. *Journal of Computer Assisted Tomography*, **20**(4), 540–6.
53. Kimura, H Grossman, RI Lenkinski, RE, et al. (1996). Proton MR spectroscopy and magnetization transfer ratio in multiple sclerosis: correlative findings of active versus irreversible plaque disease. *American Journal of Neuroradiology*, **17**(8), 1539–47.
54. Van Waesberghe, JHTM Kamphorst W, De Groot CJA, et al. Axonal loss in multiple sclerosis lesions: magnetic resonance imaging insights into substrates of disability. *Annals of Neurology*, **46**(5), 747–54.
55. Schmierer K, Scaravilli F, Altmann DR, et al. (2004). Magnetization transfer ratio and myelin in postmortem multiple sclerosis brain. *Annals of Neurology*, **56**(3), 407–15.
56. Filippi M, Campi A, Dousset V, et al. (1995). A magnetization transfer imaging study of normal-appearing white matter in multiple sclerosis. *Neurology*, **45**(3), 478–82.
57. Loevner LA, Grossman RI, Cohen JA, et al. (1995). Microscopic disease in normal-appearing white matter on conventional MR images in patients with multiple sclerosis—assessment with magnetization transfer measurements. *Radiology*, **196**(2), 511–15.
58. Lai HM, Davie CA, Gass A, et al. (1997). Serial magnetisation transfer ratios in gadolinium-enhancing lesions in multiple sclerosis. *Journal of Neurology*, **244**(5), 308–11.
59. Dousset V, Gayou A, Brochet B, et al. (1998). Early structural changes in acute MS lesions assessed by serial magnetization transfer studies. *Neurology*, **51**(4), 1150–5.
60. Filippi M, Rocca MA, Martino G. (1998). Magnetization transfer changes in the normal appearing white matter precede the appearance of enhancing lesions in patients with multiple sclerosis. *Annals of Neurology*, **43**(6), 809–14.
61. Goodkin DE, Rooney WD, Sloan R, et al. (1998). A serial study of new MS lesions and the white matter from which they arise. *Neurology*, **51**(6), 1689–97.
62. Silver NC, Lai M, Symms MR, et al. (1998). Serial magnetization transfer imaging to characterize the early evolution of new MS lesions. *Neurology*, **51**(3), 758–64.

63. Van Waesberghe JHTM, Van Walderveen MAA, Castelijns JA, et al. (1998). Patterns of lesion development in multiple sclerosis: longitudinal observations with T1-weighted spin-echo and magnetization transfer MR. *American Journal of Neuroradiology*, **19**(4), 675–83.
64. Rocca MA, Mastronardo G, Rodegher M, et al. (1999). Long-term changes of magnetization transfer-derived measures from patients with relapsing-remitting and secondary progressive multiple sclerosis. *American Journal of Neuroradiology*, **20**(5), 821–7.
65. Pike GB, De Stefano N, Narayanan S, et al. (2000). Multiple sclerosis: magnetization transfer MR imaging of white matter before lesion appearance on T2-weighted images. *Radiology*, **215**(3), 824–30.
66. Arstila AU, Riekkinen P, Rinne UK, et al. (1973). Studies on the pathogenesis of multiple sclerosis. *European Neurology*, **9**(1), 1–20.
67. Allen I, and McKeown S. (1979). A histological, histochemical and biochemical study of the macroscopically normal white matter in multiple sclerosis. *Journal of the Neurological Sciences*, **41**(1), 81–91.
68. Evangelou N, Konz D, Esiri M, et al. (2000). Regional axonal loss in the corpus callosum correlates with cerebral white matter lesion volume and distribution in multiple sclerosis. *Brain*, **123**(9), 1845–9.
69. Van Buchem MA, McGowan JC, Kolson DL, et al. (1996). Quantitative volumetric magnetization transfer analysis in multiple sclerosis: Estimation of macroscopic and microscopic disease burden. *Magnetic Resonance in Medicine*, **36**(4), 632–6.
70. Filippi M, Iannucci G, and Tortorella C. (1999). Comparison of MS clinical phenotypes using conventional and magnetization transfer MRI. *Neurology*, **52**(3), 588–94.
71. Davies GR, Tozer DJ, Cercignani M, et al. (2004). Estimation of the macromolecular proton fraction and bound pool T2 in multiple sclerosis. *Multiple Sclerosis*, **10**, 607–13.
72. Spanò B, Cercignani M, Basile B, et al. (2010). Multiparametric MR investigation of the motor pyramidal system in patients with 'truly benign' multiple sclerosis. *Multiple Sclerosis*, **16**(2), 178–88.
73. Wong KT, Grossman RI, Boorstein JM, et al. (1995). Magnetization transfer imaging of the periventricular hyperintense white matter in the elderly. *American Journal of Neuroradiology*, **16**(2), 253–8.
74. Tanabe JL, Ezekiel F, Jagust WJ, et al. (1999). Magnetization transfer ratio of white matter hyperintensities in subcortical ischemic vascular dementia. *American Journal of Neuroradiology*, **20**(5), 839–44.
75. Gupta RK, Kathuria MK, and Pradhan S. (1999). Magnetization transfer MR imaging in CNS tuberculosis. *American Journal of Neuroradiology*, **20**(5), 867–75.
76. Rovaris M, Viti B, Ciboddo G, et al. (2000). Brain involvement in systemic immune mediated diseases: magnetic resonance and magnetisation transfer imaging study. *Journal of Neurology, Neurosurgery & Psychiatry*, **68**(2), 170–7.
77. Dousset V, Armand JP, Lacoste D, et al. (1997). Magnetization transfer study of HIV encephalitis and progressive multifocal leukoencephalopathy. *American Journal of Neuroradiology*, **18**(5), 895–901.
78. Silver NC, Barker GJ, MacManus DG, et al. (1996). Decreased magnetisation transfer ratio due to demyelination: a case of central pontine myelinolysis. *Journal of Neurology, Neurosurgery & Psychiatry*, **61**(2), 208–9.
79. Iannucci G, Dichgans M, Rovaris M, et al. (2000). A magnetization transfer imaging study of individuals with CADASIL. *Neurology*, **54**, A94.
80. Bosma GP, Rood MJ, Huizinga TW, et al. (2004). Detection of cerebral involvement in patients with active neuropsychiatric systemic lupus erythematosus by the use of volumetric magnetization transfer imaging. *Arthritis & Rheumatism*, **43**(11), 2428–36.
81. Dehmeshki J, Van Buchem MA, Bosma GPT, et al. (2002). Systemic lupus erythematosus: diagnostic application of magnetization transfer ratio histograms in patients with neuropsychiatric symptoms: initial results. *Radiology*, **222**(3), 722–8.
82. Bagley L, McGowan J, Grossman R, et al. (2000). Magnetization transfer imaging of traumatic brain injury. *Journal of Magnetic Resonance Imaging*, **11**, 1–8.
83. Sinson G, Bagley LJ, Cecil KM, et al. (2001). Magnetization transfer imaging and proton MR spectroscopy in the evaluation of axonal injury: correlation with clinical outcome after traumatic brain injury. *American Journal of Neuroradiology*, **22**(1), 143–51.
84. Filippi M, Rocca MA, Moiola L, et al. (1999). MRI and magnetization transfer imaging changes in the brain and cervical cord of patients with Devic's neuromyelitis optica. *Neurology*, **53**(8), 1705–10.
85. Rocca MA, Filippi M, Herzog J, et al. (2001). A magnetic resonance imaging study of the cervical cord of patients with CADASIL. *Neurology*, **56**(10), 1392–4.
86. Inglese M, Rovaris M, Bianchi S, et al. (2001). Magnetization transfer and diffusion tensor MR imaging of the optic radiations and calcarine cortex from patients with Leber's hereditary optic neuropathy. *Journal of the Neurological Sciences*, **188**(1–2), 33–6.
87. Bozzali M, Franceschi M, Falini A, et al. (2001). Quantification of tissue damage in AD using diffusion tensor and magnetization transfer MRI. *Neurology*, **57**, 1135–7.
88. Hanyu H, Asano T, Sakurai H, et al. (2001). Magnetization transfer measurements of the hippocampus in the early diagnosis of Alzheimer's disease. *Journal of the Neurological Sciences*, **188**(1–2), 79–84.
89. Ridha BH, Symms MR, Tozer DJ, et al. (2007). Magnetization transfer ratio in Alzheimer disease: comparison with volumetric measurements. *American Journal of Neuroradiology*, **28**, 965–70.
90. Hanyu, H Asano, T Sakurai, H, et al. (2001). Magnetisation transfer measurements of the subcortical grey and white matter in Parkinson's disease with and without dementia and in progressive supranuclear palsy. *Neuroradiology*, **43**, 542–6.
91. Ferini-Strambi L, Bozzali M, Cercignani M, et al. (2000). Magnetization transfer and diffusion-weighted imaging in nocturnal frontal lobe epilepsy. *Neurology*, **54**(12), 2331–3.
92. Li LM, Narayanan S, Pike GB, et al. (2000). Magnetization transfer ratio is unable to lateralize epileptic foci in patients with temporal lobe epilepsy. *American Journal of Neuroradiology*, **21**(10), 1853–6.
93. Foong J, Symms MR, Barker GJ, et al. (2001). Neuropathological abnormalities in schizophrenia: evidence from magnetization transfer imaging. *Brain*, **124**(5), 882–92.
94. Foong J, Maier M, Barker G, et al. (2000). In vivo investigation of white matter pathology in schizophrenia with magnetisation transfer imaging. *Journal of Neurology, Neurosurgery & Psychiatry*, **68**(1), 70–4.
95. Guivel-Scharen V, Sinnwell T, Wolff SD, et al. (1998). Detection of proton chemical exchange between metabolites and water in biological tissues. *Journal of Magnetic Resonance*, **133**(1), 36–45.
96. Aime S, Barge A, Delli Castelli D, et al. (2002). Paramagnetic lanthanide(III) complexes as pH-sensitive chemical exchange saturation transfer (CEST) contrast agents for MRI applications. *Magnetic Resonance in Medicine*, **47**(4), 639–48.
97. Snoussi K, Bulte JWM, Guéron M, et al. (2003). Sensitive CEST agents based on nucleic acid imino proton exchange: detection of poly(rU) and of a dendrimer-poly(rU) model for nucleic acid delivery and pharmacology. *Magnetic Resonance in Medicine*, **49**(6), 998–1005.
98. Gilad AA, McMahon MT, Walczak P, et al. (2007). Artificial reporter gene providing MRI contrast based on proton exchange. *Nature Biotechnology*, **25**(2), 217–9.
99. Ling W, Regatte RR, Navon G, et al. (2008). Assessment of glycosaminoglycan concentration in vivo by chemical exchange-dependent saturation transfer (gagCEST). *Proceedings of the National Academy of Sciences of the United States of America*, **105**(7), 2266–70.
100. Zhou J, Blakeley JO, Hua J, et al. (2008). Practical data acquisition method for human brain tumor amide proton transfer (APT) imaging. *Magnetic Resonance in Medicine*, **60**(4), 842–9.

CHAPTER 6

Cerebral perfusion imaging

Linda Knutsson and Birgitte Fuglsang Kjølby

Introduction

For several centuries, the importance of the delivery of blood to the human brain has been known. Constant upholding of blood supply is necessary to the brain tissue viability, since the blood carries oxygen and nutrition to it through the capillaries. The capillary blood flow in tissue is called perfusion, i.e. the volume of blood passing through a given volume or mass element of tissue per unit time. It is common to also include other haemodynamic parameters related to tissue blood supply in the perfusion framework, e.g. blood volume fraction (expressed as percent by volume) or as the volume of blood in a given mass element of tissue, and the mean transit time (in units of time) of blood through the local capillary network from the arterial to the venous side.

The study of cerebral blood flow (CBF) usually given in units ml/100 g/min, has clinical applications due to the changes in perfusion associated with several neurological diseases. Therefore, the generation of quantitative maps of perfusion and perfusion-related parameters can be used to identify areas with vascular disorders. Diagnosis, lesion characterization, and follow-up of treatment in oncology, trauma, depression, dementia, and acute ischaemic stroke are examples where assessment of perfusion is of value. This chapter is dedicated to cerebral perfusion imaging techniques using modalities such as magnetic resonance imaging (MRI), computed tomography (CT), and positron emission tomography (PET) and single photon emission computed tomography (SPECT).

Magnetic resonance perfusion imaging

Dynamic contrast-enhanced MRI

Introduction to DCE-MRI

Cerebral capillaries consist of vascular endothelium that has a functional barrier preventing the passage of large molecules, such as common clinical contrast agents, e.g. non-macromolecular paramagnetic gadolinium chelates. The blood–brain barrier (BBB) effectively confines contrast agent molecules to the vascular compartment, more precisely to the blood plasma. In case of its disruption, contrast agent may distribute into the extravascular, extracellular space (EES). By injecting a contrast agent and dynamically follow the bolus, often with spoiled gradient echo (GRE) sequences, information about the haemodynamics in the microvasculature can be obtained. An example from a dynamic contrast-enhanced magnetic resonance imaging (DCE-MRI) measurement can be seen in Fig. 6.1.

Data acquisition

The kinetics of the tracer, typically a gadolinium-based contrast agent, is monitored by T_1-weighted dynamic MRI. The presence of the contrast agent leads to an increase of the longitudinal relaxation rate $R_1 = 1/T_1$, and the concentration C is proportional to the contrast-induced change in longitudinal relaxation rate, i.e. $C = (1/r_1) \cdot \Delta R_1$, where r_1 is the longitudinal relaxivity of the contrast agent.

To obtain quantitative parameters using DCE-MRI, a two-step approach for data acquisition is often carried out. First, T_1 is quantified before administration of the contrast agent, referred to as baseline T_1. Thereafter, the dynamic acquisition is performed, with a few images collected before injection of the contrast agent, providing baseline signal, and the remaining images acquired during and up to several minutes after injection of the contrast agent. T_1 is estimated during baseline and the dynamic measurements by applying appropriate signal equations. Using the relation above, the concentration can be calculated.

Tracer kinetic analysis

To extract relevant parameters from experimental data, curve-fitting approaches are often employed. Since a large number of unknown parameters might generate unreliable estimates, pharmacokinetic models used in DCE-MRI must be relative straightforward. It is therefore common to include the effects of several physiological parameters into one model parameter.

The volume transfer constant K^{trans} [s^{-1}], reflecting the diffusive flux per unit volume of tissue (in mol/s/m^3) between the blood plasma and the EES is such a combined parameter. The rate of tracer uptake in tissue (per unit volume of tissue) can be expressed as:

$$\frac{dC_t}{dt} = K^{trans}\left(C_p - \frac{C_t}{v_e}\right), \qquad [1]$$

where C_t is tissue tracer concentration [M], C_p is tracer concentration in arterial blood plasma [M], v_e is the fractional EES volume, and t is time. The physiological interpretation of K^{trans} depends on the relationship between capillary permeability and blood flow. For example, at high permeability, K^{trans} represents the plasma blood flow, while in the other limiting case, when low permeability limits the tracer leakage, K^{trans} reflects the permeability-surface area product (PS):

$$K^{trans} = \rho F(1 - Hct) \qquad (F << PS) \qquad [2]$$

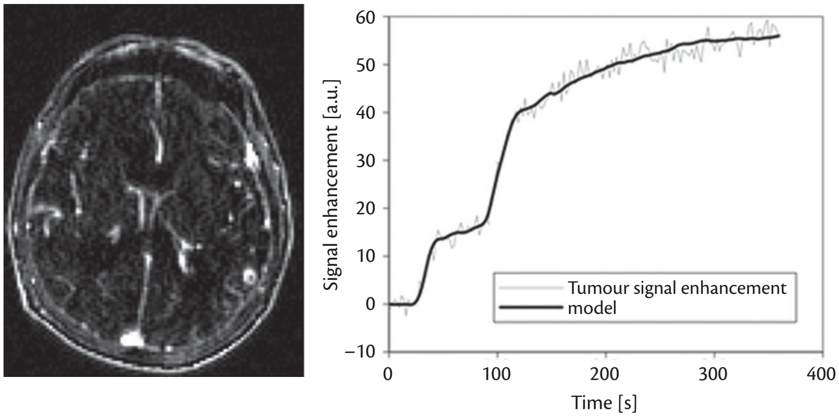

Fig. 6.1 To the left, area-under-curve map from a patient with a metastasis (left parietal) obtained using a DCE-MRI measurement. To the right, signal enhancement (in arbitrary units [a.u.] versus time in this metastasis (light grey), with two steep increases due to a dual bolus injection along with a fit of a model (black).
Courtesy of Michael Ingrisch, Ludwig-Maximilians-University Hospital, Munich, Germany.

$$K^{trans} = \rho PS \qquad \left(F >> PS\right), \qquad [3]$$

where ρ is tissue density [ml/g]. Simple two-compartment pharmacokinetic models exist for the cases of tracer flux being limited either by flow or by permeability, as well as for the intermediate case. Note, that the case of $PS = 0$ is not compatible with Tofts model [1].

Tofts model and extended version

The differential equation in Eqn 1 has the following solution (if $C_p = C_t = 0$ at $t = 0$):

$$C_t\left(t\right) = K^{trans}\int_0^t C_p\left(\tau\right)e^{-\frac{K^{trans}}{v_e}\left(t-\tau\right)}d\tau \qquad [4]$$

This is compatible with the model proposed by Kety [2] and this approach reflects the work by Tofts & Kermode [3] and Larsson et al. [4]. The equation states that the measured dynamic change in tissue concentration is modelled as a convolution of an exponential kernel and arterial blood or plasma concentration curve (i.e. arterial input function, AIF). If the blood volume cannot be neglected, a modified or extended model is applied by employing an additional term in Eqn 4, including the fractional plasma volume v_p and the arterial plasma concentration over time [5]:

$$C_t\left(t\right) = v_p C_p\left(t\right) + K^{trans}\int_0^t C_p\left(\tau\right)e^{-\frac{K^{trans}}{v_e}\left(t-\tau\right)}d\tau \qquad [5]$$

Model-independent deconvolution approach for blood flow estimation

By solving the basic tracer kinetic equation (Eqn 6) using model-independent deconvolution, perfusion F can be obtained:

$$C_t\left(t\right) = F\left[R\left(t\right)\otimes C_a\left(t\right)\right], \qquad [6]$$

where '$\otimes$' denotes convolution, C_a is tracer concentration in arterial whole blood [M], and $R(t)$ is the tissue impulse residue function, i.e. the fraction of tracer remaining in the tissue at time t, following the input of an infinitely short arterial bolus of tracer. By monitoring the first passage dynamically of a tracer bolus with high temporal resolution (of the order of 1–2 seconds) $C_a(t)$ and $C_t(t)$ can be obtained. This methodology is widely applied in dynamic susceptibility contrast magnetic resonance imaging (DSC-MRI), as will be discussed further. However, it is has also been applied in DCE-MRI [6,7].

Dynamic susceptibility contrast MRI

Introduction to DSC-MRI

Dynamic susceptibility contrast perfusion-weighted imaging is a bolus-tracking method, typically based on GRE echo planar imaging (EPI) or spin echo (SE) EPI [8,9]. The basic principle, which resembles that of DCE-MRI, is that by monitoring the passage of a contrast agent through the vascular tree in the tissue voxel of interest, dynamic information about the microvascular haemodynamics can be extracted, such as CBF, cerebral blood volume (CBV) and mean transit time (MTT; see the example in Fig. 6.2).

Data acquisition

The first passage of a rapidly-injected gadolinium-based and paramagnetic contrast agent bolus is dynamically monitored using fast imaging, often with full brain coverage. The contrast agent is confined to the intravascular compartment in the brain due to the BBB preventing it to leak out into the EES. The contrast agent affects the measured MR signal by accelerating the transverse relaxation of the water protons giving rise to a signal drop as it passes through the vascular system. The transverse relaxation is accelerated both for the water protons in the blood where the contrast agent is present, and also in a region around the contrast agent filled vessel. The latter comes from the compartmentalization of the paramagnetic contrast agent in the vessels, which gives rise to induced field inhomogeneities around the vessels.

Usually, it is assumed that a linear relation between the change in the transverse relaxation rate, ΔR_2, estimated from the measured signal and the concentration of the contrast agent, $C(t)$ exists, i.e.:

$$-\left(\frac{k}{TE}\right)\ln\left(\frac{S\left(t\right)}{S_0}\right) = k\Delta R_2 = C\left(t\right) \qquad [7]$$

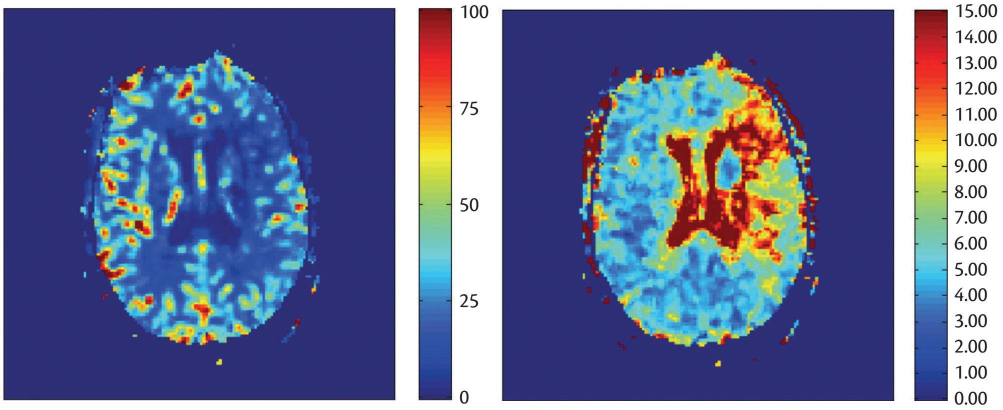

Fig. 6.2 DSC perfusion images of a stroke patient. CBF is shown to the left and MTT to the right. On the CBF image, a region with low perfusion relative to the opposite side is seen. The same region is found on the MTT image with prolonged MTT (yellow and red colours), which is typical for an ischaemic region.
Courtesy of Irene Klærke Mikkelsen, Aarhus University Hospital, Aarhus, Denmark.

where S_0 is the pre-bolus baseline signal, TE is the echo time, and k is the constant of proportionality. In most practical applications, the proportionality constant k is unknown, and the concentration is given in arbitrary units. As a first approximation, k is assumed to be independent of tissue type, and thereby equal for both tissue and blood [9].

Tracer kinetic analysis

The tracer kinetic model, which is used to extract the microvascular haemodynamics from the measured tissue concentration time-curve, requires a measurement of the input concentration time-curve to the tissue voxel of interest, also known as the AIF. It is impossible to measure the input concentration time-curve to each tissue voxel due to the limited spatial resolution. Practically, it is measured in larger arteries a distance away from the tissue voxel and usually one global input concentration time-curve is applied in the perfusion analysis of the entire brain.

The basic tracer kinetic model (see also Eqn 6) is given by:

$$C_t(t) = CBF\ R(t) \otimes C_a(t) = CBF \int_0^t R(\tau - t) C_a(\tau)\, d\tau, \qquad [8]$$

where $C_t(t)$ and $C_a(t)$ are the concentration time-curves measured in a tissue voxel, and in a voxel placed in a feeding artery, respectively [10]. The residue function, $R(t)$, describes the fraction of tracer still present in the vascular bed of the tissue voxel at time t after the bolus entered it. Therefore, $R(t)$ is a decreasing function with $R(0) \equiv 1$ and $R(\infty) = 0$ [11]. The residue function contains most of the details about the distribution and kinetics of the contrast agent in the tissue.

According to the tracer kinetic model, the product $CBF \cdot R(t)$ can be estimated by using either fitting or deconvolution, if $C_t(t)$ and $C_a(t)$ are known. In practice, CBF is estimated from:

$$CBF \;=\; max\left[CBF \cdot R(t)\right] \qquad [9]$$

The time point of which $CBF \cdot R(t)$ peaks (referred to as T_{max}) has been introduced as a predictive parameter in acute stroke imaging by several authors [12,13].

The CBV is found from the ratio of the areas under $C_t(t)$ and $C_a(t)$, respectively,

$$CBV = \frac{\int_0^t C_t(\tau)\, d\tau}{\int_0^t C_a(\tau)\, d\tau} \qquad [10]$$

The MTT is calculated by using the central volume theorem [14,15]:

$$MTT \;=\; CBV\,/\,CBF \qquad [11]$$

MTT can also be calculated using Zierler's area to height relation [10]:

$$MTT = \frac{\int_0^\infty R(t)dt}{\max\left[R(t)\right]} \qquad [12]$$

When the BBB is damaged, e.g. in tumours, the contrast agent is transported into the EES. The presence of contrast agent in the EES in some cases (but not always) leads to an elevated post-bolus signal as compared with the prebolus baseline signal. In this situation, the assumption in the previously described tracer kinetic analysis based on an intravascular contrast agent is violated. Thereby, the calculated perfusion parameters might become inaccurate unless appropriate tracer kinetic modelling is introduced [9]. Algorithms correcting for the effect of contrast agent leakage require some degree of tracer kinetic modelling and the use of appropriate pulse-sequence signal equations [16–18]. Another approach to minimize the signal enhancement is to give a predose consisting of a small amount of the contrast agent [19,20].

Arterial spin labelling

Introduction to ASL

Arterial spin labelling (ASL) is a MRI approach for the measurement of perfusion, where magnetically labelled water in the blood is used as an endogenous diffusible tracer [21]. By applying an inversion or saturation pulse to a tissue-feeding artery, labelling or tagging is accomplished, and when the arterially-labelled water

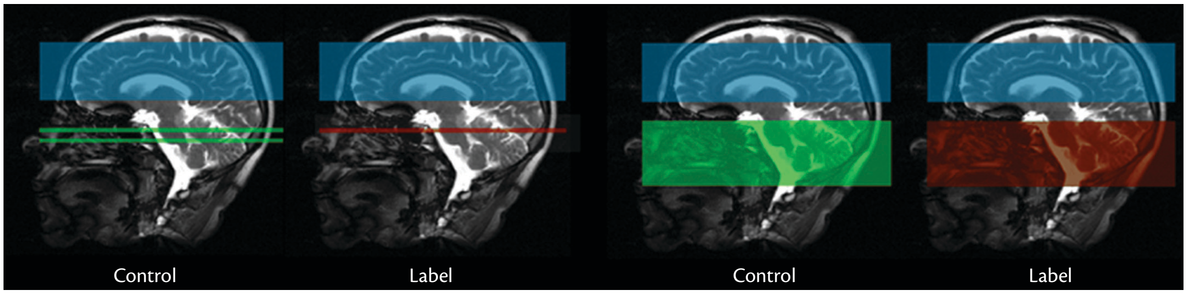

Fig. 6.3 To the left, CASL multislice experiment, using double inversion for the control experiment. To the right, PASL sequence, which labels a large volume instantly and uses two pulses resulting in a net 180° + 180° =0° for the control experiment.
Blue = imaging volume; red = labelling; green = control.

reaches the microvasculature, exchange of water between blood and tissue occurs. To ensure that all labelled water has exchanged with tissue before imaging, a delay, inversion delay (TI), between labelling and the image acquisition is inserted. The intensity difference between a label and a control experiment is directly proportional to blood perfusion. However, since the resulting ASL image has a low signal-to-noise (SNR), an ASL experiment normally requires averaging of a number of difference images.

Data acquisition

Traditionally, the labelling schemes in ASL can be divided into two groups of experiments, namely continuous arterial spin labelling (CASL) and pulsed arterial spin labelling (PASL) (Fig. 6.3).

In CASL, labelling is performed continuously through a thin plane [21,22] during a period of 1.5–2.5 seconds in order to attain adequate labelling. One of the advantages of CASL is the high SNR compared with PASL-based methods. A disadvantage of the technique is the high specific absorption rate (SAR) due to the continuous RF transmission.

In PASL, first proposed by Edelman et al. [23] as 'echo planar imaging with signal targeting with alternating frequency' (EPISTAR), spin-labelling of arterial blood is performed by applying a RF pulse of temporally short duration in an extended volume, i.e. thick slice (10–15 cm) [23]. A conceptually different PASL sequence is flow alternating inversion recovery (FAIR) [24,25], in which the label image is acquired after a slice-selective inversion and the control image after a non-selective inversion. The advantages of PASL are high labelling efficiency and reduced SAR levels, and the disadvantage is a low SNR.

In addition, a hybrid technique has also emerged called pseudo-continuous arterial spin labelling (PCASL). Using this approach the continuous labelling is replaced by a series of small RF pulses [26]. Compared with PASL, PCASL has higher SNR thereby providing whole-brain coverage, without the need of continuous labelling, Also, PCASL results in lower SAR than CASL.

CBF maps obtained using a PCASL sequence can be seen in Fig. 6.4

Tracer kinetic analysis

By using the tracer clearance theory proposed by Kety and Schmidt [27], and adapted to ASL experiments by Detre et al. [21] and Williams et al. [28] quantitative perfusion analysis can be performed. In this model, it is assumed that the labelled arterial blood water is a freely diffusible tracer that exchanges with the tissue water immediately upon arrival, described by a uniform plugged flow, to the microvasculature. The modified Bloch equation can be written as:

$$\frac{dM_t(t)}{dt} = \frac{M_{t,0} - M_t(t)}{T_{1t}} + F\left(M_a(t) - M_v(t)\right) \qquad [13]$$

where M_t is the tissue magnetization per unit mass, $M_{t,0}$ is the equilibrium value of the tissue magnetization, M_a and M_v are the magnetizations of arterial and venous water per unit volume, T_{1t} is the longitudinal relaxation time of the tissue, and F is the perfusion. The perfusion can be quantified by solving the differential equation. Improved versions of this model have later been introduced.

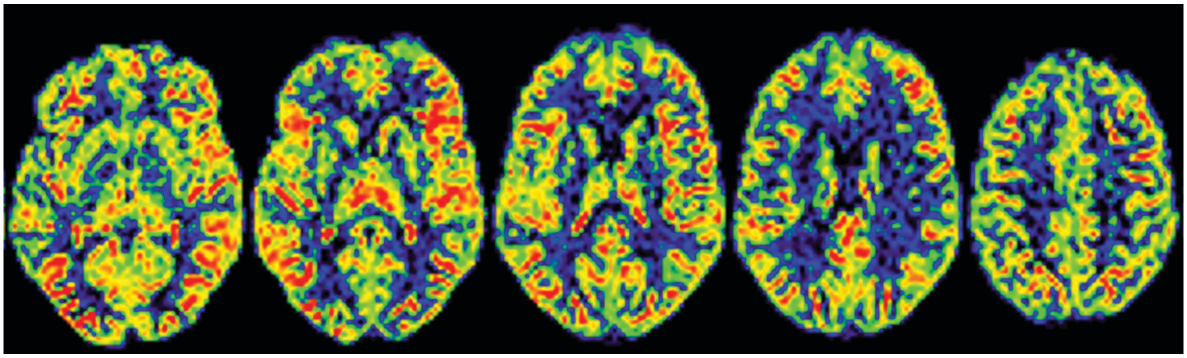

Fig. 6.4 CBF ASL images from a healthy volunteer acquired using the PCASL sequence at 3T.

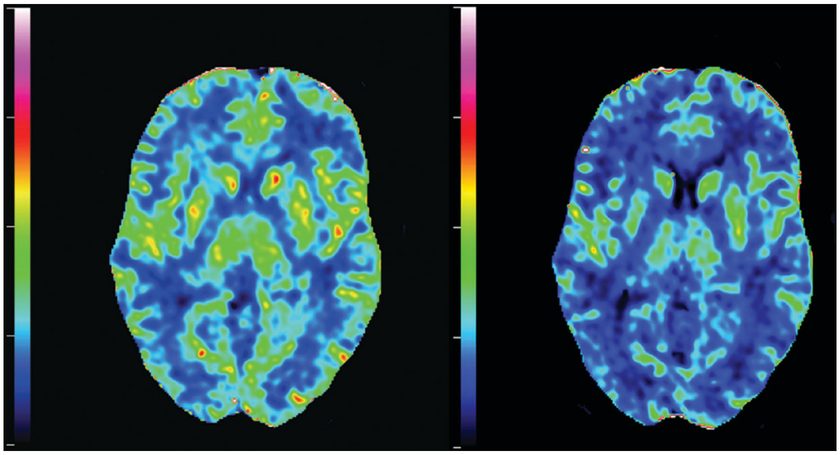

Fig. 6.5 Xe-CT CBF image showing the effect of hyperventilation in head injury. Left image shows normal CBF and to the right CBF is displayed under hyperventilation. Courtesy of Bo Bergholt, Aarhus University Hospital, Aarhus, Denmark.

In 1998, Buxton et al. proposed a general kinetic model, 'the Buxton model', including nearly all terms influencing the perfusion quantification [29]. The magnetization difference ΔM between the control and labelled images can be expressed as:

$$\Delta M(t) = 2 \cdot M_{a,0} \cdot F \int_0^t c(\tau) \cdot R(t-\tau) \cdot m(t-\tau) d\tau \qquad [14]$$

where $M_{a,0}$ is the equilibrium magnetization in arterial blood water, $c(\tau)$ is the fractional AIF, and $R(t-\tau)$ is the residue function describing the fraction of labelled spins arriving at a voxel at time τ and still remains within the voxel at time t. The factor $m(t-\tau)$ is the magnetization relaxation term that quantifies the longitudinal magnetization fraction of the labelled spins arriving at a voxel at time τ and remains at time t. This formulation is similar to the indicator dilution theory, although ASL uses a diffusible tracer. The model is applicable to any ASL experiment and can be used with different compartment models.

Computed tomography perfusion imaging

Xenon computed tomography

Introduction to Xe-CT

Xenon computed tomography (Xe-CT) provides estimates of the CBF by using stable xenon as the contrast agent. The xenon gas is inhaled and enters the bloodstream through exchange across the alveolar membranes. When the xenon reaches the brain, it freely crosses the BBB and by measuring the concentration of xenon using CT, CBF can be estimated. In Fig. 6.5 two Xe-CT images are shown, normal CBF and CBF under hyperventilation.

Data acquisition

The contrast agent is a mixture of stable xenon (~28%) with oxygen and air, which is inhaled through a mask during a period of about 4–6 minutes [30,31]. Xenon is an inert gas that freely diffuses from the vascular compartment across the BBB and, therefore, the concentration of xenon in tissue can serve as a measure of tissue perfusion. Due to the relatively high atomic number of xenon, it yields a measurable image enhancement (measured in Hounsfield units) even at low concentrations on CT images.

Prior to the xenon inhalation, a few baseline measurements are performed. During inhalation of the xenon-gas (the wash-in period), several imaging slices are acquired. This measurement is repeated around every second giving approximately six time points during xenon uptake in the tissue [32]. Sometimes only the wash-in period is acquired, but if additional measurement points on the tissue concentration time curve are warranted the wash-out period can also be measured [33]. The baseline images are then averaged and subtracted from the enhanced images obtained during xenon inhalation, producing the tissue concentration images.

The arterial concentration is measured non-invasively from the expired xenon concentration in the output tube from the mask. The arterial concentration curve is estimated from the end-tidal xenon levels by assuming that the gas close to the alveoles is in equilibrium with the concentration in the blood [30,34]. The curve is then converted into Hounsfield units [33].

Tracer kinetic analysis

The modified Kety equation for a single compartment describes the relationship between the tissue concentration $C_t(t)$ of a diffusible tracer and the arterial input function $C_a(t)$

$$C_t(t) = F \int_0^t C_a(\tau) e^{-\frac{F(t-\tau)}{\lambda}} d\tau \qquad [15]$$

where F is the perfusion, and λ the brain–blood partition coefficient of xenon, the solubility of xenon in tissue [33,35].

CBF and λ can be estimated from the modified Kety equation when the arterial- and tissue concentrations are known. The estimation is performed on a voxel-by-voxel basis by fitting routines.

Dynamic perfusion computed tomography

Introduction to pCT

Dynamic perfusion computed tomography (PCT) is a bolus tracking method used for measuring microvascular haemodynamics in terms of CBF, CBV, and MTT, using computed tomography. The method is very similar to the DSC-MRI method, which also uses an intravascular tracer to retrieve the different cerebral parameters. In Fig. 6.6, examples of CBF and MTT are shown for a stroke patient.

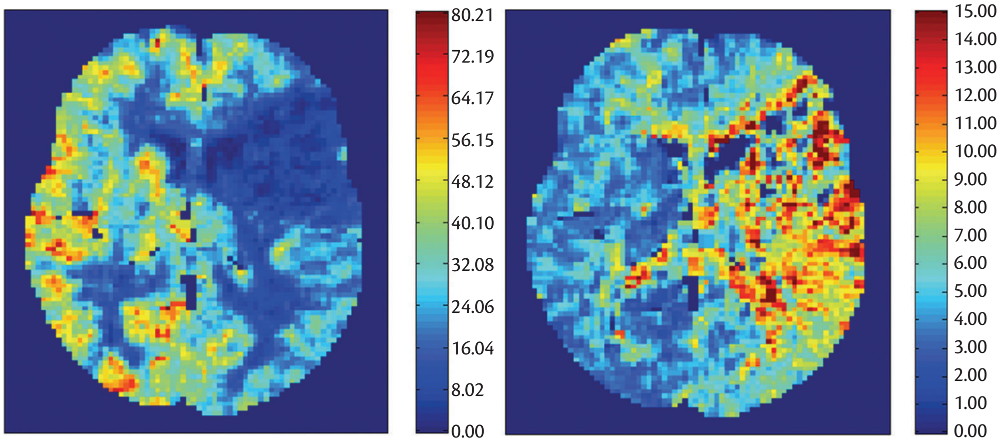

Fig. 6.6 pCT images of a stroke patient. CBF is displayed to the left and MTT to the right.
Courtesy of Irene Klærke Mikkelsen, Aarhus University Hospital, Aarhus, Denmark.

Data acquisition

The contrast agent is injected intravenously and monitored during its first circulation through the brain tissue. The contrast agent is an iodinated contrast material with an increased absorption and scattering of X-ray radiation, which results in contrast-medium enhancement on the CT image. The degree of contrast enhancement is directly related to the iodine concentration in the imaging region, and for a given voltage, the proportionality is near constant [36].

The AIF is measured in a large artery, and in order to reduce partial volume effect (mixture of signals from different tissue types) a venous concentration time-curve (venous output function (VOF)) is measured in a large draining vein, in order to scale the arterial concentration time-curve [37–39].

Due to the radiation exposure, the imaging time is minimized, which sometimes compromises a measurement of the full concentration curve length.

Tracer kinetic analysis

If constant blood flow during measurement is assumed, the tracer kinetic equation describes the relation between the tissue concentration time-curve and the scaled arterial concentration time-curve using the basic tracer kinetic equation (Eqns 6 and 8)

The product CBF · $R(t)$ can be estimated using the tracer kinetic model, if $C_t(t)$ and $C_a(t)$ are known using either fitting or deconvolution [40]. In practice, CBF is estimated using Eqn 9, but can also be retrieved using the 'maximal slope' method [35,40], where only the initial rise of the concentration curves is measured, since initially no venous outflow from the tissue voxels is assumed, hence,

$$CBF = max\left[\frac{dC_t(t)}{dt}\right] / \, max\left[C_a(t)\right] \qquad [16]$$

The CBV is found from the ratio of the areas under $C_t(t)$ and $C_a(t)$, respectively, as in Eqn 10 and the MTT is calculated using either the central volume theorem, Eqn 11 or Zierler's area to height, Eqn 12.

Perfusion imaging using nuclear medicine techniques

Positron emission tomography

Introduction to PET

PET is a modality that provides tomographic images of quantitative parameters by measuring the activity following the administration of a radioactively-labelled compound [41]. Different haemodynamic parameters, such as CBF (see Fig. 6.7 for an example), CBV, oxygen extraction fraction (rOEF), regional cerebral metabolic rate of oxygen (rCMRO) and glucose (rCMRGl) can be obtained using different PET pharmaceuticals. This section focuses on the assessment of CBF.

Data acquisition

Cerebral perfusion can be obtained either using an IV bolus injection of H_2O^{15} or a continuous inhalation of $C^{15}O_2$ over 8–10 minutes; both administrations are followed by a 1–2-minute scan [42]. The emitted positron from the isotope interacts with a neighbouring electron a few millimeters away from the decay site. In this interaction, both particles are annihilated, creating two 511 keV photons travelling in approximately the opposite directions. These photons can then be detected in rings of scintillators connected to photomultipliers. The localization of the annihilation event can be obtained by considering only those photon pairs that arrive nearly simultaneously. Images can then be obtained after different preprocessing steps and reconstruction using filtered back-projection or maximum-likelihood expectation-maximization (ML-EM) techniques. Whole-body radiation exposure by PET examination usually gives the subject 0.5–2.0 mSv per scan. Due to the short half-life of the radionuclide (122 seconds), imaging can only be carried out in close proximity to a synchrotron and a radiochemistry laboratory [42].

Tracer kinetic analysis

In both the IV bolus injection and continuous inhalation technique, CBF can be quantified using the Kety-Schmidt equation (Eqn 15) derived from the Fick's principle that states that the difference of the concentration of a tracer in the arterial and venous blood can be related to perfusion [43]. For quantitative values,

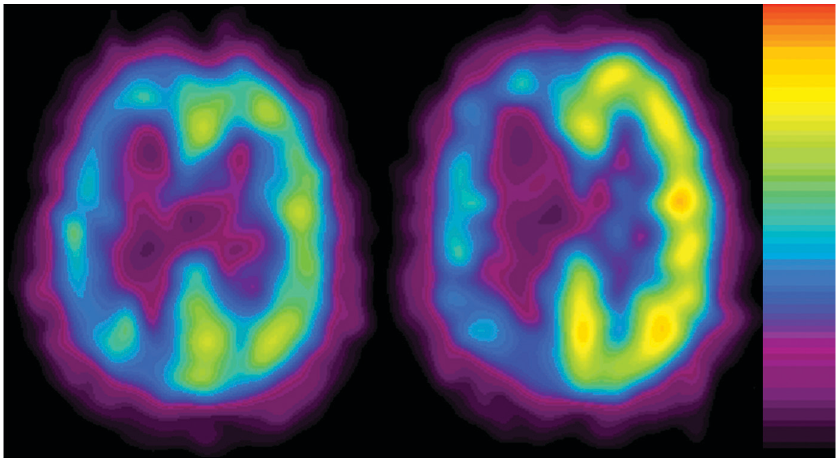

Fig. 6.7 Brain perfusion reserve in a patient with partial occlusion of right carotid artery studied by PET using 15O-water. To the left, baseline CBF image, to the right, CBF image after administration of diamox. The perfusion values ranging from 0 to 110 ml/100 ml/min are visualized using af rainbow colour scale.

Courtesy of Søren Baarsgaard Hansen, PET-Centre, Aarhus University Hospital, Aarhus, Denmark.

sampling of the arterial input function (often from a radial artery) needs to be performed.

Single photon emission tomography

Introduction to SPECT

SPECT is similar to the PET technique in that it relies on injection or inhalation of a specific radiopharmaceutical followed by generation of tomographic images [44]. Using a specific radionuclide tracer, nuclide maps of the cerebral perfusion can be obtained.

Data acquisition

In SPECT, gamma cameras that rotate around the patient are used to detect the photons emitted by the radioactive nuclide. At each position, the gamma camera captures a projection of the spatial distribution of the radionuclide, from which an image can be reconstructed using ML-EM techniques. Compared with PET, there is only one single photon that is used for the localization of the radioactive decay and this results in a lower resolution. The radionuclides that are used in SPECT normally have longer half-life and are more accessible resulting in that the technique is cheaper than PET.

For CBF determination, the freely-diffusible tracer ^{133}Xenon is historically the most used approach for measuring brain haemodynamics [44]. However, since the gamma rays emitted by ^{133}Xe are of low energy this results in limited spatial resolution. Therefore, intravascular tracers, such as ^{99m}Tc-HMPAO (hexamethylpropyleneamine oxime), ^{99m}Tc-bicisate and ^{123}I-IMP (N-isopropyl-*p*-iodoamphetamine hydrochloride), are more common in clinical SPECT imaging of cerebral perfusion.

Tracer kinetic analysis

CBF quantification relies on the microsphere principle for the Tc-99m and ^{123}I-IMP tracers. The microspheres are trapped in the capillary system of the tissue and according to Fick's principle CBF is proportional to the number of microspheres that are confined in capillaries. The multi compartmental analysis of the Kety–Schmidt equation [44] is used for retrieval of CBF maps using the ^{133}Xe inhalation technique.

Clinical applications

One major clinical application of brain perfusion measurements is in the diagnosis and characterization of acute ischaemic stroke [45], since conventional CT and MR imaging are not sufficient to fully describe the acute lesion [46]. When occlusion of a tissue-supplying artery occurs, the transport of oxygen and nutrition to the nearby cells is reduced, and this leads to cell death. In the initial phase, when perfusion starts to decrease, the CBF is initially maintained by vasodilation that results in an increase of the CBV and MTT. This autoregulation fails at a certain perfusion-pressure threshold, and below this level a decrease of CBF starts. The metabolic rate of oxygen is still maintained by an increased oxygen extraction fraction, but when the perfusion pressure decreases further to a critically low level, the metabolic rate of oxygen drops [47].

Malignant tumours need a substantial blood supply in order to grow, and to fulfil the demand of the increasing new tumour vessels that are created, a process called angiogenesis. These new vessels are more disorganized than normal vessels and contribute to an increase in CBV. An indication of the grade of malignancy of the tumour is the change in CBV. It has been shown that a low-grade tumour causes a smaller change in CBV than a high-grade tumour [20] and that the volume transfer constant, K^{trans}, is lower for low-grade gliomas than high-grade gliomas [48]. Measurement of perfusion parameters can also be used to predict clinical outcome (e.g. survival time) [49].

Vascular dementia is caused by a reduction of the supply of blood to the brain. Alzheimer's disease (AD) is a type of dementia in which cell death occurs. In perfusion studies, a reduction in the CBV is seen in patients suffering from AD. This reduction is probably partly due to loss of cerebral tissue and not only a reduction in blood-flow demand in the tissue [50–52].

Other clinical applications where perfusion abnormalities can be observed are in epilepsy, depressive disorders, migraine, and multiple sclerosis.

Acknowledgements

The authors would like to thank the following people who have helped in preparing the text: Michael Ingrisch, Ludwig Maximilians

University Hospital, Munich, Germany; Irene Klærke Mikkelsen, CFIN, Aarhus University Hospital; Bo Bergholt, Department of Neurosurgery, Aarhus University Hospital; and Søren Baarsgaard Hansen, PET-Centre, Aarhus University Hospital, Aarhus, Denmark.

References

1. Sourbron SP, and Buckley DL. (2011). On the scope and interpretation of the Tofts models for DCE-MRI. *Magnetic Resonance in Medicine*, **66**, 735–45.
2. Kety SS. (1951). The theory and applications of the exchange of inert gas at the lungs and tissues. *Pharmacological Reviews*, **3**, 1–41.
3. Tofts PS, and Kermode AG. (1991). Measurement of the blood–brain barrier permeability and leakage space using dynamic MR imaging. 1. Fundamental concepts. *Magnetic Resonance in Medicine*, **17**, 357–67.
4. Larsson HBW, Stubgaard M, Frederiksen JL, et al. (1990). Quantitation of blood-brain barrier defect by magnetic resonance imaging and gadolinium-DTPA in patients with multiple sclerosis and brain tumors. *Magnetic Resonance in Medicine*, **16**, 117–31.
5. Tofts PS. (1997). Modeling tracer kinetics in dynamic Gd-DTPA MR imaging. *Journal of Magnetic Resonance Imaging*, **7**, 91–101.
6. Larsson HBW, Hansen AE, Berg HK, et al. (2008). Dynamic contrast-enhanced quantitative perfusion measurement of the brain using T1-weighted MRI at 3T. *Journal of Magnetic Resonance Imaging*, **27**, 754–62.
7. Larsson HBW, Courivaud F, Rostrup E, et al. (2009). Measurement of brain perfusion, blood volume, and blood-brain barrier permeability, using dynamic contrast-enhanced T1-weighted MRI at 3 tesla. *Magnetic Resonance in Medicine*, **62**, 1270–81.
8. Østergaard L. (2004). Cerebral perfusion imaging by bolus tracking. *Topics in Magnetic Resonance Imaging*, **15**, 3–9.
9. Knutsson L, Ståhlberg F, and Wirestam R. (2010). Absolute quantification of perfusion using dynamic susceptibility contrast MRI: pitfalls and possibilities. *Magnetic Resonance Material Physics*, **23**, 1–21.
10. Zierler KL. (1962). Theoretical basis of indicator-dilution methods for measuring flow and volume. *Circulation Research*, **10**, 393–407.
11. Østergaard L, Sorensen AG, Kwong KK, et al. (1996). High resolution measurement of cerebral blood flow using intravascular tracer bolus passages. Part II. experimental comparison and preliminary results. *Magnetic Resonance in Medicine*, **36**, 726–35.
12. Shih LC, Saver JL, Alger JR et al. (2003). Perfusion-weighted magnetic resonance imaging thresholds identifying core, irreversibly infarcted tissue. *Stroke*, **34**, 1425–30.
13. Butcher KS, Parsons M, MacGregor L, et al. (2005). Refining the perfusion-diffusion mismatch hypothesis. *Stroke*, **36**, 1153–9.
14. Stewart GN. (1894). Researches on the circulation time in organs and on the influences which affect it. Parts I–III. *Journal of Physiology (London)*, **15**(1), 89.
15. Meier P, and Zierler KL. (1954). On the theory of the indicator-dilution method for measurement of blood flow and volume. *Journal of Applied Physiology*, **6**, 731–44.
16. Vonken EPA, van Osch MJ, Bakker CJG, et al. (2000). Simultaneous quantitative cerebral perfusion and Gd- DTPA extravasation measurement with dual-echo dynamic susceptibility contrast MRI. *Magnetic Resonance Medicine*, **43**, 820–7.
17. Haselhorst R, Kappos L, Bilecen D, et al. (2000). Dynamic susceptibility contrast MR imaging of plaque development in multiple sclerosis: application of an extended blood–brain barrier leakage correction. *Journal of Magnetic Resonance Imaging*, **11**, 495–505.
18. Boxerman JL, Schmainda KM, Weisskoff RM. (2006). Relative cerebral blood volume maps corrected for contrast agent extravasation significantly correlate with glioma tumor grade, whereas uncorrected maps do not. *AJNR American Journal of Neuroradiology*, **27**, 859–67.
19. Sorensen AG, and Reimer P. (2000). *Cerebral MR perfusion imaging: principles and current applications*. Stuttgart: Georg Thieme Verlag.
20. Aronen HJ, Gazit IE, Louis DN, et al. (1994). Cerebral blood volume maps of gliomas: comparison with tumor grade and histologic findings. *Radiology*, **191**, 41–51.
21. Detre JA, Leigh JS, Williams DS, et al. (1992). Perfusion imaging. *Magnetic Resonance Medicine*, **23**, 37–45.
22. Alsop DC, and Detre JA (1998). Multisection cerebral blood flow MR imaging with continuous arterial spin labelling. *Radiology*, **208**, 410–16.
23. Edelman RR, Siewert B, Darby DG, et al. (1994). Qualitative mapping of cerebral blood flow and functional localization with echo-planar MR imaging and signal targeting with alternating radio frequency. *Radiology*, **192**,513–20.
24. Kim SG. (1995). Quantification of relative cerebral blood flow change by flow-sensitive alternating inversion recovery (FAIR) technique: application to functional mapping. *Magnetic Resonance Medicine*, **34**, 293–301.
25. Kwong KK, Chesler DA, Weisskoff RM, et al. (1995). MR perfusion studies with T1-weighted echo planar imaging. *Magnetic Resonance Medicine*, **34**, 878–87.
26. Dai W, Garcia D, de Bazelaire C, et al. (2008). Continuous flow-driven inversion for arterial spin labeling using pulsed radio frequency and gradient fields. *Magnetic Resonance Medicine*, **60**, 1488–97.
27. Kety SS, and Schmidt CF. (1945). The determination of cerebral blood flow in man by use of nitrous oxide in low concentrations. *American Journal of Physiology*, **143**, 53–66.
28. Williams DS, Detre JA, Leigh JS, et al. (1992). Magnetic resonance imaging of perfusion using spin inversion of arterial water. *Proceedings of the National Academy of Sciences, USA*, **89**, 212–6.
29. Buxton RB, Frank LR, Wong EC, et al. (1998). A general kinetic model for quantitative perfusion imaging with arterial spin labelling. *Magnetic Resonance in Medicine*, **40**, 383–96.
30. Latchaw RE. (2004). Cerebral perfusion imaging in acute stroke. *Journal of Vascular Intervention Radiology*, **15**, S29–46.
31. Carlson AP, and Yonas H. (2010). Xenon/CT in the management of traumatic brain injury. *The open Neurosurgery Journal* **3**,64–72.
32. Chieregato A, Tanfani A, and Fainardi E (2010). A Practical Approach to Interpretation of CBF Measured by Mean of Xenon-CT in Patients with Traumatic Brain Injury. *The Open Neurosurgery Journal*, **3**, 28–58.
33. von Oettingen G, Bergholt B, Østergaard L, et al. (2000). Xenon CT cerebral blood flow in patients with head injury: influence of pulmonary trauma on the input function. *Neuroradiology*, **4**, 168–73.
34. Gur D, Wolfson SK, Yonas H Jr, et al. (1982). Progress in cerebrovascular disease: local cerebral blood flow by xenon enhanced CT. *Stroke* **13**, 750–8.
35. Wintermark M, Maeder P, Thiran JP, et al. (2001). Quantitative assessment of regional cerebral blood flows by perfusion CT studies at low injection rates: a critical review of the underlying theoretical models. *European Journal of Radiology*, **11**, 1220–30.
36. Axel L. (1980). Cerebral blood flow determination by rapid-sequence computed tomography: theoretical analysis. *Radiology*, **137**, 679–86.
37. Eastwood JD, Lev MH, and Provenzale JM. (2003). Perfusion CT with iodinated contrast material. *AJR American Journal of Roentgenology*, **180**, 3–12.
38. de Lucas EM, Sánchez E, Gutiérrez A, *et al.* (2008). CT protocol for acute stroke: tips and tricks for general radiologists. *Radiographics*, **28**(6), 1673–87.
39. Allmendinger AM, Tang ER, Lui YW, et al. (2012). Imaging of stroke: Part 1, perfusion CT–overview of imaging technique, interpretation pearls, and common pitfalls. *AJR American Journal of Roentgenology*, **198**, 52–62.
40. Fieselmann A, Kowarschik M, Ganguly A, et al. (2011). Deconvolution-based CT and MR brain perfusion measurement: theoretical model revisited and practical implementation details. *International Journal of Biomedical Imaging*, 2011, article ID 467563.
41. Ter-Pogossian M, Phelps M, Hoffman E, et al. (1975). A positron-emission transaxial tomograph for nuclear imaging (PETT). *Radiology*, **114**, 89–98.
42. Wintermark M, Sesay M, Barbier E, et al. (2005). Comparative overview of brain perfusion imaging techniques. *Stroke*, **36**, 83–99.

43. Kety SS, and Schmidt CF. (1948). The nitrous oxide method for the quantitative determination of cerebral blood flow in man: theory, procedure and normal values. *Journal of Clinical Investigation*, **27**, 476.
44. Obrist W, Thompson H Jr, Wang H, and Wilkinson W (1975). Regional cerebral blood flow estimated by 133-xenon inhalation. *Stroke*, **6**, 245–56.
45. Baird AE, and Warach S. (1998). Magnetic resonance imaging of acute stroke. *Journal of Cerebral Blood Flow Metabolism*, **18**, 583–609.
46. Mullins ME, Schaefer PW, Sorensen AG, *et al.* (2002). CT and conventional and diffusion-weighted MR imaging in acute stroke: study in 691 patients at presentation to the emergency department. *Radiology*, **224**, 353–60.
47. Powers WJ. (1991). Cerebral hemodynamics in ischemic cerebrovascular disease. *Annals of Neurology*, **29**, 231–40.
48. Jia Z, Geng D, Xie T, et al. (2012). Quantitative analysis of neovascular permeability in glioma by dynamic contrast-enhanced MR imaging, *Journal of Clinical Neuroscience*, **19**, 820–3.
49. Law M, Oh S, Babb JS, *et al.* (2006). Low-grade gliomas: dynamic susceptibility weighted contrast-enhanced perfusion MR imaging–prediction of patient clinical response. *Radiology*, **238**, 658–67.
50. Bonte FJ, Tintner R, Weiner MF, et al. (1993). Brain blood flow in the dementias: SPECT with histopathologic correlation. *Radiology*, **186**, 361–5.
51. Tanaka S, Kawamata J, Shimohama S, et al. (1998). Inferior temporal lobe atrophy and APOE genotypes in Alzheimer's disease. X-ray computed tomography, magnetic resonance imaging and Xe-133 SPECT studies. *Dementia and Geriatric Cognitive Disorders*, **9**, 90–8.
52. Londos E, Passant U, Brun A, et al. (2003). Regional cerebral blood flow and EEG in clinically diagnosed dementia with Lewy bodies and Alzheimer's disease. *Archives of Gerontology & Geriatrics*, **36**, 231–45.

CHAPTER 7

Functional magnetic resonance imaging

Ralf Deichmann and Christian Schwarzbauer

Most functional magnetic resonance imaging (fMRI) experiments are based on the blood oxygenation level dependent (BOLD) effect [1]. Since its conception in 1992 [2–4], fMRI has rapidly become the most widely used neuroimaging method to assess human brain function in health and disease. This chapter briefly explains the basics of magnetic resonance imaging (MRI) and the physiological origin of the BOLD effect. We then describe the principles of fMRI data acquisition and discuss how typical imaging artefacts can be avoided. Finally, an overview of fMRI data analysis is provided, including experimental design, data preprocessing and statistical inference.

The basics of magnetic resonance imaging

Magnetic resonance (MR) imaging is based on the physical properties of nuclear spins. Each spin carries a magnetic moment and tends to align in an external magnetic field, showing similarities to the behaviour of a compass needle. Consequently, an ensemble of polarized spins creates a magnetization that is parallel to the external magnetic field. If this magnetization is tilted via an electromagnetic radiofrequency (RF) field, it starts to rotate with a certain frequency, the so-called Larmor frequency, which depends on the magnetic field strength. During this process, the magnetization sends out an electromagnetic signal, which can be detected, provided the spin ensemble is large enough. A prerequisite for tilting the magnetization and thus for the detection of a signal is that the irradiated RF signal must have the spins' Larmor frequency. Thus, this effect is called 'magnetic resonance'.

Fig. 7.1 illustrates the principles of MR imaging, which consists of the following components:

1. *Slice selective excitation (red):* an RF pulse is irradiated, while a *slice selection gradient (GS)* is switched on. The gradient imposes a spatial dependence on the spins' Larmor frequencies, so the RF pulse will only excite spins located inside a slice perpendicular to this gradient.
2. *Phase encoding (green):* due to the *phase encoding gradient (GP)* along the first in-plane axis, spins with different coordinates will rotate with different Larmor frequencies and accumulate different phases. Thus, the respective coordinate can be derived from the phase of the acquired signal.
3. *Signal read-out and frequency encoding (blue):* due to the *read-out gradient (GR)* along the second in-plane axis, spins with different coordinates will send out signals with different Larmor frequencies. Thus, the respective coordinate can be derived from the frequency of the signal that is acquired while GR is switched on.

The step shown in Fig. 7.1 covers a single line of the so-called *k-space*, which is the data space corresponding to the frequency representation of the image. For the reconstruction of a whole image, two-dimensional (2D) k-space coverage is required, so this step has to be repeated several times with different values of the phase encoding gradient GP. The time difference between spin excitation and signal acquisition is the *echo time* (*TE*). The question arises how the choice of TE influences the signal amplitude. For a perfectly homogeneous static magnetic field (B_0) inside the MR scanner, the signal shows an exponential decay with increasing TE, governed by the *transverse relaxation time* (T_2). For the human brain, T_2 values at a field strength of 3 T are about 80 ms in white matter (WM) and 110 ms in gray matter (GM) [5]. However, inhomogeneities of B_0 accelerate the relaxation. Fig. 7.2 shows a series of MR images of a water phantom, acquired at different TEs. A tiny piece of metal is attached to the phantom (lower left), distorting B_0 in the surrounding area. As can be seen, the signal decay is much faster in this region, since the B_0 inhomogeneity causes a relatively strong spatial dependence of the Larmor frequency, giving rise to progressive spin dephasing. Thus, the signal decay is governed by the *effective transverse relaxation time* T_2* that can be considerably shorter than T_2.

For the human brain, even in the absence of major B_0 distortions, T_2* is reduced, amounting to about 50 ms in brain tissue at 3 T [5]. The field gradients used for spatial encoding in MRI experiments are artificial B_0 inhomogeneities that may give rise to spin dephasing and thus signal losses. In *gradient echo (GE) sequences*,

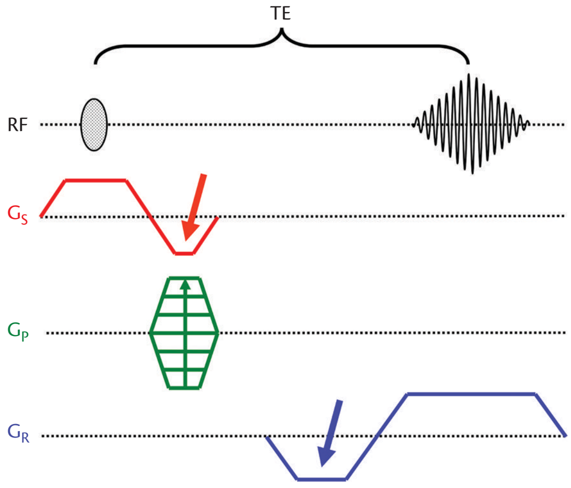

Fig. 7.1 Schematic representation of an MR imaging experiment.

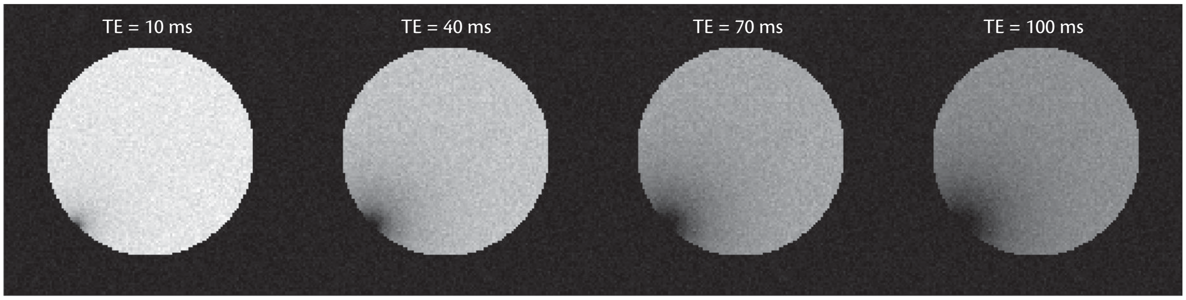

Fig. 7.2 MR images of a water phantom, acquired at different TE. A tiny piece of metal is attached to the phantom (lower left), distorting the magnetic field in the surrounding area.

this problem is solved in the following way (see Fig. 7.1): a negative read-out gradient is applied first (blue arrow), causing artificial spin dephasing. After changing the gradient polarity, this process is reversed, so the spins rephase, resulting in a build-up of the signal (the so-called *gradient echo*) in the centre of the acquisition window. Similarly, the dephasing effect of the slice selection gradient is compensated by adding a negative rephasing gradient (red arrow). Apart from the imaging gradients, no other B_0 inhomogeneities are compensated in GE sequences, which are therefore sensitive to B_0 inhomogeneities and show T_2^*-weighting. In contrast, *spin echo (SE) sequences* [6] are based on the irradiation of a second, 'refocusing' RF pulse between excitation and acquisition, causing an inversion of the magnetization, so spin dephasing is converted into rephasing, resulting in the so-called *spin echo*. This process compensates for *all* field inhomogeneities. SE sequences are therefore relatively insensitive to B_0 inhomogeneities and show T_2-weighting. In most fMRI experiments, T_2^*-weighted GE sequences are used.

To achieve the high temporal resolution required for fMRI studies, a special fast GE sequence is frequently used, dubbed *echo planar imaging (EPI)* [7], as shown in Fig. 7.3: after slice selective excitation (red), a series of gradient echoes is acquired by oscillating the read-out gradient (blue). Between adjacent gradient echoes, a constant phase encoding gradient is applied, the so-called *blip* (green). For any echo, the degree of phase encoding is given by the combined effect of the initial (negative) phase encoding gradient and the sum of all blips preceding the respective echo. Thus, each echo has a different degree of phase encoding, as required for imaging.

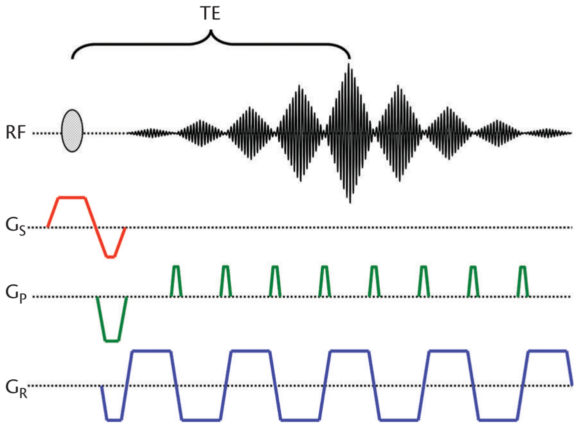

Fig. 7.3 Schematic representation of EPI.

The main difference to the GE sequence described in Fig. 7.1 is the fact that EPI requires only a single RF excitation pulse, resulting in shorter acquisition times. Typically, EPI images have a matrix size of 64 × 64 with a spatial in-plane resolution of 3 mm and an acquisition time of about 50–80 ms per slice. Thus, the acquisition time for whole brain coverage (about 40 slices with a thickness of 3 mm) is typically about 2–3 s. According to Fig. 7.3, each echo has a different TE. However, the central echo, which covers the origin of k-space, has maximum amplitude, so the respective TE is usually reported as the TE value of the sequence. This TE is relatively long, so EPI images are heavily T_2^*-weighted. This fact, combined with the short acquisition time, is the main reason why EPI is frequently used in fMRI studies.

The BOLD effect

The blood oxygenation level dependent (BOLD) effect is based on the observation that T_2^* values in brain tissue show a local increase upon neuronal activation. This effect can be explained as follows—during resting conditions, less oxygen is required, so there is a relatively high concentration of *deoxyhaemoglobin* in the blood vessels. Deoxyhaemoglobin is paramagnetic, and therefore tends to locally increase the main magnetic field B_0. In contrast, surrounding brain tissue is *diamagnetic*, tending to decrease B_0. This discrepancy of magnetic properties leads to field distortions in the vicinity of blood vessels, lowering local T_2^* values and, therefore, the signal intensity in T_2^*-weighted images. Upon neuronal activation, more oxygen is required. This stimulates a local increase in blood flow, which leads to a washout of deoxyhaemoglobin and an increased concentration of oxyhaemoglobin, which is diamagnetic, similar to brain tissue. Thus, field distortions around the blood vessels are reduced, which increases local T_2^* values. In summary, the BOLD effect allows to detect activated brain areas by means of a local signal increase in a series of T_2^*-weighted images.

A more detailed analysis of the underlying physiological principles shows that the *haemodynamic response* to brain activation depends on the interplay of three physiological parameters—the *cerebral blood flow (CBF)*, the *cerebral blood volume (CBV)*, and the *cerebral metabolic rate of oxygen consumption (CMRO2)*. The CBF is the blood volume (in ml) passing per minute through 100 g of tissue, with typical values of approximately 65 ml/(100 g)/min in GM and 33 ml/(100 g)/min in WM [8]. The CBV is the volume of blood (in ml), that is present in 100 g of tissue at a given time point, with typical values of approximately 5 ml/(100 g) in GM and 2.5 ml/(100 g) in WM [9]. The CMRO2 is the oxygen volume (in ml) that is extracted from blood per minute and 100 g of tissue, with typical values of approximately 3.7 ml/(100 g)/minute in GM and 1.4 ml/(100 g)/minute in WM [9]. The three parameters have different effects on the T_2*-weighted signal. A CBF increase yields higher oxygen transport, giving rise to higher levels of oxyhaemoglobin and, therefore, a signal increase. In contrast, increases in CMRO2 and CBV rather reduce oxygen concentrations, yielding a signal decrease (for a theoretical model of these effects, see [10]). Fig. 7.4 shows a typical *haemodynamic response function (HRF)*, i.e. the time dependence of the T_2*-weighted signal amplitude (in arbitrary units) following a stimulus at time-point zero.

The zero-level corresponds to the signal baseline during resting conditions. The main effect, the so-called (positive) *BOLD response*, is due to the increased CBF, with a maximum occurring about 5 seconds after the stimulus. There are two further, but relatively minor effects. First, the CMRO2 tends to increase earlier than the CBF and the CBV, giving rise to an initial signal decrease during the first second, the so-called *initial dip*. Secondly, CBV tends to return more slowly to baseline than CBF and CMRO2, causing a final *undershoot*. About 25 to 30 seconds after the stimulus, the signal returns to the baseline level. Details regarding the coupling between neuronal activation and haemodynamic response have not been fully elucidated yet. For an overview of the different theoretical models, the reader is referred to the literature [11].

When interpreting the results of fMRI studies, it is important to bear in mind that the BOLD signal is a surrogate measure of neuronal activation, which is based on the haemodynamic response to neuronal activation, rather than a direct measure of neuronal activation, as for example electroencephalography. Neuronal activity of a specific population of neurons may reflect the net effect of a complex balance between excitatory and inhibitory processes, which are mediated through neurotransmitters, such as glutamate or γ-aminobutyric acid (GABA). A simultaneous increase/decrease of both excitatory and inhibitory processes may therefore leave the net neuronal output unaffected, while leading to an increased/decreased BOLD signal as a result of the increased/decreased metabolic demand [12]. In a similar way, in the absences of excitatory changes, an increase of inhibitory processes may increase metabolic demand and, hence, give rise to an increased BOLD signal while reducing the net neuronal output [12]. An additional challenge regarding the interpretation of fMRI results is due to its spatial specificity. At a typical spatial resolution of $3 \times 3 \times 3$ mm^3, an fMRI voxel contains several millions of neurons. The observed BOLD signal changes therefore reflect the net effect of a very large population of neurons. While advances in scanner technology have pushed the limits of spatial resolution beyond a submillimetre voxel size, the main limitation is due to the spatial extent of the HRF which is in the order of a few millimetres depending on the spatial location in the brain and the main magnetic field strength (for further details, see [13]). The spatial extent of the HRF tends to decrease with increasing field strength as the intravascular contribution to the BOLD effect is reduced. For the same reason, spin echo (SE) sequences tend to provide improved spatial specificity compared with GE sequences.

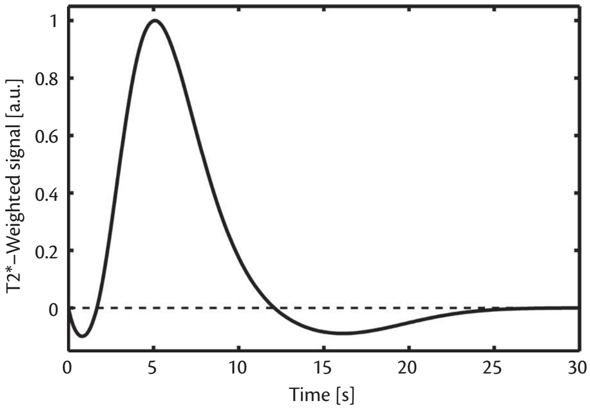

Fig. 7.4 A typical haemodynamic response function (HRF).

Acquisition of functional magnetic resonance imaging data

Based on the concepts described previously, an fMRI experiment is in principle performed as follows: a series of T_2*-weighted EPI data is acquired, each of which represents a 'data volume', i.e. a set of several slices that cover the brain area to be investigated. The time interval between the acquisition of subsequent data volumes is the *repetition time* (*TR*) and defines the temporal resolution; in general, TR is about 2–3 seconds for whole brain coverage. A typical fMRI experiment comprises several hundred volumes. During data acquisition, a specific stimulus is switched on and off several times, or the subject is requested to perform a specific task at regular intervals. Data are subsequently analysed for local signal variations that correlate with the stimulus.

As explained above, the BOLD effect depends on variations of B_0 distortions due to brain activation, which requires imaging techniques that are highly sensitive to B_0 inhomogeneities. The problem with this concept is that severe image artefacts may occur in areas suffering from macroscopic B_0 distortions, especially areas close to air–tissue interfaces, due to a mismatch of the respective so-called magnetic susceptibilities. Brain regions affected by *susceptibility artefacts* are, in particular, the orbitofrontal cortex (due to the vicinity of the nasal sinuses) and the temporal lobes (due to the vicinity of the ear canals). In these areas, EPI images may be distorted, i.e. local brain structures appear shifted in space, leading to a mismatch between fMRI and anatomical data. Spatial shifts usually occur in the phase encoding direction, since EPI acquires echoes with different phase encoding at different TEs (see Fig. 7.3). For strong field distortions, complete signal loss can occur locally, which may compromise the investigation of the affected brain areas.

Fig. 7.5 shows three slices of an anatomical data set (top) and the respective slices of an EPI data set (bottom). For a superior slice (a), EPI does not suffer from obvious distortions or signal losses, yielding a good congruency of functional and anatomical data. For more inferior slices (b, c), distortions (blue arrow) and signal losses (red arrows) occur.

Image distortions can be reduced by keeping the echo spacing (i.e. the time difference between two subsequent echoes in the EPI read-out train) as small as possible. This can be achieved by increasing the echo read-out bandwidth or by using parallel acquisition techniques (see point 6 in the list below). Residual image distortions can be corrected by acquiring a magnetic field map, yielding information about B_0 distortions that can be used to undistort the EPI images [14].

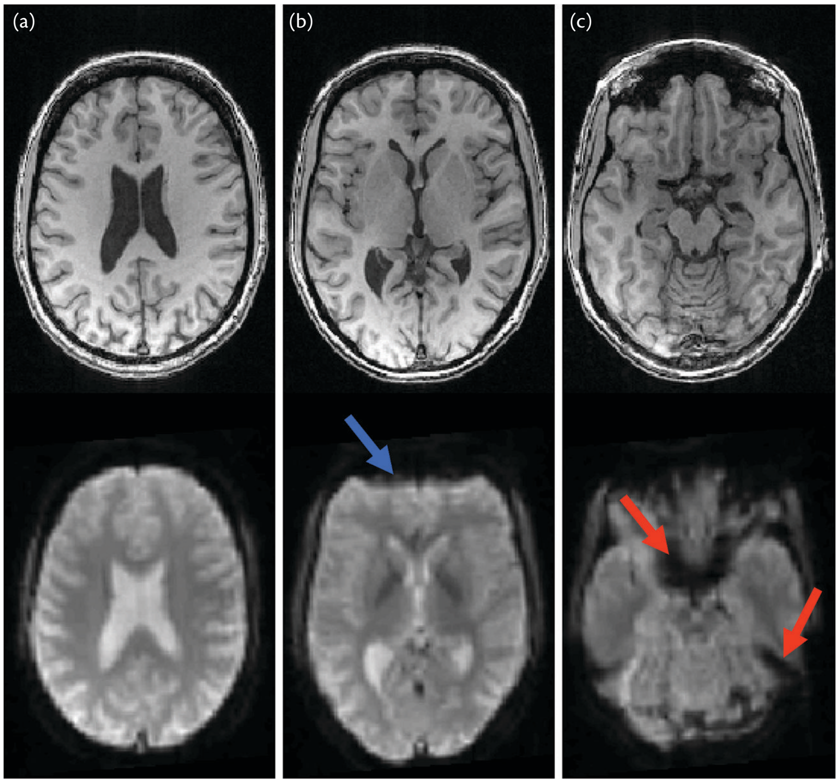

Fig. 7.5 Three slices of an anatomical data set (top) and the respective EPI data set (bottom), showing distortions (blue arrow) and signal losses (red arrows).

For reducing susceptibility-induced signal losses, several methods are available:

1. *Choice of TE:* the TE should be as short as possible to avoid major signal loss, but still long enough to obtain a measurable BOLD effect. In general, TE should be about 2/3 of the average tissue T_2* value, which depends on B_0. Recommended TE values are 50 ms at 1.5 T, 30 ms at 3 T, and 20–25 ms at 7 T.
2. *Z-shimming:* for 'through-plane' field distortions, the Larmor frequency of the spins changes across the slice, resulting in dephasing and progressive signal losses with increasing TE. This effect can be compensated by applying a gradient in slice encoding direction between excitation and acquisition. The standard implementation of this technique, dubbed 'z-shimming' [15], comprises several data sets with different compensatory gradients that are subsequently combined. The resulting data set recovers signal losses, but has a reduced temporal resolution. However, in many cases it is sufficient to acquire a single data set with a moderate z-shimming gradient, yielding a relatively effective mitigation of signal losses in areas affected by field inhomogeneities, but hardly any signal reductions in normal areas.
3. *Slice orientation:* a different orientation changes the direction of B_0 distortion gradients with respect to the slice and, therefore, the extent of signal loss. For investigations of the orbitofrontal cortex, it has been recommended to tilt the slice around the left-right axis by about 30° and apply an additional moderate z-shimming gradient [16].
4. *Spatial resolution:* certain types of signal losses, such as the U-shaped signal dropout area shown in Fig. 7.5 (bottom right), can be avoided by increasing the spatial resolution and thus the k-space coverage [17]. A list of optimum imaging parameters for the functional investigation of various brain areas affected by field inhomogeneities can be found in the literature [18].
5. *Spin-echo EPI:* compared with conventional GE EPI, SE EPI is more robust against susceptibility-induced signal loss, but generally provides lower sensitivity. Both data acquisition methods can be combined using a dual echo approach [19].
6. *Parallel imaging:* parallel imaging techniques, such as SENSE [20], GRAPPA [21], or SMASH [22], shorten the length of the data acquisition window and, therefore, reduce the effect of susceptibility-induced signal loss and image distortions. Typically, acceleration factors of 2 or 3 are used in parallel imaging.

The extent of susceptibility-induced signal loss and image distortions increases with the magnetic field strength. At field strengths of 7 T and above, susceptibility-induced signal losses in brain areas close to air-tissue interfaces (e.g. the orbitofrontal cortex) present a major challenge. However, the advantage of higher field strengths is a significant gain in sensitivity, as the signal-to-noise ratio (SNR) increases approximately linearly with the field strength. For most clinical applications, a field strength of 3 T is the best compromise to obtain a high sensitivity, while keeping susceptibility-induced image artefacts at an acceptable level.

Experimental design and analysis of functional magnetic resonance imaging data

In a typical fMRI experiment the brain is scanned every 2–3 seconds for a total duration of 5–10 minutes. During the experiment,

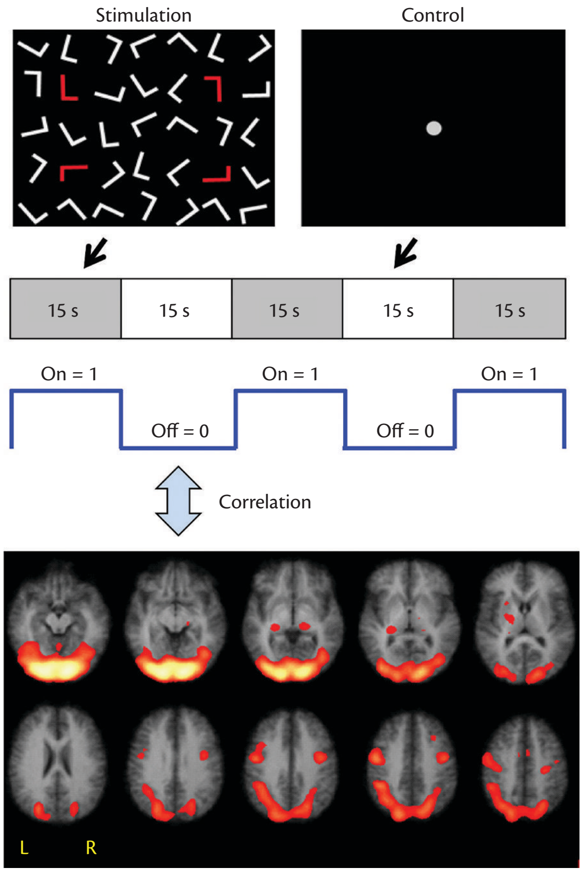

Fig. 7.6 Schematic representation of an fMRI imaging experiment, showing the stimuli corresponding to both conditions (top row), the time-course of the stimuli (second row), the boxcar function used to model this blocked design (third row), and the calculated activation maps (bottom row).

the subject engages in a specific task. A brain area is considered to be activated by this task if the BOLD signal variation in this area shows strong temporal correlation with the task. This principle is illustrated in Fig. 7.6. In this example, the subject was either looking at a screen of rotating L-shapes (condition 1) or a static fixation dot (condition 2), while being scanned. Each condition was presented for a fixed duration of 15 seconds, alternating between condition 1 and 2. This block design can be modelled by a simple boxcar function, which represents the experimental paradigm. Brain areas in which the BOLD signal variations were strongly correlated with this visual experimental paradigm are displayed in colour. As expected, activated brain areas include the visual cortex and the lateral geniculate nuclei; activation can also be seen in motor areas as the subject was instructed to press a button on the occurrence of red L-shapes.

While fMRI is conceptually simple, experimental design and data analysis can be complex. Task-induced BOLD signal changes are very small, typically in the order of a few percent or less, which results in a low contrast-to-noise ratio (CNR). To maximize the sensitivity and specificity of fMRI, a significant amount of research has been dedicated to the optimization of experimental design and data analysis strategies.

Experimental design

The order in which individual stimuli are presented is known as experimental design. In a *block design*, two or more conditions are presented in an interleaved fashion. A condition can consist of a single stimulus, like in the example shown in Fig. 7.6, or a series of short individual stimuli. For instance, to find out if there is a specialized brain area for human face perception, two different types of stimuli could be used, pictures of human faces and pictures of common objects. In analogy to the example shown in Fig. 7.6, a simple block design could be used, presenting pictures of faces during condition 1 and pictures of objects during condition 2. However, what is the optimum stimulus duration? Unfortunately, there is no generally accepted answer to this question, but a suitable choice depends on the nature of the stimulus and on the hypothesis one wishes to test. In this example, it is clear that if the stimulus duration is too short (e.g. <100 ms), it may be hard to recognize that the picture shows a human face. On the other hand, if the duration is too long (e.g. 15 seconds), the examiner's attention is likely to wander and focus on something else. Most experts would probably agree that any duration between 0.5 and 2 seconds would be a good compromise. As in the previous example, the two conditions ('faces' and 'objects') can be modelled by a simple boxcar function. When this experiment was first carried out, it revealed an area in the extrastriate cortex specialized in face perception, the so-called fusiform face area [23]. As discussed previously, the BOLD response to a stimulus is delayed due to the HRF (see Fig. 7.4). Arranging individual stimuli in a block design permits the BOLD response to reach a steady state, which maximizes the signal difference between the two conditions.

An alternative to the block design is the *event-related design*. In this design, individual stimuli are presented in a randomized order, rather than being categorized into different conditions such as in the block design. This approach has a number of advantages.

1. The response to an individual stimulus is not biased by prior categorization.

2. Stimuli can be assigned retrospectively to different categories depending on the subject's behavioural response.

3. The response to a stimulus can be investigated in the context of the preceding stimuli.

4. A real-time feedback scheme can be implemented, in which the subsequent stimulus is chosen based on the subject's response.

In an event-related design, the choice of a suitable inter-stimulus interval (ISI), which is the time between two subsequent stimuli, is an important consideration, as it determines the efficiency of the design. Optimum design efficiency means that the maximum CNR is achieved for a given contrast of interest. The design efficiency can be calculated using a linear convolution model in which the BOLD response is predicted by convolving the stimulus function with the HRF. Fig. 7.7 shows the predicted BOLD response for three different ISI values. The most efficient design is the one that produces the maximum signal variance, which is clearly the case for ISI = 15 seconds in our example. If the ISI is too short (ISI = 5 seconds), only small signal oscillations can be obtained following an initial rise. For a given amount of background noise, this will result in low sensitivity. If the ISI is too long (ISI = 40 seconds), long baseline intervals are obtained, which again result in reduced sensitivity.

To find the optimum ISI, simply plot the predicted BOLD signal variance as a function of ISI and determine the maximum which, in the example given here, occurs at ISI = 18 seconds (see Fig. 7.8).

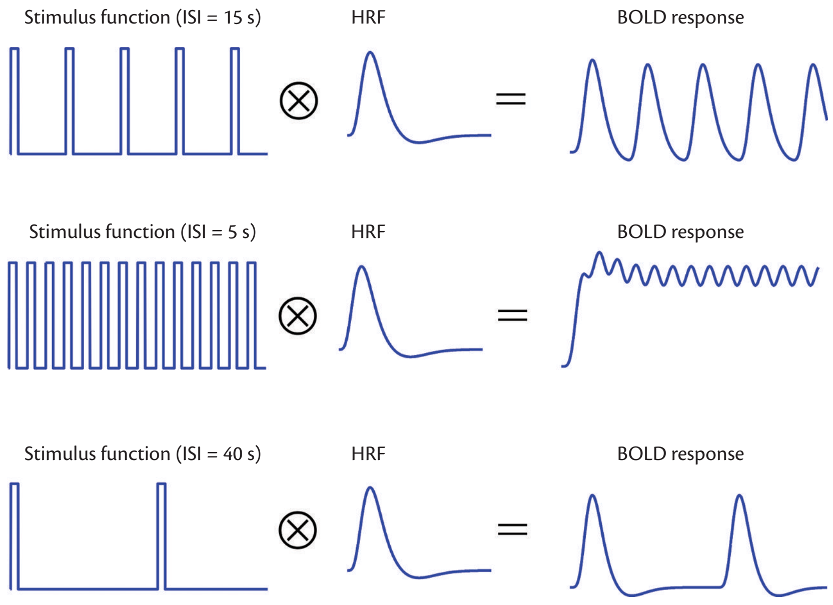
Stimulus function (ISI = 15 s)
HRF
BOLD response
Stimulus function (ISI = 5 s)
HRF
BOLD response
Stimulus function (ISI = 40 s)
HRF
BOLD response

Fig. 7.7 Predicted BOLD response for three different values of the inter-stimulus interval (ISI).

The calculation of design efficiency can be further refined by accounting for other factors, such as high-pass filtering, which is often used to reduce low-frequency noise in fMRI time series [24]. In practice, different types of stimuli that activate different brain areas can be interleaved to reduce ISI, while maintaining optimum efficiency. In our example, if three different types of stimuli are used that activate three different brain areas at an ISI of 6 seconds, each brain area will only be activated every 18 seconds, which means that the predicted BOLD signal variance is still maximal in each area.

Data preprocessing and modelling

The overall aim of data preprocessing is to improve sensitivity and spatial specificity, and to transform individual data into a standard coordinate system so that comparisons can be made across different subjects. Fig. 7.9 illustrates a typical data pre-processing scheme.

Distortion correction removes unwanted spatial image distortions by applying a set of transformation parameters that are typically derived from a magnetic field map that is acquired in addition to the fMRI data (see 'Acquisition of functional magnetic resonance imaging data'). As spatial distortion depends on individual anatomy (e.g. size of sinuses) and head orientation, distortion correction can improve spatial specificity by reducing inter-individual differences. *Realignment* of image volumes across time is used to correct for head motion during the scan; realignment is therefore often referred to as motion correction. Head movement in three-dimensional (3D) space can be characterized by an affine transformation that comprises three translational and three rotational parameters. These six realignment parameters are estimated for each image volume and the volume is then realigned to a reference volume (often the first volume of the scan) by applying an affine transformation. *Slice timing correction* accounts for small differences in timing between different slices, which are due to the fact that the slices of an image volume are acquired at slightly different times. The time difference between adjacent slices depends on the slice acquisition order (e.g. sequential or interleaved), which needs to be taken into account. Slice time correction is often carried out before the realignment, or omitted, particularly in block designs where small timing differences are less relevant.

Following this preprocessing step, there are two commonly used options regarding the further data processing stream. In the first option (as suggested in the SPM software package, Statistical Parametric Mapping, University College London), spatial normalization and smoothing is carried out before data modelling. In the second option (as suggested in the FSL software package, FMRIB Software Library, University of Oxford), data modelling is carried out before spatial normalization. *Spatial normalization*, also known as inter-subject registration, is used to transform individual brain data into a standard coordinate system, such as the MNI or Talairach coordinate system. This is particularly important for comparisons across subjects because individual brains have slightly different shapes and sizes. In addition to linear transformations consisting of translations, rotations, zooms, and shears, spatial normalization typically uses a set of non-linear deformations

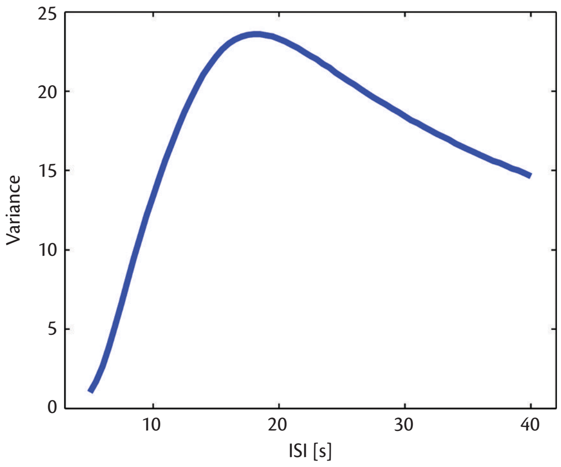

Fig. 7.8 Dependence of the predicted BOLD signal variance on the ISI.

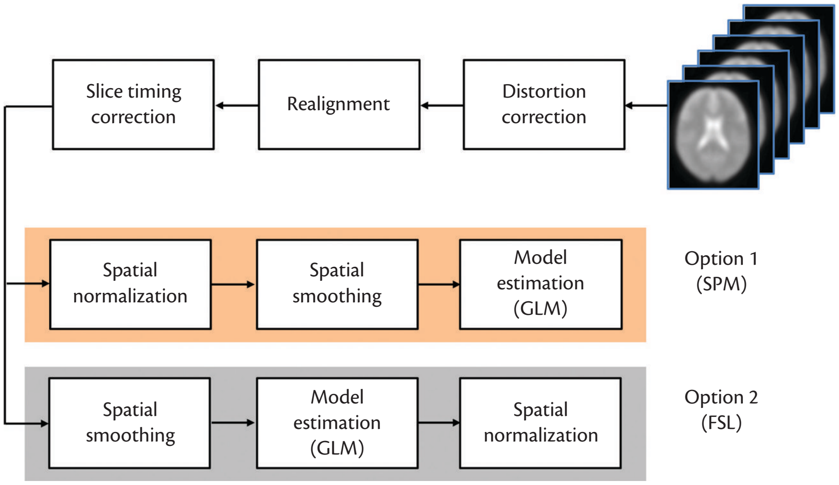

Fig. 7.9 Illustration of a typical fMRI data pre-processing scheme.

to improve inter-subject registration. Occasionally, this can lead to artefacts, particularly in the presence of lesions or other anatomical abnormalities. A careful inspection of the results is therefore recommended. *Spatial smoothing* is often applied to intentionally blur the image data by removing spatial high-frequency components. This reduces uncorrelated noise and, therefore, improves sensitivity, but at the cost of spatial specificity. Spatial smoothing will also reduce inter-individual variations that persist after spatial normalization due to imperfections in inter-subject registration. In addition, certain statistical analysis methods, such as Gaussian random field theory, require spatially smoothed data. *Data modelling* is an essential step in fMRI data analysis, which often comprises two stages—temporal filtering and the actual data modelling. Digital high-pass filters can be used to remove baseline drifts and other unwanted low frequency noise, whereas low pass filters can be applied to improve the SNR at the expense of removing high-frequency components from the signal. For the actual data modelling, a general linear model (GLM) is commonly used to predict the BOLD signal changes in each image voxel as a function of the hypothesized neuronal activity. To illustrate this principle, consider a simple example of a block design consisting of three conditions (see Fig. 7.10), during which either pictures of faces, or houses, or a fixation dot are presented. The onset and duration of each condition is described by a stimulus function and the corresponding BOLD responses are modelled by convolving each stimulus function with the HRF. The predicted BOLD responses for each condition (blue lines) are then used as regressors in a GLM.

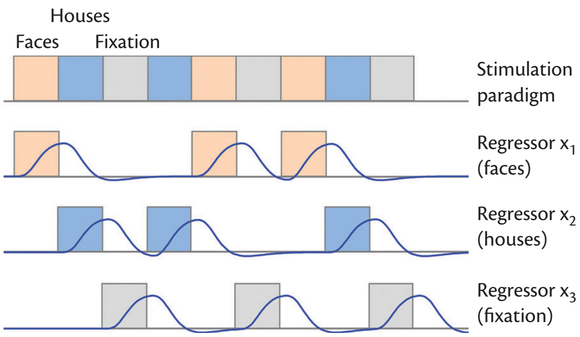

Fig. 7.10 Blocked design consisting of three conditions, during which either pictures of faces or houses or a fixation dot are presented.

The aim of this linear model is to separate the observed BOLD response in each voxel ($\mathbf{y}$) into two signal components: signal changes that are predicted by the model (i.e. by a linear combination of the regressors $\mathbf{x}_1$, $\mathbf{x}_2$, $\mathbf{x}_3$) and residual noise ($\boldsymbol{\varepsilon}$). The basic equation for the regression analysis is given by $\mathbf{y} = \beta_0 + \beta_1\mathbf{x}_1 + \beta_2\mathbf{x}_2 + \beta_3\mathbf{x}_3 + \varepsilon$. The 'betas' can be interpreted as weighting factors that determine to what extent each regressor contributes to the model. The aim of the linear regression analysis is to find the best possible model fit. This is achieved by choosing a set of weighting factors (β_0, β_1, β_2, β_3) that minimizes the residual noise component ε; β_0 models the effect of factors that are constant throughout the experiment, which can be interpreted as a 'baseline shift'. The advantage of the GLM approach is that the optimum solution can be calculated on the basis of simple matrix algebra. In addition, 'regressors of no interest' can be included in the model to remove unwanted signal variance due to baseline drift, head motion and other factors. We now return to the example shown in Fig. 7.10. The measured BOLD signal variation in a voxel in the fusiform face area is likely to be similar to the predicted BOLD signal time course described by regressor $\mathbf{x}_1$, but quite different to $\mathbf{x}_2$ and $\mathbf{x}_3$. After all, this area is associated with the perception of faces, and not houses or fixation dots. For this reason, β_1 will be considerably greater than β_2 or β_3. Conversely, for a voxel in the 'parahippocampal place area,' β_2 will be considerably greater than β_1 or β_3, as this area responds more strongly to scenes depicting places than to other kinds of visual stimuli. For a voxel in the visual cortex, high values for β_1 and β_2 would be expected, as either faces or houses will activate this area, whereas β_3 will be comparatively low, as a small fixation dot is a relatively weak visual stimulus. We now consider different linear combinations of beta values. These are known as *contrasts*. An interesting contrast is, for example, the difference $\beta_1 - \beta_2$ which will be high in the 'fusiform face area' ($\beta_1 - \beta_2 > 0$) and 'parahippocampal place area' ($\beta_1 - \beta_2 < 0$), but close to zero in other visual areas. The contrast $\beta_1 - \beta_2$ can therefore be used to identify the locations of the face and place areas; a significant positive value corresponds to the face area, whereas a significant negative value corresponds to the place area. To identify all visual areas, for example, either the contrasts $\beta_1 - \beta_3$ or $\beta_2 - \beta_3$, or a weighted average of the two could be considered: $(\beta_1 - \beta_3)/2 + (\beta_2 - \beta_3)/2$. The advantage of the latter is that it makes use of all data points and, therefore, provides better sensitivity. The elegance of the linear regression approach is that once the optimum weighting factors $(\beta_0, \beta_1, \beta_2, \beta_3)$ have been determined, any contrast of interest can be calculated post hoc, without having to rerun the linear regression analysis. In the simple example shown in Fig. 7.10, regressors were derived directly from the onsets and durations of the corresponding stimuli. Depending on the type of experiment or research question, this may not always be possible or appropriate. For example, a working memory task typically consists of a stimulus followed by a retention period and a response. To investigate aspects of working memory, a suitable regressor needs to be constructed based on the hypothesized neuronal response, rather than simply on the onsets and durations of the stimuli.

Statistical analysis

Like all experimental data, fMRI data are inherently noisy. The estimated beta values and the derived contrasts will therefore always differ from zero, even in the absence of any neuronal activation, and a statistical analysis is needed to find out whether a contrast of interest is statistically significant. A statistical analysis can be performed on a single subject level or on a group level. A *single subject analysis* is particularly relevant to diagnostic applications, such as pre-surgical planning, for example, to find out if the activation of a specific brain region is statistically significant in this particular subject. A *group analysis* is employed if the aim is to derive common effects of a specific task or intervention that can be generalized to a wider population from which the study group is drawn. To allow such a generalization, both within- and between-subject variability needs to be taken into account. This approach is known as the random-effects model. Statistical comparison of individual contrasts generally fulfils this criterion. To identify the location of the fusiform face area, for example, a group of 20 healthy normal volunteers that represent the general population could be scanned, using the stimulation paradigm illustrated in Fig. 7.10. The contrast $\beta_1 - \beta_2$ for each voxel and each subject is then calculated. We can then test the hypothesis that $\beta_1 - \beta_2 > 0$ for each voxel, for example, by using a standard *t* test; the application of a *t* test is valid, because the β and contrast values obtained in a typical fMRI experiment are approximately normally distributed. In practice, the hypothesis is tested by rejecting the null-hypothesis (i.e. $\beta_1 - \beta_2 \leq 0$) at a certain level of significance which is characterized by a *p-value*. In contrast to most other experimental sciences, where a *p*-value of 0.05 would generally be considered significant, the particular challenge with fMRI is the fact that the researcher is confronted with a substantial *multiple comparison problem*. At a typical spatial resolution of $3 \times 3 \times 3$ mm^3, an fMRI image volume includes approximately 30,000 voxels in grey matter. Since a *t* test is carried out for each voxel (i.e. 30,000 times in total), a *p*-value of 0.05 would result in approximately 1500 *false positives*. To account for multiple testing, a number of methods have been devised to derive *p*-values corrected for multiple testing. Popular correction methods rely on Gaussian random field (GRF) theory, false discovery rate (FDR) estimation, and family-wise error (FWE) correction. A FWE corrected *p*-value of 0.05 means that there is only a 5% chance of any false positive in the entire image volume or, in other words, one would have to repeat the experiment 20 times to get, on average, one false positive in any of the 20 image volumes.

Functional connectivity analysis

Conventional fMRI analysis explores the brain's response to stimulation based on the temporal correlation of an external stimulation paradigm with BOLD signal changes in the brain, as outlined in the previous section (see Fig. 7.6). Functional connectivity analysis can be regarded as an extension of this concept—rather than focusing on signal correlations with an external stimulus, functional connectivity analysis explores the brain's internal signal correlation patterns. If BOLD-related signal fluctuations of two different voxels are significantly correlated, these voxels are considered to be functionally connected. The most widely used approach is *seed-based connectivity analysis*, which considers the correlations between the BOLD signal change inside a reference voxel, the so-called *seed voxel*, and the respective signal fluctuations originating from all other voxels in the brain. In the example shown in Fig. 7.11, the seed voxel is located in the posterior cingulate cortex. The corresponding BOLD signal change in this seed voxel (blue curve) does not show any particular pattern and appears random. This signal behaviour is expected as no specific external stimulus was presented during data acquisition and the subject was instructed to lie still during the scan and not to 'think about anything in particular'. This technique is therefore often referred to as *resting state fMRI*. However, quite remarkably, a seed-based connectivity analysis shows that the signal changes in many other voxels are significantly correlated with the seed voxel signal; the corresponding brain areas are colour-coded in Fig. 7.11. These functionally connected brain areas constitute a spatially extended *functional brain network*, which includes the medial prefrontal cortex, the lateral parietal cortex and the posterior cingulate cortex. This specific functional

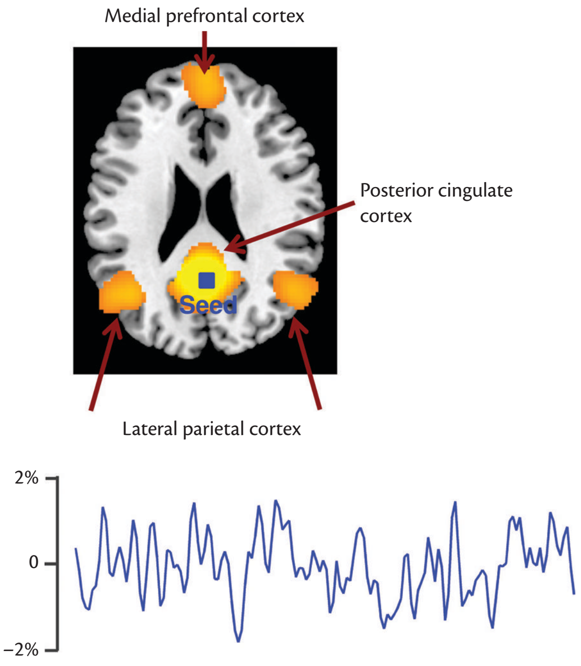

Fig. 7.11 The default mode network in a healthy volunteer derived by positioning a seed voxel in the posterior cingulate cortex. In the colour-coded areas, the respective BOLD signal correlates significantly with the signal of the seed voxel (bottom plot).

network is known as the brain's *default mode network* as it can be reliably detected in all humans with intact brain function.

The concept of functional connectivity analysis was first published by Biswal and colleagues in 1995 [25], but it took more than 10 years before the potential in medical diagnostics and brain research was recognized. Since around 2005, the number of publications investigating functional connectivity has increased almost exponentially, and a large number of robust human brain networks have been described including sensorimotor, auditory, visual, attentional, executive control and salience networks [26,27].

In principle, each voxel in the brain's grey matter can be used as a seed-voxel and the related functional brain network can be identified for each voxel. However, a whole-brain analysis of this kind produces very large data sets. Given a typical number of approximately N = 30,000 voxels in grey matter (see previous section), the total number of correlation values that can be calculated for each pair of voxels is N × N = 900 million. This 2D array of correlation values is often referred to as *similarity matrix*. For simple unidirectional correlation measures, such as Pearson's correlation coefficient, the correlation between two different voxels A and B is symmetrical, i.e. corr(A,B) = corr(B,A), and naturally the correlation of a voxel with itself is unity: corr(A,A) = 1. This reduces the total number of unique correlation values to N × (N – 1)/2, which in our example still corresponds to nearly 450 million different values.

To reduce the computational complexity, a number of methods have been devised. A straightforward approach is to subdivide the brain's grey matter into anatomically-defined regions of interest (ROIs), and to use the spatial signal average across each ROI to calculate the functional connectivity between different ROIs. The principle of *ROI-based functional connectivity analysis* is illustrated in Fig. 7.12, which is based on the 'Automated Anatomical Labeling' (AAL) template, a widely used set of ROIs that comprises N = 90 standardized ROIs in grey matter [28]. Calculating Pearson's correlation coefficient between each pair of these ROIs results in a 90 × 90 similarity matrix consisting of N × (N – 1)/2 = 4005 unique correlation values. Following a statistical test, the similarity matrix is converted into a binary connectivity matrix in which each non-zero value represents a statistically significant correlation (see black dots). The binary connectivity matrix can then be displayed as a 3D graph in which the ROIs are represented as nodes and significant connections are shown as solid lines. The analysis of such graphs is a well-established mathematical discipline known as graph theory. Graph theoretical methods are particularly useful to study the topological structure of human brain networks and to investigate their characteristic properties in health and disease [29,30].

Independent component analysis (ICA) is an alternative approach to reduce the computational complexity [31,32]. ICA can be used to group all individual voxel time courses (e.g. N = 30,000) into a fixed number of signal components (e.g. NC = 30). Each component represents the temporal properties of a spatially extended

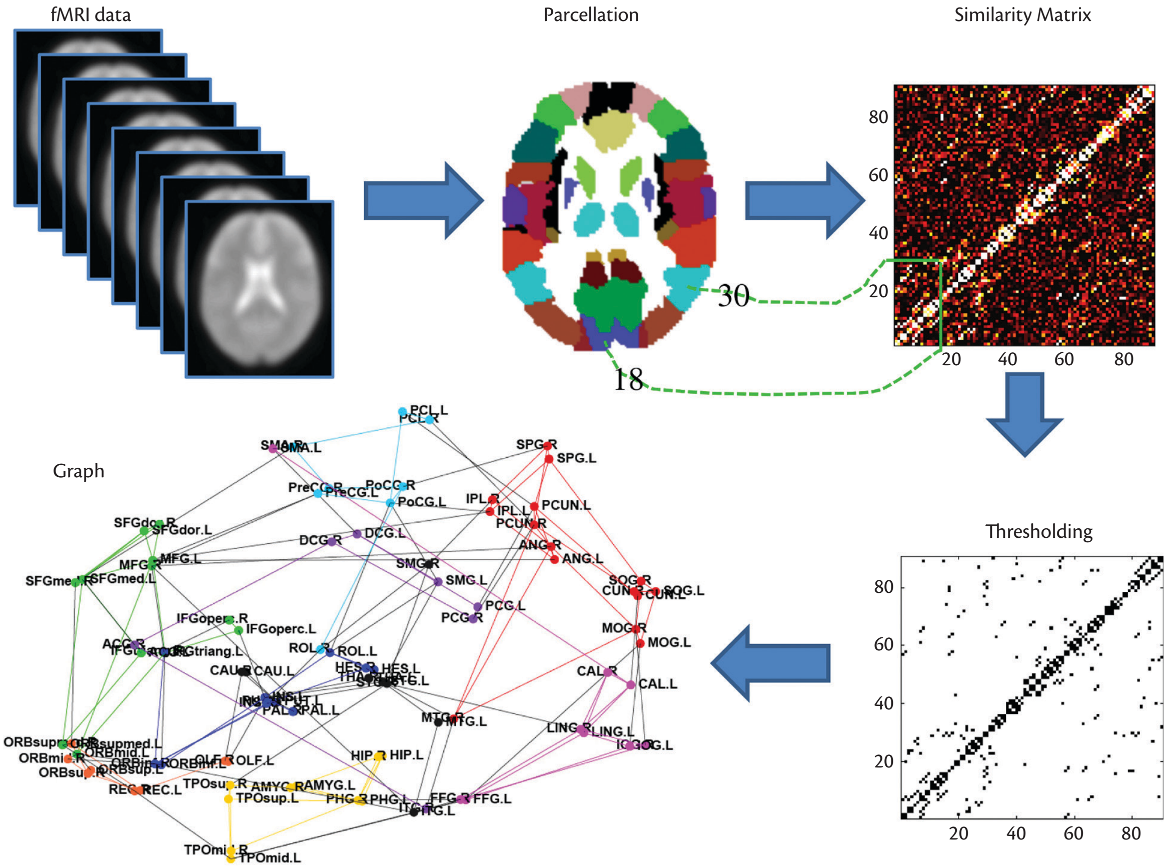
fMRI data
Parcellation
Similarity Matrix
80
60
40
20
20
40
60
80
30
18
Thresholding
80
60
40
20
20
40
60
80
Graph
PCL.L
PCL.R
SMA.R
SMA.L
SPG.R
SPG.L
PreCG.R
PreCG.L
PoCG.R
PoCG.L
IPL.R
IPL.L
PCUN.L
PCUN.R
SFGdor.R
SFGdor.L
DCG.R
DCG.L
ANG.R
ANG.L
MFG.R
MFG.L
SMG.R
SMG.L
SFGmed.R
SFGmed.L
SOG.R
CUN.R
CUN.L
SOG.L
PCG.L
PCG.R
IFGoperc.R
IFGoperc.L
MOG.R
MOG.L
ACG.R
IFGtriang.L
ROL.R
ROL.L
CAU.R
CAU.L
HES.R
HES.L
CAL.R
CAL.L
INS.L
PUT.L
PAL.R
PAL.L
MTG.R
MTG.L
LING.R
LING.L
ORBsupmed.L
ORBmid.L
ORBmid.R
ORBinf.R
ORBinf.L
OLF.R
OLF.L
ORBsup.R
ORBsup.L
HIP.R
HIP.L
REC.R
REC.L
TPOsup.R
AMYG.R
AMYG.L
TPOsup.L
PHG.R
PHG.L
FFG.R
FFG.L
ITG.R
ITG.L
TPOmid.R
TPOmid.L

Fig. 7.12 Concept of ROI-based functional connectivity analysis. The brain is parcellated into several ROIs. The correlation between respective BOLD signal time-courses is calculated pair-wise and displayed in the similarity matrix. After thresholding which leaves significant correlations only, results are displayed graphically.

pattern of individual voxels. Visual inspection or a pattern classification algorithm can be used to assign the observed spatial patterns to well-established functional brain networks, such as the default mode network. The consistency of such patterns across subjects and imaging sessions has been demonstrated [33].

Unlike seed-based connectivity analysis, which requires the choice of a suitable seed voxel on the basis of some prior hypothesis, ICA is purely data driven, which makes it particularly suitable for exploratory data analysis in the absence of a priori hypothesis. However, it is important to bear in mind that the result of an ICA will depend on the number of components chosen. The optimum number of components can be estimated by using methods of information theory such as Akaike's information criterion (AIC) or the minimum description length (MDL) criterion [34]. Due to its sensitivity to non-Gaussian features, the results of an ICA may be biased by outliers. Therefore, special care needs to be taken to avoid systematic errors due to this issue.

Data preprocessing in functional connectivity fMRI typically follows the scheme outlined in Fig. 7.9. In addition, a temporal low-pass filter with a cut-off frequency of approximately 0.1 Hz is often applied to the data. Furthermore, nuisance parameters (e.g. physiological noise and head movement), as well as global signal components may be removed from the data using linear regression. Statistical analysis of functional connectivity data may be challenging when carried out on a voxel-by-voxel level, as the number of multiple comparisons increases with the square of the number of voxels. The application of conventional statistical methods to correct for multiple comparisons (e.g. family-wise error rate and false discovery rate) may provide insufficient sensitivity when analysing larger scale networks (e.g. networks comprising N = 30,000 voxels). To address this challenge, a method referred to as *network-based statistic* has been proposed [35]. For ICA, a statistical framework known as *group ICA* has been developed that allows a comparison between different groups or conditions [34,36].

The majority of functional connectivity studies rely on temporal correlation (e.g. Pearson's correlation coefficient) as a measure of similarity between different voxel time courses. In principle, any measure of pair-wise association can be employed, such as measures that include spectral coherence or mutual information. A recent comparison of a large number of different methods for determining pair-wise association demonstrated that the correlation coefficient was a more sensitive measure than spectral coherence or mutual information. In contrast, lag-based measures such as Granger causality performed poorly which can be explained by the inherently low temporal resolution of fMRI [37].

Clinical applications

fMRI is widely used in clinical neuroscience research, and has led to a better understanding of many neurological and psychiatric conditions. Nonetheless, its translation into clinical practice is still at an early stage. Presurgical planning is currently the most common application of clinical fMRI. Recently, the potential of fMRI as a novel diagnostic tool to assess brain function in unresponsive brain injury patients has been demonstrated [38].

The clinical interpretation of fMRI data is challenging for a number of reasons. Unlike PET, fMRI does not provide an absolute measure of brain activity, but is rather restricted to the detection of changes in brain activation between two or more conditions, which are inferred from a statistical test. Confounding factors, such as even minimal patient movement during a scan, may lead to increased signal variance and, therefore, compromise the sensitivity of the statistical test. Further challenges include the choice and standardization of the task, as well as the large variability between individuals and sessions. The interpretation of the absence of activation changes presents a particular problem for clinical decision-making. The lack of an fMRI response could for instance simply be due to a malfunctioning stimulus delivery system, or the patient's inability to consistently respond to a specific task.

The clinical potential of functional connectivity MRI has recently been demonstrated in a number of clinical conditions such as Alzheimer's disease [39], Parkinson's disease [40], schizophrenia [41], depression [42], and disorders of consciousness [43]. Unlike conventional fMRI, functional connectivity MRI does not require the administration of an external stimulus or task, which greatly simplifies the application in a clinical setting and allows novel applications in unresponsive patients, for example, patients who suffer from disorders of consciousness or severe cognitive impairment. Since functional connectivity analysis is not restricted to a specific area of the brain that is activated by an external task, it can be applied to the entire brain. This is expected to facilitate the development of novel disease-specific biomarkers and diagnostic tools for clinical practice.

Further reading

For a detailed description of technical aspects of fMRI we recommend [44].

A comprehensive introduction to all aspects of fMRI can be found in [45]. For details regarding fMRI data analysis we recommend [24], [46], and [47]. Commonly used software packages for fMRI data analysis include SPM (Statistical Parametric Mapping, University College London) and FSL (FMRIB Software Library, University of Oxford).

References

1. Ogawa S, Lee TM, Nayak AS, et al. (1990). Oxygenation-sensitive contrast in magnetic resonance image of rodent brain at high magnetic fields. *Magnetic Resonance in Medicine*, **14**, 68–78.
2. Bandettini PA, Wong EC, Hinks RS, et al. (1992). Time course EPI of human brain-function during task activation. *Magnetic Resonance in Medicine*, **25**, 390–7.
3. Kwong KK, Belliveau JW, Chesler DA, et al. (1992). Dynamic magnetic resonance imaging of human brain activity during primary sensory stimulation. *Proceedings of the National Academy of Sciences, USA*, **89**, 5675–9.
4. Ogawa S, Tank DW, Menon R., et al. (1992). Intrinsic signal changes accompanying sensory stimulation—functional brain mapping with magnetic-resonance-imaging. *Proceedings of the National Academy of Sciences,* USA, **89**, 5951–5.
5. Wansapura JP, Holland SK, Dunn RS, et al. (1999). NMR relaxation times in the human brain at 3.0 tesla. *Journal of Magnetic Resonance Imaging*, **9**, 531–8.
6. Hahn EL. (1950). Spin echoes. *Physics Review*, **80**, 580–94.
7. Mansfield P. (1977). Multiplanar image formation using NMR spin echoes. *Journal of Physics C: Solid State Physics* **10**, L55–8.
8. Yen YF, Field AS, Martin EM, et al. (2002). Test-retest reproducibility of quantitative CBF measurements using FAIR perfusion MRI and acetazolamide challenge. *Magnetic Resonance in Medicine*, **47**, 921–8.

9. Leenders KL, Perani D, Lammertsma AA, et al. (1990). Cerebral blood flow, blood volume and oxygen utilization. Normal values and effect of age. *Brain*, **113**(1), 27–47.
10. Schwarzbauer C, and Deichmann R. (2012). Vascular component analysis of hyperoxic and hypercapnic BOLD contrast. *NeuroImage*, **59**, 2401–12.
11. Buxton RB, Uludag K, Dubowitz DJ, et al. (2004). Modeling the hemodynamic response to brain activation. *NeuroImage*, **23**, S220–33.
12. Logothetis NK. (2008). What we can do and what we cannot do with fMRI. *Nature*, **453**, 869–78.
13. Norris DG. (2006). Principles of magnetic resonance assessment of brain function. *Journal of Magnetic Resonance Imaging*, **23**, 794–807.
14. Hutton C, Bork A, Josephs O, et al. (2002). Image distortion correction in fMRI: a quantitative evaluation. *NeuroImage*, **16**, 217–240.
15. Ordidge RJ, Gorell JM, Deniau JC, et al. (1994). Assessment of relative brain iron concentrations using T2-weighted and T2*-weighted MRI at 3 Tesla. *Magnetic Resonance in Medicine*, **32**, 335–41.
16. Deichmann R, Gottfried JA, Hutton C, et al. (2003). Optimized EPI for fMRI studies of the orbitofrontal cortex. *NeuroImage*, **19**, 430–41.
17. Weiskopf N, Hutton C, Josephs O, et al. (2007). Optimized EPI for fMRI studies of the orbitofrontal cortex: compensation of susceptibility-induced gradients in the readout direction. *Magnetic Resonance Materials in* Physics, **20**, 39–49.
18. Weiskopf N, Hutton C, Josephs O, et al. (2006). Optimal EPI parameters for reduction of susceptibility-induced BOLD sensitivity losses: a whole-brain analysis at 3 T and 1.5 T. *NeuroImage*, **33**, 493–504.
19. Schwarzbauer C, Mildner T, Heinke W, et al. (2010). Dual echo fMRI—the method of choice for imaging brain areas affected by susceptibility artefacts? *NeuroImage* **49**, 316–26.
20. Pruessmann KP, Weiger M, Scheidegger MB, et al. (1999). SENSE: sensitivity encoding for fast MRI. *Magnetic Resonance in Medicine*, **42**, 952–62.
21. Griswold MA, Jakob PM, Heidemann RM, et al. (2002). Generalized autocalibrating partially parallel acquisitions (GRAPPA). *Magnetic Resonance in Medicine* **47**, 1202–10.
22. Sodickson DK, and Manning WJ (1997). Simultaneous acquisition of spatial harmonics (SMASH): fast imaging with radiofrequency coil arrays. *Magnetic Resonance in Medicine* **38**, 591–603.
23. Kanwisher N, McDermott J, and Chun MM (1997). The fusiform face area: a module in human extrastriate cortex specialized for face perception. *Journal of Neuroscience*, **17**, 4302–11.
24. Friston KJ, Ashburner JT, Kiebel SJ, et al. (2007). *Statistical parametric mapping*. London: Elsevier.
25. Biswal B, Yetkin FZ, Haughton VM, et al. (1995). Functional connectivity in the motor cortex of resting human brain using echo-planar MRI. *Magnetic Resonance in Medicine* **34**, 537–41.
26. Heine L, Soddu A, Gómez F, et al. (2012). Resting state networks and consciousness: alterations of multiple resting state network connectivity in physiological, pharmacological, and pathological consciousness States. *Frontiers in Psychology* **3**, Article 295.
27. Allen EA, Erhardt EB, Damaraju E, et al. (2011). A baseline for the multivariate comparison of resting-state networks. *Frontiers in Systems Neuroscience*, **5**, Article 2.
28. Tzourio-Mazoyer N, Landeau B, Papathanassiou D, et al. (2002). Automated anatomical labeling of activations in SPM using a macroscopic anatomical parcellation of the MNI MRI single-subject brain. *NeuroImage*, **15**, 273–89.
29. Bassett DS, and Bullmore ET (2009). Human brain networks in health and disease. *Current Opinions in Neurology*, **22**, 340–7.
30. Bullmore E, and Sporns O (2009). Complex brain networks: graph theoretical analysis of structural and functional systems. *Nature Reviews Neuroscience*, **10**, 186–98.
31. McKeown MJ, Makeig S, Brown GG, et al. (1998). Analysis of fMRI data by blind separation into independent spatial components. *Human Brain Mapping*, **6**, 160–88.
32. Beckmann CF, DeLuca M, Devlin JT, et al. (2005). Investigations into resting-state connectivity using independent component analysis. *Philosophical Transactions of the Royal Society B, Biological Sciences*, **360**, 1001–13.
33. Damoiseaux JS, Rombouts S, Barkhof F, et al. (2006). Consistent resting-state networks across healthy subjects. *Proceedings of the National Academy of Sciences of the United States of America*, **103**, 13848–53.
34. Calhoun VD, Adali T, Pearlson GD, et al. (2001). A method for making group inferences from functional MRI data using independent component analysis. *Human Brain Mapping*, **14**, 140–51.
35. Zalesky A, Fornito A, and Bullmore ET (2010). Network-based statistic: identifying differences in brain networks. *NeuroImage*, **53**, 1197–207.
36. Calhoun VD, Eichele T, and Pearlson G (2009). Functional brain networks in schizophrenia: a review. *Frontiers in Human Neuroscience*, **3**, Article 17.
37. Smith SM, Miller KL, Salimi-Khorshidi G, et al. (2011). Network modelling methods for FMRI. *NeuroImage*, **54**, 875–91.
38. Laureys S, and Schiff ND. (2012). Coma and consciousness: paradigms (re)framed by neuroimaging. *NeuroImage*, **61**, 478–91.
39. He Y, Chen Z, Gong GL, et al. (2009). Neuronal networks in Alzheimer's disease. *Neuroscientist*, **15**, 333–50.
40. Wu T, Wang L, Chen Y, et al. (2009). Changes of functional connectivity of the motor network in the resting state in Parkinson's disease. *Neuroscience Letters*, **460**, 6–10.
41. Calhoun VD, Liu J, and Adali T (2009). A review of group ICA for fMRI data and ICA for joint inference of imaging, genetic, and ERP data. *NeuroImage*, **45**, S163–72.
42. Perrin JS, Merz S, Bennett DM, et al. (2012). Electroconvulsive therapy reduces frontal cortical connectivity in severe depressive disorder. *Proceedings of the National Academy of Sciences, USA*, **109**, 5464–8.
43. Vanhaudenhuyse A, Noirhomme Q, Tshibanda LJF, et al. (2010). Default network connectivity reflects the level of consciousness in non-communicative brain-damaged patients. *Brain* **133**, 161–71
44. Bernstein MA, King KF, and Zhou XJ. (2004). *Handbook of MRI pulse sequences*. London: Elsevier.
45. Huettel SA, Song AW, and McCarthy G. (2009). *Functional magnetic resonance imaging*. Sunderland, MA: Sinauer Associates.
46. Poldrack RA, Mumford JA, and Nichols T. (2011). *Handbook of functional MRI data analysis*. Cambridge: Cambridge University Press.
47. Ashby FG. (2011). *Statistical analysis of fMRI data*. Cambridge, MA: MIT Press.

CHAPTER 8

Principles of brain single-photon emission computed tomography imaging

Yong Du and Habib Zaidi

Introduction

The historical development of medical imaging is marked by numerous significant technological accomplishments, driven by an unprecedented collaboration between multidisciplinary research groups. The first medical applications of tomographic imaging focused on the brain [1]. X-ray computed tomography (CT) and magnetic resonance imaging (MRI) have, for a long time, been the most widely-used imaging modalities for anatomic assessment of pathologic processes affecting the brain. Alternatively, radionuclide imaging methods, including single-photon emission computed tomography (SPECT) and positron emission tomography (PET) have emerged as useful medical imaging technologies for evaluating brain function. The development of the former technology for brain imaging dates back to 1976 when Drs Keyes and Jaszczak reported independently on the development of a brain SPECT system based on Anger camera mounted on a rotating gantry [2,3]. As nuclear medicine imaging has become integrated into clinical practice, several design trends have developed; with systems now available with a spectrum of features, from those designed for clinical whole-body applications to others designed specifically for very high-resolution brain research applications [4].

SPECT is a non-invasive 3D tomographic imaging modality that is widely used in both clinical diagnosis and academic research to assess many diseases [5–7]. In SPECT imaging, the 3D distribution of a radionuclide-labelled agent administered to a patient is measured by detecting the gamma-photons emitted from the decay of the radioactive isotopes attached to the radiotracer. Because SPECT agents can be designed to target specific physiological functions, SPECT images can provide information on physiological and physiopathological processes at a molecular level. This unique feature makes it a useful tool for *in vivo* imaging of human brain function, especially for studying dysfunction of the neurotransmission system that is related to many brain diseases [8]. As a result, brain SPECT imaging became a powerful tool for diagnosis, prognosis, evaluation of response to therapy, and choice of treatment plan for many neurodegenerative diseases [9,10].

Brain single-photon emission computed tomography instrumentation

Conventional SPECT imaging systems

Since the purpose of SPECT imaging is to measure and represent the 3D distribution of the radiopharmaceuticals administered to the patient, the energies of gamma ray photons emitted by labelling radionuclides are high enough to allow penetration through the patient's body. The emitted photons can be detected using the so-called gamma camera (Fig. 8.1) to generate a two-dimensional (2D) snapshot planar image. The 2D planar image is referred to as projection image since it represents a projected view of the three-dimensional (3D) radiotracer distribution at a certain angle. To acquire a 3D distribution, a series of projection images are taken around the patient at different discrete angles by rotating the gamma camera around the patient along the superior-inferior axis. After acquisition, the 3D distribution can then be reconstructed from the measured projection images using one of the available reconstruction techniques.

Usually, conventional SPECT imaging systems have two or three gamma cameras that are mounted on a gantry which provides mechanical support and rotation of the cameras. The main components of a gamma camera include the collimator, scintillation crystal, and photomultiplier tubes (PMTs) (Fig. 8.1).

The collimator is used to selectively detect photons travelling in a certain direction because this information is needed for image reconstruction. It is made of highly dense photon absorbing material, usually lead or tungsten, with a pattern of holes that allows only photons travelling parallel to the hole-direction to pass and reach the detector crystal. The holes can be arranged with the same direction (parallel hole collimator) or converge to certain points (for example, a cone beam collimator). The scintillator crystal, commonly sodium iodide (NaI) crystal, will absorb the photon and transfer its energy into visible or ultraviolet (UV) light photons through a process called scintillation. The number of visible or UV photons is proportional to the energy of incident photons. The visible/UV photons will travel to the PMT trough a light guide and produce an electric current signal. The PMT can multiply the

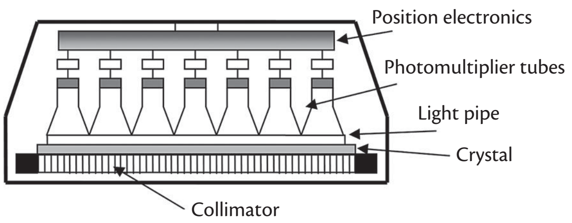

Fig. 8.1 Schematic representation of a SPECT gamma camera and its main components.

current signal by a factor of as much as a million. The signal will then be further amplified through the amplifier and sent to processing electronics to generate the position and the energy information of the incident gamma photon. The information will then be passed on to an acquisition board/computer to generate the projection images.

Many of the clinical SPECT systems commercially available today are dual-modality SPECT/CT systems that also include a CT subsystem [11]. The SPECT images and CT images are complimentary to each other: SPECT images provide functional information, while the CT images provide anatomical information about location of disease site. By fusing the two images together, an accurate interpretation of images can be achieved. In addition, CT images can also be converted into attenuation maps required for attenuation compensation to improve SPECT image quality and quantitative accuracy. A plethora of CT scanners are used on combined SPECT/CT systems. Some use diagnostic quality CT to provide images suitable for clinical usage. To reduce patient radiation dose, low-dose CT scanners have also been deployed, mostly for typical nuclear medicine applications [12]. The image quality of low-dose CT is usually low and can only be used for attenuation compensation and localization. However, with the advance of iterative CT reconstruction algorithms, low-dose CTs can now also provide images of good quality [13].

Dedicated collimators and hardware for brain imaging

Most clinical SPECT systems can be used for various applications through appropriate selection of the most suited collimator for a particular study. The collimator is the most important part of a SPECT camera and is considered to be the main component affecting spatial resolution, sensitivity, and image noise. The choice of the collimator depends on the imaged object and trade-off considerations between sensitivity and spatial resolution. Usually, collimators with better spatial resolution have lower sensitivity, thus requiring a long acquisition time as otherwise the image will be very noisy. On the other hand, collimators with higher sensitivity will provide images with lower resolution. The most commonly used collimators are parallel-hole collimators. For example, in brain imaging using ^{99m}Tc-labelled compounds, a low-energy high-resolution (LEHR) parallel-hole collimator is often used to provide images with high spatial resolution. Because high spatial resolution is desirable in brain SPECT imaging, much worthwhile research focused on designing dedicated collimators to improve spatial resolution without sacrificing sensitivity [4].

Most of these collimators are converging collimators, in which the holes are focused to a line (fan beam collimator) or a point (cone beam collimator) in front of the collimator. A number of varying focal length collimators, where the holes are focused to different points in space have also been developed and evaluated in clinical setting. The detection efficiency of converging beam collimators is higher than that of parallel-hole collimators. The spatial resolution is also slightly better. Pinhole collimators have also been designed for imaging small organs, such as the thyroid or the extremities to provide a better spatial resolution, but at the expense of detection efficiency. The efficiency can be substantially improved by using multiple pinholes [14].

Furthermore, even in the presence of high count statistics, the mechanical motions involved and the bulk of the detector heads limit the shortest time in which a complete set of projections can be recorded [15,16]. Numerous attempts have been carried out to considerably boost brain SPECT sensitivity using several detector heads or ring-like arrangement of detectors to enable the very rapid acquisition of a full set of projections. Although the use of such dedicated systems is not prevalent in the clinic for brain SPECT imaging, they are useful for research applications and could also be useful for the assessment of the potential role of advances in instrumentation in the future [17,18]. A good example of full ring detector systems is the FASTSPECT, developed at the University of Arizona, which consists of 24 position-sensitive NaI(Tl) detectors that are completely stationary, together with a stationary set of 2-mm pinhole collimators, hence, achieving high sensitivity (fast dynamic brain scans) and high spatial resolution [19]. The ring detectors from stationary systems surround the head, which makes it possible to acquire data from 360° at the same time. This is especially attractive for dynamic imaging where a short repeat-scan over a period of time is performed. Another dedicated brain scanner with stationary annular NaI(Tl) detector is the CERASPECT system, developed by Digital Scintigraphics Inc. [20], which is equipped with a rotating collimator. A modified version of this collimator is the SensOgrade, a variable focusing collimator, which samples the projections unequally, with central regions more heavily represented to compensate for attenuation from central brain structures, thus yielding a four- to nine-fold increase in sensitivity compared with conventional dual-head cameras [21]. A third example is the SPRINT II system developed at the University of Michigan, which consists of 11 detectors arranged in a polygonal fashion and a rotating collimator, which allows the acquisition of a complete set of fan-beam projection data within 1/12 of a rotation [22]. Another example of unconventional systems is the NeuroFocus™ multi-cone beam imager (Neurophysics Corporation, Shirley, MA, USA), which produces tomographic SPECT images with an intrinsic spatial resolution of ~3 mm. The operation of the NeuroFocus™ high-definition focusing emission tomographic scanner (HDFET) follows the same principles of scanning optical microscopes to obtain high-resolution 3D images of biological tissue [23]. A highly focused point of light is scanned mechanically in three-dimensions to uniformly sample the volume under observation. As an alternative to dynamic SPECT imaging using multiple, fast rotations, strategies involving the use of only a single, slow camera rotation have been proposed [24,25]. Further advances in electronics are permitting new counting strategies and advances in electronic component capability are allowing for enhanced sensitivity [26].

Data acquisition protocols

Data acquisition

During SPECT image acquisition, a series of 2D projection images are taken at different angles by rotating the camera around the patient. To acquire enough data for image reconstruction, it is important to select the correct scan arc, which defines the range of rotation and where to start. For example, for cardiac imaging a 180° rotation from right posterior oblique to left anterior oblique is used, while for brain imaging a 360° rotation is usually required. One also needs to decide the orbit to specify the distance of the camera from the patient at each angle. The orbit can be either circular or non-circular. Non-circular means that the distances of the camera from the centre of rotation, termed as the radius of rotation, are not the same for different angles. In a circular orbit, the radius of rotation is constant. For a parallel-hole collimator, the closer the patient to the camera, the better the spatial resolution is. Therefore, a non-circular orbit is often used for imaging the torso, where the camera is positioned as close to the patient as possible. In modern SPECT systems, this can be done automatically using optical sensors installed on the camera. For brain imaging, due to the round shape of the head, a circular orbit is often used where the operator can specify the radius of rotation.

The gamma photons emitted from radioactive decay have characteristic energy/energies, called peaks that are specific to the isotope. For example, ^{99m}Tc decay emits gamma photons at 140.5 keV only, while ^{123}I decay emits gamma radiation mainly at 159 keV with some other higher energy peaks with low abundance. Ideally, during SPECT imaging only photons detected with the exact peak energy will be counted as true events. However, due to the limited energy resolution of the gamma camera, the energies of detected photons are Gaussian distributed around the peak energy. To maintain a reasonable sensitivity, photons detected with energies in a certain range around the peak energy will all be counted as true events. This energy range is called the acquisition energy window. On the other hand, photons scattered in the patient body will contaminate the images and they usually have a broad energy distribution lower than the peak. To reduce the number of recorded scattered photons, the energy window should not be too wide. The choice of the energy window is dictated by a balance between recording as many peak photons as possible without significantly increasing scattered photon counts. Commonly-used energies windows are usually 15–20% wide and centred around the peak energy.

Another important parameter in SPECT is the acquisition time for each projection angle. Long acquisition times result in high counts and low image noise. However, this will also reduce patient comfort and increase chances of artefacts caused by patient movement during acquisition. Overall, the choice of scanning parameters depends on the imaging task at hand. The aim is to acquire as much complete data as possible to provide good image quality and make the process comfortable to patients. Most commercial SPECT systems have manufacturer preset or recommended acquisition protocols for common applications, such as cardiac imaging, brain imaging, tumour imaging, and bone scans. New protocols can also be set by the users to accomplish their special needs. This requires the availability of a qualified medical physicist having the required skills, expertise, and knowledge of this technology.

Dual-isotope imaging

In some situations, it may be necessary to acquire images of more than one physiological function to provide accurate diagnosis. For example, in brain imaging of the dopaminergic system, it is generally recognized that the analysis of the integrity of both the pre- and the post-synaptic neuron is crucial in distinguishing different parkinsonian syndromes. The presynaptic neurons can be imaged with an agent targeting the dopamine transporter (DAT) on the cell membrane. Agents targeting the dopamine receptors, especially type II receptor (D2R), could be used in imaging the post-synaptic neurons [27,28]. Traditionally, DAT and D2R imaging are performed on different days because most of DAT and D2R agents are labelled with the same isotope (^{123}I). Since the half-life of ^{123}I decay is 13 hours, the two scans must be separated by several days to allow the radioactivity from the first scan to decay in order to avoid contamination of the second scan. During this interval, the patient's physiological status may have changed. Moreover, the patient's position during the two scans will probably be different, which will cause registration errors between the images [29]. This is particularly relevant for patients suffering tremors, where the artefacts in the two images may have different patterns that will further complicate diagnosis.

These drawbacks can, however, be overcome by using simultaneous dual-isotope acquisition methods. Taking advantage of modern cameras' higher energy resolution and the ability to acquire multiple energy windows, simultaneous dual-isotope imaging is a method that can be used to diagnose diseases by imaging different physiological information revealed by agents labelled with different isotopes that emit gamma photons at different energies. Compared to separate imaging, simultaneous acquisition reduces acquisition time, patient discomfort and motion artefacts. Perhaps, more importantly, simultaneous acquisition ensures perfect registration of the images from both isotopes in time and space. Furthermore, motion artefacts, if any, will be the same on images of both isotopes. For example, with the introduction of ^{99m}Tc-labelled DAT ligands, such as ^{99m}Tc-TRODAT, SPECT imaging of the DAT and D2R can now be carried out simultaneously using dual-isotope ^{99m}Tc/^{123}I imaging. There is also interest in simultaneous imaging of brain perfusion using ^{99m}Tc-HMPAO and neurotransmission with ^{123}I-IBZM. However, research on simultaneous ^{99m}Tc/^{123}I dual-isotope brain imaging has shown that image quality is significantly degraded by the cross-talk contamination between the two isotopes. Cross-talk here refers to the contamination of one agent/isotope's image caused by the other isotope used in simultaneous dual-isotope imaging. Before simultaneous imaging can be adopted clinically, an efficient cross-talk compensation method must be developed and validated [30–32].

Image reconstruction

Image reconstruction techniques

SPECT image formation can be expressed as an integration of the 3D radioactivity distribution along each projection direction, i.e. line of integration, into a series of 2D data. Image reconstruction is an inverse problem that tries to estimate the 3D activity distribution from the 2D projection data. Both analytical and iterative reconstruction approaches have been devised to solve this reconstruction problem in order to provide the best estimates that are as close to the truth as possible. These two categories of reconstruction strategies are briefly summarized.

Analytical reconstruction

As described above, a projection is an integration of the activity distribution along the line of integration. The collection of these projections as a function of projection angle is referred to as the Radon transform of the object [33]. By inversing the radon transform of the projections, the original 3D activity distribution can then be reconstructed analytically. The most widely used analytical reconstruction method is the filtered back-projection (FBP) algorithm, which is still used in many image reconstruction tasks.

Analytical reconstruction methods, such as FBP, focus on the geometry and simplify the physics. They are simple, fast, and can provide accurate results when the assumed projection model matches the image formation process. However, they are sensitive to noise and missing data, which will result in artefacts and loss of reconstructed image resolution. Another major disadvantage of analytical methods is that they do not allow precise modelling of the physical and statistical characteristics of the data acquisition process, thus resulting in image artefacts and poor quantitation. This problem can, however, be solved through the use of iterative reconstruction algorithms, where image degrading factors can be modelled during the reconstruction as described in the next section.

Iterative reconstruction

Fig. 8.2 shows a generalized flow chart of an iterative reconstruction algorithm. An iterative method can be regarded as an operator working between the image space, i.e. the 3D space representing the activity distribution in the object, and projection space, which represents the SPECT measurement of the 2D projections. In an iterative method, an initial estimate is projected to generate an estimated projection of the current estimate. Estimated projections are then compared with the measured projections. The error between the two is back-projected to the image space, then used to update the current estimate. By repeating the projection–back-projection process in a feedback loop to update the image estimate until a given criterion is fulfilled, iterative methods can produce high-quality images with improved resolution and noise properties, and result in adequate quantitative accuracy.

Among all iterative reconstruction algorithms, the most successful and popular ones are statistical reconstructions, which are often simply referred to as iterative reconstruction approaches. An iterative statistical reconstruction method consists of three major components:

1. An underlying statistical model with associated objective function.
2. An iterative algorithm to find the optimal estimate in terms of the objective function.
3. A model of the image formation process often implemented using a projector–back-projector pair.

Among these, the projector–back-projector pair is very important. It serves as a bridge connecting the image space (estimate) and the projection space (measurement). It is in the projection–back-projection operators that the exact modelling of the physics and image formation process is performed. Through the iterative process, the modelling allows for the compensation of image-degrading factors, such as scatter and attenuation. The underlying statistical model and resulting objective function play the role of deciding how well the estimate matches the projections, taking into account the noise properties of the measured data and knowledge about the characteristics of the underlying activity distribution.

The most popular iterative reconstruction algorithm in SPECT is the maximum-likelihood expectation-maximization (ML-EM) algorithm and its accelerated variation, the ordered-subsets expectation-maximization (OS-EM) approach [34,35]. The ML-EM algorithm is based on the fact that photon emission and detection from radioactive decay are Poisson distributed. It attempts to maximize the statistical likelihood that the measured projections came from the reconstructed image. In OS-EM, the algorithm is made faster by using only part of the projection data, called a subset, during each update. Compared with ML-EM, OS-EM converges faster with a factor approximately equal to the number of subsets used. This category of reconstruction strategies was so successful that most current SPECT systems offer software for end users to perform ML-EM and OS-EM reconstruction with various physics modelling options. While this has been shown to be of great practical value, it should be noted that OS-EM has a relatively weak

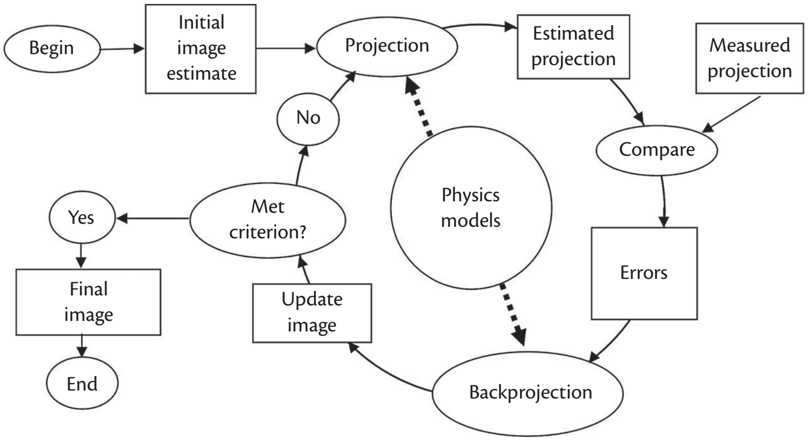

Fig. 8.2 Flow chart of an iterative reconstruction algorithm.

theoretical basis and its convergence properties are only poorly understood.

Despite their advantages and attractive properties, these technical advances have many limitations. Iterative methods can be very computationally demanding, particularly when complex models are used to model the physics of the image formation process. However, the widespread availability of high performance computing, even on desktop computers (including graphics processing unit and cloud computing), and the continuing development of rapidly converging algorithms has led to renewed interest in iterative techniques and made them a hot topic for leading manufacturers and academic research groups.

Image degrading factors

Ideally, only photons with an original path that is along the collimator hole direction can be detected in the projections. However, when gamma-photons travel inside an object, they interact with matter through a number of physical processes, such as photoelectric absorption and Compton scatter [36]. The probability of occurrence of each process depends on the energy of the photon and the electron density of the material. Those interactions could reduce the number of photons or change a photon's path and energy. The detection of those alternated photons can cause false information and degrade the image quality in multiple ways. Fig. 8.3 demonstrates the different factors that can degrade SPECT images. Among those, the most significant factors are photon attenuation, scatter, and collimator-detector response.

When photons pass through the imaging object, they can be absorbed by photoelectric absorption or diverted by Compton scatter. As a result, the intensity of the photon flux finally reaching the detector will be much smaller compared with the original one and this effect is referred to as photon attenuation. Attenuation reduces the measured projection counts. The degree depends on the photon path and the object. It can be expressed as an exponent function of the product of the attenuation coefficient of the object and the distance the photon has to travel in the object. If not compensated for, attenuation leads to reconstructed images with reduced intensity in voxels deep in the object. It can also result in visible artefacts and quantification with significant errors.

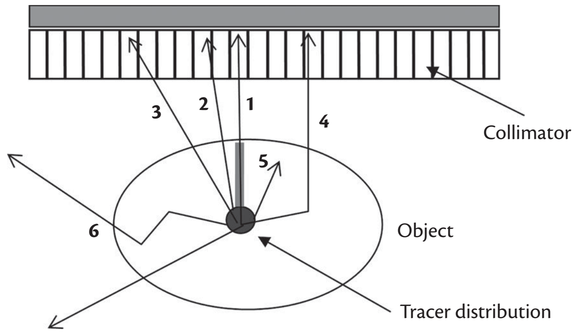

Fig. 8.3 Overview of photon detection in SPECT representing different physical degrading factors. (1 and 2) Photons pass through the collimator without interactions, 1 also shows the attenuation of the photon intensity. (3) Photon penetrates or scatters in the collimator-detector system. (4) Photon scatters inside the imaging object. (5) Photoelectric absorption; and (6) Photon escapes the object without hitting the collimator-detector system.

A number of photons emitted from the radionuclide will scatter in the patient at least once before exiting the body. The dominant scatter events are Compton scatter, which reflects a collision interaction between a gamma-photon and an outer shell electron of an atom. During the collision, gamma-photons will transfer some of their energy to the electron and change the direction of movement. The energy of the scattered photon is a function of the scattering angle, given by the Compton formula. The photon loses most of its energy when it is scattered backward (180°). When the scattering angle decreases, the energy of the scattered photon comes close to the incoming photon's energy. The probability of Compton scattering depends on the photon energy and the number of electrons available in the object. The probability of the angular distribution of the scattered photon, described by Klein–Nishina formula, is also a function of the photon energy and scattering angle [36].

Because Compton scattering reduces photon energy, usually only those photons scattered once or twice, and within a small scattering angle can be detected within the imaging energy window. Since scatter diverts the direction of scattered photons, when those photons are detected, they result in counts in voxels that they would not reach without being scattered. Scatter in projection data is spatially varying and is a function of the object attenuation properties, the imaging energy window, and the source distribution. In brain imaging using ^{123}I- or ^{99m}Tc-labelled compounds, scattered photons can contribute up to 11% of the total counts in the final images. If not compensated for, scatter could result in a structured background artefact that resembles the medium- and low-frequency character of the activity distribution, and as such reduces image contrast. Quantitatively, scatter can lead to overestimation of tracer uptake [37,38].

The collimator is the crucial element determining the sensitivity, spatial resolution and contrast of SPECT images. A perfect collimator only allows the detection of photons that travel in a direction parallel to the collimator hole. As shown in Figs 8.3 and 8.4, since a real collimator hole has a finite geometric size, photons incident within a small acceptance angle from the hole-direction can still be detected. This is referred to as geometrically-collimated photons or collimator geometric response. In addition, due to statistic variations, the position of photon absorption in the crystal is usually determined with imprecision, and is defined as intrinsic resolution. Both collimator geometric response and intrinsic resolution reduce the spatial resolution and cause blurring of the image. These effects can be modelled using geometric response functions. Typically, Gaussian functions are used to analytically model the geometric responses. The full width at half maximum of the Gaussian is, therefore, often used as an indication of the system spatial resolution [39]. In general, collimators with large holes allow more photons to pass through, but will also cause more spatial blurring. Collimators with small holes can provide better spatial resolution, but lower sensitivity. The resolution is also a function of distance: the farther the object from the collimator, the worse the resolution.

Photons incident on the collimator with large angles are usually absorbed by the septa between collimator holes. However, some high-energy photons emitted from isotopes such as ^{123}I can still penetrate the septa or pass through after scattering inside the septa as shown in Fig. 8.4. The penetrated photons from a point source usually result in a star- or stripe-shaped pattern in the projection. Collimator scattered photons usually result in a broadly distributed background in the projection. If not compensated for, these

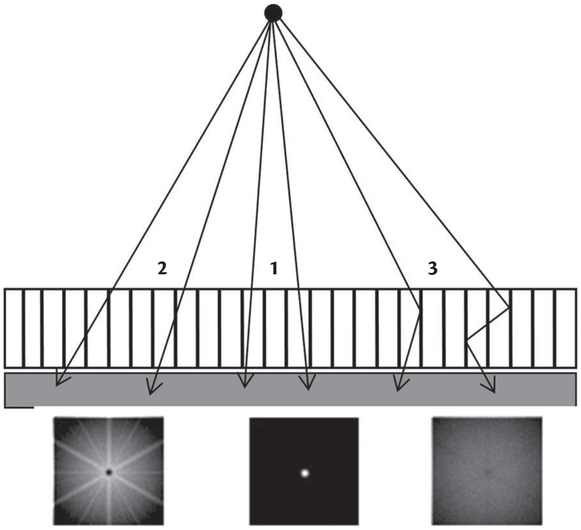

Fig. 8.4 Different components of the collimator-detector response. (1) Geometric response. (2) Collimator penetration. (3) Collimator scatter.

photons can cause artefacts in the reconstructed images. The full collimator-detector response, including geometric response, collimator penetration, and collimator scatter depends on the collimator geometry and the photon energy. It can be modelled by the collimator-detector response function (CDRF) that is measured or simulated by placing a point source at various distances from the face of the collimator.

Fig. 8.5 shows simulated SPECT images considering the different image degrading factors discussed above. The images were reconstructed using FBP without post-reconstruction filtering. From left to right, the image quality is getting worse because more degrading factors were included in the simulation process. The worst image is the last one on the right, which includes all the physical degrading factors and is the most representative of what is found in the clinic without any compensation. The images also indicate that attenuation reduces the intensity at the centre of the brain, collimator-detector response blurs images and reduces spatial resolution, and scatter reduces image contrast.

The spatial resolution in typical SPECT images is around 1–2 cm. As shown in Fig. 8.5, the finite spatial resolution results in blurred images with partial volume effects (PVEs). PVEs include both a loss of counts in structures smaller than two or three times the system resolution's full width at half maximum (partial volume) and contamination between adjacent regions (spillover). PVEs also depend on the shape, size, and relative activities of the objects of interest. The procedures applied after image acquisition, such as image reconstruction, will also affect the level of PVEs. In brain imaging, due to the fine dimensions of the structures of interest, such as the putamen and caudate, PVEs can cause large quantitative errors.

In addition, SPECT images also suffer from noise. Noise in SPECT images consists mainly of statistical noise resulting from the random nature of photon emission (following radioactive decay) and detection processes. It can be characterized by a Poisson distribution in which the variance equals the mean. Therefore, noise in SPECT data is a function of the number of detected counts—the higher the counts, the lesser the noise. Noise could significantly affect image quality and quantitative accuracy, and reduce the detectability of subtle abnormalities and their measurement. Noise can also cause image artefacts, introducing textures into uniformly-distributed regions. Increasing the count level using long acquisition times or high injection doses can reduce noise. Low pass filtering is often used to smooth out noise in the reconstructed images. Alternatively, constrains can also be applied during iterative reconstruction to reduce noise.

Cross-talk in dual-isotope imaging

In simultaneous dual-isotope imaging, a photon emitted from one isotope can be detected in another isotope's energy window owing to the finite energy resolution of the detector system, and the interaction of photons with the object and collimator-detector system. These photons can reduce image quality, degrade quantitative accuracy, and cause artefacts in the images. This effect is referred to as cross-talk contamination. Cross-talk contamination depends on the emission energies and the imaging energy windows of both isotopes. As such, the overall impact is different for various isotope combinations, making it difficult to find a universal compensation method.

Fig. 8.6 shows simulated energy spectra of a simultaneous ^{99m}Tc/^{123}I dual-isotope brain SPECT study. The spectra indicate that cross-talk from ^{99m}Tc into ^{123}I projection data originates mainly from unscattered ^{99m}Tc photons that are detected in the ^{123}I energy window as a result of the detector's finite energy resolution. The cross-talk from ^{123}I into ^{99m}Tc window, however, is complex and includes photons originating from a variety of processes. In addition to the 159 keV photons used for imaging, ^{123}I decay also emits high-energy photons with energies ranging from 182 keV to 783 keV with a total abundance of ~3% [40]. The down-scatter of these photons into both ^{99m}Tc and ^{123}I energy windows can further contaminate the images of both radionuclides.

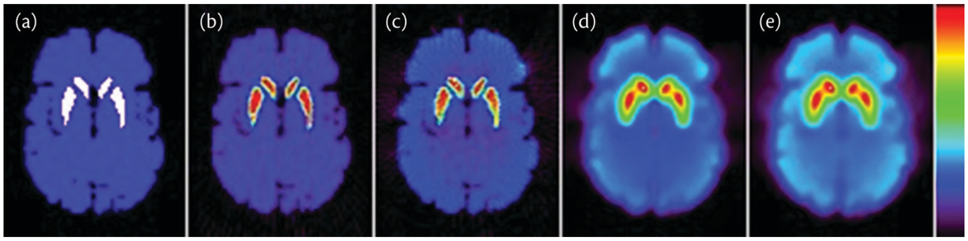

Fig. 8.5 Effects of image degrading factors. The images represent the actual tracer distribution in the striatal brain phantom (a) and reconstructed SPECT images generated without degrading factors (b); with photon attenuation (c); with attenuation and collimator-detector response blurring (d); and with attenuation, collimator-detector response blurring, and scatter (e).

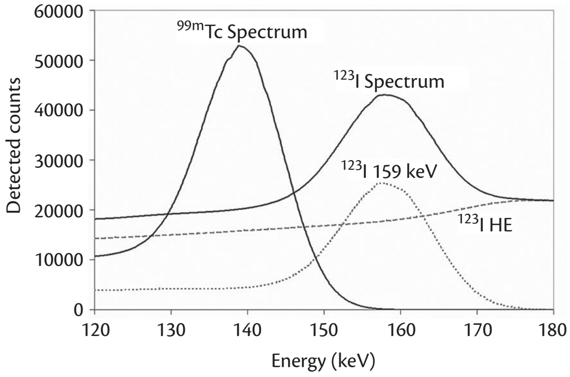

Fig. 8.6 Simulated energy spectra of a ^{99m}Tc/^{123}I dual-isotope study.

Compensation techniques

To improve image quality and quantitative accuracy, imaging degrading factors have to be compensated for. To compensate for attenuation, an attenuation map representing the spatial distribution of the patient's attenuation coefficients is required. The attenuation map can be derived by scanning the patient using either transmission sources of radionuclides having an energy close to the energy of the radionuclide used for SPECT imaging or from CT images acquired on combined SPECT-CT systems. In the past, analytical methods have been used to compensate for photon attenuation, which usually involves scaling the projection image or post-reconstruction filtering [41,42]. Because these methods often assume uniform attenuation of the medium, they can only provide an approximate compensation, and sometimes may even cause more artefacts when the object is non-homogeneous [43].

Accurate attenuation compensation can be achieved using iterative reconstruction-based compensation, where the attenuation map acquired from a transmission scan is used to model the attenuation in the projection–back-projection operators [44]. Iterative reconstruction-based attenuation compensation has been shown to significantly improve the image quality and quantitative accuracy, and is currently widely used in the clinic. Similarly, an accurate compensation of the collimator-detector response is usually achieved through iterative reconstruction-based compensation by including the CDRF models in the projection–back-projection operators [45].

Compton scatter compensation strategies can be categorized into methods that compensate for scatter directly on the projection data (pre-reconstruction), methods that compensate for scatter during the reconstruction process and post-reconstruction restoration filtering [38]. Methods that operate on projection data usually accomplish the compensation by subtracting the scatter estimate from measured projection data. Scatter is often estimated by scaling projection data acquired in one or two scatter windows with pre-determined factors [46–48]. The scatter can also be estimated by analysing the spectrum of projection data acquired in multiple narrow (1–4 keV wide) energy windows using spectral fitting techniques or artificial neural networks [49,50]. Post-reconstruction filtering usually compensates for the scatter by deconvolving the reconstructed images with a scatter response function (ScRF) acquired through experimental measurements or derived from Monte Carlo simulations [51]. Both pre- and post-reconstruction scatter compensation methods make simple assumptions about the scatter component, such as shift-invariance, which results in biased scatter estimates. Furthermore, scatter compensation is achieved by subtraction of the estimated scatter component, which is usually accompanied by a large increase in statistical noise [52,53].

Reconstruction-based scatter compensation (RBSC) methods compensate for scatter by modelling the spatially varying and object-dependent SRF in the projection–back-projection operators within the framework of an iterative reconstruction algorithm [37,54]. RBSC methods were shown to provide the most accurate scatter compensation among all methods [37,38]. Currently available scatter modelling techniques for RBSC include the slab-derived scatter estimation (SDSE) model, the effective source scatter estimation (ESSE) techniques [54,55], the non-stochastic numerical integration method [56,57], and the fast Monte Carlo simulation approach [58,59].

To demonstrate the efficacy of the various image correction techniques, Fig. 8.7 shows representative SPECT brain images reconstructed with compensation for various degrading factors. The image quality gradually improves when more degrading factors are compensated for. The best result is achieved by including compensations for all the physical degrading factors.

Most of cross-talk compensation methods have been developed based on scatter compensation methods [60–65]. The procedures include estimating the cross-talk, and subtracting it prior to reconstruction or using reconstruction-based compensation approaches. The cross-talk can be estimated using multiple energy window methods, including the triple-energy window technique or more complicated techniques, such as those using artificial neural networks, constrained spectral deconvolution, and principal component analysis. Cross-talk models were also developed for iterative reconstruction-based compensation that use estimates of the activity distribution for each isotope combined with the physics of the image-formation process to estimate the cross-talk. For

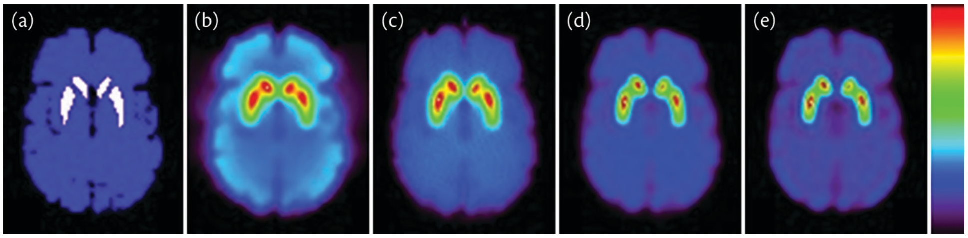

Fig. 8.7 Images reconstructed with compensation for different physical degrading factors. The images represent the actual tracer distribution in the striatal brain phantom (a) and reconstructed SPECT images obtained without compensation (b); with attenuation compensation (c); with attenuation and collimator-detector response compensation (d); and with attenuation, collimator-detector response, and scatter compensation (e).

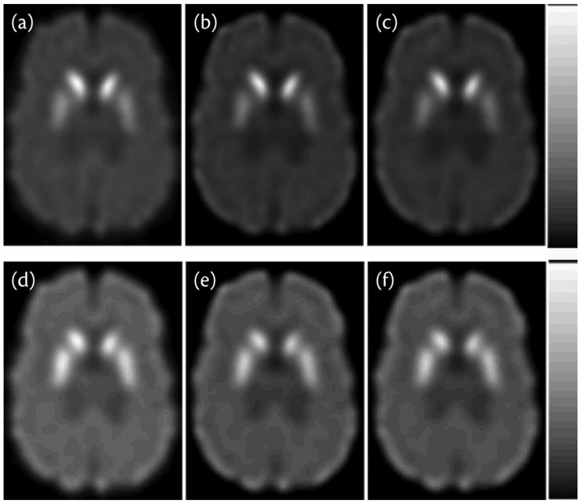

Fig. 8.8 Simultaneous dual-isotope images. Top row: ^{99m}Tc images, bottom row: ^{123}I images. Dual-isotope images without cross-talk compensation (a and d); with MBCC (b and e); and cross-talk free single-isotope images (c and f).

example, model-based cross-talk compensation (MBCC) uses the ESSE technique to model photon interactions inside objects, and collimator-detector response functions to model photon interactions within the collimator-detector and the finite energy resolution of the detector [66]. Monte Carlo simulations have also been used for cross-talk estimation [58].

Fig. 8.8 shows simultaneous ^{99m}Tc/^{123}I dual-isotope images reconstructed without cross-talk compensation and with MBCC, compared with cross-talk free single-isotope images. Overall, without compensation, the cross-talk reduced image contrast for both ^{99m}Tc and ^{123}I images. After compensation using MBCC, the images are very close to single-isotope images, indicating the efficacy of cross-talk compensation [66].

Compensation for collimator-detector response can improve image resolution and reduce PVEs. However, complete count recovery has not been achieved yet [45,66–68]. Additional partial volume effect compensation is usually required. A plethora of partial volume compensation (PVC) strategies have been proposed [69,70]. Some of these methods attempt to remove or reduce the PVEs by deconvolving the image with the system point spread function. To improve noise properties, regularization is required during deconvolution. Pixel-by-pixel template-based approaches, where spill-in and spill-out counts are modelled by their effect on template images followed by compensation using subtraction and division, were also proposed [71]. Alternative approaches directly compensate for PVEs at the regional level to provide corrected activity estimates using a transfer matrix of PVEs [72]. Application of PVC to dopaminergic neurotransmission SPECT imaging has been shown to significantly improve quantitative accuracy [73]. Reconstruction-based PVC methods have also been proposed, using for instance, the maximum a posteriori approach [74]. Methods that incorporate PVC directly into the kinetic modelling process by introducing additional parameters that model PVEs were also reported for dynamic imaging [75]. Overall, accurate PVC requires perfect knowledge of the system resolution and precise delineation of regions-of-interest (ROIs) boundaries, which can be performed through the use of registered high-resolution anatomical images such as CT or MRI.

Image quality assessment and data analysis

Qualitative versus quantitative

Traditionally, SPECT images have been qualitatively assessed by visual observation of tracer uptake in regions linked to known patterns of various diseases. The visual assessment conveys information on whether the tracer uptake is normal or abnormal, and, if abnormal, it provides an idea about the magnitude of the abnormality. In brain SPECT, the visual assessment provides information about right to left asymmetries and which structures are the most affected by disease.

However, because the uptake of an imaging tracer is often strongly correlated to the integrity of physiological functions in targeted ROIs, the quantitative measurements of tracer uptake in those ROIs can provide more information for in-depth assessment. Most importantly, quantitative analysis enables to estimate physiological parameters, such as blood flow, metabolism, and receptor concentration. These measurements can be used in clinical diagnostic work-up or in the assessment of the efficacy of therapies. For instance, the binding of DAT or D2R agents in the dopaminergic system are strongly correlated to the degree of disease progression in movement disorders. Recent research has demonstrated that the quantitative measurement of tracer uptake can provide more information for better assessment of many brain disease processes [10,76,77].

Quantification techniques

Quantitative studies usually involve defining ROIs on the images and then measuring the trace uptake inside them. One commonly used method in brain SPECT is to calculate the specific binding potential (SBP, also called specific uptake value) of the radiotracer in the ROI as the ratio between activity concentration inside the ROI and the activity concentrations in a reference region that has no specific binding for the tracer considered. The images can also be assessed using more sophisticated voxel-based quantitative methods, such as statistical parametric mapping (SPM), which automatically maps brain regions to a standardized atlas and compares the images with a database of normal subjects [77]. Compared with SPM, computing the SBP greatly simplifies data analysis and often provides a reliable measurement.

Dynamic SPECT can also be used to acquire a series of images of tracer uptake within the ROI from the injection time till the time the tracer is washed out or the distribution reaches equilibrium. Consequential kinetic analysis of the acquired dynamic data using tissue compartment models provides unique information that improves the discrimination between healthy and diseased tissue compared with static images [25].

Future perspectives

The major challenge facing the future of brain SPECT imaging is the widespread adoption and availability of PET in clinical setting. PET has better spatial resolution and higher sensitivity than SPECT. To compete with PET, future brain SPECT systems should provide images with better quality and improved quantitative accuracy that is equivalent or at least comparable with PET.

Software

Software development in SPECT is currently focusing on improving image quality and quantitative accuracy of reconstructed

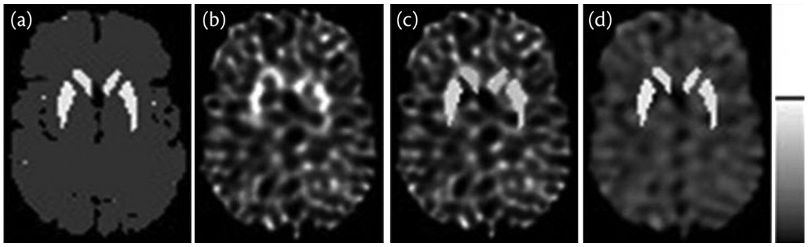

Fig. 8.9 Brain SPECT images reconstructed using different algorithms showing the actual tracer distribution in the striatal brain phantom (a). OS-EM reconstruction (b). MAP reconstruction with only a uniform prior for the striatum (c). MAP reconstruction with a smooth prior for background and a uniform prior for the striatum (d).

images. This includes the development of novel reconstruction algorithms and image correction techniques. Promising results have been achieved using maximum a posteriori (MAP) reconstruction algorithms that incorporate anatomical knowledge into the SPECT reconstruction process. The anatomical information can be obtained from MR images, which are routinely performed in the clinic for brain studies. MRI provides detailed structural information about the brain which is missing in SPECT. In MAP reconstruction, the anatomical information could be used as a prior to reduce statistical noise and improve the resolution, especially when anatomical region-based priors are used to reduce noise inside each structure but not across the boundaries [74,78,79]. Different priors can also be used for each structure based on its biological properties. Fig. 8.9 shows examples comparing OS-EM with MAP reconstructions using different regional priors. The OS-EM images contain a significant amount of noise. In the MAP reconstruction, a uniform prior was used for the striatum assuming uniform uptake. A smooth prior was used for the background to reduce noise. Images from MAP reconstruction portray much reduced noise and improved spatial resolution for the striatum compared with OS-EM reconstruction.

Hardware

A more fundamental way of improving SPECT images is to develop new detector technology that could provide images with high sensitivity and high spatial resolution. Detectors using semiconductor technology, where direct photon conversion detectors such as cadmium telluride are mostly used, acquire data at better energy resolution than conventional gamma cameras [80,81]. This could potentially provide images with less scatter and reduce cross-talk in dual-isotope imaging. Development in multimodality imaging is also being pursued. In SPECT/CT, recent developments in dual-energy CT scanners make it possible to segment soft tissues in CT images without the use of contrast agents. Simultaneous SPECT/MRI is also promising and should enable both MR and SPECT images of patient's brain to be acquired at the same time, thus providing perfectly registered images.

Acknowledgements

This work was supported by the Swiss National Science Foundation under grant SNSF 31003A-149957

References

1. Abraham T, Feng J. (2011). Evolution of brain imaging instrumentation. *Seminars in Nuclear Medicine*, **41**, 202–19.
2. Keyes J, Jr, Orlandea N, Heetderks W, et al. (1977). The Humongotron-a scintillation-camera transaxial tomograph. *Journal of Nuclear Medicine*, **18**, 381–7.
3. Jaszczak RJ, Murphy PH, Huard D, et al. (1977). Radionuclide emission computed tomography of the head with 99mTc and a scintillation camera. *Journal of Nuclear Medicine*, **18**, 373–80.
4. Accorsi R. (2008). Brain single-photon emission CT physics principles. *AJNR American Journal of Neuroradiology*, **29**, 1247–56.
5. Jaszczak RJ. (2006). The early years of single photon emission computed tomography (SPECT): an anthology of selected reminiscences. *Physics in Medicine and Biology*, **51**, R99–115.
6. Madsen MT. (2007). Recent advances in SPECT imaging. *Journal of Nuclear Medicine*, **48**, 661–73.
7. Hutton BF. (2010). New SPECT technology: potential and challenges. *European Journal of Nuclear Medicine and Molecular Imaging*, **37**, 1883–6.
8. Camargo EE. (2001). Brain SPECT in neurology and psychiatry. *Journal of Nuclear Medicine*, **42**, 611–23.
9. Catafau AM. (2001). Brain SPECT of dopaminergic neurotransmission: a new tool with proved clinical impact. *Nuclear Medicine Communications*, **22**, 1059–60.
10. Devous MD. (2002). Functional brain imaging in the dementias: role in early detection, differential diagnosis, and longitudinal studies. *European Journal of Nuclear Medicine*, **29**, 1685–96.
11. Seo Y, Mari C, and Hasegawa BH. Technological development and advances in single-photon emission computed tomography/computed tomography. *Seminars in Nuclear Medicine*, **38**, 177–98.
12. Franc BL, Myers R, Pounds TR, et al. (2012). Clinical utility of SPECT-(low-dose)CT versus SPECT alone in patients presenting for bone scintigraphy. *Clinical Nuclear Medicine*, **37**, 26–34.
13. Beister M, Kolditz D, and Kalender WA. (2012). Iterative reconstruction methods in X-ray CT. *Physics in Medicine*, **28**, 94–108.
14. Beekman F, and van der Have F. (2007). The pinhole: gateway to ultra-high-resolution three-dimensional radionuclide imaging. *European Journal of Nuclear Medicine and Molecular Imaging*, **V34**, 151–61.
15. Cherry SR. (2004). In vivo molecular and genomic imaging: new challenges for imaging physics. *Physics in Medicine*, **49**, R13–48.
16. Meikle SR, Kench P, Kassiou M, et al. (2005). Small animal SPECT and its place in the matrix of molecular imaging technologies. *Physics in Medicine and Biology*, **2005**, 22.
17. Zaidi H, (ed.) (2006). *Quantitative analysis in nuclear medicine imaging*. New York: Springer 2006.
18. Zaidi H, and El Fakhri G. (2008). Is absolute quantification of dopaminergic neurotransmission studies with 123I SPECT ready for clinical use? *European Journal of Nuclear Medicine* and *Molecular Imaging*, **35**, 1330–3.
19. Rowe RK, Aarsvold JN, Barrett HH, et al. (1993). A stationary hemispherical SPECT imager for three-dimensional brain imaging. *Journal of Nuclear Medicine*, **34**, 474–80.
20. Genna S, and Smith AP. (1988). The development of Aspect, an annular single-crystal brain camera for high-efficiency SPECT. *IEEE Transactions in Nuclear Sciences*, **35**, 654–8.
21. El Fakhri G, Ouyang J, Zimmerman RE, et al. (2006). Performance of a novel collimator for high-sensitivity brain SPECT. *Medical Physics*, **33**, 209–15.

22. Rogers WL, Clinthorne NH, Shao L, et al. (1988). SPRINT II: a second generation single photon ring tomograph. *IEEE Transactions in Nuclear Sciences*, **7**, 291–7.
23. Seibyl JP, Stobbart HA, Martin D, et al. (2002). Evaluation of high resolution NeuroFocus SPECT device for small animal imaging (abstract). *Journal of Nuclear Medicine*, **2002**, 43
24. Farncombe T, Celler A, Noll D, et al. (1999). Dynamic SPECT imaging using a single camera rotation (dSPECT). *IEEE Transactions in Nuclear Sciences*, **46**, 1055–61.
25. Gullberg GT, Reutter BW, Sitek A, et al. (2010). Dynamic single photon emission computed tomography-basic principles and cardiac applications. *Physics in Medicine and Biology*, **55**, R111–91.
26. Wong WH, Li H, Uribe J, et al. (2001). Feasibility of a high-speed gamma-camera design using the high-yield-pileup-event-recovery method. *Journal of Nuclear Medicine*, **42**, 624–32.
27. Acton PD, and Mozley PD. (1999). Single photon emission tomography imaging in parkinsonian disorders: a review. *Behavioural Neurology*, **12**, 11–27.
28. Tatsch K, Asenbaum S, Bartenstein P, et al. (2002). European association of nuclear medicine procedure guidelines for brain neurotransmission SPET using 123I-labelled dopamine transport ligands. *European Journal of Nuclear Medicine and Molecular Imaging*, **29**, BP30–5.
29. Djang DS, Janssen MJ, Bohnen N, et al. (2012). SNM practice guideline for dopamine transporter imaging with 123I-ioflupane SPECT 1.0. *Journal of Nuclear Medicine*, **53**, 154–63.
30. Devous MD, Lowe JL, Payne JK. (1992). Dual-isotope brain SPECT imaging with Technetium and I-123—Validation by phantom studies. *Journal of Nuclear Medicine*, **33**, 2030–5.
31. Devous MD, Payne JK, and Lowe JL. (1992). Dual-isotope brain SPECT imaging with Technetium and I-123—Clinical validation using Xe-133 SPECT. *Journal of Nuclear Medicine*, **33**, 1919–24.
32. Ivanovic M, Weber DA, Loncaric S, et al. (1994). Feasibility of dual radionuclide brain imaging with I-123 and Tc-99m. Medical Physics, **21**, 667–74.
33. Kak AC, and Slaney M. (1988). *Principles of computerized tomographic imaging*. IEEE Press.
34. Hudson HM, and Larkin RS. (1994). Accelerated image reconstruction using ordered subsets of projection data. *IEEE Transactions in Nuclear Sciences*, **13**, 601–9.
35. Lange K, and Carson R. (1984). EM reconstruction algorithms for emission and transmission tomography. *Journal of Computer Assisted Tomography*, **8**, 306–16.
36. Cherry SR, Sorenson JA, and Phelps ME. (2012). *Physics in nuclear medicine*, 4th edn. Philadelphia, PA: Elsevier Saunders.
37. Zaidi H, and Koral KF. (2004). Scatter modelling and compensation in emission tomography. *European Journal of Nuclear Medicine and Molecular Imaging*, **31**, 761–82.
38. Hutton BF, Buvat I, and Beekman FJ. (2011). Review and current status of SPECT scatter correction. *Physics in Medicine and Biology*, **56**, R85–112.
39. Metz CE, Atkins FB, and Beck RN. (1980). The geometric transfer function component for scintillation camera collimators with straight parallel holes. *Physics in Medicine and Biology*, **25**, 1059–70.
40. Tanaka M, Uehara S, Kojima A, et al. (2007). Monte Carlo simulation of energy spectra for 123I imaging. *Physics in Medicine and Biology*, **52**, 4409–25.
41. Budinger TF, Gullberg GT, Huesman RH. (1979). Emission computed tomography. Image reconstruction from projections: implementation and applications. **32**, 147–246.
42. Chang L-T. (1978). A method for attenuation correction in radionuclide computed tomography. *IEEE Transactions in Nuclear Sciences*, **NS-25**, 638–43.
43. Zaidi H, and Hasegawa BH. (2003). Determination of the attenuation map in emission tomography. *Journal of Nuclear Medicine*, **44**, 291–315.
44. Tsui BMW, Gullberg GT, Edgerton ER, et al. (1989). Correction of nonuniform attenuation in cardiac SPECT imaging. *Journal of Nuclear Medicine*, **30**, 497–507.
45. Tsui BMW, Zhao XD, Frey EC, et al. (1994). Quantitative single-photon emission computed-tomography—basics and clinical considerations. *Seminars in Nuclear Medicine*, **24**, 38–65.
46. Jaszczak RJ, Greer KL, Floyd CE, et al. Improved SPECT quantification using compensation for scattered photons. *Journal of Nuclear Medicine*, **25**, 893–900.
47. Ichihara T, Ogawa K, Motomura N, et al. (1993). Compton scatter compensation using the triple-energy window method for single- and dual-isotope SPECT. *Journal of Nuclear Medicine*, **34**, 2216–21.
48. King MA, Hademenos GJ, and Glick SJ. (1992). A dual-photopeak window method for scatter correction. *Journal of Nuclear Medicine*, **33**, 605–12.
49. Buvat I, Benali H, Toddpokropek A, et al. (1994). Scatter correction in scintigraphy—the state-of-the-art. *European Journal of Nuclear Medicine*, **21**, 675–94.
50. El Fakhri G, Maksud P, Kijewski MF, et al. (2000). Scatter and cross-talk corrections in simultaneous Tc-99m/I-123 brain SPECT using constrained factor analysis and artificial neural networks. *IEEE Transactions in Nuclear Sciences*, **47**, 1573–80.
51. Floyd CE, Jr, Jaszczak RJ, Greer KL, et al. (1985). Deconvolution of Compton scatter in SPECT. *Journal of Nuclear Medicine*, **26**, 403–8.
52. Gilland DR, Tsui BMW, McCartney WH, et al. (1988). Determination of the optimum filter function for SPECT imaging. *Journal of Nuclear Medicine*, **29**, 643–50.
53. Yanch JC, Flower MA, and Webb S. (1988). A comparison of deconvolution and windowed subtraction techniques for scatter compensation in SPECT. *IEEE Transactions in Nuclear Sciences*, **7**, 13–20.
54. Frey EC, and Tsui BMW. (1996). A new method for modeling the spatially-variant, object-dependent scatter response function in SPECT. In: *1996 IEEE Nuclear Science Symposium Conference Record*, pp. 1082–6. Anaheim, CA.
55. Du Y, Tsui BMW, and Frey EC. (2006). Model-based compensation for quantitative I-123 brain SPECT imaging. *Physics in Medicine and Biology*, **51**, 1269–82.
56. Cao ZJ, Frey EC, and Tsui BMW. (1994). A scatter model for parallel and converging beam SPECT based on the Klein–Nishina formula. *IEEE Transactions in Nuclear Sciences*, **41**, 1594–600.
57. Riauka TA, and Gortel ZW. (1994). Photon propagation and detection in single-photon emission computed tomograph—an analytical approach. *Medical Physics*, **21**, 1311–22.
58. Beekman FJ, de Jong HWAM, and van Geloven S. (2002). Efficient fully 3-D iterative SPECT reconstruction with Monte Carlo-based scatter compensation. *IEEE Transactions in Medical Imaging*, **21**, 867–77.
59. Lazaro D, El Bitar Z, Breton V, et al. (2005). Fully 3D Monte Carlo reconstruction in SPECT: a feasibility study. *Physics in Medicine and Biology*, **50**, 3739–54.
60. El Fakhri G, Moore SC, Maksud P, et al. (2001). Absolute activity quantitation in simultaneous I-123/Tc-99m brain SPECT. *Journal of Nuclear Medicine*, **42**, 300–8.
61. Erlandsson K, Visvikis D, Waddington WA, et al. (1999). Dual radionuclide brain imaging with Tc-99m and I-123 with crosstalk corrections using multiple energy windows. *European Journal of Nuclear Medicine*, **26**, 1186.
62. Knesaurek K, and Machac J. (1997). Enhanced cross-talk correction technique for simultaneous dual-isotope imaging: a Tl-201/Tc-99m myocardial perfusion SPECT dog study. *Medical Physics*, **24**, 1914–23.
63. Links JM, Prince JL, and Gupta SN. (1996). A vector Wiener filter for dual-radionuclide imaging. *IEEE Transactions in Medical Imaging*, **15**, 700–9.
64. Neumann DR, and Chen EQ. (1992). Convolution-based method of energy spectral crosstalk correction for simultaneous, dual-isotope SPECT. *Radiology*, **185**, 176.
65. Yang JT, Yamamoto K, Sadato N, et al. (1997). Clinical value of triple-energy window scatter correction in simultaneous dual-isotope single-photon emission tomography with 123I-BMIPP and 201Tl. *European Journal of Nuclear Medicine*, **24**, 1099–106.
66. Du Y, Tsui BMW, and Frey EC. (2007). Model-based crosstalk compensation for simultaneous Tc-99m/I-123 dual-isotope brain SPECT imaging. *Medical Physics*, **34**, 3530–43.

67. Pretorius PH, King MA, Pan TS, et al. (1988). Reducing the influence of the partial volume effect on SPECT activity quantitation with 3D modelling of spatial resolution in iterative reconstruction. *Physics in Medicine and Biology*, **43**, 407–20.
68. Soret M, Riddell C, Hapdey S, et al. (2001). Simultaneous attenuation and partial volume effect correction for SPECT I-123 dopamine receptor imaging. *Journal of Nuclear Medicine*, **42**, 57p.
69. Rousset O, Rahmim A, Alavi A, et al. (2007). Partial volume correction strategies in PET. *PET Clinics*, **2**, 235–49.
70. Erlandsson K, Buvat I, Pretorius PH, et al. (2012). A review of partial volume correction techniques for emission tomography and their applications in neurology, cardiology and oncology. *Physics in Medicine and Biology*, **57**, R119–59.
71. Meltzer CC, Zubieta JK, Links JM, et al. (1994). MRI-based correction for PET partial volume effects in the presence of heterogeneity in gray-matter radioactivity. *Journal of Nuclear Medicine*, **35**, P197.
72. Rousset OG, Ma Y, Evans AC. (1998). Correction for partial volume effects in PET: principle and validation. *Journal of Nuclear Medicine*, **39**, 904–11.
73. Du Y, Tsui BMW, Frey EC. (2005). Partial volume effect compensation for quantitative brain SPECT imaging. *IEEE Transactions in Medical Imaging*, **24**, 969–76.
74. Baete K, Nuyts J, Van Laere K, et al. (2004). Evaluation of anatomy based reconstruction for partial volume correction in brain FDG-PET. *NeuroImage*, **23**, 305–17.
75. Iida H, Law I, Pakkenberg B, et al. (2000). Quantitation of regional cerebral blood flow corrected for partial volume effect using O-15 water and PET: I. Theory, error analysis, and stereologic comparison. *Journal of Cerebral Blood Flow Metabolism*, **20**, 1237–51.
76. Acton PD, Meyer PT, Mozley PD, et al. (2000). Simplified quantification of dopamine transporters in humans using [99mTc]TRODAT-1 and single-photon emission tomography. *European Journal of Nuclear Medicine*, **27**:1714–18.
77. Habraken JB, Booij J, Slomka P, et al. (1999). Quantification and visualization of defects of the functional dopaminergic system using an automatic algorithm. *Journal of Nuclear Medicine*, **40**, 1091–7.
78. Baete K, Nuyts J, Van Paesschen W, et al. (2004). Anatomical-based FDG-PET reconstruction for the detection of hypo-metabolic regions in epilepsy. *IEEE Transactions in Medical Imaging*, **23**, 510–19.
79. Nuyts J, Baete K, Beque D, et al. (2005). Comparison between MAP and postprocessed ML for image reconstruction in emission tomography when anatomical knowledge is available. *IEEE Transactions in Medical Imaging*, **24**, 667–75.
80. Ogawa K, Ohmura N, Iida H, et al. (2009). Development of an ultra-high resolution SPECT system with a CdTe semiconductor detector. *Annals of Nuclear Medicine*, **23**, 763–70.
81. Takahashi Y, Miyagawa M, Nishiyama Y, et al. (2013). Performance of a semiconductor SPECT system: comparison with a conventional Anger-type SPECT instrument. *Annals of Nuclear Medicine*, **27**, 11–16.

CHAPTER 9

Positron emission tomography

Bart N. M. van Berckel, Adriaan A. Lammertsma,
and Ronald Boellaard

Introduction

Positron emission tomography (PET) is a medical imaging technique, which allows for quantitative *in vivo* measurements of the 3D distribution of a tracer labelled with a positron emittor. In clinical neurology, [^{18}F]-2-fluoro-2-deoxy-D-glucose (FDG) is the most common PET tracer. It provides a measure of glucose consumption of the brain and it is widely used in the diagnosis of patients with cognitive disorders, movement disorders, and brain tumours, and in the presurgical evaluation of patients with drug-resistant epilepsy [1]. The availability of many other tracers, however, makes it possible to assess several other physiological and pharmacokinetic parameters of the brain, such as blood flow, oxygen consumption and extraction, neuroreceptor density and affinity, drug delivery and uptake, and gene expression. Furthermore, PET can be used for the assessment of therapeutic efficacy and for the evaluation of new drugs. PET imaging combines quantification with high sensitivity and high spatial resolution (up to ~2.5 mm full width at half maximum for clinical PET scanners).

For some of the clinical diagnostic applications visual inspection of PET images may provide sufficient information. Nevertheless, all other applications require some form of quantification, especially when PET data are used as surrogate markers in clinical trials with disease modifying drugs. Quantification of PET studies depends on scanner settings during acquisition, scanning protocol, image reconstruction algorithm, and the method used for data analysis. It is therefore of the utmost importance to be aware as to how all these parameters may affect quantification. Potential limitations of PET quantification should be considered carefully and taken into account during the evaluation of PET studies. In this chapter some factors affecting PET quantification are discussed. The first section is a brief introduction of the physical principles of PET. The second describes various data acquisition, image reconstruction, and correction methods, together with their potential impact on PET quantification. The third section focuses on the main principles of pharmacokinetic analysis, discussing the effects of various analytical methods, including some discussion on the use of standardized uptake value (SUV) in multicentre trials.

Section I: principles of positron emission tomography

PET measures the distribution of a radioactive tracer *in vivo* [2]. Upon administration of a minute (tracer) amount (i.e. pico- or nanomoles) of a positron emitting compound to a patient, it will distribute throughout the body, including the brain. An emitted positron combines with an electron after travelling a distance of, at most, a few millimetres in tissue. This complex of positron and electron (positronium) is very unstable and will annihilate almost instantaneously, resulting in the emission of two photons, each having an energy of 511 keV, in opposite directions. PET data acquisition is based on the simultaneous (coincidence) detection of these two photons. A PET scanner consists of many photon detectors surrounding the patient. During a PET scan millions of coincidence detections are collected providing information on the distribution of the radiotracer in a given tissue. Fig. 9.1 demonstrates the principle of PET imaging.

Unfortunately, the total signal does not only consist of true coincidences, representing the true 3D distribution of the tracer. There is also background signal due to photons that are scattered before detection or by coincidence detection of two uncorrelated photons, the so-called random coincidences. Fig. 9.2 illustrates the differences between true, random, scatter, and multiple coincidences.

True coincidences arise from the simultaneous (coincident) detection of two annihilation photons originating from one positron emission. A large fraction of the emitted photons (may be up to 50%), however, is scattered before leaving the patient. This means that one or both of the emitted annihilation photons are deflected from its original path by Compton scattering before leaving the patient. When one of a pair of detected photons has been scattered it will result in a mispositioning of the original annihilation event. Moreover, a random coincidence will be recorded when two photons from two independent positron emissions are accidentally (randomly) detected simultaneously (while the others are not detected). It may be clear that these random coincidences result in image distortions (i.e. addition of a smooth background). Finally, multiple detections can occur when three or more photons are detected at the same time. These multiples usually are discarded.

For quantification of PET studies it is necessary to account for the contribution of scattered and random coincidences. Moreover, due to attenuation (i.e. scatter and absorption) of photons in the patient, a large fraction of the emitted photons will not be detected. Fortunately, in case of PET, attenuation does not depend on the exact location of the positron emission along the line of response (i.e. the line connecting the detectors where a coincidence is measured), as it depends on the total attenuation of both coincidence photons together, i.e. the total path length through the tissue. Consequently, by performing transmission scans using either an external positron emitting source or a CT scan, it is possible to correct for the effects of attenuation. In practice, however, attenuation

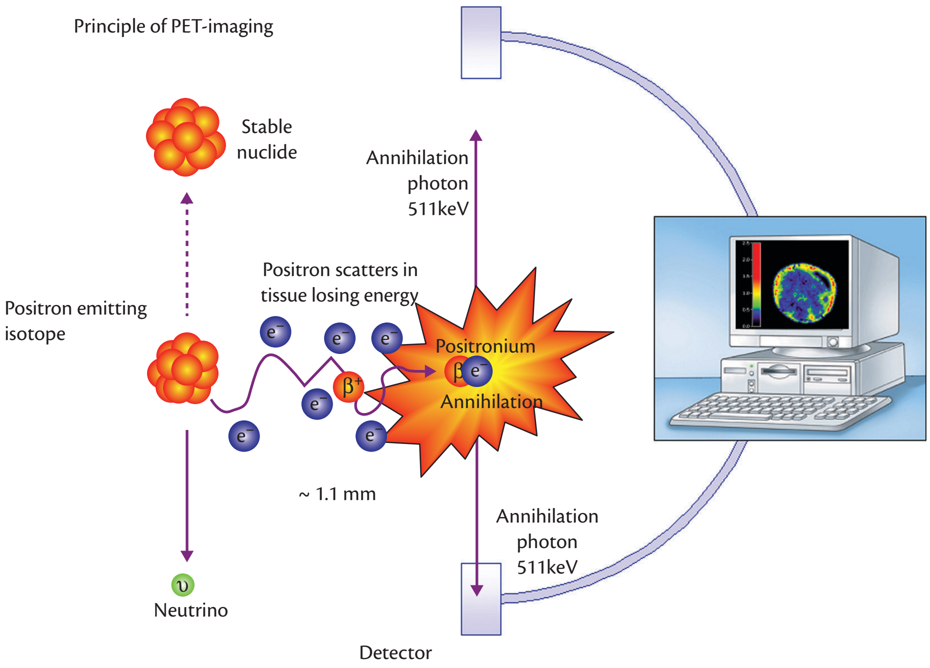
Principle of PET-imaging
Stable nuclide
Annihilation photon 511keV
Positron scatters in tissue losing energy
Positron emitting isotope
e⁻
β⁺
Positronium
β e⁻
Annihilation
~ 1.1 mm
υ
Neutrino
Annihilation photon 511keV
Detector

Fig. 9.1 Principles of PET. PET is based on the detection of the 2 annihilation photons that arise from the annihilation of an emitted positron (left part of figure) with an electron (middle of figure, indicating process of annihilation). Upon annihilation of the positron with an electron, their masses are converted into 2 photons, each with an energy of 511 keV, that are emitted simultaneously in nearly opposite directions. Next, the simultaneous (coincident) detection of these 2 photons results in a coincidence detection along a line of response. The latter is defined as the line between 2 detectors that have detected each of the 2 photons at the same time (in practice within 4–10 ns).

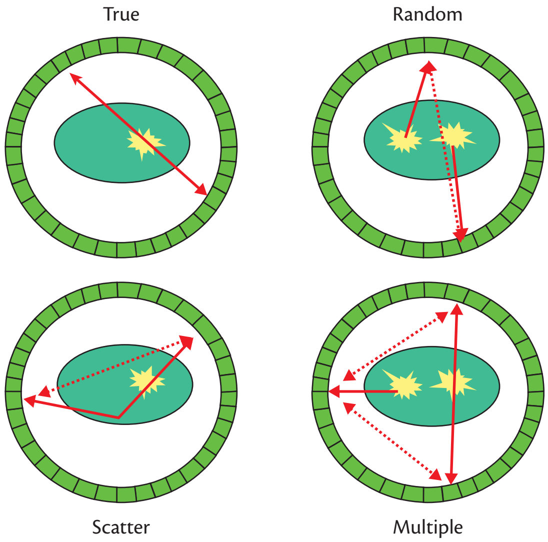

Fig. 9.2 Illustrations of true (top, left), random (top, right), scatter (bottom, left), and multiple (bottom, right) coincidences.

correction is somewhat hampered by patient motion. Random, scatter, and attenuation correction methods are discussed in more detail in the next section.

Section II: Data acquisition and image reconstruction

2D versus 3D acquisition

Although PET is a 3D imaging method, to date some PET and PET/CT scanners still are equipped with septa, i.e. lead or tungsten annular shields positioned within the field of view (FOV). These septa shield the detectors for photons emitted or scattered from outside the transverse or transaxial plane (Fig. 9.3).

The main purpose of these septa (2D mode) is to reduce the contribution of random coincidences, scattered photons, and photons originating from activity outside the FOV at the cost of reduced sensitivity compared with 3D (no septa) acquisitions. In general, it is thought that reduced contribution of random and scattered photons in the case of 2D acquisitions improves the quantitative accuracy of PET studies (smaller corrections), although this is still a matter of debate [3]. Most modern PET and PET/CT scanners are no longer equipped with septa and acquisition in 3D mode (without septa) is the only option. 3D acquisitions include lines of response (LORs) that are located in oblique planes (Fig. 9.3). 3D acquisitions have a higher detection probability, resulting in increased sensitivity, but also increased random and scatter contributions. Fortunately, most of these scanners are also equipped with new scintillation crystals (Table 9.1).

These new crystal materials result in a better count rate performance as they show a faster scintillation decay time. Consequently, a shorter coincidence time window can be used, reducing the number of random (and scatter) coincidences. Therefore, these new crystals compensate, in part, for the increase in random and scattered photons associated with 3D acquisitions. Nevertheless, 3D acquisitions still result in large fractions of random and scattered photons and, therefore, the accuracy of implemented random and scatter correction methods directly affects quantitative accuracy of PET studies.

Random corrections

As indicated in ‘2D versus 3D acquisition’, random coincidences arise from the ‘simultaneous’ detection of two uncorrelated photons,

Table 9.1 Summary of some characteristics of common scintillation crystals

Property	NaI	BGO	LSO	GSO
Density (g/ml)	3.67	7.13	7.4	6.7
Effective Z	51	74	66	61
Decay time (ns)	230	300	35–45	30–60
Photons/MeV	38,000	8200	28,000	10,000

BGO = bismuth germinate; GSO = gadolinium oxyorthosilicate; LSO = lutetium oxyorthosilicate; NaI = sodium iodide.

i.e. photons arising from two different positron emissions. As these randoms are uncorrelated, their mutual directions are also uncorrelated, and an almost uniform background is added to the measured activity distribution. Therefore, a simple strategy for random correction is to subtract a uniform or a non-uniform background (using a predefined function to describe the shape) from the reconstructed PET image. This method is still used in some modern PET scanners. As the random fraction depends on object size, attenuation distribution, and the amount of activity, the (non-)uniform background correction is generally scaled so that reconstructed activity outside the object becomes zero. Clearly, these background methods are approximations of the real distribution of randoms, as they do not take the actual 3D activity and attenuation distribution into account. Moreover, these methods need to be calibrated using specific phantoms and may only be applicable for specific clinical studies.

Due to limitations of the background subtraction methods, more sophisticated random correction methods have been developed using either block singles or delayed coincidence time windows [2].

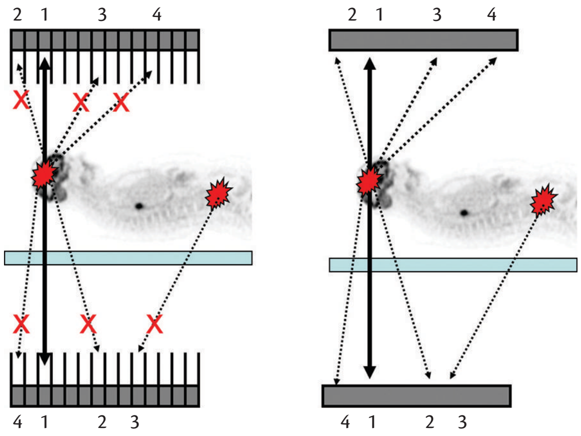

Fig. 9.3 Illustration of 2D (left) and 3D (right) acquisitions. Red crosses indicate photons that are shielded from the detectors by the septa. Indices above and below each 'detector' indicate corresponding type of coincidences. Straight (1) coincidence detections represent the simultaneous detection of both annihilation photon that are emitted along lines of responses that are located within an axial (vertical) plane. Similarly, oblique (2) coincidence detections represent detections along lines of response located in oblique planes. Random (3) coincidences arise from the simultaneous detection of 2 photons, which arise from two different unrelated or 'random' positron emissions. In this case the other 2 photons remain undetected. Finally, scattered (4) coincidences are coincidence detection where one or both photons are deflected from their original path by Compton scattering occurring within the patient. From the figure it can be deduced that 2D acquisitions have smaller contributions from random and scattered coincidences. Yet, due to the lack of oblique coincidence detections 2D acquisitions have a lower sensitivity than 3D acquisitions.

The latter is used most frequently in commercial scanners. A detailed explanation of these methods is beyond the scope of this chapter. In short, the delayed coincidence time method is based on counting coincidences using a time-shifted coincidence window. By definition, as the time window is shifted, measured coincidences must originate from photons of uncorrelated positron emissions. The 'measured' randoms using this technique provide an accurate estimate of their distribution. A random-corrected sinogram can then be obtained by subtracting such random sinogram from the measured total coincidence sinogram resulting, in a so-called 'trues' sinogram. Normally, this correction is performed online during acquisition. In general, the delayed coincidence window technique is considered to be the most accurate and it is the method of choice for random correction in case of quantitative PET.

Attenuation correction

Attenuation of photons in the patient causes loss of coincidences. The number of measured coincidences depends on the patient's 'radiological' thickness, i.e. the overall attenuation along a line of response. The effects of attenuation can easily be corrected for by making either transmission or CT scans. In short, during transmission scans the attenuation of the patient is measured for each possible LOR. Attenuation by the patient is obtained by taking the ratio of the measured transmission counts to those obtained during a blank scan, i.e. a transmission scan without the patient in the FOV. This ratio is a direct measure of the loss of counts (attenuation) for each LOR. Correction can be performed by multiplying the measured number of 'true' coincidences (true = after correction for random coincidences) by this (inverse) ratio, although a more sophisticated implementation within the reconstruction algorithm is possible [4].

In most cases transmission scans are acquired using positron emitting sources. The energy of the emitted photon (511 keV) matches that of the photons measured during emission scanning. Therefore, these transmission scans can be used for attenuation correction without any further processing. It should be noted that, in case of quantitative dynamic PET studies, usually a 10–15-minute long, transmission scan is acquired before administration of the radiotracer and thus before the start of the emission scan. In most PET/CT scanners, the CT data are used for attenuation correction (CT-AC). CT scans do not suffer from poor signal-to-noise ratios (SNR) compared with ordinary transmission scans. A CT scan is made by rotating an X-ray tube around the patient. The energy of the photons generated by the X-ray tube is much lower than 511 keV. Therefore, a CT image represents the distribution of attenuation coefficients for low photon energies (~70–90 keV). These coefficients are not valid for 511 keV and so the CT images need to be converted into '511-keV attenuation coefficient images'. Clearly, any displacement of the patient between transmission, or CT, scan and emission scan causes a spatial mismatch between both data sets and results in incorrect attenuation correction. Patient motion should therefore be prevented as much as possible.

Scatter correction

Although random and attenuation correction methods are complicated and many factors can influence their accuracy [5–8], the development of accurate scatter correction algorithms is still one of the most challenging issues in PET physics, especially in case of 3D scans (no septa). As most modern scanners are 3D only, this section summarizes scatter correction issues for 3D scans only.

Scattered coincidences occur when one or both photons are scattered and thereby deflected from their original direction(s) (Fig. 9.2). The main cause of scattering for 511-keV photons is Compton scattering, where the photon interacts with ('hits') an electron. After scattering, this photon has a lower energy, depending on the angle of deflection from its original direction. Scattering results in an almost random direction of the scattered photon (although peaked forwardly) and it results in a low frequency background signal within the image (thereby reducing contrast). A simple strategy to compensate for scatter is to apply a uniform or non-uniform background correction to the PET image, similar to the background correction described for randoms. Usually, scatter and random corrections are then combined within a single non-uniform background correction. In most cases, however, this method is far too simple to accurately correct for scatter (and randoms).

A second approach makes use of the lower energy of scattered photons. Narrowing the energy window during PET can reduce the contribution of scattered photons. The use of a smaller energy window, however, also reduces sensitivity. This reduced sensitivity is caused by the 'loss' of photons that are scattered within the detectors and thus only partially deposit their energy in the detector. Alternatively, the contribution of scatter might be estimated using two or more energy windows (dual/triple energy window techniques) [9–11]. One window is centred on 511 keV for acquisition of total counts, while another energy window is used to estimate the contribution of scattered photons. Usually, the number of photons measured in the lower energy window is rescaled in order to (more) accurately estimate the contribution of scattered photon in the 511 keV window. The rescaled scattered photons detected in the lower energy window are then subtracted from those measured in the higher (511 keV) window. One drawback of the dual (or triple) energy window technique is that it might result in poor SNR in the reconstructed data [10]. However, nowadays most PET/CT systems use a scatter simulation method to estimate and correct for the contribution of scattered photons [12,13].

Image reconstruction methods

PET measures coincidences, which are stored in sinograms. A sinogram contains the projections over all angles of the activity distribution in the patient. The process of calculating the activity distribution in the patient from these measured sinograms, including corrections for randoms, scatter, attenuation, normalization, and dead time, is called image reconstruction. Image reconstruction algorithms can be classified into analytical and iterative methods, and into 2D and 3D methods.

The most commonly used analytical image reconstruction method is filtered back-projection (FBP). This method is linear and quantitatively robust, but it is sensitive to noise and reconstructed images may contain severe streak artefacts. For these reasons iterative reconstruction algorithms have been developed, such as ordered subset expectation maximization (OSEM), least square [14], and row action maximum likelihood algorithm (RAMLA) [15]. A detailed description of all these methods is beyond the scope of this chapter (see also [16–19]).

Emerging technologies

Recently, PET scanners with time of flight (ToF) capabilities have become available. ToF is based on the difference in arrival or detection times of the two 511 keV annihilation photons when the original annihilation event occurs at a location that is not in the centre between both detectors. The difference in detection times contains information about the position of the positron emission along the line of response. ToF requires a high timing accuracy and fast detectors with high sensitivity and fast electronics, which only recently have become available. At present, assessment of the exact location (within a couple of millimetres) is still not possible. The current ToF technology provides a positional accuracy within 7–10 cm. Nevertheless, by taking the estimated position of the annihilation (and its uncertainty) into account within the reconstruction algorithm, ToF leads to a reduction in image noise. Therefore, at present, ToF is primarily used for improving image quality or SNR.

New image reconstruction algorithms that incorporate the spatial resolution characteristics of PET, expressed by the point spread function (PSF), have recently become available on several commercial PET/CT systems. These so-called PSF reconstruction methods improve both PET image resolution and SNR in the reconstructed PET images. It has been shown that PSF reconstruction methods result in higher uptake values and enhanced visibility of tumour boundaries (edge enhancement). However, the method may also give rise to artificial edge enhancements, also known as Gibbs or ring artefacts, which may result in both poorer accuracy and precision.

Section III: data analysis

As mentioned above, PET essentially measures the distribution of a tracer *in vivo*. In case of dynamic scans, this distribution can be measured as a function of time. Once data have been acquired and images reconstructed, various analyses can be performed. These analyses comprise visual inspection, semi-quantitative analysis, and full kinetic modelling. The latter is usually referred to as 'quantitative' analysis.

Visual inspection of PET images is standard practice in routine diagnostic studies, although semi-quantitative analysis like SUV is also used frequently. In the next paragraphs, some of the priniciples of SUV are addressed first. Then the principles of full kinetic analysis are discussed.

Semi-quantitative data analysis

SUV represents the uptake of a tracer in a region (e.g. a tumour) at a specific time (interval) after injection and normalized to net administered dose (corrected for decay), and a factor that takes into account the distribution within the body, such as body weight. The main advantage of SUV is that, in theory, it can be obtained relatively easily and conceptually it is very simple. There are, however, a number of restrictions that need to be taken into account when using SUV.

In general, one refers to SUV without further specification. However, apart from body weight, various other normalization factors can be used, such as body surface area and lean body mass [20]. Moreover, it has been shown that an additional correction for plasma glucose level might improve accuracy and test–retest reproducibility. Many other factors affect the SUV outcome. One of these factors is the strategy for defining a region of interest (ROI). Manually-defined 2D or 3D ROI, fixed-sized ROI, 2D and 3D iso-contour approaches, and maximum pixel values have been used to determine (average) SUV. These different ROI strategies have a large effect on the numerical values of SUV [21]. Moreover, different reconstruction methods and settings and, even more importantly, different spatial resolutions of the reconstructed images provide different SUV numbers. PET scanner and dose calibrator, used to determine the administered dose, need to be cross-calibrated frequently [22], as data from both devices are combined to derive a single SUV number. Finally, the interval between dose administration and start of the PET scan also affects SUV outcome. Fortunately, many of these ('technical') factors cancel out when SUV ratios (SUVr) are used. In case of SUVr, SUV of a particular brain region is normalized to a reference area, such as the cerebellum or pons. It is obvious that in the latter case data acquisition, image reconstruction, and data analysis procedures should be performed as consistently as possible. On the other hand, when a single cut-off (threshold) SUV is used for diagnosis or as a prognostic factor, it is important to realize that this threshold is only valid for the specific scanning conditions used. To date, many published studies do not provide enough details in order to derive a common SUV threshold applicable to all PET centres. As a result, these studies can only demonstrate the feasibility of a SUV threshold. Moreover, lack of acquisition, reconstruction, and data analysis standardization hampers the use of SUV in multicentre trials [23,24]. Therefore, when reporting SUV, it should be made very clear which SUV measure was used, how data were collected and which time interval was used.

Quantitative data analysis

SUV does not always provide a meaningful measure. The uptake of a tracer depends on time, the time course of tracer in plasma (the so-called input function) and the kinetic behaviour of tracer in tissue (e.g. extraction, retention, and clearance). The input function represents the supply of tracer to tissue over time. Clearly, differences in 'supply' of a tracer can directly affect its uptake in tissue over time. Tracer kinetics in tissue, together with the input function, determine the activity concentration in tissue as a function of time. In the case of irreversible binding or tissue trapping, the tissue concentration will increase over time, and flatten when the concentration in plasma decreases (i.e. reduction in supply). It is generally assumed that FDG is irreversible trapped in tissue (as FDG phosphate) and that the input function decreases over time. This typical behaviour of FDG allows after a fixed time after administration semi-quantitative analysis of FDG studies using SUV, although there are examples showing the opposite. However, for most other tracers (both irreversible and reversible) this is not the case and a direct relationship between uptake at a certain time point and underlying kinetic parameters does not exist. Therefore, for most PET tracers, accurate results can only be obtained by (pharmaco-)kinetic modelling.

The purpose of PET pharmacokinetic modelling is to derive a quantitative estimate of a kinetic parameter of interest [25]. This parameter may be perfusion (blood flow), metabolic rate of oxygen or glucose, or volume of distribution or binding potential of a neuroreceptor ligand, etc. Tracer kinetic modelling is based on a compartment model, which describes the fate of the tracer in tissue as a function of the input of the radiotracer. The model consists of various rate constants that describe the rate of exchange of the tracer between compartments. An example of such a model is given in Fig. 9.4.

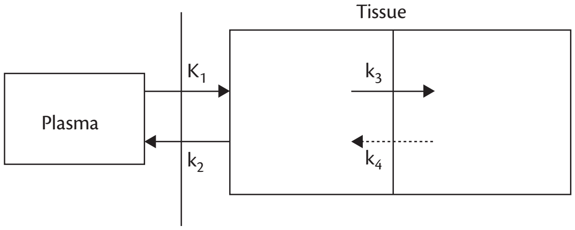

Fig. 9.4 Illustration of a two-tissue compartment model. Rate constants are indicated by K_1, k_2, k_3 and k_4. The dashed arrow, corresponding with k_4, is absent in case of irreversible binding or tracer trapping. The latter is often used in case of FDG (k_4 = 0, dashed arrow not present).

This figure shows a blood compartment (input function) and a tissue compartment. In this example, the tissue compartment is further split into two compartments, one representing free tracer in tissue and the other the tracer bound to a receptor or metabolized tracer. Rate constants, describing transport rates between these compartments, are given as k_i (i = 1, 2, 3, 4 in this example). Using non-linear regression analysis, the values of these rate constants are estimated from a dynamic PET scan and a measured input function as observed (independent) variable. In case of FDG the metabolic rate is derived from $K_1 * k_3/(k_2 + k_3)$, which is multiplied by the plasma glucose level and a so-called lumped constant. This lumped constant accounts for the different affinities of glucose and FDG for both the glucose transporter and hexokinase. For reversible tracers (k4>0) the ratio k3/k4 reflects non-displaceable binding potential (BP_{ND}), which is the parameter of interest in most neuroreceptor studies. BP_{ND} reflects the fraction of tracer in tissue that, at equilibrium, is bound to receptors. BP_{ND} depends on receptor density, affinity of the tracer for the receptor, and occupancy of the receptor by endogenous ligands. A detailed review on PET pharmacokinetic modelling can be found in Gunn *et al.* [26] and van den Hoff *et al.* [25].

As indicated above, both a dynamic PET scan and an input function are required for pharmacokinetic analysis. Therefore, during dynamic PET scanning, continuous arterial blood sampling may be performed to measure the input function directly. In case a large blood pool is present within the FOV of the PET study, the input function may be derived from the dynamic PET image themselves, providing an image derived input function. For the latter purpose, ROI may, for example, be defined over the carotid artery [27]. Depending on the tracer, additional corrections may be required to obtain a proper input function, such as corrections for the presence of radioactive metabolites in plasma, and differences between whole blood and plasma concentrations.

The need for dynamic scanning, which can take 60 minutes or longer, depending on tracer kinetics, and the need to obtain an arterial input function are serious limitations for routine clinical use of PET. On the other hand, pharmacokinetic analysis provides in-depth knowledge on the behaviour of a tracer in tissue. Especially for new tracers and/or for evaluating new drugs, it may provide valuable information that may not be obtained using simple semi-quantitative measures. Indeed, in these cases, semi-quantitative measures may provide misleading information. Sometimes pharmacokinetic analysis can be simplified [28] or it can be performed using a reference tissue approach [29]. The standard procedure for evaluating new PET tracers is therefore to compare results from full kinetic analysis with reference tissue or simplified models and with semi-quantitative parameters. Only

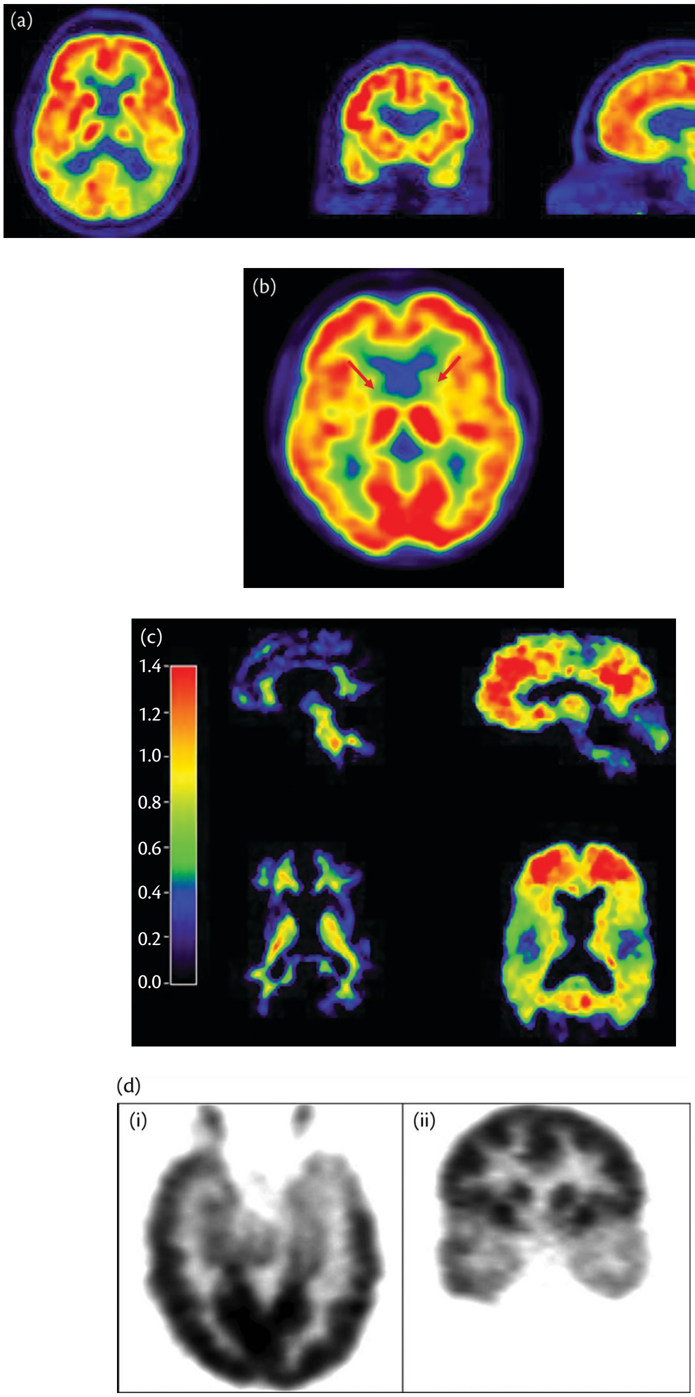

Fig. 9.5 (a) An [^{18}F]-FDG PET scan is shown of a patient with Alzheimer's disease showing diminished uptake in the parietal cortex on both sides as well as in the posterior cingulate gyrus. (b) An [^{18}F]-FDG PET scan is shown from a patient with Huntington's disease showing absent uptake in the caudate and putamen (arrows). (c) A parametric BP_{ND} image of the amyloid tracer [^{11}C]PIB is shown of a patient with Alzheimer's disease (right panel) and a healthy control (left panel) showing increased binding in the patient with Alzheimer's disease. (d) An [18F]-FDG PET scan (i: axial orientation; ii coronal orientation) is shown of a patient with epilepsy showing decreased uptake in the left medial and lateral temporal lobes.

when good correspondence between these various types of analyses has been demonstrated, use of simplified or semi-quantitative analyses may be introduced in the clinic. The interested reader is referred to an excellent educational review by van de Hoff *et al.* [25]. A concise description of the mathematical background of pharmacokinetic modelling is given by Gunn *et al.* [26].

Applications in neuroimaging

In the field on clinical neuroimaging, PET has found major implications in the diagnosis of patients suffering from cognitive disorders, epilepsy, and brain tumours.

Regarding the screening of patients with cognitive disorders, [^{18}F]-FDG PET has been used for decades for this purpose. Using

[^{18}F]-FDG PET' patients with Alzheimer's disease can be defined in a very early stage and it can be used in the differential diagnosis of patients with dementia(see Fig. 9.5). [^{18}F]-FDG PET is especially useful in the differentiation between Alzheimer's disease and frontotemporal dementia. [^{18}F]-FDG PET has a high negative predictive value for the presence of neurodegenerative disease meaning that it is highly unlikely that patients with a normal [^{18}F]-FDG PET scan will show cognitive decline within a couple of years. Since 2004, it has become possible to image amyloid depositions, the hallmark protein for Alzheimer's disease. Currently, at least five tracers are available for this purpose, [^{11}C]PIB, [^{18}F]flutemetamol, [^{18}F]florbetapir, [^{18}F]florpetapen and [^{18}F]AZD4694 (NAV4694). Currently, [^{18}F]Florbetapir and [^{18}F]flutemetamol have been approved by the FDA (USA) and the NEMA (Europe) for clinical use. The clinical role of amyloid imaging is currently being investigated.

Patients with epilepsy who do not respond adequately to anti-epileptic drugs can possibly be treated with epilepsy surgery. When it is not possible to identify the focus of the epileptic seizure with conventional methods like MRI and EEG, [^{18}F]-FDG PET can be very useful. With 'interictal' [^{18}F]-FDG PET, e.g. between episodes with seizures hypometabolic regions can sometimes reveal the epileptic focus.[^{11}C]Flumazenil, which labels benzodiazepine receptors, can also been used for this purpose, and is especially useful when the [^{18}F]-FDG PET is not informative. In patients with brain tumours, [^{18}F]-FDG PET has mainly been used to distinguish between radiation-induced necrosis and recurrence of the disease. Novel PET tracers that are used in neuro-oncology are the amino acid tracers like [^{11}C]methionine, and [^{18}F]FLT which may be more specific for this purpose.

References

1. Smith TA. (1998). FDG uptake, tumour characteristics and response to therapy: a review. *Nuclear Medicine Communications*, **19**(2), 97–105.
2. Townsend DW. (2004). Physical principles and technology of clinical PET imaging. *Annals of the Academy of Medicine, Singapore*, **33**(2), 133–45.
3. Lubberink M, Boellaard R, van der Weerdt AP, et al. Quantitative comparison of analytic and iterative reconstruction methods in 2- and 3-dimensional dynamic cardiac 18F-FDG PET. *Journal of Nuclear Medicine*, **45**(12), 2008–15.
4. Lartizien C, Kinahan PE, Swensson R, et al. (2003). Evaluating image reconstruction methods for tumor detection in 3-dimensional whole-body PET oncology imaging. *Journal of Nuclear Medicine*, **44**(2), 276–90.
5. Xu M, Cutler PD, Luk WK. (1996). Adaptive, segmented attenuation correction for whole-body PET imaging. *IEEE Transactions in Nuclear Science*, **43**(1), 331–6.
6. Visvikis D, Cheze-LeRest C, Costa DC, et al. (2001). Influence of OSEM and segmented attenuation correction in the calculation of standardised uptake values for [18F]FDG PET. *European Journal of Nuclear Medicine*, **28**(9), 1326–35.
7. van der Weerdt AP, Boellaard R, Knaapen P, et al. (2004). Postinjection transmission scanning in myocardial 18F-FDG PET studies using both filtered backprojection and iterative reconstruction. *Journal of Nuclear Medicine*, **45**(2), 169–75.
8. von Schulthess GK, Steinert HC, and Hany TF. (2006). Integrated PET/CT-3: current applications and future directions. *Radiology*, **238**(2), 405–22.
9. Shao LX, Freifelder R, and Karp JS. (1994). Triple energy window scatter correction technique in PET. *IEEE Transactions in Medical Imaging*, **13**(4), 641–8.
10. Zaidi H. (2000). Comparative evaluation of scatter correction techniques in 3D positron emission tomography. *European Journal of Nuclear Medicine*, **27**(12), 1813–26.
11. Grootoonk S, Spinks JJ, Sashin D, et al. (1996). Correction for scatter in 3D brain PET using a dual energy window method. *Physics in Medicine and Biology*, **41**(12), 2757–74.
12. Watson CC, Newport D, Casey ME, et al. (1997). Evaluation of simulation-based scatter correction for 3-D PET cardiac imaging. *IEEE Transactions on Nuclear Science*, **44**(1), 90–7.
13. Watson CC. (2000). New, faster, image-based scatter correction for 3D PET. *IEEE Transactions on Nuclear Science*, **47**(4), 1587–94.
14. Anderson JMM, Mair BA, Rao M, et al. (1997). Weighted least-squares reconstruction methods for positron emission tomography. *IEEE Transactions on Medical Imaging*, **16**(2), 159–65.
15. Browne J, and DePierro AR. (1996). A row-action alternative to the EM algorithm for maximizing likelihoods in emission tomography. *IEEE Transactions on Medical Imaging*, **15**(5), 687–99.
16. Boellaard R, van Lingen A, and Lammertsma AA. (2001). Experimental and clinical evaluation of iterative reconstruction (OSEM) in dynamic PET: quantitative characteristics and effects on kinetic modeling. *Journal of Nuclear Medicine*, **42**(5), 808–17.
17. Riddell C, Carson RE, Carrasquillo JA, et al. (2001). Noise reduction in oncology FDG PET images by iterative reconstruction: a quantitative assessment. *Journal of Nuclear Medicine*, **42**(9), 1316–23.
18. Defrise M, Kinahan PE, Townsend DW, et al. (1997). Exact and approximate rebinning algorithms for 3-D PET data. *IEEE Transactions in Med Imaging*, **16**(2), 145–58.
19. Strother SC, Casey ME, and Hoffman EJ. (1990). Measuring PET scanner sensitivity—relating countrates to image signal-to-noise ratios using noise equivalent counts. *IEEE Transactions on Nuclear Science*, **37**(2), 783–8.
20. Hoekstra CJ, Paglianiti I, Hoekstra OS, et al. (2000). Monitoring response to therapy in cancer using [F-18]-2-fluouo-2-deoxy-D-glucose and positron emission tomography: an overview of different analytical methods. *European Journal of Nuclear Medicine*, **27**(6), 731–43.
21. Boellaard R, Krak NC, Hoekstra O.S., et al. (2004). Effects of noise, image resolution, and ROI definition on the accuracy of standard uptake values: a simulation study. *Journal of Nuclear Medicine*, **45**(9), 1519–27.
22. Geworski L, Knoop BO, de Wit M, et al. (2002). Multicenter comparison of calibration and cross calibration of PET scanners. *Journal of Nuclear Medicine*, **43**(5), 635–9.
23. Shankar LK, Hoffman JM, Bacharach SL, et al. (2006). Consensus recommendations for the use of 18F-FDG PET as an indicator of therapeutic response in patients in National Cancer Institute Trials. *Journal of Nuclear Medicine*, **46**(6), 1059–66.
24. Westerterp M, Pruim J, Oyen W, et al. (2006). Quantification of FDG PET studies using standardised uptake values in multi-centre trials: effects of image reconstruction, resolution and ROI definition parameters. *European Journal of Nuclear Medicine*, 2006.
25. Van Den Hoff J. (2005). Principles of quantitative positron emission tomography. *Amino Acids*, **29**(4), 341–53.
26. Gunn RN, Gunn SR, and Cunningham VJ. (2001). Positron emission tomography compartmental models. *Journal of Cerebral Blood Flow and Metabolism*, **21**(6), 635–52.
27. van der Weerdt AP, Klein LJ, Boellaard R, et al. (2001). Image-derived input functions for determination of MRGlu in cardiac (18)F-FDG PET scans. *Journal of Nuclear Medicine*, **42**(11), 1622–9.
28. Hunter GJ, Hamberg LM, Alpert NM, et al. (1996). Simplified measurement of deoxyglucose utilization rate. *Journal of Nuclear Medicine*, **37**(6), 950–5.
29. Lammertsma AA, and Hume SP. (1996). Simplified reference tissue model for PET receptor studies. *NeuroImage*, **4**(3 Pt 1), 153–8.

CHAPTER 10

Ultrasound

Claudio Baracchini

Introduction

During the last 30 years, the field of neuroimaging has advanced rapidly and has changed the clinician's approach to the diagnosis and treatment of several neurological disorders. In comparison with other imaging techniques, neurosonology offers excellent time resolution, a bedside approach, and non-invasiveness, which makes it a unique tool for the diagnosis and monitoring of many neurological conditions. Neurosonology can be considered an extension of the neurologic examination, since it sharpens the clinician's ears and eyes by expanding his/her ability to detect, localize, and quantify disease and evaluate haemodynamic responses, thus providing tools for a thorough assessment, even at the bedside.

This chapter deals with the state of the art and future perspectives of neurosonology. Current clinical and research applications of neurosonology include determination of intima–media thickness, endothelial testing, carotid wall imaging, atherosclerotic plaque assessment, plaque perfusion, stroke prevention and diagnosis, cerebral haemodynamics in ischaemic stroke, brain perfusion imaging, sonothrombolysis, detection of micro-embolic signals, detection of right-to-left shunt, cerebral autoregulation and functional testing, cerebral and cervical venous ultrasonography, brain parenchyma imaging, neuromuscular ultrasound, and tele-ultrasound. Neurosonology is not without limitations and the most frequent criticism is that it is operator-dependent. While it is true that neurosonology requires a sound knowledge of anatomy and physiology, it is no more operator-dependent than any other imaging technique. For this reason, it is desirable that neurologists make more intensive use of these non-invasive techniques, both in daily practice and clinical research.

Basic concepts of physical and technical principles [1,2]

Physical characteristics of ultrasound

All ultrasound devices use the same principle, the piezoelectric principle, to generate ultrasound waves and receive the reflected echoes—an applied voltage deforms the crystal elements (e.g. quartz) of a transducer and creates a pressure wave; the crystals are also deformed by the reflected pressure waves and this generates an electric current, which is translated by the machine into a pixel (picture element). An ultrasound image is generated by many pixels; the brightness of the returning echoes is related to their intensity or amplitude, such that strong returning echoes translate into a white (hyperechoic) pixel, while weak returning echoes translate into a grey/black (hypo/anechoic) pixel.

Pulses of ultrasound waves with frequencies ranging between 1 and 20 MHz are used in vascular and non-vascular diagnostics, depending on the target tissue. The reason for this higher range in frequency is that spatial resolution is limited by the wavelength, which is inversely related to frequency. High frequency waves (e.g. 5–13 MHz) generate high-resolution images, but they do not penetrate long distances due to increased scattering, therefore they are used for studying superficial structures (i.e. carotid arteries). Conversely, low frequency waves (e.g. 2–4 MHz) create lower-resolution pictures, but since they can propagate more into the tissue they are used for studying deeper structures (i.e. the circle of Willis). The rate at which pulses can be transmitted (the pulse repetition frequency (PRF)) is limited by the speed of ultrasound in the tissue, and the maximum depth of interest. Ultrasound propagates in human soft tissue at an average speed of 1540 m/s and is reflected back to the transducer by tissue structures located at various depths. The time it takes for an emitted ultrasound beam to be reflected back to its source is directly proportional to the distance of a particular structure from the transducer.

As ultrasound travels through a medium, there is a progressive attenuation (i.e. reduced energy) of the sound wave, through two mechanisms—absorption and scattering. Attenuation depends on several variables:

1. The different tissue densities of the body (low attenuation coefficient for blood, fluids, fat, etc.; high attenuation for bone, air).
2. The number of interfaces encountered.
3. The wavelength (short waves penetrate less than long waves).

Consequently, ultrasound is an ideal technique for imaging soft tissues, but cannot penetrate, and is distorted and rapidly attenuated by bone. Ultrasound can be reflected back to the transducer, refracted as it crosses a boundary between different media or different tissues, scattered when it encounters a small or irregular interface, or absorbed when the mechanical energy in the beam is converted into heat causing a temperature rise. Ultrasound devices differ in resolution, according to their ability to discriminate between two closely-spaced objects: axial resolution is the ability to differentiate two objects that lie in a plane parallel to the direction of the ultrasound beam and it is directly proportional to the spatial length of the pulse. Lateral resolution is the ability to differentiate two objects that lie in a plane perpendicular to the direction of the ultrasound waves and it is highest in the focal zone [i.e. the narrowest point between converging (near-field) and diverging (far-field) parts of the ultrasound beam].

Transducers

The transducers for B-scan imaging (see below) are array transducers and the beam is steered electronically. There are two types of arrays, linear and phased arrays; they both contain a large number of very small piezoelectric elements, which transmit and receive ultrasound. In linear arrays, each beam is generated using only a limited number of adjacent array elements at any one time. Linear array transducers produce rectangular- or parallelogram-shaped fields, where all the scan lines are parallel to each other. These are the transducers of choice for imaging the carotid and vertebral arteries. In phased arrays, each beam is generated using most or even all of the elements at the same time. Phased arrays produce sector-shaped fields, where the scan lines are not parallel to each other. These are the transducers of choice for intracranial imaging because of their small footprint, which allows them to be used with the limited acoustic windows available in the skull.

There are different imaging modalities used in diagnostic ultrasound; the main ones are discussed here.

A *B-mode or brightness-mode* image is essentially a cross-sectional image of the tissue in the scan plane. It is made up of many pixels with different shades of grey according to the amplitude or intensity of the returning echoes from a given structure. Most ultrasound devices display images with 256 shades of grey, allowing the detection of subtle differences within tissues or structures. The location of pixels is related to the depth of the tissue/structure reflector, and time-gain compensation (TGC) is applied in order to improve visualization of structures with increasing depths of insonation.

M-mode or Motion-mode shows the motion of a tissue in the transducer's image plane on the y-axis and time on the x-axis. A possible application of this technique is carotid wall motion studies.

Colour-coded Doppler flow imaging relies on the frequency shift of the returning echoes reflected from moving objects (i.e. erythrocytes). According to the Doppler principle, after the Austrian physicist Christian Doppler who first described the phenomenon in 1842, objects moving towards the transducer will increase the frequency of backscattered echoes relative to the emitted frequency. Conversely, objects moving away from the transducer will decrease the frequency of backscattered echoes relative to the emitted frequency. The Doppler frequency (Fd) is the difference between the transmitted frequency (Ft) and the received frequency (Fr) and is given by the following formula:

$$\mathrm{Fd} = \mathrm{Ft} - \mathrm{Fr} = 2\mathrm{Ft}\, v \cos\theta / c$$

where v is the velocity of the target, c is the speed of sound in tissue, and θ is the angle between the ultrasound beam and the direction of motion of the target. This frequency shift is represented by changes in colour or Doppler spectrum:

1. *Colour:* at least two colours (red and blue) are used to display the direction of flow relative to the transducer position (usually red flow is toward the probe, blue flow is away from the probe).
2. *Doppler:* positive peaks mean flow toward the probe, negative peaks mean flow away from the probe.

Therefore, colour Doppler flow imaging is used to identify moving blood, display the direction of flow, and measure flow velocity. In order to obtain velocity values close to the real speed of blood, angle correction is applied. Noteworthy, no Doppler frequency shift occurs at a 90° angle between the ultrasound beam and moving bloodstream, since the cosine of 90 is 0.

Power Doppler imaging shows direction-independent and intensity-dependent changes in the energy of signals backscattered by moving objects. Its main advantages are a better visualization of tortuous and deep-located vessels, and especially its high sensitivity for detecting slow blood flow.

Image artefacts

In order not to misinterpret ultrasound findings, it is important to recognize image artefacts. *B-mode imaging artefacts* include:

1. *Acoustic shadowing*: no image can be generated along the axis of an ultrasound beam behind a strong reflector (bone, calcification, etc.), hindering the visualization of a distal structure. Shadows can extend from the strong reflector to the edge of the screen and can originate from perpendicular insonation of vessel walls, plaque calcification, and transverse vertebral processes.

2. *Reverberation:* recurrent bright arcs at equidistant intervals are displayed along the axis of the ultrasound beam when echoes bounce many times between two highly reflective structures.

3. *Refraction*: it appears as an acoustic shadow and it occurs when an ultrasound beam obliquely crosses a boundary between tissues with different propagation speeds as at the edge of a blood vessel in a transverse scan.

4. *Mirror image:* a false image deeper than the real structure due to a reflection artefact, generated when obliquely scanning a strongly reflecting boundary, such as the pleura (false 'double' subclavian artery). The false image disappears by changing the planes of visualization.

5. *Posterior acoustic enhancement:* it is a bright area located deep to an anechoic structure and it occurs when ultrasound crosses an area of low signal attenuation (e.g. blood vessels).

Colour-coded Doppler flow imaging artefacts include:

1. *Aliasing:* it occurs when a moving object is not sampled sufficiently rapidly to be able to reconstruct its true movement. If a Doppler signal is to be correctly interpreted, then the rate at which it is sampled (i.e. the PRF) must be at least twice the maximum frequency component of the Doppler signal. Failure to respect this limit leads to aliasing, which can be recognized by the cut-off peaks of the Doppler spectra and their display on the lower half of the velocity scale with an apparent reversed flow. Aliasing can be present in a normal vessel if the pulse repetition frequency is inadequately too low to display flow velocity, but also with maximum scale settings in stenosed vessels due to elevated flow velocities.

2. *Bleeding* is the apparent presence of blood flow outside the vessel and is generated by an oblique strong reflector or by tissue motion adjacent to the vessel. By changing transducer position and colour gain setting, bleeding disappears.

Power-mode artefacts: flashing is the most common artefact of this technique; it is a motion artefact and, similarly to bleeding, displays artefactual flow signals outside the vessel lumen. This can be corrected by changing the gain settings and colour box size.

Ultrasound hazards

The amount of energy leaving the transducer is called acoustic power: this should be set as low as possible, in order to avoid adverse biological effects—thermal effects and non-thermal effects. Thermal effects are due to the conversion of ultrasound energy into heat energy and are related to the temporal average intensity of the ultrasound beam and the rate at which it is absorbed by the tissue. Non-thermal effects (e.g. cavitation and streaming) are related to the peak negative pressure of the ultrasound wave as it propagates through the tissue. The potential hazards of ultrasonic examinations can be evaluated by two indices—the thermal index (ThI) and the mechanical index (MI). The TI is an estimate of the rise in tissue temperature in °C under worse case conditions. There are three different thermal indices, the soft tissue index (ThIS), the bone index (ThIB), and the cranial index (ThIC). The MI indicates the probability of mechanical damage by non-thermal processes. When these indices have a value of 1 or more, the possibility of hazard should be considered. Therefore, operators should try to maintain as low a value of ThIC and MI as is compatible with obtaining a good signal, and should be cautious when using contrast agents as they significantly lower the threshold for cavitation.

The setting

For a neurovascular ultrasound assessment, the patient usually lies in a supine position, with the head flat on the bed, the neck extended and the head slightly rotated 10–20° away from the insonated side. The examiner sits behind the patient's head, while the arm holding the probe usually rests on the examination bed.

The standard protocol

For the extracranial examination, both longitudinal and axial scanning planes should be included. The transducer most frequently used is linear, with a wide frequency range (e.g. 5–10 MHz), offering high spatial resolution and undistorted images. When the contact surface is small (e.g. origin of the vertebral artery, subclavian artery, high carotid bifurcation), a sector probe with a lower frequency range (e.g. 4–8 MHz) is the best choice, even though it offers a lower spatial resolution.

Ultrasound of the carotid system

Carotid duplex ultrasonography plays an important role both in primary and secondary stroke prevention (Fig. 10.1) [3].

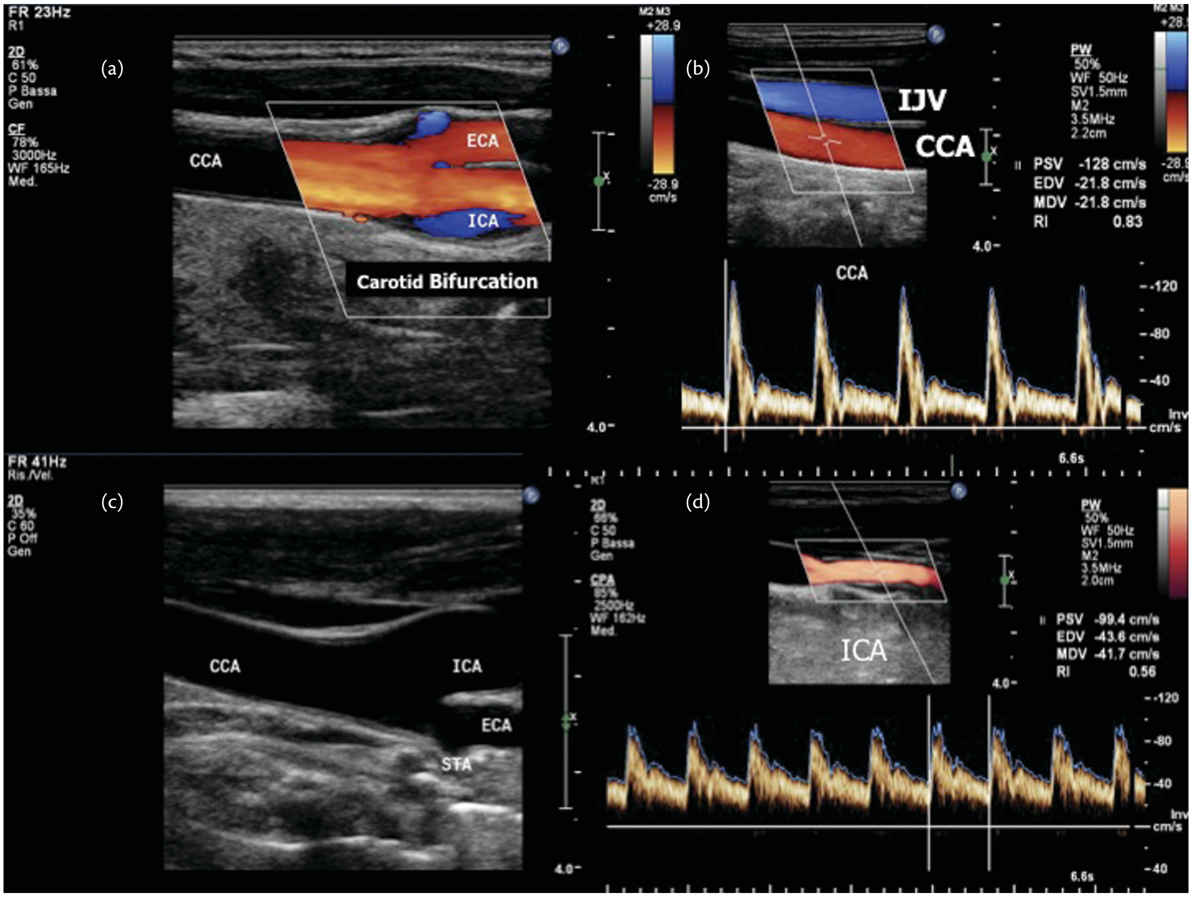
(a)
FR 23Hz
R1
2D
61%
C 50
P Bassa
Gen
CF
78%
3000Hz
WF 165Hz
Med.
CCA
ECA
ICA
Carotid Bifurcation
+28.9
-28.9 cm/s
4.0
(b)
IJV
CCA
PW
50%
WF 50Hz
SV1.5mm
M2
3.5MHz
2.2cm
PSV -128 cm/s
EDV -21.8 cm/s
MDV -21.8 cm/s
RI 0.83
CCA
-120
-80
-40
Inv cm/s
6.6s
(c)
FR 41Hz
2D
35%
C 60
P Off
Gen
CCA
ICA
ECA
STA
(d)
2D
66%
C 50
P Bassa
Gen
CPA
85%
2500Hz
WF 162Hz
Med.
PW
50%
WF 50Hz
SV1.5mm
M2
3.5MHz
2.0cm
PSV -99.4 cm/s
EDV -43.6 cm/s
MDV -41.7 cm/s
RI 0.56
ICA
-120
-80
-40
Inv cm/s
6.6s

Fig. 10.1 Normal findings in carotid ultrasound. (a) Colour-coded imaging of the carotid bifurcation. **(**b) Colour-coded and Doppler mode imaging of the common carotid artery; note the internal jugular vein with opposite direction on top. (c) B-mode imaging of the carotid bifurcation. (d) Power-mode and Doppler mode imaging of the internal carotid artery. CCA, common carotid artery; ICA, internal carotid artery; ECA, external carotid artery; STA, superior thyroid artery (a branch of ECA); IJV, internal jugular vein.

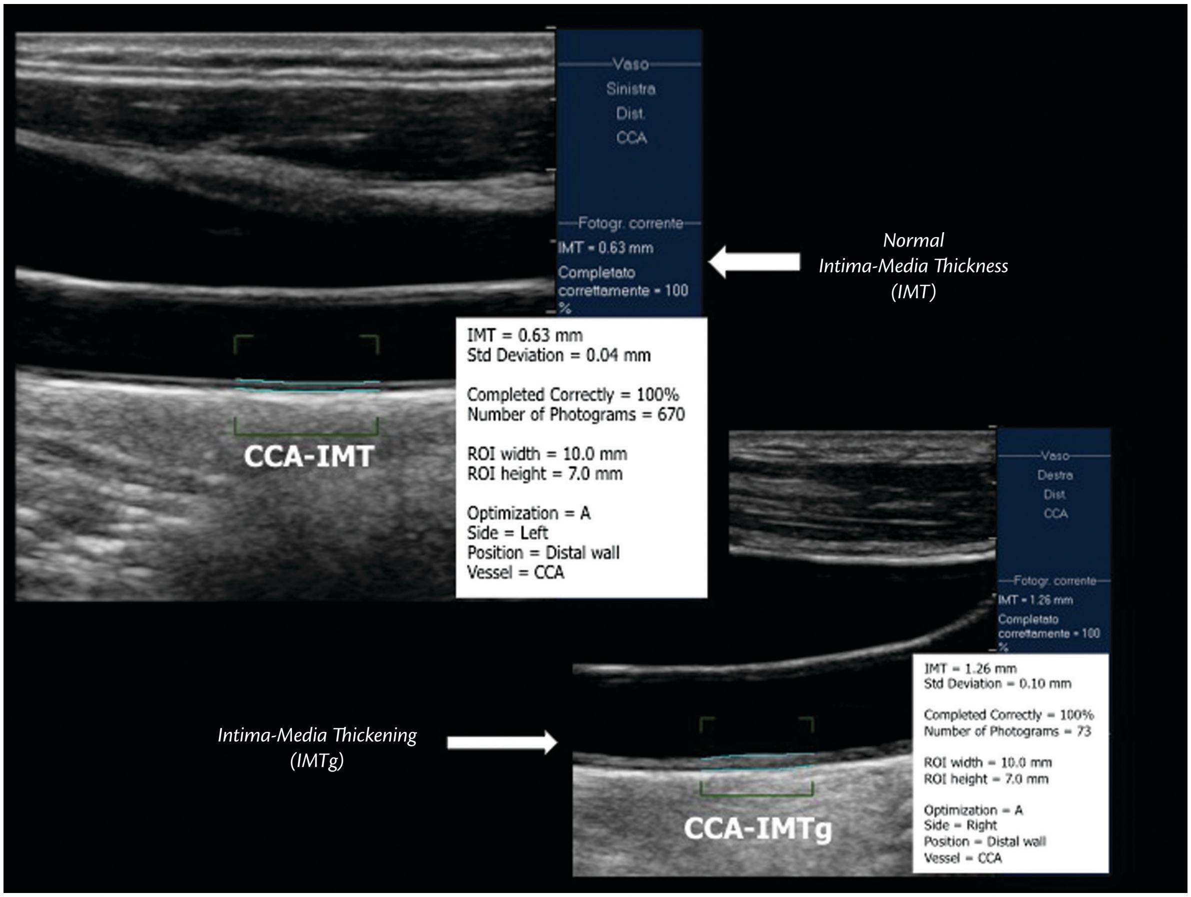
Vaso
Sinistra
Dist.
CCA
Fotogr. corrente
IMT = 0.63 mm
Completato correttamente = 100 %
Normal Intima-Media Thickness (IMT)
IMT = 0.63 mm
Std Deviation = 0.04 mm
Completed Correctly = 100%
Number of Photograms = 670
ROI width = 10.0 mm
ROI height = 7.0 mm
Optimization = A
Side = Left
Position = Distal wall
Vessel = CCA
CCA-IMT
Vaso
Destra
Dist.
CCA
Fotogr. corrente
IMT = 1.26 mm
Completato correttamente = 100 %
IMT = 1.26 mm
Std Deviation = 0.10 mm
Completed Correctly = 100%
Number of Photograms = 73
ROI width = 10.0 mm
ROI height = 7.0 mm
Optimization = A
Side = Right
Position = Distal wall
Vessel = CCA
Intima-Media Thickening (IMTg)
CCA-IMTg

Fig. 10.2 Carotid intima media thickness (IMT) measurement can be obtained very quickly thanks to a dedicated software. The operator selects a 1-cm segment of the common carotid artery, as far as possible from the carotid bifurcation and the computer after analysing the quality of the picture (100% in this case) measures the thickness of the intima media complex. Top left: normal IMT. Bottom right: intima media thickening (IMTg).

At present, the major focus is on the detection of the early stages of atherosclerosis, and the distinction between unstable and stable plaques.

Endothelial cells regulate the vascular tone by releasing vasoactive substances, such as nitrous oxide (NO), prostacyclin, endothelium-derived hyperpolarizing factor, adenosine. NO also influences atherogenesis, platelet aggregation, leukocyte adhesion, and inflammatory mechanisms. Of note is that endothelial function can be tested non-invasively by studying flow-mediated vasodilation (FMD) [4]. FMD is a response of the vessel to an increase in shear stress and the mediator of FMD is endothelial-derived NO. The FMD index is calculated by measuring the diameter of the brachial artery at rest and after a 5-minute induced ischaemia of the forearm. A reduced FMD index is a marker of endothelial dysfunction, which represents one of the early stages of atherosclerosis and is associated with an increased risk of coronary artery disease, an increased risk of transient ischaemic attack (TIA), or stroke in patients without coronary artery disease.

Carotid intima-media thickness (IMT) measurement is also part of the study of the early stages of atherosclerosis and can be obtained very quickly by ultrasound thanks to dedicated softwares [5]. Intima media thickening is the first observable morphological sign of vascular alteration, a marker of atherosclerosis, and its progression, an independent predictor of ischaemic cardiovascular events, and a reliable predictor for hypertensive organ damage in hypertensive patients (Fig. 10.2).

Carotid artery distensibility (CAD) [6] a measure of carotid artery elasticity, is the ability of the carotid to expand and contract with each cardiac pulsation and relaxation. CAD can be reliably and non-invasively assessed by high-resolution M-mode ultrasound. A decreased CAD is an expression of increased carotid wall stiffness, representing a functional change of the vessel wall, which precedes morphological abnormalities. For this reason, an impaired CAD is considered a surrogate marker for atherosclerosis, and a novel risk factor for cardiovascular disease.

Endothelial function testing, IMT measurement, and the study of carotid wall dynamics are likely to be used in the near future to monitor the efficacy of treatments on the early stages of atherosclerosis development.

A carotid plaque (Fig. 10.3a,b) is defined as a focal structure encroaching into the arterial lumen by at least 0.5 mm or 50% of the surrounding IMT value, or with a thickness of at least 1.5 mm as measured from the media-adventitia interface to the intima-lumen interface [5].

For carotid stenosis grading, the criterion of flow velocity in the stenosis has only a limited value, being influenced by multiple other factors besides narrowing of the artery. On the other hand, angiography does not reliably measure the area reduction responsible for the haemodynamic effect of a stenosis. Therefore, the correlation between velocity and the degree of stenosis as measured by angiography is suboptimal and additional criteria

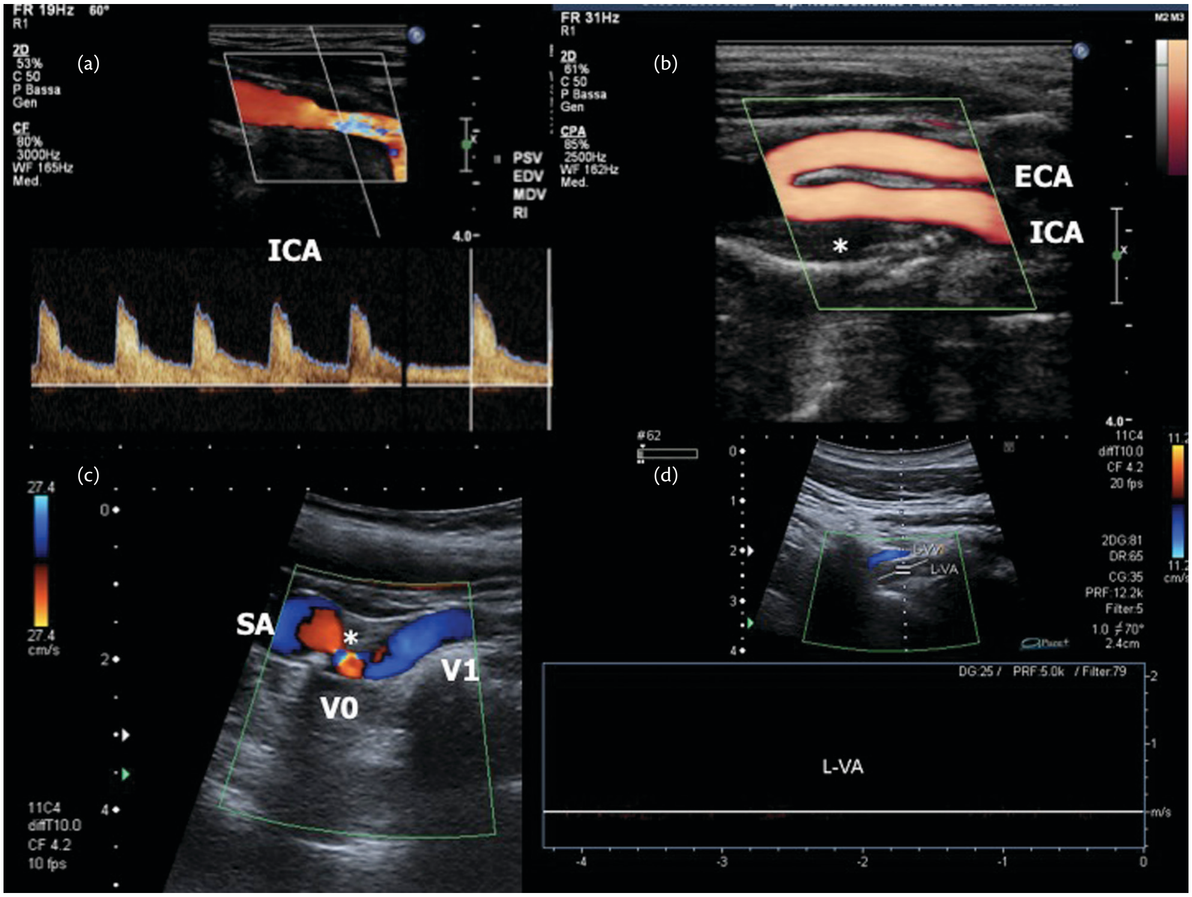

Fig. 10.3 Carotid and vertebral atherosclerotic disease. (a) Haemodynamically significant internal carotid artery stenosis: see the turbulence in the colour image and the relevant increase of velocity in the Doppler mode. (b) Power flow imaging of an internal carotid artery (ICA) plaque (*): the power mode delineates very well the surface of the plaque. (c) Stenosis at the origin of the vertebral artery: note the turbulence (*). (d) Occlusion of the vertebral artery: no flow in the vertebral artery; note the preserved flow with opposite direction in the vertebral vein. ICA, internal carotid artery; ECA, external carotid artery; SA, subclavian artery; V0, origin of the vertebral artery; V1, extraforaminal segment of the vertebral artery; L-VA, left vertebral artery; L-VV, left vertebral vein.

are mandatory. In a recent international consensus, a multiparametric approach has been proposed for the measurement of the degree of internal carotid stenosis aiming at reducing possible errors [7]. The advantage of Doppler ultrasound is to accurately describe the haemodynamic consequences of vessel narrowing, yielding important additional information in combination with other imaging modalities.

Due to the improvement of medical management in patients with high-grade asymptomatic carotid stenosis (ACS), there is uncertainty about how to best manage these patients. Recent studies demonstrate that a well-treated patient with ACS has an annual ipsilateral stroke risk of only 0.3%. Therefore, 80 patients with an ACS need be treated with a CEA to prevent one disabling stroke. Consequently, the cost-effectiveness of CEA in patients with ACS has been questioned. Nevertheless, ACS accounts for a large burden of stroke and the majority of ipsilateral strokes are unheralded. Identification of a group of ACS patients at higher risk of stroke would improve both risk- and cost-benefit ratios of surgery/endovascular procedures. Different methods have been suggested in order to identify such a high-risk group: contrast-enhanced carotid ultrasonography (CCU), and ultrasonic detection of asymptomatic embolization.

CCU is able to provide an enhanced visualization of the arterial lumen and plaque morphology. It results in:

1. Better intima-media thickness visualization.
2. Better plaque surface definition (irregularities, ulcers), especially in cases of large acoustic shadow calcified plaques.
3. More sensitive identification of plaque rupture and plaque ulcerations.
4. Improved sensibility in detecting carotid pseudo-occlusion. CCU also allows to directly visualize adventitial vasa-vasorum and carotid plaque neovascularization [8].

Plaque inflammation, adventitial vasa-vasorum, intimal angiogenesis, and plaque neovascularization have been identified in histological studies as indicators of the instability of the atheroma of carotid arteries in cerebrovascular patients [9]. Large CCU studies are now needed to clarify the prognostic value of detecting plaque vascularization in asymptomatic patients with non-severe carotid stenosis. In the future, the identification of plaque angiogenesis could be used to evaluate the effects of therapies aimed at stabilizing the plaque and hindering its growth.

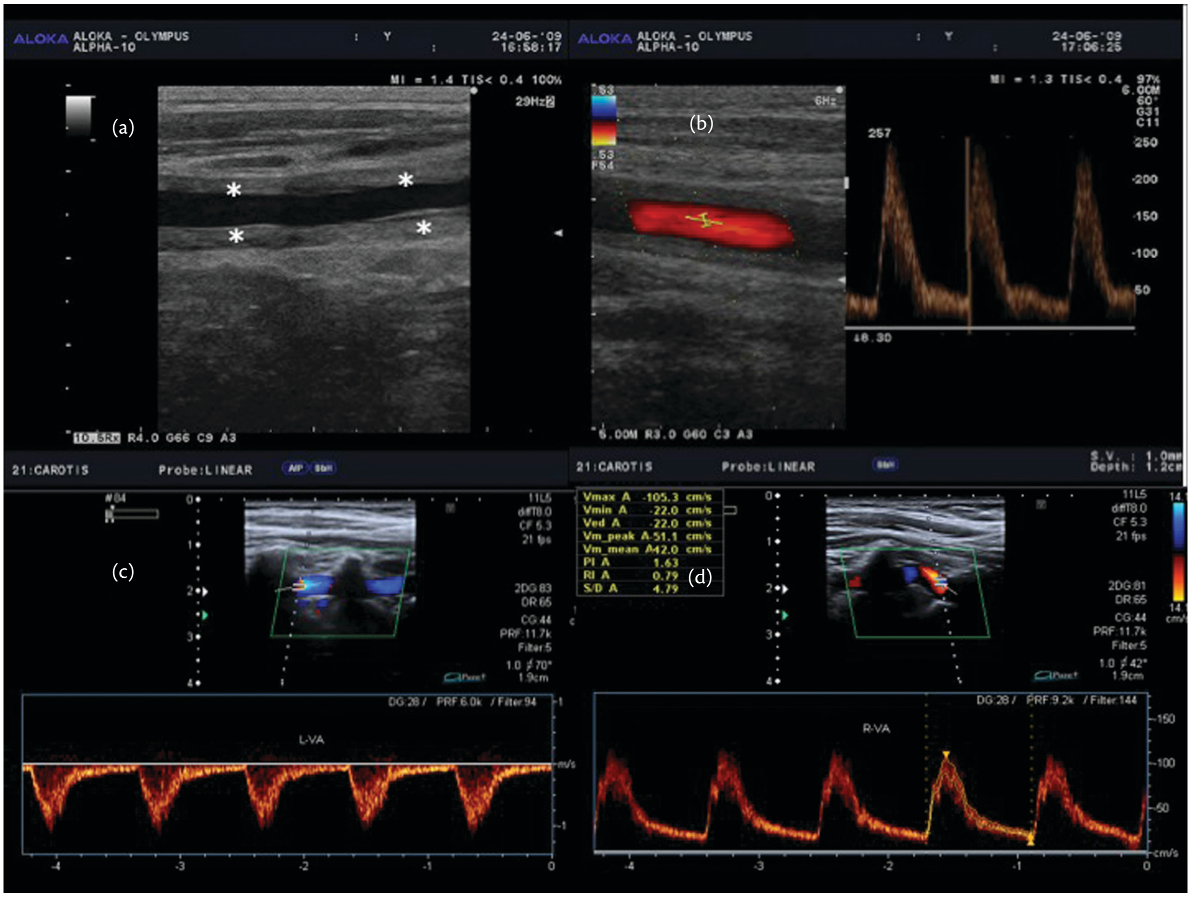

Fig. 10.4 Non-atherosclerotic disease: Takayasu arteritis with subclavian steal. (a) Concentric homogeneous swelling of the common carotid artery wall, which is seen as a mid-echoic thickening (*) often associated with stenosis or occlusion of the vessel. (b) Stenosis of the common carotid artery with significant increase of blood flow velocity. (c) Retrograde flow in the left vertebral artery indicating a subclavian steal, a frequent finding in Takayasu arteritis. (d) Compensatory flow in the right vertebral artery.

Another method to identify a high-risk group in patients with ACS is ultrasonic detection of asymptomatic embolization. Recently, a large prospective and multi-centre study (ACES, Asymptomatic Carotid Emboli Study) [10] evaluated the relationship between asymptomatic emboli and stroke risk in 467 patients with an ACS of at least 70%. The detection of emboli was associated with an increased risk for ipsilateral TIA and stroke (HR: 2.54, 95% CI: 1.2–5.36), and in particular for ipsilateral stroke (HR: 5.57, 95% CI: 1.61–19.32) during 2 years of follow-up, even after adjusting for antiplatelet therapy, degree of stenosis, and other risk factors. The absolute annual risk of ipsilateral stroke or TIA between baseline and 2 years was 7.13% in patients with embolic signals, and 3.04% in those without, and for ipsilateral stroke was 3.62% in patients with embolic signals and 0.70% in those without. The authors performed a meta-analysis of all available studies including 1144 patients. The hazard ratio for the risk of ipsilateral stroke for those with embolic signals compared with those without was 6.63 (95% CI: 2.85–15.44) with no heterogeneity between studies ($p = 0.33$).

Non-atherosclerotic disease includes vasculitis and dissection. Ultrasound can display the inflamed vessel wall in patients with large vessel vasculitides. In temporal arteritis, the wall swelling of the common superficial temporal artery is hypoechoic (halo sign in a transverse scan) [11], while in Takayasu arteritis there is a concentric homogeneous iso-echoic thickening of the common carotid artery wall (macaroni sign in a longitudinal scan) with a significant increase of blood flow velocity (Fig. 10.4a, b) [12]. Moreover, ultrasound can easily show a stenosis or a complete occlusion caused by vasculitides, as well as the effect of therapy on these vessels (i.e. reduction of the swelling and recanalization).

Spontaneous cervical vessel dissection (CAD) is caused by a haematoma in the arterial wall [13]. The typical ultrasound finding of CAD is wall thickening of low echogenicity, caused by the intramural haematoma with adjacent thrombotic material leading to a distal tapering stenosis. Other direct ultrasonographic signs of CAD (intimal flap, double lumen, pseudoaneurysm) are found infrequently, while indirect signs suggestive of CAD (high cervical stenosis, distal occlusion, increased pulsatility upstream, or decreased pulsatility downstream) are more common. However, ultrasound may show a normal picture (in case of subadventitial dissection, low-grade stenosis, mild mural haematoma, or inaccessible vessel segments) [14]. CAD diagnosis should be confirmed by MRI because of its exquisite sensitivity in detecting intramural haematoma [15]. Furthermore, in the case of a common carotid artery dissection, a chest CT scan is mandatory to exclude an aortic dissection extending to the cerebroafferent vessels (Fig. 10.5a, b).

Despite its diagnostic limitations, ultrasound is an excellent method for monitoring recanalization and recurrence, and it might help to establish whether or not to continue antithrombotic therapy (anticoagulation or antiplatelet treatment) [14,16].

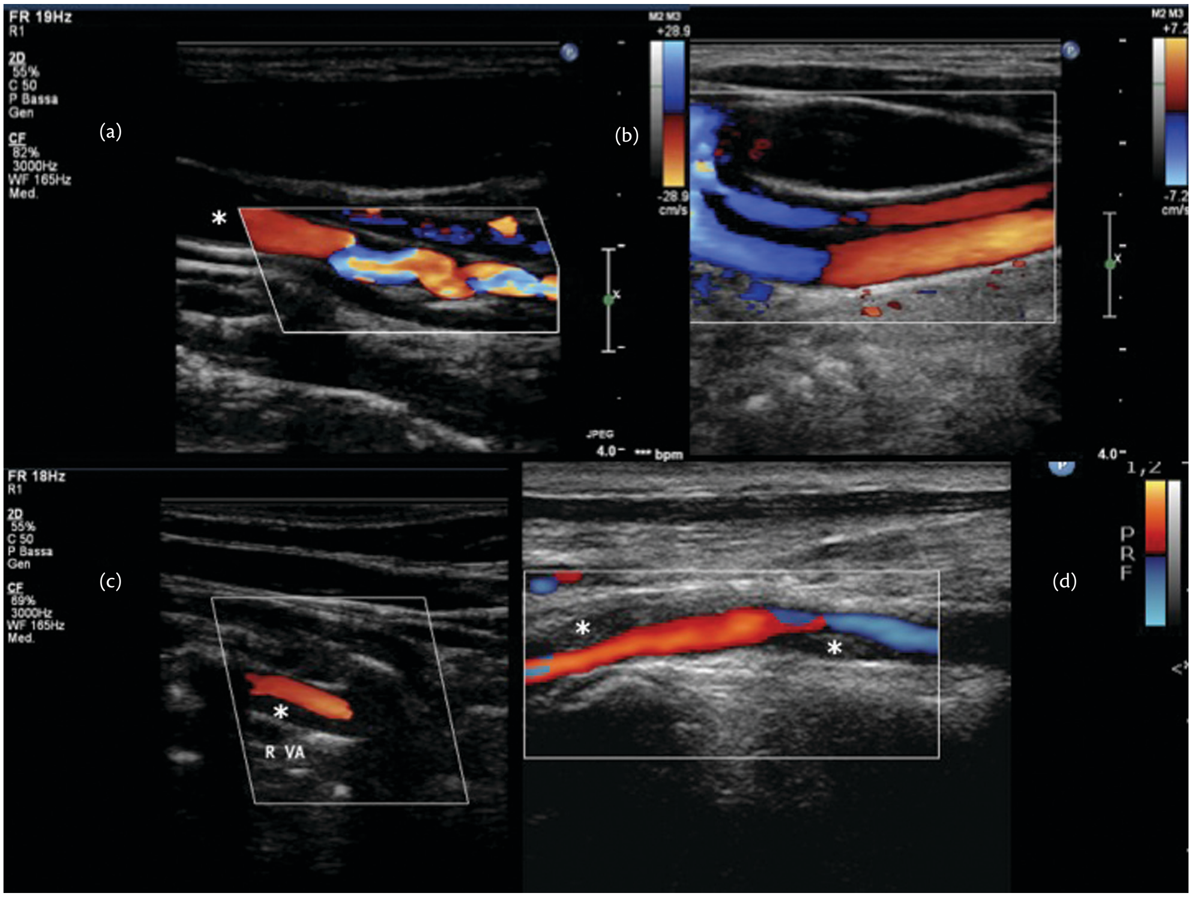

Fig. 10.5 Non-atherosclerotic disease: cervical dissection. (a) Internal carotid artery dissection; note that the stenosis is distal from the origin (*) of the vessel; the lumen is irregular and the flow is turbulent. (b) Common carotid artery dissection: subintimal dissection with a true double lumen (very rare, but pathognomonic finding). (c) Vertebral artery dissection of the V2 segment: hypoechogenic thickening of the vessel wall (*) indicating the intramural haematoma. (d) Vertebral artery dissection of the V1 segment: hypoechogenic thickening of the vessel wall (*) indicating the intramural haematoma.

Ultrasound of the vertebral system

Ultrasound imaging of vertebral stenosis is technically more complex compared with carotid stenosis, because the vertebral artery is smaller than the internal carotid artery, it arises at right angles to its feeding vessel and it is frequently asymmetrical (Fig. 10.6).

This has made clinicians reluctant to investigate for vertebral disease (Fig. 10.3c, d) and has hampered progress in managing vertebral artery stenosis.

Approximately one-quarter of ischaemic strokes involve the posterior circulation and a stenosis of the vertebral artery can account for up to 20% of these strokes [17]. Stenotic lesions, particularly at the origin of the vertebral artery, are not uncommon. In an angiographic study of 4748 patients with ischaemic stroke, some degree of proximal extracranial vertebral artery stenosis was seen in 18% of the cases on the right and 22% on the left. This was the second most common site of stenosis after internal carotid artery stenosis at the carotid bifurcation [18].

Unlike in carotid artery disease, direct morphological assessment (diameter, area) is generally not applicable, except at the origin, where plaque assessment is possible. Therefore, haemodynamic criteria (direct or indirect) are applied. Direct haemodynamic criteria include aliasing, focal velocity increase, and spectral broadening. Indirect haemodynamic criteria, observed only in haemodynamically relevant stenoses (>80%), include pre-stenotic flow signs (decreased diastolic flow, increased peripheral resistance) and post-stenotic flow signs (delayed systolic flow rise, decreased systolic velocity with a dampened waveform). In addition, a compensatory flow in the contralateral vertebral artery is frequently seen along with cervical collaterals coming from the external carotid artery. With regards to the focal velocity increase, there is no international consensus, but rather a variety of criteria which underline the hard task of grading vertebral stenosis [19–22].

To summarize, the problems with ultrasound imaging of the vertebral artery are:

1. The origin of the vertebral artery cannot be visualized when it originates directly from the aortic arch or from the posterior/inferior subclavian artery wall.
2. The full length of the vertebral artery cannot be visualized all times (tortuous course).
3. Sometimes it is not possible to show directly the site of the stenosis.
4. Indirect haemodynamic signs are present only in more severe stenosis [23–25].

It is difficult to differentiate between a dissection and an atherosclerotic stenosis, because of smaller vessel diameter and tortuous vessel

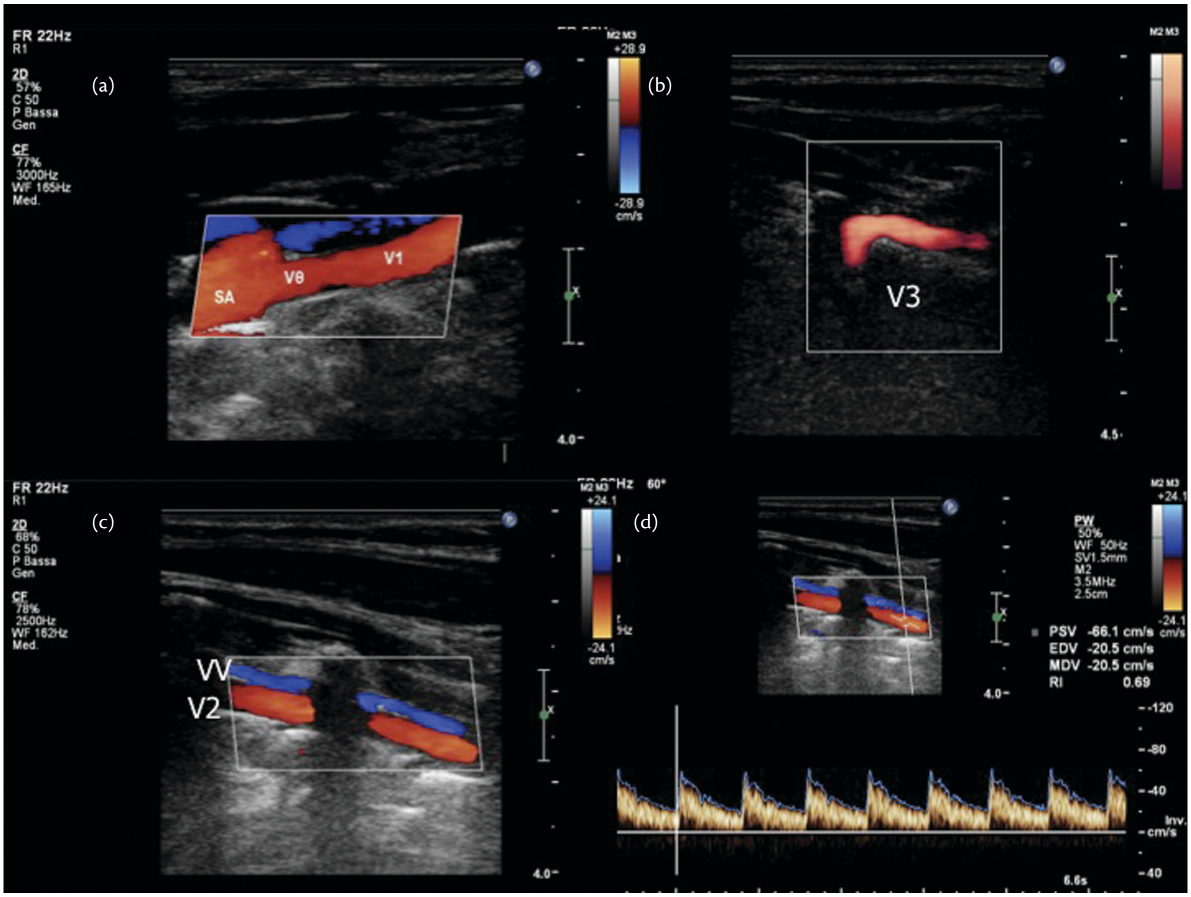

Fig. 10.6 Normal findings in vertebral ultrasound. (a) Colour-coded imaging of the vertebral artery originating from the subclavian artery. (b) Power-mode imaging of the tortuous segment, (V3) running from C2 to the foramen magnum. (c) Colour-coded imaging of the intraforaminal segment (V2) of the vertebral artery (in red) and the vertebral vein on top with opposite flow direction (in blue). (d) Colour-coded and Doppler mode imaging of the vertebral artery. SA, subclavian artery; V0, origin of the vertebral artery; V1, extraforaminal segment of the vertebral artery; V2, intraforaminal segment of the vertebral artery; V3, tortuous segment, from C2 to the foramen magnum; VV, vertebral vein.

course (sensitivity = 75–92%), unless a typical sign of dissection is evident—irregular stenosis, thickened hypo- or iso-echogenic vessel wall, indicating the presence of an intramural haematoma, a double lumen [24–26].

The vertebral artery might also present significant abnormalities of its haemodynamics secondary to subclavian artery disease. Depending on the degree of the stenosis, the subclavian artery can determine a complete or incomplete steal of blood from the vertebral artery. An incomplete steal is characterized by a systolic deceleration or slowing, at an initial stage, followed by an alternating flow (i.e. during systole the blood flows toward the arm, while during diastole it flows toward the brain). When the steal becomes complete, a retrograde flow is observed during the entire cardiac cycle, while telediastolic velocity is significantly reduced to almost zero. In addition, a contralateral vertebral compensatory flow is observed (Fig. 10.4c, d) [27].

Transcranial insonation

Transcranial colour-coded Doppler sonography (TCCS) enables the visualization of basal cerebral arteries, veins, and parenchyma through the intact skull. TCCS is called the 'doctor's stethoscope for the brain', since it provides not only imaging, but also accurate real-time information on cerebral haemodynamics and immediate bed-side results. It is also the ideal modality for monitoring disease progression and therapeutic effects [28].

Transcranial insonation can only be performed in regions of the skull called bone windows, where the bone is naturally thin, otherwise most of the energy of the ultrasound beam is reflected or absorbed. Skull acoustic reflection and absorption accounts for 94% of the energy loss in children and for 98% in white middle-aged women. The most important bone windows are the transtemporal and the transforaminal (suboccipital); while their patency depends on:.

1. Bone thickness (thick worse than thin).
2. Age of patients (old worse than young).
3. Gender of patients (female worse than male).
4. Brain atrophy (atrophy worse).

In case of a bad window or in difficult anatomical conditions, in order to increase the quality of a colour-mode image, one should reduce the depth of insonation, the size of the colour box and the PRF. A TCCS examination is technically not feasible in about 10–20% of patients, but the inability to image intracranial vessels in these cases can be overcome by the application of echo contrast

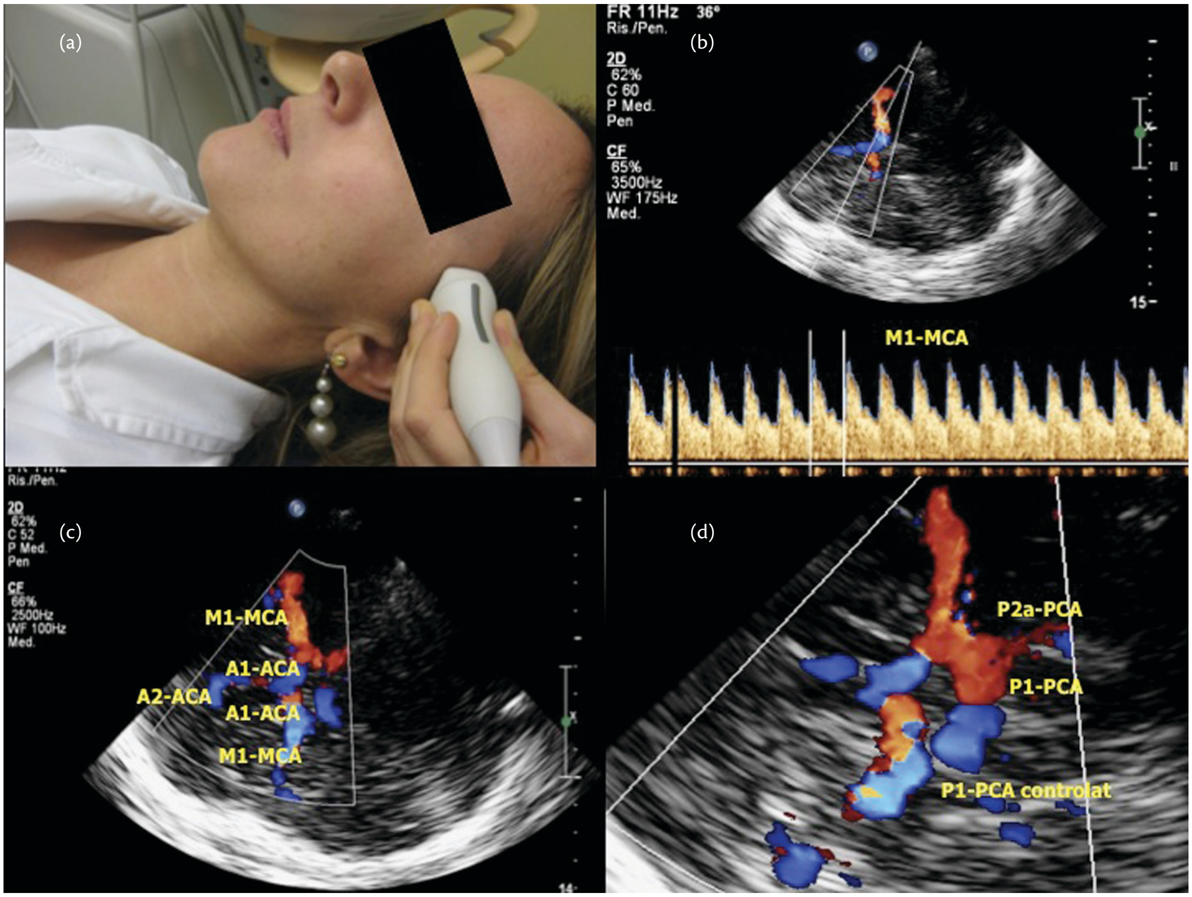

Fig. 10.7 Transtemporal approach. (a) The probe is placed on the temporal window which allows the investigation of the anterior, middle, and posterior cerebral arteries. (b) Colour-coded and Doppler mode imaging of the middle cerebral artery. (c) Colour-coded imaging of the anterior circulation (anterior and middle cerebral arteries). (d) Colour-coded imaging of the posterior circulation (posterior cerebral arteries). MCA, middle cerebral artery; ACA, anterior cerebral artery; PCA, posterior cerebral artery.

agents. Ultrasound contrast agents consist of stabilized microbubbles that improve the signal-to-noise ratio. Currently, available contrast agents are the galactose and palmitinic acid-based Levovist (Schering AG, Berlin, Germany) and the perfluorocarbon-based Sonovue (Bracco International B.V., Amsterdam, Netherlands). With these agents, visualization of intracranial vessels is improved and detection rates of basal cerebral arteries reach 90% even in the elderly population [29].

A MI up to 1.5 is acceptable for all approaches, apart from the transorbital one, which enables visualization of the ophthalmic artery and the carotid siphon, the acoustic power should be reduced to 10–15%, the MI values should be ≤0.26 and the duration of the insonation should be kept to a minimum in order to prevent any damage to the eye lens.

For the transtemporal approach (Fig. 10.7), the transducer is positioned in front of the external acoustic meatus just above the zygomatic arch. There are five main axial planes (midbrain, thalamic, ventricular, upper pontine, and lower pontine) and, by turning the probe 90° upwards, two main coronal planes (anterior, posterior). Within these planes, different structures, such as bone, parenchyma, or cerebrospinal fluid (CSF) can be assessed using conventional B-mode imaging, and they can serve as landmarks for intracranial orientation and insonation of main vessels. The midbrain plane is the most important axial plane as most vessel segments can be identified using this approach: the middle cerebral artery (MCA), the anterior cerebral artery (ACA) and the posterior cerebral artery (PCA) originating just in front of the midbrain that appears as a butterfly-shaped hypoechogenic structure surrounded by the hyperechogenic basal cisterns. The anterior coronal plane allows a complete analysis of the intracranial internal carotid artery (IntCA) to be performed. It also allows improvement in the ability to distinguish between the terminal IntCA, and the origin of the MCA and that of the ACA. The posterior coronal plane is used to study the distal segment of the basilar artery (BA) and to distinguish the proximal PCA from the superior cerebellar artery (SCA).

For the transforaminal approach (Fig. 10.8), the transducer is placed between the occipital bone and the atlas, and the anatomical landmarks are the hypoechogenic foramen magnum and the hyperechogenic clivus. There are two main planes:

1. *A lower axial plane:* the probe is pointed towards the root of the nose and it allows the study of the intracranial segment V4 of the vertebral artery and the proximal segment of the BA.
2. *An upper axial plane:* the probe is pointed at the forehead, which allows the study of the distal V4, and the proximal, the middle, and rarely the distal segments of the BA [30,31].

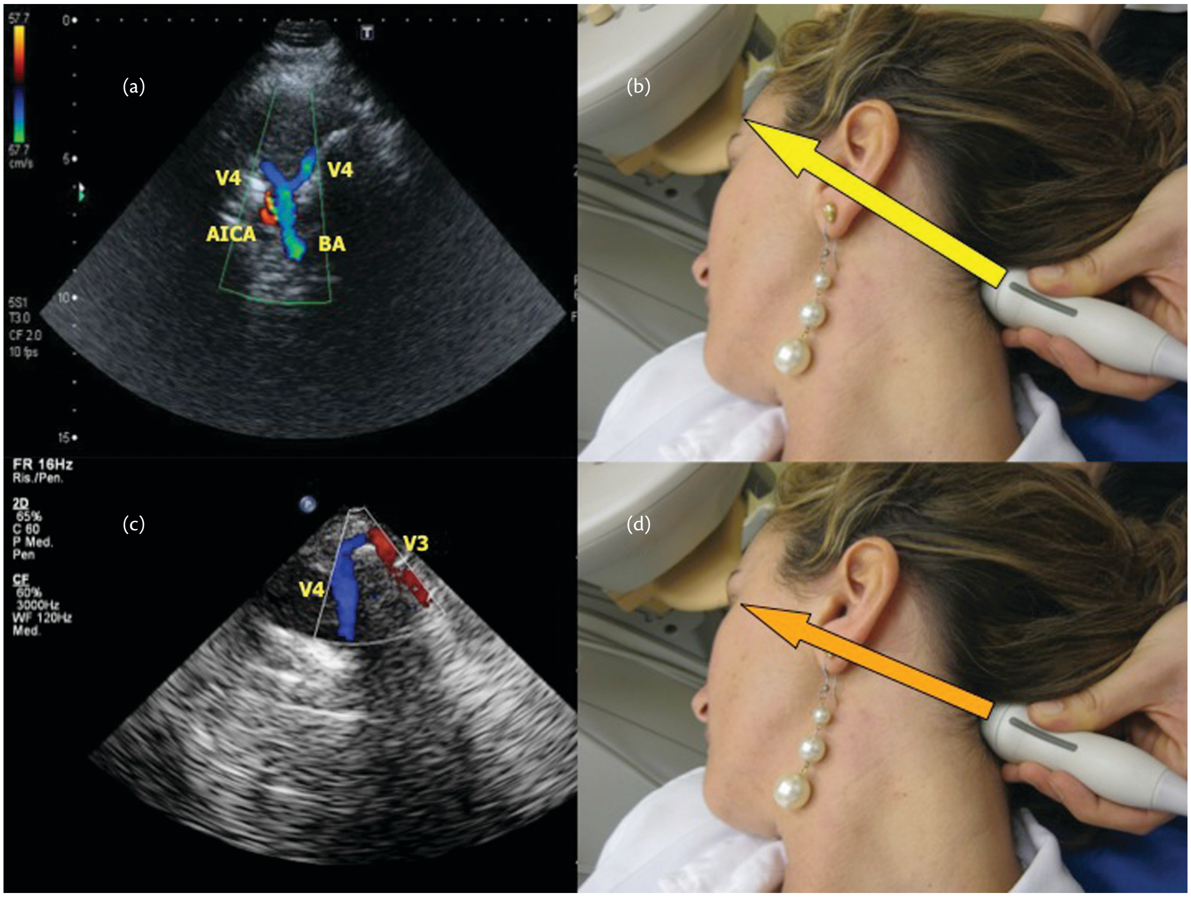

Fig. 10.8 Transforaminal approach. The probe is placed on the foraminal window, which allows the investigation of the intracranial (V4) vertebral arteries and basilar artery (BA). (a,b) The probe is aimed at the forehead (upper plane) in order to assess the confluence of V4 and origin of the BA with its braches (c,d) The probe is aimed at the root of the nose (lower plane) in order to assess the proximal part of V4 and its branches.

Ultrasound of intracranial arteries

The arteries of the circle of Willis can be identified by their anatomic location with respect to brainstem structures and by the determination of the direction of flow. Noteworthy is that a complete circle of Willis is found only in about 20% of the population, since hypoplasia or aplasia of one or more vascular segments is often present [32]. The maximum achievable flow velocity without angle-correction should be documented, except when a straight vessel segment of at least 1.5–2.0 cm can be visualized. Normal values of flow velocities, sensitivity, and specificity of TCCS in intracranial stenosis and occlusion are available for all major intracranial arteries [33]. Ultrasonographic diagnosis of a stenosis of a cerebral artery can be made on the basis of an aliasing phenomenon (usually visible in a short segment of the vessel), increased flow velocities in the area of the stenosis, and flow disturbances upstream and downstream from the lesion (Fig. 10.9).

Criteria for the diagnosis of an intracranial artery occlusion include the lack of a detectable colour-coded signal and Doppler waveform at depths of insonation corresponding to that given artery, a sufficient visibility of the neighbouring vessels, and the detection of a collateral flow.

The most established applications of transcranial ultrasound with a direct impact on clinical decision-making include:

1. *Studying the effects of a cervical arterial occlusive disease on cerebral haemodynamics:* decreased peak systolic flow velocity, delayed systolic upstroke, and the presence of collateral pathways (anterior communicating artery, posterior communicating arteries, ophthalmic artery, and leptomeningeal arteries) [34].
2. *Testing vasomotor reactivity*, i.e. the compensatory potential of the brain blood flow regulating vessels, in asymptomatic or pre-surgical symptomatic carotid stenosis: these tests assess the haemodynamic severity of carotid disease [35].
3. Assessing time course and reversibility of cerebral vasospasm after subarachnoid haemorrhage [36,37].
4. Monitoring natural history and response to treatment (drugs, angioplasty, stenting) of intracranial atherosclerotic occlusive disease.
5. Ascertaining stroke pathogenesis with TCCS in acute stroke, by identifying and locating arterial occlusion, assessing collateral circulation, selecting patients for intervention, monitoring recanalization, and identifying re-occlusion [38].
6. Detecting microemboli associated with cardioembolic disease, aortic plaques, carotid occlusive disease (Fig. 10.10a), carotid endarterectomy/stenting, and monitoring the response to anti-platelet therapy [39–42].

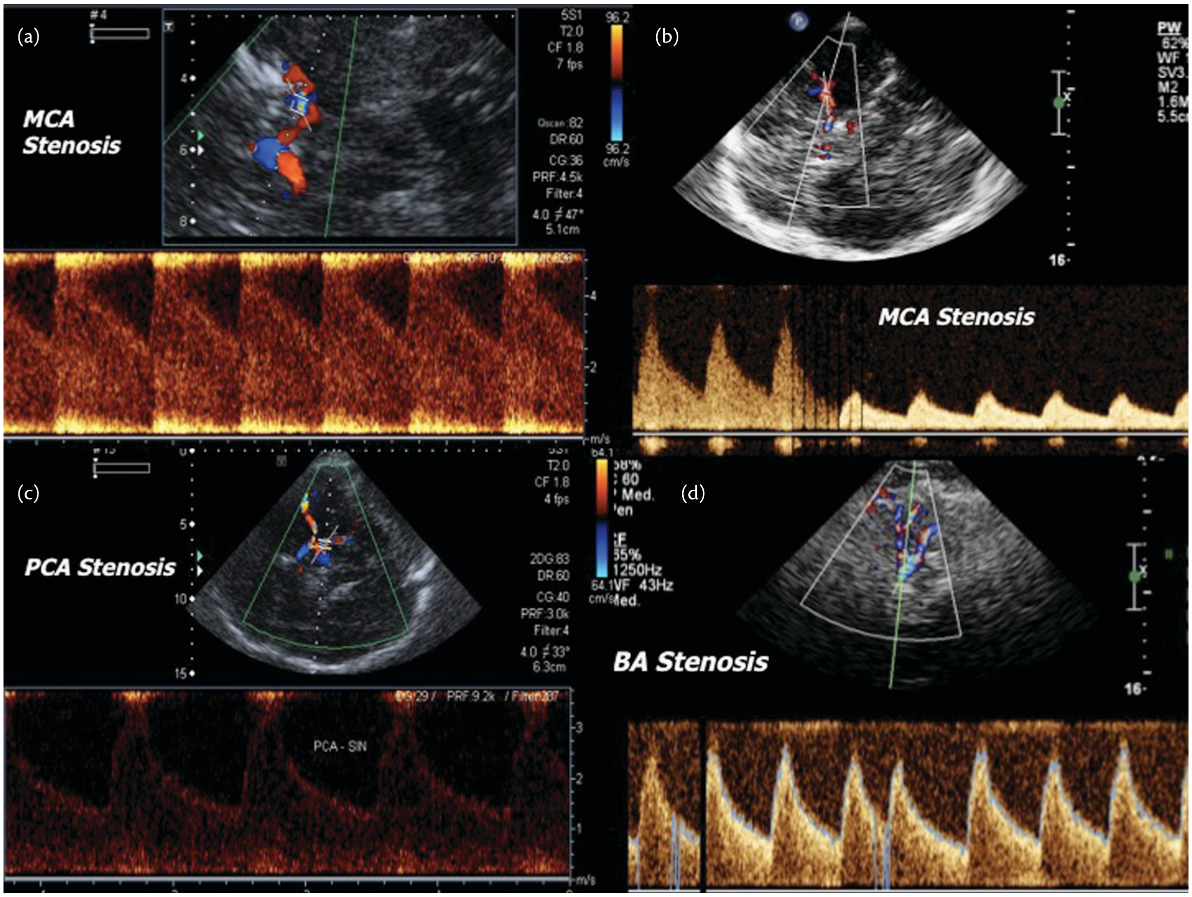

Fig. 10.9 Stenoses of the major intracranial arteries. (a) Middle cerebral artery (M1-MCA stenosis)—note the turbulent flow in the colour mode and the significant velocity increase in the Doppler mode (>4 m/s). (b) Middle cerebral artery (M1-MCA) severe stenosis—note the significant velocity increase in the Doppler mode (first three waves) and subsequent post-stenotic delayed systolic flow rise and velocity drop (indirect signs of a very tight stenosis). (c) Posterior cerebral artery (PCA) stenosis: significant velocity increase in the Doppler mode (>3 m/s). (d) Basilar artery (BA) stenosis: significant velocity increase in the Doppler mode (2.5 m/s)

7. Screening with a ‘bubble test’ for possible paradoxical cerebral embolism via a cardiac or pulmonary right-to-left shunt (RLS) in patients with cryptogenic stroke (Fig. 10.10b) [43].
8. Selecting children with sickle cell disease for blood transfusion as an effective tool in primary stroke prevention [44–48].

There are many exciting areas where the use of TCCS is likely to expand, such as cerebral perfusion imaging, sonothrombolysis, and ultrasound-targeted drug delivery to the brain. Ultrasound perfusion imaging represents the analysis of microbubble distribution in the brain parenchyma. It requires a lung-penetrating echo-contrast agent and a contrast-specific imaging modality (pulse-inversion harmonic imaging). The objective of this approach is to visualize areas of perfusion deficits in patients with acute ischaemic stroke and to predict outcome prognosis. However, there are some drawbacks:

1. Insonation artefacts, which occur in most of the patients.
2. Inability to scan the whole brain.
3. Potential side effects of the new contrast agents, which restrict the employment of these substances in severe cardiac or pulmonary disease.

Ultrasound perfusion imaging has commonly been performed by using triggered high MI scanning, so called ‘bolus kinetics’ [49]. Recently, highly sensitive, low MI imaging has been introduced and, with this new technology real-time bolus kinetics as well as refill kinetics, can be analysed without triggering [50]. Coded contrast harmonics (CCH) is a promising new pulse compression method, which improves contrast stability and image quality of low MI transcranial ultrasound perfusion studies. Microvascular imaging (MVI) is a novel processing method, which tracks the passage of microbubbles through very small vessels. The use of CCH and MVI may further increase the success rate of low MI ultrasound perfusion imaging studies in acute stroke.

There is a growing interest in the therapeutic application of ultrasound, particularly in the field of sonothrombolysis. A recent meta-analysis of all published clinical sonothrombolysis studies indicates that ultrasound and microbubbles may be effective in clot lysis of ischaemic stroke, even without additional thrombolytic drugs [51]. Ultrasound and tPA (with or without microbubbles) increase recanalization compared with tPA alone; in particular, sonothrombolysis may double the likelihood of tPA-induced recanalization, without increasing the risk of symptomatic cerebral haemorrhages. However, additional research is required for the

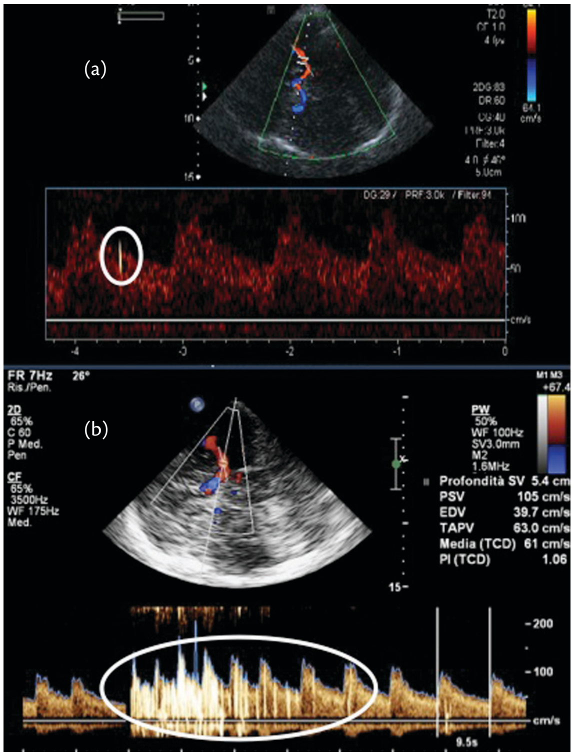

Fig. 10.10 Emboli detection. (a) Spontaneous microembolic signal (MES) in a patient with a recently symptomatic severe carotid stenosis—note the hyperintense transient signal within the flow wave of the ipsilateral middle cerebral artery. (b) Multiple MES in a patient with a patent foramen ovale. Many hyperintense transient signals some of which are tightly packed and difficult to count (shower effect).

identification and standardization of optimal ultrasound parameters. A significant evolution in this area will be to prove the efficacy of sonothrombolysis in a large number of patients worldwide, and the possibility of performing sonothrombolysis with a hands-free, operator-independent portable device.

Another exciting area of future research is the opening of the blood–brain barrier by ultrasound: this could allow targeted-delivery of drugs, monoclonal antibodies, and genes [52].

Ultrasound of cervical and intracranial veins

Venous ultrasonography has been ignored for a long time for several reasons:

1. A more complex anatomy and physiology of the venous circulation than the arterial system.
2. A number of methodological limitations especially for the study of intracranial veins and sinuses.
3. A relatively lower incidence of primary venous diseases.

However, in the last decade, several technical improvements have been achieved with ultrasound systems—an increased resolution of brain structures, which resulted in a better visualization of anatomical landmarks, and an increased sensitivity for slow velocities, which made venous flow detection easier.

This examination should be performed with a high resolution colour-coded duplex sonography scanner using a high frequency (5–10 MHz) linear probe for the cervical veins and a low frequency (1–3 MHz) phased-array probe for the intracranial veins.

For the extracranial examination (Fig. 10.11) [53], the system setting is adjusted for the analysis of low-velocity signals and, therefore, the PRF is reduced for better venous vessel detection. The patient is asked to place the head in a straight position in order to avoid flow alterations caused by unilateral or bilateral venous flow obstruction. Moreover, a large amount of gel is placed on the skin of the patient and great care is taken not to compress the cervical veins when the probe is applied over the neck, in order to obtain reliable velocity or cross-sectional area measurements. The criteria used for discriminating between a vein and an artery include the compressibility of the vein, a change in vessel diameter by breathing, and the typical Doppler signal characterized by a continuous spectral waveform of low pulsatility. Before recording the haemodynamic data, the patient is asked to rest in a given position (sitting or supine) for at least 2 minutes and take several deep breaths to allow blood redistribution in the venous system. The internal jugular veins (IJVs) and the vertebral veins (VVs) are examined by using transverse and longitudinal cervical insonation planes—the direction of flow is analysed by comparing the colour of the flow and the direction of the pulsed wave in the IJV or VV with that of the satellite carotid or vertebral artery. Longitudinal B-mode insonation of the IJV in its caudal segment is used to visualize the inferior jugular bulb and the jugular valve, and search for malformations in the IJVs (septum, valve malformation), which might reduce or block venous outflow, even during inspiration. The presence of proximal IJV stenosis is assessed by measuring the cross-sectional area of the IJV. The lack of a Doppler signal in a vein, despite several deep inspirations, and the lack of vein compressibility defines an outflow occlusion. In the case of valve incompetence, flow reversal is documented during a Valsalva manoeuvre. However, even in competent valves, there is a short physiological reflux during closure, which corresponds to the valve closing time (<0.88 s) and which must be differentiated from a pathological retrograde flow (>0.88s) in insufficient valves [54]. Care should be taken to increase the sample volume size to the size of the IJV in order not to miss retrograde jet streams along the venous wall. Up to now, the strongest link of IJV incompetence has been reported with transient global amnesia [55], although its causative role is not clear yet [56].

A complete examination of the cervical veins entails the collection of major qualitative and quantitative data, both for the jugular and the vertebral veins, in supine and sitting positions, at rest, and during a Valsalva manoeuvre. In this way, it is possible to assess:

1. The main draining system in the supine position (usually the jugulars) and in the sitting position (usually the vertebrals).
2. Internal jugular vein valve anatomy (anatomical variants, malformations) and physiology (valve incompetence).
3. Venous patency (thrombosis, stenosis).
4. Collateral flow.

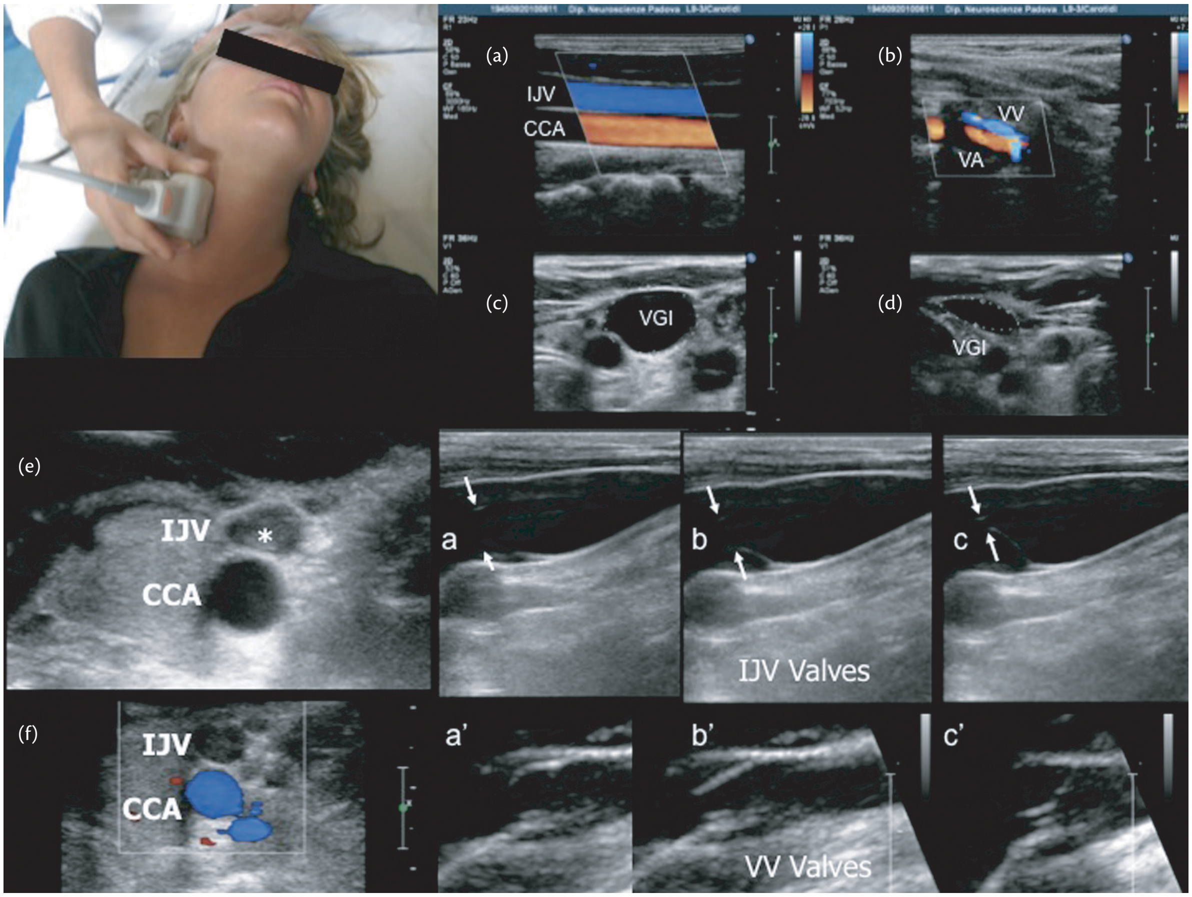

Fig. 10.11 Cervical venous ultrasound. (Top left) probe position for cervical venous assessment.

(Top right) Normal findings. (a) Colour-mode of internal jugular vein (IJV) with opposite flow direction with regards to the common carotid artery (CCA). (b) Colour-mode of vertebral vein (VV) with opposite flow direction with regards to its satellite artery, the vertebral artery (VA). (c) Internal jugular vein in the supine position. (d) Internal jugular vein in the sitting position: note its smaller diameter. Bottom left: Internal jugular vein thrombosis: (e) thrombus (*) within the IJV lumen in B-mode. (f) Colour-mode showing no colour signal in the IJV; note the colour signal in the normal common carotid artery (CCA). (Bottom right) closing of the IJV valves [a–c] and of the VV valves [a'–c']

For transcranial examination (Fig. 10.12) [57], the system setting is adjusted for the analysis of low-velocity signals and, therefore the filters are switched off, colour gain is increased, and the PRF is reduced for better venous vessel detection. The patient is examined both in a sitting and a supine position, at rest and during a Valsalva manoeuvre. Ultrasound examination is limited to the venous structures located close to the cranial base and in the posterior fossa, while cortical veins and most part of the superior sagittal sinus (except for the portion adjacent to the torcular herophili) cannot be visualized. As a consequence, TCCS cannot exclude a thrombosis of these latter veins. Examination techniques and normal velocity values for intracranial veins and sinuses are currently available, and form the basis for a correct diagnosis of intracranial venous disorders [58]. Blood flow direction and velocity of all veins are recorded; they should not be measured at junctions with other vessels, since at these points venous flow velocities could vary greatly. In healthy subjects, the detection rates of deep cerebral veins (deep middle cerebral vein, basal vein of Rosenthal, great vein of Galen) are high; however, for the posterior fossa sinuses the insonation rates are variable [58]. The reproducibility and interobserver reliability of venous measurements are high and comparable with those recorded in the arterial system [59]. Intracranial veins and sinuses do not have valves; consequently, their flow direction is governed solely by the current pressure gradient and flow resistance.

In cerebral venous thrombosis, typical findings would be absent Doppler signal in the thrombosed vein/sinus, and reversed flow direction and increased flow velocities in its tributaries. However, thrombotic occlusion or partial thrombosis cannot be differentiated from aplasia or hypoplasia by ultrasound alone. Consequently, TCCS is more suitable for follow-up examinations rather than screening for cerebral venous thrombosis.

Ultrasound of the brain parenchyma

In the last decade, thanks to technological advances, B-mode imaging can also be used to perform intracranial studies where it shows contralateral skull line, midline structures, including the third ventricle, and brain parenchymal structures. A high-resolution imaging of deep brain structures is now feasible in the majority of adults.

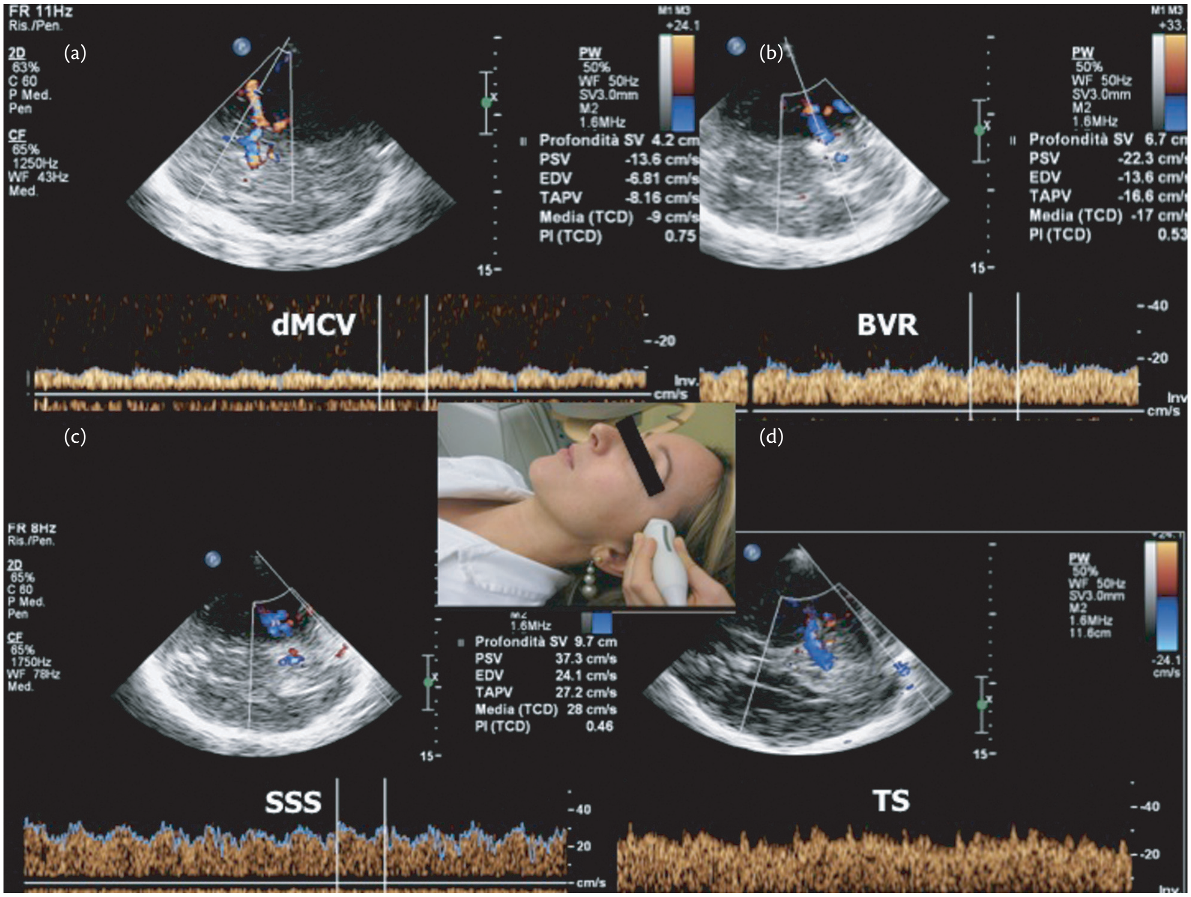
(a)
FR 11Hz
Ris./Pen.
2D
63%
C 60
P Med.
Pen
CF
65%
1250Hz
WF 43Hz
Med.
PW
50%
WF 50Hz
SV3.0mm
M2
1.6MHz
Profondità SV 4.2 cm
PSV -13.6 cm/s
EDV -6.81 cm/s
TAPV -8.16 cm/s
Media (TCD) -9 cm/s
PI (TCD) 0.75
dMCV
(b)
Profondità SV 6.7 cm
PSV -22.3 cm/s
EDV -13.6 cm/s
TAPV -16.6 cm/s
Media (TCD) -17 cm/s
PI (TCD) 0.53
BVR
(c)
FR 8Hz
Ris./Pen.
2D
65%
C 60
P Med.
Pen
CF
65%
1750Hz
WF 78Hz
Med.
1.6MHz
Profondità SV 9.7 cm
PSV 37.3 cm/s
EDV 24.1 cm/s
TAPV 27.2 cm/s
Media (TCD) 28 cm/s
PI (TCD) 0.46
SSS
(d)
PW
50%
WF 50Hz
SV3.0mm
M2
1.6MHz
11.6cm
TS

Fig. 10.12 Intracranial venous ultrasound. (Centre image) The probe is placed on the temporal window, which allows the investigation of the main intracranial venous vessels. (a) Deep middle cerebral vein (dMCV). (b) The basal vein of Rosenthal (BVR). (c) The caudal segment of the superior sagittal sinus (SSS). (d) Contralateral transverse sinus (TS).

TCCS has become a widely accepted tool in the early diagnosis and differential diagnosis of Parkinson's disease [60,61]. One main feature of TCCS is the ability to discriminate between essential tremor, Parkinson's disease (PD) related tremor and parkinsonisms. The typical finding in PD is a hyperechogenicity of the substantia nigra more evident contralaterally to the clinically more affected side [62]. The hyperechogenicity most probably reflects an increased iron content and does not seem to change with the course of the disease. Typically, patients with multisystem atrophy or progressive supranuclear palsy do not show a hyperechogenic substantia nigra, but have an increased echogenicity of the lenticular nucleus [63]. In contrast, patients with corticobasal degeneration show both a hyperechogenic substantia nigra and a hyperechogenic lenticular nucleus [64]. Deep brain stimulation (DBS) electrodes can be visualized and monitored by TCCS intra- and post-operatively, and TCCS might be used in the future to aid the insertion of DBS electrodes into the subthalamic nucleus and the globus pallidus internus [65]. Since TCCS can easily detect dislocation of DBS electrodes [65], future studies should assess the value of TCCS in the post-operative monitoring of DBS electrode position [66].

Transbulbar B-mode sonography

Transbulbar B-mode sonography of the optic nerve (Fig. 10.13) is a rather new bedside technique and represents an adjunctive diagnostic tool in different conditions leading to increased intracranial pressure (ICP), such as cerebral haemorrhage, pseudotumour cerebri, and trauma.

The optic nerve is surrounded by CSF and meninges (optic nerve sheath); in case of increased ICP, the optic nerve sheath diameter (ONSD) increases [67] and, therefore, ONSD measurement [68,69] may be used as a surrogate marker of raised ICP. Patients are examined with a medium-high frequency (7–13 MHz) linear transducer, in a supine position with the head elevated to 20–30°. In order not to expose the patient to possible side effects, especially on the lens, the power of the insonation should be reduced (MI < 0.26) and its duration should be kept to a minimum. A thick layer of ultrasound gel should be applied on the upper eyelid, before placing the probe on the temporal part of the closed upper eyelid. The probe is then adjusted to obtain a suitable angle for displaying the entry of the optic nerve into the globe—the retrobulbar part of the optic nerve, the papilla, and the optic nerve in its longitudinal course can be easily depicted. The ONSD is evaluated 3 mm behind the papilla and the distance between the external borders of the hyperechoic area surrounding the optic nerve is measured. A mean ONSD of 5.1 ± 0.5 mm has been reported in healthy subjects [70] with a good inter- and intra-observer reliability [71]. In patients with an increased ICP, a protrusion of the papilla and an increased ONSD are common

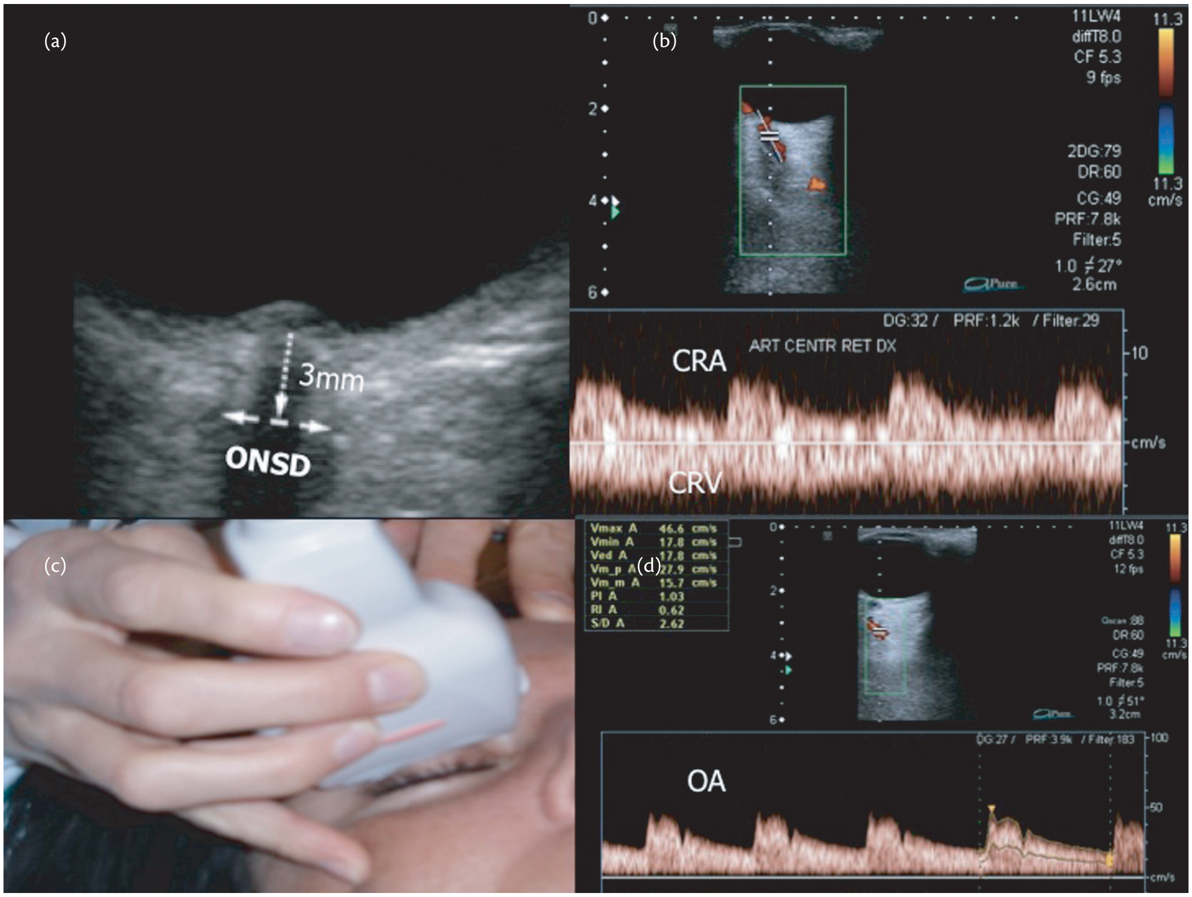

Fig. 10.13 Trans-bulbar sonography. (a) B-mode ocular sonography for measurement of optic nerve sheath diameter (ONSD) at a distance of 3 mm from the papilla. (b) Colour-mode and Doppler mode imaging for measurement of central retinal artery (CRA) and vein (CRV) blood velocity: the flow directions are normally opposite in these vessels. They are found at the entry of the optic nerve into the globe. (c) Transorbital approach: a linear probe is placed on the temporal part of the closed upper eyelid. (d) Colour-mode and Doppler mode imaging for assessing the ophthalmic artery (OA) at a depth of about 30–40 mm; the flow is towards the probe.

findings. However, the false-negative rate is about 10% [72]. Thus, absolute measurements of ICP cannot be made with transbulbar sonography, and ONSD values should be interpreted in conjunction with clinical data and other neuroimaging results. In conclusion, transbulbar sonography might be especially indicated in patients with contraindications to invasive ICP monitoring (coagulopathy, thrombocytopenia) or when the expertise for invasive monitor placement is not immediately available.

Neuromuscular ultrasound

Over the past few years, high resolution ultrasonography of peripheral nerves and muscles has evolved as an adjunctive technique in clinical neurophysiology providing complementary information to electrodiagnostic studies.

As a diagnostic tool [73], ultrasound has been shown to be valuable for the examination of patients with focal neuropathies (especially entrapment neuropathies, such as carpal tunnel and cubital tunnel syndromes), traumatic nerve lesions, several types of polyneuropathies, and nerve sheath tumours (Fig. 10.14).

Furthermore, ultrasound plays a key role in targeting therapy such as botulinum toxin. A prerequisite for successful therapy is the anatomically correct administration of the toxin into the muscle belly, to treat spastic muscles in children with cerebral palsy, and in adults with stroke sequelae or focal and cervical dystonia.

Tele-ultrasound

The use of telecommunication and information technologies in order to provide clinical healthcare at a distance is defined as telemedicine. Telemedicine is potentially beneficial for people in isolated communities and remote regions, for handicapped people not able to travel, and for healthcare professionals in multiple locations, since they can view, discuss, and assess patients' issues in order to reduce unnecessary patient transfers. Telemedicine serves also as a teaching tool, and reduces unnecessary patient transfers and the cost of healthcare.

Telestroke, an application of telemedicine, is a set of tools that enable the more efficient delivery of acute stroke care and a better quality of stroke care in neurologically-underserved areas. Depending on the level of available regional resources, Telestroke networks can support affiliated hospitals by implementing measures that improve the quality of stroke management, such as regional campaigns, stroke units and stroke teams, medical education, and programs encouraging the usage of international guidelines [74].

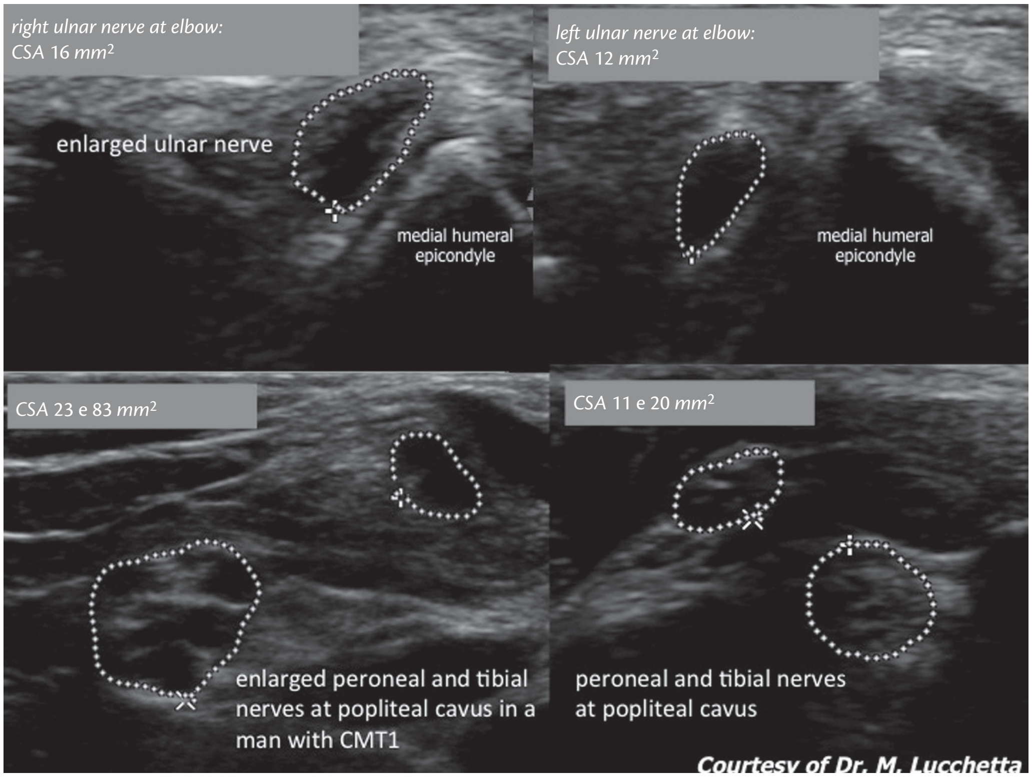
right ulnar nerve at elbow:
CSA 16 mm²
enlarged ulnar nerve
medial humeral epicondyle
left ulnar nerve at elbow:
CSA 12 mm²
medial humeral epicondyle
CSA 23 e 83 mm²
enlarged peroneal and tibial nerves at popliteal cavus in a man with CMT1
CSA 11 e 20 mm²
peroneal and tibial nerves at popliteal cavus
Courtesy of Dr. M. Lucchetta

Fig. 10.14 Ultrasonography of the peripheral nerves. (Top pictures) Enlarged ulnar nerve at the elbow in a patient with hereditary neuropathy and liability to pressure palsies (top left) versus normal findings (top right). (Bottom pictures) Enlarged peroneal and tibial nerves at the popliteal cavus in a patient with Charcot-Marie-Tooth neuropathy type 1 (bottom left) versus normal findings (bottom right).

Tele-ultrasound is a more specific application of telemedicine. There are already some reports about positive experiences of tele-ultrasound—in the acute stroke setting, to rapidly assess extracranial or intracranial occlusion [75], and during carotid endarterectomy, to monitor cerebral haemodynamics from one or more surgical theatres [76].

References

1. Kremkau FW. (1993). *Doppler ultrasound: principles and instruments*. Philadelphia: Saunders.
2. Evans DH. (2006). Physical and Technical Principles. *Frontiers in Neurology and Neuroscience*, **21**, 1–18.
3. Brott TG, Halperin JL, Abbara S, et al. (2011). ASA/ACCF/AHA/AANN/AANS/ACR/ASNR/CNS/SAIP/SCAI/SIR/SNIS/SVM/SVS guideline on the management of patients with extracranial carotid and vertebral artery disease. Report of the American College of Cardiology Foundation/American Heart Association Task Force on Practice Guidelines, and the American Stroke Association, American Association of Neuroscience Nurses, American Association of Neurological Surgeons, American College of Radiology, American Society of Neuroradiology, Congress of Neurological Surgeons, Society of Atherosclerosis Imaging and Prevention, Society for Cardiovascular Angiography and Interventions, Society of Interventional Radiology, Society of Neuro Interventional Surgery, Society for Vascular Medicine, and Society for Vascular Surgery. *Circulation* **124**, e54–130.
4. Corretti MC, Anderson TJ, Benjamin EJ, et al. (2002). International Brachial Artery Reactivity Task Force. Guidelines for the ultrasound assessment of endothelial dependent flow-mediated vasodilation of the brachial artery. *Journal of the American College of Cardiology*, **39**, 257–65.
5. Touboul PJ, Hennerici MG, Meairs S, et al. (2007). Mannheim carotid intima-media thickness consensus (2004–2006). An update on behalf of the Advisory Board of the 3rd and 4th Watching the Risk Symposium, 13th and 15th European Stroke Conferences, Mannheim, Germany, 2004, and Brussels, Belgium, 2006. *Cerebrovascular Disease*, **23**(1), 75–80.
6. Godia EC, Madhok R, Pittman J, et al. (2007). Carotid artery distensibility: a reliability study. *Journal of Ultrasound Medicine*, **26**(9), 1157–65.
7. von Reutern GM, Goertler MW, Bornstein NM, et al. (2012). Grading carotid stenosis using ultrasonic methods. *Stroke*, **43**(3), 916–21.
8. Giannoni MF, and Vicenzini E. (2009). Focus on the 'unstable' carotid plaque: detection of intraplaque angiogenesis with contrast ultrasound. Present state and future perspectives. *Current Vascular Pharmacology*, **7**(2), 180–4 [Review].
9. Dunmore BJ, McCarthy MJ, Naylor AR, et al. (2007). Carotid plaque instability and ischemic symptoms are linked to immaturity of microvessels within plaques. *Journal of Vascular Surgery*, **45**, 155–9.
10. Markus HS, King A, Shipley M, et al. (2010). Asymptomatic embolisation for prediction of stroke in the Asymptomatic Carotid Emboli Study (ACES): a prospective observational study. *Lancet Neurology*, **9**(7), 663–71.
11. Schmidt WA, Kraft HE, Vorpahl K, et al. (1997). Color duplex ultrasonography in the diagnosis of temporal arteritis. *New England Journal of Medicine*, **337**, 1336–42.
12. Maeda H, Handa N, Matsumoto M, et al. (1991). Carotid lesions detected by B-mode ultrasonography in Takayasu's arteritis: 'Macaroni sign' as an indicator of the disease. *Ultrasound in Medicine & Biology*, **17**, 695–701.
13. Debette S, and Leys D. (2009). Cervical-artery dissections: predisposing factors, diagnosis, and outcome. *Lancet Neurology*, **8**, 668–78.
14. Baracchini C, Tonello S, Meneghetti G, et al. (2010). Neurosonographic monitoring of 105 spontaneous cervical artery dissections: a prospective study. *Neurology*, **75**, 1864–70.

15. Nebelsieck J, Sengelhoff C, Nassenstein I, et al. (2009). Sensitivity of neurovascular ultrasound for the detection of spontaneous cervical artery dissection. *Journal of Clinical Neuroscience*, **16**, 79–82.
16. Dittrich R, Nassenstein I, Bachmann R, et al. (2007). Polyarterial clustered recurrence of cervical artery dissection seems to be the rule. *Neurology*, **69**, 180–6.
17. Savitz SI, and Caplan LR. (2005). Vertebrobasilar disease. *New England Journal of Medicine*, **352**, 2618–26.
18. Hass WK, Fields WS, North RR, et al. (1968). Joint study of extracranial arterial occlusion. II. Arteriography, techniques, sites and complications. *Journal of the American Medical Association*, **203**, 961–8.
19. Khan S, Rich P, Clifton A, et al. (2009). Noninvasive detection of vertebral artery stenosis: a comparison of contrast-enhanced MR angiography, CT angiography, and ultrasound. *Stroke*, **40**(11), 3499–503.
20. Koch S, Romano JG, Park H, et al. (2009). Ultrasound velocity criteria for vertebral origin stenosis. *Journal of Neuroimaging*, **19**(3), 242–5.
21. Hua Y, Meng XF, Jia LY, et al. (2009). Color Doppler imaging evaluation of proximal vertebral artery stenosis. *American Journal of Roentgenology*, **193**(5), 1434–8.
22. Yurdakul M, and Tola M. (2011). Doppler criteria for identifying proximal vertebral artery stenosis of 50% or more. *Journal of Ultrasound Medicine*, **30**(2), 163–8.
23. Khan S, Cloud G, Kerry S, et al. (2007). Imaging of vertebral artery stenosis; a systematic review. *Journal of Neurology, Neurosurgery, & Psychiatry*, **78**, 1218–25.
24. Arnold M, Bousser MG, Fahrni G, et al. (2006). Vertebral artery dissection: presenting findings and predictors of outcome. *Stroke*, **37**, 2499–503.
25. Benninger DH, and Baumgartner RW. (2006). Ultrasound diagnosis of cervical artery dissection. *Frontiers in Neurology and Neuroscience*, **21**, 70–84.
26. Nebelsieck J, Sengelhoff C, Nassenstein I, et al. (2009). Sensitivity of neurovascular ultrasound for the detection of spontaneous cervical artery dissection. *Journal of Clinical Neuroscience*, **16**, 79–82.
27. von Reutern GM, and Büdingen HJ. (1977). Doppler sonographic study of the vertebral artery in subclavian steal syndrome [in German]. *Deutsche medizinische Wochenschrift*, **102**, 140–1.
28. Garami Z, and Alexandrov AV. (2009). Neurosonology. *Neurologic Clinics*, **27**(1), 89–108.
29. Baumgartner RW. (2006). Transcranial insonation. *Frontiers in Neurology and Neuroscience* **21**, 105–16.
30. Bartels E. (1999). *Color-coded duplex ultrasonography of the cerebral vessels/atlas and manual* [Farbduplexsonographie der hirnversorgenden Gefäße/Atlas und Handbuch]. Stuttgart: Schattauer.
31. Valdueza JM, Schreiber SJ, Roehl JE, et al. (2008). *Neurosonology and neuroimaging of stroke*. Stuttgart: Thieme.
32. Riggs HE, and Rupp C. (1963). Variation in form of circle of Willis. *Archives of Neurology*, **8**, 24–30.
33. Baumgartner RW. (2003). Transcranial color duplex sonography in cerebrovascular disease: a systematic review. *Cerebrovascular Diseases*, **16**, 4–13.
34. Baumgartner RW, Baumgartner I, Mattle HP, et al. (1997). Transcranial color-coded duplex sonography in the evaluation of collateral flow through the circle of Willis. *American Journal of Neuroradiology*, **18**, 127–33.
35. Aaslid R. (2006). Cerebral autoregulation and vasomotor reactivity. *Frontiers in Neurology and Neuroscience*, **21**, 216–28.
36. Aaslid R, Huber P, and Nornes H. (1984). Evaluation of cerebrovascular spasm with transcranial Doppler ultrasound. *Journal of Neurosurgery*, **60**, 37–41.
37. Lindegaard KF, Nornes H, Bakke SJ, et al. (1988). Cerebral vasospasm after sub- arachnoid hemorrhage investigated by means of transcranial Doppler ultrasound. *Acta Neurochirugia Supplement (Wien)*, **42**, 81–4.
38. Nedelmann M, Stolz E, Gerriets T, et al. (2009). Consensus recommendations for transcranial color-coded duplex sonography for the assessment of intracranial arteries in clinical trials in acute stroke. *Stroke*, **40**, 3238–44.
39. Ritter MA, Dittrich R, Thoenissen N, et al. (2008). Prevalence and prognostic impact of microembolic signals in arterial sources of embolism. A systematic review of the literature. *Journal of Neurology*, **255**, 953–61.
40. King A, and Markus HS. (2009). Doppler embolic signals in cerebrovascular disease and prediction of stroke risk: a systematic review and meta- analysis. *Stroke*, **40**, 3711–17.
41. Markus HS, Droste DW, Kaps M, et al. (2005). Dual antiplatelet therapy with clopidogrel and aspirin in symptomatic carotid stenosis evaluated using Doppler embolic signal detection: the clopidogrel and aspirin for reduction of emboli in symptomatic carotid stenosis (CARESS) trial. *Circulation*, **111**, 2233–40.
42. Wong KS, Chen C, Fu J, et al. (2010). Clopidogrel plus aspirin versus aspirin alone for reducing embolisation in patients with acute symptomatic cerebral or carotid artery stenosis (CLAIR study): a randomised, open-label, blinded-endpoint trial. *Lancet Neurology*, **9**, 489–97.
43. Jauss M, and Zanette E. (2000). Detection of right-to-left shunt with ultrasound contrast agent and transcranial Doppler sonography. *Cerebrovascular Disease*, **10**, 490–6.
44. Adams R, McKie V, Nichols F, et al. (1992). The use of transcranial ultrasonography to predict stroke in sickle cell disease. *New England Journal of Medicine*, **326**, 605–10.
45. Adams RJ, McKie VC, Hsu L, et al. (1998). Prevention of a first stroke by transfusions in children with sickle cell anemia and abnormal results on transcranial Doppler ultrasonography. *New England Journal of Medicine*, **339**, 5–11.
46. Adams RJ, and Brambilla D. (2005). Optimizing Primary Stroke Prevention in Sickle Cell Anemia (STOP 2) trial investigators. Discontinuing prophylactic transfusions used to prevent stroke in sickle cell disease. *New England Journal of Medicine*, **353**, 2769–78.
47. Lee MT, Piomelli S, Granger S, et al. (2006). STOP study investigators. Stroke prevention trial in sickle cell anemia (STOP): extended follow-up and final results. *Blood*, **108**, 847–52.
48. Nichols FT, Jones AM, and Adams RJ. (2001). Stroke prevention in sickle cell disease (STOP) study guidelines for transcranial Doppler testing. *Journal of Neuroimaging*, **11**, 354–62.
49. Wiesmann M, and Seidel G. (2000). Ultrasound perfusion imaging of the human brain. *Stroke*, **31**, 2421–5.
50. Kern R, Diels A, Pettenpohl J, et al. (2011). Real-time ultrasound brain perfusion imaging with analysis of microbubble replenishment in acute MCA stroke. *Journal of Cerebral Blood Flow & Metabolism*, **31**, 1716–24.
51. Tsivgoulis G, Eggers J, Ribo M, et al. (2010). Safety and efficacy of ultrasound-enhanced thrombolysis: a comprehensive review and meta-analysis of randomized and nonrandomized studies. *Stroke*, **41**, 280–7.
52. Kinoshita M, McDannold N, Jolesz FA, et al. (2006). Targeted delivery of antibodies through the blood–brain barrier by MRI-guided focused ultrasound. *Biochemical and Biophysical Research Communications*, **340**, 1085–90.
53. Valdueza JM, von Munster T, and Hoffmann O, et al. (2000). Postural dependency of the cerebral venous outflow. *Lancet*, **355**, 200–1.
54. Nedelmann M, Eicke B, and Dieterich M. (2005). Functional and morphological criteria of internal jugular valve insufficiency as assessed by ultrasound. *Journal of Neuroimaging*, **15**, 70–5.
55. Nedelmann M, Eicke BM, and Dieterich M. (2005). Increased incidence of jugular valve insufficiency in patients with transient global amnesia. *Journal of Neurology*, **252**, 1482–6.
56. Baracchini C, Tonello S, Farina F, et al. (2012). Jugular veins in transient global amnesia: innocent bystanders. *Stroke*, **43**, 2289–92.
57. Stolz E, Kaps M, Kern A, et al. (1999). Transcranial color-coded duplex sonography of intracranial veins and sinuses in adults: reference data from 130 volunteers. *Stroke*, **30**, 1070–5.
58. Stolz E. (2006). Cerebral veins and sinuses. *Frontiers in Neurology and Neuroscience*, **21**, 182–93.

59. Stolz E, Babacan SS, Bödeker RH, et al. (2001). Interobserver and intraobserver reliability of venous transcranial color-coded flow velocity measurements. *Journal of Neuroimaging*, **11**, 385–92.
60. Walter U, Behnke S, Eyding J, et al. (2007). Transcranial brain parenchyma sonography in movement disorders: state of the art. *Ultrasound in Medicine and Biology*, **33**, 15–25.
61. Berg D, Godau J, and Walter U. (2008). Transcranial sonography in movement disorders. *Lancet Neurology*, **7**, 1044–55.
62. Becker G, Seufert J, Bogdahn U, et al. (1995). Degeneration of substantia nigra in chronic Parkinson's disease visualized by transcranial color-coded real-time sonography. *Neurology*, **45**, 182–4.
63. Bouwmans AE, Vlaar AM, Srulijes K, et al. (2010). Transcranial sonography for the discrimination of idiopathic Parkinson's disease from the atypical parkinsonian syndromes. *International Reviews in Neurobiology*, **90**,121–46.
64. Walter U, Dressler D, Wolters A, et al. (2004). Sonographic discrimination of corticobasal degeneration vs progressive supranuclear palsy. *Neurology*, **63**, 504–9.
65. Walter U, Kirsch M, Wittstock M, et al. (2011). Transcranial sonographic localization of deep brain stimulation electrodes is safe, reliable and predicts clinical outcome. *Ultrasound in Medicine and Biology*, **37**, 1382–91.
66. Walter U. (2010). Transcranial sonography-assisted stereotaxy and follow-up of deep brain implants in patients with movement disorders. *International Review in Neurobiology*, **90**, 274–85.
67. Hansen HC, and Helmke K. (1997). Validation of the optic nerve sheath response to changing cerebrospinal fluid pressure: ultrasound findings during intrathecal infusion tests. *Journal of Neurosurgery*, **87**(1), 34–40.
68. Helmke K, and Hansen HC. (1996). Fundamentals of transorbital sonographic evaluation of optic nerve sheath expansion under intracranial hypertension. I. Experimental study. Pediatric Radiology, **26**(10), 701–5.
69. Helmke K, and Hansen HC. (1996). Fundamentals of transorbital sonographic evaluation of optic nerve sheath expansion under intracranial hypertension. II. Patient study. *Pediatric Radiology*, **26**(10), 706–10.
70. Geeraerts T, Newcombe VF, Coles JP, et al. (2008). Use of T2-weighted magnetic resonance imaging of the optic nerve sheath to detect raised intracranial pressure. *Critical Care*, **12**(5), R114.
71. Bäuerle J, Lochner P, Kaps M, et al. (2012). Intra- and inter-observer reliability of sonographic assessment of the optic nerve sheath diameter in healthy adults. *Journal of Neuroimaging*, **22**(1), 42–5.
72. Dubourg J, Javouhey E, Geeraerts T, et al. (2011). Ultrasonography of optic nerve sheath diameter for detection of raised intracranial pressure: a systematic review and meta- analysis. *Intensive Care Medicine*, **37**(7), 1059–68.
73. Kopf H, Loizides A, Mostbeck GH, et al. (2011). Diagnostic sonography of peripheral nerves: indications, examination technique and pathological findings. *Ultraschall in der Medizin*, **32**, 242–63.
74. Müller-Barna P, Schwamm LH, and Haberl RL. (2012). Telestroke increases use of acute stroke therapy. *Current Opinions in Neurology*, **25**(1), 5–10.
75. Mikulik R, Alexandrov AV, Ribo M, et al. (2006). Telemedicine-guided carotid and transcranial ultrasound: a pilot feasibility study. *Stroke*, **37**(1), 229–30.
76. Mess WH. (2012). Teleultrasound during surgery. *Cerebrovascular Diseases*, **33**(S1), 32.

SECTION 2

Clinical applications

CHAPTER 11

Headache

Till Sprenger and Peter J. Goadsby

Introduction

Conventional neuroimaging, especially cranial MRI, is an important clinical tool to rule out secondary causes in the work-up of headache patients. However, in patients with primary (idiopathic) headache syndromes, it is not possible to confirm the diagnosis using brain MRI or CT, and the test results usually remain normal or non-contributory. On the other hand, more advanced, non-conventional structural and functional *in vivo* imaging methods have considerably improved our understanding of brain structure and function, in general, and of pain and headache processing, specifically, since the 1990s. Sophisticated structural and functional neuroimaging methods provide the means to test hypotheses gained from clinical observations not only in awake and conscious volunteers, but also in patients suffering from headache disorders. Since these are regarded as disorders of the brain [1], neuroimaging offers much in terms of understanding the physiological dysfunction that characterizes primary headache syndromes [2].

This chapter summarizes the results of neuroimaging studies, applying functional imaging or advanced measures of structural neuroimaging in primary headache syndromes. For brevity, a synthesis of the main results is provided, showing how functional and structural neuroimaging has advanced the understanding of primary headache pathophysiology, rather than to give a detailed résumé of every published study. There are several comprehensive reviews that focus on single entities of primary headache, such as migraine [3,4] or cluster headache, [5], which interested readers might consult for more detailed accounts of the syndromes.

Experimental head pain

By the use of experimental pain models, such as capsaicin or heat-pain application with contact thermodes, a consistent matrix of brain areas has been established that is activated in response to painful stimulation [6]. This matrix comprises most consistently the thalamus, insula, anterior cingulate cortex, prefrontal cortex, and primary and secondary somatosensory cortex, as well as the cerebellum [7,8]. Other than some differences related to the somatotopy of the activations and methodological aspects, basically the same network is activated when stimulating in the area of the trigeminal nerve [9], instead of the extremities or trunk, and when investigating primary headache attacks [10–13].

Although it is not yet clear which specific neurotransmitter systems contribute most to the noted activation changes, opioids are released in the same cortical network in response to painful stimulation [14,15].

Trigeminal autonomic cephalalgias

The group of trigeminal autonomic cephalalgias (TACs) [16] was introduced into the 2nd edition of the International Classification of Headache Disorders (ICHD-II) [17]. It comprises headache syndromes with a common clinical presentation, which are also likely to share pathophysiological mechanisms. The TACs are all characterized by strictly unilateral, typically periorbital, pain and concomitant cranial autonomic symptoms, which relate to sympathetic dysfunction, ptosis, miosis, and cranial parasympathetic hyperactivity, lacrimation, conjunctival injection, nasal congestion, and skin redness. The ICHD-II distinguishes cluster headache, paroxysmal hemicrania and the 'short-lasting unilateral neuralgiform headache attacks with conjunctival injection and tearing' (SUNCT) syndrome on the basis of the attack duration, which is shortest in SUNCT (seconds to minutes), and longest in cluster headache (up to 3 hours); each are typically shorter than acute migraine. In ICHD-III, hemicrania continua, a headache syndrome characterized by continuous unilateral head pain with additional shorter lasting pain exacerbations with trigeminal autonomic features has been added to this diagnostic group.

Cluster headache

Lesions at the level of the cavernous sinus might theoretically produce nearly all the essential clinical characteristics of TACs—trigeminal activation, parasympathetic activation, and sympathetic deficit—and there have been sporadic case reports of patients with such lesions suffering from cluster-like headaches, with the notable exception of the circadian and circannual features [18]. However, in the vast majority of patients with cluster headaches, there is no clinical evidence of any pathology in the cavernous sinus. Taking into account these considerations, neurogenic (sterile) inflammation of the cavernous sinus, which might not be visible on clinical MRI scans, has been postulated as an explanation for cluster headaches [19]. However, two imaging studies using single photon emission computed tomography did not report any sign of neurogenic inflammation, such as plasma protein extravasation, in this area [20,21]. Moreover, the typical circadian rhythmicity of cluster-headache attacks, which is really a hallmark of the disorder, cannot be explained by an isolated peripheral pathology.

Instead, posterior hypothalamic activation at the border to the ventral tegmental area was observed during attacks [10,22], in addition to the previously mentioned non-specific activation of the pain-processing network as a response to first division trigeminal nociceptive input. The hypothalamic region activation was initially thought to be relatively specific for cluster headaches since no such activation was observed in experimental facial pain [9]. However, hypothalamic activation is also seen in migraine, especially during the early phase of an attack [23,24], although the localization of the activation in migraine seems more anterior than is reported for the trigeminal autonomic cephalalgias, including cluster headache.

Hypothalamic involvement in the pathophysiology of cluster headache is plausible, as this brain structure is known as the generator of the biological clock and cluster headache attacks typically occur with a strong circadian and seasonal rhythmicity. Furthermore, co-localization of a structural change in the same area has been shown by voxel-based morphometry (VBM) [25], although more recent studies failed to reproduce this observation [26,27]. MR spectroscopic abnormalities have been also reported in the hypothalamus of patients with cluster headaches [28,29] and it was shown that functional connectivity is increased in a brain network where the hypothalamus is a key network node [30].

The early imaging results prompted the use of hypothalamic deep-brain stimulation in a patient with chronic cluster headaches [31], and this method has since been applied in at least 58 patients, indicating efficacy in about 60% of patients with chronic cluster headaches [32]. Ten of these stimulated patients were investigated by PET, alternately switching the hypothalamic stimulator on and off, to explore the mode of action of the deep-brain stimulation [33]. The data suggest a functional modulation of the previously-noted pain-processing network as the mode of action of hypothalamic deep brain stimulation in cluster headache [33].

Another brain structure related to the circadian rhythm and probably involved in cluster headache pathophysiology is the pineal gland, for which an alteration in opioidergic receptor status has been shown [34]. As opioids increase the secretion of melatonin, and this in turn alters beta-endorphin levels, opioidergic dysfunction in the pineal gland may relate to pathologic melatonin homeostasis in cluster headaches [35]. More recent studies have shown a reduced glucose metabolism in frontal brain circuits, which might be responsible for pain modulation/inhibition, in patients with cluster headaches [36] and another relatively large VBM study showed that in a similar network of brain areas, there is decreased gray matter density, indicating a functional and subtle structural alteration in these areas [27]. Such abnormalities might translate into insufficient pain control as one component in a more complex pathophysiology, possibly triggered by the hypothalamus.

Paroxysmal hemicrania, SUNCT, and hemicrania continua

Activation of the hypothalamic gray matter during attacks was also observed in SUNCT syndrome [37,38], paroxysmal hemicranias [39], and hemicrania continua [40]. These studies underpin the considerable clinical overlap between these syndromes [41], which is remarkably substantiated by imaging techniques. However, there is some remaining uncertainty with regard to the laterality of the hypothalamic/midbrain activations. Whereas ipsilateral activations were observed in cluster headaches [10,22], bilateral [37] or ipsilateral [38] activations were seen in SUNCT, and even a contralateral hypothalamic response in paroxysmal hemicrania [39]. These discrepancies might be related to methodological issues of the imaging studies, such as possible thresholding phenomena, and one also has to remember that the hypothalamic region as the major regulatory centre for autonomic functions is not, as such, strictly lateralized in its organization. Thus, a bilateral hypothalamic dysfunction in TAC might interact with a so-far undefined pathology to drive the clinical phenomenology to a single side of the head.

Migraine—white matter abnormalities in migraine with versus without aura

There is an ongoing debate about the significance of white matter lesions in migraine with versus without aura and the clinical implications of such findings. Current evidence suggests that white matter changes are relatively common in the deep white matter and subcortical U-fibres [41] in migraine with aura (Fig. 11.1) [42], but uncommon in migraine without aura. The cause of such white matter changes in migraine with aura is unclear. Ischaemic causes have been suggested, but are unproven. Migraine-related and multiple sclerosis (MS)-related lesions appeared to be similar on conventional MRI, but magnetization transfer ratio imaging clearly showed less tissue destruction in migraine-related lesions than in MS [43]. Moreover, migraine-related white matter changes seem to be smaller and fewer than in MS [41].

Non-conventional MRI studies applying diffusion tensor imaging have shown subtle white matter abnormalities in brain areas without overt lesions in migraineurs, such as reduced fractional anisotropy (FA), an indirect measure of fibre integrity, in the corpus callosum [44], but results are not consistent across studies [45]. Rocca et al. reported selective white matter changes (reduced FA) in the optic radiation of patients with migraine with aura, whereas patients without aura had normal FA [45]. Similarly, Granziera et al. have shown that FA is lower in migraineurs in the white matter underlying visual association areas, the superior colliculus, and the lateral geniculate ganglion [30], but their patient population included migraineurs with and without aura, and there was no significant difference between the two migraine subgroups. Altogether, white matter abnormalities seem to be more common in migraine with aura, but subtle alterations, as measured using advanced imaging techniques, may also be present in migraine without aura.

Migraine without aura

A key observation, perhaps the crucial observation of functional imaging in migraine to date, has been that brainstem areas are active during pain and that after successful treatment this activation persists, while it is not present between attacks [11–13,24,42]. The active areas are in the dorsal midbrain and the dorsolateral pons, with recent suggestions of hypothalamic activation [23,24]. This pattern of activation, specifically dorsolateral pontine activation, is also seen in chronic migraine [46] and provides a potential marker of the disorder. The dorsal midbrain activation corresponds

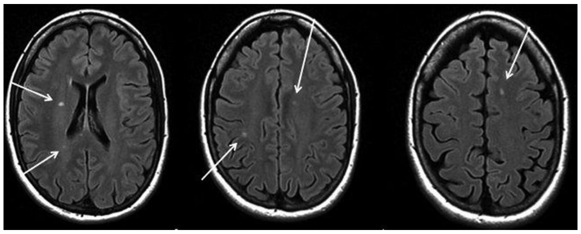

Fig. 11.1 White matter changes in a 35-year-old patient with migraine with aura, who did not have symptoms suggestive of demyelinating disease of the CNS. The axial MRI FLAIR sequence of the brain evidenced several hyperintense white matter areas. These areas did not enhance contrast in the T1 post-Gadolinium sequence. The cause of such white matter changes, which are more commonly seen in migraineurs with aura than in healthy subjects, is unknown.

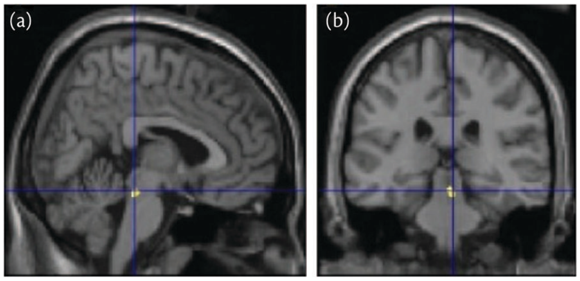

Fig. 11.2 Sagittal (a) and coronal (b) views showing statistical parametric map (SPM) regions superimposed on a high-resolution T1-weighted scan with increased gray matter (GM) density in migraine patients compared with healthy controls ($p < 0.001$, uncorrected at a voxel level; $p < 0.05$ after SVC). The PAG is visible in both sections (neurological convention).

Reproduced from Rocca MA, Ceccarelli A, Falini A, et al. (2006). Brain gray matter changes in migraine patients with T2-visible lesions: a 3-T MRI study. *Stroke*, **37**(7), p. 1765–70. Copyright (2006), with permission from Wolters Kluwer Health

with the brain region that Raskin et al. [43] initially reported, and Veloso et al. confirmed [44] as causing migraine-like headache when stimulated in patients with electrodes implanted for pain control. Moreover, lesions from, for example, MS [45] or a developmental venous anomaly [47] in these same regions also produce migraine.

Interestingly, the same area was found not to be modulated in chronic migraine treated with suboccipital stimulation [46], indicating that this potential therapy may not alter the underlying disorder.

Regarding laterality, the brainstem activations occur predominantly ipsilaterally to the manifestation of the pain, which suggests that the lateralization of the pain relates to lateralized brainstem dysfunction [13]. More recently, structural abnormalities in the brainstem, such as an increased peri-aqueductal gray matter (PAG) density, have also been demonstrated by VBM (Fig. 11.2) [48] and a perturbation of iron homeostasis in the PAG as evidenced by region-of-interest analysis of iron-susceptible MRI sequences, has been shown in patients with migraine [49]. This again suggests a pivotal role for the brainstem in migraine pathophysiology.

Furthermore, several studies using VBM have indicated widespread decreases in gray matter density within the general pain-processing network outlined in the above section on experimental head pain [48,50,51]. As these changes correlated with the duration of the disease, they may be a non-specific and probably reversible consequence of the repetitive pain attacks.

Studies applying more advanced measures of gray matter structure, such as cortical thickness and cortical surface measurements have yielded inconsistent results in the past. Cortical thickening was reported in visual motion processing areas [52] and the primary somatosensory cortex [53]. Another study replicated the thickening of the somatosensory cortex for high-frequency migraineurs (8–14 days per month), but not for low-frequency migraineurs (<2 days per month), who rather seemed to have a thinned post-central gyrus compared with healthy controls [54]. A larger study was unable to evidence any abnormality of cortical thickness in migraine [55]. However, the most recent study on cortical thickness and surface area, which included the largest patient population (63 migraineurs and 18 control subjects) studied using such techniques to date, suggested subtle abnormalities of cortical thickness with areas of both thickened and thinned brain, as well as even more pronounced abnormalities of cortical surface area [56]. The authors argued that the abnormalities of cortical surface may represent a predetermined susceptibility trait for migraine, whereas abnormal cortical thickness could be acquired throughout life potentially reflecting a consequence of repetitive migraine attacks. Larger replication studies are needed in this complex research field in order to clarify the inconsistencies across studies.

During the last few years, a growing number of studies investigated the integrity of so-called resting state networks in various neurological and psychiatric conditions suggesting alterations amongst others in Alzheimer's disease and other neurodegenerative disorders, MS, schizophrenia, and bipolar disorder. More recently, these techniques were also applied in patients with primary head pain disorders [57–63]. Three studies compared episodic migraine patients and healthy controls using independent component analysis [57,61,62]. Two studies applied a seed-based approach [58,60] and in one study the amplitude of low frequency fluctuations (ALFF) was compared between patients and controls [60]. Another study applied an unusual resting state fMRI technique on the regional homogeneity (ReHo) of the fMRI signal time course [59]. All these studies were mainly conducted in interictal patients with episodic migraine and they provided contradictory results. This observed variability between results could be due to different methodology used, different resting state networks investigated and somewhat different patient populations. Nevertheless, some of the studies seem to be convergent in that connectivity is generally increased in pain-processing networks in migraineurs [58,62,63] and this connectivity increase may worsen with more frequent attacks. On the other hand, connectivity seems to be decreased in pain modulatory circuits [58,62].

Photophobia

Photophobia is a clinical hallmark of migraine attacks and a few neuroimaging studies focused on mechanisms of this symptom. Denuelle and colleagues investigated visual cortex responses to continuous luminous stimulation in migraineurs with $H_2{}^{15}O$-PET and found evidence for visual cortex hyperexcitabilitiy during the attack. Visual cortex activation in response to low luminous stimulation was stronger during the attack compared with a period with headache relief after sumatriptan was administered. However, the activation during the headache relief phase just after the acute attack was still stronger than during an interictal scan indicating that photophobia cannot be explained as a phenomenon exclusively produced by or secondary to trigeminal pain. The same group also studied visual cortex activation in migraineurs during the interictal state compared with healthy subjects again with positron emission tomography (PET). They found increased cortical responses in migraineurs compared with non-migraineurs. In both groups, visual processing was modulated by concomittant trigeminal pain stimulation. The latter finding in the context of the previously mentioned study in acute migraine attacks indicates that, while light perception and processing can be augmented by trigeminal pain in both migraine and non-migraine subjects, the existence of photophobia in migraineurs cannot be explained by the pain only, but could rather be driven by modulatory brainstem circuits.

Clearly, migraine is far more than isolated head pain. The key clinical features, other than pain, such as photophobia, phonophobia, osmophobia, and nausea argue for a severe episodic disturbance of sensory processing located in the central nervous system (CNS). The functional imaging results support this view and show attack-related brain activation in brainstem structures key for anti-nociception and an alteration of cortical serotonin receptor availability [64].

Migraine with aura

Patients with migraine with aura experience both the typical migrainous head pain and often spectacular neurological phenomena, which usually precede the headache. Visual symptoms are most common, such as scotoma with fortifications, and about 10% of all migraine patients have a characteristic march of symptoms starting with visual and evolving into somatosensory, speech and, rarely, even motor symptoms within less than 60 minutes. Early clinical observations noted that the symptoms are consistent with a process that transiently compromises cortical function at about 3 mm/minute [65]. Leao and Morison suggested that the so-called cortical spreading depression (CSD) (suppression of cortical activity advancing at about 3 mm/minute over the cortex) was the electrophysiological correlate of slowly marching scotoma in humans. It took more than 50 years until the existence of CSD in humans was proven electrophysiologically [66–68]. In early human imaging studies using the ^{133}Xenon intra-arterial injection method in the pre-PET and fMRI era, spreading oligaemia was observed in migraineurs [69] as a surrogate of CSD. Regarding cerebral hypoperfusion, the latter results were confirmed by perfusion-weighted MRI in patients with visual migraine aura who showed decreased perfusion in the occipital cortex contralaterally to the aura symptoms [70]. However, there have also been reports of occipital activation instead of hypoperfusion during migraine aura [71]. This apparent inconsistency between activation and deactivation of the occipital cortex in migraine aura is most likely related to the course and propagation of the aura with an early activation followed by prolonged deactivation [72]. Hadjikhani et al. in an elegant study examined migraine aura in more detail taking advantage of the superior temporal and spatial resolution of fMRI [73]. They observed BOLD signal changes, decreases in stimulus-driven signal fluctuations in response to checkerboard stimulations, at a rate identical to CSD in the occipital cortex concurring with the onset of visual aura in the contralateral visual hemifield. Thereby, the retinotopic progression of the signal changes was consistent with the perceptual course and the changes crossed vascular territories. The authors located the source of the aura-related signal pertubations in the extrastriate cortex (V3A). Interestingly, the same group later showed an increased cortical thickness in patients with migraine with aura in the area previously defined as being the putative source of migraine aura [52]. Although one might conclude the alterations in V3A are the cause of migraine aura, these changes in cortical thickness might also be a trait genetically related to aura, rather than functionally. Moreover, the changes in cortical thickness have not been reproduced by other groups so far.

A recent study by Hougaard et al. found that BOLD responses to visual stimulation were selectively increased in the symptomatic hemispheres of patients with side-locked visual migraine aura [74]. This increase of activation was found in the inferior parietal lobule, the inferior frontal gyrus, and the superior parietal lobule forming a visually-driven functional network involved in oculomotor control, guidance of movement, motion perception, visual attention, and visual spatial memory. Such alterations may underlie the sometimes reported visual discomfort in migraine with aura and explain why bright or flickering light can be attack-precipitating factors in such patients [74].

Taken together, aura could be considered more broadly as a syndrome with both anatomical and physiological consequences. Longitudinal studies might help to clarify this matter.

The role of CSD in migraine without aura, which involves the concept of clinically silent CSD, is an important question. In the previously noted study evidencing abnormal cortical thickness in V3A in patients with migraine aura, identical changes were observed in patients with migraine without aura [52]. The idea of silent aura was also supported by an earlier imaging study of a patient developing an attack of migraine without aura during a PET scanning session, and evidencing propagating cortical hypoperfusion which started in the occipital cortex [75] and was believed to be the result of CSD by the authors. Although it has been questioned whether the patient studied using PET suffered from migraine with or without aura, which remains undetermined from the case description, a study of seven patients with migraine without aura from an independent group recently also reported a relative posterior cerebral hypoperfusion during migraine without aura [76]. However, hypoperfusion—co-occurring with the headache—might be the result of neuronal events in deeper brain structures, such as in the brainstem nuclei (see Section 3.2), and has certainly been reported in pain studies [77], while the marker of CSD is progression of the change in the blood flow signal, and not anatomically static hypoperfusion. Activation changes in the brainstem precede activation changes in posterior parts of the cortex [78]. Thus, these results would fit an integrated concept of migraine with a primary brainstem dysfunction leading to secondary blood flow changes in the posterior circulation. Oligaemia could then lead to CSD in susceptible patients [76].

Tension-type headache

Although tension-type headache is considered common in the general population, only a few studies have investigated this syndrome. A fundamental problem with studies of tension-type headache is that the current criteria for diagnosis have no clear external validity and are hotly debated. Without clarity of the clinical phenotype, this area will remain substantially hampered.

Schmidt-Wilcke et al. used VBM and showed reduced gray matter density in many areas belonging to the general brain pain-processing network [79]. These changes correlated with the duration of the headache disorder and are more likely to be the result, rather than the cause of the headache disorder. Similar changes in gray matter structure have been reported in migraine [50,51,56], fibromyalgia [80], and somatoform pain disorder [81]. These changes are believed to represent a common 'brain signature' in response to ongoing pain and, hence, are non-specific to the condition [82]. Some data indicate that such pain-related brain changes observed with VBM are probably reversible [83].

Specificity of results

Almost all functional imaging studies on primary headache investigated either patients with migraine or patients with TAC, but not both. Hence, there are basically no data directly investigating the specificity of the previously-cited neuroimaging results for either headache disorder. Differences in applied methodology make it difficult to compare results across studies. However, in one particular case study, a patient who had both migraine and cluster headaches [42] had a typical migraine attack in the PET scanner and the data obtained indicated brainstem activation, but no posterior hypothalamic activation, which suggested that the functional imaging data reflect the clinical phenotype.

Future research will have to implement 'head-to-head' comparisons to clarify whether findings such as brainstem involvement in migraine, or hypothalamic activation in cluster headaches, are reliable markers and specific to any disorder.

Future perspective

There is increasing interest in developing radiotracers, applicable for PET, which target specific receptors thought to be implicated in pain and headache pathogenesis, such as serotonin, glutamate, and cannabinoid receptors [84,85]. Studies using these tracers will help to map the location of disturbances in the brains of headache patients, and to evaluate the specific contribution of well-defined neuropharmacological systems. Moreover, MRI techniques are rapidly evolving that are suitable for the study of increasing numbers of small-sized brain structures and to detect subtle abnormalities. The underlying mechanisms of headache disorders are complex and it still remains difficult to 'connect the dots' from the many different studies in order to provide a comprehensive understanding of primary headache pathophysiology. Future studies aimed at reproducing previously published results and studies that combine psychophysiological, as well as multimodal imaging markers in larger patient populations may help overcome some of the inconsistencies, and improve our understanding of how different imaging markers relate to each other.

Moreover, neuroimaging studies on headache disorders have, so far, mainly been used on a group level to study the pathophysiology of the disorders. New multivariate methods, such as classification algorithms (e.g. support vector machines) may help to assess and classify individual patients. Once this becomes feasible, neuroimaging may aid the diagnosis in complex cases and facilitate the assessment of the efficacy of preventive headache drugs. Moreover, such techniques can be used to stratify patients to specific drugs.

Altogether, primary headache syndromes still have many more secrets to be uncovered, the continued study of the neurobiology involved, using functional imaging methods, will be rewarding.

References

1. Goadsby PJ, Lipton RB, and Ferrari MD. (2002). Migraine—current understanding and treatment. *New England Journal of Medicine*, **346**(4), 257–70.
2. Afridi SK, and Goadsby PJ. (2006). Neuroimaging of migraine. *Current Pain and Headache Reports*, **10**(3), 221–4.
3. Maniyar FH, and Goadsby PJ. (2013). Functional imaging in chronic migraine. *Current Pain and Headache Reports*, **17**(5), 333.
4. Lakhan SE, Avramut M, and Tepper SJ. (2013). Structural and functional neuroimaging in migraine: insights from 3 decades of research. *Headache*, **53**(1), 46–66.
5. Iacovelli E, Coppola G, Tinelli E, et al. (2012). Neuroimaging in cluster headache and other trigeminal autonomic cephalalgias. *Journal of Headache and Pain*, **13**(1), 11–20.
6. Apkarian AV, Bushnell MC, Treede RD, et al. (2005). Human brain mechanisms of pain perception and regulation in health and disease. *European Journal of Pain*, **9**(4), 463–84.
7. Valet M, Sprenger T, Boecker H, et al. (2004). Distraction modulates connectivity of the cingulo-frontal cortex and the midbrain during pain—an fMRI analysis. *Pain*, **109**(3), 399–408.
8. Peyron R, Laurent B, and Garcia-Larrea L. (2000). Functional imaging of brain responses to pain. A review and meta-analysis. *Neurophysiology Clinics*, **30**(5), 263–88.
9. May A, Kaube H, Buchel C, et al. (1998). Experimental cranial pain elicited by capsaicin: a PET study. *Pain*, **74**(1), 61–6.
10. May A, Bahra A, Buchel C, et al. (1998). Hypothalamic activation in cluster headache attacks. *Lancet*, **352**(9124), 275–8.
11. Afridi SK, Giffin NJ, Kaube H, et al. (2005). A positron emission tomographic study in spontaneous migraine. *Archives of Neurology*, **62**(8), 1270–5.
12. Weiller C, May A, Limmroth V, et al. (1995). Brain stem activation in spontaneous human migraine attacks. *Nature Medicine*, **1**(7), 658–60.
13. Afridi SK, Matharu MS, Lee L, et al. (2005). A PET study exploring the laterality of brainstem activation in migraine using glyceryl trinitrate. *Brain*, **128**(Pt 4), 932–9.
14. Sprenger T, Valet M, Boecker H, et al. (2006). Opioidergic activation in the medial pain system after heat pain. *Pain*, **122**(1–2), 63–7.
15. Zubieta JK, Smith YR, Bueller JA, et al. (2001). Regional mu opioid receptor regulation of sensory and affective dimensions of pain. *Science*, **293**(5528), 311–5.
16. Goadsby PJ, and Lipton RB. (1997). A review of paroxysmal hemicranias, SUNCT syndrome and other short-lasting headaches with autonomic feature, including new cases. *Brain*, **120**(Pt 1), 193–209.
17. Headache Classification Subcommittee of the International Headache Society. (2004). The International Classification of Headache Disorders: 2nd edition. *Cephalalgia*, **24**(Suppl 1.), 9–160.
18. Palmieri A, Mainardi F, Maggioni F, et al. (2005). Cluster-like headache secondary to cavernous sinus metastasis. *Cephalalgia*, **25**(9), 743–5.
19. Moskowitz MA. (1988). Cluster headache: evidence for a pathophysiologic focus in the superior pericarotid cavernous sinus plexus. *Headache*, **28**(9), 584–6.
20. Schuh-Hofer S, Richter M, Israel H, et al. (2006). The use of radiolabelled human serum albumin and SPECT/MRI co-registration to study inflammation in the cavernous sinus of cluster headache patients. *Cephalalgia*, **26**(9), 1115–22.
21. Sianard-Gainko J, Milet J, Ghuysen V, et al. (1994). Increased parasellar activity on gallium SPECT is not specific for active cluster headache. *Cephalalgia*, **14**(2), 132–3.
22. Sprenger T, Boecker H, Tolle TR, et al. (2004). Specific hypothalamic activation during a spontaneous cluster headache attack. *Neurology*, **62**(3), 516–17.
23. Maniyar FH, Sprenger T, Monteith T, et al. (2014). Brain activations in the premonitory phase of nitroglycerin triggered migraine attacks. *Brain*, **137**, 232–242.
24. Denuelle M, Fabre N, Payoux P, et al. (2007). Hypothalamic activation in spontaneous migraine attacks. *Headache*, **47**(10), 1418–26.
25. May A, Ashburner J, Buchel C, et al. (1999). Correlation between structural and functional changes in brain in an idiopathic headache syndrome. *Nature Medicine*, **5**(7), 836–8.
26. Absinta M, Rocca MA, Colombo B, et al. (2012). Selective decreased grey matter volume of the pain-matrix network in cluster headache. *Cephalalgia*, **32**(2), 109–15.
27. Yang FC, Chou KH, Fuh JL, et al. (2013). Altered gray matter volume in the frontal pain modulation network in patients with cluster headache. *Pain*, **154**(6), 801–7.
28. Lodi R, Pierangeli G, Tonon C, et al. (2006). Study of hypothalamic metabolism in cluster headache by proton MR spectroscopy. *Neurology*, **66**(8), 1264–6.
29. Wang SJ, Lirng JF, Fuh JL, et al. Reduction in hypothalamic 1H-MRS metabolite ratios in patients with cluster headache. *Journal of Neurology, Neurosurgery & Psychiatry*, **77**(5), 622–5.
30. Rocca MA, Valsasina P, Absinta M, et al. (2010). Central nervous system dysregulation extends beyond the pain-matrix network in cluster headache. *Cephalalgia*, **30**(11), 1383–91.

31. Leone M, Franzini A, and Bussone G. (2001). Stereotactic stimulation of posterior hypothalamic gray matter in a patient with intractable cluster headache. New England Journal of Medicine, **345**(19), 1428–9.
32. Leone M, Franzini A, Cecchini AP, et al. (2010). Hypothalamic deep brain stimulation in the treatment of chronic cluster headache. *Therapeutic Advances in Neurologic Disorders*, **3**(3), 187–95.
33. May A, Leone M, Boecker H, et al. (2006). Hypothalamic deep brain stimulation in positron emission tomography. *Journal of Neuroscience*, **26**(13), 3589–93.
34. Sprenger T, Willoch F, Miederer M, et al. (2006). Opioidergic changes in the pineal gland and hypothalamus in cluster headache: a ligand PET study. *Neurology*, **66**(7), 1108–10.
35. Barrett T, Kent S, and Voudouris N. (2000). Does melatonin modulate beta-endorphin, corticosterone, and pain threshold? *Life Science*, **66**(6), 467–76.
36. Sprenger T, Ruether KV, Boecker H, et al. (2007). Altered metabolism in frontal brain circuits in cluster headache. *Cephalalgia*, **27**(9), 1033–42.
37. Sprenger T, Berthele A, Platzer S, et al. (2005). What to learn from in vivo opioidergic brain imaging? *European Journal of Pain*, **9**(2), 117–21.
38. May A, Bahra A, Buchel C, et al. (1999). Functional magnetic resonance imaging in spontaneous attacks of SUNCT: short-lasting neuralgiform headache with conjunctival injection and tearing. *Annals of Neurology*, **46**(5), 791–4.
39. Matharu MS, Cohen AS, Frackowiak RS, et al. (2006). Posterior hypothalamic activation in paroxysmal hemicrania. *Annals of Neurology*, **59**(3), 535–45.
40. Matharu MS, Cohen AS, McGonigle DJ, et al. (2004). Posterior hypothalamic and brainstem activation in hemicrania continua. *Headache*, **44**(8), 747–61.
41. Peatfield R, Bahra A, Goadsby PJ. (1998). Trigeminal-autonomic cephalgias (TACs). *Cephalalgia*, **18**(6), 358.
42. Bahra A, Matharu MS, Buchel C, et al. (2001). Brainstem activation specific to migraine headache. *Lancet*, **357**(9261), 1016–17.
43. Raskin NH, Hosobuchi Y, and Lamb S. (1987). Headache may arise from perturbation of brain. *Headache*, **27**(8), 416–20.
44. Veloso F, Kumar K, and Toth C. (1998). Headache secondary to deep brain implantation. *Headache*, **38**(7), 507–15.
45. Haas DC, Kent PF, and Friedman DI. (1993). Headache caused by a single lesion of multiple sclerosis in the periaqueductal gray area. *Headache*, **33**, 452–5.
46. Matharu MS, Bartsch T, Ward N, et al (2004). Central neuromodulation in chronic migraine patients with suboccipital stimulators: a PET study. *Brain*, **127**(Pt 1), 220–30.
47. Goadsby PJ. (2002). Neurovascular headache and a midbrain vascular malformation- evidence for a role of the brainstem in chronic migraine. *Cephalalgia*, **22**, 107–11.
48. Rocca MA, Ceccarelli A, Falini A, et al. (2006). Brain gray matter changes in migraine patients with T2-visible lesions: a 3-T MRI study. *Stroke*, **37**(7), 1765–70.
49. Welch KM, Nagesh V, Aurora SK, et al. (2001). Periaqueductal gray matter dysfunction in migraine: cause or the burden of illness? *Headache*, **41**(7), 629–37.
50. Valfre W, Rainero I, Bergui M, et al. (2008). Voxel-based morphometry reveals gray matter abnormalities in migraine. *Headache*, **48**(1), 109–17.
51. Kim JH, Suh SI, Seol HY, et al. Regional grey matter changes in patients with migraine: a voxel-based morphometry study. *Cephalalgia*, **28**(6), 598–604.
52. Granziera C, DaSilva AF, Snyder J, et al. Anatomical alterations of the visual motion processing network in migraine with and without aura. *PLoS Medicine*, **3**(10), e402.
53. DaSilva AF, Granziera C, Snyder J, et al. (2007). Thickening in the somatosensory cortex of patients with migraine. *Neurology*, **69**(21), 1990–5.
54. Maleki N, Becerra L, Brawn J, et al. (2012). Concurrent functional and structural cortical alterations in migraine. *Cephalalgia*, **32**(8), 607–20.
55. Datta R, Detre JA, Aguirre GK, et al. (2011). Absence of changes in cortical thickness in patients with migraine. *Cephalalgia*, **31**(14), 1452–8.
56. Messina R, Rocca MA, Colombo B, et al. (2013). Cortical abnormalities in patients with migraine: a surface-based analysis. *Radiology*, **268**(1), 170–80.
57. Russo A, Tessitore A, Giordano A, et al. (2012). Executive resting-state network connectivity in migraine without aura. *Cephalalgia*, **32**(14), 1041–8.
58. Mainero C, Boshyan J, and Hadjikhani N. (2011). Altered functional magnetic resonance imaging resting-state connectivity in periaqueductal gray networks in migraine. *Annals of Neurology*, **70**(5), 838–45.
59. Yu D, Yuan K, Zhao L, et al. (2012). Regional homogeneity abnormalities in patients with interictal migraine without aura: a resting-state study. *NMR in Biomedicine*, **25**(5), 806–12.
60. Xue T, Yuan K, Cheng P, et al. (2013). Alterations of regional spontaneous neuronal activity and corresponding brain circuit changes during resting state in migraine without aura. *NMR Biomed*, **26**(9), 1051–8.
61. Xue T, Yuan K, Zhao L, et al. (2012). Intrinsic brain network abnormalities in migraines without aura revealed in resting-state fMRI. *PLoS One*, **7**(12), e52927.
62. Sprenger T, Seifert CL, Valet M, et al. (2010). Abnormal interictal large-scale brain network connectivity in episodic migraine. *Headache*, **50**(Suppl. 1), 71.
63. Jin C, Yuan K, Zhao L, et al. (2013). Structural and functional abnormalities in migraine patients without aura. *NMR in Biomedicine*, **26**(1), 58–64.
64. Lothe A, Merlet I, Demarquay G, et al. (2008). Interictal brain 5-HT1A receptors binding in migraine without aura: a 18F-MPPF-PET study. *Cephalalgia*, **28**(12), 1282–91.
65. Lashley K. (1941). Patterns of cerebral integration indicated by the scotomas of migraine. Archives of Neurology & Psychiatry, **46**, 331–9.
66. Fabricius M, Fuhr S, Bhatia R, et al. (2006). Cortical spreading depression and peri-infarct depolarization in acutely injured human cerebral cortex. *Brain*, **129**(Pt 3), 778–90.
67. Strong AJ, Fabricius M, Boutelle MG, et al. (2002). Spreading and synchronous depressions of cortical activity in acutely injured human brain. *Stroke*, **33**(12), 2738–43.
68. Mayevsky A, Doron A, Manor T, et al. (1996). Cortical spreading depression recorded from the human brain using a multiparametric monitoring system. *Brain Research*, **740**(1–2), 268–74.
69. Olesen J, Larsen B, and Lauritzen M. (1981). Focal hyperemia followed by spreading oligemia and impaired activation of rCBF in classic migraine. *Annals of Neurology*, **9**(4), 344–52.
70. Sanchez del Rio M, Bakker D, Wu O, et al. (1999). Perfusion weighted imaging during migraine: spontaneous visual aura and headache. *Cephalalgia*, **19**(8), 701–7.
71. Afridi S, Kaube H, and Goadsby PJ. (2005). Occipital activation in glyceryl trinitrate induced migraine with visual aura. *Journal of Neurology, Neurosurgery & Psychiatry*, **76**(8), 1158–60.
72. Cao Y, Welch KM, Aurora S, et al. (1999). Functional MRI-BOLD of visually triggered headache in patients with migraine. *Archives of Neurology*, **56**(5), 548–54.
73. Hadjikhani N, Sanchez Del Rio M, Wu O, et al. (2001). Mechanisms of migraine aura revealed by functional MRI in human visual cortex. Proceedings of the National Academy of Sciences, USA, **98**(8), 4687–92.
74. Hougaard A, Amin FM, Hoffmann MB, et al. (2013). Interhemispheric differences of fMRI responses in migraine with unilateral aura. *Cephalalgia*, **33**, 217.
75. Woods RP, Iacoboni M, and Mazziotta JC. (1994). Brief report: bilateral spreading cerebral hypoperfusion during spontaneous migraine headache. *New England Journal of Medicine*, **331**(25), 1689–92.
76. Denuelle M, Fabre N, Payoux P, et al. (2008). Posterior cerebral hypoperfusion in migraine without aura. *Cephalalgia*, **28**(8), 856–62.
77. Coghill RC, Sang CN, Berman KF, et al. (1998). Global cerebral blood flow decreases during pain. *Journal of Cerebral Blood Flow & Metabolism*, **18**(2), 141–7.
78. Cao Y, Aurora SK, Nagesh V, et al. (2002). Functional MRI-BOLD of brainstem structures during visually triggered migraine. *Neurology*, **59**(1), 72–8.

79. Schmidt-Wilcke T, Leinisch E, Straube A, et al. (2005). Gray matter decrease in patients with chronic tension type headache. *Neurology*, **65**(9), 1483–6.
80. Kuchinad A, Schweinhardt P, Seminowicz DA, et al. (2007). Accelerated brain gray matter loss in fibromyalgia patients: premature aging of the brain? *Journal of Neuroscience*, **27**(15), 4004–7.
81. Valet M, Gundel H, Sprenger T, et al. (2009). Patients with pain disorder show gray-matter loss in pain-processing structures: a voxel-based morphometric study. *Psychosomatic Medicine*, **71**(1), 49–56.
82. May A. (2008). Chronic pain may change the structure of the brain. *Pain*, **137**(1), 7–15.
83. Teutsch S, Herken W, Bingel U, et al. (2008). Changes in brain gray matter due to repetitive painful stimulation. *NeuroImage*, **42**(2), 845–9.
84. Li Z, Gifford A, Liu Q, et al. (2005). Candidate PET radioligands for cannabinoid CB1 receptors: [18F]AM5144 and related pyrazole compounds. *Nuclear Medicine and Biology*, **32**(4), 361–6.
85. Rstad E, Platzer S, Berthele A, et al. (2006). Towards NR2B receptor selective imaging agents for PET-synthesis and evaluation of N-[11C]-(2-methoxy)benzyl (E)-styrene-, 2-naphthyl- and 4-trifluoromethoxyphenylamidine. *Bioorganic & Medicinal Chemistry*, **14**(18), 6307–13.

CHAPTER 12

Epilepsy and related disorders

Dewi Schrader, Neda Bernasconi,
and Andrea Bernasconi

Introduction

Epilepsy, a disorder of the brain characterized by an enduring predisposition to generate epileptic seizures [1], affects over 50 million people worldwide [2]. Underlying aetiologies include structural, metabolic, and genetic abnormalities [3]. More than one third of these patients suffer from seizures that are resistant to antiepileptic drugs [4]. The consequences of recurrent seizures are severe, and include an increased risk of injury, psychosocial and economic impairment [5], and death [6]. In cases of drug-resistant focal onset epilepsy, when a structural abnormality is identified, surgical resection of the epileptogenic lesion offers patients the chance at a complete cure [6]. Temporal lobe epilepsy (TLE) secondary to mesiotemporal sclerosis and extratemporal lobe neocortical epilepsy secondary to dysplasias are the two most common drug-resistant epilepsy syndromes amenable to surgery [7,8]. Early identification of a lesion allows timely intervention with resective surgery, limits the long-term effects of recurrent seizures and medication, and has been shown to have positive consequences on cognitive outcome and brain development [9].

The overall goal of neuroimaging in epilepsy is three-fold. First, it is pivotal in revealing the underlying cause of seizures and allows for a precise definition of the various epileptic syndromes, including life-threatening conditions, such as catastrophic epilepsy in paediatric cohorts. Secondly, imaging plays an integral role in the presurgical work-up and is aimed at minimizing the risk of deficits through the identification of functional (eloquent) brain areas. Finally, imaging studies provide important insights into the organization of epileptogenic networks and the effect of ongoing seizures on the brain. This chapter provides an overview of the conventional and advanced quantitative image analysis methods used to investigate main epilepsy syndromes—TLE, neocortical extratemporal epilepsy related to cortical dysplasias, and idiopathic generalized epilepsy.

Computed tomography

The ability of computer tomography (CT) to provide an inexpensive, accessible, and rapid view of the brain makes it a useful tool in the acute assessment of patients with new onset seizures or those with exacerbation of known attacks. The most common pathologies detected in middle-aged and older adults include intracranial bleeds, infarcts, and tumours. However, in younger patients in whom the underlying pathology is usually subtle (e.g. mesiotemporal sclerosis or focal cortical dysplasia), the magnetic resonance imaging (MRI) should prevail.

Conventional structural MRI

Structural (anatomical) MRI has revolutionized the evaluation of patients with epilepsy and is the primary tool for detecting epileptogenic lesions [10]. (Box 12.1)

Multiple studies have demonstrated that the best predictor of post-surgical seizure freedom is complete resection of the lesion identified on preoperative scans [6]. However, compared with other neurological disorders, the evaluation of epilepsy can be difficult because the underlying abnormality may be subtle and easily missed when inspecting conventional MR images. Indeed, despite advances in hardware and sequences, up to 50% of patients evaluated for drug-resistant epilepsy have unremarkable structural MRI [11]. Sensitivity for detecting subtle epileptogenic lesions is enhanced by the use of specialized imaging protocols with reduced slice thickness and increased resolution, and the interpretation of scans by a reader experienced in the evaluation of epilepsy patients, with appropriate clinical information [11,12]. As an alternative visualization modality to orthogonal planes, curvilinear multiplanar reformatting might further increase the detection yields of neocortical malformative lesions [13,14]. The perpendicular orientation of the curved slices in relation to the gyri reduces artefactual cortical thickening by decreasing the obliquity of the slices in relation to the long axes of gyri and the volume averaging of different tissue types.

The advent of high-field magnets at 3 T, combined with the use of phased array coils instead of a conventional quadrature coil, has resulted in accelerated image acquisition, and improved signal-to-noise (SNR) and contrast-to-noise ratios [15–17]. The ideal sequence should be one that provides high spatial resolution, high contrast, complete brain coverage, and does so in a short period of time. Several published acquisition protocols designed to increase the sensitivity for the detection of epileptogenic lesions exist [18–21]. At a minimum, the MRI assessment should include an anatomic high-resolution T_1-weighted, a T_2-weighted, and a fluid-attenuated inversion recovery (FLAIR) sequence. In the authors experience, high-resolution T_1-weighted 3D images with millimetric or submillimetric isotropic voxels provide exquisite anatomic details. They also provide the best substrate for digital image processing. T_2 and FLAIR sequences are useful for detecting signal anomalies, usually hyperintensities, associated with pathology (e.g. gliosis). Ideally, these sequences should also provide three-dimensional (3D) images with isotropic voxel size. Otherwise, slices should be as thin as possible and acquired in at least two orthogonal planes, with coronal slices orientated perpendicular to the long axis of the

Box 12.1 Epilepsy-related structural pathology

- Mesial temporal sclerosis.
- Malformations of cortical development (dysplasias, heterotopias, polymicrogyrias).
- Trauma.
- Tumour (dysembryoplastic neuro-epithelial tumour, gliomas).
- Vascular malformations (cavernous angioma).
- Infection (cystercercosis).
- Neurocutaneous syndromes (tuberous sclerosis, Sturge–Weber syndrome).
- Stroke.

hippocampus in order to be able to examine this structure in cross section for TLE and axial slices to evaluate the neocortex.

In addition to T_1- and T_2-weighted imaging, magnetic susceptibility differences between tissue classes can be used as a new type of contrast. Susceptibility-weighed imaging uses a sequence that is sensitive to brain iron and calcium contents [22,23]. It has been applied to identify cavernous angiomatas, scar tissue related to traumatic brain injury [23,24], and is promising for the delineation of focal cortical dysplasia [15,22] and hippocampal sclerosis [25]. However, the susceptibility effects that provide advantageous T_2*-weighted contrast also cause strong artefacts degrading image quality close to pneumatized structures. Particularly, the inferior temporal lobe and the orbitofrontal region are prone to this effect because of their close relationship to the sinuses, sphenoid, and petrous bone.

The clinical value of ultra-high field strength MRI is currently unknown. High-resolution imaging at 7.0 T appears quite promising for a more detailed delineation and characterization of structural changes related to epileptogenic lesions [25]. However, because the SNR increases approximately in proportion to the field strength, under optimal conditions, the maximal gain in isotropic resolution that can be expected by increasing the static magnetic field from 3.0 to 7.0 T is only about 30% in each dimension. This incremental increase in resolution may not be clinically significant for most routine anatomic brain MRI exams. Therefore, it is not an inevitable conclusion at this time that 7.0 T MRI will replace 3.0 T systems to become the 'new standard' for routine clinical structural neuroimaging of epileptic patients.

Image processing of structural MRI

In surgical series, the two most common histopathological substrates encountered are hippocampal sclerosis and focal cortical dysplasia. The radiological spectrum of these abnormalities on MRI, includes obvious lesions that are easily detected visually to more subtle anomalies that are often overlooked due to the complexity brain folding patterns and their resemblance to normal brain tissue. By applying powerful computer algorithms to structural MRI data to mathematically model shape, folding complexity, and tissue characteristics of anatomical structures, quantitative image analysis can be used to measure *in vivo* changes in healthy and diseased brain [10,11]. These techniques can be applied to clinical MRI data without the cost of additional scanning time or exposure to ionizing radiation.

Temporal lobe epilepsy

TLE, the most common form of drug-resistant focal epilepsy, is characterized by recurrent seizures originating from mesiotemporal lobe structures. Mesiotemporal sclerosis is a general histopathological term used to describe cell loss and astrocytic gliosis seen on post-mortem and surgical specimens of these patients [26]. In addition to the hippocampus, such pathological changes are frequently seen in the amygdala [27], entorhinal cortex [28], temporopolar cortex [29], and the grey and white matter of the temporal lobe [30]. There are, however, significant variations in the degree, pattern and regional distribution of histopathological abnormalities among patients [31]. Indeed, cell loss and gliosis may be subtle throughout the hippocampus or clearly predominate in a single subfield (typically CA1), or segments (e.g. the anterior hippocampus). Alternatively, abnormalities may prevail in the amygdala or entorhinal cortex [27].

On visual inspection of conventional MRI, classical signs of mesiotemporal sclerosis consist of noticeable hippocampal atrophy, decreased T_1 signal, and loss of the internal hippocampal structure and concomitant increased T_2 signal intensity [32] (Fig. 12.1).

The T_2-signal increase is positively correlated with gliosis [33]. Temporal lobe atrophy may also be seen [34,35]. Other findings may include atrophy of the ipsilateral fornix and mammillary body [36,37]. Subtle mesiotemporal sclerosis is best visualized on 3.0 T MRI yielding high-resolution 3D images with millimetric or sub-millimetric isotropic voxels, which provide exquisite anatomic details (Fig. 12.2).

The sensitivity of conventional MRI to detect atrophy may be increased by volumetry analysis, which has been shown to be

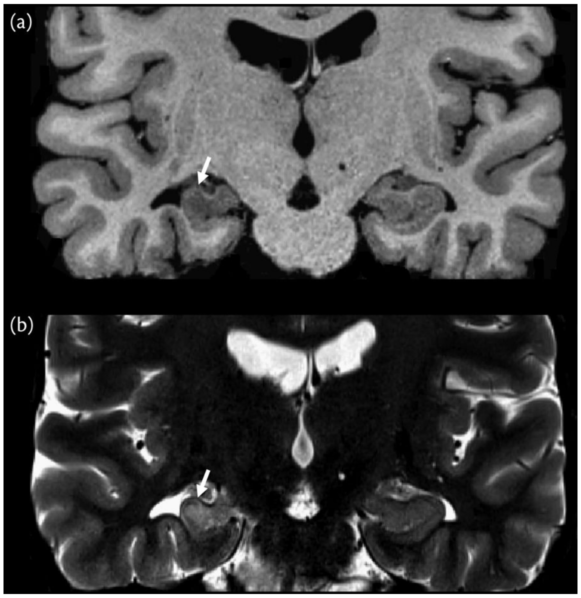

Fig. 12.1 Hippocampal sclerosis on MRI. (a) Coronal 3.0 T T_1-weighted MRI in a patient with drug-resistant left temporal lobe epilepsy shows marked atrophy and decreased signal intensity in the left hippocampal body (*arrow*). (b) Coronal T_2-weighted image in the same patient demonstrates a clear signal hyperintensity within the atrophic hippocampus (*arrow*).

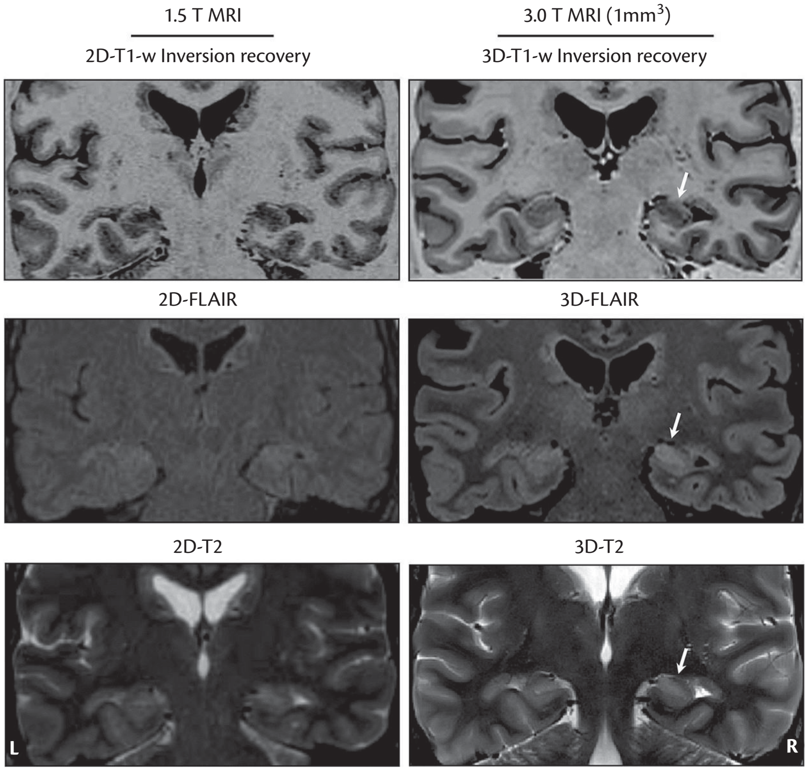

Fig. 12.2 Hippocampal sclerosis at 1.5 T (2D) and 3.0 T (3D). The 1-mm isotropic images acquired at 3.0 T in a patient with right temporal lobe epilepsy and normal hippocampal volumes (right panel) show subtle hypointensity on inversion recovery, and slight hyperintensity on FLAIR and T_2 (arrows) at the level of the right hippocampus (probably corresponding to CA4-dentate subfields). These markers of hippocampal sclerosis are not easily detectable on 2D anisotropic images (in plane resolution of 3 mm) acquired on a 1.5 T MR scanner (left panels). Indeed, the clinical MRI at 1.5 T was reported as normal.

accurate and reproducible [38–43]. Hippocampal volumetry can lateralize the seizure focus in over 90% [44] and the degree of MRI volume loss correlates with cell loss on surgical specimens [45]. In TLE, volumetry is essential for surgical target localization. Besides the hippocampus, this technique detects atrophy in the entorhinal cortex [38,39], amygdala and temporopolar region [40].

In clinical settings, manual segmentation of mesiotemporal structures is often restricted to the hippocampus, since the addition of amygdala and entorhinal cortex make it prohibitively long. Automatic hippocampal segmentation studies in TLE have been sparse and have so far provided rather poor results [46–53]. Recently, it has been shown that shape and positioning abnormalities of the hippocampus and surrounding structures hamper performance of these automated techniques [54]. Indeed, in addition to atrophy, about 40% of TLE patients show atypical shape and positioning of the hippocampus [55,56]. These features, commonly referred to as malrotation, are considered markers of neurodevelopmental abnormalities [56,57] and may contribute to the pathogenesis of this condition [58,59]. They are mainly characterized by a rounder appearance of and vertical orientation of the hippocampus, and an abnormally deep collateral sulcus [55,57]. Based on these observations, an automated segmentation algorithm that integrates deformable parametric surfaces and multiple templates in a unified framework was developed. The high performance of this algorithm regardless of atrophy and shape variants identified it as a robust segmentation tool for hippocampal volumetry compared with others [60].

Despite technical improvements in conventional techniques, including acquisitions with thin contiguous slices and 3D reformatting [61], and high field strength magnets, in up to 40% of patients with drug-resistant TLE, hippocampal volumes are normal, even though histopathological examination of the surgically resected tissue reveals subtle mesiotemporal sclerosis [41,62,63]. In tertiary care epilepsy centres worldwide the proportion of these patients with non-diagnostic MRI has gradually increased over the years. In these cases, alternative approaches to evaluate structural brain integrity include entorhinal cortex volumetry, which can lateralize the seizure focus in 25% of cases [41], and quantitation of hippocampal and temporal lobe T_2-signal [64–66], which can correctly lateralize the seizure focus in 82% of patients with a normal appearing MRI [64].

Although MRI volumetry is a valuable quantitative technique to assess pathology, it provides only a global estimate of atrophy, limiting sensitivity to detect subtle focal abnormalities. Statistical surface shape modelling allows localizing structural alterations at a sub-millimetric level. This methodology has been applied to study hippocampal and thalamic subregional atrophy in TLE [67–69].

Advanced quantitative image analysis techniques also give valuable insight in to the natural history of TLE. In a large cross-sectional study, it has been shown that there is progressive atrophy in relation to epilepsy duration of the mesial temporal structures including the hippocampus, amygdala, and entorhinal cortex ipsilateral to the seizure focus [70]. Moreover, structural abnormalities in drug-resistant TLE are not limited to the mesial temporal lobe, but

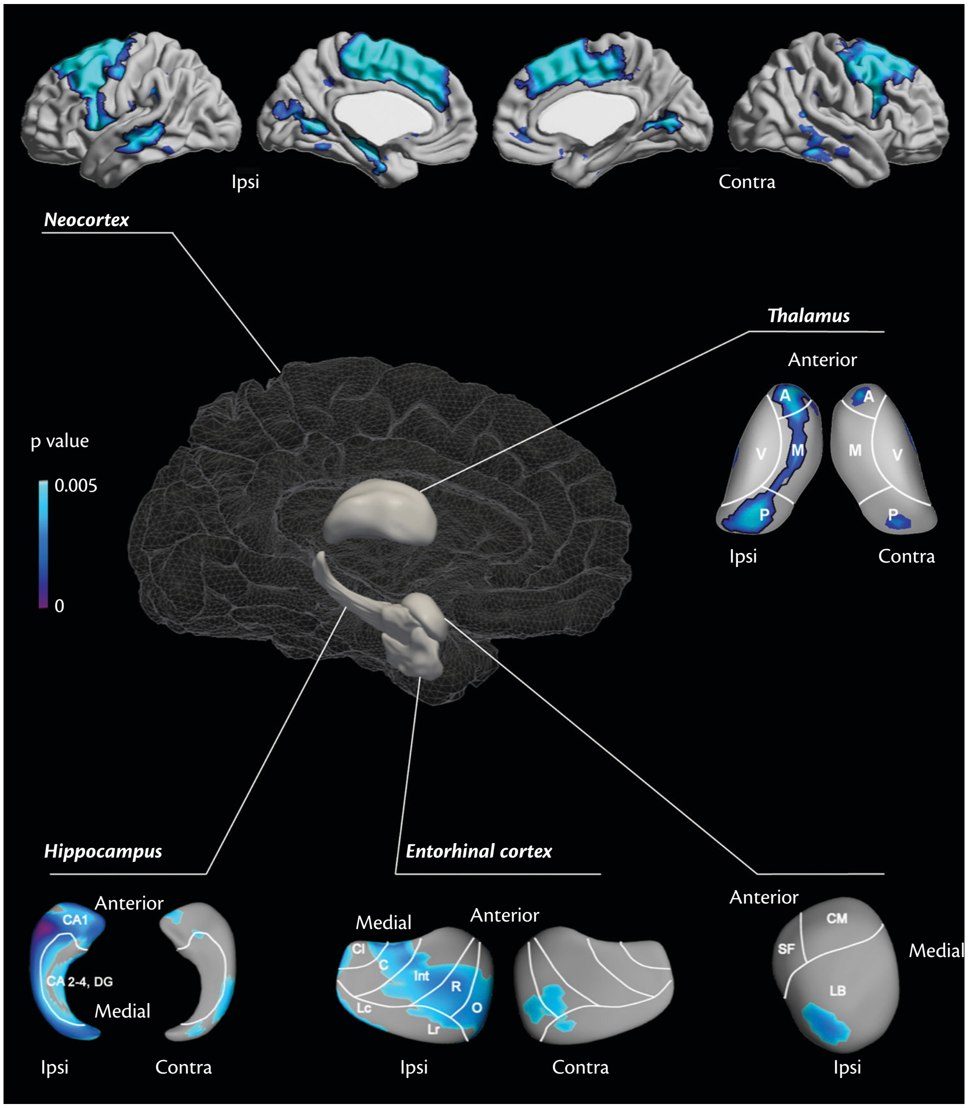

Fig. 12.3 Morphological alterations associated with drug-resistant temporal lobe epilepsy. This condition is associated with widespread histopathological anomalies (neuronal loss and gliosis) in both subcortical limbic regions and the neocortex. Morphometric MRI validates *ex vivo* neuropathological findings. Maps of atrophy are obtained using surface-based analysis of neocortical thickness and statistical shape modelling of subcortical structures. Neocortical thinning is mainly found in the fronto-central and temporal regions. Atrophy in subcortical limbic structures predominates in hippocampal CA1 subfield, latero-basal (LB) amygdalar nuclear division, orbital (O) and rostral (R) subfields of the entorhinal cortex, and thalamic medial subdivisions. Ipsi and contra refer to ipsilateral and contralateral to the epileptic focus, respectively.

also affect several neocortical regions, possibly by involvement of limbic pathways through the epileptogenic network. Indeed, whole brain studies using voxel-based morphometry [10,71–74) and measurement of cortical thickness [74–78] have shown widespread atrophy, particularly in the fronto-central areas (Fig. 12.3).

In a combined cross-sectional and longitudinal analysis, it has been demonstrated that patients suffering from epilepsy for longer than 14 years had neocortical atrophy that progressed more rapidly that in those with shorter disease duration, and showed progressive neocortical atrophy that was distinct from normal aging, likely reflecting seizure-induced damage [78]. Our findings, combined with functional data showing progressive cognitive decline in TLE [79] and evidence demonstrating that recurrent electroencephalography (EEG) discharges are associated with extension of the epileptogenic network [80], provide compelling evidence that TLE is a progressive disorder that warrants serious consideration of early surgery when seizures are medication-resistant.

Focal cortical dysplasias

The histopathological spectrum of focal cortical dysplasia, a malformation of cortical development, ranges from subtle isolated cortical dyslamination (ILAE Type I) to lesions with associated large dysplastic neurons (ILAE Type IIa), balloon cells (ILAE Type IIb), and varying degree of gliosis [81]. The most common characteristics of focal cortical dysplasia on MRI include cortical thickening, blurring of the gray matter–white matter boundary, and white matter hyperintensity on T_2 and FLAIR [7,11,82]. The funnel-shaped transmantle sign [83] is a useful marker and is apparent in the majority of patients with Type II dysplasias [82,84–89] (Fig. 12.4).

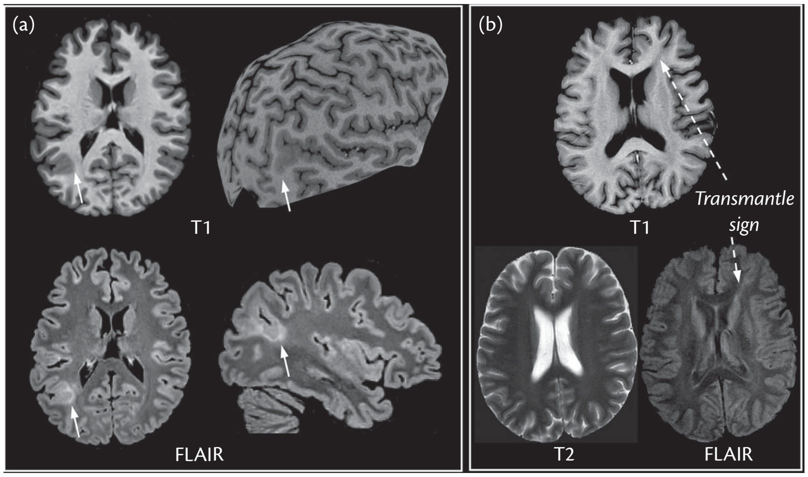

Fig. 12.4 Imaging characteristics of focal cortical dysplasia. (a) High-resolution 3.0 T sections showing focal cortical dysplasia ILAE type IIb in the right inferior parietal region. The main characteristics of dysplasia are thickening of the neocortical gray matter (shown on axial and curvilinear reformatting of T_1-weighted images, arrows), blurring of the gray–white matter transition (resulting from aggregates of large neurons, hypomyelination, and gliosis), and hyperintense signal, best seen on FLAIR (arrows). (b) High-resolution 3.0 T MRI of a 23-year-old patient with drug-resistant cryptogenic frontal lobe epilepsy. Repeated 1.5 T MRI scans had been reported to be normal. Visual evaluation of the 3.0 T volumetric T_1-weighted and FLAIR (isotropic 1-mm^3 voxel size) revealed a subtly increased white matter signal extending from the bottom of the sulcus harbouring the lesion towards the margin of the frontal horn of the lateral ventricle. This transmantle sign, a fingerprint of abnormal neuronal migration, was not visible on T_2-weighted MRI. Focal cortical dysplasia (ILAE type IIa) was diagnosed on histological examination of the resected tissue. The patient has remained seizure free with a follow-up of 3 years after surgery.

The MRI findings generally reflect the degree of the underlying histopathological abnormality [90]. In many cases, however, particularly in those displaying only disrupted laminar architecture, the dysplastic features can be very subtle, with more than 80% of patients with cortical dysplasia Type I having normal imaging [84,85,91]. Abnormal sulcation is another useful marker of cortical dysgenesis [92]. Using automated sulcal identification and labelling techniques, it has been demonstrated that 85% of small focal cortical dysplasia lesions, the vast majority of which were not seen on conventional imaging, are located at the bottom of an abnormally deep sulcus [93]. Therefore, in patients with focal seizures and apparently normal MRI, special attention should be paid to the inspection of sulcal bases to look for small subtle focal cortical dysplasia.

Voxel-based morphometry (VBM) is a method that allows for comparisons of gray matter concentration (or density) between groups [94]. This post-processing technique identified an increase in gray matter concentration overlapping with MRI-visible focal cortical dysplasia in up to 86% of cases [95–99]. Histopathological confirmation of focal cortical dysplasia in sites with increased gray matter concentration [97] suggests that VBM can also identify subtle focal cortical dysplasia lesions that may elude visual inspection. Voxel-based comparison can also be used to analyse raw intensities or intensities derived from quantitative MRI-contrasts such as T_2 relaxometry, double inversion recovery, and magnetization transfer MRI. These approaches have shown high sensitivity (87–100%) in detecting obvious malformations of cortical development [100–103]. In cases with unremarkable conventional MRI these techniques may identify areas concordant with clinical and EEG findings in up to 31%, but have low specificity [104,105]. Moreover, the histopathological substrate of these MRI signal changes remains unclear [106].

During the last decade, computer-based algorithms tailored to model the characteristic imaging features of focal cortical dysplasia have been developed [107–112]. Quantifiable abnormalities in intensity variations, increases in cortical thickness, and blurring of the gray–white matter transition are found in 87, 91, and 96% of lesions, respectively [113]. Modelling these features derived from 3D T_1-weighted images and combining them into a single composite map, demonstrated an increased sensitivity of visual identification of histologically-proven focal cortical dysplasia by 37% relative to conventional MRI (Fig. 12.5), while maintaining high specificity [109].

The detection of dysplasias can be further enhanced by the use of automated classifiers that combine the visually discernible MRI characteristics of focal cortical dysplasia (thickness, blurring, and hyperintensity) with high-order textural features that cannot be discriminated by the human eye [107,114,115]. It has been shown that this fully automated technique detects 17/20 (85%) of focal cortical dysplasia lesions, including 4/7 lesions that were undetected by conventional MRI methods [116].

One limitation of voxel-based approaches to lesion detection is that they do not fully take into account the complex topology of the cortical mantle and are therefore prone to errors due to volume averaging of non-adjacent cortex across sulci [97]. More recently, it has been shown that surface-based techniques, designed to model the previously mentioned features on an anatomically faithful representation of the cerebral cortex that allows the preservation of complex cortical topology and enhances anatomical correspondence [117], is effective in detecting small dysplastic lesions (Fig. 12.6).

C) Idiopathic generalized epilepsy

Idiopathic generalized epilepsies (IGE) form a distinct group of electroclinical syndromes characterized by absence seizures, myoclonic jerks, and generalized tonic–clonic seizures (alone or in varying combinations) in association with generalized discharges of spike-and-wave on EEG in the presence of a normal background

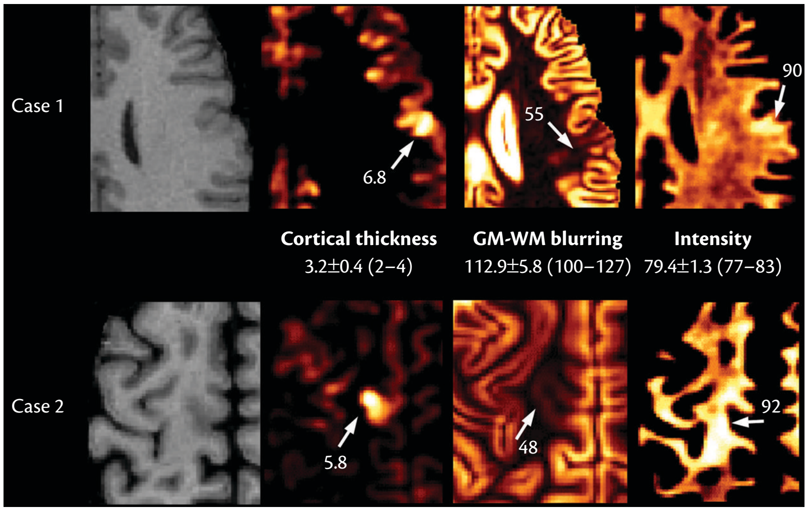

Fig. 12.5 Computational models of focal cortical dysplasia. Two cases of subtle, histologically-proven dysplasias ILAE type II. Conventional MR evaluation had been reported as normal in both cases. For each lesion, a representative slice of the T_1-weighted MRI and quantitative maps of cortical thickness, blurring of the gray-white matter transition, and tissue intensity are shown from left to right. For each feature, mean values ± standard deviation (and ranges) of healthy controls are shown.

[118]. The cellular underpinning is hypersynchronicity of thalamocortical circuits formed by the reciprocal excitatory and inhibitory connections between the cortex and thalamus [119]. These epilepsies occur in otherwise normal individuals and are believed to have a genetic, rather than structural basis [120]. While conventional MRI in this condition is usually reported to be normal, non-specific abnormalities including ventriculomegaly, enlarged perivascular spaces and white matter changes have been observed [121]. Advanced quantitative image post-processing of structural MRI, on the other hand, has identified subtle thalamic and cortical changes in this condition [122–127]. Using cortical thickness measures and thalamic volumetry, it has been shown that bilateral thalamic atrophy and widespread cortical thinning that was most prominent in fronto-central areas. Atrophy correlated with epilepsy duration. Importantly, patients with poorly-controlled seizures showed an even faster progression of atrophy of these neocortical regions, suggesting that neocortical atrophy in IGE is likely the consequence of generalized seizure activity inducing thalamocortical network remodelling [124].

Magnetic resonance spectroscopy

Proton magnetic resonance spectroscopy measures *in vivo* the concentration of metabolites, including N-acetyl aspartate [128], choline (Ch), and creatine (Cr). Depending upon the methods and hardware used, the spatial resolution of these measurements range

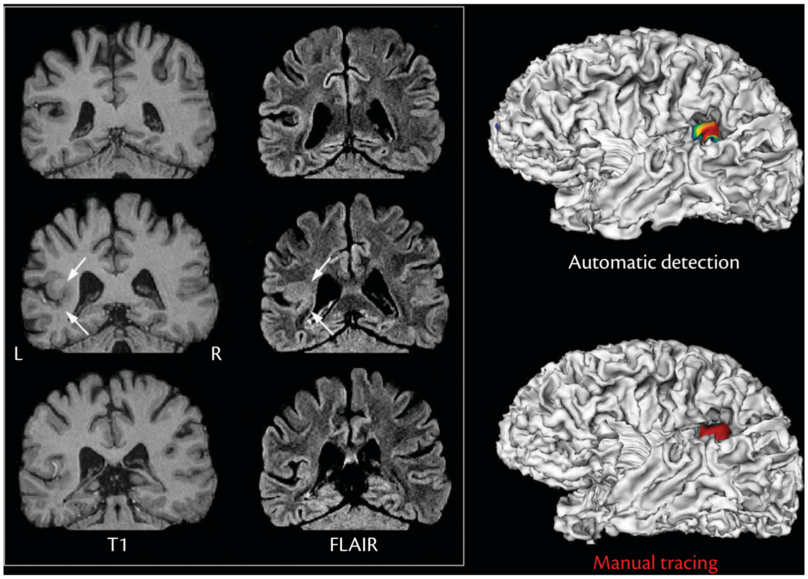

Fig. 12.6 Fully automatic classification of subtle focal cortical dysplasia. The lesional tissue detected automatically (colour map) is projected on the white matter surface. The manual tracing (red label) performed by an expert rater is shown below for comparison. Three contiguous T_1-weighted and FLAIR coronal images show the dysplasia (arrows).

from a few tens of cubic centimetres (cm^3) to several hundred microliters. To achieve spatial localization of the signal, a variety of techniques based on the concepts used in MRI have been developed to select specific regions of the brain. Most utilize spatially selective excitation and refocusing pulses to acquire a single 3D volume (single voxel), typically 1–8 cm^3. More recently, spectroscopic imaging methods have been developed that allow spectra from multiple locations to be acquired simultaneously, displaying metabolic images. Decreases in N-acetyl aspartate (NAA), a compound specific to neurons [129,130], may lateralize the seizure focus [131–133] and predict surgical outcomes [134,135] in drug-resistant TLE, thus yielding potential clinical value. Localization of seizure foci in neocortical epilepsy, on the other hand, is more challenging due to the technical constraints including limited brain coverage [136,137]. Reductions in NAA localize the focus to the correct lobe in about 60% of cases with various neocortical epilepsies [138–140].

In IGE, decreased NAA has been observed in the thalami [141–143] and the severity of the reduction correlates with epilepsy duration [143]. Reductions in NAA have also been seen in the bilateral frontal lobes suggesting an underlying dysfunction of thalamo-cortical circuits [144,145].

Using 1H magnetic resonance spectroscopy (MRS) and specialized analysis methods, it is possible to measure both glutamate and γ-aminobutyric acid (GABA) *in vivo*. Increases in glutamate, the primary excitatory neurotransmitter in human brain, have been observed in the ipsilateral hippocampus in ‘MRI-negative’ TLE [146,147], malformations of cortical development [147,148], and in the thalamus and frontal lobes in IGE [144,149]. Due to low SNR and the spectral overlap with other metabolites, attempts to measure GABA within the putative seizure focus have produced mixed results [150,151]. Notably, given the difficulties related to low SNR, the majority of studies have evaluated the occipital lobe, where small highly sensitive surface coils can be placed in close proximity to the brain. Alterations of GABA concentration occur in response to antiepileptic medication such as vigabatrin [152–154], topiramate, lamotrigine [155], and levetiracetam [156].

Overall, MRS is a technique that requires complicated analysis and is limited by sensitivity to background noise and low reproducibility. Furthermore, unlike subjects with TLE, patients with neocortical epilepsy often have poorly-defined epileptogenic regions and may have no accompanying MRI abnormality, posing significant additional demands with regard to the selection of the brain region to explore, the type of data acquisition (single voxel versus chemical shift imaging), and the analysis. Indeed, in addition to evaluating several metabolites in hundreds or thousands of locations, there are also natural variations between different lobes [157]. Depending upon the location of the region of interest, and its mixture of gray and white matter, the ‘normal’ levels of these metabolites will vary and complicate the detection of ‘abnormal’ regions. Thus, the routine use of spectroscopy in clinical epilepsy assessment is mainly restricted to patients with tumours or suspected neurometabolic diseases; in other cases, it should be regarded as a complementary investigation.

Diffusion MRI

Diffusion tensor MRI allows inferences about tissue microstructure by estimating the extent (mean diffusivity) and degree of directionality (fractional anisotropy) of passive water motion (diffusion) in a given voxel [158]. These indices are influenced by the arrangement of nerve fibres, with greater ease of diffusion parallel to tracts and perpendicular diffusion being limited by axonal membranes and myelin. Diffusion MRI may, thus, be used to assess microstructural and architectural integrity *in vivo*. The most widely used diffusion tensor parameters are fractional anisotropy (FA), an index of deviation of water diffusion from a random spherical displacement, and mean diffusion (MD), a scalar marker of bulk diffusion at each voxel.

In TLE, previous diffusion MRI studies have consistently shown decreased FA in temporo-limbic tracts such as the fornix [159,160], parahippocampal fibres [160–162], uncinate fasciculus [162–165], and cingulum bundle [160,166], as well as in several frontal and posterior fibre tracts including the inferior and superior longitudinal fascicles [160,162,165,167], internal and external capsule [166,168,169], and corpus callosum [166,168,169]. It has been postulated that these abnormalities are either a result of the direct excito-toxic effect of seizures or secondary to deafferentation due to loss of hippocampal connections [170]. Decreases in FA have been correlated with histological evidence of reduced axonal membrane circumference and decreased myelin thickness of the fimbria [171]. Relative to the widespread pattern of FA changes, MD anomalies follow a more restricted distribution [159,166,167]. In a recent study that assessed diffusion abnormalities along fibre tracts in TLE [172], this group showed that MD reduction ipsilateral to the focus decreases as a function of anatomical distance to the temporal lobe (Fig. 12.7).

In patients with MRI-visible focal cortical dysplasia, region-of-interest based [173–175] and whole-brain voxel-based analyses [176,177] have shown abnormalities in diffusion indices in the subcortical white matter adjacent to the malformation. In some patients with extratemporal epilepsy of frontal lobe origin and no visible MRI anomaly, voxel-based comparisons showed focal changes in diffusion indices that co-localized with the EEG focus [176–178]. However, diffusion abnormalities often extend beyond the epileptogenic region [176,177] highlighting the need to balance sensitivity and specificity. Moreover, given the variable direction of DT MRI indices across studies, the underlying nature of diffusion abnormalities needs to be clarified. To date, correlative studies have been limited to a single patient in whom gliosis was confirmed histologically in an area of increased diffusivity that was surgically resected [179].

In juvenile myoclonic epilepsy, a subtype of IGE, studies of diffusion have shown decreased FA in the internal capsule and thalamo-cortical white matter [180–182], as well as decreased connectivity of the supplementary motor area [183], which may relate to the myoclonus and cognitive dysfunction seen in this cohort [180,182]. Moreover, in patients with IGE, network analysis combining DT MRI and resting state functional magnetic resonance imaging (fMRI) data have shown an altered topology in regions hypothesized to play a role in the epileptogenesis of this condition including the mesial frontal cortex, putamen, and thalamus [184,185].

The ability of DT MRI tractography to delineate major white matter tract *in vivo* [186] has the potential to aid surgical planning by reducing the risk of damage to tracts connected to eloquent brain areas [187–189]. However, technical challenges, including the intra-operative shift of the brain that occurs following craniotomy, needs to be overcome for before this technique enters full clinical practice.

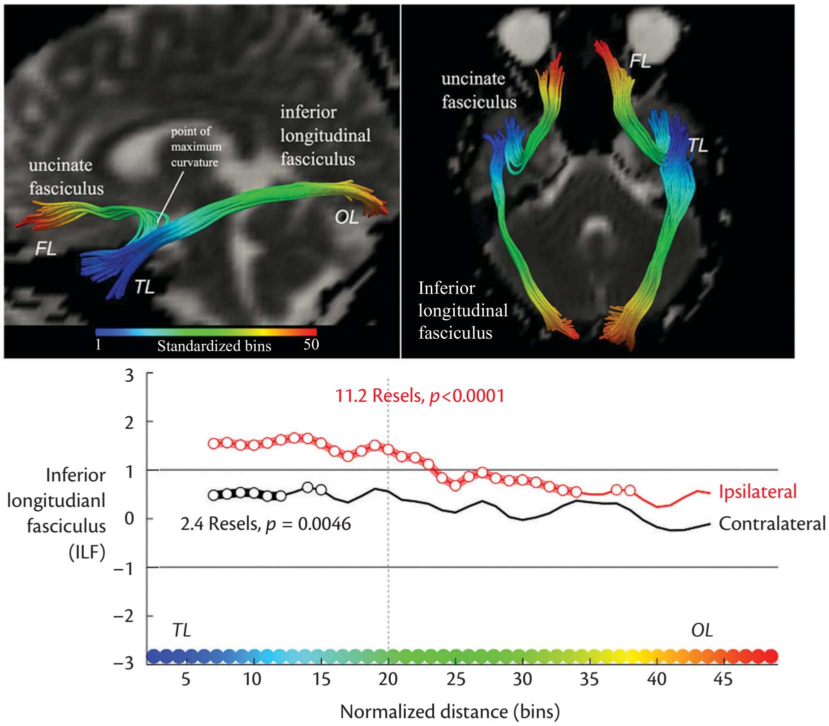

Fig. 12.7 Spatial patterns of water diffusion along white matter tracts in temporal lobe epilepsy. Seed-based deterministic tractography of the uncinate and inferior longitudinal fasciculi, overlaid on a non-diffusion T_2-weighted volume, are shown in oblique and axial views. Each tract is divided into 50 colour-coded bins, from start (blue) to end (red). Distances across tracts are standardized. The *z*-scores of mean diffusivity for the inferior longitudinal fasciculus are plotted along the normalized length of the tracts (colour-coded on the *x*-axis). Bin-wise average values of patients are compared with those obtained from healthy controls (0 on the y-axis represents the mean in healthy controls). Clusters of significant differences compared with controls are shown as circles. The vertical dashed lines on the graph separate the temporal (TL) from the occipital lobe (OL) portions of the tracts. Increased mean diffusivity is more prominent within the epileptogenic temporal lobe. Abnormalities taper off as the tract exits the temporal lobe. This centrifugal pattern of white matter diffusion abnormalities likely reflects astrogliosis and microstructure derangement related to seizure activity in the vicinity of the focus.

Magnetization transfer MRI

Magnetization transfer magnetic resonance imaging (MT MRI), based on the exchange of magnetization between protons in free water and those bound to macromolecules such as myelin, can highlight abnormally myelinated lesions. Using a voxel-based approach, MT MRI has been shown to identify malformations of cortical development, not including focal cortical dysplasia, and co-localized with electroclinical data in 33% of patients with cryptogenic epilepsy [103]. MT MRI has been shown to be helpful in the detection of cortical tubers in tuberous sclerosis and the transmantle sign in children with focal cortical dysplasia [190,191]. This technique may be considered in the evaluation of 'MRI-negative' neocortical epilepsy in children between the ages of 12–30 months when active myelination makes the detection of dysplastic lesions difficult [192].

Perfusion MRI

Cortical hyperperfusion is believed to be a marker of ictal activity. Arterial spin labelling (ASL) perfusion MRI allows the non-invasive estimation of interictal cerebral blood flow by tagging inflowing blood with a selective inversion pulse causing its longitudinal magnetization to differ from that of surrounding tissue [193]. Perfusion imaging has been used to demonstrate ictal hyperperfusion in patients with TLE [194,195]. Similarly, focal regions of interictal hypoperfusion that co-localized with clinical and EEG findings has been demonstrated in these patients [196,197], as well as in those with focal cortical dysplasia [196] and tuberous sclerosis [198]. ASL has the advantage over other methods of not requiring contrast injection or exposure to ionizing radiation, and relative ease of registration to structural MRI. However, it is technically complex, has reduced brain coverage and low SNR, and its availability is currently limited to specialized centres.

Functional MRI

fMRI maps local changes in blood flow that accompany neuronal activity by measuring variations in the ratio of oxyhaemoglobin and deoxyhaemoglobin concentrations through the blood oxygen level-dependent (BOLD) effect [199,200]. In surgical planning of patients with medically refractory partial epilepsy, its main clinical role is the localization of eloquent cortex involved in sensorimotor and language functions [201,202]. Various testing paradigms have been developed that compare the pattern of BOLD activation during a specific verbal task with a control state. Several studies have shown good concordance between fMRI for language lateralization and sodium amytal testing or cortical stimulation [203–205]. fMRI also has the potential to predict the risk of verbal episodic memory dysfunction in patients undergoing anterior temporal lobe resection for TLE [206,207]. However, as memory systems are complex, there are still challenges in developing paradigms that produce reliable and strong hippocampal activation at an individual level [208].

Neuronal activity during an epileptic discharge can be mapped using combined EEG and fMRI [209]. Mostly, EEG-fMRI has been used to record interictal discharges. These arise from the irritative zone, which is distinct from the epileptogenic zone. In rare instances, seizures are captured during monitoring, and can cause substantial movement artefacts, as well as being potentially damaging for the patient. In focal epilepsy, attempts to compare the localization of EEG-fMRI with EEG source localization or intracranial EEG have produced mixed results [210,211]. Moreover, interictal epileptiform discharges generally correlate with the BOLD signal in multiple brain regions. In some instances, no BOLD correlates of EEG spikes, or no spikes at all, are observed during the imaging session. This aspect is particularly relevant in patients with frontal lobe epilepsy and non-revealing structural MRI, who often have rare or no interictal spikes [212]. Thus, EEG-fMRI studies have mainly investigated pathophysiological mechanisms of seizure disorders. For instance, in IGE, generalized spike wave discharges have been associated with thalamic and cortical BOLD signal changes [213].

Although EEG-fMRI is unlikely to form a modality that can outline the extent of a focal abnormality, it might provide evidence for putative epileptogenic zones for further investigation [214], such as targeted MRI structural analysis or electrode implantation.

Single-photon emission computed tomography

Ictal–interictal subtraction single-photon emission computed tomography (SPECT) estimates the regional cerebral blood flow changes that occur with epileptic activity by comparing the localized uptake of radiolabelled tracer in the ictal and interictal state [215,216]. The tracer is injected at the onset of a seizure and taken up by the neuronal tissue where it will remain for about 2 hours without redistribution, allowing the patient to be injected at the bedside and then transported to the nuclear medicine facility. Ictal SPECT has low temporal resolution, as it takes up to 2 minutes for tracer to peak in the brain [217]. Furthermore, the initial onset of a seizure may be subtle and go unrecognized, delaying tracer injection. Thus, ictal SPECT perfusion patterns often include the propagation zone, as well as the epileptogenic zone of ictal onset and care must be taken when interpreting the results [218]. In TLE, ictal SPECT shows hyperperfusion in the ipsilateral anterior temporal lobe [219] that can extend into the insula and basal ganglia [220], where it is associated with ictal dystonia of the contralateral limb [219,221]. Ictal hypoperfusion has also been observed in the frontal lobes [222,223] and may account for the decreased awareness observed in complex partial seizures. SPECT can also be helpful in localizing extra-temporal neocortical epilepsy. However, false localizations can occur, particularly in regions with rapid bilateral seizure propagation such as the frontal [224] or occipital lobe [225]. In the minutes following a seizure, regions of hyperperfusion switch to relative hypoperfusion, and during the interictal period, the epileptogenic zone is often evident as a region of focal hypoperfusion [226]. Automated registration and subtraction of the interictal from the ictal study, and the co-registration of the resulting 'difference image' to MRI improves the sensitivity of SPECT [216]. SPECT is most useful in cases with non-diagnostic or discordant structural MRI, with a sensitivity of about 50 % in both temporal and extra-temporal epilepsy [227,228].

Positron emission tomography

Positron emission tomography (PET) with the glucose analogue ^{18}F-fluorodeoxyglucose (FDG) allows quantification of the alterations of cerebral metabolism associated with abnormal neuronal activity in the epileptogenic zone. Due to technical constraints involving the short half-life of FDG and its prolonged cerebral uptake of 40–60 minutes, scans are typically performed interictally, when the epileptogenic zone appears as a region of hypometabolism. Notably, this zone may extend to areas connected to the focus [217]. PET images can be coregistered to MRI [229], allowing the better localization of changes in regional metabolism in TLE [230]. In those with neocortical extra-temporal epilepsy due to cortical dysplasia, PET was able to contribute to the identification of lesions in the majority of patients with MRI negative scans [231].

Other PET ligands have been developed to target neurochemical processes and have been studied as more specific markers of epileptogenic cortex. Among them, alpha-methyl-L-tryptophan, a biomarker for the kynurenine pathway of tryptophan metabolism [232], has shown increased uptake in the epileptogenic zone and has been found to be useful in tuberous sclerosis for identifying the active tuber when there are multiple candidates for surgical resection [233]. Uptake of AMT-PET has also been shown to be increased in patients with normal volume hippocampal sclerosis on the side ipsilateral to the seizure focus [234].

Conclusions

Structural MRI is the cornerstone of epilepsy imaging. In drug-resistant epilepsy, resection of the MRI visible lesion remains the best predictor of surgical outcome. Detection of epileptogenic lesions is increased by the use of dedicated epilepsy protocols and

Box 12.2 Imaging drug-resistant epilepsy

Lesion identification

- Structural MRI (dedicated epilepsy protocol).
- Post-processing (volumetry, shape analysis, cortical thickness measurement, computational lesion modelling).

Structural MRI + post-processing negative or non-convergent with electroclinical data

- SPECT (subtraction interictal from ictal, and coregistration with structural MRI).
- PET (FDG).
- EEG-fMRI (interictal).
- MRS.

Surgical planning

- Functional MRI of eloquent cortex (sensorimotor, language, visual, memory).
- Diffusion tensor tractography (pathways).

expert evaluation. Quantitative post-processing further increases the sensitivity of structural MRI by unveiling lesions previously overlooked on visual inspection, without the downside of exposure to ionizing radiation or additional lengthy special imaging sequences. Functional techniques should be regarded as useful adjunctive investigations, particularly in situations where the epileptogenic lesion is not seen after post-processing or is discordant with electroclinical data (Box 12.2).

Ongoing developments in the non-invasive investigation of patients with refractory epilepsy is increasingly reducing the need for intracranial investigation and the life-changing benefits of epilepsy surgery to be offered to more patients.

References

1. Fisher RS, van Emde Boas W, Blume W, et al. (2005). Epileptic seizures and epilepsy: definitions proposed by the International League Against Epilepsy (ILAE) and the International Bureau for Epilepsy (IBE). *Epilepsia*, **46**(4), 470–2.
2. WHO. (2012). *Epilepsy fact sheet no. 999* [updated October 2012; cited 2013 April 8]. Available at: http://www.who.int/mediacentre/factsheets/fs999/en/.
3. Berg AT, Berkovic SF, Brodie MJ, et al. (2010). Revised terminology and concepts for organization of seizures and epilepsies: report of the ILAE Commission on Classification and Terminology, 2005–2009. *Epilepsia*, **51**(4), 676–85.
4. Kwan P, and Brodie MJ. (2000). Early identification of refractory epilepsy. *New England Journal of Medicine*, **342**(5),314–9.
5. Wiebe S. (2006). Burden of intractable epilepsy. *Advances in Neurology*, **97**, 1–4.
6. Tellez-Zenteno JF, Hernandez Ronquillo L, Moien-Afshari F, et al. (2010). Surgical outcomes in lesional and non-lesional epilepsy: a systematic review and meta-analysis. *Epilepsy Research*, **89**(2–3), 310–8.
7. Lerner JT, Salamon N, Hauptman JS, et al. (2009). Assessment and surgical outcomes for mild type I and severe type II cortical dysplasia: a critical review and the UCLA experience. *Epilepsia*, **50**(6), 1310–35.
8. Spencer S, and Huh L. (2008). Outcomes of epilepsy surgery in adults and children. *Lancet Neurology*, **7**(6), 525–37.
9. Skirrow C, Cross JH, Cormack F, et al. (2011). Long-term intellectual outcome after temporal lobe surgery in childhood. *Neurology*, **76**(15), 1330–7.
10. Bernasconi A. (2004). Quantitative MR imaging of the neocortex. *Neuroimaging Clinics of North America*, **14**(3), 425–36.
11. Bernasconi A, Bernasconi N, Bernhardt BC, et al. Advances in MRI for 'cryptogenic' epilepsies. *Nature Reviews Neurology*, **7**(2), 99–108.
12. Von Oertzen J, Urbach H, Jungbluth S, et al. (2002). Standard magnetic resonance imaging is inadequate for patients with refractory focal epilepsy. *Journal of Neurology, Neurosurgery, & Psychiatry*, **73**(6), 643–7.
13. Bastos AC, Comeau RM, Andermann F, et al. (1999). Diagnosis of subtle focal dysplastic lesions: curvilinear reformatting from three-dimensional magnetic resonance imaging. *Annals of Neurology*, **46**(1), 88–94.
14. Bastos AC, Korah IP, Cendes F, et al. (1995). Curvilinear reconstruction of 3D magnetic resonance imaging in patients with partial epilepsy—a pilot study. *Magnetic Resonance Imaging*, **13**(8), 1107–12.
15. Madan N, and Grant PE. (2009). New directions in clinical imaging of cortical dysplasias. *Epilepsia*, **50**(Suppl. 9), 9–18.
16. Knake S, Triantafyllou C, Wald LL, et al. (2005). 3T phased array MRI improves the presurgical evaluation in focal epilepsies: a prospective study. *Neurology*, **65**(7),1026–31.
17. Zijlmans M, de Kort GA, Witkamp TD, et al. (2009). 3T versus 1.5T phased-array MRI in the presurgical work-up of patients with partial epilepsy of uncertain focus. *Journal of Magnetic Resonance Imaging*, **30**(2), 256–62.
18. Urbach H. (2012). High-field magnetic resonance imaging for epilepsy. *Neuroimaging Clinics of North America*, **22**(2), 173–89, ix–x.
19. Gaillard WD, Chiron C, Cross JH, et al. (2009). Guidelines for imaging infants and children with recent-onset epilepsy. *Epilepsia*, **50**(9), 2147–53.
20. Vezina LG. (2011). MRI-negative epilepsy: protocols to optimize lesion detection. *Epilepsia*, **52**(Suppl. 4), 25–7.
21. Jackson GD, and Badawy RA. (2011). Selecting patients for epilepsy surgery: identifying a structural lesion. *Epilepsy Behaviour*, **20**(2), 182–9.
22. Haacke EM, Mittal S, Wu Z, et al. (2009). Susceptibility-weighted imaging: technical aspects and clinical applications, part 1. *AJNR American Journal of Neuroradiology*, **30**(1), 19–30.
23. Hu J, Yu Y, Juhasz C, et al. (2008). MR susceptibility weighted imaging (SWI) complements conventional contrast enhanced T1 weighted MRI in characterizing brain abnormalities of Sturge–Weber Syndrome. *Journal of Magnetic Resonance Imaging*, **28**(2), 300–7.
24. Saini J, Kesavadas C, Thomas B, et al. (2009). Susceptibility weighted imaging in the diagnostic evaluation of patients with intractable epilepsy. *Epilepsia*, **50**(6), 1462–73.
25. Breyer T, Wanke I, Maderwald S, et al. (2010). Imaging of patients with hippocampal sclerosis at 7 Tesla: initial results. *Academic Radiology*, **17**(4), 421–6.
26. Blumcke I, Coras R, Miyata H, et al. (2012). Defining clinico-neuropathological subtypes of mesial temporal lobe epilepsy with hippocampal sclerosis. *Brain Pathology*, **22**(3), 402–11.
27. Yilmazer-Hanke DM, Wolf HK, Schramm J, et al. (2000). Subregional pathology of the amygdala complex and entorhinal region in surgical specimens from patients with pharmacoresistant temporal lobe epilepsy. *Journal of Neuropathology and Experimental Neurology*, **59**(10), 907–20.
28. Du F, Whetsell WO, Abou-Khalil B, et al. (1993). Preferential neuronal loss in layer III of the entorhinal cortex in patients with temporal lobe epilepsy. *Epilepsy Research*, **16**, 223–33.
29. Bothwell S, Meredith GE, Phillips J, et al. (2001). Neuronal hypertrophy in the neocortex of patients with temporal lobe epilepsy. *Journal of Neuroscience*, **21**(13), 4789–800.
30. Thom M, Sisodiya S, Harkness W, et al. (2001). Microdysgenesis in temporal lobe epilepsy. A quantitative and immunohistochemical study of white matter neurones. *Brain*, **124**(Pt 11), 2299–309.
31. de Lanerolle NC, Kim JH, Williamson A, et al. (2003). A retrospective analysis of hippocampal pathology in human temporal lobe epilepsy: evidence for distinctive patient subcategories. *Epilepsia*, **44**(5), 677–87.
32. Jackson GD, Connelly A, Duncan JS, et al. Detection of hippocampal pathology in intractable partial epilepsy: increased sensitivity with quantitative resonance T2 relaxometry. *Neurology*, **43**, 1793–9.
33. Briellmann RS, Kalnins RM, Berkovic SF, et al. (2002). Hippocampal pathology in refractory temporal lobe epilepsy: T2-weighted signal change reflects dentate gliosis. *Neurology*, **58**(2), 265–71.
34. Meiners LC, van Gils A, Jansen GH, et al. (1994). Temporal lobe epilepsy: the various MR appearances of histologically proven mesial temporal sclerosis. *AJNR American Journal of Neuroradiology*, **15**(8), 1547–55.
35. Moran NF, Lemieux L, Kitchen ND, et al. (2001). Extrahippocampal temporal lobe atrophy in temporal lobe epilepsy and mesial temporal sclerosis. *Brain*, **124**(Pt 1), 167–75.
36. Baldwin GN, Tsuruda JS, Maravilla KR, et al. (1994). The fornix in patients with seizures caused by unilateral hippocampal sclerosis: detection of unilateral volume loss on MR images. *AJNR American Journal of Neuroradiology*, **15**(5), 1185–9.
37. Mamourian AC, Rodichok L, and Towfighi J. (1995). The asymmetric mamillary body: association with medial temporal lobe disease demonstrated with MR. *AJNR American Journal of Neuroradiology*, **16**(3), 517–22.
38. Bernasconi N, Bernasconi A, Andermann F, et al. (1999). Entorhinal cortex in temporal lobe epilepsy: a quantitative MRI study. *Neurology*, **52**(9), 1870–6.
39. Bernasconi N, Bernasconi A, Caramanos Z, et al. (2003). Mesial temporal damage in temporal lobe epilepsy: a volumetric MRI study of the hippocampus, amygdala and parahippocampal region. *Brain*, **126**(Pt 2), 462–9.

40. Sankar T, Bernasconi N, Kim H, et al. (2008). Temporal lobe epilepsy: differential pattern of damage in temporopolar cortex and white matter. Human Brain Mapping, **29**(8), 931–44.
41. Bernasconi N, Bernasconi A, Caramanos Z, et al. (2001). Entorhinal cortex atrophy in epilepsy patients exhibiting normal hippocampal volumes. *Neurology*, **56**(10), 1335–9.
42. Natsume J, Bernasconi N, Andermann F, et al. (2003). MRI volumetry of the thalamus in temporal, extratemporal, and idiopathic generalized epilepsy. *Neurology*, **60**(8), 1296–300.
43. Watson C, Andermann F, Gloor P, et al. (1992). Anatomic basis of amygdaloid and hippocampal volume measurement by magnetic resonance imaging. *Neurology*, **42**(9), 1743–50.
44. Cendes F, Andermann F, Gloor P, et al. (1993). MRI volumetric measurement of amygdala and hippocampus in temporal lobe epilepsy. *Neurology*, **43**(4), 719–25.
45. Cascino GD, Jack CR, Jr., Parisi JE, et al. (1991). Magnetic resonance imaging-based volume studies in temporal lobe epilepsy: pathological correlations. *Annals of Neurology*, **30**(1), 31–6.
46. McDonald CR, Hagler DJ, Jr, Ahmadi ME, et al. (2008). Subcortical and cerebellar atrophy in mesial temporal lobe epilepsy revealed by automatic segmentation. *Epilepsy Research*, **79**(2–3), 130–8.
47. Pardoe HR, Pell GS, Abbott DF, et al. (2009). Hippocampal volume assessment in temporal lobe epilepsy: how good is automated segmentation? *Epilepsia*, **50**(12), 2586–92.
48. Hammers A, Heckemann R, Koepp MJ, et al. (2007). Automatic detection and quantification of hippocampal atrophy on MRI in temporal lobe epilepsy: A proof-of-principle study. *NeuroImage*, **36**(1), 38–47.
49. Avants BB, Yushkevich P, Pluta J, et al. (2010). The optimal template effect in hippocampus studies of diseased populations. *NeuroImage*, **49**(3), 2457–66.
50. Pardoe HR, Pell GS, Abbott DF, et al. (2009). Hippocampal volume assessment in temporal lobe epilepsy: how good is automated segmentation? *Epilepsia*, **50**(12), 2586–92.
51. Chupin M, Hammers A, Liu RS, et al. (2009). Automatic segmentation of the hippocampus and the amygdala driven by hybrid constraints: method and validation. *NeuroImage*, **46**(3), 749–61.
52. Heckemann RA, Keihaninejad S, Aljabar P, et al. (2010). Improving intersubject image registration using tissue-class information benefits robustness and accuracy of multi-atlas based anatomical segmentation. *NeuroImage*, **51**(1), 221–7.
53. Akhondi-Asl A, Jafari-Khouzani K, Elisevich K, et al. (2011). Hippocampal volumetry for lateralization of temporal lobe epilepsy: automated versus manual methods. *NeuroImage*, **54**(Suppl. 1), S218–26.
54. Kim H, Chupin M, Colliot O, et al. (2012). Automatic hippocampal segmentation in temporal lobe epilepsy: impact of developmental abnormalities. *NeuroImage*, **59**(4), 3178–86.
55. Bernasconi N, Kinay D, Andermann F, et al. (2005). Analysis of shape and positioning of the hippocampal formation: an MRI study in patients with partial epilepsy and healthy controls. *Brain*, **128**(Pt 10), 2442–52.
56. Voets NL, Bernhardt BC, Kim H, et al. (2011). Increased temporolimbic cortical folding complexity in temporal lobe epilepsy. *Neurology*, **76**(2), 138–44.
57. Baulac M, De Grissac N, Hasboun D, et al. (1998). Hippocampal developmental changes in patients with partial epilepsy: magnetic resonance imaging and clinical aspects. *Annals of Neurology*, **44**(2), 223–33.
58. Sloviter RS, Kudrimoti HS, Laxer KD, et al. (2004). 'Tectonic' hippocampal malformations in patients with temporal lobe epilepsy. *Epilepsy Research*, **59**(2–3), 123–53.
59. Blumcke I, Thom M, and Wiestler OD. (2002). Ammon's horn sclerosis: a maldevelopmental disorder associated with temporal lobe epilepsy. *Brain Pathology*, **12**(2), 199–211.
60. Kim H, Mansi T, Bernasconi N, et al. (2012). Surface-based multi-template automated hippocampal segmentation: application to temporal lobe epilepsy. *Medical Image Analysis*, **16**(7), 1445–55.
61. Vattipally VR, and Bronen RA. (2004). MR imaging of epilepsy: strategies for successful interpretation. *Neuroimaging Clinics of North America*, **14**(3), 349–72.
62. King D, Spencer SS, Bouthillier A, et al. (1996). Medial temporal lobe epilepsy without hippocampal atrophy. *Journal of Epilepsy*, **9**, 291–7.
63. Jackson GD, Kuzniecky RI, and Cascino GD. (1994). Hippocampal sclerosis without detectable hippocampal atrophy. *Neurology*, **44**, 42–6.
64. Bernasconi A, Bernasconi N, Caramanos Z, et al. (2000). T2 relaxometry can lateralize mesial temporal lobe epilepsy in patients with normal MRI. *NeuroImage*, **12**, 739–46.
65. Townsend TN, Bernasconi N, Pike GB, et al. (2004). Quantitative analysis of temporal lobe white matter T2 relaxation time in temporal lobe epilepsy. *NeuroImage*, **23**(1), 318–24.
66. Pell GS, Briellmann RS, Pardoe H, et al. (2008). Composite voxel-based analysis of volume and T2 relaxometry in temporal lobe epilepsy. *NeuroImage*, **39**(3), 1151–61.
67. Kim H, Bernasconi N, Bernhardt B, et al. (2008). Basal temporal sulcal morphology in healthy controls and patients with temporal lobe epilepsy. *Neurology*, **70**(22 Pt 2), 2159–65.
68. Hogan RE, Wang L, Bertrand ME, et al. (2004). MRI-based high-dimensional hippocampal mapping in mesial temporal lobe epilepsy. *Brain*, **127**(Pt 8), 1731–40.
69. Hogan RE, Carne RP, Kilpatrick CJ, et al. (2008). Hippocampal deformation mapping in MRI negative PET positive temporal lobe epilepsy. *Journal of Neurology, Neurosurgery & Psychiatry*, **79**(6), 636–40.
70. Bernasconi N, Natsume J, and Bernasconi A. (2005). Progression in temporal lobe epilepsy: differential atrophy in mesial temporal structures. *Neurology*, **65**(2), 223–8.
71. Bonilha L, Rorden C, Castellano G, et al. (2004). Voxel-based morphometry reveals gray matter network atrophy in refractory medial temporal lobe epilepsy. *Archives of Neurology*, **61**(9), 1379–84.
72. Mueller SG, Laxer KD, Cashdollar N, et al. (2006). Voxel-based optimized morphometry (VBM) of gray and white matter in temporal lobe epilepsy (TLE) with and without mesial temporal sclerosis. *Epilepsia*, **47**(5), 900–7.
73. Keller SS, Mackay CE, Barrick TR, et al. (2002). Voxel-based morphometric comparison of hippocampal and extrahippocampal abnormalities in patients with left and right hippocampal atrophy. *NeuroImage*, **16**(1), 23–31.
74. Bernasconi N, Duchesne S, Janke A, et al. (2004). Whole-brain voxel-based statistical analysis of gray matter and white matter in temporal lobe epilepsy. *NeuroImage*, **23**(2), 717–23.
75. Bernhardt BC, Bernasconi N, Concha L, et al. (2010). Cortical thickness analysis in temporal lobe epilepsy: reproducibility and relation to outcome. *Neurology*, **74**(22), 1776–84.
76. Mueller SG, Laxer KD, Barakos J, et al. (2009). Widespread neocortical abnormalities in temporal lobe epilepsy with and without mesial sclerosis. *NeuroImage*, **46**(2), 353–9.
77. Bernhardt BC, Worsley KJ, Besson P, et al. (2008). Mapping limbic network organization in temporal lobe epilepsy using morphometric correlations: insights on the relation between mesiotemporal connectivity and cortical atrophy. *NeuroImage*, **42**(2), 515–24.
78. Bernhardt BC, Worsley KJ, Kim H, et al. (2009). Longitudinal and cross-sectional analysis of atrophy in pharmacoresistant temporal lobe epilepsy. *Neurology*, **72**(20), 1747–54.
79. Helmstaedter C, Kurthen M, Lux S, et al. (2003). Chronic epilepsy and cognition: a longitudinal study in temporal lobe epilepsy. *Annals of Neurology*, **54**(4), 425–32.
80. Bartolomei F, Chauvel P, and Wendling F. (2008). Epileptogenicity of brain structures in human temporal lobe epilepsy: a quantified study from intracerebral EEG. *Brain*, **131**(Pt 7), 1818–30.
81. Blumcke I, Thom M, Aronica E, et al. (2011). The clinicopathologic spectrum of focal cortical dysplasias: a consensus classification proposed by an ad hoc Task Force of the ILAE Diagnostic Methods Commission. *Epilepsia*, **52**(1), 158–74.
82. Colombo N, Tassi L, Deleo F, et al. (2012). Focal cortical dysplasia type IIa and IIb: MRI aspects in 118 cases proven by histopathology. *Neuroradiology*, **54**(10), 1065–77.
83. Barkovich AJ, Kuzniecky RI, Bollen AW, et al. (1997). Focal transmantle dysplasia: a specific malformation of cortical development. *Neurology*, **49**(4), 1148–52.

84. Cohen-Gadol AA, Ozduman K, Bronen RA, et al. (2004). Long-term outcome after epilepsy surgery for focal cortical dysplasia. *Journal of Neurosurgery*, **101**(1), 55–65.
85. Krsek P, Maton B, Korman B, et al. (2008). Different features of histopathological subtypes of pediatric focal cortical dysplasia. *Annals of Neurology*, **63**(6), 758–69.
86. Krsek P, Pieper T, Karlmeier A, et al. (2009). Different presurgical characteristics and seizure outcomes in children with focal cortical dysplasia type I or II. *Epilepsia*, **50**(1), 125–37.
87. Lerner JT, Salamon N, Hauptman JS, et al. (2009). Assessment and surgical outcomes for mild type I and severe type II cortical dysplasia: a critical review and the UCLA experience. *Epilepsia*, **50**(6), 1310–35.
88. Matsuda K, Mihara T, Tottori T, et al. (2001). Neuroradiologic findings in focal cortical dysplasia: histologic correlation with surgically resected specimens. *Epilepsia*, **42**(Suppl. 6), 29–36.
89. Urbach H, Scheffler B, Heinrichsmeier T, et al. (2002). Focal cortical dysplasia of Taylor's balloon cell type: a clinicopathological entity with characteristic neuroimaging and histopathological features, and favorable postsurgical outcome. *Epilepsia*, **43**(1), 33–40.
90. Muhlebner A, Coras R, Kobow K, et al. (2012). Neuropathologic measurements in focal cortical dysplasias: validation of the ILAE 2011 classification system and diagnostic implications for MRI. *Acta Neuropathologica*, **123**(2), 259–72.
91. Krsek P, Pieper T, Karlmeier A, et al. (2009). Different presurgical characteristics and seizure outcomes in children with focal cortical dysplasia type I or II. *Epilepsia*, **50**(1), 125–37.
92. Bronen RA, Spencer DD, and Fulbright RK. (2000). Cerebrospinal fluid cleft with cortical dimple: MR imaging marker for focal cortical dysgenesis. *Radiology*, **214**(3), 657–63.
93. Besson P, Andermann F, Dubeau F, et al. (2008). Small focal cortical dysplasia lesions are located at the bottom of a deep sulcus. *Brain*, **131**(Pt 12), 3246–55.
94. Ashburner J, and Friston KJ. (2000). Voxel-based morphometry—the methods. *NeuroImage*, **11**(6 Pt 1), 805–21.
95. Bonilha L, Montenegro MA, Rorden C, et al. (2006). Voxel-based morphometry reveals excess gray matter concentration in patients with focal cortical dysplasia. *Epilepsia*, **47**(5), 908–15.
96. Bruggemann JM, Wilke M, Som SS, et al. (2007). Voxel-based morphometry in the detection of dysplasia and neoplasia in childhood epilepsy: combined grey/white matter analysis augments detection. *Epilepsy Research*, **77**(2–3), 93–101.
97. Colliot O, Bernasconi N, Khalili N, et al. Individual voxel-based analysis of gray matter in focal cortical dysplasia. *NeuroImage*, **29**(1), 162–71.
98. Merschhemke M, Mitchell TN, Free SL, et al. (2003). Quantitative MRI detects abnormalities in relatives of patients with epilepsy and malformations of cortical development. *NeuroImage*, **18**(3), 642–9.
99. Wilke M, Kassubek J, Ziyeh S, et al. (2003). Automated detection of gray matter malformations using optimized voxel-based morphometry: a systematic approach. *NeuroImage*, **20**(1),330–43.
100. Rugg-Gunn FJ, Boulby PA, Symms MR, et al. (2006). Imaging the neocortex in epilepsy with double inversion recovery imaging. *NeuroImage*, **31**(1), 39–50.
101. Focke NK, Symms MR, Burdett JL, et al. (2008). Voxel-based analysis of whole brain FLAIR at 3T detects focal cortical dysplasia. *Epilepsia*, **49**(5), 786–93.
102. Rugg-Gunn FJ, Boulby PA, Symms MR, et al. (2005). Whole-brain T2 mapping demonstrates occult abnormalities in focal epilepsy. *Neurology*, **64**(2), 318–25.
103. Rugg-Gunn FJ, Eriksson SH, Boulby PA, et al. (2003). Magnetization transfer imaging in focal epilepsy. *Neurology*, **60**(10), 1638–45.
104. Focke NK, Bonelli SB, Yogarajah M, et al. (2009). Automated normalized FLAIR imaging in MRI-negative patients with refractory focal epilepsy. *Epilepsia*, **50**(6), 1484–90.
105. Salmenpera TM, Symms MR, Rugg-Gunn FJ, et al. (2007). Evaluation of quantitative magnetic resonance imaging contrasts in MRI-negative refractory focal epilepsy. *Epilepsia*, **48**(2), 229–37.
106. Lockwood-Estrin G, Thom M, Focke NK, et al. (2012). Correlating 3T MRI and histopathology in patients undergoing epilepsy surgery. *Journal of Neuroscience Methods*, **205**(1), 182–9.
107. Antel SB, Collins DL, Bernasconi N, et al. (2003). Automated detection of focal cortical dysplasia lesions using computational models of their MRI characteristics and texture analysis. *NeuroImage*, **19**(4), 1748–59.
108. Antel SB, Bernasconi A, Bernasconi N, et al. (2002). Computational models of MRI characteristics of focal cortical dysplasia improve lesion detection. *NeuroImage*, **17**(4), 1755–60.
109. Bernasconi A, Antel SB, Collins DL, et al. (2001). Texture analysis and morphological processing of magnetic resonance imaging assist detection of focal cortical dysplasia in extra-temporal partial epilepsy. *Annals of Neurology*, **49**(6), 770–5.
110. Bien CG, Szinay M, Wagner J, et al. (2009). Characteristics and surgical outcomes of patients with refractory magnetic resonance imaging-negative epilepsies. *Archives of Neurology*, **66**(12), 1491–9.
111. Kassubek J, Huppertz HJ, Spreer J, et al. (2002). Detection and localization of focal cortical dysplasia by voxel-based 3-D MRI analysis. *Epilepsia*, **43**(6), 596–602.
112. Srivastava S, Maes F, Vandermeulen D, et al. (2005). Feature-based statistical analysis of structural MR data for automatic detection of focal cortical dysplastic lesions. *NeuroImage*, **27**(2), 253–66.
113. Colliot O, Antel SB, Naessens VB, et al. (2006). In vivo profiling of focal cortical dysplasia on high-resolution MRI with computational models. *Epilepsia*, **47**(1), 134–42.
114. Colliot O, Mansi T, Bernasconi N, Naessens V, et al. (2005). Segmentation of focal cortical dysplasia lesions using a feature-based level set. *Medical Image Computing & Computer-Assisted Intervention: MICCAI*, **8**, 375–82.
115. Colliot O, Mansi T, Bernasconi N, et al. (2006). Segmentation of focal cortical dysplasia lesions on MRI using level set evolution. *NeuroImage*, **32**(4), 1621–30.
116. Antel SB, Collins DL, Bernasconi N, et al. (2003). Automated detection of focal cortical dysplasia lesions using computational models of their MRI characteristics and texture analysis. *NeuroImage*, **19**(4), 1748–59.
117. Besson P, Bernasconi N, Colliot O, et al. (2008). Surface-based texture and morphological analysis detects subtle cortical dysplasia. *Medical Image Computing & Computer-Assisted Intervention: MICCAI*, **11**(Pt 1), 645–52.
118. Panayiotopoulos CP. (2005). Idiopathic generalized epilepsies: a review and modern approach. *Epilepsia*, **46**(Suppl. 9), 1–6.
119. Blumenfeld H. (2005). Cellular and network mechanisms of spike-wave seizures. *Epilepsia*, **46**(Suppl. 9), 21–33.
120. Helbig I, and Lowenstein DH. (2013). Genetics of the epilepsies: where are we and where are we going? Current Opinions in Neurology, **26**(2), 179–85.
121. Betting LE, Mory SB, Lopes-Cendes I, et al. (2006). MRI reveals structural abnormalities in patients with idiopathic generalized epilepsy. *Neurology*, **67**(5), 848–52.
122. Ciumas C, and Savic I. (2006). Structural changes in patients with primary generalized tonic and clonic seizures. *Neurology*, **67**(4), 683–6.
123. Betting LE, Mory SB, Li LM, et al. Voxel-based morphometry in patients with idiopathic generalized epilepsies. *NeuroImage*, **32**(2), 498–502.
124. Bernhardt BC, Rozen DA, Worsley KJ, et al. (2009). Thalamo-cortical network pathology in idiopathic generalized epilepsy: insights from MRI-based morphometric correlation analysis. *NeuroImage*, **46**(2), 373–81.
125. Chan CH, Briellmann RS, Pell GS, et al. (2006). Thalamic atrophy in childhood absence epilepsy. *Epilepsia*, **47**(2), 399–405.
126. Kim JH, Lee JK, Koh SB, et al. (2007). Regional grey matter abnormalities in juvenile myoclonic epilepsy: a voxel-based morphometry study. *NeuroImage*, **37**(4), 1132–7.
127. O'Muircheartaigh J, Vollmar C, Barker GJ, et al. (2011). Focal structural changes and cognitive dysfunction in juvenile myoclonic epilepsy. *Neurology*, **76**(1), 34–40.
128. Glauser T, Ben-Menachem E, Bourgeois B, et al. (2006). ILAE treatment guidelines: evidence-based analysis of antiepileptic drug efficacy

and effectiveness as initial monotherapy for epileptic seizures and syndromes. *Epilepsia*, **47**(7), 1094–120.

129. Moffett JR, Namboodiri MA, Cangro CB, et al. (1991). Immunohistochemical localization of N-acetylaspartate in rat brain. *Neuroreport*, **2**(3), 131–4.
130. Urenjak J, Williams SR, Gadian DG, et al. (1993). Proton nuclear magnetic resonance spectroscopy unambiguously identifies different neural cell types. Journal of Neuroscience, **13**(3), 981–9.
131. Cendes F, Caramanos Z, Andermann F, et al. (1997). Proton magnetic resonance spectroscopic imaging and magnetic resonance imaging volumetry in the lateralization of temporal lobe epilepsy: a series of 100 patients. *Annals of Neurology*, **42**, 737–46.
132. Cendes F, Andermann F, Preul MC, et al. (1994). Lateralization of temporal lobe epilepsy based on regional metabolic abnormalities in proton magnetic resonance spectroscopic images. *Annals of Neurology*, **35**(2), 211–16.
133. Kuzniecky RI, Hugg JW, Hetherington H, et al. (1998). Relative utility of 1H spectroscopic imaging and hippocampal volumetry in the lateralization of mesial temporal lobe epilepsy. *Neurology*, **51**, 66–71.
134. Antel SB, Li LM, Cendes F, et al. (2002). Predicting surgical outcome in temporal lobe epilepsy patients using MRI and MRSI. *Neurology*, **58**(10), 1505–12.
135. Willmann O, Wennberg R, May T, et al. (2006). The role of 1H magnetic resonance spectroscopy in pre-operative evaluation for epilepsy surgery. A meta-analysis. *Epilepsy Research*, **71**(2–3), 149–58.
136. Garcia PA, Laxer KD, van der Grond J, et al. (1995). Proton magnetic resonance spectroscopic imaging in patients with frontal lobe epilepsy. *Annals of Neurology*, , **37**(2), 279–81.
137. Lundbom N, Gaily E, Vuori K, et al. (2001). Proton spectroscopic imaging shows abnormalities in glial and neuronal cell pools in frontal lobe epilepsy. *Epilepsia*, **42**(12), 1507–14.
138. Mueller SG, Laxer DL, Barakos JA, et al. Identification of the epileptogenic lobe in neocortical epilepsy with proton MR spectroscopic imaging. *Epilepsia*, **45**(12), 1580–9.
139. Maudsley AA, Domenig C, Ramsay RE, et al. (2010). Application of volumetric MR spectroscopic imaging for localization of neocortical epilepsy. *Epilepsy Research*, **88**(2–3), 127–38.
140. Krsek P, Hajek M, Dezortova M, et al. (2007). (1)H MR spectroscopic imaging in patients with MRI-negative extratemporal epilepsy: correlation with ictal onset zone and histopathology. *European Radiology*, **17**(8), 2126–35.
141. Savic I, Osterman Y, and Helms G. MRS shows syndrome differentiated metabolite changes in human-generalized epilepsies. *NeuroImage*, **21**(1), 163–72.
142. Mory SB, Li LM, Guerreiro CA, and Cendes F. (2003). Thalamic dysfunction in juvenile myoclonic epilepsy: a proton MRS study. *Epilepsia*, **44**(11), 1402–5.
143. Bernasconi A, Bernasconi N, Natsume J, et al. (2003). Magnetic resonance spectroscopy and imaging of the thalamus in idiopathic generalized epilepsy. *Brain*, **126**, 2447–54.
144. Simister RJ, McLean MA, Barker GJ, et al. (2003). Proton MRS reveals frontal lobe metabolite abnormalities in idiopathic generalized epilepsy. *Neurology*, **61**(7), 897–902.
145. Savic I, Lekvall A, Greitz D, et al. (2000). MR spectroscopy shows reduced frontal lobe concentrations of N-acetyl aspartate in patients with juvenile myoclonic epilepsy. *Epilepsia*, **41**(3), 290–6.
146. Simister RJ, Woermann FG, McLean MA, et al. (2002). A short-echo-time proton magnetic resonance spectroscopic imaging study of temporal lobe epilepsy. *Epilepsia*, **43**(9), 1021–31.
147. Woermann FG, McLean MA, Bartlett PA, et al. (1999). Short echo time single-voxel 1H magnetic resonance spectroscopy in magnetic resonance imaging-negative temporal lobe epilepsy: different biochemical profile compared with hippocampal sclerosis. *Annals of Neurology*, **45**(3), 369–76.
148. Simister RJ, McLean MA, Barker GJ, et al. (2007). Proton magnetic resonance spectroscopy of malformations of cortical development causing epilepsy. *Epilepsy Research*, **74**(2–3), 107–15.
149. Helms G, Ciumas C, Kyaga S, et al. (2006). Increased thalamus levels of glutamate and glutamine (Glx) in patients with idiopathic generalised epilepsy. *Journal of Neurology, Neurosurgery & Psychiatry*, **77**(4), 489–94.
150. Simister RJ, McLean MA, Barker GJ, et al. (2003). A proton magnetic resonance spectroscopy study of metabolites in the occipital lobes in epilepsy. *Epilepsia*, **44**(4), 550–8.
151. Petroff OA, Hyder F, Rothman DL, et al. (2001). Homocarnosine and seizure control in juvenile myoclonic epilepsy and complex partial seizures. *Neurology*, **56**(6), 709–15.
152. Verhoeff NP, Petroff OA, Hyder F, et al. (1999). Effects of vigabatrin on the GABAergic system as determined by [123I]iomazenil SPECT and GABA MRS. *Epilepsia*, **40**(10), 1433–8.
153. Petroff OA, Behar KL, Mattson RH, et al. (1996). Human brain gamma-aminobutyric acid levels and seizure control following initiation of vigabatrin therapy. *Journal of Neurochemistry*, **67**(6), 2399–404.
154. Petroff OA, Mattson RH, Behar KL, et al. (1998). Vigabatrin increases human brain homocarnosine and improves seizure control. *Annals of Neurology*, **44**(6), 948–52.
155. Kuzniecky R, Ho S, Pan J, et al. (2002). Modulation of cerebral GABA by topiramate, lamotrigine, and gabapentin in healthy adults. *Neurology*, **58**(3), 368–72.
156. Doelken MT, Hammen T, Bogner W, et al. (2010). Alterations of intracerebral gamma-aminobutyric acid (GABA) levels by titration with levetiracetam in patients with focal epilepsies. *Epilepsia*, **51**(8), 1477–82.
157. Wiedermann D, Schuff N, Matson GB, et al. (2001). Short echo time multislice proton magnetic resonance spectroscopic imaging in human brain: metabolite distributions and reliability. *Magnetic Resonance Imaging*, **19**(8), 1073–80.
158. Basser PJ, Mattiello J, and Le Bihan D. MR diffusion tensor spectroscopy and imaging. *Biophysics Journal*, **66**, 259–67.
159. Concha L, Beaulieu C, and Gross DW. (2005). Bilateral limbic diffusion abnormalities in unilateral temporal lobe epilepsy. *Annals of Neurology*, **57**(2), 188–96.
160. Ahmadi ME, Hagler DJ, Jr, McDonald CR, et al. (2009). Side matters: diffusion tensor imaging tractography in left and right temporal lobe epilepsy. *AJNR American Journal of Neuroradiology*, **30**(9), 1740–7.
161. Yogarajah M, and Duncan JS. (2008). Diffusion-based magnetic resonance imaging and tractography in epilepsy. *Epilepsia*, **49**(2):189–200.
162. McDonald CR, Ahmadi ME, Hagler DJ, et al. (2008). Diffusion tensor imaging correlates of memory and language impairments in temporal lobe epilepsy. *Neurology*, **71**(23), 1869–76.
163. Rodrigo S, Oppenheim C, Chassoux F, et al. (2007). Uncinate fasciculus fiber tracking in mesial temporal lobe epilepsy. Initial findings. *European Radiology*, **17**(7), 1663–8.
164. Diehl B, Busch RM, Duncan JS, et al. (2008). Abnormalities in diffusion tensor imaging of the uncinate fasciculus relate to reduced memory in temporal lobe epilepsy. *Epilepsia*, **49**(8), 1409–18.
165. Lin JJ, Riley JD, Juranek J, et al. Vulnerability of the frontal-temporal connections in temporal lobe epilepsy. *Epilepsy Research*, **82**(2–3), 162–70.
166. Concha L, Beaulieu C, Collins DL, et al. (2008). White matter diffusion abnormalities in temporal lobe epilepsy with and without mesial temporal sclerosis. *Journal of Neurology, Neurosurgery &* Psychiatry, **80**(3), 312–19.
167. Focke NK, Yogarajah M, Bonelli SB, et al. (2008). Voxel-based diffusion tensor imaging in patients with mesial temporal lobe epilepsy and hippocampal sclerosis. *NeuroImage*, **40**(2), 728–37.
168. Arfanakis K, Hermann BP, Rogers BP, et al. (2002). Diffusion tensor MRI in temporal lobe epilepsy. *Magnetic Resonance Imaging*, **20**(7), 511–19.
169. Gross DW, Concha L, and Beaulieu C. (2006). Extratemporal white matter abnormalities in mesial temporal lobe epilepsy demonstrated with diffusion tensor imaging. *Epilepsia*, **47**(8), 1360–3.
170. Bonilha L, Edwards JC, Kinsman SL, et al. (2010). Extrahippocampal gray matter loss and hippocampal deafferentation in patients with temporal lobe epilepsy. *Epilepsia*, **51**(4), 519–28.

171. Concha L, Livy DJ, Beaulieu C, et al. In vivo diffusion tensor imaging and histopathology of the fimbria-fornix in temporal lobe epilepsy. *Journal of Neuroscience*, **30**(3), 996–1002.
172. Concha L, Kim H, Bernasconi A, et al. (2012). Spatial patterns of water diffusion along white matter tracts in temporal lobe epilepsy. *Neurology*, **79**(5), 455–62.
173. Gross DW, Bastos A, and Beaulieu C. (2005). Diffusion tensor imaging abnormalities in focal cortical dysplasia. *Canadian Journal of Neurological Science*, **32**(4), 477–82.
174. Lee SK, Kim DI, Mori S, et al. (2004). Diffusion tensor MRI visualizes decreased subcortical fiber connectivity in focal cortical dysplasia. *NeuroImage*, **22**(4), 1826–9.
175. Widjaja E, Blaser S, Miller E, et al. (2007). Evaluation of subcortical white matter and deep white matter tracts in malformations of cortical development. *Epilepsia*, **48**(8), 1460–9.
176. Eriksson SH, Rugg-Gunn FJ, Symms MR, et al. (2001). Diffusion tensor imaging in patients with epilepsy and malformations of cortical development. *Brain*, **124**(Pt 3), 617–26.
177. Guye M, Ranjeva JP, Bartolomei F, et al. (2007). What is the significance of interictal water diffusion changes in frontal lobe epilepsies? *NeuroImage*, **35**(1), 28–37.
178. Thivard L, Adam C, Hasboun D, et al. (2006). Interictal diffusion MRI in partial epilepsies explored with intracerebral electrodes. *Brain*, **129**(Pt 2), 375–85.
179. Rugg-Gunn FJ, Eriksson SH, Symms MR, et al. (2002). Diffusion tensor imaging in refractory epilepsy. *Lancet*, **359**(9319), 1748–51.
180. Liu M, Concha L, Beaulieu C, et al. (2011). Distinct white matter abnormalities in different idiopathic generalized epilepsy syndromes. *Epilepsia*, **52**(12), 2267–75.
181. Deppe M, Kellinghaus C, Duning T, et al. (2008). Nerve fiber impairment of anterior thalamocortical circuitry in juvenile myoclonic epilepsy. *Neurology*, **71**(24), 1981–5.
182. Keller SS, Ahrens T, Mohammadi S, et al. (2011). Microstructural and volumetric abnormalities of the putamen in juvenile myoclonic epilepsy. *Epilepsia*, **52**(9), 1715–24.
183. Vulliemoz S, Vollmar C, Koepp MJ, et al. (2001). Connectivity of the supplementary motor area in juvenile myoclonic epilepsy and frontal lobe epilepsy. *Epilepsia*, **52**(3), 507–14.
184. Vollmar C, O'Muircheartaigh J, Symms MR, et al. (2012). Altered microstructural connectivity in juvenile myoclonic epilepsy: the missing link. *Neurology*, **78**(20), 1555–9.
185. Zhang Z, Liao W, Chen H, et al. (2011). Altered functional-structural coupling of large-scale brain networks in idiopathic generalized epilepsy. *Brain*, **134**(Pt 10), 2912–28.
186. Catani M, Howard RJ, Pajevic S, et al. (2002). Virtual in vivo interactive dissection of white matter fasciculi in the human brain. *NeuroImage*, **17**(1), 77–94.
187. Powell HW, Parker GJ, Alexander DC, et al. (2005). MR tractography predicts visual field defects following temporal lobe resection. *Neurology*, **65**(4), 596–9.
188. Yogarajah M, Focke NK, Bonelli S, et al. (2009). Defining Meyer's loop-temporal lobe resections, visual field deficits and diffusion tensor tractography. *Brain*, **132**(Pt 6), 1656–68.
189. Winston GP, Daga P, Stretton J, et al. (2012). Optic radiation tractography and vision in anterior temporal lobe resection. *Annals of Neurology*, **71**(3), 334–41.
190. Kadom N, Trofimova A, and Vezina GL. (2012). Utility of magnetization transfer T1 imaging in children with seizures. *AJNR American Journal of Neuroradiology*, **34**(4), 895–8 .
191. Pinto Gama HP, da Rocha AJ, Braga FT, et al. (2006). Comparative analysis of MR sequences to detect structural brain lesions in tuberous sclerosis. *Pediatric Radiology*, **36**(2), 119–25.
192. Barkovich AJ, and Raybaud C. (2012). *Pediatric Neuroimaging*. London: Wolters Kluwer Health.
193. Wheaton AJ, and Miyazaki M. (2012). Non-contrast enhanced MR angiography: physical principles. *Journal of Magnetic Resonance Imaging*, **36**(2), 286–304.
194. Oishi M, Ishida G, Morii K, et al. (2012). Ictal focal hyperperfusion demonstrated by arterial spin-labeling perfusion MRI in partial epilepsy status. *Neuroradiology*, **54**(6), 653–6.
195. Toledo M, Munuera J, Salas-Puig X, et al. (2011). Localisation value of ictal arterial spin-labelled sequences in partial seizures. *Epileptic Disorders*, **13**(3), 336–9.
196. Pendse N, Wissmeyer M, Altrichter S, et al. (2010). Interictal arterial spin-labeling MRI perfusion in intractable epilepsy. *Journal of Neuroradiology*, **37**(1), 60–3.
197. Lim YM, Cho YW, Shamim S, et al. (2008). Usefulness of pulsed arterial spin labeling MR imaging in mesial temporal lobe epilepsy. *Epilepsy Research*, **82**(2–3), 183–9.
198. Wissmeyer M, Altrichter S, Pereira VM, et al. (2010). Arterial spin-labeling MRI perfusion in tuberous sclerosis: correlation with PET. *Journal of Neuroradiology*, **37**(2), 127–30.
199. Kwong KK, Belliveau JW, Chesler DA, et al. (1992). Dynamic magnetic resonance imaging of human brain activity during primary sensory stimulation. *Proceedings of the National Academy of Sciences, USA*, **89**(12), 5675–9.
200. Ogawa S, Tank DW, Menon R, et al. (1992). Intrinsic signal changes accompanying sensory stimulation: functional brain mapping with magnetic resonance imaging. *Proceedings of the National Academy of Sciences, USA*, **89**(13), 5951–5.
201. Gaillard WD, Balsamo L, Xu B, et al. (2002). Language dominance in partial epilepsy patients identified with an fMRI reading task. *Neurology*, **59**(2), 256–65.
202. Woermann FG, Jokeit H, Luerding R, et al. (2003). Language lateralization by Wada test and fMRI in 100 patients with epilepsy. *Neurology*, **61**(5), 699–701.
203. Rutten GJ, Ramsey NF, van Rijen PC, et al. (2002). FMRI-determined language lateralization in patients with unilateral or mixed language dominance according to the Wada test. *NeuroImage*, **17**(1), 447–60.
204. Giussani C, Roux FE, Ojemann J, et al. (2010). Is preoperative functional magnetic resonance imaging reliable for language areas mapping in brain tumor surgery? Review of language functional magnetic resonance imaging and direct cortical stimulation correlation studies. *Neurosurgery*, **66**(1), 113–20.
205. Desmond JE, Sum JM, Wagner AD, et al. (1995). Functional MRI measurement of language lateralization in Wada-tested patients. *Brain*, **118**(Pt 6), 1411–19.
206. Binder JR. (2011). Preoperative prediction of verbal episodic memory outcome using FMRI. *Neurosurgical Clinics of North America*, **22**(2), 219–32, ix.
207. Dupont S, Duron E, Samson S, et al. (2010). Functional MR imaging or Wada test: which is the better predictor of individual postoperative memory outcome? *Radiology*, **255**(1), 128–34.
208. Beers CA, and Federico P. (2012). Functional MRI applications in epilepsy surgery. *Canadian Journal of Neurological Science*, **39**(3), 271–85.
209. Ives J, Warach S, Schmitt F, et al. (1993). Monitoring the patient' EEG during echo planar MRI. *Electroencephalography and Clinical Neurophysiology*, **87**, 417–20.
210. Grova C, Daunizeau J, Kobayashi E, et al. (2008). Concordance between distributed EEG source localization and simultaneous EEG-fMRI studies of epileptic spikes. *NeuroImage*, **39**(2), 755–74.
211. Richardson M. (2010). Current themes in neuroimaging of epilepsy: brain networks, dynamic phenomena, and clinical relevance. *Clinical Neurophysiology*, **121**(8), 1153–75.
212. Kellinghaus C, and Luders HO. (2004). Frontal lobe epilepsy. *Epileptic Disorders: International Epilepsy Journal with Videotape*, **6**(4), 223–39.
213. Aghakhani Y, Bagshaw AP, Benar CG, et al. (2004). fMRI activation during spike and wave discharges in idiopathic generalized epilepsy. *Brain*, **127**(Pt 5), 1127–44.
214. Thornton R, Laufs H, Rodionov R, et al. (2010). EEG correlated functional MRI and postoperative outcome in focal epilepsy. *Journal of Neurology, Neurosurgery & Psychiatry*, **81**(8), 922–7.

215. Kaiboriboon K, Lowe VJ, Chantarujikapong SI, et al. (2002). The usefulness of subtraction ictal SPECT coregistered to MRI in single- and dual-headed SPECT cameras in partial epilepsy. *Epilepsia*, **43**(4), 408–14.
216. O'Brien TJ, So EL, Mullan BP, et al. (1998). Subtraction ictal SPECT co-registered to MRI improves clinical usefulness of SPECT in localizing the surgical seizure focus. *Neurology*, **50**(2), 445–54.
217. la Fougere C, Rominger A, Forster S, et al. (2009). PET and SPECT in epilepsy: a critical review. *Epilepsy Behaviour*, **15**(1), 50–5.
218. Cho JW, Hong SB, Lee JH, et al. (2010). Contralateral hyperperfusion and ipsilateral hypoperfusion by ictal SPECT in patients with mesial temporal lobe epilepsy. *Epilepsy Research*, **88**(2–3), 247–54.
219. Chassagnon S, Namer IJ, Armspach JP, et al. (2009). SPM analysis of ictal-interictal SPECT in mesial temporal lobe epilepsy: relationships between ictal semiology and perfusion changes. *Epilepsy Research*, **85**(2–3), 252–60.
220. Kaiboriboon K, Bertrand ME, Osman MM, et al. (2005). Quantitative analysis of cerebral blood flow patterns in mesial temporal lobe epilepsy using composite SISCOM. *Journal of Nuclear Medicine*, **46**(1), 38–43.
221. Newton MR, Berkovic SF, Austin MC, et al. (1992). Dystonia, clinical lateralization, and regional blood flow changes in temporal lobe seizures. *Neurology*, **42**(2), 371–7.
222. Van Paesschen W, Dupont P, Van Driel G, et al. (2003). SPECT perfusion changes during complex partial seizures in patients with hippocampal sclerosis. *Brain*, **126**(Pt 5), 1103–11.
223. Blumenfeld H, McNally KA, Vanderhill SD, et al. (2004). Positive and negative network correlations in temporal lobe epilepsy. *Cerebral Cortex*, **14**(8), 892–902.
224. Fukuda M, Masuda H, Honma J, et al. (2006). Ictal SPECT analyzed by three-dimensional stereotactic surface projection in frontal lobe epilepsy patients. *Epilepsy Research*, **68**(2), 95–102.
225. Kun Lee S, Young Lee S, Kim DW, et al. (2005). Occipital lobe epilepsy: clinical characteristics, surgical outcome, and role of diagnostic modalities. *Epilepsia*, **46**(5), 688–95.
226. Rowe CC, Berkovic SF, Austin MC, et al. (1991). Patterns of postictal cerebral blood flow in temporal lobe epilepsy: qualitative and quantitative analysis. *Neurology*, **41**, 1096–103.
227. Knowlton RC, Elgavish RA, Limdi N, et al. (2008). Functional imaging: I. Relative predictive value of intracranial electroencephalography. *Annals of Neurology*, **64**(1), 25–34.
228. Knowlton RC, Elgavish RA, Bartolucci A, et al. (2008). Functional imaging: II. Prediction of epilepsy surgery outcome. *Annals of Neurology*, **64**(1), 35–41.
229. Lee KK, and Salamon N. (2009). [18F] fluorodeoxyglucose-positron-emission tomography and MR imaging coregistration for presurgical evaluation of medically refractory epilepsy. *AJNR American Journal of Neuroradiology*, **30**(10), 1811–16.
230. Salamon N, Kung J, Shaw SJ, et al. (2008). FDG-PET/MRI coregistration improves detection of cortical dysplasia in patients with epilepsy. *Neurology*, **71**(20), 1594–601.
231. Chassoux F, Rodrigo S, Semah F, et al. (2010). FDG-PET improves surgical outcome in negative MRI Taylor-type focal cortical dysplasias. *Neurology*, **75**(24), 2168–75.
232. Chugani DC. (2011). Alpha-methyl-L-tryptophan: mechanisms for tracer localization of epileptogenic brain regions. *Biomarker Medicine*, **5**(5), 567–75.
233. Chugani DC, Chugani HT, Muzik O, et al. (1998). Imaging epileptogenic tubers in children with tuberous sclerosis complex using alpha-[11C]methyl-L-tryptophan positron emission tomography. *Annals of Neurology*, **44**(6), 858–66.
234. Natsume J, Kumakura Y, Bernasconi N, et al. (2003). Alpha-[11C] methyl-L-tryptophan and glucose metabolism in patients with temporal lobe epilepsy. *Neurology*, **60**(5), 756–61.

CHAPTER 13

Adult neoplasia

Phiroz E. Tarapore, Corinna C. Zygourakis,
Soonmee Cha, and Mitchel S. Berger

Introduction

Neuroimaging is a cornerstone of modern practice in the fields of neurology, neuro-oncology, and neurosurgery. Techniques such as computerized tomography (CT) and magnetic resonance imaging (MRI) have revolutionized the clinician's ability to diagnose, treat, and follow patients with neoplastic processes of the central nervous system (CNS). The last two decades have seen the introduction of additional techniques that go beyond simple anatomic description, offering insights into the haemodynamics, physiology, metabolism, and cyto-architecture of both the peritumoural environment and the CNS as a whole. Additionally, functional neuroimaging techniques enable clinicians to characterize a neoplastic lesion not just in an anatomical context, but also in the context of the overall neurological function of the patient, thus reducing treatment-related morbidity. Should a lesion require surgical management, intra-operative imaging techniques have enhanced the neurosurgeon's ability to maximize extent of resection without compromising neurological function? Finally, when following patients' long term, serial imaging plays an integral role in identifying the growth or recurrence of an identified neoplastic lesion. In short, the significant improvements in morbidity and mortality associated with neoplastic lesions of the CNS are due in large part to the advancement of neuroimaging techniques.

This chapter briefly summarizes the available imaging techniques that are in common clinical use in the management of adult CNS neoplasms. For most of these modalities, a detailed discussion of underlying physics is beyond the scope of the text. However, details will be provided if they are directly relevant to understanding the clinical application. Because the management of CNS neoplasms usually involves a surgical intervention, be it biopsy, subtotal, or gross total resection, followed in some cases by adjuvant treatment, the chapter's organization reflects the phases of patient management: diagnostic/pretreatment, intra-operative, and post-operative/follow-up. Both structural and functional modalities will be covered, and cutting-edge techniques with possible future clinical applications will be discussed when adequate clinical validation exists.

World Health Organization classification system

The World Health Organization (WHO) classification system of neoplasms of the CNS, last revised in 2007, has become the *de facto* worldwide standard [1]. This system incorporates cellular morphology, cytogenetics, molecular genetics, and immunohistological parameters to form a taxonomy of CNS neoplasms that is quantitative, evidence-based, and clinically relevant. The system grades CNS tumours from grade I to IV:

1. Grade I tumours have low proliferative potential and may be cured surgically.
2. Grade II tumours are generally infiltrating, but with low mitotic index.
3. Grade III tumours demonstrate histological evidence of malignancy, increased infiltrative capability, and anaplasia.
4. Grade IV tumours are mitotically active, highly invasive, and rapidly progressive.

This grading system forms the basis of clinical tumour staging (and, consequently, treatment decisions). However, because of its reliance on histopathological parameters, without an actual specimen, definitive WHO grading cannot be achieved or treatment initiated. Nevertheless, advanced MR techniques, such as proton magnetic resonance spectroscopy (^{1}H-MRS) and diffusion-weighted imaging (DWI) have shown promise in identifying CNS tumours by type and grade prior to definitive pathological diagnosis.

Diagnostic and preoperative techniques

Structural imaging

Computed tomography and magnetic resonance imaging

A structural imaging modality, either computed tomography (CT) or magnetic resonance imaging (MRI), is the first step in the diagnosis of brain tumours. Assessment of patient age, medical history, and tumour location, combined with specific imaging characteristics on CT, T_1-weighted MRI, before and after gadolinium administration, and T_2-weighted or fluid-attenuated inversion recovery (FLAIR) MRI, are helpful in narrowing down the differential diagnosis from the many different types of known brain tumours.

CT is often the first-line technique after the acute onset of neurologic symptoms, with tissue asymmetries or changes in tissue density (either increased or decreased) suggesting a space-occupying lesion. Administration of iodinated contrast can enhance the sensitivity of CT and help characterize the lesion, offering insights into vascularity and permeability (Fig. 13.1) [2]. Despite its longer scanning time and higher cost, however, high- resolution MRI has become the gold standard for the morphologic assessment of brain tumours due to its superior soft tissue resolution, multiplanar

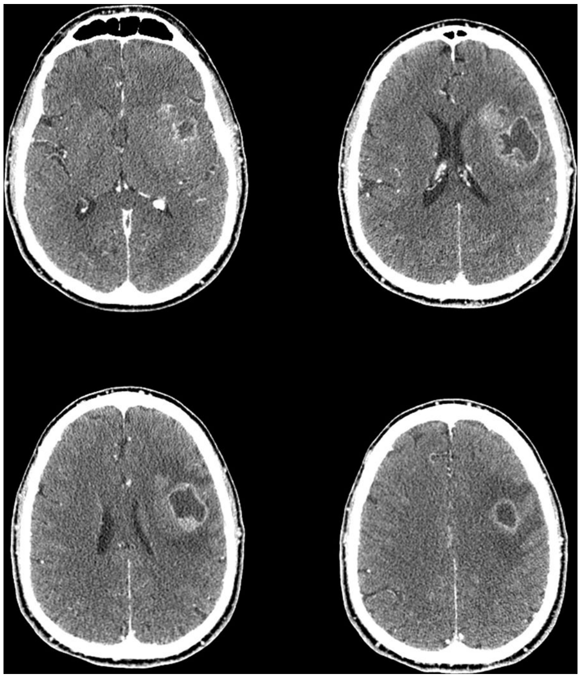

Fig. 13.1 CT with iodinated contrast shows an irregularly-shaped left frontal rim-enhancing lesion with surrounding hypodensity (oedema), consistent with a glioblastoma multiforme.

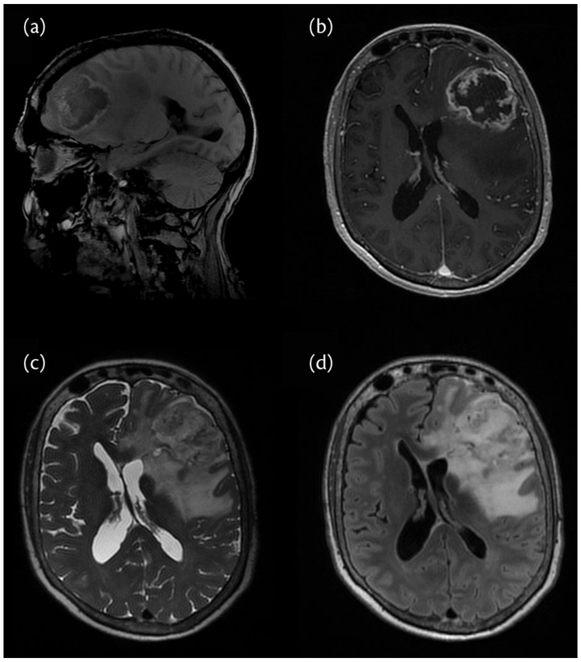

Fig. 13.2 MR of glioblastoma multiforme: (a) Sagittal T_1-weighted unenhanced MR shows a heterogeneous T_1 hypo/hyperintense irregularly-shaped left frontal lesion. (b) Axial T_1-weighted MR with gadolinium contrast shows that this left frontal lesion is avidly rim-enhancing. (c) Axial T_2-weighted MR emphasizes heterogeneous nature of this T_2 hyper/hypointense tumour (d) Axial T_2-FLAIR MR shows FLAIR abnormality surrounding left frontal lesion that is consistent with peritumoural oedema versus infiltrative tumour.

capability, and lack of ionizing radiation. Anatomic MRI relies on classic sequences, namely T_2-weighted imaging, which is particularly well-suited to imaging peritumoural oedema, and T_1-weighted imaging, in which contrast enhancement reflects breakdown of the blood–brain barrier that is seen in many high-grade tumours, such as glioblastoma multiforme, and a smaller portion of low-grade primary CNS tumours, such as pilocytic astrocytomas (Fig. 13.2) [2].

While the majority of clinical centres currently use 1.5 T or 3 T MR scanners for the evaluation of neurological diseases, there are exciting advances in the area of ultra-high field MRI. Recent studies show that 7 or 8 T MR scanners, which are not yet part of standard clinical care, may offer improved specificity, higher sensitivity, and better ability to detect, quantify, and monitor tumour activity and treatment effects due to higher resolution, greater coverage, and shorter scan times (Fig. 13.3) [3–7]. However, the ultra-high field MR scanners face challenges with respect to specific absorption rate, a measure of the rate at which energy is absorbed by the body when exposed to a radio frequency electromagnetic field, which increases with increasing strength of the MR scanner.

CT and MR perfusion

Purely anatomical CT or MRI, however, is often insufficient for making a diagnosis of a specific brain tumour, optimizing treatment planning, and monitoring treatment response. Dynamic contrast-enhanced imaging techniques with CT or MRI are now routinely used to obtain measures of tumour vascular physiology and haemodynamics. Perfusion imaging relies on the following parameters—cerebral blood volume (CBV, the volume of blood in a given region of brain tissue, in ml/100 g), cerebral blood flow (CBF, the volume of blood per unit time passing through a given region of brain tissue, in ml/min/100 g), and mean transit time (MTT, the

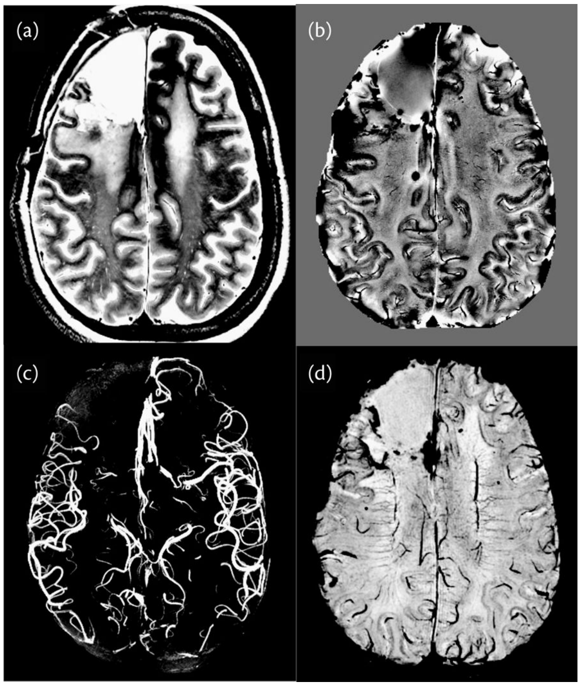

Fig. 13.3 7-T MR of grade III astrocytoma 28 months post-radiation with (a) axial high resolution 2D FSE, (b) 2D phase image generated from a T_2*-weighted GRE, (c) time-of-flight MR angiogram, and (d) 3D susceptibility-weighted image.

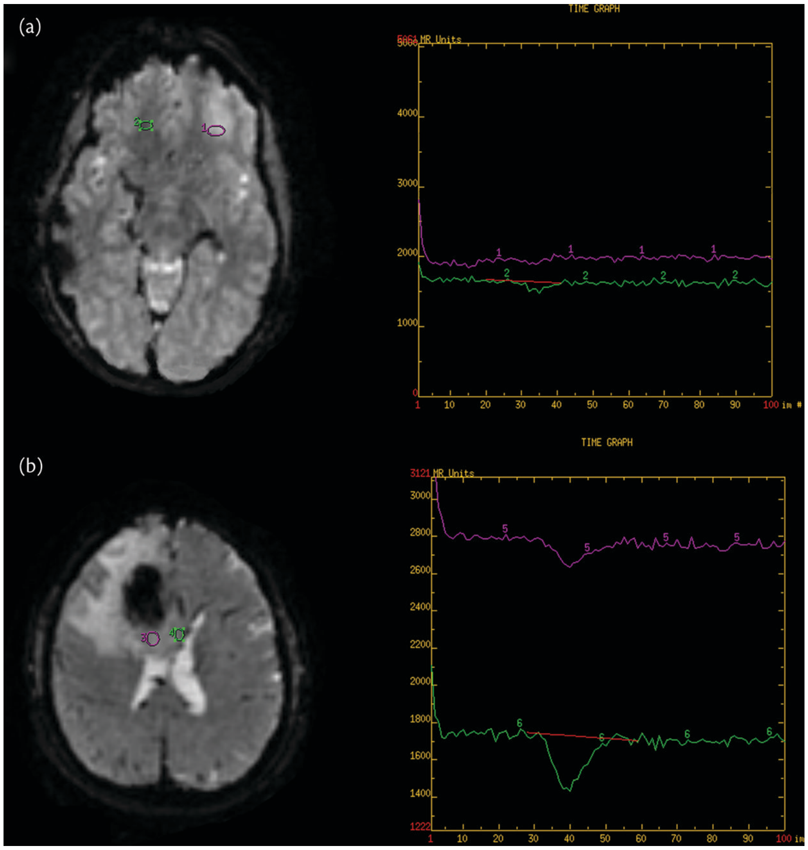

Fig. 13.4 (a) MR perfusion study of grade II astrocytoma shows that the left frontal tumour (purple) has similar cerebral blood flow/volume as compared with normal brain (green). (b) MR perfusion of grade IV astrocytoma reveals a right frontal tumour (purple) that has increased cerebral blood flow/volume as compared with normal brain (green), which is consistent with more vasculoproliferative higher grade tumours.

mean time for blood to pass through a given region of brain tissue, in seconds) [8].

In CT perfusion, a non-contrast head CT is first performed to localize the region of interest. A 50-ml bolus of non-ionic contrast is then rapidly injected (at a rate of 4–5 ml/second), and a continuous CT scan is initiated 5 seconds later. Similarly, in MR perfusion, ultrafast T_1- or T_2*-weighted MR images are obtained after the rapid injection of a paramagnetic contrast agent, gadolinium being the most common [8]. The raw data from both types of studies is then post-processed on an off-line workstation to obtain colour-coded maps of the aforementioned variables (CBV, CBF, and MTT) [9].

Since some tumours are associated with high cellular turnover and neovascularization, the increased capillary density in the intra- and peritumoural environment often leads to increased CBV and CBF. MTT may also be elevated due to the increased tortuosity of new tumour blood vessels. As a result, either CT or MR perfusion may be used to identify and distinguish tumours with relatively high CBV, CBF, and MTT from other disease processes, such as infective granulomas or tumefactive demyelination, which are hypoperfused and therefore have low values of CBV, CBF, or MTT [9]. Perfusion imaging is also helpful in differentiating low-grade tumours, which tend to have lower microvascular density (and, therefore, lower CBV and CBF) from more vasculoproliferative high-grade tumours (which have higher CBV/CBF) (Fig. 13.4). Several studies have shown a statistically significant relationship between CBV and astrocytoma grading [10–13]. In fact, one study shows that perfusion CT imaging is >80% sensitive and 100% specific for differentiating low versus high-grade gliomas [14]. Of note, perfusion values cannot be compared across brain tumour types because low grade oligodendrogliomas, for example, often have higher CBV than astrocytomas of similar grade [15].

Finally, MR perfusion can help distinguish between tumour recurrence and radiation necrosis, which often have a similar appearance on conventional MRI and are therefore a common diagnostic dilemma in the post-treatment period (see postoperative section for further details) [16].

Overall, *in vivo* perfusion imaging provides important information regarding tumour physiology and haemodynamics that complements conventional morphologic imaging. It is also a useful adjunct to histopathology because it is non-invasive, can be easily repeated, and is not prone to sampling error, therefore better reflecting the overall characteristics of a heterogeneous tumour. CT is more widely available, faster, and cheaper than MR, and some suggest that perfusion CT may provide a more robust and less biased estimation of haemodynamic parameters than perfusion MR [17]. Nevertheless, perfusion MR remains an important tool in the evaluation of brain tumours because of its higher spatial resolution.

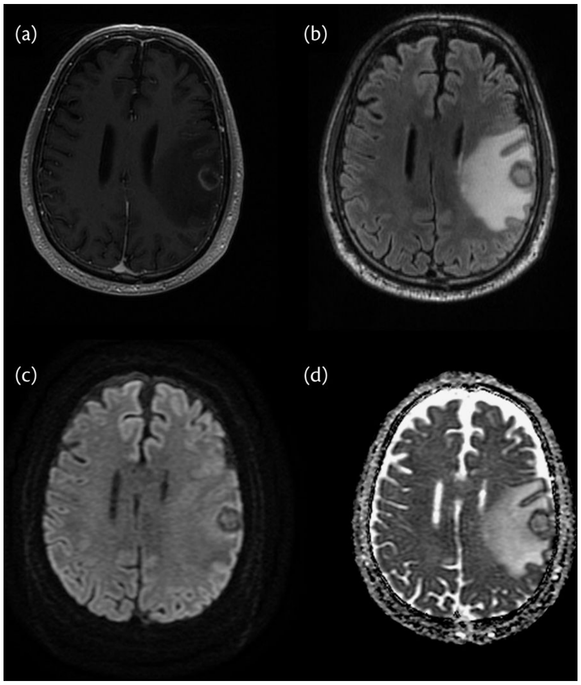

Fig. 13.5 MR of primary CNS lymphoma: (a) Axial T_1-weighted enhanced MR shows left-sided rim-enhancing lesion. (b) Axial T_2-FLAIR MR shows significant FLAIR abnormality surrounding lesion, consistent with oedema. (c) Axial DWI shows DWI hyperintensity in the centre of the lesion, reflecting reduced diffusion within the highly cellular lymphoma. DWI hypointensity surrounding the lesion indicates decreased cellularity of tumour necrosis and oedema surrounding the lesion. (d) Axial ADC shows hypointensity in centre of lesion and hyperintensity surrounding lesion, reflecting the increased cellularity of the lymphoma and decreased cellularity of surrounding tissue.

Diffusion-weighted MRI

Like MR perfusion, MR DWI is a modality that quantifies physiological processes in the *extracellular* Brownian water motion within the brain. It is based on the principle that the random motion of water molecules (Brownian motion) is constrained in certain pathologies by cellular enlargement and subsequent decrease in the extracellular space, thus restricting the diffusion of water molecules in that space [9]. For example, the diffusion of water in a highly cellular tumour, such as a primary CNS lymphoma may be reduced, appearing hyperintense on diffusion images and hypointense on the accompanying apparent diffusion coefficient (ADC) maps (Fig. 13.5) [18]. Conversely, water molecules in an area of decreased cellularity such as in tumour oedema or necrosis may diffuse more freely and therefore produce hypointense signal on DWI, with high ADC values (Fig. 13.5) [18].

Pre-operatively, DWI is helpful in the grading of brain tumours. Several studies have shown that ADC values are inversely correlated with tumour grade, probably reflecting increasing tumour cellularity with histopathological grade [19–21]. Specifically, higher ADC values are found in low-grade as compared with high-grade gliomas (ADC ≈ 1.53 μm^2/ms in WHO grade II astrocytoma, versus 0.66 μm^2/ms in grade IV glioblastoma) (Fig. 13.6) [22]. ADC has been correlated with cellularity of non-glial tumours as well, with low ADC values found in highly-cellular lymphomas [23], as well as atypical or malignant meningiomas [24]. However, the role of ADC in preoperative tumour grading remains investigational, given the considerable overlap in ADC values among tumours of different grades, as well as the significant heterogeneity of gliomas and other brain tumours [15].

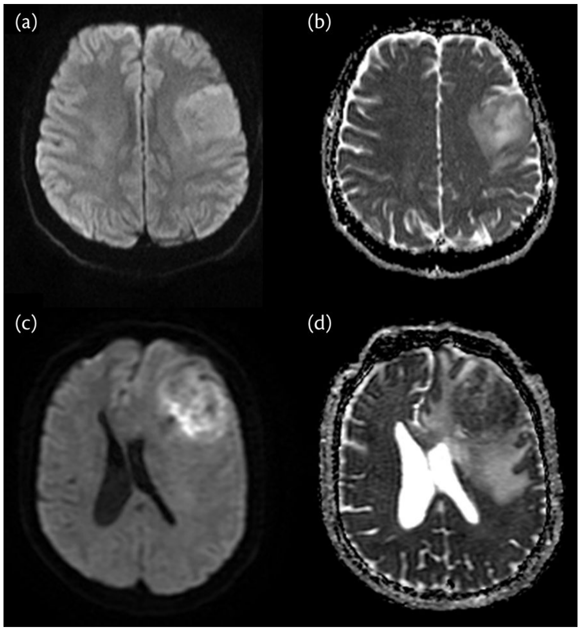

Fig. 13.6 MR of grade II astrocytoma: (a) Axial DWI shows very slightly reduced diffusion and (b) axial ADC shows only mild hypointensity, reflecting the mildly increased cellularity of a low grade neoplasm. MR of grade IV astrocytoma: (c) Axial DWI shows significantly restricted diffusion (very DWI bright), and (d) axial ADC shows significant hypointensity (ADC dark), reflecting the hypercellularity of higher grade neoplasms.

DWI can also be used to predict patient response during or after treatment for various brain tumours. Many studies show an increase in ADC after initiation of brain tumour treatment consistent with the development of vasogenic oedema or necrosis from tumour cell death. There have also been significant differences in ADC values between responders and non-responders at 2–4 weeks after stereotactic radiosurgery for a diverse array of brain tumours, including metastases, gliomas, meningiomas, and lymphomas [25]. Another investigational application of DWI is in distinguishing between vasogenic and infiltrative oedema, two types of peritumoural oedema [15]. Vasogenic oedema is caused by a disturbance in vascular permeability that leads to extravasation of plasma fluid and protein into the extracellular space, and is most commonly associated with metastatic brain tumours and other non-infiltrating brain tumours. In contrast, infiltrative oedema represents both vasogenic oedema and infiltrating tumour cells, and is associated with high-grade infiltrative tumours, such as glioblastoma multiforme. One study suggests that DWI can be used to distinguish between vasogenic and infiltrative oedema, and thereby differentiate metastatic tumours from gliomas [26]. However, the limited spatial resolution of DWI may prevent its widespread use in this area and may explain why other groups have been unable to use DWI to distinguish even more generally between cerebral tumours and peritumoural oedema [27].

Finally, MR diffusion imaging may aid in evaluating postoperative injury and in distinguishing recurrent tumour from

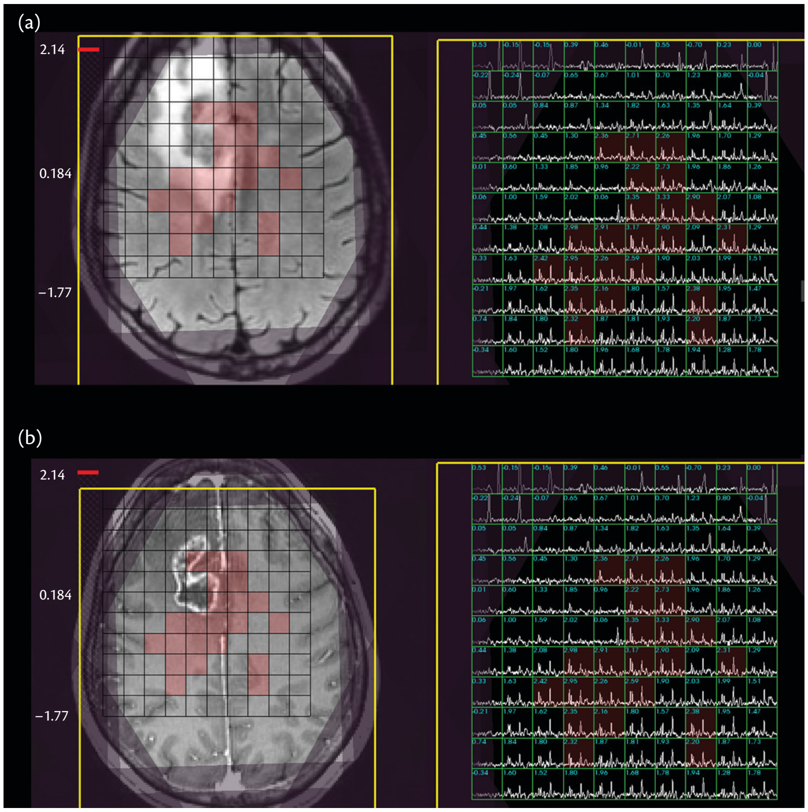

Fig. 13.7 MR spectroscopy of right frontal grade IV astrocytoma superimposed on (a) T_2-FLAIR axial sequences and (b) T_1-weighted contrast-enhanced MR sequences. Regions of interest with a choline >2.1 are highlighted in red. Higher levels of choline reflect increased membrane turnover and are found in higher-grade tumours.

radiation/treatment effect, which will be discussed further in the post-operative section of this chapter.

Proton MRS

^{1}H-MRS provides an imaging marker of tissue metabolism. It is based on the detection of molecule-specific energy spectra and, therefore, yields information about the metabolic properties in a given volume of tissue. In general, CNS neoplasms have higher levels of choline (reflecting increased membrane turnover) than non-neoplastic tissue. Tumours generally demonstrate lower N-acetyl aspartate (NAA) as a result of neuronal destruction by the tumour. They also tend to have increased levels of lactate, due to anaerobic glycolysis by tumour tissue, as well as higher lipid levels as a result of tumour necrosis (Fig. 13.7) [2].

More specifically, MRS can be used preoperatively to predict tumour grades, with choline levels >1.6 suggesting a high-grade astrocytoma [2]. However, due to presence of necrosis, glioblastoma multiforme may or may not show high choline levels due to partial volume effect. It can also guide stereotactic biopsies to assess the region with the highest membrane turnover (i.e. highest choline) in order to maximize the chance of obtaining diagnostic tissue for histopathology. MRS provides information about other metabolites, such as myoinositol, taurine, and alanine that may be useful in detecting particular brain tumours. For example, an alanine resonance peak is found in the majority of meningiomas, whereas a taurine metabolite is found in a subset of paediatric tumours. An increase in myoinositol may be found in zones of active glial activation due to infiltrating tumour cells [2].

Diffusion tensor imaging

Diffusion tensor imaging (DTI) is another magnetic resonance-based technique used to measure the restricted diffusion of water molecules in tissue. Because water molecules tend to diffuse preferentially along densely myelinated white-matter tracts, DTI can accurately trace white-matter tracts, a process known as tractography. In this modality, regions of interest that are presumed to be structurally connected are selected (e.g. primary motor cortex and cerebral peduncle). The algorithm then calculates the most likely white matter pathway connecting those regions. DTI can be performed on most modern MRI scanners, but are best suited to 3T or higher scanners. DTI-based tractography is commonly used to define the pyramidal tract [28–31] and, to a lesser extent, language [32] and visual pathways [33,34] in patients with lesions in proximity to eloquent cortical and subcortical areas (Fig. 13.8). Tractography can be rendered into a 3-dimensional (3D) volume and utilized intra-operatively for navigation during surgical resection (Fig. 13.9).

Functional imaging

Functional imaging is being utilized increasingly in the characterization of intracranial lesions, particularly in the preoperative setting to evaluate the eloquent brain region in patients with brain tumours. It is most useful in the management of lesions within or near the eloquent cortex, such as motor or visual cortex. By defining the function of perilesional parenchyma, it allows for optimization of surgical strategy by, for example, identifying the safest route

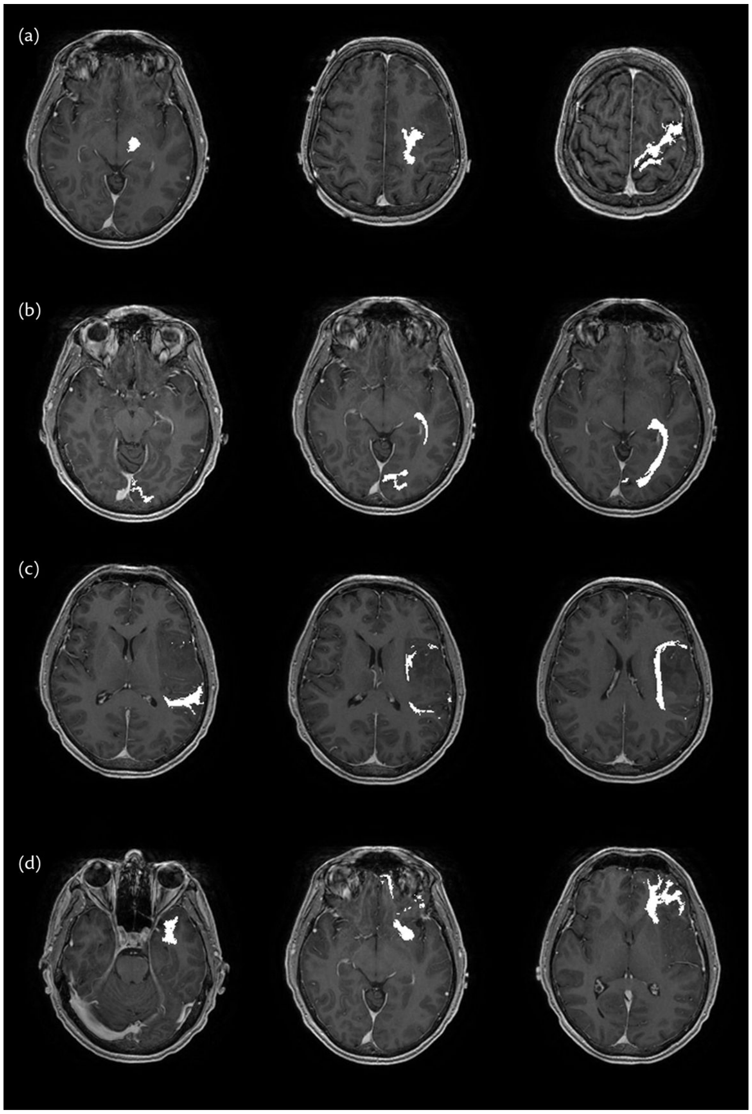

Fig. 13.8 DTI tractography of (a) corticospinal tract, (b) optic radiations, (c) arcuate fasciculus, (d) uncinate fasciculus in patient with left-sided grade II astrocytoma. Tracts are delineated in white and overlaid on axial T_1-weighted contrast-enhanced images.

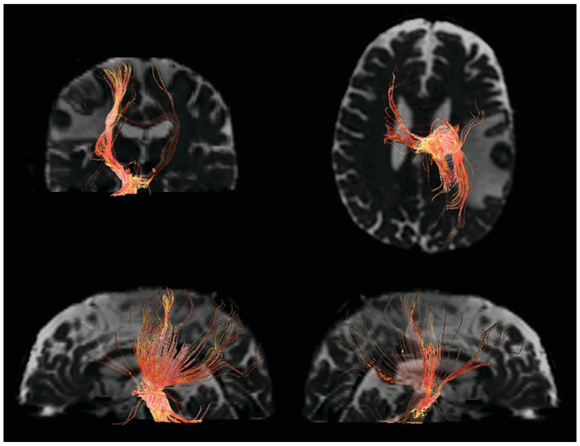

Fig. 13.9 3D representation of corticospinal tract as determined by DTI tractography and depicted in coronal, axial, right, and left sagittal projections overlaid on T_2-weighted MRI.

of access to a deep-seated lesion. It also allows clinicians to discuss the morbidity associated with a given lesion in specific and accurate terms, thereby giving patients clearer understanding of the ramifications of various management strategies (e.g. observation versus subtotal resection versus aggressive resection). Functional imaging is, therefore, an invaluable modality for identifying the clinical sequelae associated with a given lesion.

Functional MRI

Since its advent in 1991, functional magnetic resonance imaging (fMRI) has become the dominant technique for functional brain imaging. It uses the blood oxygen level dependence (BOLD) signal, which is a reflection of the changing levels of oxyhaemoglobin and deoxyhaemoglobin in functionally active brain regions. fMRI is limited by relatively poor temporal resolution (several seconds). It is a safe, non-invasive method that allows for whole-brain coverage, including the ability to examine activity in deep structures. Importantly, the widespread availability of MR scanners has made

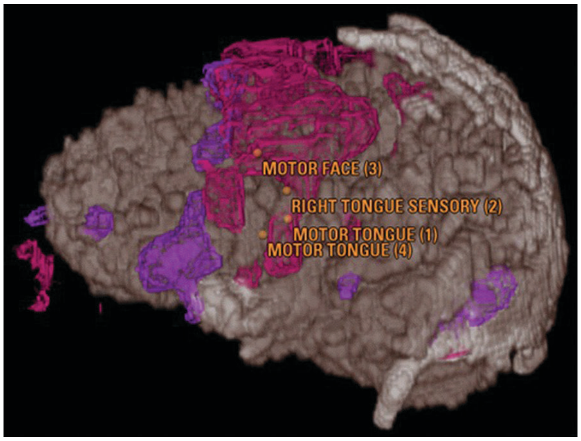
MOTOR FACE (3)
RIGHT TONGUE SENSORY (2)
MOTOR TONGUE (1)
MOTOR TONGUE (4)

Fig. 13.10 Functional MRI of motor (pink) and pre-motor areas (purple). Intra-operative direct cortical mapping results (orange dots) are overlaid on the 3D volume. The motor region (pink) defined by fMRI is more extensive than that defined by direct cortical mapping; this lack of specificity makes fMRI suboptimal as a stand-alone technique for the identification of eloquent cortical regions.

the technique easy to adopt across the medical field. In patients with brain tumours, fMRI has been used to identify sensorimotor cortex (Fig. 13.10), but other modalities, such as DTI and TMS are proving to be more accurate for this purpose. Currently, the use of fMRI to delineate regions associated with specific language tasks (i.e. word repetition, word reading, and object naming) is in the experimental stage. Similarly, language lateralization with fMRI is a subject of significant continuing research, and is rapidly reaching equivalent sensitivity and specificity to Wada testing (intracarotid sodium amobarbital procedure) [35].

Magnetoencephalography

Magnetoencephalography (MEG) measures tiny magnetic fields outside of the head that are generated by neural activity. Because it measures these fields directly, MEG offers excellent temporal resolution (<1 ms). Furthermore, magnetic fields are unimpeded by biological tissue, so MEG recordings offer an undistorted signature of underlying neural activity. MEG scanners, however, are expensive and relatively rare, so MEG is less widespread than MR-based techniques. MEG studies are useful for localization of sensory, motor, [36] and language regions (Fig. 13.11) [37]. They are also used to localize seizure foci, which is often helpful in the management of epileptogenic tumours, such as oligodendrogliomas. Finally, a recently described MEG-based algorithm for language lateralization successfully identify the language-dominant hemisphere with accuracy approaching that of Wada testing, the current gold standard [38].

Transcranial magnetic stimulation

Transcranial magnetic stimulation (TMS) is a technique that uses an externally applied, highly focused, brief magnetic pulse that is of sufficient strength to induce a depolarization in the underlying neuronal units. Depending on the frequency and location of the pulse, it can either cause neuronal excitability or have a temporary lesion

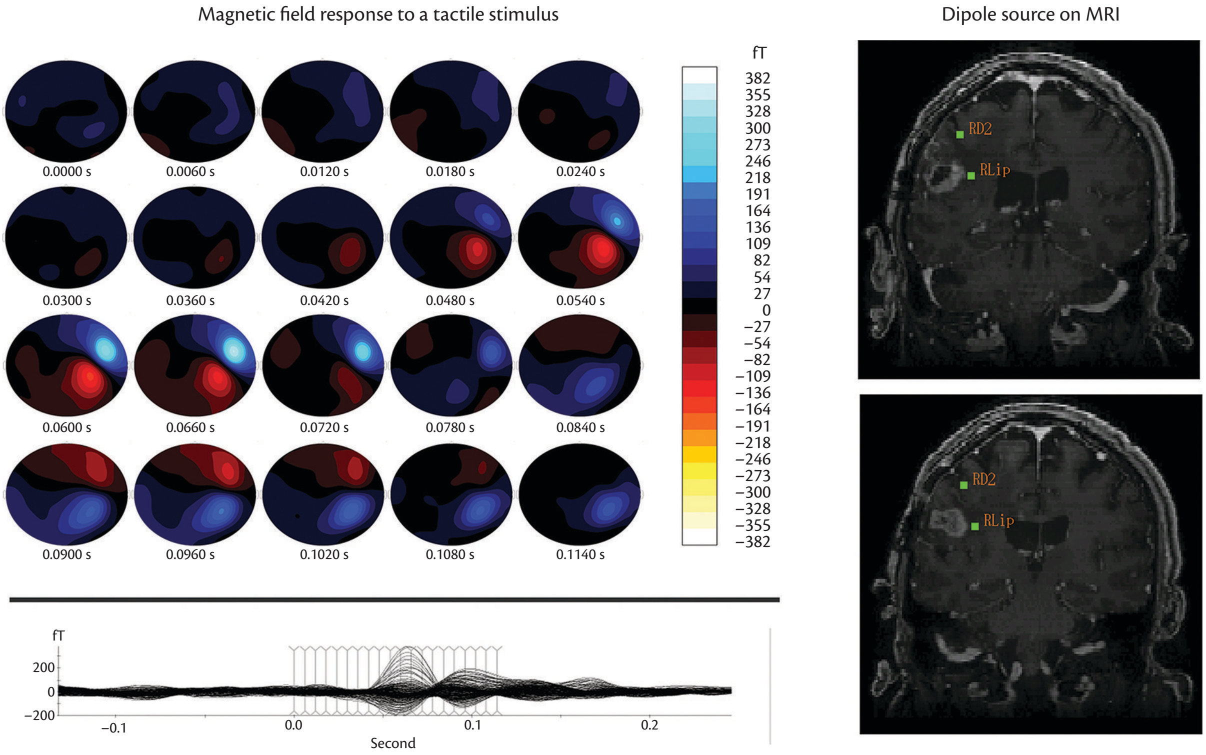
Magnetic field response to a tactile stimulus
Dipole source on MRI
0.0000 s
0.0060 s
0.0120 s
0.0180 s
0.0240 s
0.0300 s
0.0360 s
0.0420 s
0.0480 s
0.0540 s
0.0600 s
0.0660 s
0.0720 s
0.0780 s
0.0840 s
0.0900 s
0.0960 s
0.1020 s
0.1080 s
0.1140 s
fT
382
355
328
300
273
246
218
191
164
136
109
82
54
27
0
−27
−54
−82
−109
−136
−164
−191
−218
−246
−273
−300
−328
−355
−382
RD2
RLip
RD2
RLip
fT
200
0
−200
−0.1
0.0
0.1
0.2
Second

Fig. 13.11 Example MEG of somatosensory stimuli to the right lip (RLip) and right index finger (RD2). Multiple stimulus trials are performed for each site and cortical magnetic fields are recorded. The trials are averaged and a single dipole is reconstructed for each site using the least-square fit method. On the left are depicted the results in 0.006-second intervals, with the magnetic dipoles represented as red-orange (negative femto-Tesla) to blue-white (positive femto-Tesla). On the right, the resulting dipoles are then displayed on a coregistered, T_1-weighted post-gadolinium coronal MR slice. On the bottom of the figure is the overall time course of magnetic field with all trials superimposed.

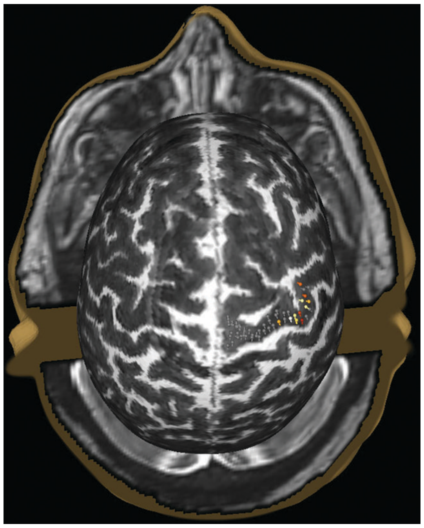

Fig. 13.12 A motor map of the precentral gyrus generated with TMS. Variably coloured pins indicate the amplitude of motor-evoked potentials in abductor pollicis brevis during the mapping procedure.

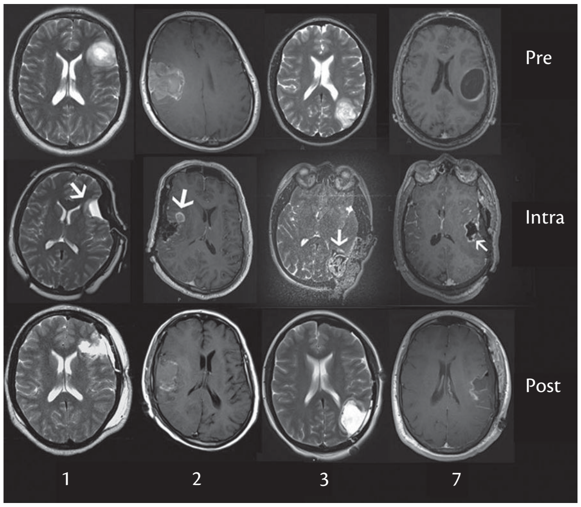

Fig. 13.13 Depiction of preoperative (top row), intra-operative (middle row), and post-operative MRI scans (bottom row) in representative patients undergoing surgery for glioma. Separate patients are shown in each column: Column 1 is T_2 MR images of left frontal tumour. Column 2 shows T_1 contrast-enhanced images of right-sided tumour. Column 3 shows T_2 MR images of left parietal tumour. Column 4 is T_1 contrast-enhanced images of left-sided tumour.

effect. Navigated TMS, in which the magnetic pulses are guided by a coregistered, preoperative MRI scan, allows for highly accurate mapping of the motor system. It is frequently used in the management of peri-Rolandic tumours, where the pyramidal tract is at highest risk of disruption from surgical resection, and has shown to correlate well with intra-operative direct cortical stimulation (Fig. 13.12) [39–41]. Additionally, TMS is currently being investigated as a modality for preoperative language mapping in patients with neoplastic lesions in peri-eloquent language regions [42,43].

Intra-operative imaging techniques

Intra-operative MRI

Intra-operative MRI utilizes a specialized scanner to acquire images within the operating room. High-field intra-operative MRI usually functions at 1.5 T or greater, and yields high-resolution scans. These units are bigger, and often require that the surgical suite be designed for rapid, easy transport of the patient to the scanner for image acquisition, such as with a motorized table that is continuous with the bore of the scanner. Low-field scanners usually function at or below 0.5 T, and are less expensive than high-field scanners. Although these images are of lower resolution, the machines are smaller and may thus be moved over a stationary patient [44].

Intra-operative MRI confers advantages over preoperative MRI, particularly in glioma surgery where extent of resection correlates with improved survival [45,46]. By allowing the surgeon to evaluate the extent of resection in real time, utilizing gadolinium contrast agent if desired, it ensures that any residual tumour may be removed. In traditional glioma surgery, this interim assessment is impossible; the surgeon must finish the case and the post-operative scan is completed the next day. Additionally, it helps the surgeon compensate for intra-operative brain shift that often occurs with longer surgeries by providing updated imaging data that accurately reflects the current anatomy.

Intra-operative MRI has been shown to improve surgical outcomes in patients with gliomas [45–47]. In comparison with traditional methods, it improves the extent of resection [48–50] in both low grade [51,52] and high grade [47,53] gliomas, and has been shown to reduce the size of residual tumour in the case of subtotal resection [54]. In a randomized, controlled trial, patients undergoing surgery for contrast-enhancing gliomas with intra-operative MRI had a significantly higher rate of gross total resection than those in the control group (Fig. 13.13) [55].

Despite the mounting evidence that glioma surgery with intra-operative MRI leads to better surgical outcomes, there is no clear data yet that it leads to increased progression-free or overall survival. Although further studies will probably demonstrate these advantages, the high cost of this technology is still an obstacle to its widespread adoption at tertiary referral centres and beyond.

Intra-operative ultrasound

Intra-operative ultrasound (IUS) is a modality that has been employed by neurosurgeons for decades. First discussed in the 1970s, IUS has been used intracranially for tumour localization, tumour biopsy, cyst drainage, and navigational guidance of ventriculo-peritoneal shunts [56]. Because it cannot penetrate the skull, IUS is not useful in the preoperative period for patients with an intact cranial vault. However, it has many advantages when used intra-operatively. IUS, like MRI, uses no ionizing radiation, but unlike MRI, ultrasound units are relatively inexpensive, portable, fast and easy to use without additional personnel.

In the last decade, IUS techniques have become more suited to neurosurgical procedures (Fig. 13.14) [57]. In particular, 3D ultrasound is increasingly able to localize meningiomas [58], gliomas, metastases [59], and other lesions [60] accurately within the brain parenchyma. Because IUS has the ability to resolve small anatomical structures, such as the small vessels on the cortical surface, it can be used to achieve highly accurate coregistration in a frameless stereotactical neuronavigation system [61]. Similarly, IUS can be used for intra-operative reregistration of an existing MRI to

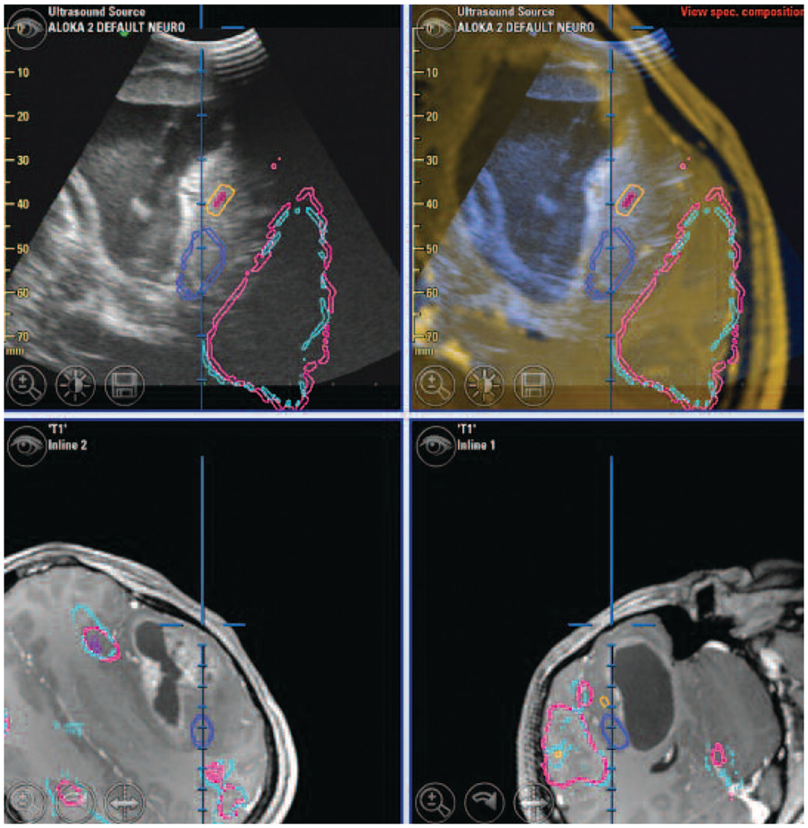

Fig. 13.14 Intra-operative ultrasound of a cystic glioma. The ultrasound image (top left and top right) is coregistered to an MRI scan (bottom left and bottom right) using a frameless stereotactical navigation system. The coloured outlines delineate specific brain regions that are identified in each modality.

account for brain shift [62]. Despite these advantages, limitations to IUS do exist. It is not optimal for deep lesions because of their distance from the probe. Additionally, it does not allow for as much tissue differentiation as other modalities, such as intra-operative MRI. Finally, it requires experience on the part of the user to be able to obtain and interpret IUS images successfully.

5-Aminolevulinic acid

5-aminolevulinic acid (5-ala) is a small molecule precursor that causes certain types of cancerous cells to synthesize or accumulate fluorescent porphyrins [63–66]. One such porphyrin, protoporphyrin IX (PPIX), specifically accumulates in glioma cells. PPIX, when illuminated with a violet-blue (375–440 nm) light, emits a red fluorescence, which can be viewed through a 455-nm long-pass filter. In effect, it makes glioma cells directly visible under the operating microscope. As such, it is not an imaging modality comparable with MR or CT, but rather a method of visualizing tumour cells directly via the microscope. 5-ala is administered as an oral solution from 6 to 24 hours prior to surgery. Intra-operatively, the tumour is resected using standard techniques. As the pseudomargins of the tumour are approached, fluorescence within cells may be used as one indicator that further resection is warranted (Fig. 13.15).

Thus far, results with 5-ala have been promising that it improves extent of resection [67,68]. In one study, it increased the rate of complete resection of the enhancing portion of GBM from 36 to 65%; the 5-ala patients also doubled their progression free survival of 6 months [69]. In another study, patients receiving 5-ala had median residual tumour volumes of 0 versus 0.5 cm in the conventional group [70]. In that study, however, patients receiving 5-ala were more likely to have short-term, temporary neurological deficits than control patients. This increased temporary morbidity is probably a result of the extended resections. 5-ala does not differentiate between eloquent and non-eloquent tissue, so the resection must not be extended to the limits of fluorescence without consideration for functional pathways. Again, in this trial, patients with complete resections had longer survival and time to neurological progression.

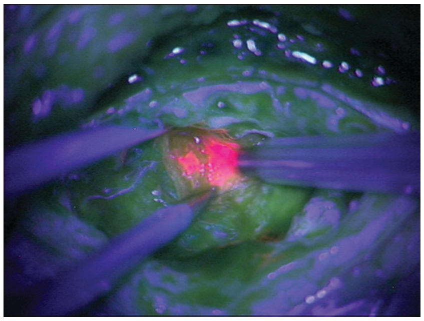

Fig. 13.15 Resection of a glioma that has been labelled with 5-ala. Under the fluorescent lighting of the operating microscope, the malignant tissue is centrally located and glowing with an apparent deep pink colour.

Post-operative and follow-up imaging techniques

Following surgical resection of a brain tumour, a post-operative MRI is usually performed within the first 48 hours. The purpose of such a scan is three-fold:

1. To determine if residual tumour is present (which would have similar MR properties as the preoperative tumour).
2. To detect stroke, retraction injury, or other intra-operative injury, which would appear diffusion restricted on the post-operative scan.
3. To identify areas of reduced diffusion that may later become contrast-enhancing and mimic the appearance of recurrent tumour [71].

These areas of contrast enhancement eventually evolve into encephalomalacia or gliosis and should therefore not be interpreted erroneously as residual tumours, which may precipitate unwarranted further therapy [15].

Subsequent to this initial post-operative scan, follow-up MRI is performed at varying frequencies depending on tumour type, ranging from 1 month (for an aggressive glioblastoma, for instance) to many years (for a benign meningioma). Adjuvant therapy also depends on tumour type, and may include systemic chemotherapy, stereotactic radiosurgery, and/or whole brain radiation. Neuroimaging plays an important role in monitoring the tumour's response to these multi-modal therapies. More specifically, repeat MRI is used to track tumour progression during chemotherapy or radiation therapy. Specific characteristics on a post-therapy scan, such as corpus callosum involvement, in conjunction with multiple enhancing lesions with or without crossing of the midline, and subependymal spread, may indicate, for example, that a high-grade glioma has recurred on conventional MRI [72].

When conventional T_1 and T_2 imaging is ambiguous, DWI helps to distinguish radiation-induced brain injury (i.e. radiation necrosis) from recurrent tumour. Several studies have shown that a recurrent tumour has significantly lower ADC values than radiation necrosis [18,73–75]. To complement DWI, perfusion MR can also be performed. Many groups have found that recurrent tumours have significantly higher cerebral blood volume and cerebral blood flow as compared with radiation necrosis. In fact, one study reported a specific relative CBV threshold that distinguishes recurrent high-grade glioma from radiation necrosis with >90% sensitivity and 100% specificity [76].

Conclusion

Neuroimaging is an integral component in the diagnosis and management of CNS neoplasms. In addition to the standard anatomical techniques, modern imaging provides insight into the physiology, metabolic profile, and architecture of the peritumoural environment, which creates a focused differential diagnosis. Additionally, functional techniques allow the treating clinicians to predict the neurological sequelae associated with the observation or treatment of a specific lesion, and to optimize treatment strategies to minimize neurological morbidity. Intra-operative imaging modalities have allowed for maximal tumour removal, while minimizing associated neurological deficits. Finally, post-operative imaging techniques aid in both long-term follow-up of a stable patient and in differentiating tumour recurrence from normal post-treatment effect. The advances in neuroimaging over the last half-century have vastly improved the quality of life and the overall survival in patients with neoplasias of the CNS. Challenges remain, however, as to how best to incorporate advanced imaging methods into treatment planning and early therapeutic assessment in order to improve clinical outcomes in patients with brain tumours.

References

1. Louis DN, Ohgaki H, Wiestler OD, et al. (2007). The 2007 WHO classification of tumours of the central nervous system. *Acta Neuropathologica*, **114**(2), 97–109.
2. Heiss WD, Raab P, and Lanfermann H. (2005). Multimodality assessment of brain tumors and tumor recurrence. *Journal of Nuclear Medicine*, **52**(10), 1585–600.
3. Lupo JM, Li Y, Hess CP, et al. (2011). Advances in ultra-high field MRI for the clinical management of patients with brain tumors. *Current Opinion in Neurology*, **24**(6), 605–15.
4. Lupo JM, Essock-Burns E, Molinaro AM, et al. (2013). Using susceptibility-weighted imaging to determine response to combined anti-angiogenic, cytotoxic, and radiation therapy in patients with glioblastoma multiforme. *Neurological Oncology*, **15**(4), 480–9.
5. Lupo JM, Chuang CF, Chang SM, et al. (2012). 7-Tesla susceptibility-weighted imaging to assess the effects of radiotherapy on normal-appearing brain in patients with glioma. *International Journal of Radiation Oncology Biology Physics*, **82**(3), e493–500.
6. Lupo JM, Banerjee S, Hammond KE, et al. (2009). GRAPPA-based susceptibility-weighted imaging of normal volunteers and patients with brain tumor at 7 T. *Magnetic Resonance Imaging*, **27**(4), 480–8.
7. Hammond KE, Lupo JM, Xu D, et al. (2008). Development of a robust method for generating 7.0 T multichannel phase images of the brain with application to normal volunteers and patients with neurological diseases. *NeuroImage*, **39**(4), 1682–92.
8. Petrella JR, and Provenzale JM. (2000). MR perfusion imaging of the brain: techniques and applications. *AJR American Journal of Roentgenology*, **175**(1), 207–19.
9. Sanghvi DA. (2009). Recent advances in imaging of brain tumors. *Indian Journal of Cancer*, **46**(2), 82–7.
10. Aronen HJ, Gazit IE, Louis DN, et al. (1994). Cerebral blood volume maps of gliomas: comparison with tumor grade and histologic findings. *Radiology*, **191**(1), 41–51.
11. Knopp EA, Cha S, Johnson G, et al. (1999). Glial neoplasms: dynamic contrast-enhanced T2*-weighted MR imaging. *Radiology*, **211**(3), 791–8.
12. Lev MH, Ozsunar Y, Henson JW, et al. (2004). Glial tumor grading and outcome prediction using dynamic spin-echo MR susceptibility mapping compared with conventional contrast-enhanced MR: confounding effect of elevated rCBV of oligodendrogliomas [corrected]. *AJNR American Journal of Neuroradiology*, **25**(2), 214–21.
13. Sugahara T, Korogi Y, Kochi M, et al. (1998). Correlation of MR imaging-determined cerebral blood volume maps with histologic and angiographic determination of vascularity of gliomas. *AJR American Journal of Roentgenology*, **171**(6), 1479–86.
14. Ellika SK, Jain R, Patel SC, et al. (2007). Role of perfusion CT in glioma grading and comparison with conventional MR imaging features. *AJNR American Journal of Neuroradiology*, **28**(10), 1981–7.
15. Cha S. (2006). Update on brain tumor imaging: from anatomy to physiology. *AJNR American Journal of Neuroradiology*, **27**(3), 475–87.
16. Jain R, Scarpace L, Ellika S, et al. (2007). First-pass perfusion computed tomography: initial experience in differentiating recurrent brain tumors from radiation effects and radiation necrosis. *Neurosurgery*, **61**(4), 778–86; discussion 86–7.
17. Jain R. (2011). Perfusion CT imaging of brain tumors: an overview. *AJNR American Journal of Neuroradiology*, **32**(9), 1570–7.
18. Gerstner ER, and Sorensen AG. (2011). Diffusion and diffusion tensor imaging in brain cancer. *Seminars in Radiation Oncology*, **21**(2), 141–6.

19. Bulakbasi N, Guvenc I, Onguru O, et al. (2004). The added value of the apparent diffusion coefficient calculation to magnetic resonance imaging in the differentiation and grading of malignant brain tumors. *Journal of Computer Assisted Tomography*, **28**(6), 735–46.
20. Kitis O, Altay H, Calli C, et al. (2005). Minimum apparent diffusion coefficients in the evaluation of brain tumors. *European Journal of Radiology*, **55**(3), 393–400.
21. Sugahara T, Korogi Y, Kochi M, et al. (1999). Usefulness of diffusion-weighted MRI with echo-planar technique in the evaluation of cellularity in gliomas. *Journal of Magnetic Resonance Imaging*, **9**(1), 53–60.
22. Maier SE, Sun Y, and Mulkern RV. (2010). Diffusion imaging of brain tumors. *NMR in Biomedicine*, **23**(7), 849–64.
23. Guo AC, Cummings TJ, Dash RC, et al. (2002). Lymphomas and high-grade astrocytomas: comparison of water diffusibility and histologic characteristics. *Radiology*, **224**(1), 177–83.
24. Filippi CG, Edgar MA, Ulug AM, et al. (2001). Appearance of meningiomas on diffusion-weighted images: correlating diffusion constants with histopathologic findings. *AJNR American Journal of Neuroradiology*, **22**(1), 65–72.
25. Tomura N, Narita K, Izumi J, et al. (2006). Diffusion changes in a tumor and peritumoral tissue after stereotactic irradiation for brain tumors: possible prediction of treatment response. *Journal of Computer Assisted Tomography*, **30**(3), 496–500.
26. Lu S, Ahn D, Johnson G, et al. (2003). Peritumoral diffusion tensor imaging of high-grade gliomas and metastatic brain tumors. *AJNR American Journal of Neuroradiology*, **24**(5), 937–41.
27. Eis M, Els T, Hoehn-Berlage M, et al. (1994). Quantitative diffusion MR imaging of cerebral tumor and edema. *Acta Neurochirugica Supplement (Wien)*, **60**, 344–6.
28. Wu JS, Zhou LF, Tang WJ, et al. (2007). Clinical evaluation and follow-up outcome of diffusion tensor imaging-based functional neuronavigation: a prospective, controlled study in patients with gliomas involving pyramidal tracts. *Neurosurgery*, **61**(5), 935–48; discussion 48–9.
29. Berman JI, Berger MS, Mukherjee P, et al. (2004). Diffusion-tensor imaging-guided tracking of fibers of the pyramidal tract combined with intraoperative cortical stimulation mapping in patients with gliomas. *Journal of Neurosurgery*, **101**(1), 66–72.
30. Berman JI, Berger MS, Chung SW, et al. (2007). Accuracy of diffusion tensor magnetic resonance imaging tractography assessed using intraoperative subcortical stimulation mapping and magnetic source imaging. *Journal of Neurosurgery*, **107**(3), 488–94.
31. Talos IF, Zou KH, Kikinis R, et al. (2007). Volumetric assessment of tumor infiltration of adjacent white matter based on anatomic MRI and diffusion tensor tractography. *Academic Radiology*, **14**(4), 431–6.
32. Henry RG, Berman JI, Nagarajan SS, et al. (2004). Subcortical pathways serving cortical language sites: initial experience with diffusion tensor imaging fiber tracking combined with intraoperative language mapping. *NeuroImage*, **21**(2), 616–22.
33. Yu CS, Li KC, Xuan Y, et al. (2005). Diffusion tensor tractography in patients with cerebral tumors: a helpful technique for neurosurgical planning and postoperative assessment. *European Journal of Radiology*, **56**(2), 197–204.
34. Werring DJ, Clark CA, Parker GJ, et al. (1999). A direct demonstration of both structure and function in the visual system: combining diffusion tensor imaging with functional magnetic resonance imaging. *NeuroImage*, **9**(3), 352–61.
35. Abou-Khalil B. (2007). An update on determination of language dominance in screening for epilepsy surgery: the Wada test and newer noninvasive alternatives. *Epilepsia*, **48**(3), 442–55.
36. Nagarajan S, Kirsch H, Lin P, et al. (2008). Preoperative localization of hand motor cortex by adaptive spatial filtering of magnetoencephalography data. *Journal of Neurosurgery*, **109**(2), 228–37.
37. Edwards E, Nagarajan SS, Dalal SS, et al. (2010). Spatiotemporal imaging of cortical activation during verb generation and picture naming. *NeuroImage*, **50**(1), 291–301.
38. Findlay AM, Ambrose JB, Cahn-Weiner DA, et al. (2012). Dynamics of hemispheric dominance for language assessed by magnetoencephalographic imaging. *Annals of Neurology*, **71**(5), 668–86.
39. Picht T, Schmidt S, Brandt S, et al. (2011). Preoperative functional mapping for Rolandic brain tumor surgery: comparison of navigated transcranial magnetic stimulation to direct cortical stimulation. *Neurosurgery*, **69**(3), 581–9.
40. Krieg SM, Shiban E, Buchmann N, et al. (2012). Utility of presurgical navigated transcranial magnetic brain stimulation for the resection of tumors in eloquent motor areas. *Journal of Neurosurgery*, **116**(5), 994–1001.
41. Tarapore PE, Tate MC, Findlay AM, et al. (2012). Preoperative multimodal motor mapping: a comparison of magnetoencephalography imaging, navigated transcranial magnetic stimulation, and direct cortical stimulation. *Journal of Neurosurgery*. 2012 Jun 15. PubMed PMID: 22702484. Epub 2012/06/19. Eng.
42. Krieg SM, Schaffner M, Shiban E, et al. (2013). Reliability of intraoperative neurophysiological monitoring using motor evoked potentials during resection of metastases in motor-eloquent brain regions. *Journal of Neurosurgery*. 2013 Mar 22. PubMed PMID: 23521547.
43. Tarapore PE, Findlay AM, Honma S, et al. (2013). Language mapping with navigated repetitive TMS: proof of technique and validation. *NeuroImage*, **82**, 260–72.
44. Leuthardt EC, Lim CC, Shah MN, et al. (2011). Use of movable high-field-strength intraoperative magnetic resonance imaging with awake craniotomies for resection of gliomas: preliminary experience. *Neurosurgery*, **69**(1), 194–205; discussion 205–6.
45. Hall WA, Liu H, Maxwell RE, et al. (2003). Influence of 1.5-Tesla intraoperative MR imaging on surgical decision making. *Acta Neurochirugica Supplement*, **85**, 29–37.
46. Nimsky C. (2011). Intraoperative MRI in glioma surgery: proof of benefit? *Lancet Oncology*, **12**(11), 982–3.
47. Kubben PL, Ter Meulen KJ, Schijns OE, et al. (2011). Intraoperative MRI-guided resection of glioblastoma multiforme: a systematic review. *Lancet Oncology*, **12**(11), 1062–70 .
48. Hatiboglu MA, Weinberg JS, Suki D, et al. (2009). Impact of intraoperative high-field magnetic resonance imaging guidance on glioma surgery: a prospective volumetric analysis. *Neurosurgery*, **64**(6), 1073–81; discussion 81.
49. Senft C, Seifert V, Hermann E, et al. (2008). Usefulness of intraoperative ultra low-field magnetic resonance imaging in glioma surgery. *Neurosurgery*, **63**(4 Suppl. 2), 257–66; discussion 66–7.
50. Nimsky C, Fujita A, Ganslandt O, et al. (2004). Volumetric assessment of glioma removal by intraoperative high-field magnetic resonance imaging. *Neurosurgery*, **55**(2), 358–70; discussion 70–1.
51. Claus EB, Horlacher A, Hsu L, et al. (2005). Survival rates in patients with low-grade glioma after intraoperative magnetic resonance image guidance. *Cancer*, **103**(6), 1227–33.
52. Pamir MN, Ozduman K, Dincer A, et al. (2010). First intraoperative, shared-resource, ultrahigh-field 3-Tesla magnetic resonance imaging system and its application in low-grade glioma resection. *Journal of Neurosurgery*, **112**(1), 57–69.
53. Hirschberg H, Samset E, Hol PK, et al. (2005). Impact of intraoperative MRI on the surgical results for high-grade gliomas. *Minimally Invasive Neurosurgery*, **48**(2), 77–84.
54. Senft C, Bink A, Heckelmann M, et al. (2011). Glioma extent of resection and ultra-low-field iMRI: interim analysis of a prospective randomized trial. *Acta Neurochirugica Supplement*, **109**, 49–53.
55. Senft C, Bink A, Franz K, et al. (2011). Intraoperative MRI guidance and extent of resection in glioma surgery: a randomised, controlled trial. *Lancet Oncology*, **12**(11), 997–1003.
56. Rubin JM, and Dohrmann GJ. (1982). Use of ultrasonically guided probes and catheters in neurosurgery. *Surgical Neurology*, **18**(2), 143–8.
57. Unsgaard G, Rygh OM, Selbekk T, et al. (2006). Intra-operative 3D ultrasound in neurosurgery. *Acta Neurochirugica*, **148**(3), 235–53; discussion 53.
58. Solheim O, Selbekk T, Lindseth F, et al. (2009). Navigated resection of giant intracranial meningiomas based on intraoperative 3D ultrasound. *Acta Neurochirugica*, **151**(9), 1143–51.

59. Unsgaard G, Selbekk T, Brostrup Muller T, et al. (2005). Ability of navigated 3D ultrasound to delineate gliomas and metastases—comparison of image interpretations with histopathology. *Acta Neurochirugica*, **147**(12), 1259–69; discussion 69.
60. Reinacher PC, and van Velthoven V. (2003). Intraoperative ultrasound imaging: practical applicability as a real-time navigation system. *Acta Neurochirugica Supplement*, **85**, 89–93.
61. Nikas DC, Hartov A, Lunn K, et al. (2003). Coregistered intraoperative ultrasonography in resection of malignant glioma. *Neurosurgery Focus*, **14**(2), e6.
62. Coenen VA, Krings T, Weidemann J, et al. (2005). Sequential visualization of brain and fiber tract deformation during intracranial surgery with three-dimensional ultrasound: an approach to evaluate the effect of brain shift. *Neurosurgery*, **56**(Suppl. 1), 133–41; discussion 141.
63. Stummer W, Stocker S, Wagner S, et al. (1998). Intraoperative detection of malignant gliomas by 5-aminolevulinic acid-induced porphyrin fluorescence. *Neurosurgery*, **42**(3), 518–25; discussion 525–6.
64. Kriegmair M, Baumgartner R, Knuchel R, et al. (1996). Detection of early bladder cancer by 5-aminolevulinic acid induced porphyrin fluorescence. *Journal of Urology*, **155**(1), 105–9; discussion 109–10.
65. Stummer W, Stocker S, Novotny A, et al. (1998). In vitro and in vivo porphyrin accumulation by C6 glioma cells after exposure to 5-aminolevulinic acid. *Journal of Photochemistry and Photobiology, Series B*, **45**(2–3), 160–9.
66. Fritsch C, Becker-Wegerich PM, Schulte KW, et al. (1996). [Photodynamic therapy and breast-plasty of an extensive superficial trunk skin basalioma of the breast. An effective combination therapy with photodynamic diagnosis]. *Hautarzt*, **47**(6), 438–42.
67. Stummer W, Pichlmeier U, Meinel T, et al. (2006). Fluorescence-guided surgery with 5-aminolevulinic acid for resection of malignant glioma: a randomised controlled multicentre phase III trial. *Lancet Oncology*, **7**(5), 392–401.
68. Stummer W, Novotny A, Stepp H, et al. (2000). Fluorescence-guided resection of glioblastoma multiforme by using 5-aminolevulinic acid-induced porphyrins: a prospective study in 52 consecutive patients. *Journal of Neurosurgery*, **93**(6), 1003–13.
69. Stepp H, Beck T, Pongratz T, et al. (2007). ALA and malignant glioma: fluorescence-guided resection and photodynamic treatment. *Journal of Environmental Pathology, Toxicology and Oncology*, **26**(2), 157–64.
70. Stummer W, Tonn JC, Mehdorn HM, et al. (2011). Counterbalancing risks and gains from extended resections in malignant glioma surgery: a supplemental analysis from the randomized 5-aminolevulinic acid glioma resection study. Clinical article. *Journal of Neurosurgery*, **114**(3), 613–23.
71. Smith JS, Cha S, Mayo MC, et al. (2005). Serial diffusion-weighted magnetic resonance imaging in cases of glioma: distinguishing tumor recurrence from postresection injury. *Journal of Neurosurgery*, **103**(3), 428–38.
72. Mullins ME, Barest GD, Schaefer PW, et al. (2005). Radiation necrosis versus glioma recurrence: conventional MR imaging clues to diagnosis. *AJNR American Journal of Neuroradiology*, **26**(8), 1967–72.
73. Hein PA, Eskey CJ, Dunn JF, et al. (2004). Diffusion-weighted imaging in the follow-up of treated high-grade gliomas: tumor recurrence versus radiation injury. *AJNR American Journal of Neuroradiology*, **25**(2), 201–9.
74. Asao C, Korogi Y, Kitajima M, et al. (2005). Diffusion-weighted imaging of radiation-induced brain injury for differentiation from tumor recurrence. *AJNR American Journal of Neuroradiology*, **26**(6), 1455–60.
75. Al Sayyari A, Buckley R, McHenery C, et al. Distinguishing recurrent primary brain tumor from radiation injury: a preliminary study using a susceptibility-weighted MR imaging-guided apparent diffusion coefficient analysis strategy. *AJNR American Journal of Neuroradiology*, **31**(6), 1049–54. PubMed PMID: 20110377. Epub 2010/01/30. eng.
76. Hu LS, Baxter LC, Smith KA, et al. (2009). Relative cerebral blood volume values to differentiate high-grade glioma recurrence from post-treatment radiation effect: direct correlation between image-guided tissue histopathology and localized dynamic susceptibility-weighted contrast-enhanced perfusion MR imaging measurements. *AJNR American Journal of Neuroradiology*, **30**(3), 552–8.

CHAPTER 14

Infections of the nervous system

Kate F. Mahady, Tarek A. Yousry, and H. Rolf Jäger

Introduction

Infection of the central nervous system (CNS) is an important, complex cause of neurological dysfunction and despite currently being only the third least common neurological disorder in the UK [1], it carries a mortality of over 50% worldwide [2].

Clinical presentation is diverse and can be late, causing delayed diagnosis and treatment, which in turn contribute to a worse clinical outcome. This makes efficient clinical, biochemical, and radiological assessment vital in the effective management of these patients [3].

Although CNS infection is more common in children, significant clinical, pathological, and radiological differences to those in adults mean this population must be considered separately.

This chapter addresses both the clinical and radiological assessment of CNS infection, first revising the anatomy of the meninges, cerebral, and spinal parenchyma as clarity here is fundamental to understanding the pathophysiology and aetiology of CNS infection. We consider infection of the meninges and neuroparenchyma as subgroups and conclude with the most clinically challenging and complex groups of CNS infections—human immunodeficiency virus (HIV)/acquired immunodeficiency syndrome (AIDS) and tuberculosis.

Although prion disease (including acquired and sporadic Creutzfeldt–Jakob disease) is communicable, it is associated with neurodegenerative clinical course, and it is discussed further in Chapter 23 of this book.

Diagnostic work-up

History and examination

A detailed clinical history of signs and symptoms, past medical, drug, family, and social histories, as well as potential exposure to pathogens (e.g. sexual, foreign travel, close contacts) should always be taken and be followed by a full physical examination.

A comprehensive examination of the central and peripheral nervous systems, including fundoscopy, should be performed by a trained specialist and routine serological analysis executed prior to referral for advanced investigations.

Investigations

Cerebrospinal fluid

Lumbar puncture is the definitive test in diagnosing CNS infection [4]. Routine analysis for glucose, cells and protein can be supplemented by cultures, PCR and immunoassays for immunoglobulins for certain microbes.

Although lumbar puncture has long been implicated in uncal and cerebellar tonsillar herniation in patients with raised intracranial pressure (ICP), this relationship has been widely disputed. The necessity of preceding cross-sectional imaging remains controversial, with little evidence of potential risks outweighing the benefit of prompt microbiological diagnosis and targeted antimicrobial treatment [5–7].

Radiology

Cross-sectional imaging of the CNS should be considered for any patient presenting with focal neurological signs, altered consciousness, intractable headache or seizures, and clinical features of infection, including pyrexia and neutrophilia, even without a known site of primary infection.

Imaging can identify potentially life-threatening complications of CNS infection. Magnetic resonance imaging (MRI) is the modality of choice, although computed tomography (CT) is indicated in certain cases that will be discussed subsequently. In the presence of inflammation, IV contrast medium administration results in tissue enhancement as a consequence of altered blood–brain barrier (BBB) permeability and inflammatory angiogenesis in more organized collections [8].

Anatomy

Anatomical knowledge of the meninges, brain, and spine is important to correctly compartmentalize CNS infection and focus the differential diagnosis. Three meningeal layers cover the brain and spinal cord. These three layers combine caudally to form the filum terminale (a fibrous band extending from the conus at L1/2 to the coccyx), which helps to anchor the spinal cord within the spinal canal. The meninges give rise to both anatomical and potential spaces, which are important in the clinical course, manifestations, and radiological signs of infection.

From deep to superficial:

1. *Pia mater:* a fragile cell layer attached to the surface of the brain and spinal cord, investing the brain's gyrae and sulci, and providing vascular supply to the neuroparenchymal surface. Pial projections (trabeculae) pass through the subarachnoid space superficially to attach the pia to the arachnoid mater. In the spine these projections form the denticulate ligaments, which pass laterally to the dura mater and anchor the spinal cord within the meninges.
2. *Subarachnoid space:* extends from the cerebral vertex and basal cisterns to approximately the S2 spinal level. This houses the cerebrospinal fluid (CSF), spinal nerve roots, cortical veins, and the cerebral and spinal arteries.

3. *Arachnoid mater:* a thin, transparent layer that fits loosely around the brain. It bears some resemblance macroscopically to a spider's web because of the previously described traversing pial projections or arachnoid trabeculations'.
4. *Subdural space:* a potential space between the arachnoid and dura mater; a strong barrier cell layer binding the two meningeal layers can be divided by collections of blood or pus. It is indented by arachnoid villi or granulations, which are involved in the CSF cycle (together with extracranial lymphatics [9]) at its inner aspect and is traversed by penetrating cortical veins, or bridging veins, *en route* to the dural venous sinuses cranially.
5. *Dura mater* comprises two layers; the outermost is periosteum of the skull's inner table meaning the layer is tightly bound to the skull bones and sutures. In the spinal canal, it is bound to the posterior longitudinal ligament in the midline and is continuous with the epineurium of the spinal nerve roots. The *inner (meningeal)* dural layer forms the superficial surface of the subdural space and includes openings which form the dural venous sinuses. *Dural reflections* separate the cerebral hemispheres (*falx cerebri*), the supra- and infratentorial brain (*tentorium cerebelli*) and indent the cerebellum posteriorly in the midline (*falx cerebelli*).
6. *Extradural (epidural) space:* another potential space that accommodates the meningeal vessels cranially. In the spine, it is predominantly fat filled and contains the extradural (or epidural) internal vertebral venous plexus.

In addition to these layers and spaces, common terms used to locate CNS lesions include *intra-* and *extra-axial*, describing a lesion's relationship to the pial layer in the brain. In the spine, *intra-* and *extra-dural*, describe the dural relationship, and *intra-* or *extra-medullary* describe the relationship to the spinal cord surface. A spinal lesion can therefore be described as intradural and extramedullary. By definition, an extradural lesion is extramedullary and an intramedullary lesion is intradural.

Meningeal infection

Inflammation of the meninges can occur as a result of pathogenic infection by bacteria, viruses, fungi, and parasites. The *leptomeninges* (constituting the pia and arachnoid mater) and *pachymeninges* (referring to the dura mater) are discussed separately on account of their differing clinical presentation, investigative findings and treatment options.

Leptomeningitis

Inflammatory infiltration of the leptomeninges (leptomeningitis) can occur by haematogenous spread of infection in patients with septicaemia or by direct invasion from infected paranasal sinuses, mastoid air cells, or exposure of the meninges in accidental or surgical trauma.

Patients typically present with acute pyrexia, severe headache, photophobia, neck stiffness, and some will be Kernig's sign positive (suffering pain on knee extension with the knee and hip flexed to 90°). The clinical course varies with the causative organism. As infection spreads, symptoms can progress to acute confusion, focal neuropathy, and reduced consciousness.

Common pathogens, imaging, and CSF findings are summarized in Table 14.1.

Bacterial leptomeningitis

Background

Untreated bacterial meningitic infection follows a devastating clinical course with mortality approaching 100%. When there is a suspicion of bacterial meningitis, empirical systemic antibiotic treatment is essential to improve clinical outcome and reduce mortality to approximately 7%. However, despite effective treatment, morbidity remains high at approximately 15% [10].

Meningococcal disease caused by *Neisseria meningitidis* in adolescents and young adults is associated with a characteristic skin rash and, if untreated, results in brain damage, hearing loss and peripheral ischaemia, progressing rapidly to coma and death.

In older patients, leptomeningitis is caused by *Streptococcus pneumonia* in approximately 50% of cases. Untreated pneumococcal meningitis can also result in permanent disability and death.

Nosocomial infection accounts for approximately 40% of meningitis in hospitalized patients and is usually caused by *Escherichia coli* or *Listeria monocytogenes* [11].

Investigative findings

Bacterial meningitis is diagnosed clinically and is confirmed by CSF analysis (Table 14.1). Radiological assessment can support the diagnosis, but its primary role is the identification of complications such as cerebritis, abscess formation (see 'Bacterial parenchymal infection'), communicating or obstructive hydrocephalus (as a result of debris/inflammatory cells causing aqueductal stenosis or obstruction of CSF absorption in the arachnoid granulations), or dural venous sinus thrombosis (DVST) and associated venous infarction.

MRI is the imaging modality of choice, however, CT and contrast-enhanced CT (CE-CT) is performed acutely, and in unstable or agitated patients unable to tolerate MRI.

In severe infection, CE-CT can show high attenuation, enhancing exudate that invests the cerebral sulci and basal cisterns (Fig. 14.4a). Cerebral oedema, early cerebritis, or infarction causes sulcal effacement and parenchymal low attenuation. Early hydrocephalus starts with dilatation of the temporal horns of the lateral ventricles.

On contrast-enhanced MRI (CE-MRI), leptomeningeal enhancement can be subtle and is demonstrated earlier by contrast-enhanced fluid-attenuated inversion recovery (FLAIR) imaging than by CE-CT or standard CE-T_1-weighted imaging (T_1WI) [12].

Complications of meningitis are better visualized by MRI with cerebral oedema and inflammation shown as T_2 white matter hyperintensity and sulcal effacement, infarction as loss of gray–white matter differentiation with water diffusion restriction on diffusion-weighted (DW) scans. Hydrocephalus can be associated with ependymal enhancement and dependant intraventricular debris, which is hypointense to CSF, implying pyogenic ventriculitis.

MRI and CT are also assessed for features of DVST and cerebral abscess as discussed in 'Parenchymal infection'.

Viral leptomeningitis

Background

Approximately 3000 cases of viral meningitis are diagnosed in the UK annually, making it more common than meningitis of any other cause with the most frequently isolated causative organisms being *Poliovirus* and *Enterovirus* species including *Coxsackie B* [13].

Acutely, patients complain of headache, neck pain and fever as patients do with bacterial meningitis, but the clinical course

Table 14.1 Summary of common pathogens, clinical and investigative findings in meningitis

	Causative organisms	**Epidemiology**	**Enhancement pattern**	**CSF [73]**
Bacterial	*N. meningitidis* *S. pneumoniae* *(E. coli,* *L. monocytogenes)*	Young Old Inpatients	None or linear leptomeningeal	OP ↑ Bacteria (60%) Glucose ↓ Protein ↑ Neutrophils + WCC > 1000/mm^3
Viral	*Enterovirus* *Coxsackie B* *Mumps virus*	Any age	None or linear leptomeningeal	OP ↔ Glucose ↔ Protein ↔ or ↑ Lymphocytes + WCC < 100/mm^3
Fungal	*Cryptococcus species* *Aspergillus species* *C. albicans*	Immunocompromised	Nodular leptomeningeal	OP variable Glucose ↓ Protein ↑ Lymphocytes + WCC < 300/mm^3
Parasitic	*A. cantonensis* *T. solium*	Foreign travel Infected pork	Rare	Parasites/ova Glucose ↓ Protein ↑ Eosinophils +
Spirochete	*B. burgdorferi*	Tick exposure	Leptomeningeal, parenchymal lesions	Glucose ↓ Protein ↑ Lymphocytes +
Mycobacteria	*M. tuberculosis*	Foreign travel Immunocompromised Ethnicity	Pachymeningeal	OP variable Glucose ↓ Protein ↑ Lymphocytes + WCC < 300/mm^3

is indolent. The condition is usually self-limiting and is associated with good clinical outcomes often negating definitive medical treatment [14]. Viral meningitis should not be confused with viral encephalitis which follows a much more aggressive course (see 'Viral encephalitis').

Investigative findings

The diagnosis of viral meningitis is made clinically and by CSF analysis, performed to exclude other causes of meningism, such as bacterial infection and subarachnoid haemorrhage. CE-CT or CE-MRI can show subtle leptomeningeal enhancement, but are usually normal.

Fungal leptomeningitis

Background

Crytpococcus neoformans and *Aspergillus* spp. are fungal species frequently associated with leptomeningitis and are fully discussed in 'Fungal infection'.

Investigative findings

CSF analysis and serology for antigen and immunoglobulins make the diagnosis of *Cryptococcal* meningitis. The role of cross-sectional imaging is in assessing parenchymal spread and complications, such as obstructive hydrocephalus caused by high exudative viscosity (see 'Parenchymal infection'). Fungal leptomeningitis causes thick, nodular enhancement on CE-CT/MRI, which is most pronounced in the basal cisterns.

Spirochete leptomeningitis

Background

Lyme's disease (*Borellia burgdorferi*) is a rare cause of meningitis and encephalitis. Ticks are transferred to humans (directly from infested animals or indirectly from long grass) and transmit the spirochete via their bite. Patients subsequently complain of flu-like symptoms and a classic skin 'target' lesion (erythaema chronicum migrans).

Neuroborreliosis is seen in approximately 15% of infected patients [15], initially causing meningitis, mononeuritis multiplex, or radiculopathy. Later in the course of the disease, there can be progressive neuropathy with or without cardiac symptoms or arthropathy.

Investigative findings

The diagnosis is made by clinical and CSF assessment, whilst the extent of the disease is assessed by CE-MRI. This typically shows meningeal enhancement associated with multiple intra-axial enhancing lesions, predominantly frontoparietal subcortical T_2 hyperintensities, and occasionally hydrocephalus.

Parasitic leptomeningitis

Parasitic meningitis is uncommon in developed countries (see cysticercosis, 'Parasitic'). As opposed to bacterial meningitis, presentation with photophobia is rare. However, severe headache and neck stiffness are common features. Helminthic parasites, the most common of which worldwide is *Angiostrongylus cantonensis* [16], infect the CSF and cause eosinophilia.

Ependymitis/ventriculitis

Background

Ventriculitis complicates approximately 30% of cases of adult bacterial meningitis, and is less commonly seen to complicate surgical ventricular catheterization, cerebral abscess, or trauma [17]. It is a potentially fatal intracranial infection that is treated clinically as a cerebral abscess (see 'Parenchymal infection'), making early diagnosis and prompt initiation of intrathecal antibiotic treatment vital for improving prognosis.

Investigative findings

Ependymal enhancement on CE-CT reflects inflammation of the ependymal cells lining the cerebral ventricles. Ventriculomegaly with extensive periventricular low attenuation on CT is seen as a result of hydrocephalus with reactive oedema and isodense inflammatory debris can pool in the occipital horns to form a dependant fluid-fluid level with CSF.

CT appearances are echoed on CE-MRI; on CE-T_1WI, there is ependymal thickening and enhancement, and dependant debris can be hyperintense because of its high protein content. T_2WI/FLAIR demonstrate hydrocephalus and hyperintense periventricular oedema.

Pachymeningitis

Pachymeningitis

Background

Pachymeningitis (dural inflammation) is typically idiopathic, iatrogenic, autoimmune, or attributable to tuberculous infection (see 'Diverse central nervous system infections'). After exclusion of infection, meningeal biopsy is sometimes indicated to identify the underlying cause. The most likely cause of dural inflammation is previous lumbar puncture.

Investigative findings

Dural thickening and enhancement at the base of the brain and over the cerebral convexities is demonstrated by CE-CT or CE-MRI (Fig. 14.4a).

Subdural empyema

Background

A subdural empyema is a collection of pus in the subdural space (above or below the tentorium) and is a recognized complication of trauma, sinusitis, mastoiditis, periorbital cellulitis, leptomeningitis, or surgery. It should be suspected in a patient with a relevant history who presents with reduced consciousness or focal neurological dysfunction because potentially fatal spread of infection is rapid and early surgical management is known to dramatically improve outcomes [18,19].

Complications such as cerebral herniation, caused by local cerebral oedema or direct mass effect from the collection, and venous sinus thrombosis (which complicates approximately 10% of subdural empyemas[16]) are diagnosed and monitored by imaging.

Investigative findings

A subdural empyema is shown by CE-CT as a peripherally enhancing, isodense crescenteric convexity collection with or without a fluid-fluid level of dependant hyperdense debris.

Assessment of the paranasal sinuses, mastoid air cells, and facial soft tissues can reveal a primary source of infection. Distension and hyperdensity of a venous sinus on CT together with a lack of opacification on CE-CT is characteristic of DVST. A venous infarct is shown by loss of gray-white matter differentiation in a non-vascular territory and can be bilateral. This can be complicated by haemorrhage that is often fragmented.

CE-MRI is more sensitive for smaller and infratentorial collections, which can be missed by CT and will show a peripherally-enhancing, T_2W/FLAIR hyperintense, T_1W iso- or hypointense, diffusion-weighted imaging (DWI) hyperintense, and apparent diffusion coefficient (ADC) hypointense (water diffusion restricted) subdural collection.

Cerebral extradural (epidural) abscess

Background

In cerebral extradural abscess, aetiology is similar to that of subdural empyema and timely imaging is important for the same reasons. In a patient presenting with Pott's puffy tumour (a tender, fluctuant, erythematous, hot forehead lesion caused by frontal sinusitis and osteomyelitis of the frontal bone), exclusion of an extradural abscess is imperative [20].

Investigative findings

On contrast-enhanced cross-sectional imaging, there is an elliptiform collection, which is bound by the skull diastases and should not cross sutures unless it is associated with a diastatic fracture. It can, however, cross the midline as, unlike subdural collections, it is not bound by the falx cerebri. Imaging characteristics are otherwise similar to those described of subdural empyema.

Spinal extradural (epidural) abscess

Background

In the spine, extradural infection is usually caused by *Staphylococcus aureus* and follows vertebral osteomyelitis caused by discitis. It is typically seen in immunocompromised or elderly patients, IV drug users, post-operative patients, or patients with established urinary tract or cardiac infections. Haematogenous microbial spread to nutrient-rich vertebral body endplates results in rapid bacterial proliferation, bone destruction, and formation of an abscess, which extends into the extradural space. Secondary infection of a traumatic spinal extradural haematoma is another recognized cause.

Patients present with back pain, sepsis, and radiculopathy. MRI assessment of the whole spine is urgent in these patients, as this can progress to myelopathy as a result of cord compression, oedema, and even infarction secondary to mass effect from large extradural collections. *Mycobacterium tuberculosis* infection should be excluded; key clinical and imaging features can aid in differentiation (see 'Diverse central nervous system infections').

Investigative findings

Discitis appears on CT as an angular kyphosis, centred on a reduced or obliterated intervertebral disc space with adjacent end plate irregularity and lucency. Soft tissue algorithms on CE-CT could reveal an adjacent peripherally enhancing paravertebral or psoas muscle collection, which can invade local structures.

On MRI, sagittal T_2W and CE-T_1W imaging demonstrate similar bony destruction and T_2 prolongation in the adjacent end plates. The disc space collection typically extends posteriorly towards the vertebral canal, where it strips the posterior longitudinal ligament from the vertebral body and compresses the theca.

Axial imaging shows a peripherally or uniformly enhancing, T_2/FLAIR hyperintense ventral extra-axial collection that is usually bilobed because the posterior longitudinal ligament dural attachment is rarely breached in the midline. This can cause central or peripheral neural compression (Fig. 14.4c). Surrounding structures, particularly the psoas muscle, should be assessed for direct extension, particularly if the abscess extends ventrally from the disc space.

Spinal subdural abscess

Background

Spinal subdural abscess is rare and its aetiology, clinical course, and management are comparable with those of spinal extradural abscess.

Investigative findings

In the spine, the extradural and subdural spaces can be difficult to differentiate radiologically. As in extradural abscess, urgent MRI is required because of the risk of spinal cord compression, oedema, and ischaemia. A circumferential (rather than elliptiform collection typically seen in extradural abscess), peripherally enhancing, T_2 hyperintense collection is demonstrated by axial imaging, with or without features of myelopathy.

Parenchymal infection

Neuroparenchymal infection by bacteria, viruses, fungi, and parasites occurs via direct spread from the adjacent meninges, haematogenously from a distant infective focus, or can be a consequence of direct exposure in surgery or trauma.

Bacterial infection is associated with the formation of a pyogenic abscess, viral infection with more diffuse encephalitis, fungal infection with leptomeningitis with or without granulomas, and parasitic infection with a variety of consequences depending upon the life cycle of the invading parasite.

Bacterial parenchymal infection

Pyogenic cerebral abscess

Background

A pyogenic cerebral abscess is an organized suppurative collection within the brain. Those in the middle cerebral artery (MCA) territory are typically a consequence of haematogenous spread of infection from a distant source, and those in the frontal or temporal lobes are likely to have been caused by the direct spread of infection from the paranasal sinuses or petrous temporal bone respectively.

Patients initially present with headache, reduced consciousness, visual disturbance, or vomiting, but whilst clinical signs of a primary infective source might be apparent, pyrexia and meningitic symptoms are seen in less than 50% [21]. If cerebral abscess is untreated, clinical deterioration with seizures and coma is rapid, making early medical antibiotic treatment, and timely neurosurgical referral important to improve the clinical outcome.

Investigative findings

The radiological stages of pyogenic abscess formation are:

1. *Early cerebritis:* occurs within 1–3 days of infection. CT is less sensitive than MRI in detecting the cerebral swelling and oedema of cerebritis, seen as a subtle loss of gray–white matter differentiation with or without local meningeal enhancement. On CE-MRI, the affected area returns high signal on T_2WI and low signal on T_1WI, with variable local post-contrast enhancement. ADC maps do not show restricted water diffusion at this stage.
2. *Late cerebritis:* occurs in the following 7–14 days. Necrosis progresses and neovascularization occurs, resulting in peripheral enhancement and central hypo-attenuation on CE-CT. Ring enhancement is also shown by CE-MRI; the centre is hyperintense on T_2WI and there is associated water diffusion restriction on DWI. This finding is important in differentiating pyogenic abscess from necrotic neoplasia, in which water diffusion is not restricted. Excessive perilesional vasogenic oedema progresses throughout cerebral abscess development and can exert mass effect resulting in local sulcal effacement, raised ICP and cerebral herniation.

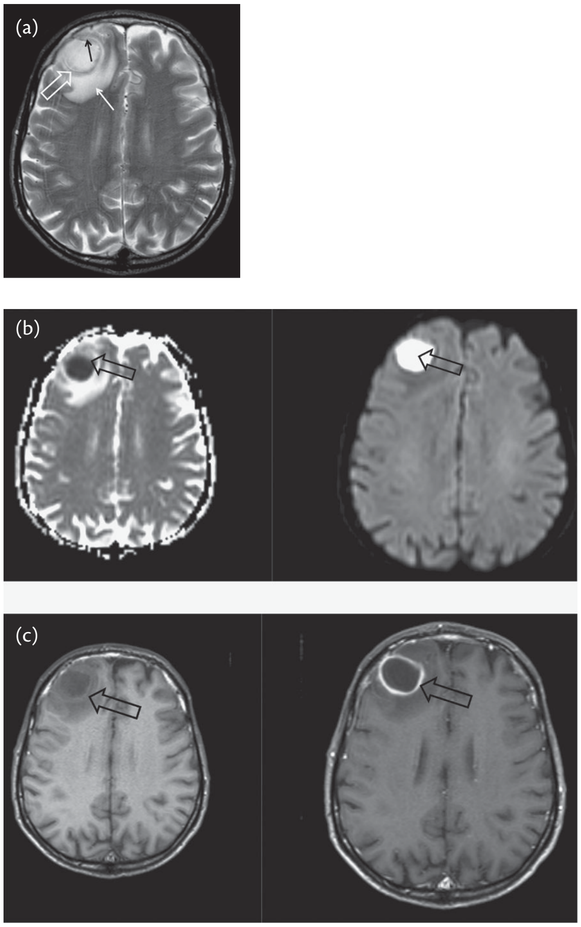

Fig 14.1 Pyogenic cerebral abscess: MRI. (a) T_2WI demonstrates a right frontal lesion (block arrow) at the grey-white matter junction. Surrounding signal change and mass effect is consistent with oedema (white line arrow). The incomplete hypointense rim (black arrow) reflects the collagen containing capsule seen in the *early capsule* stage of pyogenic abscess formation. (b) Central hypointensity on the ADC map (left) and hyperintensity on DWI (right) indicates central diffusion restriction. (c) T_1WI (left) shows capsular T_1 shortening caused by collagen within the capsular. CE-T_1WI (right) shows a complete ring of peripheral enhancement.

3. *Early capsule phase:* follows if late cerebritis is unsuccessfully diagnosed or treated, after 14 days. Optimal management then becomes surgical as a complete early capsule is formed rendering systemic treatment ineffective. A complete, but irregular ring of enhancement on CE-CT and MRI is seen. On T_2WI, the presence of collagen within the capsule causes peripheral T_2 shortening (Fig. 14.1) and on susceptibility-weighted imaging (SWI), it is displayed as a characteristic 'dual rim sign' [22]. Increased vascularity of the cerebral cortex leads to an asymmetry of lesions at the gray–white matter; the cortical aspect of the capsule is thicker than its hypovascular medial aspect.
4. *Late capsule phase:* occurs after approximately 21 days. On CE-MRI, these lesions have a thin, defined peripheral ring of enhancement and there is further capsular T_1 and T_2 shortening (hyperintense on T_1WI, hypointense on T_2WI), which can help in differentiating pyogenic abscess from resolving haematoma or necrotic neoplasm. Together with central water diffusion restriction at this stage, MRI is both highly sensitive and specific in the diagnosis of cerebral abscess.

Spinal cord abscess

Parenchymal infection of the cord is rare and can be caused by direct extension of infection from the meninges or by haematogenous seeding of infection in systemic sepsis. CE-MRI shows a small intramedullary T_2 hyperintense lesion, which enhances uniformly or peripherally, associated with local swelling and oedema.

Viral encephalitis

Herpes simplex virus

Background

The name 'Herpes' is derived from the Greek verb '*herpein*', which means 'to creep,' a fact poignant in both the clinical and investigative findings of HSV encephalitis. HSV is the causative organism in approximately 10% of encephalitis patients in whom an organism is identified. HSV-1 is implicated in immunocompetent adults and HSV-2 in children and the immune-impaired. The aetiology of HSV-1 encephalitis remains unclear, but it is thought to be a result of either acute primary infection or reactivation of latent viral infection in the dorsal root ganglia [23].

Patients are usually below 20 or above 50 years old and present with gradual (creeping) onset of behavioural, speech, and gait disturbances, progressing to seizure or coma. Death follows in up to 70% of those untreated and prompt administration of acyclovir is strongly correlated with better outcome. Of treated survivors, 30% suffer a chronic neurological deficit and empirical antiviral treatment is therefore administered where encephalitis is suspected, even when the cause is unknown [24].

In impaired immunity, HHV-6 encephalitis should be considered as a differential diagnosis because it is unresponsive to acyclovir and as such carries a poor prognosis [25].

Investigative findings

CSF analysis should be performed and although routine analysis for glucose, protein, and cells is usually abnormal, specific PCR for HSV tends to be negative especially in patients who have received empirical antiviral medication. Imaging findings are therefore fundamental to making the diagnosis.

Imaging abnormalities are typically centred on the mesial temporal lobes and can be uni- or bilateral, appearing on CT as cerebral swelling with local sulcal effacement, and on CE-CT there can be overlying leptomeningeal enhancement.

On MRI, predominantly cortical signal change on T_2WI/FLAIR is a radiological sign of HSV encephalitis and can be associated with water diffusion restriction at an early stage. Where signal change is unilateral and water diffusion is restricted, findings can

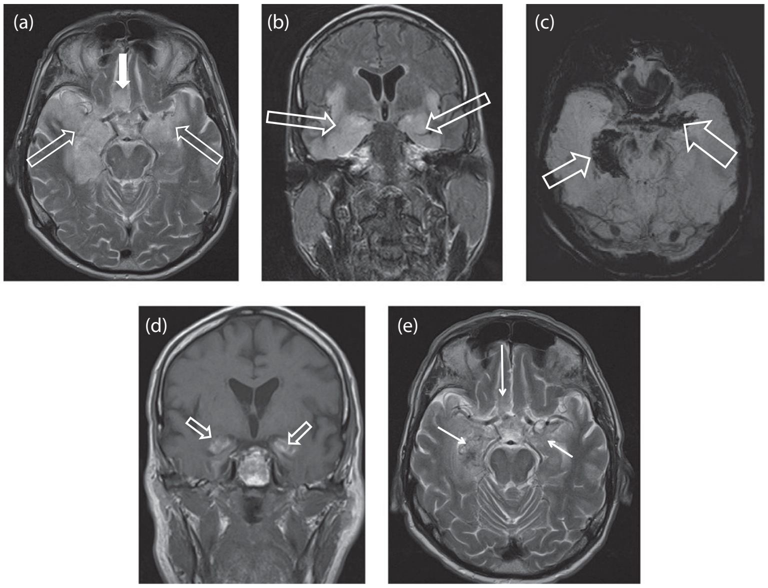

Fig 14.2 HSV encephalitis: MRI. (a) Axial T_2WI shows signal hyperintensity in both mesial temporal lobes extending into the temporal horns (block arrows). There is associated cerebral swelling. A similar appearance is seen in the right gyrus rectus (block arrow). (b) Coronal FLAIR MRI shows signal change extending into the insular cortex bilaterally. (c) + (d). 15 days later. Areas of susceptibility artefact on SWI (c, block arrows) and corresponding signal hyperintensity on T_1WI (d, arrows) in both hippocampi reflecting laminar cortical necrosis, a typical finding in late scanning of HSV encephalitis patients. (e) 30 days after presentation, T_2WI demonstrates volume loss in the mesial temporal lobes and right gyrus rectus (arrows).

be difficult to differentiate from acute MCA territory infarction, but the putamen is typically spared in HSV encephalitis and is involved in acute ischaemia.

Later, enhancement on CE-MRI can be florid and laminar cortical necrosis is sometimes seen with associated haemorrhage and calcification being demonstrated by T_1 shortening or susceptibility artefact on T_2*WI or SWI (Fig. 14.2).

Varicella zoster virus (VZV) causing herpes zoster encephalitis (even where skin blisters are absent, particularly in the elderly) should be considered. Other causes of encephalitis include paraneoplastic syndrome, other multisystem autoimmune diseases and *Epstein–Barr virus*. A definitive diagnosis can be made by brain biopsy if the cause of encephalitis is clinically important and remains in doubt.

Flavivirus infections

West Nile virus

Background

West Nile virus (WNV) is a mosquito-transmitted flavivirus, which can cause lethal meningitis and encephalitis. It is so named because it was first isolated in the West Nile region of East Africa, although summer epidemics in the USA are now well established with nearly 4000 cases reported in 2012 [26].

As in other encephalitides, patients present with pyrexia, headache, and reduced consciousness; however, motor weakness and respiratory failure predominate. A poliomyelitis-like syndrome is thought to be caused by inflammation of anterior horn cells and a Guillan–Barré-like syndrome is likely to be the result of demyelination [27].

No definitive treatment is known and although infection usually resolves within 60–90 days, many patients suffer chronic parkinsonism and fatigue.

Investigative findings

WNV is diagnosed by CSF and blood analysis for immunoglobulins/antibodies, but tests can be negative in the acute phase.

MRI typically demonstrates transient lesions in the splenium of the corpus callosum, deep gray matter, hippocampi and brainstem which are hyperintense on T_2WI and can show restricted water diffusion on DWI.

Hyperintense lesions on T_2W MRI are usually seen in the ventral spinal cord (correlating with clinical myelopathy). Associated leptomeningeal or cauda equina nerve root enhancement is often seen [28].

Japanese encephalitis virus

a. Background

Japanese encephalitis (JE) *virus* is a bird- and pig-borne, mosquito-transmitted flavivirus and is currently the leading cause of viral encephalitis in rural Asia, with rare outbreaks seen in the West. The diagnosis should primarily be considered in unvaccinated native Asian patients as the risk to visitors to Asia remains low. Untreatable meningoencephalitis occurs in approximately 1 of 250 infected patients and carries a mortality of approximately 30% [29,30].

Investigative findings

JE is similar in presentation to HSV and can cause haemorrhagic limbic encephalitis.

On T_2W MRI, typically there are hyperintense, non-enhancing inflammatory lesions of both thalami and putamina, with sparing of the red nucleus and corticospinal tract resulting in a characteristic 'panda' appearance of the brainstem on T_2WI. There can also be water diffusion restriction and features of haemorrhage, such as T_1 shortening and susceptibility artefact on SWI. Occasionally, there is pontine, cortical, cerebellar, or unilateral thalamic involvement [31].

In *Eastern equine encephalitis*, an arbovirus infection endemic to the eastern USA (which also infects horses) and transmitted by mosquitoes, imaging findings are similar to those of JE, but meningeal enhancement is sometimes seen in addition.

Tick-borne encephalitis is another arboviral infection endemic to Eastern Europe that should be included in the differential diagnosis of bilateral ganglionic and thalamic lesions in encephalitic patients [32].

Fungal infection

Fungal infection of the CNS is usually leptomeningeal but sometimes progresses to neuroparenchymal infection, more often in patients whose immunity is impaired. This can cause encephalitis or small nodular, parenchymal fungal granulomas to form. Fungal abscess is a rare complication, and is clinically and diagnostically analogous to a bacterial abscess (see 'Bacterial parenchymal infection').

Mucormycosis

Background

A disease almost exclusively of the immune-impaired, particularly of IV drug users and diabetic patients, CNS *Mucormycosis* infection is important to recognize as mortality is over 80% [33]. This opportunistic pathogen is found in soil and does not challenge a healthy immune system. In the immunocompromised, it colonizes the paranasal sinuses via direct spread from the nasal/oral cavity and subsequently invades the CNS, usually at the cribriform plate or skull base, although isolated intracranial infection has been described [34]. Within the neuroparenchyma, fungal vascular invasion causes necrotizing vasculitis with a propensity for the cavernous internal carotid artery and sinus, significantly increasing the risk of acute infarction.

Diabetic or immune-impaired patients present with black or blood-stained nasal secretions (nasal eschar), pain, and pyrexia. Where there is cavernous sinus involvement, exophthalmos and cranial neuropathy are seen, and where there is neuroparenchymal invasion, signs include reduced consciousness, seizure, and other features of encephalitis.

Otolaryngology referral is recommended for urgent surgical debridement and histological confirmation of the diagnosis, whilst the infection is treated with systemic antifungal chemotherapy.

Investigative findings

CT can show proptosis and paranasal sinusitis. Where there is bony destruction, CE-CT or MRI is recommended as the risk of calvarial breach, which usually occurs at the cribriform plate, and subsequent CNS invasion, is high.

Small, solid, intra-axial fungal granulomas associated with variable perilesional oedema (usually in the frontal lobes, because of their proximity to the paranasal sinuses) indicate parenchymal spread of infection. The enhancement pattern depends upon the patient's immune status—larger lesions typically enhance peripherally and are of low attenuation on CE-CT. Vascular invasion is frequent and can lead to intracranial haematoma or infarction.

On MRI, lesions are iso-intense to brain on T_1WI, and return to variable T_2 signal. Enhancement patterns are as on CE-CT, although local lepto- and pachymeningeal enhancement is more conspicuous. Involvement of the internal carotid artery can cause acute infarcts showing restricted water diffusion on DWI and hyperintensity on T_2WI.

4.3.2: Aspergillus *species*

Background

Aspergillus enters the body via the respiratory system from water, soil and food waste. In healthy adults, it can colonize the paranasal sinuses and directly invade the CNS. In the immune-impaired, the fungus infects the lungs and is disseminated haematologically to the CNS in up to 70% of patients.

Intra-axial *Aspergillus* infection can be extremely aggressive and has a reported mortality of over 90% [35]. Unlike most other CNS fungi, meningitis and encephalitis are complicated by abscess, rather than granuloma.

Investigative findings

Aspergillus infection should be suspected in an immunocompetent patient if widespread paranasal sinus disease encountered on CE-CT is associated with calcification, bone erosion, and enhancing soft tissue. Imaging findings usually underestimate the aggression of the underlying process and are initially normal. Poorly-defined areas of cerebral low attenuation, contrast enhancement or focal lesions are occasionally seen. If *Aspergillus* infection is suspected clinically, urgent MRI should be performed.

Aspergillus abscesses favour the basal ganglia in location, tend to be multiple and are hyperintense on T_2WI. Their thick wall usually enhances, although incomplete or absent enhancement can imply a more aggressive disease course.

Local vascular invasion (as occurs in pulmonary aspergillosis) causes infarcts demonstrated by water diffusion restriction on DWI, or haemorrhage seen as T_1-shortening or susceptibility artefact on T_2*WI and SWI.

Cryptococcus neoformans

Background

A prolific worldwide fungal infection found in pigeon faeces and Eucalyptus trees, *Cryptococcus neoformans* infection is likely to be seen in patients with impaired immunity, although up to 50% of diagnosed patients are immunocompetent and infected by serotype B.

Investigative findings

Gelatinous pseudocysts are radiologically characteristic lesions in which perivascular (Virchow–Robin) spaces are dilated and filled by fungal colonies. These can be difficult to differentiate radiologically from an idiopathic, non-pathological enlarged perivascular space. On CE-CT they are usually multiple, round, well-defined, non-enhancing, fluid-filled striatal lesions of low attenuation.

On MRI, the fluid is hypointense on T_1WI and hyperintense on T_2WI, with little or no associated peritumoural oedema. A similar appearance can be seen in the rare tick-borne bacterial infection, *Rocky Mountain Spotted Fever encephalitis*.

Cryptococcal CNS infection is an AIDS-defining illness, in the past allowing diagnosis in up to 40% of HIV patients [36]. These lesions are much more likely to be seen in the immunocompromised.

Cryptococcomas (granulomas) are rare in healthy adults and are demonstrated by cross-sectional imaging as multiple, intra-axial, uniformly-enhancing well-defined lesions of varying sizes, which are sometimes calcified.

Parasitic

Parasitic infestation of the CNS, although rare in the developed world, is of vast importance worldwide and in patients who are immunocompromised.

Cysticercosis (Fig. 14.3)

Background

Although in the UK the prevalence of reported neurocysticercosis is low, it remains the most important parasitic disease of the CNS and the commonest cause of acquired epilepsy worldwide [37]. It is a recognized eradicable disease, already reportable in several countries and likely to be declared internationally reportable by WHO. If diagnosed, the country of origin should be identified and their reporting policy observed [38].

Symptoms occur approximately 5 years after initial infection (which can be at any anatomical site) [39] making a lifelong travel history imperative in the initial assessment. Presentation is usually late, with seizures and dementia, but patients can complain of peripheral neuropathy and visual symptoms; acute symptoms of headache and confusion have been also reported. Treatment is medical with antihelminthic drugs.

Taenia solium larvae are ingested in undercooked pork or can be transmitted between humans faeco-orally. The larvae develop into tapeworms in the gastrointestinal tract, where ova burrow into the bloodstream, disseminating cysts to the neuroparenchymal and skeletal muscular end capillaries; there they mature over approximately 3 months. Host responses are prevented by the cyst wall and by the blood–brain barrier, until wall disruption upon natural or treatment-induced worm death instigates an inflammatory reaction.

Larvae are rarely disseminated into the spinal subarachnoid space from the brain and *spinal cysticercosis* is nearly always associated with cerebral disease. This presents clinically as arachnoiditis with multifocal radiculopathy or paralysis.

Neurocysticercosis can be described anatomically as:

1. *Subarachnoid-cisternal:* where infection involves the subarachnoid space and overlying meninges causing hydrocephalus, brain oedema, and volume loss.
2. '*Parenchymal*' neurocysticercosis manifests at or near the gray–white matter junction and has been shown histologically to be a subarachnoid disease of deep gyrae/perivascular spaces.
3. *Intraventricular* neurocysticercosis occurs in approximately one-third of patients, and is usually seen in the fourth or lateral ventricles.

Investigative findings

Radiological stages of neurocysticercosis are defined as:

1. *Vesicular:* on CT, small low attenuation cysts with no peri-lesional oedema, and minimal mass effect can be difficult to identify and intraventricular cysts are barely perceptible. On MRI, fluid-filled cysts measuring up to 2 cm are seen in the sylvian fissures, basal ganglia, and at the peripheral gray–white matter junction. Cyst fluid has similar signal characteristics to CSF, water diffusion is not restricted and there is no surrounding oedema. Where a

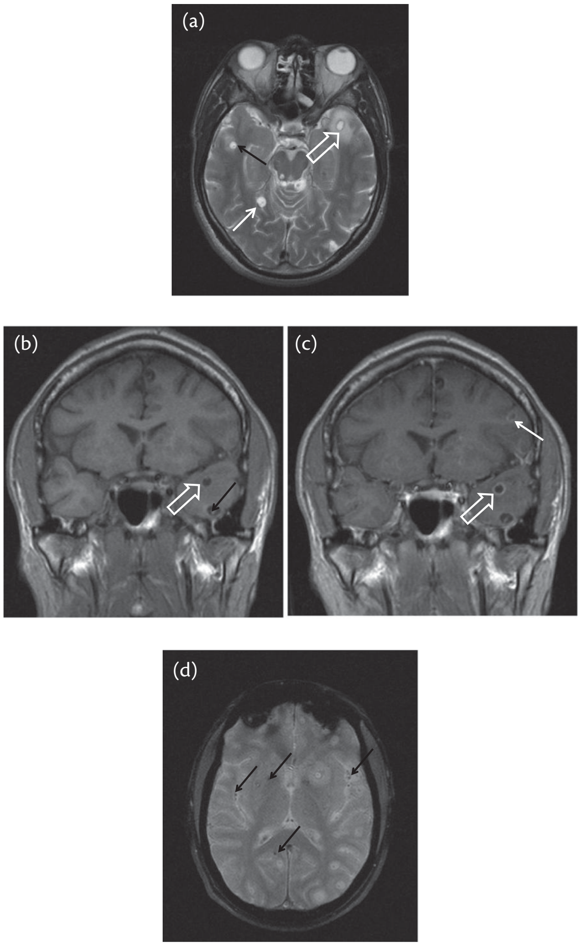

Fig 14.3 Neurocysticercosis: MRI. (a) T_2WI shows multiple, well-defined, predominantly hyperintense cystic lesions, representing neurocysterci at various radiological stages. A *vesicular* cyst is seen in the mesial right temporal lobe (white line arrow). A *colloidal vesicular* cyst at the left temporal pole (block arrow) is surrounded by a halo of oedema indicating death of the parasite and instigation of host inflammatory response. A *granular nodular* cyst anteriorly in the right temporal lobe (black line arrow) is associated with less oedema than the colloidal vesicular cyst and central hypointensity represents the scolex, or worm head. (b) T_1WI and (c) CE-T_1WI shows peripheral enhancement of the *granular nodular* cysts (arrows). T_1 shortening (black line arrow) indicates calcification of the scolex in a left temporal lesion. (d) Gradient echo (GRE) imaging demonstrates multiple foci of susceptibility artefact (arrows), each consistent with calcification of a scolex. Where these are not associated with cystic lesions, they represent the *calcified nodular* stage of neurocysticercosis.

mural nodule is seen, this represents the scolex (worm head), which does not usually enhance.

2. *Colloidal vesicular:* this is the usual stage at which patients present with seizure or encephalitis as the larva breaks down and host responses are instigated (Fig. 14.3).Multiple ring-enhancing lesions with gross peri-lesional oedema and mass effect are seen (representing the disrupted larval capsule) with or without features of global encephalitis. When compared with the vesicular stage, cyst contents are more proteinaceous and therefore appear denser than on CT. On MRI, there is corresponding T_1-shortening and T_2-prolongation.

3. *Granular nodular:* perilesional oedema progresses and the enhancing ring becomes thicker as granulomas form from retracted cysts. The scolex calcifies and can be detected by CT, gradient-echo sequences, or SWI. These can be associated with gliotic cavities.

4 *Calcified nodular*: the oedema resolves and small calcified granulomas are seen in this non-active form of neurocysticercosis. Beyond the colloidal vesicular phase, the diagnosis can be confirmed by plain radiography of the thighs, which will demonstrate multifocal muscular calcifications.

5 *Racemose* neurocysticercosis (literally meaning to take the form of a *raceme*, where individual stalked flowers grow from one central stalk) is a rare form of the disease. On CE-CT or MRI, a murally enhancing cluster of cysts ('bunch of grapes') is usually located in the subarachnoid space around the brainstem or sylvian fissures, and can be associated with local meningeal nodular enhancement or hydrocephalus. The cluster is more clearly delineated by MRI.

Echinococcus (hydatid)

Background

Dogs are definitive hosts to the *Echinococcus* (or hydatid) tapeworm, which is transmitted faeco-orally to humans. CNS involvement is seen in approximately 4% of patients with primary hepatic or pulmonary infestation.

Investigative findings

Large, isolated, unilocular, well-defined cysts are frequently seen in the parietal lobe or throughout the MCA territory as a result of haematogenous spread of embryos from the gastrointestinal tract.

On CT, mural calcification can be seen. Internal cyst fluid appears similar to CSF on both CT and MRI; the absence of perilesional oedema and post-contrast enhancement are thought to be highly suspicious of hydatid disease. Internal signal hypointensity or susceptibility artefact on MRI indicates the presence of a scolex [40].

Diverse central nervous system infections

HIV and AIDS

It is 30 years since the first case of AIDS was reported worldwide (1981) and over 120,000 patients have been diagnosed with HIV in the UK to date, approximately 22% of whom have developed AIDS. Prognosis has rapidly improved since the introduction of combination antiretroviral therapy (cART) with life expectancy now nearing normal for patients whose diagnosis is prompt [41].

Some opportunistic infections (OIs) are frequently associated with HIV/AIDS and continue to present in undiagnosed and untreated patients. Worldwide, there has been a dramatic decline in the incidence of OIs since the introduction of antiretroviral therapy and emphasis has now shifted towards neurocognitive CNS complications of HIV [42,43].

HIV encephalopathy and HIV-associated dementia

Background

Severe cognitive impairment in HIV, formerly termed AIDS dementia complex, had a prevalence of approximately 16% in patients with advanced disease before the introduction of cART. In the era of cART this is now rare, but milder forms of cognitive

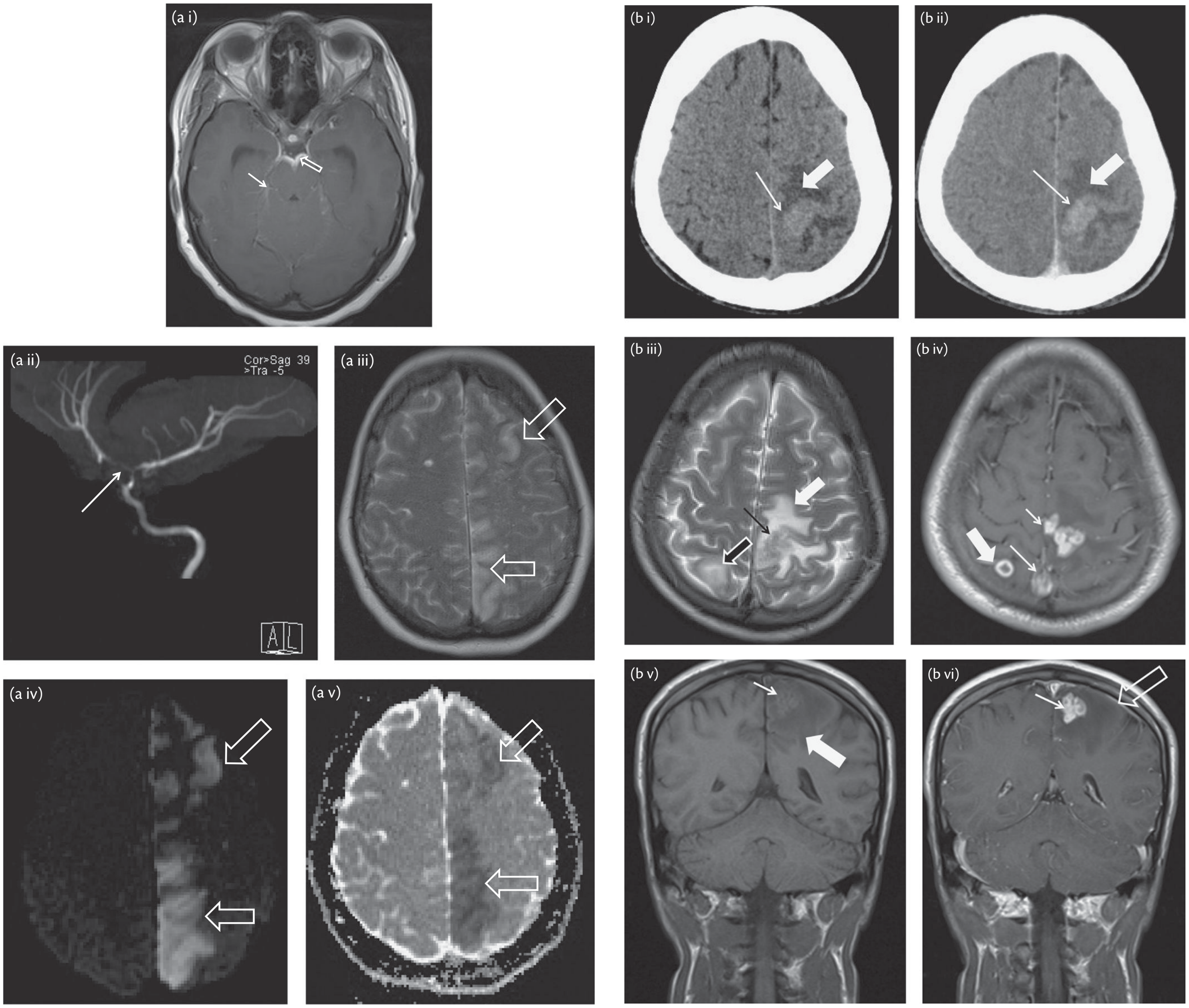

Fig 14.4 Tuberculosis.

(a) TB meningitis: meningeal disease, hydrocephalus and vasculitis are a classic triad of imaging findings. (i) CE-MRI (T_1WI) demonstrates leptomeningeal enhancement (line arrow) and pachymeningeal thickening and enhancement in the interpeduncular cistern (block arrow). The ventricular temporal horns are dilated in keeping with hydrocephalus. (ii) TOF MRI shows narrowing of the left terminal internal carotid artery, A1 segment of the ACA and M1segment of the MCA (line arrow) illustrating TB vasculitis. (iii)–(v). Cortical signal hyperintensity on T_2WI (iii) DWI (iv) and corresponding hypointensity on the ADC map (v) in the same patient demonstrate associated acute infarction.

(b) Tuberculoma. (i) CT and (ii) CE-CT show a high attenuation, enhancing lesion in the left parietal lobe (line arrow) surrounded by oedema (block arrow). (iii) The same lesion is hypointense on T_2WI (black line arrow). Perilesional oedema (block arrow) is demonstrated by hyperintense signal with local mass effect. Contralateral oedema (black block arrow) is suspicious for a second lesion. (iv) CE-T_1WI reveals a cluster of small ring enhancing lesions on the left (line arrows) and confirms the presence of a contralateral lesion not seen by CT (block arrow). Appearances are typical of multiple tuberculomas. (v) T_1WI shows some T_1 shortening in the periphery of the lesions (line arrow) and hypointense perilesional oedema (block arrow). (vi) CE-T_1WI further demonstrates the cluster of ring enhancing tuberculomas in the left parietal lobe (line arrow) and overlying meningeal thickening and enhancement (unfilled arrow).

(c) Pott disease—spinal tuberculosis. (i) In a patient complaining of dysphagia and upper limb paraesthesia, sagittal T_2WI of the cervical spine shows a large, mixed signal intensity paravertebral collection (line arrows) with vertebral canal narrowing (block arrow). (ii) Sagittal T_2WI of the cervicothoracic spine reveals an asymptomatic, non-contiguous level of involvement (at T7, block arrow). This demonstrates the importance of whole spine imaging in suspected spinal infection. (iii) Sagittal STIR imaging of the cervicothoracic spine elaborates bony oedema seen where infection involves the vertebral bodies at C5-T_1 and at T7 (line arrows). (iv) The collection enhances heterogeneously on sagittal CE-T1WI (line arrows) and there is enhancement of the C5/6 intervertebral disc (block arrow). (v) Axial imaging shows the typical 'bilobed' formation of an extradural, or epidural, collection—the midline PLL attachment (black line arrow) is intact whilst enhancing pus fills the extradural space bilaterally (white arrows). The collection contacts, but does not compress the spinal cord (*).

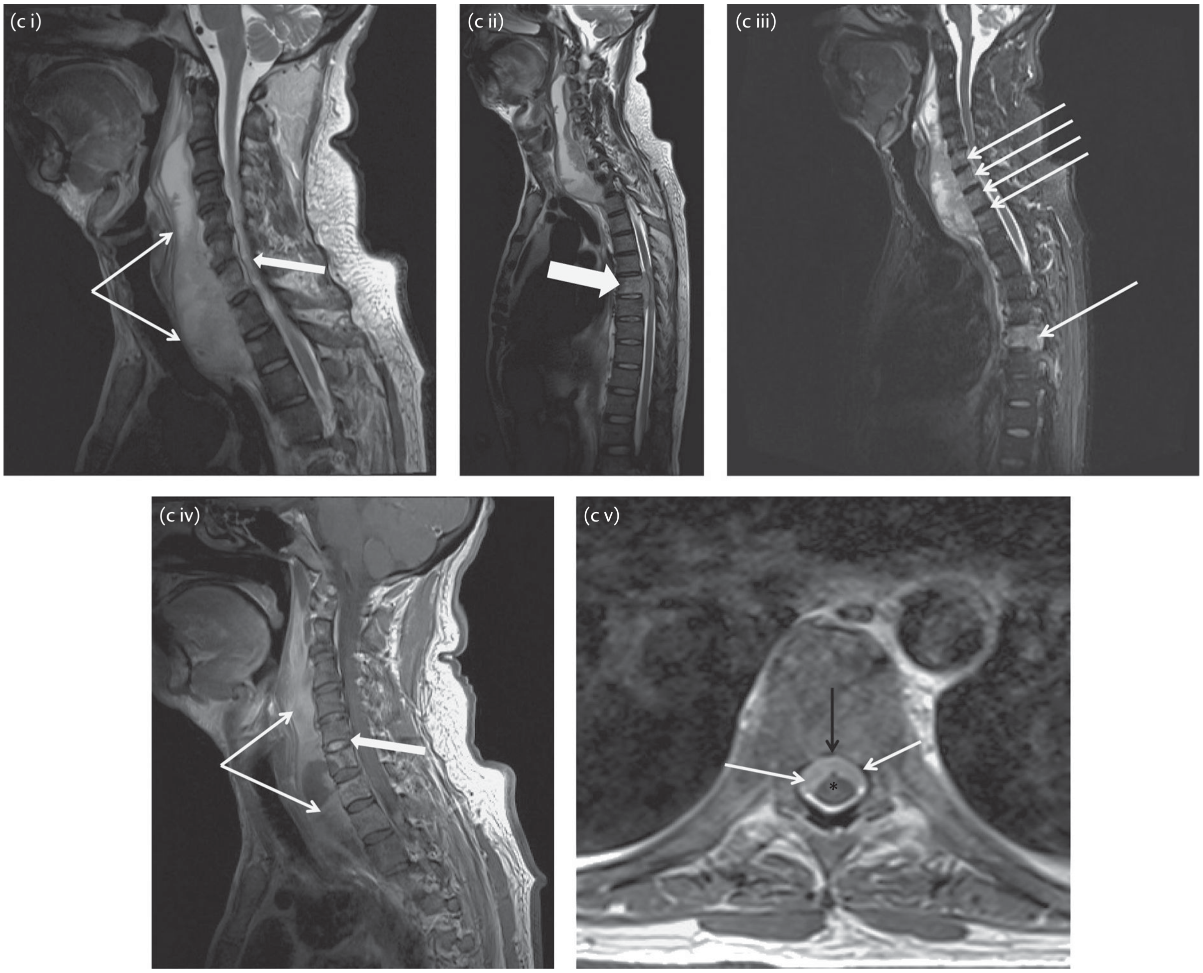

Fig 14.4 Continued

impairment are a major cause of morbidity. In 2007, a new definition of HIV-associated neurocognitive disorders (HAND) was introduced: symptomatic neurocognitive impairment (ANI), where patients have abnormal neuropsychological tests but are not impaired in their everyday life, mild neurocognitive disorder with mildly impaired functioning, and HAD corresponding to the former AIDS dementia complex [44].

HIV infects the CNS early, but does not usually cause symptoms until immunodeficiency occurs. If untreated, direct viral infection of the CNS causes lymphocytic meningitis and deep white matter inflammation resulting in gliosis [45]. There is a spectrum of disease, the earliest stage of which is HIV encephalopathy (HIVE), that rarely manifests clinically, and whose diagnosis is made by screening, imaging, or at post-mortem. As the disease advances, symptoms include motor and cognitive decline, progressing to dementia. High CSF viral load, low CD4 count, disease duration, and late seroconversion influence the likelihood of HAD.

HAND remains a diagnostic and clinical challenge in the cART era, with multiple studies demonstrating progressive cognitive decline in patients with low or even undetectable plasma, and CSF viral loads. The exact aetiology of this phenomenon remains controversial, but it is thought to involve chronic low-grade inflammation, an increase in viral exposure over time (better survival), amyloid deposition, and direct drug toxicity [44].

If diagnosed early, treatment regimens can be altered to increase CNS penetration of drugs and improve prognosis. Despite this, HAND makes a significant contribution to HIV- and AIDS-associated morbidity and mortality today.

Investigative findings

HIVE often manifests as a symmetrical white matter T_2/FLAIR hyperintensity that is ill-defined, subtle, and diffuse on MRI. It can also present as multifocal white matter lesions; involvement of gray matter, basal ganglia, or thalami is not infrequent [46]. Water diffusion is not restricted. This leukoencephalopathy can progress to leukomalacia and global cerebral atrophy, seen as prominently enlarged ventricles and sulci (Fig. 14.5).

Progressive multifocal leukoencephalopathy

a. Background

Reactivation of latent *John Cunningham virus* (*JC papovavirus*) infection occurs in patients with a CD4 count <100/mm^3 (5-10% AIDS patients) resulting in progressive multifocal leukoencephalopathy (PML), a form of progressive demyelination. PML is not isolated to HIV/AIDS patients and can also occur in patients on

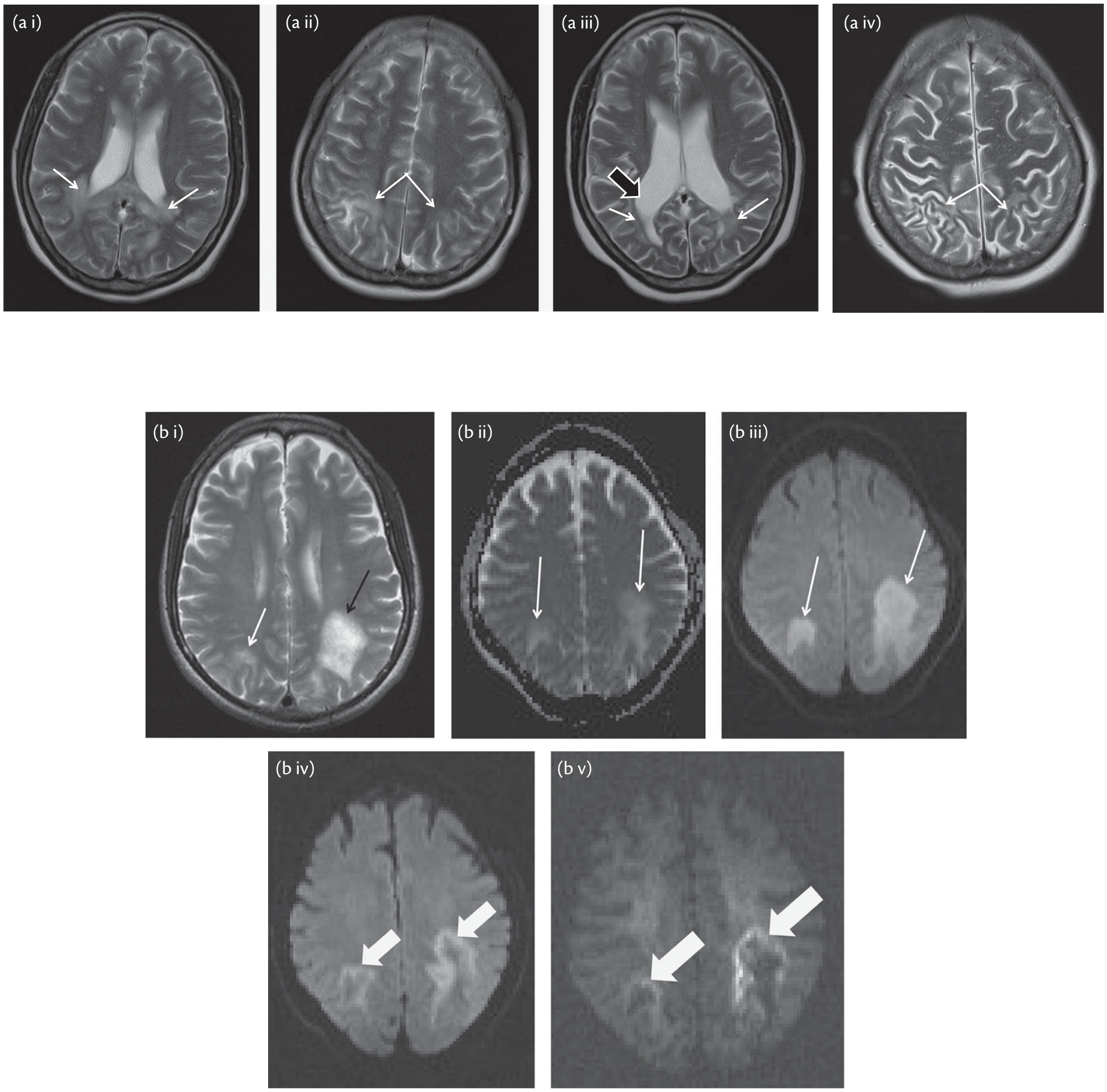

Fig 14.5 HIV/AIDS.

(a) HIV encephalopathy/AIDS Dementia Complex (A-DC). (i) In an HIV positive patient, T_2WI at presentation shows bilateral periventricular (i) and parietal (ii) deep white matter signal change which spares the subcortical fibres and does not exert mass effect (line arrows). (iii) 18 months later, there is persistent white matter signal change on T_2WI, ex-vacuodilatation of the lateral ventricles (iii, block arrow) and white matter volume loss (iii and iv, line arrows). In HIV patients with progressive dementia symptoms, these appearances are typical of HIV encephalopathy or in AIDS, A-DC.

(b) Progressive multifocal leukoencephalopathy (PML). (i) T_2WI demonstrates white matter signal change subcortically on the right (white arrow) and involving the subcortical and deep white matter on the left (black arrow). (ii) ADC and DWI at progressively increasing field strengths (iii = b1000, iv = b2000 and v = b3000) demonstrates a 'forefront' of diffusion restriction (block arrows) representing active demyelination moving from the subcortical white matter centrally. This appearance is classic for PML.

immunosuppressive drugs [47]. Patients present with a gradual cognitive impairment and personality disturbances, or acutely with focal neuropathy and seizures.

Investigative findings

The diagnosis is made by imaging together with PCR of CSF for JC papovavirus, although positive PCR is reduced in cART patients.

Unlike HIVE, PML predominantly affects the subcortical white matter, frequently involving the subcortical U-fibres. The imaging appearances are asymmetrical focal white matter abnormalities that are of low attenuation on CT. On MRI, they are iso- or hypointense on T_1WI and hyperintense on T_2WI. Enhancement and mass effect can be seen in the context of immune reconstitution and are associated with improved immunity and better outcomes [48] (see 'Immune reconstitution inflammatory syndrome').

DWI shows a characteristic peripheral hyperintense rim corresponding to the frontline of active demyelination and a central area of necrosis where water diffusion is not restricted. Gray matter involvement and lesion enhancement have been demonstrated, particularly in patients in immune recovery [49].

Immune reconstitution inflammatory syndrome

Background

Immune reconstitution inflammatory syndrome (IRIS) is defined as a 'paradoxical deterioration in clinical status attributable to the recovery of the immune system during (cART) [50]. Aggressive HIV/AIDS treatment with cART leads to an increase in CD4 cell count/function and thereby to a recovery of the immune system, which can instigate an intense inflammatory response to dead or latent organisms days to months after commencement of treatment. CD8 cell infiltration in the leptomeninges, perivascular spaces, blood vessels, and parenchyma seems to be the pathologic hallmark of CNS-IRIS. Risk factors include a rapid drop in viral load or increase in CD4+ count and young age. The most commonly associated organisms are the JC virus (PML-IRIS) and *Cryptococcus species* (spp.), but an inflammatory response to other viruses (*VZV, cytomegalovirus (CMV), HIV*), *Candida* spp., *Mycobacterium tuberculosis* or *Toxoplasma gondii* can also occur. IRIS can be diagnosed simultaneously with an OI (simultaneous IRIS), or in patients with known OI is diagnosed later (delayed IRIS) [51].

Clinical presentation is diverse and depends upon the associated OI and extent of disease. Any patient who has commenced cART within the preceding 8 weeks presenting with new CNS symptoms or progressive cognitive dysfunction despite good viral control should be investigated for HIV-related IRIS [52,53].

Recognition of IRIS in cART treated patients allows adaptation of medical management which can improve outcome and prevent death from IRIS-related illness, overall improving prognosis [53].

Investigative findings

A history of HIV/AIDS and cART treatment, or cessation of other causes of immunosupression, is key to make the diagnosis. In patients who suffer a relapse of previously treated microbial infections, or 'paradoxical' IRIS, septic screens and cultures are usually normal and should be regarded with suspicion.

On imaging, CNS-IRIS can manifest as a transient increase in parenchymal hyperintensity on FLAIR or T_2WI, hypodensity on CT, and contrast enhancement. Mass effect and water diffusion restriction can also occur [52,54].

HIV and vascular disease

Background

HIV patients have an increased risk of stroke with a cumulative increase in risk according to the duration of cART [55,56]. Several mechanisms contribute to the increase of non-haemorrhagic stroke in HIV, such as endothelial dysfunction in the presence of chronic inflammation and drug side effects [57]. Whilst HIV leads most often to premature small and large vessel disease, it can also cause frank vasculitis affecting large extracranial vessels, or small and medium-sized intracranial vessels (with or without aneurysm); vessel wall inflammation is a universal histopathological feature [58].

Investigative findings

Arterial imaging (digital subtraction angiography, computed tomography angiography, magnetic resonance angiography) of intracranial HIV arteriopathy typically shows stenosis of the distal internal carotid artery, proximal MCA, and proximal anterior cerebral artery. HIV vasculitis can be diagnosed once other causes of vasculitis (such as autoimmunity, drugs, and atypical infections, particularly VZV) are excluded. HIV-related infarcts usually involve a large territory or are hemispheric, whereas those attributable to atypical infections are more likely to be small and subcortical [59].

Aneurysms are seen in young, male patients with CD4+ <400 and are thought to be immune-mediated. cART treatment has been shown to improve prognosis [60], although endovascular treatment should be considered [61].

Spinal HIV

Background

AIDS-related vacuolar myelopathy presents late with lower limb weakness progressing to paraplegia, urinary symptoms, faecal incontinence, or male impotence [62]. This condition is typically seen in patients with advanced HIV infection or fulminant AIDS. The differential diagnosis includes focal spinal cord lesions attributable to lymphoma, necrosis, viral, toxoplasmotic, tuberculous, or syphilitic infection.

Investigative findings

MRI is recommended for HIV patients complaining of back pain with or without focal neurological signs, even if CSF examination is normal [63]. MRI in vacuolar myelopathy demonstrates T_2 hyperintense lesions in the posterior and lateral columns (predominantly in the thoracic spinal cord) or diffuse, intramedullary signal change without contrast enhancement [64].

Toxoplasmosis

Background

Acquired cerebral toxoplasmosis is an AIDS-defining infection typically seen in patients whose CD4+ is below 100 cells/mm^3. *Toxoplasma gondii* is an intracellular protozoan that infects humans via direct contact with feline excrement, or ingestion of raw or undercooked vegetables, pork, or lamb.

In healthy patients, the acute infection is asymptomatic and quickly becomes latent within the neuroparenchyma. In impaired immunity, latent infection is reactivated and patients present with headache, altered Glasgow coma score, dysphasia, seizure, or focal cranial and peripheral neuropathies [65].

Investigative findings

Typical CT findings are multiple, low attenuation, ring-enhancing abscesses centred in the basal ganglia, with perilesional oedema and mass effect typically seen on CT. Toxoplasmosis presents less often with a solitary lesion at the gray/white matter junction, in the periventricular white matter or at the cervicomedullary junction. Enhancement is not always ring-like, and can be nodular or absent.

On MRI, toxoplasmotic abscesses are usually hypointense on T_1WI, hyperintense or heterogeneous on T_2WI/FLAIR and enhance peripherally. Mural haemorrhage can cause peripheral T_1-shortening. The T_2 'target sign' is characteristic of toxoplasmosis—on T_2WI, centrally hyperintense, peripherally hypointense (mural blood) lesions are surrounded by an outer ring of hyperintense perilesional oedema. Centrally, water diffusion is not restricted, helping to differentiate

Table 14.2 Differentiating features of toxoplasmotic abscess and primary CNS lymphoma in the immunocompromised. AB: antibiotic; ↑: increase; SPECT: single photon emission tomography

Toxoplasmosis	Primary CNS lymphoma
More common	Less common
Clinical/radiological change after AB	No change after AB
No transcallosal spread	Can cross corpus callosum
Multiple > single	Single > multiple
Peripherally ↑on T_1WI, T_2 'target sign'	No ↑ on T_1WI, ↔ : white matter on T_2WI
Less uptake on thallium single photon emission computed tomography (SPECT)	↑ Uptake on thallium SPECT
Smaller lesions	Larger lesions
Basal ganglia > elsewhere	Periventricular > basal ganglia

toxoplasmosis from pyogenic abscess, although DWI can be unreliable when blood products are present.

The principal radiological differential diagnosis of toxoplasmosis is primary CNS lymphoma of the immunocompromised and many useful distinguishing features have been described (Table 14.2).

Neurosyphilis

Background

Treponema palladium is a sexually transmitted spirochete and a recognized HIV-associated infection [66]. In immunocompetent adults, the clinical and investigative profile are identical to those with impaired immunity. Doxycycline discovery caused near eradication of syphilis in the UK, but a recent resurgence saw a 600% increase in UK cases between 2000 and 2009 [67].

Neurosyphilis complicates untreated syphilis in up to 33% of untreated infected patients, usually occurring late, but disease progression is accelerated when HIV is present, making it more common in this population.

Investigative findings

White matter and cortical atrophy are typical findings on cross sectional imaging, although syphilis has been described as 'The Great Pretender' and should be considered in the differential diagnosis for any CNS infection, including HSV encephalitis [68].

Meningovascular neurosyphilis typically affects large and medium sized arteries including the circle of Willis [69]. This causes segmental arterial narrowing, and resultant infarcts of varying age and distribution that can be demonstrated by CT or MRI.

Cerebral gumma are small enhancing cortical nodules seen in neurosyphilis, which are isodense on unenhanced CT, are associated with peritumoural oedema and resolve after antibiotic treatment.

On T_2W-MRI, gummas are hyperintense, iso- or hypointense on T_1WI and on CE-MRI; local meningeal enhancement is occasionally seen in association with vasculitis and infarction [70].

Cytomegalovirus

Background

Cytomegalovirus is a latent viral infection that is reactivated when immunity is altered, causing ventriculitis and demyelination. Clinical progression to CMV encephalopathy carries a poor prognosis and can occur despite antiviral treatment.

Investigative findings

On CE-CT, ependymal enhancement in CMV ventriculitis is characteristic of the infection, but CT can also be normal.

Ependymal enhancement is better demonstrated by CE-MRI and can be associated with subependymal and periventricular white matter hyperintensity on T_2WI. Hyperintense white matter lesions can show restricted water diffusion and peripheral enhancement reflecting active inflammation/demyelination.

Aspergillus, Cryptococcus, and *Mucormycosis* are important diseases of the HIV/AIDS population that have been discussed previously.

Tuberculosis

A worldwide increase in mycobacterial CNS infection, mostly attributable to *Mycobacterium tuberculosis* (tuberculosis (TB)) is thought to be, in part, explained by the HIV epidemic. Although primary pulmonary infection should be excluded in all patients with confirmed TB infection, CNS infection occurs in approximately 5% of TB patients with isolated extrapulmonary disease [71]. The most common CNS manifestations of the infection otherwise known as the 'ultimate mimic' are discussed here. TB should be considered in most neuroradiological differential diagnoses.

TB meningitis

Background

Tuberculous meningitis is the commonest CNS manifestation of TB, principally involving the basal meninges, and less frequently the convexity sulci and sylvian fissures. The inflammation can hinder CSF absorption and cause communicating hydrocephalus. Exudates and inflammation can infiltrate the cranial nerves causing focal neuropathy or communicating hydrocephalus. Disease extension into the perivascular spaces causes vasculitis and compromise of the basal perforating vessels that can eventually lead to ganglionic and internal capsule infarcts in up to 40% of patients (Fig. 14.4a).

Investigative findings

Diagnosis is made by detection of *M. tuberculosis* in CSF as radiological appearances can be difficult to differentiate from those seen in fungal, racemose cystercicotic, neoplastic, and autoimmune meningitides.

CE-CT of clinically meningitic patients typically shows leptomeningeal thickening and enhancement that can extend along the cranial nerves and pituitary infundibulum.

Pachymeningeal disease is seen on CE-MRI as dural thickening and enhancement. Thickened meninges can also be visible on pre-contrast T_1W-magnetization transfer MRI [72].

In the cervicothoracic spine, acute tuberculous meningitis causes inflammatory exudate that fills the subarachnoid space and appears as nodular or linear enhancement on CE-MRI. Beware that in severe cases where the entire CSF space enhances, the CE-T_1WI can resemble T_2WI of a normal spine. Complications include CSF loculations and arachnoiditis (resulting in an enhancement around thickened and clumped nerve roots of the cauda equina) and syringomyelia (with a syrinx following CSF signal characteristics on all sequences).

Miliary CNS TB is a rare condition and CE-T_1WI demonstrates multiple solid enhancing lesions of below 2 mm diameter that are hyperintense on T_2WI.

Tuberculoma and tuberculous cerebritis

Background

In developed countries, the progression of TB meningitis to parenchymal TB infection is largely associated with HIV infection and AIDS, occurring only rarely in the immuno-competent. Symptoms of infection can be indolent leading to a clinical presentation analogous to those of any cerebral space occupying lesion or abscess.

Investigative findings

On CE-CT, tuberculomas are small, peripherally- or solid-enhancing round lesions; pachymeningitis can be associated. Central calcification is suggestive of tuberculoma although this can also be seen in fungal and parasitic granulomas.

On CE-MRI, signal characteristics change with time, as lesions are thought to progress through non-caseating, solid-caseating and liquid-caseating stages. Lesions are of low signal on T_1WI in all three stages, but T_2 signal (relative to gray matter) progresses from low to moderate to high respectively, and the enhancement pattern progresses from solid to peripheral with time. Peri-lesional oedema peaks at the solid-caseating stage.

Spinal TB (Fig. 14.4c)

Backgound

TB of the spine (*Pott disease*) usually presents clinically less acutely than pyogenic spinal infection. Conversely, pathological processes, such as epidural abscess or bony destruction are often more advanced.

Patients might present with a classic 'gibbus' deformity as a result of angular kyphosis and vertebral body collapse, or with myelopathy secondary to cord compression from angulation, abscess, or retropulsed bone fragments.

Investigative findings

Whole spine MRI is vital in the investigation of these patients, even where symptoms localize to only one level, as asymptomatic, large collections ('cold abscesses') can affect nearby contiguous and more distal non-contiguous spinal levels.

Findings are otherwise similar to those of pyogenic spinal infection described in 'Pachymeningitis'.

TB of the immunocompromised

A compromised immune system predisposes to a higher incidence of TB, multidrug-resistant (MDR) TB infection, and a higher rate of extrapulmonary infection in which chest imaging can be normal.

Multidrug resistant TB

Background

MDR TB has evolved as a result of non-compliance with, or inaccessibility to, a complete course of antibiotic treatment. It is associated with higher morbidity and mortality as a consequence of toxic and complex treatment regimens.

Investigative findings

Investigative and imaging features are indistinguishable from those of non MDR-TB.

Summary

We have provided a structured approach to assessment and diagnosis of common and less common CNS infections and have revised the important anatomical divisions of the brain, spinal cord, and meninges, which are important in the spread of CNS infection. We gave an overview of the clinical manifestations of CNS infections and selection of appropriate diagnostic tests, as well as discussed the value of imaging techniques.

References

1. MacDonald BK, Cockerell OC, Sander JWAS, et al. (2000). The incidence and lifetime prevalence of neurological disorders in a prospective community-based study in the UK. *Brain*, **123**(4), 665–76.
2. Brouwer MC, Tunkel AR, and van de Beek, D. (2010). Epidemiology, diagnosis, and antimicrobial treatment of acute bacterial meningitis. *Clinical Microbiology Review*, **23**(3), 467–92.
3. Kennedy PGE. (2005). Viral encephalitis. *Journal of Neurology*, **252**(3), 268–72.
4. Gorelick PB, and Biller J. (1986). Lumbar puncture: technique, indications, and complications. *Postgraduate Medicine*, **79**, 257–68.
5. Mellor DH. (1992). The place of computed tomography and lumbar puncture in suspected bacterial meningitis *Archives of Diseases of Childhood*, **67**(12), 1417–19.
6. Archer BD. (1993). Computed tomography before lumbar puncture in acute meningitis: a review of the risks and benefits. *Canadian Medical Association Journal*, **148**(6), 961–5.
7. Hasbun R, Abrahams J, Jekel J, et al. (2001). Computed tomography of the head before lumbar puncture in adults with suspected meningitis. *New England Journal of Medicine*, **345**, 1727–33.
8. Smirniotopoulos JG, Murphy FM, Rushing EJ, et al. (2007). Patterns of contrast enhancement in the brain and meninges. *RadioGraphics*, **27**, 525–51.
9. Papaiconomou C, Bozanovic-Sosic R, Zakharov A, et al. (2002). Does neonatal cerebrospinal fluid absorption occur via arachnoid projections or extracranial lymphatics? *American Journal of Physiology—Regulatory, Integrative and Comparative Physiology*, **283**(4), R869–76.
10. Van de Beek D. (2012). Progress and challenges in bacterial meningitis. *Lancet*, **380**(9854), 1623–4.
11. Durand ML, Calderwood SB, Weber DJ, et al. (1993). Acute bacterial meningitis in adults—a review of 493 episodes. *New England Journal of Medicine*, **328**, 21–8.
12. Splendiani A, Puglielli E, De Amicis R, et al. (2005). Contrast-enhanced FLAIR in the early diagnosis of infectious meningitis. *Neuroradiology*, **47**(8), 591–8.
13. Desmond RA, Accortt NA, Talley L, et al. (2006). Enteroviral meningitis: natural history and outcome of pleconaril therapy. *Antimicrobial Agents in Chemotherapy*, **50**(7), 2409–14.
14. Nagra I, Wee B, Short J, et al. (2011). The role of cranial CT in the investigation of meningitis. *Journal of the Royal Society of Medicine, Short Reports*, **2**(3): 20.
15. Auwaerter PG, Aucott J, and Dumler JS. (2004). Lyme borreliosis (Lyme disease): molecular and cellular pathobiology and prospects for prevention, diagnosis and treatment. *Expert Reviews in Molecular Medicine*, **6**, 1–22.
16. Re VL, and Gluckman SJ. (2003). Eosinophilic meningitis. *American Journal of Medicine*, **114**(3), 217–23.
17. Pezzullo JA, Tung GA, Mudigonda S, et al. (2003). Diffusion-weighted MR imaging of pyogenic ventriculitis. *American Journal of Research*, **180**, 71–5.
18. Bonis P, Anile C, Pompucci A, et al. (2009). Cranial and spinal subdural empyema. *British Journal of Neurosurgery*, **23**(3), 335–40.
19. Ratnaike TE, Das S, Gregson BA, et al. (2011). A review of brain abscess surgical treatment—78 years: aspiration versus excision. *World Neurosurgery*, **76**(5), 431–6.
20. Blumfield E, and Misra M. (2011). Pott's puffy tumor, intracranial, and orbital complications as the initial presentation of sinusitis in healthy adolescents, a case series. *Emergency Radiology*, **18**(3), 203–10.

21. Carpenter J, Stapleton S, and Holliman R. (2007). Retrospective analysis of 49 cases of brain abscess and review of the literature. *European Journal of Clinical Microbiology and Infectious Diseases*, **26**(1), 1–11.
22. Toh CH, Wei KC, Chang CN et al. (2012). Differentiation of pyogenic brain abscesses from necrotic glioblastomas with use of susceptibility-weighted imaging. *American Journal of Neurological Research*, **33**(8), 1534–8.
23. Steiner I. (2011). Herpes simplex encephalitis: new infection or reactivation? *Current Opinion in Neurology*, **24**(3), 268–74.
24. Granerod J, Ambrose HE, Davies NWS, et al. (2010). Causes of encephalitis and differences in their clinical presentations in England: a multicentre, population-based prospective study, *Lancet: Infectious Diseases* **2010**(12), 835–44.
25. Noguchi T, Yoshiura T, Hiwatashi A, et al. (2010). Original research: CT and MRI findings of human herpesvirus 6–associated encephalopathy: comparison with findings of herpes simplex virus encephalitis. *American Journal of Research*, **194**, 754–60.
26. National Centre for Emerging and Zoonotic Infectious Diseases, Centre for disease control and Prevention, USA 2012.
27. Sejvar JJ, Bode AV, Marfin AA, et al. (2005). West Nile virus-associated flaccid paralysis. *Emerging Infectious Diseases*, **11**(7), 1021–7.
28. Ali M, Safriel Y, Sohi J et al. (2005). West Nile virus infection: MR imaging findings in the nervous system. *American Journal of Neurology Research*, **26**, 289–97.
29. Solomon T, Dung NM, Kneen R, et al. (2000). Neurological aspects of tropical disease: Japanese encephalitis. *Journal of Neurology, Neurosurgery & Psychiatry*, **68**, 405–15.
30. Kumar S, Misra UK, Kalita J, et al. (1997). MRI in Japanese encephalitis. *Neuroradiology*, **39**(3), 180–4.
31. Pfister HW, Lorenzl S, Yousry T, Neuroradiographic manifestations of encephalitis.
32. *New England Journal of Medicine*, **337**(19), 1393–4.
33. Herrera DA, Dublin AB, Ormsby EL, et al. (2009). Imaging findings of rhinocerebral mucormycosis. *Skull Base*, **19**(2), 117–25.
34. Verma A, Brozman B, and Petito CK. (2006). Isolated cerebral mucormycosis: report of a case and review of the literature. *Journal of Neurological Sciences*, **240**(1–2), 65–9.
35. Ruhnke M, Kofla G, Otto K, et al. (2007). CNS aspergillosis: recognition, diagnosis and management. *CNS Drugs*, **21**, 659–76.
36. Wright D, Schneider A, and Berger JR. (1997). Central nervous system opportunistic infections. *Neuroimaging Clinics of North America*, **7**(3), 513–25.
37. Kimura-Hayama ET, Higuera JA, Corona-Cedillo R, et al. (2010). Neurocy sticercosis: radiologic-pathologic correlation. *Radiographics*, **30**, 1705–19.
38. Román G, Sotelo J, Del Brutto O et al. (2000). A proposal to declare neurocysticercosis an international reportable disease. *Bulletin of the World Health Organisation*, **78**(3), 399–406.
39. Jay A, Dhanda J, Chiodini PL, et al. (2007). Oral cysticercosis. *British Journal of Oral Maxillofacial Surgery*, **45**(4), 331–4.
40. Shahlaie K, Hawk MW, Hu BR et al. Parasitic central nervous system infections: echinococcus and schistosoma. *Reviews in Neurological Diseases*, **2**(4), 176–85.
41. Health Protection Agency. (2011). *HIV in the United Kingdom: 2011 Report*. London: Health Protection Services, Colindale.
42. Clifford DB. (2008). HIV-associated neurocognitive disease continues in the antiretroviral era. *Topics in HIV Medicine*, **16**(2), 94–8.
43. Clifford, DB. (2008). HIV-associated neurocognitive disease continues in the antiretroviral era. *HIV Neurology*, **16**(2), 94–8.
44. Antori A, Arendt G, Brew JT, et al. (2007). Updated research nosology for HIV-associated neurocognitive disorders. *Neurology*, **69**(18), 1789–99.
45. Smith AB, Smirniotopoulos JG, Rushing EJ. (2008). Central nervous system infections associated with human immunodeficiency virus infection: radiologic-pathologic correlation. *Radiographics*, **28**(7), 2033–58.
46. Manji H, Jäger HR, Winston A. (2013). HIV, dementia and antiretroviral drugs: 30 years of an epidemic. *Journal of Neurology, Neurosurgery & Psychiatry*, **84**(10), 1–11.
47. Yousry TA, Major EO, Ryschkewitsch C, et al. (2006). Evaluation of patients treated with natalizumab for progressive multifocal leukoencephalopathy. *New England Journal of Medicine*, **354**(9), 924–33.
48. Tan K, Roda R, Ostrow L, et al. (2009). PML-IRIS in patients with HIV infection: clinical manifestations and treatment with steroids. *Neurology*, **72**, 1458–64.
49. Yousy TA, Pelletier D, Cadavid D, et al. (2012). Magnetic resonance imaging pattern in natalizuman-associated progressive multifocal leukoencephalopathy. *Annals of Neurology Journal*, **72**(5), 779–87.
50. Shelburne SA, Hamill RJ, Rodriguez-Barradas MC, et al. (2002). Immune reconstitution inflammatory syndrome: emergence of a unique syndrome during highly active antiretroviral therapy. *Medicine*, **81**(3), 213–27.
51. Johnson T, and Nath A. (2010). Neurological complications of immune reconstitution in HIV-infected populations. *Annals of the New York Academy of Science*, 1184, 106–20.
52. Post MJ, Thurner MM, Clifford DB, et al. (2012). CNS-immune reconstitution inflammatory syndrome in the setting of HIV infection, part 1: overview and discussion of progressive multifocal leukoencephalopathy-immune reconstitution inflammatory syndrome and cryptococcal-immune reconstitution inflammatory syndrome. *American Journal of Neurology Research*, 2012 (EPub ahead of print).
53. Cheonis N (2005). Immune reconstitution syndrome. *BETA*, **17**(2), 12–15.
54. Post MJ, Thurner MM, Clifford DB, et al. (2012). CNS-immune reconstitution inflammatory syndrome in the setting of HIV Infection, Part 1: overview and discussion of progressive multifocal leukoencephalopathy-immune reconstitution inflammatory syndrome and cryptococcal-immune reconstitution inflammatory syndrome. *American Journal of Neurology Research* 2012 (EPub ahead of print).
55. Sen S, Rabinstein AA, Elkind MS, et al. (2012). Recent developments regarding human immunodeficiency virus and stroke. *Cerebrovascular Diseases*, **33**(3), 209–18.
56. Worm SW, Kamara DA, Reiss P, et al. (2012). Evaluation of HIV protease inhibitor use and the risk of sudden death or nonhaemorrhagic stroke. *Journal of Infectious Diseases*, **205**(4), 535–9.
57. Islam FM, Wu J, Jansson J, et al. (2012). Relative risk of cardiovascular disease among people living with HIV: a systematic review and meta-analysis. *HIV Medicine*, **13**(8), 453–68.
58. Guillevin L (2008). Vasculitides in the context of HIV infection. *AIDS*, **22**(Suppl. 3), S27–33.
59. Gutierrez J, and Ortiz G. (2011). HIV/AIDS patients with HIV vasculopathy and VZV vasculitis: a case series. *Clinical Neuroradiology*, **21**(3), 145–51.
60. Cutfield NJ, Steele H, Wilhelm T, et al. (2009). Successful treatment of HIV associated cerebral vasculopathy with HAART. *Journal of Neurology, Neurosurgery & Psychiatry*, **80**, 936.
61. Benjamin LA, Bryer A, Emsley HC, et al. (2012). HIV infection and stroke: current perspectives and future directions. *Lancet Neurology*, **11**(10), 878–90.
62. Di Rocco A, and Simpson DM. (1998). AIDS-associated vacuolar myelopathy. *AIDS Patient Care and STDs*, **12**(6), 457–61.
63. Taber KH, Hayman LA, Shandera WX, et al. (1999). Spinal disease in neurologically symptomatic HIV positive patients. *Neuroradiology*, **41**(5), 360–8.
64. Chong J, Di Rocco A, Tagliati F, et al. (1999). MR Findings in AIDS-associated myelopathy. *American Journal of Neurology Research*, **20**, 1412–16.
65. Lee GT, Antelo F, and Milkotic AA. (2009). Cerebral toxoplasmosis. *Radiographics*, **29**, 1200–5.
66. Horberg MA, Ranatunga DK, Quesenberry CP, et al. (2010). Syphilis epidemiology and clinical outcomes in HIV-infected and

HIV-uninfected patients in Kaiser Permanente Northern California. *Sexually Transmitted Diseases*, **37**(1), 53–8.

67. Health Protection Agency (2010). *STI annual data tables*.
68. Vendes E, Geraldo AF, Rodriques R, et al. (2012). Neurosyphilis versus herpes encephalitis in a patient with confusion, memory loss and T2 weighted mesiotemporal hyperintensity. *Case Reports on Infectious Diseases*, 2012, 154863.
69. Brightbill TC, Ihmeidan IH, Judith Donovan Post M, et al. (1995). Neurosyphilis in HIV positive and HIV negative patients: neuroimaging findings. *American Journal of Neurology Research*, **16**, 703–11.
70. Peng F, Hu X, Zhong X, et al. (2008). CT and MRI findings in HIV-negative neurosyphillis. *European Journal of Research*, **66**(1), 1–6.
71. Cherian A, and Thomas SV. (2011). Central nervous system tuberculosis. *African Health Sciences*, **11**(1), 116–27.
72. Kamra P, Azad R, Prasad KN, et al. (2004). Infectious meningitis: prospective evaluation with magnetization transfer MRI. *British Journal of Research*, **77**, 387–94.
73. Provan D, and Krentz A. (2005). *Oxford Handbook of Clinical and Laboratory Investigation*. Oxford: Oxford University Press.

CHAPTER 15

Multiple sclerosis and related disorders

Massimo Filippi, Paolo Preziosa, and Maria A. Rocca

Introduction

Multiple sclerosis (MS) is the most common chronic inflammatory demyelinating disease affecting the central nervous system (CNS) of young adults in Western countries leading, in most cases, to severe and irreversible clinical disability. The clinical course of MS is extremely variable. In about 85% of MS cases, patients present with a clinically-isolated syndrome (CIS) involving the optic nerve, brainstem, or spinal cord [1]. In these patients, symptoms and signs typically evolve over a period of several days, stabilize, and then often improve, resulting in a relapsing-remitting (RR) course. Persistent signs of CNS dysfunction may develop after a relapse, and the disease may progress between relapses (secondary progressive [SP] MS) [2]. Patients with benign multiple sclerosis (BMS) represent 10–20% of patients with relapsing MS and are characterized by accumulation of modest or no disability over a long period of time [3]. About 15% of patients have primary progressive (PP) MS, which is characterized by a steady progression from the clinical onset, without clear-cut relapses [4].

Magnetic resonance imaging (MRI) has a high sensitivity in revealing macroscopic tissue abnormalities in patients with MS. Conventional MR sequences, i.e. dual-echo, fluid-attenuated inversion recovery (FLAIR), and T_1-weighted, both with and without gadolinium (Gd) contrast agent administration (Fig. 15.1), provide important pieces of information for diagnosing MS, understanding its natural history, and assessing treatment efficacy. Dual-echo and FLAIR imaging have a high sensitivity in detecting MS lesions, which appear as hyperintense focal areas on these scans. However, they lack of specificity to the heterogeneous pathological substrates of individual lesions. Gd-enhanced T_1-weighted images allow active lesions to be distinguished from inactive lesions, since enhancement occurs as a result of increased blood–brain barrier (BBB) permeability and corresponds to areas with on-going inflammation. Finally, lesions that persistently appear dark on post-contrast T_1-weighted images are associated with more severe tissue damage (both demyelination and axonal loss) compared with lesions that do not appear dark on such images.

Disappointingly, the strength of the association between conventional MRI findings and the subsequent clinical manifestations of the disease remains modest in patients with MS. This is probably due to the relative lack of specificity of conventional MRI in the evaluation of the heterogeneous pathological substrates of the disease, the inability of MRI to provide accurate estimates of damage outside focal lesions, and the fact that it cannot be used to identify CNS functional reorganization after tissue injury has occurred. Structural, metabolic, and functional MR techniques have provided new markers, more closely linked to the pathological features of the disease, which may in part overcome the limitations of conventional MRI.

This chapter discusses the main insights derived from the application of MR-based techniques to diagnose MS, define its pathophysiology, and monitor the efficacy of disease-modifying treatments.

Magnetic resonance imaging and the diagnosis of multiple sclerosis

Features of MS lesions

A critical feature in the diagnostic evaluation of patients suspected of having MS is the characterization of lesion features that are suggestive of the disease. Brain MS lesions are frequently located asymmetrically in the periventricular and juxtacortical white matter (WM), the corpus callosum (CC) and infratentorial areas (with the pons and cerebellum more frequently affected than the medulla and midbrain), and are sometimes characterized by oval or elliptical shapes [5]. Consensus has also been reached on criteria useful to identify T_2-hyperintense [6] and T_1-enhancing lesions [7].

MRI diagnostic criteria

In 2001, MRI has been formally included in the diagnostic work up of patients suspected of having MS by an international panel (IP) of MS experts. [8] The definition of MRI criteria for a diagnosis of MS is based, from the one hand, on the demonstration of lesion dissemination in space (DIS) and time (DIT), and, on the other, on the exclusion of alternative neurological conditions (Table 15.1). The original IP criteria for MS diagnosis were revised in 2005 [9] to simplify the approach, while maintaining adequate sensitivity and specificity (Table 15.1). The main changes introduced by such a revision pertain to the demonstration of DIT, which can be obtained by the detection of a new T_2 lesion, if it appears at any time compared with a reference scan done at least 30 days after the onset of the first clinical event, and the clarification of the use of spinal cord MRI to demonstrate DIS [9]. Importance to clinical and imaging (brain or spinal cord) findings has been given for a diagnosis of PP MS, with less emphasis on cerebrospinal fluid (CSF) assessment.

Meanwhile several other proposals have been made to simplify further the revised IP criteria, and to make them easier to be implemented in clinical and research settings. According to the Swanton

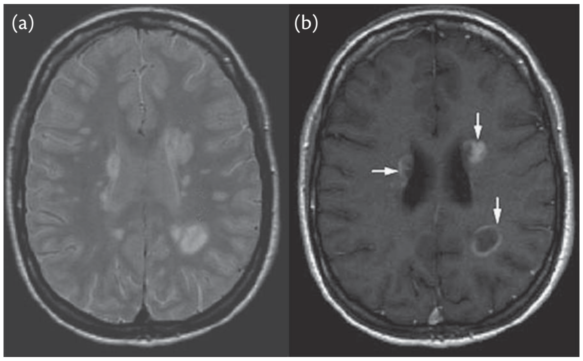

Fig. 15.1 Axial proton density-weighted (a), and post-contrast T_1-weighted (b) spin echo magnetic resonance images of the brain from a 37-year-old patient with relapsing-remitting MS. In (a), multiple hyperintense lesions are visible, which suggest multifocal white matter pathology. In (b), three of these lesions (white arrows) are clearly contrast-enhanced, which indicates the presence of local disruption of the BBB.

criteria [10], at least one subclinical T_2 lesion in at least two of the four locations defined as characteristic for MS in the revised-IP criteria (i.e. juxtacortical, periventricular, infratentorial, and spinal cord) is required for DIS (Table 15.1). Rovira et al. [11] suggested that a single brain MRI study performed early (i.e. <3 months) after the onset of a CIS is highly specific for predicting the development of definite MS in the presence of both Gd-enhancing and non-enhancing lesions, which when present simultaneously are considered to be a marker of DIT. Both the previous criteria have been included in the criteria proposed by the European Multicentre Collaborative Research Network for MRI in MS (MAGNIMS) [12], as well as in the most recent revision of the 2001 IP criteria (Table 15.1) [13]. One aspect that has not been considered in the available sets of MRI diagnostic criteria is the presence of cortical lesions (CL), which can be better visualized using double-inversion recovery (DIR) sequences [14]. The sensitivity and utility of such lesion detection in the context of MS diagnosis have been considered by Filippi and coworkers [15], who proposed a model for DIS, which includes the presence of at least one intracortical lesion (ICL), in addition to the presence of at least one infratentorial, and one spinal cord or Gd-enhancing lesion.

Another aspect that has been recently investigated is the contribution of spinal cord involvement in CIS patients in diagnosing MS according to the revised 2010 IP criteria and in predicting conversion to definite MS [16]. The presence of spinal cord lesions facilitated the diagnosis of MS and was predictive of conversion to definite MS, especially in patients without spinal CIS who did not fulfil brain MRI criteria.

MRI and differential diagnosis

A series of MRI ‘red flags’, derived from evidence-based findings and educated guesses, have been identified in the setting of clinically-suspected MS, which should alert the clinicians to prompt the performance of ‘non-routine’ tests and to reconsider differential diagnosis more extensively [17,18]. For example, the presence of symmetric, diffuse T_2-weighted hyperintensities in the deep and periventricular WM is a typical MRI finding of dystrophies. Neuromyelitis optica (NMO) should be distinguished from MS for its different course, prognosis, and response to immunomodulatory

Table 15.1 Magnetic resonance imaging criteria for dissemination in space and dissemination in time of multiple sclerosis

	DIS	DIT
IP criteria 2001 [8]	≥3 of the following: 9 T_2 lesions or 1 Gd-enhancing lesion; ≥3 periventricular lesions; ≥1 juxtacortical lesion; ≥1 posterior fossa lesion. 1 spinal cord lesion can replace 1 brain lesion	◆ A Gd-enhancing lesion ≥3 months after CIS onset, *or* ◆ A new T_2 lesion with reference to a previous scan ≥3 months after CIS onset.
Revised IP criteria 2005 [9]	≥3 of the following: 9 T_2 lesions or 1 Gd-enhancing lesion; ≥3 periventricular lesions; ≥1 juxtacortical lesion; ≥1 posterior fossa lesion or spinal cord lesion. A spinal cord lesion can replace an infratentorial lesion. Any number of spinal cord lesions can be included in total lesion count	◆ A Gd-enhancing lesion ≥3 months after CIS onset, *or* ◆ A new T_2 lesion with reference to a baseline scan obtained ≥30 days after CIS onset
Swanton 2006 [10]	≥1 lesion in each of ≥2 characteristic locations: periventricular, juxtacortical, posterior fossa, spinal cord. All lesions in symptomatic region excluded in brainstem and spinal cord syndromes	A new T_2 lesion on follow-up MRI irrespective of timing of baseline scan
MAGNIMS 2010 [12] and revised IP criteria 2010 [13]	≥1 lesion in each of ≥2 characteristic locations: periventricular, juxtacortical, posterior fossa, spinal cord All lesions in symptomatic regions excluded in brainstem and spinal cord syndromes	◆ Simultaneous presence of asymptomatic Gd-enhancing and non-enhancing lesions at any time, *or* ◆ A new T_2 and/or Gd-enhancing lesion on follow-up MRI irrespective of timing of baseline scan

Abbreviation: DIS = dissemination in space; DIT = dissemination in time; IP = international panel; MRI = magnetic resonance imaging; CIS = clinically isolated syndrome; Gd = gadolinium.

therapy. MRI and NMO-IgG, a serum biomarker, have been formally included in the diagnostic criteria of NMO [19]. Most NMO patients have a normal brain MRI or only a few, and non-specific T_2-hyperintensities that may have a predilection for regions with a high expression of aquaporin-4, including the hypothalamus, medulla, and other brainstem areas. Myelitis in this condition, unlike that which occurs in MS, is usually accompanied in the acute phase by a T_2-weighted spinal cord lesion extending over three or more spinal segments, which may be hypointense on T_1-weighted sequences and associated to varying degrees of Gd-enhancement [17,18]. Additional MRI findings of NMO are summarized in the section 'Magnetic resonance imaging in multiple sclerosis-related disorders'.

MRI and prognosis in CIS patients

In several studies, MRI findings at disease onset that showed the strongest predictive value for the subsequent development of definite MS were the number and extent of brain T_2 lesions [20–22], the presence of infratentorial lesions [22], and the presence of Gd-enhancing lesions [23]. For patients with CIS and brain MRI lesions, the chance of developing definite MS was >80% over the subsequent 20 years, in the longest follow up study to date [20,21]. Baseline T_2 lesion load is a strong predictor of disability accumulation over time in these patients [21]. In a longitudinal study [24], baseline T_1 hypointense lesion number and volume predicted the severity of executive deficits, and new T_2 lesions at a 3-month follow-up predicted slowed information processing 7 years later.

Magnetic resonance imaging and the pathophysiology of multiple sclerosis

Conventional MRI

T_2 lesions

Lesion burden on T_2-weighted MRI scans increases by about 5–10% per year. Several cross-sectional studies evaluated differences in T_2 lesion load among different MS phenotypes. T_2 lesion load is higher in SP MS in comparison to BMS, RR MS, and PP MS [25]. However, the magnitude of the correlation between T_2 lesion burden and disability in cross-sectional studies remains disappointing. A plateauing relationship between T_2 lesion load and disability has been suggested for Expanded Disability Status Scale (EDSS) scores higher than 4.5 [26]; however, this finding has not been confirmed by subsequent studies [27,28].

Gd-enhancing lesions

Post-contrast T_1-weighted scans allow to differentiate active from chronic MS lesions. Serial MRI studies have shown that enhancement occurs in almost all new lesions in patients with RR MS or SP MS and can sometimes be detected even before the onset of clinical symptoms [29]. The burden of MRI activity can be stratified on the basis of the clinical phenotype, being higher in RR MS [30] and SP MS [31] than in PP MS [31] and BMS [30]. Severely-disabled SP MS patients exhibit a substantially lower incidence of enhancing lesions when compared with those with RR MS [32], even if the trend of enhancement might vary across different cohorts of patients with the same clinical phenotype of the disease. A recent study showed a different reduction in the amount of Gd-enhancement in two different groups of SP MS patients enrolled in two clinical trials, despite these having similar inclusion and exclusion criteria, and similar MRI acquisition and analysis protocols [33]. Several studies have investigated the prognostic role of Gd-enhanced MRI findings on clinical parameters. The number of enhancing lesions increases shortly before and during clinical relapses and predicts subsequent MRI activity. As noted for T_2 lesions, contrast-enhancing lesions also show a relatively modest correlation with disability accumulation [34].

T_1-hypointense lesions

A subset of T_2 lesions (around 30–40%) appears persistently dark on post-contrast T_1-weighted images on serial scans and represent regions where irreversible axonal loss, demyelination and gliosis has occurred [35]. T_1-hypointense lesions are few in the early stage of MS and increase over the course of the disease. Studies assessing the correlations between T_1-hypointense lesion burden and disability provided conflicting results, since some of them found such a correlation to be higher than for T_2 lesions, while others did not.

New contrast agents

MRI contrast agents composed of iron particles, known as ultra-small particles of iron oxide (USPIO) or super-paramagnetic iron particles of oxide (SPIO), have been introduced to monitor the MS inflammatory process. These particles are taken by cells of the monocyte/macrophage system. As a consequence, USPIO-enhancement reflects cellular infiltration and may complement Gd enhancement [36,37]. The pattern of enhancement might differ after USPIO and Gd administration, with some lesions enhancing only with Gd, others only with USPIO, and others with both [36]. Furthermore, USPIO enhancement may precede by a few weeks Gd enhancement and may persist after Gd enhancement is ceased [36].

Recently, using dynamic contrast-enhanced (DCE) MRI, different patterns of centrifugal and centripetal Gd-enhancement have been described [38], suggesting a possible replacement of the previously accepted definition of nodular and ring-like lesions based on single post-Gd T_1-weighted scans in favour of a paradigm based on spatiotemporal enhancement dynamics.

DIR sequences and CLs

As previously discussed, DIR sequences (which use two inversion times to suppress the signal from both WM and CSF) have markedly improved the sensitivity of MRI to detect CL *in vivo* (a gain of 538% has been reported versus the use of T_2-weighted sequences; Fig. 15.2) [14]. Using DIR sequences, CLs have been detected in all the major MS clinical phenotypes, including CIS patients [39–41]. CLs are more frequently seen in patients with SP MS than in those with CIS or RR MS [39], whereas in patients with BMS they are fewer than in those with early RR MS [40]. Such lesions have also been visualized in the hippocampus [42]. Longitudinal studies have shown that new CLs continue to form in patients with early RR MS [40] and in those with the progressive disease phenotypes over one to 2-year periods of follow-up [41,43–45]. An association has been found between CL burden and progression of disability over the subsequent 2–5 years [41,43,46] in patients with different disease phenotypes, as well as between CL burden and the severity of cognitive impairment [45–47].

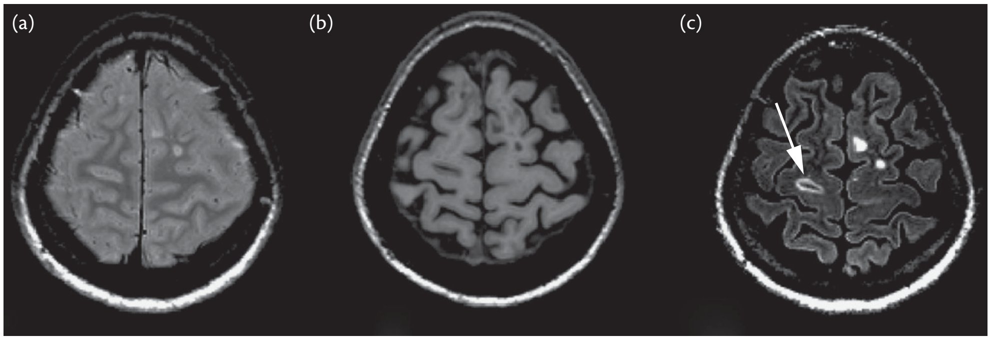

Fig. 15.2 Axial proton density-weighted (a), T_1-weighted (b) spin-echo, and double inversion recovery (c) magnetic resonance images of the brain from a 54-year-old patient with secondary progressive MS. In (a), multiple hyperintense lesions are visible. The majority of these lesions appear as hypointense in (b). In (c), one cortical lesion (white arrow), which was not clearly identifiable on the previous two sequences, is evident.

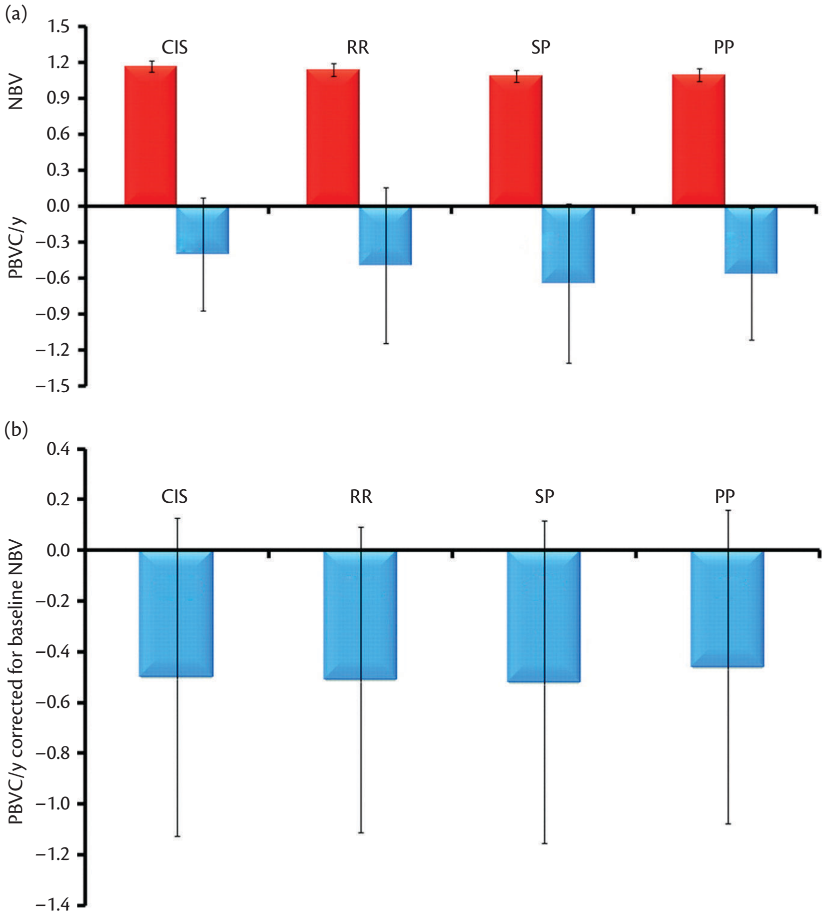

Fig. 15.3 Brain atrophy in different MS phenotypes at baseline and after 14 months. (a) Values of percent brain volume change (PBVC)/y (blue) and normalized brain volume (NBV) (expressed in litres, red). (b) Values of PBVC/y corrected for baseline NBV. Columns and error bars represent means and standard deviations of atrophy measures. Note the similar PBVC/y in the different MS subtypes when data are corrected for baseline NBV. CIS = clinically isolated syndrome; PP = primary progressive; RR = relapsing-remitting; SP = secondary progressive.

Reproduced from De Stefano N, Giorgio A, Battaglini M, et al. (2010). Assessing brain atrophy rates in a large population of untreated multiple sclerosis subtypes. *Neurology*, **74**(23), 1868–76. Copyright (2010), with permission from Wolters Kluwer Health.

DIR imaging allows to classify, on average, as ICLs only 4.6% of the overall number of gray matter (GM) lesions [39] in contrast to a figure of 59% reported by pathological studies [48]. As a consequence, a set of new strategies has been proposed to improve the detection and allow a reliable classification of these lesions, including the use of a single-slab 3D DIR sequence [49], and the combination of DIR with other sequences, such as phase-sensitive inversion recovery [50] and 3D magnetization-prepared rapid acquisition with gradient echo [51]. Nevertheless, our ability to detect CLs in MS patients *in vivo* remains suboptimal (especially for subpial lesions).

Atrophy

In MS patients, brain volume decreases on average by about 0.7–1% yearly [52]. Although it appears to be more pathologically specific than T_2 lesion load measurements, brain atrophy is at best only moderately correlated with disability in RR MS and SP MS [52,53]. The strength of the correlation increases when neuropsychological impairment is considered [54] and in longitudinal studies [55,56]. A large-scale, 14-month follow-up study [57] of untreated patients with different disease clinical phenotypes showed that the progression of brain atrophy is independent of MS phenotype, when such an assessment is corrected for brain volume at baseline (Fig. 15.3). Recently, it has been demonstrated that a higher intellectual enrichment lessens the negative impact of brain atrophy on both learning and memory [58].

Improvements in methods of analysis have allowed to quantify the extent of tissue loss in the GM and WM, separately, and also to define the distribution of atrophy at a regional level. Cross-sectional and longitudinal studies showed that GM atrophy occurs from the early stages of the disease [59,60], is associated with MS clinical disability [61–63] and cognitive deterioration [64,65], and tends to worsen over time [66]. Chen et al. [67] measured cortical thickness from patients with stable disease or progressing disability, and showed an increased rate of cortical tissue loss in the latter group. Fisher et al. [68] compared atrophy rates over 4 years across the main MS clinical phenotypes and found that GM atrophy rate increases with disease stage, from 3.4-fold normal in CIS patients converting to RR MS to 14-fold normal in SP MS.

The topography of atrophy appears to vary in the different brain structures and in different phases of the disease, as suggested by several voxel-based morphometry studies. In CIS patients, GM atrophy involves mainly the deep GM nuclei [69]. In RR MS, atrophy of the frontotemporal lobes is typically detected [70]. In SP MS patients, atrophy of deep GM structures, brainstem, cerebellum, and several cortical regions (virtually in all lobes) is observed [71]. Compared with controls, BMS patients have GM atrophy in subcortical and frontoparietal regions [72]. In comparison with BMS patients, those with SP MS have a significant GM loss in the cerebellum [72]. More recently, Riccitelli et al. [73] showed that the pattern of regional GM atrophy differs among cognitively impaired patients according to their clinical phenotype (Fig. 15.4).

Assessment of atrophy of strategic GM structures could contribute to explain deficits in selective cognitive domains, specific disease-related symptoms and disability progression. In line with this, hippocampal atrophy has been associated with deficits in memory encoding and retrieval [74], whereas atrophy of the frontal and parietal lobes has been correlated with the presence and

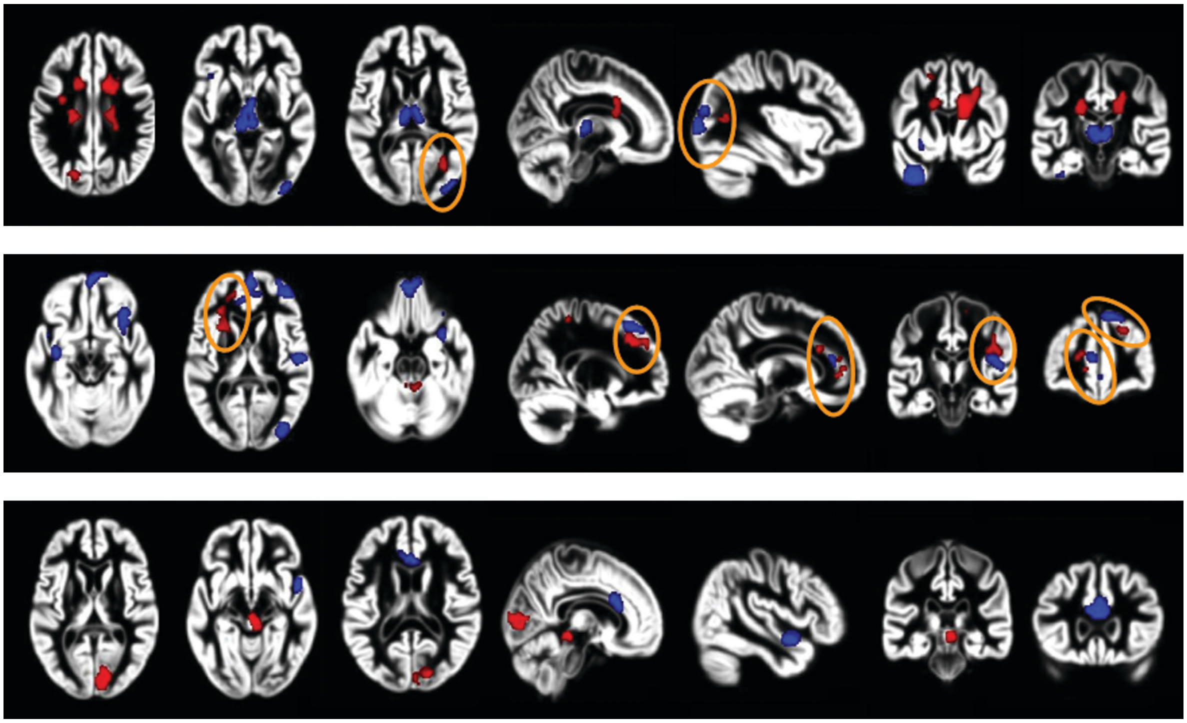

Fig. 15.4 Distribution of regions of significant cortical and subcortical atrophy (blue) and T_2-visible lesions (red) in cognitive impaired (CI) versus cognitive preserved (CP) multiple sclerosis (MS) patients according to the clinical phenotype. (Top row) Relapsing remitting (RR) MS; (middle row) secondary progressive (SP) MS; (bottom row) primary progressive (PP) MS. Orange circles identify regions with a correspondence between the presence of T_2-visible lesions and cortical atrophy. The comparison between CI versus CP patients in the three clinical phenotypes, analysed separately, shows several areas with significant tissue loss in the former groups. Differences between CI and CP patients are more prominent when considering SP MS patients. The analysis of regional distribution of T_2-visible lesions shows that while in RR MS and SP MS patients there is, at least in some regions, a correspondence between location of focal white matter lesions and cortical atrophy, in PP MS such an association was not found. Images are oriented in neurological convention.

Reproduced from Riccitelli G, Rocca MA, Pagani E, et al. (2011). Cognitive impairment in multiple sclerosis is associated to different patterns of gray matter atrophy according to clinical phenotype. *Human Brain Mapping*, **32**(10), 1535–43. Copyright (2011), with permission from John Wiley & Sons Ltd..

severity of fatigue [75,76]. Finally, thalamic atrophy has been correlated with accumulation of disability after an 8-year follow-up period in patients with relapse-onset MS [77] and after a 5-year follow-up period in PP MS patients [78].

Quantitative structural MR techniques

Quantitative MR-based techniques, including magnetization transfer (MT) [79] and diffusion tensor (DT) [80] MRI, can quantify the extent and improve the characterization of the nature of structural changes occurring within and outside focal MS lesions. Proton MR spectroscopy (^{1}H-MRS) [81] can add information on the biochemical nature of such abnormalities. T_2 hypointense areas and reduced T_2 relaxation time (RT) are thought to reflect iron deposition, which is believed to be a sign of neurodegeneration.

MT MRI

MT MRI allows the calculation of an index, the MT ratio (MTR), which, when reduced, indicates a diminished capacity of the protons bound to the brain tissue matrix to exchange magnetization with the surrounding free water. As a consequence, this index provides an estimate of the extent of MS tissue disruption. Variable degrees of MTR reduction have been reported in acute and chronic MS lesions, with the most prominent changes found in T_1-hypointense lesions. Several studies with serial scanning showed that at least in some lesions dramatic changes in normal-appearing white matter (NAWM) areas can be seen days to weeks before the development of enhancing lesions [82]. A reduction of MTR values has also been described in other areas of NAWM and GM of MS patients, including those with CIS. Such MT MRI abnormalities are more severe in patients with the progressive clinical phenotypes and tend to worsen over time [82]. MT MRI changes in the NAWM and GM correlate with the severity of clinical disability and cognitive impairment [83]. In addition, in patients with relapse-onset MS, GM MTR was found to be an independent predictor of the accumulation of disability over the subsequent eight years [84]. In PP MS patients, GM MTR decline was shown to reflect the rate of clinical deterioration over 3 years [85] and it was the best predictor of poor cognitive performance after 5.5 years [86].

Voxel-wise procedures have been applied to track longitudinal changes of MTR values within individual, newly-formed MS lesions, and to map the regional distribution of microscopic damage to the NAWM and GM. Chen et al. [87] developed a method to monitor the evolution of MTR changes of individual lesion voxels and found significant changes of MTR consistent with demyelination and remyelination that followed different temporal evolutions within some lesions and were still present in some lesions three years after their formation. MTR decrease in specific cortical regions correlated with clinical disability and Paced Auditory Serial Addition Task (PASAT) performance in patients with PP MS [88] and RR MS. [89]

DT MRI

DT MRI enables the random diffusional motion of water molecules to be measured, thus providing metrics, such as mean diffusivity (MD) and fractional anisotropy (FA), which allow the quantification of the size and geometry of water-filled spaces [90]. In line with MT MRI findings, DT MRI confirmed the heterogeneity of MS-related damage to T_2 lesions, NAWM and GM, and showed that DT MRI abnormalities may precede lesion formation. Using DT MRI, an increased FA has been found in CLs of MS patients [91–93]. Interestingly, a recent study has shown that intrinsic CL damage had high specificity, sensitivity and accuracy to discriminate BMS from SP MS [93].

DT MRI abnormalities of the NAWM, cortex and deep GM nuclei are present from the earliest stages of MS and become more pronounced with increasing disease duration and neurological impairment (see [80] for review). In addition, longitudinal DT MRI studies [94–97] demonstrated a worsening of GM damage over time in patients with RR MS [95], SP MS and PP MS [94,96,97]. The severity of GM damage has been correlated with the degree of cognitive impairment in mildly-disabled RR MS patients [98], and has been found to predict accumulation of disability over a five-year period in patients with PP MS [97].

Several approaches have been developed to investigate damage to selected WM tracts, with the ultimate goal of improving the correlation with clinical measures. These approaches include the use of DT tractography, and the quantification of abnormalities at a voxel level, by means of voxel-based or tract-based spatial statistics (TBSS) analyses. In patients with CIS and definite MS, diffusivity measures of the corticospinal tract (CST) correlate with clinical measures of motor impairment [99–101]. In patients with optic neuritis, reduced structural connectivity values in the optic radiations compared with controls have been shown [102]. Another DT MRI study [103] showed that CC damage is more pronounced in BMS patients with cognitive impairment in comparison with those without (Fig. 15.5). Similarly, in a group of 69 MS patients with different clinical phenotypes, CC DT MRI abnormalities were related to the multiple sclerosis functional composite (MSFC) and PASAT scores [104]. Two TBSS studies [105,106] have found a correlation of impaired attention, working memory and speed of information processing with decreased FA in the CC and other tracts mainly connecting prefrontal cortical regions. Using the same method, FA changes in the CC and CST have been related to clinical disability in RR MS patients [107].

Advances in DT MRI and tractography have spurred the development of brain neuro-connectivity techniques, which define and quantify anatomical links between remote brain regions by axonal fibre pathways [108]. The use of these approaches has revealed reduced network efficiency in the WM structural networks of MS patients [109], including those at the earliest stages of the disease [110].

MR spectroscopy

Using ^{1}H-MRS, dynamic changes in metabolite profiles have been shown in NAWM areas, which will become lesion [111] and in acute MS lesions, extending from the first days of lesion formation over months [81]. Several studies have found metabolite abnormalities, including reduced levels of N-acetyl aspartate (NAA, a marker of axonal viability) and choline (Cho, a marker of membrane turnover), and increased levels of myo-inositol (a marker of gliosis), in the NAWM, cortex [112–114], and subcortical GM tissue [115–118] from MS patients, including those with CIS [119,120]. A reduced concentration of glutamate-glutamine in the cortex of PP MS patients has also been detected, which was significantly correlated with the EDSS score [121]. Significant correlations have also been found between NAA decrease in frontal regions and executive function performance [122], as well as between decreased NAA in the pontine locus coeruleus and attentional measures. [123] NAWM

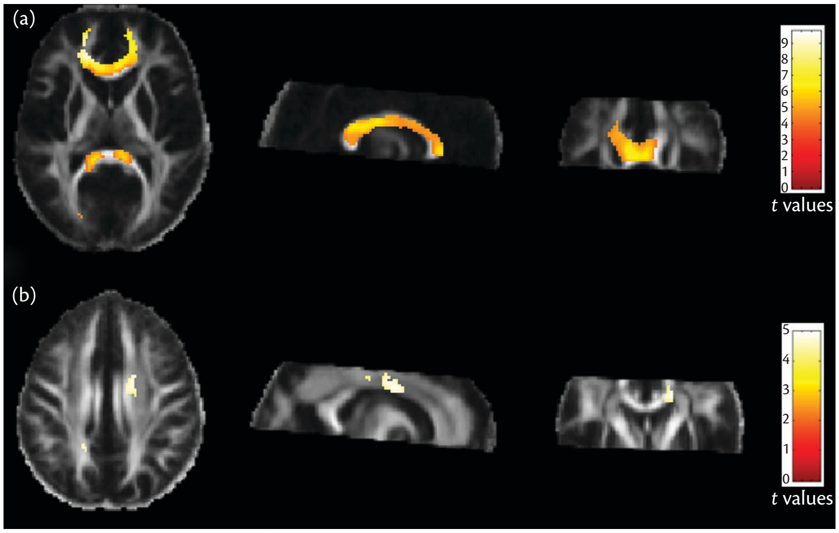

Fig. 15.5 Statistical parametric mapping analysis (colour-coded for *t* values) of corpus callosum (CC) regions with increased mean diffusivity (MD) in: (a) benign multiple sclerosis (BMS) patients ($n = 54$) versus healthy controls ($n = 21$). Compared with controls, BMS patients showed a diffuse increase of CC MD, which was more pronounced in the genu. (b) BMS patients with ($n = 9$) versus without ($n = 45$) cognitive impairment. In comparison with patients with cognitive preservation, those cognitively impaired had significant clusters of increased MD in the body and left genu of the CC. Image orientation follows the neurological convention.

Reproduced from Mesaros S, Rocca MA, Riccitelli G, et al. (2009). Corpus callosum damage and cognitive dysfunction in benign MS. *Human Brain Mapping*, **30**(8), 2656–66. Copyright (2009), with permission from John Wiley & Sons Ltd.

myo-inositol increase within three months of a CIS has been found to predict a poor performance on executive functions 7 years later [124]. A recent investigation [125] characterized metabolic abnormalities along the CST in MS patients using a novel application of chemical shift imaging (CSI) and considering the spatial variation of metabolite levels. RR MS patients showed higher CST Cho concentration than controls, and higher CST myo-inositol concentration than PP MS, suggesting greater inflammation and glial proliferation in the RR than in the PP course. In RR MS, the association between increased myo-inositol concentration and more severe disability suggested that gliosis may be relevant to disability. In PP MS, lower CST Cho and Cr concentrations correlated with more severe disability, suggesting that in the progressive stage of the disease, inflammation declines and energy metabolism reduces.

A longitudinal study showed that whole-brain NAA declines significantly (5% per year) in RR MS patients over a 2-year time period [126]. Another investigation [127] assessed the metabolic abnormalities in the GM and in the WM in early RR MS longitudinally for 3 years, and found that WM Cr, Cho, and myo-inositol concentrations were higher while WM NAA were lower at all the time points in RR MS compared with HC. No difference was found in GM metabolites, suggesting that diffuse WM glial abnormalities are larger in magnitude than axonal ones and worsen over time.

Recently, Inglese et al. [128] showed the feasibility of sodium MRI at 3.0 T in RR MS patients. In this study, an increased sodium concentration in lesions, NAWM and GM in MS patients compared with controls was found. Metabolic abnormalities were related to the extent of T_2 lesions and the severity of clinical impairment.

Imaging iron deposition

Abnormal iron deposition is thought to be the substrate of T_2 hypointense areas and reduced T_2 RT seen in the basal ganglia, thalamus, dentate nucleus, and cortical regions of MS patients [129], including those with BMS [130] and CIS [131]. Such GM T_2 hypointensities have been correlated with the severity of clinical disability and cognitive impairment in MS patients [129], as well as with clinical progression [132].

The ability to detect abnormal iron deposition increases with 3.0 T scanners. Higher basal ganglia transverse relaxation rate (R2*) values were found in RR MS than in CIS patients [133]. Increased magnetic field correlation was demonstrated in the deep GM of RR MS patients, which correlated with T_2 lesion burden and the severity of neuropsychological abnormalities [134].

Susceptibility-weighted imaging (SWI) has also been used to assess iron concentration and to evaluate cerebral venous oxygenation changes in MS patients. SWI studies found an increased iron concentration in the deep GM nuclei in MS patients compared with healthy controls [135,136]. Recently, it has been hypothesized that increased iron levels in MS brains are related to anomalies in venous outflow, termed chronic cerebrospinal venous insufficiency (CCSVI), identified by ultrasound examination [137]. This hypothesis is, at least in part, supported by the demonstration, in a pilot study of 16 RR MS patients, of a relationship between increased iron concentration, measured using SWI, and abnormalities detected at ultrasound examination [136]. However, another SWI study demonstrated a reduced visibility of the venous vasculature in the periventricular WM of RR MS patients [138], which was interpreted as a result of a decreased oxygen extraction in the diseased tissue. This, together with other studies [139] has allowed the rejection of the CCSVI hypothesis.

Functional imaging techniques

Functional imaging techniques allow the assessment of haemodynamic abnormalities in MS patients and are improving the understanding of the nature of the tissue damage, as well as the role of cortical reorganization following tissue injury.

Perfusion MRI

Brain tissue perfusion can be estimated using either exogenous tracers (e.g. Gd chelates) or endogenous arterial water (arterial

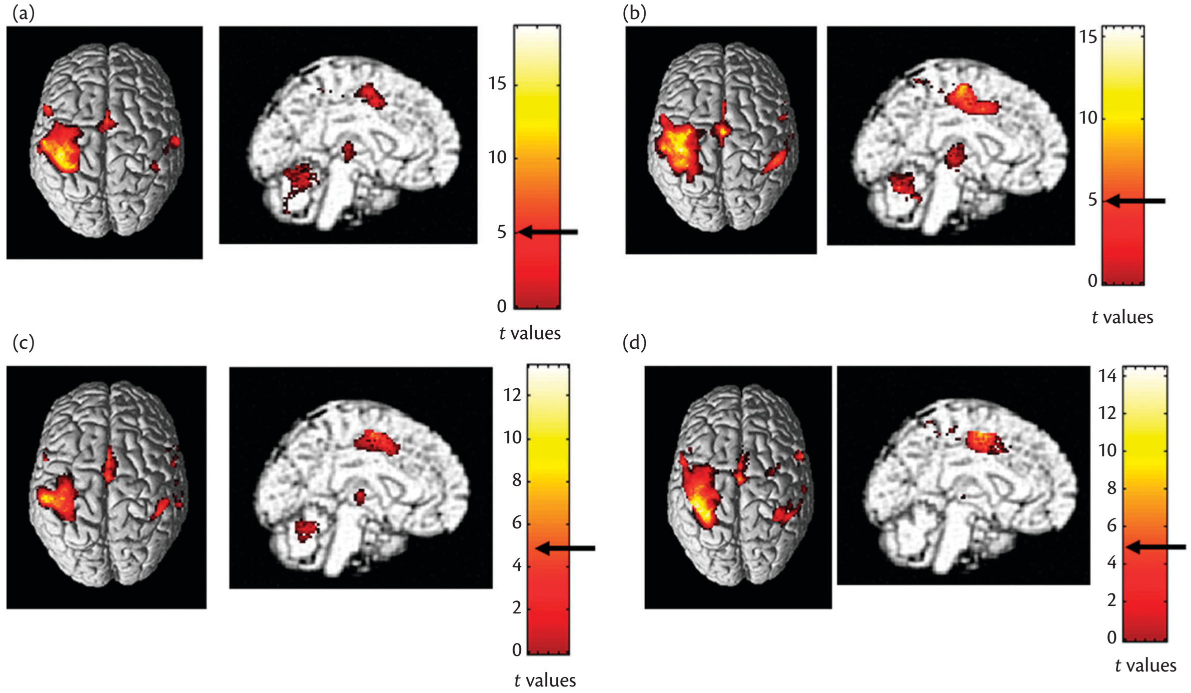

Fig. 15.6 Cortical activations in patients with multiple sclerosis (MS) during a simple, right-hand, motor task shown on a statistical parametric mapping-rendered brain. All patients were right hand dominant and clinically unimpaired. Images are colour coded for activation, and arrows show cut-off values from within-group analysis with a one-sample *t*-test ($t > 5$). In patients with clinically isolated syndromes (CIS), (a) recruitment of those areas 'normally' devoted to the performance of a motor task, such as the contralateral primary sensorimotor cortex and the supplementary motor area is noted. Activations tend to become bilateral in patients with relapsing-remitting (RR) MS (b,c). In patients with secondary progressive (SP) MS (d), a more distributed pattern of recruitment is seen. Image orientation follows the neurological convention.

Reproduced from Rocca MA, Colombo B, Falini A, et al. (2005). Cortical adaptation in patients with MS: a cross-sectional functional MRI study of disease phenotypes. *Lancet Neurology*, **4**(10), 618–26. Copyright (2005), with permission from Elsevier.

spin labelling (ASL)). While enhancing MS lesions typically show an increased perfusion, chronic lesions are characterized by a decreased perfusion. Reduced perfusion has also been recently detected in CLs of RR MS patients [140]. Several studies demonstrated a diffuse hypoperfusion in the NAWM, cortex, and deep GM of patients with different clinical phenotypes [141], including CIS [142]. Such changes have been correlated with locomotor disability [143] and neuropsychological impairment [144]. A study correlated diffusivity measures with perfusion findings in the CC of RR MS patients and provided results that are consistent with what would be seen in primary ischaemia than in secondary hypoperfusion due to Wallerian degeneration [145].

fMRI

Functional cortical changes have been demonstrated consistently in all MS phenotypes using different active paradigms. The correlation found by the majority of these studies between measures of abnormal activations and quantitative MR metrics of disease burden suggests that, at least at some stage of the disease, functional reorganization might play an adaptive role and thus limit the clinical consequences of disease-related structural damage [146]. The results of a cross-sectional study of the motor network in patients with different disease clinical phenotypes [147] support the notion of a 'natural history' of brain adaptive mechanisms in MS (Fig. 15.6). Such a study showed, at the beginning of the disease, increased recruitment in those areas 'normally' devoted to the performance of a motor task, such as the primary sensorimotor cortex and the supplementary motor area. At a later stage, a bilateral activation of these regions is seen, followed by a widespread recruitment of additional areas, which are usually recruited in normal people to perform novel/complex tasks. The preservation of a focused and strictly lateralized movement-associated pattern of cortical activations has been suggested as a possible mechanism to explain the favourable clinical outcome of patients with paediatric MS [148] and BMS [149].

There is also evidence supporting a maladaptive role of cortical functional changes in MS. In patients with progressive MS [149–151], reduced activations of 'classical' regions of the sensorimotor network and an increased recruitment of 'higher order' brain regions, such as the superior temporal sulcus and the insula have been found with motor tasks. In patients with cognitive decline, a 'reallocation' of neuronal resources and an inefficiency of neuronal processes have been associated with the extent of structural damage [152]. In RR MS patients, an abnormal recruitment of several areas of the motor network, including the thalamus and the cingulum, has been associated with the presence of fatigue [153].

The combination of measures of functional connectivity with measures of structural damage to specific WM tracts is likely to improve our understanding of the relationship between structural and functional abnormalities, as suggested by studies in patients with RR MS [154] and BMS [155].

Recently, the analysis of brain activity at rest has shown an increased synchronization of the majority of the resting-state network (RSN) in patients with CIS [156], a reduced activity of the anterior regions of the default-mode network in patients with progressive MS and cognitive impairment [157], and a complex reorganization of the visual network in normal-sighted patients who recovered from a previous optic neuritis [158]. Distributed functional abnormalities within and between large-scale neuronal networks have been shown in RR MS patients and have been related to the extent of T_2 lesions and the severity of disability [159].

Positron emission tomography

Functional abnormalities in MS patients have also been investigated using positron emission tomography (PET) [160]. A seminal investigation [161] showed an association between CC atrophy and decreased metabolic activity especially in the association cortices of the left hemisphere. Sorensen et al. [162] found a reduced cerebral metabolic rate of glucose in the cortex, putamen, thalamus, and hippocampus, which was correlated with cognitive impairment and T_2 lesion load. A decreased metabolism of cerebral glucose in several frontal areas, the putamen, and caudate nuclei, as well as an increased glucose metabolism in the cerebellar vermis and anterior cingulate cortex have been correlated to the severity of fatigue in MS [163].

A 2-year longitudinal study [164] detected a longitudinal decrease of global cortical metabolism, especially in frontal and parietal areas, which was not correlated with modification of T_2 lesions and clinical disability.

Other radio-ligands have been used to study patients with MS. Among them, [C11]-1(-2-chlorophenyl)-N-methyl-N-(-1methylpropyl)- 3-isoquinolinecarboxamide (11C-PK11195), which binds specifically to translocator protein 18KDa (TSPO), a protein that is upregulated upon exposure to various insults, might be useful to evaluate neuro-inflammation and activation of microglia. A recent PK11195 PET study [165] found that MS patients have increased cortical GM PK11195 binding relative to controls, which was correlated with disability in patients with SP MS, but not in those with RR MS. No binding in the WM was detected. Interestingly, the binding patterns suggested the presence of regional pathology, with involvement detected in the postcentral, middle frontal, anterior orbital, fusiform, and parahippocampal gyri. Patients with SP MS showed additional binding in the precentral, superior parietal, lingual and anterior superior, medial and inferior temporal gyri.

Imaging the spinal cord

MRI features of MS cord lesions have been identified [166]. MS cord lesions are more frequently observed in the cervical than in other regions, are usually peripheral, limited to two vertebral segments in length or less, occupy less than half the cross-sectional area of the cord, and typically are not T_1-hypointense (Fig. 15.7) [166]. Asymptomatic spinal cord lesions have been described in 30–40% of CIS patients and in up to 90% of patients with definite MS [166].

Although significant reduction of cervical cord size can also be observed in the early phase of MS [167], cord atrophy is more severe in the progressive forms of MS [166]. Changes at a given time point and over time in cord cross-sectional area correlate better with clinical disability than changes of T_2 lesion burden [168]. A new semi-automatic method [169], which allows segmentation of long portions of the cord, has been recently developed. The use of this method in a multicentre study of a large sample of MS patients has demonstrated that cord area differs significantly among the main MS clinical phenotypes and is correlated with EDSS, with a differential effect among phenotypes—no association in either CIS patients or in BMS, but association in RR MS, SP MS, and PP MS [170]. A voxel-wise approach has also been applied to define the regional distribution of cervical cord damage of MS patients. While RR MS patients had a few clusters of regional atrophy mainly located in the posterior and lateral columns, SP MS patients experienced a diffuse cord atrophy, which was significantly correlated with EDSS score [171]. A more recent study found no cord atrophy in CIS patients versus healthy controls, while PPMS had significant cord atrophy. Clusters of cord atrophy were found in BMS versus RR MS, and in SP MS versus RR MS, BMS, and PP MS patients, mainly involving the posterior and lateral cord segments. Cord lesion probability maps showed a significantly greater likelihood of cord abnormalities in RR MS, PP MS, and SP MS than in CIS and BMS patients. In progressive MS, regional cord atrophy was correlated with clinical disability and impairment of the pyramidal system [172].

Abnormal MT and DT MRI quantities from the cervical cord have been shown in patients with definite MS, but not in those with CIS [173]. A 2-year follow-up study of patients with relapse-onset MS found that baseline cord area and FA correlated with increased in disability at follow-up [174]. Using a MT-weighted approach, a study showed that signal abnormalities in the dorsal and lateral columns of the spinal cord are correlated with vibration sensation and strength, respectively [175]. Compared with controls, MS patients with a cervical cord relapse have reduced NAA and lower structural connectivity in the lateral CST and posterior tracts, and such abnormalities were found to be correlated with disability [176]. An increased fMRI activation of the cervical cord has been demonstrated in all the major MS clinical phenotypes and has been related

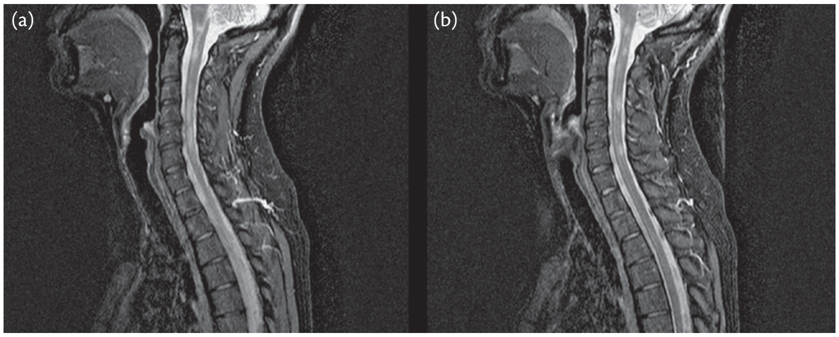

Fig. 15.7 Sagittal fast short-inversion-time inversion recovery sequence (a,b) of the cervical cord in a patient with RR MS. Multiple hyperintense lesions are visible.

to the severity of clinical disability and the extent of tissue damage [177,178].

Imaging the optic nerve

In acute monophasic optic neuritis, the most sensitive conventional MR sequences are short tau inversion recovery, fast spin echo (FSE) T_2-weighted, and spin-echo T_1-weighted pre- and post-Gd fat-suppressed. Using these sequences, the causative lesion can be frequently identified [179]. Additional typical findings include dilation of the optic nerve sheath immediately posterior to the globe on fat-saturated FSE sequences and optic nerve sheath enhancement on T_1-weighted post-contrast scans [179].

In a study of patients with an initial episode of unilateral optic neuritis, the mean cross-sectional area of the intra-orbital portion of the optic nerve was lower in the diseased eyes than in the fellow eyes and in the eyes of healthy controls [180]. MTR can be used to study longitudinally optic nerve damage. The time course of MTR changes (a progressive decline reaching a nadir after 8 months) and does not seem to match that of clinical recovery [181]. Full DT measurements from the optic nerve need to be obtained [182,183]. In patients in the chronic phase following optic neuritis, MD of the diseased optic nerve was significantly higher than in the healthy contralateral eye [182]. A multiparametric MRI study showed that, 4 years after an unilateral optic neuritis, MRI measures of optic nerve structural abnormalities (decreased FA and volume) are independently associated with visual dysfunction [184].

Ultra-high field imaging

Magnets operating at 3.0–4.0 T detect a greater number and volume of T_2 and enhancing brain lesions than those operating at 1.5 T. One study compared the performance of the MRI diagnostic criteria for MS at 1.5 T and 3.0 T in CIS patients and found that, despite an increased lesion detection, 3.0 T imaging led only to a little gain in meeting the criteria for DIS [185]. The use of DIR imaging at 3.0 T has resulted in a higher detection of infratentorial lesions compared with FLAIR and T_2-weighted sequences in patients with CIS and definite MS [186].

Ultra-high field MRI (7.0 T or more) provides a better definition of lesion location in the WM and GM, their morphology and their association with vasculature [187–189]. Using 7.0 T T_2^*-weighted MRI, the presence of a central vein in more than 40% of lesions contributed to distinguish patients with from those without definite MS [190]. This finding was found to be more predictive of MS than the presence of subcortical or periventricular lesions [190]. Using a 7.0 T scanner, Mainero et al. [191] were able to identify the three major cortical lesion patterns *in vivo* (type I: leukocortical; type II: intracortical; and type III/IV: subpial extending partly or completely through the cortical layers) described histopathologically.

Another advantage of ultra-high field MRI is an increased susceptibility to local field shifts from iron, which has allowed the demonstration of an increased local field in the caudate, putamen, and globus pallidus of MS patients relative to control subjects [188]. Ultra-high field MRI has also the potential to improve quantitative, metabolic and fMRI studies of MS. A ^{1}H-MRS study at 7.0 T [192] was able to quantify the concentration of glutathione, a marker of oxidative status, in the NAWM and GM from healthy controls and MS patients. In healthy controls, the concentration of glutathione was higher in the GM than the WM, and MS patients had a significant reduction of glutathione concentration in macroscopic lesions and the GM, but not in the NAWM, when compared with healthy individuals.

A novel approach, called diffusion tensor spectroscopy, which combines features of DT imaging and ^{1}H-MRS, has been developed to investigate the diffusion properties of intracellular, cell-type-specific metabolites. A cross-sectional pilot study [193], which measured the diffusion of the NAA in the normal-appearing CC at 7.0 T found that it was decreased in MS patients in comparison to healthy controls and that it was inversely correlated with clinical disability.

Magnetic resonance imaging in the monitoring of multiple sclerosis treatment

In MS patients, disease activity is detected much more frequently on MRI scans than with clinical assessment of relapses. This is the main reason why MRI measures are used for monitoring response to treatment. In the context of clinical trials, MRI is used as a primary outcome measure in phase II studies, where serial scans (usually monthly) are acquired to detect disease activity (new or enlarged T_2 lesions, total enhancing and new enhancing lesions and enhancing lesion volume) (Table 15.2) [194]. In phase III trials, given the uncertainty of conventional MRI in predicting clinical evolution, imaging measures (absolute or percentage increases in total T_2 lesion load) are used as secondary outcomes, and typically performed on yearly scans (Table 15.2) [195]. Despite this, two studies showed that conventional MRI quantities are valid surrogate markers of clinical activity [196,197]. In addition, recent meta-analyses [197,198] of randomized, placebo-controlled clinical trials of RR MS found a strong correlation between treatment effect on relapse and on MRI activity, which was weaker when considering EDSS worsening.

Clearly, a rigorous and valid strategy for MR-based longitudinal monitoring of MS response to treatment requires the use of standardized imaging protocols (including consistency in slice thickness and imaging planes, field strength, and patient repositioning) and evaluation procedures. As a consequence, the definition of individual patient response to MS treatment based upon routine clinical MRI scanning remains a challenging task. Patients treated with

Table 15.2 Schematic characterization of MRI-monitored trials

	Exploratory trials	**Definitive trial**
Outcome measure	Primary	Secondary
Sampling frequency	Monthly	Yearly
Main carrier	Gadolinium T_1	Unenhanced T_2
Principal target	Individual lesion	Lesion load
Method of detection	Visual	Computer assisted
Required resolution	Contrast	Spatial
Outcome parameter	Number (volume) of lesions	Change in lesion volume

Reproduced from Barkhof F, Filippi M, Miller DH, et al. (1997). Strategies for optimizing MRI techniques aimed at monitoring disease activity in multiple sclerosis treatment trials. *Journal of Neurology*, **244**(2), 76–84, Copyright (1997), with permission from Springer.

interferon (IFN) beta who developed new MRI lesions after 2 years had a higher risk of poor treatment response than those who did not [199]. In patients with RR MS treated with IFN beta, Rio et al. showed that the number of active MRI lesions detected on a MRI scan performed 12 months after treatment initiation was the most important factor related to progression of disability after 2 years [200]. In a subsequent study, the same authors found that a combination of clinical and MRI measures of disease activity during the first year of treatment allows to identify responders to IFN beta treatment after 2 and 3 years [201]. Tomassini et al. [202] demonstrated that the formation of T_1-hypointense and enhancing lesions during the first year of therapy with IFN beta was associated with relapse rate and disability progression after 6 years. Based on the degree of clinical and MRI activity, guidelines have been proposed to identify responders to disease-modifying treatments [203].

The utility of other MR techniques still needs to be validated in the context of clinical trial monitoring. For instance, the acquisition of DIR sequences has not been standardized yet across different centres and their performance has not been tested in the setting of MS clinical trials. MT MRI has been incorporated to provide additional outcome measures in limited subgroups of patients enrolled in clinical trials. In particular, two multicentre studies used MT MRI to interrogate CNS damage in CIS [204] and PP MS [205] patients. One study used ^{1}H-MRS to assess the efficacy of glatiramer acetate in PP MS patients [206], and at 3-year follow-up [207], no significant difference in metabolite ratios between treated and placebo patients was found in lesions, NAWM, and GM. Only recently, the potential of DT MRI and fMRI in prospective multicentre studies has started to be assessed [208–210].

Magnetic resonance imaging in multiple sclerosis-related disorders

The so-called classic MS variants include NMO, Balo's concentric sclerosis (BCS), Schilder's disease, acute MS (Marburg Type), and acute disseminated encephalomyelitis (ADEM). Although relatively rare, these conditions clinically important as they can cause considerable diagnostic uncertainty and might serve as 'models' to improve our understanding of the different pathophysiologic mechanisms of demyelinating diseases.

NMO is an inflammatory demyelinating condition usually characterized by optic neuritis and transverse myelitis and by the presence of a serum autoantibody (NMO-IgG) found to specifically target aquaporin-4 (AQP4).

Typical conventional MRI findings of NMO have been described in the section 'MRI and differential diagnosis'. MT MRI studies have suggested that this technique can help to distinguish patients with NMO from those with MS, since focal T_2 lesion of the brain (whenever present) have higher MTR values in NMO than in MS patients [211] and, differently from MS, NMO patients have no abnormalities in the normal-appearing brain tissue [211]. Conversely, cervical cord damage, quantified using MT MRI, is similar in NMO and MS patients [211]. However, a DT MRI study disclosed more severe cervical cord damage in NMO than in MS patients [212]. The assessment of brain NAWM and GM damage in NMO patients gave conflicting results: some authors found an isolated involvement of the GM [213], and others described an involvement of several WM tracts [214], which was more severe in the optic radiation and the CSTs [215]. As it is the case for MS patients, an increased recruitment of several cortical and subcortical areas has been also shown to occur in NMO patients using fMRI and simple motor tasks [213].

BCS is characterized by a typical pattern of pathology most often in the cerebral hemispheric WM, which consists of a concentric configuration of bands with relatively preserved myelination alternated with regions of demyelination. BCS lesions can be identified on dual-echo and T_1-weighted images. The rings may enhance, most probably in those corresponding to regions of demyelination. Synchronously enhancing, sequentially enhancing, and transiently enhancing rings have been reported. BCS lesions may present as classic large tumours in isolation associated with a fulminant clinical course or cases in which less impressive BCS-like lesions co-exist with typical MS lesions [216–219]. ^{1}H-MRS has shown metabolic abnormalities similar to those seen in very large MS lesions (increased Cho/Cr, decreased NAA/Cr, and increased lactate) [220], which tend to normalize on follow-up scans. Restricted diffusion along the surfaces of some BCS lesions may occur. These findings may normalize or become regions with increased diffusivity [221].

Schilder's disease, also known as diffuse myelinoclastic sclerosis, is a rare demyelinating disorder that occurs almost always in childhood. The following criteria [222] have been proposed for the diagnosis of this condition:

1. A subacute or chronic myelinoclastic disorder with one or two roughly symmetrical plaques at least 2 × 3 cm (large) in two of three dimensions.
2. Involvement of the centrum semiovale.
3. These being the only lesions based on clinical, paraclinical, or imaging findings
4. Adrenoleukodystropy must be excluded.

However, in some cases, small MS-like lesions have been described in addition to large areas of demyelination.

Acute MS (Marburg Type) is a rare acute inflammatory demyelinating disease, which is characterized by a rapid progression with generally frequent and severe relapses. Those cases with a particular bad course and prognosis are defined as Marburg MS. The typical MRI features of this variant might include multiple, large and often confluent lesions, that can involve the brainstem. These lesions can enhance and show perilesional oedema. It is not rare to detect simultaneously a mixture of acute, sub-acute, and chronic lesions.

ADEM is classically defined as a monophasic dysimmune demyelinating disease, commonly affecting children, generally preceded by infections or vaccinations. On MRI, ADEM is characterized by large, multifocal, diffuse, and commonly, but not exclusively symmetrically distributed lesions located in the supratentorial and infratentorial WM [223–226]. Unlike those of MS, these lesions typically have poorly-defined margins. They can involve the cortex, thalamus, basal ganglia, and, less frequently, the CC and periventricular WM [227]. Gd-enhancing lesions have been described in 30–100% of patients depending on the stage of inflammation. These lesions are often in association with non-enhancing ones. Deep GM lesions, if present, are usually bilateral and located at the GM/WM junction. The spinal cord can also be involved in ADEM, with lesions that are usually large and swollen. Follow-up MRI scans are generally very useful in the diagnostic work up of patients suspected of having ADEM, since lesions can show a partial or even a complete resolution with minimal residual evidence for injury, with no or only a few new lesions being formed. Recently, a large effort has been devoted to define those MRI parameters capable to differentiate MS from ADEM. A recent investigation has shown that the presence of either at least one T_1-hypointense lesion or one or more periventricular lesions is associated with an increased likelihood of MS [228]. Using MT MRI and DT MRI, no abnormalities of the normal-appearing brain tissue and spinal cord have been detected in ADEM patients after the acute phase of the disease [229], whereas mild DT MRI abnormalities of the basal ganglia have been described [230]. ^{1}H-MRS studies provided conflicting results in ADEM—some authors found no metabolic abnormalities in the acute stage of the disease, and others described a transient decrease of NAA in regions corresponding to T_2 lesions on the ^{1}H-MRS obtained during the acute phase which normalized after clinical recovery [231,232].

Conclusions

Conventional and advanced MR-based techniques have been applied extensively to the study of MS and such an effort has contributed to improve our ability to diagnose and monitor the disease, as well as our understanding of its pathophysiology. Nevertheless, many challenges remain. Quantitative, metabolic, and functional imaging techniques need to be optimized and standardized across multiple centres in order to adequately monitor disease evolution, either natural or modified by treatment. With the increased availability of high field and ultra-high field MR scanners, such an issue is now becoming extremely critical. Furthermore, some of the MR approaches discussed here are in their infancy and their practical utility, from a research setting to daily-life clinical practice, still needs to be investigated.

References

1. Noseworthy JH, Lucchinetti C, Rodriguez M, et al. (2000). Multiple sclerosis. *New England Journal of Medicine*, **343**(13), 938–52.
2. Lublin FD, and Reingold SC. (1996). Defining the clinical course of multiple sclerosis: results of an international survey. National Multiple Sclerosis Society (USA) Advisory Committee on Clinical Trials of New Agents in Multiple Sclerosis. *Neurology*, **46**(4), 907–11.
3. Hawkins SA, and McDonnell GV. (1999). Benign multiple sclerosis? Clinical course, long term follow up, and assessment of prognostic factors. *Journal of Neurology Neurosurgery & Psychiatry*, **67**(2), 148–52.
4. Miller DH, and Leary SM. (2007). Primary-progressive multiple sclerosis. *Lancet Neurology*, **6**(10), 903–12.
5. Ormerod IE, Miller DH, McDonald WI, et al. (1987). The role of NMR imaging in the assessment of multiple sclerosis and isolated neurological lesions. A quantitative study. *Brain*, **110**(Pt 6), 1579–616.
6. Filippi M, Gawne-Cain ML, Gasperini C, et al. (1998). Effect of training and different measurement strategies on the reproducibility of brain MRI lesion load measurements in multiple sclerosis. *Neurology*, **50**(1), 238–44.
7. Barkhof F, Filippi M, van Waesberghe JH, et al. (1997). Improving interobserver variation in reporting gadolinium-enhanced MRI lesions in multiple sclerosis. *Neurology*, **49**(6), 1682–8.
8. McDonald WI, Compston A, Edan G, et al. (2001). Recommended diagnostic criteria for multiple sclerosis: guidelines from the International Panel on the diagnosis of multiple sclerosis. *Annals of Neurology*, **50**(1), 121–7.
9. Polman CH, Reingold SC, Edan G, et al. (2005). Diagnostic criteria for multiple sclerosis: 2005 revisions to the 'McDonald Criteria'. *Annals of Neurology*, **58**(6), 840–6.
10. Swanton JK, Fernando K, Dalton CM, et al. (2006). Modification of MRI criteria for multiple sclerosis in patients with clinically isolated syndromes. *Journal of Neurology Neurosurgery & Psychiatry*, **77**(7), 830–3.
11. Rovira A, Swanton J, Tintore M, et al. (2009). A single, early magnetic resonance imaging study in the diagnosis of multiple sclerosis. *Archives of Neurology*, **66**(5), 587–92.
12. Montalban X, Tintore M, Swanton J, et al. (2010). MRI criteria for MS in patients with clinically isolated syndromes. *Neurology*, **74**(5), 427–34.
13. Polman CH, Reingold SC, Banwell B, et al. (2011). Diagnostic criteria for multiple sclerosis: 2010 Revisions to the McDonald criteria. *Annals of Neurology*, **69**(2), 292–302.
14. Geurts JJ, Pouwels PJ, Uitdehaag BM, et al. (2005). Intracortical lesions in multiple sclerosis: improved detection with 3D double inversion-recovery MR imaging. *Radiology*, **236**(1), 254–60.
15. Filippi M, Rocca MA, Calabrese M, et al. (2010). Intracortical lesions: relevance for new MRI diagnostic criteria for multiple sclerosis. *Neurology*, **75**(22), 1988–94.
16. Sombekke MH, Wattjes MP, Balk LJ, et al. (2013). Spinal cord lesions in patients with clinically isolated syndrome: a powerful tool in diagnosis and prognosis. *Neurology*, **80**(1), 69–75.
17. Charil A, Yousry TA, Rovaris M, et al. (2006). MRI and the diagnosis of multiple sclerosis: expanding the concept of 'no better explanation'. *Lancet Neurology*, **5**(10), 841–52.
18. Miller DH, Weinshenker BG, Filippi M, et al. (2008). Differential diagnosis of suspected multiple sclerosis: a consensus approach. *Multiple Sclerosis*, **14**(9), 1157–74.
19. Wingerchuk DM, Lennon VA, Pittock SJ, et al. (2006). Revised diagnostic criteria for neuromyelitis optica. *Neurology*, **66**(10), 1485–9.
20. Brex PA, Ciccarelli O, O'Riordan JI, et al. (2002). A longitudinal study of abnormalities on MRI and disability from multiple sclerosis. *New England Journal of Medicine*, **346**(3), 158–64.
21. Fisniku LK, Brex PA, Altmann DR, et al. (2008). Disability and T2 MRI lesions: a 20-year follow-up of patients with relapse onset of multiple sclerosis. *Brain*, **131**(Pt 3), 808–17.
22. Minneboo A, Barkhof F, Polman CH, et al. (2004). Infratentorial lesions predict long-term disability in patients with initial findings suggestive of multiple sclerosis. *Archives of Neurology*, **61**(2), 217–21.
23. Barkhof F, Filippi M, Miller DH, et al. (1997). Comparison of MRI criteria at first presentation to predict conversion to clinically definite multiple sclerosis. *Brain*, **120**(Pt 11), 2059–69.
24. Summers M, Fisniku L, Anderson V, et al. (2008). Cognitive impairment in relapsing-remitting multiple sclerosis can be predicted by imaging performed several years earlier. *Multiple Sclerosis*, **14**(2), 197–204.
25. Thompson AJ, Miller DH, MacManus DG, et al. (1990). Patterns of disease activity in multiple sclerosis. *British Medical Journal*, **301**(6742), 44–5.
26. Li DK, Held U, Petkau J, et al. (2006). MRI T2 lesion burden in multiple sclerosis: a plateauing relationship with clinical disability. *Neurology*, **66**(9), 1384–9.
27. Sormani MP, Rovaris M, Comi G, et al. (2009). A reassessment of the plateauing relationship between T2 lesion load and disability in MS. *Neurology*, **73**(19), 1538–42.
28. Caramanos Z, Francis SJ, Narayanan S, et al. (2012). Large, nonplateauing relationship between clinical disability and cerebral white matter lesion load in patients with multiple sclerosis. *Archives of Neurology*, **69**(1), 89–95.
29. Kermode AG, Thompson AJ, Tofts P, et al. (1990). Breakdown of the blood-brain barrier precedes symptoms and other MRI signs of new lesions in multiple sclerosis. Pathogenetic and clinical implications. *Brain*, **113**(Pt 5), 1477–89.
30. Thompson AJ, Miller D, Youl B, et al. (1992). Serial gadolinium-enhanced MRI in relapsing/remitting multiple sclerosis of varying disease duration. *Neurology*, **42**(1), 60–3.
31. Thompson AJ, Kermode AG, Wicks D, et al. (1991). Major differences in the dynamics of primary and secondary progressive multiple sclerosis. *Annals of Neurology*, **29**(1), 53–62.

32. Filippi M, Rossi P, Campi A, et al. (1997). Serial contrast-enhanced MR in patients with multiple sclerosis and varying levels of disability. *AJNR American Journal of Neuroradiology*, **18**(8), 1549–56.
33. Zhao Y, Petkau AJ, Traboulsee A, et al. (2010). Does MRI lesion activity regress in secondary progressive multiple sclerosis? *Multiple Sclerosis*, **16**(4), 434–42.
34. Kappos L, Moeri D, Radue EW, et al. (1999). Predictive value of gadolinium-enhanced magnetic resonance imaging for relapse rate and changes in disability or impairment in multiple sclerosis: a meta-analysis. Gadolinium MRI Meta-analysis Group. *Lancet*, **353**(9157), 964–9.
35. Filippi M, Rocca MA, Barkhof F, et al. (2012). Association between pathological and MRI findings in multiple sclerosis. *Lancet Neurology*, **11**(4), 349–60.
36. Vellinga MM, Oude Engberink RD, Seewann A, et al. (2008). Pluriformity of inflammation in multiple sclerosis shown by ultra-small iron oxide particle enhancement. *Brain*, **131**(Pt 3), 800–7.
37. Tourdias T, Roggerone S, Filippi M, et al. (2012). Assessment of disease activity in multiple sclerosis phenotypes with combined gadolinium- and superparamagnetic iron oxide-enhanced MR imaging. *Radiology*, **264**(1), 225–33.
38. Gaitan MI, Shea CD, Evangelou IE, et al. (2011). Evolution of the blood-brain barrier in newly forming multiple sclerosis lesions. *Annals of Neurology*, **70**(1), 22–9.
39. Calabrese M, De Stefano N, Atzori M, et al. (2007). Detection of cortical inflammatory lesions by double inversion recovery magnetic resonance imaging in patients with multiple sclerosis. *Archives of Neurology*, **64**(10), 1416–22.
40. Calabrese M, Filippi M, Rovaris M, et al. (2009). Evidence for relative cortical sparing in benign multiple sclerosis: a longitudinal magnetic resonance imaging study. *Multiple Sclerosis*, **15**(1), 36–41.
41. Calabrese M, Rocca MA, Atzori M, et al. (2009). Cortical lesions in primary progressive multiple sclerosis: a 2-year longitudinal MR study. *Neurology*, **72**(15), 1330–6.
42. Roosendaal SD, Moraal B, Vrenken H, et al. (2008). In vivo MR imaging of hippocampal lesions in multiple sclerosis. *Journal of Magnetic Resonance Imaging*, **27**(4), 726–31.
43. Calabrese M, Rocca M, Atzori M, et al. (2010). A three-year MRI study of cortical lesions in relapse-onset multiple sclerosis. *Annals of Neurology*, **67**(3), 376–83.
44. Calabrese M, Filippi M, Rovaris M, et al. (2008). Morphology and evolution of cortical lesions in multiple sclerosis. A longitudinal MRI study. *NeuroImage*, **42**(4), 1324–8.
45. Roosendaal SD, Moraal B, Pouwels PJ, et al. (2009). Accumulation of cortical lesions in MS: relation with cognitive impairment. *Multiple Sclerosis*, **15**(6), 708–14.
46. Calabrese M, Poretto V, Favaretto A, et al. (2012). Cortical lesion load associates with progression of disability in multiple sclerosis. *Brain*, **135**(Pt 10), 2952–61.
47. Calabrese M, Agosta F, Rinaldi F, et al. (2009). Cortical lesions and atrophy associated with cognitive impairment in relapsing-remitting multiple sclerosis. *Archives of Neurology*, **66**(9), 1144–50.
48. Kidd D, Barkhof F, McConnell R, et al. (1999). Cortical lesions in multiple sclerosis. *Brain*, **122**(Pt 1), 17–26.
49. Pouwels PJ, Kuijer JP, Mugler JP, 3rd, et al. (2006). Human gray matter: feasibility of single-slab 3D double inversion-recovery high-spatial-resolution MR imaging. *Radiology*, **241**(3), 873–9.
50. Nelson F, Poonawalla AH, Hou P, et al. (2007). Improved identification of intracortical lesions in multiple sclerosis with phase-sensitive inversion recovery in combination with fast double inversion recovery MR imaging. *AJNR American Journal of Neuroradiology*, **28**(9), 1645–9.
51. Nelson F, Poonawalla A, Hou P, et al. (2008). 3D MPRAGE improves classification of cortical lesions in multiple sclerosis. *Multiple Sclerosis*, **14**(9), 1214–19.
52. Miller DH, Barkhof F, Frank JA, et al. (2002). Measurement of atrophy in multiple sclerosis: pathological basis, methodological aspects and clinical relevance. *Brain*, **125**(Pt 8), 1676–95.
53. Giorgio A, Battaglini M, Smith SM, et al. (2008). Brain atrophy assessment in multiple sclerosis: importance and limitations. *Neuroimaging Clinics of North America*, **18**(4), 675–86, xi.
54. Lanz M, Hahn HK, and Hildebrandt H. (2007). Brain atrophy and cognitive impairment in multiple sclerosis: a review. *Journal of Neurology*, **254**(Suppl. 2), II43–8.
55. Fisher E, Rudick RA, Simon JH, et al. (2002). Eight-year follow-up study of brain atrophy in patients with MS. *Neurology*, **59**(9), 1412–20.
56. Khaleeli Z, Ciccarelli O, Manfredonia F, et al. (2008). Predicting progression in primary progressive multiple sclerosis: a 10-year multicenter study. *Annals of Neurology*, **63**(6), 790–3.
57. De Stefano N, Giorgio A, Battaglini M, et al. (2010). Assessing brain atrophy rates in a large population of untreated multiple sclerosis subtypes. *Neurology*, **74**(23), 1868–76.
58. Sumowski JF, Wylie GR, Chiaravalloti N, et al. (2010). Intellectual enrichment lessens the effect of brain atrophy on learning and memory in multiple sclerosis. *Neurology*, **74**(24), 1942–5.
59. Chard DT, Griffin CM, Parker GJ, et al. (2002). Brain atrophy in clinically early relapsing-remitting multiple sclerosis. *Brain*, **125**(Pt 2), 327–37.
60. De Stefano N, Matthews PM, Filippi M, et al. (2003). Evidence of early cortical atrophy in MS: relevance to white matter changes and disability. *Neurology*, **60**(7), 1157–62.
61. Tedeschi G, Lavorgna L, Russo P, et al. (2005). *Brain* atrophy and lesion load in a large population of patients with multiple sclerosis. *Neurology*, **65**(2), 280–5.
62. Sanfilipo MP, Benedict RH, Sharma J, et al. (2005). The relationship between whole brain volume and disability in multiple sclerosis: a comparison of normalized gray vs. white matter with misclassification correction. *NeuroImage*, **26**(4), 1068–77.
63. Prinster A, Quarantelli M, Lanzillo R, et al. (2010). A voxel-based morphometry study of disease severity correlates in relapsing—remitting multiple sclerosis. *Multiple Sclerosis*, **16**(1), 45–54.
64. Amato MP, Portaccio E, Goretti B, et al. (2007). Association of neocortical volume changes with cognitive deterioration in relapsing-remitting multiple sclerosis. *Archives of Neurology*, **64**(8),1157–61.
65. Benedict RH, Bruce JM, Dwyer MG, et al. (2006). Neocortical atrophy, third ventricular width, and cognitive dysfunction in multiple sclerosis. *Archives of Neurology*, **63**(9), 1301–6.
66. Valsasina P, Benedetti B, Rovaris M, et al. (2005). Evidence for progressive gray matter loss in patients with relapsing-remitting MS. *Neurology*, **65**(7), 1126–8.
67. Chen JT, Narayanan S, Collins DL, et al. (2004). Relating neocortical pathology to disability progression in multiple sclerosis using MRI. *NeuroImage*, **23**(3), 1168–75.
68. Fisher E, Lee JC, Nakamura K, et al. (2008). Gray matter atrophy in multiple sclerosis: a longitudinal study. *Annals of Neurology*, **64**(3), 255–65.
69. Henry RG, Shieh M, Okuda DT, et al. (2008). Regional grey matter atrophy in clinically isolated syndromes at presentation. *Journal of Neurology Neurosurgery & Psychiatry*, **79**(11), 1236–44.
70. Bendfeldt K, Radue EW, Borgwardt SJ, et al. (2009). Progression of gray matter atrophy and its association with white matter lesions in relapsing-remitting multiple sclerosis. *Journal of the Neurological Sciences*, **285**(1–2), 268–9; author reply 269.
71. Ceccarelli A, Rocca MA, Pagani E, et al. (2008). A voxel-based morphometry study of grey matter loss in MS patients with different clinical phenotypes. *NeuroImage*, **42**(1), 315–22.
72. Mesaros S, Rovaris M, Pagani E, et al. (2008). A magnetic resonance imaging voxel-based morphometry study of regional gray matter atrophy in patients with benign multiple sclerosis. *Archives of Neurology*, **65**(9), 1223–30.
73. Riccitelli G, Rocca MA, Pagani E, et al. (2011). Cognitive impairment in multiple sclerosis is associated to different patterns of gray matter atrophy according to clinical phenotype. *Human Brain Mapping*, **32**(10), 1535–43.
74. Sicotte NL, Kern KC, Giesser BS, et al. (2008). Regional hippocampal atrophy in multiple sclerosis. *Brain*, **131**(Pt 4), 1134–41.

75. Sepulcre J, Masdeu JC, Goni J, et al. (2009). Fatigue in multiple sclerosis is associated with the disruption of frontal and parietal pathways. *Multiple Sclerosis*, **15**(3), 337–44.
76. Pellicano C, Gallo A, Li X, et al. (2010). Relationship of cortical atrophy to fatigue in patients with multiple sclerosis. *Archives of Neurology*, 67(4):447–53.
77. Rocca MA, Mesaros S, Pagani E, et al. (2010). Thalamic damage and long-term progression of disability in multiple sclerosis. *Radiology*, **257**(2), 463–9.
78. Mesaros S, Rocca MA, Pagani E, et al. (2011). Thalamic damage predicts the evolution of primary-progressive multiple sclerosis at 5 years. *AJNR American Journal of Neuroradiology* **32**(6), 1016–20.
79. Ropele S, and Fazekas F. (2009). Magnetization transfer MR imaging in multiple sclerosis. *Neuroimaging Clinics of North America*, **19**(1), 27–36.
80. Rovaris M, Agosta F, Pagani E, et al. (2009). Diffusion tensor MR imaging. *Neuroimaging Clinics of North America*, **19**(1), 37–43.
81. Sajja BR, Wolinsky JS, and Narayana PA. (2009). Proton magnetic resonance spectroscopy in multiple sclerosis. *Neuroimaging Clinics of North America*, **19**(1), 45–58.
82. Filippi M, Rocca MA, De Stefano N, et al. (2011). Magnetic resonance techniques in multiple sclerosis: the present and the future. *Archives of Neurology*, **68**(12), 1514–20.
83. Amato MP, Portaccio E, Stromillo ML, et al. (2008). Cognitive assessment and quantitative magnetic resonance metrics can help to identify benign multiple sclerosis. *Neurology*, **71**(9), 632–8.
84. Agosta F, Rovaris M, Pagani E, et al. (2006). Magnetization transfer MRI metrics predict the accumulation of disability 8 years later in patients with multiple sclerosis. *Brain*, **129**(Pt 10), 2620–7.
85. Khaleeli Z, Altmann DR, Cercignani M, et al. (2008). Magnetization transfer ratio in gray matter: a potential surrogate marker for progression in early primary progressive multiple sclerosis. *Archives of Neurology*, **65**(11), 1454–9.
86. Penny S, Khaleeli Z, Cipolotti L, et al. (2010). Early imaging predicts later cognitive impairment in primary progressive multiple sclerosis. *Neurology*, **74**(7), 545–52.
87. Chen JT, Collins DL, Atkins HL, et al. (2008). Magnetization transfer ratio evolution with demyelination and remyelination in multiple sclerosis lesions. *Annals of Neurology*, **63**(2), 254–62.
88. Khaleeli Z, Cercignani M, Audoin B, et al. (2007). Localized grey matter damage in early primary progressive multiple sclerosis contributes to disability. *NeuroImage*, **37**(1), 253–61.
89. Ranjeva JP, Audoin B, Au Duong MV, et al. (2005). Local tissue damage assessed with statistical mapping analysis of brain magnetization transfer ratio: relationship with functional status of patients in the earliest stage of multiple sclerosis. *AJNR American Journal of Neuroradiology*, **26**(1), 119–27.
90. Rovaris M, Gass A, Bammer R, et al. (2005). Diffusion MRI in multiple sclerosis. *Neurology*, **65**(10), 1526–32.
91. Poonawalla AH, Hasan KM, Gupta RK, et al. (2008). Diffusion-tensor MR imaging of cortical lesions in multiple sclerosis: initial findings. *Radiology*, **246**(3), 880–6.
92. Calabrese M, Rinaldi F, Seppi D, et al. (2011). Cortical diffusion-tensor imaging abnormalities in multiple sclerosis: a 3-year longitudinal study. *Radiology*, **261**(3), 891–8.
93. Filippi M, Preziosa P, Pagani E, et al. (2013). Microstructural MR imaging of cortical lesion in multiple sclerosis. *Multiple Sclerosis*, **19**(4), 418–26.
94. Rovaris M, Bozzali M, Iannucci G, et al. (2002). Assessment of normal-appearing white and gray matter in patients with primary progressive multiple sclerosis: a diffusion-tensor magnetic resonance imaging study. *Archives of Neurology*, **59**(9), 1406–12.
95. Oreja-Guevara C, Rovaris M, Iannucci G, et al. (2005). Progressive gray matter damage in patients with relapsing-remitting multiple sclerosis: a longitudinal diffusion tensor magnetic resonance imaging study. *Archives of Neurology*, **62**(4), 578–84.
96. Rovaris M, Gallo A, Valsasina P, et al. (2005). Short-term accrual of gray matter pathology in patients with progressive multiple sclerosis: an in vivo study using diffusion tensor MRI. *NeuroImage*, **24**(4), 1139–46.
97. Rovaris M, Judica E, Gallo A, et al. (2006). Grey matter damage predicts the evolution of primary progressive multiple sclerosis at 5 years. *Brain*, **129**(Pt 10), 2628–34.
98. Rovaris M, Iannucci G, Falautano M, et al. (2002). Cognitive dysfunction in patients with mildly disabling relapsing-remitting multiple sclerosis: an exploratory study with diffusion tensor MR imaging. *Journal of the Neurological Sciences*, **195**(2), 103–9.
99. Lin X, Tench CR, Morgan PS, et al. (2005). 'Importance sampling' in MS: use of diffusion tensor tractography to quantify pathology related to specific impairment. *Journal of the Neurological Sciences*, **237**(1–2), 13–19.
100. Wilson M, Tench CR, Morgan PS, et al. (2003). Pyramidal tract mapping by diffusion tensor magnetic resonance imaging in multiple sclerosis: improving correlations with disability. *Journal of Neurology Neurosurgery & Psychiatry*, **74**(2), 203–7.
101. Pagani E, Filippi M, Rocca MA, et al. (2005). A method for obtaining tract-specific diffusion tensor MRI measurements in the presence of disease: application to patients with clinically isolated syndromes suggestive of multiple sclerosis. *NeuroImage*, **26**(1), 258–65.
102. Ciccarelli O, Toosy AT, Hickman SJ, et al. (2005). Optic radiation changes after optic neuritis detected by tractography-based group mapping. *Human Brain Mapping*, **25**(3), 308–16.
103. Mesaros S, Rocca MA, Riccitelli G, et al. (2009). Corpus callosum damage and cognitive dysfunction in benign MS. *Human Brain Mapping*, **30**(8), 2656–66.
104. Ozturk A, Smith SA, Gordon-Lipkin EM, et al. (2010). MRI of the corpus callosum in multiple sclerosis: association with disability. *Multiple Sclerosis*, **16**(2), 166–77.
105. Roosendaal SD, Geurts JJ, Vrenken H, et al. (2009). Regional DTI differences in multiple sclerosis patients. *NeuroImage*, **44**(4), 1397–403.
106. Dineen RA, Vilisaar J, Hlinka J, et al. (2009). Disconnection as a mechanism for cognitive dysfunction in multiple sclerosis. *Brain*, **132**(Pt 1), 239–49.
107. Giorgio A, Palace J, Johansen-Berg H, et al. (2010). Relationships of brain white matter microstructure with clinical and MR measures in relapsing-remitting multiple sclerosis. *Journal of Magnetic Resonance Imaging*, **31**(2), 309–16.
108. Guye M, Bettus G, Bartolomei F, et al. (2010). Graph theoretical analysis of structural and functional connectivity MRI in normal and pathological brain networks. *MAGMA*, **23**(5–6), 409–21.
109. Shu N, Liu Y, Li K, et al. (2011). Diffusion Tensor tractography reveals disrupted topological efficiency in white matter structural networks in multiple sclerosis. *Cerebral Cortex*, **21**, 2565–77.
110. Li Y, Jewells V, Kim M, et al. (2013). Diffusion tensor imaging based network analysis detects alterations of neuroconnectivity in patients with clinically early relapsing-remitting multiple sclerosis. *Human Brain Mapping*, **34**(12), 3376–91.
111. Narayana PA, Doyle TJ, Lai D, et al. (1998). Serial proton magnetic resonance spectroscopic imaging, contrast-enhanced magnetic resonance imaging, and quantitative lesion volumetry in multiple sclerosis. *Annals of Neurology*, **43**(1), 56–71.
112. Sharma R, Narayana PA, and Wolinsky JS. (2001). Grey matter abnormalities in multiple sclerosis: proton magnetic resonance spectroscopic imaging. *Multiple Sclerosis*, **7**(4), 221–6.
113. Chard DT, Griffin CM, McLean MA, et al. (2002). *Brain* metabolite changes in cortical grey and normal-appearing white matter in clinically early relapsing-remitting multiple sclerosis. *Brain*, **125**(Pt 10), 2342–52.
114. Sarchielli P, Presciutti O, Tarducci R, et al. (2002). Localized (1)H magnetic resonance spectroscopy in mainly cortical gray matter of patients with multiple sclerosis. *Journal of Neurology*, **249**(7), 902–10.
115. Adalsteinsson E, Langer-Gould A, Homer RJ, et al. (2003). Gray matter N-acetyl aspartate deficits in secondary progressive but not relapsing-remitting multiple sclerosis. *AJNR American Journal of Neuroradiology*, **24**(10), 1941–5.
116. Cifelli A, Arridge M, Jezzard P, et al. (2002). Thalamic neurodegeneration in multiple sclerosis. *Annals of Neurology*, **52**(5), 650–3.

117. Inglese M, Liu S, Babb JS, et al. (2004). Three-dimensional proton spectroscopy of deep gray matter nuclei in relapsing-remitting MS. *Neurology*, **63**(1), 170–2.
118. Geurts JJ, Reuling IE, Vrenken H, et al. (2006). MR spectroscopic evidence for thalamic and hippocampal, but not cortical, damage in multiple sclerosis. *Magnetic Resonance in Medicine*, **55**(3), 478–83.
119. Filippi M, Bozzali M, Rovaris M, et al. (2003). Evidence for widespread axonal damage at the earliest clinical stage of multiple sclerosis. *Brain*, **126**(Pt 2), 433–7.
120. Fernando KT, McLean MA, Chard DT, et al. (2004). Elevated white matter myo-inositol in clinically isolated syndromes suggestive of multiple sclerosis. *Brain*, **127**(Pt 6), 1361–9.
121. Sastre-Garriga J, Ingle GT, Chard DT, et al. (2005). Metabolite changes in normal-appearing gray and white matter are linked with disability in early primary progressive multiple sclerosis. *Archives of Neurology*, **62**(4), 569–73.
122. Staffen W, Zauner H, Mair A, et al. (2005). Magnetic resonance spectroscopy of memory and frontal brain region in early multiple sclerosis. *Journal of Neuropsychiatry & Clinical Neurosciences*, **17**(3), 357–63.
123. Gadea M, Martinez-Bisbal MC, Marti-Bonmati L, et al. (2004). Spectroscopic axonal damage of the right locus coeruleus relates to selective attention impairment in early stage relapsing-remitting multiple sclerosis. *Brain*, **127**(Pt 1), 89–98.
124. Summers M, Swanton J, Fernando K, et al. (2008). Cognitive impairment in multiple sclerosis can be predicted by imaging early in the disease. *Journal of Neurology Neurosurgery & Psychiatry*, **79**(8), 955–8.
125. Tur C, Wheeler-Kingshott CA, Altmann DR, et al. (2014). Spatial variability and changes of metabolite concentrations in the cortico-spinal tract in multiple sclerosis using coronal CSI. *Human Brain Mapping*, **35**(3): 993–1003
126. Rigotti DJ, Inglese M, Kirov, II, et al. (2012). Two-year serial whole-brain N-acetyl-L-aspartate in patients with relapsing-remitting multiple sclerosis. *Neurology*, **78**(18), 1383–9.
127. Kirov, II, Tal A, Babb JS, et al. (2012). Serial proton MR spectroscopy of gray and white matter in relapsing-remitting MS. *Neurology*, **80**(1), 39–46.
128. Inglese M, Madelin G, Oesingmann N, et al. (2010). *Brain* tissue sodium concentration in multiple sclerosis: a sodium imaging study at 3 tesla. *Brain*, **133**(Pt 3), 847–57.
129. Neema M, Stankiewicz J, Arora A, et al. (2007). T1- and T2-based MRI measures of diffuse gray matter and white matter damage in patients with multiple sclerosis. *Journal of Neuroimaging*, **17**(Suppl. 1), 16S–21S.
130. Ceccarelli A, Filippi M, Neema M, et al. (2009). T2 hypointensity in the deep gray matter of patients with benign multiple sclerosis. *Multiple Sclerosis*, **15**(6), 678–86.
131. Ceccarelli A, Rocca MA, Neema M, et al. (2010). Deep gray matter T2 hypointensity is present in patients with clinically isolated syndromes suggestive of multiple sclerosis. *Multiple Sclerosis*, **16**(1), 39–44.
132. Neema M, Arora A, Healy BC, et al. (2009). Deep gray matter involvement on brain MRI scans is associated with clinical progression in multiple sclerosis. *Journal of Neuroimaging*, **19**(1), 3–8.
133. Khalil M, Enzinger C, Langkammer C, et al. (2009). Quantitative assessment of brain iron by R(2)* relaxometry in patients with clinically isolated syndrome and relapsing-remitting multiple sclerosis. *Multiple Sclerosis*, **15**(9), 1048–54.
134. Ge Y, Jensen JH, Lu H, et al. (2007). Quantitative assessment of iron accumulation in the deep gray matter of multiple sclerosis by magnetic field correlation imaging. *AJNR American Journal of Neuroradiology*, **28**(9), 1639–44.
135. Haacke EM, Garbern J, Miao Y, et al. (2010). Iron stores and cerebral veins in MS studied by susceptibility weighted imaging. *International Angiology*, **29**(2), 149–57.
136. Zivadinov R, Schirda C, Dwyer MG, et al. (2010). Chronic cerebrospinal venous insufficiency and iron deposition on susceptibility-weighted imaging in patients with multiple sclerosis: a pilot case-control study. *International Angiology*, **29**(2), 158–75.
137. Zamboni P, Galeotti R, Menegatti E, et al. (2009). Chronic cerebrospinal venous insufficiency in patients with multiple sclerosis. *Journal of Neurology Neurosurgery & Psychiatry*, **80**(4), 392–9.
138. Ge Y, Zohrabian VM, Osa EO, et al. (2009). Diminished visibility of cerebral venous vasculature in multiple sclerosis by susceptibility-weighted imaging at 3.0 Tesla. *Journal of Magnetic Resonance Imaging*, **29**(5), 1190–4.
139. Filippi M, Rocca MA, Barkhof F, et al. (2011). Multiple sclerosis and chronic cerebrospinal venous insufficiency: the neuroimaging perspective. *AJNR American Journal of Neuroradiology*, **32**(3), 424–7.
140. Peruzzo D, Castellaro M, Calabrese M, et al. (2012). Heterogeneity of cortical lesions in multiple sclerosis: an MRI perfusion study. *Journal of Cerebral Blood Flow and Metabolism*, **33**(3), 457–63.
141. Inglese M, Park SJ, Johnson G, et al. (2007). Deep gray matter perfusion in multiple sclerosis: dynamic susceptibility contrast perfusion magnetic resonance imaging at 3 T. *Archives of Neurology*, **64**(2), 196–202.
142. Varga AW, Johnson G, Babb JS, et al. (2009). White matter hemodynamic abnormalities precede sub-cortical gray matter changes in multiple sclerosis. *Journal of the Neurological Sciences*, **282**(1–2), 28–33.
143. Adhya S, Johnson G, Herbert J, et al. (2006). Pattern of hemodynamic impairment in multiple sclerosis: dynamic susceptibility contrast perfusion MR imaging at 3.0 T. *NeuroImage*, **33**(4), 1029–35.
144. Inglese M, Adhya S, Johnson G, et al. (2008). Perfusion magnetic resonance imaging correlates of neuropsychological impairment in multiple sclerosis. *Journal of Cerebral Blood Flow and Metabolism*, **28**(1), 164–71.
145. Saindane AM, Law M, Ge Y, et al. (2007). Correlation of diffusion tensor and dynamic perfusion MR imaging metrics in normal-appearing corpus callosum: support for primary hypoperfusion in multiple sclerosis. *AJNR American Journal of Neuroradiology*, **28**(4), 767–72.
146. Filippi M, and Rocca MA. (2009). Functional MR imaging in multiple sclerosis. *Neuroimaging Clinics of North America*, **19**(1), 59–70.
147. Rocca MA, Colombo B, Falini A, et al. (2005). Cortical adaptation in patients with MS: a cross-sectional functional MRI study of disease phenotypes. *Lancet Neurology*, **4**(10), 618–26.
148. Rocca MA, Absinta M, Ghezzi A, et al. (2009). Is a preserved functional reserve a mechanism limiting clinical impairment in pediatric MS patients? *Human Brain Mapping*, **30**(9), 2844–51.
149. Rocca MA, Ceccarelli A, Rodegher M, et al. (2010). Preserved brain adaptive properties in patients with benign multiple sclerosis. *Neurology*, **74**(2), 142–9.
150. Filippi M, Rocca MA, Falini A, et al. (2002). Correlations between structural CNS damage and functional MRI changes in primary progressive MS. *NeuroImage*, **15**(3), 537–46.
151. Rocca MA, Matthews PM, Caputo D, et al. (2002). Evidence for widespread movement-associated functional MRI changes in patients with PPMS. *Neurology*, **58**(6), 866–72.
152. Penner IK, Rausch M, Kappos L, et al. (2003). Analysis of impairment related functional architecture in MS patients during performance of different attention tasks. *Journal of Neurology*, **250**(4), 461–72.
153. Rocca MA, Agosta F, Colombo B, et al. (2007). fMRI changes in relapsing-remitting multiple sclerosis patients complaining of fatigue after IFNbeta-1a injection. *Human Brain Mapping*, **28**(5), 373–82.
154. Rocca MA, Pagani E, Absinta M, et al. (2007). Altered functional and structural connectivities in patients with MS: a 3-T study. *Neurology*, **69**(23), 2136–45.
155. Rocca MA, Valsasina P, Ceccarelli A, et al. (2009). Structural and functional MRI correlates of Stroop control in benign MS. *Human Brain Mapping*, **30**(1), 276–90.
156. Roosendaal SD, Schoonheim MM, Hulst HE, et al. (2010). Resting state networks change in clinically isolated syndrome. *Brain*, **133**(Pt 6), 1612–21.
157. Rocca MA, Valsasina P, Absinta M, et al. (2010). Default-mode network dysfunction and cognitive impairment in progressive MS. *Neurology*, **74**(16), 1252–9.

158. Gallo A, Esposito F, Sacco R, et al. (2012). Visual resting-state network in relapsing-remitting MS with and without previous optic neuritis. *Neurology*, **79**(14), 1458–65.
159. Rocca M, Valsasina P, Martinelli V, et al. (2012). Large-scale neuronal network dysfunction in relapsing-remitting multiple sclerosis. *Neurology*, **79**(14), 1449–57.
160. Kiferle L, Politis M, Muraro PA, et al. (2011). Positron emission tomography imaging in multiple sclerosis-current status and future applications. *European Journal of Neurology*, **18**(2), 226–31.
161. Pozzilli C, Fieschi C, Perani D, et al. (1992). Relationship between corpus callosum atrophy and cerebral metabolic asymmetries in multiple sclerosis. *Journal of the Neurological Sciences*, **112**(1–2), 51–7.
162. Sorensen PS, Jonsson A, Mathiesen HK, et al. (2006). The relationship between MRI and PET changes and cognitive disturbances in MS. *Journal of the Neurological Sciences*, **245**(1–2), 99–102.
163. Roelcke U, Kappos L, Lechner-Scott J, et al. (1997). Reduced glucose metabolism in the frontal cortex and basal ganglia of multiple sclerosis patients with fatigue: a 18F-fluorodeoxyglucose positron emission tomography study. *Neurology*, **48**(6), 1566–71.
164. Blinkenberg M, Jensen CV, Holm S, et al. (1999). A longitudinal study of cerebral glucose metabolism, MRI, and disability in patients with MS. *Neurology*, **53**(1), 149–53.
165. Politis M, Giannetti P, Su P, et al. (2012). Increased PK11195 PET binding in the cortex of patients with MS correlates with disability. *Neurology*, **79**(6), 523–30.
166. Lycklama G, Thompson A, Filippi M, et al. (2003). Spinal-cord MRI in multiple sclerosis. *Lancet Neurology*, **2**(9), 555–62.
167. Brex PA, Leary SM, O'Riordan JI, et al. (2001). Measurement of spinal cord area in clinically isolated syndromes suggestive of multiple sclerosis. *Journal of Neurology, Neurosurgery & Psychiatry*, **70**(4), 544–7.
168. Losseff NA, Kingsley DP, McDonald WI, et al. (1996). Clinical and magnetic resonance imaging predictors of disability in primary and secondary progressive multiple sclerosis. *Multiple Sclerosis*, **1**(4), 218–22.
169. Horsfield MA, Sala S, Neema M, et al. (2010). Rapid semi-automatic segmentation of the spinal cord from magnetic resonance images: application in multiple sclerosis. *NeuroImage*, **50**(2), 446–55.
170. Rocca MA, Horsfield MA, Sala S, et al. (2011). A multicenter assessment of cervical cord atrophy among MS clinical phenotypes. *Neurology*, **76**(24), 2096–102.
171. Valsasina P, Horsfield MA, Rocca MA, et al. (2012). Spatial normalization and regional assessment of cord atrophy: voxel-based analysis of cervical cord 3D T1-weighted images. *AJNR American Journal of Neuroradiology*, **33**(11), 2195–200.
172. Rocca MA, Valsasina P, Damjanovic D, et al. (2013). Voxel-wise mapping of cervical cord damage in multiple sclerosis patients with different clinical phenotypes. *Journal of Neurology, Neurosurgery & Psychiatry*, **84**(1): 35–41
173. Agosta F, and Filippi M. (2007). MRI of spinal cord in multiple sclerosis. *Journal of Neuroimaging*, **17**(Suppl. 1), 46S–9S.
174. Agosta F, Absinta M, Sormani MP, et al. (2007). In vivo assessment of cervical cord damage in MS patients: a longitudinal diffusion tensor MRI study. *Brain*, **130**(Pt 8), 2211–19.
175. Zackowski KM, Smith SA, Reich DS, et al. (2009). Sensorimotor dysfunction in multiple sclerosis and column-specific magnetization transfer-imaging abnormalities in the spinal cord. *Brain*, **132**(Pt 5), 1200–9.
176. Ciccarelli O, Wheeler-Kingshott CA, McLean MA, et al. (2007). Spinal cord spectroscopy and diffusion-based tractography to assess acute disability in multiple sclerosis. *Brain*, **130**(Pt 8), 2220–31.
177. Agosta F, Valsasina P, Absinta M, et al. (2009). Primary progressive multiple sclerosis: tactile-associated functional MR activity in the cervical spinal cord. *Radiology*, **253**(1), 209–15.
178. Valsasina P, Agosta F, Absinta M, et al. (2010). Cervical cord functional MRI changes in relapse-onset MS patients. *Journal of Neurology, Neurosurgery & Psychiatry*, **81**(4), 405–8.
179. Glisson CC, and Galetta SL. (2009). Nonconventional optic nerve imaging in multiple sclerosis. *Neuroimaging Clinics of North America*, **19**(1), 71–9.
180. Hickman SJ, Brex PA, Brierley CM, et al. (2001). Detection of optic nerve atrophy following a single episode of unilateral optic neuritis by MRI using a fat-saturated short-echo fast FLAIR sequence. *Neuroradiology*, **43**(2), 123–8.
181. Hickman SJ, Toosy AT, Jones SJ, et al. (2004). Serial magnetization transfer imaging in acute optic neuritis. *Brain*, **127**(Pt 3), 692–700.
182. Hickman SJ, Wheeler-Kingshott CA, Jones SJ, et al. (2005). Optic nerve diffusion measurement from diffusion-weighted imaging in optic neuritis. *AJNR American Journal of Neuroradiology*, **26**(4), 951–6.
183. Trip SA, Schlottmann PG, Jones SJ, et al. (2006). Optic nerve atrophy and retinal nerve fibre layer thinning following optic neuritis: evidence that axonal loss is a substrate of MRI-detected atrophy. *NeuroImage*, **31**(1), 286–93.
184. Kolbe S, Chapman C, Nguyen T, et al. (2009). Optic nerve diffusion changes and atrophy jointly predict visual dysfunction after optic neuritis. *NeuroImage*, **45**(3), 679–86.
185. Wattjes MP, Harzheim M, Lutterbey GG, et al. (2008). Does high field MRI allow an earlier diagnosis of multiple sclerosis? *Journal of Neurology*, **255**(8), 1159–63.
186. Wattjes MP, Lutterbey GG, Gieseke J, et al. (2007). Double inversion recovery brain imaging at 3T: diagnostic value in the detection of multiple sclerosis lesions. *AJNR American Journal of Neuroradiology*, **28**(1), 54–9.
187. Ge Y, Zohrabian VM, and Grossman RI. (2008). Seven-Tesla magnetic resonance imaging: new vision of microvascular abnormalities in multiple sclerosis. *Archives of Neurology*, **65**(6), 812–16.
188. Hammond KE, Metcalf M, Carvajal L, et al. (2008). Quantitative in vivo magnetic resonance imaging of multiple sclerosis at 7 Tesla with sensitivity to iron. *Annals of Neurology*, **64**(6), 707–13.
189. Tallantyre EC, Brookes MJ, Dixon JE, et al. (2008). Demonstrating the perivascular distribution of MS lesions in vivo with 7-Tesla MRI. *Neurology*, **70**(22), 2076–8.
190. Tallantyre EC, Dixon JE, Donaldson I, et al. (2011). Ultra-high-field imaging distinguishes MS lesions from asymptomatic white matter lesions. *Neurology*, **76**(6), 534–9.
191. Mainero C, Benner T, Radding A, et al. (2009). In vivo imaging of cortical pathology in multiple sclerosis using ultra-high field MRI. *Neurology*, **73**(12), 941–8.
192. Srinivasan R, Ratiney H, Hammond-Rosenbluth KE, et al. (2010). MR spectroscopic imaging of glutathione in the white and gray matter at 7 T with an application to multiple sclerosis. *Magnetic Resonance Imaging*, **28**(2), 163–70.
193. Wood ET, Ronen I, Techawiboonwong A, et al. (2012). Investigating axonal damage in multiple sclerosis by diffusion tensor spectroscopy. *Journal of Neuroscience*, **32**(19), 6665–9.
194. Barkhof F, Filippi M, Miller DH, et al. (1997). Strategies for optimizing MRI techniques aimed at monitoring disease activity in multiple sclerosis treatment trials. *Journal of Neurology*, **244**(2), 76–84.
195. Filippi M, Horsfield MA, Ader HJ, et al. (1998). Guidelines for using quantitative measures of brain magnetic resonance imaging abnormalities in monitoring the treatment of multiple sclerosis. *Annals of Neurology*, **43**(4), 499–506.
196. Goodin DS. (2006). Magnetic resonance imaging as a surrogate outcome measure of disability in multiple sclerosis: have we been overly harsh in our assessment? *Annals of Neurology*, **59**(4), 597–605.
197. Sormani MP, Bonzano L, Roccatagliata L, et al. (2009). Magnetic resonance imaging as a potential surrogate for relapses in multiple sclerosis: a meta-analytic approach. *Annals of Neurology*, **65**(3), 268–75.
198. Sormani MP, Bonzano L, Roccatagliata L, et al. (2010). Surrogate endpoints for EDSS worsening in multiple sclerosis. A meta-analytic approach. *Neurology*, **75**(4), 302–9.
199. Rudick RA, Lee JC, Simon J, et al. (2004). Defining interferon beta response status in multiple sclerosis patients. *Annals of Neurology*, **56**(4), 548–55.

200. Rio J, Rovira A, Tintore M, et al. (2008). Relationship between MRI lesion activity and response to IFN-beta in relapsing-remitting multiple sclerosis patients. *Multiple Sclerosis*, **14**(4), 479–84.
201. Rio J, Castillo J, Rovira A, et al. (2009). Measures in the first year of therapy predict the response to interferon beta in MS. *Multiple Sclerosis*, **15**(7), 848–53.
202. Tomassini V, Paolillo A, Russo P, et al. (2006). Predictors of long-term clinical response to interferon beta therapy in relapsing multiple sclerosis. *Journal of Neurology*, **253**(3), 287–93.
203. Freedman MS, Patry DG, Grand'Maison F, et al. (2004). Treatment optimization in multiple sclerosis. *Can Journal of* the Neurological Sciences, **31**(2), 157–68.
204. Rocca MA, Agosta F, Sormani MP, et al. (2008). A three-year, multi-parametric MRI study in patients at presentation with CIS. *Journal of Neurology*, **255**(5), 683–91.
205. Rovaris M, Judica E, Sastre-Garriga J, et al. (2008). Large-scale, multicentre, quantitative MRI study of brain and cord damage in primary progressive multiple sclerosis. *Multiple Sclerosis*, **14**(4), 455–64.
206. Narayana PA, Wolinsky JS, Rao SB, et al. (2004). Multicentre proton magnetic resonance spectroscopy imaging of primary progressive multiple sclerosis. *Multiple Sclerosis*, **10**(Suppl. 1), S73–8.
207. Sajja BR, Narayana PA, Wolinsky JS, et al. (2008). Longitudinal magnetic resonance spectroscopic imaging of primary progressive multiple sclerosis patients treated with glatiramer acetate: multicenter study. *Multiple Sclerosis*, **14**(1), 73–80.
208. Pagani E, Hirsch JG, Pouwels PJ, et al. (2010). Intercenter differences in diffusion tensor MRI acquisition. *Journal of Magnetic Resonance Imaging*, **31**(6), 1458–68.
209. Wegner C, Filippi M, Korteweg T, et al. (2008). Relating functional changes during hand movement to clinical parameters in patients with multiple sclerosis in a multi-centre fMRI study. *European Journal of Neurology*, **15**(2), 113–22.
210. Rocca MA, Absinta M, Valsasina P, et al. (2009). Abnormal connectivity of the sensorimotor network in patients with MS: a multicenter fMRI study. *Human Brain Mapping*, **30**(8), 2412–25.
211. Filippi M, Rocca MA, Moiola L, et al. (1999). MRI and magnetization transfer imaging changes in the brain and cervical cord of patients with Devic's neuromyelitis optica. *Neurology*, **53**(8), 1705–10.
212. Benedetti B, Valsasina P, Judica E, et al. (2006). Grading cervical cord damage in neuromyelitis optica and MS by diffusion tensor MRI. *Neurology*, **67**(1), 161–3.
213. Rocca MA, Agosta F, Mezzapesa DM, et al. (2004). A functional MRI study of movement-associated cortical changes in patients with Devic's neuromyelitis optica. *NeuroImage*, **21**(3), 1061–8.
214. Liu Y, Duan Y, He Y, et al. (2012). A tract-based diffusion study of cerebral white matter in neuromyelitis optica reveals widespread pathological alterations. *Multiple Sclerosis*, **18**(7), 1013–21.
215. Zhao DD, Zhou HY, Wu QZ, et al. (2012). Diffusion tensor imaging characterization of occult brain damage in relapsing neuromyelitis optica using 3.0T magnetic resonance imaging techniques. *NeuroImage*, **59**(4), 3173–7.
216. Yao DL, Webster HD, Hudson LD, et al. (1994). Concentric sclerosis (Balo): morphometric and in situ hybridization study of lesions in six patients. *Annals of Neurology*, **35**(1), 18–30.
217. Iannucci G, Mascalchi M, Salvi F, Filippi M. (2000). Vanishing Balo-like lesions in multiple sclerosis. *Journal of Neurology Neurosurgery & Psychiatry*, **69**(3), 399–400.
218. Ng SH, Ko SF, Cheung YC, et al. (1999). MRI features of Balo's concentric sclerosis. *British Journal of Radiology*, **72**(856), 400–3.
219. Karaarslan E, Altintas A, Senol U, et al. (2001). Balo's concentric sclerosis: clinical and radiologic features of five cases. *AJNR American Journal of Neuroradiology*, **22**(7), 1362–7.
220. Khiat A, Lesage J, and Boulanger Y. (2007). Quantitative MRS study of Balo's concentric sclerosis lesions. *Magnetic Resonance Imaging*, **25**(7), 1112–15.
221. Mowry EM, Woo JH, Ances BM. (2007). Balo's concentric sclerosis presenting as a stroke-like syndrome. *Nature Clinical Practice Neurology*, **3**(6), 349–54.
222. Poser CM, Goutieres F, Carpentier MA, et al. (1986). Schilder's myelinoclastic diffuse sclerosis. *Pediatrics*, **77**(1), 107–12.
223. Dale RC, de Sousa C, Chong WK, et al. (2000). Acute disseminated encephalomyelitis, multiphasic disseminated encephalomyelitis and multiple sclerosis in children. *Brain*, **123**(Pt 12), 2407–22.
224. Hynson JL, Kornberg AJ, Coleman LT, et al. (2001). Clinical and neuroradiologic features of acute disseminated encephalomyelitis in children. *Neurology*, **56**(10), 1308–12.
225. Tenembaum S, Chitnis T, Ness J, et al. (2007). Acute disseminated encephalomyelitis. *Neurology*, **68**(16 Suppl. 2), S23–36.
226. Banwell B, Shroff M, Ness JM, et al. (2007). MRI features of pediatric multiple sclerosis. *Neurology*, **68**(16 Suppl. 2), S46–53.
227. Baum PA, Barkovich AJ, Koch TK, et al. (1994). Deep gray matter involvement in children with acute disseminated encephalomyelitis. *AJNR American Journal of Neuroradiology*, **15**(7), 1275–83.
228. Verhey LH, Branson HM, Shroff MM, et al. (2011). MRI parameters for prediction of multiple sclerosis diagnosis in children with acute CNS demyelination: a prospective national cohort study. *Lancet Neurology*, **10**(12), 1065–73.
229. Inglese M, Salvi F, Iannucci G, et al. (2002). Magnetization transfer and diffusion tensor MR imaging of acute disseminated encephalomyelitis. *AJNR American Journal of Neuroradiology*, **23**(2), 267–72.
230. Holtmannspotter M, Inglese M, Rovaris M, et al. (2003). A diffusion tensor MRI study of basal ganglia from patients with ADEM. *Journal of the Neurological Sciences*, **206**(1), 27–30.
231. Bizzi A, Ulug AM, Crawford TO, et al. (2001). Quantitative proton MR spectroscopic imaging in acute disseminated encephalomyelitis. *AJNR American Journal of Neuroradiology*, **22**(6), 1125–30.
232. Balasubramanya KS, Kovoor JM, Jayakumar PN, et al. (2007). Diffusion-weighted imaging and proton MR spectroscopy in the characterization of acute disseminated encephalomyelitis. *Neuroradiology*, **49**(2), 177–83.

CHAPTER 16

Stroke

Franz Fazekas, Stefan Ropele, and Christian Enzinger

Introduction

Until present, many radiologists still consider the exclusion of haemorrhage in the acute phase of stroke with computed tomography (CT) as a main aim of neuroimaging in cerebrovascular diseases (CVD) [1]. In fact, this is a very important goal, given the proven therapeutic efficacy of IV thrombolysis just within a short time window of currently 4.5 hours [2]. The often devastating effects of stroke also justify concentrating all efforts on an optimal use of the ever increasing armamentarium of neuroimaging techniques to better understand and define the mechanisms predicting acute stroke outcome and to guide therapeutic interventions [3–7)]. Thus, neuroimaging is expected to help in selecting those patients who may profit from vessel reopening even with extended time periods following acute stroke and to answer questions such as how to best manage patients with unclear stroke onset or those awakening with a focal deficit, or what treatment strategies to offer patients with large vessel occlusion. Over these burning questions and exciting possibilities, including the hope of generating surrogate markers for treatment trials, the many contributions of neuroimaging, especially of magnetic resonance imaging (MRI) to the diagnosis of cerebrovascular diseases in general, are sometimes neglected. This appears unfortunate as the need to perform MRI in patients with suspected CVD is easily dismissed when concentrating just on acute stroke and thrombolysis, where CT still plays an important and undisputed role. The overall higher sensitivity and specificity of MRI for vascular brain changes, however, not only improves and facilitates differential diagnosis, but even contributes to conceptual changes. Based on the high sensitivity of diffusion-weighted imaging (DWI) MRI for acute ischaemic lesions, it has been proposed that an advance toward a tissue-based definition of transient ischaemic attacks (TIA) is appropriate, i.e. to consider patients with evidence of an acute ischaemic lesion as having suffered from stroke, irrespective of the duration of symptoms [8]. MRI has also helped to better elucidate the obviously quite wide range of covert vascular damage as reflected by old silent infarcts, extensive areas of white matter hyperintensity and old microbleeds (MBs) [9]. These changes may go clinically undetected as they are not associated with acute focal symptoms, but bear a relationship to physical disability, cognitive impairment, and balance disorders [10]. Given all these developments and aspects, including haemorrhagic stroke, any discussion of neuroimaging in stroke and CVD can hardly be comprehensive. In recognition of this limitation, this contribution attempts to focus primarily on clinical relevance by:

1. Providing information on the imaging characteristics of the various abnormalities caused by CVD in relation to the tools for their detection, which is especially important for diagnostic purposes.
2. Discussing the use of the different imaging modalities in specific settings of ischaemic CVD, which addresses primarily management aspects.

Ischaemic cerebrovascular disease

Morphologic findings following acute focal ischaemic damage (ischaemic infarction)

While imaging of cerebral ischaemic infarction is regularly described in radiologic and neurologic textbooks, exact definitions of what is an infarction are actually lacking. A main reason for this are the different grades of sensitivity and a limited specificity with which neuroimaging tools can parallel histopathologic findings, although even textbooks of neuropathology contain divergent and imprecise tissue definitions of cerebral infarction [11]. Furthermore, focal acute ischaemia can have diverse aetiologies with the fate of affected tissue depending on highly variable and multifactorial processes. It needs to be considered that these aspects are partly lost in didactic descriptions of imaging findings, but strongly contribute to the actual diversity and dynamics of observations in the individual patient.

CT

With large areas of focal ischaemic damage, CT changes follow a well-recognized temporal pattern (Table 16.1).

Commonly, three main stages have been described—an initial (acute) stage, a developmental (subacute) stage, and a late or sequellar stage [12]. Historically, the initial stage was considered to be the first 24 hours after the acute event with a usually normal or near normal CT. Thus, the main purpose of obtaining a CT scan at that time was primarily to exclude cerebral haemorrhage. The 'developmental stage', which spans the period of the following day up to 4–5 weeks, shows the fundamental characteristics of ischaemic infarction, including tissue hypodensity, mass effect, and contrast enhancement, which develop to different grades depending on several factors, such as size, location, and vascular supply of the area of ischaemic tissue damage (Fig. 16.1).

In the second and third week, areas of infarction may revert back to 'false normal' density. This phenomenon of 'fogging' has been attributed to the resolution of oedema, small petechial haemorrhages, and infiltration of the infarcted tissue with macrophages, and can mask the actual extent of ischaemic damage. In the late or sequellar stage, i.e. approximately after the fourth to sixth week following infarction, an area of definite hypodensity or a cystic cavity remains, which is often associated with signs of focal atrophy, i.e. a widening of local cerebrospinal fluid (CSF) spaces (Fig. 16.1). The late stage of infarction has been also termed chronic, but it appears

Table 16.1 CT characteristics of acute ischaemic lesions and their evolution

Stages	Morphologic changes	Time
Initial (acute)	Vague blurring of gray–white matter boundaries, slight attenuation of the insular ribbon, slight indistinctness of basal ganglia gray matter, suggestion of crowding sulci (subtle mass effect), 'dense artery' sign Changes become increasingly distinct	First hours ↓
Developmental (subacute)	Distinctly hypodense area within territory of vascular supply Focal swelling/mass effect (sulcal and/or ventricular effacement) Contrast enhancement (especially of gray matter structures) 'Fogging' (area of ischaemia becomes poorly recognizable—rare)	>Day 1 to 2–4 weeks ↓ 2–3 weeks
Late (old infarct)	Demarcated area of pronounced hypodensity (close to CSF), cystic cavity focal atrophy	4–6 weeks ↓

preferable to talk of old infarcts, as this residual deficit constitutes a final stage, rather than a chronic process.

With the therapeutic option of IV thrombolysis, attention in CT interpretation has shifted strongly to the initial stage of infarction and subtle morphologic changes that may indicate an acute ischaemic infarct quite early on [13,14]. These changes mainly consist of a blurring of anatomic borders, such as of the gray/white matter interface with slight sulcal effacement and may appear already within the first 3 hours after stroke. Corresponding vessel abnormalities on CT angiography are often helpful. (Fig. 16.2a, b, Table 16.1).

However, these subtle alterations in tissue density are seen predominantly with larger infarcts and cannot fully compensate for the undisputedly lower sensitivity of CT for ischaemic tissue changes when compared with MRI [1]. Such increased sensitivity is especially desirable for patients with minor symptoms and when there are diagnostic challenges.

Magnetic resonance imaging (MRI)

MRI findings of infarction also vary with time (Table 16.2).

Similar to CT, volume changes accompany the evolution of infarction, at least if sufficiently large, which consist of swelling in the acute phase and of volume loss/focal atrophy after brain tissue has undergone necrosis. These changes may be seen directly involving large portions of the brain, but can also be restricted to only small areas or compartments such as the cortical ribbon. Mass effect and atrophy can be appreciated from changes in the widths of the cortical sulci or the ventricles. Signal changes on conventional MRI *per se*, like CT hypodensity, are not very specific. Thus, the shape and location of signal abnormalities are important aspects. As for many types of pathology, ischaemic lesions appear hyperintense on proton density (PD) and T_2-weighted sequences (Fig. 16.3).

Heavily T_2-weighted sequences are most sensitive and focal increases in signal intensity may occur as early as 90 minutes after symptom onset, but usually become apparent only within 2–3 hours. An obvious disadvantage of T_2-weighted MRI is the overlap in signal intensity of the acute lesion with that of CSF spaces, which also appear bright on this sequence. For this reason the introduction of fluid-attenuated inversion recovery (FLAIR) sequences has been an important step forward, as it allows cancelling of the signal from CSF and thus increases the conspicuity of ischaemic lesions particularly at the brain-CSF interfaces (Fig. 16.3). This

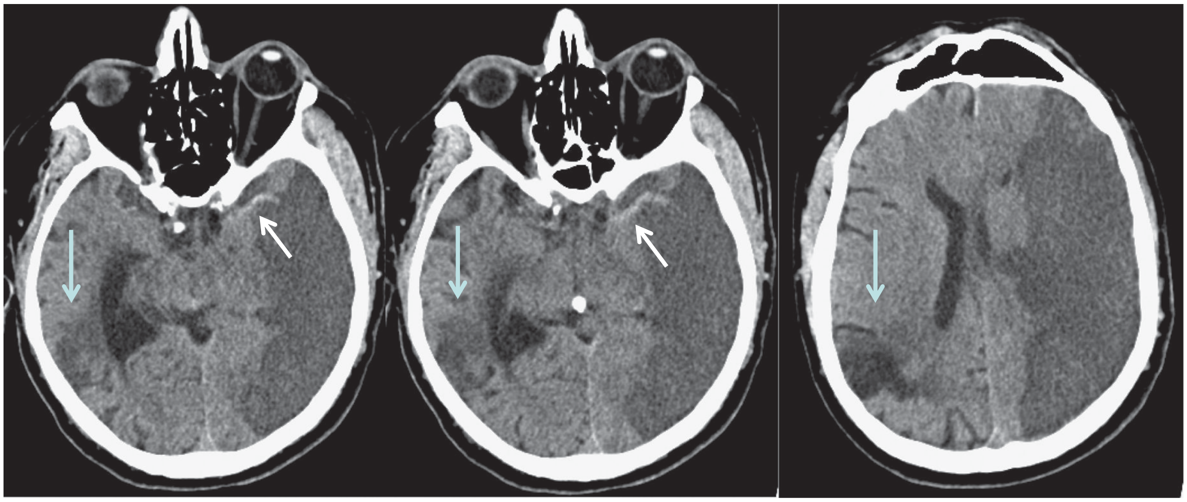

Fig. 16.1 A 72-year-old patient 40 hours after complete middle cerebral artery infarction and unsuccessful IV thrombolysis. The entire left middle cerebral artery territory is demarcated and appears hypodense. There is still evidence for a thrombus in the M1 segment of the left middle cerebral artery (white arrows) and a defect from a previous, old infarction is seen on the right (light blue arrows).

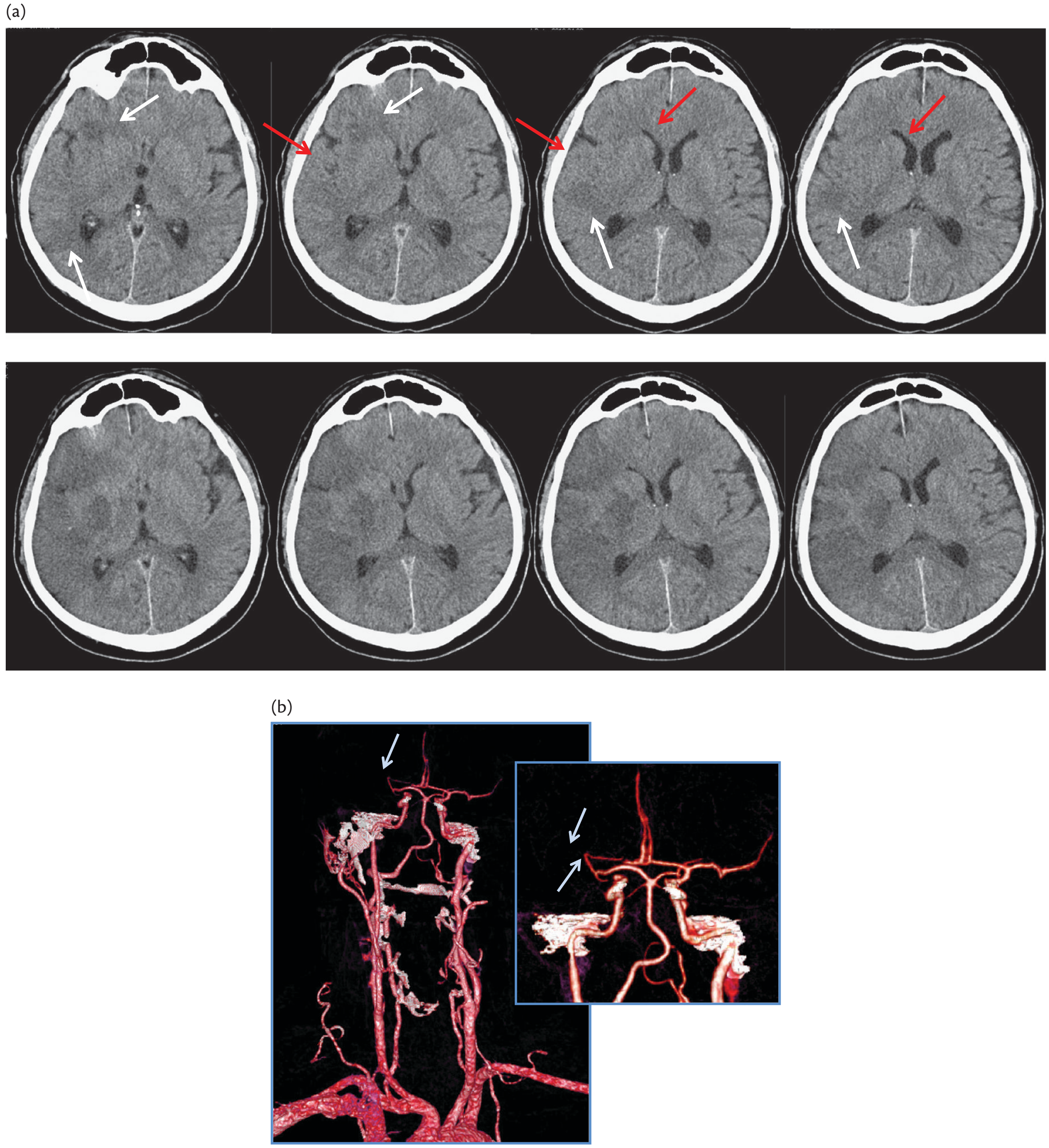

Fig. 16.2 (a) CT scan of a 56-year-old patient 6.5 hours after stuttering onset of left hemiparesis. (Upper panel) Different grades of early ischaemic changes, including some more pronounced areas of hypodensity in the frontal and temporoparietal white matter and adjacent cortex (white arrows), a blurring of the cortical white–gray matter interface when compared with the contralateral side, and slight effacement of the cortical sulci and narrowing of the right lateral ventricle as signs of early swelling (red arrows). (Lower panel) Follow-up CT 27 hours after stroke. Several areas of hypodensity are now seen in the vascular territory of the middle cerebral artery. (b) Acute CTA of extra- and intracerebral arteries shows mainstem occlusion of the middle cerebral artery (light blue arrows in original and magnified views). The combination of these CT and CTA findings suggests partial collateralization via the external carotid artery.

has also decreased the importance of PD-weighted imaging, which was intended to serve the same purpose, but with a lower sensitivity for displaying acute ischaemic lesions because of lower T_2-weighting. On T_1-weighted images most acute infarcts are first barely seen or not seen at all. With time, the ischaemic lesion becomes increasingly hypointense until it reaches iso-intensity with CSF, if complete necrosis occurs and a cystic defect remains. Table 16.2 summarizes the characteristics of lesion evolution on conventional MRI.

While conventional MRI already excelled in terms of sensitivity for tissue changes over CT, a decisive further step forward was made with the introduction of DWI [15,16]. This technique is sensitive to the motion of water protons, which differ between tissues/compartments and starts to change almost immediately after the onset of ischaemia due to the development of intracellular oedema. The shift in water from the extracellular to the intracellular compartment(s) obviously causes a reduction in the diffusivity of the water protons, which can be appreciated on a map of the

Table 16.2 MRI characteristics of acute ischaemic lesions and their evolution

Stage	Signal changes	Time
Internal (acute)	DWI hyperintensity (reduced ADC) T_2 hyperintensity (T_2-weighted sequences, FLAIR), often early on vague and indistinct No or minimal T_1 hypointensity subtle mass effect Absence of 'low void', 'vessel signs'	45–90 minutes 60 minutes to first hours
Developmental (subacute)	Bright lesion on DWI (reduced ADC), 'light bulb' Well-defined area of T_2 hyperintensity (T_2-weighted sequences, FLAIR) T_1 hypointensity Mass effect (sulcal and /or ventricular effacement) Gyriform contrast enhancement	>Day 1 to 2–4 weeks > 3–7 days
Late (old infarct)	Demarcated lesion with central iso-intensity to CSF on all sequences, i.e. cystic cavity Focal atrophy	4–6 weeks ↓

apparent diffusion coefficient (ADC). On DWI, this translates into high signal intensity of the ischaemic tissue against a background of medium to low signal intensity, which makes it light up ('light bulb phenomenon'). Thus, DWI abnormalities are the first morphologic evidence for ischaemic damage to appear and are easily detected (Fig. 16.3). As the reduction of diffusivity is also rather specific for ischaemic damage, this also helps in differential diagnosis and to identify acute lesions among pre-existing morphologic abnormalities both in the very acute setting, as well as over the first few days (Fig. 16.4 and 16.5) [17].

In rare cases and most likely due to successful reperfusion of incomplete ischaemic damage, the DWI lesion may revert to normal within hours. Otherwise, it takes 3–10 days—and sometimes even longer—before the ADC reverts back to a stage of pseudonormalization and subsequently increases up to a level of the CSF, as a consequence of tissue degradation (Fig. 16.5) [18,19].

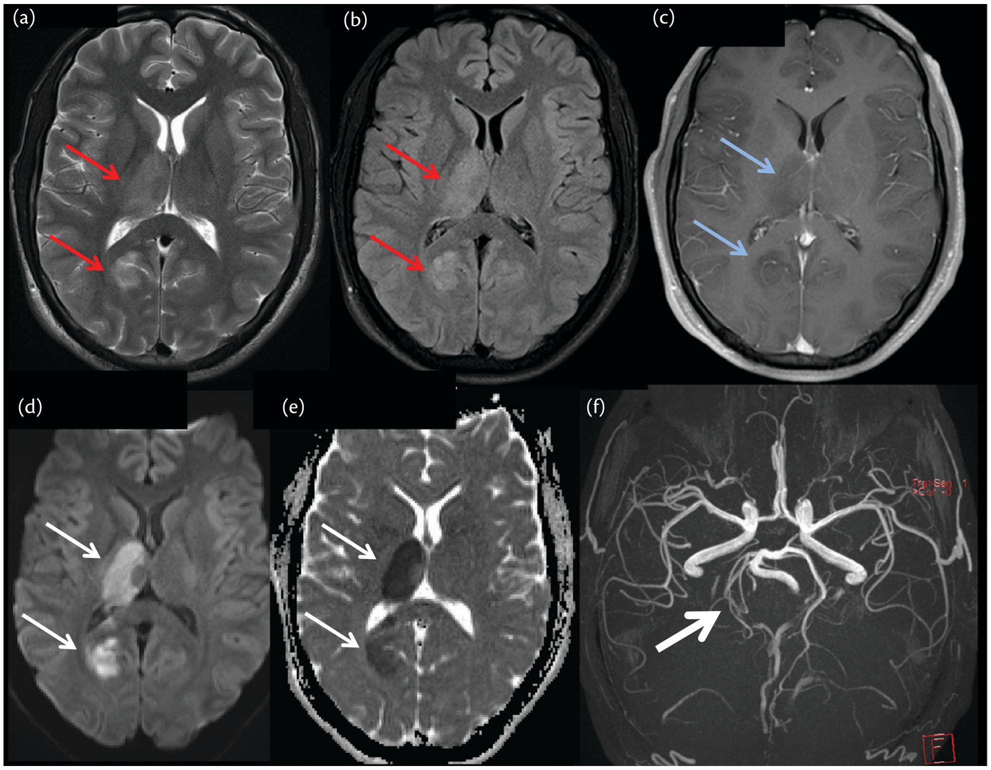

Fig. 16.3 MRI scan 12 hours after stroke onset with partial posterior cerebral artery infarction involving the thalamus and parts of the mesial occipital cortex. Hyperintense signal on the T_2-weighted (a) and fluid-attenuated inversion recovery (b) sequences (red arrows). Slight hypointensity on contrast-enhanced T_1 (light blue arrows) (c). 'Light bulb' phenomenon on the diffusion-weighted (DWI) image (d) due to the reduction in diffusivity as evidenced by the apparent diffusion coefficient (ADC) map (e) (white arrows). Intracranial time-of flight angiography shows occlusion of some branches of the right posterior cerebral artery (white arrow) (f).

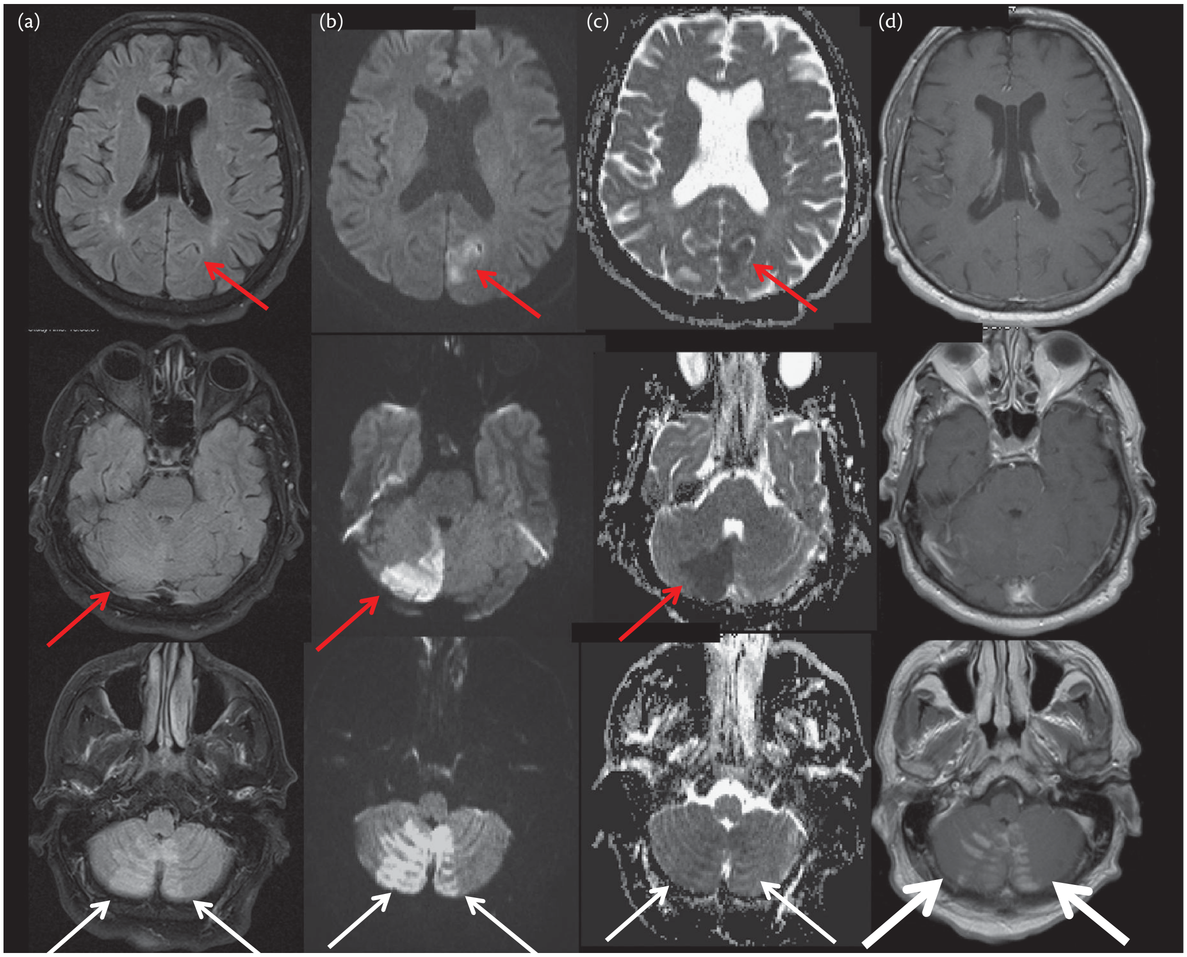

Fig. 16.4 Acute (red arrows) and subacute (white arrows) infarcts in a patient who suffered from sudden onset of vertigo and unsteady gait for 1 week before he presented with hemiataxia and visual disturbance. (a) Fluid-attenuated inversion recovery. (b) Diffusion-weighted image. (c) Apparent diffusion coefficient map. (d) Contrast-enhanced T_1. Multiple infarcts are seen in the posterior circulation. Note the lower ADC and contrast enhancement of the subacute infarcts in the posterior inferior cerebellar artery territory displayed in the lower panel (white arrows) compared with the acute infarcts (red arrows) displayed above.

It is of note that the development of signal changes from acute ischaemia, including DWI may take longer in infra—than supratentorial brain structures and especially in the brainstem. Thus, acute brainstem infarcts can remain invisible on MRI for several hours after the acute event [20]. Higher *b*-values and thin sagittal sections may help to overcome this problem. Otherwise a follow-up MRI should be considered. Further evolution of ADC changes appears also delayed, which is probably a consequence of the structural properties of the brainstem [21].

Patterns of ischaemic changes and aetiology

Acute ischaemic lesions may vary in number, size, and location in the brain partly depending on distinct territories of vascular supply [22]. Co-existing vascular damage may be evidenced by old infarcts, white matter hyperintensities (WMHs), MBs and probably atrophy (Fig. 16.6).

While this causes individual patients to usually differ quite profoundly in their imaging findings when presenting with an acute neurologic deficit, they still may share certain patterns that suggest a specific underlying aetiology. Thus, multiple acute ischaemic lesions throughout the brain are very suggestive of a cardioembolic mechanism. There is also quite good evidence that small subcortical infarcts (earlier termed lacunar infarcts in expectation of a lacune to develop) in association with old lesions of the same type, extensive WMHs, and MBs are indicative of small vessel disease [9]. Multiple, unilateral deep border zone infarcts of often different age have been closely linked to artery-to-artery embolism from an ulcerated or high-grade carotid stenosis [23]. In general, however, aetiological assumptions just on the basis of brain imaging findings are dangerous and do not obviate a complete work-up [24,25]. With this caveat, brain imaging findings certainly offer important clues to the actual cause of acute ischaemia, and are successfully used as elements of more novel classification schemes of ischaemic stroke [26,27].

Slowly-evolving ischaemic lesions

Neuroimaging has also allowed the recognition of more subtle tissue changes, originating from vascular damage especially in the context of small vessel disease, which appear to primarily affect the white matter. These abnormalities can be clinically inapparent and thus often constitute an incidental finding. When more extensive, however, they are frequently associated with general cerebral

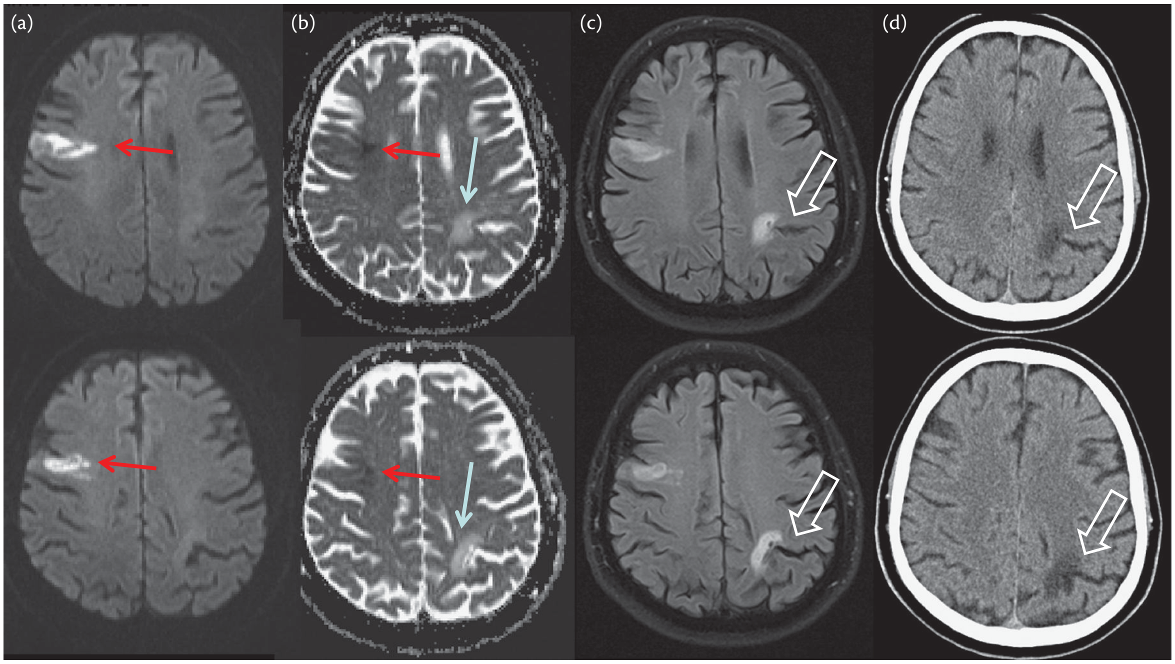

Fig. 16.5 Acute and old infarcts. The diffusion-weighted image (a) shows the acute infarct as a bright lesion with reduced diffusivity (dark) on the apparent diffusion coefficient (ADC) map (red arrows) (b). The old infarct appears bright on the ADC due to freely diffusable water within the area of parenchymal necrosis (light blue arrows), but is not seen on the diffusion-weighted image. Both infarcts appear bright on the fluid-attenuated inversion recovery image (c) with the area of the old infarct appearing slightly atrophic (open arrows). Acute CT shows only the old infarction (open white arrows) (d).

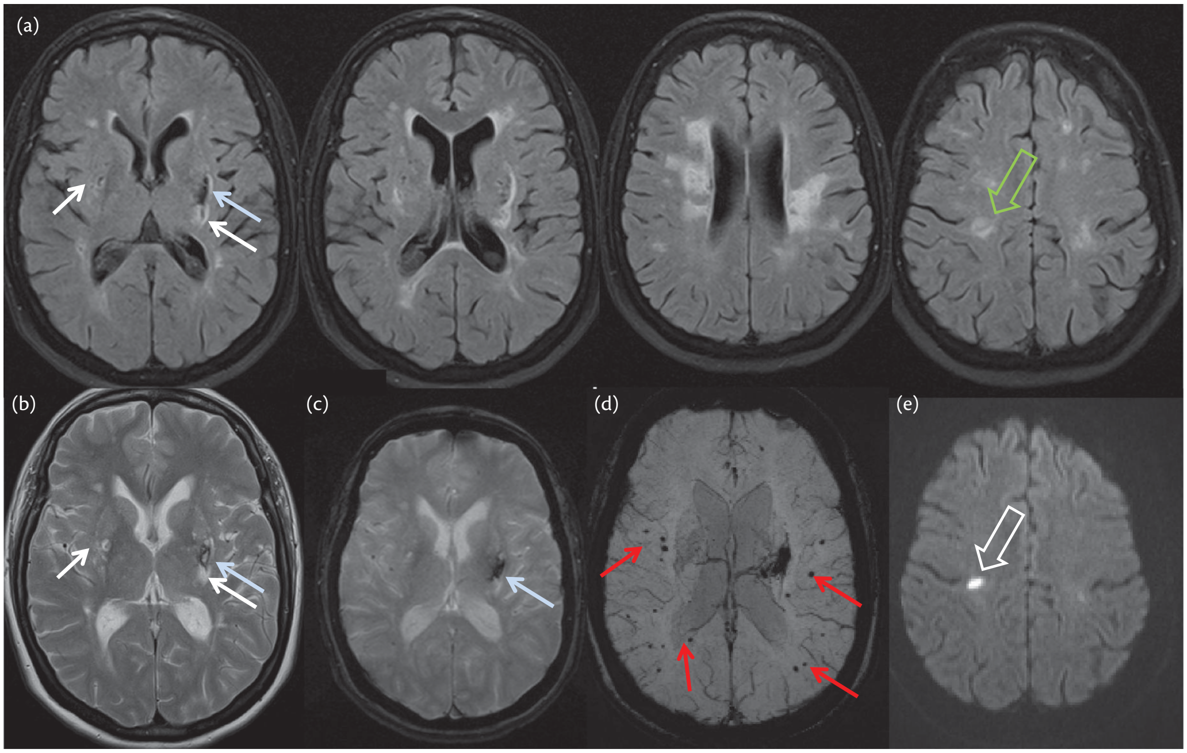

Fig. 16.6 A 49-year-old patient with acute left arm paresis and signs of widespread small vessel disease. (a) FLAIR shows signal abnormalities in the basal ganglia and patchy, partly confluent white matter hyperintensities in the centrum semiovale especially on the right. (b) The T_2-weighted image identifies the basal ganglia lesions as lacunes (white arrows). Haemosiderin deposition at the periphery of a defect in the left putamen suggests the remnants of an old haematoma (light blue arrow). (c) This is supported by corresponding findings on T_2*-gradient echo. (d) Susceptibility-weighted imaging suggests the additional presence of many old microbleeds (red arrows). (e) The diffusion-weighted image shows the acute subcortical small infarct in the right hemisphere, which is responsible for the patients symptoms (open white arrow). This infarct would have been missed as acute lesion when just using FLAIR (open green arrow in a)

dysfunction affecting cognition, gait, and to some extent also mood and bladder control [10,28].

On CT these abnormalities are characterized by a subtle decrease of X-ray attenuation. Resulting areas of mild to moderate hypodensity are characteristically ill-defined, and tend to be symmetrically distributed throughout the brain with a preference for the periventricular and deep white matter, but sparing the subcortical U-fibres. Pathologically, such areas are characterized primarily by loss of myelin and axons [29]. More extensive tissue destruction of the white matter has been equated with 'incomplete infarction' by some [30]. The corresponding rarefaction of tissue also led to the creation of the term leuko-araiosis, a term that is derived from the Greek words *'leuko-'* for 'white' and *'araios'* for 'rarefied' [31]. More recently, suggested terms for CT visible (presumably) vascular white matter changes remain more descriptive, such as 'white matter hypo-attenuation' or 'white matter hypodensities' in order to parallel MRI terminology [9].

White matter abnormalities of presumed vascular origin appear bright on T_2-weighted MRI and are therefore commonly called WMHs [32]. Unfortunately, T_2-signal hyperintensity is associated with many types of tissue damage and, thus, is an insufficient feature for a distinct aetiological classification. It is, rather, a combination of signal characteristics and the pattern of lesion distribution, which defines the MRI appearance of WMHs of presumed vascular origin. Defined as areas of only subtle tissue damage—in contrast to frank infarction or other types of complete destruction of brain parenchyma—their signal intensity is different from CSF on all sequences, i.e. they are bright on PD-weighted and FLAIR images, which ideally show CSF as low in signal intensity. On T_1-weighted images, WMHs of presumed vascular origin are not seen, or only faintly, unless one employs heavy T_1-weighting, such as by using an inversion recovery sequence. As described for CT, these white matter abnormalities occur preferentially in the deep white matter and close to the lateral ventricles, but spare the subcortical arcuate fibres. Their size is variable and in the deep white matter ranges from punctate over patchy to large confluent lesions [33]. Lesion borders are mostly indistinct and irregular. Signal abnormalities related to small vessel disease can also be seen in the brainstem and have been suggested to indicate severe microangiopathy [34]. Like supratentorial WMHs, they appear rather ill-defined, mostly involve the central portions of the brainstem and should not be associated with visible tissue destruction on T_1-weighted images. There also exist WMHs directly abutting the lateral ventricles, but their association with small vessel disease is less clear [35,36].

Vessels

Imaging of cerebral vessels adds another piece of information, which is increasingly important for patient management. Occlusion of a major cerebral artery by a thrombus can often be detected already on plain CT as increased density of portions of a vessel (Fig. 16.1). This 'dense artery sign' can be the first abnormality suggestive of ischaemic infarction and has been reported in 35–67% of patients with a major stroke, which disappears after recanalization [37]. Unfortunately, it is not always easy to separate this sign from increased attenuation of a vessel due to calcification of the vessel walls or in patients with a high haematocrit. Usually, vessel hyperdensity is then more symmetric.

Occlusion of a large vessel is also easily seen on plain MRI by a loss of flow void, i.e. signal within the blood vessel instead of no signal due to outflowing blood. This loss of flow void is only reliably interpretable with the imaging plain perpendicular to the vessel and thus mostly relevant for a first rapid evaluation of the intracranial carotid arteries. Thrombi directly in the cerebral arteries are more readily detected by susceptibility-weighted imaging, and are then characterized by an area of signal loss extending beyond the presumed vessel diameter. It has been suggested that such findings are more likely seen with cardioembolic stroke, where desaturation from oxyhaemoglobin to deoxyhaemoglobin has already occurred [38]. To what extent this might actually predict response to IV thrombolysis is still controversial [39,40]. With careful interpretation of acute stroke images, a hyperintense appearance of vessels on FLAIR images distal to the occlusion is also often noted and has to be considered another early and indirect sign of ischaemia. It is most conspicuous in the Sylvian fissure and cortical sulci, and probably indicates sluggish flow from collateral, possibly retrograde, circulation. In a recent large series, hyperintense vessels were seen in almost half of stroke patients within 12 hours of symptom onset, especially in those with proximal vessel occlusion (80%) [41].

The visualization of vessels and some of their pathologic changes on plain MRI cannot substitute for the results of direct non-invasive imaging of extra- and intracranial vessels with CT-angiography (CTA) and MR-angiography (MRA), which are increasingly used in the initial diagnostic work-up of patients with acute stroke. For the sake of space, the technical advances and possibilities of these techniques are not outlined here, but the reader is directed to recent reviews [1,7,42]. Their current contribution to the management of acute stroke patients will be discussed later in this chapter, together with a note on MR perfusion.

Haemorrhagic CVD

CT of intracranial and subarachnoid haemorrhage

Detection of acute intracranial bleeding is a mainstay of CT (Table 16.3).

As blood has a slightly higher density than brain primarily because of proteins, i.e. haemoglobin, intracerebral bleedings are seen almost immediately and density rapidly increases further with clotting (Fig. 16.7) [43].

Lower density haematomas are to be expected in patients who are severely anaemic and this may complicate haematoma detection. Differences in the extent of clotting are also associated with differences in density and may cause an inhomogenous haematoma appearance such as in patients with protracted bleeding or

Table 16.3 CT characteristics of intracerebral haemorrhage

Stage	Morphologic changes	Time
Acute	Hyperdense (~80 HU) Density may be less with anemia or coagulopathy Mass effect Perifocal oedema	Within minutes Within hours
Subacute	Isodense with brain	>10 days
Chronic (old ICH)	Cystic lesions with density similar to CSF	Several weeks ↓

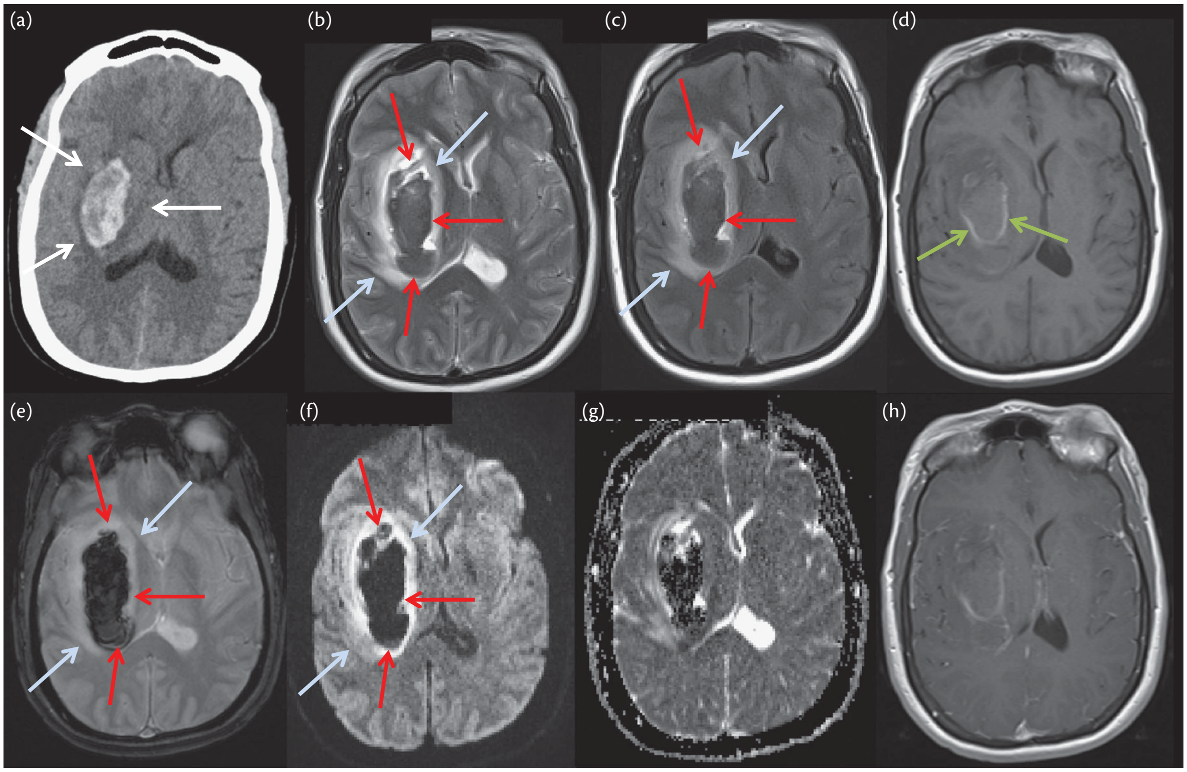

Fig. 16.7 Acute intracerebral haemorrhage in the right basal ganglia on CT (white arrows) (a). MRI follow-up 3 days later with slight extension of the haematoma (red arrows) and some perifocal oedema (light blue arrows) Note the different signal intensities on T_2 (b), fluid-attenuated inversion recovery (c), T_1, slight hyperintense rim due to methaemoglobin (green arrows) (d), T_2*-gradient echo (e), diffusion-weighted (f), apparent diffusion coefficient map (g), contrast-enhanced T_1 (h).

coagulation disorders. After several days the clot begins to lyse and the proteins are enzymatically degraded. This and the concomitant osmotic influx of water lowers attenuation in a centripetal fashion. Haematomas thus become isodense with the brain in 1–2 weeks. Following further degradation and resorption, ultimately an area of cystic encephalomalacia remains, which may be difficult to recognize as a residue of bleeding without prior knowledge or because of a suggestive shape of the defect. Thus, a slit-like cavity typically tends to remain after bleeding into the basal ganglia due to the specific and dense craniocaudal orientation of fibre tracts in this region.

Non-contrast head CT is also the cornerstone of the diagnosis of subarachnoid haemorrhage (SAH) (Fig. 16.8) [44].

Its sensitivity in the first 3 days is close to 100%, but decreases during the following days due to lysis and degradation of the extravasated blood. After 5–7 days, the rate of a false negative CT increases sharply. Therefore, lumbar puncture always should follow a negative CT in case of clinically suspected SAH [44].

MRI of intracranial and subarachnoid haemorrhage

In contrast to CT, the appearance of intracerebral blood on MRI is rather complex and variable because of the specific paramagnetic properties of the different breakdown products of haemoglobin. In this context, the state of oxidation of iron has a profound effect and causes signal intensities of a haematoma early on to change quite rapidly [43]. Besides the interval from the acute event, haematoma appearance largely depends on the respective pulse sequences employed and the magnetic field strength. Table 16.4 gives a schematic overview of the signal intensities to be expected with different pulse sequences in the various phases of an intracerebral haematoma, which is also illustrated in Fig. 16.7.

For some time, concerns existed regarding the sensitivity and specificity of MRI for haematoma detection in the peracute setting of stroke. The introduction of T_2*-weighted gradient-echo images and subsequently of DWI put an end to this debate. Acute bleeding appears hypointense at least at the periphery of the haematoma on both sequences, which is clearly different from an acute ischaemic lesion. Thus, acute bleeds often have mixed signal intensity on both sequences with a target-like appearance [45]. Using these sequences, a similar sensitivity and specificity for the detection of intracerebral bleeding was also confirmed in a large head-to-head comparison [46].

Completely new insights have come from the ability of MRI to detect residues of intracranial bleeds, which have occurred in the parenchyma or the subarachnoid spaces because of deposited haemosiderin. The paramagnetic effects of haemosiderin cause a loss of signal on T_2-weighted images, which allows lasting identification of defects from prior intracerebral bleeds by their hypointense rim [43]. Susceptibility sensitive sequences, such as T_2*-weighted gradient-echo images, are yet more sensitive and can detect even very small amounts of haemosiderin deposition by a kind of 'blooming' artefact. This has led to the recognition of the so called MBs, which are a consequence of minimal blood leakage through small vessels [47]. Several lines of evidence indicate their association, especially with hypertensive microangiopathy or cerebral amyloid angiopathy, but also hereditary angiopathies,

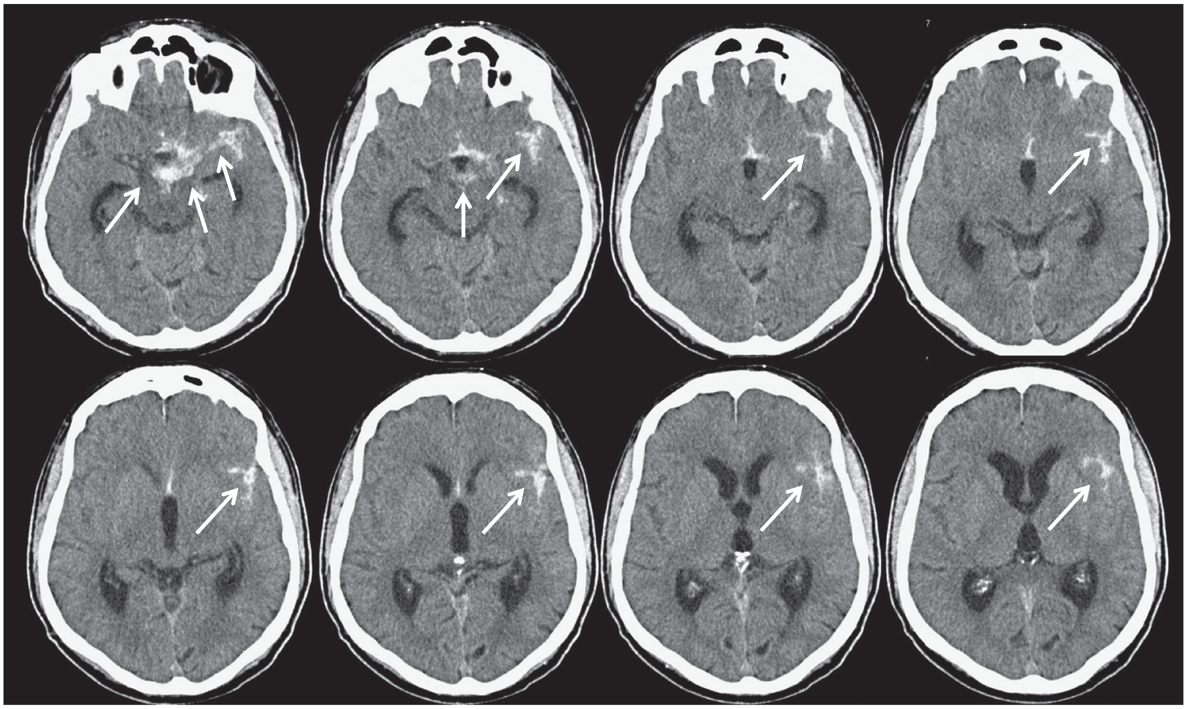

Fig. 16.8 Acute CT scan showing subarachnoid haemorrhage in basal cisterns and left Sylvian fissure (arrows).

Table 16.4 MRI characteristics of intracerebral haemorrhage

Stage	Signal intensity			Other characteristics
	T_1	T_2	T_2*	
Hyperacute (minutes to hours)		↑	Periphery ↓↓ Centre ↑	
Acute (hours to several days)	↓	↓	↓	Surrounding high signal of oedema on T_2
Subacute (several days to weeks)	↑↑↑	Early ↓ then ↑↑	↓↓	Change of signal intensities starts at periphery of haematoma
Chronic (old ICH) (> several weeks)	↓	Periphery ↓ central ↑↑	Periphery ↓↓↓ Central ↑	Focal atrophy/ cystic cavity

such as 'cerebral autosomal dominant arteriopathy with subcortical infarcts and leukoencephalopathy' (CADASIL) and they are now an accepted hallmark finding of cerebral small vessel diseases [9,48]. Recent experience shows that susceptibility-weighted imaging is even more sensitive and reliable for the detection of MBs (Fig. 16.6) [49]. While especially propagated for being used in ischaemic CVD, which also appears to associate with intracerebral bleeds more often than previously expected [50], MRI can add a wealth of additional information in patients with intracerebral bleeds. In support of practical experience a small systematic series has also shown that the additional insights provided by MRI can influence both diagnosis and management of patients with intracerebral haemorrhage to a significant extent [51].

Some investigators have claimed that specific MRI sequences, such as FLAIR, are as sensitive as CT in detecting subarachnoid blood. In fact, MRI is often still positive when CT has already normalized. From practical experience, however, MRI is certainly inferior to CT for diagnosing SAH, as several mechanisms may lead to signal increases intrasulcally and in other subarachnoid spaces, including artefacts, especially in the posterior fossa. T_2*-weighted gradient-echo images can also serve to visualize acute subarachnoid or intraventricular blood, but are much less reliable than CT in substantiating SAH (Fig. 16.9).

The contribution of MRI comes from outlining remnants of SAH in the meninges, i.e. from the detection of haemosiderin deposits together with concomitant morphologic findings. This first became evident by the possibility for in vivo diagnosis of the rare condition of meningeal haemosiderosis. More recently, this has helped to shed light on the clinical manifestations of convexal SAH and its causes, including a probable association with cerebral amyloid angiopathy in elderly patients [52].

Neuroimaging in the management of stroke and other cerebrovascular diseases

As outlined previously, and in other chapters of this book, available tools and technologies provides a range of potentially informative insights, but also have specific limitations and requirements, such as the time needed for an examination and its interpretation, the degree of invasiveness of a procedure, the need for contrast

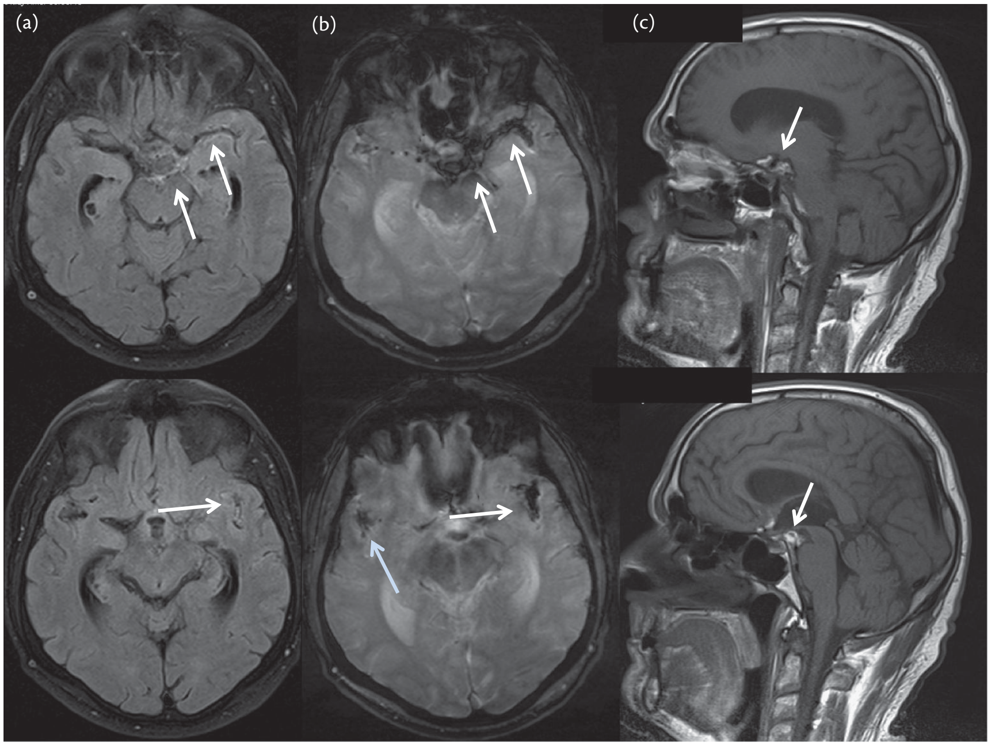

Fig. 16.9 MRI 4 days after subarachnoid haemorrhage of same patient as in Figure 16.7. (a) There is some signal abnormality in the basal cisterns and left Sylvian fissure on fluid-attenuated inversion recovery (white arrows), but it is less conspicuous than on CT. (b) The abnormality is more pronounced on T_2*-gradient echo images that now also show some blood in the right Sylvian fissure (light blue arrow). (c) T_1-weighted images show a hyperintense signal in the basal cisterns due to methaemoglobin (white arrows).

material, etc. The use of imaging tools needs to be tailored according to the maximum benefit and least burden/cost for patients [53]. With this goal, algorithms of how to employ available techniques must be strongly driven by the actual impact of imaging findings on patient management and therapy. For illustrative purpose some scenarios and situations of specific clinical relevance are discussed.

Systemic thrombolysis within the approved window of efficacy

In patients who present with a stroke that is potentially amenable to systemic thrombolysis within 4.5 hours [54,55], major emphasis has to be put on the exclusion of a bleeding condition, such as an intracerebral or subarachnoid haemorrhage. This can be reliably achieved with cranial CT. The rather low sensitivity of CT for displaying evidence of acute focal ischaemia is usually not critical for such a decision. As outlined previously, MRI is as sensitive and specific for the detection of intracerebral haemorrhage as CT when using appropriate sequences, including gradient-echo T_2*-weighted and diffusion weighted imaging [46]. For the detection of SAH, MRI still may not be as sensitive as CT. In most instances, however, SAH will be already suspected on clinical grounds and, in the absence of focal symptoms, will lead to the use of CT as the preferred imaging technique. As a consequence, American Heart Association/American Stroke Association (AHA/ASA) guidelines on the management of acute ischaemic stroke indicate that CT or MRI can be used for brain imaging and conclude that, in most cases, CT findings suffice for adequate patient management [56]. The increased sensitivity of MRI for most morphologic changes makes it the preferred imaging technique if this does not cause any delay in the time to thrombolysis [57]. MRI should also be considered in patients with uncertain clinical findings.

These recommendations are well supported for the 3-hour time window. Large stroke centres have pooled their data to compare their experience with systemic thrombolysis based on CT or MRI within the 3-hour time window. No major differences in patient outcome were seen, although a trend towards a lower rate of haemorrhages following MRI-based thrombolysis has been suggested by some [58,59]. However, the possibility that a certain selection bias regarding patients who are shifted to acute MRI examinations may have impacted on these results cannot be excluded. Also, there is no complete agreement if patients with a certain extent of visible ischaemic brain damage should be excluded from systemic thrombolysis within the 3-hour time window. The AHA/ASA guidelines do not foresee the need to withhold thrombolysis based on presumed infarct size [56]. However, patients with a hypo-attenuating lesion that exceeds one-third of the middle cerebral artery (MCA) territory may benefit less from thrombolysis. The use of a scoring scheme has proven helpful both for recording signs of early infarction on CT and to predict outcome following thrombolytic therapy [60]. Irrespective of considerations of infarct size, the presence of a well-demarcated infarct should alert the treating physician towards the possibility of a longer interval from the acute event than 3 hours or even the coexistence of another less acute infarction. Regarding MRI-based selection criteria for systemic thrombolysis, several experienced institutions assume a higher risk of haemorrhagic complications with abnormality of more than 50% of the MCA on DWI [61,62]. In addition, the AHA/ASA guidelines note that evidence for MCA occlusion is indicative of a poor outcome [56]. They also highlight the need for expert reading of brain images to maximize the contribution of neuroimaging to the management of stroke [56].

Identification of patients for thrombolysis beyond approved criteria

Assessment of morphologic and functional changes after stroke by multimodal MRI and positron emission tomography (PET) suggests that many patients still have salvageable tissue as long as 24 hours after stroke onset. This assumption comes from the observation of much larger areas of the brain with a reduction in perfusion-threatening tissue viability than the region with visible ischaemic damage. This mismatch between morphologic and perfusion changes, i.e. the zone of purely functional changes or 'penumbra' around the core of an infarct, may indicate the potential for successful therapeutic intervention beyond the 4.5-hour time window.

Support for the feasibility and efficacy of treating acute stroke patients with systemic thrombolysis based on the presence of a 'penumbra' as defined by a mismatch between diffusion/perfusion abnormalities has come from several non-randomized studies [59,63]. The diffusion and perfusion imaging evaluation for understanding stroke evolution (DEFUSE) study investigating patients receiving systemic thrombolysis within 3–6 hours after stroke, found favourable results of the administration of recombinant tissue plasminogen activator (rtPA) only in patients with a clear diffusion/perfusion mismatch [64]. In individuals without evidence for any DWI/perfusion-weighted imaging (PWI) mismatch, no impact of systemic thrombolysis was found. A group of patients with very large DWI lesions and corresponding perfusion deficits even appeared to deteriorate following vessel recanalization and this pattern of MRI abnormalities was thus considered as consistent with a malignant profile [64]. The DEFUSE 2 trial largely replicated these results over a 12-hour time window in 100 patients scheduled to have endovascular treatment [65]. Reperfusion was associated with more favourable clinical outcomes in the presence of a target DWI/PWI mismatch identified by an automated system, while no association between reperfusion and outcome was seen in patients without target mismatch [65]. Unfortunately, placebo-controlled trials have come up with controversial results and delayed thrombolysis in patients selected for their mismatch was not confirmed to improve clinical outcome [66]. Thus, mismatch selection currently cannot yet be recommended as part of routine care [54,66] (Fig. 16.2).

Identification of patients for interventional thrombectomy

Systemic application of rtPA does not allow rapid reperfusion to be achieved in all instances and to a more limited extent with occlusion of the main extra- and intracerebral vessels. For these patients, interventional thrombectomy has been suggested as an effective alternative. Larger occlusions are commonly associated with more severe stroke. In an analysis of patients who underwent conventional arteriography within 6 hours of symptom onset in carotid stroke and within 12 hours in vertebrobasilar stroke, a National Institutes of Health Stroke Scale (NIHSS) score ≥10 has a 96097% positive predictive value to show arterial occlusions [67]. When considering and being able to offer the option of thrombectomy to patients with presumed main stem occlusions of intracerebral arteries it may thus be recommended to routinely perform intracranial CTA or MRA in all patients with more severe stroke (e.g. NIHSS score ≥10). This can also serve to assess the length of the thrombus, which has also been found to predict the likelihood of recanalization [68]. Unfortunately, recently randomized trials have not confirmed superiority of interventional thrombectomy [69], but it is certainly still an option in selected patients with remaining large vessel occlusion following IV rtPA or in case of specific contraindications for systemic thrombolysis.

Work-up of patients with unclear onset time of stroke

Approximately 15–20% of ischaemic stroke patients awaken with their neurological deficit which precludes a clear definition of the time of onset [70,71].Thus, although many of these wake-up stroke patients might be good candidates to receive thrombolytic treatment, under the current guidelines they are not eligible for thrombolysis because of the uncertain time of stroke onset. It has been speculated that imaging might provide information which could serve to estimate the length of pre-existing cerebral ischemia. In a first study of 94 consecutive patients with stroke who underwent an MRI within 12 hours after known symptom onset, negative FLAIR had a sensitivity of 46% and a specificity of 79% for allocating patients to a time window of less than 4.5 hours [72]. A subsequent multicentre observational study repeated this evaluation in 543 patients [73]. Ischaemic lesions were identified on DWI in 95% and on FLAIR in 50% of these patients. A DWI–FLAIR mismatch, i.e. the presence of only DWI signal abnormality identified patients within 4.5 hours of symptom onset with 62% sensitivity and 78% specificity (Fig. 16.10).

Interobserver agreement for acute ischaemic lesion visibility was moderate. Taken together, these findings indicate some variability in the evolution of signal abnormalities, but suggest that patients with an acute ischaemic lesion detected with DWI, but not seen on FLAIR are likely to be in a time window for which thrombolysis is safe [73]. Besides that it could also be argued that a negative FLAIR scan might indicate a greater benefit from systemic thrombolysis and/or a lower risk for haemorrhage irrespective of the time interval. These hypotheses are currently tested in prospective studies.

Identification of patients (especially those suffering from transient symptoms) with high risk for subsequent attacks

Accumulating evidence suggests a strong impact of neuroimaging, especially of MRI, on the management of patients with TIA, which has traditionally been defined clinically by a resolution of focal neurologic deficits within 24 hours from symptom onset. While CT can just serve to exclude rare non-ischaemic causes of transient focal neurologic episodes, MRI findings actually predict the reoccurrence of ischaemia. Studies using conventional MRI have already shown the frequent occurrence of infarcts in patients who had suffered from a TIA [74]. Consistent with the notion of transient symptoms, they often were seen not in an area that corresponded to the patient's neurologic symptoms, but rather in clinically silent regions of the brain. The introduction of DWI has further increased the recognition of acute ischaemic lesions in TIA, which in a small proportion, may also be transient. Ay et al. were among the first to consider the association of 'transient symptoms with infarction (TSI)' as something specific [75]. Their study suggested that TSI patients may have different risk factors than those

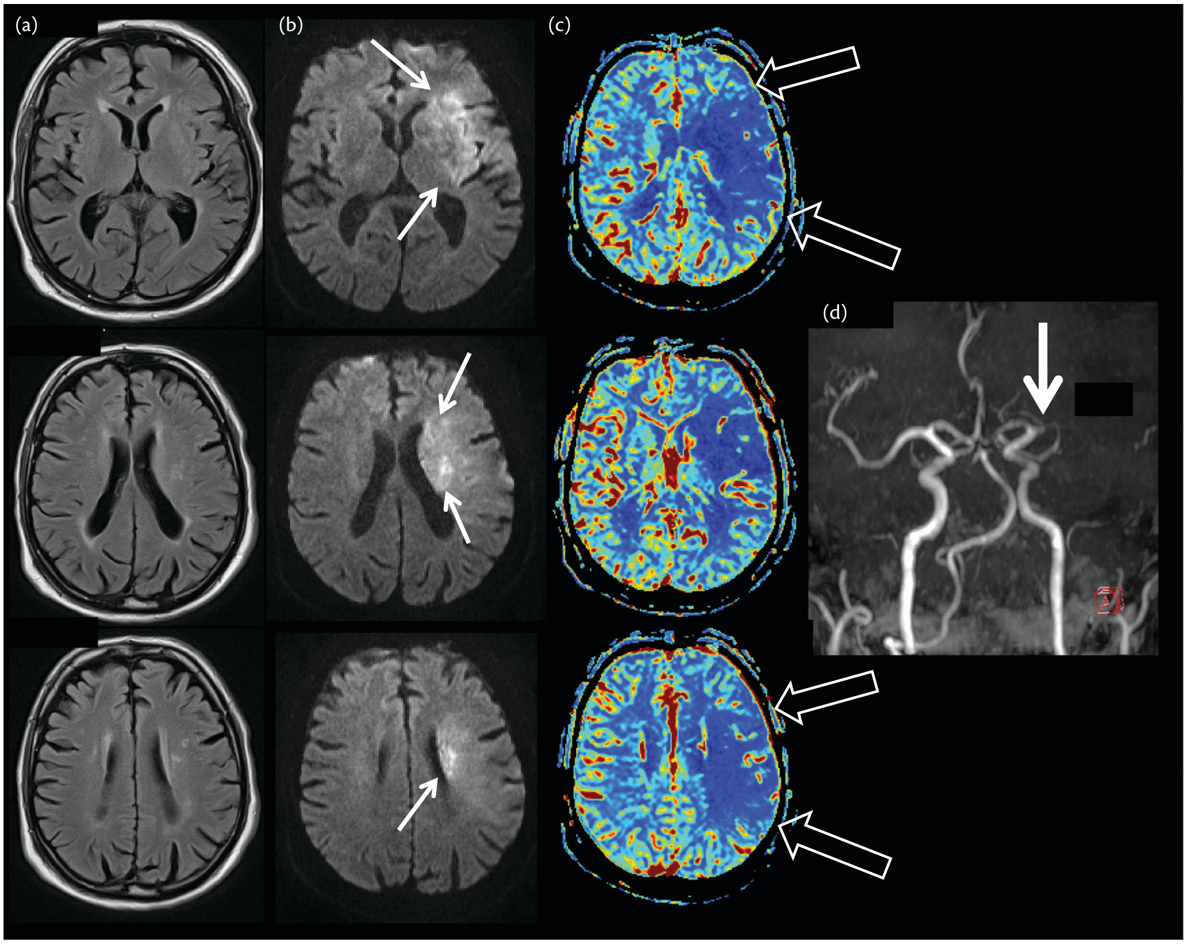

Fig. 16.10 Wake-up stroke with dense right hemiparesis. (a) Fluid-attenuated inversion recovery shows no clear signal abnormalities. (b) Diffusion abnormality in anterior and central portions of middle cerebral artery territory (MCA) (white arrows). (c) Hypoperfusion of most parts of the brain supplied by the MCA (open white arrows). (d) Corresponding MCA main stem occlusion on intracranial time-of flight MR-angiography (thick white arrow).

TIA patients without a DWI abnormality on MRI. Along the same lines, Coutts et al. performed MRI and MRA in a series of 156 patients with minor stroke and TIA [76]. Over a follow-up period of 3 months, they observed that the risk of a next stroke and of developing disability increased with the presence of a DWI lesion and was further enhanced by evidence for an occluded intracerebral vessel. These and other studies, indicating a significantly higher risk of further vascular events among patients with clinically defined TIA and DWI lesions consistent with acute focal ischaemia when compared with patients with no DWI abnormality [77,78], also lend support to the recommendation of a tissue-based diagnosis of TIA, which should be established just in patients with 'a brief episode of neurological dysfunction caused by focal brain or retinal ischaemia, with clinical symptoms typically lasting less than one hour, and without evidence of acute infarction' [79]. Patients with evidence for an acute ischaemic lesion should be considered as having suffered from stroke irrespective of the duration of symptoms [8]. Along these lines, a subanalysis of the MRI data of the 'Stroke in Young Fabry Patients Study (sifap1)' has been performed, which enrolled 5023 young patients with stroke and TIA ≤55 years, with a central collection and analysis of imaging data [80]. Besides an unexpectedly high rate of silent old infarcts of 21.7% in patients with ischaemic stroke and 9.9% in patients with a clinical diagnosis of TIA, overall morphologic findings in patients with TIA and evidence for acute infarction on DWI were much more like those in stroke patients than in patients with a clinical TIA and no DWI abnormality [81]. All these observations support the move towards a morphology-based diagnosis of TIA, but also alert for the obvious subtlety of clinical signs and symptoms associated with focal cerebral ischaemia, which may often be overlooked [82]. It is, therefore, recommended that 'TIA patients should undergo neuroimaging evaluation within 24 hours of symptom onset, preferably with magnetic resonance imaging, including diffusion sequences' [8], and in this case it is also reasonable to add intracranial MRA for its ease and non-invasiveness. What tools are used to perform the non-invasive assessment of the extracranial vessel will and should depend on the local availability and access.

Conclusions

As outlined in this chapter, CT and MRI have different potential to assess and define the different acute and chronic cerebrovascular diseases. It is important to use these possibilities to the maximum benefit of patients, weighing provided information against burden to the patient or other disadvantages such as a delay in treatment in the very acute setting of stroke. Table 16.5 summarizes

Table 16.5 Suggestion of imaging tools and techniques for specific scenarios or situations

Clinical settings	Diagnostic goals	Imaging tools
Candidates for systemic thrombolysis ≤4.5 hours	Exclude intracranial bleeding or other contraindications for iv rtPA	CT or MRI (FLAIR, DWI, T_2^*-GRE)
Acute ischaemic stroke patients >4.5–9 hours	Selection for iv rtPA beyond 4.5 hours	MRI (DWI, PWI)
(Presumed) non-responders to systemic thrombolysis	Selection for interventional recanalization (e.g. thrombectomy)	CT + CTA or MRI (DWI) + IC MRA (EC MRA optional)
Unclear stroke onset (e.g. wake-up stroke)	Identification of candidates for thrombolysis	MRI (FLAIR / DWI mismatch)
Transient ischaemic attack	Identify patients at high risk for recurrence	MRI (DWI) + IC MRA (EC MRA optional)

CT = computed tomography, CTA = CT angiography, DWI = diffusion-weighted imaging, EC = extracranial, GRE = gradient echo imaging, IC = intracranial, MRA = magnetic resonance angiography, MRI = magnetic resonance imaging, PWI = perfusion-weighted imaging.

recommendations derived from the discussion of some specific aspects of the management of patients with suspected acute focal cerebral ischaemia.

These recommendations will certainly have to be modified further with advancements in imaging technology and treatment options, and need to be adapted to the local situation. All this requires very close interaction of the involved specialists on the basis of a profound understanding of available options.

References

1. Lovblad KO, and Baird AE. (2010). Computed tomography in acute ischemic stroke. *Neuroradiology*, **52**(3), 175–87.
2. Hacke W, Kaste M, Bluhmki E, et al. (2008). Thrombolysis with alteplase 3 to 4.5 hours after acute ischemic stroke. *New England Journal of Medicine*, **359**(13), 1317–29.
3. Muir KW, Buchan A, von Kummer R, et al. (2006). Imaging of acute stroke. *Lancet Neurology*, **5**(9), 755–68.
4. Merino JG, and Warach S. (2010). Imaging of acute stroke. *Nature Reviews Neurology*, **6**(10), 560–71.
5. Leiva-Salinas C, Wintermark M, and Kidwell CS. (2011). Neuroimaging of cerebral ischemia and infarction. *Neurotherapeutics*, **8**(1), 19–27.
6. Wintermark M, Albers GW, Broderick JP, et al. (2013). Acute stroke imaging research roadmap II. *Stroke*, **44**(9), 2628–39.
7. Kloska SP, Wintermark M, Engelhorn T, et al. (2010). Acute stroke magnetic resonance imaging: current status and future perspective. *Neuroradiology*, **52**(3), 189–201.
8. Easton JD, Saver JL, Albers GW, et al. (2009). Definition and evaluation of transient ischemic attack: a scientific statement for healthcare professionals from the American Heart Association/American Stroke Association Stroke Council; Council on Cardiovascular Surgery and Anesthesia; Council on Cardiovascular Radiology and Intervention; Council on Cardiovascular Nursing; and the Interdisciplinary Council on Peripheral Vascular Disease. The American Academy of Neurology affirms the value of this statement as an educational tool for neurologists. *Stroke*, **40**(6), 2276–93.
9. Wardlaw JM, Smith EE, Biessels GJ, et al. (2013). Neuroimaging standards for research into small vessel disease and its contribution to ageing and neurodegeneration. *Lancet Neurology*, **12**(8), 822–38.
10. Poggesi A, Pantoni L, Inzitari D, et al. (2011). 2001–2011: a decade of the LADIS (Leukoaraiosis And DISability) Study: what have we learned about white matter changes and small-vessel disease? Cerebrovascular Diseases, 32(6), 577–88.
11. Saver JL. (2008). Proposal for a universal definition of cerebral infarction. *Stroke*, **39**(11), 3110–15.
12. Bories J, Derhy S, and Chiras J. (1985). CT in hemispheric ischaemic attacks. *Neuroradiology*, **27**(6), 468–83.
13. Beauchamp NJ, Jr, Barker PB, Wang PY, et al. (1999). Imaging of acute cerebral ischemia. *Radiology*, **212**(2), 307–24.
14. von Kummer R. (2000). CT of acute cerebral ischemia. *Radiology*, **216**(2), 611–13.
15. Warach S, Gaa J, Siewert B, et al. (1995). Acute human stroke studied by whole brain echo planar diffusion-weighted magnetic resonance imaging. *Annals of Neurology*, **37**(2), 231–41.
16. Bammer R, Stollberger R, Augustin M, et al. (1999). Diffusion-weighted imaging with navigated interleaved echo-planar imaging and a conventional gradient system. *Radiology*, **211**(3), 799–806.
17. Augustin M, Bammer R, Simbrunner J, et al. (2000). Diffusion-weighted imaging of patients with subacute cerebral ischemia: comparison with conventional and contrast-enhanced MR imaging. *AJNR American Journal of Neuroradiology*, **21**, 1596–602.
18. Schlaug G, Siewert B, Benfield A, et al. (1997). Time course of the apparent diffusion coefficient (ADC) abnormality in human stroke. *Neurology*, **49**(1), 113–19.
19. Eastwood JD, Engelter ST, MacFall JF, et al. (2003). Quantitative assessment of the time course of infarct signal intensity on diffusion-weighted images. *AJNR American Journal of Neuroradiology*, **24**(4), 680–7.
20. Toi H, Uno M, Harada M, et al. (2003). Diagnosis of acute brain-stem infarcts using diffusion-weighed MRI. *Neuroradiology*, **45**(6), 352–6.
21. Axer H, Grassel D, Bramer D, et al. (2007). Time course of diffusion imaging in acute brainstem infarcts. *Journal of Magnetic Resonance Imaging*, **26**(4), 905–12.
22. Tatu L, Moulin T, Bogousslavsky J, et al. (1998). Arterial territories of the human brain: cerebral hemispheres. *Neurology*, **50**(6), 1699–708.
23. Wong KS, Gao S, Chan YL, et al. (2002). Mechanisms of acute cerebral infarctions in patients with middle cerebral artery stenosis: a diffusion-weighted imaging and microemboli monitoring study. *Annals of Neurology*, **52**(1), 74–81.
24. Chowdhury D, Wardlaw J, and Dennis M. Are multiple acute small subcortical infarctions caused by embolic mechanisms? *Journal of Neurology, Neurosurgery & Psychiatry*, **75**(10), 1416–20.
25. Seifert T, Enzinger C, Storch M, et al. (2005). Acute small subcortical infarctions on diffusion weighted MRI: clinical presentation and aetiology. *Journal of Neurology, Neurosurgery & Psychiatry*, **76**(11), 1520–4.
26. Ay H, Benner T, Arsava EM, et al. (2007). A computerized algorithm for etiologic classification of ischemic stroke: the Causative Classification of Stroke System. *Stroke*, **38**(11), 2979–84.
27. Amarenco P, Bogousslavsky J, Caplan LR, et al. (2009). New approach to stroke subtyping: the A-S-C-O (phenotypic) classification of stroke. *Cerebrovascular Diseases*, **27**(5), 502–8.
28. Pantoni L. (2010). Cerebral small vessel disease: from pathogenesis and clinical characteristics to therapeutic challenges. *Lancet Neurology*, **9**(7), 689–701.
29. Janota I, Mirsen T, Hachinski V, et al. (1989). Neuropathologic correlates of leuko-araiosis. *Archives of Neurology*, **46**, 1124–8.
30. Brun A, and Englund E. (1986). A white matter disorder in dementia of the Alzheimer type: a pathoanatomical study. *Annals of Neurology*, **19**, 253–62.
31. Hachinski V, Potter P, and Merskey H. (1987). Leuko-araiosis. *Archives of Neurology*, **44**, 21–3.
32. Wardlaw J. (2014). Morphological, distributional, volumetric and intensity characterisation of periventricular hyperintensities. *American Journal of Neuroradiology*, **35**(1), 55–62.

33. Fazekas F, Chawluk JB, Alavi A, et al. (1987). MR signal abnormalities at 1.5 T in Alzheimer's dementia and normal aging. *AJR American Journal of Roentogenology*, **149**(2), 351–6.
34. Pullicino P, Ostrow P, Miller L, et al. (1995). Pontine ischemic rarefaction. *Annals of Neurology*, **37**(4), 460–6.
35. Gouw AA, Seewann A, van der Flier WM, et al. (2011). Heterogeneity of small vessel disease: a systematic review of MRI and histopathology correlations. *Journal of Neurology, Neurosurgery & Psychiatry*, **82**(2), 126–35.
36. Schmidt R, Schmidt H, Haybaeck J, et al. (2011). Heterogeneity in age-related white matter changes. *Acta Neuropathologica*, **122**(2), 171–85.
37. Schuknecht B, Ratzka M, Hofmann E. (1990). The 'dense artery sign'—major cerebral artery thromboembolism demonstrated by computed tomography. *Neuroradiology*, **32**(2), 98–103.
38. Cho KH, Kim JS, Kwon SU, et al. (2005). Significance of susceptibility vessel sign on T2*-weighted gradient echo imaging for identification of stroke subtypes. *Stroke*, **36**(11), 2379–83.
39. Schellinger PD, Chalela JA, Kang DW, et al. (2005). Diagnostic and prognostic value of early MR Imaging vessel signs in hyperacute stroke patients imaged <3 hours and treated with recombinant tissue plasminogen activator. *AJR American Journal of Neuroradiology*, **26**(3), 618–24.
40. Kimura K, Iguchi Y, Shibazaki K, et al. (2009). M1 susceptibility vessel sign on T2* as a strong predictor for no early recanalization after IV-t-PA in acute ischemic stroke. *Stroke*, **40**(9), 3130–2.
41. Cheng B, Ebinger M, Kufner A, et al. (20120. Hyperintense vessels on acute stroke fluid-attenuated inversion recovery imaging: associations with clinical and other MRI findings. *Stroke*, **43**(11), 2957–61.
42. Jadhav AP, and Jovin TG. (2012). Vascular imaging of the head and neck. *Seminars in Neurology*, **32**(4), 401–10.
43. Kidwell CS, and Wintermark M. (2008). Imaging of intracranial haemorrhage. *Lancet Neurology*, **7**(3), 256–67.
44. Connolly ES, Jr, Rabinstein AA, Carhuapoma JR, et al. (2012). Guidelines for the management of aneurysmal subarachnoid hemorrhage: a guideline for healthcare professionals from the American Heart Association/American Stroke Association. *Stroke*, **43**(6), 1711–37.
45. Fiebach JB, Schellinger PD, Gass A, et al. (2004). Stroke magnetic resonance imaging is accurate in hyperacute intracerebral hemorrhage: a multicenter study on the validity of stroke imaging. *Stroke*, **35**(2), 502–6.
46. Chalela J, Kidwell C, Nentwich L, et al. (2007). Magnetic resonance imaging and computed tomography in emergency assessment of patients with suspected acute stroke: a prospective comparison. *Lancet*, **369**(9558), 293–8.
47. Fazekas F, Kleinert R, Roob G, et al. (1999). Histopathologic analysis of foci of signal loss in gradient-echo T2*-weighted MR images in patients with spontaneous intracerebral hemorrhage: evidence of microangiopathy-related microbleeds. *AJNR American Journal of Neuroradiology*, **20**,637–42.
48. Charidimou A, Krishnan A, Werring DJ, et al. (2013). Cerebral microbleeds: a guide to detection and clinical relevance in different disease settings. *Neuroradiology*, **55**(6), 655–74.
49. Cheng AL, Batool S, McCreary CR, et al. (2013). Susceptibility-weighted imaging is more reliable than T2*-weighted gradient-recalled echo MRI for detecting microbleeds. *Stroke*, **44**(10), 2782–6.
50. Kang DW, Han MK, Kim HJ, et al. (2012). New ischemic lesions coexisting with acute intracerebral hemorrhage. *Neurology*, **79**(9), 848–55.
51. Wijman CA, Venkatasubramanian C, Bruins S, et al. (2010). Utility of early MRI in the diagnosis and management of acute spontaneous intracerebral hemorrhage. *Cerebrovascular Diseases*, **30**(5), 456–63.
52. Beitzke M, Gattringer T, Enzinger C, et al. (2011). Clinical presentation, etiology, and long-term prognosis in patients with nontraumatic convexal subarachnoid hemorrhage. *Stroke*, **42**(11), 3055–60.
53. Fazekas F, Niederkorn K, Ebner F, et al. (2009). Relevance of neuroimaging in the evaluation of cerebral ischemia. *Cerebrovascular Diseases*, **27**(Suppl. 1), 1–8.
54. Committee TESOEECatEW. (2008). Guidelines for management of ischaemic stroke and transient ischaemic attack 2008. *Cerebrovascular Diseases*, **25**, 457–507.
55. Del Zoppo GJ, Saver JL, Jauch EC, et al. (2009). Expansion of the time window for treatment of acute ischemic stroke with intravenous tissue plasminogen activator: a science advisory from the American Heart Association/American Stroke Association. *Stroke*, **40**(8), 2945–8.
56. Adams H, del Zoppo G, Alberts M, et al. (2007). Guidelines for the early management of adults with ischemic stroke: a guideline from the American Heart Association/American Stroke Association Stroke Council, Clinical Cardiology Council, Cardiovascular Radiology and Intervention Council, and the Atherosclerotic Peripheral Vascular Disease and Quality of Care Outcomes in Research Interdisciplinary Working Groups: the American Academy of Neurology affirms the value of this guideline as an educational tool for neurologists. *Stroke*, **38**(5), 1655–711.
57. Schellinger PD, Bryan RN, Caplan LR, et al. (2010). Evidence-based guideline: the role of diffusion and perfusion MRI for the diagnosis of acute ischemic stroke: report of the Therapeutics and Technology Assessment Subcommittee of the American Academy of Neurology. *Neurology*, **75**(2), 177–85.
58. Köhrmann M, Jüttler E, Fiebach J, et al. (2006). MRI versus CT-based thrombolysis treatment within and beyond the 3 h time window after stroke onset: a cohort study. *Lancet Neurology*, **5**(8), 661–7.
59. Schellinger P, Thomalla G, Fiehler J, et al. (2007). MRI-based and CT-based thrombolytic therapy in acute stroke within and beyond established time windows: an analysis of 1210 patients. *Stroke*, **38**(10), 2640–5.
60. Barber P, Demchuk A, Zhang J, et al. (2000). Validity and reliability of a quantitative computed tomography score in predicting outcome of hyperacute stroke before thrombolytic therapy. ASPECTS Study Group. Alberta Stroke Programme Early CT Score. *Lancet*, **355**, 1670–4.
61. Schellinger P, Fiebach J, and Hacke W. (2003).Imaging-based decision making in thrombolytic therapy for ischemic stroke: present status. *Stroke*, **34**(2), 575–83.
62. Hjort N, Butcher K, Davis S, et al. (2005). Magnetic resonance imaging criteria for thrombolysis in acute cerebral infarct. *Stroke*, **36**(2), 388–97.
63. Kohrmann MJ, Fiebach J, Huttner H, et al. (2006). MRI versus CT-based thrombolysis treatment within and beyond the 3 h time window after stroke onset: a cohort study. *Lancet Neurology*, **5**(8), 661–7.
64. Albers G, Thijs V, Wechsler L, et al. Magnetic resonance imaging profiles predict clinical response to early reperfusion: the diffusion and perfusion imaging evaluation for understanding stroke evolution (DEFUSE) study. *Annals of Neurology*, **60**(5), 508–17.
65. Lansberg MG, Straka M, Kemp S, et al. (2012). MRI profile and response to endovascular reperfusion after stroke (DEFUSE 2): a prospective cohort study. *Lancet Neurology*, **11**(10), 860–7.
66. Mishra NK, Albers GW, Davis SM, et al. (2010). Mismatch-based delayed thrombolysis: a meta-analysis. *Stroke*, **41**(1), e25–33.
67. Fischer U, Arnold M, Nedeltchev K, et al. (2005). NIHSS score and arteriographic findings in acute ischemic stroke. *Stroke*, **36**(10), 2121–5.
68. Riedel CH, Zimmermann P, Jensen-Kondering U, et al. (2011). The importance of size: successful recanalization by intravenous thrombolysis in acute anterior stroke depends on thrombus length. *Stroke*, **42**(6), 1775–7.
69. Hennerici MG, Kern R, and Szabo K. (2013). Non-pharmacological strategies for the treatment of acute ischaemic stroke. *Lancet Neurology*, **12**(6), 572–84.
70. Mackey J, Kleindorfer D, Sucharew H, et al. (2011). Population-based study of wake-up strokes. *Neurology*, **76**(19), 1662–7.
71. Koton S, Tanne D, and Bornstein NM. (2012). Ischemic stroke on awakening: patients' characteristics, outcomes and potential for reperfusion therapy. *Neuroepidemiology*, **39**(3–4), 149–53.
72. Ebinger M, Galinovic I, Rozanski M, et al. (2010). Fluid-attenuated inversion recovery evolution within 12 hours from stroke onset: a reliable tissue clock? *Stroke*, **41**(2), 250–5.

73. Thomalla G, Cheng B, Ebinger M, et al. (2011). DWI-FLAIR mismatch for the identification of patients with acute ischaemic stroke within 4.5 h of symptom onset (PRE-FLAIR): a multicentre observational study. *Lancet Neurology*, **10**(11), 978–86.
74. Fazekas F, Fazekas G, Schmidt R, et al. (1996). Magnetic resonance imaging correlates of transient cerebral ischemic attacks. *Stroke*, **27**(4), 607–11.
75. Ay H, Koroshetz W, Benner T, et al. (2005). Transient ischemic attack with infarction: a unique syndrome? *Annals of Neurology*, **57**(5), 679–86.
76. Coutts S, Simon J, Eliasziw M, et al. (2005). Triaging transient ischemic attack and minor stroke patients using acute magnetic resonance imaging. *Annals of Neurology*, **57**(6), 848–54.
77. Purroy F, Montaner J, Rovira A, et al. (2004). Higher risk of further vascular events among transient ischemic attack patients with diffusion-weighted imaging acute ischemic lesions. *Stroke*, **35**(10), 2313–19.
78. Prabhakaran S, Chong J, and Sacco R. (2007). Impact of abnormal diffusion-weighted imaging results on short-term outcome following transient ischemic attack. *Archives of Neurology*, **64**(8), 1105–9.
79. Albers GW, Caplan LR, Easton JD, et al. (2002). Transient ischemic attack—proposal for a new definition. *New England Journal of Medicine*, **347**(21), 1713–16.
80. Rolfs A, Fazekas F, Grittner U, et al. (2013). Acute cerebrovascular disease in the young: the stroke in young fabry patients study. *Stroke*, **44**(2), 340–9.
81. Fazekas F, Enzinger C, Schmidt R, et al. (2013). MRI in acute cerebral ischemia of the young: the Stroke in Young Fabry Patients (sifap1) study. *Neurology*, **81**, 1914–21.
82. Paul NL, Simoni M, and Rothwell PM. (2013). Transient isolated brainstem symptoms preceding posterior circulation stroke: a population-based study. *Lancet Neurology*, **12**(1), 65–71.

CHAPTER 17

Neuroimaging in vascular cognitive impairment

Structural and functional imaging in vascular dementia

Lars-Olof Wahlund, Lena Bronge,
Irina Savitcheva, and Rimma Axelsson

Background

Cognitive decline due to diseases of the brain vessels is common. The best known concept is vascular dementia (VaD), which is regarded as the second most common dementia disorder after Alzheimer's disease (AD). VaD is caused by changes in the brain vessels, usually of arteriosclerotic origin, but in rare cases other abnormalities, such as inflammation and deposition of amyloid in the vessel walls, can cause cognitive symptoms. Also cerebral bleedings can sometimes cause VaD.

It is difficult to define the different subgroups of VaD and several diagnostic criteria for VaD have been published [1,2]. Usually, the presence of cognitive decline together with evidence of cerebrovascular damage and correlation in time between these two phenomena is mandatory for a diagnosis. In the criteria published lately, findings on a structural computed tomography (CT) or magnetic resonance imaging (MRI) scans [2] can be regarded as evidence of cerebrovascular damage. Moreover, since the concept of dementia is under discussion and will not be present in the new DSM-5 criteria, this chapter also discusses vascular cognitive impairment (VCI).

VCI is an umbrella term, including 'VCI without dementia', VaD, and cognitive impairment of mixed origin (AD and VaD). The VCI construct also includes the concept of 'mild VCI', similar to mild cognitive impairment (MCI) in neurodegenerative disorders. This means that mild cognitive deficits are recognized as belonging to a disorder entity before these deficits have reached the dementia stage. The concept takes into account the fact that there are mechanisms of cerebrovascular disease other than strategic infarcts, multiple infarcts and white matter (WM) changes accounting for the pattern of cognitive deficits associated with VaD; for example, chronic hypoperfusion [3].

Generally, VaD can be divided into cognitive decline due to large vessel disease, small vessel disease, cerebral autosomal dominant arteriopathy with subcortical infarcts and leuco-encephalopathy (CADASIL) and cerebral amyloid angiopathy (CAA).

Large vessel disease

Arteriosclerotic changes in the large brain vessels can, for instance, cause territorial infarctions, as well as multiple smaller infarcts. This is recognized in the NINDS-AIREN criteria for VaD [2]. The concept includes infarcts in specific arterial territories, as well as watershed infarcts. Watershed infarcts are lesions that occur in the border zone regions between the main arterial territories. Posterior watershed infarcts in the parietal region are located between the cortical supply of the middle cerebral artery and that of the posterior cerebral artery. Watershed infarcts in the superior frontal area are located between the cortical supply of the anterior cerebral artery and that of the middle cerebral artery.

Typically, large vessel infarcts can cause a picture of VaD, when they are located in the dominant hemisphere or—in the case of anterior cerebral artery territories—when they are bilateral. On the other hand, infarcts in the non-dominant hemisphere alone are not sufficient radiological support for a diagnosis of VaD [2].

Sometimes small infarcts in strategic areas can result in pronounced cognitive decline. For instance, such strategic areas can be in the thalami, angular gyrus, or hippocampus (Fig. 17.1). The clinical picture of this type of VaD is dependent on where the ischaemic lesions are located. In general, VaD is characterized by a stepwise course of cognitive deterioration, and with a picture of psychomotor retardation, revealed by tests that are time-dependent. Cognitive decline in connection with stroke is another example of large vessel disease. If an area such as the hippocampus is damaged by a stroke, a picture similar to AD might occur (Fig. 17.1).

Small vessel disease

Ischaemic damage due to arteriosclerosis of the small vessels of the brain results either in changes (previously denoted as Binswangers disease) in the white matter (WM changes) or multiple lacunes (status lacunare). Today, the NINDS-AIREN criteria state that multiple lacunes or extensive WM changes and bilateral lesions in the thalamus are sufficient to diagnose VaD [2]. Small vessel disease is regarded as the most common form of VaD.

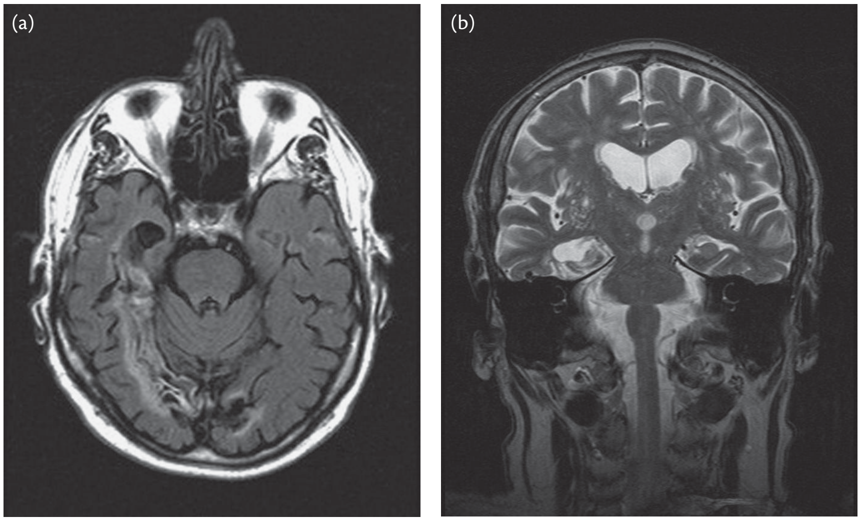

Fig. 17.1 Strategic infarct in medial part of right temporal lobe, engaging most of right hippocampus. (a) FLAIR image in the axial plane. (b) T_2-weighted coronal image.

White matter changes

In elderly individuals, areas of high signal intensity in the WM are seen on T_2-weighted MR images. On CT these changes are less conspicuous and appear as areas of low attenuation.

The significance of such changes has been debated since they are seen not only in connection with cognitive impairment and cerebrovascular disease, but also in otherwise healthy elderly individuals. However, there is mounting evidence that such changes are clinically important and represent ischaemic injury caused by cerebral small vessel pathology [4,5]. The most important risk factor connected to WM changes, besides increasing age, is hypertension.

The histopathological substrates of the abnormalities seen on MRI scans include a spectrum of tissue damage ranging from mild demyelination to loss of parenchymal elements with gliosis and necrosis. The severity of the disease seems to increase with lesion size, although the MR signal abnormalities are identical.

Typically, WM changes present as two different types; as lines or bands along the lateral ventricular walls (periventricular changes) and as irregular areas in the deep WM or subcortical regions (deep WM changes) (Fig. 17.2). In the more severe cases, these two types merge. The periventricular and deep WM changes are thought to have different aetiology and significance, and thin periventricular lines or bands can even be a normal finding.

More extensive WM changes have been linked not only to cognitive impairment, but also to motor and gait disturbances, incontinence, and mood disorders like depression. Although there is a great overlap, WM changes are more often found in demented patients than in healthy people, and more often in patients with VaD than in those with other dementias. Moreover, WM changes significantly increase the risk for dementia [5].

Severe WM changes can cause cognitive impairment with a 'subcortical' pattern. This includes decline in specific cognitive functions, such as processing speed, attention and executive function, verbal fluency, and visuoconstructional praxis, but also a poor performance in global cognitive tests [5].

WM changes alone might not be enough to cause dementia, but when reaching a certain degree of severity they can interact with other pathologic processes. In the diagnostic radiological criteria the amount of WM changes considered to be sufficient as to be a cause of VaD is set at involvement of at least 25% of the WM [2].

There is a need for methods to assess the amount of WM changes for both clinical purposes and in the research setting. Automatic

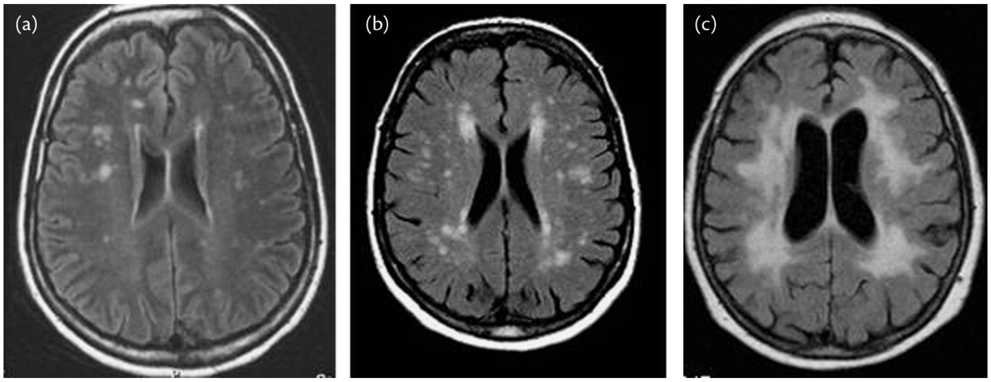

Fig. 17.2 Pictures of different grades of WM changes. The images were obtained using FLAIR. According to the Fazekas scale (see [6]): (a) grade 1, multiple punctate lesions; (b) grade 2, beginning confluency (bridging) of lesions; (c) grade 3, large confluent lesions.

computerized methods that measure the volume of WM changes exist, but they require high image quality and post-processing facilities. The use of visual rating scales, on the other hand, offers a simple, swift, and robust method that has been shown to be reliable. There are a number of different rating scales and one of the simplest ones has also been widely used for clinical purposes. This scale was developed by Fazekas et al. [6], and it rates deep WM changes as mild (punctiform), moderate (beginning confluence) or severe (confluent lesions) 0–3, and periventricular changes on a separate scale (Fig. 17.2).

The age-related white matter changes (ARWMC) changes scale was developed for both CT and MRI images, and rates lesions in separate brain areas [7].

Lacunes

Lacunes are small subcortical infarcts measuring 3–20 mm in diameter, occurring in territories supplied by the small perforating arteries (Fig. 17.3) [8]. On MRI, they can be detected as round or oval lesions with CSF-like intensity on all MR sequences, surrounded by WM or subcortical gray matter and sometimes by a rim of high signal (gliosis) on T_2 and FLAIR. Usually, lacunes are located in the basal ganglia, internal capsule, thalamus, paramedian, and lateral regions of the brainstem, corona radiata, and centrum semiovale.

They may be clinically silent, but are sometimes accompanied by a history of transient ischaemic attacks or stroke. Lacunes in the thalamus are important, since it plays a crucial role in many cognitive functions, and even small lesions in this structure may result in cognitive deficits (Fig. 17.4). If a diagnosis of VaD is to be based on the presence of lacunes, there should be evidence of multiple (at least two) lacunes in the basal ganglia and frontal WM.

Lacunes should be distinguished from enlarged Virchow–Robin spaces (VRS). VRS are dilated perivascular spaces, and are located typically at the vertex and around the anterior commissure near the substantia perforate (Fig. 17.5). An association between VRS and WM changes has been described in healthy elderly subjects, but the number of VRS was not independently related to cognitive function [8]. It was recently shown that VRS are present even in healthy young subjects, and are to be considered a normal finding [9]. When VRS appear in large numbers (*état criblé*, occurring especially in the basal ganglia), this is probably due to focal brain atrophy around blood vessels.

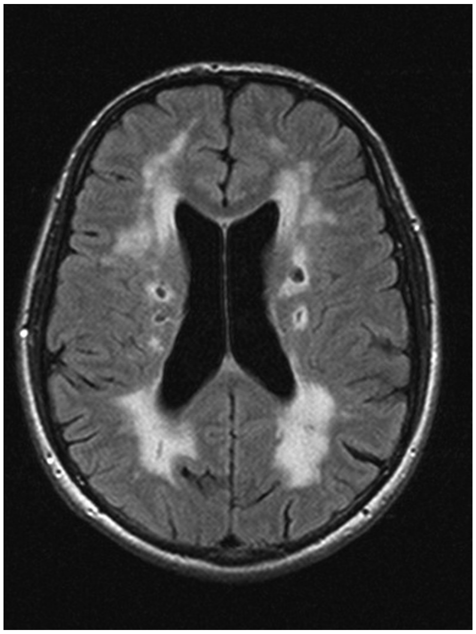

Fig. 17.3 Axial FLAIR image in a patient with CADASIL, showing extensive WM lesions and multiple lacunes.

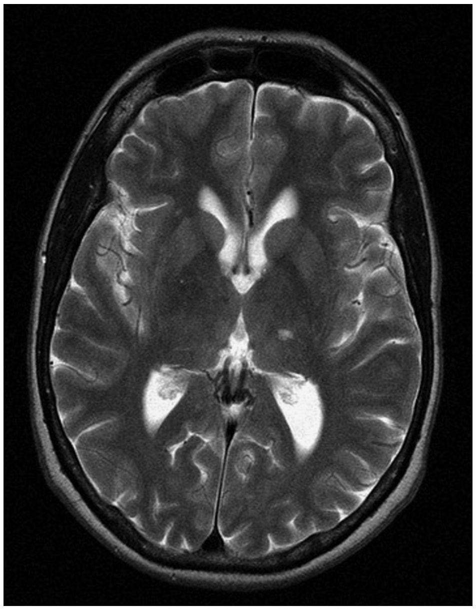

Fig. 17.4 T_2-weighted axial image showing small lacunar infarct in left thalamus.

Microbleeds

Microbleeds are small rounded lesions detected on T_2* MR images (Fig. 17.6). They are seen as black dots due to haemosiderin deposition.

Cerebral microbleeds are composed of small collection of blood breakdown products, in particular haemosiderin within perivascular macrophages [10]. Microbleeds can be observed in cortical/subcortical, basal ganglia/thalamus, and infratentorial areas, and should be distinguished from calcification or iron deposits that are often observed symmetrically in the globi pallidi, and flow void artefacts of the pial blood vessels. Microbleeds are observed in subjects with hypertension and in diseases with amyloid depletion in the brain vessels, e.g. Alzheimers disease, CAA, and CADASIL. Microbleeds are usually associated with other manifestations of small vessel disease such as WM changes. The frequency of microbleeds differs between different populations [11]. In community-based populations, the prevalence of microbleeds is relatively low, in the order of 5%. Prevalence of microbleeds in stroke populations and in VaD is far higher, around 50–70% [11].

The prevalence might differ also depending on the image parameters and scanners used. More modern equipment with higher field strengths and microbleeds sensitive image parameters detect more microbleeds.

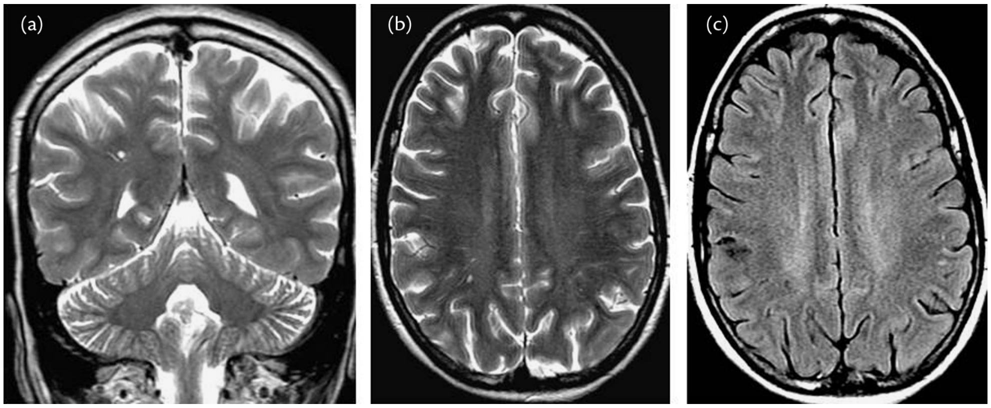

Fig. 17.5 (a) T_2-weighted coronal image showing dilated perivascular spaces (VRS) in the WM of the centrum semiovale in the right parietal lobe. The VRS appear to be well-defined and mostly tubular, but sometimes round or ovoid, structures with MRI-signal as CSF on all sequences. (b) Axial T_2-weighted image in the same patient. (c) Axial FLAIR image in the same patient showing a subtle area of low signal. No surrounding gliosis is seen.

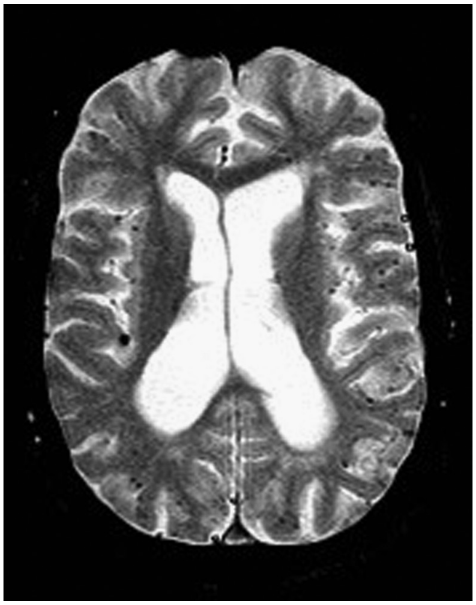

Fig. 17.6 T_2*-weighted axial image showing multiple microhaemorrhages (the black dots) in both cerebral hemispheres

Hereditary forms of VaD

There are some hereditary forms of vascular cognitive dementia. CADASIL is one such example. This disease usually starts in early middle age with migraine and ischaemic events (transient ischaemic attacks and ischaemic strokes). Gradually cognitive impairment develops and repeated ischaemic events are common. CADASIL is regarded as a model for VaD. Typical brain changes are WM changes and lacunes on MRI. The WM changes are located in the anterior temporal areas of the brain. In addition, lacunes are present in the centrum semiovale centre, the thalamus, the basal ganglia, and the pons [12] (Fig. 17.3). Microbleeds are frequently observed in a large proportion of these patients [13].

Neurodegeneration

VCI and VaD are associated with brain atrophy. Hippocampal atrophy may not be specific for Alzheimer disease. In fact, hippocampal atrophy is typically seen in other types of dementia such as fronto-temporal dementia and VaD [14]. It is unclear whether hippocampal atrophy in VaD is always due to concomitant Alzheimer-type pathology, or if another type of neuropathology causes neuronal loss in this region, and eventually leads to atrophy. VaD and AD are two strongly age-related disorders and they frequently co-exist. The hippocampus is highly vulnerable to ischaemia, which may contribute to hippocampal atrophy in VaD. In support of this hypothesis, it has been shown that vascular risk factors are related to hippocampal atrophy [15,16].

Imaging, computed tomography

CT is generally sufficient to rule out other potentially treatable conditions that could cause cognitive disturbances, such as tumours, subdural haematomas or hydrocephalus. Furthermore, with modern CT technology, more subtle changes like small vessel pathology and regional atrophy are detectable. However MRI is superior to CT due to its better spatial resolution, tissue characterization and increased sensitivity to pathology.

If CT is used for evaluation of cognitive impairment, reconstruction of images in all three planes is recommended. This contributes to the assessment of regional atrophy, especially in the temporal lobes. The coronal reformatted images should preferably be perpendicular to the long axis of the temporal lobe for optimal visualization of the hippocampus. The acquisition protocol should also have a fairly good signal-to-noise ratio to be able to detect WM changes and small lacunes.

Magnetic resonance imaging

The MRI protocol should include as a minimum: T_2-weighted and FLAIR images, a coronal (3D) T_1-weighted sequence with thin slices, and a T_2*-weighted gradient-echo.

T_2 and FLAIR images, preferably in the axial plane, show lacunar and cortical infarcts, as well as WM changes with high sensitivity. On T_2 sequences, all these changes are seen as bright areas;

on FLAIR images cavities can be seen as dark areas. This facilitates the differentiation of lacunes or enlarged perivascular spaces from WM changes. Compared with T_2, FLAIR sequences have, however, a reduced sensitivity for lesions in the infra-tentorial region as well as in the diencephalon (including the thalamus).

T_1-weighted sequences are used for regional atrophy assessment and should be obtained in a coronal plane parallel to the brainstem, orthogonal to the long axis of hippocampus. Coronal images can be reformatted from a sagittal 3D sequence.

T_2* sequences are the best to detect microbleeds, haemorrhages, and calcifications.

Other magnetic resonance imaging techniques

Later in this chapter, methods to image vascular brain function are described, e.g. PET and SPECT. MRI technique offers one imaging modality to study brain perfusion (ASL) and one to study tissue diffusion (DTI).

Arterial spin labelling

ASL is a non-invasive method, which allows brain perfusion to be measured. The technique is based on the labelling of protons in the blood entering the brain. Due to differences in the magnetic properties of blood protons the amount of blood going into different brain areas can be measured. Basically, this technique provides the same information as the one that can be obtained by using PET or SPECT without being invasive and using radioactive compounds. Both small infarcts, as well as WM changes can be detected using ASL [17].

Diffusion tensor imaging

Since conventional MRI images show all WM changes as hyperintense areas on T_2-weighted images, there is a demand for more specific methods. Modern MRI techniques, such as diffusion tensor imaging (DTI) and magnetization transfer imaging (MTI) can assess WM integrity in a more quantitative way. Studies using such methods have indicated that different types or grades of pathology provide different clinical expression. The application of these techniques has also revealed changes in the ‘normal-appearing’ WM that seems to be connected to cognitive decline [18,19].

It is hoped that these techniques will, in the future, help us to better understand the underlying mechanisms through which WM changes impair brain function.

Functional imaging using SPECT and PET in VaD

The purpose of functional imaging in clinical practice is to increase the diagnostic accuracy in order to differentiate among different dementia disorders.

The modern three-dimensional (3D) techniques used for functional imaging are imaging of regional cerebral blood flow (rCBF) with single photon emission computed tomography (SPECT) and glucose metabolism using positron emission tomography (PET). However, there are only a few studies of brain receptors with SPECT and they have not yet been tested in clinical settings.

Imaging of rCBF and FDG-PET was used in clinical practice for over more than 25 years and the extent of found abnormalities is well correlated with the severity of cognitive impairments and the clinical stage of dementia [20].

Regional cerebral blood flow detected with SPECT

Different dementias are characterized by specific blood flow patterns. The majority of studies in this area have been performed on AD and fewer have focused on VaD. It is well documented that AD patients tend to have reduced blood flow in the temporal and parietal association cortex, while frontotemporal dementia (FTD) patients shows reduced blood flow in the frontal and anterior temporal parts of the brain [21].

It is difficult to categorize a specific perfusion pattern in VaD with the goal of differentiating it from AD and other dementias, as well as from normality. In an early review by Jagust et al., it was reported that it was difficult to differentiate multiple infarct dementias from AD using SPECT due to a variety of findings in VaD patients [22]. These findings included temporal/parietal and multiple focal hypoperfusion, as well as patchy and global rCBF reductions (Fig. 17.7). Two findings on visual interpretation most consistent with VaD are ‘patchy’ patterns and a reduction in rCBF in the frontal lobes [23,24].

Using statistical parametric mapping (SPM) to analyse rCBF patterns in VaD [25], a clear relationship between the reduction of CBF in the anterior and posterior associated areas [26], and the severity of dementia was reported.

In order to increase the capacity of rCBF to differentiate VaD from other dementias, a ‘stereotactic surface projection’ method was used [27]. Using a pixel-by-pixel analysis, this method evaluates the severity, extent and localization of abnormal rCBF. This allowed the authors to distinguish three perfusion patterns, (a) anterior cerebral hypoperfusion, (b) posterior cerebral hypoperfusion, and (c) diffuse cerebral hypoperfusion. It was also reported that patients with Binswanger’s disease showed a decreased blood flow in the frontal lobes and in the anterior cingulate cortex, while AD patients showed a decrease in the temporoparietal and in the posterior cingulate cortices.

Another computerized image method called ‘Fractal dimension analysis’ (FD) has been developed [28]. Fractal dimension is an index of heterogeneity of rCBF, and a higher FD indicates uneven rCBF in SPECT images. Higher FD values were found in VaD and AD subjects as compared to controls. Moreover, the heterogeneity of rCBF SPECT images was larger in the anterior parts of the brain in VaD compared with AD.

These analysis methods confirm earlier findings establishing that in patients with VaD a reduction in rCBF appears in the anterior parts of the brain and that the rCBF reductions are more heterogeneously distributed.

Diagnostic value of SPECT

In a systematic review by Dougall et al., the regional cerebral blood flow in VaD patients was compared with AD to assess its diagnostic usefulness [29]. The authors reported the results from 13 studies. The overall pooled weighted sensitivity of ^{99m}Tc-HMPAO-SPECT in discriminating clinically defined AD from VD was 71.3%; its specificity was 75.9%. The pooled weighted sensitivity and specificity for AD versus FTD were 71.5 and 78.2%, respectively. However, it is important to note that meta-analysis results are conservative since the latest

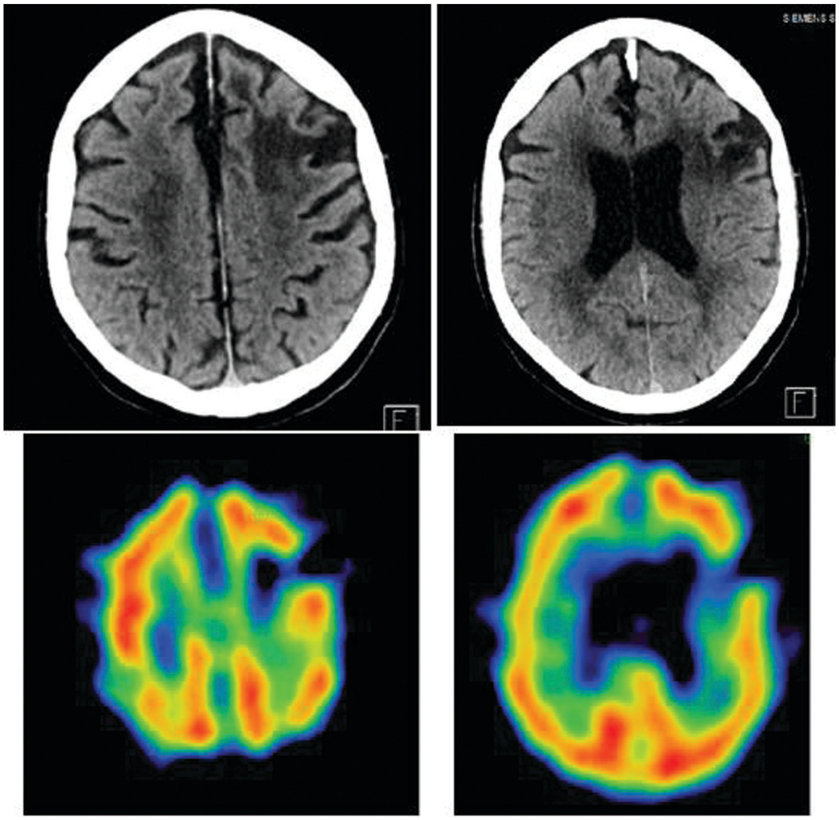

Fig. 17.7 CT transaxial slices (upper row) in patients with multi-infarct dementia. 99m-Tc-HMPAO transaxial SPECT slices (lower row) in the same patient. The hypoperfusion in several cortical regions corresponding to CT findings.

publications are usually not included. Another aspect regarding the included studies is that they were sometimes carried out on severely demented patients with more evident pathological changes.

The results from Dougall et al. were, to some extent, supported by a study by Talbot et al. who compared rCBF as a diagnostic tool in VaD and other dementias including AD, Lewy–Body disease (DLBD), FTD) and progressive aphasia [24]. Among 363 patients, a bilateral posterior CBF abnormality was found to significantly increase the odds of having AD as opposed to VaD or FTD. Bilateral anterior CBF abnormality significantly increased the odds of FTD as opposed to AD, VaD or DLBD. 'Patchy' CBF changes significantly increased the odds of a patient having VaD as opposed to AD. They found ^{99m}Tc-HMPAO SPECT to be most useful in distinguishing AD from VaD and FTD, and least useful in differentiating between AD and DLBD, and between VaD, FTD, and progressive aphasia. It was suggested that CBF SPECT should be used selectively and as an adjunct to clinical evaluation and CT.

PET imaging in VaD

Compared with SPECT, PET is generally characterized by a higher sensitivity and specificity in the diagnosis of dementia [30]. The study of glucose metabolism using [^{18}F]-2-fluoro-2-deoxy-D-glucose (FDG) is the most commonly applied and well-established method in the diagnosis of dementia. Neuronal dysfunction or/and neuron loss, usually present in all dementia diseases, results in a decrease of synaptic activity and a consequent reduction of energy demand and thus metabolism of glucose, the main source of energy supply in the brain.

As with SPECT, no specific metabolic pattern indicating VaD can be demonstrated with PET. A reduction of global brain metabolism and CBF, widespread and patchy patterns of regional hypometabolism in cortical regions, basal ganglia, cerebellum, and brainstem are described in the literature (Fig. 17.8). A frontal hypometabolism is the most common sign in VaD, which is often seen in patients with lacunes in basal ganglia and thalamus [31].

Frontal metabolic changes are probably due to disruption of subcortical-frontal projections leading to reduction of synaptic activity in the frontal cortex. Yao et al. [32] reported widespread reduction of CBF and oxygen metabolism in cortical regions and WM in Binswanger´s type of VaD as compared with normal controls. Widespread hypometabolism in different cortical and subcortical regions was demonstrated in VaD, which may overlap with hypometabolic changes in AD [33]. However, reduction of metabolic activity in sensorimotor areas and cerebellum is more pronounced in VaD, compared with AD, in which these areas show a preserved metabolism. To summarize, diffuse patchy hypometabolism in the cortical region, including sensorimotor areas and subcortical hypometabolism, can help to distinguish VaD from AD.

An early diagnosis of a prodromal stage of VaD (subcortical vascular MCI, svMCgI) is important because by modifying the vascular risk factors one may influence the disease course. Seo et al. [34] have compared metabolic changes in svMCgI with amnestic types of MCI (aMCgI) and demonstrated different patterns of metabolic changes in these two groups. In svMCgI, hypometabolism was seen bilaterally in the thalamus, insula, anterior cingulate gyrus, left superior temporal gyrus, right basal ganglia,

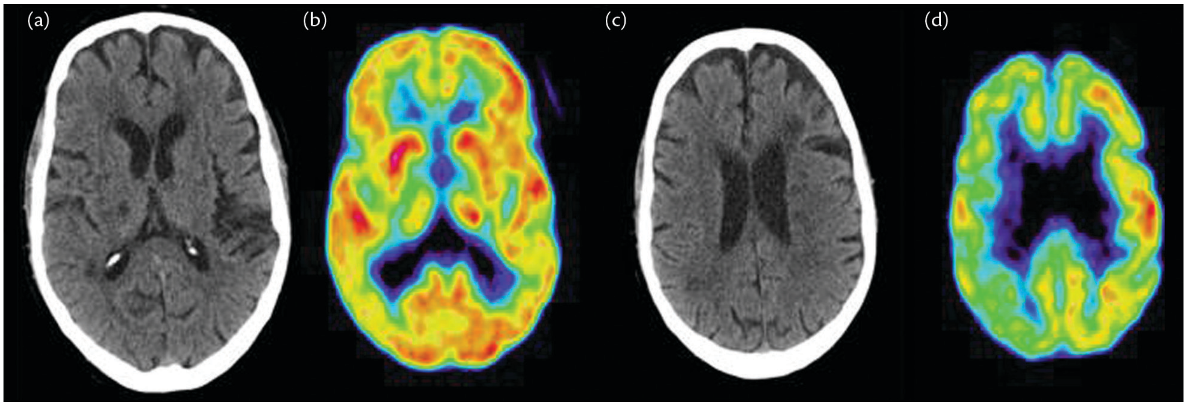

Fig. 17.8 Brain CT of a patient with dementia. (a,c) Transaxial slices at the thalamic and upper cortical levels show a lacune in the right thalamus and diffuse WM changes. Corresponding PET images (b,d) show hypometabolism in the right thalamus (b) and metabolic changes in the right frontal and parietal cortices, as well as in the left medial frontal cortex (d).

cerebellum, and brainstem. In svMCgI, hypometabolic changes are more severe in the right thalamus, brainstem and cerebellum compared with aMCgI, where the most prominent hypometabolism is seen in the left parahippocampal gyrus, cerebellar vermis, and bilaterally in the orbitofrontal gyrus. The different pattern of metabolic changes can provide a better understanding of the mechanisms leading to neurobehavioural syndromes in the prodromal stage of dementia and help to distinguish between the different types of MCI.

Beta-amyloid markers used in dementia diagnosis in recent years can potentially rule out AD in MCI patients, but their role in VaD remains unclear.

Summary

Imaging plays an important role in diagnosing VCI. Structural imaging modalities, such as MRI and CT are used to monitor the presence of WM changes, infarcts, and bleedings. The presence of cognitive decline similar to dementia together with significant WM changes or lacunes strongly support a VaD diagnose. Modern MRI technique, such as DTI or ASL presents a good opportunity for studying brain vascular function and will probably, in the future, further increase our understanding of how vascular cognitive decline develops.

Despite the fact that functional imaging reflects brain perfusion and the fact that VaD is the consequence of pathological changes in brain vessels, there is little consensus on a specific brain perfusion pattern in VaD. This is in contrast to primary degenerative disorders such as AD and FTD, which usually show a more distinct pattern of brain perfusion and metabolism. In clinical practice, rCBF SPECT of VaD shows a reduction in the anterior lobes and a patchy reduction of blood perfusion. For clinical purposes it is clear, according to the meta review by Dougall et al. [29], that the clinical usefulness of SPECT in differentiating AD from VaD is limited. Despite this fact SPECT might be considered as a complement in the dementia work-up to differentiate between different primary degenerative disorders and VaD since this at times provides relevant and useful information.

A PET investigation of glucose metabolism shows the same pattern of reduction in glucose metabolism as is seen with rCBF-SPECT, but has a greater sensitivity and specificity in differentiating dementia diseases. However, SPECT is still more available and less costly than PET imaging and, therefore, more applicable in the dementia work-up in primary and secondary settings. The question of whether modern PET imaging with new ligands such as b-amyloid markers contributes to the evaluation of VaD needs to be further investigated.

References

1. Erkinjuntti T, Inzitari D, Pantoni L, et al. (2000). Research criteria for subcortical vascular dementia in clinical trials. *Journal of Neural Transmission*, **59**(Suppl.), 23–30.
2. Román GC, Tatemichi TK, Erkinjuntti T, et al. (1993). Vascular dementia: diagnostic criteria for research studies. Report of the NINDS-AIREN International Workshop (see comments). *Neurology*, **43**(2), 250–60.
3. Moorhouse P, and Rockwood K. (2008). Vascular cognitive impairment: current concepts and clinical developments. *Lancet Neurology*, **7**, 246–55.
4. The LADIS study group, 2001–2011 (2011). A decade of the LADIS (Leukoaraiosis And DISability) Study: what have we learned about white matter changes and small-vessel disease? *Cerebrovascular Diseases*, **32**, 577–88.
5. Debette S, and Markus HS. (2010). The clinical importance of white matter hyperintensities on brain magnetic resonance imaging: systematic review and meta-analysis. *British Medical Journal*, **341**, c3666.
6. Fazekas F, Chawluk JB, Alavi A, et al. (1987). MR signal abnormalities at 1.5 T in Alzheimer´s dementia and normal aging. *AJR American Journal of Roentgenology*, **149**(2), 351–6.
7. Wahlund L.O, Barkhof F, Fazekas F, et al. (2001). A new rating scale for age-related white matter changes applicable to MRI and CT. *Stroke*, **32**, 1318–22.
8. Longstreth WT, Jr, Bernick C, Manolio TA, et al. (1998). Lacunar infarcts defined by magnetic resonance imaging of 3660 elderly people: the Cardiovascular Health Study. *Archives of Neurology*, **55**(9), 1217–25.
9. Maclullich AM, Wardlaw JM, Ferguson KJ, et al. (2004). Enlarged perivascular spaces are associated with cognitive function in healthy elderly men. *Journal of Neurology, Neurosurgery & Psychiatry*, **75**(11), 1519–23.
10. Groeschel S, Chong WK, Surtees R, et al. (2006). Virchow–Robin spaces on magnetic resonance images: normative data, their dilation, and a review of the literature. *Neuroradiology*, **48**(10), 745–54.
11. Koennecke HC. (2006). Cerebral microbleeds on MRI: prevalence associations, and potential clinical implications. *Neurology*, **66**(2), 165–71.
12. Van Den BR, Lesnik Oberstein SA, van Duinen SG, et al. (2002). Subcortical lacunar lesions: an MR imaging finding in patients with cerebral autosomal dominant arteriopathy with subcortical infarcts and leukoencephalopathy. *Radiology*, **224**(3), 791–6.

13. Lesnik Oberstein SA, van Den BR, van Buchem MA, et al. (2001). Cerebral microbleeds in CADASIL. *Neurology*, **57**(6), 1066–70.
14. Du AT, Schuff N, Laakso MP, et al. (2002). Effects of subcortical ischemic vascular dementia and AD on entorhinal cortex and hippocampus. *Neurology*, **58**(11), 1635–41.
15. Korf ES, White LR, Scheltens P, et al. (2004). Midlife blood pressure and the risk of hippocampal atrophy: the Honolulu Asia Aging Study. *Hypertension*, **44**(1), 29–34.
16. Van der Flier WM, Staekenborg Salka, S, Barkhof F, et al. (2009). Structural neuroimaging: CT and MRI. In: Wahlund L-O, Erkinjuntti T and Gauthier S (eds) *Vascular cognitive impairment in clinical practice*. Cambridge: Cambridge Press.
17. Hendriksen J, Petersen ET, and Golay X. (2012). Vascular disorders: insights from arterial spin labeling. *Neuroimaging Clinics of North America*, **22**, 259–69.
18 Viana-Baptista M, Bugalho P, Jordao C, et al. (2008). Cognitive function correlates with frontal white matter apparent diffusion coefficients in patients with leukoaraiosis, *Journal of Neurology*, **255**, 360–6.
19. Yan Zhou, Qun-Xu, Lin-di Qin, et al. (2011). A primary study of diffusion tensor imaging-based histogram analysis in vascular cognitive impairment with no dementia, *Clinical Neurology and Neurosurgery*, **113**(2), 92–7.
20. Farid K, Caillat-Vigneton N, and Sibon I. (2011). Is brain SPECT useful in degenerative dementia diagnosis? *Journal of Computer Assisted Tomography*, **35**, 1–3.
21. Torosyan N, and Silverman DHS. (2012). Neuronuclear Imaging in the Evaluation of Dementia and Mild Decline in cognition. *Seminars in Nuclear Medicine*, **42**(N6), 415–22.
22. Jagust WJ, Johnson KA, and Holman BL. (1995). SPECT perfusion imaging in the diagnosis of dementia. *Journal of Neuroimaging*, **5**(Suppl. 1), S45–52.
23. Yoshikawa T, Murase K, Oku N, et al. (2003). Statistical image analysis of cerebral blood flow in vascular dementia with small-vessel disease. *Journal of Nuclear Medicine*, **44**(4), 505–11.
24. Talbot PR, Lloyd JJ, Snowden JS, et al. (1998). A clinical role for 99mTc-HMPAO SPECT in the investigation of dementia? *Journal of Neurology, Neurosurgery, and Psychiatry*, **64**(3), 306–13.
25. Shim YS, Yang DW, Kim BS, et al. (2006). Comparison of regional cerebral blood flow in two subsets of subcortical ischemic vascular dementia: statistical parametric mapping analysis of SPECT. *Journal of Neurological Sciences*, **250**(1–2), 85–91.
26. Yang DW, Kim BS, Park JK, et al. (2002). Analysis of cerebral blood flow of subcortical vascular dementia with single photon emission computed tomography: adaptation of statistical parametric mapping. *Journal of Neurological Sciences*, 203–204, 199–205.
27. Hanyu H, Shimuzu S, Tanaka Y, et al. (2004). Cerebral blood flow patterns in Binswanger's disease: a SPECT study using three-dimensional stereotactic surface projections. *Journal of Neurological Sciences*, **220**(1–2),79–84.
28. Yoshikawa T, Murase K, Oku N, et al. (2003). Heterogeneity of cerebral blood flow in Alzheimer disease and vascular dementia. *American Journal of Neurological Research*, **24**(7), 1341–7.
29. Dougall NJ, Bruggink S, and Ebmeier KP. (2004). Systematic review of the diagnostic accuracy of 99mTc-HMPAO-SPECT in dementia. *American Journal of Geriatric Psychiatry*, **12**(6), 554–70.
30. Mielke R, Pietrzyk U, Jacobs A, et al. (1994). HMPAO SPET and FDG PET in Alzheimer's disease and vascular dementia: comparison of perfusion and metabolic pattern. *European Journal of Nuclear Medicine*, **21**(10), 1052–60.
31. Sultzer DL, Mahler ME, Cummings JL, et al. (1995). Cortical abnormalities associated with subcortical lesions in vascular dementia. Clinical and position emission tomographic findings. *Archives of Neurology*, **52**(8), 773–80.
32. Yao H, Sadoshima S, Kuwabara Y, et al. (1990). Cerebral blood flow and oxygen metabolism in patients with vascular dementia of the Binswanger type. *Stroke*, **21**, 1694–1699.
33. Mielke R, Herholz K, Grond M, et al. (1992). Severity of vascular dementia is related to volume of metabolically impaired tissue. *Archives of Neurology*, **49**(9), 909–13.
34. Seo SW, Cho SS, Park A, et al. (2009). Subcortical vascular versus amnestic mild cognitive impairment: comparison of cerebral glucose metabolism. *Journal of Neuroimaging*, **19**(3), 213–19.

CHAPTER 18

Alzheimer's disease

Massimo Filippi and Federica Agosta

Introduction

Alzheimer's disease (AD) is the most common cause of dementia in the elderly. Autopsy case series of AD patients showed the sequential accumulation of neurofibrillary tangles and amyloid β (Aβ) plaques, as well as the progression of neuronal loss through the cerebral cortex. Neuroimaging has traditionally been considered an ancillary procedure in the diagnosis of AD. In most cases, clinicians use brain imaging to rule out other pathologies, such as tumours and haemorrhages. As the clinical approach to dementia changes, several factors require clinicians to rely more heavily on brain imaging for diagnosis and patient management [1]. First, according to current diagnostic criteria [2–5], the diagnosis of AD is based on clinical history, neurologic and psychiatric examination, neuropsychological testing, and supportive measures, including structural and functional neuroimaging and cerebrospinal fluid (CSF) tests to improve specificity and reach a diagnosis of AD before the onset of manifest dementia (Table 18.1). Furthermore, the most important anticipated development in dementia will be the use of treatments targeted at specific molecular pathologies, e.g. eradication of toxic Aβ in patients with AD. This will increase the importance of making accurate aetiological diagnoses to avoid inappropriate exposure of patients to potentially dangerous medications. In addition, parameters obtained from neuroimaging, such as metabolism or cerebral volume, can be measured much more accurately than changes in memory abilities or other clinical parameters, making imaging an attractive technique for measuring response to treatment, both in research and clinical practice. Finally, as reviewed in this chapter, AD is associated with the development of pathologic changes long before the development of functional impairment (dementia). Thus, neuroimaging has a potential role in diagnosing AD at the prodromal stage (i.e. mild cognitive impairment (MCI) that are likely to progress to AD) [4] (Table 18.1). For all these reasons, researchers are increasingly turning to neuroimaging to establish its role in early and accurate diagnosis, as well as to investigate how changes in brain structure and function can be measured over time. A variety of imaging techniques are available. The goal of this chapter is to provide an overview of the various methods used to image AD.

Diagnosis of Alzheimer's disease: the new guidelines

All current diagnostic criteria require structural imaging to be done at the initial evaluation of a patient suspected of having AD [2–5]. This is needed not only to exclude other brain disease, but also to identify the earliest and most specific abnormalities that would allow a diagnosis of AD. Indeed, biomarkers, including those from neuroimaging, have been formally incorporated in the most recent revisions of the diagnostic criteria for AD and MCI [2–5] (Table 18.1). Two major classes of biomarkers have been identified: biomarkers of *disease state* (i.e. biomarkers of Aβ accumulation, which are abnormal (increased) tracer retention on amyloid positron emission tomography (PET) imaging and abnormal (low) CSF Aβ42), and biomarkers of *disease stage* (i.e. biomarkers of neuronal injury, which are elevated CSF tau, decreased fluorine-18 (^{18}F)-2-fluoro-2-deoxy-D-glucose (FDG) uptake on PET in the temporoparietal cortex, and atrophy on structural magnetic resonance imaging (MRI) in a suggestive topographic pattern involving medial, basal, and lateral temporal lobes, and medial and lateral parietal cortices). Regardless of whether clinical criteria for possible AD are fulfilled, when both Aβ and neuronal injury biomarkers are negative, the dementia is unlikely to be due to AD pathology [2–5] (Table 18.1).

Structural neuroimaging findings

Because it was the first technique to provide a detailed image of the brain, computed tomography (CT) has the longest history of use in dementia. CT scanning adequately addresses the most basic needs for imaging in neurodegenerative disease, which are to rule out alternate pathologies, and to evaluate the presence and extent of cerebrovascular disease. However, in a large study of patients referred to a memory clinic, CT failed to reveal any reversible causes that were not identified clinically in 362 patients with dementia [6]. Although CT is still regularly used for the diagnostic assessment, research on most aspects of degenerative dementia has moved away from CT because this technique typically has lower resolution than MRI and is not as sensitive to many types of abnormalities seen in AD.

Neurodegeneration in AD leads to a marked reduction of brain tissue. Indeed, typical late onset, amnestic AD (arbitrarily defined as age at onset >65 years) is characterized by global atrophy on MRI. The medial temporal lobes (MTL), especially the hippocampus and entorhinal cortex, are among the earliest sites of pathologic involvement [7]. Other severely affected regions include the posterior part of the cingulate gyrus, precuneus, and splenium of the corpus callosum on the medial surface, and the parietal, posterior superior temporal, and frontal regions on the lateral cerebral surfaces [8–10] (Fig. 18.1).

Of all the structural markers of AD, hippocampal atrophy assessed on coronal T_1-weighted images (or conventional CT) is the best established and validated. MRI-autopsy studies have convincingly

Table 18.1 Diagnostic criteria for Alzheimer's disease (AD) and mild cognitive impairment (MCI) incorporating biomarkers. Recommendations from the National Institute on Aging–Alzheimer's Association workgroups on diagnostic guidelines for AD

Diagnostic category	**Biomarker probability of AD aetiology**	**Amyloid β (PET or CSF)**	**Neuronal injury (CSF tau, FDG-PET, structural MRI)**
Probable AD dementia			
Based on clinical criteria	Uninformative	Unavailable, conflicting or indeterminate	Unavailable, conflicting or indeterminate
With three levels of evidence of AD pathophysiological process	Intermediate	Unavailable or indeterminate	Positive
	Intermediate	Positive	Unavailable or indeterminate
	High	Positive	Positive
Possible AD dementia (atypical clinical presentation)			
Based on clinical criteria	Uninformative	Unavailable, conflicting or indeterminate	Unavailable, conflicting or indeterminate
With evidence of AD pathophysiological process	High, but does not rule out second aetiology	Positive	Positive
Dementia unlikely due to AD	Lowest	Negative	Negative
MCI-core clinical criteria	Uninformative	Conflicting, indeterminant, untested	Conflicting, indeterminant, untested
MCI due to AD-intermediate likelihood	Intermediate	Positive	Untested
		Untested	Positive
MCI due to AD-high likelihood	Highest	Positive	Positive
MCI-unlikely due to AD	Lowest	Negative	Negative

Abbreviations: AD = Alzheimer's disease; CSF = cerebrospinal fluid; FDG = fluorine-18 (^{18}F)-2-fluoro-2-deoxy-D-glucose; MCI = mild cognitive impairment; MRI = magnetic resonance imaging; PET = positron emission tomography.

Modified from Albert MS, DeKosky ST, Dickson D, et al. (2011). The diagnosis of mild cognitive impairment due to Alzheimer's disease: recommendations from the National Institute on Aging-Alzheimer's Association workgroups on diagnostic guidelines for Alzheimer's disease. *Alzheimer's & Dementia*, **7**, 270–9. Copyright (2011), with permission from Elsevier; McKhann GM, Knopman DS, Chertkow H, et al. (2011). The diagnosis of dementia due to Alzheimer's disease: recommendations from the National Institute on Aging-Alzheimer's Association workgroups on diagnostic guidelines for Alzheimer's disease. *Alzheimer's & Dementia*, **7**, 263–9. Copyright (2011), with permission from Elsevier.

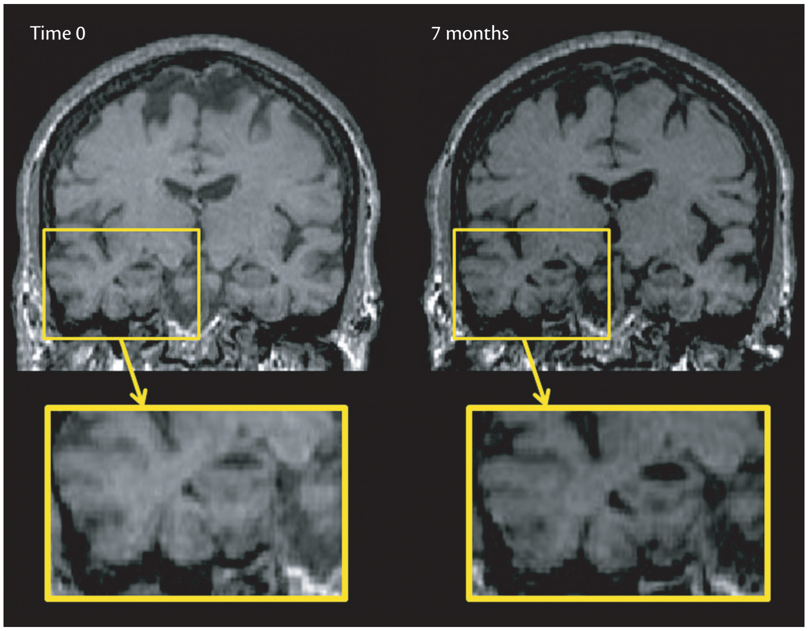

Fig. 18.1 Serial coronal MRI of a patient with Alzheimer's disease (AD). Progressive hippocampal atrophy is clearly shown (magnified region outlined in yellow) associated with ventricular and sulcal enlargement after 7 months in a 70-year-old AD patient.

corroborated that hippocampal volumes measured from ante mortem MRI scans correlate with Braak neurofibrillary tangle pathologic staging [11,12]. MTL atrophy is now one of the supportive biomarkers to make a diagnosis of AD in the presence of memory loss proposed by the new diagnostic criteria [2,3,5]. MRI is superior to conventional CT in the evaluation of MTL atrophy [13,14]. However, the possibility of evaluating the pattern of atrophy using CT has been improved with the advent of multidetector row CT, due to the availability of high resolution coronally reformatted images [15]. MTL atrophy can be detected by qualitative ratings based on visual scoring, or by linear measurements and quantitative volumetry of regions of interest (referenced to a well-characterized population with age norms). Several visual rating scales to quantify degree of MTL atrophy have been developed and are widely used [16–19]. These scales have a high accuracy in determining the extent of atrophy in cross-sectional studies relative to more labour-intensive manual volumetry of the hippocampus, and reached an accuracy of about 89% in discriminating AD patients from controls in a small sample of subjects [18]. By contrast, the use of a visual rating scale to determine rates of atrophy over time only reached accuracy at chance level relative to volumetric measures, suggesting that this approach may not be useful as a secondary end point in clinical trials [20]. However, at present, accepted standards for quantitative analysis of hippocampal volumetry are lacking [21]. Manual hippocampal segmentation is the most validated procedure to estimate a quantitative hippocampal volume, but different laboratories use different anatomical landmarks and measurement approaches [21]. The utility of structural imaging will certainly be increased further by automated segmentation algorithms developed in the last few years, which are the only feasible methods in the context of large studies, such as clinical trials.

MRI has also been used to study patients with MCI, who have subjective cognitive concerns and impairment on cognitive testing that are not impeding daily function. Structural MRI studies in MCI have produced mixed results, both in terms of hippocampal, as well as posterior cingulate and parietal involvement (absent, unilateral, or bilateral) [22–25]. The reasons for this variability may be due to different subject selection (i.e. diverse diagnostic inclusion criteria), small sample size (i.e. studies are not adequately powered to detect differences even at the group level), and methodological differences. It is also worth noting that the major source of variance in MCI studies is likely to be the intrinsic heterogeneity of the MCI population, since a relevant proportion of these subjects do not have AD pathology and will not progress to AD. MCI patients with predominant memory impairment (amnestic MCI), who are at increased risk of developing AD, have atrophy in a consistent set of cortical regions, the 'cortical signature of AD', including the MTL and temporoparietal cortex (Fig. 18.2). Conversely, non-amnestic MCI show a different pattern of atrophy characterized by a relative sparing of the MTL and a regional involvement, which is typically highly consistent with the observed clinical deficits (Fig. 18.2).

Clinical population studies have reported that hippocampal volumes in mild AD patients are 15–40% smaller than controls [26], and in MCI the volume is reduced by 10–15% [27]. MTL volume can separate mild to moderate AD patients from normal controls with sensitivity and specificity greater than 85% [26]. MTL volumes can separate AD patients and MCI subjects from healthy controls, with accuracy ranging from 70% for early stages of MCI

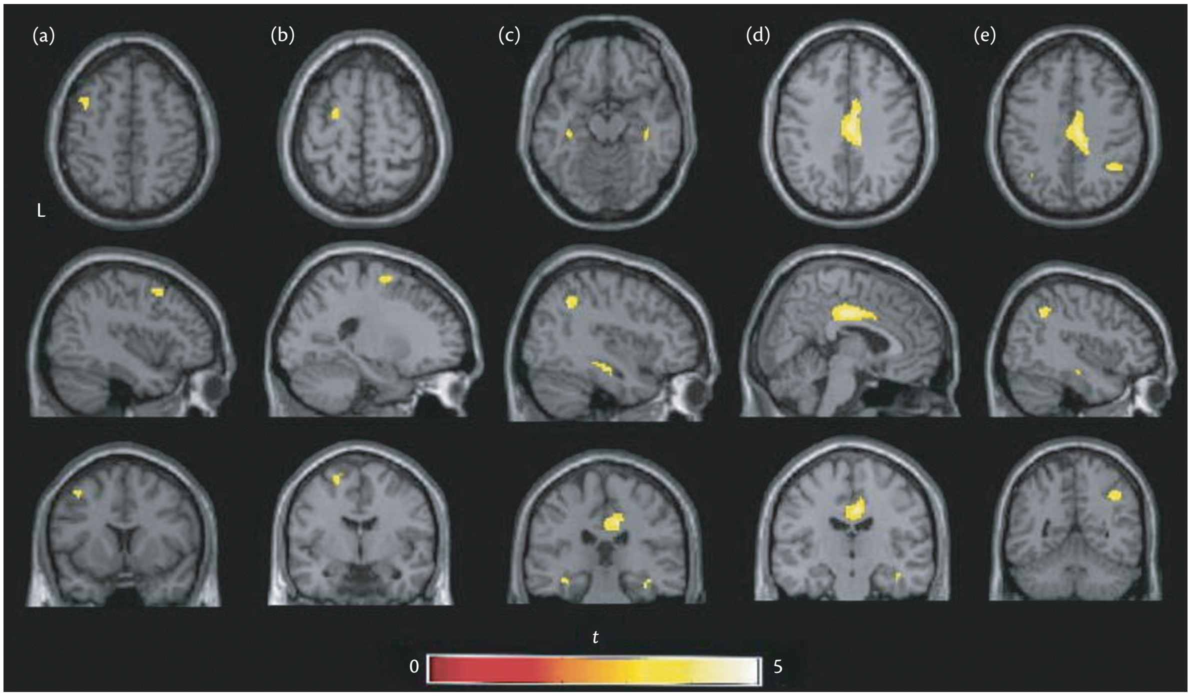

Fig. 18.2 Gray matter atrophy in mild cognitive impairment (MCI) subgroups. Gray matter loss in (a) dorsolateral prefrontal cortex and (b) dorsomedial prefrontal cortex in dysexecutive MCI compared with controls. Gray matter loss in (c) bilateral hippocampus, (d) posterior cingulate gyrus, and (e) right parietal cortex in amnestic MCI compared with controls. Colour bar represents *t* values.

Reproduced from Pa J, Boxer A, Chao LL, et al. (2009). Clinical-neuroimaging characteristics of dysexecutive mild cognitive impairment. *Annals of Neurology*, **65**, 414–23. Copyright (2009), with permission from John Wiley & Sons Ltd.

to complete group separation for advanced stages of AD dementia [26]. Furthermore, volumes of both hippocampus and entorhinal cortex predict future conversion to AD in individuals with MCI with an accuracy of around 80–85%. The predictive value of entorhinal cortex volume seems to be slightly superior over that of hippocampus [28–32]. A meta-analysis estimated that MTL volume, as assessed on structural MRI, has 73% sensitivity and 81% specificity for predicting whether patients with MCI will convert to AD [33]. Subjects with amnestic MCI who progress to AD, also show atrophy of gray matter regions beyond the MTL, including

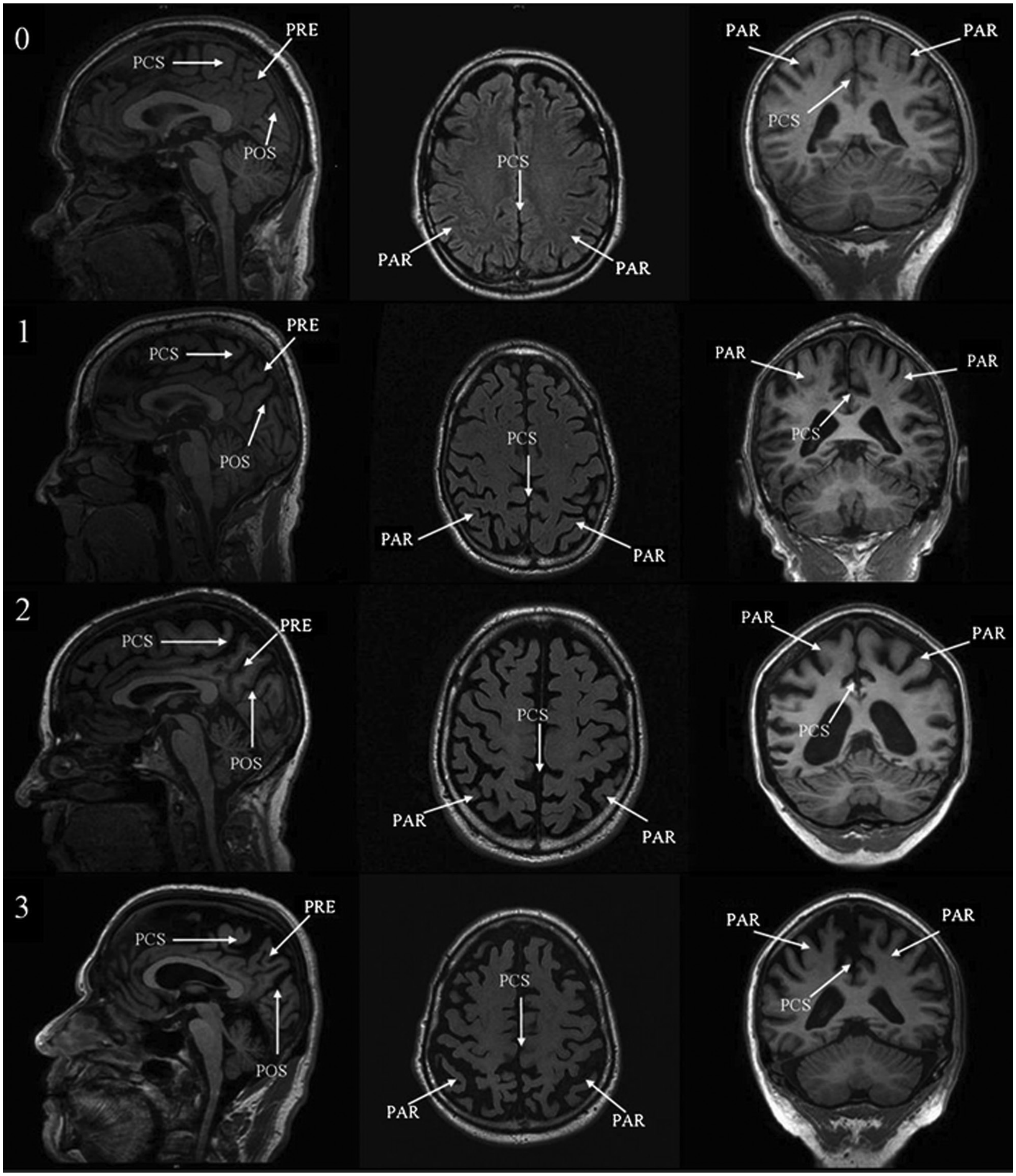

Fig. 18.3 Visual rating scale for the posterior brain regions in Alzheimer's disease patients. In sagittal, axial, and coronal orientation, this rating scale rates 0 = no atrophy, 1 = minimal atrophy, 2 = moderate atrophy and 3 = severe atrophy. In sagittal orientation, widening of the posterior cingulated sulcus and parieto-occipital sulcus, and atrophy of the precuneus is evaluated. In axial orientation, widening of the posterior cingulate sulcus and sulcal dilatation in the parietal lobes is evaluated. In coronal orientation, the widening of the posterior cingulate sulcus and sulcal dilatation in the parietal lobes is evaluated.

Abbreviations: PSC= posterior cingulate sulcus; POS = parieto-occipital sulcus; PRE = precuneus; PAR = parietal lobe.

Reproduced from Koedam EL, Lehmann M, van der Flier WM, et al. (2011). Visual assessment of posterior atrophy development of a MRI rating scale. *European Radiology*, **21**, 2618–25, Copyright (2011), reproduced under Creative Commons License 2.0

the medial and inferior temporal lobes, temporoparietal association neocortex, and frontal lobes [22,23,34–36].

Especially informative for the study of earliest structural changes in the course of AD are the MRI data of longitudinally followed elderly who were completely asymptomatic at the time of the MRI scan and later developed cognitive impairment leading to a diagnosis of MCI or AD. Using such data, a few studies were able to show that volumetric reduction of the anterior MTL, including the hippocampus, the amygdala, and the entorhinal cortex, precedes the onset of cognitive deterioration by several years [37–39]. Volumes of the amygdala and the hippocampus in clinically-declining subjects were found to be, on average, 5% smaller than in stable controls as early as 6 years before the diagnosis of dementia was made. It should be emphasized, however, that MTL atrophy may occur in other diseases as well [40–44]; thus, MTL atrophy alone lacks specificity and cannot confidently be used to exclude other dementia, particularly in patients at the MCI stage.

Early onset AD patients (i.e. subjects showing onset of symptoms before the age of 65 years) showed less prominent MTL atrophy and greater involvement of the parietal, lateral temporal, and frontal regions compared with late onset AD cases [45–47]. A specific visual rating scale has been designed, evaluating the posterior cingulate, precuneus, and superior parietal regions to provide diagnostic information at a single subject level [48] (Fig. 18.3). This scale was found to be robust, reproducible, and easily applicable in the clinical setting [48–50]. The utility of such a scale has been assessed in pathologically-proven (mostly early onset) AD and frontotemporal lobar degeneration (FTLD) patients [49]. Thirty per cent of AD patients had posterior atrophy in the absence of abnormal MTL atrophy, whereas only 7% of the FTLD group had abnormal posterior atrophy score and normal MTL [49]. Adding posterior atrophy to the MTL visual rating score improved discrimination of early onset AD from normal controls, and all AD from FTLD cases [49].

Serial MRI may be helpful to demonstrate the progression of the disease (Fig. 18.1). Rates of whole brain atrophy in AD have been estimated at 1.4–2.2% per year, whereas rates of atrophy during normal ageing (at a mean age of 70 years) do not usually exceed 0.7% per year [51]. A meta-analysis showed that mean annualized hippocampal atrophy rates are 4.7% for AD subjects and 1.4% for controls [52]. Atrophy rate from serial MRI studies was found to be associated with time to subsequent clinical conversion to a more impaired state, in both cognitively healthy elderly subjects and subjects with amnestic MCI [53,54].

AD pathology can manifest itself with clinically atypical presentations, i.e. in some patients memory is not the primary deficit, but visuospatial and visuoperceptual, and/or language disturbances are prominent symptoms. Atypical presentations are more often seen in early onset AD patients. In atypical, focal AD presentations, the MTL is relatively spared [55,56]. Two quantitative MRI studies of pathology-proven AD cases suggested that a pattern of temporoparietal atrophy or cortical thinning may suggest AD pathology even in subjects presenting with non-amnestic clinical syndromes [56,57]. The temporoparietal cortex volume provided also better discrimination between atypical AD and FTLD groups than the hippocampal volume (81 versus 74% accuracy) [56]. Two common progressive, focal cortical syndromes associated with AD pathology are posterior cortical atrophy (PCA) and primary progressive aphasia (PPA). Structural MRI scans of patients with PCA show atrophy of parieto-occipital and posterior temporal cortices [55,58] (Fig. 18.4). Compared with typical AD cases, PCA patients have greater parietal and less MTL atrophy [55]. Among the PPA variants, the logopenic one is most frequently associated with AD pathology. In the logopenic PPA variant, the pattern of

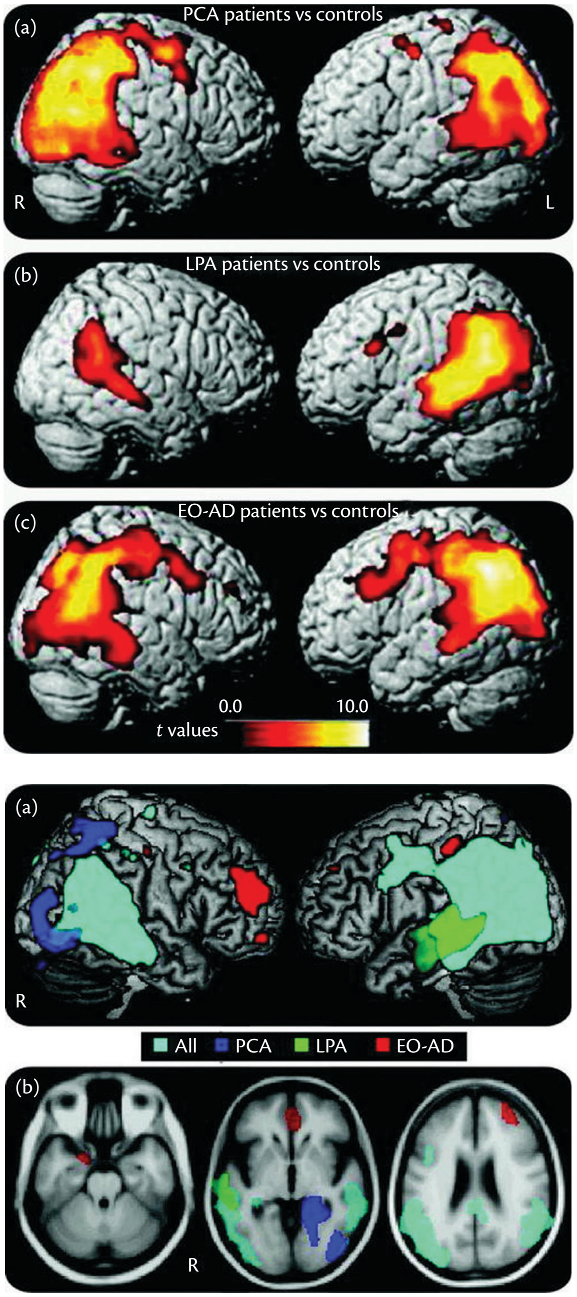

Fig. 18.4 Gray matter atrophy in atypical, focal presentation of early-onset Alzheimer's disease. (Left panel) Gray matter areas with significant atrophy in (a) posterior cortical atrophy (PCA), (b) logopenic primary progressive aphasia (LPA), and (c) early age at onset AD (EO-AD) compared with controls. (Right panel) Gray matter (GM) atrophy common to all patients versus controls is shown in cyan, while GM regions specifically atrophied in each group compared with controls are indicated in blue for PCA, green for LPA, and red for EO-AD. Results are superimposed on the 3D rendering of the Montreal Neurological Institute standard brain.

Reproduced from Migliaccio R, Agosta F, Rascovsky K, et al. (2009). Clinical syndromes associated with posterior atrophy: early age at onset AD spectrum. *Neurology*, **73**, 1571–8. Copyright (2009), with permission from Wolters Kluwer Health.

atrophy primarily affects the left temporoparietal junction, including the left posterior superior and middle temporal gyri, as well as the inferior parietal lobule [55,59] (Fig. 18.4). The involvement of the left MTL is reported less consistently [59]. Such a posterior temporoparietal pattern of atrophy may help discriminating this syndrome from the other subtypes of PPA (see Chapter 19 for further details).

Beside atrophy, cerebrovascular pathology has been associated with AD, especially in the late onset form. White matter hyperintensities, lacunae, and microbleeds can be observed on MRI scans of AD patients. An overlap with vascular dementia (VaD) may occur and patients may actually fulfil both criteria for AD and VaD (see Chapter 17 for further details).

Functional imaging findings

Cerebral blood flow (CBF) single-photon emission computed tomography (SPECT) and FDG-PET have been shown to have high sensitivity and specificity for detecting AD throughout the course of the disease, including the early prodromal stage. CBF-SPECT and FDG-PET scans of typical AD patients demonstrate predominant hypoperfusion or reduced glucose metabolism of the temporoparietal regions, including the precuneus and posterior cingulate cortex [60] (Fig. 18.5).

Functional frontal lobe involvement is also often reported in AD, but usually in conjunction with and characteristically less severe than temporoparietal involvement [61]. Overall hypoperfusion or hypometabolism in early onset AD is much greater in magnitude and extent than that of late onset AD patients with similar dementia severity [62–64]. Early onset AD patients typically show more severe hypometabolism of parietal, frontal, occipital, and subcortical areas [63,64]. The primary visual and sensorimotor cortices, cerebellum, thalamus, and basal ganglia are relatively spared in AD [61]. SPECT is technically less demanding and more widely available, while PET is more sensitive, mainly due to its higher resolution [65], but comes at the cost of more complex detector system and tracer production facilities. In general, the magnitude of hypometabolism seen with FDG-PET is greater than the amplitude of hypoperfusion seen with CBF-SPECT [65].

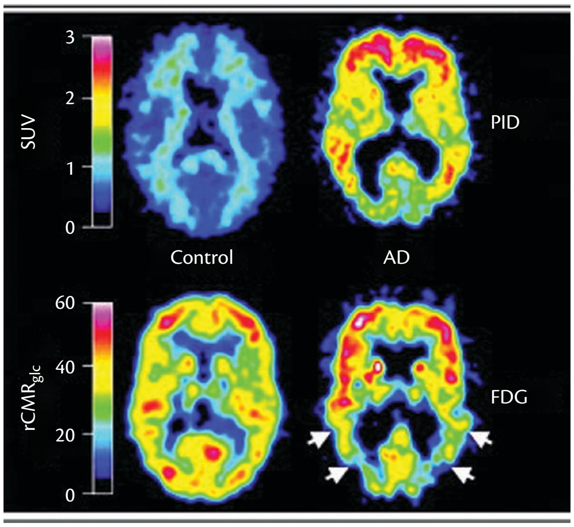

Fig. 18.5 Fluorine-18 (^{18}F)-2-fluoro-2-deoxy-D-glucose (FDG) and ^{11}C-labelled Pittsburgh Compound-B (^{11}C-PIB) positron emission tomography (PET) in Alzheimer's disease (AD). FDG and PIB standardized uptake value (SUV) PET images of a 67-year-old healthy control subject (left) and a 79-year-old AD patient (MMSE = 21; right). The left column shows lack of PIB retention in the entire gray matter of the healthy subject (top left) and normal FDG uptake (bottom left). Non-specific PIB retention is seen in the white matter (top left). The right column shows high PIB retention in the frontal and temporoparietal cortices of the AD patient (top right) and a typical pattern of FDG hypometabolism present in the temporoparietal cortex (arrows; bottom right) along with preserved metabolic rate in the frontal cortex. FDG and PIB-PET scans were obtained within 3 days of each other.

Abbreviation: rCMRGlc = regional cerebral metabolic rate of glucose. Reproduced from Klunk WE, Engler H, Nordberg A, et al. (2004). Imaging brain amyloid in Alzheimer's disease with Pittsburgh Compound-B. *Annals of Neurology*, **55**, 306–19. Copyright (2004), with permission from John Wiley & Sons Ltd..

Most existing studies compared FDG-PET with a clinical diagnosis [66–70]. A recent review showed, for those studies that used clinical assessment as the reference standard, that FDG-PET has a pooled diagnostic accuracy of 93% for differentiating AD subjects from normal subjects, with a sensitivity of 96% and a specificity of 90% [60]. A prospective study of 102 individuals, presenting consecutively to a primary care centre for the examination of suspected early onset dementia, showed a sensitivity of 78% and specificity of 81% of FDG-PET scans against clinical diagnosis of AD [71]. Some studies compared the accuracy of FDG-PET with that of neuropathologic diagnosis of dementia [61,72–74]. A multicentre analysis in 138 patients with histopathological diagnoses reported that FDG-PET correctly identified the presence or absence of AD in 88% of the cases, with a sensitivity of 94% and a specificity of 73% [72]. A single-centre cohort study of 44 subjects with variable levels of cognitive impairment and autopsy confirmation showed that the diagnostic accuracy of FDG-PET at an initial clinical evaluation (sensitivity, 84%; specificity, 74%) was better than that of initial clinical evaluation alone (sensitivity, 76%; specificity, 58%), and was similar to that of longitudinal clinical diagnosis over approximately 4 years [73]. The clinical diagnosis of AD was associated with a 70% probability of detecting AD pathology, but with a positive FDG-PET scan this increased to 84%; with a negative FDG-PET scan it decreased to 31% [73]. A diagnosis of not-AD at an initial clinical evaluation was associated with a 35% probability of AD pathology, increasing to 70% with a positive PET scan [73].

Multiple studies have shown that AD-type metabolic patterns can be found in CBF-SPECT and FDG-PET scans at the prodromal stages. Amnestic MCI typically shows regional hypometabolism consistent with AD, although the magnitude of reduction is milder than that in clinically probable AD cases (Fig. 18.6) [69,75–80].

Longitudinal studies of patients with MCI found that if the baseline FDG-PET shows an AD-like pattern, the probability of clinical progression within a few years is extremely high [81–85]. A meta-analysis estimated that an AD-like FDG-PET pattern observed at baseline in MCI patients had a sensitivity of 89% and a specificity of 85% in distinguishing converters from stable subjects within a follow-up ranging from 12 to 37 months [33]. However, several MCI patients do not have amnestic symptoms. The few CBF-SPECT and FDG-PET studies that considered amnestic and non-amnestic MCI patients separately, provided evidence for a high variability in non-amnestic subjects [69,76,77,86]. A large multicentre study examining FDG-PET scans from 114 MCI subjects (amnestic and non-amnestic) found an AD-like PET pattern

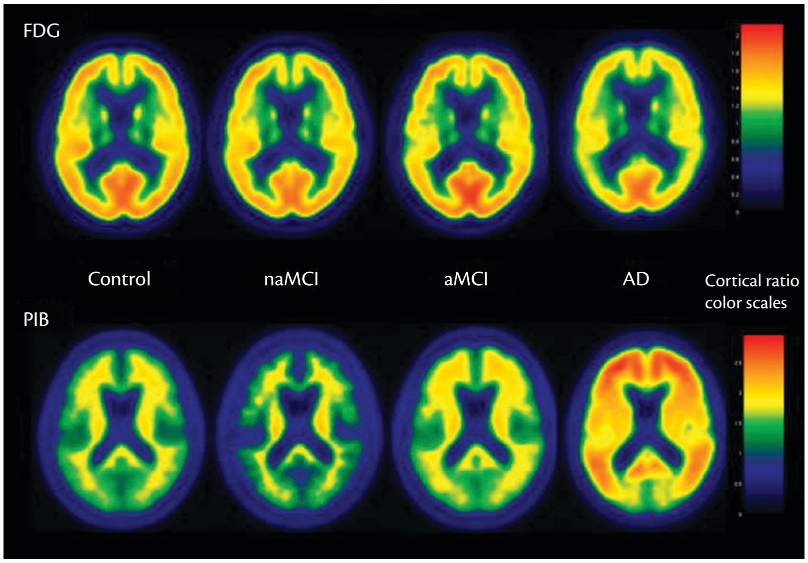

Fig. 18.6 Fluorine-18 (^{18}F)-2-fluoro-2-deoxy-D-glucose (FDG) and ^{11}C-labelled Pittsburgh Compound-B (^{11}C-PIB) positron emission tomography (PET) in amnestic (aMCI) and non-amnestic (naMCI) MCI relative to AD. FDG and PIB-PET images from controls, naMCI, aMCI, and AD subjects show a better visual separation of groups using PIB-PET scans. Scaling shown to right uses pons and cerebellar normalization, respectively. Regions with activity similar to these regions of normalization are coloured in 1.0 colour ranges (green), whereas regions with greater uptake show up in yellow and red. Colour scaling is slightly different for FDG and PIB-PET groups given different range of cortical ratios. Reproduced from Lowe VJ, Kemp BJ, Jack CR Jr, et al. (2009). Comparison of 18F-FDG and PiB PET in cognitive impairment. *Journal of Nuclear Medicine*, **50**, 878-86. Copyright (2009), with permission from the Journal of Nuclear Medicine

in 25% of subjects, and a dementia with Lewy bodies (DLB) or frontotemporal dementia (FTD)-like PET patterns in 10% of subjects [69] (see Chapters 20 and 19 for further details on DLB and FTD, respectively). An AD pattern was found in the majority (79%) of the MCI patients with deficits in multiple cognitive domains, frequently with additional frontal hypometabolism, and in 31% of amnestic MCI patients [69]. The remaining amnestic MCI patients showed primarily hypometabolism restricted to the hippocampus and posterior cingulate cortex [69]. Non-amnestic MCI patients showed more variable FDG-PET profiles, from no hypometabolism (9%) and isolated hippocampal deficits (18%), to distributed FDG uptake consistent with DLB (18%) or with AD and FTLD (9%) [69].

The value of functional imaging biomarkers might also differ in the setting of atypical, focal AD presentations, in which the topographical distribution of functional abnormalities needs to be considered separately in each syndrome. Only a few studies provide guidance about the degree of sensitivity and specificity of CBF-SPECT or FDG-PET in the diagnostic work up of atypical AD cases. A retrospective study of 94 patients with a clinical diagnosis of MCI or dementia (typical or atypical), who had a FDG-PET within 2 months of their diagnosis, showed that FDG-PET findings significantly lowered the number of atypical/unclear diagnoses from 39 to 16% [87]. Data from functional imaging studies demonstrate a comparable involvement of temporoparietal cortex and precuneus in PCA and typical AD, with extension of hypoperfusion or hypometabolism into occipital and posterior temporal lobes in PCA patients [88–92]. In addition to posterior regions, FDG-PET in PCA has indicated specific areas of hypometabolism in the frontal eye fields bilaterally, which can occur secondary to the loss of input from occipitoparietal regions and be the cause of oculomotor apraxia in these patients [88,90]. Logopenic PPA patients usually show a pattern of left posterior temporoparietal hypometabolism on FDG-PET scans [92–94].

Amyloid imaging

Amyloid imaging, such as ^{11}C-labelled Pittsburgh Compound-B (^{11}C-PIB) PET has very high (90% or greater) sensitivity for AD [95]. Use of ^{11}C-PIB PET has been limited to research centres because of the short half-life of the carbon-11 radiolabel (20 minutes). Aβ tracers labelled with fluorine-18 have subsequently been developed for clinical use (Fig. 18.7), with one recently approved by the US Food and Drug Administration [96]. Amyloid tracer binding is diffuse and symmetric, with high uptake consistently found in the prefrontal cortex, precuneus, and posterior cingulate cortex, followed by the lateral parietal, lateral temporal cortex, and striatum (Fig. 18.5 and 18.7). This pattern closely mirrors the distribution of plaques found at autopsy [97]. Early onset AD patients showed increased ^{11}C-PIB uptake throughout frontal, parietal and lateral temporal cortices, and striatum [64,98]. Of particular interest is the potential of PET amyloid imaging to differentiate mixed AD with cerebrovascular disease from pure AD or vascular dementia [99], and AD from FTD which is not associated with amyloid deposition [100,101]. See Chapters 17 and 19–21 for further details on the differential diagnosis of dementia using amyloid imaging.

As a group, 52–87% of MCI patients show elevated ^{11}C-PIB binding in a similar regional distribution to AD [102,103] (Fig. 18.6). Patients with amnestic MCI are more likely to be ^{11}C-PIB-positive than patients with non-amnestic presentations [103]. Studies using ^{18}F tracers report similar findings, with positive scans found in 45–60% of MCI patients [104–106]. In longitudinal studies, ^{11}C-PIB-positive subjects with MCI are significantly more likely to convert to AD than ^{11}C-PIB-negative patients [31,107–109],

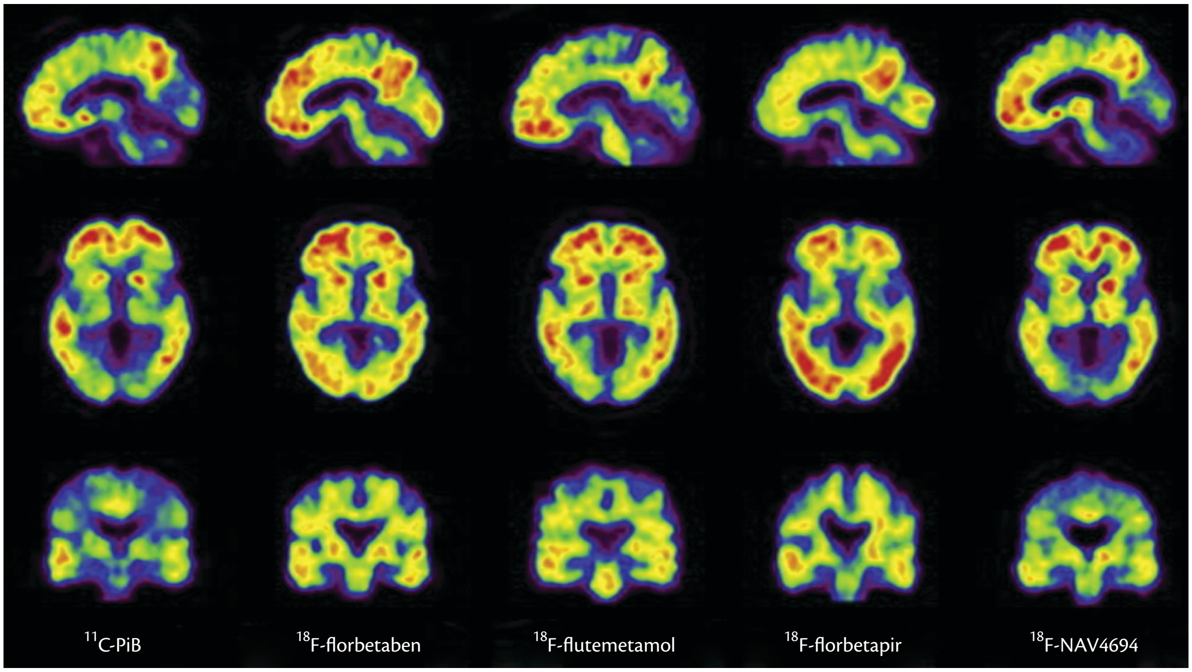

Fig. 18.7 Amyloid β (Aβ) imaging radiotracers in Alzheimer's disease (AD). Representative sagittal (top row), transaxial (middle row), and coronal (bottom row) positron emission tomography (PET) images from AD patients obtained with different Aβ imaging radiotracers. From left to right, ^{11}C-PIB, ^{18}F-florbetaben, ^{18}F-flutemetamol, ^{18}F-florbetapir, and ^{18}F-NAV4694 (previously named AZD4694). The images show the typical pattern of tracer retention in AD, with the highest retention in frontal, temporal, posterior parietal, and posterior cingulate cortices, reflecting Aβ plaque burden.

Reproduced from Rowe CC, and Villemagne VL. (2013). Amyloid imaging with PET in early Alzheimer disease diagnosis. *Medical Clinics of North America*, **97**, 377–98. Copyright (2013), with permission from Elsevier

with 1-year conversion rates to AD ranging from 38 to 47% in ^{11}C-PIB-positive MCI subjects versus virtually no conversion in ^{11}C-PIB-negative subjects [108,109]. Faster amnestic MCI converters have higher ^{11}C-PIB retention than slower converters in the anterior cingulate, frontal, and temporal cortices [108]. However, some healthy elderly controls show high ^{11}C-PIB binding. The frequency of increased cortical ^{11}C-PIB binding in controls increases rapidly from 10% or less below the age of 70 to 30–40% at the age of 80 years [110].

In vivo studies using ^{11}C-PIB PET in patients with an atypical clinical presentation of AD have reported greater PIB uptake in occipital cortex in PCA [67,111–113], and left temporoparietal regions in PPA [67] in single cases or in small series studies. However, larger studies have found no difference in PIB retention patterns in PCA or PPA compared with amnestic AD [91,93,100,114]. All showed diffuse ^{11}C-PIB uptake throughout frontal, temporoparietal, and occipital cortex [91,93,100,114].

Amyloid imaging is not yet recommended for routine use in the clinical setting, especially in the diagnostic work-up of patients with straightforward clinical AD, as these patients are very likely to have positive scans [1,115]. Amyloid imaging is likely to find clinical utility in the following fields (Box 18.1):

1. Stratification of MCI patients into those with and without underlying AD pathology.
2. Assessment of patients satisfying core clinical criteria for possible AD because of unclear clinical presentation, either an atypical clinical course or an aetiologically mixed presentation.
3. Evaluation of early onset patients, as these patients often present with atypical symptoms and are pathologically heterogeneous syndromes that are variably associated with AD pathology.

In addition, to date, only few studies have evaluated the effect of amyloid imaging on patient management and treatment in a clinical setting. In a recent decision, the US Centers for Medicare & Medicaid Services concluded that there are insufficient data that amyloid imaging affects clinical outcomes to justify reimbursing scans. A recent retrospective clinical study evaluated the effect of amyloid imaging on clinical decision making in an academic dementia centre [116], showing that discordant PIB-PET had a greater effect on diagnostic changes and treatment plan than discordant FDG-PET and influence on diagnosis is greater than on treatment.

Non-conventional magnetic resonance imaging

Hippocampus subfields

The wide availability of high-field MRI at 3 T and the increasing availability of ultra-high field MRI at 7 T rendered subfield measurements of the hippocampus a feasible diagnostic approach. Pathologic evidence suggests a selective vulnerability of hippocampal subfields in AD. Both manual volumetric and atlas-based automated measurements have been used to determine volumes of CA1 to CA4, dentate gyrus, and subiculum. In studies of a small

Box 18.1 Appropriate use criteria for amyloid positron emission tomography as defined by the Society of Nuclear Medicine and Molecular Imaging and the Alzheimer's Association joint Amyloid Imaging Task Force 2012

Amyloid imaging is appropriate in the situations listed here for individuals with all of the following characteristics:

- A cognitive complaint with objectively confirmed impairment;
- AD as a possible diagnosis, but when the diagnosis is uncertain after a comprehensive evaluation by a dementia expert.
- When knowledge of the presence or absence of amyloid β pathology is expected to increase diagnostic certainty and alter management.

Appropriate situations

- Patients with persistent or progressive unexplained MCI.
- Patients satisfying core clinical criteria for possible AD because of unclear clinical presentation, either an atypical clinical course or an aetiologically mixed presentation.
- Patients with progressive dementia and atypically early age of onset (usually defined as 65 years or less in age).

Inappropriate situations

- Patients with core clinical criteria for probable AD with typical age of onset.
- To determine dementia severity.
- Based solely on a positive family history of dementia or presence of apolipoprotein E ε4.
- Patients with a cognitive complaint that is unconfirmed on clinical examination.
- In lieu of genotyping for suspected autosomal mutation carriers.
- In asymptomatic individuals.
- Non-medical use (e.g. legal, insurance coverage, or employment screening).

Abbreviations: AD = Alzheimer's disease; MCI = mild cognitive impairment.

Reproduced from Johnson KA, Minoshima S, Bohnen NI, et al. (2013). Appropriate use criteria for amyloid PET: a report of the Amyloid Imaging Task Force, the Society of Nuclear Medicine and Molecular Imaging, and the Alzheimer's Association. *Alzheimer's & Dementia*, **9**, e-1–16. Copyright (2013), with permission from Elsevier.

number of subjects, the assessment of CA1 and CA2 using manual delineation [117], and CA2 to CA3 using automated delineation [118] was more accurate than total hippocampus volume in discriminating MCI subjects from controls. 7 T scanners provide access to even finer substructures of the hippocampus [119,120] (Fig. 18.8). The clinical relevance of these measures, however, is still unclear.

^{1}H-MRS

Proton magnetic resonance spectroscopic (^{1}H-MRS) studies have reported that the neuronal metabolite N-acetyl aspartate (NAA) is consistently decreased and the glial metabolite myo-inositol is increased in AD and amnestic MCI patients [121–126] compared with cognitively normal elderly. Post-mortem assessment of AD brains showed correlations between ^{1}H-MRS metabolites and density of neurofibrillary tangles and senile plaques in the tissue [127]. Ante mortem posterior cingulate gyrus NAA and myo-inositol levels correlate with the likelihood of post-mortem AD pathology at autopsy [128]. The NAA/myo-inositol ratio enabled the differentiation of patients with AD from cognitively healthy subjects with relatively high sensitivity (57–90%) and specificity (73–95%) [129–132]. Whilst these findings are robust on a group level, diagnostic value at an individual patient level is still suboptimal.

DT MRI

The loss of cortical neurons in AD is invariably accompanied by axonal degeneration along white matter pathways. Diffusion tensor magnetic resonance imaging (DT-MRI) studies in AD have found altered diffusion properties compared with controls in several white matter regions, especially in temporal and frontal lobes, posterior cingulum, and corpus callosum [133]. A posterior-to-anterior gradient in the severity of white matter abnormalities has been observed, with posterior regions being affected more severely [133] (Fig. 18.9). Early onset AD patients showed the most severe damage to the posterior fibres of cingulum and corpus callosum [134] (Fig. 18.9).

White matter abnormalities in AD generally follow the anatomical pattern of cortical atrophy [135]. Two recent meta-analyses showed that differences between amnestic MCI and controls parallel those between AD and controls, but fewer white matter regions reached statistical significance [133,136]. Interestingly, in patients with amnestic MCI, damage to the majority of white matter tracts was not correlated with cortical atrophy [135], thus suggesting that, in the early phases of the disease, white matter abnormalities may reflect primary white matter tract damage over and above cortical pathology. Similar findings have been reported in cognitively normal individuals who were later diagnosed with amnestic MCI at 2-year follow up [137]. White matter alterations at baseline in these subjects were predictive of subsequent cognitive decline, in the absence of significant correlation with cortical atrophy [137]. These studies suggest that microstructural white matter changes may serve as a potential imaging marker of early AD-related brain damage.

For DT MRI to be useful in the clinical setting, one must be able to make inferences at the level of the individual, rather than the group. Adding DT MRI measurements of the posterior cingulum to hippocampal volume significantly improves the accuracy in separating AD and amnestic MCI subjects from healthy controls (from 63 to 74% in amnestic MCI, and from 78 to 91% in AD) [138]. Diffusivity abnormalities of the left posterior cingulum were able to distinguish subjects with amnestic MCI from those with non-amnestic MCI with an accuracy of 85% [139]. In addition, hippocampal diffusivity measurements were found to be more sensitive than hippocampal volume in predicting

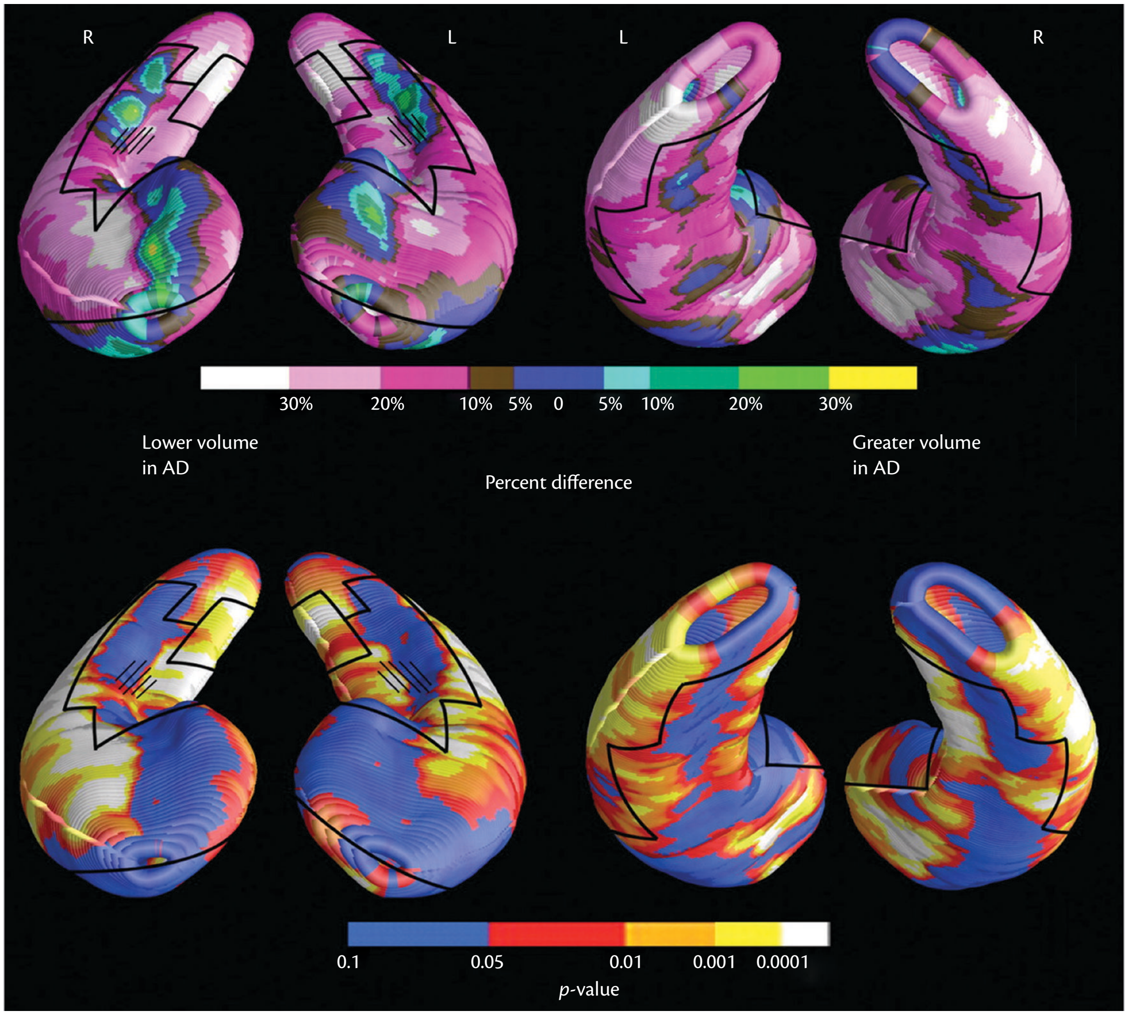

Fig. 18.8 Hippocampal subfields at 3T in normal aging and Alzheimer's disease (AD). Maps of the percentage and statistical differences of regional hippocampal volume between AD and healthy elderly controls. Hippocampal subfields are mapped on blank MR-based models of the hippocampal formation of a healthy subject.

Reproduced from Frisoni GB, Ganzola R, Canu E, et al. (2008). Mapping local hippocampal changes in Alzheimer's disease and normal ageing with MRI at 3 Tesla. *Brain*, **131**, 3266–76. Copyright (2008), with permission from Oxford University Press

conversion to AD in patients with amnestic MCI [140–142]. The severity of microstructural damage beyond the MTL was also associated with an increased short-term risk to develop AD in amnestic MCI patients [143]. A reduction of FA of the fornix has been recently proposed as an imaging sign that may be helpful in order to differentiate AD patients from normal controls with an accuracy of 75%, as well as to predict conversion from normal cognitive status to amnestic MCI and from amnestic MCI to AD (with an accuracy of 96% and 92%, respectively) [144]. An individual classification of MCI cases using support vector machine analysis of DTI data allowed for an individual classification with an accuracy up to 91% (healthy controls versus MCI) and 98% (stable versus progressive MCI at one year) [145]. Furthermore, such an approach resulted in a highly accurate individual classification of stable versus progressive MCI patients at one year, regardless of the MCI subtype. This indicates that it might become a tool for early detection of MCI subjects evolving to overt dementia [145].

Functional MRI

A number of investigators have examined brain activation patterns in dementia using functional MRI (fMRI), with complex results. Task-based fMRI studies have used episodic memory tasks in studying memory-related activation of the MTL. While several studies have shown increased activation in AD or MCI [146,147], others have shown a combination of increased activation in some regions and decreased activation in others [148]. Increased activations are often interpreted as evidence of compensatory processing, but whether this is true and what the nature of this compensation is, are unknown. In some cases, the degree of regional activation is correlated with cognitive performance [149,150].

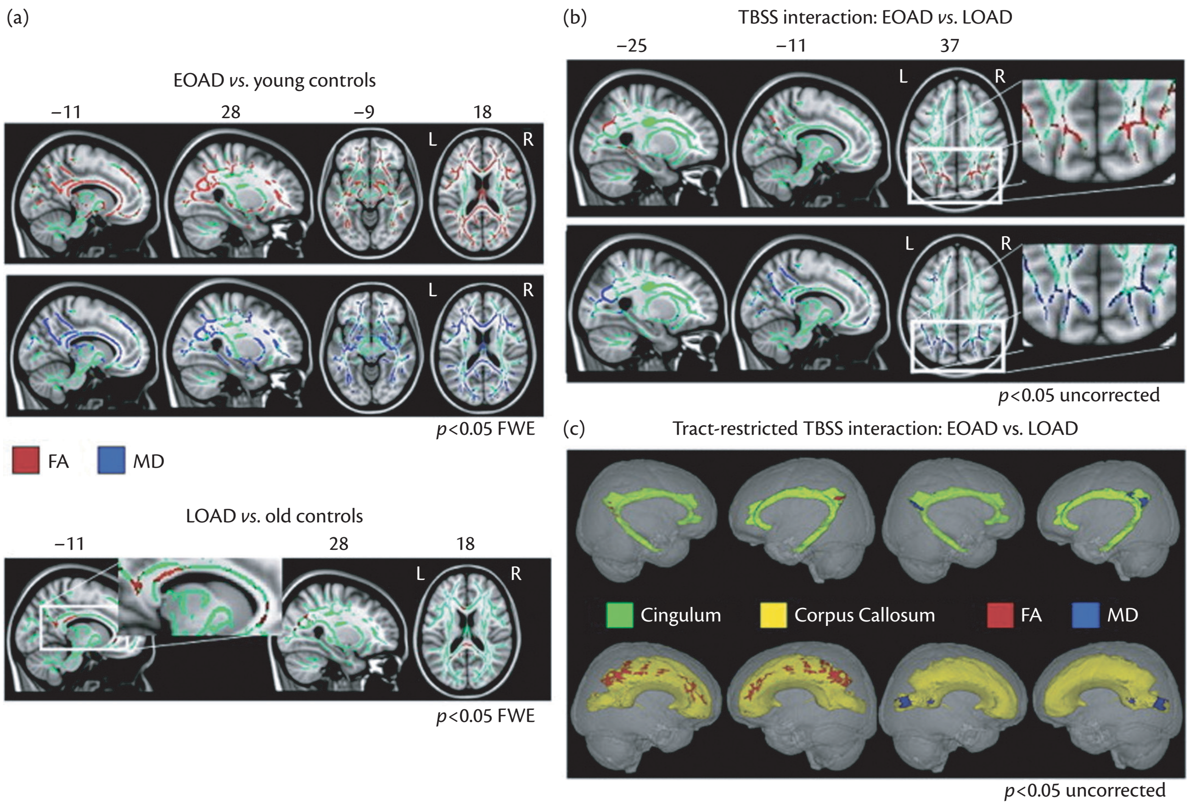

Fig. 18.9 Pattern of white matter tract damage in Alzheimer's disease (AD). Tract-based spatial statistics (TBSS) results in late onset and early onset AD patients versus age-matched healthy controls (a), and each other (b, interaction analysis). Voxel-wise group differences are shown in red (fractional anisotropy [FA]) and blue (mean diffusivity [MD]). Results are overlaid on the white matter skeleton (light green) and displayed on the sagittal and axial sections of the Montreal Neurological Institute (MNI) standard brain in neurological convention (right is right). (c) Tract-restricted TBSS results showing more severe damage of the cingulum and corpus callosum in EOAD versus LOAD patients (interaction analysis). Voxel-wise group differences are shown in red (FA) and blue (MD). Results are overlaid on the cingulum (light green) or corpus callosum (yellow) tractography maps.

Reproduced from Canu E, Frisoni GB, Agosta F, et al. (2013). Early and late onset Alzheimer's disease patients have distinct patterns of white matter damage. *Neurobiology of Aging*, **33**, 1023–33. Copyright (2013), with permission from Elsevier.

A substantial body of neuroimaging research in AD has focused on resting state fMRI, which is a promising new tool for the investigation of the intrinsic connectivity of brain networks in patient populations. The default mode network, which includes the posterior cingulate, inferior parietal, inferolateral temporal, ventral anterior cingulate, and hippocampal regions, has received the greatest attention, and has been shown to be dysfunctional in AD [151–154] and MCI [153,155–157] patients (Fig. 18.10). Sensitivity of RS fMRI measures in differentiating AD patients from healthy elderly controls ranges from 72 to 85% and specificity from 77 to 80% [151,158,159]. The impaired posteromedial cortex deactivation in amnestic MCI patients was also found to be predictive of clinical conversion to AD [160,161].

Concluding remarks

1. Structural imaging should be carried out at least once in the diagnostic work-up of patients suspected of having AD, and serves at least three purposes—to exclude other, potentially-treatable diseases; to recognize vascular lesions; and to identify specific findings in order to help distinguish AD from other forms of neurodegenerative dementia.
2. MRI is currently the imaging modality of choice for assessing subjects with suspected AD. T_1-weighted images should be carefully evaluated to assess specific patterns of focal atrophy, especially of the MTL, biparietal regions, and posterior cingulate cortex. However, in cases of atypical AD presentations, the involvement of the MTL is reported less consistently than that of lateral temporal and medial parietal regions.
3. Although typical cases of dementia may not benefit from routine CBF-SPECT or FDG-PET imaging, these tools are recommended in those cases where diagnosis remains in doubt after clinical and structural MRI work-up.
4. The overall regional pattern of metabolic impairment of the posterior cingulate/precuneus and lateral temporoparietal cortices, more accentuated than frontal cortex deficits, together with the relative preservation of the primary sensorimotor and visual cortices, basal ganglia, and cerebellum defines the distinct metabolic phenotype of AD.
5. Prediction of subsequent AD in individuals with amnestic MCI can be obtained with MRI volumetric measures of the MTL and FDG-PET.
6. Amyloid imaging is likely to find clinical utility in several fields, including the stratification of patients with mild cognitive

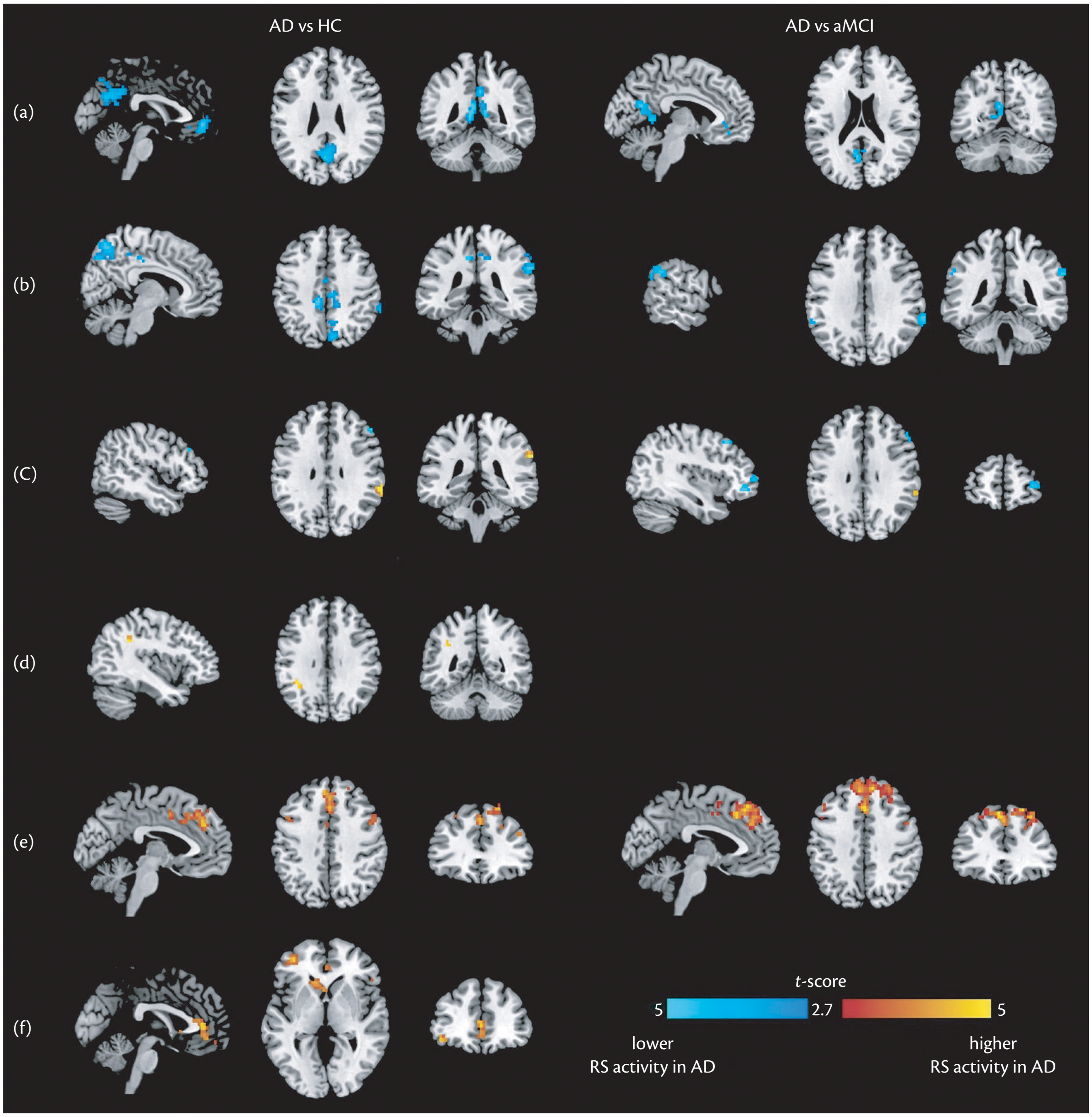

Fig. 18.10 Resting state functional MRI (fMRI) in Alzheimer's disease (AD) and amnestic mild cognitive impairment (aMCI). Contrasts of the resting state networks between (left columns) patients with AD and healthy controls (HC), and (right columns) patients with AD and patients with aMCI. (a,b) Default mode network (DMN I and II); (c) right fronto-parietal network; (d) left fronto-parietal network II; (e) executive network; and (f) ventral salience network. Colour maps represent significant voxels in the corresponding contrast. *t*-values are colour-coded with cyan to blue (from 2.7 to 5.0) = lower resting state fMRI signal in AD *vs* other groups, and red to yellow (from 2.7 to 5.0) = higher resting state fMRI signal in AD *vs*. other groups. Results are shown on the Montreal Neurological Institute standard brain, in neurological convention.

Reproduced from Agosta F, Pievani M, Geroldi C, et al. (2012). Resting state fMRI in Alzheimer's disease: beyond the default mode network. *Neurobiology of Aging*, **33**, 1564–78. Copyright (2012), with permission from Elsevier.

impairment into those with and without underlying AD and the evaluation of atypical AD presentations.

7. At present, advanced MRI techniques provide useful information on the pathophysiology of AD. Their role in the diagnosis, routine assessment, and monitoring of AD has yet to be fully explored.

References

1. Filippi M, Agosta F, Barkhof F, et al. (2012). EFNS task force: the use of neuroimaging in the diagnosis of dementia. *European Journal of Neurology*, **19**, e131–40, 1487–501.
2. Dubois B, Feldman HH, Jacova C, et al. (2007). Research criteria for the diagnosis of Alzheimer's disease: revising the NINCDS-ADRDA criteria. *Lancet Neurology*, **6**, 734–46.
3. Dubois B, Feldman HH, Jacova C, et al. (2010). Revising the definition of Alzheimer's disease: a new lexicon. *Lancet Neurology*, **9**, 1118–27.
4. Albert MS, DeKosky ST, Dickson D, et al. (2011). The diagnosis of mild cognitive impairment due to Alzheimer's disease: recommendations from the National Institute on Aging–Alzheimer's Association workgroups on diagnostic guidelines for Alzheimer's disease. *Alzheimer's & Dementia*, **7**, 270–9.
5. McKhann GM, Knopman DS, Chertkow H, et al. (2011). The diagnosis of dementia due to Alzheimer's disease: recommendations from the

National Institute on Aging–Alzheimer's Association workgroups on diagnostic guidelines for Alzheimer's disease. *Alzheimer's & Dementia*, **7**, 263–9.

6. Farina E, Pomati S, and Mariani C. (1999). Observations on dementias with possibly reversible symptoms. *Aging (Milano)*, **11**, 323–8.
7. Thompson PM, Hayashi KM, de Zubicaray G, et al. (2003). Dynamics of gray matter loss in Alzheimer's disease. *Journal of Neuroscience*, **23**, 994–1005.
8. Fox NC, Crum WR, Scahill RI, et al. (2001). Imaging of onset and progression of Alzheimer's disease with voxel-compression mapping of serial magnetic resonance images. *Lancet*, **358**, 201–5.
9. Thompson PM, Mega MS, Woods RP, et al. (2001). Cortical change in Alzheimer's disease detected with a disease-specific population-based brain atlas. *Cerebral Cortex*, **11**, 1–16.
10. Teipel SJ, Bayer W, Alexander GE, et al. (2002). Progression of corpus callosum atrophy in Alzheimer disease. *Archives of Neurology*, **59**, 243–8.
11. Gosche KM, Mortimer JA, Smith CD, et al. (2002). Hippocampal volume as an index of Alzheimer neuropathology: findings from the Nun Study. *Neurology*, **58**, 1476–82.
12. Csernansky JG, Hamstra J, Wang L, et al. (2004). Correlations between antemortem hippocampal volume and postmortem neuropathology in AD subjects. *Alzheimer Disease and Associated Disorders*, **18**, 190–5.
13. De Leon MJ, George AE, Golomb J, et al. (1997). Frequency of hippocampal formation atrophy in normal aging and Alzheimer's disease. *Neurobiology of Aging*, **18**, 1–11.
14. O'Brien JT, Metcalfe S, Swann A, et al. (2000). Medial temporal lobe width on CT scanning in Alzheimer's disease: comparison with vascular dementia, depression and dementia with Lewy bodies. *Dementia and Geriatric Cognitive Disorders*, **11**, 114–8.
15. Wattjes MP, Henneman WJ, van der Flier WM, et al. (2009). Diagnostic imaging of patients in a memory clinic: comparison of MR imaging and 64-detector row CT. *Radiology*, **253**, 174–83.
16. Scheltens P, Leys D, Barkhof F, et al. (1992). Atrophy of medial temporal lobes on MRI in 'probable' Alzheimer's disease and normal ageing: diagnostic value and neuropsychological correlates. *Journal of Neurology, Neurosurgery & Psychiatry*, **55**, 967–72.
17. Erkinjuntti T, Lee DH, Gao F, et al. (1993). Temporal lobe atrophy on magnetic resonance imaging in the diagnosis of early Alzheimer's disease. *Archives of Neurology*, **50**, 305–10.
18. Bresciani L, Rossi R, Testa C, et al. (2005). Visual assessment of medial temporal atrophy on MR films in Alzheimer's disease: comparison with volumetry. *Aging Clinical and Experimental Research*, **17**, 8–13.
19. Duara R, Loewenstein DA, Potter E, et al. (2008). Medial temporal lobe atrophy on MRI scans and the diagnosis of Alzheimer disease. *Neurology*, **71**, 1986–92.
20. Ridha BH, Barnes J, van de Pol LA, et al. (2007). Application of automated medial temporal lobe atrophy scale to Alzheimer disease. *Archives of Neurology*, **64**, 849–54.
21. Frisoni GB and Jack CR (2011). Harmonization of magnetic resonance-based manual hippocampal segmentation: a mandatory step for wide clinical use. *Alzheimer's & Dementia*, **7**, 171–4.
22. Chetelat G, Landeau B, Eustache F, et al. (2005). Using voxel-based morphometry to map the structural changes associated with rapid conversion in MCI: a longitudinal MRI study. *NeuroImage*, **27**, 934–46.
23. Bozzali M, Filippi M, Magnani G, et al. (2006). The contribution of voxel-based morphometry in staging patients with mild cognitive impairment. *Neurology*, **67**, 453–60.
24. Whitwell JL, Przybelski SA, Weigand SD, et al. (2007). 3D maps from multiple MRI illustrate changing atrophy patterns as subjects progress from mild cognitive impairment to Alzheimer's disease. *Brain*, **130**, 1777–86.
25. Pengas G, Hodges JR, Watson P, et al. (2010). Focal posterior cingulate atrophy in incipient Alzheimer's disease. *Neurobiology of Aging*, **31**, 25–33.
26. Scheltens P, Fox N, Barkhof F, et al. (2002). Structural magnetic resonance imaging in the practical assessment of dementia: beyond exclusion. *Lancet Neurology*, **1**, 13–21.
27. Shi F, Liu B, Zhou Y, et al. (2009). Hippocampal volume and asymmetry in mild cognitive impairment and Alzheimer's disease: meta-analyses of MRI studies. *Hippocampus*, **19**, 1055–64.
28. Jack CR, Jr., Petersen RC, Xu YC, et al. (1999). Prediction of AD with MRI-based hippocampal volume in mild cognitive impairment. *Neurology*, **52**, 1397–403.
29. Apostolova LG, Dutton RA, Dinov ID, et al. (2006). Conversion of mild cognitive impairment to Alzheimer disease predicted by hippocampal atrophy maps. *Archives of Neurology*, **63**, 693–9.
30. Desikan RS, Cabral HJ, Fischl B, et al. (2009). Temporoparietal MR imaging measures of atrophy in subjects with mild cognitive impairment that predict subsequent diagnosis of Alzheimer disease. *AJNR American Journal of Neuroradiology*, **30**, 532–8.
31. Jack CR, Jr, Wiste HJ, Vemuri P, et al. (2010). Brain beta-amyloid measures and magnetic resonance imaging atrophy both predict time-to-progression from mild cognitive impairment to Alzheimer's disease. *Brain*, **133**, 3336–48.
32. Prestia A, Caroli A, van der Flier WM; et al. (2013). Prediction of dementia in MCI patients based on core diagnostic markers for Alzheimer disease. *Neurology*, **80**, 1048–56.
33. Yuan Y, Gu ZX, and Wei WS. (2009). Fluorodeoxyglucose-positron-emission tomography, single-photon emission tomography, and structural MR imaging for prediction of rapid conversion to Alzheimer disease in patients with mild cognitive impairment: a meta-analysis. *AJNR American Journal of Neuroradiology*, **30**, 404–10.
34. Whitwell JL, Shiung MM, Przybelski SA et al. (2008). MRI patterns of atrophy associated with progression to AD in amnestic mild cognitive impairment. *Neurology*, **70**, 512–20.
35. Pa J, Boxer A, Chao LL, et al. (2009). Clinical-neuroimaging characteristics of dysexecutive mild cognitive impairment. *Annals of Neurology*, **65**, 414–23.
36. Misra C, Fan Y, and Davatzikos C. (2009). Baseline and longitudinal patterns of brain atrophy in MCI patients, and their use in prediction of short-term conversion to AD: results from ADNI. *NeuroImage*, **44**, 1415–22.
37. Kaye JA, Swihart T, Howieson D, et al. (1997). Volume loss of the hippocampus and temporal lobe in healthy elderly persons destined to develop dementia. *Neurology*, **48**, 1297–304.
38. Martin SB, Smith CD, Collins HR, et al. (2010). Evidence that volume of anterior medial temporal lobe is reduced in seniors destined for mild cognitive impairment. *Neurobiology of Aging*, **31**, 1099–106.
39. Smith CD, Chebrolu H, Weckstein DR, et al. (2007). Brain structural alterations before mild cognitive impairment. *Neurology*, **68**, 1268–73.
40. Barber R, Gholkar A, Scheltens P, et al. (1999). Medial temporal lobe atrophy on MRI in dementia with Lewy bodies. *Neurology*, **52**, 1153–8.
41. Bastos-Leite AJ, van der Flier WM, van Straaten EC, et al. (2007). The contribution of medial temporal lobe atrophy and vascular pathology to cognitive impairment in vascular dementia. *Stroke*, **38**, 3182–5.
42. Laakso MP, Partanen K, Riekkinen P, et al. (1996). Hippocampal volumes in Alzheimer's disease, Parkinson's disease with and without dementia, and in vascular dementia: an MRI study. *Neurology*, **46**, 678–81.
43. Chan D, Fox NC, Scahill RI, et al. (2001). Patterns of temporal lobe atrophy in semantic dementia and Alzheimer's disease. *Annals of Neurology*, **49**, 433–42.
44. van de Pol LA, Hensel A, van der Flier WM, et al. (2006). Hippocampal atrophy on MRI in frontotemporal lobar degeneration and Alzheimer's disease. *Journal of Neurology, Neurosurgery & Psychiatry*, **77**, 439–42.
45. Frisoni GB, Pievani M, Testa C, et al. (2007). The topography of grey matter involvement in early and late onset Alzheimer's disease. *Brain*, **130**, 720–30.
46. Canu E, Frisoni GB, Agosta F, et al. (2010). Early and late onset Alzheimer's disease patients have distinct patterns of white matter damage. *Neurobiology of Aging*, **33**(6), 1023–33.
47. van de Pol LA, Hensel A, Barkhof F, et al. (2006). Hippocampal atrophy in Alzheimer disease: age matters. *Neurology*, **66**, 236–8.

48. Koedam EL, Lehmann M, van der Flier WM, et al. (2011). Visual assessment of posterior atrophy development of a MRI rating scale. *European Radiology*, **21**, 2618–25.
49. Lehmann M, Koedam EL, Barnes J, et al. (2012). Posterior cerebral atrophy in the absence of medial temporal lobe atrophy in pathologically-confirmed Alzheimer's disease. *Neurobiology of Aging*, **33**, 627 e1–12.
50. Moller C, van der Flier WM, Versteeg A, et al. (2014). Quantitative regional validation of the visual rating scale for posterior cortical atrophy. *European Radiology*, **24**, 397–404.
51. Frisoni GB, Fox NC, Jack CR Jr, et al. (2010). The clinical use of structural MRI in Alzheimer disease. *Nature Reviews in Neurology*, **6**, 67–77.
52. Barnes J, Bartlett JW, van de Pol LA, et al. (2009). A meta-analysis of hippocampal atrophy rates in Alzheimer's disease. *Neurobiology of Aging*, **30**, 1711–23.
53. Geroldi C, Rossi R, Calvagna C, et al. (2006). Medial temporal atrophy but not memory deficit predicts progression to dementia in patients with mild cognitive impairment. *Journal of Neurology, Neurosurgery & Psychiatry*, **77**, 1219–22.
54. Jack CR, Jr., Shiung MM, Weigand SD, et al. (2005). Brain atrophy rates predict subsequent clinical conversion in normal elderly and amnestic MCI. *Neurology*, **65**, 1227–31.
55. Migliaccio R, Agosta F, Rascovsky K, et al. (2009). Clinical syndromes associated with posterior atrophy: early age at onset AD spectrum. *Neurology*, **73**, 1571–8.
56. Whitwell JL, Jack CR, Jr., Przybelski SA, et al. (2011). Temporoparietal atrophy: a marker of AD pathology independent of clinical diagnosis. *Neurobiology of Aging*, **32**, 1531–41.
57. Lehmann M, Rohrer JD, Clarkson MJ, et al. (2010). Reduced cortical thickness in the posterior cingulate gyrus is characteristic of both typical and atypical Alzheimer's disease. *Journal of Alzheimer's Disease*, **20**, 587–98.
58. Whitwell JL, Jack CR, Jr., Kantarci K, et al. (2007). Imaging correlates of posterior cortical atrophy. *Neurobiology of Aging*, **28**, 1051–61.
59. Gorno-Tempini ML, Brambati SM, Ginex V, et al. (2008). The logopenic/phonological variant of primary progressive aphasia. *Neurology*, **71**, 1227–34.
60. Bohnen NI, Djang DS, Herholz K, et al. (2012). Effectiveness and safety of 18F-FDG PET in the evaluation of dementia: a review of the recent literature. *Journal of Nuclear Medicine*, **53**, 59–71.
61. Minoshima S, Foster NL, Sima AA, et al. (2001). Alzheimer's disease versus dementia with Lewy bodies: cerebral metabolic distinction with autopsy confirmation. *Annals of Neurology*, **50**, 358–65.
62. Kemp PM, Holmes C, Hoffmann SM, et al. (2003). Alzheimer's disease: differences in technetium-99m HMPAO SPECT scan findings between early onset and late onset dementia. *Journal of Neurology, Neurosurgery & Psychiatry*, **74**, 715–9.
63. Kim EJ, Cho SS, Jeong Y, et al. (2005). Glucose metabolism in early onset versus late onset Alzheimer's disease: an SPM analysis of 120 patients. *Brain*, **128**, 1790–801.
64. Rabinovici GD, Furst AJ, Alkalay A, et al. (2010). Increased metabolic vulnerability in early-onset Alzheimer's disease is not related to amyloid burden. *Brain*, **133**, 512–28.
65. Herholz K, Schopphoff H, Schmidt M, et al. (2002). Direct comparison of spatially normalized PET and SPECT scans in Alzheimer's disease. *Journal of Nuclear Medicine*, **43**, 21–6.
66. Mosconi L, Tsui WH, Pupi A, et al. (2007). (18)F-FDG PET database of longitudinally confirmed healthy elderly individuals improves detection of mild cognitive impairment and Alzheimer's disease. *Journal of Nuclear Medicine*, **48**, 1129–34.
67. Ng S, Villemagne VL, Berlangieri S, et al. (2007). Visual assessment versus quantitative assessment of 11C-PIB PET and 18F-FDG PET for detection of Alzheimer's disease. *Journal of Nuclear Medicine*, **48**, 547–52.
68. Chen WP, Samuraki M, Yanase D, et al. (2008). Effect of sample size for normal database on diagnostic performance of brain FDG PET for the detection of Alzheimer's disease using automated image analysis. *Nuclear Medicine Communications*, **29**, 270–6.
69. Mosconi L, Tsui WH, Herholz K, et al. (2008). Multicenter standardized 18F-FDG PET diagnosis of mild cognitive impairment, Alzheimer's disease, and other dementias. *Journal of Nuclear Medicine*, **49**, 390–8.
70. McMurtray AM, Licht E, Yeo T, et al. (2008). Positron emission tomography facilitates diagnosis of early-onset Alzheimer's disease. *European Neurology*, **59**, 31–7.
71. Panegyres PK, Rogers JM, McCarthy M, et al. (2009). Fluorodeoxyglucose-positron emission tomography in the differential diagnosis of early-onset dementia: a prospective, community-based study. *BMC Neurology*, **9**, 41.
72. Silverman DH, Small GW, Chang CY, et al. (2001). Positron emission tomography in evaluation of dementia: Regional brain metabolism and long-term outcome. *Journal of the American Medical Association*, **286**, 2120–7.
73. Jagust W, Reed B, Mungas D, et al. (2007). What does fluorodeoxyglucose PET imaging add to a clinical diagnosis of dementia? *Neurology*, **69**, 871–7.
74. Foster NL, Heidebrink JL, Clark CM, et al. (2007). FDG-PET improves accuracy in distinguishing frontotemporal dementia and Alzheimer's disease. *Brain*, **130**, 2616–35.
75. Nestor PJ, Fryer TD, Smielewski P, et al. (2003). Limbic hypometabolism in Alzheimer's disease and mild cognitive impairment. *Annals of Neurology*, **54**, 343–51.
76. Mosconi L, De Santi S, Li Y, et al. (2006). Visual rating of medial temporal lobe metabolism in mild cognitive impairment and Alzheimer's disease using FDG-PET. *European Journal of Nuclear Medicine and Molecular Imaging*, **33**, 210–21.
77. Mosconi L, Tsui WH, De Santi S, et al. (2005). Reduced hippocampal metabolism in MCI and AD: automated FDG-PET image analysis. *Neurology*, **64**, 1860–7.
78. Minoshima S, Giordani B, Berent S, et al. (1997). Metabolic reduction in the posterior cingulate cortex in very early Alzheimer's disease. *Annals of Neurology*, **42**, 85–94.
79. Drzezga A, Lautenschlager N, Siebner H, et al. (2003). Cerebral metabolic changes accompanying conversion of mild cognitive impairment into Alzheimer's disease: a PET follow-up study. *European Journal of Nuclear Medicine and Molecular Imaging*, **30**, 1104–13.
80. Mosconi L, Perani D, Sorbi S, et al. (2004). MCI conversion to dementia and the APOE genotype: a prediction study with FDG-PET. *Neurology*, **63**, 2332–40.
81. Arnaiz E, Jelic V, Almkvist O, et al. (2001). Impaired cerebral glucose metabolism and cognitive functioning predict deterioration in mild cognitive impairment. *Neuroreport*, **12**, 851–5.
82. Anchisi D, Borroni B, Franceschi M, et al. (2005). Heterogeneity of brain glucose metabolism in mild cognitive impairment and clinical progression to Alzheimer disease. *Archives of Neurology*, **62**, 1728–33.
83. Landau SM, Harvey D, Madison CM, et al. (2010). Comparing predictors of conversion and decline in mild cognitive impairment. *Neurology*, **75**, 230–8.
84. Morbelli S, Piccardo A, Villavecchia G, et al. (2010). Mapping brain morphological and functional conversion patterns in amnestic MCI: a voxel-based MRI and FDG-PET study. *European Journal of Nuclear Medicine and Molecular Imaging*, **37**, 36–45.
85. Galluzzi S, Geroldi C, Amicucci G, et al. (2012). Supporting evidence for using biomarkers in the diagnosis of MCI due to AD. *Journal of Neurology*, **260**, 640–50.
86. Huang C, Wahlund LO, Almkvist O, et al. (2003). Voxel- and VOI-based analysis of SPECT CBF in relation to clinical and psychological heterogeneity of mild cognitive impairment. *NeuroImage*, **19**, 1137–44.
87. Laforce R, Jr., Buteau JP, Paquet N, et al. (2010). The value of PET in mild cognitive impairment, typical and atypical/unclear dementias: A retrospective memory clinic study. *American Journal of Alzheimer's Disease and Other Dementias*, **25**, 324–32.
88. Nestor PJ, Caine D, Fryer TD, et al. (2003). The topography of metabolic deficits in posterior cortical atrophy (the visual variant of Alzheimer's disease) with FDG-PET. *Journal of Neurology, Neurosurgery & Psychiatry*, **74**, 1521–9.

89. Schmidtke K, Hull M, and Talazko J. (2005). Posterior cortical atrophy: variant of Alzheimer's disease? A case series with PET findings. *Journal of Neurology*, **252**, 27–35.
90. Kas A, de Souza LC, Samri D, et al. (2011). Neural correlates of cognitive impairment in posterior cortical atrophy. *Brain*, **134**(Pt 5), 1464–78.
91. Rosenbloom MH, Alkalay A, Agarwal N, et al. (2011). Distinct clinical and metabolic deficits in PCA and AD are not related to amyloid distribution. *Neurology*, **76**, 1789–96.
92. Lehmann M, Ghosh PM, Madison C, et al. (2013). Diverging patterns of amyloid deposition and hypometabolism in clinical variants of probable Alzheimer's disease. *Brain*, **136**, 844–58.
93. Rabinovici GD, Jagust WJ, Furst AJ, et al. (2008). A beta amyloid and glucose metabolism in three variants of primary progressive aphasia. *Annals of Neurology*, **64**, 388–401.
94. Josephs KA, Duffy JR, Fossett TR, et al. (2010). Fluorodeoxyglucose F18 positron emission tomography in progressive apraxia of speech and primary progressive aphasia variants. *Archives of Neurology*, **67**, 596–605.
95. Herholz K, and Ebmeier K (2011). Clinical amyloid imaging in Alzheimer's disease. *Lancet Neurology*, **10**, 667–70.
96. Yang L, Rieves D, and Ganley C. (2012). Brain amyloid imaging—FDA approval of florbetapir F18 injection. *New England Journal of Medicine*, **367**, 885–7.
97. Braskie MN, Klunder AD, Hayashi KM, et al. (2008). Plaque and tangle imaging and cognition in normal aging and Alzheimer's disease. *Neurobiology of Aging*, **31**, 1669–78.
98. Ossenkoppele R, Zwan MD, Tolboom N, et al. (2012). Amyloid burden and metabolic function in early-onset Alzheimer's disease: parietal lobe involvement. *Brain*, **135**, 2115–25.
99. Lee JH, Kim SH, Kim GH, et al. (2011). Identification of pure subcortical vascular dementia using 11C-Pittsburgh compound B. *Neurology*, **77**, 18–25.
100. Leyton CE, Villemagne VL, Savage S, et al. (2011). Subtypes of progressive aphasia: application of the International Consensus Criteria and validation using beta-amyloid imaging. *Brain*, **134**, 3030–43.
101. Rabinovici GD, Rosen HJ, Alkalay A, et al. (2011). Amyloid vs FDG-PET in the differential diagnosis of AD and FTLD. *Neurology*, **77**, 2034–42.
102. Kemppainen NM, Aalto S, Wilson IA, et al. (2007). PET amyloid ligand [11C]PIB uptake is increased in mild cognitive impairment. *Neurology*, **68**, 1603–6.
103. Pike KE, Savage G, Villemagne VL, et al. (2007). Beta-amyloid imaging and memory in non-demented individuals: evidence for preclinical Alzheimer's disease. *Brain*, **130**, 2837–44.
104. Fleisher AS, Chen K, Liu X, et al. (2011). Using positron emission tomography and florbetapir F18 to image cortical amyloid in patients with mild cognitive impairment or dementia due to Alzheimer disease. *Archives of Neurology*, **68**, 1404–11.
105. Villemagne VL, Ong K, Mulligan RS, et al. (2011). Amyloid imaging with (18)F-florbetaben in Alzheimer disease and other dementias. *Journal of Nuclear Medicine*, **52**, 1210–7.
106. Vandenberghe R, Van Laere K, Ivanoiu A, et al. (2010). 18F-flutemetamol amyloid imaging in Alzheimer disease and mild cognitive impairment: a phase 2 trial. *Annals of Neurology*, **68**, 319–29.
107. Forsberg A, Engler H, Almkvist O, et al. (2008). PET imaging of amyloid deposition in patients with mild cognitive impairment. *Neurobiology of Aging*, **29**, 1456–65.
108. Okello A, Koivunen J, Edison P, et al. (2009). Conversion of amyloid positive and negative MCI to AD over 3 years: an 11C-PIB PET study. *Neurology*, **73**, 754–60.
109. Wolk DA, Price JC, Saxton JA, et al. (2009). Amyloid imaging in mild cognitive impairment subtypes. *Annals of Neurology*, **65**, 557–68.
110. Rowe CC, Ng S, Ackermann U, et al. (2007). Imaging beta-amyloid burden in aging and dementia. *Neurology*, **68**, 1718–25.
111. Formaglio M, Costes N, Sequin J, et al. (2011). In vivo demonstration of amyloid burden in posterior cortical atrophy: a case series with PET and CSF findings. *Journal of Neurology*, **258**, 1841–51.
112. Kambe T, Motoi Y, Ishii K, et al. (2010). Posterior cortical atrophy with [11C] Pittsburgh compound B accumulation in the primary visual cortex. *Journal of Neurology*, **257**, 469–71.
113. Tenovuo O, Kemppainen N, Aalto S, et al. (2008). Posterior cortical atrophy: a rare form of dementia with in vivo evidence of amyloid-beta accumulation. *Journal of Alzheimer's Disease*, **15**, 351–5.
114. de Souza LC, Corlier F, Habert MO, et al. (2011). Similar amyloid-beta burden in posterior cortical atrophy and Alzheimer's disease. *Brain*, **134**, 2036–43.
115. Johnson KA, Minoshima S, Bohnen NI, et al. (2013). Appropriate use criteria for amyloid PET: a report of the Amyloid Imaging Task Force, the Society of Nuclear Medicine and Molecular Imaging, and the Alzheimer's Association. *Alzheimer's & Dementia*, **9**, e-1–16.
116. Sanchez-Juan P, Ghosh PM, Hagen J, et al. (2014). Practical utility of amyloid and FDG-PET in an academic dementia center. *Neurology*, **82**, 230–8.
117. Mueller SG, and Weiner MW (2009). Selective effect of age, Apo e4, and Alzheimer's disease on hippocampal subfields. *Hippocampus*, **19**, 558–64.
118. Hanseeuw BJ, Van Leemput K, Kavec M, et al. (2011). Mild cognitive impairment: differential atrophy in the hippocampal subfields. *AJNR American Journal of Neuroradiology*, **32**, 1658–61.
119. Kerchner GA, Hess CP, Hammond-Rosenbluth KE, et al. (2010). Hippocampal CA1 apical neuropil atrophy in mild Alzheimer disease visualized with 7-T MRI. *Neurology*, **75**, 1381–7.
120. Kerchner GA, Deutsch GK, Zeineh M, et al. (2012). Hippocampal CA1 apical neuropil atrophy and memory performance in Alzheimer's disease. *NeuroImage*, **63**, 194–202.
121. Kantarci K, Jack CR, Jr., Xu YC, et al. (2000). Regional metabolic patterns in mild cognitive impairment and Alzheimer's disease: A 1H MRS study. *Neurology*, **55**, 210–7.
122. Kantarci K (2007). 1H magnetic resonance spectroscopy in dementia. *British Journal of Radiology*, **80**(Spec. Iss. 2), S146–52.
123. Kantarci K, Reynolds G, Petersen RC, et al. (2003). Proton MR spectroscopy in mild cognitive impairment and Alzheimer disease: comparison of 1.5 and 3 T. *AJNR American Journal of Neuroradiology*, **24**, 843–9.
124. Falini A, Bozzali M, Magnani G, et al. (2005). A whole brain MR spectroscopy study from patients with Alzheimer's disease and mild cognitive impairment. *NeuroImage*, **26**, 1159–63.
125. Wang Z, Zhao C, Yu L, et al. (2009). Regional metabolic changes in the hippocampus and posterior cingulate area detected with 3-Tesla magnetic resonance spectroscopy in patients with mild cognitive impairment and Alzheimer disease. *Acta Radiologica*, **50**, 312–9.
126. Chantal S, Braun CM, Bouchard RW, et al. (2004). Similar 1H magnetic resonance spectroscopic metabolic pattern in the medial temporal lobes of patients with mild cognitive impairment and Alzheimer disease. *Brain Research*, 1003, 26–35.
127. Klunk WE, Panchalingam K, Moossy J, et al. (1992). N-acetyl-L-aspartate and other amino acid metabolites in Alzheimer's disease brain: a preliminary proton nuclear magnetic resonance study. *Neurology*, **42**, 1578–85.
128. Kantarci K, Knopman DS, Dickson DW, et al. (2008). Alzheimer disease: postmortem neuropathologic correlates of antemortem 1H MR spectroscopy metabolite measurements. *Radiology*, **248**, 210–20.
129. Kantarci K, Xu Y, Shiung MM, et al. (2002). Comparative diagnostic utility of different MR modalities in mild cognitive impairment and Alzheimer's disease. *Dementia and Geriatric Cognitive Disorders*, **14**, 198–207.
130. Zhu X, Schuff N, Kornak J, et al. (2006). Effects of Alzheimer disease on fronto-parietal brain N-acetyl aspartate and myo-inositol using magnetic resonance spectroscopic imaging. *Alzheimer's Disease & Associated Disorders*, **20**, 77–85.

131. Martinez-Bisbal MC, Arana E, Martí-Bonmatí L, et al. (2004). Cognitive impairment: classification by 1H magnetic resonance spectroscopy. *European Journal of Neurology*, **11**, 187–93.
132. Fernandez A, Garcia-Segura JM, Ortiz T, et al. (2005). Proton magnetic resonance spectroscopy and magnetoencephalographic estimation of delta dipole density: a combination of techniques that may contribute to the diagnosis of Alzheimer's disease. *Dementia and Geriatric Cognitive Disorders*, **20**, 169–77.
133. Sexton CE, Kalu UG, Filippini N, et al. (2011). A meta-analysis of diffusion tensor imaging in mild cognitive impairment and Alzheimer's disease. *Neurobiology of Aging*, **32**, 2322 e5–18.
134. Canu E, Frisoni GB, Agosta F, et al. (2013). Early and late onset Alzheimer's disease patients have distinct patterns of white matter damage. *Neurobiology of Aging*, **33**, 1023–33.
135. Agosta F, Pievani M, Sala S, et al. (2011). White matter damage in Alzheimer disease and its relationship to gray matter atrophy. *Radiology*, **258**, 853–63.
136. Clerx L, Visser PJ, Verhey F, et al. (2012). New MRI markers for Alzheimer's disease: a meta-analysis of diffusion tensor imaging and a comparison with medial temporal lobe measurements. *Journal of Alzheimer's Disease*, **29**, 405–29.
137. Zhuang L, Sachdev PS, Trollor JN, et al. (2012). Microstructural white matter changes in cognitively normal individuals at risk of amnestic MCI. *Neurology*, **79**, 748–54.
138. Zhang Y, Schuff N, Jahng GH, et al. (2007). Diffusion tensor imaging of cingulum fibers in mild cognitive impairment and Alzheimer disease. *Neurology*, **68**, 13–9.
139. Chua TC, Wen W, Chen X, et al. (2009). Diffusion tensor imaging of the posterior cingulate is a useful biomarker of mild cognitive impairment. *American Journal of Geriatric Psychiatry*, **17**, 602–13.
140. Fellgiebel A, Dellani PR, Greverus D, et al. (2006). Predicting conversion to dementia in mild cognitive impairment by volumetric and diffusivity measurements of the hippocampus. *Psychiatry Research*, **146**, 283–7.
141. Kantarci K, Petersen RC, Boeve BF, et al. (2005). DWI predicts future progression to Alzheimer disease in amnestic mild cognitive impairment. *Neurology*, **64**, 902–4.
142. Muller MJ, Greverus D, Weibrich C, et al. (2007). Diagnostic utility of hippocampal size and mean diffusivity in amnestic MCI. *Neurobiology of Aging*, **28**, 398–403.
143. Scola E, Bozzali M, Agosta F, et al. (2010). A diffusion tensor MRI study of patients with MCI and AD with a 2-year clinical follow-up. *Journal of Neurology, Neurosurgery & Psychiatry*, **81**, 798–805.
144. Oishi K, Mielke MM, Albert M, et al. (2012). The fornix sign: a potential sign for Alzheimer's disease based on diffusion tensor imaging. *Journal of Neuroimaging*, **22**, 365–74.
145. Haller S, Nguyen D, Rodriguez C, et al. (2010). Individual prediction of cognitive decline in mild cognitive impairment using support vector machine-based analysis of diffusion tensor imaging data. *Journal of Alzheimer's Disease*, **22**, 315–27.
146. Saykin AJ, Flashman LA, et al. (1999). Neuroanatomic substrates of semantic memory impairment in Alzheimer's disease: patterns of functional MRI activation. *Journal of the International Neuropsychology Society*, **5**, 377–92.
147. Dickerson BC, Salat DH, Frutiger SA, et al. (2004). Medial temporal lobe function and structure in mild cognitive impairment. *Annals of Neurology*, **56**, 27–35.
148. Gron G, Bittner D, Schmitz B, et al. (2002). Subjective memory complaints: objective neural markers in patients with Alzheimer's disease and major depressive disorder. *Annals of Neurology*, **51**, 491–8.
149. Dickerson BC, Salat DH, Greve DN, et al. (2005). Increased hippocampal activation in mild cognitive impairment compared to normal aging and AD. *Neurology*, **65**, 404–11.
150. Diamond EL, Miller S, Dickerson BC, et al. (2007). Relationship of fMRI activation to clinical trial memory measures in Alzheimer disease. *Neurology*, **69**, 1331–41.
151. Greicius MD, Srivastava G, Reiss AL, et al. (2004). Default-mode network activity distinguishes Alzheimer's disease from healthy aging: evidence from functional MRI. *Proceedings of the National Academy of Sciences, USA*, **101**, 4637–42.
152. Zhang HY, Wang SJ, Liu B, et al. (2010). Resting brain connectivity: changes during the progress of Alzheimer disease. *Radiology*, **256**, 598–606.
153. Agosta F, Pievani M,Geroldi C, et al. (2012). Resting state fMRI in Alzheimer's disease: beyond the default mode network. *Neurobiology of Aging*, **33**, 1564–78.
154. Binnewijzend MA, Schoonheim MM, Sanz-Arigita E, et al. (2011). Resting-state fMRI changes in Alzheimer's disease and mild cognitive impairment. *Neurobiology of Aging*, **33**(9), 2018–28.
155. Qi Z, Wu X, Wang Z, et al. (2010). Impairment and compensation coexist in amnestic MCI default mode network. *NeuroImage*, **50**, 48–55.
156. Sorg C, Riedl V, Mühlau M, et al. (2007). Selective changes of resting-state networks in individuals at risk for Alzheimer's disease. *Proceedings of the National Academy of Sciences, USA*, **104**, 18760–5.
157. Wang J, Zuo X, Dai Z, et al. (2013). Disrupted functional brain connectome in individuals at risk for Alzheimer's disease. *Biological Psychiatry*, **73**, 472–81.
158. Li SJ, Li Z, Wu G, et al. (2002). Alzheimer disease: evaluation of a functional MR imaging index as a marker. *Radiology*, **225**, 253–9.
159. Supekar K, Menon V, Rubin D, et al. (2008). Network analysis of intrinsic functional brain connectivity in Alzheimer's disease. *PLoS Computer Biology*, **4**, e1000100.
160. Petrella JR, Prince SE, Wang L, et al. (2007). Prognostic value of posteromedial cortex deactivation in mild cognitive impairment. *PLoS ONE*, **2**, e1104.
161. Petrella JR, Sheldon FC, Prince SE, et al. (2011). Default mode network connectivity in stable vs progressive mild cognitive impairment. *Neurology*, **76**, 511–7.
162. Klunk WE, Engler H, Nordberg A, et al. (2004). Imaging brain amyloid in Alzheimer's disease with Pittsburgh Compound-B. *Annals of Neurology*, **55**, 306–19.
163. Lowe VJ, Kemp BJ, Jack CR Jr, et al. (2009). Comparison of 18F-FDG and PiB PET in cognitive impairment. *Journal of Nuclear Medicine*, **50**, 878–86.
164. Rowe CC, and Villemagne VL (2013). Amyloid imaging with PET in early Alzheimer disease diagnosis. *Medical Clinics of North America*, **97**, 377–98.
165. Frisoni GB, Ganzola R, Canu E, et al. (2008). Mapping local hippocampal changes in Alzheimer's disease and normal ageing with MRI at 3 Tesla. *Brain*, **131**, 3266–76.

CHAPTER 19

Frontotemporal lobar degeneration

Massimo Filippi and Federica Agosta

Introduction

Frontotemporal lobar degeneration (FTLD) represents the second most common early onset neurodegenerative dementia. FTLD is a pathologically heterogeneous spectrum of disorders, which encompasses distinct clinical syndromes, including the behavioural variant of frontotemporal dementia (bvFTD) and the language variant. bvFTD presents with marked changes in personality and behaviour [1], and pathologically is associated with all the three major FTLD pathologies, characterized by abnormal cellular inclusions containing either tau, TAR DNA-binding protein 43 (TDP-43), or fused in sarcoma (FUS) protein [2]. In the language variant known as primary progressive aphasia (PPA), a prominent, isolated language deficit is the dominant feature during the initial phase of the disease [3]. Distinct profiles of language impairment define the three clinical phenotypes of PPA [4]:

1. The non-fluent/agrammatic (for convenience hereafter called non-fluent), characterized by agrammatism in language production and effortful speech with motor speech deficits.
2. The semantic, characterized by a progressive loss of knowledge about words and objects in the context of relatively preserved fluency of speech.
3. The logopenic, characterized by impaired naming and repetition in the context of spared syntactic and motor speech abilities.

The non-fluent variant is most commonly associated with tau pathology [5,6], and the semantic with a TDP-43 proteinopathy [7–9]. The logopenic variant is mainly caused by Alzheimer's pathology, rather than FTLD pathology [9,10] and is discussed in detail in Chapter 18.

In the last few years, neuroimaging has contributed to the phenotypic characterization of frontotemporal dementia (FTD). The most commonly used neuroimaging approaches to assess FTD are structural magnetic resonance imaging (MRI) and functional molecular techniques, i.e. single photon emission computed tomography (SPECT) and positron emission tomography (PET). The designation of probable bvFTD by the revised diagnostic criteria [11] restricts diagnosis to patients with demonstrable functional decline and typical neuroimaging findings, including frontal and/or temporal atrophy, and hypoperfusion or hypometabolism on PET or SPECT (Box 19.1). Similarly, in patients clinically diagnosed with PPA, an 'imaging-supported' diagnosis can be made for each subtype if the expected pattern of focal atrophy on structural MRI scans or functional involvement on SPECT and [^{18}F]-2-fluoro-2-deoxy-D-glucose (FDG) is found (Box 19.2) [4].

Recent years have also witnessed impressive advances in the development of novel imaging approaches that, with varying degrees of success, have improved the ability to understand the pathophysiology of the disease. Alterations in the brain microstructure associated with FTD have the potential to modify water diffusion characteristics, which can be measured using diffusion tensor (DT) MRI. The ability to image amyloid β (Aβ) using new PET ligands may allow distinction of FTD from AD with a greater accuracy than that of other structural and functional imaging techniques. Functional MRI (fMRI) is likely to be a useful tool for detecting alterations in brain function that may be present very early in the course of FTLD. In particular, resting state (RS) functional MRI (fMRI) allows the characterization of low-frequency, spontaneous fluctuations of blood oxygenation level-dependent signals across the brain that are organized into distinct, tightly correlated functional-anatomic networks, some of which are typically disrupted in this condition.

This chapter reviews the state-of-the-art of neuroimaging in the study of FTD spectrum of disorders, and envisages which of them will be novel neuroimaging markers that have the potential to improve *in vivo* detection of the underlying pathology. This will be central in the design of treatment trials of new drugs targeting the pathological processes associated with FTD, which are likely to emerge in the near future. In this chapter, the term FTLD will be used to indicate cases with a pathological diagnosis, while the term FTD will be used to refer to the clinical syndrome.

Atrophy patterns

bvFTD

Structural MRI studies showed that classical bvFTD presents with a combination of medial frontal, orbital-insular, and anterior temporal cortical atrophy [12–19], mostly on the right hemisphere (Fig. 19.1a and 19.2). Such an atrophy pattern can be readily appreciated on coronal T_1-weighted MRI scans (knife-edge atrophy) (Fig. 19.1a). The medial temporal lobe (MTL) is more affected anteriorly, i.e. the amygdala is more damaged than the hippocampus and posterior hippocampus often appears normal. Brain atrophy in bvFTD also involves several subcortical structures, such as the striatum [13,16,20], thalamus [16,20,21], bilaterally, and hypothalamus [22]

Box 19.1 International consensus criteria for behavioural variant of frontotemporal dementia

I. Neurodegenerative disease

The following symptom must be present to meet criteria for bvFTD:

Shows progressive deterioration of behaviour and/or cognition by observation or history (as provided by a knowledgeable informant).

II. Possible bvFTD

Three of the following behavioural/cognitive symptoms (A–F) must be present to meet criteria. Ascertainment requires that symptoms be persistent or recurrent, rather than single or rare events.

A.Early behavioural disinhibition [one of the following symptoms (A.1–A.3) must be present]:

A.1. Socially inappropriate behaviour.

A.2. Loss of manners or decorum.

A.3. Impulsive, rash or careless actions.

B.Early apathy or inertia [one of the following symptoms (B.1–B.2) must be present]:

B.1. Apathy.

B.2. Inertia.

C.Early loss of sympathy or empathy [one of the following symptoms (C.1–C.2) must be present]:

C.1. Diminished response to other people's needs and feelings.

C.2. Diminished social interest, interrelatedness or personal warmth.

D.Early perseverative, stereotype, or compulsive/ritualistic behaviour [one of the following symptoms (D.1–D.3) must be present]:

D.1. Simple repetitive movements.

D.2. Complex, compulsive or ritualistic behaviours.

D.3. Stereotypy of speech.

E.Hyperorality and dietary changes [one of the following symptoms (E.1–E.3) must be present]:

E.1. Altered food preferences.

E.2. Binge eating, increased consumption of alcohol or cigarettes.

E.3. Oral exploration or consumption of inedible objects.

F.Neuropsychological profile: executive/generation deficits with relative sparing of memory and visuospatial functions [all of the following symptoms (F.1–F.3) must be present]:

F.1. Deficits in executive tasks.

F.2. Relative sparing of episodic memory.

F.3. Relative sparing of visuospatial skills.

III. Probable bvFTD

All of the following symptoms (A–C) must be present to meet criteria:

A.Meets criteria for possible bvFTD.

B.Exhibits significant functional decline (by caregiver report or as evidenced by Clinical Dementia Rating Scale or Functional Activities Questionnaire scores).

C.Imaging results consistent with bvFTD [one of the following (C.1–C.2) must be present]:

C.1. Frontal and/or anterior temporal atrophy on MRI or CT.

C.2. Frontal and/or anterior temporal hypoperfusion/hypometabolism on PET/SPECT.

IV. Behavioural variant FTD with definite FTLD pathology

Criterion A and either criterion B or C must be present to meet criteria:

A.Meets criteria for possible or probable bvFTD.

B.Histopathological evidence of FTLD on biopsy or at post-mortem.

C.Presence of a known pathogenic mutation.

V. Exclusionary criteria for bvFTD

Criteria A and B must be answered negatively for any bvFTD diagnosis. Criterion C can be positive for possible bvFTD, but must be negative for probable bvFTD:

A.Pattern of deficits is better accounted for by other non-degenerative nervous system or medical disorders.

B.Behavioural disturbance is better accounted for by a psychiatric diagnosis.

C.Biomarkers strongly indicative of AD or other neurodegenerative process.

Abbreviations: Abbreviations: AD, Alzheimer disease; bvFTD, behavioural variant of frontotemporal dementia; FTLD, frontotemporal lobar degeneration.

Reproduced from Rascovsky K, Hodges JR, Knopman D, et al. (2011). Sensitivity of revised diagnostic criteria for the behavioural variant of frontotemporal dementia. *Brain*, **134**, 2456–77. Copyright (2011), with permission from Oxford University Press

(Fig. 19.2). Significant atrophy has also been found in the brainstem, including the midbrain and pontine tegmentum in some cases [16,23,24].

Atrophy in bvFTD has been shown to be progressive [25–29] and faster compared with Alzheimer's disease (AD) cases [25,27]. In a cross-sectional voxel-based morphometry (VBM) study, patients with bvFTD were stratified based on their clinical dementia rating (CDR) score and atrophy patterns were determined at the different clinical stages [16]. Patients with mild dementia severity (CDR = 0.5) showed circumscribed gray matter (GM) atrophy in anterior brain regions, including paralimbic (anterior cingulate cortex, fronto-insula, and lateral orbitofrontal cortex), frontal neocortical (dorsolateral, rostromedial, and frontal polar), limbic (hippocampus), and subcortical (ventral striatum and dorsomedial thalamus) areas, as well as the precentral gyrus, with a predominant

Box 19.2 Diagnostic criteria for the non-fluent and semantic variants of primary progressive aphasia

Non-fluent/agrammatic variant PPA

I. Clinical diagnosis of non-fluent/agrammatic variant PPA

At least one of the following core features must be present:

1. Agrammatism in language production.
2. Effortful, halting speech with inconsistent speech sound errors and distortions (apraxia of speech).

At least 2 of 3 of the following other features must be present:

1. Impaired comprehension of syntactically complex sentences.
2. Spared single-word comprehension.
3. Spared object knowledge.

II. Imaging-supported non-fluent/agrammatic variant diagnosis

Both of the following criteria must be present:

1. Clinical diagnosis of non-fluent/agrammatic variant PPA.
2. Imaging must show one or more of the following results:
   a. Predominant left posterior fronto-insular atrophy on MRI; or
   b. Predominant left posterior fronto-insular hypoperfusion or hypometabolism on SPECT or PET.

III. Non-fluent/agrammatic variant PPA with definite pathology

Clinical diagnosis (criterion 1 below) and either criterion 2 or 3 must be present:

1. Clinical diagnosis of non-fluent/agrammatic variant PPA.
2. Histopathologic evidence of a specific neurodegenerative pathology (e.g. FTLD-tau, FTLD-TDP, AD, other).
3. Presence of a known pathogenic mutation.

Semantic variant PPA

I. Clinical diagnosis of semantic variant PPA

Both of the following core features must be present:

1. Impaired confrontation naming.
2. Impaired single-word comprehension.

At least three of the following other diagnostic features must be present:

1. Impaired object knowledge, particularly for low frequency or low-familiarity items.
2. Surface dyslexia or dysgraphia.
3. Spared repetition.
4. Spared speech production (grammar and motor speech).

II. Imaging-supported semantic variant PPA diagnosis

Both of the following criteria must be present:

1. Clinical diagnosis of semantic variant PPA.
2. Imaging must show one or more of the following results:
   a. Predominant anterior temporal lobe atrophy.
   b. Predominant anterior temporal hypoperfusion or hypometabolism on SPECT or PET.

III. Semantic variant PPA with definite pathology

Clinical diagnosis (criterion 1 below) and either criterion 2 or 3 must be present:

1. Clinical diagnosis of semantic variant PPA.
2. Histopathologic evidence of a specific neurodegenerative pathology (e.g. FTLD-tau, FTLD.TDP, AD, other).
3. Presence of a known pathogenic mutation.

Abbreviations: Abbreviations: AD, Alzheimer disease; FTLD, frontotemporal lobar degeneration; PPA, primary progressive aphasia.

Reproduced from Gorno-Tempini ML, Hillis AE, Weintraub S, et al. (2011). Classification of primary progressive aphasia and its variants. *Neurology*, **76**, 1006–14. Copyright (2011), with permission from Wolters Kluwer Health

involvement of the right hemisphere. At CDR = 0.5, white matter (WM) loss was minimal, with only small subfrontal and basal pontine foci detected. In patients with a CDR score of 1, GM atrophy was more extensive and bilateral, involving most of the medial frontal surface, dorsolateral frontal regions, and striatal-thalamic structures. WM loss involved the subfrontal, parahippocampal, and mid-callosal regions, and cerebral peduncles. In patients with CDR scores of 2 or 3, which indicate moderate and severe dementia, respectively, GM of the frontal lobe was markedly involved, as well as the posterior insula, posterior hippocampus, and parietal lobes, bilaterally. In these stages, tissue loss affected the entire corpus callosum, as well as several cortical regions (including parahippocampal areas and parietal lobes). Longitudinal studies showed that the greatest rates of atrophy in bvFTD is observed in the frontal lobe [30,31], particularly the medial frontal cortex [32].

BvFTD is pathologically heterogeneous. The typical frontotemporal pattern is not necessarily present in all cases [33–35], particularly in patients with FTD and motor neuron disease (MND), and the pattern of atrophy in bvFTD varies significantly across different cohorts [36,37]. In some cases, bvFTD presents with a remarkable atrophy of the right anterior temporal lobe and a less severe involvement of the frontal regions [18,38]. A large VBM study using cluster analysis suggested that bvFTD may be divided into four separate neuroanatomical groups, two of which are associated with a prominent frontal atrophy (i.e. frontal dominant and frontotemporal variants) and two with prominent temporal lobe atrophy (i.e. temporal dominant, and temporo-frontoparietal subtypes) (Fig. 19.3) [18].

In addition to these anatomical variants, it has also been recognized that some bvFTD patients do not show any observable atrophy on MRI, despite presenting with the clinical features of bvFTD [39,40]. These subjects have been referred to as having a bvFTD ‘phenocopy syndrome’ and tend to progress very slowly clinically. Some of these subjects may not have an underlying FTLD pathology and instead may be a psychiatric phenocopy [41].

Despite variation and overlap of atrophy patterns, visual inspection of regional atrophy on MRI may aid in discriminating FTD from AD. Several studies comparing FTD and typical AD

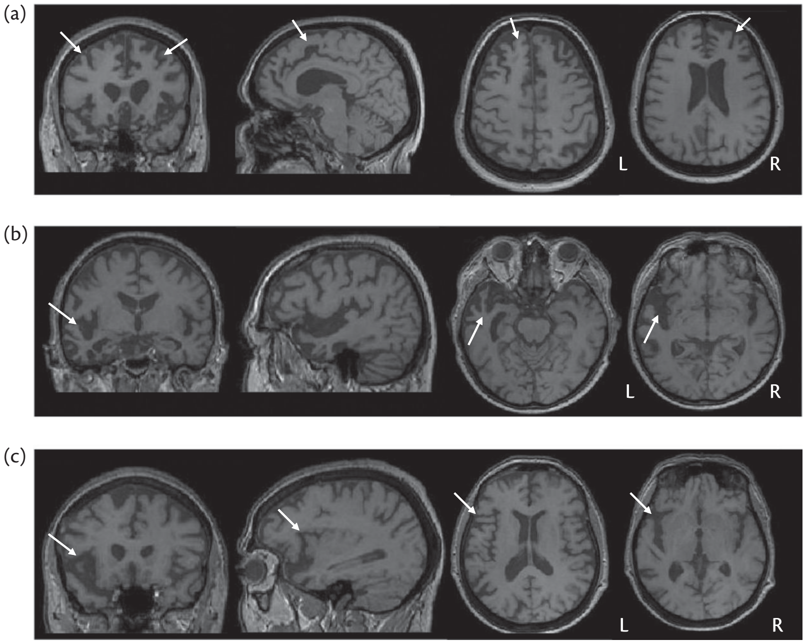

Fig. 19.1 T_1-weighted MRI scans showing the typical brain atrophy patterns of the bvFTD and each PPA variant. (a) A typical bvFTD patient, aged 49 years. The arrows show atrophy of the medial and dorsolateral frontal cortices. (b) A semantic PPA patient, aged 66 years. The arrow shows left-lateralized atrophy of the anterior temporal lobe. (c) A patient with the non-fluent PPA variant, aged 63 years. The arrows show asymmetric left-lateralized atrophy of the insula and inferior frontal gyrus.

Modified from Agosta F, Canu E, Sarro L, et al. (2011). Neuroimaging findings in frontotemporal lobar degeneration spectrum of disorders. *Cortex*, **48**, 389–413. Copyright (2011), with permission from Elsevier.

cases have shown that FTD is associated with a greater frontal insular-cingulate and striatum atrophy, while AD is characterized by a more severe posterior parietal, precuneus, and occipital damage [42]. Diagnostic criteria based on finding of either severe frontal atrophy or asymmetry were highly diagnostic (sensitivity 71%, specificity 93%) of bvFTD compared with non-FTD dementia cases (i.e. AD and vascular dementia) [43]. In a study investigating the diagnostic accuracy of visual inspection of MRI scans in patients with pathologically-confirmed diagnosis, atrophy of the anterior, inferior, and lateral temporal lobes was associated

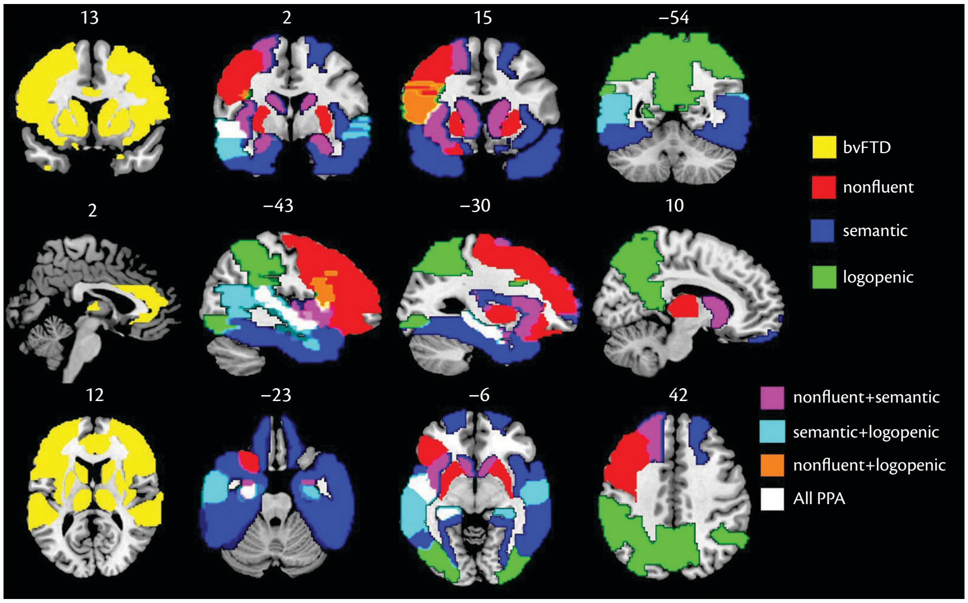

Fig. 19.2 An illustrative figure of the patterns of gray matter atrophy in patients with the bvFTD and each PPA variant, as derived from available literature. Regions of gray matter atrophy are overlaid on the sagittal, coronal and axial slices of the Montreal Neurological Institute template.

Modified from Agosta F, Canu E, Sarro L, et al. (2011). Neuroimaging findings in frontotemporal lobar degeneration spectrum of disorders. *Cortex*, **48**, 389–413. Copyright (2011), with permission from Elsevier.

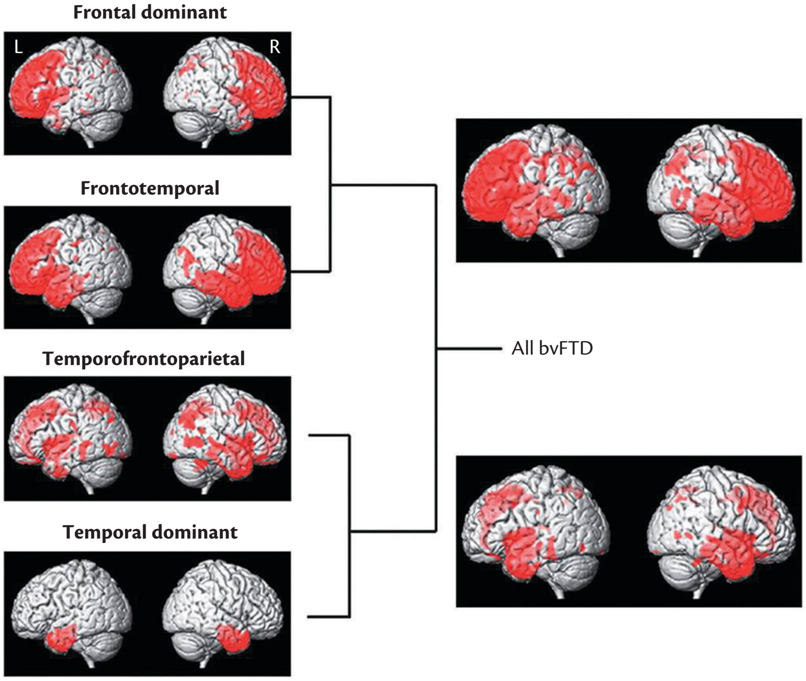

Fig. 19.3 Three-dimensional surface renderings showing patterns of cortical loss in each of the four subtypes of behavioural variant of frontotemporal dementia. The results are shown on a schematic version of the dendrogram in order to illustrate the relationship between patterns of atrophy and cluster position. Patterns of cortical loss are also shown at the level of the dendrogram when the bvFTD subjects are divided into two groups.

Reproduced from Whitwell JL, Przybelski SA, Weigand SD, et al. (2009). Distinct anatomical subtypes of the behaviour variant of frontotemporal dementia: a cluster analysis study. *Brain*, **132**, 2932–46. Copyright (2009), with permission from Oxford University Press.

with the highest sensitivity (≥90%) for discriminating FTLD from AD patients, and anterior greater than posterior gradient and hemispheric asymmetry of atrophy were each at least 85% specific for FTLD versus AD [44]. A prospective study of 134 patients with clinically-suspected bvFTD demonstrated that evidence of frontotemporal atrophy on structural MRI scans, in the absence of abnormalities in more posterior areas of the brain, had a sensitivity of 63% and specificity of 70% against a 2-year diagnosis based on clinical findings only [34]. Automated methods of classification using support vector machines have shown the ability to accurately differentiate typical AD and bvFTD with relatively high sensitivity and specificity [45,46]. Studies comparing bvFTD with more atypical phenotypes of AD have suggested that, independent of clinical phenotype, a cortical thinning of the anterior temporal and frontal lobes is indicative of the presence of FTLD pathology [47]. Conversely, a cortical thinning or atrophy of the posterior cingulate gyrus, parietal lobe, and frontal pole is suggestive of AD pathology independent of clinical presentations (i.e. even in patients with behavioural or language deficits) [47, 48].

Less commonly, bvFTD can be mistaken for dementia with Lewy bodies (DLB); this may well be because some patients with bvFTD clinical syndromes can develop delusions and/or visual hallucinations. One small study suggested that MRI is not helpful in differentiating bvFTD from DLB [49]. Another recent study has shown that an accurate differentiation between these two conditions can be reached using ^{123}I-MIBG scintigraphy in which uptake is markedly reduced in DLB, but normal in bvFTD [50].

Primary progressive aphasia

Semantic variant PPA is associated with anterior temporal atrophy (temporal pole) affecting the lateral and ventral temporal surfaces, as well as the anterior hippocampus, amygdala and fusiform gyrus [12,51–53] (Fig. 19.1b and 19.2). Semantic patients may have hippocampal atrophy that is at least as severe as that seen in AD patients [25,52,54,55]. In semantic patients, hippocampal atrophy is predominantly located anteriorly, with a relative preservation of the posterior regions [25,54]. Temporal lobe atrophy is also mainly inferior (often with a severe involvement of the fusiform gyrus) with a relative sparing of the superior temporal gyrus [25,54]. In the most common variant, there is left greater than right temporal lobe atrophy, with the opposite pattern seen less frequently [56]. As the disease progresses, a more severe atrophy of posterior and superior regions of the left temporal lobe, areas of the left frontal lobe (orbitofrontal, inferior frontal and cingulate gyri), and insula can be detected [57,58]. A similar pattern of tissue loss over time is observed in the right temporal lobe of these patients [57,58]. Patients with the semantic variant also experience temporal WM atrophy [24,59], which is predominant in the left temporal lobe and includes areas likely to represent the fornix, inferior longitudinal fasciculus (ILF), and uncinate fasciculus [59].

The non-fluent PPA variant is associated with a characteristic pattern of left anterior peri-sylvian atrophy involving inferior, opercular and insular portions of the frontal lobe [53,60] (Fig. 19.1c and 19.2). Motor and premotor regions, and Broca's area are also involved [53,60] (Fig. 19.1c and 19.2). In non-fluent PPA patients, bilateral atrophy of the basal ganglia [20,53], thalamus [20], and amygdala [20] has been observed (Fig. 19.2). Compared with controls, non-fluent patients also have atrophy of the left hippocampus

[61]; however, it is less severe than that in AD patients [61]. Although atrophy in non-fluent PPA is most prominent in the left inferior frontal regions, the left lateral temporal cortex, anterior parietal lobe and middle and superior regions of the frontal lobe are increasingly affected as language deficits worsen [57,60].

Atrophy patterns associated with genetic abnormalities

A high proportion of FTD subjects have familial disease with an autosomal dominant pattern of inheritance. A number of genetic mutations responsible for FTD have been identified, including mutations in the progranulin gene (*GRN*), the microtubule-associated protein tau (*MAPT*) gene, and the recently identified hexanucleotide repeat expansion in C9Orf72. Mutations in the *MAPT* gene and the C9Orf72 repeat expansion are more frequently associated with bvFTD, while semantic PPA is often associated with *MAPT* mutations. The clinical phenotypes associated with *GRN* mutations are more diverse, and include bvFTD and non-fluent PPA, as well as corticobasal syndrome.

There are relatively few detailed neuroimaging studies in genetic FTD showing different patterns of atrophy associated with the different gene mutations (Fig. 19.4). *GRN* mutations are more likely to show strongly asymmetrical atrophy affecting either the left or right hemispheres, and involving the inferior frontal, temporal, and inferior parietal lobes [62–64]. *MAPT* mutations are associated with a more symmetrical pattern of atrophy localized predominantly to the anterior temporal lobes and involving orbitofrontal cortices and fornix [62,63,65]. GRN mutations are also associated with faster rates of brain atrophy than MAPT mutations. The pattern of atrophy associated with the C9Orf72 repeat expansion has only recently been assessed, with some variability across studies. Most studies have found that this genetic abnormality is associated with relatively symmetric patterns of atrophy, mostly in the frontal lobes [36,37,66], with an unusual and characteristic atrophy observed in the cerebellum [36,37]. Cortical atrophy is, however, widespread, with a severe involvement of the posterior regions, in addition to the frontal lobes [37,66]. Patients with *GRN* and *MAPT* gene mutations tend to show a greater atrophy of the temporal lobes compared with those carrying the C9Orf72 repeat expansion [36,37]. In addition, longitudinal studies found that *GRN* mutations are associated with faster rates of whole brain atrophy than *MAPT* mutations [63] and the C9Orf72 repeat expansion [36].

Atrophy patterns associated with FTLD pathologies

MRI studies that have assessed autopsy-confirmed cases have demonstrated specific anatomical signatures associated with the different FTLD pathologies, independent of the clinical syndromes (Fig. 19.4).

Two common tau pathologies in FTLD are Pick's disease with Pick bodies and MAPT-associated FTLD (with *MAPT* gene

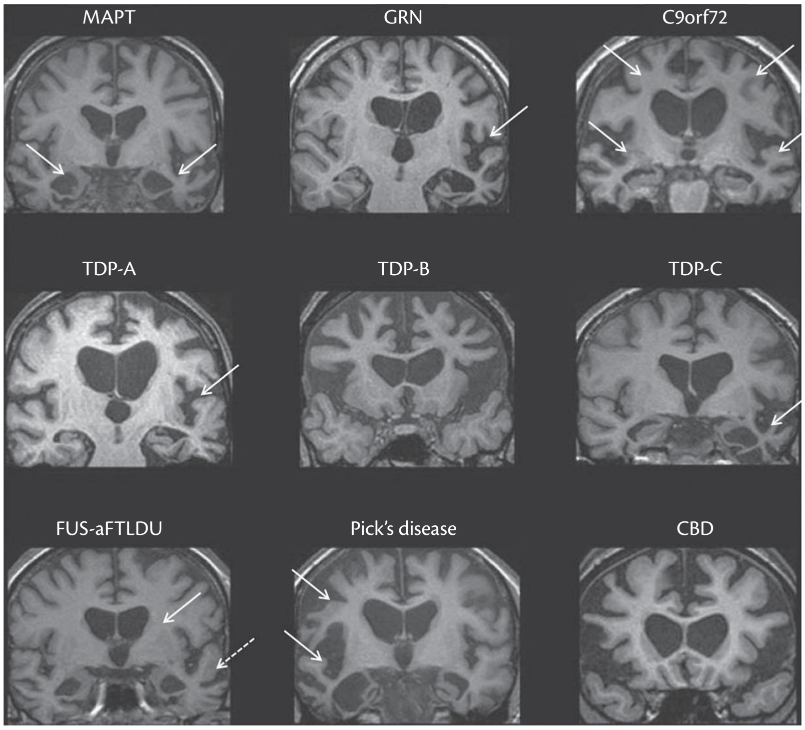

Fig. 19.4 Coronal T_1-weighted MR images showing illustrative examples of gray matter atrophy in genetically- and pathologically-defined frontotemporal dementia. In *MAPT* gene mutations, a relatively symmetrical medial temporal atrophy can be appreciated (arrows); in *GRN* mutations there is asymmetrical temporo-frontoparietal atrophy, affecting the left hemisphere in this case (arrow); in C9Orf72 repeat expansion, a relatively symmetrical fronto-temporal atrophy is seen (arrows). In TDP-A pathology there is asymmetrical temporo-frontoparietal atrophy, left-sided predominant in this case (arrow). In TDP-B pathology there is a more symmetrical atrophy affecting the frontal lobe, insula and anteromedial temporal lobe. In TDP-C pathology, asymmetrical antero-inferior temporal lobe atrophy can be appreciated, which is left-side predominant in this case (arrow). In FUS pathology there is caudate (arrow) and anterior temporal lobe (dashed arrow) atrophy. In Pick's disease, there is asymmetrical fronto-insula-temporal atrophy, right-sided predominant in this case (arrows); in CBD, fronto-parietal atrophy can be seen.

Modified from Rohrer JD, and Rosen HJ. (2013). Neuroimaging in frontotemporal dementia. *International Review of Psychiatry*, **25**, 221–9. Copyright (2013), with permission from Informa.

mutations). Progressive supranuclear palsy (PSP) and corticobasal degeneration (CBD) can also occur. Pick's diseases is associated with asymmetrical frontal (particularly dorsolateral and orbitofrontal), insular, and anterior temporal lobe atrophy. As discussed previously, *MAPT* mutations are associated with anterior temporal lobe atrophy. More focal patterns of atrophy are associated with PSP and CBD pathologies. Atrophy of cortical GM, particularly involving the premotor and posterior frontal cortex, has been identified in both CBD and PSP, but it is more distributed and severe in patients with CBD [67–70]. CBD is often associated with parietal lobe atrophy [67–70]. Atrophy of the basal ganglia is greater in CBD than in PSP [68]. Compared with CBD, cases with PSP pathology show preferential involvement of the brainstem and degeneration of the superior cerebellar peduncle [67,68].

A harmonized classification system subdivided FTLD pathology characterized by deposition of TDP-43 (FTLD-TDP) into four different types (A–D) according to the morphology of the inclusions. Distinct patterns of atrophy among the pathological subtypes of FTLD-TDP have been identified [37,70]. Type A is associated with an asymmetrical pattern of atrophy of frontal, temporal, and parietal lobes, and caudate involvement. It is of note that, within the TDP-43 type A group, patients carrying *GRN* mutations have more lateral temporal lobe atrophy than those without, and patients with MND have a similar pattern of atrophy, independent of the type of FTLD-TDP pathology [66]. Type B patients have predominant frontal atrophy. Type C is associated with asymmetric, either left- or right-sided, antero-inferior temporal lobe atrophy with involvement of the insula [37,70]. No neuroimaging study so far has assessed the atrophy pattern of FTLD-type D.

FTLD pathology characterized by the presence of FUS mutations are much rarer than tau and TDP-43 pathologies. A marked atrophy of the caudate nucleus in FTD patients has been consistently shown to be predictive of FUS pathology [70–72].

Taken together, the results of these studies suggest that the patterns of atrophy may contribute to the *in vivo* prediction of the underlying FTLD pathology. However, caution should be exercised when interpreting these findings, because the samples of patients studied so far are usually small.

White matter microstructural damage

bvFTD

In bvFTD, several studies found DT MRI abnormalities in WM tracts located in the frontal lobes, such as the anterior cingulum, genu of the corpus callosum, and superior longitudinal fasciculus (SLF), and in those tracts passing through the temporal lobes, such as the uncinate, ILF, and inferior fronto-occipital fasciculus (IFOF) (Fig. 19.5) [21,73–78]. Some studies also identified diffusivity abnormalities in more posterior WM regions, such as those containing the posterior SLF and the posterior cingulum (Fig. 19.5) [73,75,76]. Recently, a DT MRI study has investigated the overlap of bvFTD with MND, and has shown that patients with FTD-MND have a similar pattern of involvement of the frontal and temporal WM tracts as bvFTD, but with greater corticospinal tract damage [79].

DT MRI may improve the diagnostic differentiation between bvFTD and AD. When compared with AD, bvFTD was associated with greater reductions of fractional anisotropy (FA) in frontal

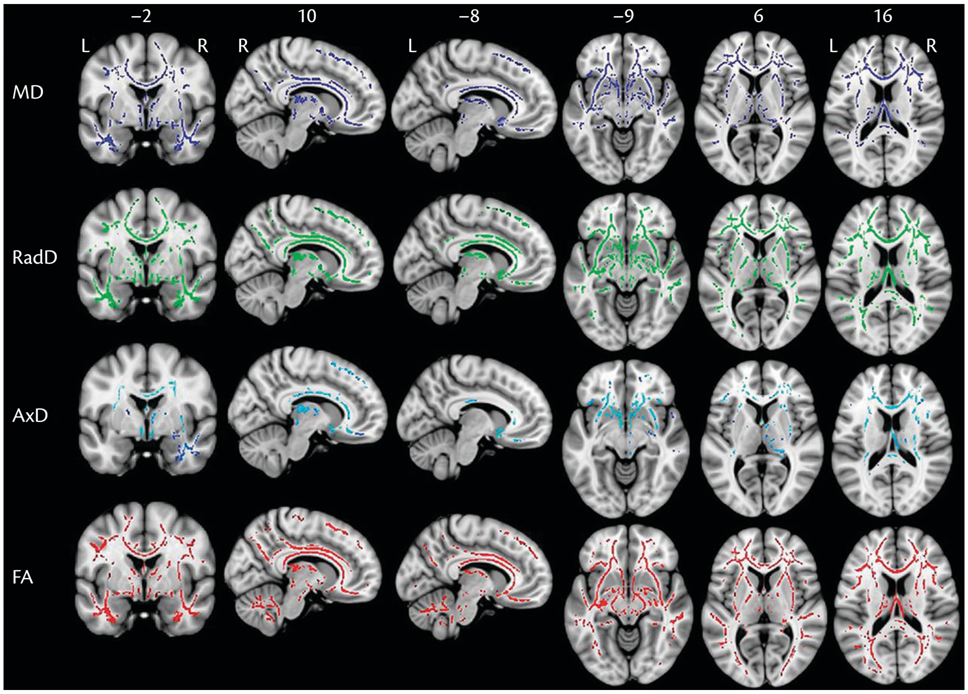

Fig. 19.5 Diffusion tensor MRI findings in patients with the behavioural variant of frontotemporal dementia compared with age-matched healthy controls. Voxel-wise group differences are shown in blue (mean diffusivity), green (radial diffusivity), cyan (axial diffusivity), and red (fractional anisotropy). Results are overlaid on the coronal, sagittal, and axial sections of the Montreal Neurological Institute standard brain in neurological convention (right is right).

Reproduced from Agosta F, Scola E, Canu E, et al. (2012). White matter damage in frontotemporal lobar degeneration spectrum. *Cerebral Cortex*, **22**, 2705–14. Copyright (2012), with permission from Oxford University Press.

WM regions, whereas no regions in AD showed greater DT MRI abnormalities compared with bvFTD [76]. One recent study combined cortical thickness measurement and DT MRI to compare 25 FTD (13 bvFTD, seven non-fluent, five semantic) and 24 AD patients, with autopsy- or cerebrospinal fluid (CSF)-confirmed disease [78]. The direct comparison of these two groups showed a significantly greater atrophy of inferior frontal, medial frontal, and prefrontal cortical regions, and a reduced FA of the genu of the corpus callosum, left IFOF, cingulum, uncinated, and bilateral corona radiata in FTD cases relative to AD [78]. Conversely, AD patients showed no areas of significant reduction in cortical thickness or WM damage relative to FTD patients [78]. These studies suggest that WM injury is likely to be more prominent in bvFTD than in AD.

Primary progressive aphasia

Several studies have investigated the patterns of WM abnormalities in small samples of non-fluent and semantic PPA patients using DT MRI [73,75,77,80–85]. The most consistent findings are a more ventral WM involvement in semantic patients and a more widespread frontal involvement in non-fluent cases (Fig. 19.6). However, recent studies using a voxel-based approach suggested a spreading of diffusion abnormalities beyond the typical sites of damage in both PPA variants.

In semantic PPA, abnormalities of WM tract diffusivity were identified in the major inferior and superior temporal connections of the left hemisphere, mirroring the severe atrophy affecting the same regions—the ILF, IFOF, and uncinate fasciculus of the ventral stream, and the arcuate and the temporoparietal component of the SLF of the dorsal stream [73,75,77,80–85]. Although tractography studies have argued that the frontoparietal connections are relatively spared in SV [80,82], a finding that couples with the absence of syntactic deficits in these patients, a few studies using tract-based spatial statistics (TBSS) have provided evidence for an involvement of the left prefrontal and parietofrontal WM, contributing to the SLF and corona radiata [73,84].

Non-fluent PPA is characterized by the prominent involvement of the left SLF [73,75,77,81, 82,84,85]. In contrast, the ventral tracts connecting the temporal lobe with the occipital and orbitofrontal cortices (i.e. ILF and uncinate fasciculi) are relatively spared [75,82]. TBSS studies showed that non-fluent patients not only have damage to the fronto-parietotemporal connections, but also an involvement of the corpus callosum, cingulum bundle, external capsule, several regions of the prefrontal and orbitofrontal

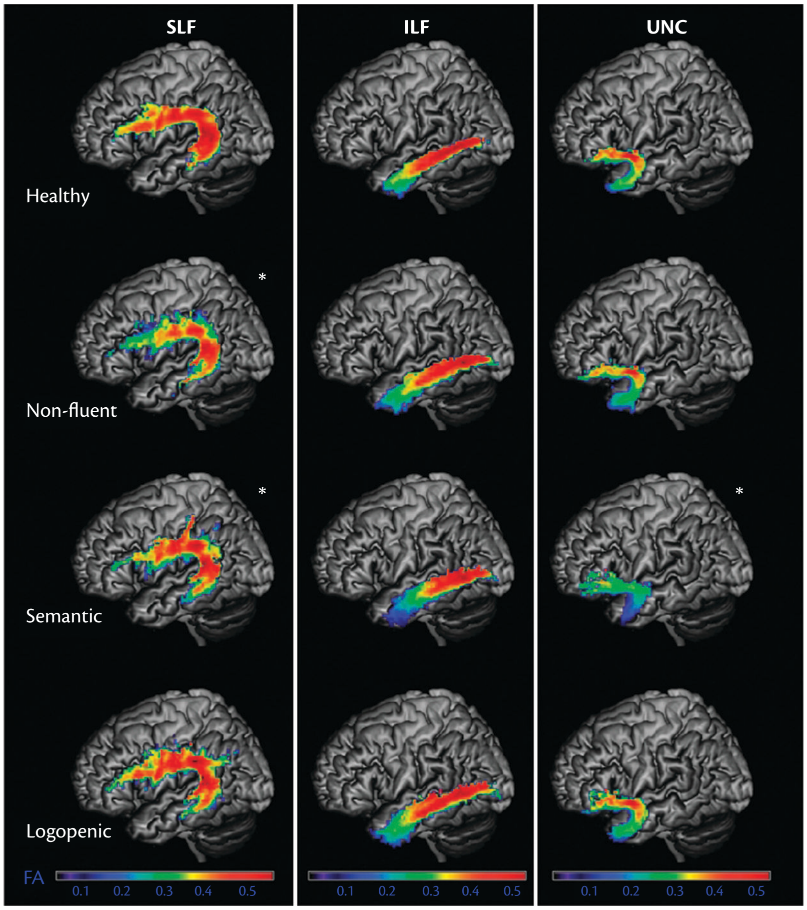

Fig. 19.6 Fractional anisotropy (FA) values of the left SLF, ILF, and uncinate fasciculus (UNC) in patients with PPA, overlaid on a standard Montreal Neurological Institute brain. Only voxels that are in common in at least 20% of the subjects in each group were included in the probability maps. Asterisks denotes significant difference relative to normal controls. The chromatic scale represents average FA values ranging from lower (violet–blue) to higher values (yellow–red).

Reproduced from Galantucci S, Tartaglia MC, Wilson SM, et al. (2011). White matter damage in primary progressive aphasias: a diffusion tensor tractography study. *Brain*, **134**, 3011–29. Copyright (2011), with permission from Oxford University Press. For further details on the logopenic variant PPA see Chapter 18.

WM, parietotemporal WM, and temporal regions, mainly in the left hemisphere [73,84]. Recent studies also found that portions of the ILF are not spared in non-fluent cases [81,84]. In patients with prominent apraxia of speech, rather than agrammatism, the premotor components of the SLF are the most affected region [86].

WM tract damage associated with genetic abnormalities

There have been a very few DT MRI studies assessing WM tract damage in patients with genetically-defined FTD. Involvement of the SLF, ILF, uncinate fasciculus, anterior cingulum, corpus callosum, but also corticospinal tracts and thalamic radiations, has been found in patients carrying the C9Orf72 repeat expansion [36]. More posterior brain regions were also damaged in these patients [36]. Studies of presymptomatic subjects at-risk of developing genetic FTD showed WM abnormalities years before the onset of symptoms [87,88] .

Perfusion and metabolic brain alterations

bvFTD

bvFTD is identified on SPECT or PET scans by patterns of hypoperfusion or hypometabolism in frontal, insular and anterior temporal regions that are typically quite asymmetrically centred around the frontolateral cortex [89–91] (Fig. 19.7). The regions that are most impaired are the medial frontal cortex, followed by the frontolateral

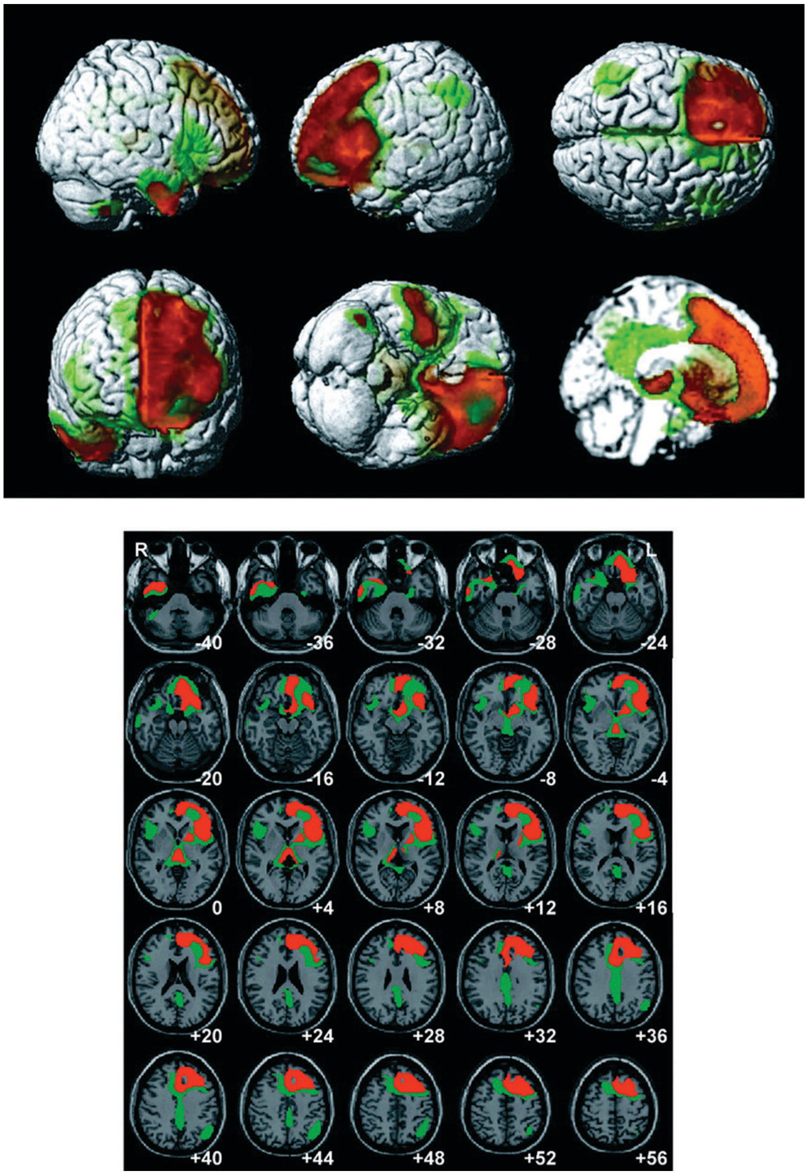

Fig. 19.7 Regions of hypometabolism in patients with frontotemporal dementia compared with healthy controls. These regions are displayed on surface-rendered (top) and transaxial (bottom) images. Hypometabolic regions were displayed according to two different thresholds in green ($p < 0.01$; corrected, $t = 5.18$) and red ($p < 0.0005$; corrected, $t = 6.29$). Number in each transaxial brain image indicates distance (mm) from anterior commissure–posterior commissure plane.

Reproduced from Jeong Y, Cho SS, Park JM, et al. (2005). 18F-FDG-PET findings in frontotemporal dementia: an SPM analysis of 29 patients. *Journal of Nuclear Medicine*, **46**, 233–9. Copyright (2005), with permission from the Journal of Nuclear Medicine.

and anterior temporal cortices. A prospective study of 134 patients with suspected bvFTD demonstrated that a predominant frontal, anterior temporal, or frontotemporal hypoperfusion or hypometabolism on initial SPECT or PET scans has a sensitivity of 90 and specificity of 75% against a clinical diagnosis after 2 years [34]. However, metabolic abnormalities are not limited to these regions. As dementia progresses, the severity and topographic extent of perfusion and metabolic impairment also increases and starts to involve other association areas [92].

The regional pattern of predominantly frontal functional involvement in FTD, with relative sparing of posterior brain regions, usually allows a clear distinction between these patients and those with AD [43,90,93–96]. Using an anterior–posterior cerebral blood flow (CBF) SPECT ratio (medial superior frontal gyrus/medial temporal lobes), patients with clinical bvFTD were successfully distinguished from AD patients, with a sensitivity of 87%, and a specificity of 96% versus early onset AD patients and 80% versus late onset AD patients [93]. A few studies have looked at the accuracy of SPECT or FDG-PET findings in relation to the pathological diagnoses [97,98]. A reduction of frontal CBF is more commonly seen in pathologically confirmed FTLD than in AD cases and is of diagnostic value (sensitivity 80%, specificity 65%) [97]. When the pattern of bilateral frontal CBF reduction is not associated with a bilateral parietal CBF abnormality, the diagnosis is even more accurate (sensitivity 80%, specificity 81%) [97]. However, an overlap of abnormalities between these two conditions exists, since AD can involve frontal regions and FTLD may not spare the temporoparietal cortex [99]. In a study of autopsy-proven FTLD and AD patients, the addition of FDG-PET scans significantly improved the accuracy of a FTLD diagnosis more than that of an AD diagnosis [98]. However, FDG-PET scans from FTLD patients were more difficultly interpreted than those from AD cases, resulting in lower sensitivity (70% for FTLD versus 98% for AD) and diagnostic confidence [98]. The disagreement in interpretation of scans in patients with FTLD primarily occurred when there was a temporoparietal hypometabolism [99]. Hypometabolism of anterior cingulate and anterior temporal regions indicates a high likelihood of FTLD, even when temporoparietal hypometabolism is detected [99].

Primary progressive aphasia

In patients with semantic variant PPA, FDG-PET studies showed asymmetrical hypometabolism of the temporal lobes, more marked on the left side (Fig. 19.8) [100–103]. A functional deficit of the left frontal opercular regions has been reported in non-fluent variant PPA patients (Fig. 19.8) [102,104–107]. In these cases, a functional involvement of bilateral caudate nuclei and thalami was also described [107].

A study comparing semantic PPA and very early AD patients using structural MRI and FDG-PET revealed hippocampal atrophy and hypometabolism in both groups; however, a strikingly reduced metabolism of the posterior cingulate cortex was seen in patients with AD, which was not detected in those with semantic variant PPA [100]. A functional imaging study of non-fluent patients demonstrated that a pattern of bilateral temporoparietal involvement is predictive of AD pathology, while a unilateral (left) temporoparietal cortex hypometabolism/perfusion was seen in cases with FTLD pathology [108]. On the contrary, a bilaterally normal temporoparietal cortical perfusion or metabolism was predictive of FTLD pathology [108].

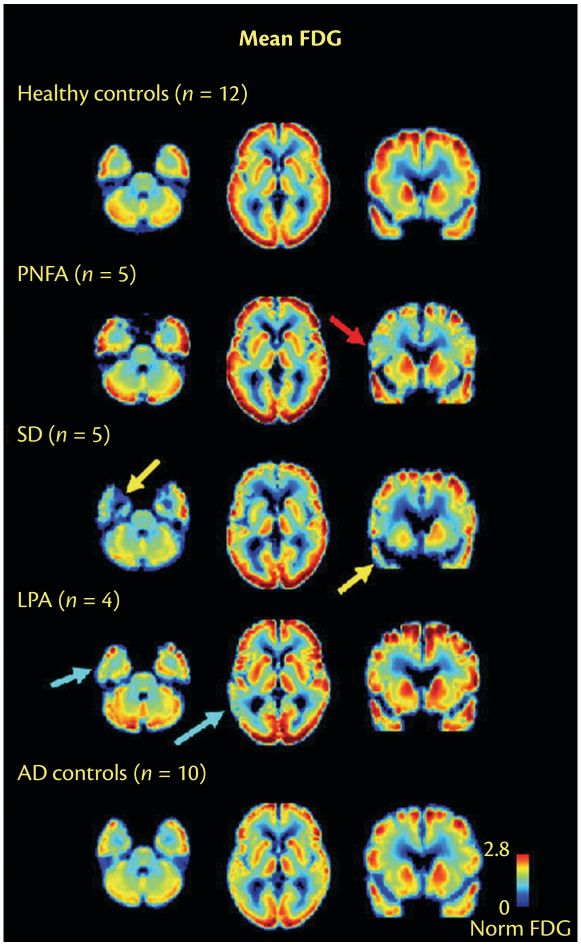

Fig. 19.8 Axial and coronal slices of mean atrophy-corrected FDG-PET images from (top to bottom) normal control subjects, patients with non-fluent variant of PPA, patients with semantic variant PPA, patients with logopenic variant PPA, and patients with Alzheimer's disease. Images are in neurological convention. Non-fluent PPA is characterized by left frontal hypometabolism (red arrow), semantic PPA by left greater than right anterior temporal hypometabolism (yellow arrows), and logopenic PPA by asymmetric left temporoparietal hypometabolism (light blue arrows).

Reproduced from Rabinovici GD, Jagust WJ, Furst AJ, et al. (2008). A beta amyloid and glucose metabolism in three variants of primary progressive aphasia. *Annals of Neurology*, **64**, 388–401. Copyright (2008), with permission from John Wiley & Sons Ltd. For further details on the logopenic variant PPA see Chapter 18.

Amyloid imaging

Amyloid imaging is expected to be helpful in distinguishing FTD, which is not associated with amyloid deposition, from AD, particularly in case of young patients. Generally, low cortical ^{11}C-Pittsburgh compound B (PIB) retention [109–113] or ^{18}F-florbetaben positivity [114,115] were observed in patients with FTD. In a large study of 62 AD patients and 45 FTD patients, ^{11}C-PIB scans were positive in 87% of AD cases and 16% of FTD cases [113]. ^{11}C-PIB visual reads had a higher sensitivity for AD than FDG-PET (89% versus 77%), with similar specificity (83% versus 84%). When scans were classified quantitatively, PIB had higher sensitivity (89% versus 73%), while FDG-PET had higher specificity (83% versus 98%) [113]. ^{11}C-PIB outperformed FDG-PET in classifying the 12 patients with known pathology (97 versus 87% overall accuracy combining visual reads and quantitative classification) [113].

In small PPA case series [102,112], the semantic and non-fluent groups showed the lowest proportion of ^{11}C-PIB-positive cases, while amyloid deposition was more common in patients with the logopenic variant with a pattern that was indistinguishable from that of typical AD [102,112].

Functional connectivity abnormalities

An early study exploring the RS functional connectivity in patients with bvFTD [116] found that, while AD patients have a disrupted connectivity of the default-mode network (DMN), bvFTD is associated with an altered connectivity of the salience network, which is linked to emotional salience processing capacities [117], most notably in the frontal and anterior insula, mid-cingulate and numerous subcortical, limbic, and brainstem nodes. BvFTD patients also experienced an increased left parietal connectivity of the DMN [116]. Salience network disruption and DMN enhancement correlate with clinical severity in bvFTD patients [116]. A combination of salience network and DMN connectivity scores was found to be able to classify healthy subjects, AD patients, and bvFTD patients with a 92% accuracy, and to separate AD and bvFTD patients with a 100% accuracy [116]. The reduced connectivity of the salience network has been replicated in further studies of patients with bvFTD (Fig. 19.9) [118–120]. Baseline measures of salience network connectivity involving the left insula were also found to predict behavioural changes in patients with bvFTD and semantic PPA [121].

Network-based analysis of brain structural and functional connections has provided a novel instrument to study the human brain in healthy and diseased individuals. Graph theory provides a powerful tool to quantitatively describe the topological organization of brain connectivity. Using such a framework, the brain can be depicted as a set of nodes connected by edges. Distinct modifications of brain network topology have been identified during development and normal ageing, whereas disrupted functional and structural connectivities have been associated with several neurological conditions, including AD [122]. Graph theoretical analysis was recently applied to RS fMRI data from patients with bvFTD [123]. Global and local functional network properties were altered in bvFTD patients relative to normal subjects. Such abnormalities were located in structures known to harbour the neuropathological changes of bvFTD, such as the frontotemporal lobes and subcortical regions (Fig. 19.10). Overall, these findings contribute to support the theory of a selective vulnerability of large-scale brain networks in neurodegenerative diseases [124].

Three studies have examined the use of RS fMRI in presymptomatic subjects carrying *MAPT* or *GRN* mutations, but the results are conflicting [88,120,125]. Presymptomatic *MAPT* mutation carriers showed no abnormalities of the salience network, but a reduced connectivity of nodes of the DMN (lateral temporal and medial prefrontal cortex) with an increased connectivity of other components of the network (medial parietal) [120]. On the contrary, presymptomatic *GRN* mutation carriers showed an increased connectivity of the salience network, with no abnormalities of the DMN [125]. A larger study showed a reduced functional connectivity of the

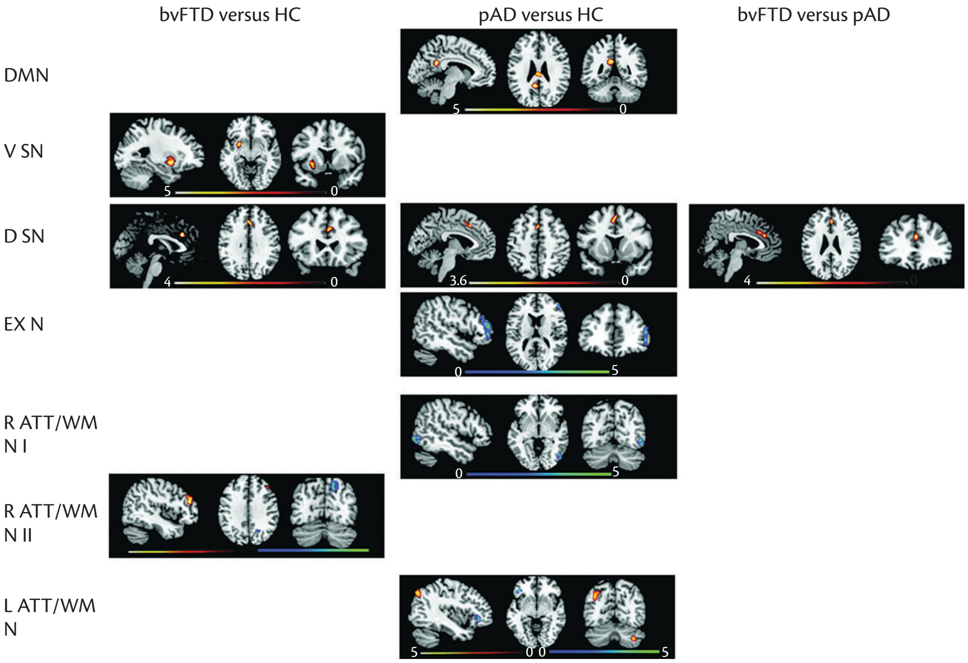

Fig. 19.9 Contrasts of resting state networks between (left column) patients with the bvFTD and healthy controls (HC), (central column) patients with probable Alzheimer's disease (pAD) and HC, and (right column) bvFTD patients and pAD patients. Colour maps represent significantly different voxels in the corresponding contrast. T values are colour-coded with red to yellow = decreased RS functional MRI (fMRI) connectivity, and cyan to blue = increased RS fMRI connectivity. Results are shown on the Montreal Neurological Institute standard brain, in neurological convention.

Abbreviations: ATT/WM, attention/working memory; bvFTD, behavioural variant frontotemporal dementia; DMN, default mode network; D SN, dorsal salience network; EX N, executive network; HC, healthy controls; pAD, probable Alzheimer's disease; V SN, ventral salience network.

Reproduced from Filippi M, Agosta F, Scola E, et al. (2012). Functional network connectivity in the behavioral variant of frontotemporal dementia. *Cortex*, **49**, 2389–401. Copyright (2012), with permission from Elsevier.

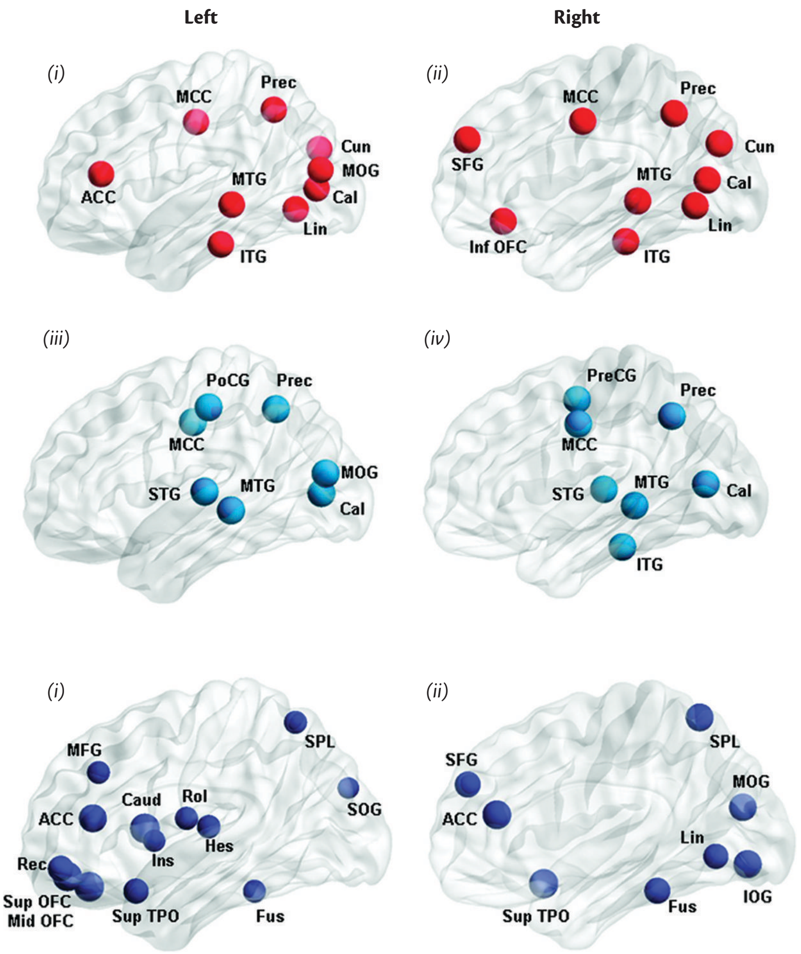

Fig. 19.10 (a) Cortical hubs of brain functional networks in healthy controls (i,ii) and patients with the bvFTD (iii,iv). (b) Regions showing decreased integrated nodal degree (i,ii) in patients with bvFTD compared to healthy controls. Node size is proportional to the difference in the value of the integrated nodal parameters between the two groups.

Abbreviations: ACC, anterior cingulate cortex; Cal, calcarine cortex; Caud, caudate nucleus; Cun, cuneus; Fus, fusiform gyrus; Hes, Heschl gyrus; Ins, insula; IOG, inferior occipital gyrus; ITG, inferior temporal gyrus; Lin, lingual gyrus; MCC, middle cingulate cortex; MFG, middle frontal gyrus; MOG, middle occipital gyrus; MTG, middle temporal gyrus; OFC, orbitofrontal cortex; Prec, precuneus; PoCG, post-central gyrus; PreCG, precentral gyrus; Rec, gyrus rectus; Rol, Rolandic operculum; SFG, superior frontal gyrus; SOG, superior occipital gyrus; SPL, superior parietal lobule; STG, superior temporal gyrus; TPO, temporal pole.

Reproduced from Agosta F, Sala S, Valsasina P, et al. (2013). Brain network connectivity assessed using graph theory in frontotemporal dementia. *Neurology*, **81**, 134–43. Copyright (2013), with permission from Wolters Kluwer Health.

anterior mid-cingulate cortex in both *MAPT* and *GRN* mutation carriers with no alterations of the posterior cingulate connectivity. Despite such incongruent results, all three studies did not find structural abnormalities on T_1-weighted images in presymptomatic subjects at-risk of developing FTD [88,120,125], suggesting that RS fMRI changes may predate atrophy.

Little is known regarding task-related functional activity of FTD patients. In this context, fMRI studies are warranted to clarify the neural correlates of the behavioural and linguistic symptoms of these patients.

Conclusions

The detection of distinct patterns of atrophy on structural MRI and functional abnormalities on SPECT and PET scans has been shown to contribute to establishing the correct diagnosis of FTD, and help to distinguish FTD patients from those with AD. The diagnostic ability of structural and functional imaging techniques is further improved if the image analysis methods that provide single-subject classification are employed. Furthermore, a multimodal approach, such as one that combines neuropsychological testing, MRI, and PET/SPECT can improve *in vivo* distinction of FTD from AD cases. Nevertheless, it has to be stated that clinical criteria, neuropsychological profiles, and structural and functional imaging may all fail to correctly predict the underlying pathology when this does not adhere to common anatomic patterns. In these cases, molecular imaging, such as PET with Aβ ligands, may be decisive.

A major clinical challenge, to date, is the need to improve the prediction of the specific histopathology, causing each of the FTLD variants during life. Preliminary studies in genetically and pathologically proven cases suggest that distinct patterns of tissue loss could help. However, the results of these reports are limited by the small numbers of patients enrolled. As a consequence, larger studies are needed to verify whether specific patterns of regional atrophy constitute signatures of specific FTLD pathologies. In this context, the discovery of novel radioactive compounds to detect tau or TDP-43 pathology with PET scanning will be central. An improved reliability in distinguishing FTLD pathological variants using neuroimaging techniques may become important in the near future, as a aetiology-specific modifying treatments are likely to be developed and thus enter the clinical arena.

References

1. Neary D, Snowden JS, Gustafson L, et al. (1998). Frontotemporal lobar degeneration: a consensus on clinical diagnostic criteria. *Neurology*, **51**, 1546–54.
2. Mackenzie IR, Neumann M, Bigio EH, et al. (2010). Nomenclature and nosology for neuropathologic subtypes of frontotemporal lobar degeneration: an update. *Acta Neuropathologica*, **119**, 1–4.
3. Mesulam MM (2001). Primary progressive aphasia. *Annals of Neurology*, **49**, 425–32.
4. Gorno-Tempini ML, Hillis AE, Weintraub S, et al. (2011). Classification of primary progressive aphasia and its variants. *Neurology*, **76**, 1006–14.
5. Josephs KA, Duffy JR, Strand EA, et al. (2006). Clinicopathological and imaging correlates of progressive aphasia and apraxia of speech. *Brain*, **129**, 1385–98.
6. Knibb JA, Xuereb JH, Patterson K, et al. (2006). Clinical and pathological characterization of progressive aphasia. *Annals of Neurology*, **59**, 156–65.
7. Grossman M, Wood EM, Moore P, et al. (2007). TDP-43 pathologic lesions and clinical phenotype in frontotemporal lobar degeneration with ubiquitin-positive inclusions. *Archives of Neurology*, **64**, 1449–54.
8. Hodges JR, Davies RR, Xuereb JH, et al. (2004). Clinicopathological correlates in frontotemporal dementia. *Annals of Neurology*, **56**, 399–406.
9. Mesulam M, Wicklund A, Johnson N, et al. (2008). Alzheimer and frontotemporal pathology in subsets of primary progressive aphasia. *Annals of Neurology*, **63**, 709–19.
10. Josephs KA, Whitwell JL, Duffy JR; et al. (2008). Progressive aphasia secondary to Alzheimer disease vs FTLD pathology. *Neurology*, **70**, 25–34.
11. Rascovsky K, Hodges JR, Knopman D, et al. (2011). Sensitivity of revised diagnostic criteria for the behavioural variant of frontotemporal dementia. *Brain*, **134**, 2456–77.
12. Rosen HJ, Gorno-Tempini ML, Goldman WP, et al. (2002). Patterns of brain atrophy in frontotemporal dementia and semantic dementia. *Neurology*, **58**, 198–208.
13. Boccardi M, Sabattoli F, Laakso MP, et al. (2005). Frontotemporal dementia as a neural system disease. *Neurobiology of Aging*, **26**, 37–44.
14. Perry RJ, Graham A, Williams G, et al. (2006). Patterns of frontal lobe atrophy in frontotemporal dementia: a volumetric MRI study. *Dementia and Geriatric Cognitive Disorders*, **22**, 278–87.
15. Du AT, Schuff N, Kramer JH, et al. (2007). Different regional patterns of cortical thinning in Alzheimer's disease and frontotemporal dementia. *Brain*, **130**, 1159–66.
16. Seeley WW, Crawford R, Rascovsky K, et al. (2008). Frontal paralimbic network atrophy in very mild behavioral variant frontotemporal dementia. *Archives of Neurology*, **65**, 249–55.
17. Richards BA, Chertkow H, Singh V, et al. (2009). Patterns of cortical thinning in Alzheimer's disease and frontotemporal dementia. *Neurobiology of Aging*, **30**, 1626–36.
18. Whitwell JL, Przybelski SA, Weigand SD, et al. (2009). Distinct anatomical subtypes of the behavioural variant of frontotemporal dementia: a cluster analysis study. *Brain*, **132**, 2932–46.
19. Rabinovici GD, Seeley WW, Kim EJ, et al. (2007). Distinct MRI atrophy patterns in autopsy-proven Alzheimer's disease and frontotemporal lobar degeneration. *American Journal of Alzheimer's Disease and Other Dementias*, **22**, 474–88.
20. Garibotto V, Borroni B, Agosti C, et al. (2011). Subcortical and deep cortical atrophy in Frontotemporal Lobar Degeneration. *Neurobiology of Aging*, **32**, 875–84.
21. Borroni B, Brambati SM, Agosti C, et al. (2007). Evidence of white matter changes on diffusion tensor imaging in frontotemporal dementia. *Archives of Neurology*, **64**, 246–51.
22. Piguet O, Petersen A, Yin Ka Lam B, et al. (2011). Eating and hypothalamus changes in behavioral-variant frontotemporal dementia. *Annals of Neurology*, **69**, 312–9.
23. Cardenas VA, Boxer AL, Chao LL; et al. (2007). Deformation-based morphometry reveals brain atrophy in frontotemporal dementia. *Archives of Neurology*, **64**, 873–7.
24. Chao LL, Schuff N, Clevenger EM, et al. (2007). Patterns of white matter atrophy in frontotemporal lobar degeneration. *Archives of Neurology*, **64**, 1619–24.
25. Chan D, Fox NC, Scahill RI, et al. (2001). Patterns of temporal lobe atrophy in semantic dementia and Alzheimer's disease. *Annals of Neurology*, **49**, 433–42.
26. Whitwell JL, Jack CR, Jr, Parisi JE, et al. (2007). Rates of cerebral atrophy differ in different degenerative pathologies. *Brain*, **130**, 1148–58.
27. Whitwell JL, Jack CR, Jr, Pankratz VS, et al. (2008). Rates of brain atrophy over time in autopsy-proven frontotemporal dementia and Alzheimer disease. *NeuroImage*, **39**, 1034–40.
28. Knopman DS, Jack CR, Jr, Kramer JH, et al. (2009). Brain and ventricular volumetric changes in frontotemporal lobar degeneration over 1 year. *Neurology*, **72**, 1843–9.
29. Gordon E, Rohrer JD, Kim LG; et al. (2010). Measuring disease progression in frontotemporal lobar degeneration: a clinical and MRI study. *Neurology*, **74**, 666–73.
30. Frings L, Mader I, Landwehrmeyer BG, et al. (2012). Quantifying change in individual subjects affected by frontotemporal lobar degeneration using automated longitudinal MRI volumetry. *Human Brain Mapping*, **33**, 1526–35.
31. Krueger CE, Dean DL, Rosen HJ, et al. (2010). Longitudinal rates of lobar atrophy in frontotemporal dementia, semantic dementia, and Alzheimer's disease. *Alzheimer's Disease and Associated Disorders*, **24**, 43–8.
32. Brambati SM, Renda NC, Rankin KP, et al. (2007). A tensor based morphometry study of longitudinal gray matter contraction in FTD. *NeuroImage*, **35**, 998–1003.
33. Knopman DS, Boeve BF, Parisi JE, et al. (2005). Antemortem diagnosis of frontotemporal lobar degeneration. *Annals of Neurology*, **57**, 480–8.
34. Mendez MF, Shapira JS, McMurtray A, et al. (2007). Accuracy of the clinical evaluation for frontotemporal dementia. *Archives of Neurology*, **64**, 830–5.
35. Pijnenburg YA, Mulder JL, van Swieten JC, et al. (2008). Diagnostic accuracy of consensus diagnostic criteria for frontotemporal dementia in a memory clinic population. *Dementia and Geriatric Cognitive Disorders*, **25**, 157–64.
36. Mahoney CJ, Beck J, Rohrer JD, et al. (2012). Frontotemporal dementia with the C9ORF72 hexanucleotide repeat expansion: clinical, neuroanatomical and neuropathological features. *Brain*, **135**, 736–50.
37. Whitwell JL, Weigand SD, Boeve BF, et al. (2012). Neuroimaging signatures of frontotemporal dementia genetics: C9ORF72, tau, progranulin and sporadics. *Brain*, **135**, 794–806.
38. Shimizu H, Hokoishi K, Fukuhara R, et al. (2009). Two cases of frontotemporal dementia with predominant temporal lobe atrophy. *Psychogeriatrics*, **9**, 204–7.
39. Davies RR, Kipps CM, Mitchell J, et al. (2006). Progression in frontotemporal dementia: identifying a benign behavioral variant by magnetic resonance imaging. *Archives of Neurology*, **63**, 1627–31.
40. Kipps CM, Davies RR, Mitchell J, et al. (2007). Clinical significance of lobar atrophy in frontotemporal dementia: application of an MRI visual rating scale. *Dementia and Geriatric Cognitive Disorders*, **23**, 334–42.
41. Josephs KA, Whitwell JL, Jack CR, et al. (2006). Frontotemporal lobar degeneration without lobar atrophy. *Archives of Neurology*, **63**, 1632–8.
42. Agosta F, Canu E, Sarro L, et al. (2011). Neuroimaging findings in frontotemporal lobar degeneration spectrum of disorders. *Cortex*, **48**, 389–413.

43. Varma AR, Adams W, Lloyd JJ, et al. (2002). Diagnostic patterns of regional atrophy on MRI and regional cerebral blood flow change on SPECT in young onset patients with Alzheimer's disease, frontotemporal dementia and vascular dementia. *Acta Neurologica Scandinavica*, **105**, 261–9.
44. Likeman M, Anderson VM, Stevens JM, et al. (2005). Visual assessment of atrophy on magnetic resonance imaging in the diagnosis of pathologically confirmed young-onset dementias. *Archives of Neurology*, **62**, 1410–5.
45. Horn JF, Habert MO, Kas A, et al. (2009). Differential automatic diagnosis between Alzheimer's disease and frontotemporal dementia based on perfusion SPECT images. *Artificial Intelligence Medicine*, **47**, 147–58.
46. Kloppel S, Stonnington CM, Chu C, et al. (2008). Automatic classification of MR scans in Alzheimer's disease. *Brain*, **131**, 681–9.
47. Lehmann M, Rohrer JD, Clarkson MJ, et al. (2010). Reduced cortical thickness in the posterior cingulate gyrus is characteristic of both typical and atypical Alzheimer's disease. *Journal of Alzheimer's Disease*, **20**, 587–98.
48. Whitwell JL, Jack CR, Jr, Przybelski SA, et al. (2011). Temporoparietal atrophy: a marker of AD pathology independent of clinical diagnosis. *Neurobiology of Aging*, **32**, 1531–41.
49. Claassen DO, Parisi JE, Giannini C, et al. (2008). Frontotemporal dementia mimicking dementia with Lewy bodies. *Cognitive Behavioural Neurology*, **21**, 157–63.
50. Novellino F, Bagnato A, Salsone M, et al. (2010). Myocardial (123) I-MIBG scintigraphy for differentiation of Lewy bodies disease from FTD. *Neurobiology of Aging*, **31**, 1903–11.
51. Mummery CJ, Patterson K, Price CJ, et al. (2000). A voxel-based morphometry study of semantic dementia: relationship between temporal lobe atrophy and semantic memory. *Annals of Neurology*, **47**, 36–45.
52. Galton CJ, Patterson K, Graham K, et al. (2001). Differing patterns of temporal atrophy in Alzheimer's disease and semantic dementia. *Neurology*, **57**, 216–25.
53. Gorno-Tempini ML, Dronkers NF, Rankin KP, et al. (2004). Cognition and anatomy in three variants of primary progressive aphasia. *Annals of Neurology*, **55**, 335–46.
54. Boxer AL, Rankin KP, Miller BL, et al. (2003). Cinguloparietal atrophy distinguishes Alzheimer disease from semantic dementia. *Archives of Neurology*, **60**, 949–56.
55. van de Pol LA, Hensel A, Barkhof F, et al. (2006). Hippocampal atrophy in Alzheimer disease: age matters. *Neurology*, **66**, 236–8.
56. Josephs KA, Whitwell JL, Knopman DS, et al. (2009). Two distinct subtypes of right temporal variant frontotemporal dementia. *Neurology*, **73**, 1443–50.
57. Rohrer JD, Warren JD, Modat M, et al. (2009). Patterns of cortical thinning in the language variants of frontotemporal lobar degeneration. *Neurology*, **72**, 1562–9.
58. Brambati SM, Rankin KP, Narvid J, et al. (2009). Atrophy progression in semantic dementia with asymmetric temporal involvement: a tensor-based morphometry study. *Neurobiology of Aging*, **30**, 103–11.
59. Rohrer JD, Ridgway GR, Crutch SJ, et al. (2010). Progressive logopenic/phonological aphasia: erosion of the language network. *NeuroImage*, **49**, 984–93.
60. Rogalski E, Cobia D, Harrison TM, et al. (2011). Progression of language decline and cortical atrophy in subtypes of primary progressive aphasia. *Neurology*, **76**, 1804–10.
61. van de Pol LA, Hensel A, van der Flier WM, et al. (2006). Hippocampal atrophy on MRI in frontotemporal lobar degeneration and Alzheimer's disease. *Journal of Neurology, Neurosurgery & Psychiatry*, **77**, 439–42.
62. Whitwell JL, Jack CR, Jr., Boeve BF, et al. (2009). Voxel-based morphometry patterns of atrophy in FTLD with mutations in MAPT or PGRN. *Neurology*, **72**, 813–20.
63. Rohrer JD, Ridgway GR, Modat M, et al. (2010). Distinct profiles of brain atrophy in frontotemporal lobar degeneration caused by progranulin and tau mutations. *NeuroImage*, **53**, 1070–6.
64. Beck J, Rohrer JD, Campbell T, et al. (2008). A distinct clinical, neuropsychological and radiological phenotype is associated with progranulin gene mutations in a large UK series. *Brain*, **131**, 706–20.
65. Spina S, Farlow MR, Unverzagt FW, et al. (2008). The tauopathy associated with mutation +3 in intron 10 of Tau: characterization of the MSTD family. *Brain*, **131**, 72–89.
66. Boxer AL, Mackenzie IR, Boeve BF, et al. (2011). Clinical, neuroimaging and neuropathological features of a new chromosome 9p-linked FTD-ALS family. *Journal of Neurology, Neurosurgery & Psychiatry*, **82**, 196–203.
67. Boxer AL, Geschwind MD, Belfor N, et al. (2006). Patterns of brain atrophy that differentiate corticobasal degeneration syndrome from progressive supranuclear palsy. *Archives of Neurology*, **63**, 81–6.
68. Josephs KA, Whitwell JL, Dickson DW, et al. (2008). Voxel-based morphometry in autopsy proven PSP and CBD. *Neurobiology of Aging*, **29**, 280–9.
69. Rankin KP, Mayo MC, Seeley WW, et al. (2011). Behavioral variant frontotemporal dementia with corticobasal degeneration pathology: phenotypic comparison to bvFTD with Pick's disease. *Journal of Molecular Neuroscience*, **45**, 594–608.
70. Rohrer JD, Lashley T, Schott JM, et al. (2011). Clinical and neuroanatomical signatures of tissue pathology in frontotemporal lobar degeneration. *Brain*, **134**, 2565–81.
71. Josephs KA, Whitwell JL, Parisi JE, et al. (2010). Caudate atrophy on MRI is a characteristic feature of FTLD-FUS. *European Journal of Neurology*, **17**, 969–75.
72. Seelaar H, Klijnsma KY, de Koning I, et al. (2010). Frequency of ubiquitin and FUS-positive, TDP-43-negative frontotemporal lobar degeneration. *Journal of Neurology*, **257**, 747–53.
73. Agosta F, Scola E, Canu E, et al. (2012). White matter damage in frontotemporal lobar degeneration spectrum. *Cerebral Cortex*, **22**, 2705–14.
74. Matsuo K, Mizuno T, Yamada K, et al. (2008). Cerebral white matter damage in frontotemporal dementia assessed by diffusion tensor tractography. *Neuroradiology*, **50**, 605–11.
75. Whitwell JL, Avula R, Senjem ML, et al. (2011). Gray and white matter water diffusion in the syndromic variants of frontotemporal dementia. *Neurology*, **74**, 1279–87.
76. Zhang Y, Schuff N, Du AT, et al. (2009). White matter damage in frontotemporal dementia and Alzheimer's disease measured by diffusion MRI. *Brain*, **132**, 2579–92.
77. Zhang Y, Tartaglia MC, Schuff N, et al. (2013). MRI signatures of brain macrostructural atrophy and microstructural degradation in frontotemporal lobar degeneration subtypes. *Journal of Alzheimer's Disease*, **33**, 431–44.
78. Avants BB, Cook PA, Ungar L, et al. (2010). Dementia induces correlated reductions in white matter integrity and cortical thickness: a multivariate neuroimaging study with sparse canonical correlation analysis. *NeuroImage*, **50**, 1004–16.
79. Lillo P, Mioshi E, Burrell JR, et al. (2012). Grey and white matter changes across the amyotrophic lateral sclerosis-frontotemporal dementia continuum. *PLoS One*, **7**, e43993.
80. Agosta F, Henry RG, Migliaccio R, et al. (2010). Language networks in semantic dementia. *Brain*, **133**, 286–99.
81. Agosta F, Galantucci S, Canu E, et al. (2013). Disruption of structural connectivity along the dorsal and ventral language pathways in patients with nonfluent and semantic variant primary progressive aphasia: A DT MRI study and a literature review. *Brain and Language*, **127**(2), 157-66.
82. Galantucci S, Tartaglia MC, Wilson SM, et al. (2011). White matter damage in primary progressive aphasias: a diffusion tensor tractography study. *Brain*, **134**, 3011–29.
83. Acosta-Cabronero J, Patterson K, Fryer TD, et al. (2011). Atrophy, hypometabolism and white matter abnormalities in semantic dementia tell a coherent story. *Brain*, **134**, 2025–35.
84. Schwindt GC, Graham NL, Rochon E; et al. (2013). Whole-brain white matter disruption in semantic and nonfluent variants of primary progressive aphasia. *Human Brain Mapping*, **34**, 973–84.

85. Mahoney CJ, Malone IB, Risgway GR, et al. (2013). White matter tract signatures of the progressive aphasias. *Neurobiology of Aging*, **34**, 1687–99.
86. Josephs KA, Duffy JR, Strand EA, et al. (2012). Characterizing a neurodegenerative syndrome: primary progressive apraxia of speech. *Brain*, **135**, 1522–36.
87. Borroni B, Alberici A, Premi E; et al. (2008). Brain magnetic resonance imaging structural changes in a pedigree of asymptomatic progranulin mutation carriers. *Rejuvenation Research*, **11**, 585–95.
88. Dopper EG, Rombouts SA, Jiscoot LC; et al. (2013). Structural and functional brain connectivity in presymptomatic familial frontotemporal dementia. *Neurology*, **80**, 814–23.
89. Miller BL, Cummings JL, Villanueva-Meyer J, et al. (1991). Frontal lobe degeneration: clinical, neuropsychological, and SPECT characteristics. *Neurology*, **41**, 1374–82.
90. Ishii K, Sakamoto S, Sasaki M, et al. (1998). Cerebral glucose metabolism in patients with frontotemporal dementia. *Journal of Nuclear Medicine*, **39**, 1875–8.
91. Jeong Y, Cho SS, Park JM, et al. (2005). 18F-FDG PET findings in frontotemporal dementia: an SPM analysis of 29 patients. *Journal of Nuclear Medicine*, **46**, 233–9.
92. Diehl-Schmid J, Grimmer T, Drzezga A, et al. (2007). Decline of cerebral glucose metabolism in frontotemporal dementia: a longitudinal 18F-FDG-PET-study. *Neurobiology of Aging*, **28**, 42–50.
93. Sjogren M, Gustafson L, Wikkelsö C, et al. (2000). Frontotemporal dementia can be distinguished from Alzheimer's disease and subcortical white matter dementia by an anterior-to-posterior rCBF-SPET ratio. *Dementia and Geriatric Cognitive Disorders*, **11**, 275–85.
94. Ibach B, Poljansky S, Marienhagen J, et al. (2004). Contrasting metabolic impairment in frontotemporal degeneration and early onset Alzheimer's disease. *NeuroImage*, **23**, 739–43.
95. Charpentier P, Lavenu I, Defebvre L, et al. (2000). Alzheimer's disease and frontotemporal dementia are differentiated by discriminant analysis applied to (99m)Tc HmPAO SPECT data. *Journal of Neurology, Neurosurgery & Psychiatry*, **69**, 661–3.
96. Kanda T, Ishii K, Uemura T, et al. (2008). Comparison of grey matter and metabolic reductions in frontotemporal dementia using FDG-PET and voxel-based morphometric MR studies. *European Journal of Nuclear Medicine and Molecular Imaging*, **35**, 2227–34.
97. McNeill R, Sare GM, Manoharan M, et al. (2007). Accuracy of single-photon emission computed tomography in differentiating frontotemporal dementia from Alzheimer's disease. *Journal of Neurology, Neurosurgery & Psychiatry*, **78**, 350–5.
98. Foster NL, Heidebrink JL, Clark CM, et al. (2007). FDG-PET improves accuracy in distinguishing frontotemporal dementia and Alzheimer's disease. *Brain*, **130**, 2616–35.
99. Womack KB, Diaz-Arrastia R, Aizenstein HJ, et al. (2011). Temporoparietal hypometabolism in frontotemporal lobar degeneration and associated imaging diagnostic errors. *Archives of Neurology*, **68**, 329–37.
100. Nestor PJ, Fryer TD, Hodges JR. (2006). Declarative memory impairments in Alzheimer's disease and semantic dementia. *NeuroImage*, **30**, 1010–20.
101. Diehl J, Grimmer T, Drzezga A, et al. (2004). Cerebral metabolic patterns at early stages of frontotemporal dementia and semantic dementia. A PET study. *Neurobiology of Aging*, **25**, 1051–6.
102. Rabinovici GD, Jagust WJ, Furst AJ, et al. et al. (2008). A beta amyloid and glucose metabolism in three variants of primary progressive aphasia. *Annals of Neurology*, **64**, 388–401.
103. Drzezga A, Grimmer T, Henriksen G, et al. (2008). Imaging of amyloid plaques and cerebral glucose metabolism in semantic dementia and Alzheimer's disease. *NeuroImage*, **39**, 619–33.
104. Nestor PJ, Graham NL, Fryer TD, et al. (2003). Progressive non-fluent aphasia is associated with hypometabolism centred on the left anterior insula. *Brain*, **126**, 2406–18.
105. Zahn R, Buechert M, Overmans J, et al. (2005). Mapping of temporal and parietal cortex in progressive nonfluent aphasia and Alzheimer's disease using chemical shift imaging, voxel-based morphometry and positron emission tomography. *Psychiatry Research*, **140**, 115–31.
106. Panegyres PK, McCarthy M, Campbell A, et al. (2008). Correlative studies of structural and functional imaging in primary progressive aphasia. *American Journal of Alzheimer's Disease and Other Dementias*, **23**, 184–91.
107. Perneczky R, Diehl-Schmid J, Pohl C, et al. (2007). Non-fluent progressive aphasia: cerebral metabolic patterns and brain reserve. *Brain Research*, 1133, 178–85.
108. Nestor PJ, Balan K, Cheow HK, et al. (2007). Nuclear imaging can predict pathologic diagnosis in progressive nonfluent aphasia. *Neurology*, **68**, 238–9.
109. Rabinovici GD, Furst AJ, O'Neil JP, et al. (2007). 11C-PIB PET imaging in Alzheimer disease and frontotemporal lobar degeneration. *Neurology*, **68**, 1205–12.
110. Rowe CC, Ng S, Ackermann U, et al. (2007). Imaging beta-amyloid burden in aging and dementia. *Neurology*, **68**, 1718–25.
111. Engler H, Santillo AF, Wang SX, et al. (2008). In vivo amyloid imaging with PET in frontotemporal dementia. *European Journal of Nuclear Medicine and Molecular Imaging*, **35**, 100–6.
112. Leyton CE, Villemagne VL, Savage S, et al. (2011). Subtypes of progressive aphasia: application of the International Consensus Criteria and validation using beta-amyloid imaging. *Brain*, **134**, 3030–43.
113. Rabinovici GD, Rosen HJ, Alkalay A, et al. (2011). Amyloid vs FDG-PET in the differential diagnosis of AD and FTLD. *Neurology*, **77**, 2034–42.
114. Villemagne VL, Ong K, Mulligan RS, et al. (2011). Amyloid imaging with (18)F-florbetaben in Alzheimer disease and other dementias. *Journal of Nuclear Medicine*, **52**, 1210–7.
115. Rowe CC, Ackerman U, Browne W, et al. (2008). Imaging of amyloid beta in Alzheimer's disease with 18F-BAY94-9172, a novel PET tracer: proof of mechanism. *Lancet Neurology*, **7**, 129–35.
116. Zhou J, Greicius MD, Gennatas ED; et al. (2010). Divergent network connectivity changes in behavioural variant frontotemporal dementia and Alzheimer's disease. *Brain*, **133**, 1352–67.
117. Seeley WW, Menon V, Schatzberg AF, et al. (2007). Dissociable intrinsic connectivity networks for salience processing and executive control. *Journal of Neuroscience*, **27**, 2349–56.
118. Farb NA, Grady CL, Strother S, et al. (2013). Abnormal network connectivity in frontotemporal dementia: evidence for prefrontal isolation. *Cortex*, **49**, 1856–73.
119. Filippi M, Agosta F, Scola E, et al. (2012). Functional network connectivity in the behavioral variant of frontotemporal dementia. *Cortex*, **49**(9), 2389–401.
120. Whitwell JL, Josephs KA, Avula R, et al. (2011). Altered functional connectivity in asymptomatic MAPT subjects: a comparison to bvFTD. *Neurology*, **77**, 866–74.
121. Day GS, Farb NA, Tang-Wai DF, et al. (2013). Salience Network Resting-State Activity: prediction of frontotemporal dementia progression. *Journal of the American Medical Association: Neurology*, **70**(10), 1249–53
122. Filippi M, van den Heuvel M, Fornito A, et al. (2013). Assessing brain system dysfunction through MRI-based connectomics. *Lancet Neurology*, **12**(12), 1189–99.
123. Agosta F, Sala S, Valsasina P, et al. (2013). Brain network connectivity assessed using graph theory in frontotemporal dementia. *Neurology*, **81**, 134–43.
124. Seeley WW, Crawford RK, Zhou J, et al. (2009). Neurodegenerative diseases target large-scale human brain networks. *Neuron*, **62**, 42–52.
125. Borroni B, Alberici A, Cercignani M, et al. (2012). Granulin mutation drives brain damage and reorganization from preclinical to symptomatic FTLD. *Neurobiology of Aging*, **33**, 2506–20.
126. Rohrer JD, and Rosen HJ. (2013). Neuroimaging in frontotemporal dementia. *International Review of Psychiatry*, **25**, 221–9.

CHAPTER 20

Dementia with Lewy bodies

Michael J. Firbank and John T. O'Brien

Introduction

Lewy bodies (LB) are spherical, neuronal inclusions that were first described in cases of 'paralysis agitans' by the neuropathologist Friedrich Lewy [1]. Lewy body disease was considered as a rare cause of dementia until the use of improved neuropathological techniques, such as anti-ubiquitin immunocytochemistry, allowed enhanced visualization of cortical LB. A series of studies in Europe and North America in the late 1980s identified LB at autopsy in the brains of 15–20% of elderly demented cases [2,3], establishing it as the second most common form of degenerative dementia in old age.

Clinically, the characteristic features that distinguish dementia with Lewy bodies (DLB) from other forms of dementia include fluctuating cognitive impairment, prominent or vivid and recurrent visual hallucinations, and spontaneous extrapyramidal symptoms. Other important features are REM sleep-behaviour disorder and neuroleptic (antipsychotic) hypersensitivity. Diagnosis is made according to the current International Consensus Criteria [4].

Dementia develops frequently in people with Parkinson's disease [5], and DLB is similar to Parkinson's disease dementia (PDD) in clinical, neurochemical, and pathological features. It has been argued that the two disorders should be seen as two ends of a Lewy body disease spectrum [6]. Currently, DLB is distinguished from PDD by the duration of extrapyramidal motor symptoms prior to the onset of dementia—if motor features have been present for less than a year, the diagnosis is DLB, and if over a year, then PDD.

Positron emission tomography (PET)/single photon emission computed tomography (SPECT) imaging

Dopaminergic system

In DLB, as in Parkinson's disease, there is significant nigrostriatal degeneration in most cases, paralleled by a marked loss of the presynaptic dopamine transporter in the striatum. Several SPECT and PET ligands, which show high specificity for the dopamine transporter, or the monaminergic transporter, have been developed. Of these, the dopamine transporter ligand [I-123]-2beta-carbomethoxy-3beta-(4-iodophenyl)-N-(3-fluoropropyl) nortropane (FP-CIT, DaTSCAN^{TM}) has been the most widely studied in DLB. In normal subjects and those with AD, the ligand is taken up in the caudate and putamen where neurones expressing the dopamine transporter are concentrated. In DLB, however, uptake is almost absent in the putamen, and is reduced in the caudate (Fig. 20.1).

The presence of abnormal FP-CIT uptake has very good diagnostic accuracy for DLB/PDD with a sensitivity of around 80% and specificity of 90% [7]. Sensitivity is probably limited because not all DLB subjects show the classic brainstem, limbic, neocortical model of alpha-synuclein progression described by Braak [8], with around 10% of subjects showing limbic or neocortical pathology without significant nigrostriatal loss [9]. The latest revision of the Consensus Criteria for DLB diagnosis [4] allows a diagnosis of probable DLB to be made in the presence of one core feature of DLB plus low dopamine transporter uptake demonstrated by SPECT or PET imaging, and this part of the new criteria has been validated as having very high positive predictive value for probable DLB [10].

Assessment of the dopaminergic system is also possible with PET [18F]-DOPA, which reflects dopamine synthesis activity, and with [11C]-dihydrotetrabenazine (DTBZ)—a ligand for the vesicular monoamine transporter type-2, which transports the dopamine to vesicles for release into the synapse [11]. Images from these ligands are similar in appearance to dopamine transporter scans.

Perfusion/glucose metabolism

Glucose metabolism has been investigated in DLB with PET and [^{18}F]-2-fluoro-2-deoxy-D-glucose (FDG), and perfusion with SPECT and a number of different tracers: ^{99m}Tc hexamethylpropylene amine oxime (HMPAO, exametazime), N-isopropyl-p-[^{123}I]iodoamphetamine (IMP) and ^{99m}Tc-ethyl cysteinate dimer (ECD). There is a widespread pattern of reduced glucose metabolism [12–14] and perfusion [15,16] in the midline and lateral parietal lobes, and frontal lobe which resembles that of AD. However, in distinction to AD, there is a hypoperfusion/metabolism of the occipital lobe [12,17] and relatively preserved medial temporal lobes [14,18] (Fig. 20.2). There is also evidence that in the midline parietal area, the posterior cingulate is more affected in AD, whilst DLB have relatively greater reduction in perfusion/metabolism in the precuneus region [18,19]. The diagnostic accuracy of FDG-PET for distinguishing AD from DLB is in the range of 75–85% [13,14,19] and for SPECT perfusion 70–80% [15,18].

One issue in interpreting the perfusion and metabolism images is that they are often acquired in relative, rather than absolute units. Hence, a reference region is required to determine relative hyper- or hypo-perfusion/metabolism. Since there is profound reduction of metabolism in large cortical regions in DLB, using the whole brain (or gray matter) average as a reference region results in unaffected areas appearing relatively hyperperfused [20]. The choice of a reference region is not completely standard—the cerebellum has been shown to be a good choice in AD, since it is relatively unaffected [21,22].

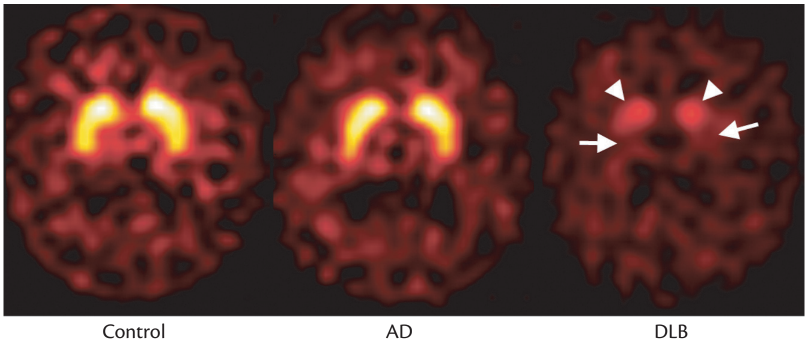

Fig. 20.1 Image showing FP-CIT scans in healthy control, AD and DLB subject. In the DLB, reduced uptake is evident in the caudate (arrow head) and putamen (arrows).

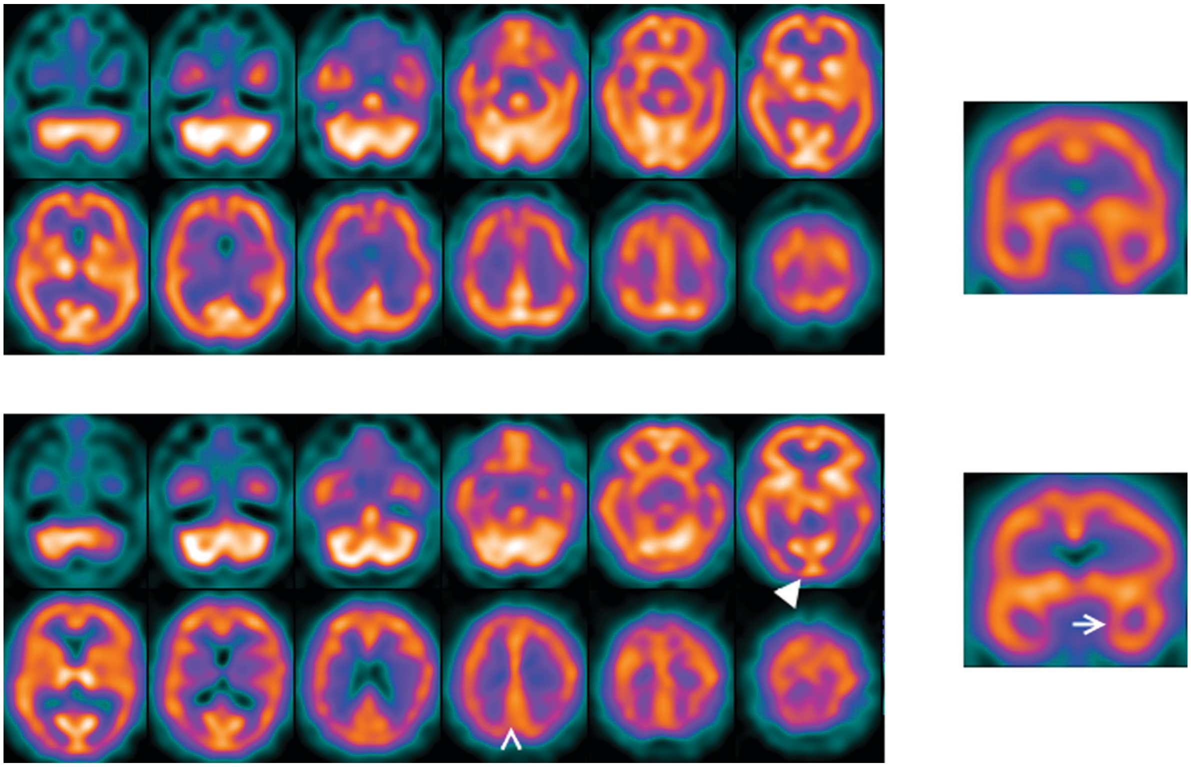

Fig. 20.2 SPECT perfusion scan: normal scan above, DLB below, showing occipital (solid arrow head) and precuneus perfusion deficit (arrow head). Medial temporal perfusion (on the coronal image on the right hand panel) is relatively preserved in DLB (arrow).

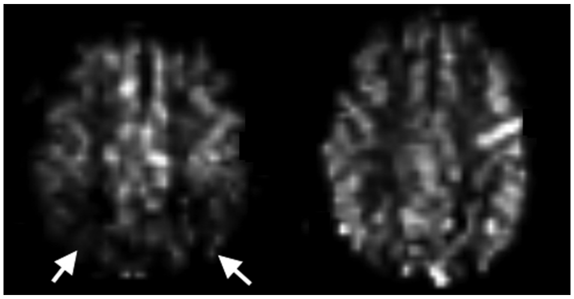

Fig. 20.3 Axial perfusion ASL image showing DLB on the left, and normal on the right. Deficits in the parietal lobe are evident on the DLB (arrows).

Perfusion has also more recently been investigated with MRI [23,24] using arterial spin-labelling (ASL), (Fig. 20.3) with similar results to the SPECT perfusion findings.

Amyloid PET imaging

Over the last 10 years, the use of the PET tracer Pittsburgh compound B (PiB) has established itself as a sensitive and specific marker of amyloid-β deposition *in vivo* [25]. Most of the research done with this tracer has been in AD, which shows strong uptake, particularly in the pre-frontal cortex, midline, and lateral parietal cortex, temporal cortex, and striatum. Imaging is usually performed approximately 90 minutes after the injection of the tracer, and the cerebellum is used as a reference region (since it has low amyloid-β deposition) to calculate uptake ratios.

The studies performed in DLB have had some variability in results, with some reporting similar uptake in DLB to AD [26,27], and some low levels of uptake [28]. However, most studies find DLB intermediate between AD and controls [29–31], with some normal appearing and some AD-like scans. It seems likely that PDD cases can also have elevated amyloid-β deposition [28,29], but to a lesser extent than DLB [30], which would fit with pathological studies suggesting greater cortical AD pathology in DLB [32]. Increased PiB binding has been associated with the apolipoprotein E4 (ApoE4) allele and worse cognitive score [29]. Overall, at least half of DLB have elevated PiB levels, and from the studies to date, no obvious differences in regional distribution have been noted compared with AD.

One disadvantage of PiB is that the radioactive carbon isotope has a very short half-life (20 minutes), and thus it needs to be prepared on site, limiting its use to centres with their own cyclotron. Recently, amyloid-β tracers utilizing radioactive fluorine (half-life 110 minutes) have been developed, which give similar results to PiB [33], albeit with slightly lower binding levels. These include 2-(1-{6-[(2-[F-18]fluoroethyl)(methyl)amino]-2-naphthyl}ethylidene) malononitrile (FDDNP, Siemens), which binds to both tau neurofibrillary tangles and amyloid plaques [34], AV-45 (florbetapir, Avid/Lilly) [35], which is already FDA approved for clinical use, GE-067 (flutemetamol, GE Healthcare) and Bay 94-9172 (florbetaben, Bayer healthcare) [33].

Cholinergic imaging

Neuropathological studies have found marked cholinergic deficits in DLB [36,37], and a number of PET and SPECT ligands have been developed to depict the cholinergic nervous system *in vivo*.

Activity of acetylcholinesterase (the enzyme that breaks down acetylcholine), has been investigated with the ligands N-[11C] methylpiperidin-4-yl acetate ([11C]MP4A) and propionate ([11C] MP4P) [38]. In DLB, there is a widespread reduction of acetylcholinesterase activity [39], most marked in posterior regions, and including the thalamus [40], which has cholinergic input from pontine brainstem cholinergic neurons. This is very similar to that seen in PD [41], whereas in AD, the deficits are most marked in the temporal lobes [42] and normal in the thalamus [40].

Imaging with SPECT of muscarinic receptors using (R,R) I-123-iodo-quinuclidinyl-benzilate (QNB) [43] and of nicotinic receptors with 125I-5-Iodo-3-[2(S)-2-azetidinylmethoxy] pyridine (5IA-85380) has found decreases in the temporal and frontal lobes of PDD and DLB, and a relative increase in uptake of both ligands in the occipital lobe, with the nicotinic ligand uptake being higher in DLB subjects with recent hallucinations [44].

Cardiac imaging

Cardiovascular autonomic dysfunction is common in DLB [45], and impairment of the peripheral sympathetic nervous system can occur in the earliest clinical stage of PD [46]. Cardiac scintigraphy using iodine-123 metaiodobenzylguanidine, (123I-MIBG) an analogue of noradrenaline, has been used for estimating local myocardial sympathetic nerve damage. Most studies have acquired images 3–4 hours after injection of the tracer. The ratio of uptake in the heart to the mediastinum is calculated using a region of interest. This ratio has been found to be reduced in DLB in comparison with AD and healthy subjects with a diagnostic accuracy for DLB versus AD of sensitivity and specificity of approximately 95% [47].

One potential advantage of MIBG over FP-CIT is that myocardial MIBG can distinguish PD and DLB from atypical parkinsonian syndromes such as multiple system atrophy, corticobasal degeneration, and progressive supranuclear palsy [48]. However, it is important to note that reduced MIBG uptake has also been reported in patients with cerebrovascular disease [49]. It is also markedly abnormal in severe heart failure, where it is used clinically as a marker of poor cardiac outcome [50], and may be abnormal in those with more severe ischaemic heart disease. Most studies of MIBG have been undertaken on carefully selected populations, where cardiac disease, and sometimes even cardiac risk factors, have been excluded [47]. How it performs in more ‘real world’ samples of older people with comorbid vascular disease remains to be determined. As such, although MIBG scintigraphy seems to be a useful tool to aid the diagnosis of DLB, and is listed as a supportive feature in current criteria, there is a need for larger clinical multisite studies and investigation of the confounding effect of heart disease.

Magnetic resonance imaging

Structural imaging

Anatomical T_1-weighted MR scans have been used to compare DLB with healthy subjects and AD. The most consistent finding is that in the medial temporal lobe/ hippocampus, there is less atrophy in DLB than AD [51–56], although the presence of medial temporal atrophy does not rule out the diagnosis of DLB [57].

In the medial temporal lobe, studies of hippocampus morphology have found a different spatial distribution of atrophy in DLB compared with AD, with the CA2 and CA3 regions being more affected in DLB, and the CA1 and subiculum in AD [58,59].

In general, DLB has less atrophy than AD of a similar disease severity, both in cross-sectional [55,56,60] and longitudinal studies [61,62]. The most commonly affected area is the temporal lobe (Fig. 20.4), although the occipital, parietal, and frontal regions are also affected. The midbrain has been reported to be more atrophied in DLB than AD [60,63], which may relate to the greater cholinergic deficit in DLB [36] and/or the presence of midbrain synuclein pathology [64]. Putamen volume reduction (of about 15%) has been observed in DLB [65,66], which again may be the result of increased striatal synuclein pathology. Studies comparing structural brain changes with a pathology have shown an association between hippocampal atrophy in DLB and underlying tau (tangle) pathology [67] and smaller amygdala (but not hippocampus) volume associated with greater synuclein pathology [68]. This latter finding is interesting, given the known vulnerability of the amygdala to synuclein pathology in AD [69].

White matter hyperintensities on T_2-weighted images are perhaps more common in DLB than in healthy subjects, but no more so than in AD [70,71]. They probably reflect concomitant subcortical ischaemic vascular disease, but may partly reflect amyloid angiopathy.

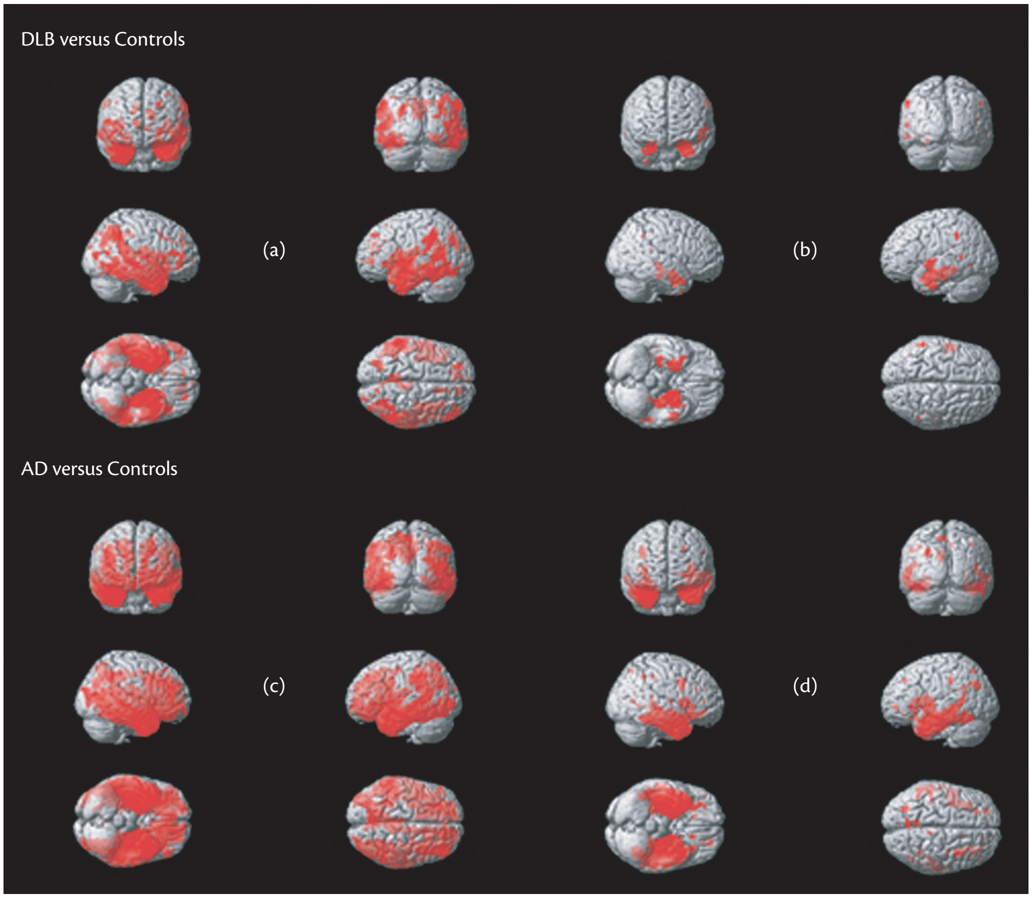

Fig. 20.4 Areas of significantly reduced grey matter volume in DLB and AD displayed on surface rendering of a standard brain (data from [56] using voxel-based morphometry, significance threshold (a) and (c) are $p < 0.001$ uncorrected; (b) and (d) are $p < 0.05$ family wise corrected for multiple comparisons).

Modified from Watson R, O'Brien JT, Barber R, et al. (2011). Patterns of gray matter atrophy in dementia with Lewy bodies: a voxel-based morphometry study. *International Psychogeriatrics*, **24**(4), 532–40. Copyright (2011), with permission from Cambridge University Press.

Diffusion tensor MRI

Studies with diffusion tensor MRI have found a broad pattern of increased mean diffusivity and reduced fractional anisotropy in DLB. The changes in DLB are quite similar to AD, but with perhaps more posterior white matter changes (Fig. 20.5) and, similar to atrophy findings, more temporal lobe changes in AD and more subcortical changes in DLB [72]. The inferior longitudinal fasciculus (which connects the occipital to temporal lobe) has been the focus of several reports [73–75], showing greater change in DLB compared to healthy controls, which may relate to visual symptoms of the disease [73].

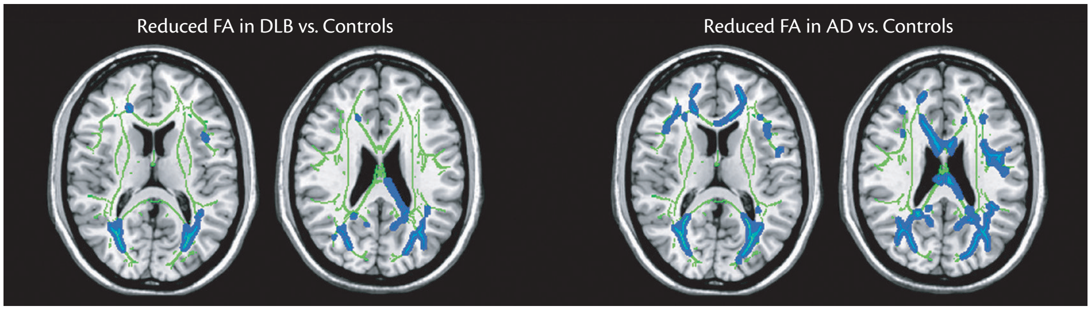

Fig. 20.5 Results from analysis of FA in DLB and AD compared to controls. Blue is areas of significantly lower FA compared to controls ($p < 0.05$ corrected for multiple comparisons) [72]. The analysis was performed using the tract-based spatial statistics method [76], which compares FA values over white matter tracts common to all subjects (shown in green).

Modified from Watson R, Blamire AM, Colloby SJ, et al. (2012). Characterizing dementia with Lewy bodies by means of diffusion tensor imaging. *Neurology*, **79**(9), 906–14. Copyright (2012), with permission from Wolters Kluwer Health.

^{1}H-MRS

There have been few studies of ^{1}H-MRS in DLB. The neuronal marker N-acetyl aspartate, which is reduced in many neurodegenerative diseases, including AD, was not found to be reduced in the parietal grey matter of DLB [77,78], although it has been reported to be reduced in medial temporal lobe [79] and parietal white matter [78]. Unlike AD, the concentration of myo-inositol does not appear to be increased in DLB, indicating perhaps an absence of gliosis [77,78]. Further studies would be required to more precisely determine ^{1}H-MR spectroscopy changes in DLB, but they are probably not particularly distinctive.

Functional MRI

There have been very few papers describing the use of task-related fMRI in DLB. These have focused on investigating the visual system. Taylor et al. [23] performed fMRI, whilst subjects looked at three different types of image—a flashing chequer board versus a grey screen; a set of moving dots versus flickering dots; and pictures of objects versus scrambled pictures. They found no difference between DLB and controls in the primary visual cortex in response to the chequer board, but there was significantly lower activation of the motion sensitive area V5/MT in response to the moving dots in DLB.

Sauer et al. [80] compared fMRI in DLB, AD, and controls on visual tasks of colour, face, and biological motion (dots moving in the pattern of a walking person). Similar to Taylor et al. when performing the motion task, there was lower activity in the V5/MT region in the DLB group compared with AD or controls, which was accounted for by poorer performance on the task. They also found increased activity in DLB relative to AD in the superior temporal sulcus—a region previously reported to be involved in processing biological motion.

The default mode network (DMN) is a set of brain regions, including lateral and midline parietal, and anterior frontal regions, which are typically active when people are not actively engaged in a task [81]. Deactivation of these regions is frequently seen during task performance, with the level of deactivation associated with degree of focus on task in normal individuals [82]. Sauer et al. found reduced deactivation in the DMN of DLB and AD, and that this reduced deactivation was related to poorer performance on the tasks [80].

The DMN has also been investigated by the analysis of resting state fMRI. Galvin et al. [83] looked at regional correlations with the time course of the signal in the precuneus, and found in DLB versus controls increased connectivity with regions in the dorsal attention network and the putamen, but decreased connectivity between the precuneus and other DMN regions and visual cortices. Kenny et al. [84], using a similar method, found no significant differences in DLB in regional correlations to the precuneus, but greater connectivity to the adjacent posterior cingulate region in a number of locations. One difference between the two studies is that Kenny et al. used individually placed regions, whereas Galvin et al. had their region placed via registration to a standard brain template, and it is possible that brain atrophy in their subjects led to imprecise positioning of their region. Kenny et al. [84] also investigated functional connectivity of the occipital cortex in DLB, and found it to be normal. A number of functional brain networks have been identified [85], but we are not aware of any resting state studies investigating them in DLB.

Microbleeds

T_2*-weighted MRI allows acquisition of images that are sensitive to inhomogeneities in the magnetic field. In older people, small dark areas are often visible on these images, and have been interpreted as depicting microbleeds [86]. These microbleeds have been associated with amyloid angiopathy when in lobar distribution, and with hypertensive brain disease when present in deep structures such as the basal ganglia [86]. In AD, microbleeds are frequently found in lobar distribution, which is consistent with the presence of amyloid pathology in AD [87]. No studies have been performed in DLB as yet, although it is likely that, similar to findings with amyloid PET imaging, that microbleeds will be more frequent in DLB than controls, but less so than AD.

Conclusions

The most distinguishing imaging finding in DLB is reduction of dopaminergic activity in the basal ganglia. Cerebral perfusion or metabolism has a distinctive pattern of parieto-occipital reduction, with relative preservation of posterior cingulate and temporal lobe, although there is some overlap with AD. Cardiac sympathetic denervation can be visualized using MIBG imaging, and has the potential to become a diagnostic tool, but research is required to investigate the influence of comorbid vascular disease. There is scope for further research into patterns of brain activity depicted with fMRI, the frequency, and severity of amyloid-β deposition, and the role of white matter changes in DLB.

References

1. Lewy FH. (1912). Paralysis agitans I. Pathologische Anatomie. In: Lewandowsky M (ed.) *Handbuch der Neurologie III*, pp.920–33. Berlin: Springer.
2. Perry RH, Irving D, Blessed G, et al. (1990). Senile dementia of Lewy body type: a clinically and neuropathologically distinct form of Lewy body dementia in the elderly. *Journal of Neurological Sciences*, **95**, 119–39.
3. Hansen L, Salmon D, Galasko D, et al. (1990). The Lewy body variant of Alzheimers disease—a clinical and pathological entity. *Neurology*, 40(1), 1–8.
4. McKeith IG, Dickson DW, Lowe J, et al. (2005). Diagnosis and management of dementia with Lewy bodies: third report of the DLB consortium. *Neurology*, **65**(12), 1863–72.
5. Aarsland D, Andersen K, Larsen JP, et al. (2001). Risk of dementia in Parkinson's disease—a community-based, prospective study. *Neurology*, **56**(6), 730–6.
6. McKeith I. (2009). Commentary: DLB and PDD: the same or different? Is there a debate? *International Psychogeriatric*, **21**(2), 220–4.
7. Papathanasiou ND, Boutsiadis A, Dickson J, et al. (2012). Diagnostic accuracy of [123]I-FP-CIT (DaTSCAN) in dementia with Lewy bodies: a meta-analysis of published studies. *Parkinsonism Related Disorders*, **18**(3), 225–9.
8. Braak H, Ghebremedhin E, Rüb U, et al. (2004). Stages in the development of Parkinson's disease-related pathology. *Cell and Tissue Research*, **318**(1), 121–34.
9. Colloby SJ, McParland S, O'Brien JT, et al. (2012). Neuropathological correlates of dopaminergic imaging in Alzheimer's disease and Lewy body dementias. *Brain*, **135**(9), 2798–808.
10. O'Brien JT, McKeith IG, Walker Z, et al. (2009). Diagnostic accuracy of I-123-FP-CIT SPECT in possible dementia with Lewy bodies. *British Journal of Psychiatry*, **194**(1), 34–9.
11. Cummings JL, Henchcliffe C, Schaier S, et al. (2011). The role of dopaminergic imaging in patients with symptoms of dopaminergic system neurodegeneration. *Brain*, **134**(11), 3146–66.

12. Teune LK, Bartels AL, de Jong BM, et al. (2010). Typical cerebral metabolic patterns in neurodegenerative brain diseases. *Movement Disorders*, **25**(14), 2395–404.
13. Ishii K, Soma T, Kono AK, et al. (2007). Comparison of regional brain volume and glucose metabolism between patients with mild dementia with Lewy bodies and those with mild Alzheimer's disease. *Journal of Nuclear Medicine*, **48**, 704–11.
14. Mosconi L, Tsui WH, Herholz K, et al. (2008). Multicenter standardized 18F-FDG PET diagnosis of mild cognitive impairment, Alzheimer's disease, and other dementias. *Journal of Nuclear Medicine*, **49**, 390–8.
15. Minoshima S, Foster NL, Sima AAF, et al. (2001). Alzheimer's disease versus dementia with Lewy bodies: cerebral metabolic distinction with autopsy confirmation. *Annals of Neurology*, **50**(3), 358–65.
16. Yong SW, Yoon JK, An YS, et al. (2007). A comparison of cerebral glucose metabolism in Parkinson's disease, Parkinson's disease dementia and dementia with Lewy bodies. *European Journal of Neurology*, **14**(12), 1357–62.
17. Sato T, Hanyu H, Hirao K, et al. (2007). Deep gray matter hyperperfusion with occipital hypoperfusion in dementia with Lewy bodies. *European Journal of Neurology*, **14**(11), 1299–301.
18. Colloby SJ, Taylor JP, Firbank MJ, et al. (2010). Covariance Tc-99m Exametazime SPECT patterns in Alzheimer's disease and dementia with Lewy bodies. *Journal of Geriatric Psychiatry and Neurology*, **23**(1), 54–62.
19. Lim SM, Katsifis A, Villemagne VL, et al. (2009). The 18F-FDG PET cingulate island sign and comparison to 123I-beta-CIT SPECT for diagnosis of dementia with Lewy bodies. *Journal of Nuclear Medicine*, **50**(10), 1638–45.
20. Borghammer P, Jonsdottir KY, Cumming P, et al. (2008). Normalization in PET group comparison studies—the importance of a valid reference region. *NeuroImage*, **40**(2), 529–40.
21. Soonawala D, Amin T, Ebmeier KP, et al. (2002). Statistical parametric mapping of 99mTc-HMPAO-SPECT images for the diagnosis of Alzheimer's disease: normalizing to cerebellar tracer uptake. *NeuroImage*, **17**, 1193–202.
22. Yakushev I, Landvogt C, Buchholz HG, et al. (2008). Choice of reference area in studies of Alzheimer's disease using positron emission tomography with fluorodeoxyglucose-F18. *Psychiatric Research—Neuroimaging*, **164**(2), 143–53.
23. Taylor JP, Firbank MJ, He J, et al. (2012). Visual cortex in dementia with Lewy bodies: magnetic resonance imaging study. *British Journal of Psychiatry*, **200**(6), 491–8.
24. Fong TG, Inouye SK, Dai W, et al. (2011). Association cortex hypoperfusion in mild dementia with Lewy bodies: a potential indicator of cholinergic dysfunction. *Brain Imaging and Behavior*, **5**, 25–35.
25. Quigley H, Colloby SJ, and O'Brien JT. (2011). PET imaging of brain amyloid in dementia: a review. *International Journal of Geriatric Psychiatry*, **26**(10), 991–9.
26. Gomperts SN, Rentz DM, Moran E, et al. (2008). Imaging amyloid deposition in Lewy body diseases. *Neurology*, **71**(12), 903–10.
27. Claassen DO, Lowe VJ, Peller PJ, et al. (2011). Amyloid and glucose imaging in dementia with Lewy bodies and multiple systems atrophy. *Parkinsonism Related Disorders*, **17**(3), 160–5.
28. Foster ER, Campbell MC, Burack MA, et al. (2010). Amyloid imaging of Lewy body-associated disorders. *Movement Disorders*, **25**(15), 2516–23.
29. Maetzler W, Liepelt I, Reimold M, et al. (2009). Cortical PIB binding in Lewy body disease is associated with Alzheimer-like characteristics. *Neurobiology of Disease*, **34**(1), 107–12.
30. Edison P, Rowe CC, Rinne JO, et al. (2008). Amyloid load in Parkinson's disease dementia and Lewy body dementia measured with [11C]PIB positron emission tomography. *Journal of Neurology, Neurosurgery & Psychiatry*, **79**(12), 1331–8.
31. Rowe CC, Ng S, Ackermann U, et al. (2007). Imaging beta-amyloid burden in aging and dementia. *Neurology*, **68**(20), 1718–25.
32. Halliday GM, Song YJC, and Harding AJ. (2011). Striatal beta-amyloid in dementia with Lewy bodies but not Parkinson's disease. *Journal of Neural Transmission*, **118**(5), 713–19.
33. Villemagne VL, Ong K, Mulligan RS, et al. (2011). Amyloid imaging with 18F-Florbetaben in Alzheimer disease and other dementias. *Journal of Nuclear Medicine*, **52**, 1210–7
34. Braskie MN, Klunder AD, Hayashi KM, et al. (2010). Plaque and tangle imaging and cognition in normal aging and Alzheimer's disease. *Neurobiology of Aging*, **31**(10), 1669–78.
35. Joshi AD, Pontecorvo MJ, Clark CM, et al. (2012). Performance characteristics of amyloid PET with florbetapir F-18 in patients with Alzheimer's disease. *Journal of Nuclear Medicine*, **53**(3), 378–84.
36. Perry EK, Irving D, Kerwin JM, et al. (1993). Cholinergic transmitter and neurotrophic activities in Lewy body dementia—similarity to Parkinson and distinction from Alzheimer disease. *Alzheimer Disease and Associated Disorders*, **7**(2), 69–79.
37. Tiraboschi P, Hansen LA, Alford M, et al. (2002). Early and widespread cholinergic losses differentiate dementia with Lewy bodies from Alzheimer disease. *Archives of General Psychiatry*, **59**(10), 946–51.
38. Namba H, Fukushi K, Nagatsuka S, et al. (2002). Positron emission tomography: quantitative measurement of brain aceytlcholinesterase activity using radiolabeled substrates. *Methods*, **27**, 242–50.
39. Klein JC, Eggers C, Kalbe E, et al. (2010). Neurotransmitter changes in dementia with Lewy bodies and Parkinson disease dementia in vivo. *Neurology*, **74**(11), 885–92.
40. Kotagal V, Müller MLTM, Kaufer DI, et al. (2012). Thalamic cholinergic innervation is spared in Alzheimer disease compared to parkinsonian disorders. *Neuroscience Letters*, **514**, 169–72.
41. Hilker R, Thomas AV, Klein JC, et al. (2005). Dementia in Parkinson disease—Functional imaging of cholinergic and dopaminergic pathways. *Neurology*, **65**(11), 1716–22.
42. Bohnen NI, Kaufer DI, Ivanco LS, et al. (2003). Cortical cholinergic function is more severely affected in Parkinsonian dementia than in Alzheimer disease. *Archives of Neurology*, **60**(12), 1745–8.
43. Colloby SJ, Pakrasi S, Firbank MJ, et al. (2006). In vivo SPECT imaging of muscarinic acetylcholine receptors using (R,R) I-123-QNB in dementia with Lewy bodies and Parkinson's disease dementia. *NeuroImage*, **33**(2), 423–9.
44. O'Brien JT, Colloby SJ, Pakrasi S, et al. (2008). Nicotinic alpha4beta2 receptor binding in dementia with Lewy bodies using 123I-5IA-85380 SPECT demonstrates a link between occipital changes and visual hallucinations. *NeuroImage*, **40**(3), 1056–63.
45. Allan LM, Ballard CG, Allen J, et al. (2007). Autonomic dysfunction in dementia. *Journal of Neurology, Neurosurgery & Psychiatry*, **78**(7), 671–8.
46. Spiegel J, Möllers MO, Jost WH, et al. (2005). FP-CIT and MIBG scintigraphy in early Parkinson's disease. *Movement Disorders*, **20**(5), 552–61.
47. Treglia GC, and Giordano, A. (2012). Diagnostic performance of myocardial innervation imaging using MIBG scintigraphy in differential diagnosis between dementia with Lewy bodies and other dementias: a systematic review and a meta-analysis. *Journal of Neuroimaging*, **22**(2), 111–17.
48. Kashihara K, Ohno M, Kawada S, et al. (2006). Reduced cardiac uptake and enhanced washout of I-123-MIBG in pure autonomic failure occurs conjointly with Parkinson's disease and dementia with Lewy bodies. *Journal of Nuclear Medicine*, **47**(7), 1099–101.
49. Nagayama H, Hamamoto M, Ueda M, et al. (2005). Reliability of MIBG myocardial scintigraphy in the diagnosis of Parkinson's disease. *Journal of Neurology, Neurosurgery & Psychiatry*, **76**(2), 249–51.
50. Perrone-Filardi P, Paolillo S, Dellegrottaglie S, et al. (2011). Assessment of cardiac sympathetic activity by MIBG imaging in patients with heart failure: a clinical appraisal. *Heart*, **97**(22), 1828–33.
51. Barber R, Ballard C, McKeith IG, et al. (2000). MRI volumetric study of dementia with Lewy bodies. *Neurology*, **54**(6), 1304–9.
52. Beyer MK, Larsen JP, and Aarsland D. (2007). Gray matter atrophy in Parkinson disease with dementia and dementia with Lewy bodies. *Neurology*, **69**(8), 747–54.
53. Burton EJ, Karas G, Paling SM, et al. (2002). Patterns of cerebral atrophy in dementia with Lewy bodies using voxel based morphometry. *NeuroImage*, **17**, 618–30.

54. Tam CW, Burton EJ, McKeith IG, et al. (2005). Temporal lobe atrophy on MRI in Parkinson disease with dementia: a comparison with Alzheimer disease and dementia with Lewy bodies. *Neurology*, **64**(5), 861–5.
55. Takahashi R, Ishii K, Miyamoto N, et al. (2010). Measurement of gray and white matter atrophy in dementia with Lewy bodies using diffeomorphic anatomic registration through exponentiated Lie algebra: a comparison with conventional voxel-based morphometry. *American Journal of Neuroradiology*, **31**(10), 1873–8.
56. Watson R, O'Brien JT, Barber R, et al. (2011). Patterns of gray matter atrophy in dementia with Lewy bodies: a voxel-based morphometry study. *International Psychogeriatrics*, **24**(4), 532–40.
57. Barkhof F, Polvikoski TM, Van Straaten ECW, et al. (2007). The significance of medial temporal lobe atrophy: a postmortem MRI study in the very old. *Neurology*, **69**(15), 1521–7.
58. Sabattoli F, Boccardi M, Galluzzi S, et al. (2008). Hippocampal shape differences in dementia with Lewy bodies. *NeuroImage*, **41**(3), 699–705.
59. Firbank MJ, Blamire AM, Teodorczuk A, et al. (2010). High resolution imaging of the medial temporal lobe in Alzheimer's disease and dementia with Lewy bodies. *Journal of Alzheimer's Disease*, **21**(4), 1129–40.
60. Vemuri P, Simon G, Kantarci K, et al. (2011). Antemortem differential diagnosis of dementia pathology using structural MRI: Differential-STAND. *NeuroImage*, **55**(2), 522–31.
61. O'Brien JT, Paling S, Barber R, et al. (2001). Progressive brain atrophy on serial MRI in dementia with Lewy bodies, AD, and vascular dementia. *Neurology*, **56**(10), 1386–8.
62. Whitwell JL, Jack CR, Parisi JE, et al. (2007). Rates of cerebral atrophy differ in different degenerative pathologies. *Brain*, **130**, 1148–58.
63. Whitwell JL, Weigand SD, Shiung MM, et al. (2007). Focal atrophy in dementia with Lewy bodies on MRI: a distinct pattern from Alzheimer's disease. *Brain*, **130**, 708–19.
64. Jellinger KA. (2004). Lewy body related alpha-synucleinopathy in the aged human brain. *Journal of Neural Transmission*, **111**, 1219–35.
65. Cousins DA, Burton EJ, Burn D, et al. (2003). Atrophy of the putamen in dementia with Lewy bodies but not Alzheimer's disease: an MRI study. *Neurology*, **61**(9), 1191–5.
66. Geng DY, Li YX, and Zee CS. (2006). Magnetic resonance imaging-based volumetric analyses of basal ganglia nuclei and substantia nigra in patients with Parkinson's disease. *Neurosurgery*, **58**(2), 256–61.
67. Burton EJ, Barber R, Mukaetova-Ladinska EB, et al. (2009). Medial temporal lobe atrophy on MRI differentiates Alzheimer's disease from dementia with Lewy bodies and vascular cognitive impairment: a prospective study with pathological verification of diagnosis. *Brain*, **132**(1), 195–203.
68. Burton EJ, Mukaetova-Ladinska EB, Perry RH, et al. (2012). Neuropathological correlates of volumetric MRI in autopsy-confirmed Lewy body dementia. *Neurobiology and Aging*, **33**, 1228–36.
69. Hamilton RL. (2000). Lewy bodies in Alzheimer's disease: a neuropathological review of 145 cases using alpha-synuclein immunohistochemistry. *Brain Pathology*, **10**(3), 378–84.
70. Barber R, Scheltens P, Gholkar A, et al. (1999). White matter lesions on magnetic resonance imaging in dementia with Lewy bodies, Alzheimer's disease, vascular dementia, and normal aging. *Journal of Neurology, Neurosurgery & Psychiatry*, **67**, 66–72.
71. Burton EJ, McKeith IG, Burn DJ, et al. (2006). Progression of white matter hyperintensities in Alzheimer disease, dementia with Lewy bodies, and Parkinson disease dementia: a comparison with normal aging. *American Journal of Geriatric Psychiatry*, **14**(10), 842–9.
72. Watson R, Blamire AM, Colloby SJ, et al. (2012). Characterizing dementia with Lewy bodies by means of diffusion tensor imaging. *Neurology*, **79**(9), 906–14.
73. Kantarci K, Avula R, Senjem ML, et al. (2010). Dementia with Lewy bodies and Alzheimer disease: Neurodegenerative patterns characterized by DTI. *Neurology*, **74**(22), 1814–21.
74. Ota M, Sato N, Ogawa M, et al. (2009). Degeneration of dementia with Lewy bodies measured by diffusion tensor imaging. *NMR in Biomedicine*, **22**(3), 280–4.
75. Kiuchi K, Morikawa M, Taoka T, et al. (2011). White matter changes in dementia with Lewy bodies and Alzheimer's disease: A tractography-based study. *Journal of Psychiatric Research*, **45**(8), 1095–100.
76. Smith SM, Jenkinson M, Johansen-Berg H, et al. (2006). Tract-based spatial statistics: voxelwise analysis of multi-subject diffusion data. *NeuroImage*, **31**(4), 1487–505.
77. Kantarci K, Petersen RC, Boeve BF, et al. (2004). H-1 MR spectroscopy in common dementias. *Neurology*, **63**(8), 1393–8.
78. Molina JA, Garcis-Segura JM, Benito-Leon J, et al. (2002). Proton magnetic resonance spectroscopy in dementia with Lewy bodies. *European Neurology*, **48**, 158–63.
79. Xuan XQ, Ding MP, and Gong XY. (2008). Proton magnetic resonance spectroscopy detects a relative decrease of N-acetylaspartate in the hippocampus of patients with dementia with Lewy bodies. *Journal of Neuroimaging*, **18**(2), 137–41.
80. Sauer J, ffytche DH, Ballard C, et al. (2006). Differences between Alzheimer's disease and dementia with Lewy bodies: an fMRI study of task-related brain activity. *Brain*, **129**(7), 1780–8.
81. Raichle ME, MacLeod AM, Snyder AZ, et al. (2001). A default mode of brain function. *PNAS*, **98**(2), 676–82.
82. Thompson GJ, Magnuson ME, Merritt MD, et al. (2012). Short-time windows of correlation between large-scale functional brain networks predict vigilance intraindividually and interindividually. *Human Brain Mapping*, **34**(12), 3280–98.
83. Galvin JE, Price JL, Yan Z, et al. (2011). Resting BOLD fMRI differentiates dementia with Lewy bodies vs Alzheimer disease. *Neurology*, **76**(21), 1797–803.
84. Kenny ER, Blamire AM, Firbank MJ, et al. (2012). Functional connectivity in cortical regions in dementia with Lewy bodies and Alzheimer's disease. *Brain*, **135**(2), 569–81.
85. De Luca M, Beckmann CF, De Stefano N, et al. (2006). fMRI resting state networks define distinct modes of long-distance interactions in the human brain. *NeuroImage*, **29**(4), 1359–67.
86. Greenberg SM, Vernooij MW, Cordonnier C, et al. (2009). Cerebral microbleeds: a guide to detection and interpretation. *Lancet Neurology*, **8**, 165–74.
87. Cordonnier C, and van der Flier WM. (2011). Brain microbleeds and Alzheimer's disease: innocent observation or key player? *Brain*, **134**, 335–44.

CHAPTER 21

Movement disorders

Parkinson's disease and atypical parkinsonisms

Massimo Filippi and Federica Agosta

Introduction

Idiopathic Parkinson's disease (PD) is by far the most common cause of parkinsonism and should always be the diagnosis if a definite secondary cause cannot be identified. Other forms of parkinsonism are broadly classified as atypical parkinsonian syndromes (multiple system atrophy-parkinsonism (MSA-P), progressive supranuclear palsy (PSP), corticobasal syndrome (CBS)), and secondary (symptomatic, acquired) parkinsonisms. Less frequently, patients who receive an initial clinical diagnosis of PD are found to have parkinsonian features as part of other diseases, such as dementia with Lewy bodies (DLB) or Alzheimer's disease (AD).

The definitive diagnosis of idiopathic PD requires histological demonstration of intraneuronal Lewy body inclusions in the substantia nigra (SN) pars compacta [1]. In most cases, the diagnosis of probable PD can be made on clinical grounds and no ancillary investigations are needed. However, in early PD the full triad of clinical symptoms and signs (bradykinesia, tremor at rest and rigidity) may not be manifested yet [2]. This chapter summarizes the role of nuclear medicine techniques, magnetic resonance imaging (MRI) and transcranial sonography to the diagnostic work-up of patients with parkinsonism. The potential of neuroimaging techniques in elucidating the physiopathology of parkinsonian diseases is also highlighted.

Parkinson's disease

Functional imaging with PET and SPECT

Imaging dopaminergic function

PD is characterized by a progressive degeneration of the dopaminergic neurons in the SN projecting to the striatum that begins several years before clinical onset. It is estimated that the interval between onset of dopaminergic degeneration and appearance of symptoms is about 5 years, when a neuronal loss of 40–60% in the SN has occurred [3]. Single-photon emission computed tomography (SPECT) and positron emission tomography (PET) allow objective measurement of the loss of dopaminergic function and thus are utilized in the diagnostic work-up of parkinsonian syndromes (Fig. 21.1).

Presynaptic dopaminergic integrity can be assessed *in vivo* in three different ways [3]:

1. Presynaptic dopamine uptake through the dopamine transporter (DAT) is the primary mechanism of dopamine removal from the striatal synaptic cleft. Striatal DAT availability provides a measure of dopamine terminal function and can be assessed with a variety of SPECT and PET tracers, such as ^{123}I-2β-carbomethoxy-3β-(4-iodophenyl)-tropane (^{123}I-β-CIT), ^{123}I-*N*-3-fluoropropyl-2β-carbomethoxy-3β-(4-iodophenyl)nortropane (^{123}I-FP-CIT or DaTSCAN^{TM}), and ^{123}I-2β-carbomethoxy-3β-(4-fluorophenyl (-*N*-(1-iodoprop-1-en-3-yl)nortropane (^{123}I-Altropane) for SPECT and 2β-carbomethoxy-3β-(4-fluorophenyl)tropane (11C-β-CFT), 11C-N-(2-fluoroethyl)-2β-carbomethoxy-3β-(4-iodophenyl)nortropane (^{11}C-β-CIT-FE), ^{18}F-β-CFT, and ^{18}F-FP-CIT for PET (Fig. 21.1).
2. ^{18}F-3,4-dihydroxyphenylalanine (^{18}F-dopa) PET provides a marker of dopaminergic terminal dopa decarboxylase activity and dopamine turnover, since the tracer is taken up by L-aromatic amino acid decarboxylase (AADC), converted to ^{18}F-fluorodopamine, and packaged in synaptic vesicles (Fig. 21.1). However, ^{18}F-dopa uptake is not restricted to dopaminergic neurons, since AADC is also present in serotonergic and noradrenergic neurons.
   - Vesicular monoamine transporter (VMAT2) availability in dopamine terminals can be examined with either ^{11}C- or ^{18}F-dihydrotetrabenazine (DTBZ) PET (Fig. 21.1).

In PD, all these presynaptic dopaminergic function tracers show a characteristic pattern of asymmetric reduction of striatal uptake, more pronounced contralaterally to the clinically more affected side of the body (Fig. 21.2) [3]. Typically, the nigrostriatal dopaminergic projections to the posterior (dorsal-caudal) putamen are affected earlier and more severely than those to the caudate nucleus. In early hemiparkinsonian cases, bilaterally reduced putamen tracer uptake is also seen, activity being most depressed in the putamen contralateral to the affected limbs [4]. Reductions in striatal tracer uptake correlate with pathological measures (i.e. cell loss) and degree of motor disability, particularly bradykinesia and, to a lesser extent, rigidity.

Progression of the disease can be monitored using these tracers in longitudinal studies, as reported by numerous clinical trials assessing efficacy of putative neuroprotective agents [4].

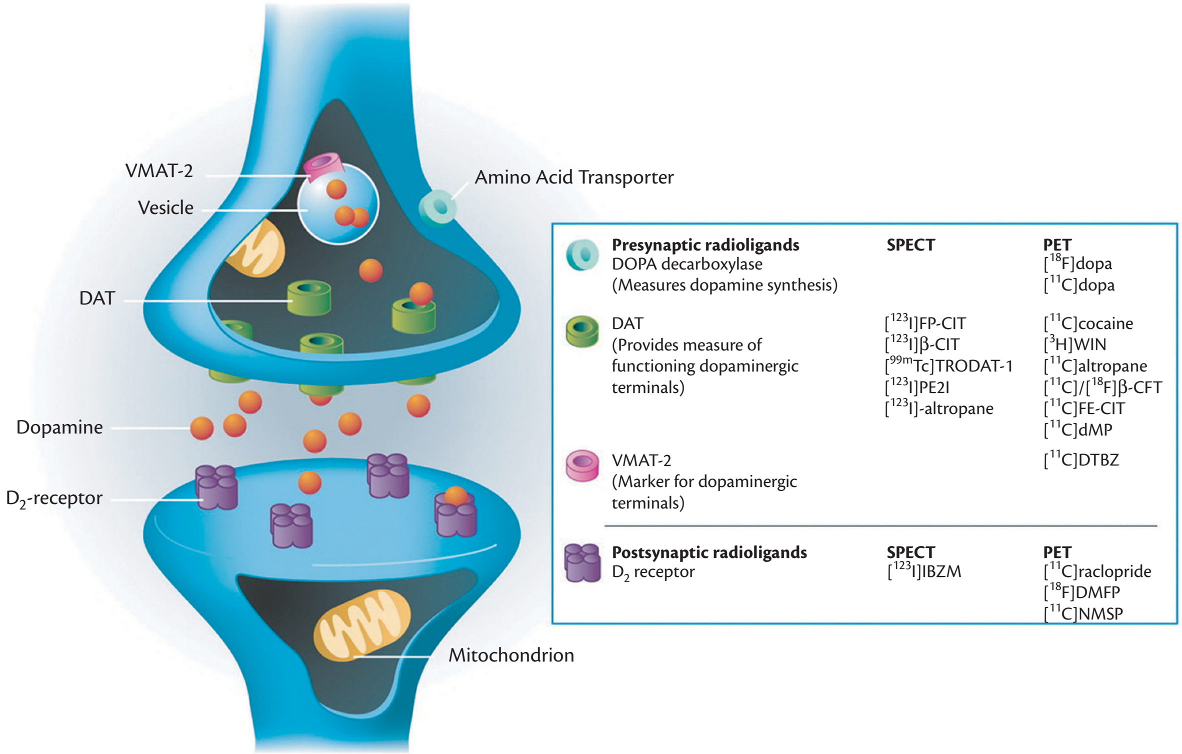

Presynaptic radioligands	**SPECT**	**PET**
DOPA decarboxylase (Measures dopamine synthesis)		[^{18}F]dopa [^{11}C]dopa
DAT (Provides measure of functioning dopaminergic terminals)	[^{123}I]FP-CIT [^{123}I]β-CIT [^{99m}Tc]TRODAT-1 [^{123}I]PE2I [^{123}I]-altropane	[^{11}C]cocaine [^{3}H]WIN [^{11}C]altropane [^{11}C]/[^{18}F]β-CFT [^{11}C]FE-CIT [^{11}C]dMP
VMAT-2 (Marker for dopaminergic terminals)		[^{11}C]DTBZ
Postsynaptic radioligands	**SPECT**	**PET**
D_2 receptor	[^{123}I]IBZM	[^{11}C]raclopride [^{18}F]DMFP [^{11}C]NMSP

Fig. 21.1 Dopaminergic single-photon emission computed tomography and positron emission tomography radioligands. These radioligands image either presynaptic targets—dopamine transporter, vesicular monoamine transporter or dihydroxyphenylalanine (DOPA) decarboxylase activity (reflecting dopamine synthesis)—or post-synaptic D2 dopamine receptors.

Abbreviations: β-CFT, 2β-carbomethoxy-3β-(4-fluorophenyl)tropane; DAT = dopamine transporter; dopa, dihydroxyphenylalanine; DMFP, desmethoxyfallypride; dMP, d-threo methylphenidate; DTBZ, dihydrotetrabenazine; FE-CIT, (*N*-(2-fluoroethyl)-2β-carbomethoxy-3β-(4-iodophenyl)nortropane; IBZM, iodobenzamide; NMSP, 3-*N*-methylspiperone; PE2I, *N*-(3-iodoprop-(2E)-enyl)-2β-carboxymethoxy-3β-(4′-methylphenyl)nortropane; TRODAT-1, [2-[[2-[[[3-(4-chlorophenyl)-8-methyl-8-azabicyclo]3.2.1]oct-2-yl]methyl](2-mercaptoethyl)amino]ethyl]amino] ethanethiolato(3-)-*N*2,*N*20,*S*2,*S*20]oxo-[1R-(exo-exo)]; VMAT, vesicular monoamine transporter; WIN, WIN 55,212-2 cannabinoid receptor agonist.

Reproduced from Cummings JL, Henchcliffe C, Schaier S, et al. (2011). The role of dopaminergic imaging in patients with symptoms of dopaminergic system neurodegeneration. *Brain*, **134**, 3146–66. Copyright (2011), with permission from Oxford University Press.

Notably, nigrostriatal damage is demonstrated using both DAT imaging and ^{18}F-dopa in subjects with increased risk to develop PD, such as presymptomatic carriers of genetic mutations associated with parkinsonism (e.g. Parkin) [5], asymptomatic relatives of familial PD cases [6], elderly patients with hyposmia [7], or rapid-eye-movement sleep behaviour disorders [8,9]. A prospective study of non-parkinsonian subjects with a positive family history of PD showed that 10% of those with hyposmia and reduced

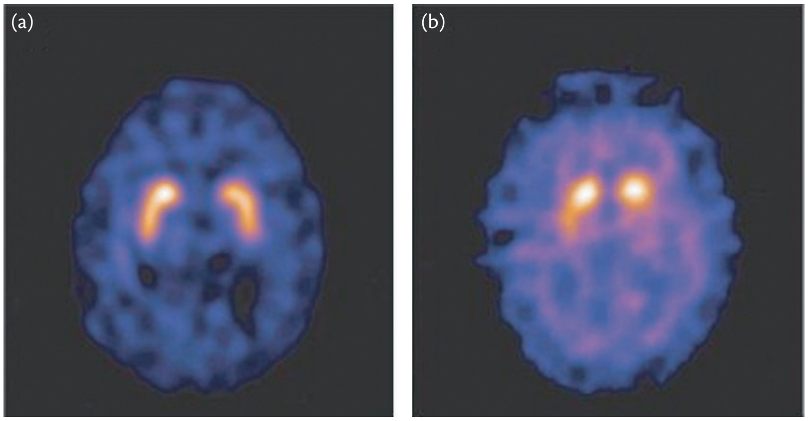

Fig. 21.2 Dopamine transporter (DAT) single-photon emission computed tomography with ^{123}I-*N*-3-fluoropropyl-2β-carbomethoxy-3β-(4-iodophenyl)nortropane (^{123}I-FP-CIT or DaTSCAN^{TM}) shows normal striatal DAT availability in healthy subject (a) and asymmetric DAT loss in patient with Parkinson's disease (b).

Reproduced from McKeith I, O'Brien J, Walker Z, et al. (2007). Sensitivity and specificity of dopamine transporter imaging with 123I-FP-CIT SPECT in dementia with Lewy bodies: a phase III, multicentre study. *Lancet Neurology*, **6**, 305–13. Copyright (2007), with permission from Elsevier.

DAT SPECT binding at baseline developed PD over a two year follow-up period [7].

Presynaptic dopaminergic imaging is clinically useful in differentiating PD from multiple other conditions that may overlap with features of PD, such as drug-induced parkinsonism, essential tremor, and psychogenic parkinsonism/tremor [10]. DaTSCAN^{TM} has been approved for evaluating parkinsonian syndromes and for distinguishing PD from essential tremor. However, it cannot differentiate PD from other forms of presynaptic parkinsonism, such as MSA-P, PSP, and CBS, although PD is associated with a rostro-caudal putamen gradient of dopamine dysfunction compared with the more uniform dysfunction detected in atypical parkinsonisms (see section 'Atypical parkinsonisms' for further details).

It is worth noting that up to 15% of patients suspected of having an early PD have a normal DAT SPECT or PET scan (i.e. subjects with scans without evidence of dopaminergic deficit—SWEDD) [4]. While such a finding is still not fully understood, follow-up studies of SWEDD cases suggest that there is no disease progression, the response to dopaminergic medication is questionable [11], dopamine innervations remain intact, and the glucose metabolic pattern is normal [12]. These findings support the notion that normal dopaminergic imaging excludes the presence of a degenerative parkinsonian syndrome.

Post-synaptic dopamine function can be assessed using PET or SPECT with ligands for D1 and D2 receptor subtypes. Theoretically, abnormalities in ligand binding reflect either receptor density or affinity. Tracers with high affinity can be used to assess the availability of dopamine receptors in extrastriatal sites, while ligands with low affinity for the D2 receptor (e.g. ^{11}C-raclopride) compete with endogenous dopamine and can be used to estimate dopamine release (i.e. alterations of synaptic dopamine concentrations) in response to a variety of pharmacological, physical, and behavioural interventions [4]. In early, untreated PD patients, striatal D2 receptor binding is increased (probably due to receptor up-regulation) and returns to normal or slightly reduced levels once dopamine replacement treatment is started [13]. Again, the initial increase of striatal binding is higher in putamen (posterior > anterior) than in the caudate nucleus. In contrast, striatal D2 binding is reduced in MSA-P and PSP (see below 'Atypical parkinsonism' section). Striatal D1 receptor density is unchanged in PD compared to controls [14].

Glucose metabolism and regional cerebral blood flow

In PD, ^{18}F-fluorodeoxyglucose (FDG) PET reveals a characteristic regional profile characterized by an increased metabolism in the putamen/globus pallidus, thalamus, cerebellum, pons, and sensorimotor cortex, and low metabolism in the lateral frontal, paracentral, and parieto-occipital areas (Fig. 21.3a) [15]. This abnormal pattern, which is called the Parkinson's disease-related covariance pattern (PDRP), correlates linearly with clinical motor ratings (mainly with bradykinesia and rigidity, rather than tremor), increases with disease progression, and can be normalized by successful levodopa treatment or deep brain stimulation. Abnormal PDRP activity was shown to precede motor symptoms by about 2 years [16].

FDG-PET can be helpful for separating PD from atypical parkinsonian syndromes, since glucose metabolism of the lentiform nucleus is preserved or raised in PD, whereas it is reduced in most atypical cases (see below 'Atypical parkinsonism' section).

The Parkinson's disease cognitive-related network pattern (PDCP) defined by FDG-PET involves hypometabolism in the frontal and parietal association cortices, in parallel with relative increases in the cerebellar hemispheres and dentate nuclei [17]. Values of PDCP correlated with cognitive function of cognitively normal PD patients and increased stepwise, depending on the extent of cognitive dysfunction (cognitively unimpaired PD patients < PD patients with a single-domain mild cognitive impairment (MCI) < PD patients with multiple domain MCI < PD patients with dementia (PDD)) [18]. FDG-PET scans of frankly demented PD patients show an AD pattern of impaired brain glucose utilization, posterior parietal and temporal association areas being most affected [4]. Additionally, PDD patients had involvement of the basal ganglia, and frontal and occipital lobes [4]. Patients with PD-MCI have hypometabolism in the same areas when compared to PD subjects without cognitive impairment [19]. A longitudinal study found that early metabolic changes in the visual association and posterior cingulate cortices are associated with incident dementia in PD [20].

Imaging cholinergic function

Molecular imaging studies demonstrated a widespread cholinergic dysfunction in PD, more pronounced and extensive in those with PDD. ^{123}I-iodobenzovesamicol SPECT is a marker of acetylcholine vesicle transporter binding in cholinergic nerve terminals. A reduced ^{123}I-iodobenzovesamicol binding has been found only in the parietal and occipital cortices of cognitively unimpaired PD patients, while it involves all cortical regions in PDD [21]. Another marker of cholinergic function is the level of acetylcholinsterase activity, which can be assessed with 1-^{11}C-methylpiperidin-4-yl acetate (^{11}C-PMP) PET. Cortical binding of ^{11}C-PMP is reduced in PDD when compared to PD patients with no cognitive impairment [22].

Amyloid imaging

Limbic and neocortical Lewy body pathology has been claimed to be the main determinant of the development of cognitive impairment in PD, while cortical β-amyloid deposition seems to determine the rate of progression to dementia [23]. Therefore, of particular interest is the potential of PET amyloid imaging. Both ^{11}C and ^{18}F ligands are available.

While the majority of DLB patients show an increased ^{11}C-Pittsburgh compound B (PIB) binding in associative cortical regions, some degree of amyloid deposition is observed only in a minority of PDD cases (from 17 to 33%) and it is more rarely present in PD patients without dementia (from 0 to 23%) [24]. Thus, amyloid imaging may be useful to distinguish AD and DLB from PD and PDD. The different pattern of amyloid imaging between PDD and DLB is an intriguing finding since distinction between the two disorders is primarily based on the relative timing of onset of dementia and parkinsonism. In a prospective study of cognitively normal PD patients, amyloid accumulation was found to contribute to cognitive, but not motor, decline over up to 5 years of follow-up, although amyloid burden did not distinguish PD-MCI from cognitively unimpaired PD patients at baseline [25]. In this study, PD patients had generally modest PIB retention, well below the values observed in the majority of AD cases [25]. A cross-sectional study of 40 PD patients at risk for developing dementia (with MCI or other known dementia risk factors) had an increased cerebral PIB retention similar to that seen in AD in six patients only; a significant correlation was found between cortical binding values and

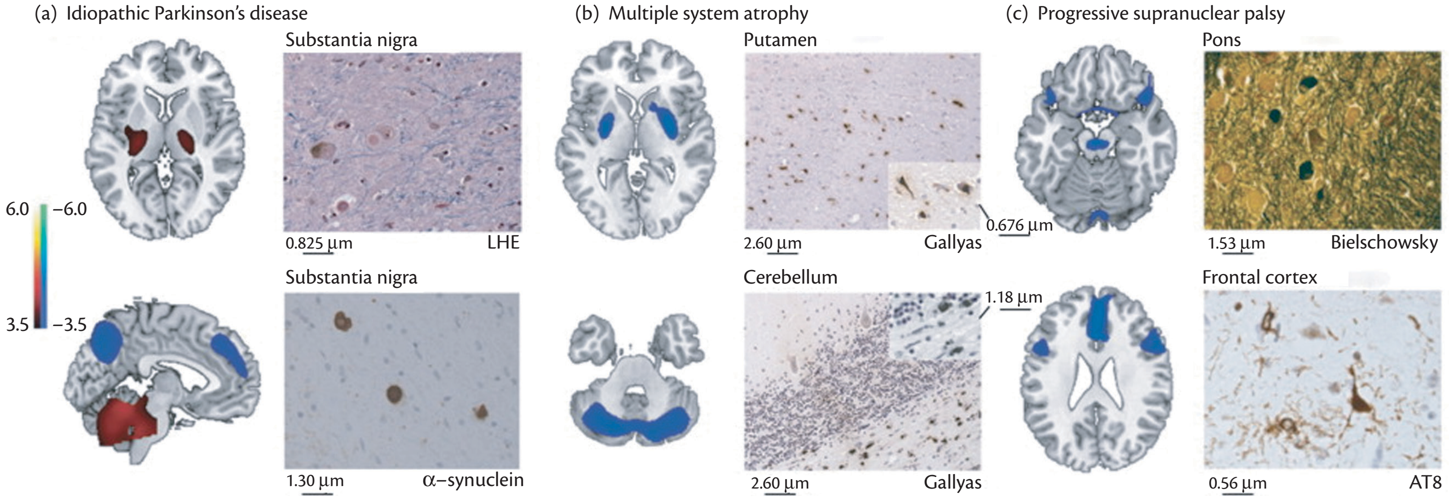
(a) Idiopathic Parkinson's disease
Substantia nigra
6.0
−6.0
3.5
−3.5
0.825 μm
LHE
Substantia nigra
1.30 μm
α−synuclein
(b) Multiple system atrophy
Putamen
2.60 μm
Gallyas
0.676 μm
Cerebellum
1.18 μm
2.60 μm
Gallyas
(c) Progressive supranuclear palsy
Pons
1.53 μm
Bielschowsky
Frontal cortex
0.56 μm
AT8

Fig. 21.3 Disease-related metabolic patterns assessed using FDG positron emission tomography (PET) and post-mortem findings. (a) The pattern related to idiopathic Parkinson's disease (PD, left) is characterized by increased (red areas) pallidothalamic and pontocerebellar metabolic activity associated with relative reductions (blue areas) in the premotor cortex, supplementary motor area, and parietal association regions. Neuropathological findings (right) from the substantia nigra pars compacta of a patient classified as having idiopathic PD with a likelihood of 99% on the basis of FDG-PET 5.8 years before death. Diagnosis was confirmed at post-mortem examination, with the demonstration of Lewy-body containing neurons and severe cell loss in this region (top). Neuronal inclusions stained positively for α-synuclein (bottom). (b) The multiple system atrophy (MSA)-related pattern (left) is characterized by bilateral metabolic reductions in putamen and cerebellar activity. Neuropathological findings (right) from a patient classified as having MSA-P with a likelihood of 98% on the basis of FDG-PET 3 years before death. Autopsy revealed characteristic abnormalities of hypometabolic pattern areas, with neuronal loss and gliosis in the putamen (top) and cerebellum (bottom). Insets: putamen and cerebellum. (c) The progressive supranuclear palsy (PSP)-related pattern (left) is characterized by metabolic reductions in the upper brainstem, medial frontal cortex, and medial thalamus. Neuropathological findings (right) from a patient classified as having PSP with a likelihood of 99% on the basis of FDG-PET 3.9 years before death. Post-mortem examination confirmed this diagnosis, with characteristic histopathological abnormalities of hypometabolic areas in the pons (top) and frontal cortex (bottom). Argyrophilic globosum neuronal tangles were noted in the basis pontis. A neuronal tangle with cytoplasmic inclusions and neuropil threads is displayed from the fifth cortical layer of the prefrontal region. Tufted astrocytes (not shown) were present in this cortical region, the amygdala, globus pallidus, and claustrum.

Reproduced from Tang CC, Poston KL, Eckert T, et al. (2010). Differential diagnosis of parkinsonism: a metabolic imaging study using pattern analysis. *Lancet Neurology*, **9**, 149–58. Copyright (2010), with permission from Elsevier.

measures of cognitive impairment in this cohort [26]. These findings suggest that low levels of amyloid are likely to contribute to the development of dementia in α-synucleinopathies [25].

Computed tomography and MRI

In PD patients, computed tomography (CT) scans can show non-specific atrophy with enlarged ventricles and sulci. Conventional T_1, T_2, fluid-attenuated inversion recovery (FLAIR) and proton density-weighted imaging at 1.5 T does not reveal PD-specific abnormalities and usually MRI is normal, particularly in early phases [27]. Therefore, the main clinical role of MRI is to exclude subcortical vascular pathology, rare secondary causes of parkinsonism (e.g. basal ganglia tumours, toxic necrosis, granulomas, or calcification; Wilson's disease; manganese-induced parkinsonism; normal pressure hydrocephalus), and in differentiating atypical parkinsonisms. With disease progression, findings remain non-specific, although a lateral to medial gradient of signal increased of SN on T_2-weighted images, smudging of the hypointensity in the SN toward the red nucleus or signal loss can be detected on inversion recovery MRI scans [28]. Mild frontal and hippocampal atrophy can also be observed in the later stage of the disease [28]. Enlargement of lateral ventricles, possibly reflecting gray (GM) and white matter (WM) loss, can be observed in PDD patients [29].

Structural MRI studies of the SN

Volumetric T_1-weighted MRI studies at 1.5 T have failed to detect a reduction of the SN volume in PD, partly because of the difficulty in defining the borders of this structure [30]. Advanced MR techniques, particularly if implemented on high and ultra-high field systems, are promising for a better SN visualization [31,32], although further studies in large groups of patients are warranted to assess the reproducibility of the results and their usefulness in clinical practice:

1. Several 3.0 T MRI studies have reported decreased T_2 and T_2^* relaxation times, and increased relaxation rates (R2 and R2*) in the SN of PD patients compared with controls [33–35], possibly reflecting increased iron content.
2. Diffusion tensor (DT) MRI at 3.0 T showed that SN fractional anisotropy (FA) values are reduced in PD patients compared with controls [36]. Approaches combining FA and R2* alterations of the SN at 3.0 T showed high accuracy in distinguishing PD patients from controls [35,37]. Whereas SN volume discriminated insufficiently PD patients and controls, a combination of SN volumetry and its connectivity with the thalamus assessed with DT MRI at 3.0 T provided 100% sensitivity and 80% specificity [38].

- At 3.0 T, the so-called 'neuromelanin-sensitive' MR sequence is able to visualize neuromelanin containing nuclei (SN and locus coeruleus) as distinct high-intensity areas compared with the surrounding brain tissue. This technique showed signal attenuation in the SN and locus coeruleus in PD patients compared to controls [39,40], with sensitivities and specificities of 73 and 87% in lateral SN and 82 and 90% in locus coeruleus [41].
- High-resolution 2D and 3D T_2^*-weighted gradient echo sequences obtained at 7.0 T result in an improved delineation of the shapes and boundaries of the SN (Fig. 21.4) [42–44].

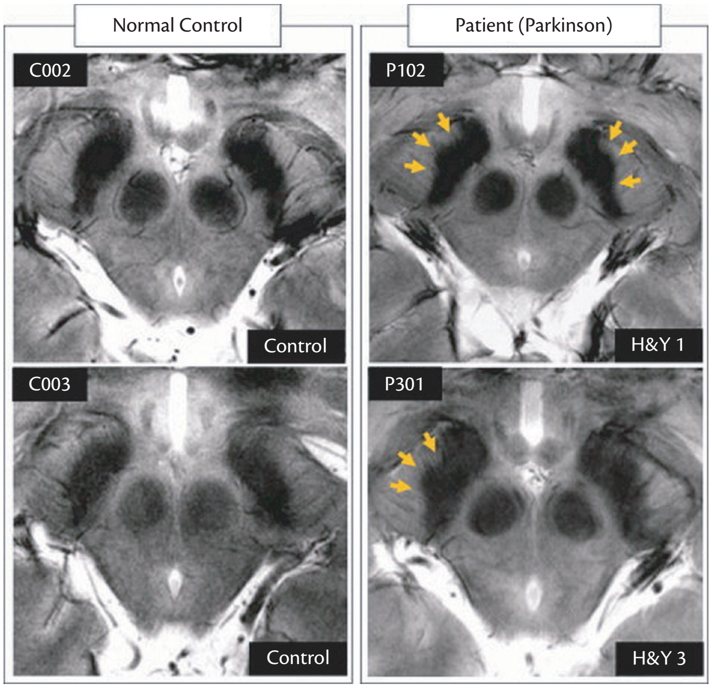

Fig. 21.4 7.0 T T_2^*-weighted magnetic resonance images of the midbrain from two healthy controls and Parkinson's disease (PD) patients showing the substantia nigra (SN), cerebral peduncle, and red nucleus. Note the smooth 'arch' shape boundary between the SN and cerebral peduncle in healthy subjects. In the two PD cases (Hoehn and Yahr (H&Y) 1 and 3, respectively), the lateral boundaries of SN are no longer 'smooth-arch' shaped but rather appear serrated and distorted (yellow arrows), likely due to the degradation of cells in the SN.

Reproduced from Cho ZH, Oh SH, Kim JM, et al. (2011). Direct visualization of Parkinson's disease by in vivo human brain imaging using 7.0T magnetic resonance imaging. *Movement Disorders*, **26**, 713–18. Copyright (2011), with permission from John Wiley & Sons Ltd.

Morphometric studies of brain atrophy

Morphometric studies have shown GM loss in PD patients, which becomes more extensive as cases develop MCI and then PDD. In early PD, significant cortical atrophy in cognitively intact patients is not detected using voxel-based morphometry (VBM) [45]. Cortical thickness measurements may be more sensitive to early GM loss detection in PD patients without dementia, in whom cortical thinning of the frontal, temporal, parietal and occipital lobes has been observed (Fig. 21.5) [46,47].

In established PDD, cortical atrophy involves the frontal, temporoparietal, and occipital lobes [4,27]. Although less severe than in AD, and not a universal finding [48,49], hippocampal atrophy is reported in PDD [50–53]. A pattern of atrophy similar to that noted in AD has been related to cognitive performance in PD and could be used to predict global cognitive decline in non-demented patients [54]. Atrophy of the caudate nucleus, putamen, and thalamus has been also reported in PDD [48,55]. Loss of brain volume was 0.31% per year in PD, but raised to 1.12% in PDD patients [56]. In patients with PD-MCI, a milder degree of atrophy of the frontal, temporal and parietal cortices has been detected [53,57–59]. A number of VBM studies, however, failed to find significant atrophy in PD-MCI relative to cognitively normal PD patients [45].

Diffusion tensor MRI of WM damage

DT MRI studies of cognitively normal, early, idiopathic PD patients showed subtle WM alterations along the nigrostriatal projections, in the frontal regions, including premotor areas, and corpus callosum [60–64]. In early PD, diffusion changes precede atrophy that is detectable with conventional MRI, specifically within voxels containing the olfactory tracts [65]. DT MRI methods might be useful for differentiating between idiopathic PD and atypical parkinsonisms, for instance DT MRI parameters of the middle cerebellar peduncles (MCP) can be used to differentiate MSA-P, while DT MRI measures of the superior cerebellar peduncles (SCP) differentiate PSP (see 'Atypical parkinsonism' section for further details).

WM damage is emerging as an important pathological substrate of cognitive deficits in PD patients [66–73]. A large study of idiopathic non-demented PD cases at different disease stages showed that WM damage is more marked with increasing PD severity and is associated with the degree of global cognitive impairment [71]. DT MRI studies exploring WM tract abnormalities in PD-MCI patients showed an involvement of the corpus callosum, cingulum, and major association WM tracts [70,72,74]. Notably, PD patients carrying glucocerebrosidase gene mutations showed a pattern of WM abnormalities involving the interhemispheric, frontal corticocortical, and parahippocampal tracts, which may partly account for the clinical manifestations of the disease including cognitive impairment [75]. Finally, new methods of analysing diffusion properties, such as diffusion kurtosis, might prove useful in the diagnosis of PD [76,77].

Functional MRI

Recent task-based and resting state functional MRI (fMRI) studies have reproduced several of the altered connectivity patterns identified using FDG-PET in PD patients.

fMRI studies investigating brain activations in PD patients during self-initiated movements have found evidence of reduced neural responses in the rostral SMA (pre-SMA), along with concomitant increases in the lateral premotor cortex and parietal cortex [78–80]. Off-medication reductions in activation

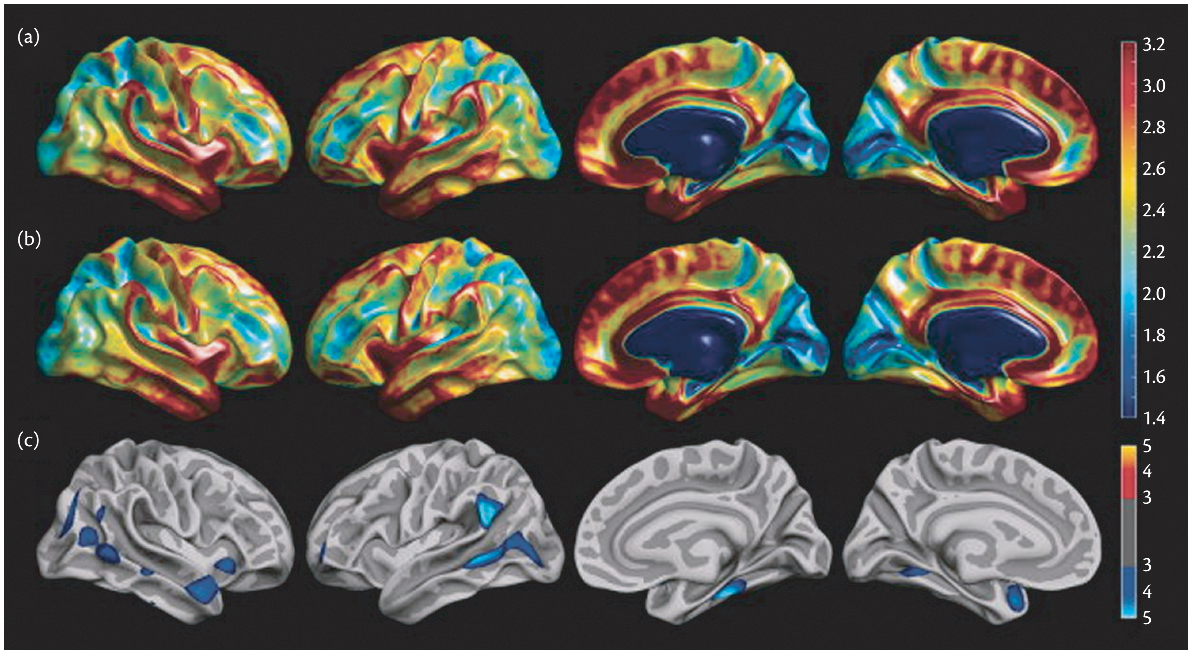

Fig. 21.5 The average regional cortical thickness of healthy controls (a) and patients with Parkinson's disease (PD) without dementia (b) are expressed as colour scale. (c) The cortical areas where the thickness is thinner in patients with PD than in controls are expressed as cold colours. Compared with controls, patients with PD showed a significant cortical thinning of the temporal, inferior parietal, rostral frontal, and orbitofrontal cortices. The upper colour scale bar shows cortical thickness (mm) and the lower colour scale bar shows logarithmic scale of *p*-values (= $\log_{10}$P).

Reproduced from Lyoo CH, Ryu YH, and Lee MS. (2010). Topographical distribution of cerebral cortical thinning in patients with mild Parkinson's disease without dementia. *Movement Disorders*, **25**, 496–9. Copyright (2010), with permission from John Wiley & Sons Ltd..

responses in the SMA complex have been noted to improve with levodopa administration [81,82] and subthalmic nucleus stimulation [83]. More recently, fMRI has been used to investigate the alterations of effective connectivity between the SMA and other cortico-striato-pallido-thalamocortical nodes in PD patients. Early PD patients studied off-medication exhibited increased effective connectivity between the pre-SMA, primary motor and premotor regions, and cerebellum, as well as diminished connectivity between the putamen, cortical motor regions (including SMA) and cerebellum [84]. Interestingly, these patients had similar task performance to the matched control group [84], suggesting that the observed increased effective connectivity was compensatory. Of note, fMRI has also shown common compensatory activity in the rostral SMA and premotor cortex in individuals who were heterozygous for mutations in PARK2 and PINK1 [85].

Some investigations have also used task-based fMRI to study cortical-subcortical network connectivity associated with non-motor PD manifestations, such as cognitive impairment and freezing of gait. Event-related fMRI with tasks of executive function was obtained in non-demented PD patients and showed a reduced deactivation of regions of the default mode network (DMN), such as the posterior cingulate and precuneus [86]. A large fMRI study showed that PD patients had a reduced recruitment of the frontostriatal brain network during a verbal two-back working memory task. In the PD group, patients with MCI had an additional reduced recruitment of the bilateral anterior cingulate cortex compared with patients with PD without MCI [87]. Interestingly, PD-MCI patients also showed a lower SPECT dopamine presynaptic uptake in the right caudate than patients without MCI, which correlated with striatal fMRI signal [87]. The relationship between cognitive impairment and frontostriatal dysfunction was also suggested by a study showing the patients with PD-MCI displayed a reduced activity of the premotor cortex and cognitive corticostriatal loop, which includes the caudate nucleus and prefrontal cortex, while planning a set shift during fMRI, whereas non-MCI patients experienced activation patterns similar to those of healthy participants [88].

During motor imagery of gait, PD patients with freezing of gait had an increased activation of the mesencephalic locomotor region than those without freezing of gait; on the contrary, they had decreased responses in the mesial frontal and posterior parietal regions [89]. Gait-related hyperactivity of the mesencephalic locomotor region correlated with severity of freezing of gait and disease duration [89]. More recently, PD patients with freezing of gait demonstrated a functional decoupling between the basal ganglia network and the cognitive control network during a virtual reality gait task [90]. This decoupling was also associated with paroxysmal motor arrests [90]. These results provide novel insights into the pathophysiology underlying freezing of gait and lend support to models of freezing of gait that implicate dysfunction across coordinated neural networks.

Resting-state fMRI is useful in PD, since motor deficits, as well as comorbidities such as apathy preclude active engagement in complex motor or cognitive tasks that are normally required in task-related fMRI studies. A recent study was able to reliably distinguish participants with PD from healthy controls with 92% sensitivity and 87% specificity using resting state fMRI data [91]. When resting state fMRI was combined with GM and WM volumetry, 87% accuracy was obtained (79% sensitivity, 93% specificity) [92].

Several studies assessed the RS fMRI pattern of the cortico-striatal-thalamocortical circuits in patients with mild to moderate PD, most of which reported both reduced and decreased functional connectivity relative to healthy controls [93–100]. A levodopa-induced spatial remapping of the cortico-striatal connectivity has been detected in chronically treated PD patients [95–98], suggesting that the clinical improvement associated with dopaminergic treatment could be related to the dopaminergic modulation of RS functional connectivity. Of note, two recent studies have suggested that dopaminergic-related changes in functional connectivity occur also in drug-naïve PD cases [101,102].

A few studies used resting state fMRI to explore other brain networks outside the corticostriatal circuit. PD patients showed decreased connectivity of a number of regions, including the frontal cortex and the key nodes of the DMN. Decreased resting state activity of the DMN was associated with cognitive impairment [103]. After 3 months of rivastigmine treatment, spontaneous brain activity in cognitively impaired PD patients was found to be restored in the SMA, premotor cortex, and inferior frontal gyrus [104]. Treatment-related increased activity of the premotor and inferior frontal cortices correlated with parallel reaction time improvement on a test of controlled attention [104]. A recent study applied graph analysis to resting state fMRI data in PD-MCI [105]. Patients with PD-MCI had connectivity reductions predominantly affecting long-range connections, as well as increased local interconnectedness manifested as higher measures of clustering, small-worldness, and modularity [105]. The latter measures tended to correlate negatively with cognitive performance in visuospatial/visuoperceptual and memory functions [105]. Brain hub structure is also reorganized in PD patients: normal hubs displayed reduced centrality and degree in PD-MCI patients [105]. These studies indicate that cognitive deficits in PD are likely associated with abnormalities of functional brain networks. In PD patients, an association was found between a decreased resting state fMRI connectivity of regions of the ventral and dorsal attention networks and visual hallucinations [106].

Transcranial sonography

Transcranial sonography detects unique bilaterally increased echogenicity in the lateral midbrain of patients with PD, which is likely to reflect SN iron deposition (Fig. 21.6).

Guidelines for the assessment of SN echogenicity have been published [107,108], and for an accurate examination a qualified investigator is requested. The differentiation into normal or abnormal SN echogenicity is based on cut-off values derived from percentile ranks obtained in healthy subjects (i.e. these values must be established for each laboratory and ultrasound system): *marked* hyperechogenicity refers to hyperechogenicity above the 90th percentile, while *moderate* values are between the 75th and 90th percentiles obtained in the healthy population [107,108]. Whereas 90% of subjects have a suitable pre-auricular acoustic bone window, in 10% no echoes can be detected [107,108].

An initial study showed that about 90% of patients with PD show SN hyperechogenicity [109]. SN hyperechogenicity can be present in the presymptomatic stages of PD, and most studies were not able to show a correlation between its extent and disease progression, suggesting that midbrain hyperechogenicity is a trait, rather than a state marker for susceptibility to parkinsonism [107]. However, increased midbrain echogenicity has also been reported in 17% of

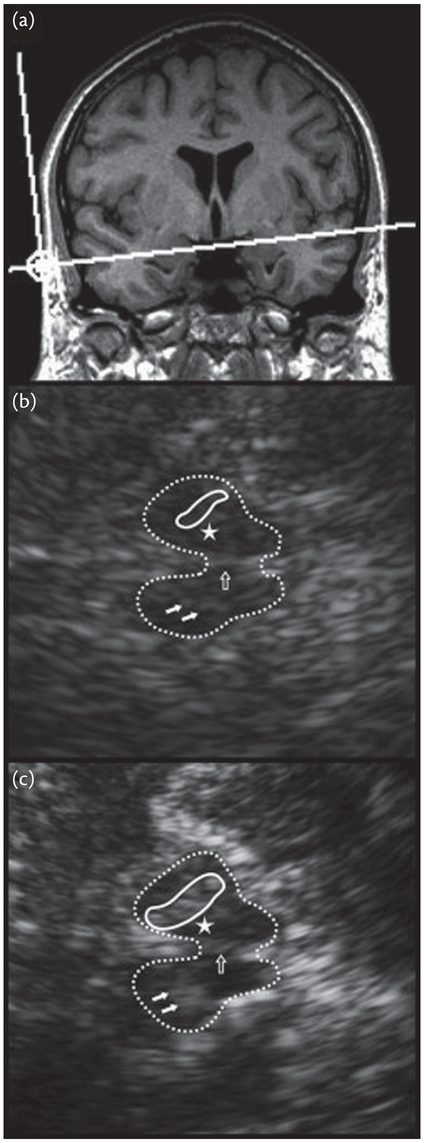

Fig. 21.6 Transcranial sonography of the midbrain. (a) Midbrain scanning plane parallel to the orbito-meatal line. (b) Midbrain (surrounded by dotted line) of a healthy control with normal echogenicity of the substantia nigra (SN, encircled ipsilaterally and marked with arrows contralaterally to the insonating probe), the area of the red nucleus (asterisk), and the hyperechogenic midline raphe (open arrow). (c) In a patient with Parkinson's disease, the area of hyperechogenicity at the anatomical site of the SN is enlarged (encircled ipsilaterally and marked with arrows contralaterally).

Reproduced from Berg D, Steinberger JD, Warren Olanow C, et al. (2011). Milestones in magnetic resonance imaging and transcranial sonography of movement disorders. *Movement Disorders*, **26**, 979–92. Copyright (2011), with permission from John Wiley & Sons Ltd.

patients with essential tremor, 40% of depressed patients without parkinsonism, and 10% of healthy subjects [107], suggesting that the specificity of this technique is suboptimal. Also, interpretation of the images in patients with severe tremor and associated movement artefacts may be challenging.

The utility of transcranial sonography has been suggested in conjunction with other screening tests for an early diagnosis of PD in clinically unclear cases, for the detection of subjects at risk for PD including asymptomatic mutation carriers for monogenic forms of PD, and for the differential diagnosis of PD from atypical parkinsonisms and secondary parkinsonian syndromes (e.g. vascular parkinsonism, hydrocephalus, trace metal accumulation, and calcifications of the basal ganglia) [10]. In addition, transcranial sonography may be particularly useful to distinguish PD patients from patients with SWEDD and suspected parkinsonism (SN hyperechogenicity reported in only 9% of SWEDD patients) [110].

Atypical parkinsonisms

Atypical parkinsonisms can be caused by different neurodegenerative syndromes, such as MSA-P, PSP, and CBS, which are frequently accompanied by denervation of both pre- and post-synaptic dopaminergic pathways and are usually levodopa resistant.

MSA is a progressive, neurodegenerative disorder characterized clinically by autonomic dysfunction, parkinsonism, cerebellar ataxia, and pyramidal signs [111]. MSA can be classified into two subgroups, a cerebellar and a parkinsonian (MSA-P) variant [111]. The histological hallmarks of MSA are α-synuclein-positive glial cytoplasmic inclusions in the oligodendroglia, which are required for the diagnosis of definite MSA [111].

PSP and CBD are pathologically distinct causes of progressive atypical parkinsonism, characterized by hyperphosphorylated tau aggregates in the brain accompanied by neuronal loss and gliosis in a characteristic distribution [112]. The large majority of PSP patients presents with Richardson's syndrome, also known as PSP syndrome [113], characterized by postural instability leading to backward falls within the first year of symptom onset, axial rigidity, progressive vertical opthalmoplegia, dementia, and personality changes. CBD pathology can cause multiple different neurologic syndromes, including CBS, PSP syndrome, frontotemporal dementia, or primary progressive aphasia. CBS includes a mixed movement disorder (e.g. levodopa-unresponsive rigidity associated with apraxia, dystonia, myoclonus, and alien limb) and impaired cognition [114].

Outside specialized centres and especially in the early stage of the diseases, differential diagnosis among different atypical parkinsonian syndromes and each of them with PD is challenging because of similarity of symptoms and lack of preclinical markers of the disease.

Functional imaging with PET and SPECT

SPECT and PET tracers investigating pre-synaptic dopaminergic function cannot differentiate PD from atypical parkinsonisms, given a similar nigrostriatal involvement in these conditions, although asymmetry of binding loss tends to be more pronounced in PD. A reduced midbrain ^{123}I-β-CIT uptake was found in patients with MSA-P and allowed a correct classification of 95% patients with MSA-P from PD cases [115]. Imaging with other D2 receptor ligands, such as ^{123}I-IBZM, ^{123}I-IBF and ^{123}I-epidepride, has been shown to be useful for the differentiation of PD from MSA-P and PSP [116], since the post-synaptic component of the dopaminergic system is not affected in patients with PD except in advanced disease stages. However, ^{123}I-IBZM SPECT cannot itself discriminate among different atypical parkinsonisms [117].

The pattern of striatal abnormalities in CBS consists of a decreased uptake of DAT and F-DOPA, which is predominant contralateral to the side of prominent symptoms with a balanced involvement of caudate and putamen [118]. Frequently, D2 receptor uptake is normal in CBS [3].

FDG-PET studies can contribute in the diagnostic work-up between atypical parkinsonisms and PD. In contrast to PD, atypical parkinsonian syndromes show a reduced lentiform nucleus glucose metabolism (Fig. 21.3b, c), which continues to decline as disease progresses. In addition, FDG-PET shows bilateral hypometabolism of the putamen, brainstem and cerebellum in MSA-P and hypometabolism of the brainstem, thalamus and frontal cortex in PSP [119] (Fig. 21.3b, c). Perhaps the best method to diagnostically characterize patients with parkinsonism using radiotracer imaging is to combine two techniques: FDG-PET and a dopaminergic scan. With such an approach and using automated imaging analysis, subjects with PD, MSA-P, and PSP can be reliably classified with specificities in the 94–97% range [120]. The FDG-PET pattern of CBS is characterized by a unilateral hypometabolism contralateral to the clinically affected side with a predominance in the parietotemporal, prefrontal, cingular, and motor cortices, as well as in the caudate and thalamus [121,122]. A recent study showed a recognizable pattern of hypometabolism bilaterally in the caudate and SMA, with asymmetric hypometabolism in the midbrain and thalamus in 10 patients with a pathologically proven (4R)-tauopathy [123].

MRI

Conventional MRI

Conventional brain MRI can aid in the classification of these patients, and several neuroimaging signs have been described for differentiating atypical parkinsonism syndromes from PD.

A number of conventional MRI findings have been described as suggestive of MSA-P. These include atrophy and signal alterations at 1.5 T of the putamen and several infratentorial regions compared with PD, PSP, and controls, such as:

1. Posterolateral putaminal decreased signal intensity on T_2-weighted images, mainly due to iron deposition, covered by a rim of increased signal, mainly due to gliosis (Fig. 21.7a, b).
2. If pontocerebellar degeneration is present, lateral and longitudinal pontine fibres become evident as high signal manifesting as the 'hot cross bun' (i.e. there is a cruciform linear area of high signal on T_2-weighted images in the pons with tiny round darker areas within the checkerboard of the cross) (Fig. 21.7d).

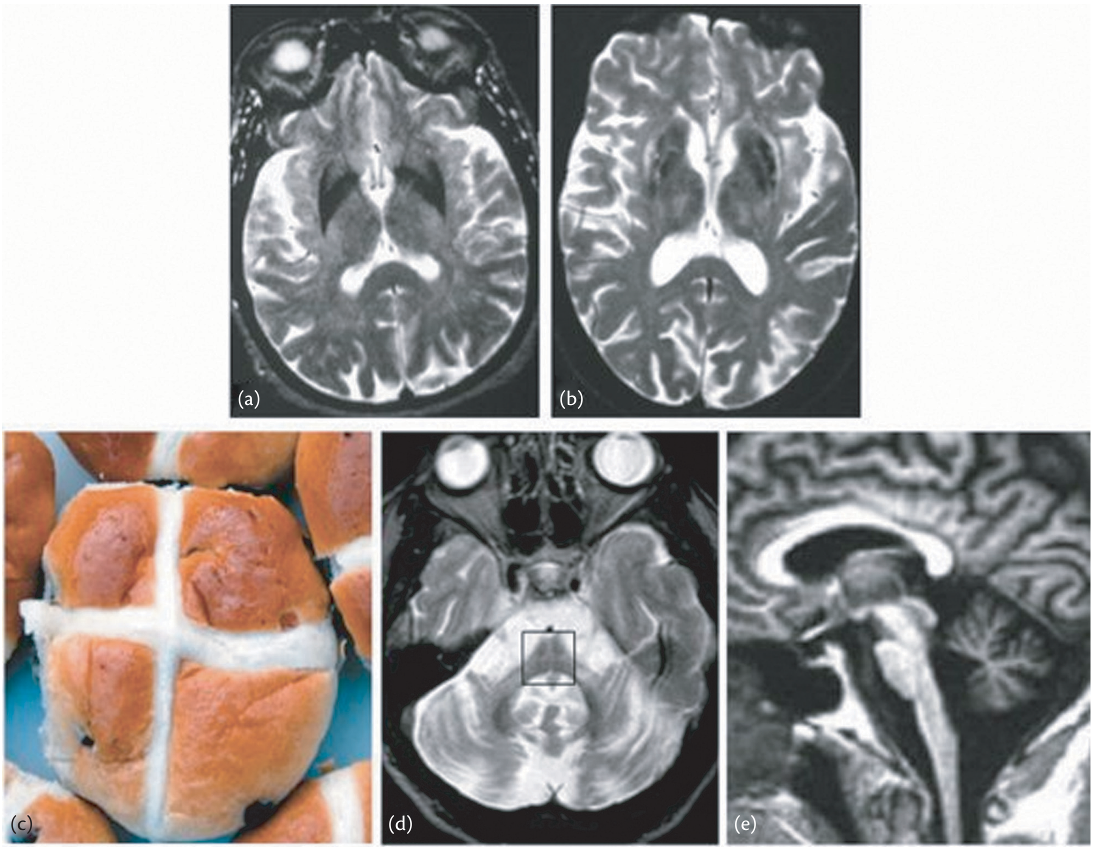

Fig. 21.7 Axial T_2*-weighted gradient echo (a) and T_2-weighted turbo spin echo (b) magnetic resonance (MR) images show symmetric abnormally low signal intensity of the putamen in two different patients with multiple system atrophy parkinsonian type (MSA-P), which is surrounded by a regular hyperintense rim in (b). 'Hot cross bun' (c). Axial T_2-weighted turbo spin echo (d) MR image shows a subtle diffuse hyperintensity of the white matter of the pons, middle cerebellar peduncles, and cerebellar white matter with sparing of the corticospinal tracts in the basis pontis which creates the 'hot cross bun' sign (empty box). Note the marked thinning of the basis pontis and middle cerebellar peduncles. Sagittal T_1-weighted gradient echo MR image (e) demonstrates diffuse atrophy of the brainstem, which is more pronounced in the basis pontis, and thinning of the folia of the cerebellar vermis.

Reproduced from Mascalchi M, Vella A, and Ceravolo R. (2012). Movement disorders: role of imaging in diagnosis. *Journal of Magnetic Resonance Imaging*, **35**, 239–56. Copyright (2012), with permission from John Wiley & Sons Ltd.

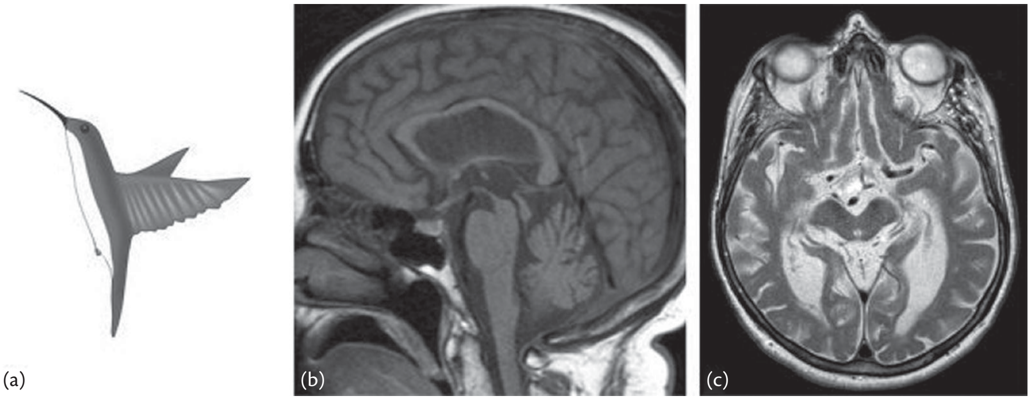

Fig. 21.8 Hummingbird (a). Sagittal T_1-weighted magnetic resonance (MR) image from a patient with progressive supranuclear palsy (b) shows the characteristic thinning of the anteroposterior diameter and the abnormal shape of the rostral midbrain tegmentum exhibiting a concave upper profile and the posterior and central portions of floor of the third ventricle resembling the hummingbird's long, thin, sharp beak. Axial T_2-weighted MR image (c) shows thinning of the midbrain and hypointensity of the substantia nigra.

Reproduced from Mascalchi M, Vella A, and Ceravolo R. (2012). Movement disorders: role of imaging in diagnosis. *Journal of Magnetic Resonance Imaging*, **35**, 239–56. Copyright (2012), with permission from John Wiley & Sons Ltd.

3. Cerebellar and pontine atrophy can be visually detected along with hyperintensity of the MCP (Fig. 21.7d, e).

While putaminal atrophy appears to discriminate MSA-P from PD, T_2 putaminal hypointensity and a putaminal hyperintense rim may also occur in the latter condition [27]. In addition, it is worth noting that, at higher magnetic field strengths (3T and above), some of these signal-intensity patterns can also be found in healthy elderly subjects and their clinical utility is, therefore, currently debated [27]. Specificity of those abnormalities in differentiating MSA-P from PD and healthy controls is considered to be relatively high; in contrast, sensitivity seems to be insufficient especially in the early stages of disease [27].

Specific brain MRI findings associated with PSP include:

1. Significant dorsal midbrain atrophy, especially of the anteroposterior diameter. Indirect signs of midbrain atrophy are: the 'penguin silhouette' or 'humming bird' signs on sagittal views [27] where the shapes of the midbrain tegmentum, i.e. the bird's head, and pons, i.e. the bird's body, resemble a lateral view of a standing king penguin or humming bird, and an abnormal superior midbrain profile—flat or concave versus convex aspect in healthy subjects (Fig. 21.8b, c).
2. Enlargement of the third ventricle (Fig. 21.8b, c).
3. Signal increase on T_2-weighted images of the midbrain and inferior olives.
4. Atrophy and increased signal of the SCP on T_2-weighted and FLAIR images (Fig. 21.9).
5. Hypointense putamen on T_2-weighted images, due to increase iron content.
6. Frontal and parietal lobe atrophy.

Several studies have investigated the usefulness of the assessment of various supratentorial and infratentorial structures on MRI with manual or semi-automatic segmentation techniques for differentiating MSA-P, PSP, and PD. A decreased MCP width points the diagnosis towards MSA-P compared with PD and controls [124]. The area of the pons measured on mid-sagittal T_1-weighted images is smaller in MSA-P patients compared with controls and patients with PD and PSP, albeit overlap at the individual level can occur [125, 126]. A reduced anterior–posterior midbrain diameter was able to discriminate between PSP, PD, and controls, while an overlap of anterior-posterior midbrain diameter between PSP and MSA-P patients was found [127]. A reduced ratio between midbrain and pontine areas [125,126], as well as an increased MR parkinsonism index (i.e. [pons area/midbrain area]*[MCP widths/SCP width]) [126,128] can point the diagnosis towards PSP relative to PD, MSA-P, and controls at individual patient level (Fig. 21.9). In a large study of MSA-P and PSP, 627 MRI data sets were evaluated (297 PSP; 330 MSA-P) [129]. Four meaningful clusters of covarying parameters with respect to regional volume or signal alterations were defined (i.e. brainstem and cerebellum; midbrain; putamen; other basal ganglia) with good to excellent internal consistency and moderate to excellent reliability. The total score significantly discriminated for disease severity or diagnosis and was considered to be a reliable and consistent measure of MRI abnormalities in PSP and MSA-P [129].

Only a few conventional MRI studies have assessed CBS patients; despite this, several suggestive findings have been described. These include:

- Characteristically asymmetric frontal and/or parietal atrophy (including the pre- and post-central gyri and central sulcus), with less frequent involvement of the temporal lobe (sometimes even global and symmetric) (Fig. 21.10).
- Subcortical gliosis in the atrophic cortical gyri seen as high intensity on T_2-weighted images.

Unfortunately, none of these MRI abnormalities is considered to be of clearly diagnostic or even pathognomonic relevance for CBS, mainly due to the pathological heterogeneity of this syndrome.

Sensitivity to early findings may be improved using higher resolution imaging and sequences with greater sensitivity to PD-related pathological abnormalities, such as iron-related R2* relaxometry measurements and diffusion-weighted imaging.

Until now, there have been only a few attempts to characterize the iron content of brain structures to differentiate PD from atypical parkinsonisms, especially during the early phase of the disease.

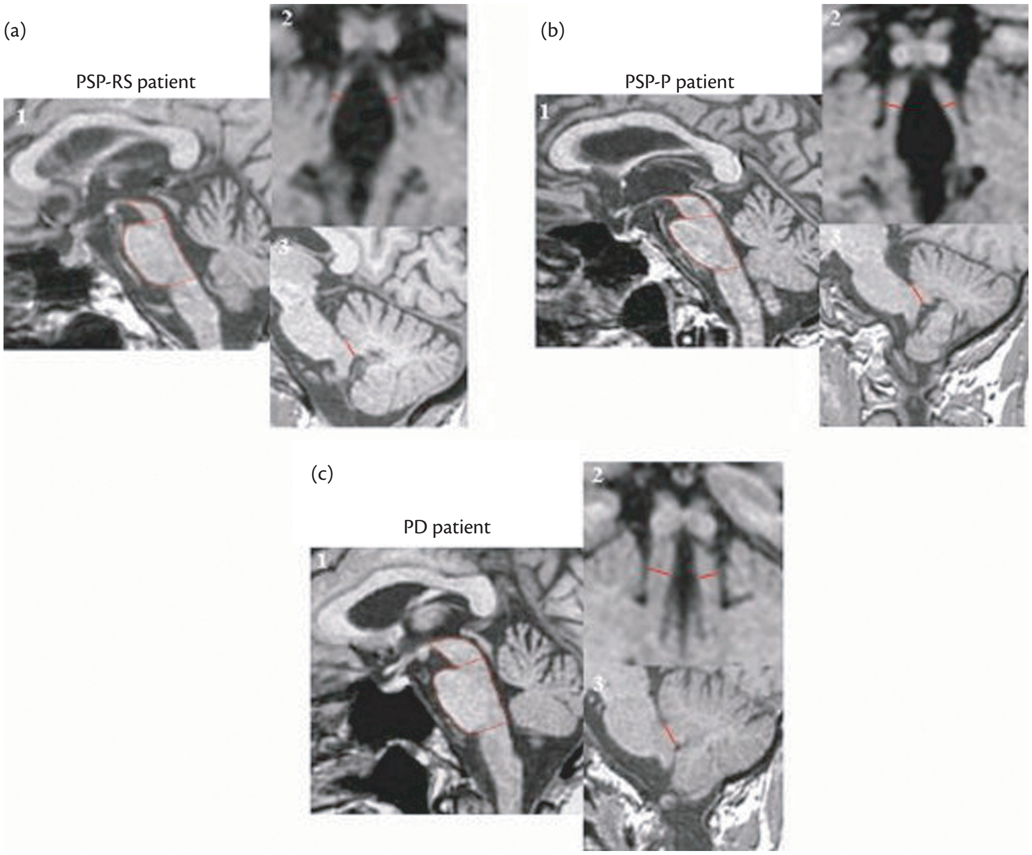

Fig. 21.9 Sagittal and coronal 3D T_1-weighetd images showing in red (1) pons and midbrain areas, as well as (2) superior cerebellar peduncle (SCP) and (3) middle cerebellar peduncle (MCP) widths in (a) a patient with Richardson's syndrome (PSP-RS), (b) a patient with PSP-parkinsonism (PSP-P), and (c) a patient with Parkinson's disease (PD). MRI measurements values were as follows: (a) midbrain area = 48.9 mm^2, pons area = 375.3 mm^2, SCP width = 1.7 mm, MCP width = 5.6 mm; (b) midbrain area = 107.6 mm^2, pons area = 461.2 mm^2, SCP width = 3.1 mm, MCP width = 7.9 mm; and (c) midbrain area = 139.0 mm^2, pons area = 525.8 mm^2, SCP width = 3.6 mm, MCP width = 8.9 mm.

Reproduced from Longoni G, Agosta F, Kostić VS, et al. (2011). MRI measurements of brainstem structures in patients with Richardson's syndrome, progressive supranuclear palsy-parkinsonism, and Parkinson's disease. *Movement Disorders*, **26**, 247–55. Copyright (2011), with permission from John Wiley & Sons Ltd.

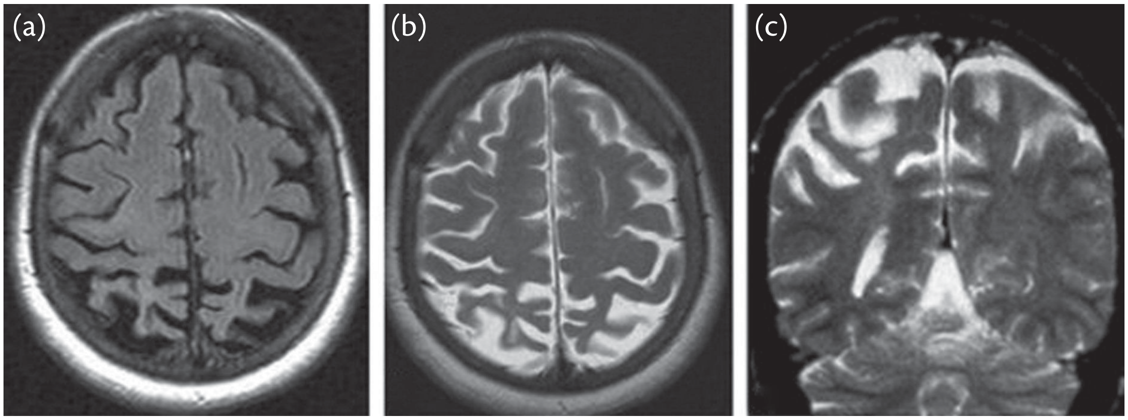

Fig. 21.10 Axial fluid-attenuated inversion recovery (a) and T_2-weighted spin echo (b) magnetic resonance images demonstrate thinning of the sulci in the parietal cortex combined with subtle hyperintensity of the subcortical white matter in a patient with corticobasal syndrome. The asymmetric involvement with a right side predominance is better appreciated on a coronal T_2-weighted spin echo image (c).

Reproduced from Mascalchi M, Vella A, Ceravolo R. (2012). Movement disorders: role of imaging in diagnosis. *Journal of Magnetic Resonance Imaging*, **35**, 239–56. Copyright (2012), with permission from John Wiley & Sons Ltd.

These studies showed an increased iron content in the putamen of MSA-P patients [130,131] and in the striatum and globus pallidus in PSP patients [132].

Diffusion-weighted (DW) MRI using regions of interest allows the differentiation of MSA-P from PD and healthy controls on the basis of increased putaminal diffusivity in MSA-P patients [133,134]. Putaminal diffusivity is also increased in PSP, but with considerable overlap, so that an increased putaminal diffusivity can point the diagnosis towards MSA-P versus PD and controls [133,134]. Abnormal diffusivity measures in the MCP and SCP can differentiate MSA-P and PSP from controls, respectively, and from each other [133,135]. A recent DT MRI study examined multiple basal ganglia and cerebellum regions simultaneously in patients with movement disorders [136]. Receiver operating characteristic analyses demonstrated an area under the curve of 0.99 (sensitivity 90%, specificity 100%) in distinguishing PD from atypical parkinsonism [136]. Areas under the curves of 0.99, 0.96, and 0.97 were achieved for distinguishing PD versus MSA-P, PD versus PSP, and MSA-P versus PSP, respectively, with unique diffusion MRI measures and subcortical regions-of-interest (ROIs) for each group [136]. The study also found an excellent separation between PD and essential tremor [136]. Notably, a comparison between DW MRI to IBZM-SPECT in patients with MSA-P and PD found striatal diffusivity to have a significantly higher predictive accuracy than D2 binding with IBZM (97 versus 75%) [137], suggesting that DW MRI may be more accurate compared with IBZM SPECT in distinguishing MSA-P from PD. A discrimination between CBS patients and other groups, including PSP was reached only when applying a hemispheric symmetry ratio (i.e. smaller to the larger median value of diffusivity histograms of left and right hemispheres) [138].

Morphometric MRI studies

In MSA-P, VBM revealed GM loss mainly in the putamen, caudate nucleus, cerebellar vermis and lobes, dorsal midbrain, and several cortical regions, including the insular cortex and motor area [139,140]. VBM has also been used to investigate the progression of cortical and subcortical atrophy patterns in MSA-P and revealed early tissue loss in the basal ganglia followed by later onset cortical atrophy [141].

VBM studies of patients with PSP reported concordant results on the presence of midbrain atrophy, which was variably associated with tissue loss in the basal ganglia, frontotemporal cortices, SCP, corticospinal tract, and premotor and prefrontal WM regions [142–146]. Some studies interrogated the clinical utility of VBM results as a guide for the differential diagnosis of PSP from PD at individual subject level. Allocating the subject to either PSP or 'non-PSP,' based on the presence or absence of the atrophy on T_1-weighted images, one study achieved a sensitivity of 83% and a specificity of 79% [147]. In a more recent VBM study, severe midbrain and cerebellar tissue loss achieved a 97% accuracy for the differentiation of individual PSP patients versus PD [148].

VBM was used to compare structural patterns of atrophy between patients with PSP and CBS. Midbrain structures were more atrophic in PSP, whereas dorsal frontal and parietal cortices were more atrophic in CBS [144]. In a recent study of CBS patients with pathological verification [149], the most common pathologic substrates for clinical CBS were found to be CBD (35%), AD (23%), PSP (13%), and frontotemporal lobar degeneration (FTLD) with transactive response DNA binding protein (TDP) inclusions (13%). VBM showed that CBS was associated with peri-Rolandic atrophy irrespective of underlying pathology [149]. In CBS due to FTLD (tau or TDP), atrophy extended into prefrontal cortex, striatum, and brainstem, whereas in CBS due to AD, atrophy extended into temporoparietal cortex and precuneus [149].

Diffusion tensor MRI of WM damage

Apart from the pontine transverse fibres [150], only a few studies assessed other WM tracts in patients with MSA-P. Damage was found in the corticospinal tract [151,152].

DT MRI studies of PSP underlined the role of WM degeneration, especially of the SCP. Some studies also showed DT MRI abnormalities of the corpus callosum, internal capsule, and association tracts [152–160]. Along with frontal cortical and basal ganglia involvement, WM damage is likely to contribute to the motor manifestations as well as to the development of the dysexecutive and behavioural abnormalities of PSP [155,161]. Furthermore, adding DT MRI measures to the MR parkinsonism index was found to improve the diagnostic accuracy in discriminating among different clinical PSP syndromes [162].

WM tract degeneration is also a feature of CBS, with degeneration occurring in frontoparietal WM tracts and corpus callosum [163–165]. In CBS, limb apraxia correlated with parietal atrophy and FA reduction of the parietofrontal associative fibres [163]. CBS patients showed a more supratentorial and posterior pattern of degeneration with greater involvement of the splenium of the corpus callosum, premotor and motor regions, and parietal lobes than PSP patients [165]. Findings in CBS were also highly asymmetric [165].

Functional MRI

The use of fMRI in patients with atypical parkinsonisms is still in its infancy. Resting state fMRI has been applied in patients with PSP. Patients with PSP showed resting state functional connectivity disruptions within a network, including brainstem, cerebellar, diencephalic, basal ganglia, and cortical regions, involved in skeletomotor, oculomotor, and executive control [166]. Patients with more severe functional impairment showed lower mean network connectivity scores [166]. In PSP patients, the altered functional connectivity of the thalamocortical network was found to be correlated with microstructural damage of the SCP, assessed using DT MRI [156].

Cardiac imaging in the diagnostic work-up of parkinsonisms

^{123}I-metaiodobenzylguanidine (MIBG) SPECT imaging is useful for visualizing catecholaminergic terminals and, hence, in detecting cardiac sympathetic denervation. In PD, there is a significant loss of ^{123}I-MIBG binding in the heart, whereas in vascular parkinsonism and atypical parkinsonian syndromes there is only a mild reduction of cardiac sympathetic innervations [167]. A meta-analysis reported a pooled sensitivity of MIBG SPECT to detect PD of 89%, and a pooled specificity to discriminate between PD and MSA-P of 77% [168]. Nevertheless, possible causes of false positive and false negative results should be considered when interpreting MIBG SPECT results, as it is well known that various heart diseases and diabetes may damage the postganglionic sympathetic neurons [169].

Conclusions

Although the clinical diagnosis of PD may be straightforward in cases with classic presentations, accurate distinction among different parkinsonisms may be challenging, particularly in the early stages. Nuclear medicine techniques, including PET and SPECT, permit the confirmation of the clinical suspicion of PD by demonstrating presynaptic loss of the dopamine transporter. These techniques may also be useful as a premotor marker of PD, as dopaminergic deficits are evident many years before the appearance of the motor manifestations of PD. However, radiotracer neuroimaging is not widely available, is expensive, and cannot differentiate between PD and other forms of presynaptic parkinsonism reliably. In addition, symptomatic therapy may modify imaging results with radiotracer ligands. Conventional MRI enables to detect suggestive findings in symptomatic and atypical causes of parkinsonism. However, it does not show specific findings in PD. Modern neuroimaging markers, especially at ultra-high field strengths, hold a substantial promise for early diagnosis. Because manual MRI approaches are heavily operator-dependent and time-consuming, some authors have investigated automated machine learning and pattern recognition methods as potential alternative tools for computer-aided diagnosis. Recently, support vector machines have been applied with success to the analysis of multimodal MRI data in patients with PD and PSP [148,170]. fMRI measures neuronal activity at rest or during the performance of specific tasks, but it is too early to determine the clinical utility of this tool as a diagnostic marker of PD and atypical parkinsonisms. Transcranial ultrasound has been shown to detect increased echogenicity in the SN of PD patients, with a relatively high accuracy. This technique is somewhat limited by the requirement of a good temporal bone window and still lacks validation against other conditions.

References

1. Gibb WR, and Lees AJ. (1988). The relevance of the Lewy body to the pathogenesis of idiopathic Parkinson's disease. *Journal of Neurology, Neurosurgery & Psychiatry*, **51**, 745–52.
2. Massano J, and Bhatia KP (2012). Clinical approach to Parkinson's disease: features, diagnosis, and principles of management. *Cold Spring Harbor Perspectives in Medicine*, **2**, a008870.
3. Cummings JL, Henchcliffe C, Schaier S, et al. (2011). The role of dopaminergic imaging in patients with symptoms of dopaminergic system neurodegeneration. *Brain*, **134**, 3146–66.
4. Brooks DJ. (2010). Imaging approaches to Parkinson disease. *Journal of Nuclear Medicine*, **51**, 596–609.
5. Khan NL, Scherfler C, Graham E, et al. (2005). Dopaminergic dysfunction in unrelated, asymptomatic carriers of a single parkin mutation. *Neurology*, **64**, 134–6.
6. Piccini P, Morrish PK, Turjanski N, et al. (1997). Dopaminergic function in familial Parkinson's disease: a clinical and 18F-dopa positron emission tomography study. *Annals of Neurology*, **41**, 222–9.
7. Ponsen MM, Stoffers D, Booij J, et al. (2004). Idiopathic hyposmia as a preclinical sign of Parkinson's disease. *Annals of Neurology*, **56**, 173–81.
8. Eisensehr I, Linke R, Noachtar S, et al. (2000). Reduced striatal dopamine transporters in idiopathic rapid eye movement sleep behaviour disorder. Comparison with Parkinson's disease and controls. *Brain*, **123**(Pt 6), 1155–60.
9. Iranzo A, Lomena F, Stockner H, et al. (2010). Decreased striatal dopamine transporter uptake and substantia nigra hyperechogenicity as risk markers of synucleinopathy in patients with idiopathic rapid-eye-movement sleep behaviour disorder: a prospective study [corrected]. *Lancet Neurology*, **9**, 1070–7.
10. Berardelli A, Wenning GK, Antonini A, et al. (2013). EFNS/MDS-ES/ENS [corrected] recommendations for the diagnosis of Parkinson's disease. *European Journal of Neurology*, **20**, 16–34.
11. Marshall VL, Patterson J, Hadley DM, et al. (2006). Two-year follow-up in 150 consecutive cases with normal dopamine transporter imaging. *Nuclear Medicine Communications*, **27**, 933–7.
12. Eckert T, Feigin A, Lewis DE, et al. (2007). Regional metabolic changes in parkinsonian patients with normal dopaminergic imaging. *Movement Disorders*, **22**, 167–73.
13. Antonini A, Schwarz J, Oertel WH, et al. (1997). Long-term changes of striatal dopamine D2 receptors in patients with Parkinson's disease: a study with positron emission tomography and [11C]raclopride. *Movement Disorders*, **12**, 33–8.
14. Shinotoh H, Inoue O, Hirayama K, et al. (1993). Dopamine D1 receptors in Parkinson's disease and striatonigral degeneration: a positron emission tomography study. *Journal of Neurology, Neurosurgery & Psychiatry*, **56**, 467–72.
15. Eidelberg D, Moeller JR, Dhawan V, et al. (1990). The metabolic anatomy of Parkinson's disease: complementary [18F]fluorodeoxyglucose and [18F]fluorodopa positron emission tomographic studies. *Movement Disorders*, **5**, 203–13.
16. Tang CC, Poston KL, Dhawan V, et al. (2010). Abnormalities in metabolic network activity precede the onset of motor symptoms in Parkinson's disease. *Journal of Neuroscience*, **30**, 1049–56.
17. Huang C, Mattis P, Tang C, et al. (2007). Metabolic brain networks associated with cognitive function in Parkinson's disease. *NeuroImage*, **34**, 714–23.
18. Hirano S, Shinotoh H, Eidelberg D. (2012). Functional brain imaging of cognitive dysfunction in Parkinson's disease. *Journal of Neurology, Neurosurgery & Psychiatry*, **83**, 963–9.
19. Pappata S, Santangelo G, Aarsland D, et al. (2011). Mild cognitive impairment in drug-naive patients with PD is associated with cerebral hypometabolism. *Neurology*, **77**, 1357–62.
20. Bohnen NI, Koeppe RA, Minoshima S, et al. (2011). Cerebral glucose metabolic features of Parkinson disease and incident dementia: longitudinal study. *Journal of Nuclear Medicine*, **52**, 848–55.
21. Kuhl DE, Minoshima S, Fessler JA, et al. (1996). In vivo mapping of cholinergic terminals in normal aging, Alzheimer's disease, and Parkinson's disease. *Annals of Neurology*, **40**, 399–410.
22. Hilker R, Thomas AV, Klein JC, et al. (2005). Dementia in Parkinson disease: functional imaging of cholinergic and dopaminergic pathways. *Neurology*, **65**, 1716–22.
23. Compta Y, Parkkinen L, O'Sullivan SS, et al. (2011). Lewy- and Alzheimer-type pathologies in Parkinson's disease dementia: which is more important? *Brain*, **134**, 1493–505.
24. Brooks DJ. (2009). Imaging amyloid in Parkinson's disease dementia and dementia with Lewy bodies with positron emission tomography. *Movement Disorders*, **24**(Suppl. 2), S742–7.
25. Gomperts SN, Locascio JJ, Rentz D, et al. (2013). Amyloid is linked to cognitive decline in patients with Parkinson disease without dementia. *Neurology*, **80**, 85–91.
26. Petrou M, Bohnen NI, Mueller ML, et al. (2012). A beta-amyloid deposition in patients with Parkinson disease at risk for development of dementia. *Neurology*, **79**, 1161–7.
27. Seppi K, and Poewe W. (2010). Brain magnetic resonance imaging techniques in the diagnosis of parkinsonian syndromes. *Neuroimaging Clinics of North America*, **20**, 29–55.
28. Zarei M, Ibarretxe-Bilbao N, Compta Y, et al. (2013). Cortical thinning is associated with disease stages and dementia in Parkinson's disease. *Journal of Neurology, Neurosurgery & Psychiatry*, **84**(8), 875–81.
29. Camicioli R, Sabino J, Gee M, et al. (2011). Ventricular dilatation and brain atrophy in patients with Parkinson's disease with incipient dementia. *Movement Disorders*, **26**, 1443–50.
30. Geng DY, Li YX, and Zee CS. (2006). Magnetic resonance imaging-based volumetric analysis of basal ganglia nuclei and substantia nigra in patients with Parkinson's disease. *Neurosurgery*, **58**, 256–62; discussion 262.
31. Lehericy S, Sharman MA, Dos Santos CL, et al. (2012). Magnetic resonance imaging of the substantia nigra in Parkinson's disease. *Movement Disorders*, **27**, 822–30.
32. Stoessl AJ, Martin WW, McKeown MJ, et al. (2011). Advances in imaging in Parkinson's disease. *Lancet Neurology*, **10**, 987–1001.
33. Martin WR, Wieler M, Gee M. (2008). Midbrain iron content in early Parkinson disease: a potential biomarker of disease status. *Neurology*, **70**, 1411–17.

34. Ordidge RJ, Gorell JM, Deniau JC, et al. (1994). Assessment of relative brain iron concentrations using T2-weighted and T2*-weighted MRI at 3 Tesla. *Magnetic Resonance in Medicine*, **32**, 335–41.
35. Peran P, Cherubini A, Assogna F, et al. (2010). Magnetic resonance imaging markers of Parkinson's disease nigrostriatal signature. *Brain*, **133**, 3423–33.
36. Vaillancourt DE, Spraker MB, Prodoehl J, et al. (2009). High-resolution diffusion tensor imaging in the substantia nigra of de novo Parkinson disease. *Neurology*, **72**, 1378–84.
37. Du G, Lewis MM, Styner M, et al. (2011). Combined R2* and diffusion tensor imaging changes in the substantia nigra in Parkinson's disease. *Movement Disorders*, **26**, 1627–32.
38. Menke RA, Scholz J, Miller KL, et al. (2009). MRI characteristics of the substantia nigra in Parkinson's disease: a combined quantitative T1 and DTI study. *NeuroImage*, **47**, 435–41.
39. Sasaki M, Shibata E, Tohyama K, et al. (2006). Neuromelanin magnetic resonance imaging of locus ceruleus and substantia nigra in Parkinson's disease. *Neuroreport*, **17**, 1215–8.
40. Schwarz ST, Rittman T, Gontu V, et al. (2011). T1-weighted MRI shows stage-dependent substantia nigra signal loss in Parkinson's disease. *Movement Disorders*, **26**, 1633–8.
41. Ohtsuka C, Sasaki M, Konno K, et al. (2013). Changes in substantia nigra and locus coeruleus in patients with early-stage Parkinson's disease using neuromelanin-sensitive MR imaging. *Neuroscience Letters*, **541**, 93–8.
42. Cho ZH, Oh SH, Kim JM, et al. (2011). Direct visualization of Parkinson's disease by in vivo human brain imaging using 7.0T magnetic resonance imaging. *Movement Disorders*, **26**, 713–8.
43. Kwon DH, Kim JM, Oh SH, et al. (2012). Seven-Tesla magnetic resonance images of the substantia nigra in Parkinson disease. *Annals of Neurology*, **71**, 267–77.
44. Cosottini M, Frosini D, Pesaresi I, et al. (2014). MR Imaging of the substantia nigra at 7 T enables diagnosis of Parkinson disease. *Radiology*, **271**(3), 831–8.
45. Duncan GW, Firbank MJ, O'Brien JT, et al. (2013). Magnetic resonance imaging: a biomarker for cognitive impairment in Parkinson's disease? *Movement Disorders*, **28**, 425–38.
46. Pereira JB, Ibarretxe-Bilbao N, Marti MJ, et al. (2011). Assessment of cortical degeneration in patients with Parkinson's disease by voxel-based morphometry, cortical folding, and cortical thickness. *Human Brain Mapping*, **33**, 2521–34.
47. Lyoo CH, Ryu YH, and Lee MS. (2010). Topographical distribution of cerebral cortical thinning in patients with mild Parkinson's disease without dementia. *Movement Disorders*, **25**, 496–9.
48. Burton EJ, McKeith IG, Burn DJ, et al. (2004). Cerebral atrophy in Parkinson's disease with and without dementia: a comparison with Alzheimer's disease, dementia with Lewy bodies and controls. *Brain*, **127**, 791–800.
49. Apostolova LG, Beyer M, Green AE, et al. (2010). Hippocampal, caudate, and ventricular changes in Parkinson's disease with and without dementia. *Movement Disorders*, **25**, 687–95.
50. Nagano-Saito A, Washimi Y, Arahata Y, et al. (2005). Cerebral atrophy and its relation to cognitive impairment in Parkinson disease. *Neurology*, **64**, 224–9.
51. Summerfield C, Junque C, Tolosa E, et al. (2005). Structural brain changes in Parkinson disease with dementia: a voxel-based morphometry study. *Archives of Neurology*, **62**, 281–5.
52. Tam CW, Burton EJ, McKeith IG, et al. (2005). Temporal lobe atrophy on MRI in Parkinson disease with dementia: a comparison with Alzheimer disease and dementia with Lewy bodies. *Neurology*, **64**, 861–5.
53. Beyer MK, Janvin CC, Larsen JP, et al. (2007). A magnetic resonance imaging study of patients with Parkinson's disease with mild cognitive impairment and dementia using voxel-based morphometry. *Journal of Neurology, Neurosurgery & Psychiatry*, **78**, 254–9.
54. Weintraub D, Dietz N, Duda JE, et al. (2012). Alzheimer's disease pattern of brain atrophy predicts cognitive decline in Parkinson's disease. *Brain*, **135**, 170–80.
55. Almeida OP, Burton EJ, McKeith I, et al. (2003). MRI study of caudate nucleus volume in Parkinson's disease with and without dementia with Lewy bodies and Alzheimer's disease. *Dementia and Geriatric Cognitive Disorders*, **16**, 57–63.
56. Burton EJ, McKeith IG, Burn DJ, et al. (2005). Brain atrophy rates in Parkinson's disease with and without dementia using serial magnetic resonance imaging. *Movement Disorders*, **20**, 1571–6.
57. Lee JE, Park HJ, Song SK, et al. (2010). Neuroanatomic basis of amnestic MCI differs in patients with and without Parkinson disease. *Neurology*, **75**, 2009–16.
58. Song SK, Lee JE, Park HJ, et al. (2011). The pattern of cortical atrophy in patients with Parkinson's disease according to cognitive status. *Movement Disorders*, **26**, 289–96.
59. Melzer TR, Watts R, MacAskill MR, et al. (2012). Grey matter atrophy in cognitively impaired Parkinson's disease. *Journal of Neurology, Neurosurgery & Psychiatry*, **83**, 188–94.
60. Yoshikawa K, Nakata Y, Yamada K, et al. (2004). Early pathological changes in the parkinsonian brain demonstrated by diffusion tensor MRI. *Journal of Neurology, Neurosurgery & Psychiatry*, **75**, 481–4.
61. Karagulle Kendi AT, Lehericy S, Luciana M, et al. (2008). Altered diffusion in the frontal lobe in Parkinson disease. *AJNR American Journal of Neuroradiology*, **29**, 501–5.
62. Zhang K, Yu C, Zhang Y, et al. (2011). Voxel-based analysis of diffusion tensor indices in the brain in patients with Parkinson's disease. *European Journal of Radiology*, **77**, 269–73.
63. Haller S, Badoud S, Nguyen D, et al. (2012). Individual detection of patients with Parkinson disease using support vector machine analysis of diffusion tensor imaging data: initial results. *AJNR American Journal of Neuroradiology*, **33**, 2123–8.
64. Gattellaro G, Minati L, Grisoli M, et al. (2009). White matter involvement in idiopathic Parkinson disease: a diffusion tensor imaging study. *AJNR American Journal of Neuroradiology*, **30**, 1222–6.
65. Scherfler C, Schocke MF, Seppi K, et al. (2006). Voxel-wise analysis of diffusion weighted imaging reveals disruption of the olfactory tract in Parkinson's disease. *Brain*, **129**, 538–42.
66. Matsui H, Nishinaka K, Oda M, et al. (2007). Wisconsin Card Sorting Test in Parkinson's disease: diffusion tensor imaging. *Acta Neurologica Scandinavica*, **116**, 108–12.
67. Lee JE, Park HJ, Park B, et al. (2010). A comparative analysis of cognitive profiles and white-matter alterations using voxel-based diffusion tensor imaging between patients with Parkinson's disease dementia and dementia with Lewy bodies. *Journal of Neurology, Neurosurgery & Psychiatry*, **81**, 320–6.
68. Lee JE, Park B, Song SK, et al. (2010). A comparison of gray and white matter density in patients with Parkinson's disease dementia and dementia with Lewy bodies using voxel-based morphometry. *Movement Disorders*, **25**, 28–34.
69. Bertrand JA, Bedetti C, Postuma RB, et al. (2010). Color discrimination deficits in Parkinson's disease are related to cognitive impairment and white-matter alterations. *Movement Disorders*, **27**, 1781–8.
70. Hattori T, Orimo S, Aoki S, et al. (2012). Cognitive status correlates with white matter alteration in Parkinson's disease. *Human Brain Mapping*, **33**, 727–39.
71. Agosta F, Canu E, Stojković T, et al. (2012). The topography of brain damage at different stages of Parkinson's disease. *Human Brain Mapping*, **34**(11), 2798–807.
72. Deng B, Zhang Y, Wang L, et al. (2013). Diffusion Tensor Imaging Reveals White Matter Changes Associated With Cognitive Status in Patients With Parkinson's Disease. *American Journal of Alzheimer's Disease and Other Dementias*, **28**(2), 154–64.
73. Rae CL, Correia MM, Altena E, et al. (2012). White matter pathology in Parkinson's disease: the effect of imaging protocol differences and relevance to executive function. *NeuroImage*, **62**, 1675–84.
74. Agosta F, Canu E, Stefanova E, et al. (2013). Mild cognitive impairment in PD is associated with a distributed pattern of brain white matter damage. *Human Brain Mapping*, **35**(5), 1921–9.

75. Agosta F, Kostic VS, Davidovic K, et al. (2013). White matter abnormalities in Parkinson's disease patients with glucocerebrosidase gene mutations. *Movement Disorders*, **28**, 772–8.
76. Giannelli M, Toschi N, Passamonti L, et al. (2012). Diffusion kurtosis and diffusion-tensor MR imaging in Parkinson disease. *Radiology*, **265**, 645–6; author reply 646–7.
77. Wang JJ, Lin WY, Lu CS, et al. (2011). Parkinson disease: diagnostic utility of diffusion kurtosis imaging. *Radiology*, **261**, 210–7.
78. Sabatini U, Boulanouar K, Fabre N, et al. (2000). Cortical motor reorganization in akinetic patients with Parkinson's disease: a functional MRI study. *Brain*, **123**(Pt 2), 394–403.
79. Wu T, and Hallett M (2005). A functional MRI study of automatic movements in patients with Parkinson's disease. *Brain*, **128**, 2250–9.
80. Wu T, Wang L, Hallett M, et al. (2010). Neural correlates of bimanual anti-phase and in-phase movements in Parkinson's disease. *Brain*, **133**, 2394–409.
81. Buhmann C, Glauche V, Stürenburg HJ, et al. (2003). Pharmacologically modulated fMRI—cortical responsiveness to levodopa in drug-naive hemiparkinsonian patients. *Brain*, **126**, 451–61.
82. Haslinger B, Erhard P, Kämpfe N, et al. (2001). Event-related functional magnetic resonance imaging in Parkinson's disease before and after levodopa. *Brain*, **124**, 558–70.
83. Grafton ST, Turner RS, Desmurget M, et al. (2006). Normalizing motor-related brain activity: subthalamic nucleus stimulation in Parkinson disease. *Neurology*, **66**, 1192–9.
84. Wu T, Wang L, Hallett M, et al. (2011). Effective connectivity of brain networks during self-initiated movement in Parkinson's disease. *NeuroImage*, **55**, 204–15.
85. van Nuenen BF, Weiss MM, Bloem BR, et al. (2009). Heterozygous carriers of a Parkin or PINK1 mutation share a common functional endophenotype. *Neurology*, **72**, 1041–7.
86. van Eimeren T, Monchi O, Ballanger B, et al. (2009). Dysfunction of the default mode network in Parkinson disease: a functional magnetic resonance imaging study. *Archives of Neurology*, **66**, 877–83.
87. Ekman U, Eriksson J, Forsgren L, et al. (2012). Functional brain activity and presynaptic dopamine uptake in patients with Parkinson's disease and mild cognitive impairment: a cross-sectional study. *Lancet Neurology*, **11**, 679–87.
88. Nagano-Saito A, Habak C, Mejía-Constaín B, et al. (2014). Effect of mild cognitive impairment on the patterns of neural activity in early Parkinson's disease. *Neurobiology of Aging*, **35**, 223–31.
89. Snijders AH, Leunissen I, Bakker M, et al. (2011). Gait-related cerebral alterations in patients with Parkinson's disease with freezing of gait. *Brain*, **134**, 59–72.
90. Shine JM, Matar E, Ward PB, et al. (2013). Freezing of gait in Parkinson's disease is associated with functional decoupling between the cognitive control network and the basal ganglia. *Brain*, **136**, 3671–81.
91. Skidmore FM, Yang M, von Deneen KM, et al. (2013). Reliability analysis of the resting state can sensitively and specifically identify the presence of Parkinson disease. *NeuroImage*, **75**, 249–61.
92. Long D, Wang J, Xuan M, et al. (2012). Automatic classification of early Parkinson's disease with multi-modal MR imaging. *PLoS One*, **7**, e47714.
93. Hacker CD, Perlmutter JS, Criswell SR, et al. (2012). Resting state functional connectivity of the striatum in Parkinson's disease. *Brain*, **135**, 3699–711.
94. Helmich RC, Derikx LC, Bakker M, et al. (2010). Spatial remapping of cortico-striatal connectivity in Parkinson's disease. *Cerebral Cortex*, **20**, 1175–86.
95. Kwak Y, Peltier S, Bohnen NI, et al. (2010). Altered resting state cortico-striatal connectivity in mild to moderate stage Parkinson's disease. *Frontiers in Systems Neuroscience*, **4**, 143.
96. Kwak Y, Peltier SJ, Bohnen NI, et al. (2012). L-DOPA changes spontaneous low-frequency BOLD signal oscillations in Parkinson's disease: a resting state fMRI study. *Frontiers in Systems Neuroscience*, **6**, 52.
97. Wu T, Long X, Zang Y, et al. (2009). Regional homogeneity changes in patients with Parkinson's disease. *Human Brain Mapping*, **30**, 1502–10.
98. Wu T, Wang L, Zang Y, et al. (2009). Changes of functional connectivity of the motor network in the resting state in Parkinson's disease. *Neuroscience Letters*, **460**, 6–10.
99. Yang H, Zhou XJ, Zhang MM, et al. (2013). Changes in spontaneous brain activity in early Parkinson's disease. *Neuroscience Letters*, **549**, 24–8.
100. Yu R, Liu B, Wang L, et al. (2013). Enhanced functional connectivity between putamen and supplementary motor area in Parkinson's disease patients. *PLoS One*, **8**, e59717.
101. Choe IH, Yeo S, Chung KC, et al. (2013). Decreased and increased cerebral regional homogeneity in early Parkinson's disease. *Brain Research*, 1527, 230–7.
102. Esposito F, Tessitore A, Giordano A, et al. (2013). Rhythm-specific modulation of the sensorimotor network in drug-naive patients with Parkinson's disease by levodopa. *Brain*, **136**, 710–25.
103. Tessitore A, Esposito F, Vitale C, et al. (2012). Default-mode network connectivity in cognitively unimpaired patients with Parkinson disease. *Neurology*, **79**, 2226–32.
104. Possin KL, Kang GA, Fine EM, et al. (2013). Rivastigmine is associated with restoration of left frontal brain activity in Parkinson's disease. *Movement Disorders*, **28**, 1384–90.
105. Baggio HC, Sala-Llonch R, Segura B, et al. (2014). Functional brain networks and cognitive deficits in Parkinson's disease. *Human Brain Mapping*, **35**(9), 4620–34.
106. Shine JM, Halliday GM, Gilat M, et al. (2014). The role of dysfunctional attentional control networks in visual misperceptions in Parkinson's disease. *Human Brain Mapping*, **35**, 2206–19.
107. Berg D, Godau J, Walter U. (2008). Transcranial sonography in movement disorders. *Lancet Neurology*, **7**, 1044–55.
108. Walter U, Behnke S, Eyding J, et al. (2007). Transcranial brain parenchyma sonography in movement disorders: state of the art. *Ultrasound in Medicine and Biology*, **33**, 15–25.
109. Becker G, Seufert J, Bogdahn U, et al. (1995). Degeneration of substantia nigra in chronic Parkinson's disease visualized by transcranial color-coded real-time sonography. *Neurology*, **45**, 182–4.
110. Stockner H, Schwingenschuh P, Djamshidian A, et al. (2012). Is transcranial sonography useful to distinguish scans without evidence of dopaminergic deficit patients from Parkinson's disease? *Movement Disorders*, **27**, 1182–5.
111. Gilman S, Wenning GK, Low PA, et al. (2008). Second consensus statement on the diagnosis of multiple system atrophy. *Neurology*, **71**, 670–6.
112. Dickson DW, Kouri N, Murray ME, et al. (2011). Neuropathology of frontotemporal lobar degeneration-tau (FTLD-tau). *Journal of Molecular Neuroscience*, **45**, 384–9.
113. Litvan I, Agid Y, Calne D, et al. (1996). Clinical research criteria for the diagnosis of progressive supranuclear palsy (Steele–Richardson–Olszewski syndrome): report of the NINDS-SPSP international workshop. *Neurology*, **47**, 1–9.
114. Armstrong MJ, Litvan I, Lang AE, et al. (2013). Criteria for the diagnosis of corticobasal degeneration. *Neurology*, **80**, 496–503.
115. Scherfler C, Seppi K, Donnemiller E, et al. (2005). Voxel-wise analysis of [123I]beta-CIT SPECT differentiates the Parkinson variant of multiple system atrophy from idiopathic Parkinson's disease. *Brain*, **128**, 1605–12.
116. van Royen E, Verhoeff NF, Speelman JD, et al. (1993). Multiple system atrophy and progressive supranuclear palsy. Diminished striatal D2 dopamine receptor activity demonstrated by 123I-IBZM single photon emission computed tomography. *Archives of Neurology*, **50**, 513–6.
117. Vlaar AM, de Nijs T, Kessels AG, et al. (2008). Diagnostic value of 123I-ioflupane and 123I-iodobenzamide SPECT scans in 248 patients with parkinsonian syndromes. *European Neurology*, **59**, 258–66.
118. Sawle GV, Brooks DJ, Marsden CD, et al. (1991). Corticobasal degeneration. A unique pattern of regional cortical oxygen hypometabolism and striatal fluorodopa uptake demonstrated by positron emission tomography. *Brain*, **114**(Pt 1B), 541–56.

119. Eckert T, Barnes A, Dhawan V, et al. (2005). FDG PET in the differential diagnosis of parkinsonian disorders. *NeuroImage*, **26**, 912–21.
120. Tang CC, Poston KL, Eckert T, et al. (2010). Differential diagnosis of parkinsonism: a metabolic imaging study using pattern analysis. *Lancet Neurology*, **9**, 149–58.
121. Garraux G, Salmon E, Peigneux P, et al. (2000). Voxel-based distribution of metabolic impairment in corticobasal degeneration. *Movement Disorders*, **15**, 894–904.
122. Hosaka K, Ishii K, Sakamoto S, et al. (2002). Voxel-based comparison of regional cerebral glucose metabolism between PSP and corticobasal degeneration. *Journal of the Neurological Sciences*, **199**, 67–71.
123. Zalewski N, Botha H, Whitwell JL, et al. (2014). FDG-PET in pathologically confirmed spontaneous 4R-tauopathy variants. *Journal of Neurology*, **261**, 710–6.
124. Nicoletti G, Fera F, Condino F, et al. (2006). MR imaging of middle cerebellar peduncle width: differentiation of multiple system atrophy from Parkinson disease. *Radiology*, **239**, 825–30.
125. Oba H, Yagishita A, Terada H, et al. (2005). New and reliable MRI diagnosis for progressive supranuclear palsy. *Neurology*, **64**, 2050–5.
126. Quattrone A, Nicoletti G, Messina D, et al. (2008). MR imaging index for differentiation of progressive supranuclear palsy from Parkinson disease and the Parkinson variant of multiple system atrophy. *Radiology*, **246**, 214–21.
127. Warmuth-Metz M, Naumann M, Csoti I, et al. (2001). Measurement of the midbrain diameter on routine magnetic resonance imaging: a simple and accurate method of differentiating between Parkinson disease and progressive supranuclear palsy. *Archives of Neurology*, **58**, 1076–9.
128. Longoni G, Agosta F, Kostić VS, et al. (2011). MRI measurements of brainstem structures in patients with Richardson's syndrome, progressive supranuclear palsy-parkinsonism, and Parkinson's disease. *Movement Disorders*, **26**, 247–55.
129. Rolland Y, Verin M, Payan CA, et al. (2011). A new MRI rating scale for progressive supranuclear palsy and multiple system atrophy: validity and reliability. *Journal of Neurology, Neurosurgery & Psychiatry*, **82**, 1025–32.
130. Focke NK, Helms G, Pantel PM, et al. (2011). Differentiation of typical and atypical Parkinson syndromes by quantitative MR imaging. *AJNR American Journal of Neuroradiology*, **32**, 2087–92.
131. Wang Y, Butros SR, Shuai X, et al. (2012). Different iron-deposition patterns of multiple system atrophy with predominant parkinsonism and idiopathetic Parkinson diseases demonstrated by phase-corrected susceptibility-weighted imaging. *AJNR American Journal of Neuroradiology*, **33**, 266–73.
132. Boelmans K, Holst B, Hackius M, et al. (2012). Brain iron deposition fingerprints in Parkinson's disease and progressive supranuclear palsy. *Movement Disorders*, **27**, 421–7.
133. Nicoletti G, Lodi R, Condino F, et al. (2006). Apparent diffusion coefficient measurements of the middle cerebellar peduncle differentiate the Parkinson variant of MSA from Parkinson's disease and progressive supranuclear palsy. *Brain*, **129**, 2679–87.
134. Seppi K, Schocke MF, Esterhammer R, et al. (2003). Diffusion-weighted imaging discriminates progressive supranuclear palsy from PD, but not from the parkinson variant of multiple system atrophy. *Neurology*, **60**, 922–7.
135. Nicoletti G, Tonon C, Lodi R, et al. (2008). Apparent diffusion coefficient of the superior cerebellar peduncle differentiates progressive supranuclear palsy from Parkinson's disease. *Movement Disorders*, **23**, 2370–6.
136. Prodoehl J, Li H, Planetta PJ, et al. (2013). Diffusion tensor imaging of Parkinson's disease, atypical parkinsonism, and essential tremor. *Movement Disorders*, **28**, 1816–22.
137. Seppi K, Schocke MF, Donnemiller E, et al. (2004). Comparison of diffusion-weighted imaging and [123I]IBZM-SPECT for the differentiation of patients with the Parkinson variant of multiple system atrophy from those with Parkinson's disease. *Movement Disorders*, **19**, 1438–45.
138. Rizzo G, Martinelli P, Manners D, et al. (2008). Diffusion-weighted brain imaging study of patients with clinical diagnosis of corticobasal degeneration, progressive supranuclear palsy and Parkinson's disease. *Brain*, **131**, 2690–700.
139. Brenneis C, Seppi K, Schocke MF, et al. (2003). Voxel-based morphometry detects cortical atrophy in the Parkinson variant of multiple system atrophy. *Movement Disorders*, **18**, 1132–8.
140. Minnerop M, Specht K, Ruhlmann J, et al. (2007). Voxel-based morphometry and voxel-based relaxometry in multiple system atrophy-a comparison between clinical subtypes and correlations with clinical parameters. *NeuroImage*, **36**, 1086–95.
141. Brenneis C, Egger K, Scherfler C, et al. (2007). Progression of brain atrophy in multiple system atrophy. A longitudinal VBM study. *Journal of Neurology*, **254**, 191–6.
142. Cordato NJ, Duggins AJ, Halliday GM, et al. (2005). Clinical deficits correlate with regional cerebral atrophy in progressive supranuclear palsy. *Brain*, **128**, 1259–66.
143. Paviour DC, Price SL, Stevens JM, et al. (2005). Quantitative MRI measurement of superior cerebellar peduncle in progressive supranuclear palsy. *Neurology*, **64**, 675–9.
144. Boxer AL, Geschwind MD, Belfor N, et al. (2006). Patterns of brain atrophy that differentiate corticobasal degeneration syndrome from progressive supranuclear palsy. *Archives of Neurology*, **63**, 81–6.
145. Josephs KA, Whitwell JL, Dickson DW, et al. (2008). Voxel-based morphometry in autopsy proven PSP and CBD. *Neurobiology of Aging*, **29**, 280–9.
146. Agosta F, Kostic VS, Galantucci S, et al. (2010). The in vivo distribution of brain tissue loss in Richardson's syndrome and PSP-parkinsonism: a VBM-DARTEL study. *European Journal of Neuroscience*, **32**, 640–7.
147. Price S, Paviour D, Scahill R, et al. (2004). Voxel-based morphometry detects patterns of atrophy that help differentiate progressive supranuclear palsy and Parkinson's disease. *NeuroImage*, **23**, 663–9.
148. Focke NK, Helms G, Scheewe S, et al. (2011). Individual voxel-based subtype prediction can differentiate progressive supranuclear palsy from idiopathic Parkinson syndrome and healthy controls. *Human Brain Mapping*, **32**, 1905–15.
149. Lee SE, Rabinovici GD, Mayo MC, et al. (2011). Clinicopathological correlations in corticobasal degeneration. *Annals of Neurology*, **70**, 327–40.
150. Nilsson C, Markenroth Bloch K, Brockstedt S, et al. (2007). Tracking the neurodegeneration of parkinsonian disorders—a pilot study. *Neuroradiology*, **49**, 111–9.
151. Ito M, Watanabe H, Atsuta N, et al. (2008). Fractional anisotropy values detect pyramidal tract involvement in multiple system atrophy. *Journal of the Neurological Sciences*, **271**, 40–6.
152. Surova Y, Szczepankiewicz F, Lätt J, et al. (2013). Assessment of global and regional diffusion changes along white matter tracts in parkinsonian disorders by MR tractography. *PLoS One*, **8**, e66022.
153. Padovani A, Borroni B, Brambati SM, et al. (2006). Diffusion tensor imaging and voxel based morphometry study in early progressive supranuclear palsy. *Journal of Neurology, Neurosurgery & Psychiatry*, **77**, 457–63.
154. Ito S, Makino T, Shirai W, et al. (2008). Diffusion tensor analysis of corpus callosum in progressive supranuclear palsy. *Neuroradiology*, **50**, 981–5.
155. Whitwell JL, Master AV, Avula R, et al. (2011). Clinical correlates of white matter tract degeneration in progressive supranuclear palsy. *Archives of Neurology*, **68**, 753–60.
156. Whitwell JL, Avula R, Master A, et al. (2011). Disrupted thalamocortical connectivity in PSP: a resting-state fMRI, DTI, and VBM study. *Parkinsonism and Related Disorders*, **17**, 599–605.
157. Canu E, Agosta F, Baglio F, et al. (2011). Diffusion tensor magnetic resonance imaging tractography in progressive supranuclear palsy. *Movement Disorders*, **26**(9), 1752-5.
158. Wang J, Wai Y, Lin WY, et al. (2011). Microstructural changes in patients with progressive supranuclear palsy: a diffusion tensor imaging study. *Journal of Magnetic Resonance Imaging*, **32**, 69–75.

159. Saini J, Bagepally BS, Sandhya M, et al. (2012). In vivo evaluation of white matter pathology in patients of progressive supranuclear palsy using TBSS. *Neuroradiology*, **54**, 771–80.
160. Sajjadi SA, Acosta-Cabronero J, Patterson K, et al. (2013). Diffusion tensor magnetic resonance imaging for single subject diagnosis in neurodegenerative diseases. *Brain*, **136**, 2253–61.
161. Agosta F, Galantucci S, Svetel M, et al. (2014). Clinical, cognitive, and behavioural correlates of white matter damage in progressive supranuclear palsy. *Journal of Neurology*, **261**(5), 913–24.
162. Agosta F, Pievani M, Svetel M, et al. (2012). Diffusion tensor MRI contributes to differentiate Richardson's syndrome from PSP-parkinsonism. *Neurobiology of Aging*, **33**, 2817–26.
163. Borroni B, Garibotto V, Agosti C, et al. (2008). White matter changes in corticobasal degeneration syndrome and correlation with limb apraxia. *Archives of Neurology*, **65**, 796–801.
164. Boelmans K, Kaufmann J, Bodammer N, et al. (2009). Involvement of motor pathways in corticobasal syndrome detected by diffusion tensor tractography. *Movement Disorders*, **24**, 168–75.
165. Whitwell JL, Schwarz CG, Reid RI, et al. (2014). Diffusion tensor imaging comparison of progressive supranuclear palsy and corticobasal syndromes. *Parkinsonism and Related Disorders*, **20**(5), 493–8.
166. Gardner RC, Boxer AL, Trujillo A, et al. (2013). Intrinsic connectivity network disruption in progressive supranuclear palsy. *Annals of Neurology*, **73**, 603–16.
167. Courbon F, Brefel-Courbon C, Thalamas C, et al. (2003). Cardiac MIBG scintigraphy is a sensitive tool for detecting cardiac sympathetic denervation in Parkinson's disease. *Movement Disorders*, **18**, 890–7.
168. Treglia G, Stefanelli A, Cason E, et al. (2011). Diagnostic performance of iodine-123-metaiodobenzylguanidine scintigraphy in differential diagnosis between Parkinson's disease and multiple-system atrophy: a systematic review and a meta-analysis. *Clinical Neurology and Neurosurgery*, **113**, 823–9.
169. Rascol O, and Schelosky L. (2009). 123I-metaiodobenzylguanidine scintigraphy in Parkinson's disease and related disorders. *Movement Disorders*, **24**(Suppl. 2), S732–41.
170. Cherubini A, Morelli M, Nisticó R, et al. (2014). Magnetic resonance support vector machine discriminates between Parkinson disease and progressive supranuclear palsy. *Movement Disorders*, **29**, 266–9.
171. McKeith I, O'Brien J, Walker Z, et al. (2007). Sensitivity and specificity of dopamine transporter imaging with 123I-FP-CIT SPECT in dementia with Lewy bodies: a phase III, multicentre study. *Lancet Neurology*, **6**, 305–13.
172. Berg D, Steinberger JD, Warren Olanow C, et al. (2011). Milestones in magnetic resonance imaging and transcranial sonography of movement disorders. *Movement Disorders*, **26**, 979–92.
173. Mascalchi M, Vella A, and Ceravolo R. (2012). Movement disorders: role of imaging in diagnosis. *Journal of Magnetic Resonance Imaging*, **35**, 239–56.

CHAPTER 22

Neuroimaging of prion diseases

Eduardo Caverzasi, Leonel Takada, Paolo Vitali,
Marina Pan, and Michael D. Geschwind

Introduction

Prion diseases are a group of rare and invariably fatal diseases that occur in humans and animals. Prion diseases (PrDs) are presumed to be caused by misfolding of a normal protein in the nervous system, the prion protein, or PrPC (in which PrP stands for prion-related protein and C stands for the normal cellular form of the protein), into an abnormal, disease-causing conformation called the prion, or PrPSc (in which Sc stands for scrapie, the prion disease of sheep and goats) [1]. In human prion disease (hPrD), deposition of PrPSc as diffuse deposits and/or plaques of various morphologies is usually accompanied by the classic histologic triad: vacuolar degeneration of the gray matter (GM) neuropil, gliosis, and neuronal loss [2].

Some animal prion diseases include scrapie of sheep and goat, bovine spongiform encephalopathy (BSE; 'mad cow disease'), chronic wasting disease (CWD) of mule deer, elk, and moose, and others. Human prion diseases are unique in medicine as they occur in three different ways: sporadic (spontaneous), genetic (also called familial), and acquired (iatrogenic or environmental). Sporadic prion diseases are referred to as sporadic Jakob–Creutzfeldt (or Creutzfeldt–Jakob) disease (sCJD). Based on clinical and pathological features genetic prion diseases are historically divided into three forms, specifically familial Creutzfeldt–Jakob (fCJD), Gerstmann–Sträussler–Scheinker disease (GSS) and fatal familial insomnia (FFI). Acquired PrDs (aPrDs) include the notorious Kuru, a disease caused by endocannibalism among the Fore ethnic group in Papua New Guinea, which is nearly extinct due to the elimination of cannibalism, variant Creutzfeldt–Jakob (vCJD, linked to BSE) and iatrogenic Creutzfeldt–Jakob (iCJD) [3,4].

Unlike many other neurodegenerative diseases, brain magnetic resonance imaging (MRI) has been shown to be particularly useful in the diagnosis of certain forms of prion diseases. Although atrophy in CJD had been known for many years [5], the first report of specific T2-weighted abnormalities in sCJD, primarily hyperintensities in the deep nuclei, was published in 1988, suggesting that MRI might distinguish CJD from other neurodegenerative diseases [6]. With the advent of fluid-attenuated inversion recovery (FLAIR) MRI, hyperintensity of cortical gyri ('cortical ribboning') was more clearly noted [7]. In 1999, diffusion-weighted imaging (DWI) MRI abnormalities were first reported in sCJD [8,9]. These changes were much more obvious than most T2/FLAIR abnormalities and had a non-vascular distribution, helping to differentiate from stroke [8,9]. Most importantly for clinical diagnosis is that there is significant restricted diffusion on DWI sequences, in most human PrDs (hPrDs), particularly sCJD, many forms of fCJD, and iCJD [10–12]. Overall, DWI has been shown to have the higher diagnostic utility for hPrD diagnosis [12–14] than current clinically available cerebrospinal fluid (CSF) biomarkers, such as 14-3-3, total tau, and neuron-specific enolase (NSE) [15–17]. Unfortunately, the majority of MRIs in patients with sCJD have been misread. These MRIs are often misread because either the T2-weighted or DWI hyperintensities are not noted or these signal changes are noted, but not recognized as being due to hPrDs [18,19]. In this chapter, we will discuss the major forms of hPrDs and present typical imaging features, including MRI and positron emission tomography (PET).

Sporadic CJD

CJD is the most common form of hPrD, comprising about 85–90% of all hPrDs and is classically characterized by rapidly progressive dementia with ataxia and myoclonus, typically leading to akinetic mutism and death within about a year or less from onset (many patients survive less than 6 months). sCJD is rare and appears to be evenly distributed worldwide with an annual incidence of ~ 1 per million [1]. sCJD typically begins with cognitive, behavioural, and/or cerebellar deficits, although other symptoms, such as more subtle constitutional symptoms (e.g. headache, weight loss, fatigue, insomnia, etc.) might occur first [20,21]. Extra-pyramidal and pyramidal symptoms, myoclonus, aphasia, and/or visual disturbances often develop. In the last phase of disease, patients often develop akinetic mutism (not moving, not speaking) before death, which is usually due to aspiration pneumonia. The mean and peak incidence of age of onset of sCJD is in the 60s. Unlike other more common neurodegenerative dementias, such as Alzheimer's disease (AD) and Parkinson's disease, the incidence of CJD does not increase with age [1,22].

Although a rapid course is the most common and typical of classical sCJD, it can have a greatly varied course and symptomatology [23–27], with survivals even of more than 3 years, overlapping with the duration of other neurodegenerative dementias and making diagnosis more difficult [25,28–31]. This heterogeneity in sCJD is, in part, explained by a combination of a gene polymorphism at codon 129 in the prion protein gene (*PRNP*), which can be methionine or valine homozygous or heterozygous (*MM, VV*, or *MV*), as well as the type of prion based on the molecular weight of the protease-k treated unglycosylated fragment when run on a gel. When prions are digested with proteinase K and run on a Western Blot, if the lowest, unglycosylated, band runs at 21 kDa, these are considered type 1 prions; if the unglycosylated band runs at 19 kDa, these are considered type 2 prions. Based on these variables, six sCJD subtypes (MM1/MV1, MV2, MM2-cortical, MM2-thalamic, VV1 and VV2) have been defined, and variations in the sensitivities of diagnostic tests for the different subtypes have been reported [23]. MM1 and MV1 were combined into one category due to their high clinicopathological overlap, whereas MM2 was divided into two subtypes [23]. This combination of codon 129 polymorphism and prion typing is referred to as 'molecular classification'. This classification, however, has become more complicated with the finding that many patients have a combination of type 1 and type 2 prions, depending on the brain region sampled [32–34].

Clinical diagnostic criteria

Most clinical diagnostic criteria for possible sCJD require progressive dementia (usually rapidly progressive) with the presence of two of four of the following combinations of symptoms:

1. Pyramidal/extrapyramidal.
2. Visual/cerebellar.
3. Myoclonus.
4. Akinetic mutism.

Criteria for 'probable' sCJD generally require a positive ancillary test, such as a characteristic electroencephalogram (EEG) showing ~1 Hz periodic sharp wave complexes (PSWCs) [35] a positive brain MRI, or a positive CSF protein 14-3-3. The EEG has relatively high specificity [36], but not very high sensitivity for sCJD [16]; only about two-thirds of sCJD patients will develop these EEG findings during the entire course of their illness [37]. In 1998, revised WHO diagnostic criteria for probable sCJD, an elevated/positive CSF test for the 14-3-3 protein was also allowed to substitute for a positive EEG for a probable sCJD diagnosis [35]. The CSF 14-3-3 protein is a controversial diagnostic test, with vastly differing reports of sensitivity and specificity [15,16,38–41]. At best, the diagnostic utility of the 14-3-3 varies greatly among the various molecular classifications of sCJD [16,42] and is even less sensitive in vCJD, aPrDs, and certain sCJD molecular subtypes [15]. As the molecular classification, with prion typing, requires brain tissue, interpretation of a positive or negative CSF 14-3-3 test might be difficult pre-mortem or without brain biopsy. Other CSF biomarkers tests, such as total tau, NSE, S100ß, might be more useful, particularly with higher specificity, than 14-3-3 [15,38,39,43,44) but none of these seem to be as useful as brain MRI [45,46].

MRI features

MRI has become increasingly important in the clinical diagnosis of sCJD, both by excluding non-prion forms of rapidly progressive dementias (npRPD) and by demonstrating features considered typical of hPrD. FLAIR and especially DWI sequences allow the detection of hyperintensity both of subcortical GM (striatum and thalamus) and in cortical GM (so called 'cortical ribboning') [12,14,47–52]. Such MRI findings help differentiate sCJD from other form of RPD with high sensitivity and specificity [12,17], and often are found early in the illness [47,53]. These DWI signal changes usually are more evident and frequently positive earlier in the disease than on T2 or FLAIR images (Fig. 22.1) [12,13]. As DWI hyperintensities might occur from either T2 increase and/or restricted mean diffusivity, concomitant evaluation of the apparent diffusion coefficient (ADC), and/or exponential ADC map, is important in order to identify a possible 'T2 shine through' [54] effect and confirm a restriction of water molecules movements with signal hypointensity on the ADC maps. The underlying phenomenon causing restriction of water molecules in the brain of patients with prion disease is still not completely understood [55]. DWI signal changes seems to correlate with specific histopathological findings, in particular

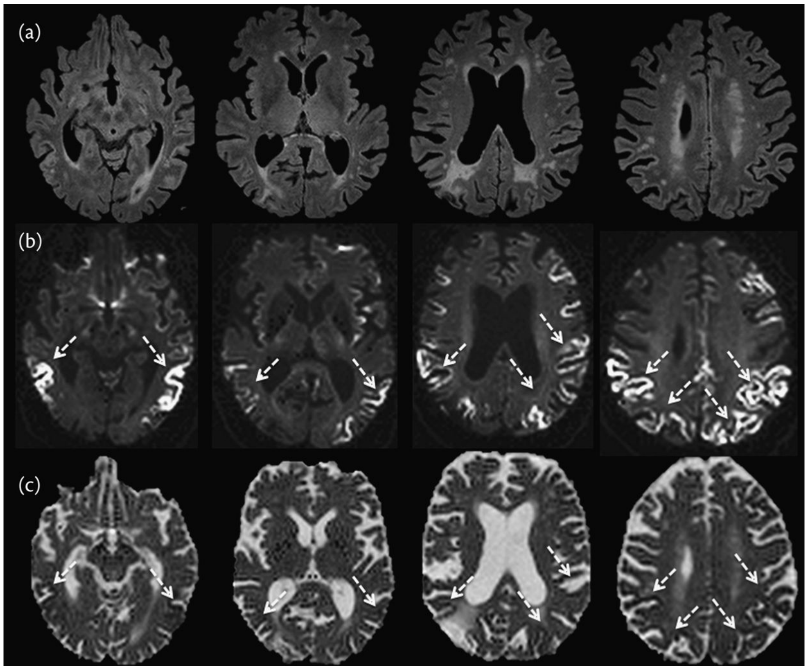

Fig. 22.1 Cortical involvement on brain MRI in sCJD. Brain MRI of a 71-year-old male with MM1 subtype of sCJD with predominantly cortical involvement on (a) FLAIR, (b), DWI, and (c) ADC map. There is diffuse hyperintense signal mainly in bilateral parietal and temporal cortex (dashed arrows) greater than frontal, but no significant subcortical abnormalities.

vacuolation occurring in the neuropil, whereas less correlation was observed with gliosis and prion deposition [55,56]. Typical vacuoles (spongiform change) in sCJD initially are small (around 5–25 μ) fluid-filled vesicles in the dendrites [57, 58]. It is thought that vacuoles around 16 μ or less are sufficient to restrict normal water movement in typical DWI pulse intervals [59,60].

MRI features as diagnostic criteria

The growing evidence of the diagnostic role of MRI in CJD necessitated an update of CJD diagnostic criteria [13,17,61]. The 2009 European criteria for probable sCJD allow high signal intensity in FLAIR or DWI to be considered as an equivalent diagnostic finding as either elevated CSF 14-3-3 protein or as periodic sharp and slow wave complexes on the EEG. Thus, for a patient to meet probable sCJD criteria, they need to have a positive ancillary test—either MRI, EEG, or CSF 14-3-3 required for probable sCJD diagnosis [17]. Focusing on the pattern of involvement in sCJD at a lobar level, Zerr and colleagues observed that specific cortical (at least two cortical regions—parietal, occipital or temporal, but not frontal) and subcortical GM (striatum—caudate nucleus and putamen) involvement had a higher power of discrimination between sCJD and controls subjects. They found that inclusion of frontal cortical involvement has led to too many false positive readings. Therefore, updating of probable sCJD diagnostic criteria by including MRI findings was suggested (Table 22.1) [17,61].

In clinical practice, sCJD is frequently misdiagnosed as other conditions [62], but MRI should help differentiate sCJD from many other conditions [12,13,17]. Vitali and colleagues highlighted four MRI features, which they found to be helpful in differentiating sCJD from non-prion diagnoses in their cohort [12]:

1. Greater hyperintensity on DWI than on FLAIR.
2. Subcortical GM hyperintensities on DWI should have associated ADC hypointensity (i.e. restricted diffusion).
3. Cortical GM involvement usually not isolated to only limbic structures.
4. Characteristic neuroanatomical pattern of involvement (see Table 22.2 UCSF 2011 proposal criteria for CJD diagnosis [12].

Table 22.1 MRI-CJD Consortium criteria for sporadic Creutzfeldt-Jakob disease

Clinical signs 1. Dementia 2. Cerebellar or visual 3. Pyramidal or extrapyramidal 4. Akinetic mutism
Tests 1. PSWCs in EEG 2. 14-3-3 detection in CSF (in patients with a disease duration of less than 2 years) 3. High signal abnormalities in caudate nucleus and putamen or at least two cortical regions (temporal-parietal-occipital) either in DWI or FLAIR
Probable CJD Two from 'Clinical Signs' and at least one from 'Tests'
Possible CJD Two from 'Clinical signs' and less than 2 years duration

Zerr I, Kallenberg K, Summers DM, et al. (2009). Updated clinical diagnostic criteria for sporadic Creutzfeldt–Jakob disease. *Brain*, **132**(Pt 10), 2659-68.

MRI hyperintensities in sCJD rarely affect only limbic structures, and they usually present with a typical neuroanatomical pattern of involvement [12,63]. Three main patterns of GM involvement are usually present on DWI and/or FLAIR images [14,48,63]—concomitant cortical and subcortical involvement (~2/3 of the patients), only cortical involvement (less than a 1/3), or subcortical alone (rarely) (Fig. 22.2) [12,14]. The MRI signal changes in sCJD are almost always brighter and more evident on the DWI images than on FLAIR [12].

Based on the UCSF 2011 MRI criteria, classic pathognomonic MRI features for sCJD are at the cortical level involvement of cingulate cortex and a concomitant involvement of >1 cortical gyri, in particular often precuneus, angular, superior, or middle frontal gyri; the cortical ribboning frequently involves both hemispheres, often asymmetrically, especially midline structures [12,14]. At a subcortical level, striatal involvement is supportive for sCJD diagnosis, frequently showing an anterior-posterior gradient, with the caudate head and anterior putamen being brighter than the posterior putamen [12,14]. Brain MRI is probably the most accurate method for the diagnosis of sCJD, with approximate sensitivity of 92–96% and specificity of 92–94% using DWI MRI [12,13].

Thalamic DWI involvement in CJD is often coupled with bilateral striatal involvement and is usually more symmetric, involving the dorso-median and posterior (pulvinar) regions. This pattern is similar to, but typically less intense than the 'double hockey stick' sign often observed in vCJD cases. In sCJD the pulvinar usually is not brighter than anterior putamen (true 'pulvinar sign' in vCJD), although there are rare exceptions (Fig. 22.3) [64,65]. Often if there is focal thalamic involvement on DWI images, a more diffuse thalamic hypointensity is seen on the ADC maps.

MRI features in sCJD subtypes

To some extent, visual assessment and quantitative analysis suggest that the pattern of DWI MRI involvement in sCJD depends on the molecular subtype [63,66]. Prominent subcortical GM hyperintensities seems to occur most frequently in MV2, VV2, and MM1 in the striatum. VV2 and MV2 often show striatal and thalamic involvement without significant cortical involvement. More widely-distributed cortical ribboning is more frequently seen in VV1, MM2, and MV1 subtypes [63], as shown in MM1 cases in Figs 22.1, and 22.4b, c. Our own quantitative analysis suggests a correlation between type 1 prions and more reduced cortical MD and between codon 129 VV and more reduced MD in the deep nuclei [66].

The patterns of involvement do not always fit as reported in Meissner et al. [63], however, as shown in Fig. 22.4a with an MM2 case showing prominent cortical and subcortical involvement. Fig. 22.4 also shows the extremely wide heterogeneity of possible DWI gyral involvement, not only between various subtypes, but also between patients with the same CJD subtype disease. The pattern of involvement in sCJD seems to change over the disease course, with possible normalization (relative normalization) of MD in areas previously affected by reduced MD [66]

The areas most commonly affected on DWI by visual inspection in a cohort of sCJD subjects are shown in Fig. 22.5. Although, on visual inspection, the Rolandic cortex and pallidum are not

Table 22.2 UCSF 2005 and 2010 proposal of MRI criteria for CJD diagnosis

Diagnosis	**UCSF 2005 criteria**	**UCSF 2011 proposed modifications/additions**
	FLAIR and DWI (or DWI alone) hyperintensity in	**DWI > FLAIR hyperintensity in**
MRI definitely CJD	Cortex (>1 gyrus) and striatum	Classic pathognomic: cingulate, striatum, and >1 neocortical gyrus (often precuneus, angulate, superior, or middle frontal gyrus). *Supportive for subcortical involvement:* ◆ Striatum with anterior–posterior gradient. ◆ Subcortical ADC hypointensity *Supportive for cortical involvement:* ◆ Asymmetric involvement of midline neocortex or cingulate ◆ Sparing of the precentral gyrus ◆ ADC cortical ribboning hypointensity
	Cortex only (>3 gyri)	Cortex only (>3 gyri); see 'Supportive for cortical involvement', above
MRI probably CJD	Unilateral striatum or cortex ≤gyri	Unilateral striatum or cortex ≤3 gyri; see 'Supportive for subcortical involvement', above; see 'Supportive for cortical involvement', above
	Bilateral striatum or posteromesial thalamus	Bilateral striatum or posteromesial thalamus; see 'Supportive for subcortical involvement', above
	FLAIR > DWI hyperintensities	Moved to probably not CJD; see 'MRI probably not CJD', below
MRI probably not CJD	Only FLAIR/DWI abnormalities in limbic areas, where hyperintensity can be normal (insula, cingulate)	Only FLAIR/DWI abnormalities in limbic areas, where hyperintensity can be normal (e.g. insula, anterior cingulate, hippocampi) and ADC map does not show restricted diffusion in these areas
	DWI hyperintensities due to artefact (signal distortion)	DWI hyperintensities due to artefact (signal distortion); see other MRI issues (below)
	FLAIR > DWI hyperintensities	FLAIR > DWI hyperintensities; see 'Other MRI issues', below
MRI definitely not CJD	Normal	No change from prior criteria
	Abnormalities not consistent with CJD	No change from prior criteria
Other MRI issues	In prolonged courses of sCJD (~>1 year) brain MRI might show significant atrophy with loss of DWI hyperintensity, particularly in areas previously with restricted diffusion	
	To help distinguish abnormality from artefact, obtain sequences in multiple directions (e.g. axial and coronal)	

Modified from *Neurology*, **76**(20), Vitali P, Maccagnano E, Caverzasi E, et al., Diffusion-weighted MRI hyperintensity patterns differentiate CJD from other rapid dementias, p. 1711–19, Copyright (2011), with permission from Wolters Kluwer Health.

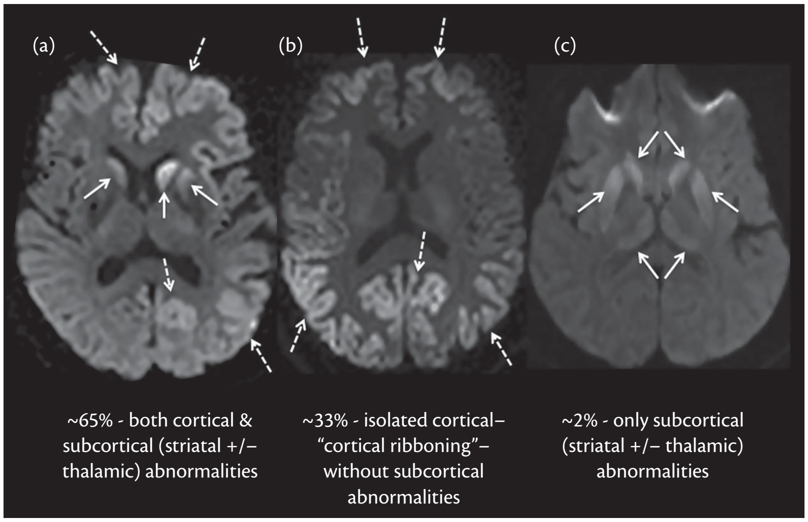

~65% - both cortical & subcortical (striatal +/– thalamic) abnormalities

~33% - isolated cortical– "cortical ribboning"– without subcortical abnormalities

~2% - only subcortical (striatal +/– thalamic) abnormalities

Fig. 22.2 Three common DWI MRI patterns in sporadic CJD: (a) both cortical and subcortical, (b) predominantly cortical, (c) predominantly subcortical involvement (basal ganglia and/or thalamus). Cortical (dashed arrows) and subcortical hyperintensity (solid arrows)

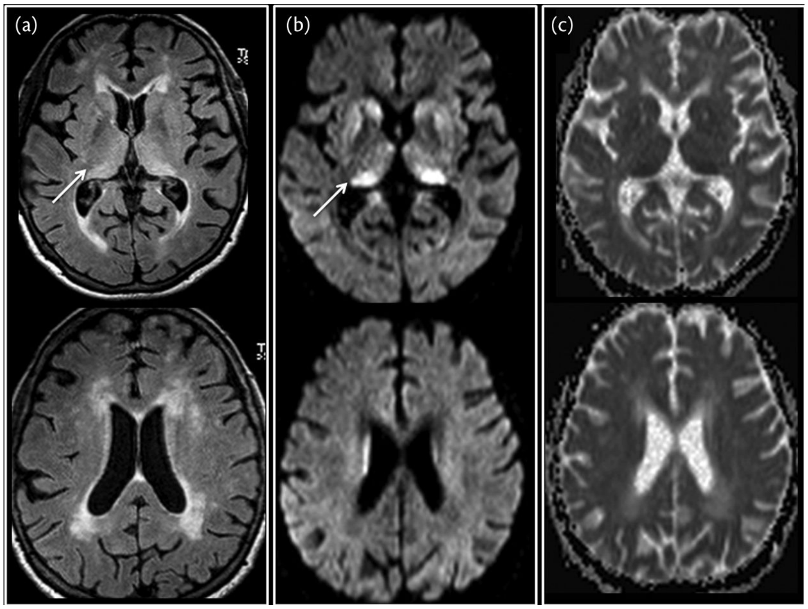

Fig. 22.3 Pulvinar sign is not specific for variant CJD. Brain MRI of a 72 year old woman with MV1-2 sCJD with (a) FLAIR, (b) DWI and (c) ADC sequences showing the pulvinar sign on MRI with the pulvinar (solid arrow) being brighter than the anterior putamen. Note that the pulvinar sign is present on FLAIR, DWI and ADC sequences, but this sign was devised based on T_2/FLAIR and not diffusion sequences [80].

usually involved on FLAIR/DWI MRI [14], whether or not these areas are affected on MRI is controversial as the apparent preservation of these structures on some sequences might be due to some intrinsic regional characteristic (i.e. iron deposition) causing an underestimation of involvement on FLAIR or DWI images (T2 black-out effect). Quantitative studies have shown decreased ADC/MD values in this region [66,67]. ADC maps are important for the confirmation of restriction of diffusion, and are particularly useful

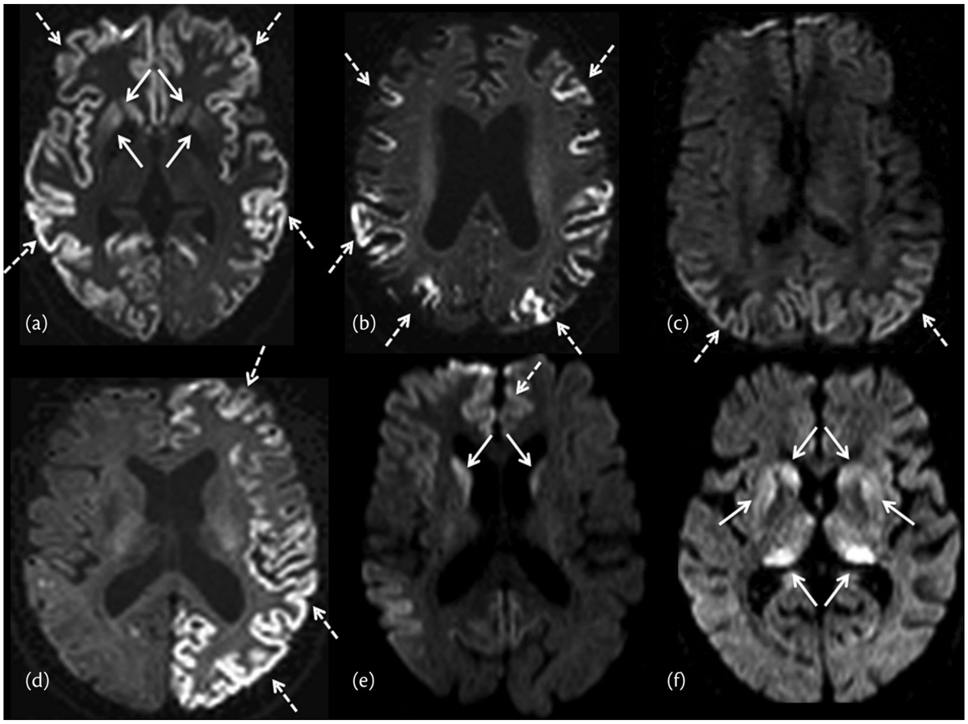

Fig. 22.4 Heterogeneity of MRI patterns of involvement in sCJD. (a) Bilateral cortical and subcortical pattern in a 60-year-old woman with MM2 sCJD. (b) Isolated cortical ribboning in a 71-year-old man with MM1 subtype of sCJD. (c) 74-year-old MM2 sCJD man. (D) MRI showing only unilateral cortical involvement in an sCJD subject. (e) 70-year-old man with MM1 sCJD. (f) A 73-year-old woman with MV1-2 sCJD. Note the 'pulvinar sign,' with the posterior thalamus (pulvinar) being more hyperintense than the anterior putamen. Despite this MRI finding, her clinical story was not consistent with vCJD and she did not technically have the pulvinar sign, which requires a clinical history compatible with vCJD [80]. Autopsy showed sCJD, not vCJD. Cortical (dashed arrows) and subcortical hyperintensity (solid arrows).

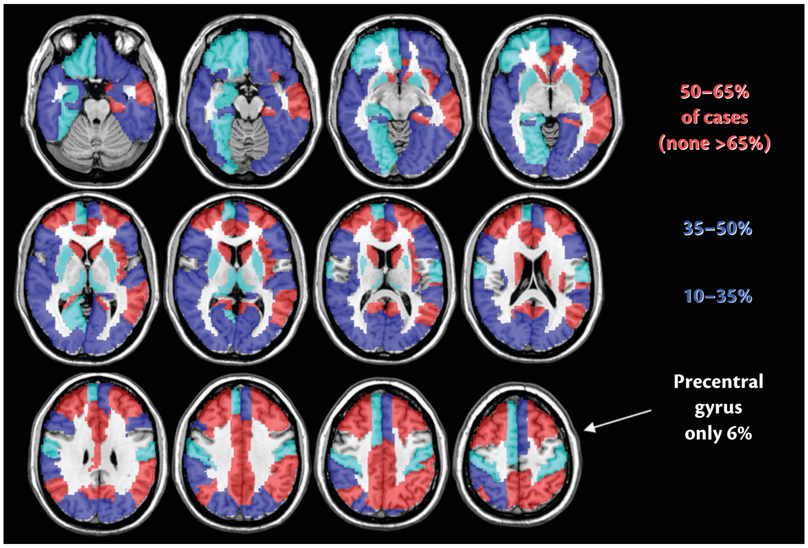

Fig. 22.5 Patterns of average gray matter involvement on DWI by visual assessment in 48 sCJD subjects. Colours depict percent of sCJD subjects with that region involved on DWI. Figure shown in radiological orientation (left side is right brain).

Modified from Vitali P, Maccagnano E, Caverzasi E, et al. (2011). Diffusion-weighted MRI hyperintensity patterns differentiate CJD from other rapid dementias. *Neurology*, **76**(20), 1711–19. Copyright (2011), with permission from Wolters Kluwer Health

for determining of DWI cortical ribboning is real (i.e. reduced diffusion) or artefact (Fig. 22.1). If the DWI shows deep nuclei hyperintensity in sCJD, the ADC usually will confirm this with concomitant hypointensity (Fig. 22.3). Unfortunately, ADC maps do not always show hypointense cortical ribboning due to the diffusion imaging distortion [68]. For a correct interpretation of the sCJD pattern of involvement on DWI images, it is important to note that DWI images are susceptible to geometric distortion and signal loss due to magnetic field inhomogeneity near air-tissue boundaries. Certain cortical regions, such as the cingulate cortex and insula, are known to be areas of DWI/FLAIR hyperintensity in healthy normal subjects [69]. These regions, as well as the frontal cortex are often bright in non-CJD patients, sometimes causing false-positive readings (see section, 'Differential diagnosis of rapidly progressive dementias and radiological mimickers of CJD'). Quantitative analysis seems to confirm a relative sparing of the frontal and anterior cingulate cortices, whereas a preferential involvement of posterior cingulate, parietal and temporal lobes [17,48,66].

The majority of sCJD cases present with a rapid course, surviving usually only a few months and, typically, less than 1 year [21,23], and thus it is rare to observe significant atrophy in the early phase of the disease, when DWI changes are already significant [66]. In sCJD patients who survive longer than a few months, and particularly longer than 1 year frequently show a progressive volume loss in the last phase of the disease [70,71]. The progressive atrophy is frequently associated with T2-weighted white matter hyperintensities, probably due to degeneration secondary to late stage neuronal loss [5]. White matter abnormalities have also been reported in the so-called 'panencephalopathic' form of CJD, mostly in Asia, but particularly in Japan [72–74]. It is not clear if this form represents a distinct entity. Many believe that this form of CJD merely represents the end-stage of patients with prolonged survival, often more than 18 months [75], rather than primary pathological events. Only recently for the first time, a widespread reduced mean diffusivity within the WM of sCJD subjects has been described in association with astrocytic gliosis and microglial activation. These imaging and histopathological findings may reflect direct white matter damages occurring during the early stages of sCJD [76].

Variant CJD

vCJD usually affects younger subjects (mean age 28–29 years old) with a longer mean disease course (14 months) compared with sCJD. Subjects usually first develop psychiatric and sensory symptoms (dysaesthesias); later in the course of the disease cerebellar signs and involuntary movements such as dystonia, myoclonus and chorea become more evident [77,78].

The imaging hallmark of vCJD is bilateral hyperintensity of the posterior portion of the thalamus (pulvinar), which is brighter than the anterior putamen (pulvinar sign) [79,80]. In a study on the sensitivity of the pulvinar sign on FLAIR sequences in vCJD, there was 90% sensitivity (74/82) in a prospective analysis and 100% (30/30) sensitivity in a retrospective analysis. According to that study, a pulvinar sign should be recorded to be present if:

1. The patient meets vCJD clinical criteria [78].
2. There is bilateral hyperintensity in the pulvinar, greater than the signal intensity in the anterior half of the putamen.
3. Appropriate imaging sequences have been performed, including an axial FLAIR sequence [80].

In an analysis of the first 150 UK vCJD cases, only seven of 150 did not have an MRI consistent with vCJD, and most of these seven cases did not have a FLAIR MRI, the sequence in which the pulvinar sign is most often identified [78]. The literature on the diagnostic utility of brain MRI in vCJD has focused on T2-weighted sequences (i.e. proton-density, T2 and FLAIR), but has not examined the utility of DWI sequences [78]. This is, in part, because most cases have been identified in the UK, where the use of DWI sequences is not common. Hyperintensity of the medio-dorsal nuclei (double hockey stick sign) is also common in vCJD (Fig. 22.6), although

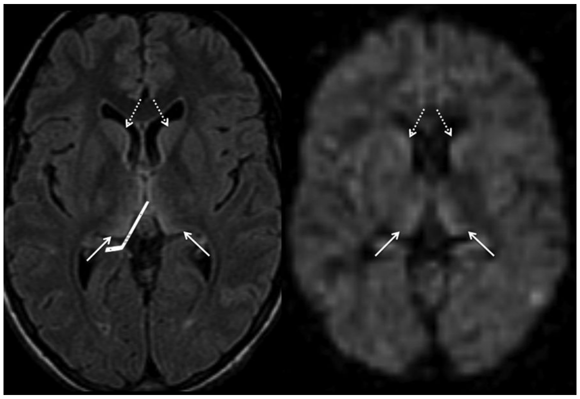

Fig. 22.6 Variant form of CJD. Thalamic involvement on FLAIR and DWI MRI in variant CJD. A 21-year-old woman with probable variant CJD with MRI showing bilateral thalamic hyperintensity in the mesial pars (mainly dorsomedian nucleus; solid arrows) and posterior pars (pulvinar) of the thalamus, the so-called 'double hockey stick sign'. A sample hockey stick is drawn depicting hyperintensity pattern in the right thalamus. The MRI probably also shows the pulvinar sign as the pulvinar is brighter than the anterior putamen. The caudate heads are also slightly hyperintense (dotted arrows). Both the pulvinar and especially the double-hockey stick sign are not specific for vCJD, and can be seen in sCJD and other, particularly metabolic, disorders.

this finding is also found in other forms of CJD [65,79,81]. Even the pulvinar sign rarely can be found in sCJD (Fig. 22.3) [64].

Other acquired CJD forms (iCJD)

The first iatrogenic (post-corneal transplantation) transmission of CJD (iCJD) was reported in 1974 [82]. Several parenteral transmission mechanisms have been identified in the following years due to surgical procedures (through instruments, dura graft, deep brain stimulation electrodes) or hormones (human pituitary-derived gonadotropins and growth hormone) [83]. In a study of 10 dura mater (DM) graft-associated iCJD cases, brain MRI reportedly showed cortical and basal ganglia signal increase each in eight out of 10 patients and thalamic hyperintensity in five [84]. All thalamic positive cases interestingly were homozygous for methionine at codon 129, suggesting that this polymorphism might play a role in iCJD MRI patterns, as molecular classification does in sCJD [63]. We reported a growth hormone case of iCJD, which typically present with cerebellar symptoms at onset, and cerebellar DWI hyperintensity [10], which is unusual in other hPrDs [12].

Neuroimaging of genetic prion diseases

Genetic PrDs are all caused by autosomal dominant mutations in the gene that encodes the prion protein (PRNP). Currently there are more than 40 known mutations in PRNP [85,86] and each mutation often is associated with one of the phenotypes (fCJD, GSS, or FFI). The classification is somewhat outdated as it predates molecular genetic diagnosis and is based on molecular and neuropathological characteristics [87]. Thus, some mutations do not fit neatly into these three classifications and even within a mutation there can be clinicopathological variability [22,87]. Two types of mutations are known in PRNP—point mutations (mostly missense, with rare stop codons) and octapeptide repeat insertions (or rarely deletions, but these are thought to be polymorphisms and not mutations) [87]. Octapeptide repeat mutations are phenotypically heterogeneous; whereas most cause fCJD, some have been described in GSS [22]. The most common genetic prion disease (gPrD) mutations worldwide probably are E200K (causing fCJD), P102L (causing GSS), V210I (causing fCJD) and D178N (causing fCJD or FFI), and several OPRI mutations (causing fCJD and GSS), but the prevalence of mutations differs greatly by region and ethnicity [88–90].

Studies on neuroimaging aspects of gPrD in cohorts of mutation carriers are limited, and most of the evidence available is based on small series of patients or case reports. The sensitivity of MRI, particularly DWI, in gPrD varies greatly depending on the type of gPrD and the specific mutation, but is overall lower than in sCJD [12,89]. Functional neuroimaging (PET or single-photon emission computed tomography [SPECT]) may be informative in some situations, as will be discussed below.

Familial CJD

The clinical presentation of fCJD (particularly with the E200K mutation) is similar to sCJD, although age at onset may be slightly earlier (around 60 years) and the average duration of disease longer (median survival is around 4 months) [87,91]. Nevertheless, there is high variability depending on the mutation [89,92]. The term familial CJD is probably not entirely appropriate, as many cases do not necessarily have a positive family history. In fact, in a large European study of gPrD, up to 60% of patients did not have a positive family history [89]. This is, in part, because of reduced penetrance of certain mutations, such as E200K, such that not everyone with a mutation will develop disease [93,94]. In other cases, such as V180I mutation, it is not entirely known why the genetic disease is not usually familial [90]. Thus, genetic CJD (gCJD), might be a better term than fCJD [89]; for this chapter, however, we will continue to use the term fCJD to avoid confusion with past literature. The most commonly reported worldwide mutations causing fCJD probably are E200K, V210I, and D178N–129V [89,91], but there are significant regional and ethnic differences in the frequencies and types of mutations. For example, the E200K mutation was the most common in the EUROCJD study and has been described in clusters among Libyan Jews and in Slovakia, whereas in Japan the V180I mutation is the most common followed by E200K for fCJD (which in turn are rare or absent in Europe) [89,90,95].

DWI and/or FLAIR hyperintensities may be indistinguishable from the ones observed in sCJD (Fig. 22.7), although the sensitivity of MRI in fCJD might be lower. Across studies, the MRI scans of 50–100% of patients with fCJD showed cortical and/or subcortical FLAIR/DWI hyperintensities [12,89,90,96–100]. Thalamic hyperintensities may be found in 40% of cases (96), whereas cerebellar changes are absent or rare [97].

Specific to the E200K mutation, previous studies have suggested that isolated basal ganglia hyperintensities might be more common than cortical hyperintensities [96,100]. It must be noted, however, that the neuroimaging features of E200K should not automatically be extended to other mutations. Recent imaging findings seem to suggest that the sensitivity of MRI in fCJD differs depending on the mutation [89,90,97,99].

Gerstmann–Sträussler–Scheinker

GSS is an autosomal dominant progressive ataxia and/or dementia, and its defining neuropathological finding is the presence of multicentric PrP-positive amyloid plaques [101]. Onset most commonly occurs between the third and seventh decades of life, and the duration of disease is usually between 2 and 7 years (although

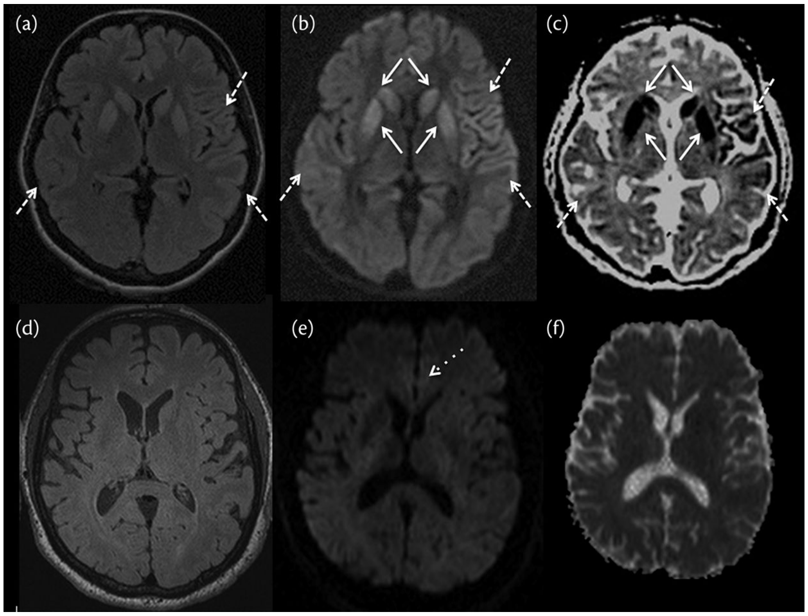

Fig. 22.7 Brain MRI in genetic prion diseases. MRI of a 48-year-old patient with the fCJD due to the PRNP D178N-129V mutation (a–c), showing bilateral hyperintensities in the striatum (solid arrow), as well as cortical ribboning in frontal and temporal regions (more prominent on the left; dashed arrows) on axial FLAIR (a) and DWI (b) sequences. The ADC map (c) showed corresponding hypointensities, in frontal and temporal regions (dashed arrows) and striatum bilaterally (solid arrows). MRI of a 49-year-old patient with a A117V mutation causing Gerstmann–Sträussler–Scheinker syndrome (GSS) (d–f) showing mild global atrophy and periventricular white matter changes, but no restricted diffusion on axial FLAIR (d), DWI (e), and ADC map (f) sequences. The cingulate cortex (dashed arrow) and insula, areas that are known to be DWI/FLAIR hyperintense in healthy normal subjects, are likely bright due to air-brain artefact [70].

longer survival, of more than one decade, has been reported) [22]. Pyramidal and/or extrapyramidal signs may also be found during the disease course. The most common mutations in PRNP are P102L, P105L, and A117V.

The literature on neuroimaging findings in GSS is scarce. Most of the available literature is based on a single mutation, P102L, and neuroimaging data on other mutations are based on case reports or small series. GSS is most commonly associated with focal cerebellar or generalized brain atrophy, particularly in later stages of disease, or a normal MRI (Fig. 22.7d–f) [102,103], but hyperintensities consistent with sCJD can also be found [104]. In a large study of European gPrD cases, Kovacs et al. found that around 30% of MRIs of GSS patients (n = 17) were consistent with sCJD [89] and Nozaki et al. reported MRI hyperintensities in 34% (14/41) patients with GSS (P102L = 14/36 cases and P105L = 0/5 cases) [90]. It was not clear in these studies, however, how many subjects had DWI, which is much more sensitive than T2-weighted sequences [13]. Our group found abnormalities in only one case out of seven GSS patients, all of whom had DWI [12]. The positive scan was of a patient with a F198S mutation; one patient with A117V and another with F198S mutation had only possible limbic hyperintensities (thus not meeting UCSF MRI criteria for CJD) and one P102L and three A117V patients had negative scans [12].

In the largest series of P102L cases published so far, Webb et al. [102] reported findings of 15 MRI scans of patients, none of which had cortical or basal ganglia hyperintensities. Generalized atrophy was observed in three patients and focal cerebellar atrophy in one. Five scans were considered normal from 1 to 3 years after the onset of symptoms. Among 11 patients with the P102L mutation, Arata et al. [103] found one with cortical hyperintensities on DWI. Brain or cerebellar atrophy was only observed in more advanced stages. White matter abnormalities also have been described in GSS patients [102,105].

Because PrP-amyloid deposition is a defining feature of GSS, there has been some interest in studying the use of PET imaging with amyloid ligands. Two small studies have shown increased binding of [18F]FDDNP, a radiotracer that binds to beta-amyloid and neurofibrillary tangles and used in AD neuroimaging, in patients with GSS (6-OPRI, P102L, and F198S mutations) and in some presymptomatic mutation carriers [106,107], but its utility in clinical practice is still a matter of further research. Pittsburgh compound B (PiB), used to identify Aβ amyloid deposition in AD, does not appear to detect PrP-amyloid in prion disease [106,108].

FFI

FFI is a rare form of gPrD that is caused by the PRNP D178N mutation when the cis (i.e. located in the same chromosome) codon 129 polymorphism is methionine (129M). When the cis codon 129 polymorphism is valine, then the disease usually presents as fCJD, with a clinical presentation similar to sCJD [109]. A sporadic form of fatal insomnia in sCJD has also been described (also referred to as the MM2-thalamic form of CJD) with similar clinical and neuropathological findings [110]. FFI clinically presents with progressive insomnia and dysautonomia; with the progression of disease, hallucinations, motor, and cognitive symptoms appear [111]. Onset is around the fifth or sixth decades of life, with a mean disease duration of 15 months [92].

Kovacs et al. reported MRI hyperintensities in 18% of cases, but it was not stated which type of hyperintensities (i.e. thalamic, striatal, cortical) was present and on what sequences. Most probably they did not acquire DWI sequences. Structural MRI most commonly shows non-specific changes, such as non-localized atrophy (particularly later in the disease course) [89]. Functional neuroimaging with fluorodeoxyglucose (FDG) PET typically reveals early and prominent thalamic hypometabolism. This reflects the neuropathological finding of focal thalamic gliosis in patients with FFI, although the hypometabolism might be more widespread than the neuronal loss [112].

Differential diagnosis of rapidly progressive dementias and radiological mimickers of CJD

Although MRI in sCJD and most fCJD has very high diagnostic specificity and sensitivity [12] and has been included amongst the European criteria for probable sCJD [17], there are other conditions that may have similar MRI findings, from basal ganglia hyperintensities (T2-weighted and/or restricted diffusion) to cortical ribboning. PrDs are often misdiagnosed because they are rare and can mimic many other clinical conditions [26,62,113]. When evaluating a patient with an RPD or suspected PrD, we find helpful to use the mnemonic VITAMINS in order to consider other possible causes of RPD:

1. ***V***ascular (e.g. strokes, vasculitis, intravascular lymphoma).
2. ***I***nfectious (e.g. HIV, Lyme, encephalitis, Whipple's, fungal, parasites).
3. ***T***oxic-metabolic (e.g. heavy metals, medications, B12, Bismuth, Wernicke's, porphyria).
4. ***A***utoimmune (e.g. antibody-mediated, Hashimoto's encephalitis).
5. ***M***etastases/neoplastic (e.g. primary central nervous system lymphoma (PCNSL), gliomatosis cerebri, paraneoplastic).
6. ***I***atrogenic.
7. ***N***eurodegenerative (e.g. dementia with Lewy bodies (DLB), AD, frontotemporal dementia (FTD), corticobasal syndrome (CBS), progressive supranuclear palsy (PSP));
8. ***S***ystemic/seizures/structural (e.g. Sarcoid, Beçhet's, non-convulsive status epilepticus (NCSE), masses).

The most frequent CJD neuroimaging mimickers probably are seizures, metabolic, autoimmune (antibody-mediated paraneoplastic and non-paraneoplastic) encephalopathies, infection, and possibly stroke. Importantly, many treatable conditions, including infections, vasculitis, toxic-metabolic and lymphoma, might mimic CJD both clinically and radiologically [114]. In the section 'Deep nuclei involvement', we will discuss some CJD radiological mimickers, based on pattern of involvement, including cortical ribboning, deep nuclei hyperintensity, and both. Aetiologies for CJD MRI mimickers representing each pattern of involvement are discussed in the next section in order of the 'VITAMINS' mnemonic.

Deep nuclei involvement

Vascular

Many strokes can lead to hyperintensity of deep nuclei, which can be associated with restricted diffusion. Embolic stroke can present with focal cortical areas of restricted diffusion; this can be included among CJD mimickers in that single stroke dementia, particularly involving the angular gyrus in the parietal lobe , has been described in literature [115]. These true diffusion restriction scenarios due to vascular involvement can often be readily differentiated from CJD due to the concurrent cortical swelling and subcortical involvement that occurs during cytotoxic oedema that appears as a hyperintense signal on FLAIR sequences. Moreover on contrast enhanced T1 weighted sequence, vascular engorgement with pial contrast enhancement is identified in acute phase of stroke whereas in the subacute phase blood–brain barrier breakdown with parenchimal cortical-subcortical enhancement. Also the cortical involvement, such as hippocampal hyperintensity, might show diffuse hyperintensity and not just hyperintensity of the cortical ribboning of CJD. Strokes might also lead to oedema or adjacent white matter involvement which should not be seen in CJD [12]. Deep venous thrombosis and Percheron artery occlusion can cause bilateral thalamic diffusion restriction, often sparing the striatum [116]. A case was reported of clinically diagnosed sCJD, with DWI positive medial thalamic and periaqueductal gray involvement, consistent with PrD [48,117]; brain autopsy, however, showed multiple infarcts and hypoxia, and no evidence of prion disease [118].

Infection

Bartonella infection, particularly *B. henselae*, the cause of cat-scratch disease, can cause encephalopathy and encephalitis. This condition has been reported to cause thalamic hyperintensity, particularly on FLAIR and DWI sequences, including pulvinar hyperintensity [119], which can look identical to pulvinar sign of vCJD [79,80,120]. Murray Valley encephalitis virus, an endemic arbovirus in Australia, a flavirus antigenically-related to Japanese encephalitis virus and West Nile virus, causes an encephalitis that often involves thalamus and basal ganglia particularly on T_2/FLAIR sequences [121]. Cerebral peduncles and other regions are also involved, and oedema, which argues against PrD. Some patients with AIDS due to HIV infection who present acutely, often with seizures, might show bilateral T_2 basal ganglia hyperintensity, but this is often with mass effect and involvement of adjacent white matter, thalamus and brainstem [122]. Many infections that often are accompanied by seizures can have deep nuclei involvement on MRI. Some of these are discussed under 'Systemic/seizures/sarcoid'.

Toxic-metabolic

Acute hyperammonemic encephalopathy occurs from neurotoxicity due to consistent and prolonged elevated blood ammonia levels. MRI usually shows diffuse leukoencephalopathy. Cases with severe onset and progression, however, have shown diffuse cortical, thalamic and/or striatal abnormalities on DWI sequences [123,124], but may differ somewhat from sCJD. Hyperammonemic encephalopathy might be very symmetric in the deep nuclei (although this can occur in hPrDs), but often with greater involvement of the thalamus, rather than striatum, although this can mimic vCJD. Hyperammonemic encephalopathy also often shows diffuse subcortical white matter T2-hyperintensities [123,124].

Osmotic extrapontine myelinosis from rapid sodium shifts or corrections of hyponatraemia can cause symmetric striatal T_2/FLAIR and DWI hyperintensity, often with reduced diffusion [125–127]. These abnormalities can persist for weeks, but in our experience they eventually resolve, particularly with restricted diffusion, unlike in PrD in which the abnormalities usually progress to involve other brain regions.

Severe hypoglycaemic encephalopathy, which often shows extensive cortical diffusion restriction, has a worse prognosis when there is subcortical involvement, particularly in the striatum and internal capsule [128]. Carbon monoxide poisoning typically causes symmetric T2/FLAIR hyperintensities in the basal ganglia, but this is

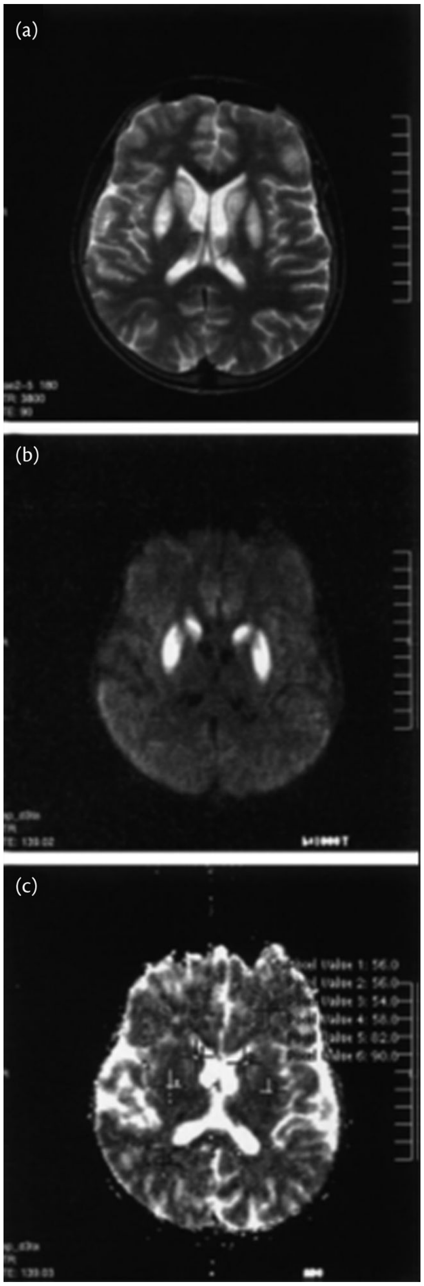

Fig. 22.8 Cytotoxic oedema-like pattern in Wilson's disease in an 11-year-old girl. (a) The T_2-weighted image reveals bilateral high signal in the putamina and in the heads of the caudate nuclei. (b) Heavily diffusion-weighted image reveals high signal changes similar to cytotoxic oedema. (c) ADC map. Low signal, and low ADC values: 0.56, 0.56, 0.54, 0.58 × 10^{-3} mm^2/s are noted in the corresponding regions, compared with normal ADC values from the unaffected regions of the parenchyma.

Reproduced from Sener RN. (2008). Diffusion MRI findings in Wilson's disease. *Computerized Medical Imaging and Graphics*, **27**(1), 17–21. Copyright (2003), with permission from Elsevier.

usually in the globus pallidum and not in the striatum as seen in CJD [116].

Wernicke's encephalopathy is caused by neural death due to exhaustion of B-vitamin reserves, in particular thiamine, or by its difficulties in accessing the mitochondria. Wernicke's encephalopathy can show symmetric DWI hyperintensity in the deep GM nuclei, mainly the posteromesial thalamic nuclei, thus resembling the hockey-stick sign. Other cases have shown bilateral caudate head involvement, but this type of deficiency encephalopathy often also affects mammillary bodies and periaqueductal GM [129].

In Wilson's disease, an autosomal recessive genetic disorder in which copper accumulates in the tissues, brain MRI in early phases of brain involvement can show striatal diffusion restriction (Fig. 22.8) [130]. This pattern of striatal hyperintensity, however, differs from most PrD cases, which usually have an anterior to posterior gradient of decreasing hyperintensity [12].

Several disorders of inborn errors of metabolism, such as ethylmalonic encephalopathy, which usually presents in children, show T2/FLAIR hyperintensities in the striatum [131].

Autoimmune and paraneoplastic encephalopathies

Although the more common MRI abnormality in limbic encephalopathies involves medial temporal lobe cortical hyperintensities, striatal hyperintensity can be seen in some antibody-mediated dementias [132–134]. The paraneoplastic condition associated with anti-CV2 (i.e. anti-CRMP5) antibodies often shows bilateral, symmetric striatal, hippocampal or insula T2/FLAIR hyperintensity (Fig. 22.9) [132]. The striatal involvement on T2/FLAIR, might mimic CJD, but unlike CJD, in anti-CV2 these hyperintensities are usually not diffusion-restricted.

Metastases/neoplasm

Neoplasms, particularly PCNSL can involve the deep nuclei, with T2/FLAIR, as well as DWI hyperintensities. The MRI abnormalities can be asymmetric or sometimes very symmetric, involving striatum [135,136]. Other abnormalities, such as associated oedema, white matter involvement, and contrast enhancement, however, should argue against CJD [12].

Neurodegenerative

Neurofilament inclusion body disease (NIBD), a relatively recently described clinicopathological entity that often presents either as a FTD or CBS, has been reported to have bilateral striatal FLAIR hyperintensity. Structural and functional imaging typically shows frontal and temporal as well as striatal involvement [137].

Seizures

Although seizures, particularly status epilepticus, typically cause cortical ribboning (see below), deep nuclei hyperintensities with restricted diffusion can occur as well, including in the caudate, thalamus, and pulvinar [138–140].

Cortical ribboning

True diffusion restriction resembling cortical ribboning seen in CJD occurs most commonly in three non-prion conditions—acute encephalitis, focal epileptic status, and embolic stroke. These and other conditions are discussed below. It is important, however, not to misinterpret MRI artefacts as restricted diffusion. For example, in one paper, some cases reported to mimic CJD on DWI MRI appeared to the authors of this chapter to be artefacts, and most were not consistent with CJD based on our UCSF CJD MRI criteria (Fig. 22.10).

Vascular

A pattern of diffuse cortical with or without striatal diffusion restriction pattern is described in severe hypoxic encephalopathy (i.e. patients with brain death or in vegetative state) with cortical

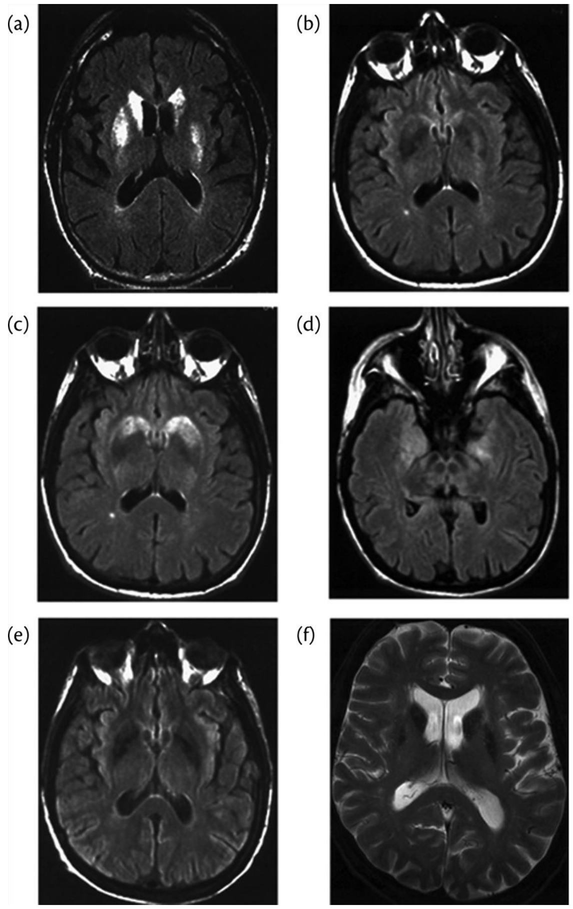

Fig. 22.9 Magnetic resonance imaging (MRI) findings in patients with paraneoplastic chorea (due to anti-CRMP5, also called CV2, antibodies). (a) In Patient 1, 1 week after the onset of hemichorea, fluid-attenuated inverse recovery (FLAIR) revealed asymmetric signal hyperintensity in the caudate and putamen. (b) In Patient 2, cranial MRI performed to evaluate forgetfulness (4 months before the onset of chorea) was normal except for minimal FLAIR hyperintensity of the caudate head and left putamen. (c,d) In Patient 2, 1 month after the onset of chorea, cranial MRI showed marked FLAIR hyperintensity in the caudate head and anterior putamen bilaterally, as well as in the mesial temporal lobes. Chorea improved dramatically after chemotherapy for small-cell lung carcinoma. (e) In Patient 2, clinical improvement was accompanied by the resolution of FLAIR signal abnormalities in the basal ganglia. (f) In Patient 3, cranial MRI nine months after the onset of chorea was unremarkable except for low T_2 signals in the caudate and putamen.

Reproduced from Vernino S, Tuite P, Adler CH, et al. (2002). Paraneoplastic chorea associated with CRMP-5 neuronal antibody and lung carcinoma. *Annals of Neurology*, **51**(5), 625–30. Copyright (2002), with permission from John Wiley & Sons Ltd.

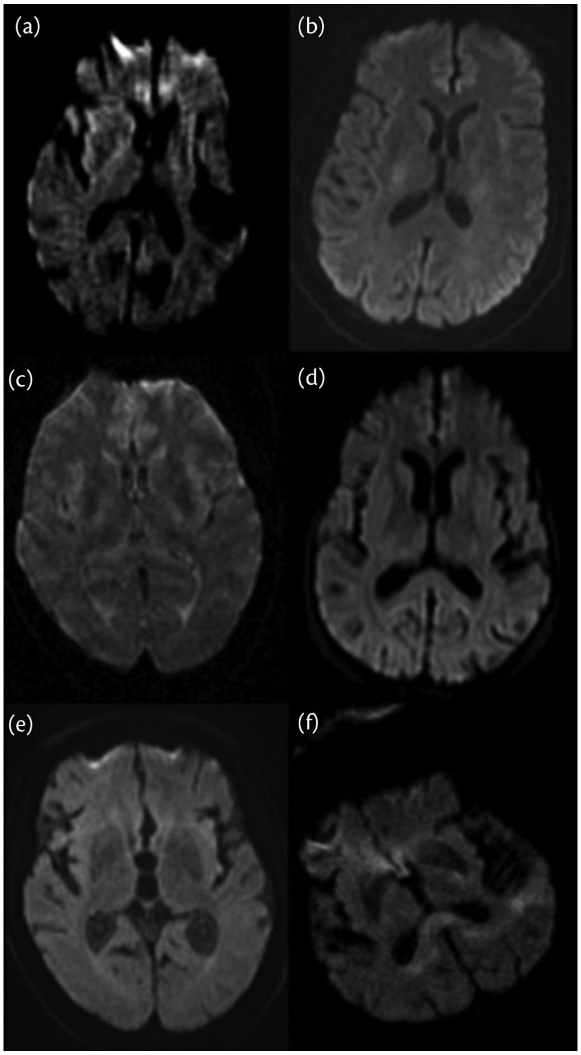

Fig. 22.10 MRIs in non-CJD cases read as consistent with CJD in the literature. Diffusion-weighted images of patients presenting with suspected CJD including urosepsis (a), neurosarcoid (b), left temporal lobe epilepsy (c), alcohol intoxication (d), CNS vasculitis (e), and non-Hodgkin's lymphoma (f). Figure with permission from [114]. It is not clear, however, from our reading of these images, that most of them should have been read as consistent with CJD, with the exception of possibly (b) and (d). Even in these cases, however, the ADC sequence might have been helpful distinguishing true abnormality from artefact [12]. The authors of this chapter would have not read the other DWI sequences as consistent with CJD.

Reproduced from Newey CR, Sarwal A, Wisco D, et al. (2013). Variability in diagnosing Creutzfeldt–Jakob disease using standard and proposed diagnostic criteria. *Journal of Neuroimaging*, **23**(1), 58–63. Copyright (2013), with permission from John Wiley & Sons Ltd.

laminar necrosis [123]. CNS vasculitis might rarely show cortical ribboning, with a clinical picture mimicking CJD (Fig. 22.10) [114].

Infection

Rasmussen's, herpes simplex type 1 encephalitis, and meningoencephalitis secondary to Neisseria meningitis all have been shown to cause cortical ribboning on T2-weighted and DWI. It is not clear what component of this might be due to, or independent of seizure activity [141]. Herpes simplex encephalitis (HSE), the most common viral encephalitis, usually presents with predominant temporomesial involvement [142,143]. Similarly, human herpes virus 6 (HHV6) encephalitis also shows the same pattern of hippocampal and extrahippocampal involvement with DWI abnormalities in temporomesial areas [144,145] rarely sparing these structures [146]. Although quantitative studies in HSE demonstrated that diffusion restriction does occur in early phases, DWI hyperintensity is mostly due to T2 shine-through and vasogenic oedema [147]. Other viral encephalopathies, often affecting children, namely subacute sclerosing panencephalitis (SSPE) [148] and enterovirus 71, a cause of hand, foot, and mouth disease [149], influenza virus encephalitis [150], or other encephalitis with unknown aetiology (151,152] can present with extensive cortical involvement and positive diffusion restriction abnormalities. Bacterial encephalitis and neurosyphilis can show temporomesial or tempolateral cortical ribboning [153]. Most of these infections, however, either have GM hyperintensities that are not restricted to the cortical ribbon and involve adjacent white matter or have isolated medial temporal lobe involvement; neither of these findings are common in PrD [12,13,48].

Toxic-metabolic

Cortical ribboning, involving diffusively the neocortex and insula has been reported in acute hepatic encephalopathy, associated with hyperammonemia. Abnormalities appear on both FLAIR and DWI sequences. These changes, however, are often reversible with treatment of the underlying metabolic disturbance [124,154]. In addition to deep nuclei T2, FLAIR, and DWI hyperintensities, severe hypoglycaemic encephalopathy can also present with extended cortical diffusion restriction [128].

Autoimmune paraneoplastic and non-paraneoplastic

Patients with voltage-gated potassium channel complex (VGKCC) associated autoimmune encephalopathy can not only mimic CJD clinically, but also might have cortical ribboning [155]. Most patients with VGKCC and related antibody-mediated encephalopathies show normal MRI, medial temporal lobe hyperintensity or sometimes white matter disease. Cortical ribboning is rare and to our knowledge, when it occurs, it does not usually show restricted diffusion [155]. Predominance of T2 or FLAIR hyperintensity in limbic areas, mainly temporomesial structures, is the hallmark sign of limbic encephalopathies; isolated limbic involvement is probably very uncommon in hPrD [12]. It is crucial to recognize autoimmune and paraneoplastic encephalopathies early in the course of the diseases, because these pathologies can be effectively treated in their early stages [26]. Cortical ribboning has been reported in neurosarcoid [114], although the images might not have been very convincing and simply due to artefacts (Fig. 22.10).

Systemic/seizures/sarcoid

One of the most common non-CJD causes of cortical ribboning, and conditions that might clinically mimic CJD, are seizures, particularly status epilepticus, either convulsive or non-convulsive [139,140,156]. Focal epileptic status, which can occur in autoimmune encephalopathy, infections and other conditions, might show hippocampal and pulvinar diffusion restriction [138–140], but can often involve neocortical structures mimicking cortical ribboning [139,157]. Even single seizures can results in reduced cortical diffusion [158]. Even NCSE can cause diffuse cortical ribboning, reminiscent of CJD [156]. Once the seizures are controlled, however, the DWI cortical ribboning and diffusion abnormalities (in the deep nuclei as well) should resolve usually in a matter of days [139,140], unlike in PrD in which these abnormalities might be present until significant atrophy occurs.

Conclusion

Human prion diseases are relatively unique among not only neurodegenerative diseases, but most neurological conditions, in that they have virtually pathognomonic MRI findings. Neuroimaging has had a crucial leading role, both in the redefinition of diagnostic criteria for sCJD and in the differential diagnosis between the various types and subtypes of prion diseases and other neurological syndromes. DWI and FLAIR, in particular, have been found to be essential sequences, with the greatest sensitivity and specificity among all the diagnostic tools available at this time. However, CJD and other hPrDs cannot only clinically mimic many other conditions, but other conditions sometimes present with similar MRI findings. It is vital to be able to differentiate these conditions from PrD, as many MRI mimickers are treatable, if not reversible [113,159].

References

1. Prusiner SB. (1998). Prions. *Proceedings of the National Academy of Sciences, USA*, **95**(23), 13363–83.
2. Kretzschmar HA, Ironside JW, DeArmond SJ, et al. (1996). Diagnostic criteria for sporadic Creutzfeldt–Jakob disease. *Archives of Neurology*, **53**(9), 913–20.
3. Brown P, Brandel JP, Preece M, et al. (2006). Iatrogenic Creutzfeldt–Jakob disease: the waning of an era. *Neurology*, **67**(3), 389–93.
4. Will RG. (2003). Acquired prion disease: iatrogenic CJD, variant CJD, kuru. *British Medical Bulletin*, **66**, 255–65.
5. Kovanen J, Erkinjuntti T, Iivanainen M, et al. (1985). Cerebral MR and CT imaging in Creutzfeldt–Jakob disease. *Journal of Computer Assisted Tomography*, **9**(1), 125–8.
6. Gertz HJ, Henkes H, and Cervos-Navarro J. (1988). Creutzfeldt–Jakob disease: correlation of MRI and neuropathologic findings. *Neurology*, **38**(9), 1481–2.
7. Saito T, Isozumi K, Komatsumoto S, et al. (2000). [A case of codon 232 mutation-induced Creutzfeldt–Jakob disease visualized by the MRI-FLAIR images with atypical clinical symptoms]. *Rinsho Shinkeigaku*, **40**(1), 51–4.
8. Demaerel P, Heiner L, Robberecht W, et al. (1999). Diffusion-weighted MRI in sporadic Creutzfeldt–Jakob disease. *Neurology*, **52**(1), 205–8.
9. Nagaoka U, Kurita K, Hosoya T, et al. (1999). [Diffusion images on brain MRI in Creutzfeldt–Jakob disease]. *Rinsho Shinkeigaku*, **39**(4), 468–70.
10. Lewis AM, Yu M, DeArmond SJ, et al. (2006). Human growth hormone-related iatrogenic Creutzfeldt–Jakob disease with abnormal imaging. *Archives of Neurology*, **63**(2), 288–90.
11. Vitali P, Migliaccio R, Agosta F, et al. (2008). Neuroimaging in dementia. *Seminars in Neurology*, **28**(4), 467–83.
12. Vitali P, Maccagnano E, Caverzasi E, et al. (2011). Diffusion-weighted MRI hyperintensity patterns differentiate CJD from other rapid dementias. *Neurology*, **76**(20), 1711–19.
13. Shiga Y, Miyazawa K, Sato S, et al. (2004). Diffusion-weighted MRI abnormalities as an early diagnostic marker for Creutzfeldt–Jakob disease. *Neurology*, **163**, 443–9.
14. Young GS, Geschwind MD, Fischbein NJ, et al. (2005). Diffusion-weighted and fluid-attenuated inversion recovery imaging in Creutzfeldt–Jakob disease: high sensitivity and specificity for diagnosis. *AJNR American Journal of Neuroradiology*, **26**(6), 1551–62.
15. Sanchez-Juan P, Green A, Ladogana A, et al. (2006). CSF tests in the differential diagnosis of Creutzfeldt–Jakob disease. *Neurology*, **67**(4), 637–43.
16. Collins SJ, Sanchez-Juan P, Masters CL, et al. (2006). Determinants of diagnostic investigation sensitivities across the clinical spectrum of sporadic Creutzfeldt–Jakob disease. *Brain*, **129**(Pt 9), 2278–87.
17. Zerr I, Kallenberg K, Summers DM, et al. (2009). Updated clinical diagnostic criteria for sporadic Creutzfeldt–Jakob disease. *Brain*, **132**(Pt 10), 2659–68.
18. Geschiwnd MD, Kuryan C, Cattaruzza T, et al. (2010). Brain MRI in sporadic Jakob–Creutzfeldt disease Is often misread. *Neurology*, **78**(Suppl. 1), P03.018.
19. Carswell C, Thompson A, Lukic A, et al. (2012). MRI findings are often missed in the diagnosis of Creutzfeldt–Jakob disease. *BMC Neurology*, **12**(1), 153.
20. Rabinovici GD, Wang PN, Levin J, et al. (2006). First symptom in sporadic Creutzfeldt–Jakob disease. *Neurology*, **66**(2), 286–7.
21. Brown P, Cathala F, Castaigne P, et al. (1986). Creutzfeldt–Jakob disease: clinical analysis of a consecutive series of 230 neuropathologically verified cases. *Annals of Neurology*, **20**(5), 597–602.

22. Brown K, and Mastrianni JA. (2010). The prion diseases. *Journal of Geriatric Psychiatry and Neurology*, **23**(4), 277–98.
23. Parchi P, Giese A, Capellari S, et al. (1999). Classification of sporadic Creutzfeldt–Jakob disease based on molecular and phenotypic analysis of 300 subjects. *Annals of Neurology*, **46**(2), 224–33.
24. Mandell AM, Alexander MP, and Carpenter S. (1989). Creutzfeld–Jakob disease presenting as isolated aphasia. *Neurology*, **39**(1), 55–8.
25. Johnson DY, Dunkelberger DL, Henry M, et al. (2013). Sporadic Jakob-Creutzfeldt disease presenting as primary progressive aphasia. [Case Reports Research Support, N.I.H., Extramural]. *Journal of the American Medical Association: Neurology*, **70**(2), 254–7.
26. Paterson RW, Takada LT, Geschwind MD. (2012). Diagnosis and treatment of rapidly progressive dementias. *Neurology: Clinical Practice*, **2**(3), 187–200.
27. Rinne ML, McGinnis SM, Samuels MA, et al. (2012). A startling decline. *New England Journal of Medicine*, **366**(9), 836–42.
28. Vingerhoets FJ, Hegyi I, Aguzzi A, et al. (1998). An unusual case of Creutzfeldt–Jakob disease. [Case Reports Research Support, Non-U.S. Gov't]. *Neurology*, **51**(2), 617–19.
29. Iida T, Doh-ura K, Kawashima T, et al. (2001). An atypical case of sporadic Creutzfeldt–Jakob disease with Parkinson's disease. [Case Reports]. *Neuropathology*, **21**(4), 294–7.
30. Shimamura M, Uyama E, Hirano T, et al. (2003). A unique case of sporadic Creutzfeldt-Jacob disease presenting as progressive supranuclear palsy. *Internal Medicine*, **42**(2), 195–8.
31. Meissner B, Westner IM, Kallenberg K, et al. (2005). Sporadic Creutzfeldt–Jakob disease: clinical and diagnostic characteristics of the rare VV1 type. *Neurology*, **65**(10), 1544–50.
32. Polymenidou M, Stoeck K, Glatzel M, et al. (2005). Coexistence of multiple PrPSc types in individuals with Creutzfeldt–Jakob disease. *Lancet Neurology*, **4**(12), 805–14.
33. Parchi P, Strammiello R, Notari S, et al. (2009). Incidence and spectrum of sporadic Creutzfeldt–Jakob disease variants with mixed phenotype and co-occurrence of PrPSc types: an updated classification. *Acta Neuropathologica*, **118**(5), 659–71.
34. Puoti G, Bizzi A, Forloni G, et al. (2012). Sporadic human prion diseases: molecular insights and diagnosis. [Research Support, N.I.H., Extramural Research Support, Non-U.S. Gov't Research Support, U.S. Gov't, P.H.S. Review]. *Lancet Neurology*, **11**(7), 618–28.
35. WHO. (1998). Global surveillance, diagnosis and therapy of human transmissible spongiform encephalopathies: report of a WHO consultation Geneva, Switzerland 9–11 February 1998. Geneva, Switzerland: World Health Organization. Report No.
36. Sanchez-Juan P, Sanchez-Valle R, Green A, et al. (2007). Influence of timing on CSF tests value for Creutzfeldt–Jakob disease diagnosis. *Journal of Neurology*, **254**(7), 901–6.
37. Steinhoff BJ, Zerr I, Glatting M, et al. (2004). Diagnostic value of periodic complexes in Creutzfeldt–Jakob disease. *Annals of Neurology*, **56**(5), 702–8.
38. Hamlin C, Puoti G, Berri S, et al. (2012). A comparison of tau and 14-3-3 protein in the diagnosis of Creutzfeldt–Jakob disease. *Neurology*, **79**(6), 547–52.
39. Coulthart MB, Jansen GH, Olsen E, et al. (2011). Diagnostic accuracy of cerebrospinal fluid protein markers for sporadic Creutzfeldt–Jakob disease in Canada: a 6-year prospective study. *BMC Neurology*, **11**, 133.
40. Geschwind MD, Martindale J, Miller D, et al. (2003). Challenging the clinical utility of the 14-3-3 protein for the diagnosis of sporadic Creutzfeldt–Jakob disease. *Archives of Neurology*, **60**(6), 813–16.
41. Chapman T, McKeel DW, Jr, Morris JC. (2000). Misleading results with the 14-3-3 assay for the diagnosis of Creutzfeldt–Jakob disease. *Neurology*, **55**(9), 1396–7.
42. Castellani RJ, Colucci M, Xie Z, et al. (2004). Sensitivity of 14-3-3 protein test varies in subtypes of sporadic Creutzfeldt–Jakob disease. *Neurology*, **63**(3), 436–42.
43. Forner SA, Wong KS, Bostrom A, et al. (2012). CSF biomarkers findings in a large rapidly progressive dementia cohort. *Neurology: AAN Meeting Abstract*, **78**, S14.004.
44. Chohan G, Pennington C, Mackenzie JM, et al. (2010). The role of cerebrospinal fluid 14-3-3 and other proteins in the diagnosis of sporadic Creutzfeldt–Jakob disease in the UK: a 10-year review. *Journal of Neurology, Neurosurgery & Psychiatry*, **81**(11), 1243–8.
45. Wong K, Forner S, Haman A, et al. (2011). CSF biomarkers findings in a large rapidly progressive dementia cohort. *Neurology*, **76**(9), A551.
46. Vitali P, Haman A, Torres-Chae C, et al. (2008). Improving MRI Criteria for Jakob–Creutzfeldt Disease (CJD) by the pattern of gray matter involvement on FLAIR and DWI MRI (IN2-2.005). *Neurology*, **70**(Suppl. 1), A8.
47. Satoh K, Shirabe S, Tsujino A, et al. (2007). Total tau protein in cerebrospinal fluid and diffusion-weighted MRI as an early diagnostic marker for Creutzfeldt–Jakob disease. *Dementia and Geriatric Cognitive Disorders*, **24**(3), 207–12.
48. Tschampa HJ, Kallenberg K, Kretzschmar HA, et al. (2007). Pattern of cortical changes in sporadic Creutzfeldt–Jakob disease. *AJNR American Journal of Neuroradiology*, **28**(6), 1114–18.
49. Tschampa HJ, Zerr I, and Urbach H. (2007). Radiological assessment of Creutzfeldt–Jakob disease. *European Radiology*, **17**(5), 1200–11.
50. Galanaud D, Haik S, Linguraru MG, et al. (2010). Combined diffusion imaging and MR spectroscopy in the diagnosis of human prion diseases. *AJNR American Journal of Neuroradiology*, **31**(7), 1311–18.
51. Meissner B, Kallenberg K, Sanchez-Juan P, et al. (2008). Isolated cortical signal increase on MR imaging as a frequent lesion pattern in sporadic Creutzfeldt–Jakob disease. *AJNR American Journal of Neuroradiology*, **29**(8), 1519–24.
52. Fujita K, Nakane S, Harada M, et al. (2008). Diffusion tensor imaging in patients with Creutzfeldt–Jakob disease. [Letter Research Support, Non-U.S. Gov't]. *Journal of Neurology, Neurosurgery & Psychiatry*, **79**(11), 1304–6.
53. Ukisu R, Kushihashi T, Kitanosono T, et al. (2005). Serial diffusion-weighted MRI of Creutzfeldt–Jakob disease. *American Journal of Roentgenology*, **184**(2), 560–6.
54. Mandell DM, Mikulis DJ, Kiehl TR, et al. (2012). T2-dark restricted diffusion. [Case Reports]. *Canadian Journal of Neurological Sciences*, **39**(5), 664–6.
55. Geschwind MD, Potter CA, Sattavat M, et al. (2009). Correlating DWI MRI with pathologic and other features of Jakob-Creutzfeldt disease. *Alzheimer's Disease Associated Disorders*, **23**(1), 82–7.
56. Manners DN, Parchi P, Tonon C, et al. (2009). Pathologic correlates of diffusion MRI changes in Creutzfeldt–Jakob disease. *Neurology*, **72**(16), 1425–31.
57. Lampert PW, Gajdusek DC, and Gibbs CJ, Jr (1972). Subacute spongiform virus encephalopathies. Scrapie, kuru and Creutzfeldt–Jakob disease: a review. *American Journal of Pathology*, **68**, 626–52.
58. DeArmond SJ, Kretzschmar HA, and Prusiner SB. (2002). Prion diseases. In: Godwin Greenfield J, Graham DI, Lantos PL (eds) *Greenfield's Neuropathology*, 7th edn. London: CRC Press, 273–323.
59. Moseley ME, Cohen Y, Mintorovitch J, et al. (1990). Early detection of regional cerebral ischemia in cats: comparison of diffusion- and T2-weighted MRI and spectroscopy. *Magnetic Resonance Medicine*, **14**(2), 330–46.
60. Mourmans J, Majoie CB, Barth PG, et al. (2006). Sequential MR imaging changes in nonketotic hyperglycinemia. *AJNR American Journal of Neuroradiology*, **27**(1), 208–11.
61. Geschwind MD, Josephs KA, Parisi JE, et al. (2007). A 54-year-old man with slowness of movement and confusion. *Neurology*, **69**(19), 1881–7.
62. Paterson RW, Torres-Chae CC, Kuo AL, et al. (2012). Differential diagnosis of Jakob-Creutzfeldt disease. *Archives of Neurology*, **69**(12), 1578–82.
63. Meissner B, Kallenberg K, Sanchez-Juan P, et al. (2009). MRI lesion profiles in sporadic Creutzfeldt–Jakob disease. *Neurology*, **72**(23), 1994–2001.
64. Haik S, Brandel JP, Oppenheim C, et al. (2002). Sporadic CJD clinically mimicking variant CJD with bilateral increased signal in the pulvinar. *Neurology*, **58**(1), 148–9.

65. Martindale J, Geschwind MD, De Armond S, et al. (2003). Sporadic Creutzfeldt–Jakob disease mimicking variant Creutzfeldt–Jakob disease. *Archives of Neurology*, **60**(5), 767–70.
66. Caverzasi E, Henry RG, Vitali P, et al. (2014) Application of quantitative DTI metrics in sporadic CJD. *Neuroimage Clinic*, **4**, 426–35.67.
67. Lin YR, Young GS, Chen NK, et al. (2006). Creutzfeldt–Jakob disease involvement of Rolandic cortex: a quantitative apparent diffusion coefficient evaluation. *AJNR American Journal of Neuroradiology*, **27**(8), 1755–9.
68. Le Bihan D, Poupon C, Amadon A, et al. (2006). Artifacts and pitfalls in diffusion MRI. *Journal of Magnetic Resonance Imaging*, **24**(3), 478–88.
69. Asao C, Hirai T, Yoshimatsu S, et al. (2008). Human cerebral cortices: signal variation on diffusion-weighted MR imaging. *Neuroradiology*, **50**(3), 205–11.
70. Finkenstaedt M, Szudra A, Zerr I, et al. (1996). MR imaging of Creutzfeldt–Jakob disease. *Radiology*, **199**(3), 793–8.
71. Uchino A, Yoshinaga M, Shiokawa O, et al. (1991). Serial MR imaging in Creutzfeldt–Jakob disease. *Neuroradiology*, **33**(4), 364–7.
72. Berciano J, Berciano MT, Polo JM, et al. (1990). Creutzfeldt–Jakob disease with severe involvement of cerebral white matter and cerebellum. *Virchows Archive A: Pathological Anatomy and Histopathology*, **417**(6), 533–8.
73. Kruger H, Meesmann C, Rohrbach E, et al. (1990). Panencephalopathic type of Creutzfeldt–Jakob disease with primary extensive involvement of white matter. *European Neurology*, **30**(2), 115–19.
74. Matsusue E, Kinoshita T, Sugihara S, et al. (2004). White matter lesions in panencephalopathic type of Creutzfeldt–Jakob disease: MR imaging and pathologic correlations. *AJNR American Journal of Neuroradiology*, **25**(6), 910–18.
75. Jansen C, Head MW, Rozemuller AJ, et al. (2009). Panencephalopathic Creutzfeldt–Jakob disease in the Netherlands and the UK: clinical and pathological characteristics of nine patients. *Neuropathology and Applied Neurobiology*, **35**(3), 272–82.
76. Caverzasi E, Mandelli ML, DeArmond SJ, et al. (2014). White matter involvement in sporadic Creutzfeldt–Jakob disease. *Brain*, **137**(Pt 12), 3339–54.
77. UK National CJD Surveillance Unit. (2012, December 2012). Variant Creutzfeldt–Jakob disease worldwide current data (December 2012). Available at: http://www.cjd.ed.ac.uk/documents/worldfigs.pdf (accessed April 15, 2013).
78. Heath CA, Cooper SA, Murray K, et al. (2011). Diagnosing variant Creutzfeldt–Jakob disease: a retrospective analysis of the first 150 cases in the UK. *Journal of Neurology, Neurosurgery & Psychiatry*, **82**(6), 646–51.
79. Zeidler M, Sellar RJ, Collie DA, et al. (2000). The pulvinar sign on magnetic resonance imaging in variant Creutzfeldt- Jakob disease. *Lancet*, **355**(9213), 1412–18.
80. Collie DA, Summers DM, Sellar RJ, et al. (2003). Diagnosing variant Creutzfeldt–Jakob disease with the pulvinar sign: MR imaging findings in 86 neuropathologically confirmed cases. *AJNR American Journal of Neuroradiology*, **24**(8), 1560–9.
81. Linguraru MG, Ayache N, Gonzalez Ballester MA, et al. (2005). New ratios for the detection and classification of CJD in multisequence MRI of the brain. *Med Image Comput Comput Assist Interv Int Conf Med Image Comput Comput Assist Interv*, **8**(Pt 2), 492–9.
82. Duffy P, Wolf J, Collins G, et al. (1974). Letter: possible person-to-person transmission of Creutzfeldt–Jakob disease. *New England Journal of Medicine*, **290**(12), 692–3.
83. Brown P, Preece M, Brandel JP, et al. (2000). Iatrogenic Creutzfeldt–Jakob disease at the millennium. *Neurology*, **55**(8), 1075–81.
84. Meissner B, Kallenberg K, Sanchez-Juan P, et al. (2009). MRI and clinical syndrome in dura mater related Creutzfeldt–Jakob disease. *Journal of Neurology*, **256**(3), 355–63.
85. Colby DW, and Prusiner SB. (2011). Prions. *Cold Spring Harbor Perspectives in Biology*, **3**(1), a006833.
86. Kong Q, Surewicz WK, Petersen RB, et al. (2004). Inherited prion diseases. In: Prusiner SB (ed.), *Prion Biology and Diseases*, 2nd edn. Cold Spring Harbor: Cold Spring Harbor Laboratory Press, pp. 673–775.
87. Mead S. (2006). Prion disease genetics. *European Journal of Human Genetics*, **14**(3), 273–81.
88. Kong Q, Surewicz WK, Petersen RB, et al. (2004). Inherited prion diseases. In: Prusiner SB (ed.), Prion Biology and Diseases, 2nd edn. Cold Spring Harbor: Cold Spring Harbor Laboratory Press, pp. 673–776.
89. Kovacs GG, Puopolo M, Ladogana A, et al. (2005). Genetic prion disease: the EUROCJD experience. *Human Genetics*, **118**(2), 166–74.
90. Nozaki I, Hamaguchi T, Sanjo N, et al. (2010). Prospective 10-year surveillance of human prion diseases in Japan. [Research Support, Non-U.S. Gov't]. *Brain*, **133**(10), 3043–57
91. Johnson RT. (2005). Prion diseases. [Review]. *Lancet Neurology*, **4**(10), 635–42.
92. Pocchiari M, Puopolo M, Croes EA, et al. (2004). Predictors of survival in sporadic Creutzfeldt–Jakob disease and other human transmissible spongiform encephalopathies. *Brain*, **127**(10), 2348–59.
93. Mitrova E, and Belay G. (2002). Creutzfeldt–Jakob disease with E200K mutation in Slovakia: characterization and development. *Acta Virologica*, **46**(1), 31–9.
94. Chapman J, Ben-Israel J, Goldhammer Y, et al. (1994). The risk of developing Creutzfeldt–Jakob disease in subjects with the PRNP gene codon 200 point mutation. *Neurology*, **44**(9), 1683–6.
95. Lee HS, Sambuughin N, Cervenakova L, et al. (1999). Ancestral origins and worldwide distribution of the PRNP 200K mutation causing familial Creutzfeldt–Jakob disease. *American Journal of Human Genetics*, **64**(4), 1063–70.
96. Fulbright RK, Hoffmann C, Lee H, et al. (2008). MR imaging of familial Creutzfeldt–Jakob disease: a blinded and controlled study. *AJNR American Journal of Neuroradiology*, **29**(9), 1638–43.
97. Breithaupt M, Romero C, Kallenberg K, et al. (2013). Magnetic resonance imaging in E200K and V210I mutations of the prion protein gene. [Research Support, Non-U.S. Gov't]. *Alzheimer's Disease and Associated Disorders*, **27**(1), 87–90
98. Begue C, Martinetto H, Schultz M, et al. (2011). Creutzfeldt–Jakob disease surveillance in Argentina, 1997–2008. [Research Support, Non-U.S. Gov't]. *Neuroepidemiology*, **37**(3–4), 193–202.
99. Schelzke G, Kretzschmar HA, and Zerr I. (2012). Clinical aspects of common genetic Creutzfeldt–Jakob disease. [Comparative Study Letter]. *European Journal of Epidemiology*, **27**(2), 147–9.
100. Appel SA, Chapman J, Prohovnik I, et al. (2012). The EEG in E200K familial CJD: relation to MRI patterns. *Journal of Neurology*, **259**(3), 491–6.
101. Budka H. (2003). Neuropathology of prion diseases. *British Medical Bulletin*, **66**, 121–30.
102. Webb TE, Poulter M, Beck J, et al. (2008). Phenotypic heterogeneity and genetic modification of P102L inherited prion disease in an international series. *Brain*, **131**(Pt 10), 2632–46.
103. Arata H, Takashima H, Hirano R, et al. (2006). Early clinical signs and imaging findings in Gerstmann-Straussler-Scheinker syndrome (Pro102Leu). *Neurology*, **66**(11), 1672–8.
104. Irisawa M, Amanuma M, Kozawa E, et al. (2007). A case of Gerstmann–Straussler–Scheinker syndrome. *Magnetic Resonance Medical Science*, **6**(1), 53–7.
105. Karmon Y, Kurzweil A, Lindzen E, et al. (2011). Gerstmann-Straussler-Scheinker syndrome masquerading as multiple sclerosis. [Case Reports Research Support, Non-U.S. Gov't]. *J Neurological Science*, **309**(1–2), 55–7.
106. Boxer AL, Rabinovici GD, Kepe V, et al. (2007). Amyloid imaging in distinguishing atypical prion disease from Alzheimer disease. *Neurology*, **69**(3), 283–90.
107. Kepe V, Ghetti B, Farlow MR, et al. (2010). PET of brain prion protein amyloid in Gerstmann–Straussler–Scheinker disease. *Brain Pathology*, **20**(2), 419–30.
108. Hyare H, Ramlackhansingh A, Gelosa G, et al. (2012). 11C-PiB PET does not detect PrP-amyloid in prion disease patients including variant Creutzfeldt–Jakob disease. [Comment Letter Research Support, Non-U.S. Gov't]. *Journal of Neurology, Neurosurgery, and Psychiatry*, **83**(3), 340–1.

109. Goldfarb LG, Petersen RB, Tabaton M, et al. (1992). Fatal familial insomnia and familial Creutzfeldt–Jakob disease: disease phenotype determined by a DNA polymorphism. *Science*, **258**(5083), 806–8.
110. Parchi P, Capellari S, Chin S, et al. (1999). A subtype of sporadic prion disease mimicking fatal familial insomnia. *Neurology*, **52**(9), 1757–63.
111. Mastrianni JA. (2010). The genetics of prion diseases. *Genet Medicine*, **12**(4), 187–95.
112. Montagna P, Gambetti P, Cortelli P, et al. (2003). Familial and sporadic fatal insomnia. [Research Support, Non-U.S. Gov't Review]. *Lancet Neurology*, **2**(3), 167–76.
113. Chitravas N, Jung RS, Kofskey DM, et al. (2011). Treatable neurological disorders misdiagnosed as Creutzfeldt–Jakob disease. *Annals of Neurology*, **70**(3), 437–44.
114. Newey CR, Sarwal A, Wisco D, et al. (2013). Variability in diagnosing Creutzfeldt–Jakob disease using standard and proposed diagnostic criteria. *Journal of Neuroimaging: Journal of the American Society of Neuroimaging*, **23**(1), 58–63
115. Auchus AP, Chen CP, Sodagar SN, et al. (2002). Single stroke dementia: insights from 12 cases in Singapore. *Journal of Neurological Sciences*, 203–204, 85–9.
116. Lim CC. (2009). Magnetic resonance imaging findings in bilateral basal ganglia lesions. *Annals of the Academy of Medicine, Singapore*, **38**(9), 795–8.
117. Zerr I, Bodemer M, Racker S, et al. (1995). Cerebrospinal fluid concentration of neuron-specific enolase in diagnosis of Creutzfeldt–Jakob disease. *Lancet*, **345**(8965), 1609–10.
118. Mittelbronn M, Capper D, Bader B, et al. (2008). Severe hypoxia and multiple infarctions resembling Creutzfeldt–Jakob disease. *Folia Neuropathologica*, **46**(2), 149–53.
119. Singhal AB, Newstein MC, Budzik R, et al. (2003). Diffusion-weighted magnetic resonance imaging abnormalities in Bartonella encephalopathy. *Journal of Neuroimaging: Journal of the American Society of Neuroimaging*, **13**(1), 79–82.
120. Zeidler M, Collie DA, Macleod MA, et al. (2001). FLAIR MRI in sporadic Creutzfeldt–Jakob disease. *Neurology*, **56**(2), 282.
121. Speers DJ, Flexman J, Blyth CC, et al. (2013). Clinical and radiological predictors of outcome for Murray Valley encephalitis. *American Journal of Tropical Medicine and Hygiene*, **88**(3), 481–9.
122. Meltzer CC, Wells SW, Becher MW, et al. (1998). AIDS-related MR hyperintensity of the basal ganglia. *AJNR American Journal of Neuroradiology*, **19**(1), 83–9.
123. McKinney AM, Teksam M, Felice R, et al. (2004). Diffusion-weighted imaging in the setting of diffuse cortical laminar necrosis and hypoxic-ischemic encephalopathy. *AJNR American Journal of Neuroradiology*, **25**(10), 1659–65.
124. Capizzano AA, Sanchez A, Moritani T, et al. (2012). Hyperammonemic encephalopathy: time course of MRI diffusion changes. *Neurology*, **78**(8), 600–1.
125. de Souza A, Desai PK. (2012). More often striatal myelinolysis than pontine? A consecutive series of patients with osmotic demyelination syndrome. *Neurology Research*, **34**(3), 262–71.
126. Chua GC, Sitoh YY, Lim CC, Chua HC, Ng PY. (2002). MRI findings in osmotic myelinolysis. *Clinical Radiology*, **57**(9), 800–6.
127. Martin RJ. (2004). Central pontine and extrapontine myelinolysis: the osmotic demyelination syndromes. *Journal of Neurology, Neurosurgery & Psychiatry*, **75**(Suppl. 3), iii22–8.
128. Lim CC, Gan R, Chan CL, et al. (2009). Severe hypoglycemia associated with an illegal sexual enhancement product adulterated with glibenclamide: MR imaging findings. [Research Support, Non-U.S. Gov't]. *Radiology*, **250**(1), 193–201.
129. Chu K, Kang DW, Kim HJ, et al. (2002). Diffusion-weighted imaging abnormalities in wernicke encephalopathy: reversible cytotoxic edema? *Archives of Neurology*, **59**(1), 123–7.
130. Sener RN. (2003). Diffusion MRI findings in Wilson's disease. *Computerized Medical Imaging and Graphics*, **27**(1), 17–21.
131. Grosso S, Mostardini R, Farnetani MA, et al. (2002). Ethylmalonic encephalopathy: further clinical and neuroradiological characterization. [Case Reports]. *Journal of Neurology*, **249**(10), 1446–50.
132. Vernino S, Tuite P, Adler CH, et al. (2002). Paraneoplastic chorea associated with CRMP-5 neuronal antibody and lung carcinoma. *Annals of Neurology*, **51**(5), 625–30.
133. Rosenbloom MH, Smith S, Akdal G, et al. (2009). Immunologically mediated dementias. *Current Neurology and Neuroscience Reports*, **9**(5), 359–67.
134. Rosenbloom MH, and Atri A. (2011). The evaluation of rapidly progressive dementia. *Neurologist*, **17**(2), 67–74.
135. Hegde AN, Mohan S, Lath N, et al. (2011). Differential diagnosis for bilateral abnormalities of the basal ganglia and thalamus. *Radiographics*, **31**(1), 5–30.
136. Kuker W, Nagele T, Korfel A, et al. (2005). Primary central nervous system lymphomas (PCNSL): MRI features at presentation in 100 patients. *Journal of Neurooncology*, **72**(2), 169–77.
137. Josephs KA, Holton JL, Rossor MN, et al. (2003). Neurofilament inclusion body disease: a new proteinopathy? *Brain*, **126**(Pt 10), 2291–303.
138. Caraballo RH, Fortini S, Cersosimo R, et al. (2013). Rasmussen syndrome: an Argentinean experience in 32 patients. *Seizure: Journal of the British Epilepsy Association*, **22**(5), 360–7.
139. Milligan TA, Zamani A, Bromfield E. (2009). Frequency and patterns of MRI abnormalities due to status epilepticus. [Research Support, Non-U.S. Gov't]. *Seizure: Journal of the British Epilepsy Association*, **18**(2), 104–8.
140. Szabo K, Poepel A, Pohlmann-Eden B, et al. (2005). Diffusion-weighted and perfusion MRI demonstrates parenchymal changes in complex partial status epilepticus. *Brain*, **128**(Pt 6), 1369–76.
141. Sener RN. (2002). Diffusion MRI in Rasmussen's encephalitis, herpes simplex encephalitis, and bacterial meningoencephalitis. *Computerized Medical Imaging and Graphics*, **26**(5), 327–32.
142. Kuker W, Nagele T, Schmidt F, et al. (2004). Diffusion-weighted MRI in herpes simplex encephalitis: a report of three cases. [Case Reports]. *Neuroradiology*, **46**(2), 122–5.
143. Kiroglu Y, Calli C, Yunten N, et al. (2006). Diffusion-weighted MR imaging of viral encephalitis. *Neuroradiology*, **48**(12), 875–80.
144. Provenzale JM, Engelter ST, Petrella JR, et al. (1999). Use of MR exponential diffusion-weighted images to eradicate T2 'shine-through' effect. *AJR American Journal of Roentgenology*, **172**(2), 537–9.
145. Seeley WW, Marty FM, Holmes TM, et al. (2007). Post-transplant acute limbic encephalitis: clinical features and relationship to HHV6. *Neurology*, **69**(2), 156–65.
146. Yoshinari S, Hamano S, Ito T, et al. (2005). [MRI-diffusion weighted images of encephalopathy associated with human herpesvirus 6 infection]. *No to hattatsu Brain and Development*, **37**(5), 374–9.
147. Herweh C, Jayachandra MR, Hartmann M, et al. (2007). Quantitative diffusion tensor imaging in herpes simplex virus encephalitis. *Journal of Neurovirology*, **13**(5), 426–32.
148. Sener RN. (2004). Subacute sclerosing panencephalitis findings at MR imaging, diffusion MR imaging, and proton MR spectroscopy. [Case Reports]. *AJNR American Journal of Neuroradiology*, **25**(5), 892–4.
149. Lian ZY, Huang B, He SR, et al. (2012). Diffusion-weighted imaging in the diagnosis of enterovirus 71 encephalitis. [Research Support, Non-U.S. Gov't]. *Acta Radiologica*, **53**(2), 208–13.
150. Tokunaga Y, Kira R, Takemoto M, et al. (2000). Diagnostic usefulness of diffusion-weighted magnetic resonance imaging in influenza-associated acute encephalopathy or encephalitis. [Case Reports]. *Brain & Development*, **22**(7), 451–3.
151. Nouranifar RK, Ali M, and Nath J. (2003). The earliest manifestation of focal encephalitis on diffusion-weighted MRI. [Case Reports Review]. *Clinical Imaging*, **27**(5), 316–20.
152. Yoshikawa H, and Kitamura T. (2006). Serial changes on diffusion-weighted magnetic resonance imaging in encephalitis or encephalopathy. [Case Reports Research Support, Non-U.S. Gov't]. *Pediatric Neurology*, **34**(4), 308–11.

153. Bash S, Hathout GM, and Cohen S. (2001). Mesiotemporal T2-weighted hyperintensity: neurosyphilis mimicking herpes encephalitis. [Case Reports]. *AJNR American Journal of Neuroradiology*, **22**(2), 314–16.
154. McKinney AM, Lohman BD, Sarikaya B, et al. (2010). Acute hepatic encephalopathy: diffusion-weighted and fluid-attenuated inversion recovery findings, and correlation with plasma ammonia level and clinical outcome. *AJNR American Journal of Neuroradiology*, **31**(8), 1471–9.
155. Geschwind MD, Tan KM, Lennon VA, et al. (2008). Voltage-gated potassium channel autoimmunity mimicking Creutzfeldt–Jakob disease. *Archives of Neurology*, **65**(10), 1341–6.
156. Chu K, Kang DW, Kim JY, et al. (2001). Diffusion-weighted magnetic resonance imaging in nonconvulsive status epilepticus. *Archives of Neurology*, **58**(6), 993–8.
157. Di Bonaventura C, Bonini F, Fattouch J, et al. (2009). Diffusion-weighted magnetic resonance imaging in patients with partial status epilepticus. [Case Reports Comparative Study]. *Epilepsia*, **50**(Suppl. 1), 45–52.
158. Hufnagel A, Weber J, Marks S, et al. (2003). Brain diffusion after single seizures. *Epilepsia*, **44**(1), 54–63.
159. Geschwind MD, Shu H, Haman A, et al. (2008). Rapidly progressive dementia. *Annals of Neurology*, **64**(1), 97–108.

CHAPTER 23

Motor neuron diseases

Massimo Filippi and Federica Agosta

Introduction

Motor neuron diseases (MND) are progressive neurodegenerative conditions that lead to severe disability and death [1]. There is considerable variability in presentation, clinical course, and prognosis. These conditions are divided into several different clinical subtypes [1]. Amyotrophic lateral sclerosis (ALS) is the most common (90% of all MND cases) and is characterized by upper (UMN) and lower (LMN) motor neuron involvement of the bulbar, upper, and lower limb territories. Primary lateral sclerosis (PLS) causes exclusive UMN involvement and progressive muscular atrophy (PMA) involves only the LMN. The spectrum of MND also includes hereditary spastic paraplegias (HSP), which are a clinically and genetically heterogeneous group of conditions characterized by the presence of lower limb spasticity and weakness due to corticospinal tract (CST) damage [2]. Traditionally, HSP has been divided into pure (uncomplicated) and complicated, depending on the presence of other neurological features in addition to spastic paraparesis, and all modes of inheritance (autosomal dominant, autosomal recessive, or x-linked) have been reported [2].

There is as yet no definitive diagnostic test available for MND. Diagnosis is made mainly on clinical grounds, with the use of paraclinical and laboratory tests aimed at excluding other causes [3]. The greatest contribution of neuroimaging of the brain and the spinal cord to the diagnosis of MND so far is due to its sensitivity to detect abnormalities suggestive of alternative diagnoses [4]. Reliable objective markers of both UMN and LMN involvement are critical for the early diagnosis and monitoring of disease progression in patients with MND. Diffusion tensor (DT) magnetic resonance imaging (MRI), cortical thickness measures, and proton magnetic resonance spectroscopic imaging (^{1}H-MRSI) hold particular promise for grading UMN injury [5]. Functional neuroimaging techniques, such as positron emission tomography (PET) and functional MRI (fMRI), are providing a more complete picture of extramotor involvement, and are disclosing how functional changes interact with structural damage to determine the clinical outcome.

Clinical, genetic, and neuropathological data suggest that ALS and frontotemporal dementia (FTD) might form part of a disease continuum, with pure ALS at one extreme and pure FTD at the other [6]. Cognitive and behavioural dysfunction affects up to 50% of ALS patients, with frank FTD (ALS-FTD) occurring less commonly (15%) [6]. A disease-segregating expanded hexanucleotide repeat in the *C9orf72* gene accounts for up to 60% of familial ALS and up to 10% of sporadic ALS [7,8].

This chapter summarizes the main results obtained from the application of conventional and non-conventional neuroimaging techniques in MND patients, with a greater focus on ALS and other 'classic' MND phenotypes (i.e. PLS and PMA). Neuroimaging findings in HSP patients are summarized in the last section.

Conventional magnetic resonance imaging

Although a detailed clinical assessment remains the basis of the evaluation of patients suspected of having MND, current international diagnostic criteria [3] and European guidelines [4] recommend that 'all patients suspected of having a MND, where a plausible alternative unifying neuroanatomical explanation exists, should undergo an MRI of either or both the brain and whole cord depending on the clinical presentation'. Indeed, routine brain and spinal cord MRI can be useful in excluding several ALS mimic syndromes, including cerebral lesions (e.g. multiple sclerosis and cerebrovascular disease), skull base lesions, cervical spondylotic myelopathy, other myelopathy (e.g. foramen magnum lesions, intrinsic and extrinsic tumours, and syringomyelia), conus lesions, and thoracolumbar-sacral radiculopathy [9].

CST hyperintensities on T_2-weighted, proton density-weighted, and fluid-attenuated inversion recovery images are frequently found in ALS patients [10–20]. CST hyperintensities, which are best followed on coronal scans, have been reported mostly bilaterally and are most frequently seen in the caudal portion of the posterior limb of the internal capsule (Fig. 23.1). They typically extend downward to the ventral portion of the brainstem, and less consistently upward through the corona radiata. Such lesions may occur more often in younger patients with greater disability [15]. However, the reported frequency of conventional MRI abnormalities in ALS patients is very heterogeneous, ranging from 15 to 76%. More importantly, increased CST signal intensity has also been described in healthy individuals [16], and, strikingly, in patients with other conditions, such as Krabbe disease [21], x-linked Charcot–Marie Tooth neuropathies [22], adrenomyeloneuropathy [23], and after hepatic transplantation [24].

In ALS patients, the precentral cortex can present a low signal intensity (hypointense rim) on T_2-weighted images [11,14,15,17,18,25]. This so called 'ribbon-like' hypointensity is sharply contrasted by the hyperintense signal of cerebrospinal fluid in the adjacent sulci (Fig. 23.1).

Voxel-based morphometry and cortical thickness measures

In ALS, voxel-based morphometry (VBM) has shown limited sensitivity for abnormalities of the precentral gyrus. Cross-sectional VBM studies, with sample sizes ranging from 16 to 34 patients, have

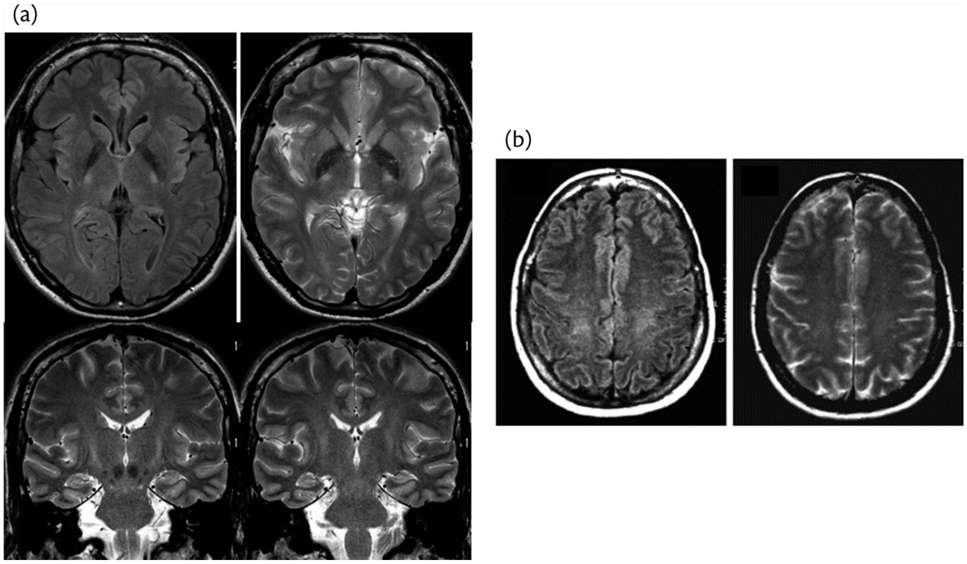

Fig. 23.1 Conventional MRI findings in patients with amyotrophic lateral sclerosis (ALS).

(a) Axial fluid-attenuated inversion recovery (FLAIR) and axial and coronal T_2-weighted fast spin-echo images showing CST high signal in a 55-year-old patient with moderate ALS. (b) Hyperintensity of the centrum semiovale on FLAIR and T_2-weighted images of a 66-year-old ALS patient.

Modified from Hecht MJ, Fellner F, Fellner C, et al. (2001). MRI-FLAIR images of the head show corticospinal tract alterations in ALS patients more frequently than T2-, T1- and proton-density-weighted images. *Journal of Neurological Science*, **186**, 37–44. Copyright (2001), with permission from Elsevier.

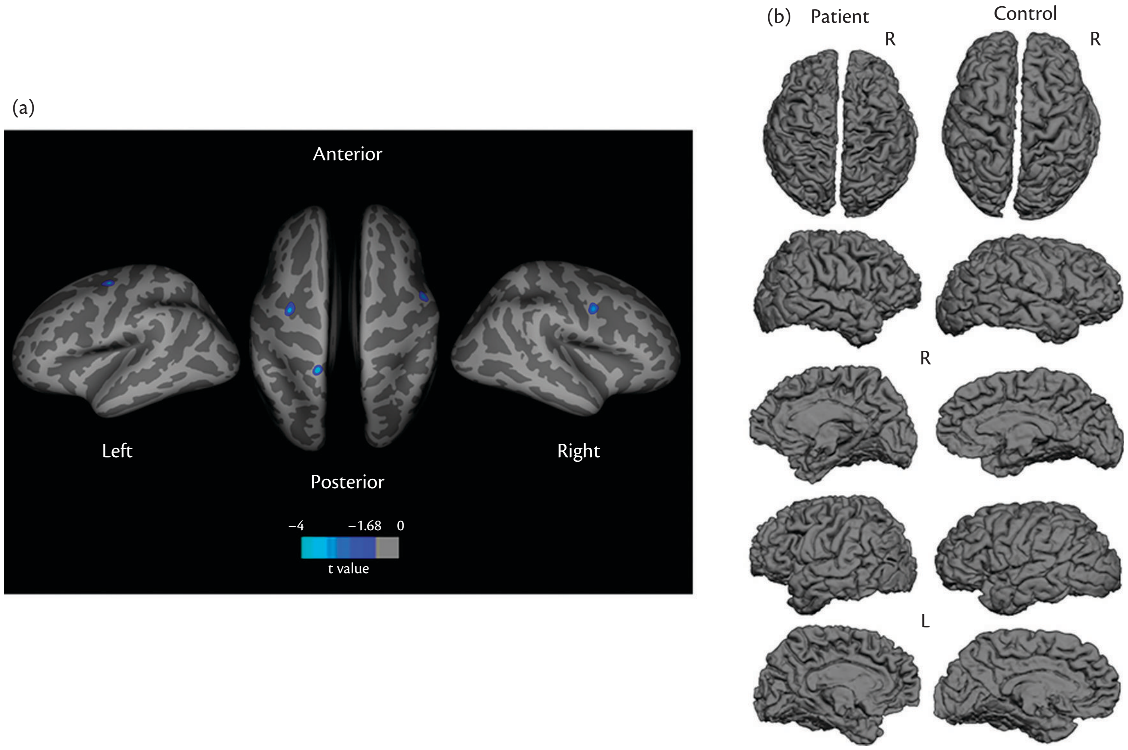

Fig. 23.2 Cortical thinning in patients with amyotrophic lateral sclerosis (ALS) and primary lateral sclerosis (PLS). (a) Regions of significantly thinner cortex in patients with amyotrophic lateral sclerosis compared with healthy controls represented on an averaged brain map. Colour bar represents t values. (b) Freesurfer reconstruction of brain volume of a patient with primary lateral sclerosis and a control. The superior, right, and left lateral and medial views illustrate striking atrophy in the patient's brain, most pronounced in the frontal lobe. L = left; R = right.

Reproduced from (a) Agosta F, Valsasina P, Riva N, et al. (2012). The cortical signature of amyotrophic lateral sclerosis. *PLoS ONE*, **7**, 1236–41. Copyright (2012), reproduced under the Creative Commons License 3.0. (b) Tartaglia MC, Laluz V, et al. (2009)., Brain atrophy in primary lateral sclerosis. *Neurology*, **72**, 1236–41. Copyright (2009), with permission from Wolters Kluwer Health.

yielded inconsistent results regarding the presence of motor/premotor cortical atrophy in ALS, which was found by some [26–31], but not all authors [32,33]. On the contrary, studies of surface-based morphometry in ALS have all revealed cortical thinning of the precentral gyrus (Fig. 23.2) [34–37].

Routine clinical MRI frequently demonstrates marked precentral gyrus atrophy in cases of PLS. A study of surface-based morphometry found a significant thinning of the precentral cortex in PLS patients, which was associated with disease severity (Fig. 23.2) [38].

With respect to the regional distribution of brain atrophy beyond the primary motor cortex, the pattern and extent of volume loss in MND patients vary across studies. Differences in image pre-processing and statistical analysis, as well as in the clinical, cognitive, and genetic characteristics of the cohorts of patients studied, may all contribute to explain this variability. For instance, some studies have included patients with an ALS-FTD syndrome, while others restrict their sample to non-demented patients with and without cognitive impairment.

In ALS patients with no cognitive impairment, several MRI studies found extra-motor regional grey matter loss or thinning of the frontotemporal and parietal regions [26–31,33,36,37,39]. Studies that have investigated the cognitive status of the patients have revealed that ALS-FTD compared with ALS-only patients show more severe gray matter atrophy of the frontal regions (left middle and inferior frontal and medial premotor cortex) [28]. Compared with cognitively normal patients, sporadic ALS patients with even subthreshold variants of cognitive or behavioural impairment (not meeting criteria for dementia) showed atrophy of frontal, parietal and limbic lobes [40].

Patients with ALS and the C9orf72 repeat expansion showed a considerable non-motor cortical atrophy (right inferior frontal and superior frontal gyri) when compared with ALS patients without the repeat expansion (Fig. 23.3) [41].

A VBM study showed that cortical atrophy in patients homozygous for the D90A (*homD90A*) mutation of the superoxide dismutase 1 (*SOD1*) gene is more pronounced in the frontal lobes, while sporadic ALS patients had areas of atrophy mainly confined to motor and premotor cortices bilaterally [42]. Mutations of the *Senataxin* gene are associated with autosomal dominant juvenile ALS (*ALS4*) and autosomal recessive ataxia-ocular apraxia 2 (*AOA2*). In a two-generation family, whose affected individuals had a clinical phenotype combining typical features of *AOA2* and *ALS4*, MRI revealed severe cerebellar atrophy [43].

In ALS patients, white matter tissue loss along the CST has been observed [29,39]. Extra-motor white matter atrophy, which included the anterior (prefrontal) corpus callosum, cerebellum, and frontotemporal and occipital regions [29,32], was also found,

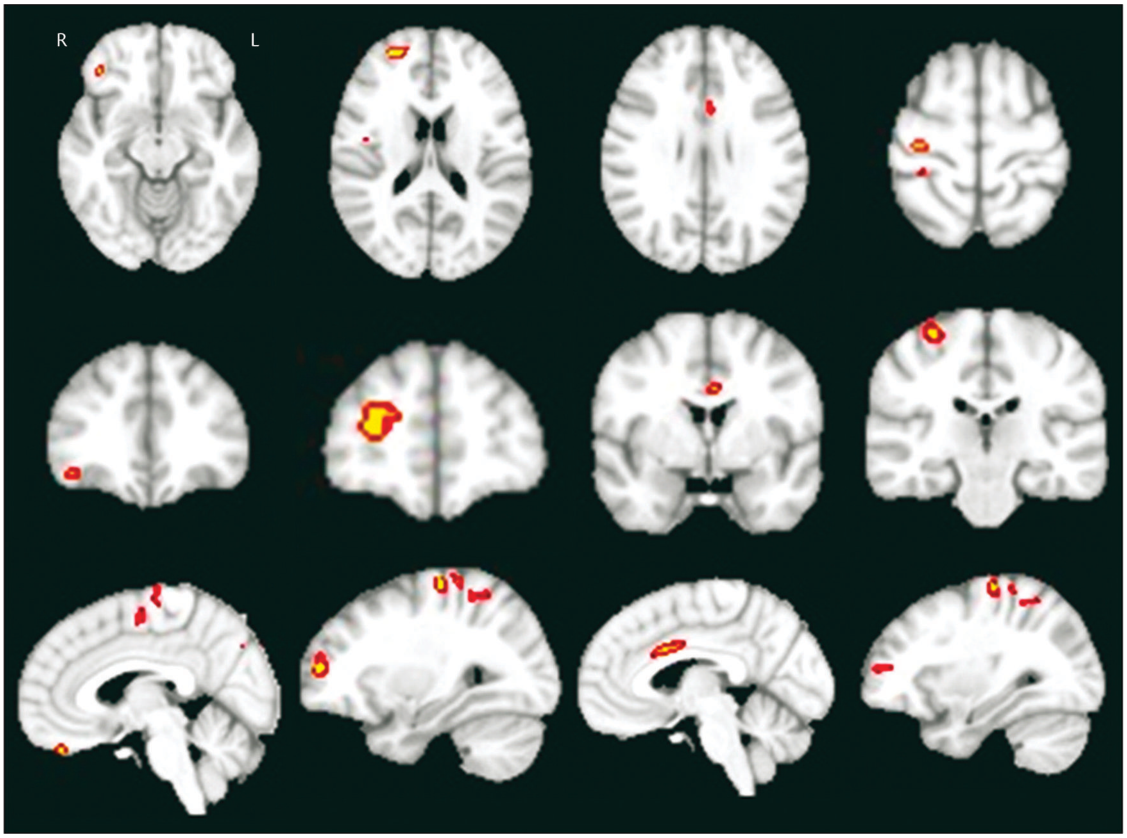

Fig. 23.3 Brain atrophy in amyotrophic lateral sclerosis patients with C9orf72 hexanucleotide repeat expansion. Clusters of significant grey matter atrophy in a cohort of 10 patients with amyotrophic lateral sclerosis (ALS) and the pathological expanded C9orf72 hexanucleotide repeat compared with 30 matched ALS patients without the repeat expansion. The four columns show the four clusters (from left to right: in the right inferior frontal gyrus, right superior frontal gyrus, left anterior cingulate gyrus, and the right precentral gyrus) in the three main radiological planes in each row (top to bottom: axial, coronal, sagittal). L = left; R = right.

Reproduced from Byrne S, Elamin M, Bede P, et al. (2012). Cognitive and clinical characteristics of patients with amyotrophic lateral sclerosis carrying a C9orf72 repeat expansion: a population-based cohort study. *Lancet Neurology*, **11**, 232–40. Copyright (2012), with permission from Elsevier.

but this finding was not confirmed by other authors [27,28,31]. One study reported a greater white matter atrophy of the frontotemporal regions in cognitively impaired (non-demented) ALS patients compared with those with no evidence of cognitive impairment [32]. Corpus callosum atrophy has been reported in PLS patients [38].

A few longitudinal studies have attempted to assess quantitatively the dynamics of brain atrophy in patients with ALS [44–46]. Two longitudinal VBM studies have demonstrated progressive atrophy in extramotor, as well as motor regions [44,46]. Patients with more rapidly progressive ALS accelerated frontal lobe and motor cortex atrophy [44,46]. A significant increase of cortical atrophy in motor and premotor areas after a follow up of about 5 months was found in four patients with ALS-FTD compared with controls [45].

Diffusion tensor magnetic resonance imaging

DT MRI studies of ALS patients have consistently reported decreased fractional anisotropy (FA) of the CST (Fig. 23.4) [34,47–60], which was found to correlate with disease severity [48,49,54,59,61,62], rate of disease progression [47,58], and clinical [49,51,53] or electrophysiological [52,55] measures of UMN degeneration. Patients with bulbar-onset have the most marked FA decreases [49,63,64].

Importantly, two studies demonstrated that CST DT MRI measures have a prognostic value in ALS patients (Fig. 23.5) [60,65].

ALS patients show FA decrease of the corpus callosum (Fig. 23.4) [26,53,55,57,59,62,66–69], which has been found to correlate with disease severity [53,66] and central motor conduction time obtained by transcranial magnetic stimulation [55]. The strongest FA decrease was found in the middle-posterior parts of the corpus callosum, linking to the motor and premotor cortices [53]. Corpus callosum involvement in ALS might reflect secondary Wallerian degeneration due to bilateral primary motor cortex degeneration, or might equally be the conduit for an interhemispheric spread of pathology [53]. The involvement of the corpus callosum appears to be a common pathway in UMN disorders. Indeed, PLS patients showed FA decrease of the CST and the mid-body of the corpus callosum compared with healthy controls [64,67,70–72]. A DT MRI study investigating FA abnormalities in PLS and ALS patients [67] showed that PLS patients have lower FA in the body of the corpus callosum than those with ALS [67]. More recently, DT MRI tractography was used to reconstruct the CST and three regions of the corpus callosum (i.e. genu, splenium, and callosal fibres connecting the motor cortices) in PLS and ALS patients [71]. Both patient groups had reduced FA and increased mean diffusivity (MD) of the CST and callosal motor fibres compared with controls [71]. In patients with PLS, the most severe FA and MD abnormalities occurred in the subcortical white matter in the vicinity of the primary motor cortex [71].

DT MRI has the potential to offer markers of early, clinically silent UMN involvement. Patients with PMA have FA values in the posterior limb of the internal capsule that are similar to those of patients with UMN signs [54]. Voxel-based DT MRI studies of patients with PMA [55,64] showed decreased FA in the white matter in the vicinity of the right primary motor cortex [64] and the CST [55], including those patients that later developed ALS [55]. A study of eight presymptomatic *SOD1* mutation carriers reported decreased FA in the posterior limb of the internal capsule compared with healthy controls [73]. These findings might be among the earliest detectable changes in those subjects who are at risk for UMN involvement.

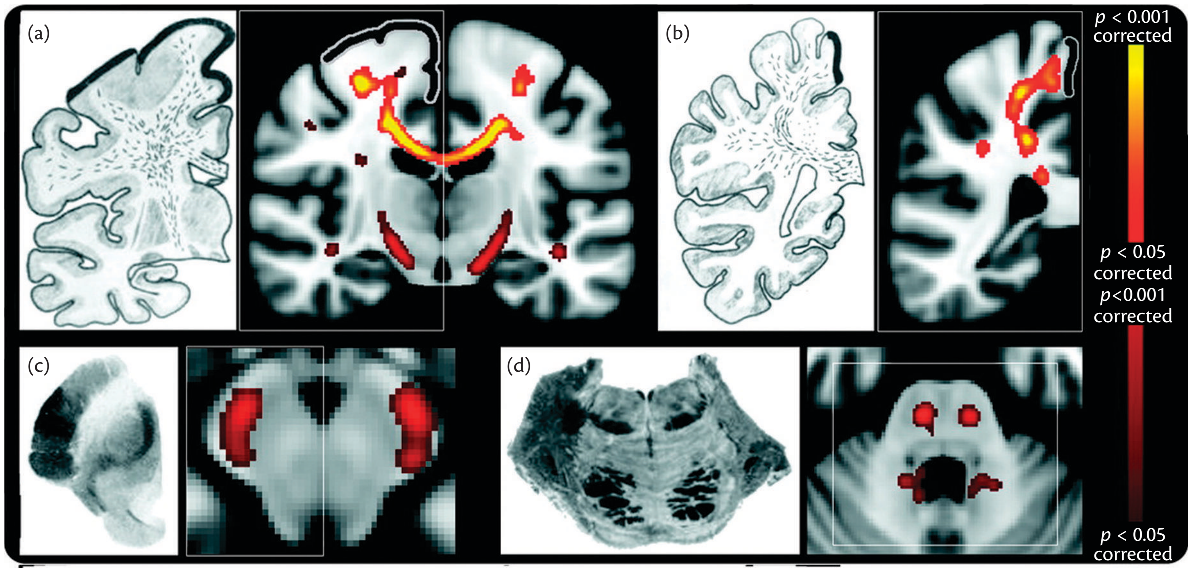

Fig. 23.4 Corticospinal tract (CST) and corpus callosum involvement in patients with amyotrophic lateral sclerosis (ALS) as assessed using diffusion tensor MRI. Regional fractional anisotropy (FA) reductions in ALS patients compared with healthy controls, alongside published postmortem (161) (left side images of a–d), confirmed prominent involvement of the corpus callosum and rostral CST (a and b, thick black lines indicating primary motor cortex), with caudal CST changes seen in uncorrected FA results (a, c, and d). Images shown were corrected (red–yellow scale) and uncorrected (red-only scale) for multiple comparisons ($p< 0.05$; radiologic convention).

Reproduced from Filippini N, Douaud G, Mackay CE, et al. (2010). Corpus callosum involvement is a consistent feature of amyotrophic lateral sclerosis. *Neurology*, **75**, 1645–52. Copyright (2010), with permission from Wolters Kluwer Health.

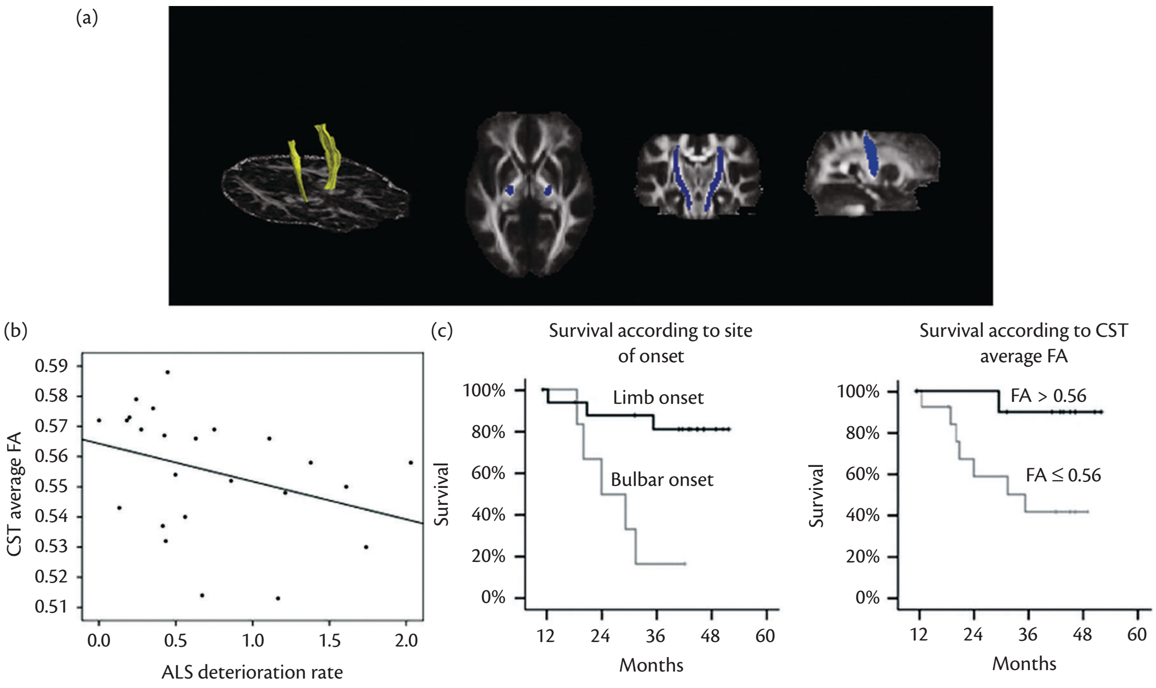

Fig. 23.5 Corticospinal tract (CST) damage as assessed by diffusion tensor MRI tractography in patients with amyotrophic lateral sclerosis. (a) Reconstruction of the corticospinal tracts (CST) (yellow) in a reference healthy control superimposed on the single subject's fractional anisotropy (FA) images, and illustration of the CST probability maps (blue) obtained from reference healthy subjects. Probability map is superimposed on axial, coronal and sagittal sections of the FA atlas. (b) Scatterplot of the correlation between the progression rate over 3.4 year follow-up measured with the Amyotrophic Lateral Sclerosis Rating scale (ALSFRS) score and the average FA of the CST in ALS patients. (c) Kaplan–Meier plots of survival probabilities according to: the site of symptoms at onset, and the average FA of the CST at baseline in ALS patients.

Modified from Agosta F, Pagani E, Petrolini M, et al. (2010). MRI predictors of long-term evolution in amyotrophic lateral sclerosis. *European Journal of Neuroscience*, **32**, 1490–6. Copyright (2010), with permission from John Wiley & Sons Ltd.

DT MRI studies that employed a voxel-wise approach to investigate differences in FA between ALS patients and controls, reported a decreased FA in regions outside the 'classic' motor network [26,55,59,62,67,74]. FA decrease was found in the prefrontal [59,62,67,74] and temporal [59,62] white matter. Using DT MRI tractography, decreased FA [75], and increased axial diffusivity [47] were reported in the uncinate fasciculus in ALS patients. Performances in cognitive tests assessing attention and executive functions correlated with DT MRI changes in the corpus callosum, CST and long association tract, including the cingulum, inferior longitudinal, inferior fronto-occipital, and uncinate fasciculi [76].

Despite a similar degree of clinical UMN dysfunction and disability, less extensive white matter changes in motor and extramotor pathways were found in patients homozygous for the homD90A *SOD1* mutation compared to sporadic ALS patients [77,78].

Longitudinal studies used DT MRI to track brain white matter changes over time in MND [59,60,64,79–82]. Two studies reported a significant progression of brain CST damage after 8-month follow up in ALS patients [59,82], which was moderately correlated with the concomitant worsening of disability [59]. Axial diffusivity significantly increased in the posterior limb of the internal capsule after approximately 6 months [60]. DT MRI changes after 6 months were reported in the CST, corpus callosum and several regions in the frontal and temporal lobes in both ALS and PMA patients (Fig. 23.6) [64]. However, significant brain DT MRI changes over time were not reported by other studies [79–81].

Proton magnetic resonance spectroscopic imaging

Nearly all ^{1}H-MRSI studies in ALS have demonstrated that either N-acetyl aspartate (NAA) concentrations [81,83–86] or NAA/creatine (Cr) [81,87–90], NAA/choline (Cho) [85,87] and NAA/Cr+Cho [86,90,91] ratios are reduced in the motor cortex of these patients. The reduction of the NAA/Cr ratio in the motor cortex was found to vary from 5 to 32% [81,88–90,92,93]. NAA/Cho is reduced more than NAA/Cr in the motor cortex in those studies that measured both [61,85–87,92,94,95]. NAA/Cr and NAA/Cho ratios are reduced along the full length of the intracranial CST from the motor cortex to the cerebral peduncles, but this reduction is most significant rostrally in the precentral gyrus and corona radiata [95]. However, ^{1}H-MRSI abnormalities in the brainstem have also been reported in ALS patients, with the greatest decrease of the NA (NAA+N-acetyl aspartylglutamate)/Cr ratio in the pons and upper medulla of patients with prominent UMN or bulbar signs [96]. The finding of reduced NAA concentrations or NAA ratios was confirmed by studies performed at 3.0 T [61,94,97].

^{1}H-MRSI studies reported significant correlations between motor cortex NAA concentrations (or ratios) and disease severity (revised ALSFRS [61,81,98]), the Norris limb scale [99], UMN signs [81,90,100,101], maximum finger tapping rate [90], and disease progression [85,95], suggesting that ^{1}H-MRSI might contribute to the understanding of phenotype heterogeneity. Bulbar onset patients have a lower NAA/Cho+Cr ratio in the motor

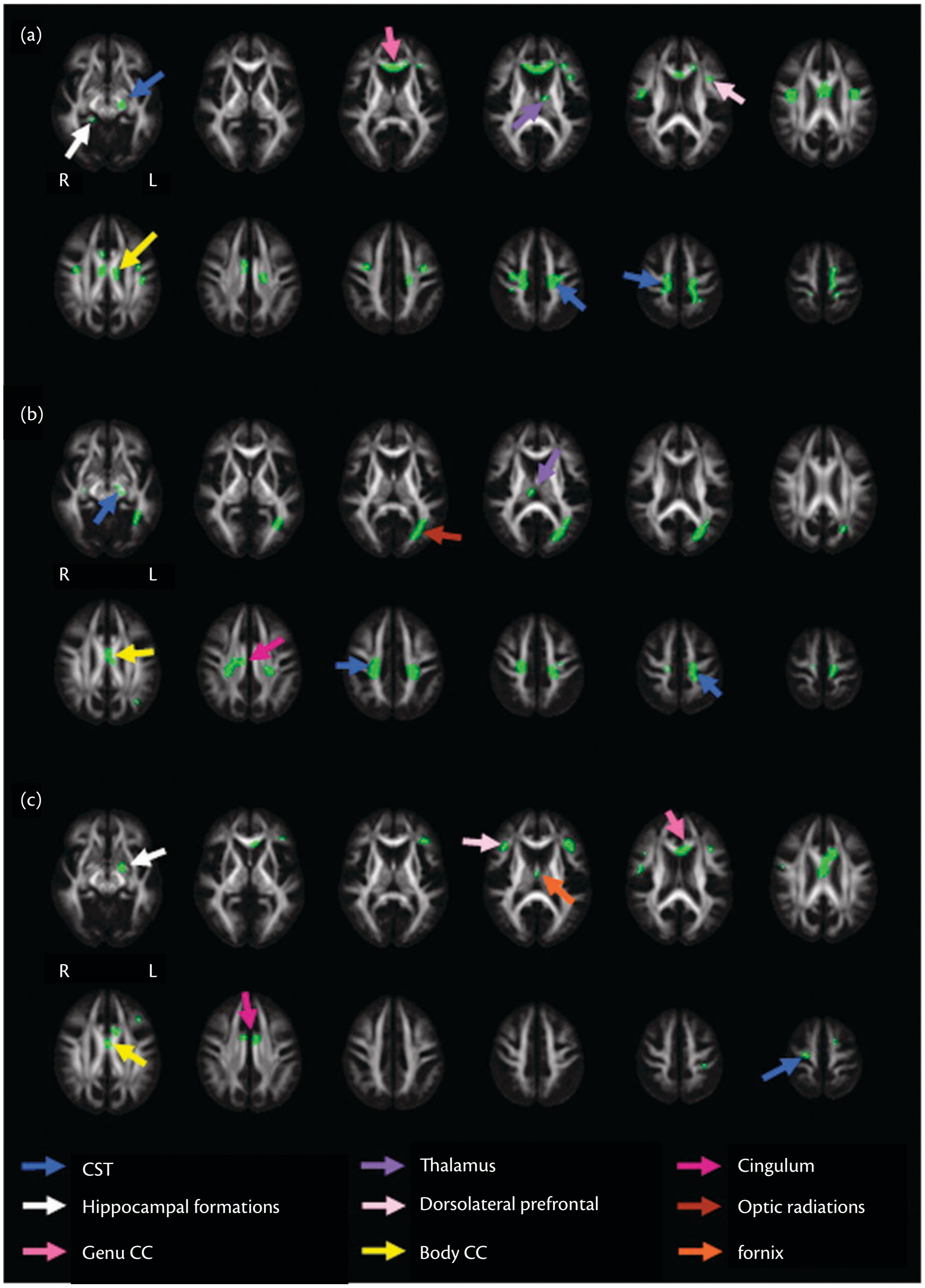

Fig. 23.6 Longitudinal brain diffusion tensor MRI changes in patients with amyotrophic lateral sclerosis (ALS) and progressive muscular atrophy (PMA). Regions in which fractional anisotropy (FA) is significantly reduced in patients with bulbar-onset ALS (a), limb-onset ALS (b) or PMA (c) over time are shown in green, overlaid on axial slices of the FA map of the population-based diffusion tensor MRI atlas. Specific anatomical locations/white matter structures are indicated by coloured arrows (see colour legend in figure).

CC = corpus callosum; CST = corticospinal tract; L = left; R = right.

Reproduced from van der Graaff MM, Sage CA, Caan MW, et al. (2011). Upper and extra-motoneuron involvement in early motoneuron disease: a diffusion tensor imaging study. *Brain*, **134**, 1211–28. Copyright (2011), with permission from Oxford University Press.

cortex compared with limb onset patients [98]. In a multiparametric study, T_2 hypointensity of the motor cortex and bulbar-onset were associated independently with the degree of NAA loss [84]. In a prospective ^{1}H-MRSI study of patients with probable or definite ALS, a multivariate analysis showed reduced survival for individuals with lower NAA/Cho, older age, and shorter symptom duration [97]. Patients with NAA/Cho < 2.11 had a survival of 19.4 versus 31.9 months of the others [97].

In two studies including PLS patients, mean NAA/Cr values were significantly different relative to control subjects [81,102]: when the optimal cut-off was set (2.5), NAA/Cr values were found to be abnormal in 67% of patients. Two studies of patients with PMA found normal NAA levels in the motor cortex [83,102]. However, a modest reduction in NAA/Cr ratio was found in nine PMA patients relative to controls [81], and abnormal ^{1}H-MRSI was found in 63% of 27 patients with PMA [100]. This variability may be explained by the different size of samples and methodological issues (i.e. single-voxel versus multi-voxel ^{1}H-MRSI).

^{1}H-MRSI studies have found decreased NAA/Cho in regions beyond the motor cortex such as the thalamus and basal ganglia [103], mid-cingulate cortex [104], and the frontal and parietal lobes [91] of patients with ALS. In ALS patients, decreased NAA/Cr ratios have been observed in premotor regions, primary sensory cortex, and extramotor frontal regions, with relative sparing of the parietal lobe [89,99]. Decreased frontal NAA/Cr ratio correlated with cognitive dysfunction [99]. ALS patients with bulbar onset and greater cognitive impairment had a decrease in the NAA/Cr ratio in the cingulate gyrus compared to those with limb onset [105].

Myo-inositol (mI), a spectroscopic marker of glial activity, was found to be increased in the motor cortex of ALS patients [87,101]. Increased mI levels were associated with motor cortex hypointensity on T_2-weighted images [101]. The NAA/mI ratio may have a better sensitivity and specificity for detecting ALS than the other metabolites ratios, as was shown by a cross-sectional study of ALS patients using a 3.0 T scanner [97]. In this study, decreased NAA/Cr and increased Ins/Cr had high sensitivity but low specificity, and decreased NAA/Cho had low sensitivity, but high specificity; while the NAA/Ins ratio had moderate sensitivity (71%), the highest specificity (93%), and the best sensitivity and specificity profile among the four metabolite ratios [97].

^{1}H-MRSI studies with an adequate follow up are scanty. Moreover, these studies most often have a relatively short follow up of no more than 28 months [106], and variable assessment schedule. Together with the variety of image analysis used, this makes comparisons between studies virtually impossible. Nevertheless, longitudinal ^{1}H-MRSI studies have reported a progressive reduction of NAA [86,91,107] and NAA/Cho [85,106] in the primary motor cortex of patients with ALS. In one study, changes of metabolite ratios were significantly correlated with progression of clinical deficits [85]. However, one prospective study, using multivoxel ^{1}H-MRSI in 30 patients with ALS, did not confirm these findings [81]. A significant decrease of NAA levels outside the motor cortex was observed after 9 months in ALS patients [91]. These findings were not confirmed by another study [86].

^{1}H-MRSI has been used to evaluate therapeutic effects on brain metabolites in ALS. An increase of 6% of NAA/Cr in the primary motor cortex of 11 patients after administration of riluzole for three weeks was noted, whereas it decreased by 4% in a group of untreated patients [108]. A study of oral creatine therapy revealed increased creatine (8%) and reduced glutamine (18%) in the frontal cortex 19 days after treatment initiation [109].

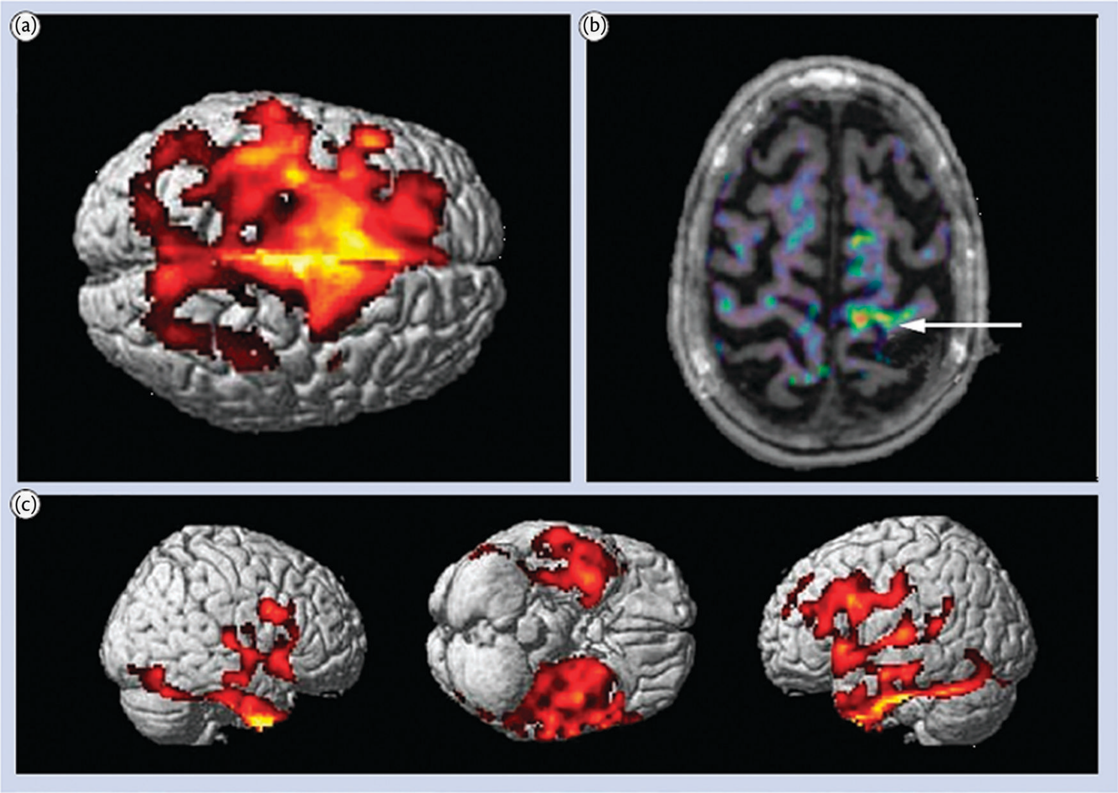

Fig. 23.7 Composite image from ligand positron emission tomography (PET) studies in amyotrophic lateral sclerosis (ALS). (a) A large area of motor and pre-motor cortex showed reduced binding of the GABA-A receptor ligand 11C-flumazenil in ALS patients, supporting the concept of loss of interneuronal inhibitory circuits. (b) Evidence of activated microglia, as demonstrated by binding of 11C-PK11195, was clearly localized to the left motor cortex (arrow) of a patient with weakness lateralized to the right sided limbs. (c) Right, inferior, and left views of the brain show strikingly frontotemporal localization of significantly reduced binding of the serotonin 5-HT$_1$A receptor ligand 11C-WAY100635, in keeping with the pathological links between ALS and frontotemporal dementia.

Reproduced from Turner MR, Agosta F, Bede P, et al. (2012). Neuroimaging in ALS. *Biomarkers in Medicine*, **6**(3), 319–37. Copyright (2012), with permission from Future Medicine.

Functional imaging

Positron emission tomography

Patients with ALS have decreased glucose uptake in the frontal lobe as assessed using PET with [18F]2-fluoro-2-deoxy-D-glucose (FDG), and some have additional abnormalities in the temporal, parietal, and right thalamic regions [110,111]. One study linked glucose hypometabolism of the frontal lobes to ALS-associated neuropsychological deficits, particularly verbal fluency impairment [112]. Non-demented ALS patients with decreased verbal fluency scores also have reduced regional cerebral blood flow of the frontal cortex, insular cortex, and thalamus compared to those patients who were cognitively intact [113,114].

Using ligand-based PET, a reduction of cortical ^{11}C-flumazenil binding has been detected in the motor/premotor [115–117] and extramotor [115] cortical regions of patients with ALS (Fig. 23.7).

A poorer performance on verbal fluency correlated with decreased ^{11}C-flumazenil binding in frontotemporal regions, while a poorer performance on a confrontation naming test correlated with decreased binding in the left middle frontal gyrus and cuneus [118]. A less extensive and more frontal pattern of reduced ^{11}C-flumazenil binding was observed in patients with homD90A SOD1 compared with similarly-disabled patients with sporadic ALS [116,117].

One PET study with ^{11}C-WAY100635, which binds selectively to the 5-hydroxytryptamine (5-HT) 1A receptor on cortical pyramidal neurons, revealed marked binding reductions in the precentral and cingulate gyri, and frontotemporal regions of ALS patients (Fig. 23.7) [119]. Such reduced 5-HT$_1$A receptor binding was also seen in similar areas in FTD patients [120]. The reduction in the cortical binding of ^{11}C-WAY100635 was less severe in homD90A SOD1 patients than in those with sporadic ALS [121].

A significantly increased ^{11}C(R)-PK11195 binding, which is a sign of microglial activation, was found in the motor cortex, pons, prefrontal cortex and thalamus; a significant correlation between binding in the motor cortex and clinical UMN signs was also found (Fig. 23.7) [122]. An increased uptake of ^{11}C(L)-deprenyl, which allows to localize astrocytosis *in vivo*, has been demonstrated in ALS patients in the pons and white matter [123].

A PET study using a ligand previously applied to Parkinson's disease patients, namely 18F-6-fluorodopa, provided evidence for loss of nigral dopaminergic cells in ALS [124].

Task-related functional MRI

During tasks of limb movements, fMRI demonstrated an increased activation of the contralateral sensorimotor cortex and the supplementary motor area in ALS patients relative to controls [125–128]. An increased sensorimotor activation was also reported in the hemisphere ipsilateral to the movement [127]. A spatial shift of

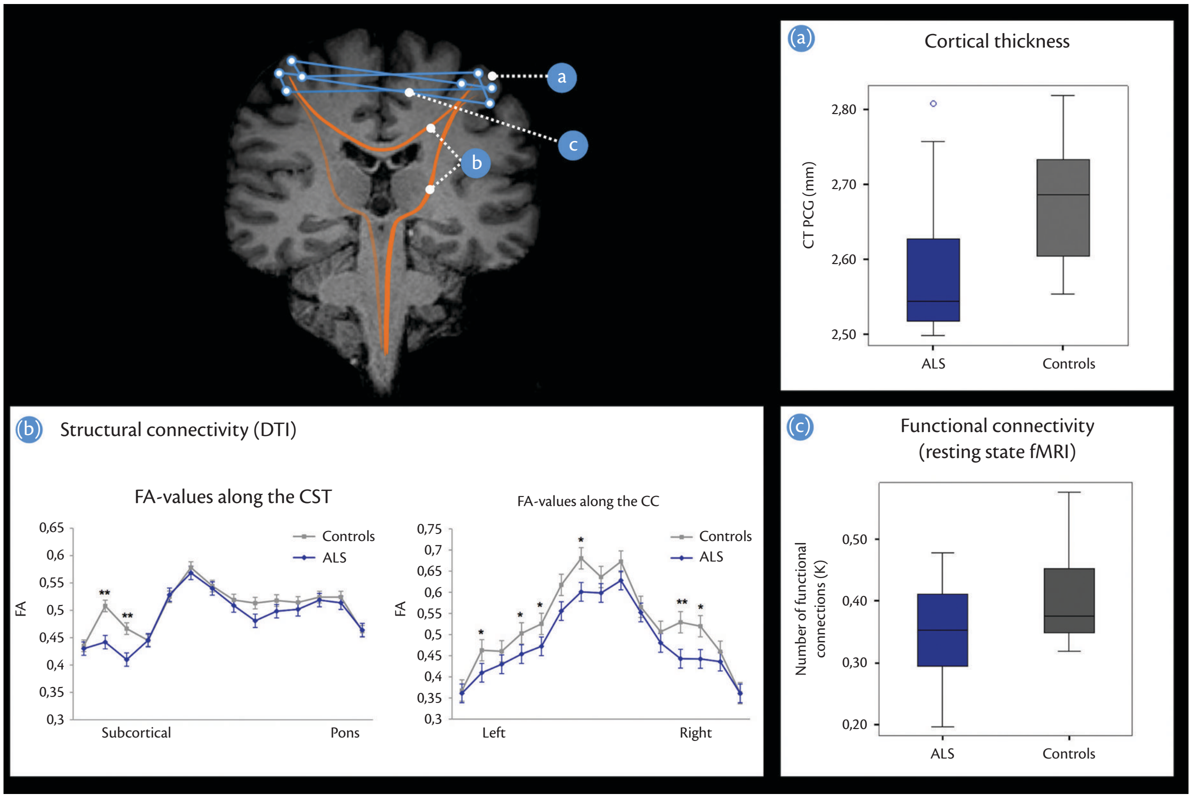

Fig. 23.8 Relationship between motor network measures in patients with amyotrophic lateral sclerosis (ALS). (a) Cortical thickness in patients with ALS relative to controls in the precentral gyrus in mm ($p = 0.04$). (b) Fractional anisotropy (FA) values along the corticospinal tract (CST) and the corpus callosum (CC) in patients with ALS and controls (**$p < 0.01$; *$p < 0.05$). (c) Number of functional connections based on resting state functional MRI (fMRI) in patients with ALS and controls ($p = 0.14$).

CT = cortical thickness; DTI = diffusion tensor imaging; PCG = precentral gyrus.

Reproduced from Verstraete E, van den Heuvel MP, Veldink JH, et al. (2010). Motor network degeneration in amyotrophic lateral sclerosis: a structural and functional connectivity study. *PLoS ONE*, **5**, e13664. Copyright (2010), reproduced under the Creative Commons License 3.0.

recruitment to more anterior regions of the premotor cortex during upper limb movement was also observed in ALS patients [125,129,130]. Such changes might reflect compensatory cortical plasticity in response to a loss of pyramidal cells of the primary motor cortex, or a reduced local inhibitory (presumed interneuronal) function. In ALS patients, an increased recruitment of the inferior parietal cortex during a motor task has also been reported; a relationship with task difficulty [127] or a compensatory role of parietal areas [125,128] have been suggested. Activation of cerebral regions involved in motor learning has been noted in ALS patients, including the basal ganglia and cerebellum [126,131]. An increase in movement-associated cortical activations beyond the primary motor cortex is associated with the degree of UMN involvement [131].

Overall, fMRI data provide evidence for a multi-system involvement of cognitive, emotional and sensory processing pathways in ALS. In ALS patients, a letter fluency fMRI task revealed significantly impaired recruitment of frontal, parietal and temporal lobes [132]. A confrontation naming fMRI task revealed an impaired activation of a prefrontal region (including Broca's area) and areas of the temporal, parietal, and occipital lobes [132]. This pattern of dysfunction corresponded to the presence of cognitive deficits on both letter fluency and confrontation naming [132]. Processing of socio-emotional stimuli was noted to be altered in non-demented ALS patients [133,134].

Resting state functional MRI

The difficulty to control task performance in ALS patients may be responsible for the variability of the results of the motor fMRI studies. Initial resting state fMRI studies of ALS reported significantly decreased functional connectivity within the sensorimotor network [135–137], in keeping with the altered structural connectivity. However, subsequent studies have identified regions of increased functional connectivity, including somatosensory areas (Fig. 23.8) [35,138,139]. In a study using a seed-based functional connectivity method, the pattern of increased functional connectivity to the left primary motor cortex was more widespread when considering only patients with no CST DT MRI abnormalities than the whole group of patients [138], suggesting that these changes might have a role in compensate for (limited) structural damage and might exhaust with increasing burden of pathology. In another study using a pre-defined 'ALS-specific' cortical network, increased functional connectivity was found over a large area spanning sensorimotor, premotor, prefrontal, and thalamic regions, which largely overlapped the areas of structural abnormalities identified using DT MRI [139]. The observation that patients with the highest rates of disease progression also had the highest level of functional connectivity lends support to a pathogenic loss of local inhibitory circuitry, rather than compensatory recruitment [139].

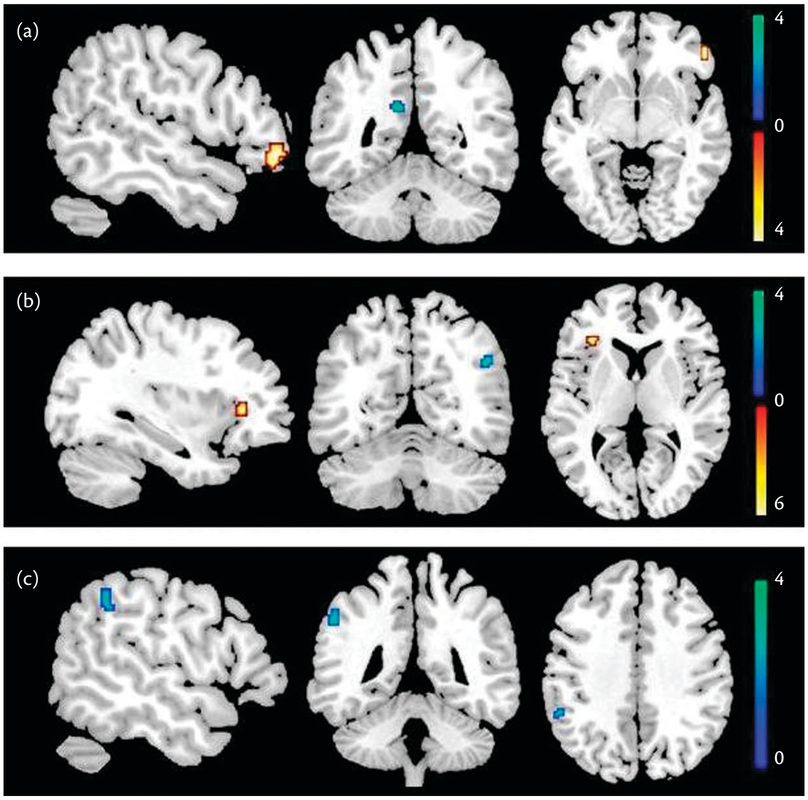

Fig. 23.9 Resting state functional connectivity of the brain networks related to cognition in patients with amyotrophic lateral sclerosis (ALS). Results of the resting state networks comparison between ALS patients and controls, accounting for grey matter volume differences: (a) default mode network; (b) right frontoparietal network; and (c) left frontoparietal network. Colour maps represent significant voxels ($p < 0.001$, uncorrected) in the corresponding contrast. *t*-values are colour-coded with red to yellow = decreased connectivity, and cyan to blue = increased connectivity in patients versus controls. Results are shown on the Montreal Neurological Institute standard brain, in neurological convention.

Reproduced from Agosta F, Canu E, Valsasina P, et al. (2013). Divergent brain network connectivity in amyotrophic lateral sclerosis. *Neurobiology of Aging*, **34**, 419–27. Copyright (2013), with permission from Elsevier.

In ALS, resting state fMRI demonstrated not only sensorimotor network alterations, but also an abnormal connectivity of brain networks related to cognition and behaviour [135,136,140]. In a recent study [140], ALS patients compared with controls showed divergent connectivity patterns, with a decreased connectivity of the frontal cortex and an increased connectivity of the parietal regions in the default mode and frontoparietal networks (Fig. 23.9). The enhanced parietal connectivity was found to be associated with the clinical and cognitive deficits of the patients [140], suggesting that it may have a role in maintaining cognitive efficiency in the presence of structural frontotemporal injury.

Spinal cord

T_2-weighted [17,141] or T_1-weighted [18] hyperintensities of the anterolateral columns of the cervical cord have been observed in ALS patients. T_1-hyperintensity of the anterolateral cervical cord has been associated with a younger age and a more rapid disease progression [18]. However, specificity and sensitivity of these findings in ALS vary greatly, making them unsuitable as markers of the disease.

Compared with controls, ALS patients demonstrated a decreased cervical cord cross-sectional area [142]. This finding was not confirmed by a second study [143]. However, a longitudinal study showed a significant development of cord atrophy in these patients over a nine month follow-up [79].

DT MRI has been successfully used to grade the extent of cervical cord damage associated with ALS [142,144]. A correlation was found between cervical cord FA and measures of disease severity such as the ALSFRS [142,144], forced vital capacity, average finger and foot tapping speed [144]. The analysis of DT MRI parameters from individual cervical segments, as well as profile plots along the length of the cervical cord, showed largest differences in FA and radial diffusivity at more distal cervical segments [144], providing evidence that supports the 'dying-back' hypothesis of neurodegeneration in ALS. After a mean follow up of 9 months [79], ALS patients showed a significant decrease of cord FA and a significant increase of cord MD.

Reduced NAA ratios in the cervical cord appear to correlate with reduced forced vital capacity in ALS [145]. A pivotal ^{1}H-MRS study of pre-symptomatic carriers of pathogenic *SOD1* mutations identified reduced metabolite ratios in the cervical cord similar to affected ALS patients [146], suggesting that these measures have the potential to serve as very early biomarkers.

Conventional and advanced neuroimaging techniques in hereditary spastic paraplegia

In HSP cases, brain and spinal cord conventional MRI are important to rule out other frequent neurological conditions, such as multiple sclerosis, leucodystrophies, intramedullar tumours, but also to detect associated abnormalities such as cerebellum and corpus callosum atrophy, as well as white matter lesions.

Conventional brain MRI is usually normal in patients with pure HSP and spastic paraplegia type 4 (*SPG4*) mutations [2]. MRI abnormalities of the posterior fossa that fall within the Dandy–Walker continuum were found in members of a large family with autosomal dominant spastic paraparesis due to SPG4 mutations (Fig. 23.10) [147]. MRI reveals variable degrees of cerebellar atrophy in patients with SPG7 mutations, which account for 5% of autosomal recessive HSP (Fig. 23.10), although cerebellar signs are not necessarily detected on clinical examination [148,149].

Autosomal recessive HSP with thin corpus callosum (HSP TCC) and mental impairment are genetically heterogeneous. *SPG11* is the most frequent form (Fig. 23.10) [150], followed by *SPG15* [151]. The occurrence of global atrophy and white matter abnormalities increases the chance of identifying SPG11 mutations [152]. In addition, the presence of the 'ears of the lynx' abnormality in the forceps minor of the corpus callosum in HSP TCC cases (i.e. the frontal horn region bore a remarkable resemblance to the ears of a lynx, with the areas of abnormal signal reminiscent of the tufts of hair crowning the tips of the ears of this animal) has been linked to the presence of a mutation in the *SPG11* gene [153]. Mutations in the proteolipoprotein gene (formerly SPG2) have been found mainly in families with complicated HSP with associated peripheral neuropathy and white matter changes on MRI [154].

On MRI, the spinal cord of HSP patients can appear atrophic, but other abnormalities are not usually seen. A quantitative study using standardized spinal cord planimetry showed a significant atrophy of the cervical and thoracic spinal cord compared with controls in both pure and complicated HSP, with no difference between patient groups [155].

Only a few studies have employed advanced MRI techniques in the evaluation of HSP patients with heterogeneous phenotypes. VBM was used to identify brain regional volume changes associated with pure and complicated HSP [156]. Pure HSP patients showed only small regional grey matter volume reduction, whereas significantly decreased grey matter volumes were localized in frontal and parietal lobes in complicated HSP [156]. In the white matter, several small areas of regional volume reduction (including the posterior part of the corpus callosum) were observed in pure HSP patients, whereas the complicated HSP group exhibited large volume reductions in the entire corpus callosum [156]. Using DT MRI in 24 HSP patients (19 cases with an autosomal-dominant inheritance—six SPG4 patients), a study showed abnormalities of the CST, dorsal part of the corpus callosum, capsula extrema, and brainstem (Fig. 23.11) [70]. DT MRI alterations were also found in the limbic system and its projectional fibre system [70].

In six *SPG4* patients, DT MRI showed distributed abnormalities of white matter, mainly affecting the corticospinal tracts and temporal lobes [157]. With longer disease duration, frontal regions were also found to be involved [157]. Five patients with *SPG11* mutations had decreased FA in the subcortical white matter of the temporal and frontal lobes, corpus callosum, brainstem, and regions in the vicinity of the cingulate gyrus, and cuneus [158]. On ^{1}H-MRS, NAA/Cr values of white matter periventricular regions were lower in *SPG11* patients compared with healthy controls, suggesting a pronounced neuroaxonal injury or loss [159]. NAA/Cr of the superior region of the corona radiata correlated with disability [159].

Conclusions

The use of routine MRI of the brain and spinal cord in patients suspected of having a MND is recommended to exclude mimics [4].

Over the past 10 years, there have been significant advances in the identification of neuroimaging patterns in MND [5]. International consensus was reached about essential and desirable protocols for MRI for studies in ALS (Table 23.1) [160], which are of the utmost importance in multicentre and longitudinal settings.

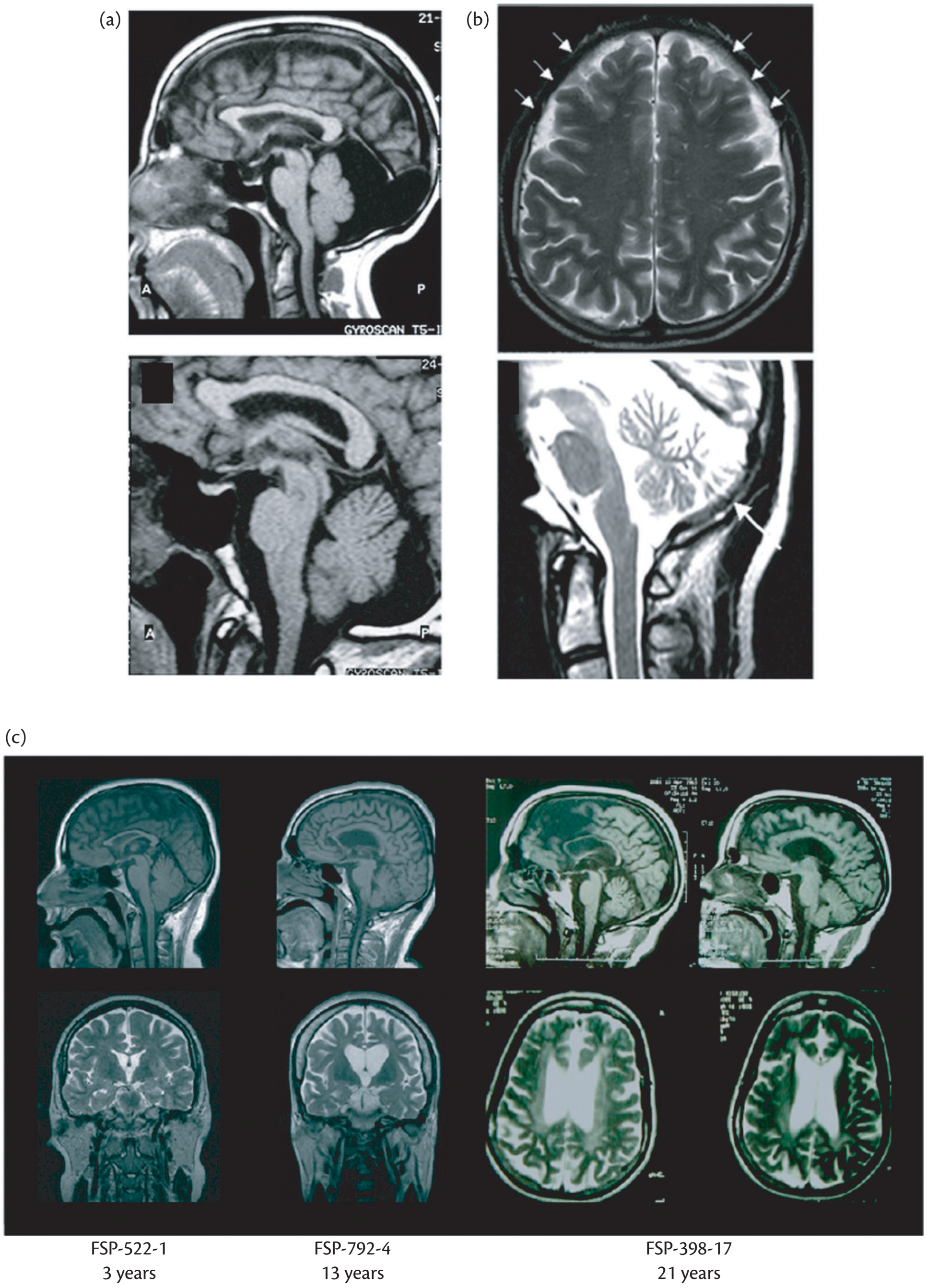

Fig. 23.10 Conventional MRI findings in patients with hereditary spastic paraplegias. (a) Sagittal T_1-weighted images of SPG4 patients: upper image shows posterior fluid collection with hypoplastic vermis and tentorial defect (note the atlanto-occipital assimilation); lower image shows posterior fluid collection with mild displacement of the vermis. (b) T_2-weighted MRI showing mild frontal cortical atrophy (upper, white arrows) and cerebellar atrophy (lower, white arrows) in two siblings with a SPG7 mutation. (c) Brain MRI images of three SPG11 patients with different disease durations. Upper panel: T_1-weighted sagittal image show thin corpus callosum and global cortical atrophy. Lower panel: T_2-fast spin echo weighted axial and coronal images showing periventricular hyperintensities of variable severity according to disease duration.

Modified from (a) Scuderi C, Fichera M, Calabrese G, et al. (2009). Posterior fossa abnormalities in hereditary spastic paraparesis with spastin mutations. *Journal of Neurology, Neurosurgery & Psychiatry*, **80**, 440–3. Copyright (2009), with permission from the BMJ Publishing Group Ltd. (b) Warnecke T, Duning T, Schwan A, et al. (2007). A novel form of autosomal recessive hereditary spastic paraplegia caused by a new SPG7 mutation. *Neurology*, **69**, 368–75. Copyright (2007), with permission from Wolters Kluwer Health. (c) Stevanin G, Azzedine H, Denora P, et al. (2008). Mutations in SPG11 are frequent in autosomal recessive spastic paraplegia with thin corpus callosum, cognitive decline and lower motor neuron degeneration. *Brain*, **131**, 772–84. Copyright (2008), with permission from Oxford University Press.

In the absence of definitive biomarkers of UMN involvement, a significant cortical thinning of the precentral gyrus [36,37], damage to the CST and corpus callosum assessed using DT MRI [55,64], and altered NAA levels in the primary motor cortex and CST [100] should be considered suggestive of MND and hold promise for detecting an UMN involvement before clinical symptoms become apparent. Importantly, DT MRI measures of the CST have also a prognostic value in ALS patients [60,65]. Furthermore, patterns of

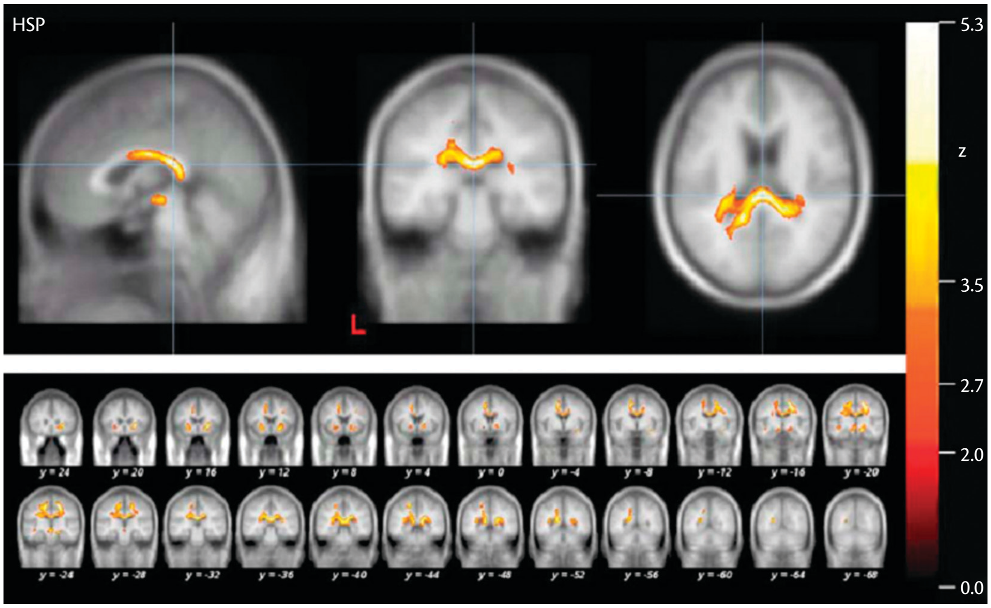

Fig. 23.11 Pattern of white matter damage in patients with hereditary spastic paraplegias (HSP). Results of the whole brain-based fractional anisotropy analysis in HSP patients. The upper panel shows the local maximum of decreased fractional anisotropy (FA) values (thresholded at $p < 0.05$, corrected for multiple comparisons) in the dorsal part of the corpus callosum in patients with HSP. The multi-slice views in the lower panel shows significantly reduced FA values in subcortical white matter areas of the motor and limbic system.

Reproduced from Unrath A, Muller HP, Riecker A, et al. (2010). Whole brain-based analysis of regional white matter tract alterations in rare motor neuron diseases by diffusion tensor imaging. *Human Brain Mapping*, **31**, 1727–40. Copyright (2010), with permission from John Wiley & Sons Ltd.

Table 23.1 Consensus guidelines on MRI protocol for studies of amyotrophic lateral sclerosis

MR technique	**Essential**	**Desirable**
Voxel-based morphometry	◆ T_1 (MP-RAGE or equivalent high-resolution 3D pulse sequence) ◆ Isotropic voxels (maximum 1 mm^3)	High gray matter–white matter contrast
Diffusion tensor imaging	◆ Minimum 12 gradient directions ◆ Isotropic voxels (maximum 2.5 mm slice thickness) ◆ T_2, FLAIR (to consider other white matter pathology, such as cerebrovascular disease) ◆ Minimum *b*-value 800 s/mm^2	◆ Axial acquisition (to maximize brainstem coverage) ◆ More than one cycle to allow averages to be calculated ◆ Cervical cord and brain ◆ Consideration of parallel imaging ◆ B0 field map
Functional MRI	◆ Resting-state sequence (in addition to any task-based measure) ◆ EPI, isotropic voxels (maximum 3 mm slice thickness) ◆ Consistent, either eyes open–fixed target, or eyes closed–not asleep for resting-state acquisition	◆ Axial acquisition (to maximize brainstem coverage) ◆ Pulse-waveform and respiratory-waveform monitoring to allow physiological noise correction ◆ Task-based protocol for both motor and cognitive functions ◆ B0 field map
Spectroscopy	◆ Standardized methodology ◆ NAA-based measures within primary motor cortex	Myo-inositol, glutamate, and gamma-aminobutyric acid measurements

For all imaging methods, a minimum scanner field strength of 1.5 T is essential, and 3.0 T plus a multiple-channel head coil (12-channel to 32-channel) is desirable.

Abbreviations: EPI = echo planar imaging; FLAIR = fluid-attenuated inversion recovery; MP-RAGE = magnetization-prepared rapid gradient echo; NAA = N-acetyl aspartate.

Reproduced from Turner MR. (2011). Towards a neuroimaging biomarker for amyotrophic lateral sclerosis. *Lancet Neurology*, **10**, 400–3. Copyright (2011), with permission from Elsevier.

brain damage are emerging that allow to identify patients prone to develop dementia or have a rapid progression [5].

It is strongly advisable to incorporate measures derived from advanced neuroimaging techniques into new clinical trials as exploratory outcomes to gain additional insights into the value of these techniques in the assessment of MND at an individual patient level and to validate them further in the context of multicentre, longitudinal studies. Finally, neuroimaging techniques need to be further applied in familial ALS with mutations of newly identified genes.

References

1. Kiernan MC, Vucic S, Cheah BC, et al. (2011). Amyotrophic lateral sclerosis. *Lancet*, **377**, 942–55.
2. Salinas S, Proukakis C, Crosby A, et al. (2008). Hereditary spastic paraplegia: clinical features and pathogenetic mechanisms. *Lancet Neurology*, **7**, 1127–38.
3. Brooks BR, Miller RG, Swash M, et al. (2000). El Escorial revisited: revised criteria for the diagnosis of amyotrophic lateral sclerosis. *Amyotrophic Lateral Sclerosis and Other Motor Neuron Disorders*, **1**, 293–9.
4. Filippi M, Agosta F, Abrahams S, et al. (2010). EFNS guidelines on the use of neuroimaging in the management of motor neuron diseases. *European Journal of Neurology*, **17**, 526–e20.
5. Turner MR, Agosta F, Bede P, et al. (2012). Neuroimaging in ALS. *Biomarkers in Medicine*, **6**(3), 319–37.
6. Phukan J, Pender NP, and Hardiman O. (2007). Cognitive impairment in amyotrophic lateral sclerosis. *Lancet Neurology*, **6**, 994–1003.
7. Dejesus-Hernandez M, Mackenzie IR, Boeve BF, et al. (2011). Expanded GGGGCC hexanucleotide repeat in noncoding region of C9ORF72 causes chromosome 9p-linked FTD and ALS. *Neuron*, **72**, 245–56.
8. Renton AE, Majounie E, Waite A, et al. (2011). A hexanucleotide repeat expansion in C9ORF72 is the cause of chromosome 9p21-linked ALS-FTD. *Neuron*, **72**, 257–68.
9. Kato S, Shaw P, Wood-Allum C, et al. (2003).Amyotrophic lateral sclerosis. In: Dickson DW (ed.) *Neurodegeneration: the molecular pathology of dementia and movement disorders*. Basel: ISN Neuropath Press, pp. 350–71.
10. Abe K, Fujimura H, Kobayashi Y, et al. (1997). Degeneration of the pyramidal tracts in patients with amyotrophic lateral sclerosis. A premortem and postmortem magnetic resonance imaging study. *Journal of Neuroimaging*, **7**, 208–12.
11. Cheung G, Gawel MJ, Cooper PW, et al. (1995). Amyotrophic lateral sclerosis: correlation of clinical and MR imaging findings. *Radiology*, **194**, 263–70.
12. Goodin DS, Rowley HA, and Olney RK.. (1988). Magnetic resonance imaging in amyotrophic lateral sclerosis. *Annals of Neurology*, **23**, 418–20.
13. Hecht MJ, Fellner F, Fellner C, et al. (2001). MRI-FLAIR images of the head show corticospinal tract alterations in ALS patients more frequently than T2-, T1- and proton-density-weighted images. *Journal of the Neurological Sciences*, **186**, 37–44.
14. Hecht MJ, Fellner F, Fellner C, et al. (2002). Hyperintense and hypointense MRI signals of the precentral gyrus and corticospinal tract in ALS: a follow-up examination including FLAIR images. *Journal of the Neurological Sciences*, **199**, 59–65.
15. Ishikawa K, Nagura H, Yokota T, et al. (1993). Signal loss in the motor cortex on magnetic resonance images in amyotrophic lateral sclerosis. *Annals of Neurology*, **33**, 218–22.
16. Mirowitz S, Sartor K, Gado M, et al. (1989). Focal signal-intensity variations in the posterior internal capsule: normal MR findings and distinction from pathologic findings. *Radiology*, **172**, 535–9.
17. Thorpe JW, Moseley IF, Hawkes CH, et al. (1996). Brain and spinal cord MRI in motor neuron disease. *Journal of Neurology, Neurosurgery, & Psychiatry*, **61**, 314–7.
18. Waragai M (1997). MRI and clinical features in amyotrophic lateral sclerosis. *Neuroradiology*, **39**, 847–51.
19. Basak M, Erturk M, Oflazoğlu B, et al. (2002). Magnetic resonance imaging in amyotrophic lateral sclerosis. *Acta Neurologica Scandinavica*, **105**, 395–9.
20. Charil A, Corbo M, Filippi M, et al. (2009). Structural and metabolic changes in the brain of patients with upper motor neuron disorders: a multiparametric MRI study. *Amyotrophic Lateral Sclerosis*, **10**, 269–79.
21. Satoh JI, Tokumoto H, Kurohara K, et al. (1997). Adult-onset Krabbe disease with homozygous T1853C mutation in the galactocerebrosidase gene. Unusual MRI findings of corticospinal tract demyelination. *Neurology*, **49**, 1392–9.
22. Kassubek J, Bretschneider V, and Sperfeld AD. (2005). Corticospinal tract MRI hyperintensity in X-linked Charcot–Marie–Tooth disease. *Journal of Clinical Neuroscience*, **12**, 588–9.
23. Teriitehau C, Adamsbaum C, Merzoug V, et al. (2007). [Subtle brain abnormalities in adrenomyeloneuropathy]. *Journal of Radiology*, **88**, 957–61.
24. Turner MR (2005). Reversible diffusion MRI abnormalities and transient mutism after liver transplantation. *Neurology*, **64**, 177; author reply.
25. Oba H, Araki T, Ohtomo K, et al. (1993). Amyotrophic lateral sclerosis: T2 shortening in motor cortex at MR imaging. *Radiology*, **189**, 843–6.
26. Agosta F, Pagani E, Rocca MA, et al. (2007). Voxel-based morphometry study of brain volumetry and diffusivity in amyotrophic lateral sclerosis patients with mild disability. *Human Brain Mapping*, **28**, 1430–8.
27. Grosskreutz J, Kaufmann J, Frädrich J, et al. (2006). Widespread sensorimotor and frontal cortical atrophy in Amyotrophic Lateral Sclerosis. *BMC Neurology*, **6**, 17.
28. Chang JL, Lomen-Hoerth C, Murphy J, et al. (2005). A voxel-based morphometry study of patterns of brain atrophy in ALS and ALS/FTLD. *Neurology*, **65**, 75–80.
29. Kassubek J, Unrath A, Huppertz HJ, et al. (2005). Global brain atrophy and corticospinal tract alterations in ALS, as investigated by voxel-based morphometry of 3-D MRI. *Amyotrophic Lateral Sclerosis and Other Motor Neuron Disorders*, **6**, 213–20.
30. Grossman M, Anderson C, Khan A, et al. (2008). Impaired action knowledge in amyotrophic lateral sclerosis. *Neurology*, **71**, 1396–401.
31. Thivard L, Pradat PF, Lehéricy S, et al. (2007). Diffusion tensor imaging and voxel based morphometry study in amyotrophic lateral sclerosis: relationships with motor disability. *Journal of Neurology, Neurosurgery & Psychiatry*, **78**, 889–92.
32. Abrahams S, Goldstein LH, Suckling J, et al. (2005). Frontotemporal white matter changes in amyotrophic lateral sclerosis. *Journal of Neurology*, **252**, 321–31.
33. Mezzapesa DM, Ceccarelli A, Dicuonzo F, et al. (2007). Whole-brain and regional brain atrophy in amyotrophic lateral sclerosis. *AJNR American Journal of Neuroradiology*, **28**, 255–9.
34. Roccatagliata L, Bonzano L, Mancardi G, et al. (2009). Detection of motor cortex thinning and corticospinal tract involvement by quantitative MRI in amyotrophic lateral sclerosis. *Amyotrophic Lateral Sclerosis*, **10**, 47–52.
35. Verstraete E, van den Heuvel MP, Veldink JH, et al. (2010). Motor network degeneration in amyotrophic lateral sclerosis: a structural and functional connectivity study. *PLoS ONE*, **5**, e13664.
36. Verstraete E, Veldink JH, Hendrikse J, et al. (2011). Structural MRI reveals cortical thinning in amyotrophic lateral sclerosis. *Journal of Neurology, Neurosurgery & Psychiatry*, **83**, 383–8.
37. Agosta F, Valsasina P, Riva N, et al. (2012). The cortical signature of amyotrophic lateral sclerosis. *PLoS ONE*, **7**, e42816.
38. Tartaglia MC, Laluz V, Rowe A, et al. (2009). Brain atrophy in primary lateral sclerosis. *Neurology*, **72**, 1236–41.
39. Ellis CM, Suckling J, Amaro E Jr, et al. (2001). Volumetric analysis reveals corticospinal tract degeneration and extramotor involvement in ALS. *Neurology*, **57**, 1571–8.
40. Murphy JM, Henry RG, Langmore S, et al. (2007). Continuum of frontal lobe impairment in amyotrophic lateral sclerosis. *Archives of Neurology*, **64**, 530–4.
41. Byrne S, Elamin M, Bede P, et al. (2012). Cognitive and clinical characteristics of patients with amyotrophic lateral sclerosis carrying a C9orf72 repeat expansion: a population-based cohort study. *Lancet Neurology*, **11**, 232–40.
42. Turner MR, Hammers A, Allsop J, et al. (2007). Volumetric cortical loss in sporadic and familial amyotrophic lateral sclerosis. *Amyotrophic Lateral Sclerosis*, **8**, 343–7.

43. Schols L, Arning L, Schule R, et al. (2008). 'Pseudodominant inheritance' of ataxia with ocular apraxia type 2 (AOA2). *Journal of Neurology*, **255**, 495–501.
44. Agosta F, Gorno-Tempini ML, Pagani E, et al. (2009). Longitudinal assessment of grey matter contraction in amyotrophic lateral sclerosis: A tensor based morphometry study. *Amyotrophic Lateral Sclerosis*, **10**, 168–74.
45. Avants B, Khan A, McCluskey L, et al. (2009). Longitudinal cortical atrophy in amyotrophic lateral sclerosis with frontotemporal dementia. *Archives of Neurology*, **66**, 138–9.
46. Senda J, Kato S, Kaga T, et al. (2011). Progressive and widespread brain damage in ALS: MRI voxel-based morphometry and diffusion tensor imaging study. *Amyotrophic Lateral Sclerosis*, **12**, 59–69.
47. Agosta F, Pagani E, Petrolini M, et al. (2010). Assessment of white matter tract damage in patients with amyotrophic lateral sclerosis: a diffusion tensor MR imaging tractography study. *AJNR American Journal of Neuroradiology*, **31**, 1457–61.
48. Cosottini M, Giannelli M, Siciliano G, et al. (2005). Diffusion-tensor MR imaging of corticospinal tract in amyotrophic lateral sclerosis and progressive muscular atrophy. *Radiology*, **237**, 258–64.
49. Ellis CM, Simmons A, Jones DK, et al. (1999). Diffusion tensor MRI assesses corticospinal tract damage in ALS. *Neurology*, **53**, 1051–8.
50. Toosy AT, Werring DJ, Orrell RW, et al. (2003). Diffusion tensor imaging detects corticospinal tract involvement at multiple levels in amyotrophic lateral sclerosis. *Journal of Neurology, Neurosurgery & Psychiatry*, **74**, 1250–7.
51. Abe O, Yamada H, Masutani Y, et al. (2004). Amyotrophic lateral sclerosis: diffusion tensor tractography and voxel-based analysis. *NMR in Biomedicine*, **17**, 411–16.
52. Iwata NK, Aoki S, Okabe S, et al. (2008). Evaluation of corticospinal tracts in ALS with diffusion tensor MRI and brainstem stimulation. *Neurology*, **70**, 528–32.
53. Filippini N, Douaud G, Mackay CE, et al. (2010). Corpus callosum involvement is a consistent feature of amyotrophic lateral sclerosis. *Neurology*, **75**, 1645–52.
54. Graham JM, Papadakis N, Evans J, et al. (2004). Diffusion tensor imaging for the assessment of upper motor neuron integrity in ALS. *Neurology*, **63**, 2111–19.
55. Sach M, Winkler G, Glauche V, et al. (2004). Diffusion tensor MRI of early upper motor neuron involvement in amyotrophic lateral sclerosis. *Brain*, **127**, 340–50.
56. Schimrigk SK, Bellenberg B, Schluter M, et al. (2007). Diffusion tensor imaging-based fractional anisotropy quantification in the corticospinal tract of patients with amyotrophic lateral sclerosis using a probabilistic mixture model. *AJNR American Journal of Neuroradiology*, **28**, 724–30.
57. Senda J, Ito M, Watanabe H, et al. (2009). Correlation between pyramidal tract degeneration and widespread white matter involvement in amyotrophic lateral sclerosis: A study with tractography and diffusion-tensor imaging. *Amyotrophic Lateral Sclerosis*, 10, 288-94.
58. Ciccarelli O, Behrens TE, Altmann DR, et al. (2006). Probabilistic diffusion tractography: a potential tool to assess the rate of disease progression in amyotrophic lateral sclerosis. *Brain*, **129**, 1859–71.
59. Sage CA, Peeters RR, Gorner A, et al. (2007). Quantitative diffusion tensor imaging in amyotrophic lateral sclerosis. *NeuroImage*, **34**, 486–99.
60. Menke RA, Abraham I, Thiel CS, et al. (2012). Fractional anisotropy in the posterior limb of the internal capsule and prognosis in amyotrophic lateral sclerosis. *Archives of Neurology*, **69**, 1493–9.
61. Wang S, Poptani H, Woo JH, et al. (2006). Amyotrophic lateral sclerosis: diffusion-tensor and chemical shift MR imaging at 3.0 T. *Radiology*, **239**, 831–8.
62. Sage CA, Van Hecke W, Peeters R, et al. (2009). Quantitative diffusion tensor imaging in amyotrophic lateral sclerosis: Revisited. *Human Brain Mapping*, **30**(11), 3657–75.
63. Aoki S, Iwata NK, Masutani Y, et al. (2005). Quantitative evaluation of the pyramidal tract segmented by diffusion tensor tractography: feasibility study in patients with amyotrophic lateral sclerosis. *Radiation Medicine*, **23**, 195–9.
64. van der Graaff MM, Sage CA, Caan MW, et al. (2011). Upper and extra-motoneuron involvement in early motoneuron disease: a diffusion tensor imaging study. *Brain*, **134**, 1211–28.
65. Agosta F, Pagani E, Petrolini M, et al. (2010). MRI predictors of long-term evolution in amyotrophic lateral sclerosis. *European Journal of Neuroscience*, **32**, 1490–6.
66. Bartels C, Mertens N, Hofer S, et al. (2008). Callosal dysfunction in amyotrophic lateral sclerosis correlates with diffusion tensor imaging of the central motor system. *Neuromuscular Disorders*, **18**, 398–407.
67. Ciccarelli O, Behrens TE, Johansen-Berg H, et al. (2009). Investigation of white matter pathology in ALS and PLS using tract-based spatial statistics. *Human Brain Mapping*, **30**, 615–24.
68. Rose S, Pannek K, Bell C, et al. (2012). Direct evidence of intra- and interhemispheric corticomotor network degeneration in amyotrophic lateral sclerosis: An automated MRI structural connectivity study. *NeuroImage*, **59**(3), 2661–9.
69. Cirillo M, Esposito F, Tedeschi G, et al. (2012). Widespread microstructural white matter involvement in amyotrophic lateral sclerosis: a whole-brain DTI study. *AJNR American Journal of Neuroradiology*, **33**, 1102–8.
70. Unrath A, Muller HP, Riecker A, et al. (2010). Whole brain-based analysis of regional white matter tract alterations in rare motor neuron diseases by diffusion tensor imaging. *Human Brain Mapping*, **31**, 1727–40.
71. Iwata NK, Kwan JY, Danielian LE, et al. (2011). White matter alterations differ in primary lateral sclerosis and amyotrophic lateral sclerosis. *Brain*, **134**, 2642–55.
72. Muller HP, Unrath A, Huppertz HJ, et al. (2012). Neuroanatomical patterns of cerebral white matter involvement in different motor neuron diseases as studied by diffusion tensor imaging analysis. *Amyotrophic Lateral Sclerosis*, **13**, 254–64.
73. Ng MC, Ho JT, Ho SL, et al. (2008). Abnormal diffusion tensor in nonsymptomatic familial amyotrophic lateral sclerosis with a causative superoxide dismutase 1 mutation. *Journal of Magnetic Resonance Imaging*, **27**, 8–13.
74. Canu E, Agosta F, Riva N, et al. (2011). The topography of brain microstructural damage in amyotrophic lateral sclerosis assessed using diffusion tensor MR imaging. *AJNR American Journal of Neuroradiology*, **32**, 1307–14.
75. Sato K, Aoki S, Iwata NK, et al. (2010). Diffusion tensor tract-specific analysis of the uncinate fasciculus in patients with amyotrophic lateral sclerosis. *Neuroradiology*, **52**, 729–33.
76. Sarro L, Agosta F, Canu E, et al. (2011). Cognitive functions and white matter tract damage in amyotrophic lateral sclerosis: a diffusion tensor tractography study. *AJNR American Journal of Neuroradiology*, **32**, 1866–72.
77. Stanton BR, Shinhmar D, Turner MR, et al. (2009). Diffusion tensor imaging in sporadic and familial (D90A SOD1) forms of amyotrophic lateral sclerosis. *Archives of Neurology*, **66**, 109–15.
78. Blain CR, Brunton S, Williams VC, et al. (2011). Differential corticospinal tract degeneration in homozygous 'D90A' SOD-1 ALS and sporadic ALS. *Journal of Neurology, Neurosurgery & Psychiatry*, **82**, 843–9.
79. Agosta F, Rocca MA, Valsasina P, et al. (2009). A longitudinal diffusion tensor MRI study of the cervical cord and brain in amyotrophic lateral sclerosis patients. *Journal of Neurology, Neurosurgery & Psychiatry*, **80**, 53–5.
80. Blain CR, Williams VC, Johnston C, et al. (2007). A longitudinal study of diffusion tensor MRI in ALS. *Amyotrophic Lateral Sclerosis*, **8**, 348–55.
81. Mitsumoto H, Ulug AM, Pullman SL, et al. (2007). Quantitative objective markers for upper and lower motor neuron dysfunction in ALS. *Neurology*, **68**, 1402–10.
82. Zhang Y, Schuff N, Woolley SC, et al. (2011). Progression of white matter degeneration in amyotrophic lateral sclerosis: A diffusion tensor imaging study. *Amyotrophic Lateral Sclerosis*, **12**, 421–9.
83. Gredal O, Rosenbaum S, Topp S, et al. (1997). Quantification of brain metabolites in amyotrophic lateral sclerosis by localized proton magnetic resonance spectroscopy. *Neurology*, **48**, 878–81.

84. Sarchielli P, Pelliccioli GP, Tarducci R, et al. (2001). Magnetic resonance imaging and 1H-magnetic resonance spectroscopy in amyotrophic lateral sclerosis. *Neuroradiology*, **43**, 189–97.
85. Pohl C, Block W, Karitzky J, et al. (2001). Proton magnetic resonance spectroscopy of the motor cortex in 70 patients with amyotrophic lateral sclerosis. *Archives of Neurology*, **58**, 729–35.
86. Suhy J, Miller RG, Rule R, et al. (2002). Early detection and longitudinal changes in amyotrophic lateral sclerosis by (1)H MRSI. *Neurology*, **58**, 773–9.
87. Block W, Karitzky J, Traber F, et al. (1998). Proton magnetic resonance spectroscopy of the primary motor cortex in patients with motor neuron disease: subgroup analysis and follow-up measurements. *Archives of Neurology*, **55**, 931–6.
88. Jones AP, Gunawardena WJ, Coutinho CM, et al. (1995). Preliminary results of proton magnetic resonance spectroscopy in motor neurone disease (amytrophic lateral sclerosis). *Journal of the Neurological Sciences*, **129**(Suppl.), 85–9.
89. Pioro EP, Antel JP, Cashman NR, et al. (1994). Detection of cortical neuron loss in motor neuron disease by proton magnetic resonance spectroscopic imaging in vivo. *Neurology*, **44**, 1933–8.
90. Rooney WD, Miller RG, Gelinas D, et al. (1998). Decreased N-acetylaspartate in motor cortex and corticospinal tract in ALS. *Neurology*, **50**, 1800–5.
91. Rule RR, Suhy J, Schuff N, et al. (2004). Reduced NAA in motor and non-motor brain regions in amyotrophic lateral sclerosis: a cross-sectional and longitudinal study. *Amyotrophic Lateral Sclerosis and Other Motor Neuron Disorders*, **5**, 141–9.
92. Kalra S, Vitale A, Cashman NR, et al. (2006). Cerebral degeneration predicts survival in amyotrophic lateral sclerosis. *Journal of Neurology, Neurosurgery & Psychiatry*, **77**, 1253–5.
93. Kalra S, Tai P, Genge A, et al. (2006). Rapid improvement in cortical neuronal integrity in amyotrophic lateral sclerosis detected by proton magnetic resonance spectroscopic imaging. *Journal of Neurology*, **253**, 1060–3.
94. Nelles M, Block W, Traber F, et al. (2008). Combined 3T diffusion tensor tractography and 1H-MR spectroscopy in motor neuron disease. *AJNR American Journal of Neuroradiology*, **29**, 1708–14.
95. Pyra T, Hui B, Hanstock C, et al. (2010). Combined structural and neurochemical evaluation of the corticospinal tract in amyotrophic lateral sclerosis. *Amyotrophic Lateral Sclerosis*, 11, 157-65.
96. Cwik VA, Hanstock CC, Allen PS, et al. (1998). Estimation of brainstem neuronal loss in amyotrophic lateral sclerosis with in vivo proton magnetic resonance spectroscopy. *Neurology*, **50**, 72–7.
97. Kalra S, Hanstock CC, Martin WR, et al. (2006). Detection of cerebral degeneration in amyotrophic lateral sclerosis using high-field magnetic resonance spectroscopy. *Archives of Neurology*, **63**, 1144–8.
98. Ellis CM, Simmons A, Andrews C, et al. (1998). A proton magnetic resonance spectroscopic study in ALS: correlation with clinical findings. *Neurology*, **51**, 1104–9.
99. Abe K, Takanashi M, Watanabe Y, et al. (2001). Decrease in N-acetylaspartate/creatine ratio in the motor area and the frontal lobe in amyotrophic lateral sclerosis. *Neuroradiology*, **43**, 537–41.
100. Kaufmann P, Pullman SL, Shungu DC, et al. (2004). Objective tests for upper motor neuron involvement in amyotrophic lateral sclerosis (ALS). *Neurology*, **62**, 1753–7.
101. Bowen BC, Pattany PM, Bradley WG, et al. (2000). MR imaging and localized proton spectroscopy of the precentral gyrus in amyotrophic lateral sclerosis. *AJNR American Journal of Neuroradiology*, **21**, 647–58.
102. Chan S, Shungu DC, Douglas-Akinwande A, et al. (1999). Motor neuron diseases: comparison of single-voxel proton MR spectroscopy of the motor cortex with MR imaging of the brain. *Radiology*, **212**, 763–9.
103. Sharma KR, Saigal G, Maudsley AA, et al. (2011). 1H MRS of basal ganglia and thalamus in amyotrophic lateral sclerosis. *NMR in Biomedicine*, **24**, 1270–6.
104. Sudharshan N, Hanstock C, Hui B, et al. (2011). Degeneration of the mid-cingulate cortex in amyotrophic lateral sclerosis detected in vivo with MR spectroscopy. *AJNR American Journal of Neuroradiology*, **32**, 403–7.
105. Strong MJ, Grace GM, Orange JB, et al. (1999). A prospective study of cognitive impairment in ALS. *Neurology*, **53**, 1665–70.
106. Block W, Traber F, Flacke S, et al. (2002). In-vivo proton MR-spectroscopy of the human brain: assessment of N-acetylaspartate (NAA) reduction as a marker for neurodegeneration. *Amino Acids*, **23**, 317–23.
107. Unrath A, Ludolph AC, and Kassubek J. (2007). Brain metabolites in definite amyotrophic lateral sclerosis. A longitudinal proton magnetic resonance spectroscopy study. *Journal of Neurology*, **254**, 1099–106.
108. Kalra S, Cashman NR, Genge A, et al. (1998). Recovery of N-acetylaspartate in corticomotor neurons of patients with ALS after riluzole therapy. *Neuroreport*, **9**, 1757–61.
109. Atassi N, Ratai EM, Greenblatt DJ, et al. (2010). A phase I, pharmacokinetic, dosage escalation study of creatine monohydrate in subjects with amyotrophic lateral sclerosis. *Amyotrophic Lateral Sclerosis*, **11**, 508–13.
110. Dalakas MC, Hatazawa J, Brooks RA, et al. (1987). Lowered cerebral glucose utilization in amyotrophic lateral sclerosis. *Annals of Neurology*, **22**, 580–6.
111. Hatazawa J, Brooks RA, Dalakas MC, et al. (1988). Cortical motor-sensory hypometabolism in amyotrophic lateral sclerosis: a PET study. *Journal of Computer Assisted Tomography*, **12**, 630–6.
112. Ludolph AC, Langen KJ, Regard M, et al. (1992). Frontal lobe function in amyotrophic lateral sclerosis: a neuropsychologic and positron emission tomography study. *Acta Neurologica Scandinavica*, **85**, 81–9.
113. Abrahams S, Goldstein LH, Kew JJ, et al. (1996). Frontal lobe dysfunction in amyotrophic lateral sclerosis. A PET study. *Brain*, **119**(Pt 6), 2105–20.
114. Abrahams S, Leigh PN, Kew JJ, et al. (1995). A positron emission tomography study of frontal lobe function (verbal fluency) in amyotrophic lateral sclerosis. *Journal of the Neurological Sciences*, **129**(Suppl.), 44–6.
115. Lloyd CM, Richardson MP, Brooks DJ, et al. (2000). Extramotor involvement in ALS: PET studies with the GABA(A) ligand [(11)C] flumazenil. *Brain*, **123**(Pt 11), 2289–96.
116. Turner MR, Hammers A, Al-Chalabi A, et al. (2005). Distinct cerebral lesions in sporadic and 'D90A' SOD1 ALS: studies with [11C]flumazenil PET. *Brain*, **128**, 1323–9.
117. Turner MR, Osei-Lah AD, Hammers A, et al. (2005). Abnormal cortical excitability in sporadic but not homozygous D90A SOD1 ALS. *Journal of Neurology, Neurosurgery & Psychiatry*, **76**, 1279–85.
118. Wicks P, Turner MR, Abrahams S, et al. (2008). Neuronal loss associated with cognitive performance in amyotrophic lateral sclerosis: an (11C)-flumazenil PET study. *Amyotrophic Lateral Sclerosis*, **9**, 43–9.
119. Turner MR, Rabiner EA, Hammers A, et al. (2005). [11C]-WAY100635 PET demonstrates marked 5-HT1A receptor changes in sporadic ALS. *Brain*, **128**, 896–905.
120. Bowen DM, Procter AW, Mann DM, et al. (2008). Imbalance of a serotonergic system in frontotemporal dementia: implication for pharmacotherapy. *Psychopharmacology (Berlin)*, **196**, 603–10.
121. Turner MR, Rabiner EA, Al-Chalabi A, et al. (2007). Cortical 5-HT1A receptor binding in patients with homozygous D90A SOD1 vs sporadic ALS. *Neurology*, **68**, 1233–5.
122. Turner MR, Cagnin A, Turkheimer FE, et al. (2004). Evidence of widespread cerebral microglial activation in amyotrophic lateral sclerosis: an [11C](R)-PK11195 positron emission tomography study. *Neurobiology of Disease*, **15**, 601–9.
123. Johansson A, Engler H, Blomquist G, et al. (2007). Evidence for astrocytosis in ALS demonstrated by [11C](L)-deprenyl-D2 PET. *Journal of the Neurological Sciences*, **255**, 17–22.
124. Takahashi H, Snow BJ, Bhatt MH, et al. (1993). Evidence for a dopaminergic deficit in sporadic amyotrophic lateral sclerosis on positron emission scanning. *Lancet*, **342**, 1016–8.
125. Konrad C, Henningsen H, Bremer J, et al. (2002). Pattern of cortical reorganization in amyotrophic lateral sclerosis: a functional magnetic resonance imaging study. *Experimental Brain Research*, **143**, 51–6.

126. Konrad C, Jansen A, Henningsen H, et al. (2006). Subcortical reorganization in amyotrophic lateral sclerosis. *Experimental Brain Research*, **172**, 361–9.
127. Schoenfeld MA, Tempelmann C, Gaul C, et al. (2005). Functional motor compensation in amyotrophic lateral sclerosis. *Journal of Neurology*, **252**, 944–52.
128. Stanton BR, Williams VC, Leigh PN, et al. (2007). Altered cortical activation during a motor task in ALS. Evidence for involvement of central pathways. *Journal of Neurology*, **254**, 1260–7.
129. Lule D, Diekmann V, Kassubek J, et al. (2007). Cortical plasticity in amyotrophic lateral sclerosis: motor imagery and function. *Neurorehabilitation and Neural Repair*, **21**, 518–26.
130. Cosottini M, Pesaresi I, Piazza S, et al. (2012). Structural and functional evaluation of cortical motor areas in Amyotrophic Lateral Sclerosis. *Experimental Neurology*, **234**, 169–80.
131. Tessitore A, Esposito F, Monsurro MR, et al. (2006). Subcortical motor plasticity in patients with sporadic ALS: An fMRI study. *Brain Research Bulletin*, **69**, 489–94.
132. Abrahams S, Goldstein LH, Simmons A, et al. (2004). Word retrieval in amyotrophic lateral sclerosis: a functional magnetic resonance imaging study. *Brain*, **127**, 1507–17.
133. Lule D, Diekmann V, Anders S, et al. (2007). Brain responses to emotional stimuli in patients with amyotrophic lateral sclerosis (ALS). *Journal of Neurology*, **254**, 519–27.
134. Palmieri A, Naccarato M, Abrahams S, et al. (2010). Right hemisphere dysfunction and emotional processing in ALS: an fMRI study. *Journal of Neurology*, **257**, 1970–8.
135. Mohammadi B, Kollewe K, Samii A, et al. (2009). Changes of resting state brain networks in amyotrophic lateral sclerosis. *Experimental Neurology*, **217**, 147–53.
136. Tedeschi G, Trojsi F, Tessitore A, et al. (2010). Interaction between aging and neurodegeneration in amyotrophic lateral sclerosis. *Neurobiology of Aging*, **33**, 886–98.
137. Jelsone-Swain LM, Fling BW, Seidler RD, et al. (2011). Reduced interhemispheric functional connectivity in the motor cortex during rest in limb-onset amyotrophic lateral sclerosis. *Frontiers in Systems Neuroscience*, **4**, 158.
138. Agosta F, Valsasina P, Absinta M, et al. (2011). Sensorimotor functional connectivity changes in amyotrophic lateral sclerosis. *Cerebral Cortex*, **21**, 2291–8.
139. Douaud G, Filippini N, Knight S, et al. (2011). Integration of structural and functional magnetic resonance imaging in amyotrophic lateral sclerosis. *Brain*, **134**, 3470–9.
140. Agosta F, Canu E, Valsasina P, et al. (2013). Divergent brain network connectivity in amyotrophic lateral sclerosis. *Neurobiology of Aging*, **34**, 419–27.
141. Terao S, Sobue G, Yasuda T, et al. (1995). Magnetic resonance imaging of the corticospinal tracts in amyotrophic lateral sclerosis. *Journal of the Neurological Sciences*, **133**, 66–72.
142. Valsasina P, Agosta F, Benedetti B, et al. (2007). Diffusion anisotropy of the cervical cord is strictly associated with disability in amyotrophic lateral sclerosis. *Journal of Neurology, Neurosurgery & Psychiatry*, **78**, 480–4.
143. Sperfeld AD, Bretschneider V, Flaith L, et al. (2005). MR-pathologic comparison of the upper spinal cord in different motor neuron diseases. *European Neurology*, **53**, 74–7.
144. Nair G, Carew JD, Usher S, et al. (2011). Diffusion tensor imaging reveals regional differences in the cervical spinal cord in amyotrophic lateral sclerosis. *NeuroImage*, **53**, 576–83.
145. Carew JD, Nair G, Pineda-Alonso N, et al. (2011). Magnetic resonance spectroscopy of the cervical cord in amyotrophic lateral sclerosis. *Amyotrophic Lateral Sclerosis*, **12**, 185–91.
146. Carew JD, Nair G, Andersen PM, et al. (2011). Presymptomatic spinal cord neurometabolic findings in SOD1-positive people at risk for familial ALS. *Neurology*, **77**, 1370–5.
147. Scuderi C, Fichera M, Calabrese G, et al. (2009). Posterior fossa abnormalities in hereditary spastic paraparesis with spastin mutations. *Journal of Neurology, Neurosurgery & Psychiatry*, **80**, 440–3.
148. Elleuch N, Depienne C, Benomar A, et al. (2006). Mutation analysis of the paraplegin gene (SPG7) in patients with hereditary spastic paraplegia. *Neurology*, **66**, 654–9.
149. Warnecke T, Duning T, Schwan A, et al. (2007). A novel form of autosomal recessive hereditary spastic paraplegia caused by a new SPG7 mutation. *Neurology*, **69**, 368–75.
150. Stevanin G, Santorelli FM, Azzedine H, et al. (2007). Mutations in SPG11, encoding spatacsin, are a major cause of spastic paraplegia with thin corpus callosum. *Nature Genetics*, **39**, 366–72.
151. Goizet C, Boukhris A, Maltete D, et al. (2009). SPG15 is the second most common cause of hereditary spastic paraplegia with thin corpus callosum. *Neurology*, **73**, 1111–9.
152. Stevanin G, Azzedine H, Denora P, et al. (2008). Mutations in SPG11 are frequent in autosomal recessive spastic paraplegia with thin corpus callosum, cognitive decline and lower motor neuron degeneration. *Brain*, **131**, 772–84.
153. Riverol M, Samaranch L, Pascual B, et al. (2009). Forceps minor region signal abnormality 'ears of the lynx': an early MRI finding in spastic paraparesis with thin corpus callosum and mutations in the spatacsin gene (SPG11) on chromosome 15. *Journal of Neuroimaging*, **19**, 52–60.
154. Battini R, Bianchi MC, Boespflug-Tanguy O, et al. (2003). Unusual clinical and magnetic resonance imaging findings in a family with proteolipid protein gene mutation. *Archives of Neurology*, **60**, 268–72.
155. Sperfeld AD, Baumgartner A, and Kassubek J. (2005). Magnetic resonance investigation of the upper spinal cord in pure and complicated hereditary spastic paraparesis. *European Neurology*, **54**, 181–5.
156. Kassubek J, Juengling FD, Baumgartner A, et al. (2007). Different regional brain volume loss in pure and complicated hereditary spastic paraparesis: a voxel-based morphometric study. *Amyotrophic Lateral Sclerosis* , **8**, 328–36.
157. Duning T, Warnecke T, Schirmacher A, et al. (2010). Specific pattern of early white-matter changes in pure hereditary spastic paraplegia. *Movement Disorders*, **25**, 1986–92.
158. Franca MC, Jr., Yasuda CL, Pereira FR, et al. (2012). White and grey matter abnormalities in patients with SPG11 mutations. *Journal of Neurology, Neurosurgery & Psychiatry*, **83**, 828–33.
159. Stromillo ML, Malandrini A, Dotti MT, et al. (2011). Structural and metabolic damage in brains of patients with SPG11-related spastic paraplegia as detected by quantitative MRI. *Journal of Neurology*, **258**, 2240–7.
160. Turner MR, Grosskreutz J, Kassubek J, et al. (2011). Towards a neuroimaging biomarker for amyotrophic lateral sclerosis. *Lancet Neurology*, **10**, 400–3.

CHAPTER 24

Cerebellar ataxia and related disorders

Mario Mascalchi and Alessandra Vella

Introduction

Ataxia from the Greek a-taxis, namely lack of order, can be defined as an inability to coordinate voluntary muscle movements that is not due to weakness or involuntary muscle activity [1].

Classifications of ataxias are multiple, variably complex, and overlapping. The distinction between ataxias with an acute course, in which symptoms and signs appear suddenly or within a few days, and ataxias with a chronic, usually progressive, course, also termed degenerative ataxias, is the most useful for the purpose of illustrating the imaging features of these conditions (Table 24.1).

Ataxia with onset in childhood has peculiar features, since it can be associated with malformation of the cerebellum and the brainstem in cases of congenital ataxia or with tumours of the posterior cranial fossa and metabolic disorders in cases of acquired syndrome. A further distinction between inherited and sporadic ataxia can be adopted, but this classification has practical limitations, since several inherited conditions also present as sporadic disease, notably the recessively inherited ataxias and those that are X-linked [2,3]. Moreover, many inherited and sporadic conditions share the same imaging findings.

Patients with ataxia can be examined with several imaging modalities, but magnetic resonance imaging (MRI) is now the fundamental examination. This chapter reviews MRI findings in the most common ataxias and in those rare ataxias for which MRI can provide a valuable hint to the diagnosis. Also the contribution of magnetic resonance spectroscopy (MRS) and nuclear medicine techniques, including single photon emission computed tomography (SPECT) and positron emission tomography (PET) to the evaluation of patients with ataxia, that was reviewed in detail elsewhere [3,4], will be summarized.

In contrast, the imaging features of primary tumours or metastasis of the cerebellum or brainstem in children and adults are not discussed here [5,6]. As well prenatal ultrasounds and MRI of foetal cerebellar and brainstem abnormalities are not reviewed here [7].

Magnetic resonance imaging and magnetic resonance spectroscopy

MRI enables an optimal visualization of the cerebellum, brainstem and spinal cord which are the elective sites of damage in ataxic diseases, without the hazards of ionizing radiations.

While large amounts of data were obtained with conventional MRI, more technically and methodologically demanding techniques such as diffusion tensor imaging (DTI) and functional MRI (fMRI) are being increasingly used for characterization of the tissue microstructural changes and brain physiopathology in patients with ataxias. Moreover, proton MRS can be utilized to investigate the biochemical abnormalities associated to ataxia conditions.

Visual assessment of T_1- and T_2-weighted spin echo and diffusion-weighted (DWI) echo planar images, supplemented by IV contrast administration and, where an ischaemic insult is suspected, magnetic resonance angiography (MRA), is usually sufficient for the diagnostic work-up of patients presenting with acute ataxia.

In patients with chronic ataxia, contrast administration and MRA are generally not required, and diagnosis can often be achieved or suspected based on T_1- and T_2-weighted spin echo images. These must take into consideration the variable combination and distribution of visually appreciable changes of sizes, and signal intensity in the brainstem, cerebellum, spinal cord, and, occasionally, supratentorial brain. However, high-resolution gradient echo T_1-weighted images are recommended in these patients since they enable multiplanar reconstruction, which can help in delineation of malformations of the brainstem and cerebellum in congenital ataxia, and the three main atrophy patterns observed in chronic ataxias (see 'Chronic ataxias'. Moreover, in the latter conditions, high-resolution gradient echo T_1-weighted images are preferable for determination of bi-dimensional or volume morphometric measurements [7–11] and are essential for more complex analyses as volumetry or voxel-based morphometry (VBM) or tensor-based morphometry (TBM) that are potentially useful for characterizing the pattern of atrophy of each disease [12–21] and monitoring disease progression [22,23]. For the same purposes, DTI is preferable to DWI, since is allows a more sensitive analysis of the microstructural damage of the remaining nervous tissue, generally in terms of increased mean diffusivity (MD) and decreased fractional anisotropy (FA) [24] or decreased mode of the diffusion tensor [25]. A variety of approaches including region-of-interest (ROI) [24, 26–30], histograms of large regions or volumes of the brain [26,30], tract-based spatial statistics (TBSS) [16,17,25], and tractography [31–33] can be used to analyse the DTI maps.

The exact role of fMRI in patients with ataxias is uncertain. It was used to investigate the physiopathology of inherited chronic ataxias with assessment of brain activation patterns during the execution of motor tasks [34–36] and to evaluate the effects of therapy in a pilot study in patients with ataxia telangiectasia [37]. In consideration of the disability that often precludes a correct execution of motor

Table 24.1 Classification of the most common ataxias

Acute ataxias
Alcohol consumption
Cerebrovascular insult (ischaemic or haemorrhagic)
Drugs (anticonvulsivants, antineoplastics, lithium, amiodarone, diphenoxylate-atropine, cyclosporine, bismuth, bromides, mefloquine, isoniazid, lindane, perhexyline maleate, cimetidine, cocaine, heroin)
Toxic agents (heavy metals, insecticides and herbicides, eucalyptus oil, nicotine, cyanide, toluene/benzene derivatives, carbon monoxide)
Electrolyte disturbances (hyponatraemia hypocalcaemia, hypomagnesaemia)
Cerebellitis
Bickerstaff 's encephalitis
Infections:
Rhomboencephalitis,
Basal meningitis,
Tuberculoma,
Abscess,
Creutzfeldt–Jakob disease
Wernicke's encephalopathy (vitamin 1 deficiency)
Decompensation of inborn errors of metabolism
Chronic ataxias
Inherited ataxias
Autosomal recessive ataxias
Joubert syndrome and related disorders
Friedreich's ataxia
Vitamin E deficiency
Ataxia telangectasia
Cerebellar ataxia with oculomotor apraxia 1,2
Autosomal Recessive Spastic Ataxia of Charlevoix–Saguenay
Cerebrotendineous xanthomatosis
Niemann–Pick type C
Early onset cerebellar ataxia with retained tendon reflexes
Childhood ataxia with CNS hypomyelination/vanishing white matter
Autosomal recessive cerebellar ataxia type 1 and 2
Marinesco–Sjögren syndrome
Leukodystrophies
Inborn errors of metabolism
Autosomal dominant ataxias
Spinocerebellar ataxia
Episodic ataxia type 1-7
Dentatorubral-pallido luysian atrophy (DRPLA)
Familial hemiplegic migraine with progressive cerebellar ataxia
Leukodystrophies
X-linked ataxias
Fragile X premutation syndrome
Adrenoleukodystrophy
Sporadic ataxias
Known causes
Alcoholic cerebellar degeneration
Toxic agents (methylmercury poisoning)
Paraneoplastic cerebellar degeneration
Immune-mediated ataxias
Gluten ataxia
Anti-GAD associated ataxia
Siderosis of the CNS
Chronic lymphocytic inflammation with perivascular pontine enhancement responsive to steroids (CLIPPERS)
Acquired vitamin E deficiency
Gerstmann–Straussler–Scheinken disease
Idiopathic
Sporadic adult onset ataxia
Multi-system atrophy—cerebellar type (MSA-C)

tasks by patients with ataxia, it is predicted that resting state fMRI would provide a major contribution to the investigation of physiopathology and possibly the effects of therapy in ataxias, but so far only three studies have been published with this technique [38–40].

Single voxel proton and, more rarely, phosphorus MRS have been applied to the investigation of patients with acute and especially chronic ataxias for almost 20 years [4]. Proton MRS can reveal abnormalities in the brainstem, cerebellum, and cerebral hemispheres, generally in terms of decreased ratios between the neuronal marker N-acetyl aspartate (NAA) and creatine (Cr), between the marker of membrane turnover choline (Cho) and Cr, and of increased ratio between the glial marker myo-inositol (mIns) and Cr, which are correlated with severity of the clinical deficit [3,4,41–49]. In a few, very rare metabolic ataxias of children proton MRS can demonstrate specific or characteristic abnormalities [7]. Moreover proton MRS at 3 T or above, by exploiting the improved definition of the neurochemical profiles with determination of the concentration of 10–15 metabolites, can assist in the differential diagnosis of apparently sporadic chronic ataxias in adults [49].

Despite its potentials, especially as progression and surrogate biomarker in degenerative ataxias, limitations of MRS include long acquisition time with three single voxel acquisitions requiring about 1 hour, the relatively low spatial resolution, the non-specificity of the most common findings, need of cerebrospinal fluid (CSF) correction for computation of metabolite concentration, and the imperfect interscanner reproducibility.

Single photon emission computed tomography and positron emission tomography

Nuclear medicine brain investigations are utilized in the diagnostic work-up of patients with ataxias in only a few conditions, including cerebellitis, paraneoplastic cerebellar degeneration and multi-system atrophy (MSA)(see below). Moreover they can provide interesting information on the complex pathophysiology of the ataxic diseases [4,50–53].

Three categories of photon emission tracers are employed to investigate patients with acute or chronic ataxias, including blood flow tracers, and tracers of dopamine transporter (DaT-imaging) and dopamine D2 receptors in the basal ganglia.

The majority of PET studies in patients with ataxia have employed the tracer of glucose metabolism [^{18}F]-fluoro-2-deoxy-D-glucose (FDG), which reveals regional hypometabolism with a variable distribution in patients with different types of ataxias. Positron emission tracers are also available to investigate nigro-striatal projections and dopamine D2 receptors.

Acute ataxias

MRI has a significant role in establishing the diagnosis of some causes of acute ataxia. MRI findings in children and adults are essentially the same.

Infarct and haemorrhage

Unenhanced computed tomography (CT) is still the imaging modality of choice for the evaluation of the patient with acute stroke, since it readily demonstrates intra- or extra-axial haemorrhage as hyperdensity. MRI is generally performed when the CT is negative. It can demonstrate brainstem and cerebellar infarcts as areas of decreased diffusion on DWI within a few hours following the clinical onset and, later, of increased signal intensity on T_2-weighted images (Fig.24.1).

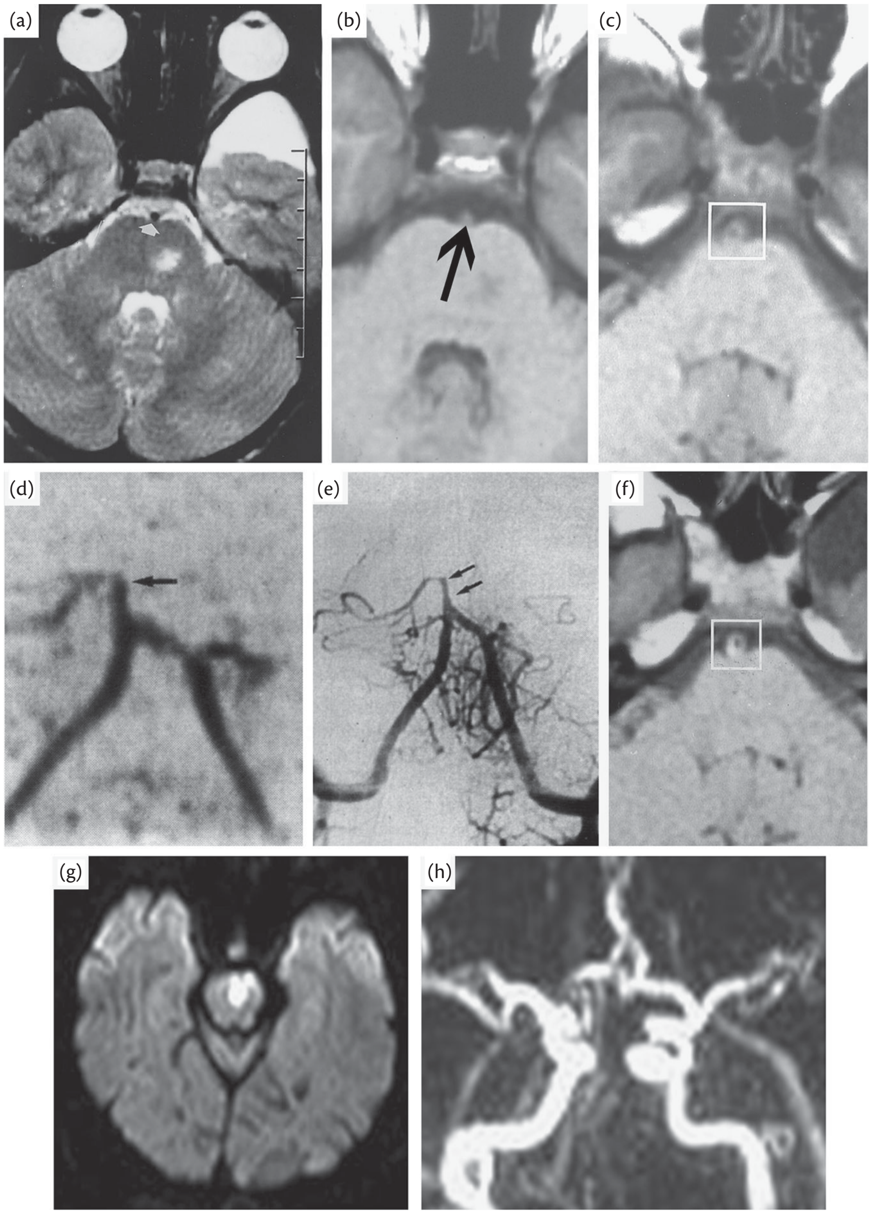

Fig. 24.1 (a–h) MRI of vertebrobasilar infarcts. (a–f) Acute pontine infarct due to dissection of the basilar artery in 10-year-old boy. MRI shows a small area of high signal in the left pons in axial T_2-weighted image (a). The basilar artery shows normal flow void in (a), but abnormal intermediate signal intensity on the axial T_1-weighted image consistent with occlusion (b, arrow). Thickening of the vascular wall of intermediate signal on the axial T_1-weighted image, proximal to the occlusion, is observed in (c) (square). Lack of basilar artery flow (arrow) is revealed in a coronal reconstruction of MRA (d), which is also seen in digital subtraction arteriography AP projection (e, arrows). Two days later the thickening of the basilar artery wall proximal to the occlusion shows high signal intensity in axial T_1-weighted image (f, square), consistent with methaemoglobin formation in the wall of the vessel consistent with arterial dissection. (g–h) Diagnosis with MR of basilar occlusion in a 62-year-old woman. Axial diffusion weighted image (g) demonstrates an area of high signal consistent with decreased diffusion and acute ischaemia in the basis pontis. Coronal reconstruction of MRA (h) shows complete lack of flow signal in the basilar artery consistent with occlusion.

Reproduced from Scazzeri F, et al. (1997). MRI and MR angiography of basilar artery dissection in a child. *Neuroradiology*, **39**, 654–7. Copyright (1997), with permission from Springer.

The combination of MRI and MRA demonstrating possible flow and vascular wall abnormalities in the vertebrobasilar arteries represents the standard of reference for evaluation of stroke in the posterior circulation territories (Fig. 24.1). In children, MRI is sometimes performed without prior CT, and diagnosis of haemorrhage can be difficult and requires acquisition of T_2*-weighted gradient echo images to identify susceptibility effects due to the presence of haemoglobin by-products in the clot.

MRS and nuclear medicine brain imaging have no role in the diagnostic assessment of patients with acute ataxia due to stroke.

Drugs and toxic agents

Acute ataxia can occur after administration of several drugs including phenytoin, lithium, amiodarone, diphenoxylate-atropine, cystostatics 5-fluorouracil, and cytosine arabinoside, as well as after poisoning with heavy metals, such as mercury and thallium (Table 24.1). Additional causes of acute ataxia following intoxication include methanol, methadone, and methyl bromide (Table 24.1). Generally, MRI after acute drug intoxication or poisoning can demonstrate a non-specific pattern of cortical cerebellar atrophy variably combined with symmetric high signal intensity of the subcortical white matter of the cerebellar hemispheres and dentate nuclei, as well as signal changes in other parts of the brain [54–57].

Electrolyte disturbances

Ataxia with subacute onset has rarely been described in patients with hyponatraemia and hypocalcaemia [58,59]. MRI shows cerebellar atrophy. In hypomagnesaemia a condition observed on the background of intestinal malabsorption, reversible T_2 signal hyperintensity, and diffusion restriction of the cerebellar folia were reported [60,61].

Cerebellitis

Acute cerebellar damage can develop after an infectious, usually viral, illness in children and young adults. The pathophysiology of this condition, termed cerebellitis, has not been established yet, but direct viral invasion of the cerebellum or an autoimmune response are two possible mechanisms. Clinical features are variable, but in the child cerebellitis can underlie mutism or even have a pseudo-tumoural presentation. Conventional MRI can demonstrate symmetric or unilateral areas of increased signal on T_2-weighted images in the cerebellar cortex and underlying white matter (Fig. 24.2) [62], variably combined with non-specific leptomeningeal contrast enhancement [63].

Proton MRS shows decreased NAA/Cr in the cerebellum [62]. However, both conventional MRI and MRS findings are not sensitive appearing only several days after onset. Since prompt diagnosis is important in consideration of the potential fatal outcome associated with obstructive hydrocephalus or herniation in the foramen magnum, some reports have emphasized the contribute of DWI to the early diagnosis of cerebellitis [63,64]. In fact, DWI shows marked hyperintensity of the dentate nuclei as early as 1 day after onset with extension of the areas of decreased diffusion to the vermis and cerebellar hemispheres in the following days (Fig. 24.2). The contribution of perfusion SPECT examination to the early diagnosis of cerebellitis has been purported by several studies, which demonstrated areas of hyper- or hypoperfusion in the cerebellum [4].

Bickerstaff's encephalitis

Bickerstaff's encephalitis often develops after infections and shares some features with Miller Fisher syndrome (a variant of acute inflammatory demyelinating polyradiculoneuropathy, i.e. Guillain–Barré syndrome). It is characterized by progressive ophthalmoplegia and ataxia, disturbed consciousness and hyperreflexia. In about one-third of the patients, MRI shows high intensity on T_2-weighted images and swelling of the brainstem, thalamus, cerebral white matter, and cerebellum [65]. Contrast enhancement can be absent [66]. Diagnosis is supported by demonstration in the serum of anti-GQ1b antibodies, increased cell count, and protein in the CSF and predominantly axonal motor dysfunction at nerve conduction studies.

Rhombencephalitis

The term rhombencephalitis applies to an inflammatory syndrome of the brainstem and cerebellum caused by viral or bacterial infections, most commonly by *Listeria monocytogenes* [67]. MRI typically demonstrates high-signal lesions on proton density, T_2-weighted, and FLAIR images with variable nodular or ring contrast enhancement [68]. Diagnosis is achieved by isolation of the

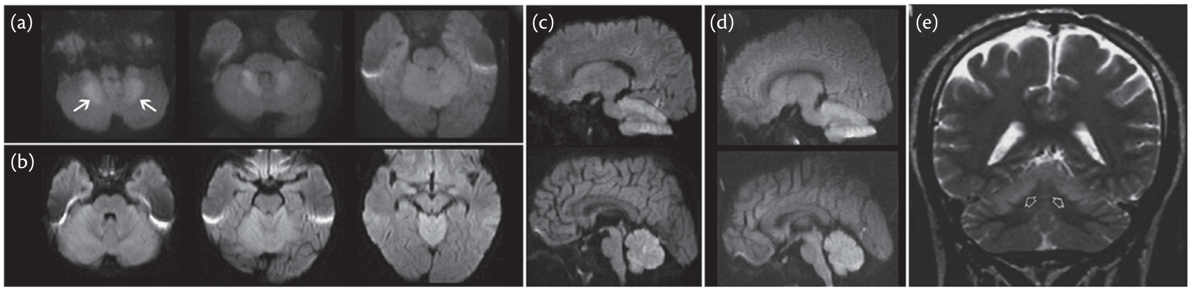

Fig. 24.2 (a–e). MRI of cerebellitis. (a–d) Serial axial (a,b) and sagittal (c,d) diffusion-weighted images in a case of rotavirus-associated cerebellitis in a 38-month-old boy obtained on days 1 (a), 3 (b), 9 (c), and 15 (d) after clinical onset. The initial marked hyperintensity in the bilateral dentate nucleus (arrows in a) is followed by diffuse hyperintensity in the vermis and cerebellar hemisphere in b–d). (e) Coronal T_2-weighted MRI in a case of cerebellitis of unknown cause in a 36-year-old man shows a mild symmetric hyperintensity in the cortical-subcortical junction in the superior vermis and paravermian regions (arrows) 7 days after clinical onset

Reproduced from (a–d) Kubota T, et al. (2011). Chronological diffusion-weighted imaging changes and mutism in the course of rotavirus-associated acute cerebellitis/cerebellopathy concurrent with encephalitis/encephalopathy. *Brain & Development*, **33**, 21–7. Copyright (2011), with permission from Elsevier. (e) Guerrini L, et al. (2002). Proton MRS of cerebellitis. *Magnetic Resonance Imaging*, **20**, 619–22. Copyright (2002), with permission from Elsevier.

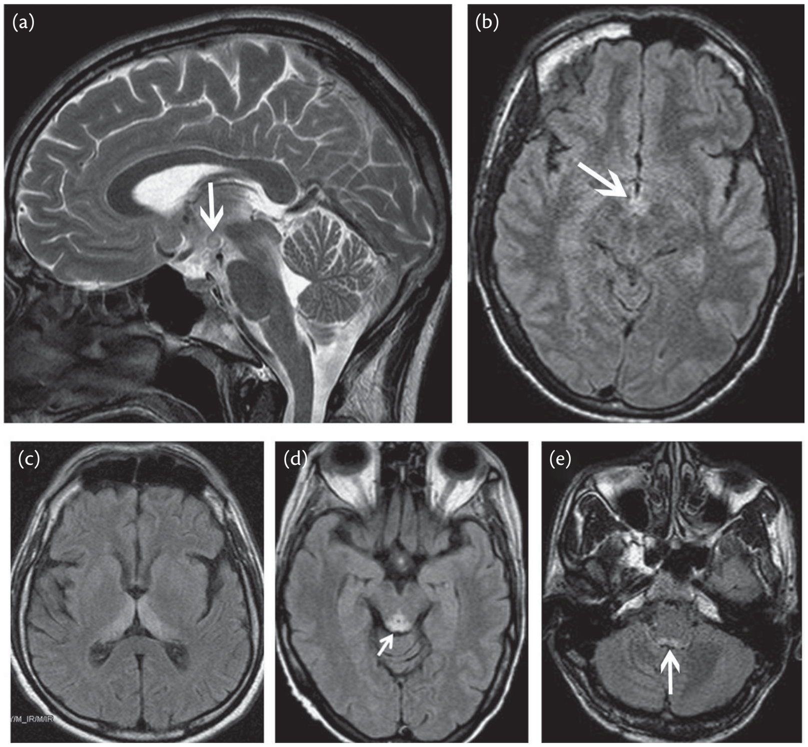

Fig. 24.3 (a–e). MRI of Wernicke encephalopathy in a 56-year-old man with background of alcoholism. Sagittal T_2-weighted image (a) and axial FLAIR image (b) demonstrate high signal intensity in the mammillary bodies (arrows). Other cases (c–e) exemplify the areas typically exhibiting symmetrically increased signal on axial T_2 and FLAIR images in Wernicke encephalopathy, including the medial thalami (c), midbrain tectum and peri-acqueductal gray matter (arrow in d), and posterior medulla (arrow in e).

infective agents in blood and CSF cultures. Prognosis is poor, with high mortality and residual morbidity, but differs among the various aetiologies.

Wernicke's encephalopathy

Wernicke encephalopathy is due to thiamine (vitamin B1) deficiency and is characterized by the clinical triad of acute ataxia, oculomotor disturbances, and confusional state. It can develop on the background of alcoholism or follow malabsorption, hyperemesis gravidarum, chemotherapy and severe malnutrition caused by prolonged voluntary starvation or anorexia nervosa. Failure to recognize Wernicke encephalopathy can be fatal, but the clinical symptoms are non-specific. Hence, MRI has an important role in the diagnosis by revealing symmetric areas of high signal on proton density and T_2-weighted images which are typically localized in the medial thalami, mammillary bodies, and peri-aqueductal white matter and are better visible on FLAIR images (Fig. 24.3) [69].

Other less common sites of signal change include the dorsal medulla (Fig. 24.3), tectal plate, the basal ganglia and the frontal and sensorimotor cortices [70,71]. Contrast enhancement is variable and usually associated with alcohol abuse [70,71]. The role of DWI for the diagnosis of Wernicke encephalopathy is not established yet.

In two patients examined in the acute phase of Wernicke encephalopathy proton MRS showed decreased NAA/Cr without lactate in the thalami [72]. The biochemical abnormalities cleared together with clinical improvement after the administration of thiamine. A PET study documented increased cerebellar glucose metabolism in the acute phase of Wernicke encephalopathy, which subsequently decreased with recovery of cerebellar function in two patients [73].

Acute decompensation of inborn error of metabolism

In children, acute ataxia may be associated with exacerbation of mitochondrial disorders, organic aciduria, or urea cycle disorders. Although the diagnosis of these uncommon and often inherited conditions rests completely on biochemical and genetic testing, once ischaemic, inflammatory, or toxic causes are excluded, MRI may suggest such a diagnostic possibility by revealing symmetric areas of increased signal on T_2-weighted images or decreased diffusion (Fig. 24.4) [74].

Other causes of acute ataxias in which MRI can have a central role for the diagnosis include multiple sclerosis and infections of the posterior cranial fossa determining meningitis, and abscess or tuberculoma formation.

Chronic ataxias

The terms chronic or degenerative ataxias are used for some ataxias with childhood onset and a progressive course, and for all progressive ataxias of adulthood.

In chronic ataxias, conventional MRI demonstrates three main patterns of atrophy, named spinal atrophy (SA), cortical cerebellar atrophy (CCA) and pontocerebellar atrophy (PtCA), which can be associated with symmetric signal changes of the brainstem, cerebellum, spinal cord, or cerebral hemispheres. The atrophy patterns are better seen on T_1-weighted spin echo or high-resolution 3D gradient echo images in which the high signal intensity of CNS

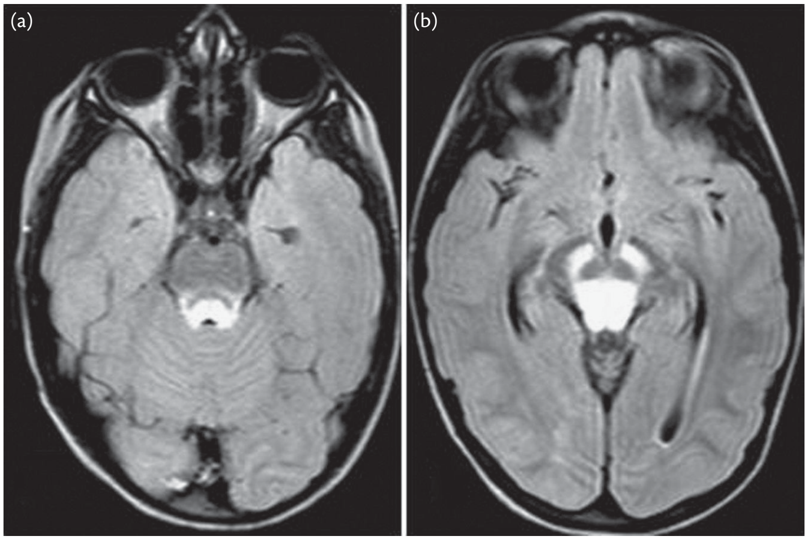

Fig. 24.4 (a,b) MRI of Leigh syndrome in a 4-year-old boy presenting with ataxia, nystagmus and gaze palsy. Axial FLAIR images demonstrate symmetric high signal intensity in the peri-aqueductal gray matter, superior cerebellar peduncles (a), tectum, and substantia nigra (b) with sparing of the red nucleus. The upper midbrain is swollen (b).

structures stands out on the background of the very low signal from the CSF.

In SA, in which the neurons of the sensory ganglion of the spinal nerves and of the Clark columns in the spinal gray matter are predominantly affected, MRI shows atrophy of the spinal cord extending to the medulla with a slight widening of the fourth ventricle without overt loss of bulk of the cerebellum and cerebral hemispheres (Fig. 24.5).

In CCA, in which the damage of the Purkinje cells of the cerebellar cortex is largely predominant, MRI demonstrates atrophy of the cerebellum with widening of the cerebellar sulci and of the fourth ventricle (Fig. 24.6). The volume of the brainstem and spinal cord is normal. No abnormality in the supratentorial compartment is generally observed.

The MRI features of PtCA , in which there is predominant damage to the pontine gray nuclei, include characteristic atrophy of the lower portion of the basis pontis, medulla, inferior, and middle cerebellar peduncles, cerebellar hemispheres, and vermis (Fig. 24.7). There is a widening of the IV ventricle, but supratentorial atrophic changes are variable. Although this pattern was initially labelled as olivo-PtCA, pathological, and imaging data have demonstrated that the inferior olives are substantially spared.

The relationship among the macroscopic pattern of atrophy demonstrated by MRI and the aetiologies of chronic ataxias is summarized in Table 24.2.

This represents a valuable step in the diagnostic algorithm of chronic ataxia at an individual patient level.

As anticipated, the three main patterns of atrophy can be appreciated visually on MRI [75–77], but in the not-advanced cases, the application of morphometric (linear, surface or volume) measurements of structures of interest is essential [8]. VBM or TBM represent alternative or complementary approaches to volumetry for investigation of brain volume changes in homogeneous groups of subjects. VBM has been applied to the investigation of brain structural changes in several chronic ataxias to delineate the diseases pattern of atrophy as compared with control subjects, as well as to

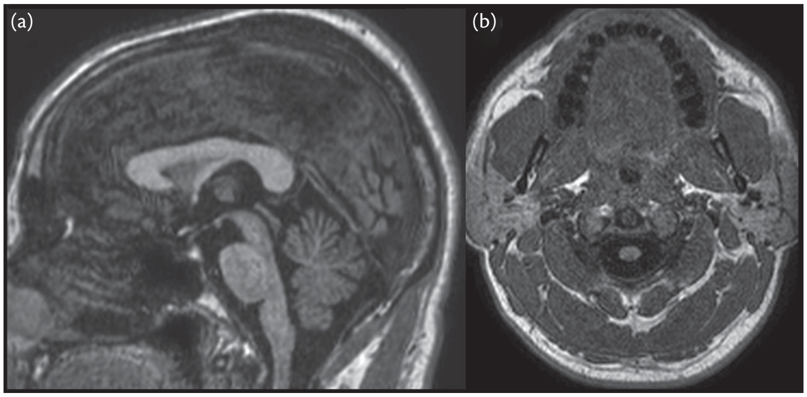

Fig. 24.5 (a,b). MRI in an 18-year-old woman with Friedreich ataxia showing the typical features of spinal atrophy. Sagittal 3D T_1-weighted gradient echo image (a) shows normal volume of the pons and cerebellar vermis but thinning of the upper cervical spinal cord. Axial reconstruction of the 3D data set (b) confirms that the anterior-posterior diameter of the cervical spinal cord at C2 is reduced and shows corresponding widening of the perimedullary CSF spaces.

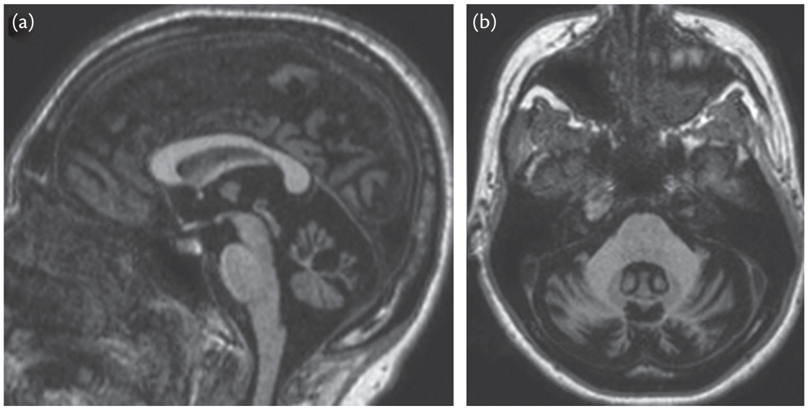

Fig. 24.6 (a,b) MRI in a 48-year-old man with sporadic adult onset ataxia showing the typical features of cortical cerebellar atrophy. The sagittal 3D T_1-weighted gradient echo image (a) shows atrophy of the vermis with normal volume of the pons and of the cervical spinal cord. Axial reconstruction of the 3D data set (b) confirms severe atrophy of the cerebellar vermis with normal volume of the pons. It also shows atrophy of cerebellar hemispheres with normal size of the middle cerebellar peduncles.

explore the correlation between clinical and genetic findings, and the distribution and severity of regional volume [12–17,19–21], and more recently the regional progression of atrophy [18,23]. For the latter purpose TBM was also recently used [22].

In some chronic ataxias, the morphometry changes are frequently associated with characteristic, usually symmetric areas of increased or decreased signal intensity on T_2- or T_2*-weighted MR images (see below).

Ataxias with childhood onset

A distinction of chronic cerebellar ataxias with childhood onset based on MRI findings, showing malformative or degenerative changes often involving the brainstem, has recently been proposed [74].

The malformative pattern

Cerebellar ataxias with childhood onset showing a malformative pattern on MRI are typically congenital ataxias with a stable, non-progressive course. Their clinical counterpart is extremely variable from complex and severe conditions, in which the cerebellar deficit is often overwhelmed by additional clinical features due to supratentorial malformative changes, to subtle and often overlooked impairment, when isolated. The most common hindbrain malformations include localized or generalized cerebellar hypoplasia (small cerebellum with fissures of normal size compared with the folia), and cerebellar dysplasia (abnormal folial pattern or the presence of heterotopic nodules of gray matter, often associated with abnormalities of the cerebral cortical development). The best characterized dysplastic variant of isolated hindbrain malformation is the Jourbert syndrome and related disorders [7]. The term comprises a number of conditions with autosomal recessive inheritance, sharing abnormal function of the primary cilia (ciliopathies). These are specialized membrane-bound structures projecting from the neuron and ependyma surface and serving many functions in development of the brain, kidneys, and eyes. Patients with Joubert syndrome present with hypotonia, oculomotor apraxia, facial dysmorphism, irregular neonatal breathing, and cognitive deficits, and show small dysmorphic vermis and midbrain, a thin midbrain-pons junction, a triangular-shaped IV ventricle, and the distinctive 'molar tooth' sign on axial MR images due to enlarged superior cerebellar peduncles (Fig. 24.8).

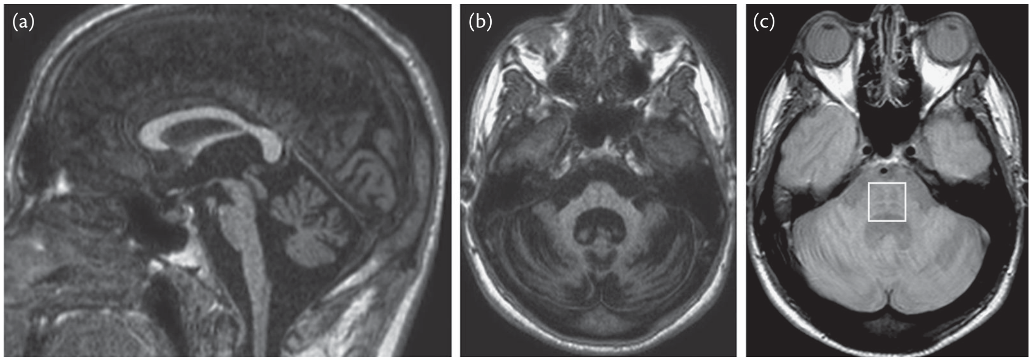

Fig. 24.7 (a–c). MRI in a 36-year-old woman with spinocerebellar ataxia type 2 showing the typical features of ponto-cerebellar atrophy. The sagittal 3D T_1-weighted gradient echo image (a) shows atrophy of the brainstem, more pronounced in the inferior portion of the basis pontis, and of the vermis. The axial reconstruction of the 3D data set (b) confirms severe atrophy of the pons and reveals the decreased size of the middle cerebellar peduncles and of the cerebellar hemispheres. The axial proton density-weighted image (c) shows a diffusely and mild increase of the signal intensity of the white matter of the pons, middle cerebellar peduncels and cerebellar white matter with sparing of the corticospinal tracts in the central portion of basis pontis featuring the 'hot cross bun' sign (white box).

Table 24.2 MR imaging-aetiological correlation in chronic ataxias

SA	CCA	PtCA
FRDA	AT	DRPLA
AVED	AOA1-2	EOCA
	EA-2	MSA-C
	EOCA	SCA1
	Gluten ataxia	SCA2
	SAOA	SCA3
	SCA4	SCA7
	SCA5	SCA13
	SCA6	
	SCA8	
	SCA10	
	SCA12	
	SCA14	
	SCA15	
	SCA16	
	SCA17	
	SCA18	
	SCA19	
	SCA21	
	SCA22	
	SCA25	

AOA = ataxia oculomotor ataxia; AVED = ataxia with vitamin E deficiency; AT = ataxia telangectasia; CCA = corticocerebellar atrophy; DRPLA = dentato-rubro-paliido-luysian atrophy; EA-2 = episodic ataxia type 2; EOCA = early onset cerebellar ataxia with retained tendon reflexes; FRDA = Friedreich ataxia; MSA-C= multiple systema atrophy- cerebellar type; PtCA = pontocerebellar atrophy; SA = spinal atrophy; SAOA = sporadic adult onset ataxia; SCA = spinocerebellar ataxia.

The degenerative pattern

Childhood ataxias with a degenerative pattern show a progressive clinical course and typically exhibit a SA or CCA pattern. The SA patters is characteristic of Friedreich ataxia (FRDA) (Fig. 24.5), the most common inherited ataxia (see below), whereas the CCA pattern (Fig. 24.6) corresponds to other inherited ataxias including ataxia telangectasia (AT) and ataxia oculomotor apraxia (AOA) (see below and Table 24.2) and to the former clinical category of early onset cerebellar ataxia (EOCA) with retained tendon reflexes, whose genetic causes are being increasingly discovered [78–80]. Moreover, a CCA pattern of variable severity may be observed in children with metabolic diseases presenting with ataxia. These include leukodistrophies, alteration of amino acids, lysosomal, peroxysomal, and glicosilation metabolism, urea cycle, lactic acidosis, and mitochondropathie [7]. In these cases, however, overt abnormalities in terms of hypomyelination or altered signal changes are usually present in the white matter and gray matter of the cerebral hemispheres and cerebellum [7,74]. Notably, in several of these very rare conditions proton MRS can usefully complement MRI to orientate the diagnosis in the single patient [7]. For instance, a lactate peak at 1.33 ppm is observed in mitochondropathies and in neuronal ceroid lipofuscinosis, a galacticol peak at 3.67/3.74 ppm in galactosaemia type 1, a phenylalanine at 7.37 ppm in phenylketonuria, branched-chain amino acids and ketoacids at 0.9 ppm in maple syrup urine disease, whereas NAA is abnormally increased in Canavan's disease.

For the sake of schematism, several inherited degenerative ataxias with possible onset in childhood or adolescence will be treated in the section 'Ataxias with later onset', once subdivided according to the type of inheritance.

Ataxias with later onset

Usually chronic ataxias with onset after childhood are subclassified as inherited and sporadic, and the former according to the type of inheritance (Table 24.1).

Recessive inherited ataxias

This is a very heterogenous group of diseases for which several characteristic or pathognomonic laboratory, and neurophysiological findings can help in the differential diagnosis [80].

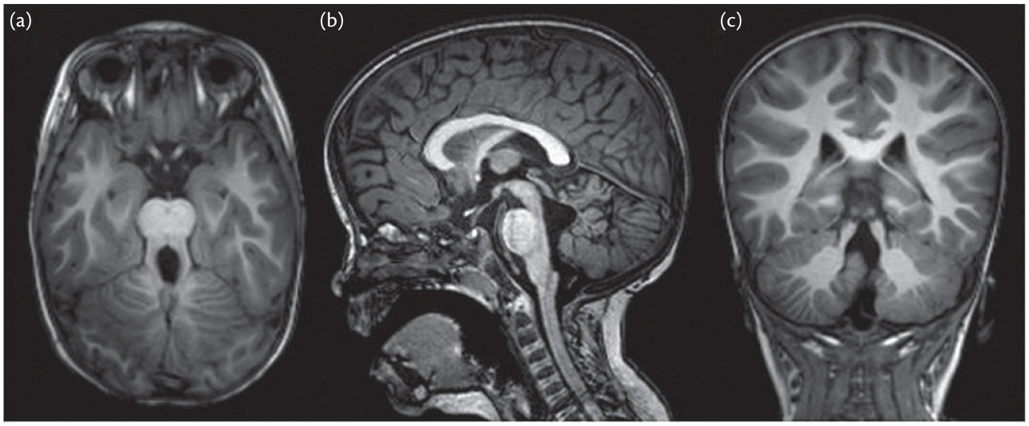

Fig. 24.8 (a–c) MRI in a 3-year-old girl with delayed psychomotor development and macrocephalia showing dysgenesis of the hindbrain in Joubert syndrome. Axial T_1-weighted gradient echo image (a) shows thickened superior cerebellar peduncles featuring the characteristic 'molar tooth' sign and abnormally thin cerebellar folia. Sagittal T_1-weighted gradient echo image (b) confirm the severe dysmorphism of the superior vermis. Coronal T_1-weighted gradient echo (c) displays the abnormally thickened superior cerebellar peduncles.

Friedreich's ataxia

FRDA is the most common inherited ataxia and is commonly due to an expanded GAA trinucleotide repeat in both the alleles of a gene encoding a mitochondrial protein named 'frataxin'. A late onset (after 25 years of age) variant of FRDA is recognized, which is associated with a smaller GAA expansion. Although deep tendon reflexes are characteristically lost in FRDA, a variant of FRDA with retained reflexes exists. Pathological hallmark of FRDA is neuronal loss and shrinkage of the spinal ganglion cells, and Clarke column of the spinal cord with degeneration of peripheral nerves, and spinocerebellar gracilis and cuneatus tracts [81]. The cerebellar cortex is spared, whereas there is cell loss in the dentate nuclei and gliosis of the cerebellar white matter. Cerebral cortical gray matter abnormalities are usually limited to the primary motor cortex, although damage to the visual cortex can occur. Hypertrophic cardiomyopathy is often a cause of death in advanced phases. MRI reveals a SA pattern (Fig. 24.5) [8,82,83] and symmetric signal changes in the posterior and lateral columns of the cervical spinal cord [82]. Atrophy of the cerebellar or cerebral cortical gray matter in FRDA is not remarkable and usually late [8,16], whereas volume loss of the deep cerebellar white matter, which correlates with severity of the clinical deficits, was reported [16]. Atrophy of the posterior cyngulate gyrus, paracentral lobule, and middle frontal gyrus was also reported in a VBM study [84]. Recent morphometry and DTI studies have documented atrophy and microstructural changes of the superior cerebellar peduncles, containing the main efferent fibres of the dentate nuclei, which closely correlates with the severity of the neurological deficits [10,16,85]. Moreover, a recent tractography study demonstrated correlation between microstructural damage in the dentate-rubral, dentate-thalamic and thalamocortical white matter fibres and cognitive profile in FRDA [33]. Other brain white matter tracts showing microstructual damage on DWI or DTI in FRDA include inferior cerebellar peduncles, corticospinal tracts in the internal capsule and pyramis, and optic radiations [16,30]. An abnormally increased T_2* relaxation rate assumed to reflect increased iron content was reported in the dentate nuclei [86,87]. A mixed activation pattern of the brain was documented during motor tasks in FRDA patients [36]. Right hand tapping and writing of the '8' revealed areas of significantly lower activation in the left primary sensory-motor cortex, thalamus, and dorsolateral prefrontal cortex and right cerebellum, compared with healthy control subjects. These hypoactive areas were associated with hyperactive areas in the right parietal and precentral cortex, globus pallidus, and putamen during execution of the more demanding task, namely the writing of the '8'. The decreased activation of the primary motor cortex and cerebellum might reflect a regional neuronal damage, the decreased activation of the left thalamus and primary sensory cortex could be secondary to deafferentation phenomena, and the increased activation of the right parietal cortex and striatum might have a possible compensatory significance.

In FRDA two types of single voxel MRS studies were performed—proton MRS of the brain, and phosphorus MRS of the heart and muscle. A mild decrease of the NAA/Cr ratio and of the NAA concentration, and increase of the Cr and mIns concentration were observed in the deep cerebellar hemisphere in FRDA patients [44,46.88.89]. Lower NAA/Cr ratio and mildly decreased concentrations of the NAA and increased concentration of mIns were reported in the pons [44,88,89]. Finally a decrease of NAA was also found in the frontal lobe [90].

The impaired muscle metabolism and cardiomyopathy characteristic of FRDA are nicely reflected in alteration of phosphorus MRS with evidence of decreased maximum rate of ATP production and delayed recovery of phosphocreatine after ischaemic exercise in the muscle [91], and decreased ratio between phosphocreatine and ATP in the heart [92]. As such, muscle and heart phosphorus MRS have been applied as surrogate biomarker in clinical trials of FRDA [91].

FDG-PET demonstrated a distinctive pattern of diffusely-increased glucose metabolism in the brain of FRDA patients with mild to moderate clinical impairment [93]. Conversely, in patients with a more severe deficit, a normal pattern or a decrease of glucose metabolism in the cerebral cortex, the cerebellum, and the brainstem was observed [93].

Ataxia telangectasia

AT is the most common inherited degenerative ataxia in the child below 4 years of age. It is transmitted as a recessive trait and is due to the *AT* mutated gene localized to chromosome 11q23. AT is a multisystem disease consisting of progressive cerebellar ataxia, progressive oculomucocutaneous telangiectases, and susceptibility to sinus and lung infections, neoplasms and ionizing radiation damage. Purkinje cell loss is the most prominent neuropathological feature of AT. MRI in AT shows a CCA pattern combined with foci of hypointensity on T_2*-weighted gradient echo images, possibly corresponding to brain capillary telangectasias best appreciated on 3T MR systems [94,95]. An increased apparent diffusion coefficient (ADC) of the cerebellar white matter and cortex was reported in patients with AT as compared to healthy controls [96].

Two proton MRS studies in AT provided partially contradictory results. One study using spectroscopic imaging acquisition reported a marked decrease of the normalized NAA, Cho, and Cr signal in the vermis of AT patients [97], whereas one single voxel study reported a significantly lower NAA/Cho ratio and higher Cho/Cr ratio with a normal NAA/Cr ratio, suggesting an increased Cho content in the cerebellum of AT patients [95].

Ataxia oculomotor apraxia type 2

Ataxia oculomotor apraxia type 2 (AOA-2) is the second most frequent recessive ataxia after FRDA in Spain and Portugal with onset between 10 and 30 years. It is associated with increased serum alpha-foetoprotein in 50% of patients. MRI in AOA-2 shows a CCA pattern [44].

In a proton MRS study an array of abnormalities was found in the pons, vermis, and cerebellar hemispheres in patients with AOA-2 [44]. This included lower NAA, consistent with neuronal loss/dysfunction in the cerebellar vermis and hemispheres, increased mIns indicative of gliosis in the pons and vermis, and decreased glutamate in the vermis. The cerebellar NAA concentrations correlated with a clinical scale of cerebellar deficit.

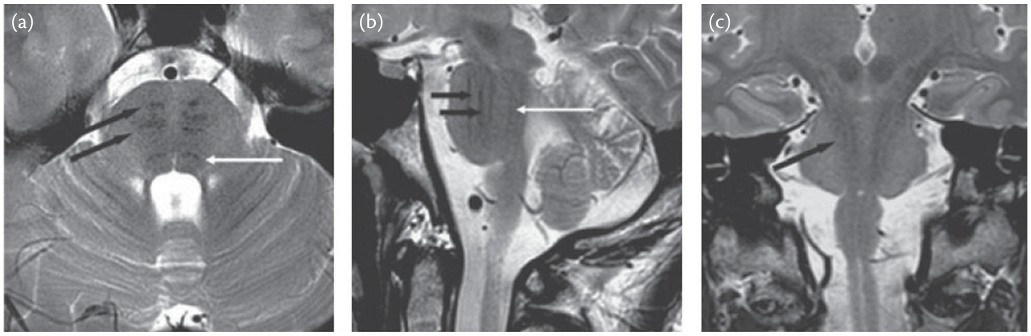

Fig. 24.9 (a–c) MRI of autosomal recessive spastic ataxia of Charlevoix–Saguenay. Axial (a), sagittal (b) and coronal (c) T_2-weighted images from a 18-year-old patient show highly characteristic low signal intensity stripes (black arrows) corresponding to the corticospinal tracts in a bulky basis pontis. The white arrow in (a) indicates the medial lemniscus.

Reproduced from Prodi E, et al. (2013). Supratentorial and pontine MRI abnormalities characterize recessive spastic ataxia of Charlevoix-Saguenay. A comprehensive study of an Italian series. *European Journal of Neurology*, **20**, 138–46. Copyright (2013), with permission from John Wiley & Sons Ltd.

Autosomal recessive spastic ataxia of Charlevoix–Saguenay

Geographic distribution of autosomal recessive spastic ataxia of Charlevoix–Saguenay (ARSACS) is much heterogeneous. In the Netherlands, ARSACS is responsible for 30% of recessive ataxias after exclusion of FRDA. Onset is usually in early childhood, but the clinical onset can occur until 30 years of age. The clinical features include pyramidal and cerebellar signs, and peripheral neuropathy. MRI can significantly contribute to the diagnosis of this recessive disease that can present as a sporadic condition. MRI reveals a constellation of characteristic findings, including atrophy of the superior cerebellar vermis, a bulky pons exhibiting T_2-hypointense stripes, identified as the corticospinal tract (Fig. 24.9), thinning of the corpus callosum and a rim of T_2-hyperintensity around the thalami [98].

DTI reveals grossly over-represented transverse pontine fibres and microstructural alterations in the supratentorial white matter of forceps, cingulum, and superior longitudinal fasciculus pointing to a possible developmental component in the pathogenesis of the disease [98].

A proton MRS study showed decreased concentration of NAA and increased concentration of mIns in the vermis and cerebellar hemispheres in ARSACS patients versus healthy controls [90].

Cerebrotendineous xanthomatosis

Cerebrotendineous xanthomatosis is a disorder of bile acid metabolism that is characterized by serum increase of cholestanol and is treatable with chenodeoxycholic acid. The clinical presentation with onset between 10 and 30 years comprises ataxia, cutaneous and tendon xhantomas, cataract and diarrhoea. Additional neurological features include spasticity, seizures, and extra-pyramidal disturbances. MRI reveals characteristic symmetric high signal in the hilum of the dentate cerebellar nuclei on T_2-weighted images (Fig. 24.10) [41,99,100].

A decrease of NAA combined with increase of lactate was observed in the supracallosal brain, which correlated with clinical disability and in the deep cerebellar white matter [41].

Niemann–Pick type C

Niemann–Pick disease type C is a rare inherited neurovisceral disease with accumulation of cholesterol and glycosphingolipids in the brain and other tissues.

Onset of neurological symptoms and signs, including oculomotor palsy, ataxia, dystonia, and epilepsy, occurs in childhood and adulthood. MRI can support the diagnostic suspicion by showing cerebral and cerebellar atrophy [101], and non-specific cerebral white matter hyperintensities associated with a thinned corpus callosum that correlates with disease duration and severity of clinical deficit [102]. In a proton spectroscopic imaging study the NAA/Cr ratio was decreased in the frontal and parietal cortices, centrum semiovale, and caudate nucleus, whereas the Cho/Cr ratio was increased in the frontal cortex and centrum semiovale [42]. Significant correlations were found between 1H-MRSI abnormalities and staging clinical scale.

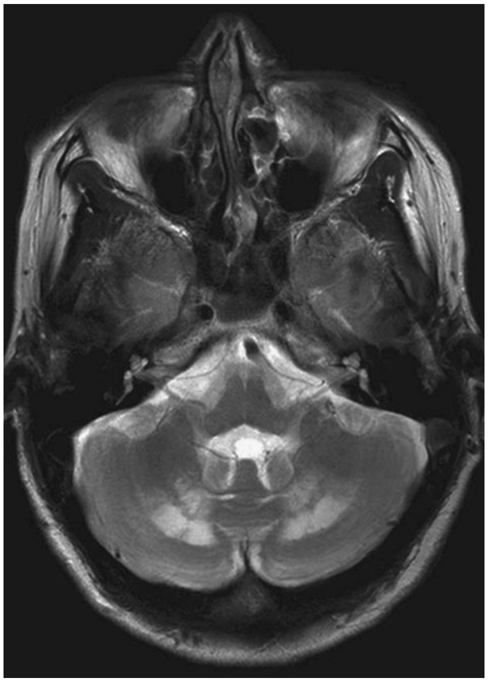

Fig. 24.10 MRI of cerebrotendineous xanthomatosis. An axial T_2-weighted image from a 37-year-old woman shows symmetric areas of high signal intensity in the cerebellar white matter.

Reproduced from Rafiq M, et al. (2011). A neurological rarity not to be missed: cerebrotendinous xanthomatosis. *Practical Neurology*, **11**, 296–300. Copyright (2011), with permission from Elsevier.

Autosomal dominant inherited ataxias

Many different genotypes of autosomal dominant inherited ataxias, comprehensively termed spinocerebellar ataxias , have been identified. The clinical [103], genetic and pathogenetic features [78], as well as the neuropathological findings [104] of spinocerebellar ataxias are reviewed elsewhere.

The geographic distribution of the spinocerebellar ataxias is much heterogeneous. The diagnosis can be easily suspected when there is already an affected individual in the kindred.

This chapter reports the MRI findings in the most common variants of spinocerebellar ataxias.

SCA1

On MRI SCA1 exhibits the typical atrophy features of PtCA, which is combined in advanced cases with the 'hot cross bun' sign (Fig.24.7) [105]. Volumetric MRI measurements and VBM studies in patients with SCA1 demonstrate a decreased volume of the brainstem, notably of the pons, middle cerebellar peduncles, cerebellar gray and white matter, putamen, and caudate without cerebral atrophy [19,106–108]. The degree of atrophy, particularly of the pons, correlates with the neurological deficit [108]. Regional atrophy is already present in presymptomatic gene carriers [109]. DTI studies [17,27,32,39] have documented a distributed pattern of microstructural damage to the white matter tracts in the brainstem and cerebellar peduncles in patients with SCA1, whose severity correlated with the clinical status.

In an fMRI study using a simple motor task, a decreased or absent cerebellar activity with increased activity in the controlateral cerebral cortex and thalamus was observed in SCA1 patients when compared with controls [35]. Changes in the intrinsic functional connectivity of the lateral cerebellum and thalamus of SCA1 as compared with healthy controls were demonstrated in a pilot resting state fMRI study [39].

A recent longitudinal volumetric and VBM study in patients with SCA1 [23] revealed progressive volume loss of brainstem that was more pronounced in the pons, cerebellum, and basal ganglia. The volume changes were not correlated with the interim modifications of the clinical measurements and exceeded them.

Proton MRS in SCA1 shows a decrease of the NAA/Cr ratio, and Cho/Cr ratio, as well as of NAA and glutamate concentration, and increased concentration of Cr, glutamine and the glial marker mIns in the pons, deep cerebellar hemispheres, and vermis, which are correlated with severity of ataxia [45,47,105,108]. Importantly, the NAA/Cr and Cho/Cr ratio abnormalities are already detectable in presymptomatic carriers of the SCA1 gene [105].

A decrease of metabolism in the brainstem, cerebellum and cerebral cortex and subcortical gray nuclei was reported in a FDG-PET study [110], whereas no abnormalities of the dopamine active transporter in the striatum were observed [111].

SCA2

At clinical onset SCA2 patients usually exhibit an evident PtCA pattern on MRI (Fig. 24.7), which was combined with the 'hot cross bun' sign in 25% of the cases of a series [112]. Morphometric MRI and VBM studies in patients with SCA2 demonstrate a marked decrease of the volume of the cerebellum and brainstem [12,17,106,108], combined with cerebral cortical atrophy in patients with advanced disease [12,17]. Putamen, caudate, and pallidus are usually of normal size and signal [17,106]. A variable correlation between the gray or white matter volume loss and the severity of the clinical deficit was reported [12,17,108,113].

The PtCA pattern is already detectable in presymptomatic gene carriers [109,114].· A recent longitudinal TBM study indicated that SCA2 is associated with a progressive pontocerebellar atrophy [22].

Two studies using DTI [17,27] have revealed that white matter tract microstructural damage in SCA2 patients involves the brainstem, cerebellar peduncles, and intracerebellar white matter, as well as the corticospinal tracts in the internal capsule and cerebral peduncles. A recent longitudinal studies indicated the capability of DTI to show progression of white matter microstructural damage in SCA2 in terms of decreasing mode of the diffusion tensor in the brainstem, cerebellum, cerebellar peduncles, cerebral hemispheres and corpus callosum [25].

A resting state fMRI has revealed decreased connectivity within the basal ganglia-thalamus-cortical motor loop in both asymptomatic and symptomatic SCA2 gene carriers compared with healthy controls, which was combined with increased connectivity in the corticocortical motor, corticocerebellar, cortico-brainstem, and part of the basal ganglia-thalamus-cortical motor circuits in the asymptomatic carriers [40]. Notably, the above abnormalities were relatively normalized after levodopa administration.

Proton MRS demonstrated a decrease of the NAA/Cr and Cho/Cr ratio and of NAA concentration, combined with increase of mIns and lactate in the pons and cerebellum [47,48,90,108,115].

In a FDG-PET study, reduced glucose metabolism was observed in the brainstem, cerebellum and parietal cortex of patients with SCA2 [111]. The decreased glucose metabolism was already detectable in presymptomatic gene carriers [114].

Driven by the description of a subgroup of patients with SCA2 presenting with a parkinsonian syndrome[116], several SPECT and PET studies have reported a decreased uptake of dopamine active transporter and concentration of D2 receptors in the neostriatum of SCA2 also in patients without parkinsonian syndrome [4,111,117].

SCA3

This is the most common SCA worldwide. Signs of extrapyramidal, pyramidal, and lower motor neuron involvement often accompany and can mask ataxia. MRI studies in SCA3/Machado–Joseph disease show heterogeneous findings. In German families, mild atrophy of the cerebellum and brainstem with significant volumetric decreases of the putamen and caudate were described [106], whereas in Japanese families atrophy of the brainstem, cerebellum, and superior cerebellar peduncles is more frequent [118,119]. The 'hot cross bun' sign was observed in 1.3% of patients with SCA3 in a series from Taiwan [112]. In SCA3 patients from South America, atrophy involved the pons, inferior olives, cerebellum, and frontal lobes [120]. Finally, a decreased size of the upper spinal cord was reported in SCA3 patients from Germany [121].

Volumetry and VBM studies of German kindreds confirmed atrophy of the brainstem, cerebellar hemispheres and vermis, putamen and caudate nuclei, and lack of substantial atrophy of the cerebral cortex [19,122]. Clinical dysfunction correlated with total brainstem atrophy. A longitudinal MRI study [23] revealed a progressive loss of bulk of brainstem, cerebellar and basal ganglia volume in SCA3, with putaminal volume being the most sensitive to change, which was not correlated with the rate of modification of the clinical scales and exceeded them.

DTI studies indicated that in SCA3 the neurological deficit correlates with severity of white matter tract damage in the brainstem and cerebellum and that white matter damage occurred also in the cerebral hemispheres [123,124].

Proton MRS shows a decrease of the NAA/Cr ratio in the deep cerebellum, vermis and cerebral white matter of SCA3 patients [47,48,125]. A strong correlation between the NAA/Cr ratio in the vermis and deep cerebellar hemispheres on the one hand, and the severity of ataxia was documented in a recent study [48].

SCA3 has been the object of intensive investigations with nuclear medicine techniques [4]. FDG-PET studies in SCA3 demonstrated a decrease of glucose metabolism in the brainstem, cerebellum, thalamus, putamen, and cerebral cortex [111], which was already present in asymptomatic gene carriers [126].

Decreased F-dopa uptake and dopamine transporter binding in the striatum were reported in both symptomatic and asymptomatic SCA3 gene carriers using PET and SPECT radiotracers [111,127].

SCA6

MRI in SCA6 shows a pattern of CCA [107,128] and SCA6 was indeed considered a prototype of neurodegenerative processes leading to CCA [129]. Atrophy of the cerebellum correlates with the neurological deficit in SCA6 [19,130]. However, volumetry and VBM have recently documented a mild volume decrease of the brainstem [19,122], and a longitudinal volumetry and VBM study [23] a progressive volume loss of the brainstem, cerebellar, and basal ganglia (the most sensitive to change being the caudate volume).

Proton MRS in SCA6 shows a mild decrease of the NAA/Cr in the cerebellum, which is not correlated with severity of ataxia [46–48].

PET demonstrated a decrease of glucose metabolism in the cerebellum and putamen with normal dopamine transporter in the striatum in SCA6 [111]. However, in a SPECT study a variable decrease of the dopamine active transporter was documented which was correlated with clinical evidence of parkinsonisms in some SCA6 patients [51].

Overall the MRI and nuclear medicine data are consistent with the new view that, in SCA6, neuronal dysfunction may not be confined to the cerebellar cortex [131].

SCA17

In line with the typical clinical presentation of combined ataxia, extra-pyramidal signs and psychiatric disturbances, MRI in SCA17 shows a generalized atrophy involving the cerebral hemispheres, in particular the limbic system, the parietal lobes, the putamen, caudatus and thalamus, and the cerebellum [14,50,132]. The severity of the regional brain atrophy correlates with spectrum of clinical disturbance and the cerebellar atrophy with the number of the expanded CAG triplet in the abnormal gene [21].

In a longitudinal VBM study, progression of gray matter atrophy in cerebellar and cerebral motor networks correlated with deterioration of the motor function, whereas progression of atrophy in frontal, limbic, parietal, and cerebellar correlated with severity of psychiatric disturbance [18].

Proton MRS in SCA17 shows decreased NAA/Cr in the cerebellum vermis and deep cerebellar hemisphere [47].

A PET study using different radiotracers demonstrated decreased glucose metabolism in the striatum, as well as in the cuneus, cingulum, and parietal lobe in SCA17 patients, including presymptomatic mutation carriers with a correlation with the scales of motor and cognitive involvement [50]. Evaluation of the striatum showed decreased post-synaptic receptors in only symptomatic gene carriers in the absence of presynaptic dopamine dysfunction. However, several SPECT studies documented decreased dopamine active transporter activity in symptomatic SCA17 patients [4,133].

Episodic ataxia type 2

Episodic ataxia type 2 (EA-2) is due to mutations in the *CACNA1A* gene, which encodes the alpha1 subunits of neuronal Cav2.1 (P/Q-type) calcium channels, expressed mainly in the Purkinje cells. Onset of EA-2 is usually in childhood with recurrent attacks of ataxia lasting hours to days. Occurrence of progressive cerebellar ataxia is inconstant and usually takes place later in life.

Since MRI shows CCA only in a minority of patients with EA-2 [134], a role for phosphorus and proton MRS for diagnosis of EA-2 has been advocated [134,135]. Characteristic phosphorus MRS findings in EA-2 include decreased high-energy phosphate ratios in the occipital lobes, and increased pH (alkalosis) in the cerebellum and occipital lobes, both of which normalize after acetazolamide administration. Proton MRS findings are less specific, including high lactate peaks in the cerebellum and cerebrum irrespective of acetazolamide treatment, and decreased creatine concentration in the vermis and deep cerebellar hemispheres.

X-linked inherited ataxias

Fragile X tremor ataxia syndrome

Expansion in excess of 200 of a CGG triplet in the fragile X mental retardation 1 gene is the most common hereditary form of mental retardation. Elderly men with CGG repeat expansions in the range of 55–200 repeats (premutation) of the same gene on the X chromosome, typically the grandfather of the boy with mental retardation due to the full expansion, can develop a progressive syndrome characterized mainly by tremor, cerebellar ataxia with decrease deep tendon, and cognitive dysfunction. However a familial history of mental retardation is present in only in 57% of cases, and MRI has a central role for the diagnosis of fragile X tremor ataxia syndrome, which can present as a sporadic condition also in women [136,137]. On T_2-weighted images, characteristic symmetric area of hyperintensity in the peridentate white matter, and middle cerebellar peduncles combined with symmetric signal changes in the periventricular cerebral white matter and in the splenium corpus callosum can be seen (Fig. 24.11).

Signal changes in the peridentate regions correlated with severity of ataxia, whereas signal changes in the corpus callosum splenium was a marker of severe disease progression [137]. There is a diffuse atrophy of the brain in the supra and infratentorial compartments, but the oval shape of the basis pontis is preserved [138].

A VBM study [20] demonstrated that the atrophy of the anterior lobe and the superior posterior lobe in both vermis and cerebellar hemispheres were combined with areas of atrophy in the medial surface of the cerebral hemispheres, including the dorsomedial prefrontal cortex, anterior cingulate cortex, and precuneus, the lateral prefrontal cortex, orbitofrontal cortex, amygdala, and insula. Notably, gray matter loss in the vermis correlates with severity of motor symptoms, gray matter loss in the left amygdala correlates with increased levels of obsessive–compulsiveness and depression, and gray matter loss in the left inferior frontal cortex and anterior cingulate cortex with poor working memory performance.

SPECT studies have revealed decreased uptake of the dopamine transporter and post-synaptic D2 receptors in the striata, accounting for the extrapyramidal symptoms often observed in patients with fragile X tremor ataxia syndrome [139–140].

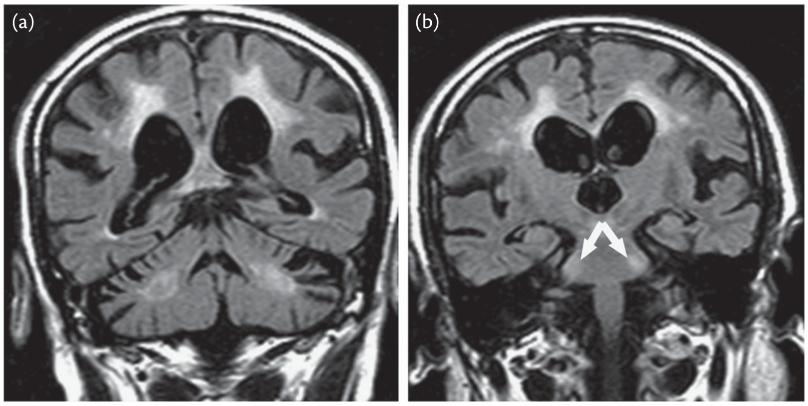

Fig. 24.11 (a–b) MRI from a 70-year-old man with fragile X premutation syndrome. Coronal FLAIR weighted image (a) shows symmetric area of high signal in white matter of the cerebellar hemispheres and the periventricular white matter of the cerebral hemispheres and the splenium of the corpus callosum. The cerebellar and cerebral sulci are widened. A coronal FLAIR image obtained more anteriorly (b) shows the characteristic high signal intensity of the middle cerebellar peduncles (arrows), whereas the signal of the basis pontis is normal.

Sporadic ataxias

Alcoholic cerebellar degeneration

In about 30% of cases, chronic alcohol consumption is accompanied by cerebellar ataxia and vermal atrophy at autopsy. A MRI study reported a correlation between vermal atrophy and serum thiamine levels in chronic alcoholics suggesting that thiamine deficiency, rather than a direct neurotoxic effect of alcohol, might be responsible for cerebellar degeneration in these patients [141].

Hypometabolism in the superior cerebellar vermis and in the medial frontal region of the cerebral cortex was reported in a FDG-PET study in symptomatic patients with alcoholic cerebellar degeneration [142].

Drugs and toxic agents

Epileptic patients receiving chronic phenytoin therapy often show on MRI a diffuse cerebellar atrophy without consistent clinical correlates [9,143].

Cerebellar syndrome typically is part of the symptoms of methylmercury poisoning observed in Minamata and Iraqi outbreaks, as well as in occupational methylmercury poisoning cases [144]. In patients with Minamata disease MRI shows atrophy of the visual cortex, the cerebellar vermis, and hemispheres, and the post-central cortex and T_2 signal hyperintensity of the visual cortex [145].

Paraneoplastic cerebellar degeneration

A rapid (typically within 6 months) progression of ataxia from onset to wheelchair with normal MRI should raise the suspicion of paraneoplastic cerebellar degeneration. In fact, MRI findings including cortical cerebellar atrophy [146], and diffuse symmetric T_2 hyperintensity in the cerebellar white matter and cortex [147] are inconsistently reported. A recent study pointed out the capability of MRS of the superior vermis to detect cerebellar abnormalities in terms of decreased NAA/Cr ratio in patients with paraneoplastic cerebellar degeneration [148]. Since negative results of search for serum antibodies do not exclude this diagnosis, there is an increasing consensus to perform whole-body FDG-PET to detect the occult primary malignancy (typically ovarian, breast or lung) in patients with suspected paraneoplastic cerebellar degeneration and unknown cancer [149–151]. In paraneoplastic degeneration FDG-PET demonstrates diffuse hypometabolism of the cerebellar cortex, variably combined with hypometabolism of the basal ganglia and cerebral cortex [152], but hypermetabolism of the cerebellum was also observed [153].

Gluten and immune-mediated ataxia

Ataxia is the commonest neurological manifestation in individuals with a heightened immunological response to ingested gluten on a background of genetic predisposition [3]. However, the diagnosis of gluten ataxia should rest on the demonstration of both increased serum antigliadin antibodies and typical histological findings at duodenal biopsy in patients who usually lack gastrointestinal symptoms [154]. Increased serum antigliadin antibodies alone is not a specific finding being reported in patients with other ataxic diseases. A pattern of cerebellar cortical atrophy is demonstrated by MRI in about 60% of patients with gluten ataxia [154]. Proton MRS showed a decrease of NAA and NAA/Cr ratio and an increase of the Cho/Cr ratio in the deep cerebellum in patients with gluten ataxia [43].

Immunological mechanisms are also assumed to underlie cerebellar syndrome that can observed in patients with glutamic acid decarboxylase antibodies in whom MRI shows cerebellar atrophy [155,156].

Siderosis of the CNS

Progressive sensorineural deafness, cerebellar ataxia, and pyramidal syndrome are the clinical features of superficial siderosis of the CNS that is an uncommon condition due to haemosiderin deposition in the subpial layers of the brain, spinal cord, and the second and eight cranial nerves [157]. Superficial siderosis of the CNS is associated with repeated and chronic, often clinically silent, bleeding in the subarachnoid spaces related to post-traumatic or post-surgical dural lesions of the spine or haemorrhagic tumours, vascular malformations and aneurysms [157]. Since most of these causes are surgically treatable, diagnosis of superficial siderosis is mandatory. MRI has a critical role for such a diagnosis [158], since it demonstrates symmetric areas of low signal on T_2- and T_2*-weighted images of the affected structures (Fig. 24.12).

In a patient examined longitudinally with PET a progressive decrease of blood flow and metabolic rate of oxygen in cerebellar hemispheres and the occipital cortices, matching the distribution of haemosiderin as revealed by MRI, was reported [159].

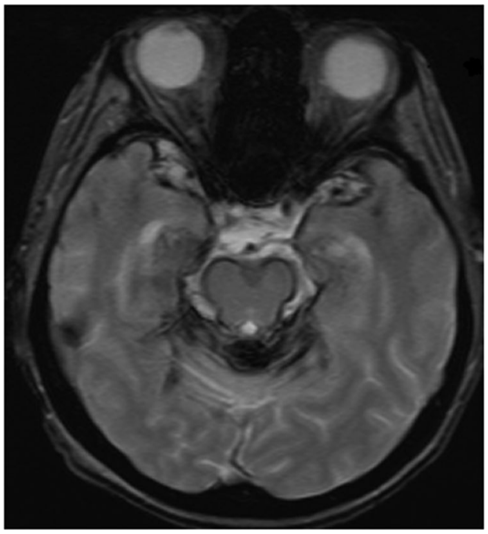

Fig. 24.12 MRI of superficial siderosis of the central nervous system in a 67-year-old man who presented with ataxia and bilateral sensorineural loss and had suffered a severe spinal trauma at age 48. The axial T_2*-weighted gradient echo image shows hypointensity of the cerebellar folia of the superior vermis and paravermian cerebellar hemispheres and a linear hypointensity of the surface of the midbrain.

Courtesy of Dr Mirco Cosottini, Department of Neuroradiology, University of Pisa.

Chronic lymphocytic inflammation with perivascular pontine enhancement responsive to steroids (CLIPPERS)

Chronic lymphocytic inflammation with perivascular pontine enhancement responsive to steroids (CLIPPERS) is a rare, chronic inflammatory syndrome affecting the CNS with a relapsing–remitting course [160]. Patients present with ataxia, diplopia, nystagmus, and perioral and facial paraesthesia. MRI has a fundamental role for the diagnosis of CLIPPERS by demonstrating patchy or punctate increased signal in T_2-weighted images, and contrast enhancement is referred to as 'peppering' in the pons and cerebellum (Fig. 24.13).

Similar features can also be observed in the basal ganglia cerebral cortex and spinal cord [160]. Increased number of lymphocytes and amount of proteins are usually present in the CSF. The main differential diagnosis of CLIPPERS on MRI is pontine capillary telangiectasia, which is usually asymptomatic representing an incidental finding, is restricted to the basis pontis, shows characteristic low signal on T_2*-weighted gradient-echo images, and is sometimes associated with an enlarged draining vein [161].

Idiopathic

Two conditions, both of unknown aetiology, can be recognized clinically, based on neuropathological and imaging findings, namely sporadic adult onset ataxia (SAOA) formerly labelled 'pure' idiopathic late onset cerebellar ataxia, and multi-system atrophy cerebellar type (MSA-C). In SAOA involvement of pyramidal tracts, posterior columns of the spinal cord and peripheral nervous system is uncommon and mild, and life-expectancy is close to normal [2]. In MSA-C, involvement of different neuronal systems, in particular the extrapyramidal and autonomic, is the rule; REM-sleep behaviour disorders and cognitive decline and psychiatric symptoms are common, and patients have a median survival after disease onset of 8–10 years [162]. Onset with parkinsonism enables identification of a parkinsonian type of MSA (MSA-P), which tends to merge with MSA-C in a single severe MSA syndrome as the disease progresses.

SAOA

SAOA patients typically show a CCA pattern on MRI (Fig. 24.6) [77,163]. In some patients, however, brainstem or spinal cord atrophy is also present [163]. The ADC was found to be significantly increased in the cerebellum and brainstem in patients with SAOA possibly reflecting a mild diffuse structural damage of the cerebellar cortical gray matter or cerebello-petal and cerebello-fugal white matter tracts [26]. Conversely, in a DTI study of patients with SAOA, no microstructural abnormalities were observed in the cerebellar peduncles [31] that are typically spared at the neuropathological examination [164].

Proton MRS reveals a decrease of the NAA/Cr ratio in the cerebellum, pons, and frontal cortex, but not in the putamen in patients with SAOA with correlation between the decrease of the NAA/Cr ratio and the severity of cerebellar clinical signs [165].

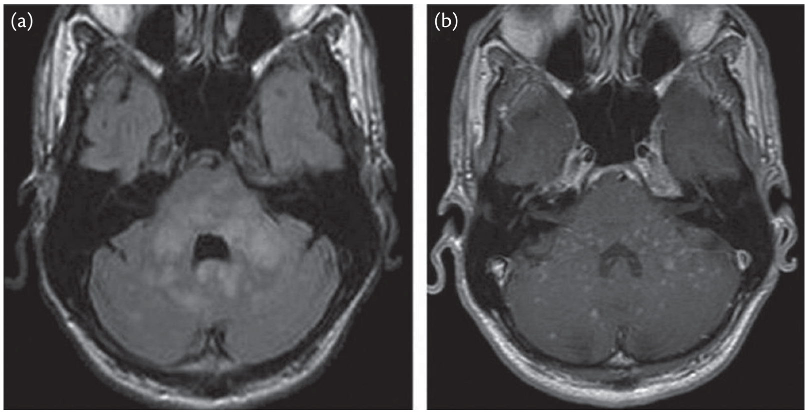

Fig. 24.13 (a,b) MRI of CLIPPERS in a 40-year-old man presenting with dizziness, ataxia, and diplopia. Axial FLAIR image (a) shows pontine and cerebellar patchy T_2-hyperintense areas associated with punctuate and curvilinear contrast-enhancement in axial T_1-weighted image (b).

Reproduced from Pesaresi I, Sabato M, Desideri I, et al. (2013). 3.0T MR investigation of CLIPPERS: Role of susceptibility weighted and perfusion weighted imaging. *Magnetic Resonance Imaging*, **31**(9), 1640–2. Copyright (2013), with permission from Elsevier.

A SPECT study in patients with ILOCA showed decreased blood flow in the cerebellum and frontal cortex with significant correlation between the perfusion of the frontal lobe and cerebellum [166].

MSA-C

MRI in patients with advanced MSA-C shows a PtCA pattern [77] that is accompanied by the 'hot cross bun' sign in 80% of the cases [167,168]. Basal ganglia signal changes on T_2-weighted images (hypo- or hyperintensities) (Fig. 24.14) are not useful for the differential diagnosis between MSA-C and SAOA [163]. Conversely, measurements of the thickness of middle cerebellar peduncles can contribute to the diagnosis by demonstrating thinning of these structures in MSA [169].

VBM studies confirmed the PtCA pattern in MSA by demonstrating a volume loss of the brainstem, cerebellar gray and white and middle cerebellar peduncles [13,15]. In one study, a correlation between the amount of volume loss in the brainstem and cerebellar hemispheres, and the severity of cerebellar ataxia was found [15]. A decrease of the supratentorial gray matter in the frontal, temporomesial, and insular cortical areas was also reported [15]. Atrophy of putamen and cerebellum can be used as marker of disease progression [170].

A DWI study showed that diffusivity was increased in the putamen, cerebellum, and middle cerebellar peduncles of MSA-C patients [28]. Moreover, disease duration correlated with increased diffusivity in the cerebellum and middle cerebellar peduncles. Longitudinal data of the same cohort of patients [29] indicated progression of the microstructural changes in terms of increased proton diffusion in the putamen, pons, cerebellar white matter, thalamus and frontal white matter over a 12-month period, which were not correlated with the clinical evolution. A DTI study [31] demonstrated that microstructural changes selectively involve the middle cerebellar peduncles and spare the inferior and superior cerebellar peduncles in patients with MSA-C.

A preliminary investigation with resting state fMRI in MSA patients reported cerebral cortical areas with both decreased and increased low frequency spontaneous fluctuation of blood oxygen level dependent signal as compared with controls [38], in line with the hypothesis that motor cortex areas can be functionally involved in MSA.

A decrease of the NAA/Cr ratio in the cerebellum, pons, frontal cortex, and,

notably, the putamen, and a decrease of the pontine and cerebellar Cho/Cr ratio were reported in proton MRS studies in patients with sporadic PtCA or MSA-C [47,88,115,165]. The putaminal MRS abnormality can assist in the differential diagnosis between MSA and SAOA. The decrease of the NAA/Cr ratio in the pons correlated with the severity of the global neurological deficit [88,115].

A decrease of the NAA/Cr ratio was observed in the pons and putamen of MSA patients without MR signal changes in the same regions or clinical symptoms of cerebellar or basal ganglia dysfunction [171], suggesting that proton MRS of the pons may be useful for the differential diagnosis between MSA-parkinsonian type and Parkinson's disease.

Finally, since due to similarities in clinical presentation and age of onset the differential diagnosis between MSA-C and spinocerebellar ataxias, especially SCA2, can be challenging, one study investigated the potential of proton MRS at 4 T for this purpose[49]. Utilizing selected neurochemical levels from the cerebellum and the pons a 89% accurate classification of a cohort of patients with SCA1, SCA2, SCA6 and MSA-C and controls was achieved.

MSA has been intensively investigated with nuclear medicine techniques and several radiotracers [4]**.** In MSA-C, FDG-PET demonstrates widespread pattern of areas of decreased metabolism in the cerebellum, striatum and frontal and parietal cortices [52,172]. Hypometabolism of the putamen, cerebellum, or brainstem supports a diagnosis of possible MSA [173]. Perfusion SPECT might support the differential diagnosis between MSA-C and SAOA by revealing more pronounced hypoperfusion in the pons in

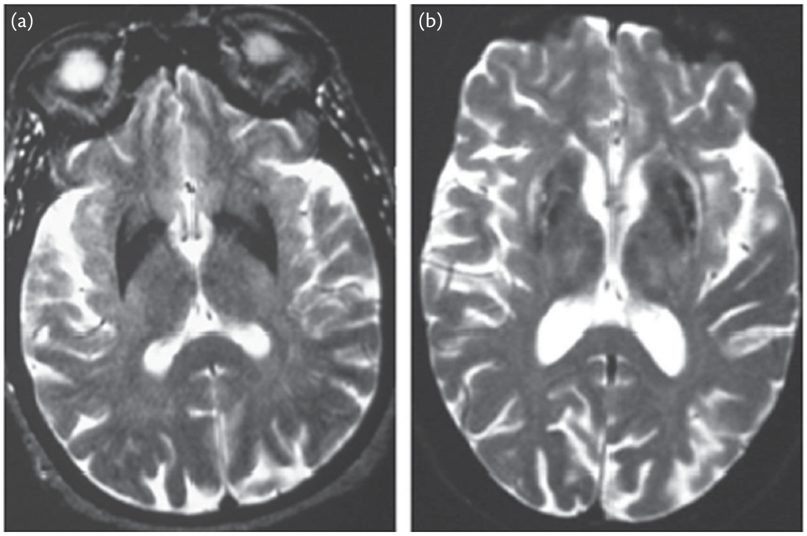

Fig. 24.14 (a,b) MRI of the basal ganglia in multiple system atrophy. Axial T_2*-weighted gradient echo (a) and T_2-weighted turbo spin echo (b) images from two patients with MSA showing symmetric abnormally low signal intensity of the putamen. In (b) a regular hyperintense rim in the external border of the putamen is also present.

Reproduced from Mascalchi M, et al. (2012). Movement disorders: role of imaging in diagnosis. *Journal of Magnetic Resonance Imaging*, **35**, 239–56. Copyright (2012), with permission from John Wiley & Sons Ltd.

the former condition [174]. PET and SPECT show decreased striatal uptake of both pre- and post-synaptic radiolabels [175,176]. The decreased post-synaptic D2 receptors uptake is a distinguishing feature of MSA compared with early Parkinson's disease in which the nigrostriatal dysfunction is typically associated with an increased or normal D2 receptors uptake [176].

References

1. Sanger TD, Chen D, Delgado MR, et al. (2006). Definition and classification of negative motor signs in childhood. *Pediatrics*, **118**, 2159–67.
2. Abele M, Burk K, Schols L, et al. (2002). The aetiology of sporadic adult-onset ataxia. *Brain*, **125**, 961–8.
3. Currie S, Hadjivassiliou M, Craven IK, et al. (2013). Magnetic resonance imaging biomarkers in patients with progressive ataxia: current status and future direction. *Cerebellum*, **12**, 245–66.
4. Mascalchi M, and Vella A. (2012). Magnetic resonance and nuclear medicine imaging in ataxias. *Handbook of Clinical Neurology*, **103**, 85–110.
5. Tortori-Donati P, and Rossi A. (2005). *Pediatric neuroradiology: brain, head, neck and spine*. Berlin: Springer.
6. Osborn AG. (2012). *Osborn's brain. Imaging, pathology and anatomy*. Baltimore: Lippincott-Williams and Wilkins.
7. Baldarcara L, Currie S, Hadjivassiliou M, et al. (2014). Consensus paper: radiological biomarkers of cerebellar disorders. *Cerebellum*, Nov 11 2014 [Epub ahead of print].
8. Wullner U, Klockgether T, Petersen D, et al. (1993). Magnetic resonance imaging in hereditary and idiopathic ataxia. *Neurology*, **43**, 318–25.
9. Luef G, Burtscher J, Kremser C, et al. (1996). Magnetic resonance volumetry of the cerebellum in epileptic patients after phenytoin overdosages. *European Neurology*, **36**, 273–7.
10. Akhlaghi H, Corben L Georgiou-Karistianis N, et al. (2011). Superior cerebellar peduncle atrophy in Friedreich's ataxia correlates with disease symptoms. *Cerebellum*, **10**, 81–7.
11. Jacobi H, Hauser TK, Giunti P, et al. (2012). Spinocerebellar ataxia types 1, 2, 3 and 6: the clinical spectrum of ataxia and morphometric brainstem and cerebellar findings. *Cerebellum*, **11**, 155–66.
12. Brenneis C, Bosch SM, Schocke M, et al. (2003). Atrophy pattern in SCA2 determined by voxel-based morphometry. *Neuroreport*, **14**, 1799–802.
13. Specht K, Minnerop M, Muller-Hubenthal J, et al. (2005). Voxel-based analysis of multiple-system atrophy of cerebellar type: complementary results by combining voxel-based morphometry and voxel-based relaxometry. *NeuroImage*, **25**, 287–93.
14. Lasek K, Lencer R, Gaser C, et al. (2006). Morphological basis for the spectrum of clinical deficits in spinocerebellar ataxia 17 (SCA17). *Brain*, **129**, 2341–52.
15. Brenneis C, Boesch SM, Egger KE, et al. (2006). Cortical atrophy in the cerebellar variant of multiple system atrophy: a voxel-based morphometry study. *Movement Disorders*, **21**, 159–65.
16. Della Nave R, Ginestroni A, Tessa C, et al. (2008). Brain white matter tracts degeneration in Friedreich ataxia. An in vivo MRI study using tract-based spatial statistics and voxel based morphometry. *NeuroImage*, **40**, 19–25.
17. Della Nave R, Ginestroni A, Tessa C, et al. (2008). Brain white matter damage in SCA1 and SCA2. An in vivo study using voxel-based morphometry, histogram analysis of mean diffusivity and tract-based spatial statistics. *NeuroImage* , **43**, 10–19.
18. Reetz K, Lencer R, Hagenah JM, et al. (2010). Structural changes associated with progression of motor deficits in spinocerebellar ataxia 17. *Cerebellum*, **9**, 210–17.
19. Schulz JB, Borkert J, Wolf S, et al. (2010). Visualization, quantification and correlation of brain atrophy with clinical symptoms in spinocerebellar ataxia types 1, 3 and 6. *NeuroImage*, **49**, 158–68.
20. Hashimoto R, Javan AK, Tassone F, et al. (2011). A voxel-based morphometry study of grey matter loss in fragile X-associated tremor/ataxia syndrome. *Brain*, **134**, 863–78.
21. Reetz K, Kleiman A, Klein C, et al. (2011). CAG repeats determine brain atrophy in spinocerebellar ataxia 17: a VBM study. *PLoS ONE*, **6**, e15125.
22. Mascalchi M, Diciotti S, Giannelli M, et al. (2014). Progression of brain atrophy in SCA2. A longitudinal TBM study. *PLoS ONE*, **9**, e89410.
23. Reetz K, Costa AS, Mirzazade S, et al. (2013). Genotype specific patterns of atrophy progression is more sensitive than clinical decline in SCA1, SCA3 and SCA6. A longitudinal MRI study. *Brain*, **136**, 905–17.
24. Mascalchi M, Filippi M, Floris R, et al. (2005). Diffusion-weighted MR of the brain: methodology and clinical applications. *Radiology Medicine*, **109**, 155–97.
25. Mascalchi M, Toschi N, Giannelli M, et al. Progression of microstructural damage in spinocerebellar ataxia type 2. A longitudinal diffusion tensor study. *AJNR American Journal of Neuroradiology* (in press).
26. Della Nave R, Foresti S, Tessa C, et al. (2004). ADC mapping of neurodegeneration in the brainstem and cerebellum of patients with progressive ataxias. *NeuroImage*, **22**, 698–705.
27. Mandelli ML, De Simone T, Minati L, et al. (2007). Diffusion tensor imaging of spinocerebellar ataxias types 1 and 2. *AJNR American Journal of Neuroradiology*, **28**, 1996–2000.
28. Pellecchia MT, Barone P, Mollica C et al. (2009). Diffusion-weighted imaging in multiple system atrophy: a comparison between clinical subtypes. *Movement Disorders*, **24**, 689–96.
29. Pellecchia MT, Barone P, Vicidomini C, et al. (2011). Progression of striatal and extrastriatal degeneration in multiple system atrophy: a longitudinal diffusion-weighted MR study. *Movement Disorders*, **26**, 1303–9.
30. Rizzo G, Tonon C, Valentino ML, et al. (2011). Brain diffusion-weighted imaging in Friedreich's ataxia. *Movement Disorders*, **26**, 705–12.
31. Taoka T, Kin T, Nakagawa H, et al. (2007). Diffusivity and diffusion anisotropy of cerebellar peduncles in cases of spinocerebellar degenerative disease. *NeuroImage*, **37**, 387–93.
32. Prakash N, Hageman N, Hua X, et al. (2009). Patterns of fractional anisotropy changes in white matter of cerebellar peduncles distinguish spinocerebellar ataxia-1 from multiple system atrophy and other ataxia syndromes. *NeuroImage*, **47**, T72–81.
33. Akhlaghi H, Yu J, Corben L, et al. (2014). Cognitive deficits in Friedreich ataxia correlate with micro-structural changes in dentatorubral tract. *Cerebellum*, **13**, 187–98.
34. Mantovan MC, Martinuzzi A, Squarzanti F, et al. (2006). Exploring mental status in Friedreich's ataxia: a combined neuropsychological, behavioral and neuroimaging study. *European Journal of Neurology*, **13**, 827–35.
35. Jayakumar PN, Desai S, Pal PK, et al. (2008). Functional correlates of incoordination in patients with spinocerebellar ataxia 1: a preliminary fMRI study. *Journal of Clinical Neuroscience*, **15**, 269–77.
36. Ginestroni A, Diciotti S, Cecchi P, et al. (2012). Neurodegeneration in Friedreich's ataxia is associated with a mixed activation pattern of the brain. A fMRI study. *Human Brain Mapping*, **33**, 1780–91.
37. Quarantelli M, Giardino G, Prinster A, et al. (2013). Steroid treatment in Ataxia-Telangiectasia induces alterations of functional magnetic resonance imaging during prono-supination task. *European Journal of Paediatric Neurology*, **17**, 135–40.
38. You H, Wang J, Wang H, et al. (2011). Altered regional homogeneity in motor cortices in patients with multiple system atrophy. *Neuroscience Letters*, **502**, 18–23.
39. Solodkin A, Peri E, Chen EE, et al. (2011). Loss of intrinsic organization of cerebellar networks in spinocerebellar ataxia type 1: correlates with disease severity and duration. *Cerebellum*, **10**, 218–32.
40. Wu T, Wang C, Wang J, et al. (2013). Preclinical and clinical neural network changes in SCA2 parkinsonism. *Parkinsonism Related Disorders*, **19**, 158–64.
41. De Stefano N, Dotti MT, Mortilla M, et al. (2001). Magnetic resonance imaging and spectroscopic changes in brain of patients with cerebrotendineous xanthomatosis. *Brain*, **124**, 121–31.
42. Tedeschi G, Bonavita S, Barton NW, et al. (1998). Proton magnetic resonance spectroscopic imaging in the clinical evaluation of patients

with Niemann-Pick type C disease. *Journal of Neurology, Neurosurgery & Psychiatry*, **65**, 72–9.

43. Wilkinson ID, Hadjivassiliou M, Dickson JM, et al. (2005). Cerebellar abnormalities on proton MR spectroscopy in gluten ataxia. *Journal of Neurology, Neurosurgery & Psychiatry*, **76**, 1011–13.
44. Iltis I, Hutter D, Bushara KO, et al. (2010). 1H MR spectroscopy in Friedreich's ataxia and ataxia with oculomotor apraxia type 2. *Brain Research*, 1358, 200–10.
45. Oz G, Hutter D, Tkac I, et al. (2010). Neurochemical alterations in spinocerebellar ataxia type 1 and their correlations with clinical status. *Movement Disorders*, **25**, 1253–61.
46. Hadjivassiliou M, Wallis LI, Hoggard N, et al. (2012). MR spectroscopy and atrophy in Gluten, Friedreich's and SCA6 ataxias. *Acta Neurologica Scandinavica*, **126**, 138–43.
47. Lirng JF, Wang PS, Chen HC, et al. (2012). Differences between spinocerebellar ataxias and multiple system atrophy-cerebellar type on proton magnetic resonance spectroscopy. *PLoS ONE*, **7**, e47925.
48. Wang PS, Chen HC, Wu HM, et al. (2012). Association between proton magnetic resonance spectroscopy measurements and CAG repeat number in patients with spinocerebellar ataxias 2, 3, or 6. *PLoS ONE*, **7**, e47479.
49. Oz G, Iltis I, Hutter D, et al. (2011). Distinct neurochemical profiles of spinocerebellar ataxias 1, 2, 6, and cerebellar multiple system atrophy. *Cerebellum*, **10**, 208–17.
50. Brockmann K, Reimold M, Globas C, et al. (2012). PET and MRI reveal early evidence of neurodegeneration in spinocerebellar ataxia type 17. *Journal of Nuclear Medicine*, **53**, 1074–80.
51. Kim JM, Lee JY, Kim HJ, et al. (2010). The wide clinical spectrum and nigrostriatal dopaminergic damage in spinocerebellar ataxia type 6. *Journal of Neurology, Neurosurgery & Psychiatry*, **81**, 529–32.
52. Lyoo CH, Jeong Y, Ryu YH, et al. (2008). Effects of disease duration on the clinical features and brain glucose metabolism in patients with mixed type multiple system atrophy. *Brain*, **131**, 438–46.
53. Wang PS, Liu RS, Yang BH, et al. (2007). Topographic brain mapping of the international cooperative ataxia rating scale. A positron emission tomography study. *Journal of Neurology*, **254**, 722–8.
54. Kuruvilla T, and Bharucha NE. (1997). Cerebellar atrophy after acute phenytoin intoxication. *Epilepsia*, **38**, 500–2.
55. Roy M, Stip E, Black D, et al. (1998). Cerebellar degeneration following acute lithium intoxication. *Revue Neurologie (Paris)*, **154**, 546–8.
56. Suwanlaong K, and Phanthumchinda K. (2008). Neurological manifestations of methylbromide intoxication. *Journal of the Medical Association of Thailand*, **91**, 421–6.
57. Xiao L, Lin X, Cao J, et al. (2011). MRI findings in 6 cases of children by inadvertent ingestion of diphenoxylate-atropine. *European Journal of Radiology*, **79**, 432–6.
58. Asokumar P, Gogate YV, Gangadhar P, et al. (2011). Reversible cerebellar ataxia: a rare presentation of depletional hyponatremia. *Neurology India*, **59**, 631–2.
59. Nguyen HV, and Gan SK. (2005). Neurological sequelae of chronic profound hypocalcaemia. *Medical Journal of Australia*, **182**, 123.
60. Sedehizadeh S, Keogh M, and Will AJ. (2011). Reversible hypomagnesaemia-induced subacute cerebellar syndrome. *Biological Trace Element Research*, **142**, 127–9.
61. Boulos MI, Shoamanesh A, Aviv RI, et al. (2012). Severe hypomagnesemia associated with reversible subacute ataxia and cerebellar hyperintensities on MRI. *Neurologist*, **18**, 223–5.
62. Guerrini L, Belli G, Cellerini M, et al. Proton MR spectroscopy of cerebellitis. *Magnetic Resonance Imaging*, **20**, 619–22.
63. Donmez FY, Agildere AM, Tore HG, et al. (2008). Abnormal diffusion-weighted imaging findings in an adult patient with acute cerebellitis presenting with a normal magnetic resonance imaging. *Journal of Computer Assisted Tomography*, **32**, 156–8.
64. Kubota T, Suzuki T, Kitase Y, et al. (2011). Chronological diffusion-weighted imaging changes and mutism in the course of rotavirus-associated acute cerebellitis/cerebellopathy concurrent with encephalitis/encephalopathy. *Brain & Development*, **33**, 21–7.
65. Odaka M, Yuki N, Yamada M, et al. (2003). Bickerstaff's brainstem encephalitis: clinical features of 62 cases and a subgroup associated with Guillain-Barre syndrome. *Brain*, **126**, 2279–90.
66. Mondejar RR, Santos JMG, and Villalba EF. MRI findings in a remitting-relapsing case of Bickerstaff encephalitis. *Neuroradiology*, **44**, 411–14.
67. Moragas M, Martinez-Yelamos S, Majos C, et al. (2011). Rhombencephalitis: a series of 97 patients. *Medicine (Baltimore)*, **90**, 256–61.
68. Mrowka M, Graf LP, and Odin P. (2002). MRI findings in mesen-rhombencephalitis due to *Listeria monocytogenes*. *Journal of Neurology, Neurosurgery & Psychiatry*, **73**, 775.
69. Gallucci M, Bozzao A, Splendiani A, et al. (1990). Wernicke encephalopathy. MR findings in five patients. *AJNR American Journal of Neuroradiology* **11**, 887–92.
70. Mascalchi M, Simonelli P, Tessa C, et al. (1999). Do acute lesions of Wernicke's encephalopathy show contrast enhancement? Report of three cases and review of the literature. *Neuroradiology*, **41**, 249–54.
71. Zuccoli G, Santa Cruz D, Bertolini M, et al. (2009). MR imaging findings in 56 patients with Wernicke encephalopathy: nonalcoholics may differ from alcoholics. *AJNR American Journal of Neuroradiology*, **30**, 171–6.
72. Mascalchi M, Belli G, Guerrini L, et al. (2002). Proton MR spectroscopy of Wernicke encephalopathy. *AJNR American Journal of Neuroradiology*, **23**, 1803–6.
73. Fellgiebel A, Siessmeier T, Winterer G, et al. (2004). Increased cerebellar PET glucose metabolism corresponds to ataxia in Wernicke–Korsakoff syndrome. *Alcohol and Alcoholism*, **39**, 150–3.
74. Vedolin L, Gonzalez G, Souza CF, et al. (2013). Inherited cerebellar ataxia in childhood: a pattern-recognition approach using brain MRI. *AJNR American Journal of Neuroradiology*, **34**, 925–34.
75. Bradac GB, Riva A, Mortara P, et al. (1989). Primary progressive cerebellar ataxia. *Neuroradiology*, **31**, 16–18.
76. Savoiardo M, Strada L, Girotti F, et al. (1990). Olivopontocerebellar atrophy: MR diagnosis and relationship to multi-system atrophy. *Radiology*, **174**, 693–6.
77. Ormerod IEC, Harding AE, Miller DH, et al. (1994). Magnetic resonance imaging in degenerative ataxic disorders. *Journal of Neurology, Neurosurgery & Psychiatry*, **57**, 51–7.
78. Klockgether T. (2011). Update on degenerative ataxias. *Current Opinions in Neurology*, **24**, 339–45.
79. Anheim M, Fleury M, Monga B, et al. (2010). Epidemiological, clinical, paraclinical and molecular study of a cohort of 102 patients affected with autosomal recessive progressive cerebellar ataxia from Alsace, Eastern France: implications for clinical management. *Neurogenetics*, **11**, 1–12.
80. Anheim M, Tranchant C, and Koenig M. (2012). The Autosomal recessive cerebellar ataxias. *New England Journal of Medicine*, **366**, 636–46.
81. Koeppen AH. (2011). Friedreich's ataxia: Pathology, pathogenesis, and molecular genetics. *Journal of Neurological Science*, **303**, 1–12.
82. Mascalchi M, Salvi F, Piacentini S, et al. (1994). Friedreich 's ataxia: MR findings involving the cervical portion of the spinal cord. *AJR American Journal of Roentgenology*, **163**, 187–91.
83. Schols L, Amoiridis G, Przuntek H, et al. (1997). Friedreich's ataxia. Revision of the phenotype according to molecular genetics. *Brain*, **120**, 2131–40.
84. Franca MC Jr, D'Abreu A, Yasuda CL, et al. (2009). A combined voxel-based morphometry and 1H-MRS study in patients with Friedreich's ataxia. *Journal of Neurology*, **256**, 1114–20.
85. Pagani E, Ginestroni A, Salvi F, et al. (2010). Assessment of brain white matter fibre bundle atrophy in patients with Friedreich's ataxia. *Radiology*, **255**, 882–9.
86. Waldvogel D, van Gelderen P, and Hallet M. (1999). Increased iron in the dentate nucleus of patients with Friedreich's ataxia. *Annals of Neurology*, **46**, 123–5.
87. Boddaert N, Le Quan Sang KH, Rotig A, et al. (2007). Selective iron chelation in Friedreich ataxia: biologic and clinical implications. *Blood*, **110**, 401–8.

88. Mascalchi M, Cosottini M, Lolli F, et al. (2002). Proton MR spectroscopy of the cerebellum and pons in patients with degenerative ataxia. *Radiology*, **223**, 371–8.
89. Guerrini L, Belli G, Mazzoni L, et al. (2009). Impact of cerebrospinal fluid contamination on brain metabolites evaluation with 1H-MR spectroscopy: a single voxel study of the cerebellar vermis in patients with degenerative ataxias. *Journal of Magnetic Resonance Imaging*, **30**, 11–17.
90. Viau M, Machand L, Bard C, et al. (2005). 1H magnetic resonance spectroscopy of autosomal ataxias. *Brain Research*, 1049, 191–202.
91. Nachbauer W, Boesch S, Schneider R, et al. (2013). Bioenergetics of the calf muscle in Friedreich ataxia patients measured by 31P-MRS before and after treatment with recombinant human erythropoietin. *PLoS ONE*, **8**, e69229.
92. Bunse M, Bit-Avragim N, and Riefflin A. (2003). Cardiac energetics correlates to myocardial hypertrophy in Friedreich's ataxia. *Annals of Neurology*, **53**, 121–3.
93. Gilman S, Junck L, Markel DS, et al. (1990). Cerebral glucose hypermetabolism in Friedreich's ataxia detected with positron emission tomography. *Annals of Neurology*, **28**, 750–7.
94. Tavani F, Zimmerman RA, Berry GT, et al. (2003). Ataxia-telangiectasia: the pattern of cerebellar atrophy on MRI. *Neuroradiology*, **45**, 315–19.
95. Wallis LI, Griffith PD, Ritchie SJ et al. (2007). Proton spectroscopy and imaging at 3T in ataxia-telangectasia. *AJNR American Journal of Neuroradiology*, **28**, 79–83.
96. Firat AK, Karakas HM, Firat Y, et al. (2005). Quantitative evaluation of brain involvement in ataxia telangectasia by diffusion weighted MR Imaging. *European Journal of Radiology*, **26**, 1357–62.
97. Lin DD, Crawford TO, Lederman HM, et al. (2006). Proton MR spectroscopic imaging in ataxia-telangiectasia. *Neuropediatrics*, **37**, 241–6.
98. Prodi E, Grisoli M, Panzeri M, et al. (2013). Supratentorial and pontine MRI abnormalities characterize recessive spastic ataxia of Charlevoix–Saguenay. A comprehensive study of an Italian series. *European Journal of Neurology*, **20**, 138–46.
99. Barkhof F, Verrips A, Wesseling P, et al. (2000). Cerebrotendinous xanthomatosis: the spectrum of imaging findings and the correlation with neuropathologic findings. *Radiology*, **217**, 869–76.
100. Rafiq M, Sharrack N Shaw PJ, et al. (2011). A neurological rarity not to be missed: cerebrotendinous xanthomatosis. *Practical Neurology*, **11**, 296–300.
101. Sevin M, Lesca G, N. Baumann N, et al. (2007). The adult form of Niemann–Pick disease type C. *Brain*, **130**, 120–33.
102. Walterfang M, Fahey M, Abel L, et al. (2011). Size and shape of the corpus callosum in adult Niemann–Pick type C reflects state and trait illness variables, *AJNR American Journal of Neuroradiology*, **32**, 1340–6.
103. Klockgether T. (2008). The clinical diagnosis of autosomal dominant spinocerebellar ataxias. *Cerebellum*, **7**, 101–5.
104. Seidel K, Siswanto S, Brunt ER, et al. (2012). Brain pathology of spinocerebellar ataxias. *Acta Neuropathologica*, **124**, 1–21.
105. Mascalchi M, Tosetti M, Plasmati R, et al. (1998), Proton magnetic resonance spectroscopy in an Italian family with spinocerebellar ataxia type 1. *Annals of Neurology*, **43**, 244–52.
106. Klockgether T, Skalej M, Wedekind D et al. (1998). Autosomal dominant cerebellar ataxia type I. MRI-based volumetry of posterior fossa structures and basal ganglia in spinocerebellar ataxia types 1, 2 and 3. *Brain*, **121**, 1678–93.
107. Nagaoka U, Suzuki Y, Kawanami T et al. (1999). Regional differences in genetic subgroup frequency in hereditary cerebellar ataxia, and a morphometric study of brain MR images in SCA1, MJD and SCA6. *Journal of Neurology Sciences*, **164**, 187–94.
108. Guerrini L, Lolli F, Ginestroni A, et al. (2004). Brainstem neurodegeneration correlates with clinical dysfunction in SCA1 but not in SCA2. A volumetric, diffusion and quantitative proton spectroscopy MR study. *Brain*, **127**, 1785–95.
109. Jacobi H, Reetz K, du Montcel ST, et al. (2013). Biological and clinical characteristics of individuals at risk for spinocerebellar ataxia types 1, 2, 3, and 6 in the longitudinal RISCA study: analysis of baseline data. *Lancet Neurology*, **12**, 650–8.
110. Gilman S, Sima AA, Junck L, et al. (1996). Spinocerebellar ataxia type 1 with multiple system degeneration and glial cytoplasmic inclusions. *Annals of Neurology*, **39**, 241–55.
111. Wullner U, Reimold M, Abele M, et al. (2005). Dopamine transporter positron emission tomography in spinocerebellar ataxias type 1, 2, 3, and 6. *Archives of Neurology*, **62**, 1280–5.
112. Lee YC, Liu CS, Wu HM, et al. (2009). The 'hot cross bun' sign in the patients with spinocerebellar ataxia. *European Journal of Neurology*, **16**, 513–16.
113. Ying SH, Choi SI, Perlman SL, et al. (2006). Pontine and cerebellar atrophy correlate with clinical disability in SCA2. *Neurology*, **66**, 424–6.
114. Inagaki A, Iida A, Matsubara M, et al. (2005). Positron emission tomography and magnetic resonance imaging in spinocerebellar ataxia type 2: a study of symptomatic and asymptomatic individuals. *European Journal of Neurology*, **12**, 725–8.
115. Boesch SM, Wolf C, Seppi K, et al. (2007). Differentiation of SCA2 from MSA-C using proton magnetic resonance spectroscopic imaging. *Journal of Magnetic Resonance Imaging*, **25**, 564–9.
116. Shan DA, Soong BW, Sun CM, et al. (2001). Spinocerebellar Ataxia type 2 presenting as familial levodopa-responsive parkinsonism. *Annals of Neurology*, **50**, 812–5.
117. Varrone A, Salvatore E, De Michele G, et al. (2004). Reduced striatal [123I]FP-CIT binding in SCA2 patients without parkinsonism. *Annals of Neurology*, **55**, 426–30.
118. Murata Y, Yamaguchi S, Kawakami H, et al. (1998). Characteristic magnetic resonance imaging findings in Machado-Joseph disease. *Archives of Neurology*, **55**, 33–7.
119. Tokumaru AM, Kamakura K, Maki T, et al. (2003). Magnetic resonance imaging findings of Machado-Joseph disease: histopathologic correlation. *Journal of Computer Assisted Tomography*, **27**, 241–8.
120. Etchebehere EC, Cendes F, Lopes-Cendes I, et al. (2001). Brain single-photon emission computed tomography and magnetic resonance imaging in Machado-Joseph disease. *Archives of Neurology*, **58**, 1257–63.
121. Lukas C, Hahn HK, Bellenberg B, et al. Spinal cord atrophy in spinocerebellar ataxia type 3 and 6: impact on clinical disability. *Journal of Neurology*, **255**, 1244–9.
122. Eicher L, Bellenberg B, Hahn HK et al. (2011). Quantitative assessment of brain stem and cerebellar atrophy in spinocerebellar ataxia types 3 and 6: impact on clinical status. *AJNR American Journal of Neuroradiology*, **32**, 890–7.
123. Guimaraes RP, D'Abreu A, Yasuda CL et al. (2013). A multimodal evaluation of microstructural white matter damage in spinocerebellar ataxia type 3. *Movement Disorders*, **28**, 1125–32.
124. Kang JS, Klein JC, Baudrexel S et al. (2014). White matter damage is related to ataxia severity in SCA3. *Journal of Neurology*, **261**, 291–9.
125. D'Abreu A, Franca M Jr, Appenzeller S et al. (2009). Axonal dysfunction in the deep white matter in Machado-Joseph disease. *Journal of Neuroimaging*, **19**, 9–12.
126. Soong B, and Liu R. (1998). Positron emission tomography in asymptomatic gene carriers of Machado Joseph disease. *Journal of Neurology, Neurosurgery & Psychiatry*, **64**, 499–504.
127. Yen YC, Tzen KY, Chen MC, et al. (2002). Dopamine transporter concentration is reduced in asymptomatic Machado–Joseph disease gene carriers. *Journal of Nuclear Medicine*, **43**, 153–9.
128. Schols L, Kruger R, Amoiridis G, et al. (1998). Spinocerebellar ataxia type 6: genotype and phenotype in German kindreds. *Journal of Neurology, Neurosurgery & Psychiatry*, **64**, 67–73.
129. Jung BC, Cho SI, Du AX, et al. (2012). Principal component analysis of cerebellar shape on MRI separates SCA types 2 and 6 into two archetypal modes of degeneration. *Cerebellum*, **11**, 887–95.

130. Richter S, Dimitrova A, Maschke M, et al. (2005). Degree of cerebellar ataxia correlates with three-dimensional MRI-based cerebellar volume in pure cerebellar degeneration. *European Neurology*, **54**, 23–7.
131. Soong B, Liu R, Wu L, et al. (2001). Metabolic characterization of spinocerebellar ataxia type 6. *Archives of Neurology*, **58**, 300–4.
132. Rolfs A, Koeppen AH, Bauer I, et al. (2003). Clinical features and neuropathology of autosomal dominant spinocerebellar ataxia(SCA17). *Annals of Neurology*, **54**, 367–75.
133. Salvatore E, Varrone A, Sansone V, et al. (2006). Characterization of nigrostriatal dysfunction in spinocerebellar ataxia 17. *Movement Disorders*, **21**, 872–5.
134. Harno H, Heikkinen S, Kaunisto MA, et al. (2005). Decreased cerebellar creatine in episodic ataxia type 2: a 1H MRS study. *Neurology*, **64**, 542–4.
135. Sappey-Marinier D, Vighetto A, Peyron R, et al. (1999). Phosphorus and proton magnetic resonance spectroscopy in episodic ataxia type 2. *Annals of Neurology*, **46**, 256–9.
136. Brunberg JA, Jacquemont S, Hagerman RJ, et al. (2002). Fragile X premutation carriers: characteristic MR imaging findings of adult male patients with progressive cerebellar and cognitive dysfunction. *AJNR American Journal of Neuroradiology*, **23**, 1757–66.
137. Apartis E, Blancher A, Meissner WG, et al. (2012). FXTAS: new insights and the need for revised diagnostic criteria. *Neurology*, **79**, 1898–907.
138. Ginestroni A, Guerrini L, Della Nave R, et al. (2007). Morphometry and 1H- MR spectroscopy of the brainstem and cerebellum in three patients with fragile-X premutation. *AJNR American Journal of Neuroradiology*, **28**, 486–8.
139. Scaglione C, Ginestroni A, Vella A, et al. (2008). MRI and SPECT of midbrain and striatal degeneration in fragile X-associated tremor/ataxia syndrome. *Journal of Neurology*, **255**, 144–6.
140. Healy DG, Bressman S, Dickson J, et al. (2009). Evidence for pre and postsynaptic nigrostriatal dysfunction in the fragile X tremor-ataxia syndrome. *Movement Disorders*, **24**, 1245–7.
141. Maschke M, Weber J, Bonnet U, et al. (2005). Vermal atrophy of alcoholics correlate with serum thiamine level but not with dentate iron concentrations as estimated by MRI. *Journal of Neurology*, **252**, 704–11.
142. Gilman S, Adams K, Koeppe RA, et al. (1990). Cerebellar and frontal hypometabolism in alcoholic cerebellar degeneration studied with positron emission tomography. *Annals of Neurology*, **28**, 775–85.
143. Ney G, Lantos G, Barr WB, et al. (1994). Cerebellar atrophy in patients with long-term phenytoin exposure and epilepsy. *Archives of Neurology*, **51**, 767–71.
144. Satoh H. (2000). Occupational and environmental toxicology of mercury and its compounds. *Industrial Health*, **38**, 153–64.
145. Korogi Y, Takahashi M, Okajima T, et al. (1998). MR findings of Minamata disease—organic mercury poisoning. *Journal of Magnetic Resonance Imaging*, **8**, 308–16.
146. Schlake HP, Husstedt IW, Grotemeyer KH, et al. (1989). Paraneoplastic subacute cerebellar degeneration in Hodgkin's disease. Report of three cases and review of the literature. *Clinical Neurology and Neurosurgery*, **91**, 329–35.
147. Gilmore CP, Elliott I, Auer D, et al. (2010). Diffuse cerebellar MR signal changes in anti-Yo positive paraneoplastic cerebellar degeneration. *Journal of Neurology* 2010; 257:490–1.
148. Hadjivassiliou M, Currie S, and Hoggard N. (2013). MR spectroscopy in paraneoplastic cerebellar degeneration. *Journal of Neuroradiology*, **40**, 310–12.
149. Berner U, Menzel C, Rinne D, et al. (2003). Paraneoplastic syndrome: detection of malignant tumors using 18FDG-PET. *Q Journal of Nuclear Medicine*, **47**, 85–9.
150. Basu S, and Alavi A. (2008). Role of FDG-PET in the clinical management of paraneoplastic neurological syndrome: detection of the underlying malignancy and the brain PET-MRI correlates. *Molecular Imaging Biology*, **10**, 131–7.
151. Hadjivassiliou M, Alder SJ, Van Beek EJR, et al. (2009). PET scan in clinically suspected paraneoplastic neurological syndromes: a six year prospective study in a regional neuroscience unit. *Acta Neurologica Scandinavica*, **119**, 186–93.
152. Clapp AJ, Hunt CH, Johnson GP, et al.(2013). Semiquantitative analysis of brain metabolism in patients with paraneoplastic neurologic syndrome. *Clinical Nuclear Medicine*, **38**, 241–7.
153. Choi KD, Kim JS, Park SH, et al (2006). Cerebellar hypermetabolism in paraneoplastic cerebellar degeneration. *Journal of Neurology, Neurosurgery & Psychiatry*, **77**, 525–8.
154. Burk K, Bosch S, Muller CA, et al. (2001). Sporadic cerebellar ataxia associated with gluten sensitivity. *Brain*, **124**, 1013–19.
155. Honnorat J, Saiz A, Giometto B, et al. (2001). Cerebellar ataxia with anti-glutamic acid decarboxylase antibodies: study of 14 patients. *Archives of Neurology*, **58**, 225–30.
156. Nanri K, Niwa H, Mitoma H, et al. (2013). Low-titer anti-GAD-antibody-positive cerebellar ataxia. *Cerebellum*, **12**, 171–5.
157. Fearnley JM, Stevens JM, and Rudge P. (1995). Superficial siderosis of the central nervous system. *Brain*, **118**, 1051–6.
158. Bracchi M, Savoiardo M, Triulzi F, et al. (1993).Superficial siderosis of the CNS: MR diagnosis and clinical findings. *AJNR American Journal of Neuroradiology*, **14**, 227–36.
159. Terashi H, Nagata K, Tsutsumi K, et al. (1998). Long-term follow up study with PET in a case of superficial siderosis. *Rinsho Shinkeigaku*, **38**, 506–11.
160. Simon NG, Parratt JD, Barnett MH, et al. (2012). Expanding the clinical, radiological and neuropathological phenotype of chronic lymphocytic inflammation with pontine perivascular enhancement responsive to steroids (CLIPPERS). *Journal of Neurology, Neurosurgery & Psychiatry*, **83**, 15–22.
161. Scaglione C, Salvi F, Riguzzi P, et al. (2001). Symptomatic unruptured capillary telangectasia of the brainstem: report of three cases and review of the literature. *Journal of Neurology, Neurosurgery & Psychiatry*, **71**, 390–3.
162. Klockgether T, Ludke R, Kramer B, et al. (1998). The natural history of degenerative ataxia: a retrospective study in 466 patients. *Brain*, **121**, 589–600.
163. Burk K, Buhring U, Schulz JB, et al. (2005). Clinical and magnetic resonance imaging characteristics of sporadic cerebellar ataxia. *Archives of Neurology*, **62**, 981–5.
164. Lowe J, Lennox G, and Leigh PN. (1997). Disorders of movement and system degeneration. In: DL Graham, PL Lantos (eds), *Greenfield's Neuropathology*, Vol. 2, 6th edn. London; Arnold, pp. 281–366.
165. Terakawa H, Abe K, Watanabe Y, et al. (1999). Proton magnetic resonance spectroscopy (1H MRS) in patients with sporadic cerebellar degeneration. *Journal of Neuroimaging*, **9**, 72–7.
166. Tachibana H, Kawabata K, Tomino Y, et al. (1999). Prolonged P3 latency and decreased brain perfusion in cerebellar degeneration. *Acta Neurologica Scandinavica*, **100**, 310–6.
167. Watanabe H, Saito Y, Terao S, et al. (2002). Progression and prognosis in multiple system atrophy—an analysis of 230 Japanese patients. *Brain*, **125**, 1070–83.
168. Horimoto Y, Aiba I, Yasuda T, et al. (2002). Longitudinal MRI study of multiple system atrophy—when do the findings appear, and what is the course? *Journal of Neurology*, **249**, 847–54.
169. Quattrone A, Nicoletti G, Messina D, et al. (2008). MR imaging index for differentiation of progressive supranuclear palsy from Parkinson's disease and parkinsonian variant of multi system atrophy. *Radiology*, **246**, 214–21.
170. Hauser T, Luft A, Skalej M, et al. (2006). Visualization and quantification of disease progression in multiple system atrophy. *Movement Disorders*, **18**, 85–92.

171. Watanabe H, Fukatsu H, Katsuno M, et al. (2004). Multiple regional 1H-MR spectroscopy in multiple system atrophy: NAA/Cr reduction in pontine base as a valuable diagnostic marker. *Journal of Neurology, Neurosurgery & Psychiatry*, **75**, 103–9.
172. Lee PH, An YS, Yong SW, et al. (2008). Cortical metabolic changes in the cerebellar variant of multiple system atrophy: a voxel-based FDG-PET study in 41 patients. *NeuroImage*, **40**, 796–801.
173. Gilman S, Wenning GK, Low PA, et al. (2008). Second consensus statement on the diagnosis of multiple system atrophy. *Neurology*, **71**, 670–6.
174. Kimura N, Kumamoto T, Masuda T, et al. (2009). Evaluation of regional cerebral blood flow in cerebellar variant of multiple system atrophy using FineSRT. *Clinical Neurology and Neurosurgery*, **11**, 829–34.
175. Gilman S. (2001). Biochemical changes in multiple system atrophy detected with positron emission tomography. *Parkinsonism Related Disorders*, **7**, 253–6.
176. Cilia R, Marotta G, Benti R, et al. (2005). Brain SPECT imaging in multiple system atrophy. *Journal of Neural Transmission*, **112**, 1635–45.

CHAPTER 25

Spinal cord injury

Patrick Freund, Siawoosh Mohammadi,
Nikolaus Weiskopf, and Armin Curt

Introduction

Quantitative neuroimaging of the spinal cord and brain is an advancing field in neuroimaging with the provision to increase our understanding of disease development, as well as the possibility to monitor functional, as well as anatomical changes following injury to the central nervous system. This chapter focuses on traumatic spinal cord injury (SCI) as a role model to gain insights into the underlying pathology and also how this can provide important new information in neurological conditions with spinal involvement.

The clinical diagnosis of SCI is a life-changing event as patients are generally left with the impairment of voluntary motor control and autonomic disabilities, such as loss of sensory and motor functions, but also autonomic dysfunction such as loss of bladder and bowel control. However, due to improved acute management and intensive rehabilitation interventions, SCI patients can show some improvements in function within the first year after injury, but the majority will remain permanently disabled. The degree of recovery depends on the lesion level and extent. SCI patients with incomplete lesions show substantial recovery within a greater range of upper and lower limb functions, while patients with complete lesions show primarily segmental improvements close to the level of lesion. However, for patients with a cervical lesion, the greatest desire is to regain skilled hand function, the greatest desire for paraplegic patients is to regain bladder–bowel–sexual function [1]. To respond to these desires, the quest to find effective therapies for spinal cord repair is on-going and trials evaluating agents with the potential to repair the injured spinal cord are imminent [2–4]. At present, potential agents are tested focusing either on neuroprotection, axonal regeneration, or a combination of the two. Some of these agents have even entered clinical phase I trials. However, success in translating such interventions into therapies with patient benefit depends on carefully-designed outcome measures. Consequently, there is a pressing need to identify non-invasive accurate and sensitive surrogate outcomes, which can assess the safety by means of phase I clinical trials, preliminary efficacy, and evaluation of 'proof of concepts' in the context of phase IIa and IIb trials [5]. While reliable, clinical outcome measures are still poorly sensitive to detect subtle changes in phase I and IIa/b trials; non-invasive MRI markers may therefore prove to be essential as surrogate outcomes.

The advantage of employing MRI as a surrogate of safety and efficacy is that clinical neuroimaging outcomes are objective and may be sensitive to detect subtle structural changes (i.e. drug responsive changes), which contribute to resolving neurological deficits prior to the threshold required for conventional clinical outcome measures. Importantly, recent developments in structural MRI of the spinal cord and brain have the potential to detect both anatomical changes and functional reorganization following SCI, which are clinically rather obscure. However, spinal cord MRI is still very challenging. Due to the high demands on the scanner hardware (i.e. very high in-plane resolution and unilateral (dorsal) coil coverage), it is prone to instrumental artefacts such as eddy currents [6,7], gradient inhomogeneities [8,9], and vibration artefacts [10]. Due to the small structure of interest with bone-CSF-GM-WM transitions, it is subject to CSF pulsation, swallowing, and physiological artefacts, e.g. cardiac pulsation and respiration [11]. To get reliable results for clinical studies these artefacts have to be understood, controlled, and where possible corrected.

This chapter will therefore discuss the potential value of quantitative neuroimaging applicable both in research, but also routine clinical care. It also might become applicable in clinical studies to improve the sensitivity of clinical trial protocols.

Spinal cord magnetic resonance imaging

While computer tomography is preferentially used for imaging the condition of the spine (i.e. any damage of vertebras, mineralization, and tumour formation, as well as condition of joints), MRI of the spinal cord has been established as the gold standard in the evaluation of cord pathology.

Most commonly, conventional MRI of the spinal cord comprises both T_1-weighted (T1w) and T_2-weighted (T2w) fat-supressed pulse sequences, acquired in both the axial and sagittal planes to optimize evaluation of spinal cord damage. T1w sequences are preferentially applicable to reveal morphological changes because on T1w images fat, vertebrae, and the spinal cord are hyperintense (i.e. brighter), while water and cerebral spinal fluid (CSF) appear hypointense (i.e. darker). Conversely, on T2w scans, the CSF appears brighter than the spinal cord, which facilitates depiction of pathological processes as these are associated with increased water content due to reactive fluid accumulation and inflammation within soft tissue structures, and between ligaments (Fig. 25.1). Another sequence of interest, although less frequently employed, is the gradient echo (GRE) sequence. This sequence best demonstrates susceptibility effects (i.e. blooming artefact) resulting from haemosiderin accumulation secondary to cord haemorrhage or haematoma.

In acute SCI, both traumatic and non-traumatic, MRI is the most sensitive tool to define the site and nature of the injury in addition to associated disc herniations, injuries to the ligaments and

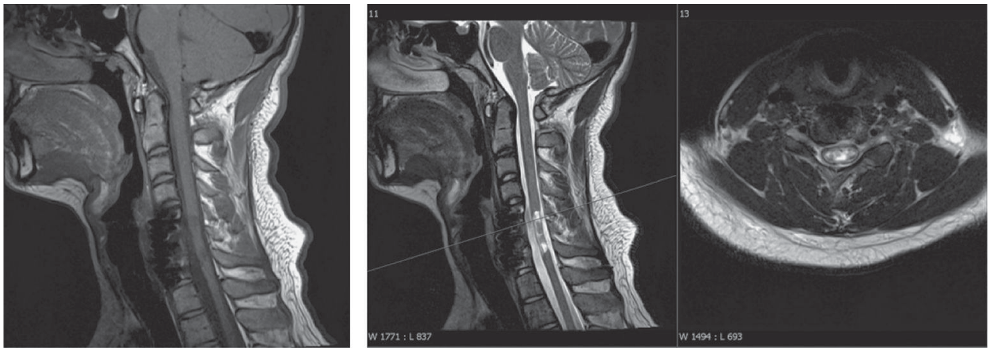

Fig. 25.1 (a) T_1- and (b) T_2-weighted images of a patient with a chronic cervical spinal cord lesion showing an increased MR signal intensity from cervical level C5 to C7 on the T_2-weighted sagittal scan. The axial T_2-weighted scan demonstrated the cross-sectional extent of the injured spinal tissue. The high signal intensity on the latter scan corresponds to a cyst.

vertebras. Using conventional MRI, four different patterns of MR signal intensities within the spinal cord (i.e. intramedullary damage) can be observed in the very acute phase on T2w scans (Fig. 25.2) [12]. Pattern 1 corresponds to a normal MR signal of the cord, while pattern 2 (haemorrhage) is characterized by a large area of low signal intensity on T2w images, which is attributed to haemorrhagic contusion within the spinal cord. Pattern 3 (oedema) demonstrates a large area of high signal intensity on the same set of images representing cord oedema, and pattern 4 (combined haemorrhage and oedema) is representative of a mixed combination of patterns 2 and 3. In this fourth pattern, a low signal intensity change is surrounded by a high signal intensity change [13]. In the acute phase of injury a hyperintense area on GRE scans represents oedema or haemorrhage due to haemosiderin deposits, while T_2-hyperintense signal changes have been associated with cystic degeneration [14].

However, in some cases, where a SCI is clinically suspected, but where there is no radiographic evidence of a fracture or dislocation (i.e. spinal cord injury without radiographic abnormality (SCIWORA)), conventional MRI has been shown to be sensitive in the detection of tissue changes—reflected by a T_2-hyperintensity at the level of the neurological impairment.

Following transition from the acute to chronic phase of injury, conventional MRI applied serially is able to reveal the devastating macroscopic sequels (i.e. neural damage and cell loss) following the traumatic impact (Fig. 25.3). However, the timeline of deterioration does not correspond well with neurological deficits. This is because neurological deficits appear immediately, while the lesion area only becomes visible following the resolution of the initial oedema. The most common pattern of changes entail a high intensity area on T2w scans immediately following injury, which over time varies in intensity, becoming either more intense or iso-intense, while a low intensity area appears on T1w images. Based on histopathological features of traumatic SCI, this combination of varying intensity changes is thought to represent degenerative processes, such as gliosis and/or myelomalacia (i.e. morbid softening of the spinal cord). As a consequence of a traumatic impact, the primary induced neurodegenerative processes cumulate into a post-traumatic intramedullary cyst, which represents the final morphological stage of SCI.

Correlates of structural magnetic resonance imaging changes to neurologic outcome

Besides the value of MR images in visualizing spinal cord pathology, the interpretation of MRI findings, such as intramedullary haemorrhage, oedema, soft-tissue and ligamentous injury, haematoma, and herniated disk has been correlated with the degree of neurological impairment [15]. Importantly, intramedullary haemorrhage, cord swelling, canal compromise, and spinal cord compression have been identified as key predictors of neurologic recovery after traumatic cervical SCI [16]. Therefore, based on the

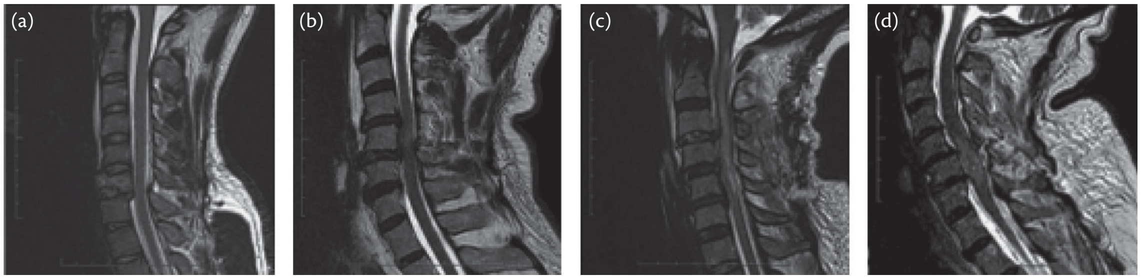

Fig. 25.2 The four injury MR signal intensity patterns that can be identified using sagittal T_2-weighted sequences. (a) Burst fracture of C6 and retrolisthesis of C6 on C7 by 4 mm with normal cord (pattern 1). (b) Single-level oedema due to a severe central stenosis C5–6 and C5 fracture (pattern 2). (c) Multi-level oedema C1–C5 with C3–C4 disk herniation (pattern 3). (d) Haemorrhage and surrounding oedema centred at C6 (pattern 4) in a patient with bilateral C5 lamina fractures, inferior facet fractures, and grade one anterolisthesis of C5 on C6.

Modified from Bozzo A, Marcoux J, Radhakrishna M, et al. (2013). The role of magnetic resonance imaging in the management of acute spinal cord injury. *Journal of Neurotrauma*, **28**, 1401–11. Copyright (2013), with permission from Mary Ann Liebert Inc. publishers.

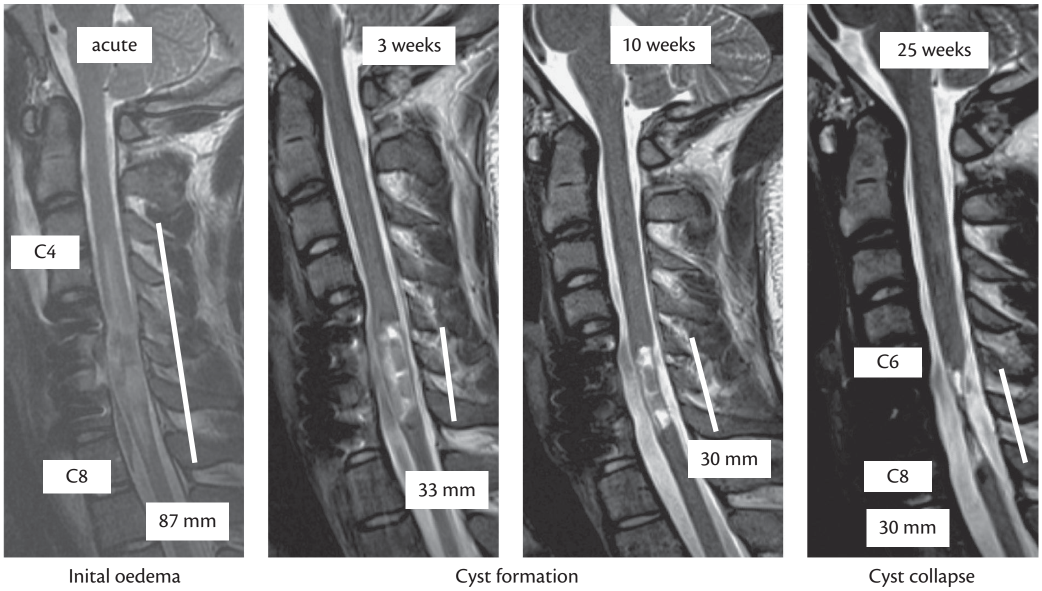

Fig. 25.3 Images from a patient with cervical traumatic SCI (C6 AIS-A) presenting the typical evolution of the spinal tissue changes within the first 25 weeks following the traumatic injury. Between 1 and 10 weeks the oedema resolves and the full extent of the post-traumatic cyst becomes apparent covering two spinal segments with a final length of about 30 mm. At 25 weeks post-injury, the cyst at the lesion centre collapses.

Reproduced and modified from Curt A. (2012). The translational dialogue in spinal cord injury research. *Spinal Cord*, **50**, 352–7. Copyright (2012), with permission from Nature Publishing Group.

current literature, it is tempting to conclude that SCI patients with no MRI signal abnormality during the acute phase are those with a more favourable outcome compared with those patients with early MRI signal changes.

Need for advanced spinal cord magnetic resonance imaging

So far, however, conventional MRI has not been shown to be more predictive than the initial neurological examination. This might in part be due to technical challenges posed by imaging of the spinal cord with the inhomogeneous anatomy of the spine and the difference in magnetic susceptibility between adjacent air- and fluid-filled structures [17]. Moreover, imaging the injured spinal cord is even more challenging as one has to cope with MR signal drop out due to spinal fixation constructs employing non-ferromagnetic orthopaedic fixative screws and bolts. However, imaging technology is rapidly evolving and it is likely that in the near future this MR signal drop out caused by the spinal fixation constructs can be minimized, with potential improved diagnostic and predictive capabilities. Nevertheless, the relatively weak predictive value of routine clinical MRI examinations for further functional recovery calls for improved MRI techniques or for strategies that bypass the impediment posed by MR signal drop out due to the orthopaedic fixative constructs at the focal injury level.

Measures of neural changes within the brain at a microstructural level have become possible as the extent of myelination, iron deposition, and changes in neuronal microstructure are reflected in MR relaxation times and diffusion-weighted images, which now can be measured with high resolution and speed [18–20]. Furthermore, spinal cord imaging suffers from the effects of involuntary subjects' motion during acquisition that can considerably degrade the image quality. The use of a cervical collar, as used in emergency medicine, to reduce involuntary head motion during acquisition has been shown to increase the contrast between gray and white matter of the cervical cord (Fig. 25.4) [21].

Measuring cross-sectional spinal cord area

One strategy, to overcome problems caused by fixative artefacts, is to assess trauma-induced anatomical changes in the upper cervical cord (i.e. above) far away from the site of trauma. As most MRI sequences of the brain cover also the upper spinal cord (i.e. C2/C3) the optimized MR sequences for brain morphometry can be applied to investigate cord changes. Recently, cross-sectional spinal cord area measurement, which was first developed for quantifying tissue damage in patients with multiple sclerosis (MS) and suspected spinal involvement, was applied to the field of SCI [22–24]. This technique allows for measuring changes of the cross-sectional spinal cord area accurately at C2 level based on the regional specific contrast differences between the CSF and the myelon on three-dimensional T1w images. In MS, it has been shown to be sensitive by disclosing subtle changes as the disease progresses [25]. Moreover, it has been used as an objective outcome measure in MS clinical trials promoting remyelination and axonal repair [26].

First data in SCI have been acquired in the very chronic stage of SCI (>10 years post-injury) where global atrophy is evident at C2 and it has been shown that cord area had shrunk by more than 30% in tetraplegic patients (Fig. 25.5). While spinal atrophy at the level of injury [27] is primarily induced by ischaemia and excitotoxicity [28], distant atrophic changes, as revealed by this method, are likely to be the result of changes in the cellular microstructure of the injured spinal cord [29–31].

The degree of cervical atrophy correlates with upper limb impairment in chronic tetraplegic patients (Fig. 25.5e). For example, performance on the Nine Hole Peg test was slowest in those patients with the more severe atrophy as compared with those patients with an equally extensive lesion, but lower degrees of atrophy. These

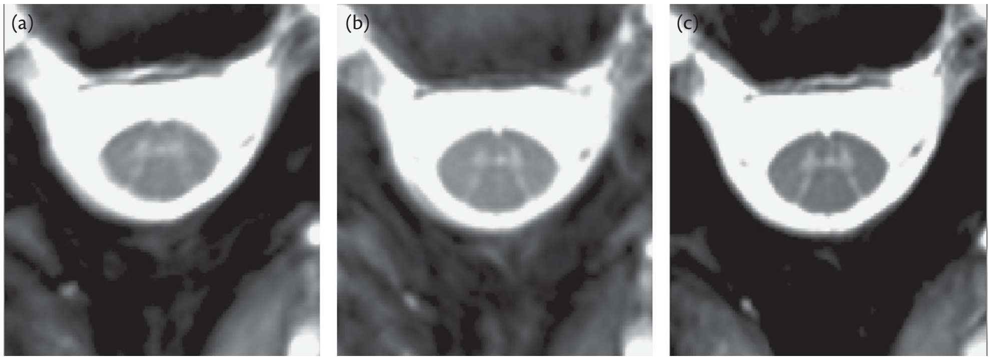

Fig. 25.4 (a) Axial 3D-FFE image (resolution 0.5 × 0.5 × 5 mm^3) through the C2–3 intervertebral disc acquired with standard immobilization padding (without the use of the MRI compatible cervical collar) displaying motion artefacts (note the blurred edges at the WM/GM interface within the cord); (b) Axial 3D-FFE image at the same position as in a) acquired still without the use of the cervical collar, but with less motion artefacts; (c) axial 3D-FFE image at the same position as in A and B, this time acquired with the use of the cervical collar, demonstrating the major effect of the immobilization procedure.

Modified from Yiannakas MC, Kearney H, Samson RS, et al. (2012). Feasibility of grey matter and white matter segmentation of the upper cervical cord in vivo: a pilot study with application to magnetisation transfer measurements. *NeuroImage*, **63**, 1054–9. Copyright (2012), with permission from Elsevier.

clinical eloquent correlations between changes in cord area and clinical impairment indicate the potential of this to offer markers in clinical trials of spinal cord repair and also for prognosis in individual cases, similar to what has been shown in MS [25,26]. Moving beyond the feasibility studies in the chronic stages of SCI showing clinically relevant relationships, it is important to increase our understanding of the dynamic sequence of structural and functional changes at the spinal and the brain level, and their impact on the clinical outcome.

At present, the major drawback for the applicability of this method is the low resolution of the sequences employed. Therefore, it is not possible to distinguish whether tissue loss arises from retrograde/anterograde axonal degeneration of motor and sensory pathways, and/or atrophic changes of motor neurons or demyelination. With the advent of high resolution imaging sequences (e.g. MEDIC) [32], which allow a clear differentiation between the butterfly-shaped gray matter and the surrounding white matter, it is possible to measure changes to cord white and gray matter in a fully automatic way. The feasibility of segmenting gray and white in the upper cervical spinal cord in healthy subjects using high-resolution 3D images acquired with a commercially available gradient-echo sequence and a 3T MR system has been recently

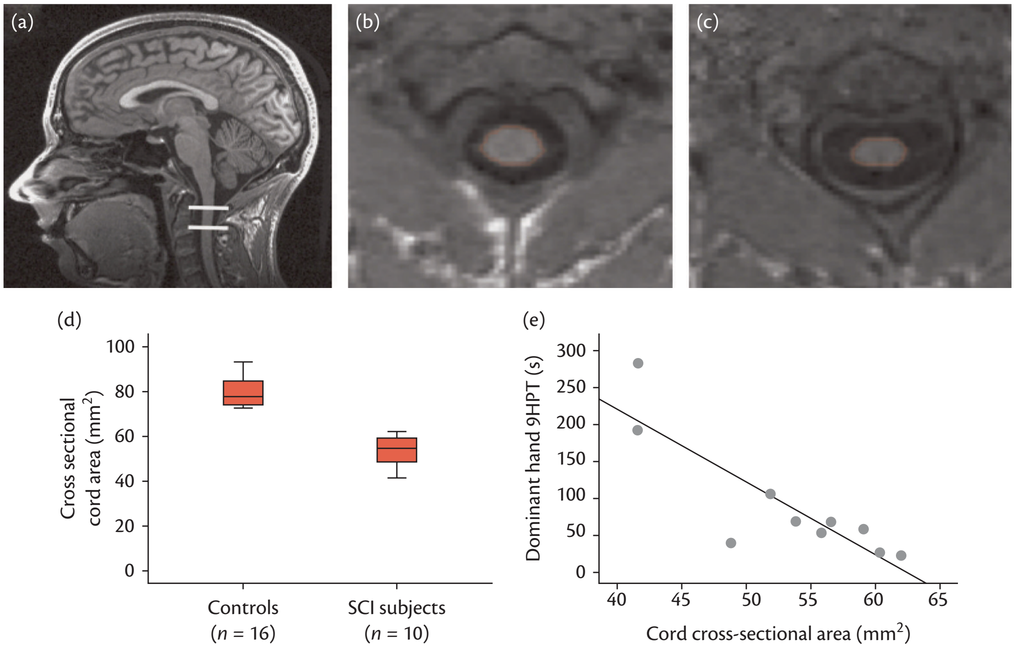

Fig. 25.5 Spinal cord atrophy following SCI. (a) T_1-weighted scan of the brain and cervical spinal cord showing the region of cross-sectional cord area measurement (within white horizontal bars). (b,c) Cord area in a control and subject with SCI, respectively. (d) Box and whisker plots showing a 30% reduction in cord area in subjects with SCI compared with controls. (e) Greater atrophy relates to greater impairment of manual dexterity.

Reproduced and modified from Freund P, Weiskopf N, Ward NS, et al. (2011). Disability, atrophy and cortical reorganization following spinal cord injury. *Brain*, **134**, 1610–22. Copyright (2011), reproduced under the Creative Commons License 2.5.

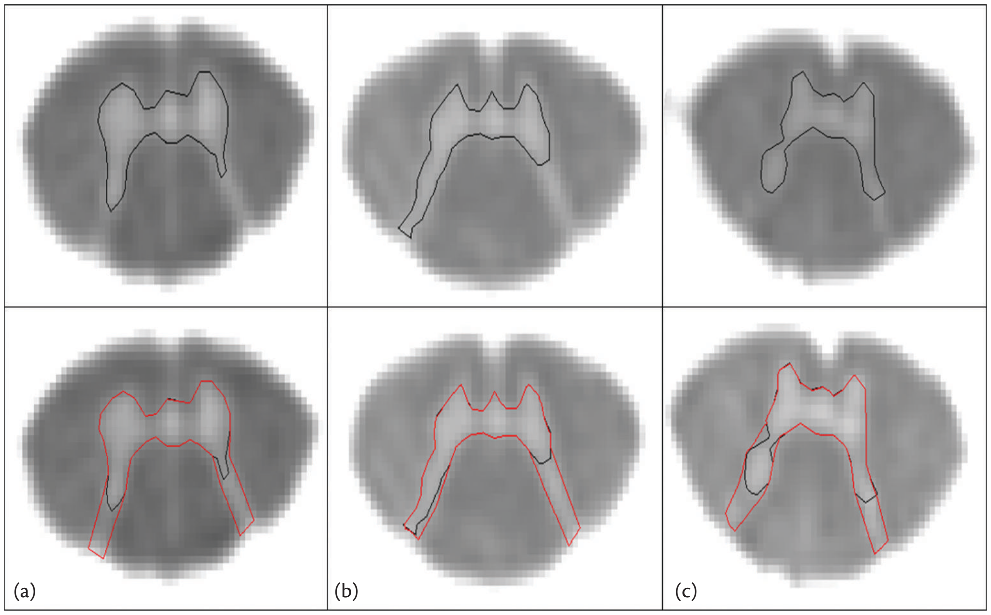

Fig. 25.6 Examples of gray matter cross-sectional area (TGMA) segmentation in three healthy subjects measured at C2; (a–c) top row shows the unedited TGMA contours and bottom row shows the unedited TGMA contours (in black) and how these have been edited by the operator (the final contours are shown in red).
Modified from Yiannakas MC, Kearney H, Samson RS, et al. (2012). Feasibility of grey matter and white matter segmentation of the upper cervical cord in vivo: a pilot study with application to magnetisation transfer measurements. *NeuroImage*, **63**, 1054–9. Copyright (2012), with permission from.

demonstrated (Fig. 25.6) [21]. Further improvement in acquisition protocols, imaging post-processing [33] (Fig. 25.8) and fully computational neuroanatomy analysis techniques [34,35] will eventually allow voxel wise quantification, similar to voxel-based morphometry (VBM) [36] and voxel-based quantification (VBQ) of spinal gray and white matter changes similar to that achieved already for the brain

Voxel-based morphometric analysis of cranial gray and white matter

Beyond looking at the spinal cord itself, it is important to understand the impact of trauma on brain white and gray matter, secondary to those at the local (spinal) level. For the brain, imaging sequences and analysis softwares are well established for assessing functional and structural changes. Voxel-based analysis, such as VBM, and cortical thickness (CT) measurements [37] are valid and sensitive (and spatially unbiased) automated methods that quantify changes in white and gray matter volume and cortical thinning, respectively, on 3D T1w high resolution images. As a result, the combined application of both techniques can provide complementary results as has been shown in ageing [38] and disease [22].

VBM of white matter volume revealed decreases in spatially distinct areas of the corticospinal tract (CST), such as the pyramids and cerebral peduncles in chronic and acute SCI patients [22,39] (Fig. 25.7). In line with the decrease in white matter volume, volumetric changes of gray matter have been observed specifically in the denervated leg area of the primary motor (M1) and sensory cortex (S1) [22,40]. Moreover, CT measurements revealed next to and beyond the leg area of the sensorimotor cortex cortical thinning (Fig. 25.7). However, the latter findings have not been uniformly confirmed in all studies [23,41]. Possible explanations for a failure to reproduce these findings might be the nature of the underlying volumetric changes assessed by VBM—the changes might not only

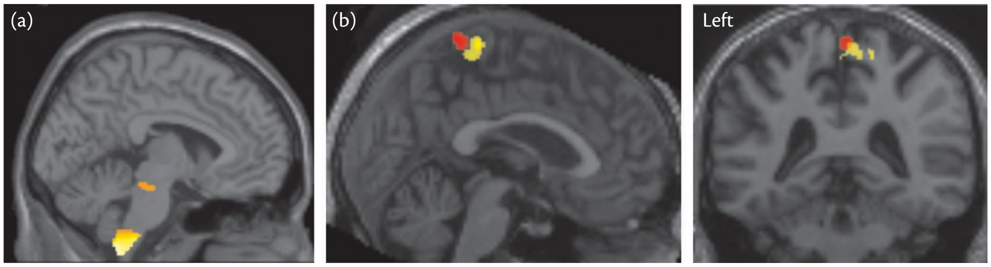

Fig. 25.7 (Sub)-cortical atrophy in chronic tetraplegic patients compared to healthy volunteers. (a) Statistical parametric map (SPM) showing significant white matter volume reduction in regions encompassing the corticospinal tract (yellow) in patients compared to controls using voxel-based morphometry (VBM). (b) SPMs of gray matter volume reduction (yellow) and cortical thinning (red) in the sensorimotor cortices in patients compared to controls using VBM and cortical thickness (CT).
Modified from Freund P, Weiskopf N, Ward NS, et al. (2011). Disability, atrophy and cortical reorganization following spinal cord injury. *Brain*, **134**, 1610–22. Copyright (2011), reproduced under the Creative Commons License 2.5.

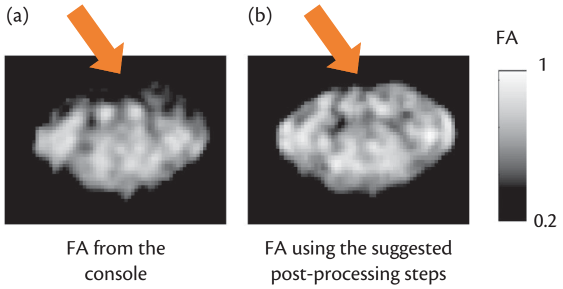

Fig. 25.8 Effect of post-processing on spinal cord fractional anisotropy (FA) image. (a) The FA as it is estimated from the un-processed data directly from the console. Artificial low FA values in the white matter (WM) are visible (highlighted by arrow). (b) The FA after post-processing (i.e. slice-wise eddy current and motion correction [7], and robust tensor fitting [10] was employed). Due to the post-processing, the artificial low white matter FA was corrected, and the butterfly-shaped gray matter structure became better visible.

represent degeneration, but also activity-dependent changes that are dynamic and follow distinct temporal patterns.

Recent studies in patients have revealed activity-dependent cortical volumetric changes either through suppression (i.e. immobilization) or enhancement (i.e. training) of manual activity. Interestingly, these changes were bi-directional either showing contraction or increases in the gray matter volume of primary motor cortex (M1) [42,43]. For example, writer's cramp patients with immobilization of the hand or neurological intact patients with casting of the upper limb due to a fracture have shown decreases in gray matter thickness in contralateral M1, together with a decrease in corticomotor excitability as assessed by transcranial magnetic stimulation (TMS) [42]. Subsequent training reversed the cortical volumetric effects of immobilization. Therefore, it is tempting to speculate that re-training may have induced a re-integration of the local neuronal networks previously implied in manual dexterity. Similar activity-dependent effects might be expected in acute and chronic SCI patients based on the intensity (training duration, frequency, repetition, etc.) and type of rehabilitation intervention (active versus passive movements, task-specificity, etc.), as well as the overall levels of activity (post-traumatic immobilization versus mobilization in a wheelchair or locomotion).

Diffusion-weighted imaging

Gaining insights into the sequel of a SCI at a microscopic level, however, would permit exploration of the extent degeneration contributes to volumetric changes. Diffusion tensor imaging (DTI) data provide the opportunity to explore the integrity of the microstructure of the spinal cord and brain. While fractional anisotropy (FA) has been reported to be a marker of both axonal count [44] and myelin content [45], axial diffusivity and radial diffusivity have been reported to be more specific to the integrity of axons and myelin in the injured spinal cord, respectively [46–49]. Recently, it has been reported that the simple diffusion tensor approach [50] and the relation between axial diffusivity and radial diffusivity on the one side, and axonal and myelin on the other side [51] do not fully describe the complex microstructure of the brain. However, for the spinal cord, the simple diffusion tensor model and its indices might be the right approach, because of the simple geometry of its major fibre bundles (most axons are aligned along the head-feet directions). Thus, in spinal cord DTI, axial diffusivity, and radial diffusivity have the potential to disclose additional information on axonal integrity besides FA.

DTI applied to the chronic injured spinal cord has demonstrated widespread changes in DTI indexes at the lesion site and more rostral to it suggesting trauma-induced degenerative processes in ascending and descending central pathways. Moreover, tractography showed a reduction in the integrity of the CST in chronic SCI patients indicative of the presence of axonal degeneration and demyelination [51]. Lower FA measured within a region of interest that encompassed the corticospinal tract at the cervical level correlated with a poorer performance on a manual dexterity task [52]. Thus, trauma-induced distal neuronal damage spreads supraspinally and induces degenerative changes at the microstructural level in major spinal pathways, which are clinically eloquent [53]. However, the pathological processes underlying these changes within the white matter are not completely understood and may be the result of multiple microstructural changes such as axonal degeneration, demyelination, loss of large diameter axons and/or death of oligodendrocytes [28]. Studies, which will combine different indices sensitive to myelin and axonal integrity, together with histological findings, have the potential to confirm the relative specificity of axial diffusivity and radial diffusivity to chronic demyelination and axonal degeneration in the injured SC. Thus, DTI holds promise to quantify the degree of white matter integrity, to predict recovery and to monitor the effects of therapeutic interventions.

Future perspectives

From neuroimaging studies conducted in chronic SCI, it is commonly understood that trauma to the spinal cord induces atrophic changes in spatially distinct areas of the sensorimotor system in the spinal cord and brain, and that the degree of atrophy relates to disability. However, the onset and rate of these changes are just being assessed in the acute phase of injury [39]. Improving our understanding of the neuronal mechanisms that subtend clinical recovery is essential for individual patient therapy.

The interpretation of signal changes at the microstructural level, however, needs to be treated with care, as they often result in a mix of different types of MR relaxation mechanisms and tissue characteristics [18,54]. For example, increased iron content can look like a reduction of free water on standard T1w images. This confounds the interpretation of signal changes and consequently reduces specificity. Beside DTI, quantitative MRI and, in particular, a new multi-parameter mapping (MPM) approach may increase our understanding of disease progression of the spinal cord and brain in SCI patients. The MPMs yield accurate and precise measures of four major contrast parameters in a clinically feasible scan time of 20 minutes at 1 mm isotropic resolution: longitudinal relaxation rate (R1), apparent transverse relaxation rate (R2*), proton density (PD) and magnetization transfer saturation (MT). Each quantitative parameter reflects a single contrast mechanism that predominantly depends on a specific tissue property, e.g. MT and R1 are highly correlated with myelination, R2* with iron content and PD with free water [18]. These MPM derived measures and DTI indices can be assessed conjointly in spinal and cortical areas of volumetric decline following SCI, in order to further establish the correlates of central volumetric changes.

Another important emerging field is the application of spinal functional magnetic resonance imaging (fMRI), however, results remain controversial due to its low reproducibility [55,56]. Recent advances in the acquisition of spinal functional MRI sequences in humans with improved contrast mechanism due to signal enhancement from extravascular water protons (SEEP) [58] and new *post-hoc* correction methods [59,60] have opened an avenue into the clinical setting for fMRI. For example, increased blood oxygenation level dependent (BOLD) signal intensity changes were observed following stimulation of dermatomes with normal sensation in patients suffering from a traumatic SCI. Interestingly, the degree of sensory impairment, as assessed by the ASIA sensory scale, was inversely correlated with the number of voxels with task-related increases in BOLD signal [61]. The next step would be to assess with quantitative and functional MRI acute changes in the spinal cord and brain in longitudinal multicentre studies in order to validate the sensitivity of the emerging MRI markers and their relationship to central reorganization and predictive value for functional recovery.

Conclusion

MRI of the spinal cord and brain is an excellent clinical and research tool to quantify trauma induced changes across the entire neuroaxis. The degrees of the changes, both at a structural and functional level, are to some extent associated with the degree of disability. These clear relationships provide a conceptual basis for future studies looking at longitudinal changes from the acute to the chronic phase of SCI. Ideally, these will allow for discerning changes that relate to trauma from those that are treatment induced.

References

1. Anderson KD. (2004). Targeting recovery: priorities of the spinal cord-injured population. *Journal of Neurotrauma*, **21**, 1371–83.
2. Freund P, Schmidlin E, Wannier T, et al. (2006). Nogo-A-specific antibody treatment enhances sprouting and functional recovery after cervical lesion in adult primates. *Nature Medicine*, **12**, 790–2.
3. Wang D, Ichiyama RM, Zhao R, et al. (2011). Chondroitinase combined with rehabilitation promotes recovery of forelimb function in rats with chronic spinal cord injury. *Journal of Neuroscience*, **31**, 9332–44.
4. Cummings BJ, Uchida N, Tamaki SJ, et al. (2005). Human neural stem cells differentiate and promote locomotor recovery in spinal cord-injured mice. *Proceedings of the National Academy of Sciences USA*, **102**, 14069–74.
5. Barkhof F, Calabresi PA, Miller DH, et al. (2009). Imaging outcomes for neuroprotection and repair in multiple sclerosis trials. *Nature Reviews Neurology*, **5**, 256–66.
6. Jezzard P, Barnett AS, and Pierpaoli C. (1998). Characterization of and correction for eddy current artifacts in echo planar diffusion imaging. *Magnetic Resonance Medicine* 39: 801–12.
7. Mohammadi S, Moller HE, Kugel H, et al. (2010). Correcting eddy current and motion effects by affine whole-brain registrations: evaluation of three-dimensional distortions and comparison with slicewise correction. *Magnetic Resonance Medicine*, **64**, 1047–56.
8. Bammer R, Markl M, Barnett A, et al. (2003). Analysis and generalized correction of the effect of spatial gradient field distortions in diffusion-weighted imaging. *Magnetic Resonance Medicine*, **50**, 560–9.
9. Mohammadi S, Nagy Z, Moller HE, et al. (2012). The effect of local perturbation fields on human DTI: characterisation, measurement and correction. *NeuroImage*, **60**, 562–70.
10. Mohammadi S, Nagy Z, Hutton C, et al. (2012). Correction of vibration artifacts in DTI using phase-encoding reversal (COVIPER). *Magnetic Resonance Medicine* **68**, 882–9.
11. Mohammadi S, Freund P, Feiweier T, Curt A, Weiskopf N. (2013). The impact of post-processing on spinal cord diffusion tensor imaging. *NeuroImage*, **70**, 377–85.
12. Mohammadi S, Hutton C, Nagy Z, et al. (2012). Retrospective correction of physiological noise in DTI using an extended tensor model and peripheral measurements. *Magnetic Resonance Medicine*, **70**(2), 358–69.
13. Bozzo A, Marcoux J, Radhakrishna M, et al. (2011). The role of magnetic resonance imaging in the management of acute spinal cord injury. *Journal of Neurotrauma*, **28**, 1401–11.
14. Weber T, Vroemen M, Behr V, et al. (2006). In vivo high-resolution MR imaging of neuropathologic changes in the injured rat spinal cord. *AJNR American Journal of Neuroradiology*, **27**, 598–604.
15. Shimada K, and Tokioka T. (1999). Sequential MR studies of cervical cord injury: correlation with neurological damage and clinical outcome. *Spinal Cord*, **37**, 410–15.
16. Miyanji F, Furlan JC, Aarabi B, et al. (2007). Acute cervical traumatic spinal cord injury: MR imaging findings correlated with neurologic outcome—prospective study with 100 consecutive patients. *Radiology*, **243**, 820–7.
17. Andre JB, and Bammer R. (2010). Advanced diffusion-weighted magnetic resonance imaging techniques of the human spinal cord. *Topics in Magnetic Resonance Imaging*, **21**, 367–78.
18. Sereno MI, Lutti A, Weiskopf N, et al. (2012). Mapping the human cortical surface by combining quantitative T1 with retinotopy. *Cerebral Cortex*, **23**(9), 2261–8. 19. Barazany D, Basser PJ, and Assaf Y. (2009). In vivo measurement of axon diameter distribution in the corpus callosum of rat brain. *Brain*, **132**, 1210–20.
20. Draganski B, Ashburner J, Hutton C, et al. (2011). Regional specificity of MRI contrast parameter changes in normal ageing revealed by voxel-based quantification (VBQ). *NeuroImage*, **55**, 1423–34.
21. Yiannakas MC, Kearney H, Samson RS, et al. (2012). Feasibility of grey matter and white matter segmentation of the upper cervical cord in vivo: a pilot study with application to magnetisation transfer measurements. *NeuroImage*, **63**, 1054–9.
22. Freund P, Weiskopf N, Ward NS, et al. (2011). Disability, atrophy and cortical reorganization following spinal cord injury. *Brain*, **134**, 1610–22.
23. Lundell H, Barthelemy D, Skimminge A, et al. (2011). Independent spinal cord atrophy measures correlate to motor and sensory deficits in individuals with spinal cord injury. *Spinal Cord*, **49**, 70–5.
24. Cohen-Adad J, El Mendili MM, Lehericy S, et al. (2011). Demyelination and degeneration in the injured human spinal cord detected with diffusion and magnetization transfer MRI. *NeuroImage*, **55**(3), 1024–33.
25. Stevenson VL, Leary SM, Losseff NA, et al. (1998). Spinal cord atrophy and disability in MS: a longitudinal study. *Neurology*, **51**, 234–8.
26. Kalkers NF, Barkhof F, Bergers E, et al. (2002). The effect of the neuroprotective agent riluzole on MRI parameters in primary progressive multiple sclerosis: a pilot study. *Multiple Sclerosis*, **8**, 532–3.
27. Tuszynski MH, Gabriel K, Gerhardt K, et al. (1999). Human spinal cord retains substantial structural mass in chronic stages after injury. *Journal of Neurotrauma*, **16**, 523–31.
28. Dusart I, and Schwab ME. (1994). Secondary cell death and the inflammatory reaction after dorsal hemisection of the rat spinal cord. *European Journal of Neuroscience*, **6**, 712–24.
29. Buss A, Pech K, Merkler D, et al. (2005). Sequential loss of myelin proteins during Wallerian degeneration in the human spinal cord. *Brain*, **128**, 356–64.
30. Becerra JL, Puckett WR, Hiester ED, et al. (1995). MR-pathologic comparisons of wallerian degeneration in spinal cord injury. *AJNR American Journal of Neuroradiology*, **16**, 125–33.
31. Wu CW, and Kaas JH. (2000). Spinal cord atrophy and reorganization of motoneuron connections following long-standing limb loss in primates. *Neuron*, **28**, 967–78.
32. Schmid MR, Pfirrmann CW, Koch P, et al. (2005). Imaging of patellar cartilage with a 2D multiple-echo data image combination sequence. *AJR American Journal of Roentgenology*, **184**, 1744–8.

33. Mohammadi S, Freund P, Feiweier T, et al. (2013). The impact of post-processing on spinal cord diffusion tensor imaging. *NeuroImage*, **70**, 377–85.
34. Rocca MA, Valsasina P, Damjanovic D, et al. (2013). Voxel-wise mapping of cervical cord damage in multiple sclerosis patients with different clinical phenotypes. *Journal of Neurology, Neurosurgery & Psychiatry*, **84**, 35–41.
35. Valsasina P, Rocca MA, Horsfield MA, et al. (2012). Regional cervical cord atrophy and disability in multiple sclerosis: a voxel-based analysis. *Radiology*, **266**(3), 853–61.
36. Ashburner J, and Friston KJ. (2000). Voxel-based morphometry—the methods. *NeuroImage*, **11**, 805–21.
37. Hutton C, De VE, Ashburner J, Deichmann R, et al. (2008). Voxel-based cortical thickness measurements in MRI. *NeuroImage*, **40**, 1701–10.
38. Hutton C, Draganski B, Ashburner J, et al. (2009). A comparison between voxel-based cortical thickness and voxel-based morphometry in normal aging. *NeuroImage*, **48**, 371–80.
39. Freund P, Weiskopf N, Ashburner J, et al. (2013). MRI investigation of the sensorimotor cortex and the corticospinal tract after acute spinal cord injury: a prospective longitudinal study. *Lancet Neurology*, **12**(9), 873–81. Erratum: *Lancet Neurology*, **12**(9), 846.
40. Jurkiewicz MT, Crawley AP, Verrier MC, et al. (2006). Somatosensory cortical atrophy after spinal cord injury: a voxel-based morphometry study. *Neurology*, **66**, 762–4.
41. Granert O, Peller M, Gaser C, et al. (2011). Manual activity shapes structure and function in contralateral human motor hand area. *NeuroImage*, **54**, 32–41.
42. Langer N, Hanggi J, Muller NA, et al. (2012). Effects of limb immobilization on brain plasticity. *Neurology*, **78**, 182–8.
43. Gouw AA, Seewann A, Vrenken H, et al. (2008). Heterogeneity of white matter hyperintensities in Alzheimer's disease: post-mortem quantitative MRI and neuropathology. *Brain*, **131**, 3286–98.
44. Schmierer K, Wheeler-Kingshott CA, Boulby PA, et al. (2007). Diffusion tensor imaging of post mortem multiple sclerosis brain. *NeuroImage*, **35**, 467–77.
45. Ou X, Sun SW, Liang HF, et al. (2009). The MT pool size ratio and the DTI radial diffusivity may reflect the myelination in shiverer and control mice. *NMR in Biomedicine*, **22**(5), 480–7.
46. Song SK, Sun SW, Ramsbottom MJ, et al. (2002). Dysmyelination revealed through MRI as increased radial (but unchanged axial) diffusion of water. *NeuroImage*, **17**, 1429–36.
47. Song SK, Yoshino J, Le TQ, et al. (2005). Demyelination increases radial diffusivity in corpus callosum of mouse brain. *NeuroImage*, **26**, 132–40.
48. Zhang J, Jones M, DeBoy CA, et al. (2009). Diffusion tensor magnetic resonance imaging of Wallerian degeneration in rat spinal cord after dorsal root axotomy. *Journal of Neuroscience*, **29**, 3160–71.
49. Jones DK, Knosche TR, and Turner R. (2012). White matter integrity, fiber count, and other fallacies: the do's and don'ts of diffusion MRI. *NeuroImage*, **73**, 239–54.
50. Wheeler-Kingshott CA, and Cercignani M. (2009). About 'axial' and 'radial' diffusivities. *Magnetic Resonance Medicine*, **61**, 1255–60.
51. Budde MD, Kim JH, Liang HF, et al. (2008). Axonal injury detected by in vivo diffusion tensor imaging correlates with neurological disability in a mouse model of multiple sclerosis. *NMR in Biomedicine*, **21**, 589–97.
52. Freund P, Schneider T, Nagy Z, et al. (2012). Degeneration of the injured cervical cord is associated with remote changes in corticospinal tract integrity and upper limb impairment. *PLoS ONE*, **7**(12), e51729.
53. Wrigley PJ, Gustin SM, Macey PM, et al. (2009). Anatomical changes in human motor cortex and motor pathways following complete thoracic spinal cord injury. *Cerebral Cortex*, **19**, 224–32.
54. Draganski B, Ashburner J, Hutton C, et al. (2011). Regional specificity of MRI contrast parameter changes in normal ageing revealed by voxel-based quantification (VBQ). *NeuroImage*, **55**, 1423–34.
55. Bouwman CJ, Wilmink JT, Mess WH, et al. (2008). Spinal cord functional MRI at 3 T: gradient echo echo-planar imaging versus turbo spin echo. *NeuroImage*, **43**, 288–96.
56. Giove F, Garreffa G, Giulietti G, et al. (2004). Issues about the fMRI of the human spinal cord. *Magnetic Resonance Imaging*, **22**, 1505–16.
57. Stroman PW, Kornelsen J, Lawrence J, et al. (2005). Functional magnetic resonance imaging based on SEEP contrast: response function and anatomical specificity. *Magnetic Resonance Imaging*, **23**, 843–50.
58. Stroman PW, Figley CR, and Cahill CM. (2008). Spatial normalization, bulk motion correction and coregistration for functional magnetic resonance imaging of the human cervical spinal cord and brainstem. *Magnetic Resonance Imaging*, **26**, 809–14.
59. Xie G, Piche M, Khoshnejad M, et al. (2012). Reduction of physiological noise with independent component analysis improves the detection of nociceptive responses with fMRI of the human spinal cord. *NeuroImage*, **63**, 245–52.
60. Cadotte DW, Bosma R, Mikulis D, et al. (2012). Plasticity of the injured human spinal cord: insights revealed by spinal cord functional MRI. *PLoS ONE*, **7**, e45560.
61. Curt A. (2012). The translational dialogue in spinal cord injury research. *Spinal Cord*, **50**, 352–7.

CHAPTER 26

Spinal cord diseases

Maria A. Rocca, Paolo Preziosa, and Massimo Filippi

Introduction

The spinal cord is a portion of the central nervous system (CNS) that lies within the spinal canal inside the spine, and is surrounded by a variable layer of cerebrospinal fluid (CSF), and by a thick layer of bone or cartilaginous discs between the vertebral bodies. The spinal cord is a thin structure, with the widest region at the level of the cervical enlargement of only ≈15 mm, with an average length of approximately 45 cm in adult humans. The pulsating CSF flow and arterial pulsation cause the spinal cord to move within the spinal canal, with an amplitude that diminishes with greater distance from the head. Moreover, the spinal cord is close to the heart and lungs, which might further promote and determine spinal cord movements.

The anatomical arrangement of the spinal cord is the reverse to that of the brain, with the gray matter (GM; largely nerve cell bodies, glial cells, and interneurons) within a characteristic butterfly-shaped cross-section at the centre of the cord, surrounded by white matter (WM) tracts. The main arteries supplying the cord lie along the cord surface, one above the anterior median fissure and two along the posterior side of the cord, and these are connected by lateral branches. The anterior artery sends branches into the anterior median fissure with further branching to supply the GM from the centre outward. Venules and small veins carry blood radially from the GM to the cord surface.

Due to these anatomical and topographical features, imaging the spinal cord is challenging. When planning to study this structure, one should therefore consider:

1. The spatial inhomogeneity of the magnetic field strength in this regions.
2. The small physical dimension of the spinal cord cross-section area.
3. Physiological motions.

These points are discussed in detail in Chapter 25.

This chapter summarizes the major contributions obtained using conventional and advanced magnetic resonance imaging (MRI) techniques for the *in vivo* diagnosis and monitoring of various diseases other than spinal cord injury involving this CNS structure.

Inflammatory/demyelinating diseases

CNS demyelinating diseases are a group of heterogeneous neurological conditions mainly characterized by damage to the myelin sheaths covering axons, which are secondary to different aetiologies (e.g. autoimmune, post-infective, disimmune, etc.).

Multiple sclerosis

Multiple sclerosis (MS) is the most common chronic inflammatory demyelinating disease affecting the CNS. The application of conventional and advanced MRI techniques for the diagnosis and monitoring of MS and future possible application of MRI in MS are discussed in Chapter 15.

Concerning the spinal cord, conventional MRI features of MS cord lesions have been identified (Fig. 26.1) [1]. Specifically, MS cord lesions are more frequently observed in the cervical than in other cord regions, are usually peripheral, limited to two vertebral segments in length or less, and occupy less than half the cross-sectional area of the cord (Fig. 26.1) [1]. A set of new strategies has been proposed to improve the detection of spinal cord lesions, including the use of an axial 3D gradient echo sequence with or without magnetization transfer (MT)-prepulse [2] and of an optimized T_1 magnetization-prepared-rapid-acquisition-gradient-echo (MPRAGE) sequence [3].

Although a significant reduction of cervical cord size can be observed since the early phase of MS [4], cord atrophy is more severe in the progressive forms of the disease [1]. Abnormalities at a given time point and changes over time of cord cross-sectional area correlate better with clinical disability than changes of brain T_2 lesion burden [5]. A new semi-automatic method [6], which allows segmentation of long portions of the cord, has been recently developed. The use of this approach in a multicentre study of a large sample of MS patients has demonstrated that the cord area differs significantly among the main MS clinical phenotypes and is correlated with locomotor disability [7] with a differential effect among phenotypes: no association in either clinically isolated syndromes (CIS) or benign multiple sclerosis (BMS) patients; association in relapsing-remitting (RR) MS, secondary progressive (SP) MS and primary progressive (PP) MS [8]. A voxel-wise approach has also been developed and applied to define the regional distribution of cervical cord damage of MS patients. While RR MS patients had a few clusters of regional atrophy mainly located in the posterior and lateral columns, SP MS patients experienced a diffuse cord atrophy, which was significantly correlated with disability [9]. A more recent voxel-based study [10] found no cord atrophy in CIS patients versus healthy controls, while PP MS had significant cord atrophy. Clusters of cord atrophy were found in BMS versus RR MS, and in SP MS versus RR MS, BMS and PP MS patients, mainly involving the posterior and lateral cord segments. Cord lesion probability maps showed a significantly greater likelihood of cord abnormalities in RR MS, PP MS and SP MS than in CIS and BMS patients. In progressive MS, regional cord atrophy was correlated with clinical disability and impairment of the pyramidal system [9,10].

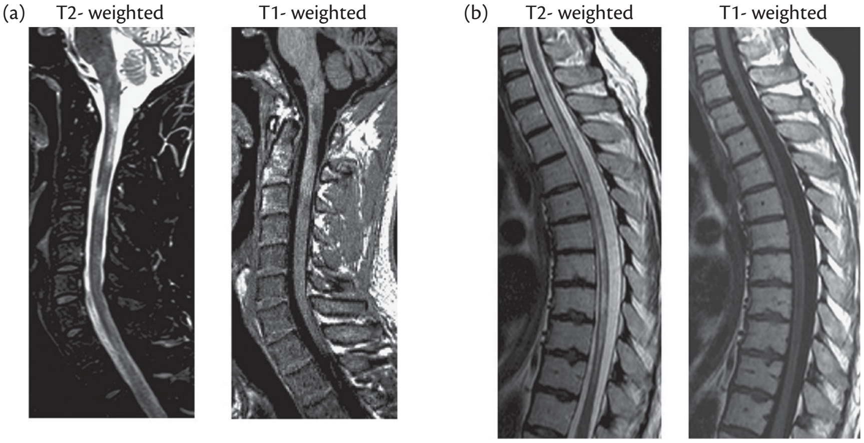

Fig. 26.1 Spinal cord sagittal T_2- and T_1-weighted magnetic resonance images from a patient with relapsing-remitting (RR) multiple sclerosis (MS) (a) and a patient with neuromyelitis optica (NMO) (b). In RR MS, several oval-shape cervical cord lesions, hyperintense on T_2-weighted scan, and hypointense on T_1-weighted images, are evident. In NMO, a T_2 hyperintense lesion extending for several segments of the cervical and thoracic cord is present. Hypointensity on T_1-weighted sequence is also visible.

Magnetization transfer ratio (MTR) can also be measured in the cervical cord [11–16]. A reduction of MTR of the cervical cord has been described in all MS phenotypes, except for CIS, which correlated with disability [16,17]. A study showed that MTR abnormalities located in the dorsal and lateral columns of the spinal cord are associated with deficits of vibration sensation and strength, respectively [18]. In patients with RR MS, reduced cervical cord GM average MTR was correlated with the severity of disability [19].

Abnormal diffusion tensor magnetic resonance imaging (DT-MRI) quantities from the cervical cord have been shown in patients with definite MS, but not in those with CIS [20]. A two-year longitudinal study of patients with relapse-onset MS found that baseline cord area and fractional anisotropy (FA) correlated with increased in disability at follow-up [21]. Compared with controls, MS patients with a cervical cord relapse have reduced N-acetyl aspartate (NAA) and lower structural connectivity in the lateral corticospinal tract and posterior tracts, and such abnormalities were found to correlate with disability [22]. Recently, diffusional kurtosis MRI has been applied to assess non-Gaussian diffusion in cervical cord from MS patient. This approach has provided a more comprehensive evaluation, especially of GM cord pathology [23]. A cross-sectional study, which combined different MR modalities (DT MRI, MTR and atrophy) to quantify cervical cord damage in a large sample of MS patients, showed that a multiparametric MR approach contributes to discriminate patients with high from those with low levels of disability [24].

An increased functional MRI (fMRI) activation of the cervical cord has been demonstrated in all major MS clinical phenotypes and has been related to the severity of disability and the extent of tissue damage [25,26]. An abnormal recruitment of the spinal cord has been correlated with same of the clinical manifestations of the disease, such as fatigue [27].

Variants of multiple sclerosis and neuromyelitis optica

Conventional and advanced imaging features of spinal cord damage in patients with neuromyelitis optica (NMO) and the so-called classic MS variants (i.e. Balo's concentric sclerosis, Schilder's disease, acute MS, and acute disseminated encephalomyelitis) are discussed in Chapter 15.

Other inflammatory and immuno-mediated diseases

Spinal cord involvement can be detected in many other inflammatory and immuno-mediated diseases, including sarcoidosis, systemic lupus erythematosus (SLE) and CNS vasculitis.

Central and peripheral nervous system can be involved in approximately 5–16% of patients with sarcoidosis. Neurosarcoidosis is most commonly associated with granulomatous infiltrates involving the leptomeninges, dura, hypothalamus, pituitary gland, and cranial nerves. Spinal cord neurosarcoidosis is rare with an incidence estimated at 0.43–1% of all patients and is usually characterized by the presence of T_2-hyperintense lesions, associated with a variable degree of T_1-hypointensity and patchy/nodular contrast-enhancement on conventional MRI [28]. A classification of intramedullary spinal sarcoidosis in different stages has been proposed by Junger et al. [29] based on the analysis of a retrospective series:

1. *Phase 1:* early inflammation showing linear leptomeningeal enhancement after gadolinium (Gd) administration along the spinal surface.
2. *Phase 2:* secondary centripetal spread of the leptomeningeal inflammatory process through the Virchow–Robin spaces, showing parenchymal involvement with faint enhancement and diffuse swelling.
3. *Phase 3:* less prominent swelling and possible normal-sized spinal cord, associated with focal or multiple enhancement.
4. *Phase 4:* resolution of the inflammatory process with normal size or atrophy of the spinal cord, and no enhancement.

Phases 2 and 3 are the most frequently detected at clinical presentation (Fig. 26.2). Other rare cord findings, such as calcifications, cyst formation, and extradural involvement have also been described.

Acute transverse myelitis occurs in 1–2% of SLE patients [30,31], generally involving less than four vertebral bodies. In these patients, spinal cord MRI may reveal longitudinally extensive lesions with cases of continuous transverse myelitis affecting more than four

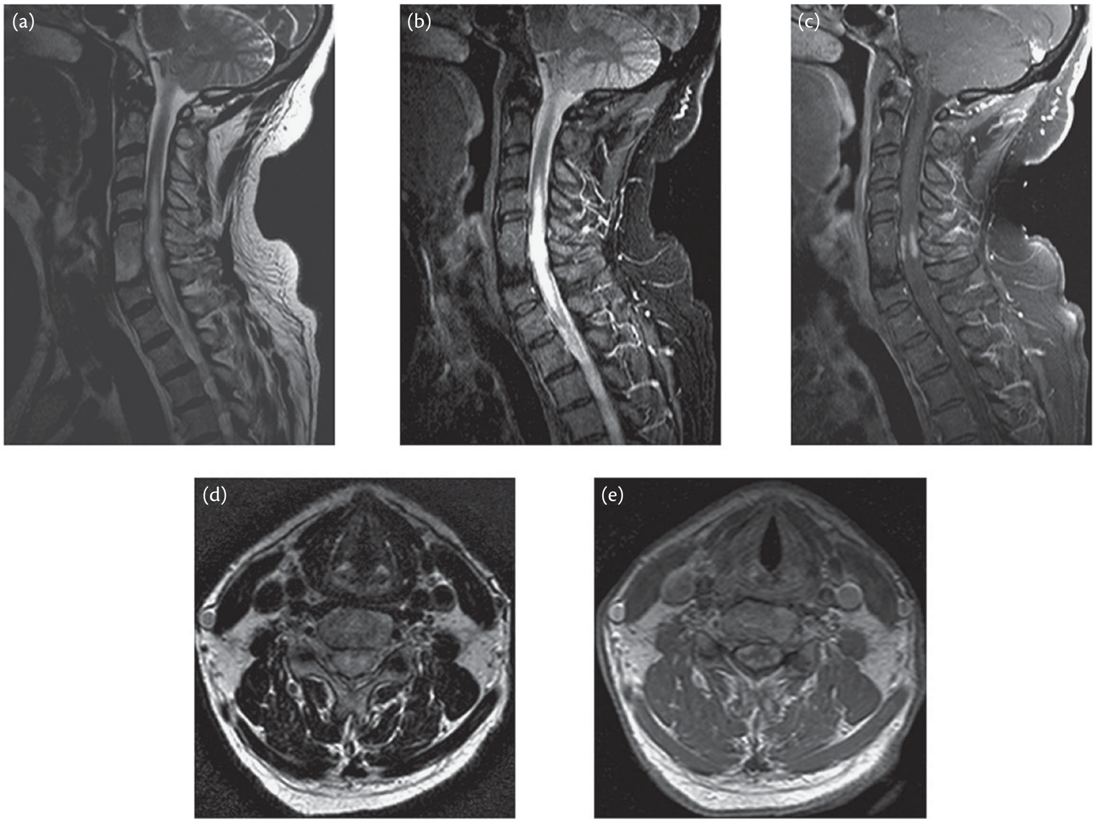

Fig. 26.2 Spinal cord sagittal and axial T_2-weighted (a,d), sagittal short tau inversion recovery (STIR) (b) and sagittal and axial (c,e) post-Gd T_1-weighted magnetic resonance images from a patient with neurosarcoidosis. A large T_2 hyperintense lesion surrounded by oedema and associated to spinal cord swelling is visible (a,b,d). A peripheral enhancement of the spinal cord involving the meninges is also evident (c and e).

spinal segments, and sometimes involving the entire length of the spinal cord. Resolution of these lesions correlates with clinical improvement [30,31].

Spinal cord involvement is reported in 20–34% of all patients with Sjögren's syndrome (SS) and it is occasionally the initial manifestation of this systemic disease [32]. In these patients, cord involvement is generally characterized by longitudinally extensive spinal cord lesions (more than seven segments) [32,33]. Several studies suggest that there is considerable overlap between SS and NMO-spectrum disorders. Indeed, patients with NMO often have accompanying autoantibodies or autoimmune disorders, and SS is one of the most frequently found autoimmune disorders in these patients, suggesting a common underlying mechanism or predisposition [32,33].

Patients with Behçet's disease and spinal cord involvement generally show a single lesion, which might look like a demyelinating plaque, but might extend over two or three segments. Enhancement and surrounding oedema is also common [34].

Spinal cord involvement, characterized by the presence of T_2-hyperintense lesions, generally showing Gd enhancement, and commonly affecting the dorsal portion of the cord, has also been described in up to 5% of patients with primary CNS vasculitis [35].

Infectious diseases

Infective and para-infective conditions (caused by viral, bacterial or parasitic agents) can cause myelopathies.

Infectious agents that are particularly liable to be involved in directly causing spinal cord lesions are herpes viruses (herpes simplex virus (HSV) [36], varicella zoster virus (VZV) [37], Epstein–Barr virus (EBV) and cytomegalovirus (CMV) [38]), human immunodeficiency virus (HIV) [39–41], human T-lymphotrophic virus (HTLV-1) [42], *Borrelia burgdorferi* [43], *Treponema pallidum* [44,45], *Mycobacterium* [46] and *Schistosoma* [47].

Viral infections of the CNS are uncommon but are important in the differential diagnosis of acute myelopathy [48]. Acute viral myelitis can present as acute flaccid paralysis (poliomyelitis) or neurologic dysfunction due to involvement of the WM. Such an involvement usually affects only part of the transverse section of the spinal cord and manifests as asymmetric motor and sensory symptoms. MRI of the patient with viral myelitis can demonstrate a wide range of findings, including a normal appearing spinal cord. In this latter case, repeating MRI after 1 or 2 days may reveal abnormalities. It is not unusual for T_2-hyperintensity to extend over multiple vertebral segments. In HSV myelitis, haemorrhagic necrosis within the lesions can lead to hyperintensity on T_1-weighted images [36]. In acute lesions, Gd administration classically reveals enhancement of the cord and sometimes of the adjacent meninges and roots. Contrast-enhancement disappears within days. Cord enlargement, due to focal cord oedema may also be observed in the lesion.

Spinal symptoms in HIV-positive patients are a diagnostic challenge, since they may have acute or chronic myelopathy, radiculopathy, and/or peripheral neuropathy [49]. HIV itself has been described as causing myelitis. HIV myelitis has been reported to involve the GM of the spinal cord and to be frequently associated with severe HIV-encephalitis. Vacuolar myelopathy, which presents clinically as a progressive myelopathy, is the most common chronic myelopathy associated with late stage HIV infection or AIDS. Spinal cord MRI characteristically reveals symmetrical high signal on T_2 scans with a predilection for the dorsal columns and lateral corticospinal tracts in multiple contiguous sections. The lesions usually do not enhance following Gd administration [39–41].

Polioviruses are classically associated with acute flaccid paralysis. Spinal MRI findings include T_2 hyperintense signal involving bilateral anterior horns with a variable longitudinal extension [50] and Gd-enhancement of the anterior portion of the cord in some cases, indicating an acute anterior horn infection [51]. In the later stages, cavitation and atrophy of the anterior horns can be seen.

HTLV-I is associated with adult T-cell leukaemia and a chronic progressive disease of the CNS termed HTLV-I–associated myelopathy/tropical spastic paraparesis. Several cases of myelopathy associated with HTLV-I infection have been described, which are characterized by spinal cord swelling with hyperintense T_2 signal and contrast enhancement mainly of the cervical and thoracic portions. At follow-up, a progressive decrease of spinal cord swelling with the disappearance of T_2 hyperintensities has been observed [42].

Acute *Borrelia burgdorferi* myelitis represents less than 5% of all cases of neuroborreliosis. Spinal cord MRI is typically characterized by T_2 hyperintense lesions, associated to various degrees of cord swelling. Contrast enhancement of the spinal cord and the meninges are common findings [43]. A combined DT MRI and MT MRI study showed no microstructural tissue abnormalities of the cervical cord of 20 patients with neuroborreliosis, which might help in the differential diagnosis with other conditions, such as MS [52].

Patients with neurosyphilis can show three types of spinal cord lesions—syphilitic meningomyelitis, spinal meningovascular syphilis (anterior spinal artery syndrome), and tabes dorsalis. In syphilitic myelitis, generally there is a primary involvement of the meninges and vessels. Meningeal and subpial inflammation can cause abnormal Gd-enhancement in the superficial portions of the spinal cord. In some cases, vascular changes of the meninges predominate and ischaemia of the spinal cord occurs, thus determining T_2-hypeintensity [44,45].

Spinal cord involvement following infection of *Mycobacterium tuberculosis*, especially in active disease, can develop secondary to mechanical compression by abscess, granulation tissue, tubercular debris, caseous tissues, and localized pressure of internal salient and/or pathological subluxation/dislocation of the vertebrae. The spinal cord may develop oedema, cord atrophy with myelomalacia and syrinx, thickening of dura-arachnoid complex and/or arachnoiditis, and interstitial gliosis [46].

Symptomatic spinal cord involvement is rare but well described in schistosomiasis. A non-specific intramedullary expansion of the caudal spinal cord is the most common finding of conventional and computed myelography. In eight cases of confirmed schistosomiasis, MRI showed a mild to moderate enlargement of the caudal part of the spinal cord and of the conus medullaris from D9 to L3 [47]. This abnormality was usually T_1 iso-intense and patchy hyperintense on T_2-weighted images. Contrast enhancement was present in all patients, with three different patterns:

1. Intramedullary nodular enhancement, often multiple and of different sizes.
2. Peripheral enhancing lesions on the cord surface, especially in the anterior regions of the cord.
3. Enhancing thickened nerve roots and cauda equina.

Short segment transverse myelitis and longitudinally extensive transverse myelitis can occur as a para-infectious phenomenon. Considering a sample of 17 para-infectious myelitis patients, Pradhan et al. [53] defined three different patterns of MRI features:

1. Focal segmental myelitis: focal cord lesions with long tract signs and good clinical prognosis.
2. Ascending myelitis: continuous lesions from conus to mid-cord with upper and lower motor neuron signs, dysautonomia and poor clinical outcome.
3. Disseminated myelitis: discrete lesions scattered throughout the cord with subtle signs in spinal segmental distribution, above and below the transverse level and moderate clinical outcome.

Neoplasm

Myelopathy is an important and severe neurological complication of cancer and might be due to several reasons. Epidural spinal cord compression (SCC) is the most common cause, occurring in approximately 5% of patients with cancer (Fig. 26.3).

MRI of the entire spine is the initial study of choice, with up to one-third of patients showing multiple sites of compression at initial diagnosis [54]. Other disorders, such as intramedullary spinal cord metastases, primary spinal cord neoplasms, adverse effects of therapy, and paraneoplastic spinal cord syndromes, might also occur. Ependymomas, astrocytomas, and haemangioblastomas are the three most frequently seen primary intramedullary tumours [55,56]. MRI should be performed as soon as possible whenever an intrinsic spinal cord lesion is suspected clinically. MRI assessment should include systematically T_1- and T_2-weighted images, as well as Gd-enhanced T_1-weighted images. The entire spinal cord should be studied with dedicated phased-array spinal surface coils. At least two different imaging planes must be used in order to locate the tumour properly and to differentiate intra- from extramedullary tumours.

Spinal ependymomas are the most common intramedullary tumour. The typical cellular ependymoma is located in the cervical region and associated large satellite cysts are frequently seen. Ependymomas originate from ependymal linings and hence tend to be located more centromedullary compared with astrocytomas, which are also frequently seen in the cervical region. The myxopapillary subtype, which makes up nearly 30% of all spinal ependymomas, is found almost exclusively in the cauda equina and filum terminale. The mean size of cellular subtype ependymomas corresponds to an average height of three to four vertebral bodies. These tumours are slow-growing and often present with features of osseous remodelling, such as canal expansion and scalloping of the posterior vertebral bodies. Nearly all ependymomas show hyperintense signal on T_2-weighted images. Ependymomas enhance homogeneously and usually have well-defined borders. A so-called 'cap sign' is often seen and corresponds to low signal intensity areas capping both sides of the tumour limits; these caps are haemosiderin deposits due to chronic haemorrhage.

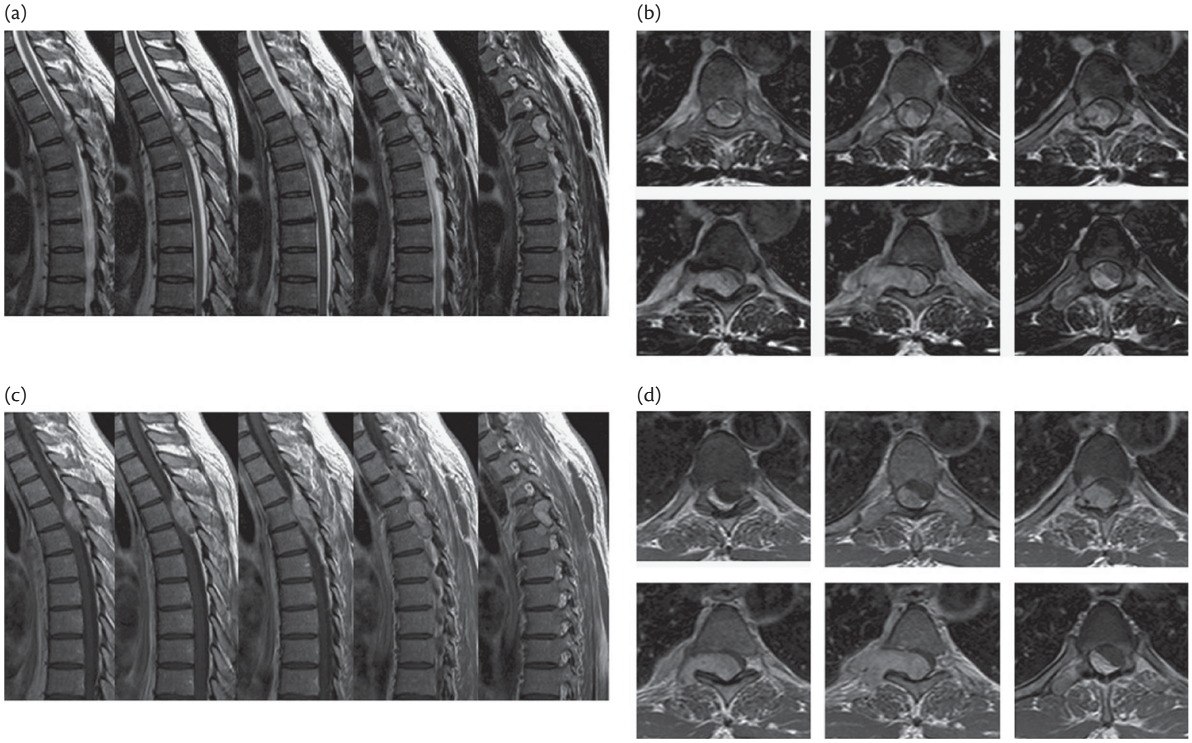

Fig. 26.3 Spinal cord sagittal (a,c) and axial (b,d) T2-weighted (a,b) and post-contrast T_1-weighted (c,d) magnetic resonance images from a patient with a sarcoma causing a spinal cord compression. A dishomogeneous lesion on T_2-weighted images, with diffuse contrast enhancement on T_1-weighted images, and cord displacement is evident.

Astrocytomas, which tend to be located to the (cervico)-thoracic region, account for 24–30% of intramedullary tumours in adults, and up to 90% of tumours in children. On T_2-weighted images, areas of increased signal represent a combination of tumour mass and extensive surrounding cord oedema. Astrocytomas are usually eccentrically located in the cord and show heterogeneous, moderate and partial contrast enhancement. The tumour borders are frequently ill-defined, asymmetric or 'lumpy'.

Hemangioblastomas are richly vascularized tumours, usually located eccentrically, intramedullary, and posteriorly in the cord. These tumours can be either solitary or multiple, and are most frequently located in the thoracic regions. Tumour nodules are usually small and they are typically associated with extensive hydrosyringomyelia. The typical appearance is of a well-defined high T_2 signal intensity ovoid or rounded cystic tumour with a strongly enhancing mural nodule. Extensive hydrosyringomyelia may be present in up to 50–70% of cases.

Intramedullary spinal cord metastases are rare, representing 4% of all the intramedullary tumours. No specific MRI characteristics are reported. Usually metastases are small, nodular, well-defined lesions, hyperintense on T_2-weighted images. The enhancement pattern may be either ring-like or homogeneous. Often, the extensive oedema involves several segments of the spinal cord resulting in hyperintensity and cord expansion.

Cancer treatment itself might results in myelopathy. Drugs including cisplatin, doxorubicin, vincristine, cytosine arabinoside, and intrathecal methotrexate might cause cord damage. Spinal cord MRI acquired very early after treatment initiation might be normal, even though T_2-hyperintensities may be described early. Other abnormalities include spinal cord swelling, contrast enhancement, sometimes limited to the lateral column and/or being located peripherally [57].

Radiation-induced myelopathy can present with four different clinical syndromes [58], including acute transient myelitis, chronic-progressive radiation myelopathy, lower motor neuron disease of the extremities, and acute paraplegia. Radiation-induced damage causes extensive demyelination and neuronal loss, and spinal cord MRI might be normal or might reveal increased T_2 signal sometimes associated with contrast enhancement [54,55].

Although rare, paraneoplastic syndromes can cause myelopathy [54,59]. The pathogenesis is believed to be an autoimmune reaction to antigen shared between the tumour and the CNS. The hallmark MRI finding in paraneoplastic myelopathy is longitudinally extensive, symmetric, tract-specific signal abnormalities within the spinal cord that often enhance after Gd administration. This pattern most commonly involves the lateral columns, but dorsal columns or central GM can also be involved. MRI may be normal in up to 50% of the cases.

Although the application of proton MR spectroscopy (1H-MRS) in the spinal cord is not straightforward, and great care is required to attain optimal spectral quality, a few studies have investigated metabolic abnormalities in spinal cord tumours [60]. A study [61] evaluated 14 patients with mass lesions and detected abnormal choline peaks in all tumours except for ependymoma. Such a finding was absent in other benign conditions, including disc herniation (mimicking spinal cord tumours), dermoid cyst, tuberculosis, and non-MS myelitis. Spectral patterns of meningiomas, schwannomas, metastasis from renal cell carcinoma, and ependymomas of the spinal cord were similar to those of brain tumours.

Syringomyelia

Syringomyelia literally means 'cavity within the spinal cord' and is typically a progressive chronic condition. The syrinx is either a fluid-filled, gliosis-lined cavity within the cord parenchyma or a focal dilatation of the central canal, in which case it is called hydromyelia [62]. Most lesions are located between C2 and T9, but they can descend down to the conus medullaris, or extend upward into the brainstem (i.e syringobulbia). Syringomyelia usually occurs in the setting of congenital anomalies, most commonly the Arnold–Chiari type I malformation and tethered cord. Acquired forms are also described, which are thought to be caused by disturbance in normal CSF circulation following conditions, such as infections, inflammation, trauma, hydrocephalus, spinal canal stenosis, and extramedullary lesions.

Imaging of the spinal cord has greatly improved the diagnosis of syringomyelia, since the demonstration of malformation and/or abnormalities in CSF circulation are very specific signs. Nevertheless, the visualization of intramedullary cavities or peri-medullary CSF flow disturbances is challenging. Common spinal cord MRI findings include the visualization of a syrinx characterized by T_2-hyperintensity and T_1-hypointensity, similar to CSF extending along the cervical and thoracic cord (Fig. 26.4). To detect sometimes subtle, extramedullary arachnoid adhesions or membranes, advanced imaging techniques, such as three-dimensional (3D) constructive interference in steady state (CISS) sequences, can be very helpful. Using electrocardiographically-gated flow-sensitive techniques, such as four-dimensional (4D) phase contrast (PC) MRI, CSF flow dynamics can be studied to distinguish physiological from complex pathological flow patterns at the craniocervical junction, and cervical and thoracic spine, and to detect cystic spaces not communicating with normal CSF spaces [62–65].

Vascular disorders

Acute spinal cord infarction can mimic myelitis and the ischaemic area can extend over several vertebral segments, thus mimicking longitudinal extended transverse myelitis. The onset of spinal cord ischaemia is usually sudden and associated with pain. The anterior two-thirds of the spinal cord are most often involved in acute infarcts, owing to disruption or blockage of the anterior spinal artery (Fig. 26.5). Important mechanisms of ischaemia include the disruption of atheromatous plaque with resultant micro-emboli, aortic dissection, and hypotension with hypoperfusion. The major arterial supply to the thoracolumbar segment of the spinal cord is the artery of Adamkiewicz, which is a single, prominent radicular artery that originates most often from the left intercostal artery between T8 and T11. Mawad et al. [66] described four imaging patterns on MR proportional to the degree of ischaemia. First, axial T_2-weighted MRI scans can show a so-called 'snake eye' or 'owl's eye' pattern of bilateral hyperintensities of the anterior horns of the GM. Then, the posterior horn region is involved; subsequently the posterolateral WM tracts and, finally, the entire transverse area of the cord. The dorsal part of the vertebral body in the affected region can show increased signal on T_2-weighted scans as an indicator of cord infarction, since the vertebral body and spinal cord share the same segmental blood supply. After some days, T_2-weighted images can show hyperintense lesions with spinal cord swelling.

DT MRI can help to visualize diffusion restriction as a sign of acute ischaemic infarction. Thurnher et al. [67] found a decreased apparent diffusion coefficient (ADC) in the first hours after the onset of symptoms, suggestive of restricted diffusion, with a progressive resolution of MRI abnormalities within 1 week.

Spinal dural arteriovenous fistulae can also cause diffuse T_2-hyperintense spinal cord lesions that might extend over more than three vertebral segments (Fig. 26.6). Unlike inflammatory

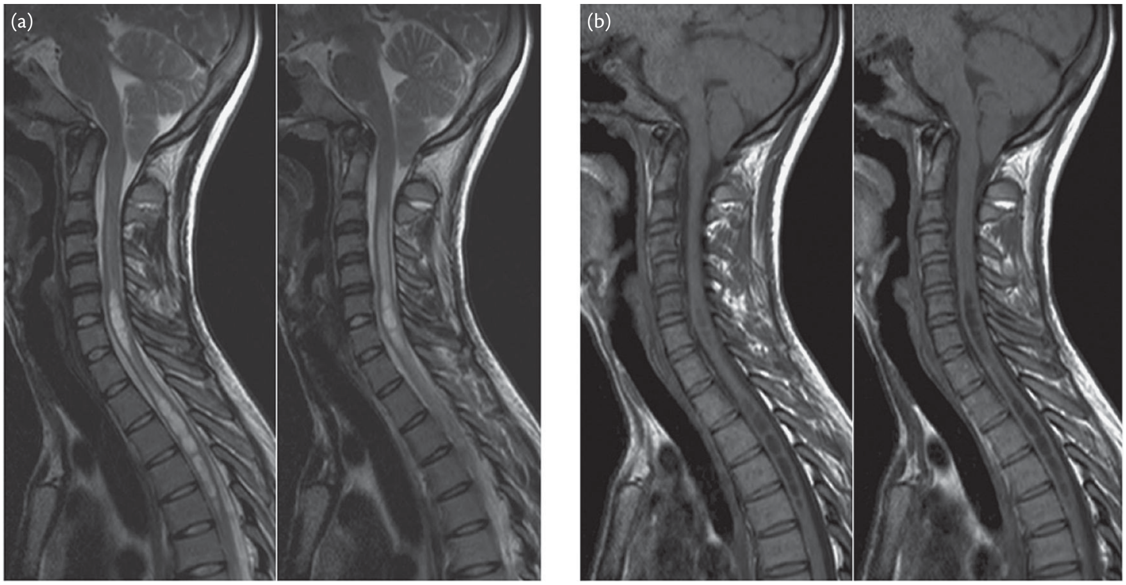

Fig. 26.4 Spinal cord sagittal T_2-weighted (a) and T_1-weighted (b) magnetic resonance images from a patient with Arnold–Chiari Type I malformation and syringomyelia. A syrinx fluid-filled, characterized by T_2-hyperintensity and T_1-hypointensity similar to cerebrospinal fluid (CSF) is evident along the cervical and thoracic cord.

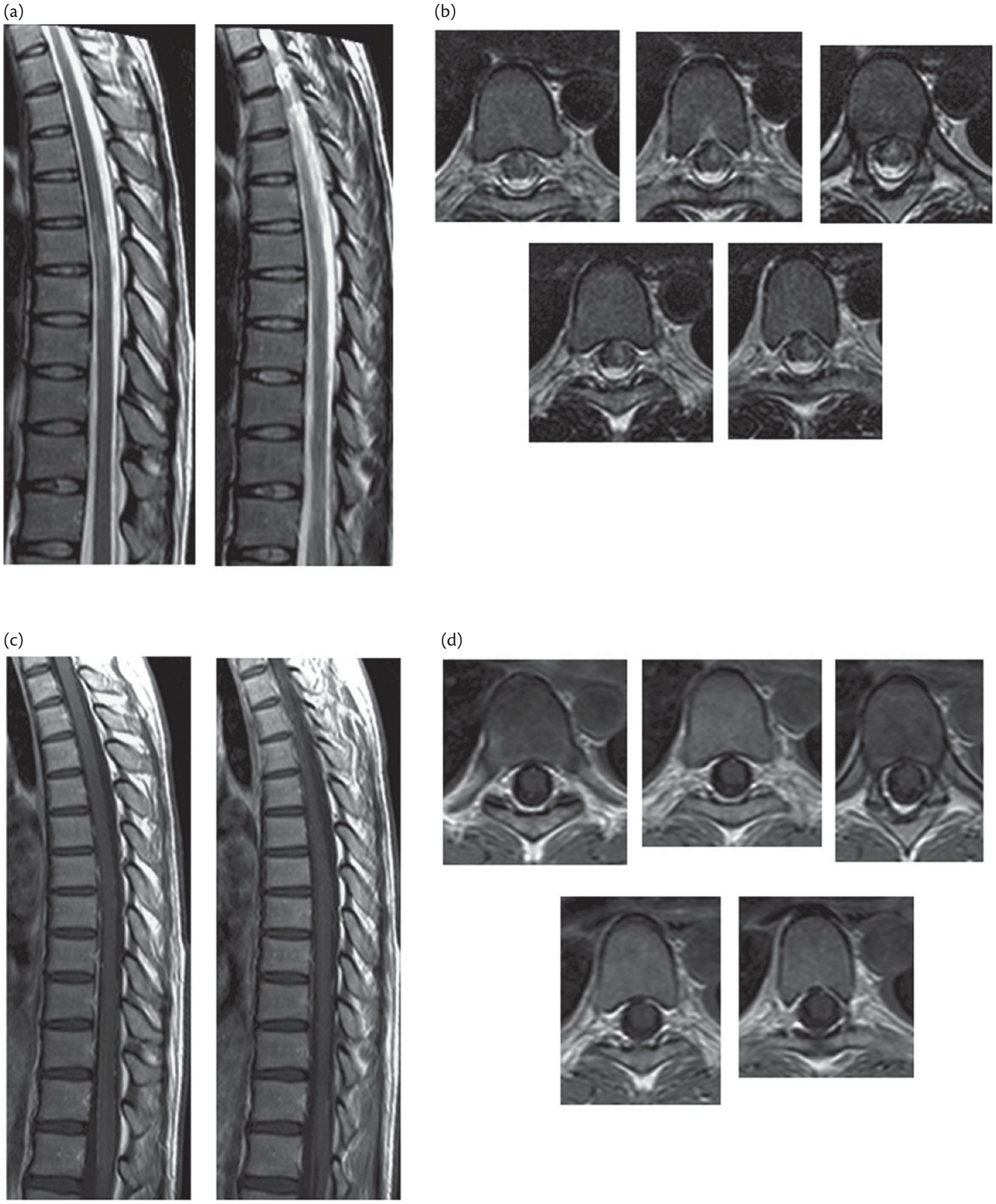

Fig. 26.5 Spinal cord sagittal (a,c) and axial (b,d) T_2-weighted (a,b) and post-contrast T_1-weighted (c,d) magnetic resonance images from a patients with sub-acute ischaemic myelopathy secondary to a atheromatous micro-embolus. A well-defined T_2 hyperintense lesion localized in the anterior portion of the thoracic spinal cord and extending for more than two segments is visible, which does not enhance.

diseases, such as MS and NMO, spinal cord abnormalities are usually seen below the mid- to lower thoracic cord.

Increased peri-medullary flow voids on T_2-weighted MRI and vascular-type enhancement after Gd administration with dilated, tortuous peri-medullary vessels are signs of venous enlargement, which can accompany medullary venous congestion. Enlarged peri-medullary veins are indirect signs of spinal cord arterio-venous shunts and should direct further diagnostic work-up, including spinal digital subtraction angiography (Fig. 26.6) [68].

Metabolic and toxic diseases

Myelopathy and myeloneuropathy related to metabolic, nutritional, and toxic causes are not rare clinical conditions. Identification of causative deficiencies or excesses, and toxic conditions may lead to treatment decisions that will cure, if not arrest the symptoms of these disabling conditions.

Subacute combined degeneration (SCD) is a cause of demyelination of the dorsal and lateral columns of the spinal cord, and of the

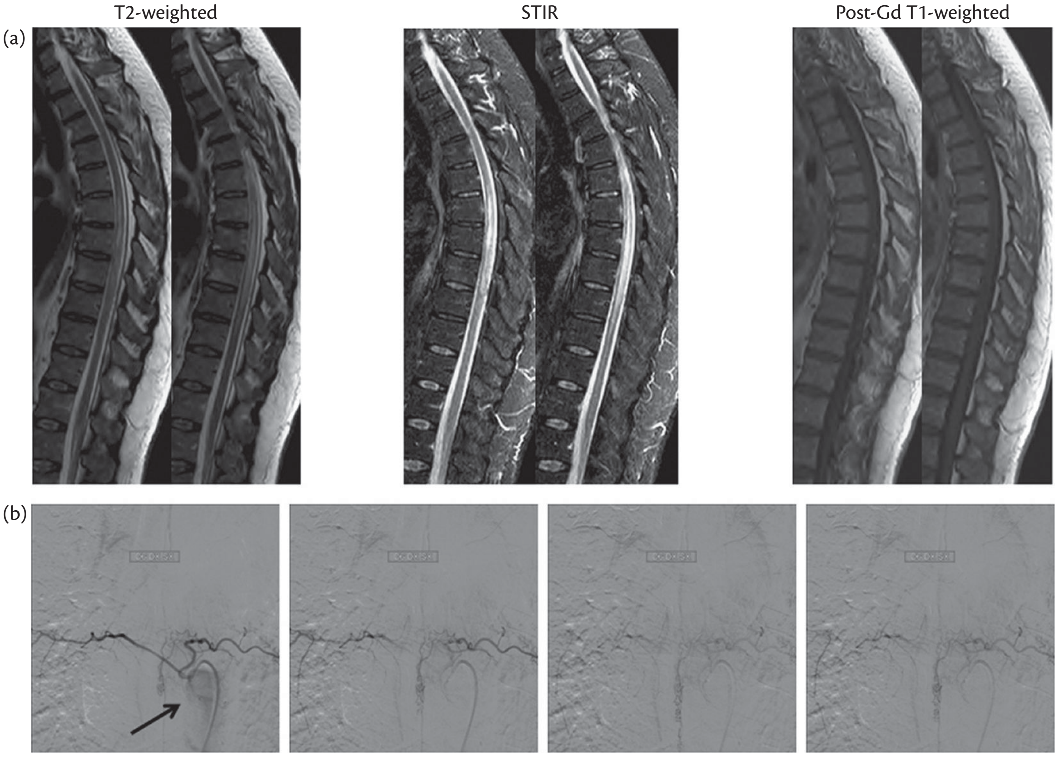

Fig. 26.6 (a) Spinal cord sagittal T_2-weighted, short tau inversion recovery (STIR) and post-contrast T_1-weighted magnetic resonance images from a patients with an arteriovenous fistula involving the thoracic spinal cord. A longitudinally extensive T_2 hyperintense lesion, white spotted regions of contrast enhancement is evident. (b) Angiography shows the tortuous arteriovenous shunt occurring in the spinal cord.

brain pyramidal and spinocerebellar tracts, usually related to vitamin B12 deficiency. Spinal cord MRI shows high-signal intensity on T_2-weighted scans of the posterior or lateral columns, which might be visible in up to 87.5% of patients, with contiguous involvement of multiple segments [69–71] (Fig. 26.7). Atrophy [72], and abnormal MT MRI and DTI MRI values in the spinal cord have also been described [73].

Copper deficiency has been also associated with myelopathy, characterized by the presence of a segment of T_2-hyperintensity in the spinal cord, involving both cervical and thoracic portion [74], with imaging features similar to those described for SCD. Contrast enhancement has not been described. Signal abnormalities most often involve the central and dorsal midline, with an increased signal in the posterior and lateral columns. These signal abnormalities may partially recover after copper supplementation [75].

Spinal MRI findings in patients with vitamin E deficiency typically include T_2-hyperintesities in the posterior columns.

Myelopathy is known to occur with heroin abuse, by either inhalation or IV use. The onset is acute and there is evidence of spinal cord T_2-weighted hyperintensities resembling those seen in transverse myelitis, with cord hyperintensities on T_2 affecting posterior and lateral columns.

Degenerative and neurodegenerative diseases

Degenerative spine disease

Spinal cord compression can be caused by various pathological processes, such as disc herniation, neoplasms, epidural abscess, degenerative abnormalities, inflammatory processes, lumbar spinal stenosis, cervical spine instability, and trauma [76].

Degenerative spine disease is the most common and is due to the progressive compression of the spinal cord due to narrowing of the spinal canal. Spinal cord MRI shows a combination of increased T_2-weighted and decreased T_1-weighted signal intensities. A long segment of increased T_2-weighted signal intensity or patchy areas of increased T_2-weighted signal intensity are predictive of reduced neurological recovery after surgical intervention. The application of advanced MRI techniques, such as DT MRI, might allow a more sensitive evaluation of the normal appearing WM, particularly in the initial stages of the disease, when the correlation between imaging and clinical findings is poor. A significant correlation between FA reduction at the compressed level and clinical scales has been described [77]. Such FA abnormalities can be detected in stenotic segments even without T_2 signal alterations [78]. The utility of DT MRI measures in predicting clinical outcome following surgery has been suggested by a recent study, which has shown that patients with higher ADC values tended to have a poorer clinical recovery [79].

Using 1H-MRS, reduced N-acetyl aspartate/creatine ratio has been found in patients with *cervical spondylotic myelopathy*, suggesting axonal and neuronal injury. An abnormal lactate signal was present in nearly one-third of the patients, supporting the role of ischaemia in the pathogenesis of cervical spinal myelopathy [80].

Neurodegenerative spine diseases

Neurodegenerative diseases include a wide spectrum of conditions that are characterized by a progressive and irreversible accumulation of CNS damage, which leads to severe disability and death.

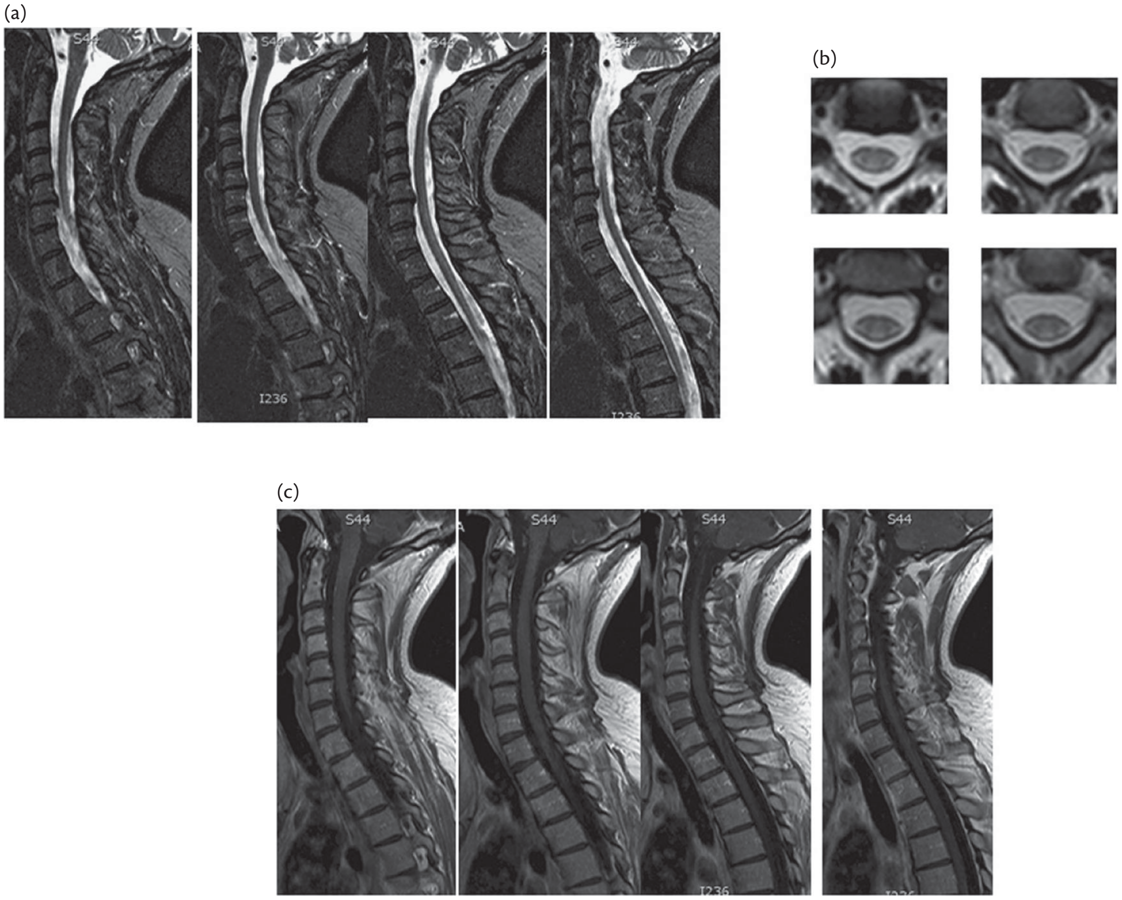

Fig. 26.7 Spinal cord sagittal (a) and axial (b) T_2-weighted, and sagittal post-contrast T_1-weighted (c) magnetic resonance images from a patient with subacute combined degeneration. T_2 hyperintensity of the posterior and lateral columns extending for multiple segments is evident, without contrast enhancement.

Among them, motor neuron diseases and hereditary spastic paraplegia are discussed in Chapter 23. Spinocerebellar ataxia are discussed in Chapter 24.

Hirahyama disease is a rare condition characterized by asymmetric progressive muscle weakness and atrophy at C8–T_1, which develops classically in young males. The pathogenesis is not completely defined yet, but it has been hypothesized that an insufficient growth of the dura relative to the spinal column during puberty might promote the displacement of the dura in flexion with compression of the spinal cord, leading to

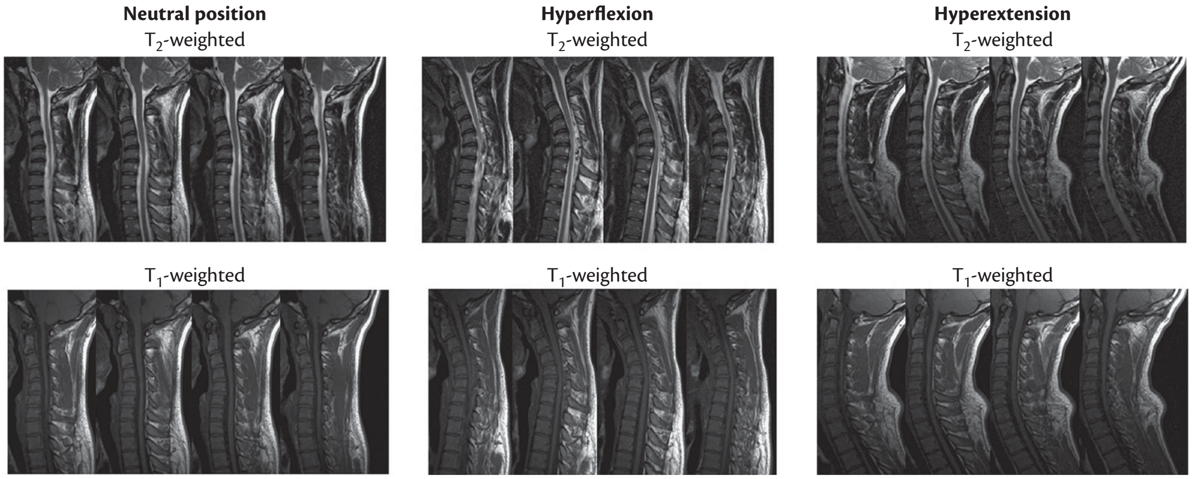

Fig. 26.8 Spinal cord sagittal T_2-weighted and T_1-weighted magnetic resonance images from a patient with Hyrayama disease. In the neutral position, T_2 hyperintensity in the cervical spine, associated with regional atrophy is evident. During hyperflexion a displacement of the dura in flexion with compression of the spinal cord, leading to ischaemia of the anterior horn cells is visible. During hyperextension, no clear spinal cord compression and dural displacement is visible.

ischaemia of the anterior horn cells at C8 and T_1 [81]. Classical MRI findings include loss of attachment of the dura to the lamina, asymmetric lower cervical spinal cord atrophy, spinal cord T_2-hyperintense lesions, loss of cervical lordosis in the neutral position, and forward displacement of the dura with flexion MRI (Fig. 26.8) [82].

Conclusions

Significant advances in spinal cord imaging methods have emerged in the past decade. The application of conventional and advanced MRI techniques to study the spinal cord has allowed us to improve our ability to diagnose and monitor a wide spectrum of conditions which involve this clinically relevant portion of the CNS, as well as to ameliorate our knowledge of the pathophysiological mechanisms of these diseases. Despite this, many challenges still remain, related to spinal cord anatomy and topography, and to methodologic limitations. Improvements in technology associated with an increased availability of novel imaging modalities might contribute to overcome these limitations.

References

1. Lycklama G, Thompson A, Filippi M, et al. (2003). Spinal-cord MRI in multiple sclerosis. Lancet N*eurology*, **2**(9), 555–62.
2. Ozturk A, Aygun N, Smith SA, et al. (2013). Axial 3D gradient-echo imaging for improved multiple sclerosis lesion detection in the cervical spinal cord at 3T. *Neuroradiology*, **55**(4), 431–9.
3. Nair G, Absinta M, and Reich DS. (2013). Optimized T1-MPRAGE sequence for better visualization of spinal cord multiple sclerosis lesions at 3T. *AJNR* American J*ournal of Neuroradiology*, **34**(11), 2215–22.
4. Brex PA, Leary SM, O'Riordan JI, et al. (2001). Measurement of spinal cord area in clinically isolated syndromes suggestive of multiple sclerosis. *Journal of Neurology, Neurosurgery & Psychiatry*, **70**(4), 544–7.
5. Losseff NA, Kingsley DP, McDonald WI, et al. (1996). Clinical and magnetic resonance imaging predictors of disability in primary and secondary progressive multiple sclerosis. *Multiple Sclerosis*, **1**(4), 218–22.
6. Horsfield MA, Sala S, Neema M, et al. (2010). Rapid semi-automatic segmentation of the spinal cord from magnetic resonance images: application in multiple sclerosis. *NeuroImage*, **50**(2), 446–55.
7. Kurtzke JF. (1983). Rating neurologic impairment in multiple sclerosis: an expanded disability status scale (EDSS). *Neurology*, **33**(11), 1444–52.
8. Rocca MA, Horsfield MA, Sala S, et al. (2011). A multicenter assessment of cervical cord atrophy among MS clinical phenotypes. *Neurology*, **76**(24), 2096–102.
9. Valsasina P, Rocca MA, Horsfield MA, et al. (2013). Regional cervical cord atrophy and disability in multiple sclerosis: a voxel-based analysis. *Radiology*, **266**(3), 853–61.
10. Rocca MA, Valsasina P, Damjanovic D, et al. (2012). Voxel-wise mapping of cervical cord damage in multiple sclerosis patients with different clinical phenotypes. *Journal of Neurology, Neurosurgery & Psychiatry*.
11. Bozzali M, Rocca MA, Iannucci G, et al. (1999). Magnetization-transfer histogram analysis of the cervical cord in patients with multiple sclerosis. *AJNR American Journal of Neuroradiology*, **20**(10), 1803–8.
12. Filippi M, Rocca MA, Moiola L, et al. (1999). MRI and magnetization transfer imaging changes in the brain and cervical cord of patients with Devic's neuromyelitis optica. *Neurology*, **53**(8), 1705–10.
13. Rovaris M, Bozzali M, Santuccio G, et al. (2000). Relative contributions of brain and cervical cord pathology to multiple sclerosis disability: a study with magnetisation transfer ratio histogram analysis. *Journal of Neurology, Neurosurgery & Psychiatry*, **69**(6), 723–7.
14. Bot JC, Blezer EL, Kamphorst W, et al. (2004). The spinal cord in multiple sclerosis: relationship of high-spatial-resolution quantitative MR imaging findings to histopathologic results. *Radiology*, **233**(2), 531–40.
15. Rovaris M, Gallo A, Riva R, et al. (2004). An MT MRI study of the cervical cord in clinically isolated syndromes suggestive of MS. *Neurology*, **63**(3), 584–5.
16. Charil A, Caputo D, Cavarretta R, et al. (2006). Cervical cord magnetization transfer ratio and clinical changes over 18 months in patients with relapsing-remitting multiple sclerosis: a preliminary study. *Multiple Sclerosis*, **12**(5), 662–5.
17. Rovaris M, Bozzali M, Santuccio G, et al. (2001). In vivo assessment of the brain and cervical cord pathology of patients with primary progressive multiple sclerosis. *Brain*, **124**(Pt 12), 2540–9.
18. Zackowski KM, Smith SA, Reich DS, et al. (2009). Sensorimotor dysfunction in multiple sclerosis and column-specific magnetization transfer-imaging abnormalities in the spinal cord. *Brain*, **132**(Pt 5), 1200–9.
19. Agosta F, Pagani E, Caputo D, et al. (2007). Associations between cervical cord gray matter damage and disability in patients with multiple sclerosis. *Archives of Neurology*, **64**(9), 1302–5.
20. Agosta F, and Filippi M. (2007). MRI of spinal cord in multiple sclerosis. *Journal of Neuroimaging*, **17**(Suppl. 1), 46S–9S.
21. Agosta F, Absinta M, Sormani MP, et al. (2007). In vivo assessment of cervical cord damage in MS patients: a longitudinal diffusion tensor MRI study. *Brain*, **130**(Pt 8), 2211–19.
22. Ciccarelli O, Wheeler-Kingshott CA, McLean MA, et al. (2007). Spinal cord spectroscopy and diffusion-based tractography to assess acute disability in multiple sclerosis. *Brain*, **130**(Pt 8), 2220–31.
23. Raz E, Bester M, Sigmund EE, et al. (2013). A better characterization of spinal cord damage in multiple sclerosis: a diffusional kurtosis imaging study. *AJNR American Journal of Neuroradiology*, **34**(9), 1846–52.
24. Oh J, Saidha S, Chen M, et al. (2013). Spinal cord quantitative MRI discriminates between disability levels in multiple sclerosis. *Neurology*, **80**(6), 540–7.
25. Agosta F, Valsasina P, Absinta M, et al. (2009). Primary progressive multiple sclerosis: tactile-associated functional MR activity in the cervical spinal cord. *Radiology*, **253**(1), 209–15.
26. Valsasina P, Agosta F, Absinta M, et al. (2010). Cervical cord functional MRI changes in relapse-onset MS patients. *Journal of Neurology, Neurosurgery & Psychiatry*, **81**(4), 405–8.
27. Rocca MA, Absinta M, Valsasina P, et al. (2012). Abnormal cervical cord function contributes to fatigue in multiple sclerosis. *Multiple Sclerosis*, **18**(11), 1552–9.
28. Segal BM. (2013). Neurosarcoidosis: diagnostic approaches and therapeutic strategies. Current O*pinions in Neurology*, **26**(3), 307–13.
29. Junger SS, Stern BJ, Levine SR, et al. (1993). Intramedullary spinal sarcoidosis: clinical and magnetic resonance imaging characteristics. *Neurology*, **43**(2), 333–7.
30. Espinosa G, Mendizabal A, Minguez S, et al. (2010). Transverse myelitis affecting more than 4 spinal segments associated with systemic lupus erythematosus: clinical, immunological, and radiological characteristics of 22 patients. *Seminars in Arthritis and Rheumatism*, **39**(4), 246–56.
31. Provenzale JM, Barboriak DP, Gaensler EH, et al B. (1994). Lupus-related myelitis: serial MR findings. *AJNR American Journal of Neuroradiology*, **15**(10), 1911–17.
32. Kim SM, Waters P, Vincent A, et al. (2009). Sjögren's syndrome myelopathy: spinal cord involvement in Sjögren's syndrome might be a manifestation of neuromyelitis optica. *Multiple Sclerosis*, **15**(9), 1062–8.
33. Kitley JL, Leite MI, George JS, et al. (2012). The differential diagnosis of longitudinally extensive transverse myelitis. *Multiple Sclerosis*, **18**(3), 271–85.
34. Al-Araji A, and Kidd DP. (2009). Neuro-Behçet's disease: epidemiology, clinical characteristics, and management. *Lancet Neurology*, **8**(2), 192–204.

35. Salvarani C, Brown RD, Jr, Calamia KT, et al. (2008). Primary CNS vasculitis with spinal cord involvement. *Neurology*, **70**(24 Pt 2), 2394–400.
36. Nakajima H, Furutama D, Kimura F, et al. (1998). Herpes simplex virus myelitis: clinical manifestations and diagnosis by the polymerase chain reaction method. *European Neurology*, **39**(3), 163–7.
37. Hung CH, Chang KH, Kuo HC, et al. (2012). Features of varicella zoster virus myelitis and dependence on immune status. *Journal of Neurological Sciences*, **318**(1–2), 19–24.
38. Karunarathne S, Govindapala D, Udayakumara Y, et al. (2012). Cytomegalovirus associated transverse myelitis in an immunocompetent host with DNA detection in cerebrospinal fluid; a case report. *BMC Research Notes*, **5**, 364.
39. Bou-Haidar P, Peduto AJ, and Karunaratne N. (2009). Differential diagnosis of T2 hyperintense spinal cord lesions: part B. *Journal of Medical Imaging & Radiation Oncology*, **53**(2), 152–9.
40. Sartoretti-Schefer S, Blattler T, Wichmann W. (1997). Spinal MRI in vacuolar myelopathy, and correlation with histopathological findings. *Neuroradiology*, **39**(12), 865–9.
41. Chong J, Di Rocco A, Tagliati M, et al. (1999). MR findings in AIDS-associated myelopathy. *AJNR American Journal of Neuroradiology*, **20**(8), 1412–16.
42. Umehara F, Nose H, Saito M, et al. (2007). Abnormalities of spinal magnetic resonance images implicate clinical variability in human T-cell lymphotropic virus type I-associated myelopathy. *Journal of Neurovirology*, **13**(3), 260–7.
43. Meurs L, Labeye D, Declercq I, et al. (2004). Acute transverse myelitis as a main manifestation of early stage II neuroborreliosis in two patients. *European Neurology*, **52**(3), 186–8.
44. Chilver-Stainer L, Fischer U, Hauf M, et al. (2009). Syphilitic myelitis: rare, nonspecific, but treatable. *Neurology*, **72**(7), 673–5.
45. Kikuchi S, Shinpo K, Niino M, et al. (2003). Subacute syphilitic meningomyelitis with characteristic spinal MRI findings. *Journal of Neurology*, **250**(1), 106–7.
46. Jain AK, and Kumar J. (2013). Tuberculosis of spine: neurological deficit. *European Spine Journal*, **22**(Suppl. 4), 624–33.
47. Saleem S, Belal AI, and El-Ghandour NM. (2005). Spinal cord schistosomiasis: MR imaging appearance with surgical and pathologic correlation. *AJNR American Journal of Neuroradiology*, **26**(7), 1646–54.
48. Kincaid O, and Lipton HL. (2006). Viral myelitis: an update. *Current Neurology and Neuroscience Reports*, **6**(6), 469–74.
49. Thurnher MM, Post MJ, and Jinkins JR. (2000). MRI of infections and neoplasms of the spine and spinal cord in 55 patients with AIDS. *Neuroradiology*, **42**(8), 551–63.
50. Choudhary A, Sharma S, Sankhyan N, et al. (2010). Midbrain and spinal cord magnetic resonance imaging (MRI) changes in poliomyelitis. *Journal of Child Neurology*, **25**(4), 497–9.
51. Kornreich L, Dagan O, and Grunebaum M. (1996). MRI in acute poliomyelitis. *Neuroradiology*, **38**(4), 371–2.
52. Agosta F, Rocca MA, Benedetti B, et al. (2006). MR imaging assessment of brain and cervical cord damage in patients with neuroborreliosis. *AJNR American Journal of Neuroradiology*, **27**(4), 892–4.
53. Pradhan S, Gupta RK, and Ghosh D. (1997). Parainfectious myelitis: three distinct clinico-imagiological patterns with prognostic implications. *Acta Neurologica Scandinavica*, **95**(4), 241–7.
54. Graber JJ, and Nolan CP. (2010). Myelopathies in patients with cancer. *Archives of Neurology*, **67**(3), 298–304.
55. Bou-Haidar P, Peduto AJ, and Karunaratne N. (2008). Differential diagnosis of T2 hyperintense spinal cord lesions: Part A. *Journal of Medical Imaging & Radiation Oncology*, **52**(6), 535–43.
56. Baleriaux DL. (1999). Spinal cord tumors. *European Radiology*, **9**(7), 1252–8.
57. Counsel P, and Khangure M. (2007). Myelopathy due to intrathecal chemotherapy: magnetic resonance imaging findings. *Clinical Radiology*, **62**(2), 172–6.
58. Reagan TJ, Thomas JE, and Colby MY, Jr (1968). Chronic progressive radiation myelopathy. Its clinical aspects and differential diagnosis. *Journal of the American Medical Association*, **203**(2), 106–10.
59. Flanagan EP, and Keegan BM. (2013). Paraneoplastic myelopathy. *Neurology Clinics*, **31**(1), 307–18.
60. Hock A, Henning A, Boesiger P, et al. (2013). (1)H-MR spectroscopy in the human spinal cord. *AJNR American Journal of Neuroradiology*, **34**(9), 1682–9.
61. Kim YG, Choi GH, Kim DH, et al. (2004). In vivo proton magnetic resonance spectroscopy of human spinal mass lesions. *Journal of Spinal Disorders & Techniques*, **17**(5), 405–11.
62. Vandertop WP. (2014). Syringomyelia. *Neuropediatrics*, **45**(1), 3–9.
63. Chavhan GB, Babyn PS, Jankharia BG, et al. (2008). Steady-state MR imaging sequences: physics, classification, and clinical applications. *Radiographics*, **28**(4), 1147–60.
64. Roser F, Ebner FH, Danz S, et al. (2008). Three-dimensional constructive interference in steady-state magnetic resonance imaging in syringomyelia: advantages over conventional imaging. *Journal of Neurosurgery: Spine*, **8**(5), 429–35.
65. Bunck AC, Kroeger JR, Juettner A, et al. (2012). Magnetic resonance 4D flow analysis of cerebrospinal fluid dynamics in Chiari I malformation with and without syringomyelia. *European Radiology*, **22**(9), 1860–70.
66. Mawad ME, Rivera V, Crawford S, et al. (1990). Spinal cord ischemia after resection of thoracoabdominal aortic aneurysms: MR findings in 24 patients. *AJNR American Journal of Neuroradiology*, **11**(5), 987–91.
67. Thurnher MM, and Bammer R. (2006). Diffusion-weighted MR imaging (DWI) in spinal cord ischemia. *Neuroradiology*, **48**(11), 795–801.
68. Mull M, Nijenhuis RJ, Backes WH, et al. (2007). Value and limitations of contrast-enhanced MR angiography in spinal arteriovenous malformations and dural arteriovenous fistulas. *AJNR American Journal of Neuroradiology*, **28**(7), 1249–58.
69. Lee WJ, Hsu HY, and Wang PY. (2008). Reversible myelopathy on magnetic resonance imaging due to cobalamin deficiency. *Journal of the Chinese Medical Association*, **71**(7), 368–72.
70. Katsaros VK, Glocker FX, Hemmer B, et al. (1998). MRI of spinal cord and brain lesions in subacute combined degeneration. *Neuroradiology*, **40**(11), 716–19.
71. Sun HY, Lee JW, Park KS, et al. (2014). Spine MR imaging features of subacute combined degeneration patients. *European Spine Journal*, **23**(5), 1052–8.
72. Kalita J, and Misra UK. (2008). Vitamin B12 deficiency neurological syndromes: correlation of clinical, MRI and cognitive evoked potential. *Journal of Neurology*, **255**(3), 353–9.
73. Filippi M, Rocca MA, Rossi P, et al. (2003). Demyelination and cortical reorganization: functional MRI data from a case of subacute combined degeneration. *NeuroImage*, **18**(2), 558–63.
74. Kumar N, Ahlskog JE, Klein CJ, et al. (2006). Imaging features of copper deficiency myelopathy: a study of 25 cases. *Neuroradiology*, **48**(2), 78–83.
75. Goodman BP, Chong BW, Patel AC, et al. (2006). Copper deficiency myeloneuropathy resembling B12 deficiency: partial resolution of MR imaging findings with copper supplementation. *AJNR American Journal of Neuroradiology*, **27**(10), 2112–14.
76. Wheeler-Kingshott CA, Stroman PW, Schwab JM, et al. (2014). The current state-of-the-art of spinal cord imaging: applications. *NeuroImage*, **84**, 1082–93.
77. Budzik JF, Balbi V, Le Thuc V, et al. (2011). Diffusion tensor imaging and fibre tracking in cervical spondylotic myelopathy. *European Radiology*, **21**(2), 426–33.
78. Kara B, Celik A, Karadereler S, et al. (2011). The role of DTI in early detection of cervical spondylotic myelopathy: a preliminary study with 3-T MRI. *Neuroradiology*, **53**(8), 609–16.

79. Sato T, Horikoshi T, Watanabe A, et al. (2012). Evaluation of cervical myelopathy using apparent diffusion coefficient measured by diffusion-weighted imaging. *AJNR American Journal of Neuroradiology*, **33**(2), 388–92.
80. Holly LT, Freitas B, McArthur DL, et al. (2009). Proton magnetic resonance spectroscopy to evaluate spinal cord axonal injury in cervical spondylotic myelopathy. *Journal of Neurosurgery: Spine*, **10**(3), 194–200.
81. Lehman VT, Luetmer PH, Sorenson EJ, et al. (2013). Cervical spine MR imaging findings of patients with Hirayama disease in North America: a multisite study. *AJNR American Journal of Neuroradiology*, **34**(2), 451–6.
82. Chen CJ, Hsu HL, Tseng YC, et al. (2004). Hirayama flexion myelopathy: neutral-position MR imaging findings—importance of loss of attachment. *Radiology*, **231**(1), 39–44.

CHAPTER 27

Traumatic brain injury

Matilde Inglese and Elan J. Grossman

Introduction

Traumatic brain injury (TBI) represents one of the most serious public health problems confronting the modern world [1]. In the United States alone, current estimates indicate that more than 2 million such injuries are reported annually by hospital emergency departments [2]. Of these cases, 10% result in fatality and another 10% result in long-term or permanent cognitive and affective impairment, costing about $60 billion per year in health care utilization and lost productivity [2]. TBI is defined as a bump, blow, or jolt to the head that disrupts normal brain functioning. It is most commonly graded in severity according to a patient's state of consciousness as determined by an assessment of eye, motor, and verbal responses using the Glasgow Coma Scale (GCS) [3]. Approximately 80% of patients score between 13 and 15, or a classification of mild, 10% score between 9 and 12, or a classification of moderate, and 10% score between 3 and 8, or a classification of severe. The leading causes of TBI are falls, motor vehicle accidents, collisions with stationary or moving objects, and assaults [1]. Particularly at high risk are children aged 0–4 years old, adolescents aged 15–19 years old, and adults aged 35–44 years old and 75 years or older [1,4]. A better understanding of TBI and the ability to forecast outcome could be of central importance in managing the condition because it may be possible to identify early medical and rehabilitative interventions which reduce the risk of persistent neurologic impairment. Unfortunately, however, clinical and cognitive predictors are suboptimal due to wide intra- and interpatient variability, and the confounding effects of psychological and motivational factors.

The problem is further complicated by the fact that more objective measures such as computed tomography (CT) and conventional magnetic resonance imaging (MRI) also exhibit significant limitations. CT is often used for the initial evaluation of patients with TBI to detect the presence of intracranial haemorrhages that require acute neurosurgical intervention, but it lacks sensitivity. Conventional MRI can identify abnormalities even in cases where other radiography findings are vague or completely absent, but it also demonstrates important restrictions:

1. It underestimates tissue damage severity.
2. It lacks pathological specificity.
3. It poorly correlates with cognitive impairment.
4. It does not provide biomarkers that can be used to determine prognosis and/or monitor treatment response.
5. It is less effective for evaluating cases of mild and moderate TBI since the damage tends to be microscopic and therefore more challenging to detect.

A great deal of research focused on overcoming the limitations of CT and conventional MRI has been conducted in recent years, and led to the development of advanced imaging techniques, such as susceptibility-weighted imaging (SWI), proton magnetic resonance spectroscopy (^{1}H-MRS), diffusion MRI, perfusion imaging, blood oxygen level-dependent (BOLD) MRI, and fluorine-18 deoxyglucose positron emission tomography (FDG-PET). There is growing evidence to suggest that each of these approaches may be particularly valuable for the understanding and management of TBI.

Susceptibility-weighted imaging

In SWI [5], data are acquired using three-dimensional (3D) long echo gradient echo (GRE) MRI to improve detection of signal intensity loss caused by the presence of inhomogeneous magnetic fields in tissue. The magnitude data are combined with the phase data, which reflect such susceptibility differences, to produce an enhanced-contrast magnitude image that is exceptionally sensitive to paramagnetic tissue compounds, such as deoxyhaemoglobin, ferritin, haemosiderin, and methaemoglobin and diamagnetic tissue compounds, such as dystrophic calcifications.

SWI studies of adults with TBI

A few studies [6,7] have applied SWI to adults in cohorts containing patients with a mix of mild, moderate, and severe TBI (Fig. 27.1). Akiyama et al. [6] examined 15 patients within 2 weeks following injury, and found that the mean number of hypointense spotty lesions detected by SWI was 76 ± 52 with a total of 1132 as compared with T_2*-weighted (T2*w) MRI which was 21 ± 19 with a total of 316. Chastain et al. [7] examined 38 patients at the time of injury, and reported that although T_2-weighted (T2w) MRI and fluid-attenuated inversion recovery (FLAIR) MRI best predicted group outcomes based on median total lesion volume, median volume per lesion, median number of lesions, and zonal distribution of lesions, SWI was more sensitive to detecting intraparenchymal lesions, and tended to better predict group outcomes based on median number of lesions in the gray–white matter junction and deeper regions of the brain.

SWI studies of children and adolescents with TBI

Tong et al. [8,9] and Babikian et al. [10] applied SWI to children and adolescents in cohorts containing patients with a mix of mild, moderate, and severe TBI in three related studies designed to assess the potential role of using this technique to detect injury and predict outcome. The first study [9] examined seven children and adolescents within a mean of 5 days following injury, and reported

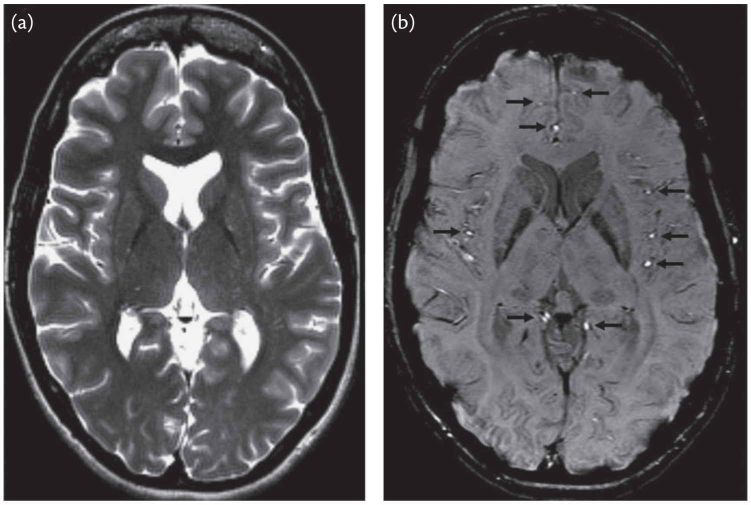

Fig. 27.1 T2w MRI image (a) showing no evidence of injury and a corresponding SWI image (b) with foci (arrows) demonstrating the locations of parenchymal lesions in a 40-year-old male with mild TBI.

that the number of haemorrhagic lesions detected by SWI was 1038 as compared with T2*w two-dimensional (2D) GRE MRI, which was 162, and the apparent total haemorrhagic volume detected by SWI was 57,946 mm^3 as compared with T2*w 2D GRE MRI, which was 28,893 mm^3. The second study [8] examined 40 children and adolescents within a mean of 7 days following injury, and reported that greater average number and volume of haemorrhagic lesions detected by SWI was associated with prolonged coma, lower GCS scores, and neurologic outcome 6–12 months following injury as determined by the Pediatric Cerebral Performance Category Scale (PCPCS), which quantifies the overall functional neurologic morbidity and cognitive impairment of infants and children. The third study [10] examined 18 children and adolescents within a mean of 6 days following injury, and reported that greater number and volume of haemorrhagic lesions detected by SWI in the thalamus and the basal ganglia was associated with decreased performance in cognitive measures for intelligence, executive functioning, attention, visuoperceptual skills, language, verbal and non-verbal memory, motor functioning, and academic achievement.

Proton magnetic resonance spectroscopy

^{1}H-MRS, which uses the same principles and technology as conventional MRI, but by contrast acquires signals from hydrogen nuclei in molecules other than water to derive a measure of tissue chemistry, is discussed in Chapter 3. ^{1}H-MRS studies of TBI have mostly focused on quantification of the neurometabolites N-acetyl aspartate (NAA), which is a marker for neuronal integrity, choline (Cho), which is a marker for membrane metabolism, creatinine (Cr), which is a marker for energy supply, and lactate (Lac), which is a marker for anaerobic glycolysis.

^{1}H-MRS studies of adults with TBI

Several studies [11–16] have applied ^{1}H-MRS to adults in cohorts containing patients with a mix of mild and/or moderate and severe TBI. These studies have reported finding cortical gray and white matter regions and deep gray matter regions with decreased NAA, suggesting neuronal damage (Fig. 27.2), increased Cho, suggesting neuronal membrane and myelin shearing and reactive astrocytosis, and decreased NAA/Cr, suggesting neuronal loss. In patients with moderate and severe TBI, decreased NAA in the basal ganglia was associated with cognitive measures for attention, speed, and motor scanning, suggesting involvement of the frontostriatal networks [11] In patients with severe TBI, combined analysis of NAA/Cr with conventional MRI in the brainstem, or NAA/Cr with diffusion MRI in the thalamus, the pons, and the insula, were associated with long-term neurologic outcome [12,16].

^{1}H-MRS studies of children and adolescents with TBI

A number of studies [17-20] have applied ^{1}H-MRS to children and adolescents in cohorts containing patients with a mix of mild, moderate, and severe TBI. These studies have reported finding that in children examined within 7 days following injury, decreased NAA/Cho and NAA/Cr in occipital gray matter predicted neurologic outcome at 6–12 months following injury as determined by the PCPCS [19]. In infants and children examined at a mean of 6.5 days following injury, the presence of Lac was able to predict neurologic outcome at 6–12 months following injury (96% of patients) better than clinical evaluation (77–86% of patients) [17]. In children examined at a mean of 6 days following injury, NAA averaged from the corpus callosum, frontal white matter, frontal gray matter, parieto-occipital white matter, and parieto-occipital gray matter was associated with cognitive functioning 1-4 years following injury [18].

Diffusion magnetic resonance imaging

Diffusion weighted (DW) MRI, which measures the magnitude of water diffusion in tissue, and diffusion tensor (DT) MRI, which measures the magnitude as well as the directionality of water diffusion in tissue, are discussed in Chapter 4. Another MRI technique that has been developed more recently is diffusional kurtosis imaging (DKI) [21], which measures the diffusional complexity of water movement in tissue and can provide information in regions where DT MRI is less effective, such as gray matter and where white matter fibres cross and/or divide.

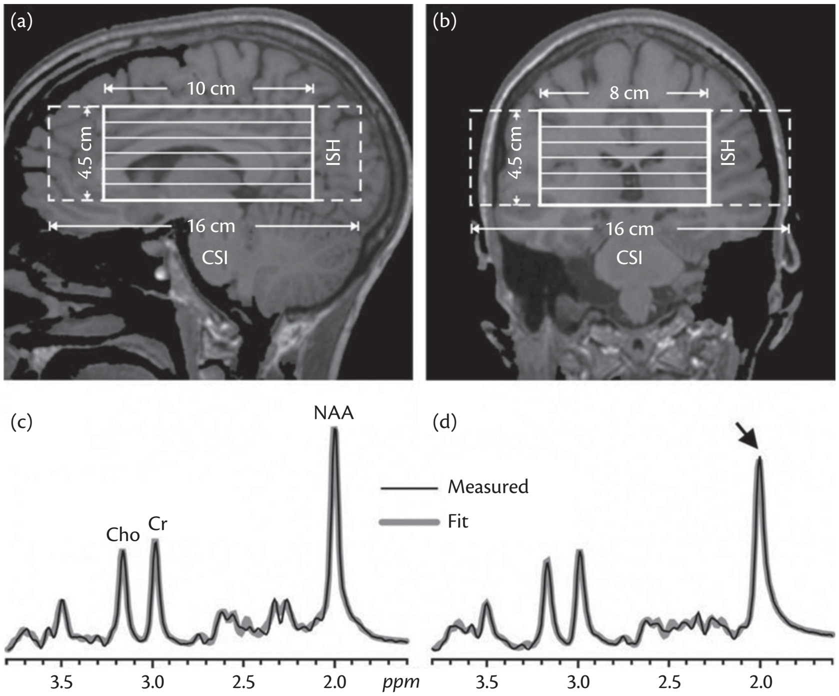

Fig. 27.2 Top row shows sagittal (a) and coronal (b) T1w MRI images of an 18-year-old male with mild TBI demonstrating no evidence of injury on which are superimposed an ^{1}H-MRS volume of interest (8 × 10 × 4.5 cm; thick solid white lines) and field of view (16 × 16 × 4.5 cm; dashed white lines) consisting of six slices that are 80 (1 × 1 × 0.75 cm) voxels each (CSI, chemical shift imaging; HSI, Hadamard spectroscopic imaging). Bottom row shows average spectra (thin black lines) with a fitted model function (thick gray lines) on common intensity and chemical shift scales from the volume of interest for a matched control (c) and the patient (d) indicating a lower NAA peak in the patient (arrow).

Figure courtesy of Ivan I. Kirov, PhD, New York University School of Medicine, New York.

DW MRI studies of adults with TBI

Various studies [22–26] have applied DW MRI to adults in cohorts containing patients with a mix of mild, moderate, and severe TBI. These studies have reported that DW MRI was able to detect more white matter lesions than either T2w fast spin echo (FSE) MRI or T2*w GRE MRI. These studies also found that DW MRI was able to detect increases and decreases of diffusion in white matter lesions, suggesting that it may enable differentiation between vasogenic oedema, which is reversible, and cytotoxic oedema, which is irreversible. In addition, these studies observed that DW MRI was able to detect changes of diffusion, and total number and volume of white matter lesions at very early stages of injury, which were associated with indicators for cognitive functioning and outcome at hospital discharge.

DT MRI studies of adults with TBI

A substantial number of studies [27–42] have applied DT MRI to adults in cohorts containing patients with mild or a mix of mild, moderate, and/or severe TBI. Most of these studies found that within a short-term period following injury, patients exhibited decreased fractional anisotropy (FA) (Fig. 27.3) [27,29–32,34,39,42] and within a long-term period following injury patients experiencing post-concussion symptoms exhibited decreased FA and increased mean diffusivity (MD) [29–33,38,42]. Some studies [28,37], however, reported that within a short-term period following injury, patients also exhibited increased FA and decreased MD in the corpus callosum and other white matter tracts. One possible explanation for these differences is that the occurrence of axonal swelling within a short-term period following injury could restrict both the interstitial and overall movement of water molecules, and lead to increased FA and decreased MD, respectively.

There are a few DT MRI studies [33,34,37] that have investigated patients with TBI using axial diffusivity and radial diffusivity. Kraus et al. [33] examined 37 patients with mild and moderate to severe TBI at a mean of 92.55 months following injury, and found, in cases of mild TBI, increased axial diffusivity and normal radial diffusivity in the sagittal striatum and the superior longitudinal fasciculus. This suggested less irreversible myelin damage than was found in cases of moderate to severe TBI, which exhibited increased axial diffusivity and radial diffusivity in both of these regions, as well as the corticospinal tract and the whole brain. Kumar et al. [34], however, examined 26 patients with mild TBI at a mean of 8.9 days following injury, and found normal axial diffusivity and increased radial diffusivity in the genu and the splenium of the corpus callosum. Mayer et al. [37], for that matter, also examined 22 patients with mild TBI at a mean of 12.5 days following injury, and found decreased radial diffusivity in the corpus callosum and several left hemisphere tracts. One possible explanation for these differences is that Kraus et al. [33] examined patients with mild TBI over a long-term period following injury when recovery had taken place, while Kumar et al. [34] and Mayer et al. [37] examined patients with mild TBI over a shorter-term period following injury when changes in radial diffusivity could be observed because demyelination was still occurring. The discrepancy between these two early stage investigations might then further reflect varying inflammatory responses that can cause fluctuations in the water content of myelin sheath [37].

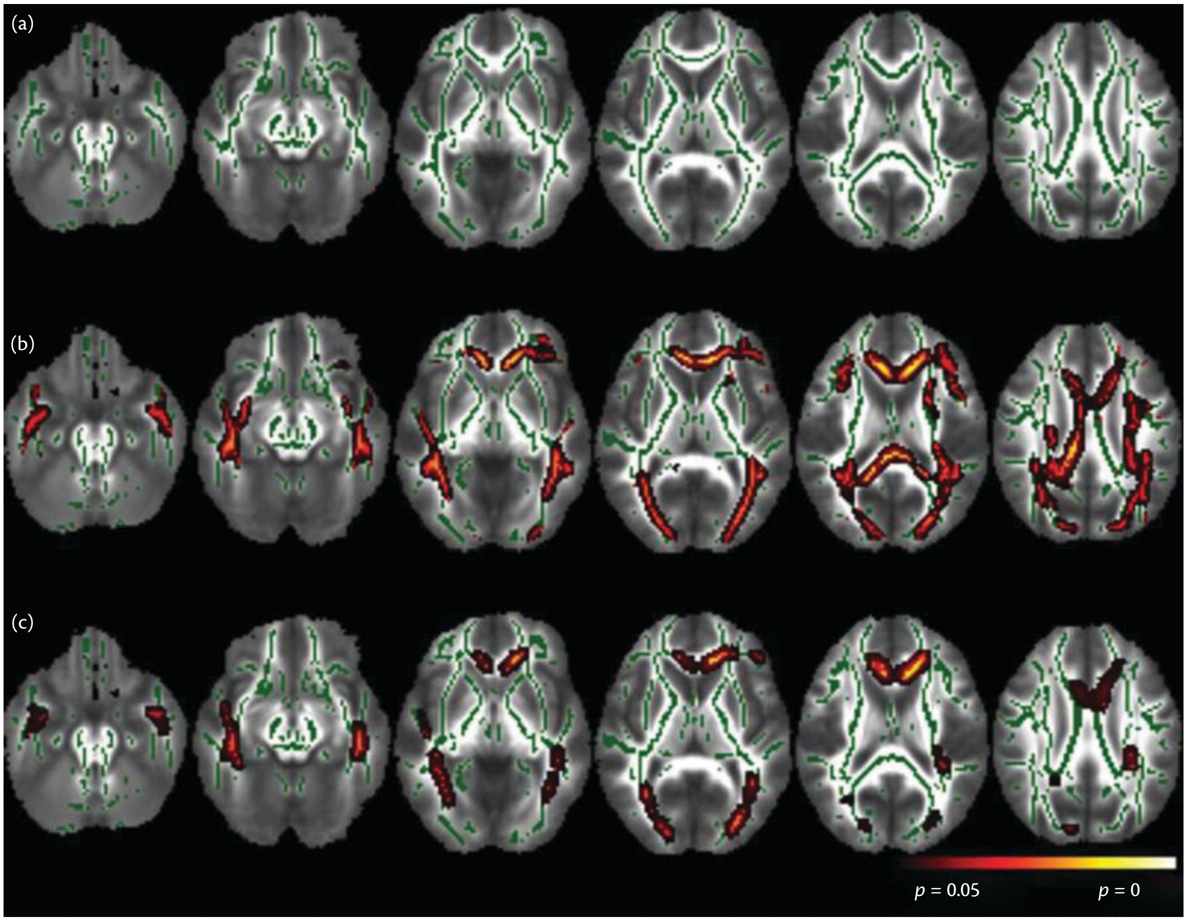

Fig. 27.3 DT MRI subject group averaged white matter tract analyses displayed on a reference brain showing that, in adults with mild TBI during subacute phase injury, patients having a good outcome exhibit no differences in FA (green) compared with controls (a), patients having a poor outcome exhibit regions with decreased FA (red and yellow) compared with controls (b), and patients having a poor outcome exhibit regions with decreased FA (red and yellow) compared with patients having a good outcome (c). Differences between subject groups were considered significant at $p < 0.05$ corrected for multiple comparisons.

Modified from Messe A, Caplain S, Paradot G, et al. (2011). Diffusion tensor imaging and white matter lesions at the subacute stage in mild traumatic brain injury with persistent neurobehavioral impairment. *Human Brain Mapping*, **32**, 999–1011. Copyright (2011), with permission from John Wiley & Sons Ltd.

Recently, some DT MRI studies [35,40–42] have investigated patients with TBI using tractography. Le et al. [35] examined one patient with severe TBI at 3 days following injury during a first visit, and at 12 weeks following injury during a second visit, and found that, at baseline, an interruption along the white matter fibres in the postero-inferior aspect of the splenium was associated with a left hemialexia, which was absent at follow-up. Rutgers et al. [40,41] conducted two investigations of patients with mild, moderate, and severe TBI. They reported that only a minority of sites with decreased FA were associated with fibre bundles showing discontinuity (Fig. 27.4), suggesting that such abnormalities could be related to oedema, haemosiderin deposition, axonal degeneration, or fibre misalignment, rather than fibre disruption.

Many DT MRI studies [28–31,33,34,36–39,42] of patents with TBI have also evaluated whether the severity of damage detected was associated with behavioural and cognitive measures for impairment. Most of these studies [28–31,33,34,36–39,42] have focused on white matter regions, and have found that the integrity of the frontal and temporal pathways are associated with executive functioning, attention, memory, and learning deficits. Some recent studies [30,31,36,38], however, have also examined the thalamus and found that, in addition to white matter, this region may be an important further site of damage, which is associated with executive functioning, attention, and memory deficits, as well as persistent post-concussion symptoms.

Longitudinal DT MRI studies [27,29,31,35,37,42] of patients with TBI are sparse and have investigated only two time points, spanning a very limited time frame. Sidaros et al. [42] examined 30 patients with severe TBI at a mean of 8 weeks following injury during a first visit, and 23 patients at a mean of 12 months following injury during a second visit. They found, at baseline, decreased FA in all white matter regions and, at follow-up, decreased FA in all white matter regions for cases with an unfavourable outcome, and increased FA in the internal capsule and the centrum semiovale for cases with a favourable outcome. Bendlin et al. [29] examined 46 patients with moderate to severe TBI at a mean of 2 months following injury during a first visit, and 42 patients at a mean of 12.7 months following injury during a second visit. They reported differences between baseline and

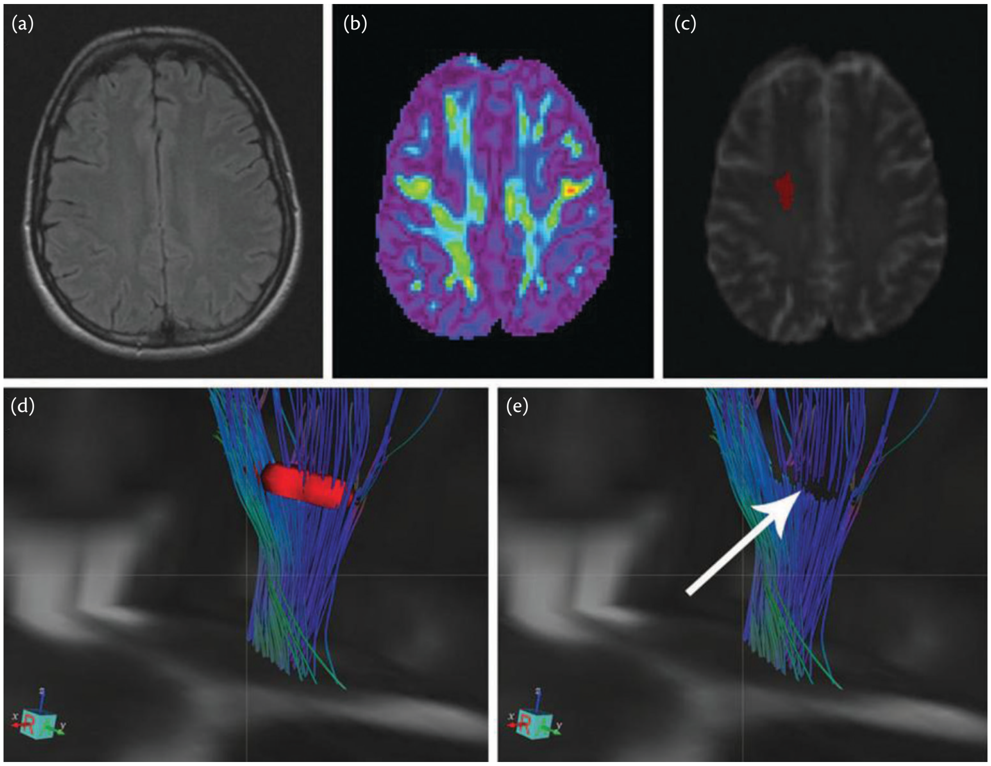

Fig. 27.4 FLAIR MRI image (a) of a 38-year-old male with mild TBI showing no evidence of injury and a corresponding FA map (b) that when analysed and displayed on a T2w MRI image (c) reveals a region of decreased diffusivity in the centrum semiovale (red) and when superimposed from a postero-laterosuperior view using multiplanar quantitative tractography (d,e) demonstrates discontinuous projection fibres (arrow).

Modified from Rutgers DR, Toulgoat F, Cazejust J, et al. (2008). White matter abnormalities in mild traumatic brain injury: a diffusion tensor imaging study. *American Journal of Neuroradiology*, **29**, 514–19. Copyright (2008), with permission from the American Journal of Neuroradiology.

follow-up, which included decreased FA in several white matter tracts, suggesting Wallerian degeneration, decreased MD in several white matter tracts, suggesting repair, and an improvement in the performance of cognitive tasks, suggesting functional reorganization.

DKI studies of adults with TBI

Grossman et al. [30,31] applied DKI to adults with mild TBI in both a cross-sectional (Fig. 27.5) and a longitudinal study. They found that patients examined within 1 month following injury and more than 9 months following baseline exhibited decreased mean kurtosis (MK), a measure of the diffusional complexity of water molecule movement, in the thalamus and different white matter regions, and that MK in the thalamus was associated with performance on cognitive measures for attention, concentration, and processing speed, as well as cognitive impairment. While there is still no precise understanding of DKI in relation to the underlying cellular environment, recent analytical and animal modelling investigations suggest that it has the potential to detect aspects of injury in TBI for which DT MRI lacks sensitivity [21]. For example, if neuronal recovery and/or degeneration are occurring, then MK might reflect specific underlying dynamic complexities of these processes, such as subtle precursory changes in axonal and myelin density, or the presence of inflammation marked by reactive astrogliosis. FA and MD, however, might reflect more general results of these processes, such as overall axonal and myelin integrity [21,30,31].

DW MRI, DT MRI, and DKI studies of children and adolescents with TBI

Several studies [43–48] have applied DW MRI and DT MRI, but not DKI, to children and/or adolescents in cohorts containing patients with mild or a mix of mild, moderate, and/or severe TBI. Galloway et al. [44] applied DW MRI to 37 children and adolescents with mild to moderate and severe TBI at a mean of 7 days following injury. It was found that, for 84% of patients, whole brain average diffusion correctly predicted neurologic outcome at 6–12 months following injury as determined by the PCPCS. Another set of studies [43,47,48] applied tractography to adolescents with mild TBI at a short-term period following injury. These reported that increased FA and decreased MD and radial diffusivity in several white matter tracts was consistent with the presence of cytotoxic oedema, and was associated with poor performance on cognitive measures for episodic verbal learning and memory tasks, as well as severity of post-concussion symptoms. In another set of studies [45,46], which applied tractography to children with moderate to severe TBI at a long-term period following injury, it was reported that decreased FA in the corpus callosum was associated with poor performance on cognitive measures for processing speed and speed of interference resolution on an inhibition task, as well as global outcome.

Perfusion imaging

To assess disturbances of perfusion in TBI, a number of studies [49–52] have investigated using the nuclear medicine techniques of

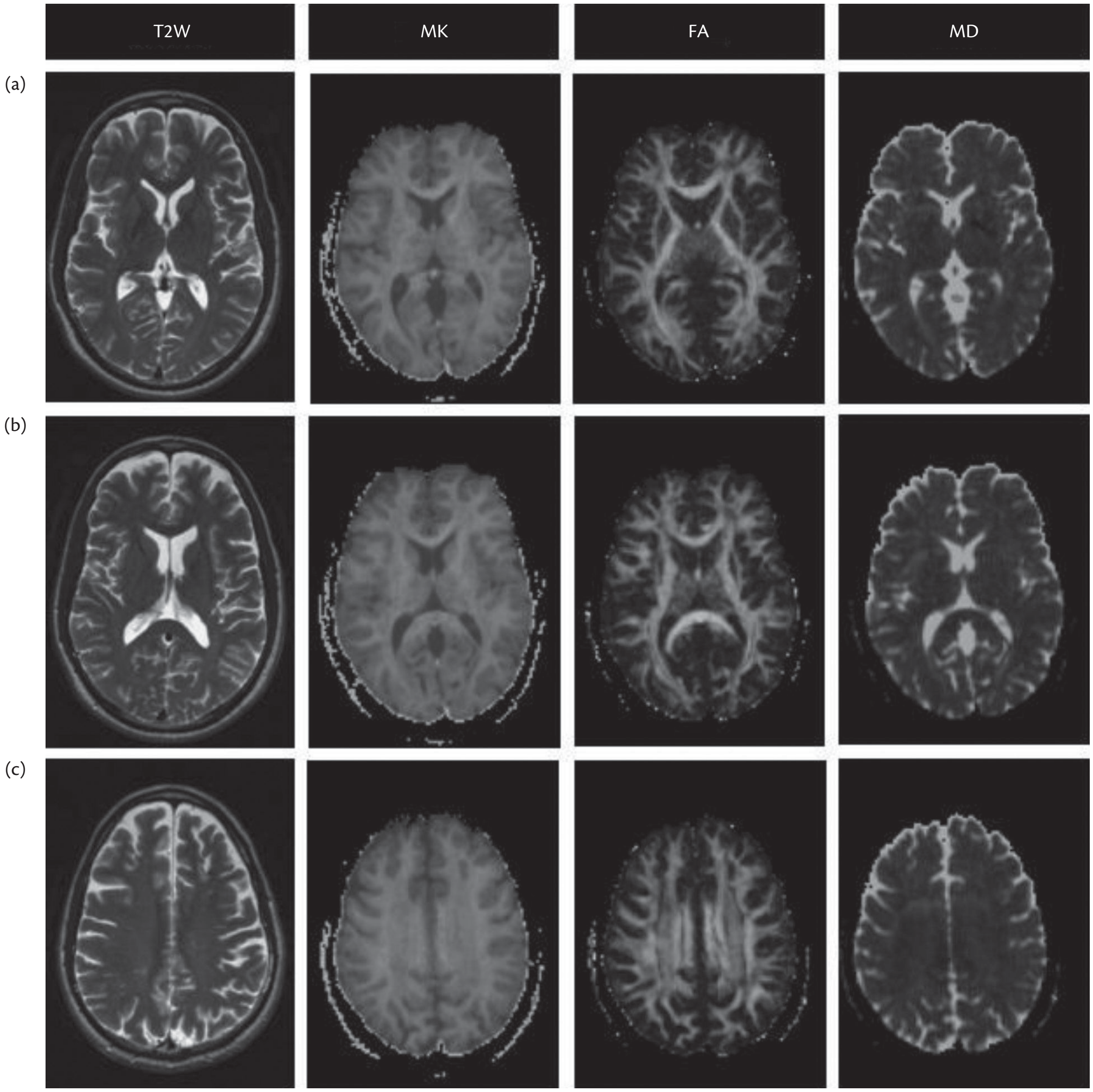

Fig. 27.5 T2w MRI images and corresponding MK, FA, and MD maps (a–c) of a 49-year-old male with mild TBI.
Modified from Grossman EJ, Ge Y, Jensen JH, et al. (2012). Thalamus and cognitive impairment in mild traumatic brain injury: a diffusional kurtosis imaging study. *Journal of Neurotrauma*, **29**, 2318–27. Copyright (2012), with permission from Mary Ann Liebert Inc. publishers.

single photon emission CT (SPECT), xenon enhanced CT (Xe-CT), and oxygen-15 water PET, which are discussed in Chapters 6, 8, and 9. These studies examined adults in cohorts containing patients with a mix of acute stage mild and moderate to severe TBI. It was found that there were regional and global changes in cerebral blood flow (CBF) and metabolism resulting from direct vascular damage, indirect vasospasm, and failure of cerebral autoregulation. These were associated with severity of trauma, suggesting the evaluation of ischaemic abnormalities might be useful as an early indicator and prognostic measure for outcome. Nuclear medicine techniques, however, are limited by the fact that they require radioactive exogenous endovascular contrast agents, which preclude serial scannning, exhibit low spatial resolution, are relatively expensive, and are available only at a small number of highly specialized centres. The only method currently available to measure perfusion that can overcome these limitations is the MRI technique of arterial spin labelling (ASL) [53], which utilizes blood water as an endogenous, freely-diffusible tracer.

ASL studies of adults with TBI

A limited number of studies [31,54–56] have applied ASL to adults in cohorts containing patients with a mix of mild and/or moderate and severe TBI. Garnett et al. [54] examined 18 patients with mild, moderate, and severe TBI at a mean of 10 days following injury, and found that six patients who exhibited focal contusions or oedema on T1w GRE MRI or T2w FSE MRI, also had decreased CBF volume and were associated with poorer outcome. Kim et al. [56] examined 27 patients with moderate and severe TBI at a mean of 65.7 days following injury. They found that focal lesions in the superior and middle frontal cortices, and diffuse lesions in

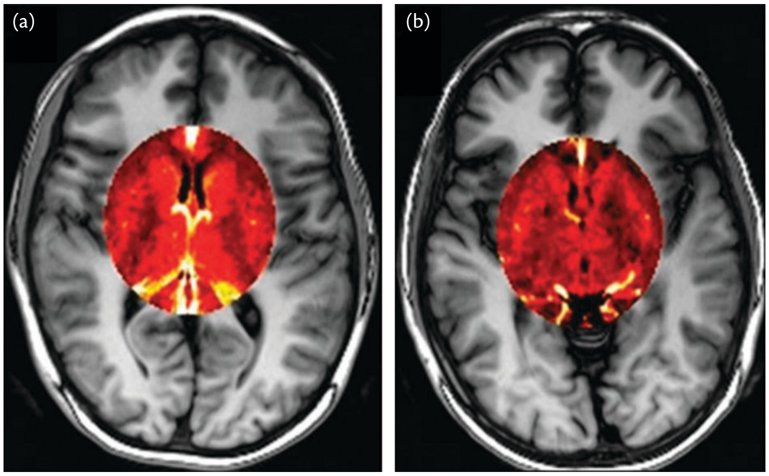

Fig. 27.6 T1w MRI images with superimposed segmented True-FISP ASL images showing that compared with a matched control (a) an adult with mild TBI (b) exhibits diminished signal intensity indicating decreased CBF in the region of the thalamus.

the thalami and posterior cingulate cortices were associated with volume loss and decreased CBF. This may reflect alterations in the default mode network, contributing to attentional deficits common in head trauma. Ge et al. [55], using a segmented true-fast imaging with steady-state precession (True-FISP) version of ASL [53], developed to overcome susceptibility artefacts, which encumber imaging of deep gray matter in standard echo-planar MRI versions of ASL, examined 21 patients with mild TBI at a median of 24.6 months following injury. They found decreased CBF in the thalamus (Fig. 27.6) that was associated with cognitive measures for impairment in executive functioning, memory, learning, processing speed, and response time. Grossman et al. [31], using the same technique, examined 22 patients with mild TBI at a mean of 22.1 days following injury during a first visit, and at mean of 369.6 days following baseline during a second visit. They found persistent decreased CBF in the thalamus that, at baseline, was moderately associated with DT MRI and DKI measures, suggesting the influence of both primary injury, due to direct traumatic insult, and secondary injury, due to longer-term degenerative processes, such as neuroaxonal dysfunction and loss.

ASL studies of children and adolescents with TBI

Newsome et al. [57] applied ASL to seven adolescents with moderate to severe TBI at a mean of 2.4 years following injury, and found a disruption in the association between CBF in prefrontal regions and functional activation in non-prefrontal regions during performance of social cognition tasks. There was, however, a stronger association between CBF in prefrontal regions and whole brain functional activation in non-prefrontal regions, suggesting CBF in prefrontal regions may be involved with the rerouting of neuronal resources needed to complete the social cognition tasks.

Blood oxygen level-dependent MRI

BOLD MRI or functional magnetic resonance imaging (fMRI), which assesses metabolic activity based on changes in the T2* signal intensity from deoxygenated haemoglobin in venous blood, is discussed in Chapter 7. fMRI studies of TBI have focused on both task-related and resting-state connectivity analyses.

BOLD MRI studies of adults with TBI

A considerable number of studies [58–67] have applied fMRI to adults in cohorts containing patients with mild or moderate and/or severe TBI. Most of these studies [58,62,64] have conducted task-related connectivity analysis within a short-term period following injury. It was found that patients exhibited increased functional activation in the prefrontal cortex, the anterior cingulate cortex, and the parietal cortex during performance of working memory tasks. Studies focusing on task-related connectivity analysis within a longer-term period following injury reported that, at a mean of 31.7 days, patients exhibited increased functional activation in the frontomedian cortex and the anterior cingulate cortex during performance of evaluative judgment tasks (Fig. 27.7) [66]. At a mean of 3 months, patients exhibited increased functional activation in the thalamus, the cingulate gyrus, and other structures thought to mediate visual attention and cognitive control during performance of a stimulus response compatibility task [65]. These results have generally been interpreted as reflecting adaptive or compensatory responses to injury, although an alternative explanation may be that the neural networks are no longer functioning efficiently [64]

Studies [59,61,67] investigating resting-state connectivity analysis found that acutely-injured patients with mild TBI exhibited decreased functional connectivity within the default mode network, which was associated with cognitive complaints. Chronically-injured patients with mild, moderate, and severe TBI exhibited decreased functional connectivity within the default mode network and the motor network, which was associated with functional activation during performance of cognitive tasks. These results suggest that in patients with TBI, cognitive impairment might be partly associated with decreased coupling between control networks [67].

Longitudinal fMRI studies [60,63] of patients with TBI are very scant and have investigated only task-related connectivity analysis at two time points spanning a very limited time frame. These studies have reported finding that in patients with moderate and severe TBI, functional activation during performance of working memory tasks, or motor and visual memory tasks, progressively improved and eventually normalized over a period of 6 months to 1 year following injury.

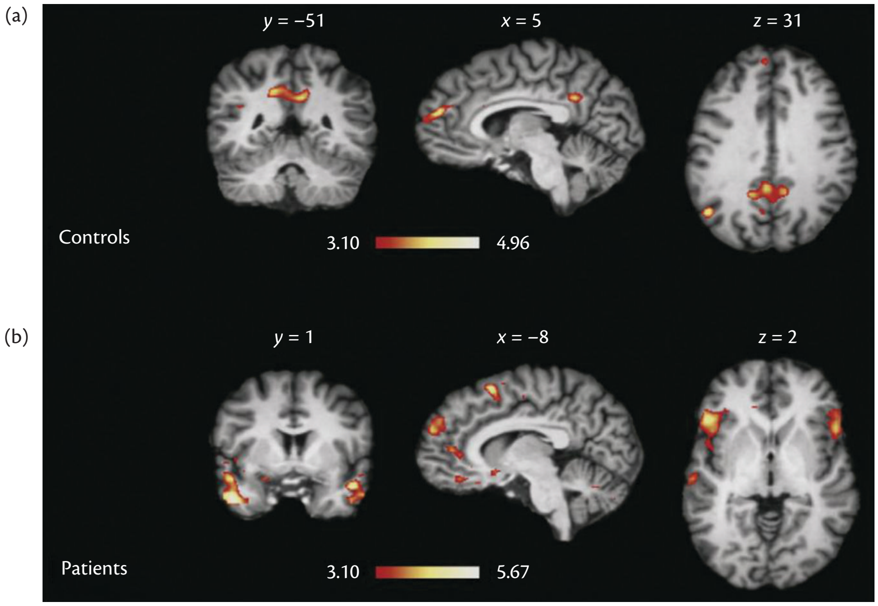

Fig. 27.7 BOLD MRI subject group averaged functional activation maps displayed on a reference brain showing differences between controls (a) and adults with severe TBI (b), while performing contrasting evaluative judgment and semantic memory retrieval tasks. Controls exhibit increased functional activation in the pregenual anterior cingulate cortex and the inferior precuneus, while patients exhibit increased functional activation in the left inferior frontal gyrus, the anterior insula, both temporal poles, and the left cerebellum. Coordinates are in Talairach space and the *z*-value was thresholded at $z = 3.10$ with $p < 0.001$.

Modified from Schroeter M, Ettrich B, Menz M, et al. (2010). Traumatic brain injury affects the frontomedian cortex-an event-related fMRI study on evaluative judgments. *Neuropsychologia*, **48**, 185–93, Copyright (2010), with permission from Elsevier.

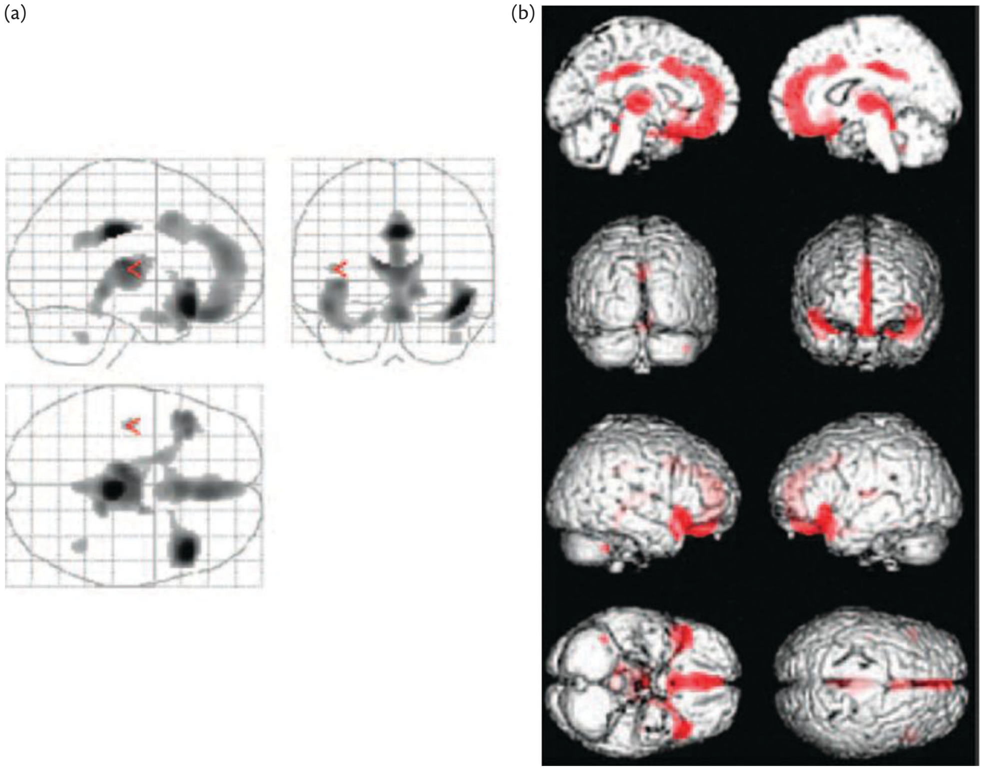

Fig. 27.8 FDG-PET subject group averaged CMR_{glu} displayed on a glass brain (a) and a reference brain (b), showing regions where, compared with controls, adults with mild, moderate, and severe TBI, exhibit decreased cerebral metabolism. Patients exhibit decreased CMR_{glu} in the right and left thalamus, the right cingulate gyrus, the right parahippocampal gyrus, the right rectal gyrus, the left insula, the right and left superior temporal gyrus, and the right cerebellum.

Modified from Kato T, Nakayama N, Yasokawa Y, et al. (2007). Statistical image analysis of cerebral glucose metabolism in patients with cognitive impairment following diffuse traumatic brain injury. *Journal of Neurotrauma*, **24**, 919–26. Copyright (2007), with permission from Mary Ann Liebert Inc. publishers.

BOLD MRI studies of children and adolescents with TBI

A small number of studies [57,68–70] have applied fMRI to children in cohorts containing patients with a mix of mild, moderate, and severe TBI using task-related connectivity analysis. They have found that within a long-term period following injury, patients exhibited increased functional activation in the frontal cortex and the parietal cortex during performance of sustained attention tasks, the peri-sylvian areas during performance of language tasks, regions posterior to the prefrontal area during performance of social cognition tasks, and the medial and anterior parietal areas and the posterior cerebellum during performance of motor control tasks.

Fluorine-18 deoxyglucose positron emission tomography

FDG-PET, which assesses metabolic activity using the radioactive isotope fluorine-18 as a tracer for glucose consumption, is discussed in Chapter 9. Despite the limitations previously discussed concerning nuclear medicine techniques, FDG-PET provides unique physiological information that potentially has important clinical implications, since glucose consumption is a central component in cellular metabolism and neuronal activation.

FDG PET studies of adults with TBI

Only a few studies [71–74] have applied FDG-PET to adults in cohorts containing patients with mild, moderate, and/or severe TBI. These studies have reported finding that within a short-term period following injury, patients exhibited decreased cerebral metabolic rate of glucose (CMR_{glu}) in the thalamus, the cerebellum, and the brain stem, which was associated with post-traumatic level of consciousness. Within a long-term period following injury, patients exhibited decreased CMR_{glu} in the thalamus, the cerebellum, and several regions of the cortex, including the frontal and temporal lobes (Fig. 27.8), which was associated with cognitive impairment and neurologic outcome.

FDG PET studies of children and adolescents with TBI

Worley et al. [75] applied FDG-PET to 22 children and adolescents with severe TBI and reported that decreased CMR_{glu} in the thalamus, the striatum, the cerebellum, the frontal lobe, the temporal lobe, the parietal lobe, and the occipital lobe was associated with outcome at a baseline visit with a median of 55 days following injury, but not at a follow-up visit with a median of 21.9 months later. While CMR_{glu} levels demonstrated improvement in patients which underwent rehabilitation between baseline visit and follow-up visit, this improvement was not associated with changes in their neurologic condition. This, however, was an early FDG-PET investigation, and since the technique has undergone more recent advancements and yielded encouraging results when applied to adults with TBI, further examination of the potential value it might have for the study of children and adolescents with TBI is worthwhile pursuing.

Conclusions

The lack of evidence for injury in TBI on CT and conventional MRI has led to the examination of SWI, ^{1}H-MRS, diffusion MRI, perfusion imaging, BOLD MRI, and FDG-PET as possible individual and/or complimentary approaches to detecting microstructural and functional changes that have the potential to help grade damage severity, track its development, and provide prognostic markers for clinical outcome. Although many studies have yielded promising results, there is still a need for more research, since some of these techniques lack validation as diagnostic tools and very few investigations have been conducted, most of which examined small cohorts of patients with mixed grades of TBI severity at a single time point following injury. Nevertheless, these studies have helped to improve understanding of TBI pathophysiology and suggest that neuroimaging techniques might, indeed, provide early markers for tissue damage, which better enable the monitoring of medical and rehabilitative interventions.

References

1. Langlois JA, Rutland-Brown W, and Wald MM. (2006). The epidemiology and impact of traumatic brain injury: a brief overview. *Journal of Head Trauma Rehabilitation*, **21**, 375–8.
2. Finkelstein E, Corso P, and Miller T. (2006). *The incidence and economic burden of injuries in the United States*. New York: Oxford University Press.
3. Teasdale G, and Jennett B. (1974). Assessment of coma and impaired consciousness. A practical scale. *Lancet*, **2**, 81–4.
4. Bazarian JJ, McClung J, Shah MN, et al. (2005). Mild traumatic brain injury in the United States, 1998-2000. *Brain Injury*, **19**, 85–91.
5. Haacke EM, Xu Y, Cheng Y-CN, et al. (2004). Susceptibility weighted imaging (SWI). *Magnetic Resonance in Medicine*, **52**,612–18.
6. Akiyama Y, Miyata K, Harada K, et al. (2009). Susceptibility-weighted magnetic resonance imaging for the detection of cerebral microhemorrhage in patients with traumatic brain injury. *Neurologia Medico-chirurgica*, **49**, 97–9.
7. Chastain C, Oyoyo U, Zipperman M, et al. (2009). Predicting outcomes of traumatic brain injury by imaging modality and injury distribution. *Journal of Neurotrauma*, **26**, 1183–96.
8. Tong KA, Ashwal S, Holshouser BA, et al. (2004). Diffuse axonal injury in children: clinical correlation with hemorrhagic lesions. *Annals of Neurology*, **56**, 36–50.
9. Tong KA, Ashwal S, Holshouser BA, et al. (2003). Hemorrhagic shearing lesions in children and adolescents with posttraumatic diffuse axonal injury: improved detection and initial results. *Radiology*, **227**, 332–9.
10. Babikian T, Freier MC, Tong KA, et al. (2005). Susceptibility weighted imaging: neuropsychologic outcome and pediatric head injury. *Pediatric Neurology*, **33**, 184–94.
11. Ariza M, Junqué C, Mataró M, et al. (2004). Neuropsychological correlates of basal ganglia and medial temporal lobe NAA/Cho reductions in traumatic brain injury. *Archives of Neurology*. 2004;61:541–4.
12. Carpentier A, Galanaud D, Puybasset L, et al. (2006). Early morphologic and spectroscopic magnetic resonance in severe traumatic brain injuries can detect ‘invisible brain stem damage’ and predict ‘vegetative states’. *Journal of Neurotrauma*. 2006;23:674–85.
13. Cohen BA, Inglese M, Rusinek H, et al. (2007). Proton MR spectroscopy and MRI-volumetry in mild traumatic brain injury. *AJNR American Journal of Neuroradiology*, **28**, 907–13.
14. Garnett MR, Corkill RG, Blamire AM, et al. (2001). Altered cellular metabolism following traumatic brain injury: a magnetic resonance spectroscopy study. *Journal of Neurotrauma*, **18**, 231–40.
15. Kirov II, Tal A, Babb JS, et al. (2013). Diffuse axonal injury in mild traumatic brain injury: a 3D multivoxel proton MR spectroscopy study. *Journal of Neurology*, **260**, 242–452.
16. Tollard E, Galanaud D, Perlbarg V, et al. (2009). Experience of diffusion tensor imaging and 1H spectroscopy for outcome prediction in severe traumatic brain injury: preliminary results. *Critical Care Medicine*, **37**, 1448–55.

17. Ashwal S, Holshouser BA, Shu SK, et al. (2000). Predictive value of proton magnetic resonance spectroscopy in pediatric closed head injury. *Pediatric Neurology*, **23**, 114–25.
18. Babikian T, Freier M-C, Ashwal S, et al. (2006). MR spectroscopy: predicting long-term neuropsychological outcome following pediatric TBI. *Journal of Magnetic Resonance Imaging*, **24**, 801–11.
19. Holshouser BA, Ashwal S, Luh GY, et al. (1997). Proton MR spectroscopy after acute central nervous system injury: outcome prediction in neonates, infants, and children. *Radiology*, **202**, 487–96.
20. Yeo RA, Phillips JP, Jung RE, et al. (2006). Magnetic resonance spectroscopy detects brain injury and predicts cognitive functioning in children with brain injuries. *Journal of Neurotrauma*, **23**, 1427–35.
21. Jensen JH, and Helpern JA. (2010). MRI quantification of non-Gaussian water diffusion by kurtosis analysis. *NMR in Biomedicine*, **23**, 698–710.
22. Hou DJ, Tong KA, Ashwal S, et al. (2007). Diffusion-weighted magnetic resonance imaging improves outcome prediction in adult traumatic brain injury. *Journal of Neurotrauma*, **24**, 1558–69.
23. Kurca E, Sivak S, and Kucera P. (2006). Impaired cognitive functions in mild traumatic brain injury patients with normal and pathologic magnetic resonance imaging. *Neuroradiology*, **48**, 661–9.
24. Schaefer PW, Huisman TAGM, Sorensen AG, et al. (2004). Diffusion-weighted MR imaging in closed head injury: high correlation with initial Glasgow Coma Scale score and score on modified Rankin scale at discharge. *Radiology*, **233**, 58–66.
25. Shanmuganathan K, Gullapalli RP, Mirvis SE, et al. (2004). Whole-brain apparent diffusion coefficient in traumatic brain injury: correlation with Glasgow Coma Scale score. *AJNR American Journal of Neuroradiology*, **25**, 539–44.
26. Zheng WB, Liu GR, Li LP, et al. (2007). Prediction of recovery from a post-traumatic coma state by diffusion-weighted imaging (DWI) in patients with diffuse axonal injury. *Neuroradiology*, **49**, 271–9.
27. Arfanakis K, Haughton VM, Carew JD, et al. (2002). Diffusion tensor MR imaging in diffuse axonal injury. *AJNR American Journal of Neuroradiology*, **23**, 794–802.
28. Bazarian JJ, Zhong J, Blyth B, et al. (2007). Diffusion tensor imaging detects clinically important axonal damage after mild traumatic brain injury: a pilot study. *Journal of Neurotrauma*, **24**, 1447–59.
29. Bendlin BB, Ries ML, Lazar M, et al. (2008). Longitudinal changes in patients with traumatic brain injury assessed with diffusion-tensor and volumetric imaging. *NeuroImage*, **42**, 503–14.
30. Grossman EJ, Ge Y, Jensen JH, et al. (2012). Thalamus and cognitive impairment in mild traumatic brain injury: a diffusional kurtosis imaging study. *Journal of Neurotrauma*, **29**, 2318–27.
31. Grossman EJ, Jensen JH, Babb JS, et al. (2013). Cognitive impairment in mild traumatic brain injury: a longitudinal diffusional kurtosis and perfusion imaging study. *AJNR American Journal of Neuroradiology*, **34**, 951–7.
32. Inglese M, Makani S, Johnson G, et al. (2005). Diffuse axonal injury in mild traumatic brain injury: a diffusion tensor imaging study. *Journal of Neurosurgery*, **103**, 298–303.
33. Kraus MF, Susmaras T, Caughlin BP, et al. (2007). White matter integrity and cognition in chronic traumatic brain injury: a diffusion tensor imaging study. *Brain*, **130**, 2508–19.
34. Kumar R, Gupta RK, Husain M, et al. (2009). Comparative evaluation of corpus callosum DTI metrics in acute mild and moderate traumatic brain injury: its correlation with neuropsychometric tests. *Brain Injury*, **23**, 675–85.
35. Le TH, Mukherjee P, Henry RG, et al. (2005). Diffusion tensor imaging with three-dimensional fiber tractography of traumatic axonal shearing injury: an imaging correlate for the posterior callosal 'disconnection' syndrome: case report. *Neurosurgery*, **56**, 189.
36. Little DM, Kraus MF, Joseph J, et al. (2010). Thalamic integrity underlies executive dysfunction in traumatic brain injury. *Neurology*, **74**, 558–64.
37. Mayer AR, Ling J, Mannell MV, et al. (2010). A prospective diffusion tensor imaging study in mild traumatic brain injury. *Neurology*, **74**,643–50.
38. Messe A, Caplain S, Paradot G, et al. (2011). Diffusion tensor imaging and white matter lesions at the subacute stage in mild traumatic brain injury with persistent neurobehavioral impairment. *Human Brain Mapping*, **32**, 999–1011.
39. Miles L, Grossman RI, Johnson G, et al. (2008). Short-term DTI predictors of cognitive dysfunction in mild traumatic brain injury. *Brain Injury*, **22**, 115–22.
40. Rutgers DR, Fillard P, Paradot G, et al. (2008). Diffusion tensor imaging characteristics of the corpus callosum in mild, moderate, and severe traumatic brain injury. *AJNR American Journal of Neuroradiology*, **29**, 1730–5.
41. Rutgers DR, Toulgoat F, Cazejust J, et al. (2008). White matter abnormalities in mild traumatic brain injury: a diffusion tensor imaging study. *AJNR American Journal of Neuroradiology*, **29**, 514–19.
42. Sidaros A, Engberg AW, Sidaros K, et al. (2008). Diffusion tensor imaging during recovery from severe traumatic brain injury and relation to clinical outcome: a longitudinal study. *Brain*, **131**, 559–72.
43. Chu Z, Wilde EA, Hunter JV, et al. (2010).Voxel-based analysis of diffusion tensor imaging in mild traumatic brain injury in adolescents. *AJNR American Journal of Neuroradiology*, **31**, 340–6.
44. Galloway NR, Tong KA, Ashwal S, et al. (2008). Diffusion-weighted imaging improves outcome prediction in pediatric traumatic brain injury. *Journal of Neurotrauma*, **25**, 1153–62.
45. Levin HS, Wilde EA, Chu Z, et al. (2008). Diffusion tensor imaging in relation to cognitive and functional outcome of traumatic brain injury in children. *Journal of Head Trauma Rehabilitation*, **23**, 197–208.
46. Wilde EA, Chu Z, Bigler ED, et al. (2006). Diffusion tensor imaging in the corpus callosum in children after moderate to severe traumatic brain injury. *Journal of Neurotrauma*, **23**, 1412–26.
47. Wilde EA, McCauley SR, Hunter JV, et al. (2008). Diffusion tensor imaging of acute mild traumatic brain injury in adolescents. *Neurology*, **70**, 948–55.
48. Wu TC, Wilde EA, Bigler ED, et al. (2010). Evaluating the relationship between memory functioning and cingulum bundles in acute mild traumatic brain injury using diffusion tensor imaging. *Journal of Neurotrauma*, **27**, 303–7.
49. Bouma GJ, Muizelaar JP, Stringer WA, et al. (1992). Ultra-early evaluation of regional cerebral blood flow in severely head-injured patients using xenon-enhanced computerized tomography. *Journal of Neurosurgery*, **77**, 360–8.
50. Nakamizo A, Inamura T, Amano T, et al. (2002). Decreased thalamic metabolism without thalamic magnetic resonance imaging abnormalities following shearing injury to the substantia nigra. *Journal of Clinical Neuroscience*, **9**, 685–8.
51. Nakayama N, Okumura A, Shinoda J, et al. (2006). Relationship between regional cerebral metabolism and consciousness disturbance in traumatic diffuse brain injury without large focal lesions: an FDG-PET study with statistical parametric mapping analysis. *Journal of Neurology, Neurosurgery & Psychiatry*, **77**, 856–62.
52. Stamatakis EA, Wilson JT, Hadley DM, et al. (2002). SPECT imaging in head injury interpreted with statistical parametric mapping. *Journal of Nuclear Medicine*, **43**, 476–83.
53. Grossman EJ, Zhang K, An J, et al. (2009). Measurement of deep gray matter perfusion using a segmented true-fast imaging with steady-state precession (True-FISP) arterial spin-labeling (ASL) method at 3T. *Journal of Magnetic Resonance Imaging*, **29**, 1425–31.
54. Garnett MR, Blamire AM, Corkill RG, et al. (2001). Abnormal cerebral blood volume in regions of contused and normal appearing brain following traumatic brain injury using perfusion magnetic resonance imaging. *Journal of Neurotrauma*, **18**, 585–93.
55. Ge Y, Patel MB, Chen Q, et al. (2009). Assessment of thalamic perfusion in patients with mild traumatic brain injury by true FISP arterial spin labelling MR imaging at 3T. *Brain Injury*, **23**, 666–74.
56. Kim J, Whyte J, Patel S, et al. (2010). Resting cerebral blood flow alterations in chronic traumatic brain injury: an arterial spin labeling perfusion FMRI study. *Journal of Neurotrauma*, **27**, 1399–411.

57. Newsome MR, Scheibel RS, Chu Z, et al. (2012). The relationship of resting cerebral blood flow and brain activation during a social cognition task in adolescents with chronic moderate to severe traumatic brain injury: a preliminary investigation. *International Journal of Developmental Neuroscience*, **30**, 255–66.
58. Christodoulou C, DeLuca J, Ricker JH, et al. (2001). Functional magnetic resonance imaging of working memory impairment after traumatic brain injury. *Journal of Neurology, Neurosurgery & Psychiatry*, **71**, 161–8.
59. Kasahara M, Menon DK, Salmond CH, et al. (2010). Altered functional connectivity in the motor network after traumatic brain injury. *Neurology*, **75**, 168–76.
60. Mani TM, Miller LS, Yanasak N, et al. (2007). Evaluation of changes in motor and visual functional activation over time following moderate-to-severe brain injury. *Brain Injury*, **21**, 1155–63.
61. Mayer AR, Mannell MV, Ling J, et al. (2011). Functional connectivity in mild traumatic brain injury. *Human Brain Mapping*, **32**, 1825–35.
62. McAllister TW, Sparling MB, Flashman LA, et al. (2001). Differential working memory load effects after mild traumatic brain injury. *NeuroImage*, **14**, 1004–12.
63. Sanchez-Carrion R, Fernandez-Espejo D, Junque C, et al. (2008). A longitudinal fMRI study of working memory in severe TBI patients with diffuse axonal injury. *NeuroImage*, **43**, 421–9.
64. Scheibel RS, Newsome MR, Steinberg JL, et al. (2007). Altered brain activation during cognitive control in patients with moderate to severe traumatic brain injury. *Neurorehabilitation and Neural Repair*, **21**, 36–45.
65. Scheibel RS, Newsome MR, Troyanskaya M, et al. (2009). Effects of severity of traumatic brain injury and brain reserve on cognitive-control related brain activation. *Journal of Neurotrauma*, **26**, 1447–61.
66. Schroeter M, Ettrich B, Menz M, et al. (2010). Traumatic brain injury affects the frontomedian cortex-an event-related fMRI study on evaluative judgments. *Neuropsychologia*, **48**, 185–93.
67. Sharp DJ, Beckmann CF, Greenwood R, et al. (2011). Default mode network functional and structural connectivity after traumatic brain injury. *Brain*, **134**, 2233–47.
68. Caeyenberghs K, Wenderoth N, Smits-Engelsman BCM, et al. (2009). Neural correlates of motor dysfunction in children with traumatic brain injury: exploration of compensatory recruitment patterns. *Brain*, **132**, 684–94.
69. Karunanayaka PR, Holland SK, Yuan W, et al. (2007). Neural substrate differences in language networks and associated language-related behavioral impairments in children with TBI: a preliminary fMRI investigation. *NeuroRehabilitation*, **22**, 355–69.
70. Kramer ME, Chiu C-YP, Walz NC, et al. (2008).Long-term neural processing of attention following early childhood traumatic brain injury: fMRI and neurobehavioral outcomes. *Journal of the International Neuropsychology Society*, **14**, 424–35.
71. Garcia-Panach J, Lull N, Lull JJ, et al. (2011). A voxel-based analysis of FDG-PET in traumatic brain injury: regional metabolism and relationship between the thalamus and cortical areas. *Journal of Neurotrauma*, **28**, 1707–17.
72. Hattori N, Huang SC, Wu HM, et al. (2003). Correlation of regional metabolic rates of glucose with Glasgow Coma Scale after traumatic brain injury. *Journal of Nuclear Medicine*, **44**, 1709–16.
73. Kato T, Nakayama N, Yasokawa Y, et al. (2007). Statistical image analysis of cerebral glucose metabolism in patients with cognitive impairment following diffuse traumatic brain injury. *Journal of Neurotrauma*, **24**, 919–26.
74. Zhang J, Mitsis EM, Chu K, et al. (2010). Statistical parametric mapping and cluster counting analysis of [18F] FDG-PET imaging in traumatic brain injury. *Journal of Neurotrauma*, **27**, 35–49.
75. Worley G, Hoffman JM, Paine SS, et al. (1995). 18-Fluorodeoxyglucose positron emission tomography in children and adolescents with traumatic brain injury. *Developmental Medicine & Child Neurology*, **37**, 213–20.

CHAPTER 28

Neuroimaging in disorders of consciousness

Olivier Bodart, Vanessa Charland-Verville, Steven Laureys, and Olivia Gosseries

Introduction

Evaluation of patients with an altered level of consciousness is and has always been a difficult task. Indeed, they are, by definition, non-communicative patients, sometimes with important vigilance fluctuation, some with little or no motor output, and most with language impairment and/or aphasia [1]. Each patient has a different medical history, their brain injuries are all unique, as well as their residual levels of consciousness. Clinical and behavioural evaluations remain the gold standard in the diagnostic work-up of disorders of consciousness (DOC), but they may lead to a high rate of misdiagnosis when not assessed with standardized scales [2]. The neuroimaging techniques developed during the last 10 years have completely changed this field of research.

Definition of consciousness

The concept of consciousness in itself is difficult to sense and there is still no internationally accepted definition of it. For neuroscientists and clinicians, such a concept has two main components—arousal and awareness—representing, respectively, the level of wakefulness, and the level of awareness of self and environment [3]. Arousal and awareness are positively correlated in healthy people (with the notable exception of paradoxical sleep). In disorders of consciousness, these components can be dissociated (Fig. 28.1).

Definition of disorders of consciousness

Patients who survive severe brain injuries can remain temporarily or permanently in various states of altered consciousness. The deepest state is coma, characterized by the loss of both arousal and awareness for at least 1 hour [4] and up to a few weeks. The patients may either die, or recover arousal or awareness. Recovery of arousal alone is characteristic of the vegetative state [5]. These patients in a vegetative state are able to open their eyes, but remain unaware of their environment and themselves. This condition has recently been renamed 'unresponsive wakefulness syndrome' (UWS) to lower the public impression of these patients being 'vegetable-like' [6,7]. They may further evolve to a minimally conscious state (MCS). Patients in MCS show signs of awareness of their surroundings, such as command following, visual pursuit or localization of pain stimulation [8]. MCS has been recently subcategorized in 'MCS+' for patients who present high-order behavioural responses to stimuli (with preservation of language processing ability) and 'MCS–' for patients who only show low-level non-reflexive responses to stimuli (e.g. visual pursuit) [9]. However, MCS patients cannot communicate functionally. Recovery of the ability to functionally communicate or to use objects adequately is necessary for the diagnosis of the emergence of MCS (Fig. 28.2).

Clinical assessment and related issues

To date, behavioural assessment of consciousness is the gold standard for diagnosis of the different states of DOC. There are several scales to rate the level of consciousness, but the most sensitive and validated one is the Coma Recovery Scale-Revised (CRS-R) [10,11]. The CRS-R is composed of six subscales (auditory, visual, motor, oromotor, communication, and arousal scales) each assessing the presence or absence of signs of consciousness. This scale permits the distinction of UWS from MCS. Behavioural scales mainly assess the level of awareness by looking for a motor response to a recent query. Thus, patients require a preservation of the sensory networks, the absence of motor impairment (paralysis or spasticity), and the capacity to understand language. Other sources of diagnostic errors are fluctuations of patient's arousal, and administration of sedating drugs and painkillers. Clearly, if the patient is assessed by someone who is not familiar with the behavioural scale, or not suitably trained to detect subtle signs of consciousness, the risk of misdiagnosis is increased [12]. Furthermore, some behavioural signs (such as visual fixation [13]) remain ambiguous, and not all clinicians and neuroscientists share the same opinion about their ability to reflect consciousness. All these limitations explain the need for more objective and direct techniques to assess the level of consciousness.

To be considered conscious—even minimally—or unconscious greatly influences caregivers in regard to pain treatment and end-of-life decision-making [14,15]. This shows that making the correct diagnosis is not only a scientific goal, but also has important ethical implications. Access to a rehabilitation centre can also be influenced by the diagnosis, since sometimes it is necessary for the patient to be able to actively take part in the treatment programme [16]. Finally, prognosis and functional outcome of patients in MCS are better than those with UWS [17,18]. MCS patients with a traumatic brain injury aetiology have the best prognosis, with up to 48% emerging from this state at 12 months, whereas UWS patients

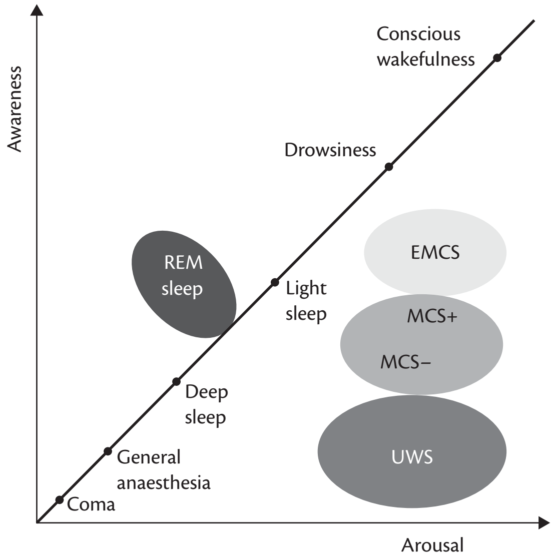

Fig. 28.1 Arousal versus awareness. In physiological condition, the awareness and wakefulness components of consciousness are positively correlated, with the notable exception of rapid eye movement sleep. In disorders of consciousness, there is a dissociation between these two components. Arousal often improves more than awareness, resulting in an unresponsive wakefulness syndrome in patients who are awake but not aware.

REM sleep, rapid eye movement sleep; UWS, unresponsive wakefulness syndrome; MCS, minimally Casali AG, Gosseries O, Rosanova M, et al. (2013). A theoretically based index of consciousness independent of sensory processing and behavior. Science Translational Medicine, 5(198), 198ra105conscious state; EMCS, emergence of the MCS.

Modified from Laureys S. (2005). The neural correlate of (un)awareness: lessons from the vegetative state. *Trends in Cognitive Science*, **9**(12), 556–9. Copyright (2005), with permission from Elsevier.

with a non-traumatic aetiology have a worse one, with only 1% emerging from MCS [19].

Neuroimaging studies

Structural MRI

Conventional magnetic resonance imaging (MRI) can provide valuable pieces of information about the structural integrity of the brain. As the variability in the severity and localization of lesions is extreme, people have tried to identify key areas of the brain that would be linked with favourable or unfavourable prognosis. When comatose patients are scanned in the subacute phase, MRI lesions in the brainstem and basal ganglia are associated to a poor prognosis, especially if they are bilateral [20–23]. However, this cannot explain why, with the same kind and distribution of lesions, some patients remain in an UWS, while other progress to a MCS [24].

Diffusion-tensor imaging (DTI) metrics have been found to be correlated with the CRS-R scores, and have been shown to be able to distinguish between UWS and MCS patients at a group level (Fig. 28.3) [25,26]. In the latter study, Fernandez-Espejo et al. showed that mean diffusivity histograms of UWS patients have a lower peak height and an increased peak width in the thalami and the subcortical white matter, when compared with MCS patients. The authors suspect that this could reflect the presence of more damage to the white matter in that population. In UWS, DTI can detect white matter lesions unseen on conventional MRI, and, in traumatic injuries aetiology only, disconnection of the brainstem's tracts [27]. DTI has also been used as a predictor of outcome. Fractional anisotropy of the splenium of the corpus callosum and the internal capsule correlates with the Glasgow Coma Scale (GCS, [28]) and the Modified Rankin Score [29] at the time of discharge [30]. A noteworthy case of a MCS patient recovering after several years in this state was studied with DTI. The results showed clues of possible axonal regrowth in the cerebellar midline white matter and along the splenium of the corpus callosum [31].

Resting state

When the patients are not receiving any external stimulation and are not performing any active task, their brain is considered to be at rest. Brain metabolic activity in this resting state condition is not null and can be studied even in non-collaborative patients. Using positron emission tomography (PET), several studies have demonstrated a global decrease in brain metabolism in UWS patients [32–34]. However, recovery of consciousness is not always linked to an increase of the global metabolism [35]. It seems that some brain areas are more important than others for the emergence of consciousness. Indeed, a widespread network encompassing midline (mesiofrontal and precuneus areas) and lateral associative cortices (prefrontal and parietal areas) is necessary for the emergence of UWS [36–39]. The metabolic

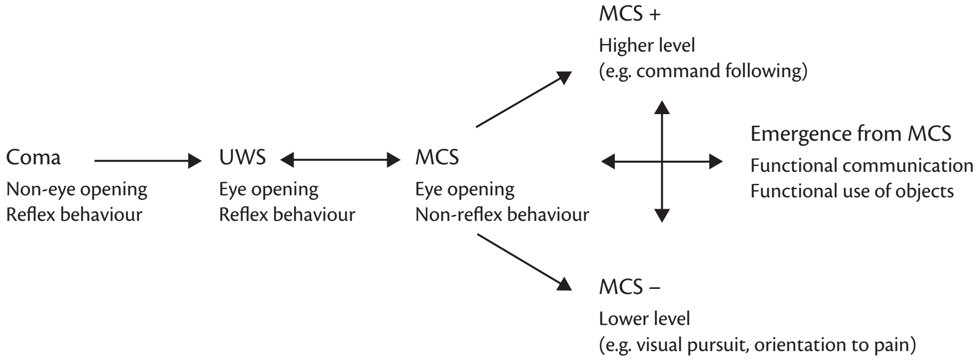

Fig. 28.2 Evolution of nosology in disorders of consciousness. The nosology of disorders of consciousness is rapidly changing. As new diagnostic tools are designed, new conditions are described, each with its own prognosis of outcome and survival. However, the boundaries between each of these more precisely defined conditions are less and less clear-cut.

UWS, unresponsive wakefulness syndrome; MCS, minimally conscious state.

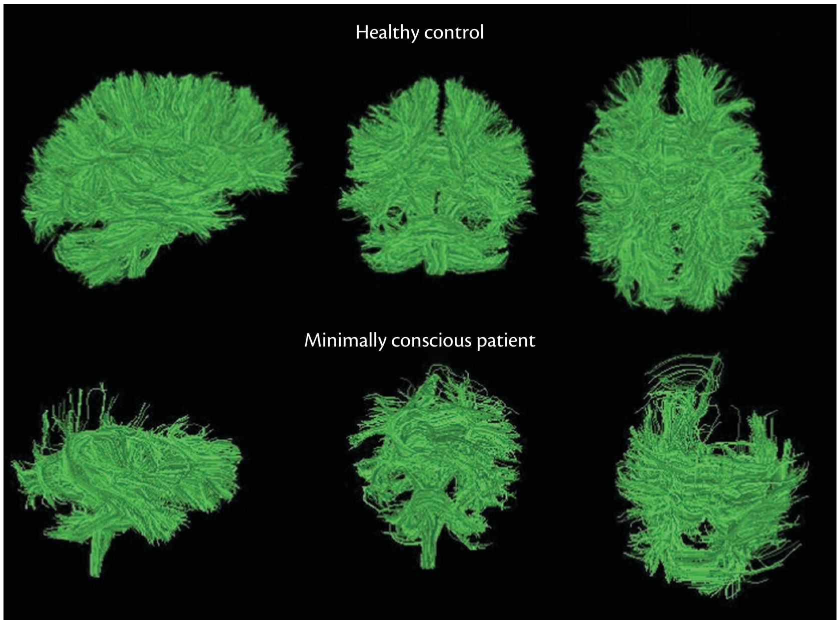

Fig. 28.3 Use of DTI in patients with disorders of consciousness. Top row shows axonal tracts in a healthy control with views, respectively, from the right side, front side, and the top of the brain. Below is an example of a DTI map in a patient in a minimally conscious state (10 months post-trauma), showing a global decrease in the number of axonal tracts and demonstrating a loss of structural connectivity.

activity in this network is linked with the level of consciousness (Fig. 28.4) [40–42], suggesting that UWS might be the result of a disconnection syndrome [3]. Thalamus can also play a role in consciousness, as deep gray matter structures have proved to promote arousal, behavioural responses as assessed by the CRS-R, and motor control in one patient [43]. In the clinical setting, these PET data can also be used to train classifiers that can distinguish conscious from unconscious patients [44].

This resting state brain can also be assessed using functional MRI (fMRI). A similar frontoparietal and thalamo-cortical network was identified and named the default mode network (DMN) encompassing midlines cortices (i.e. anterior cingulate/mesofrontal and posterior cingulate/precuneus) [45]. Functional connectivity in this network is linked to the level of consciousness ranging from maximal in healthy controls, locked-in patients, and MCS, to minimal in UWS and coma patients [46] (Fig. 28.5). This activity is not found in brain dead patients [47]. Moreover, recovery of functional connectivity in this network has been correlated with the level of recovery of consciousness [48].

Further research has identified two different networks: the network for the awareness of the self and the network associated with environment processing (Fig. 28.6) [49]. The DMN is thought to reflect self-awareness (i.e. spontaneous thoughts, inner speech, and mind wandering) [49,50]. In the clinical setting, these data could be used to infer the patients' residual level of consciousness [51], but at first motion artefacts and traumatic brain deformations should be corrected for this approach to work at an individual patient level [52]. The perception of the environment (i.e. stimulus-dependent thoughts, sensation, and perception of external stimuli, such as visual or auditory stimulations) is related to activation of the external network encompassing lateral parts of the frontoparietal network, and has been investigated though passive external stimulation and active paradigms.

Passive external stimulation

Brain metabolic reactions to passive stimulations have been studied using PET and fMRI. In healthy volunteers, a stimulus activates the corresponding primary cortices and higher-level associative areas (e.g. see [53]). Activation of these latter brain regions seems to reflect a sign of conscious information processing. Metabolic brain reaction to passive stimuli has therefore been investigated in DOC patients. Using PET, in response to appropriate stimuli, UWS patients only show activation of auditory and somatosensory primary cortices, while MCS patients experience a distributed activation of associative areas [54]. More recent fMRI studies support these results [55–57]. Nevertheless, it remains challenging to define consciousness in itself. Indeed, it is controversial that passive activations of brain areas or networks could be a sign of consciousness in the sense of a volitional cerebral activity since this could also reflect automatic processing [50].

Nonetheless, some of these studies may have an important impact in the clinical setting, especially for those on pain perception. Painful stimulation in UWS patients seems to activate low-level brain regions only (and not the associative areas thought to be essential for a conscious perception of the painful stimulus) [58], while MCS patients show full pain network's activation [53]. Several states' laws about termination of artificial nutrition and hydration in the United States require that pain treatment is unnecessary for UWS patients [59]. However, such a statement is controversial knowing that diagnosis errors are still high, and pain treatment should definitely be given to MCS patients.

Active paradigms

Paradigms have been developed to detect wilful modulations of brain activity, which would be unambiguously considered as a sign of awareness. In the study of Owen et al. [60], one patient was asked to imagine playing tennis and walking around her house.

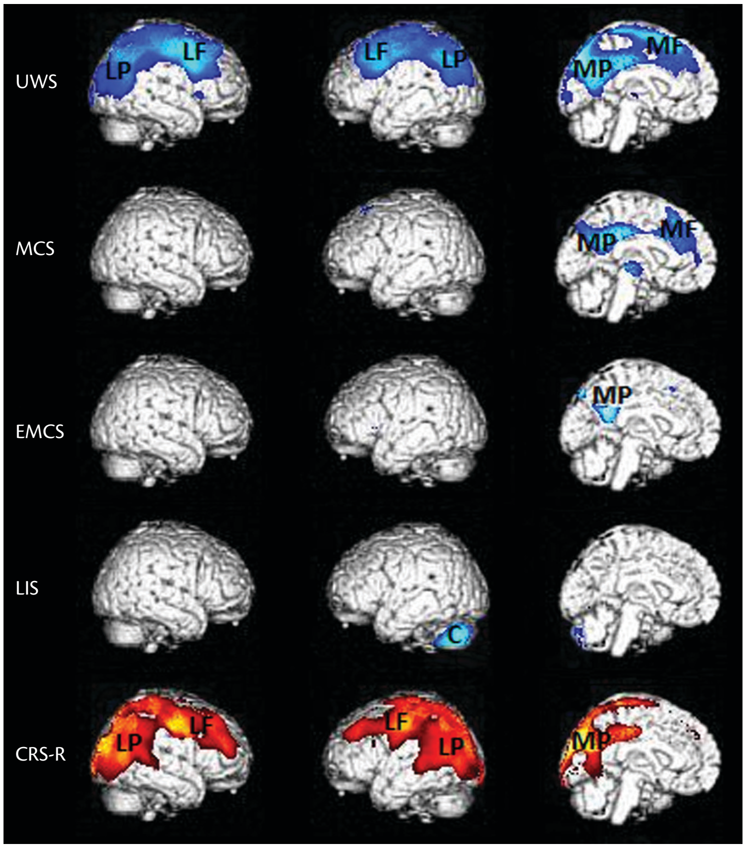

Fig. 28.4 Metabolic impairment in patients with disorders of consciousness using FDG-PET. Areas with significant metabolic impairment (blue) in unresponsive wakefulness syndrome (UWS), minimally conscious state (MCS), emergence from MCS (EMCS) and locked-in syndrome (LIS) compared with age-matched controls. The lower panel shows the areas where metabolic activity correlated with Coma Recovery Scale-Revised (CRS-R) scores.

LP, lateral parietal cortices; LF, lateral prefrontal cortices; MP, midline precuneus/posterior cingulated cortices; MF, mesiofrontal/anterior cingulate cortices; C, cerebellum.

Reproduced from Thibaut A, Bruno MA, Chatelle C, et al. (2012). Metabolic activity in external and internal awareness networks in severely brain damaged patient. *Journal of Rehabilitation Medicine*, **44**(6), 487–94. Copyright (2012), under Creative Commons License 2.0.

Interestingly, this patient behaviourally diagnosed as UWS was able to respond to the commands, resulting respectively in the activation of the supplementary motor area and parahippocampal cortex. These patterns of activation were similar to those observed in healthy volunteers [61]. This paradigm was adapted by Monti et al. [62] into a communication protocol and they showed that one MCS patient was able to communicate by answering 'yes' or 'no' to a set of questions (Fig. 28.7), although no signs of communication was observed with behavioural examination. Now, real-time fMRI communication protocols begin to develop [63,64]. Several adaptations of the paradigm exist with the use of other commands, resulting in activation of the language network [65], the attention network [66], the supplementary motor area [67], the premotor cortex [68], and the visual cortex [69], which sometimes allow to assess some communication capacities (e.g. [67,70]). Such approaches have also been implemented at the patient's bedside using electroencephalography (EEG) [71] and electromyography [72].

It is worth noting that negative results should not be taken as proof of unconsciousness [73]. There are many factor that can lead to a false negative, either technical (movement or other artefacts) or patient-related (arousal fluctuations) issues [74]. Moreover, these tasks need preserved cognitive capacity (i.e. auditory, language, memory functions need to be spared). Positive results on the other hand are a straightforward indication of consciousness, since these modulations of brain activity are volitional and are answers to commands given to the patient.

A combination of all these neuroimaging tools might be used to better explore consciousness and to study patients with DOC. In a recent study, Bruno and colleagues combined DTI with PET (using [^{18}F]-2-fluoro-2-deoxy-D-glucose (FDG)) and fMRI to study two cases of chronic DOC. Both patients showed functional impairment in the left hemisphere while the right hemisphere was preserved and this was correlated with DTI findings of low interhemispheric connectivity [75].

Perturbational approach using transcranial magnetic stimulation and electroencephalography

While active paradigms can offer strong pieces of evidence of consciousness, they require the subject to be in a scanner for a while, and to record brain responses for several seconds in order to be interpretable. Compared with MRI and PET techniques, EEG has the ability to study brain activity on a time scale of milliseconds, but lacks spatial resolution, as it can only give data on the most superficial neurons. Transcranial magnetic stimulation (TMS) can induce a focal neuronal discharge at the cortex surface. By combining TMS with high-density EEG at the bedside of the patient, one

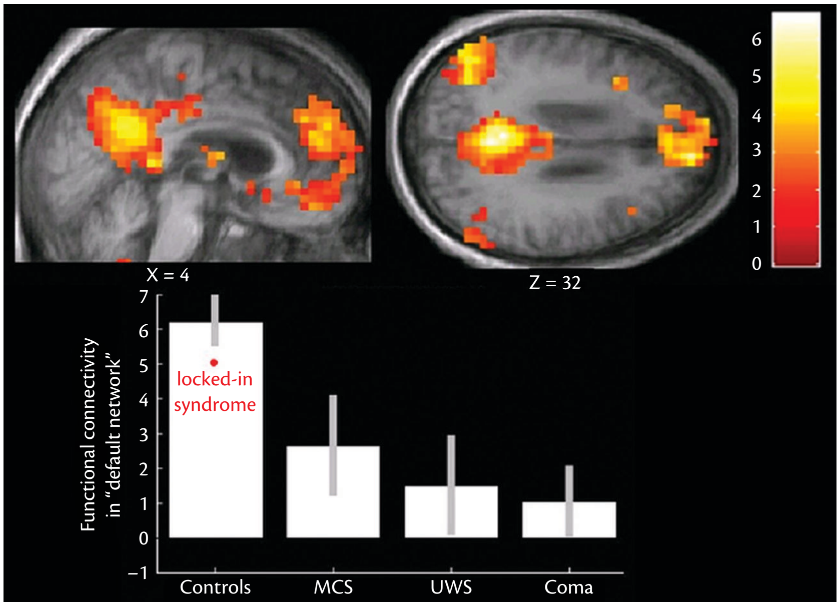

Fig. 28.5 The default-mode network's functional connectivity assessed with fMRI. This internal network involves midlines cortices (i.e. anterior cingulate/mesofrontal and posterior cingulate/precuneus) and is correlated with the level of consciousness.

UWS, unresponsive wakefulness syndrome; MCS, minimally conscious state.

Reproduced from Vanhaudenhuyse A, Noirhomme Q, Tshibanda LJ, et al. (2010). Default network connectivity reflects the level of consciousness in non-communicative brain damaged patients. *Brain*, **133**(1), 161–171. Copyright (2010), with permission from Oxford University Press.

can introduce a perturbation in the neuronal state of the brain and record its electrical response, both locally and at a distance. Thus, TMS/high-density EEG can study effective connectivity, which represents the direct connection between the initial perturbed area and those responding remotely, connections that must be supported both anatomically and functionally [76]. Using advanced analysis, it is possible to detect the effect of an initial stimulation on the rest of the brain both in space and time (Fig. 28.8).

Recent studies in sleep [77], anaesthesia [78], and patients with DOC [79] showed two categories of neuronal responses: healthy volunteers, MCS and people in the paradoxical stage of sleep all show rapid complex differentiated and distributed responses after TMS stimulations, while in unconscious volunteers and patients in UWS TMS triggers only simple stereotyped and local responses. This was interpreted as a variation of effective connectivity that correlates with the level of consciousness. Importantly, it was shown that effective connectivity recovers when the level of consciousness

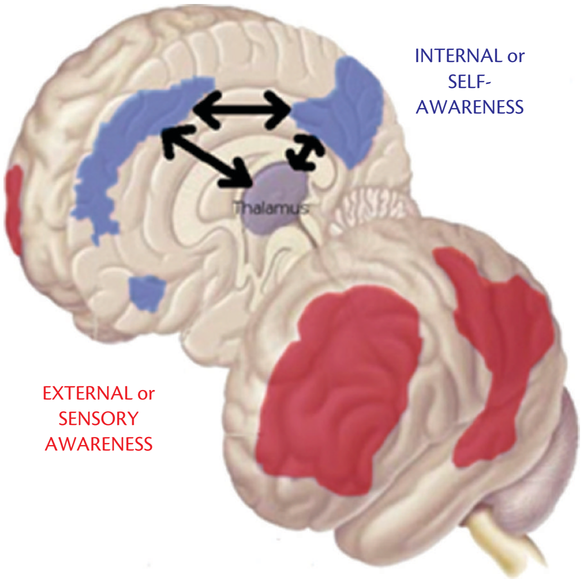

Fig. 28.6 Two networks for awareness—internal or self-awareness, and external or sensory awareness. Internal network encompasses midline structures whereas external network comprises lateral areas of the frontoparietal network and its connections with the thalamus.

Reproduced from Laureys S. (2007). Eyes open, brain shut: the vegetative state. *Scientific American*, **296**(5), 84–9. Copyright (2007), with permission from Scientific American.

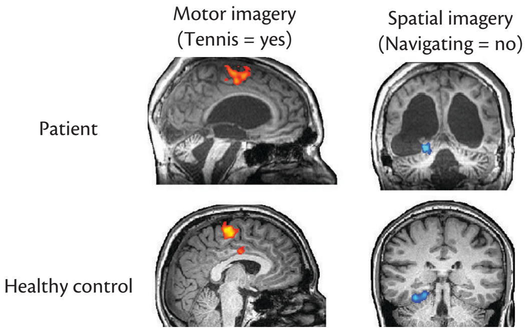
Motor imagery (Tennis = yes)
Spatial imagery (Navigating = no)
Patient
Healthy control

Fig. 28.7 Communication with a MCS patient using fMRI. The observed activity patterns in this patient were very similar to that observed in healthy controls when imaging playing tennis (i.e. activity in the supplementary motor area in orange) and when imaging walking into his house (i.e. activity in parahippocampal cortices in blue), which here indicates a 'yes' and a 'no' response, respectively.

Reproduced from Monti MM, Vanhaudenhuyse A, Coleman MR, et al. (2010). Wilful modulation of brain activity in disorders of consciousness, p. *New England Journal of Medicine*, **362**, 579–89. Copyright (2010), with permission from Massachusetts Medical Society.

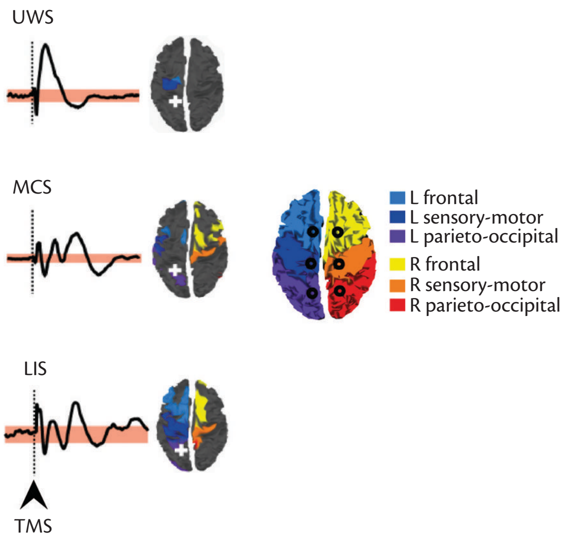

Fig. 28.8 Source mapping in TMS-EEG. This figure illustrates the neuronal responses to a transcranial magnetic stimulation targeting the white cross. The graph on the left side illustrates the time dispersion of the local response, while the brain template on the right side illustrates the spatial dispersion of the neuronal response. While the response is limited, both in time and space, in the UWS, patients in a MCS and in locked-in syndrome show time and spatial dispersion of the cortical response. This pattern is similar to those seen in healthy controls. Colours correspond to the localization of the brain activity (L: left; R: right).

TMS, transcranial magnetic stimulation; UWS, unresponsive wakefulness syndrome; MCS, minimally conscious state; LIS: locked-in syndrome.

Reproduced from Rosanova M, Gosseries O, Casarotto S, et al. (2012). Recovery of cortical effective connectivity and recovery of consciousness in vegetative patients. *Brain*, **135**, 1308–20. Copyright (2012), with permission from Oxford University Press.

improves in DOC patients [79]. Recently, the perturbational complexity index (PCI) has been calculated from the TMS/EEG signal. This quantification measure showed to be a reliable index of the level of consciousness across various states, including DOC, sleep and general anaesthesia [80]. Clearly, such an approach is appealing to study consciousness, as it does not require any participation from the patient, no motor output and no language processing to assimilate commands.

Conclusion

To summarize, the last decade left us with a better understanding of consciousness neural correlates. These advancements have a major clinical impact on patients' diagnosis, care, and prognosis. In fact, due to the challenge in attributing the right level of consciousness in non-communicative, severely brain-damaged people, neuroimaging techniques offer an objective and complementary approach. Similarly, the fact that a minority of patients who are behaviourally diagnosed as 'unresponsive' can show brain activations that are similar to those seen in conscious healthy controls is highlighted. As a consequence, the neuroimaging techniques may allow locked-in syndrome or non-communicative patients in a MCS to express their consciousness (e.g. [81]). Why these patients show this pattern of brain activity and how clinicians should be dealing with it should be the focus of future studies. Indeed, these techniques and paradigms still need to be validated in larger samples, especially in the acute phase to track patient's evolution and provide prognosis clues for clinicians and families. Moreover, multicentre studies must be conducted in order to address the sensitivity and specificity of the neuroimaging or electrophysiological tools. This seems also essential to gather comparable data about the potential prognostic value of each of the techniques discussed [56,82]. On an ethical note, these findings must be taken into account for patients' future care needs and to promote adequate policies to keep up with the scientific advancement. In fact, consciousness research leads to the redefinition of recovery, clinical criteria for diagnosis, and has an increasing impact on prognosis [83,84].

Acknowledgement

This work was supported by the Belgian National Funds for Scientific Research (FNRS), Fonds Léon Frédericq, Belgian American Education Foundation, Wallonie-Bruxelles International, James S. McDonnell Foundation, Mind Science Foundation, European Commission (Mindbridge, DISCOS, DECODER & COST), Concerted Research Action (ARC 06/11-340), Public Utility Foundation 'Université Européenne du Travail', 'Fondazione Europea di Ricerca Biomedica' and the University of Liège.

References

1. Majerus S, Bruno MA, Schnakers C, et al. (2009). The problem of aphasia in the assessment of consciousness in brain-damaged patients. *Progress in Brain Research*, **177**,49–61.
2. Schnakers C, Vanhaudenhuyse A, Giacino J, et al. (2009). Diagnostic accuracy of the vegetative and minimally conscious state: clinical consensus versus standardized neurobehavioral assessment. *BMC Neurology*, **9**, 35.
3. Laureys S. (2005). The neural correlate of (un)awareness: lessons from the vegetative state. *Trends in Cognitive Science*, **9**(12), 556–9.
4. Plum F, and Posner JB. (1972). The diagnosis of stupor and coma. *Contemporary Neurology Series*, **10**, 1–286.
5. The Multi-Society Task Force on PVS (1994). Medical aspects of the persistent vegetative state (1). The Multi-Society Task Force on PVS. *New England Journal of Medicine*, **330**(21), 1499–508.
6. Laureys S, Celesia GG, Cohadon F, *et al.* (2010). Unresponsive wakefulness syndrome: a new name for the vegetative state or apallic syndrome. *BMC Medicine*, **8**, 68.
7. Gosseries O, Bruno MA, Chatelle C, *et al.* (2011). Disorders of consciousness: what's in a name? *NeuroRehabilitation*, **28**(1), 3–14.
8. Giacino JT, Ashwal S, Childs N, *et al.* (2002). The minimally conscious state: definition and diagnostic criteria. *Neurology*, **58**(3), 349–53.
9. Bruno MA, Vanhaudenhuyse A, Thibaut A, et al. (2011). From unresponsive wakefulness to minimally conscious PLUS and functional locked-in syndromes: recent advances in our understanding of disorders of consciousness. *Journal of Neurology*, **258**(7), 1373–84.
10. Giacino JT, Kalmar K, and Whyte J. (2004). The JFK Coma Recovery Scale-Revised: measurement characteristics and diagnostic utility. *Archives of Physical Medicine and Rehabilitation*, **85**(12), 2020–9.
11. Seel RT, Sherer M, Whyte J, et al. (2010). Assessment scales for disorders of consciousness: evidence-based recommendations for clinical practice and research. *Archives of Physical Medicine and Rehabilitation*, **91**(12), 1795–813.
12. Vanhaudenhuyse A, Schnakers C, Bredart S, et al. (2008). Assessment of visual pursuit in post-comatose states: use a mirror. *Journal of Neurology, Neurosurgery & Psychiatry*, **79**(2), 223.
13. Bruno MA, Vanhaudenhuyse A, Schnakers C, et al. (2010). Visual fixation in the vegetative state: an observational case series PET study. *BMC Neurology*, **10**, 35.
14. Demertzi A, Ledoux D, Bruno MA, *et al.* (2011). Attitudes towards end-of-life issues in disorders of consciousness: a European survey. *Journal of Neurology*, **258**(6), 1058–65.

15. Demertzi A, Schnakers C, Ledoux D, *et al.* (2009). Different beliefs about pain perception in the vegetative and minimally conscious states: a European survey of medical and paramedical professionals. *Progress in Brain Research*, **177**, 329–38.
16. Whyte J, Gosseries O, Chervoneva I, *et al.* (2009). Predictors of short-term outcome in brain-injured patients with disorders of consciousness. *Progress in Brain Research*, **177**, 63–72.
17. Noe E, Olaya J, Navarro MD, et al. (2012). Behavioral recovery in disorders of consciousness: a prospective study with the Spanish version of the Coma Recovery Scale-Revised. *Archives of Physical Medicine and Rehabilitation*, **93**(3), 428–33 e12.
18. Hirschberg R, and Giacino JT. (2011). The vegetative and minimally conscious states: diagnosis, prognosis and treatment. *Neurology Clinics*, **29**(4), 773–86.
19. Ledoux D, Bruno M, Schnakers C, *et al.* (2008). Outcome prediction in brain-injured patients. In: *Eighteenth Meeting of the European Neurological Society*, Nice, France, 7–11 June, 2008**255**(2), 24.
20. Kampfl A, Schmutzhard E, Franz G, et al. (1998). Prediction of recovery from post-traumatic vegetative state with cerebral magnetic-resonance imaging. *Lancet*, **351**(9118), 1763–7.
21. Karantanas A, and Paterakis K. (2000). Magnetic resonance imaging and brainstem injury. *Journal of Neurosurgery*, **92**(5), 896–7.
22. Yanagawa Y, Tsushima Y, Tokumaru A, *et al.* (2000). A quantitative analysis of head injury using T2*-weighted gradient-echo imaging. *Journal of Trauma*, **49**(2), 272–7.
23. Galanaud D, Naccache L, and Puybasset L. (2007). Exploring impaired consciousness: the MRI approach. *Current Opinions in Neurology*, **20**(6), 627–31.
24. Tshibanda L, Vanhaudenhuyse A, Boly M, et al. (2010). Neuroimaging after coma. *Neuroradiology*, **52**(1), 15–24.
25. Tshibanda L, Vanhaudenhuyse A, Galanaud D, et al. (2009). Magnetic resonance spectroscopy and diffusion tensor imaging in coma survivors: promises and pitfalls. *Progress in Brain Research*, **177**, 215–29.
26. Fernandez-Espejo D, Bekinschtein T, Monti MM, et al. (2011). Diffusion weighted imaging distinguishes the vegetative state from the minimally conscious state. *NeuroImage*, **54**(1), 103–12.
27. Newcombe VF, Williams GB, Scoffings D, *et al.* (2010). Aetiological differences in neuroanatomy of the vegetative state: insights from diffusion tensor imaging and functional implications. *Journal of Neurology, Neurosurgery & Psychiatry*, **81**(5), 552–61.
28. Teasdale G, and Jennett B. (1974). Assessment of coma and impaired consciousness. A practical scale. *Lancet*, **2**(7872), 81–4.
29. Bamford JM, Sandercock PA, Warlow CP, et al. (1989). Interobserver agreement for the assessment of handicap in stroke patients. *Stroke*, **20**(6), 828.
30. Huisman TA, Schwamm LH, Schaefer PW, et al. (2004). Diffusion tensor imaging as potential biomarker of white matter injury in diffuse axonal injury. *AJNR American Journal of Neuroradiology*, **25**(3), 370–6.
31. Voss HU, Uluc AM, Dyke JP, et al. (2006). Possible axonal regrowth in late recovery from the minimally conscious state. *Journal of Clinical Investigations*, **116**(7), 2005–11.
32. Tommasino C, Grana C, Lucignani G, et al. (1995). Regional cerebral metabolism of glucose in comatose and vegetative state patients. *Journal of Neurosurgical Anesthesiology*, **7**(2), 109–16.
33. Rudolf J, Ghaemi M, Haupt WF, et al. (1999). Cerebral glucose metabolism in acute and persistent vegetative state. *Journal of Neurosurgical Anesthesiology*, **11**(1), 17–24.
34. Beuthien-Baumann B, Handrick W, Schmidt T, *et al.* (2003). Persistent vegetative state: evaluation of brain metabolism and brain perfusion with PET and SPECT. *Nuclear Medicine Communications*, **24**(6), 643–9.
35. Laureys S, Owen AM, and Schiff ND. (2004). Brain function in coma, vegetative state, and related disorders. *Lancet Neurology*, **3**(9), 537–46.
36. Laureys S, Goldman S, Phillips C, et al. (1999). Impaired effective cortical connectivity in vegetative state: preliminary investigation using PET. *NeuroImage*, **9**(4), 377–82.
37. Nakayama N, Okumura A, Shinoda J, et al. (2006). Relationship between regional cerebral metabolism and consciousness disturbance in traumatic diffuse brain injury without large focal lesions: an FDG-PET study with statistical parametric mapping analysis. *Journal of Neurology, Neurosurgery & Psychiatry*, **77**(7), 856–62.
38. Silva S, Alacoque X, Fourcade O, et al. (2010). Wakefulness and loss of awareness: brain and brainstem interaction in the vegetative state. *Neurology*, **74**(4), 313–20.
39. Lull N, Noe E, Lull JJ, et al. (2010). Voxel-based statistical analysis of thalamic glucose metabolism in traumatic brain injury: relationship with consciousness and cognition. *Brain Injury*, **24**(9), 1098–107.
40. Laureys S, Faymonville ME, Luxen A, et al. (2000). Restoration of thalamocortical connectivity after recovery from persistent vegetative state. *Lancet*, **355**(9217), 1790–1.
41. Thibaut A, Bruno MA, Chatelle C, et al. (2012). Metabolic activity in external and internal awareness networks in severely brain-damaged patients. *Journal of Rehabilitation Medicine*, **44**(5), 487–94.
42. Stender J, Gosseries O, Bruno MA, et al. (2014). Diagnostic precision of PET imaging and functional MRI in disorders of consciousness: a clinical validation study. *Lancet*, **384**(9942), 514–22.
43. Schiff ND, Giacino JT, Kalmar K, et al. (2007). Behavioural improvements with thalamic stimulation after severe traumatic brain injury. *Nature*, **448**(7153), 600–3.
44. Phillips CL, Bruno MA, Maquet P, et al. (2011). 'Relevance vector machine' consciousness classifier applied to cerebral metabolism of vegetative and locked-in patients. *NeuroImage*, **56**(2), 797–808.
45. Heine L, Soddu A, Gomez F, *et al.* (2012). Resting state networks and consciousness: alterations of multiple resting state network connectivity in physiological, pharmacological, and pathological consciousness States. *Frontiers in Psychology*, **3**, 295.
46. Vanhaudenhuyse A, Noirhomme Q, Tshibanda LJ, et al. (2010). Default network connectivity reflects the level of consciousness in non-communicative brain-damaged patients. *Brain: a Journal of Neurology*, **133**(Pt 1), 161–71.
47. Boly M, Tshibanda L, Vanhaudenhuyse A, et al. (2009). Functional connectivity in the default network during resting state is preserved in a vegetative but not in a brain dead patient. *Human Brain Mapping*, **30**(8), 2393–400.
48. Norton L, Hutchison RM, Young GB, et al. (2012). Disruptions of functional connectivity in the default mode network of comatose patients. *Neurology*, **78**(3), 175–81.
49. Vanhaudenhuyse A, Demertzi A, Schabus M, *et al.* (2011). Two distinct neuronal networks mediate the awareness of environment and of self. *Journal of Cognitive Neuroscience*, **23**(3), 570–8.
50. Soddu A, Boly M, Nir Y, et al. (2009). Reaching across the abyss: recent advances in functional magnetic resonance imaging and their potential relevance to disorders of consciousness. *Progress in Brain Research*, **177**, 261–74.
51. Baars BJ, Ramsoy TZ, and Laureys S. (2003). Brain, conscious experience and the observing self. *Trends in Neuroscience*, **26**(12), 671–5.
52. Soddu A, Vanhaudenhuyse A, Bahri MA, et al. (2012). Identifying the default-mode component in spatial IC analyses of patients with disorders of consciousness. *Human Brain Mapping*, **33**(4), 778–96.
53. Boly M, Faymonville ME, Schnakers C, *et al.* (2008). Perception of pain in the minimally conscious state with PET activation: an observational study. *Lancet Neurology*, **7**(11), 1013–20.
54. Boly M, Faymonville ME, Peigneux P, et al. (2004). Auditory processing in severely brain injured patients: differences between the minimally conscious state and the persistent vegetative state. *Archives of Neurology*, **61**(2), 233–8.
55. Di HB, Yu SM, Weng XC, et al. (2007). Cerebral response to patient's own name in the vegetative and minimally conscious states. *Neurology*, **68**(12), 895–9.
56. Coleman MR, Davis MH, Rodd JM, et al. (2009). Towards the routine use of brain imaging to aid the clinical diagnosis of disorders of consciousness. *Brain: a Journal of Neurology*, **132**(Pt 9), 2541–52.
57. Schiff ND, Rodriguez-Moreno D, Kamal A, et al. (2005). fMRI reveals large-scale network activation in minimally conscious patients. *Neurology*, **64**(3), 514–23.

58. Laureys S, Faymonville ME, Peigneux P, et al. (2002). Cortical processing of noxious somatosensory stimuli in the persistent vegetative state. *NeuroImage*, **17**(2), 732–41.
59. Larriviere D, and Bonnie RJ. (2006). Terminating artificial nutrition and hydration in persistent vegetative state patients: current and proposed state laws. *Neurology*, **66**(11), 1624–8.
60. Owen AM, Coleman MR, Boly M, et al. (2006). Detecting awareness in the vegetative state. *Science*, **313**(5792), 1402.
61. Boly M, Coleman MR, Davis MH, *et al.* (2007). When thoughts become action: an fMRI paradigm to study volitional brain activity in non-communicative brain injured patients. *NeuroImage*, **36**(3), 979–92.
62. Monti MM, Vanhaudenhuyse A, Coleman MR, *et al.* (2010). Willful modulation of brain activity in disorders of consciousness. *New England Journal of Medicine*, **362**(7), 579–89.
63. Sorger B, Reithler J, Dahmen B, et al. (2012). A real-time fMRI-based spelling device immediately enabling robust motor-independent communication. *Current Biology*, **22**(14), 1333–8.
64. Chatelle C, Chennu S, Noirhomme Q, et al. (2012). Brain-computer interfacing in disorders of consciousness. *Brain Injury*, 26(12), 1510–22.
65. Rodriguez Moreno D, Schiff ND, Giacino J, et al. (2010). A network approach to assessing cognition in disorders of consciousness. *Neurology*, **75**(21), 1871–8.
66. Naci L, and Owen AM. (2013). Making every word count for nonresponsive patients. *Journal of the American Medical Association Neurology*, **70**, 1235–41.
67. Bardin JC, Schiff ND, and Voss HU. (2012). Pattern classification of volitional functional magnetic resonance imaging responses in patients with severe brain injury. *Archives of Neurology*, **69**(2), 176–81.
68. Bekinschtein TA, Manes FF, Villarreal M, et al. (2011). Functional imaging reveals movement preparatory activity in the vegetative state. *Frontiers in Human Neuroscience*, **5**, 5.
69. Monti MM, Pickard JD, and Owen AM (2012). Visual cognition in disorders of consciousness: From V1 to top-down attention. *Human Brain Mapping*, **34**(6), 1245–53.
70. Liang X, Kuhlmann L, Johnston LA, et al. (2012). Extending communication for patients with disorders of consciousness. *Journal of Neuroimaging*, **24**(1), 31–8.
71. Schnakers C, Perrin F, Schabus M, et al. (2008). Voluntary brain processing in disorders of consciousness. *Neurology*, **71**(20), 1614–20.
72. Bekinschtein TA, Coleman MR, Niklison J, 3rd, et al. (2008). Can electromyography objectively detect voluntary movement in disorders of consciousness? *Journal of Neurology, Neurosurgery & Psychiatry*, **79**(7), 826–8.
73. Bardin JC, Fins JJ, Katz DI, et al. (2011). Dissociations between behavioural and functional magnetic resonance imaging-based evaluations of cognitive function after brain injury. *Brain: a Journal of Neurology*, **134**(Pt 3), 769–82.
74. Soddu A, Vanhaudenhuyse A, Demertzi A, et al. (2011). Resting state activity in patients with disorders of consciousness. *Functional Neurology*, **26**(1), 37–43.
75. Bruno MA, Fernandez-Espejo D, Lehembre R, et al. (2011). Multimodal neuroimaging in patients with disorders of consciousness showing 'functional hemispherectomy'. *Progress in Brain Research*, **193**, 323–33.
76. Friston K. (2002). Beyond phrenology: what can neuroimaging tell us about distributed circuitry? *Annual Reviews in Neuroscience*, **25**, 221–50.
77. Massimini M, Ferrarelli F, Huber R, et al. (2005). Breakdown of cortical effective connectivity during sleep. *Science*, **309**(5744), 2228–32.
78. Ferrarelli F, Massimini M, Sarasso S, et al. (2010). Breakdown in cortical effective connectivity during midazolam-induced loss of consciousness. *Proceedings of the National Academy of Sciences, USA*, **107**(6), 2681–6.
79. Rosanova M, Gosseries O, Casarotto S, et al. (2012). Recovery of cortical effective connectivity and recovery of consciousness in vegetative patients. *Brain: a Journal of Neurology*, **135**(Pt 4), 1308–20.
80. Casali AG, Gosseries O, Rosanova M, et al. (2013). A theoretically based index of consciousness independent of sensory processing and behavior. *Science Translational Medicine*, **5**(198), 198ra105.
81. Gosseries O, Bruno M-Al, Vanhaudenhuyse A, et al. (2009). Consciousness in the locked-in syndrome. In: Steven L, Giulio T (eds), *The Neurology of Consciousness*, pp. 191–203. San Diego: Academic Press.
82. Di H, Boly M, Weng X, Ledoux D, et al. (2008). Neuroimaging activation studies in the vegetative state: predictors of recovery? *Clinical Medicine*, **8**(5), 502–7.
83. Fins JJ. (2009). Being conscious of their burden: severe brain injury and the two cultures challenge. *Annals of the New York Academy of Sciences*, 1157, 131–47.
84. Fins JJ. (2009). The ethics of measuring and modulating consciousness: the imperative of minding time. *Progress in Brain Research*, **177**, 371–82.

CHAPTER 29

Congenital malformations of the brain and skull

Sara Nuñez, Sonia Bermudez, Mónica C. Vargas,
Andrés Puerta, and María T. Mantilla

Introduction

The pathogenesis of the congenital malformations, in some cases, is not clearly understood, and definitions and limits among different diseases are not apparent. Recent advances in neuroimaging had aid in new classifications. Considering the complexity of congenital abnormalities of the brain, this chapter reviews the subject, based on clinical approach, embryological development, developmental biology, neuroimaging, and molecular genetics. There are still several areas of poor knowledge and controversy. In some cases, the radiologist does not know the relevant data from the medical chart, such as the prenatal or family history among others, that lead him to a diagnosis based only on the imaging findings. A classification system cannot be made based on neuroimaging criteria only.

Embryology of the brain stem and cerebellum

By 24–27 days gestational age, the neural tube divides into three primary brain vesicles—the prosencephalon, mesencephalon, and rhombencephalon; this early differentiation of the neural tube is called patterning [1,2]. The metencephalon and the myelencephalon stem from the rhombencephalon. The metencephalon derives into the protuberance and the cerebellum. The myelencephalon develops into the medulla oblonga. The alar plate hypertrophies at its medial aspect and creates the rhombic lips at 5 weeks´ of gestation. The neuroepithelial zones, in the roof of the fourth ventricle and the rhombic lips, are the locations of the germinal matrices. The cerebellar primordium or tuberculum cerebelli come from the fusion of the rhombic lips at the midline, above the roof of the fourth ventricle and covers the most rostral portion of the roof of a prominent IV ventricle. The fusion continues in a caudal and mediolateral direction, and creates the rest of the cerebellum and the vermis by 15 weeks´ gestational age. The plica choroidea invaginates into the lumen of the fourth ventricle and forms a rudimentary choroid plexus that divides the rhombencephalic roof into two membranes: the area membranacea superior (AMS) and the area membranacea inferior (AMI). Active multiplication continues at the cerebelar cortex and generates the fastigium in the roof of the fourth ventricle, anterior to the cerebellum. The superior subdivision, limited on its inferior aspect by the plica choroidea, thickens in the craniocaudal direction, and forms the vermis. Intense neuroblastic activity during the third month produces extraventricular prominence of the cerebellum that starts to subdivide. The inferior area membranacea, an ependymal membrane, expands posteriorly to form a recess (Blake´s pouch), which then disappears, leaving a median aperture (Blake´s pouch metapore), precursor of the foramen of Magendie of around 8 weeks´ gestational age. Disorders in this process result in cysts of the posterior fossa.

Cerebellar malformations

Various classifications and descriptions of posterior fossa malformations can be found in the medical literature [3–7]. It is difficult to know whether an abnormal cerebellum represents atrophy, hypoplasia, or malformation. Although a classification based on images is practical, it has limitations. Truly developmental malformations are sometimes placed in the same category as disruptions. An integrated classification of such malformations based on morphologic appearance, embryology, and molecular neurogenetics will be helpful. [2, 4–6]. There are also some useful MRI criteria that can be used for the evaluation of the posterior fossa malformations:

1. *Vermis and cerebellar hemisphere anomaly:* focal or generalized.
2. *Vermis and cerebellar folial pattern:* normal or abnormal.
3. *Fastigial point:* normal or abnormal.
4. *Craniocaudal vermian axis:* normal or rotated (Fig. 29.1).
5. *Ratio anterior/posterior vermian lobes* (47%/53%).
6. Vermis and cerebellar hemispheres characteristics: dysplastic, hypoplastic, or absent.
7. *Brainstem development:* normal, hypoplastic, or dysplastic.
8. *Posterior fossa cerebrospinal fluid (CSF) collection*: present or absent.
9. *Size of the posterior fossa:* reduced, normal, or increased.
10. *Mass effect:* present or absent.

Cerebellar hypoplasia

Cerebellar hypoplasia is usually asymmetric, implying a small cerebellum with normal-size fissures compared with the folia, and is a disorder of formation with early termination of cellular production

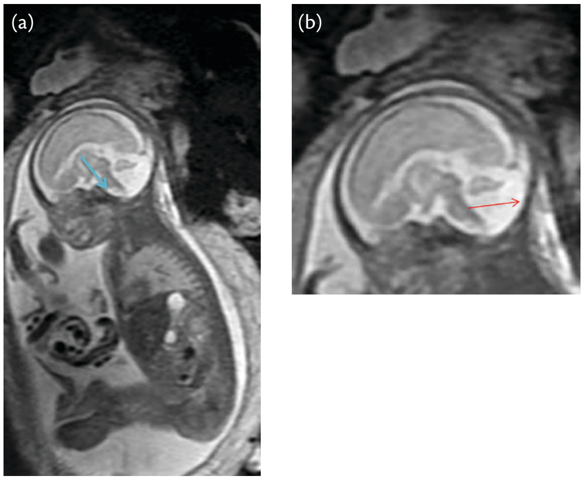

Fig. 29.1 Abnormally upward rotated craniocaudal vermian axis. Sagittal single shot fast spin echo (SSFSE) T_2-weighted foetal image. The normal axis should be parallel to the brainstem (blue arrow) in (a). The abnormal upward cerebellar axis (red arrow) is shown in (b).

Reproduced from Nuñez S, Mantilla MT, Sonia Bermúdez S. (2011). Midline congenital malformations of the brain and skull. *Neuroimaging Clinics of North America*, **21**(3), 429–482. Copyright (2011), with permission from Elsevier.

and migration (incomplete formation). It can be seen in heterogeneous conditions, both malformations and disruptions [8]. It may be the consequence of a variety of causes, such as prenatal vascular injury, prenatal infections (cytomegalovirus), prenatal exposure to teratogens, chromosomal aberrations, metabolic disorders, isolated (genetic) cerebellar hypoplasias, complex (genetic) malformations, (genetic) migration disorders, some types of congenital muscular dystrophies, and pontocerebellar hypoplasias.

Cystic malformations of the posterior fossa

Cystic malformations of the posterior fossa overlap clinically, radiologically, and pathologically. There is no consensus on the criteria for their diagnosis. Differential diagnosis may be difficult or even impossible.

Dandy–Walker continuum or Dandy–Walker complex

Classic Dandy–Walker Malformation

The cause of this anomaly is unknown, and heterogeneous. There are some predisposing factors such as gestational exposure to rubella, cytomegalovirus, toxoplasmosis, coumadin, and alcohol. Some authors reports normal intellectual development in approximately 50% to 75% of patients[3, 4]. If supratentorial anomalies are present the prognosis is less favourable. The classic triad includes:

1. Dysgenesis, complete or partial agenesis of the vermis,
2. Cystic dilatation of the fourth ventricle,
3. Enlarge posterior fossa with upward displacement of the vermis, venous sinuses, tentorium and torcula.

Hydrocephalus should be considered a complication and not a part of the malformation itself. Associated CNS anomalies are present in approximately 68% of the cases. The most common is dysgenesis of the corpus callosum. The patient usually presents with characteristic dolichocephaly, with a bulging occipital region and macrocrania. A dysplastic vermis is rotated posterosuperiorly. The cerebellar hemispheres are hypoplastic, asymmetric, or symmetric in size. The fax cerebelli is absent. (Fig. 29.2)

Cerebellar-vermian hypoplasia-dysplasia or Dandy–Walker variant

Cerebellar-vermian hypoplasia-dysplasia is more common than the classic Dandy–Walker malformation and represents approximately one-third of all posterior fossa malformations. This group is clinically and radiologically difficult to differentiate. Some authors believe that these conditions represent steps on a continuum of developmental anomalies. Barkovich et al. used the term Dandy–Walker complex and includes the classic Dandy–Walker malformation, Dandy–Walker variant, and mega cistern magna. Other authors suggest abandoning the term *Dandy–Walker variant* because in the majority of cases they do not believe it corresponds to the same spectrum of Dandy–Walker malformation. The posterior fossa is normal in size, with varying degrees of cerebellar-vermian hypoplasia-dysplasia (never agenesis), normal position of the vermis, or minimal upward rotation. There is also a prominent cerebrospinal fluid retrocerebellar space that communicates freely through a prominent vallecula with a normal or minimal dilated fourth ventricle, but not a cyst, the tentorium cerebelli has normal position (Fig. 29.3).

Associated supratentorial anomalies can also be found. The intrauterine noxa occurs in the same embryological period than the classic form. Ventriculomegaly with secondary macrocrania is present approximately in 32% of patients. Developmental delay is associated with the presence of supratentorial anomalies, mild ataxia could be present.

Mega cisterna magna

Anatomically the magna cistern occupies the vallecula cerebelli and extends inferiorly, the posterior limit is the arachnoid membrane extends from the upper cervical cord to the posteroinferior surface of the cerebellum. The arachnoid separates the cisterna magna from the supravermian cistern. There are no definitive measurements for its size. The mega cisterna magna is a common developmental variation of the posterior fossa and *does not necessarily indicate a malformation*, it is considered to be an inaccurate term by some authors. The posterior part of the cistern is divided by the falx cerebelli in 60% of cases. (Fig. 29.4).

This cystic collection can be very large and may extend beyond the normal anatomic limits or extend supratentorially with a high position of the tentorium, without compressive effects on the cerebellum. The cerebellar hemispheres and the vermis are always normal. Most cases are detected incidentally. However, some patients may present with hydrocephalus.

Blake's pouch cyst

This posterior fossa malformation is believed to derive from the persistence of the transient Blake pouch that arises from the inferior area membranacea, that normally regresses at 5 to 8 weeks gestational age. The cyst protrudes through either the Magendie or Luschka foramina. The diagnosis is made by histological examination, actually is not a diagnosis made by imaging methods.

Arachnoid cyst

The arachnoid cyst is derived from the meninx primitive, it is believed that the developing arachnoid membrane may split and

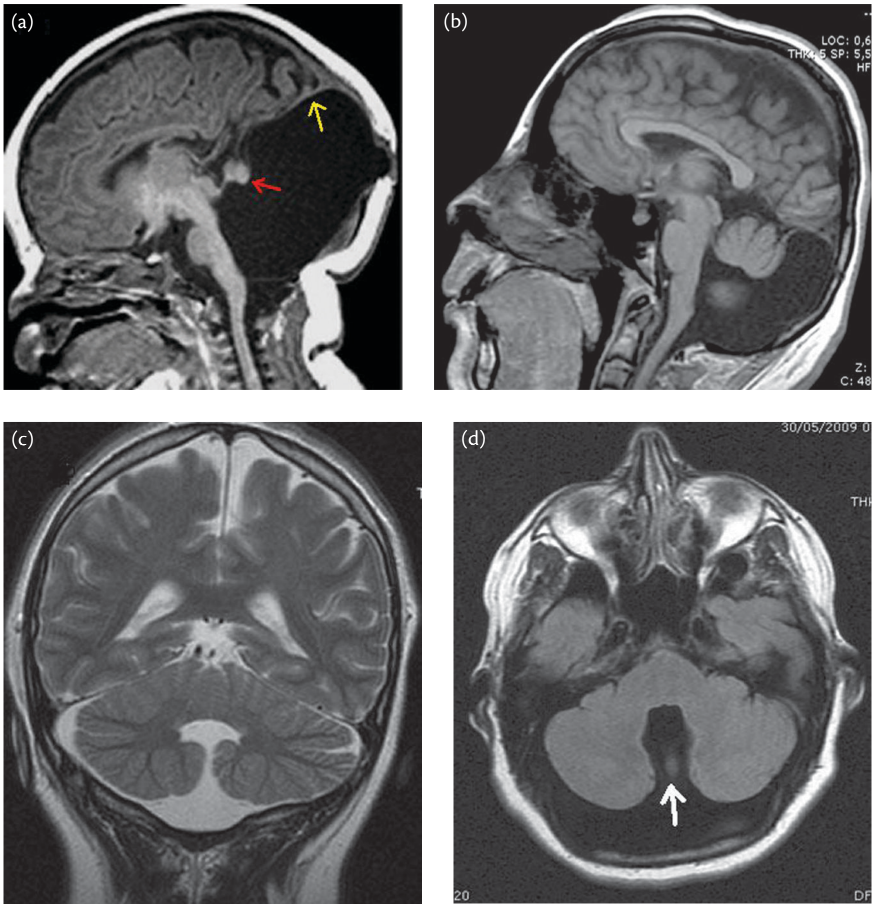

Fig. 29.2 (a) Classic Dandy–Walker malformation. Sagittal T_1-weighted image. Dysgenesis, severe hypoplasia and superior rotation of the vermis (red arrow) associated with a cystic dilatation of the 4th ventricle, enlarged posterior fossa with upward displacement of tentorium (yellow arrow). (b–d) Classic Dandy–Walker malformation in another patient with a milder variant in this continuum, less severe vermian/cerebellar hypoplasia with a dilated 4th ventricle (white arrow) are seen. (b) Sagittal T_1-weighted image. (c) Coronal T_2-weighted image. (d) axial FLAIR image.

Reproduced from Nuñez S, Mantilla MT, Sonia Bermúdez S. (2011). Midline congenital malformations of the brain and skull. *Neuroimaging Clinics of North America*, **21**(3), 429–482. Copyright (2011), with permission from Elsevier.

secrete fluid into the cleft with similar composition to CSF. It presents with an infratentorial location in 16–23% of the cases and a retrocerebellar location in 9–16% of them. May exert mass effect on adjacent brain or bone, sometimes with bone remodelling and the posterior fossa may present increase volume.

In many cases, imaging diagnosis of the posterior fossa cystic malformations is not possible [9] because infratentorial cysts may present a similar appearance, some publications propose using the term ‘retrocerebellar cyst or collection’ if the histology of the cyst wall is unknown. They consider ‘speculative terms’ should be avoided, like Dandy–Walker variation, mega cisterna magna or arachnoid cyst [10]. The diagnosis should be an opinion based on the patient’s medical picture. Patients with isolated hypoplasia of the vermis or cerebellar unilateral hypoplasia may present with normal intelligence, so as in mega cisterna magna, Blake’s pouch cyst, and congenital arachnoid cyst.

Brainstem anomalies

Pontine tegmental cap dysplasia

This is a severe and rare regional developmental defect, probably secondary to an abnormal axonal path. It is characterized by an hypoplastic flat ventral pons, as a consequence of the absence of normal ventral decussation of the middle cerebellar peduncles, a band of horizontally-orientated axons, with a vaulted dorsal pons that projects into the fourth ventricle, hypoplasia of the middle cerebellar peduncles, hypoplasia, and malformation of the vermis, short mesencephalic isthmus with molar tooth sign, with hypoplasia of the VII and VIII cranial nerves, and the internal auditory meati (Fig. 29.5).

Clinical findings may be motor and cognitive deficits, gaze abnormalities, hearing, loss, and seizures.

Cerebellar focal dysplasias

Rhombencephalosynapsis

This is a rare (0.13%), sporadic malformation that mainly affects the midline cerebellar structures. The diagnosis is confirm by MR images, there is absence or hypogenesis, dysgenesis of the vermis, especially in its anterior lobe, and fusion of the cerebellar hemispheres, as well as the dentate nuclei, the small superior cerebellar peduncles, middle peduncles, and tectum, a small brainstem and hypoplastic cerebellar hemispheres. Supratentorial anomalies seem to be responsible for neurologic and cognitive impairments,

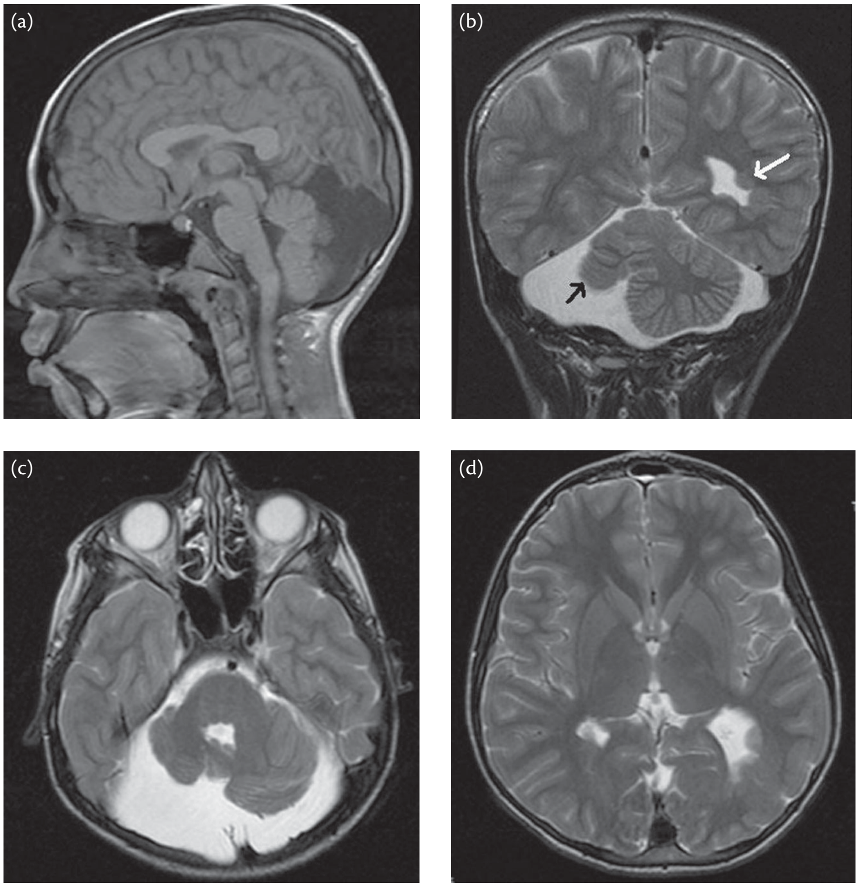

Fig. 29.3 Cerebellar-vermian hypoplasia-dysplasia (CVH). (a) Sagittal T_1-weighted image shows a posterior fossa normal in size, prominent CSF retrocerebellar space, normal position of the hypoplastic vermis relative to the brainstem, and normal position of the tentorium cerebelli. (b) Coronal T_2-weighted image shows asymmetric cerebellar hypoplasia (black arrow) and left nodular heterotopias (white arrow). (c–d) Axial T_2-weighted image, display a CVH (never agenesis). (d) Shows associated occipital nodular heterotopias.

Reproduced from Nuñez S, Mantilla MT, Sonia Bermúdez S. (2011). Midline congenital malformations of the brain and skull. *Neuroimaging Clinics of North America*, **21**(3), 429–482. Copyright (2011), with permission from Elsevier.

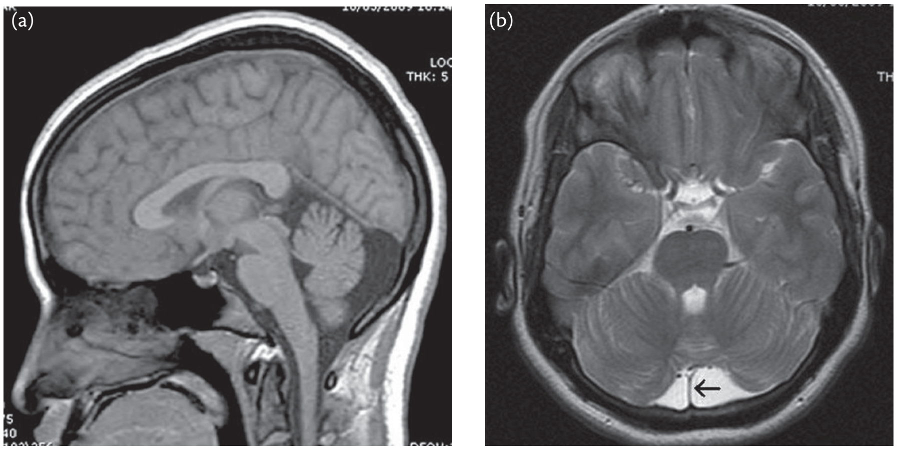

Fig. 29.4 Mega cisterna magna. (a) Sagittal T_1-weighted image showing retrocerebellar fluid collection that freely communicates with the subarachnoid space, normal vermis, no rotated craniocaudal vermian axis. (b) Axial T_2-weighted image shows normal cerebellar hemispheres and vermis with presence of the falx cerebelli (black arrow).

Reproduced from Nuñez S, Mantilla MT, Sonia Bermúdez S. (2011). Midline congenital malformations of the brain and skull. *Neuroimaging Clinics of North America*, **21**(3), 429–482. Copyright (2011), with permission from Elsevier.

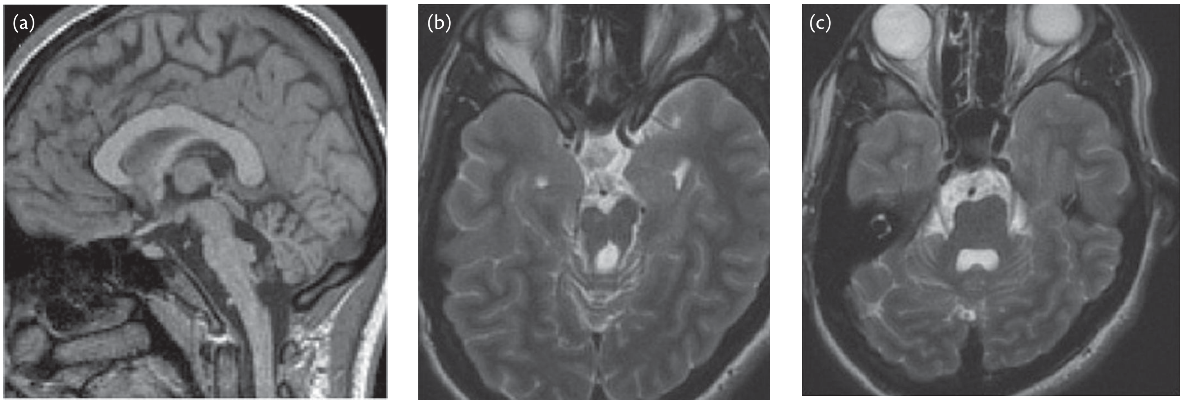

Fig. 29.5 Pontine tegmental cap dysplasia. (a) Sagittal T_1-weighted image. Hypoplastic brainstem with flattened ventral pons and dorsal tegmental cap (white arrow). Hypoplastic and dysplastic vermis with abnormal vermian foliation and fastigial point. (b,c) Axial T_2-weighted images. Hypoplastic pons, superior, and middle cerebellar peduncles with dysplastic vermis.

Reproduced from Nuñez S, Mantilla MT, Sonia Bermúdez S. (2011). Midline congenital malformations of the brain and skull. *Neuroimaging Clinics of North America*, **21**(3), 429–482. Copyright (2011), with permission from Elsevier.

associated supratentorial anomalies include the absence of the septum pellucidum, in almost 50% of the cases, ventriculomegaly or hydrocephalus, fused thalami and fornices, polymicrogyria and/or hypoplastic anterior commissure. Severely affected patients may present mental retardation, epilepsy, spasticity, and strabismus (Fig. 29.6).

Diffuse molar tooth dysplasias associated with defects in ciliary proteins, Joubert syndrome and related disorders/syndromes with molar tooth malformation

The Joubert Syndrome has evolved to a more complex entity that incorporates multiple syndromes with genetic heterogeneity. The last classification divided these malformation syndromes into four disorders:

1. Joubert syndrome.
2. COACH syndrome (cerebellar vermis hypoplasia, oligophrenia, ataxia, ocular coloboma, hepatic fibrosis).
3. CORS (cerebro-oculo-renal syndrome).
4. Oculo-facial-digital syndrome Type IV (OFD-IV syndrome) (11).

In all of these entities patients have hypotonia, ataxia, developmental delay (cognitive and motor), oculomotor apraxia, and in MR images the molar tooth sign. MRI diagnosis is made in the axial, sagittal, and coronal planes. The superior cerebellar peduncles are enlarged and follow a more horizontal course between the pons and the cerebellum, caused by lack of decussation of peduncular fibre tracts. A thin isthmic region is seen in the sagittal view. Severe

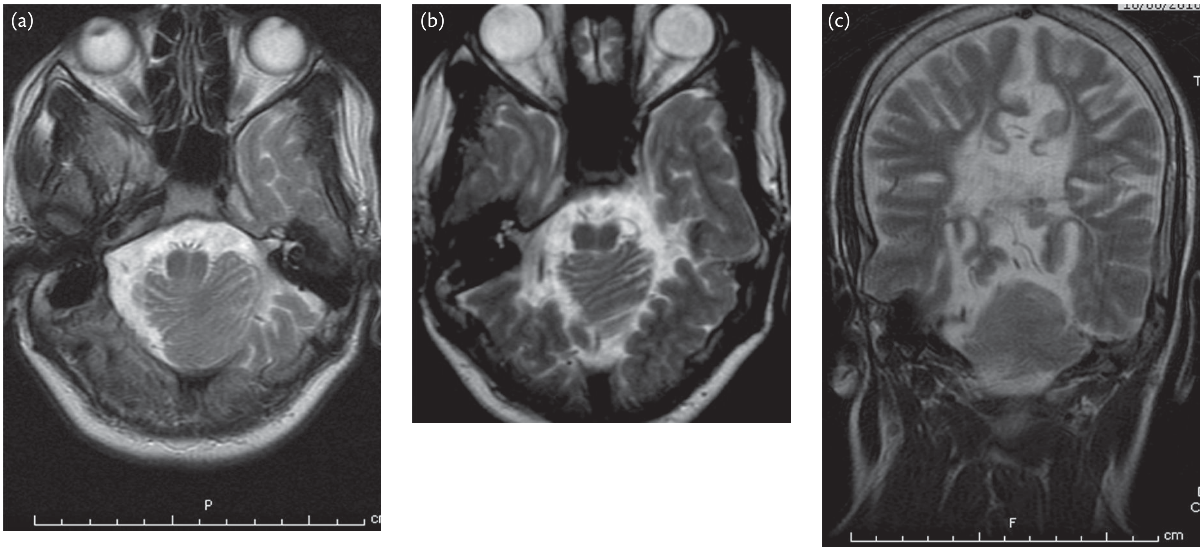

Fig. 29.6 Rhombencephalosynapsis, 13-year-old boy with mental retardation. (a,b) Axial T_2-weighted images. Fused and hypoplastic cerebellar hemispheres, absent vermis, hypoplastic pons with midline cleft. (c) Coronal T_2-weighted image. Fused and hypoplastic cerebellar hemispheres, absent vermis.

Reproduced from Nuñez S, Mantilla MT, Sonia Bermúdez S. (2011). Midline congenital malformations of the brain and skull. *Neuroimaging Clinics of North America*, **21**(3), 429–482. Copyright (2011), with permission from Elsevier.

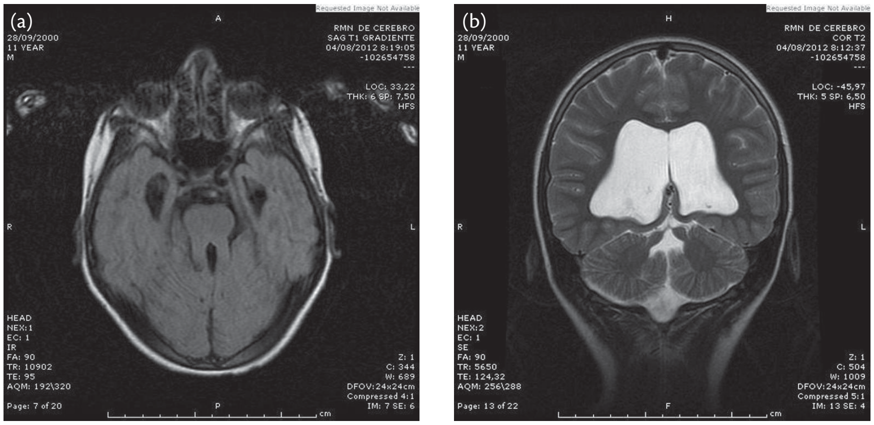

Fig. 29.7 Molar tooth malformation. (a) Axial FLAIR image. Enlarge horizontal superior cerebellar peduncles with molar tooth appearance at the level of midbrain. (b) Coronal T_2-weighted image. Enlarge superior cerebellar peduncles. Ventriculomegaly, enlarge fourth ventricle.

Reproduced from Nuñez S, Mantilla MT, Sonia Bermúdez S. (2011). Midline congenital malformations of the brain and skull. *Neuroimaging Clinics of North America*, **21**(3), 429–482. Copyright (2011), with permission from Elsevier.

hypoplasia of the brainstem and pontomesencephalic clefting may be present, as well as vermian agenesis. All these changes in the axial view produce the molar tooth appearance at the level of the midbrain, and an enlarged fourth ventricle with a bat wing or triangular configuration. Near total absence of pyramidal decussations with reduce volume of the cervicomedullary union are also seen. Supratentorial anomalies include PMG, unsegmented midbrain tectum and agenesis of the corpus callosum. Occasional features are seen in all forms are mental retardation, in infancy respiratory disturbances, episodes of hyperpnoea or apnoea, postaxial polydactyly, and mild retinopathy (Fig. 29.7).

Arnold Chiari malformations

Chiari type I malformation

A bony malformation that causes a small posterior fossa may be considered the primary abnormality (occipital dysplasia) and the neural malformation the secondary. A symmetrical or asymmetrical caudal extension of at least 3–5 mm of the cerebellar tonsils below the foramen magnum, is considered for the diagnosis, sometimes also descent of the inferior vermis can be seen. On sagittal T_1-weighted MR images, the McRae line through the foramen magnum is use to confirm the diagnosis, the coronal T_1- or T_2-weighted image also are used (Fig. 29.8).

The herniation correlates positively with the amount of occipital bone thickening. Chiari type I malformation may be associated with platybasia, occipito-atlantal assimilation, and Klippel–Feil syndrome, syringohidromyelia in 25–65%, and with hydrocephalus. There is a high incidence of complex craniosynostosis, skull base, and cervical spine anomalies [12–15].

Related signs and symptoms include chronic headache, neck pain, torticollis, lower cranial nerve palsies, nystagmus, ataxia, motor and sensory deficits, scoliosis, sleep-apnoeas, seizures, psychiatric complaints, and unexplained episodes of unconsciousness.

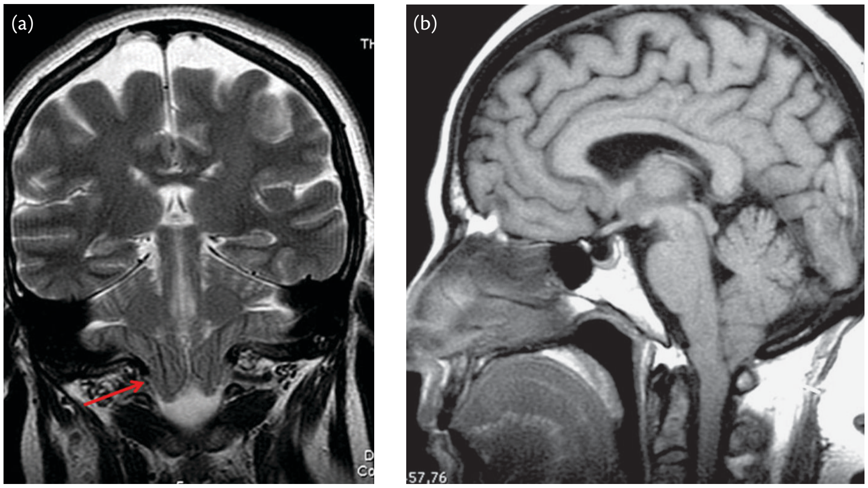

Fig. 29.8 Chiari type I malformation. (a) Coronal T_2-weighted image. (b) Sagittal T_1-weighted image. Inferior displacement of the cerebellar tonsils below the foramen magnum (red arrow in (a)). Flat and small posterior fossa (occipital dysplasia). No associated supratentorial anomalies.

Reproduced from Nuñez S, Mantilla MT, Sonia Bermúdez S. (2011). Midline congenital malformations of the brain and skull. *Neuroimaging Clinics of North America*, **21**(3), 429–482. Copyright (2011), with permission from Elsevier.

Chiari type II malformation

This is a complex malformation that involves the spinal cord and the hindbrain, all or nearly all cases present with myelomeningocele at birth [16]. There is herniation of the inferior vermis, medulla, pons, and fourth ventricle into the cervical or thoracic spinal canal with a small posterior fossa. The medulla buckles posterior to the cervical spinal cord in severe cases. The quadrigeminal plate has a typical beaked shape and the cerebellum can wrap itself around the brainstem. Primary causes of neural tube defects are variable and still debated. Intra-uterine hydrocephalus and hydromyelia leading to the herniation have also been proposed as abnormal traction by tethering of the distal spinal cord, primary hindbrain dysgenesis, or a primary mesodermal defect. Supratentorial brain abnormalities of the corpus callosum are present in 75–90% of cases, the splenium is nearly always hypoplastic or absent, and in severe cases there could be agenesis of the corpus callosum. Absence of the septum pellucidum could also be present. The abnormal gyral pattern in the posterior parietal and occipital regions is termed 'stenogyria', with multiple small gyri. Gyri interdigitation through fenestrations of the fax cerebri are also frequent. All these findings are not always present, but depend on the severity of the case (Fig. 29.9).

Chiari III malformation

This malformation includes both the herniation of the contents of the low occipital and upper cervical regions for diagnosis. The cephalocele sac variably includes the brainstem, occipital lobes, subarachnoid or ventricular CSF spaces, and the dural venous sinuses. Hypoplasia or agenesis of the corpus callosum, occipital and cervical osseous defects, dorsal clivus and petrous bones scalloping, as well as craniolacunia could be associated.

Progress in understanding embryology, developmental biology, and the creation of multidisciplinary expert groups with a clinical, neuroimaging, and molecular genetics approach, will make easier the classification of posterior fossa malformations.

Holoprosencephaly and associated variants

Holoprosencephaly is a complex developmental anomaly of the brain and skull, resulting from an injury to the CNS during

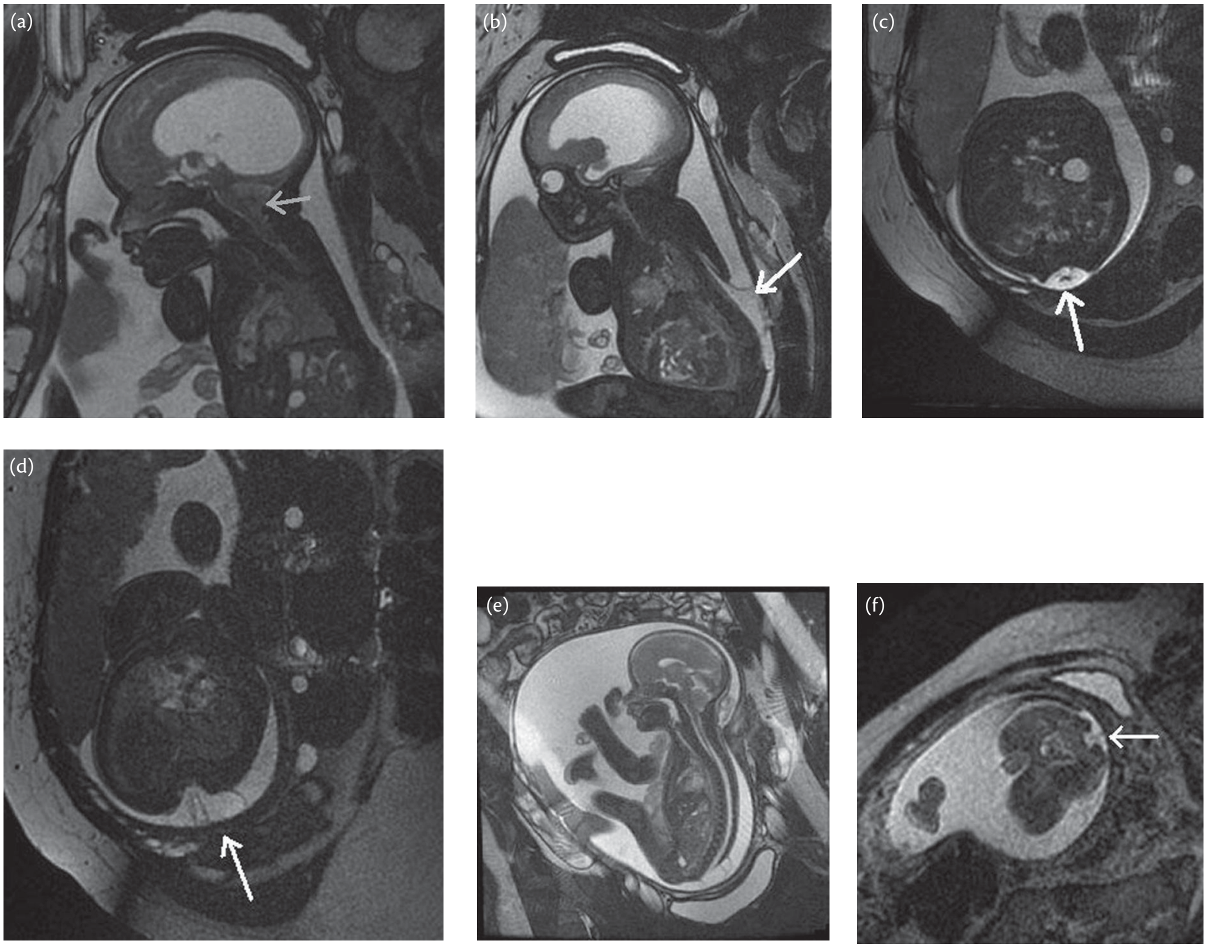

Fig. 29.9 Chiari type II malformation. Foetal MRI, 22 weeks. (a) Sagittal SSFSE T_2-weighted images showing the inferior displacement of the cerebellar tonsils and the inferior vermis bellow the foramen magnum, until the middle cervical spinal canal level (white arrow). Flat and small posterior fossa (occipital dysplasia) and hydrocephalus. Mielomeningocoele. Foetal MRI 22 weeks thoracolumbar level, (b) Sagittal SSFSE T_2-weighted image (white arrow). (c,d) Axial SSFSE T_2-weighted image (white arrow). Foetal MRI 21 weeks lumbosacral level. (e) Sagittal T_2. (f) Axial T_2 weighted image (white arrow).

Reproduced from Nuñez S, Mantilla MT, Sonia Bermúdez S. (2011). Midline congenital malformations of the brain and skull. *Neuroimaging Clinics of North America*, **21**(3), 429–482. Copyright (2011), with permission from Elsevier.

prosencephalic cleavage, in 4–6 weeks of gestation [17, 18]. It is characterized by hypoplasia of the rostral portions of the neural tube and absence of midline structures, in a spectrum ranging from septo-optic dysplasia to the most severe alobar holoprosencephaly.

Genetic anomalies have been demonstrated, being the most common mutation identified in the *SHH* (sonic hedgehog) gene at 7q36. Associations with early or advanced maternal age, eclampsia, exposure to metals, herbicides or pesticides, drug abuse, and radiation have been described. Main characteristics of this continuum are listed as follows:

Alobar holoprosencephaly (Fig. 29.10)

1. A rudimentary ventricle without septum pellucidum communicated with a large cyst located in the suprapineal recess[19].
2. Absence of the anterior falx cerebri, superior sagittal sinus, corpus callosum, third ventricle, and pituitary gland.
3. Hypoplasia and fusion of the frontal lobes.
4. Unique thalamus, basal nuclei, and hypothalamic fusion.
5. Olfactory and optic nerves could be absent.
6. Facial abnormalities are frequently associated (cyclopia, ethmocephaly)[19].

Semilobar holoprosencephaly

1. Rudimentary lateral ventricles with temporal horns.
2. Third ventricle partially formed, without roof.
3. Septum pellucidum absent.
4. Fusion of the frontal lobes cortex and hypothalamus.
5. Incomplete fusion of thalami and basal ganglia.
6. Interhemispheric fissure and falx cerebri developed posteriorly.
7. Posterior dysplastic corpus callosum.

Lobar holoprosencephaly

1. Better formed lateral ventricles. Frontal horns hypoplastic.
2. Septum pellucidum absent.
3. Frontal lobes may be partially fused or completely separated.
4. Absence of rostrum and genu of corpus callosum. Body extension is useful to differentiate from semilobar variant.
5. Basal ganglia and thalamus fusion mild or absent.
6. Normal or mild facial anomalies (mild hypotelorism) (Fig. 29.11).

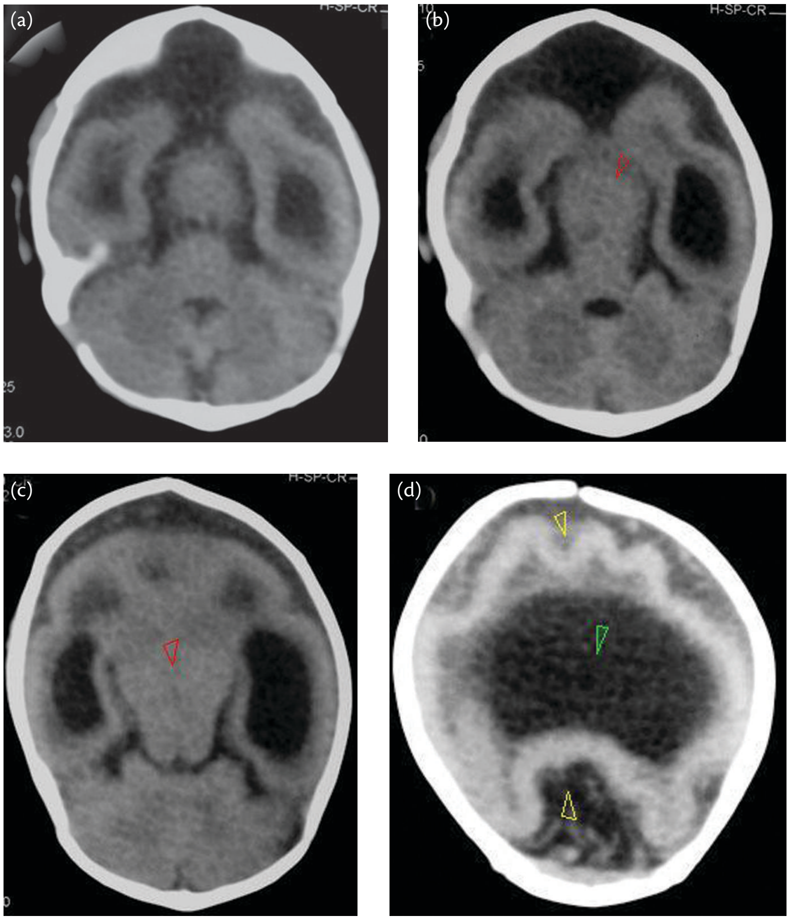

Fig. 29.10 Alobar holoprosencephaly. CT axial images in a 4-week-old baby boy. (a–c) Thalami and basal ganglia fusion (red arrowheads). (d) Monoventricle (green arrowhead), frontal lobe hypoplasia, cortical dysplasia and rudimentary anterior and posterior interhemispheric fissure (yellow arrowheads).

Reproduced from Nuñez S, Mantilla MT, Sonia Bermúdez S. (2011). Midline congenital malformations of the brain and skull. *Neuroimaging Clinics of North America*, **21**(3), 429–482. Copyright (2011), with permission from Elsevier.

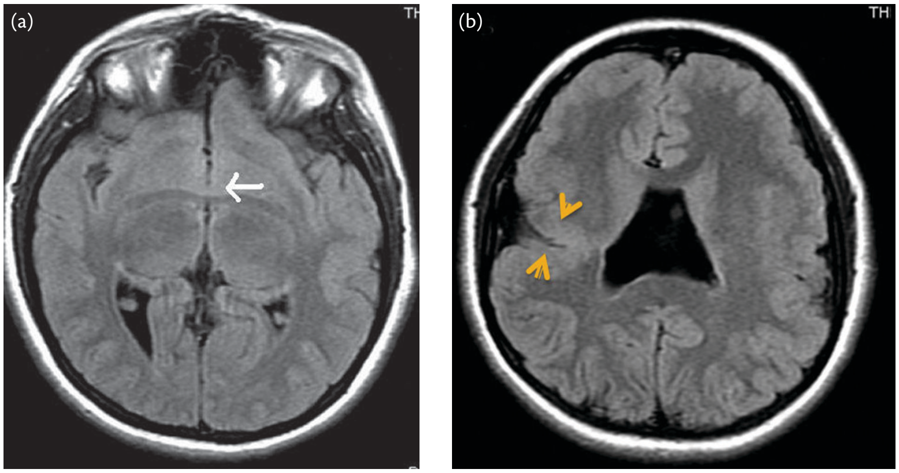

Fig. 29.11 Lobar holoprosencephaly, 16-year-old female. (a,b) MRI FLAIR axial images: (a) transversal band of frontal parenquima fusion, anterior to the anterior commissure (white arrow). (b) The absence of frontal horns of lateral ventricles and the frontal lobe cortical dysplasia with close lip schizencephaly (yellow arrows).

Reproduced from Nuñez S, Mantilla MT, Sonia Bermúdez S. (2011). Midline congenital malformations of the brain and skull. *Neuroimaging Clinics of North America*, **21**(3), 429–482. Copyright (2011), with permission from Elsevier.

Middle interhemispheric variant or syntelencephaly

1. Peri-Rolandic fusion of brain lobes.
2. Normal or hypoplastic frontal horns. Posterior monoventricle. Third ventricle formed.
3. Interhemispheric fusion of the Sylvian fissures.
4. Normal basal ganglia, thalamus variably fused, separated hypothalamus.
5. Septum pellucidum absent.
6. Cortical dysplasia and heterotopias frequently associated.
7. Low incidence of endocrine manifestations and hypothalamic dysfunction[20,21].

Septo-optic dysplasia

1. Septum pellucidum absent or incomplete.
2. Frontal horns anteriorly square shaped.
3. Optic nerves uni- or bilaterally absent or small.
4. Mild anterior dysgenesis of corpus callosum.
5. No fusion of midline structures [22] (Fig. 29.12).

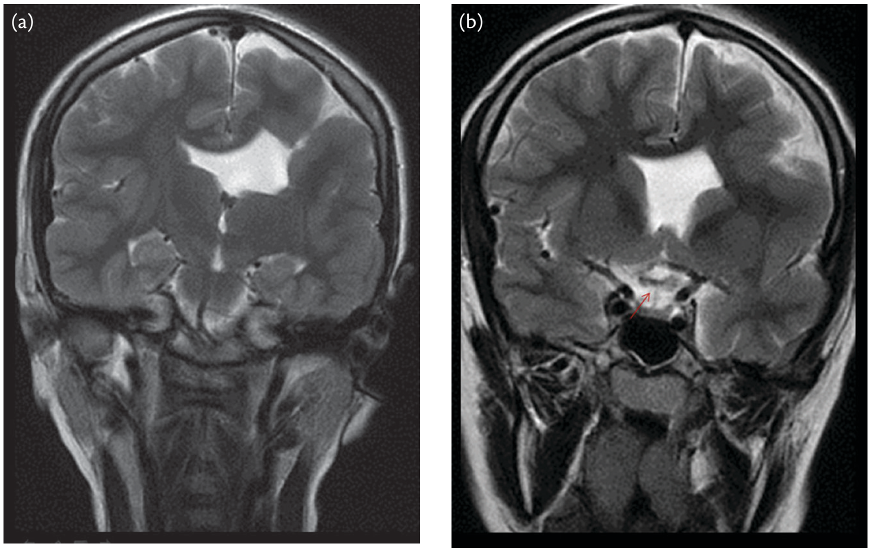

Fig. 29.12 Septo-optic dysplasia with close lip schizencephaly and dysplastic cortex. (a,b) MRI coronal T_2-weighted images—square, irregular and inferior pointed frontal horns, septum pellucidum absence and right optic nerve hypoplasia (red arrow) in (b).

Reproduced from Nuñez S, Mantilla MT, Sonia Bermúdez S. (2011). Midline congenital malformations of the brain and skull. *Neuroimaging Clinics of North America*, **21**(3), 429–482. Copyright (2011), with permission from Elsevier.

Neuronal migration and cortical organization disorders

Neuronal migration is a complex process that essentially allows migration of neuronal precursors from their site of origin at the periventricular germinative neuroepithelium to their final location at the cortical plate, which becomes, at the end of this process, the cerebral cortex [23]. This process must occur in a highly ordered way in order to be normal, but recently a large number of molecular mechanisms have been described as being involved in this process [24]. These mechanisms can be affected by a great number of genetic diseases, as well as environmental factors.

This heterogeneous group of disorders is one of the most significant causes of psychomotor problems in the infant population, including epilepsy and a variable degree of mental retardation. In the majority of cases, seizures do not respond to treatment and permanent sequelae are common according to the type of malformation.

Barkovich [25] classified malformations of cortical development in three categories as follows:

1. Stem cell proliferation or apoptosis (microcephaly, macrocephaly, cortical hamartomas, focal cortical dysplasia type II, dysembryoplastic neuroepithelial tumour (DNET), ganglioglioma).
2. Neuronal migration (lissencephaly, band heterotopia, cobblestone complex, subependymal heterotopia).
3. Late migration and cortical organization (polymicrogiria, schizencephaly, focal cortical dysplasia type I, III, microdysgenesis).

Lissencephaly

Lissencephaly literally means ‘smooth brain’; it consists of a group of disorders characterized by a lack of sulcation of the cortical plate, varying from *agyria*, with an absence of normal convolutions to *pachygyria*, in which there is a reduction of the gyral pattern and cortical thickening.

Mutations in multiple genes have been involved in the pathogenesis of this disease:

1. In classical lissencephaly (previously type 1) *LIS1, DCX*, and *TUBA1A* are involved.
2. In cobblestone lissencephaly (previously type 2) mutations have been described in genes *POMT*$_1$, *POMT*$_2$, *FKTN, FKRP, LARGE*.
3. In X-linked lissencephaly with agenesis of the corpum callosum, alterations of the gene *ARX* have been found.
4. In lissencephaly with cerebellar hypoplasia *RELN* and *VLDRL* genes can be altered.

The distribution of areas of agyria and pachygyria has been described precisely for some of the genes previously described [26].

In classical lissencephaly most children have early developmental delay, a wide spectrum of seizure types, spastic quadriparesis, mental retardation, and infantile spasms, while in cobblestone lissencephaly nearly half of patients have associated seizure disorders and up to 30% intractable [27].

A severe classic lissencephaly has been described in children with Miller–Dieker syndrome, associated with facial dysmorphism and, in some cases, cryptorchidism, omphaloceles, cardiac, and renal anomalies. Three syndromes associated with cobblestone lissencephaly are well known; Walker–Warburg syndrome (WWS) with generalized hypotonia, hydrocephalus, mental retardation, severe seizures, different ocular abnormalities, with or without encephalocele; muscle–eye–brain (MEB) disease with a severe congenital muscular dystrophy and mental retardation; and Fukuyama congenital muscular dystrophy with severe hypotonia, progressive weakness and mental retardation [28].

MRI findings in classic lissencephaly include a flat, thickened cortical surface (5–10 mm), with poorly-developed sylvian and Rolandic fissures, with figure eight-shaped appearance in axial images. In cobblestone lissencephaly, the cortex is usually thinner than in the classic form, and cerebellar and brainstem malformations can be associated, such as the pontine hypogenesis common in WWS and MEB.

Heterotopia

This migration disorder consists of clusters of neurons in abnormal locations, caused by damage of radial glial fibres, with migration arrest at different sites. Three groups have been described [27,28]:

1. *Periventricular nodular heterotopia* (Fig. 29.13): caused by mutation of the *FLNA* gene (X q28), *ARFGEF2* gene (20q

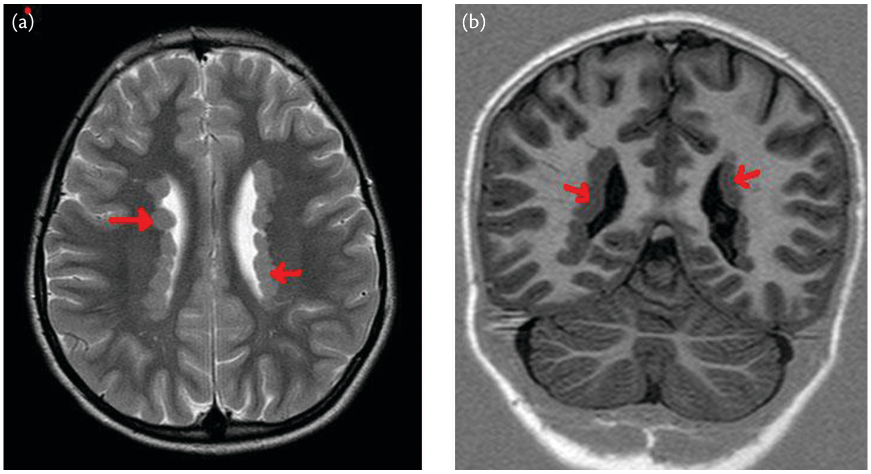

Fig. 29.13 Periventricular nodular heterotopias. (a) Axial T$_2$-weighted image and (b) coronal MR T$_1$ IR 3D image, show nodules of heterotopic gray matter protruding in the ventricular surface (red arrows).

Reproduced from Nuñez S, Mantilla MT, Sonia Bermúdez S. (2011). Midline congenital malformations of the brain and skull. *Neuroimaging Clinics of North America*, **21**(3), 429–482. Copyright (2011), with permission from Elsevier.

13.13—recessive form), duplication of chromosome 5, and deletion on chromosome 6 or 7. Sporadic forms associated with infections or prenatal injuries have been described. In the X-linked mutation bilateral symmetric gray matter nodules contiguous to the ventricular wall are present. In the unilateral form gray matter nodules are usually in the paratrigonal zone of lateral ventricles. Up to 90% of patients have epilepsy with auras, requiring surgical intervention.

2. *Subcortical band heterotopia:* consists of gray matter bands interposed between the cortex and the lateral ventricles. Two genes have been involved, *LIS1* at 17p13.32 and *DCX* at Xq22.3-q23.3. Seizures are the most common manifestation, but intellectual impairment varies depending the band thickness and degree of pachygyria.
3. *Marginal zoneheterotopias* or *leptomeningeal glioneuronal heterotopias*.

Polymicrogyria

This disorder occurs during late neuronal migration and cortical organization, with a macroscopic appearance of excessive in-folding of the cortex resulting in abnormal small gyri separated by shallow sulci (Fig. 29.14).The distribution is highly variable, uni- or bilateral and neurologic manifestations depend on location and extent of anomaly.

The pathogenesis is not well understood, and some genes have been involved, including *SRPX2, PAX6, TBR2, KIAA1279, RAB3GAP1*, and *COL18A1*. Also associations with Aicardi syndrome, Zellweger and WWS support a genetic basis in the pathogenesis. [27,28].

This is the most frequent cause of partial seizures in paediatric population, seizures start at 4–12 years and, similar to other migration disorders, do not respond to medication; most frequent are atypical absences, or tonic or atonic drop attacks.

Schizencephaly

This structural abnormality consists of uni- or bilateral congenital clefts of brain hemisphere(s), communicating the lateral ventricle(s) with the subarachnoid space [29]. The walls of the cleft are surrounded by gray matter, often polymicrogyric, and can be separated by CSF (open lips) or abut on another (closed lips). (Fig. 29.15)

Pathogenesis includes multifactorial causes, including vascular, toxic, metabolic, and infectious factors (CMV) [27]. Associations with septo-optic dysplasia, absent septum pellucidum, and optic nerve hypoplasia are not uncommon [30].

Unilateral closed lip cleft associates with seizures and mild hemiparesis, while bilateral clefts lead to severe mental retardation and motor anomalies, even spastic quadriparesis.

Focal cortical dysplasia

Focal cortical dysplasia (FCD) is defined as an area of malformed cerebral cortex with cortical disorganization that is usually correlated with focal epilepsy. FCD was first described by Taylor [11] and numerous classifications have been proposed since that first description. Currently, the ILAE task force divides FCDs into three types [31]

Type I FCDs are related to abnormal cortical layering. These are further subdivided in types Ia, Ib, and Ic. Type Ia FCDs are associated with compromise of the radial migration and maturation of neurons, type Ib FCDs are associated with compromise of the tangential composition of the neocortex, and the combination of both variants is classified as FCD Type Ic. Almost 50% of patients with type I FCDs have a normal MRI in the remaining cases, where the abnormality is visible by imaging, the most common presentation is a focal blurring of the cortical white matter that can be associated with some degree of volume lost, although in almost all cases the abnormality is very subtle [32].

Type II FCDs are related to disrupted cortical lamination with specific cytological abnormalities. Like type I FCDs they are subdivided in subtypes. Type IIa, refers to FCDs with dysmorphic neurons WITHOUT balloon cells and type IIb to FCDs with dysmorphic neurons *and* balloon cells. On MRI, type II cortical dysplasias are also characterized by blurring of the gray–white matter junction and mimic increased cortical thickness, changes that are more pronounced than in type I FCDs. These findings are usually associated with subcortical white matter signal abnormalities, and

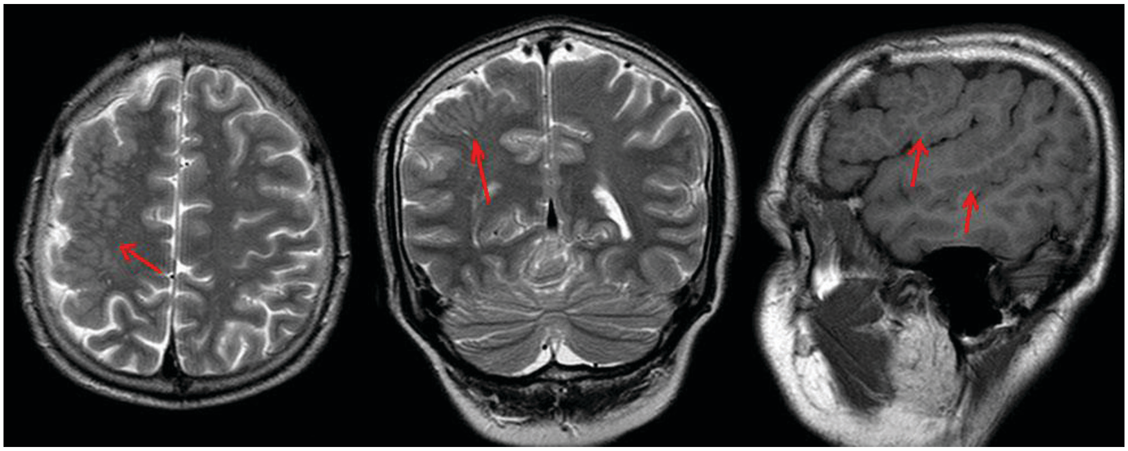

Fig. 29.14 Polymicrogyria. Axial and coronal T_2-weighted images and sagittal T_1-weighted image, show right frontoparietal polymicrogyria with slightly thick cortex with a 'bumpy' surface (red arrows).

Reproduced from Nuñez S, Mantilla MT, Sonia Bermúdez S. (2011). Midline congenital malformations of the brain and skull. *Neuroimaging Clinics of North America*, **21**(3), 429–482. Copyright (2011), with permission from Elsevier.

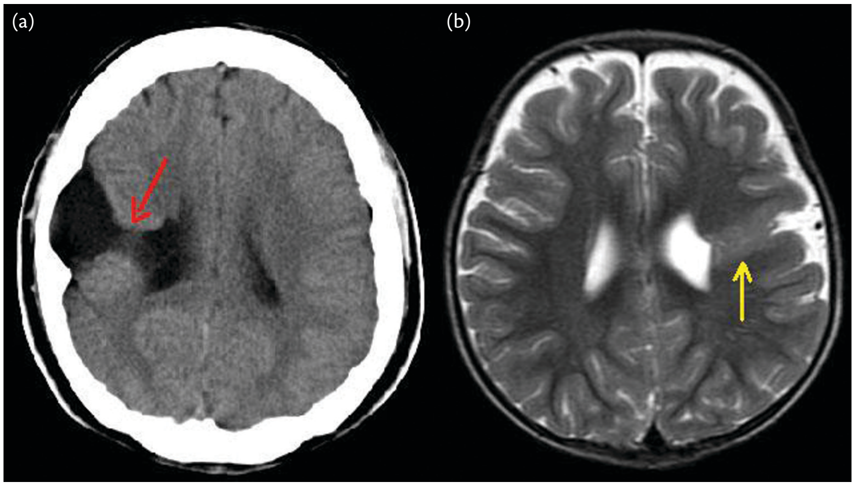

Fig. 29.15 (a) Axial CT scan shows right open-lip schizencephaly with a small cleft with continuity of CSF from the subarachnoid space to the ventricle. (b). Axial T_2-weighted image shows left closed-lip schizencephaly with an irregular track of gray matter extending from the cortex to the ventricular surface.
Reproduced from Nuñez S, Mantilla MT, Sonia Bermúdez S. (2011). Midline congenital malformations of the brain and skull. *Neuroimaging Clinics of North America*, **21**(3), 429–482. Copyright (2011), with permission from Elsevier.

with cortical gyration and sulcation abnormalities, especially in type IIb FCDs.

Type III FCD refers to FCDs associated with an additional abnormality, usually adjacent to, or affecting the same cortical area or lobe. They are subdivided into:

1. FCD type IIIa when associated with hippocampal sclerosis.
2. FCD type IIIb when associated with neoplasms.
3. FCD type IIIc when associated with vascular malformation.
4. FCD type IIId when associated with other lesion.

The MRI imaging findings of type III would be, in consequence, various, according to the subjacent abnormality associated with the FCD.

Cephaloceles

The permanent connection between a protruded cerebral tissue and meninges, and the intracranial cavity, through a congenital bony defect is the so-called cephalocele. The cephaloceles are classified according to the location of the skull defect—anterior or posterior in relation to the coronal sutures (Fig. 29.16).

Their names depend on their location. Anterior cephaloceles include interfrontal, fronto-ethmoidal (naso-frontal, naso-ethmoidal, naso-orbital), and nasopharyngeal (transsphenoidal, transethmoidal, spheno-ethmoidal, basioccipital) cephaloceles [33]. Posterior cephaloceles are divided in parietal (the defect is between the bregma and the lambda), and occipital (the defect arises between the lambda and the foramen magnum, possibly including one or more of the cervical vertebrae) [34].

Atretic cephaloceles are forms frustré of cephaloceles, which contain a small, non-cystic, flat, or nodular lesion. This lesion is situated in the midline of the scalp, either near the vertex (parietal) or just cephalic to the external occipital protuberance (occipital form) [10,35].

Cephaloceles can also be classified according to the involvement of the cranial vault (interfrontal, parietal, occipital, and lateral) or the skull base (temporal, fronto-ethmoidal, nasopharyngeal, spheno-orbital and sphenomaxillary) [10]. Nasopharyngeal, temporal, and spheno-orbital types are classified as basal cephaloceles by other authors [36,37]. A detailed histologic examination allows for another classification according to their content—pure meninges (meningocele), meninges and brain (encephalomeningoceles), part of the ventricle (encephalocystocele), or glial-lined cyst containing CSF (gliocele) [9].

The incidence of cephaloceles is approximately 0.8–3.0 per 10,000 births [10,38] and varies in relation to their location: 66–89% for occipital cephaloceles [10], l5% for fronto-ethmoidal and 10% for basal [36,37]. There is a relatively high incidence (1:5000 live births) of fronto-ethmoidal cephaloceles in southeast Asia [39,40]. The factors that influence the incidence of neural tube defects (NTD), include different genetic alterations, nutrition and the health status of women, frequency of prenatal diagnosis resulting in an elective abortion, and exposure to NTD-inducing toxic agents [41].

Although the review of the embryology is beyond the scope of this chapter, it is important to remember that processes of neurulation, disjunction, and migration of the neural crest cells [42–44], precede the formation of the prosencephalon, which then differentiates into the diencephalon and telencephalon [45].

The mechanisms leading to faulty closure of the neural tube are still unknown. Recently, Trovato et al. proposed NTD may be due to p53 down-regulation or disruption, which diminishes the expression of hepatocyte growth factor/scatter factor (*HGF*), *c-met*, and *STAT3* genes [41].

Clinical and radiological features

Cephaloceles present both swelling (the protruded tissue) and an underlying bony defect. There are certain features shared by patients with cephaloceles—facial malformations in anterior cephaloceles, dysgenesis of corpus callosum, hydrocephalus, optic nerve atrophy, and intracranial malformations in both anterior and posterior cephaloceles. While Dandy–Walker cyst, Chiari II malformation, venous anomalies, and prominent supracerebellar cistern

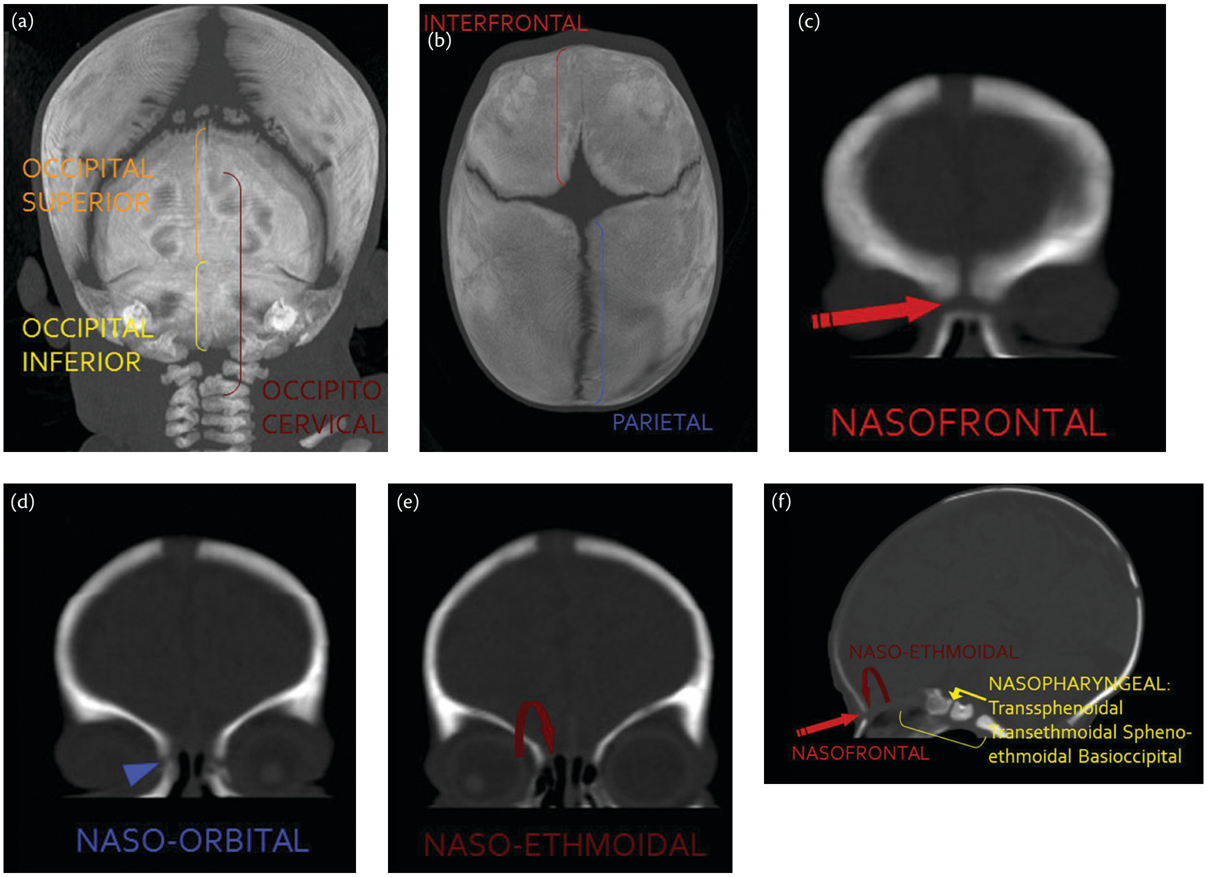

Fig. 29.16 Classification of cephaloceles according to the skull defect. (a) Three-dimensional CT. Posterior view of occipital bone demonstrates the location of different occipital cephaloceles: superior, inferior, occipitocervical. (b) Three-dimensional CT of head. Superior view of skull illustrates sites of interfrontal and parietal cephaloceles. (c) CT coronal image at nasofrontal sutures (straight arrow), where nasofrontal cephaloceles occur. (d) CT coronal image at the level of the middle third of the medial orbital wall (arrowhead), where naso-orbital cephaloceles protrude. (e) CT coronal image at fronto-ethmoidal level (curved arrow), where naso-ethmoidal cephaloceles are found. (f) CT midline sagittal image. Different points of probable nasopharyngeal (transsphenoidal: angled arrow) and fronto-ethmoidal cephaloceles are shown.

Reproduced from Nuñez S, Mantilla MT, Sonia Bermúdez S. (2011). Midline congenital malformations of the brain and skull. *Neuroimaging Clinics of North America*, **21**(3), 429–482. Copyright (2011), with permission from Elsevier.

are shared by parietal and occipital cephaloceles. Chiari III malformation, cerebral and cerebellar migration anomalies are found in occipital cephaloceles [40,43,46]. Agenesis of the corpus callosum is demonstrated in approximately 80% of patients with nasopharyngeal cephaloceles [42].

The location of the bony defect in occipital cephaloceles may be infratentorial, supratentorial or combined [46]. The occipital cephalocele can be small or large (>50 mm), and it is rarely larger in size than the head (giant cephalocele) of the patient [47]. The occipital encephalocele is part of the Chiari III malformation. Intracranial malformations and syndromes are associated with occipital cephaloceles.

The bony defect in parietal cephaloceles more commonly lies near the posterior or anterior fontanelle. Under this bony defect, there is a fenestrated falx or dural dehiscence leading to widening of the ostium and the interhemispheric fissure.

Anterior cephaloceles can be:

1. Fronto-ethmoidal (naso-ethmoidal, nasofrontal and naso-orbital).
2. Nasopharyngeal.
3. Interfrontal.

Naso-ethmoidal (intranasal) cephaloceles are usually evident in the paediatric age group and cause complex deformities in the frontal, orbital, and nasal regions. Sometimes it is a small defect and only manifests late in adulthood. In this setting, misdiagnosis is common as either a nasal polyp, intracerebral tumour that has invaded down through the skull base into the nasal anlage, or cerebral intranasal heterotopia. Biopsy is contraindicated in these cephaloceles due to potential CSF leaks, seizures, or meningitis [37,48]. Cisternography with heavily T_2-weighted images with thin sections may be useful in the diagnosis [37].

Hypertelorism is constantly seen in nasopharyngeal and nasofrontal cephaloceles, and is commonly associated with naso-ethmoidal and naso-orbital cephaloceles. Other facial malformations, such as labial, palatine, and median nasal fissure are demonstrated in nasopharyngeal and fronto-ethmoidal cephaloceles [42,46].

Since naso-orbital cephaloceles protrude into the orbit, they typically present proptosis and a slightly pulsatile mass [46].

Elster et al. [49] classify nasopharyngeal or basal cephaloceles into six types. The basal cephaloceles are not obviously seen on clinical examination. Since they are occult, they are discovered towards the end of the first postnatal decade. In order to rule out a nasopharyngeal encephalocele, it is mandatory to do a neuroradiological evaluation in patients with hypertelorism, with diminished visual acuity and hypothalamic-pituitary dysfunction and/or nasopharyngeal mass [46]. These symptoms are due to the stretching of the inferior portion of the third ventricle, hypothalamus, and optic chiasm, into the sac [42,45]. The transalar sphenoidal cephalocele causes headache with non-localizing symptoms [49].

Interfrontal cephaloceles may occupy the entire length of the suture, which allows the passage to the anterior tips of the frontal lobes or the anterior halves of the cerebral hemispheres. The protrusion of the brain could be asymmetrical and extensive, leading to a rotation of the intracranial hemisphere. The associated cerebral malformations, such as agyria and holotelencephaly (prosencephaly with arrhinencephaly), hydrocephalus, and the compression of the herniated brain contribute to the poor prognosis of the interfrontal cephalocele [46].

MRI is the method of choice to evaluate of all of these abnormalities, even though computed tomography (CT) is more precise than MRI in delineating the margins and extensions of the bony defect [37,47,50,51].

Nasal dermoids, intranasal cerebral heterotopia, and dermal sinus

Abnormalities of closure and formation of frontonasal suture and foramen caecum result in anomalies at this level. If brain tissue protrudes through the fonticulus frontalis and communicates with the intracranial cavity, a frontonasal cephalocele is formed. If the fonticulus frontalis closes after the protrusion of the brain tissue, the entrapped tissue constitutes a prenasal cerebral heterotopia (nasal glioma).

When the protrusion of the brain tissue is through the prenasal space, without regression of this tissue, and connects to the intracranial cavity, a naso-ethmoidal encephalocele arises.

If dysplastic brain tissue remains separated from the intracranial CSF, after its protrusion through the prenasal space, an intranasal cerebral heterotopia (intranasal glioma) is formed. There is a stalk of tissue in approximately 15% of cases, without direct fluid-filled tract connection with intracranial subarachnoid spaces. The partial regression of the most superior portion of the dural diverticulum is the postulated explanation for both the prenasal and the intranasal cerebral heterotopia [25].

When the dural diverticulum reaches the dermis and remains attached (incomplete disjunction of the neuroectoderm and cutaneous ectoderm) to the skin in its regression through the prenasal space, a dermal sinus tract is created leaving a dimple at its orifice. The dermal sinus tract may extend superiorly along the path of the dural diverticulum for a variable distance, and can communicate with the intracranial cavity. Some of the tissue within the sinus dermal tract can originate dermoid and/or epidermoid cysts due to persistent ectodermal elements at sites of suture closure, brain diverticulation, and neural tube closure [42]. These cysts can also be found along the following midline locations: the anterior fontanelle, glabella, nasion, vertex, and subocciput [52], at the level of foramen caecum (adjacent to the crista galli), and adjacent to the anterior margin of the third ventricle [53].

MRI is the best choice to achieve the objective sought in studying these lesions, evaluating the nature (imaging features of the tissue), locating site of origin and determining the extension of the lesion (19,28).

All of the aforementioned lesions can be surgically resected. The nasal dermoid and epidermoid cysts are removed in order to avoid potential CNS infection if there is intracranial connection [52].

Corpus callosum malformations

The three-telencephalic commissures are the anterior commissure (paleocortical), the hippocampal commissure (archicortical), and the corpus callosum (neocortical). The corpus callosum emerges as a new phylogenetic feature in placental mammals [54]. Even though, the anatomy [55], the embryology [54], and the different factors (cellular tunnels, midline glia, guidance, and defasciculation) [56] that intervene in the development of these commissures are not the topic of this review, it is important to recall that the corpus callosum is completed at weeks 14–15, with the fusion of the splenium with the lamina rostralis, genu, and body. The lamina rostralis is present before the genu and the splenium develop [55]. There is a front-to-back translation of the splenium as result from the back-to-front expansion of the frontal lobes and the progressive accumulation of fibres in the anterior callosal segment. The translation of the splenium is not due to a front-to-back progression of the corpus callosum [54,57]. The myelination of the isthmus and splenium, which contain the fibres of the primary cortical areas (somatosensory, motor, auditory, visual), precedes the myelination of the body, genu, and rostrum related to the more anterior associative areas.

Agenesis of the corpus callosum

The agenesis of the corpus callosum (ACC) has an incidence of 0.5–70 in 10,000 [58]. ACC is not a malformation in itself, but an anatomical feature of many different diseases [54,59]. It is found in genetic defects (autosomal dominant, autosomal recessive, and X-linked mode of inheritance), familial or not, identified or not, syndromic or not [54,58].

Most clinical findings in patients with ACC described in the literature include mental retardation (60%), visual problems (33%), speech delay (29%), seizures (25%), and abnormal muscular tone (25%) [58].

MRI findings in patients with ACC include bundles of Probst, cingulate cortex and midline anatomy changes, parallel lateral ventricles, colpocephaly, as well as ventricular abnormalities and cysts (Fig. 29.17) [54,60,61].

Agenesis of the anterior commissure and the bundles of Probst may or may not be present in ACC [54, 61]. The Probst bundles are found in 59% of patients with ACC and 30% with commissural hypogenesis [59].

Commissural agenesis associated with midline meningeal dysplasia

Interhemispheric cystic meningeal dysplasia

The agenesis of the commissures with interhemisperic cysts may be related to meningeal disorders. The interhemispheric cysts are classified in two classes—communicating and non-communicating. The communicating cysts result from expansion of the ventricular telachoroidea, while the non-communicating cysts are a multiloculated meningeal cystic dysplasia. A morphological classification for interhemispheric cysts associated to ACC was presented by Barcovich et al., according to morphologic data. The interhemispheric cysts are iso-intense to CSF, except for 2b, which is hyperintense [62].

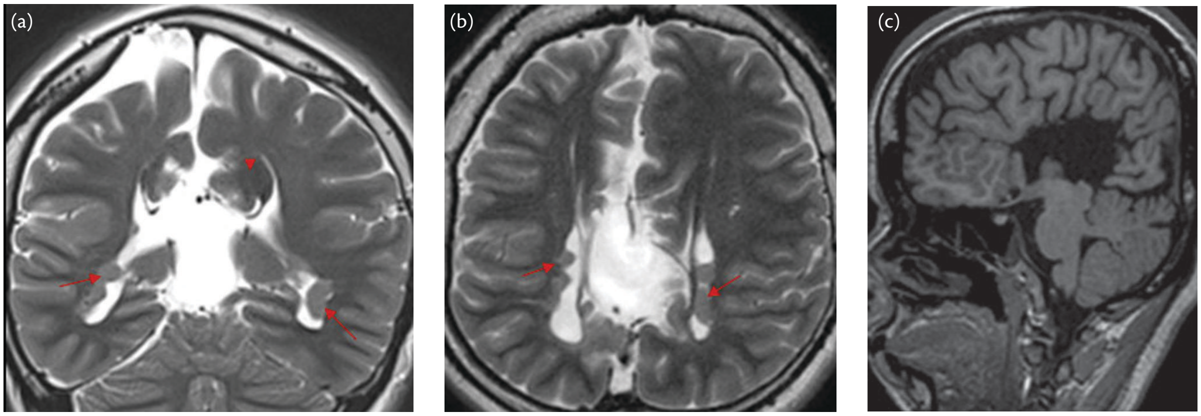

Fig. 29.17 Agenesis of corpus callosum. (a) Hypointense bundles of Probst (arrowhead), persistent eversion of the cingulate gyrus and subependymal heterotopias (arrows) are demonstrated on a coronal T_2-weighted image. (b) On an axial T_2-weighted image, the ventricles are parallel and subependymal heterotopias (arrows) are seen. (c) Sagittal T_1-weighted image shows absence of both the corpus callosum and the cingulated sulcus.

Reproduced from Nuñez S, Mantilla MT, Sonia Bermúdez S. (2011). Midline congenital malformations of the brain and skull. *Neuroimaging Clinics of North America*, **21**(3), 429–482. Copyright (2011), with permission from Elsevier.

Interhemispheric meningeal lipomas

The interhemispheric meningeal lipoma is located in the leptomeninges and is considered to result from an abnormal differentiation of the meninx primitiva. Dysplastic vessels are often associated to this lipoma, which may calcify. The abnormality of the commissures varies according to the location of the lipoma: the anterior or tubulonodular kind (15%) is associated with major commissural hypogenesis, the more posterior transitional or global (24%) to a complete, but hypoplastic commissural plate, the posterior or curvilinear (48%), to minor shortening or tapering of the splenium, and the inferior (12%) to minor commissural abnormalities only, if any. The lipoma is isointense to fat on T_2- and T_1-weighted sequences, and hypointense on fat saturation sequences, without increase of signal intensity on T_1-weighted contrast sequence. There is a chemical shift artefact associated with the lipoma, due to different chemical shift of fat and water protons [63].

Conclusions

It's very important to review the embryologic development of the brain and skull in order to understand malformations, as well as the impact these have on the patient. Classifying the different malformations is difficult. The objective must be the creation of multidisciplinary expert groups with a clinical, neuroimaging, and molecular genetics approach. Obtaining high-quality images with thin sections and high resolution volumetric acquisitions, must always be the goal, as well as obtaining true sagittal and coronal views in the different modalities of diagnostic imaging, to avoid erroneous diagnosis. The advent of diffusion tensor imaging with colour fractional anisotropy maps, may help in the analysis of the malformations, and facilitate the diagnosis.

Acknowledgements

We are grateful to Dr. Manohar Shroff (Hospital for Sick Children, Toronto, Canada) for his critical review of this chapter.

References

1. Patel, S, and Barkovich AJ. (2002). Analysis and classification of cerebellar malformations. *AJNR American Journal of Neuroradiology*, **23**(7), 1074–87.
2. Barkovich AJ, Millen KJ, and Dobyns WB. (2009). A developmental and genetic classification for midbrain-hindbrain malformations. *Brain*, **132**(Pt 12), 3199–230.
3. Kollias SS, Ball, WS Jr, and Prenger EC. (1993). Cystic malformations of the posterior fossa: differential diagnosis clarified through embryologic analysis. *Radiographics*, **13**(6), 1211–31.
4. Parisi MA, and Dobyns WB. (2003). Human malformations of the midbrain and hindbrain: review and proposed classification scheme. *Molecular Genetics and Metabolism*, **80**(1–2), 36–53.
5. Nelson MD, Jr, Maher K, and Gilles FH. (2004). A different approach to cysts of the posterior fossa. *Pediatric Radiology*, **34**(9), 720–32.
6. Alkan O, Kizilkilic O, and Yildirim T. (2009). Malformations of the midbrain and hindbrain: a retrospective study and review of the literature. *Cerebellum*, **8**(3), 355–65.
7. Robinson AJ, Blaser S, Toi A, et al. (2007). The fetal cerebellar vermis: assessment for abnormal development by ultrasonography and magnetic resonance imaging. *Ultrasound Q*, **23**(3), 211–23.
8. Poretti A, Prayer D, and Boltshauser E. (2009). Morphological spectrum of prenatal cerebellar disruptions. *European Journal of Paediatric Neurology*, **13**(5), 397–407.
9. Suwanwela C, and Suwanwela N. (1972). A morphological classification of sincipital encephalomeningoceles. *Journal of Neurosurgery*, **36**(2), 201–11.
10. Naidich TP, Altman NR, Braffman BH, et al. (1992). Cephaloceles and related malformations. *AJNR American Journal of Neuroradiology*, **13**(2), 655–90.
11. Taylor DCF, Falconer MA, Bruton CJ, et al. (1971). Focal dysplasia of the cerebral cortex in epilepsy. *Journal of Neurology, Neurosurgery & Psychiatry*, **34**(4), 369–87.
12. dos Santos AV, Matias S, Saraiva P, et al. (2006). MR imaging features of brain stem hypoplasia in familial horizontal gaze palsy and scoliosis. *AJNR American Journal of Neuroradiology*, **27**(6), 1382–3.
13. Naidich TP, Pudlowski RM, Naidich JB, et al. (1980). Computed tomographic signs of the Chiari II malformation. Part I: Skull and dural partitions. *Radiology*, **134**(1), 65–71.
14. McLeary RD, Kuhns LR, and Barr M, Jr. (1984). Ultrasonography of the fetal cerebellum. *Radiology*, **151**(2), 439–42.

15. Poretti A, Leventer RJ, Cowan FM, et al. (2008). Cerebellar cleft: a form of prenatal cerebellar disruption. *Neuropediatrics*, **39**(2), 106–12.
16. Boltshauser E. (2004). Cerebellum-small brain but large confusion: a review of selected cerebellar malformations and disruptions. *American Journal of Medical Genetics A*, **126A**(4), 376–85.
17. Thakur S, Singh R, Pradhan M, et al. (2004). Spectrum of holoprosencephaly. *Indian Journal of Pediatrics*, **71**(7), 593–7.
18. Alfonso I, Papazian O, and Sinisterra S. (2003). [Cerebral malformation in the newborn: holoprosencephaly and agenesis of the corpus callosum]. *Reviews in Neurology*, **36**(2), 179–84.
19. Fitz CR. (1983). Holoprosencephaly and related entities. *Neuroradiology*, **25**(4), 225–38.
20. Hahn JS, and Barnes PD. (2010). Neuroimaging advances in holoprosencephaly: Refining the spectrum of the midline malformation. *American Journal of Medical Genetics C Seminars in Medical Genetics*, **154C**(1), 120–32.
21. Barkovich AJ, and Quint DJ. (1993). Middle interhemispheric fusion: an unusual variant of holoprosencephaly. *AJNR American Journal of Neuroradiology*, **14**(2), 431–40.
22. Barkovich AJ, Fram EK, and Norman D. (1989). Septo-optic dysplasia: MR imaging. *Radiology*, **171**(1), 189–92.
23. Guerrini R, and Parrini E. (2010). Neuronal migration disorders. *Neurobiology of Disease*, **38**(2), 154–66.
24. Meyer G. (2007). Genetic control of neuronal migrations in human cortical development. *Advances in Anatomy, Embryology and Cell Biology*, **189**, 1–111.
25. Barkovich AJ. (2012). Congenital malformations of the brain and skull. In: Barkovich AJ, and Raybaud C. (eds). *Pediatric Neuroimaging*, 5th edn. Philadelphia: Lippincott Williams and Wilkins, pp. 389–90.
26. Mochida GH. (2009). Genetics and biology of microcephaly and lissencephaly. *Semininars in Pediatric Neurology*, **16**(3), 120–6.
27. Spalice A, Parisi P, Nicita F, et al. (2009). Neuronal migration disorders: clinical, neuroradiologic and genetics aspects. *Acta Paediatrica*, **98**(3), 421–33.
28. Verrotti A, Spalice A, Ursitti F, et al. (2010). New trends in neuronal migration disorders. *European Journal of Paediatric Neurology*, **14**(1), 1–12.
29. Granata T, Freri E, Caccia C, et al. (2005). Schizencephaly: clinical spectrum, epilepsy, and pathogenesis. *Journal of Child Neurology*, **20**(4), 313–18.
30. Leventer RJ, Guerrini R, and Dobyns WB. (2008). Malformations of cortical development and epilepsy. *Dialogues in Clinical Neuroscience*, **10**(1), 47–62.
31. Blümcke I, Thom M, Aronica E, et al. (2011). The clinicopathologic spectrum of focal cortical dysplasias: a consensus classification proposed by an ad hoc Task Force of the ILAE Diagnostic Methods Commission. *Epilepsia*, **52**(1), 158–74.
32. Colombo N, Tassi L, Galli C, et al. (2003). Focal cortical dysplasias: MR imaging, histopathologic, and clinical correlations in surgically treated patients with epilepsy. *AJNR American Journal of Neuroradiology*, **24**(4), 724–33.
33. Mahapatra AK, and Suri A. (2002). Anterior encephaloceles: a study of 92 cases. *Pediatric Neurosurgery*, **36**(3), 113–18.
34. Brown MS, and Sheridan-Pereira M. (1992). Outlook for the child with a cephalocele. *Pediatrics*, **90**(6), 914–19.
35. Patterson RJ, Egelhoff JC, Crone KR, et al. (1998). Atretic parietal cephaloceles revisited: an enlarging clinical and imaging spectrum? *AJNR American Journal of Neuroradiology*, **19**(4), 791–5.
36. Czech T, Reinprecht A, Matula C, et al. (1995). Cephaloceles—experience with 42 patients. *Acta Neurochirugia (Wien)*, **134**(3–4), 125–9.
37. Lowe LH, Booth TN, Joglar JM, et al. (2000). Midface anomalies in children. *Radiographics*, **20**(4), 907–22; quiz 1106–7, 1112.
38. Martinez-Lage JF, Poza M, Sola J, et al. (1996). The child with a cephalocele: etiology, neuroimaging, and outcome. *Childs Nervous System*, **12**(9), 540–50.
39. David DJ, and Proudman TW. (1989). Cephaloceles: classification, pathology, and management. *World Journal of Surgery*, **13**(4), 349–57.
40. Hoving EW. (2000). Nasal encephaloceles. *Childs Nervous System*, **16**(10–11), 702–6.
41. Trovato M, D'Armiento M, Lavra L, et al. (2007). Expression of p53/HGF/c-met/STAT3 signal in fetuses with neural tube defects. *Virchows Archives*, **450**(2), 203–10.
42. Barkovich AJ, Kuzniecky RI, Jackson GD, et al. (2005). A developmental and genetic classification for malformations of cortical development. *Neurology*, **65**(12), 1873–87.
43. Padmanabhan R. (2006). Etiology, pathogenesis and prevention of neural tube defects. *Congenital Anomalies (Kyoto)*, **46**(2), 55–67.
44. Langman J. (2004). Second Week of Development: Trilaminar Germ Disc 65. In: Sadler TW, and Langman J (eds). *Langman's medical embryology*. Philadelphia: Lippincott Williams & Wilkins, p. x.
45. Blustajn J, Netchine I, Frédy D, et al. (1999). Dysgenesis of the internal carotid artery associated with transsphenoidal encephalocele: a neural crest syndrome? *AJNR American Journal of Neuroradiology*, **20**(6), 1154–7.
46. Diebler C, and Dulac O. (1983). *Cephaloceles: clinical and neuroradiological appearance. Associated cerebral malformations. Neuroradiology*, **25**(4), 199–216.
47. Kotil K, Kilinc B, and Bilge T. (2008). Diagnosis and management of large occipitocervical cephaloceles: a 10-year experience. *Pediatric Neurosurgery*, **44**(3), 193–8.
48. Allbery SM, Chaljub G, Cho NL, et al. (1995). MR imaging of nasal masses. *Radiographics*, **15**(6), 1311–27.
49. Elster AD, and Branch, CL, Jr (1989). Transalar sphenoidal encephaloceles: clinical and radiologic findings. *Radiology*, **170**(1 Pt 1), 245–7.
50. Hofmann E, Behr R, and Schwager K. (2009). Imaging of cerebrospinal fluid leaks. *Klinische Neuroradiologie*, **19**(2), 111–21.
51. Morioka T, Hashigushi K, Samura k, et al. (2009). Detailed anatomy of intracranial venous anomalies associated with atretic parietal cephaloceles revealed by high-resolution 3D-CISS and high-field T2-weighted reversed MR images. *Childs Nervous System*, **25**(3), 309–15.
52. Moron FE, Morriss MC, Jones JJ, et al. (2004). Lumps and bumps on the head in children: use of CT and MR imaging in solving the clinical diagnostic dilemma. *Radiographics*, **24**(6), 1655–74.
53. Hedlund, G. (2006). Congenital frontonasal masses: developmental anatomy, malformations, and MR imaging. *Pediatrics Radiology*, **36**(7), 647–62; quiz 726–7.
54. Raybaud, C. (2010). The corpus callosum, the other great forebrain commissures, and the septum pellucidum: anatomy, development, and malformation. *Neuroradiology*, **52**(6), 447–77.
55. Kier EL, and Truwit CL. (1997). The lamina rostralis: modification of concepts concerning the anatomy, embryology, and MR appearance of the rostrum of the corpus callosum. *AJNR American Journal of Neuroradiology*1997. **18**(4), 715–22.
56. Richards LJ. (2002). Axonal pathfinding mechanisms at the cortical midline and in the development of the corpus callosum. *Brazilian Journal of Medical and Biological Research*, **35**(12), 1431–9.
57. Kier EL, and Truwit CL. (1996). The normal and abnormal genu of the corpus callosum: an evolutionary, embryologic, anatomic, and MR analysis. *AJNR American Journal of Neuroradiology*, **17**(9), 1631–41.
58. Schell-Apacik CC, Wagner K, Bihler M, et al. (2008). Agenesis and dysgenesis of the corpus callosum: clinical, genetic and neuroimaging findings in a series of 41 patients. *American Journal of Medical Genetics A*, **146A**(19), 2501–11.
59. Hetts SW, Sherr EH, Chao S, et al. (2006). Anomalies of the corpus callosum: an MR analysis of the phenotypic spectrum of associated malformations. *AJR American Journal of Roentgenology*, **187**(5), 1343–8.
60. Kuker W, Mayrhofer H, Mader I, et al. (2003). Malformations of the midline commissures: MRI findings in different forms of callosal dysgenesis. *European Radiology*, **13**(3), 598–604.
61. Utsunomiya H, Ogasawara T, Hayashi T, et al. (1997). Dysgenesis of the corpus callosum and associated telencephalic anomalies: MRI. Neuroradiology, **39**(4), 302–10.
62. Stroustrup Smith A, and Levine D. (2004). Appearance of an interhemispheric cyst associated with agenesis of the corpus callosum. *AJNR American Journal of Neuroradiology*, **25**(6), 1037–40.
63. Yildiz H, Hakyemez B, Koroglu M, et al. (2006). Intracranial lipomas: importance of localization. *Neuroradiology*, **48**(1), 1–7.

CHAPTER 30

Paediatrics

Central nervous system inflammatory disorders

Leonard H. Verhey and Brenda Banwell

Introduction

Acute central nervous system (CNS) inflammatory disorders represent a broad spectrum of illnesses that result when activated immune cells target CNS structures, such as myelin or other proteins, neurons, or blood vessels. Brain inflammation can occur in the context of an underlying systemic condition (systemic lupus erythematosus, Behçet's disease, sarcoidosis) or may manifest as a primary idiopathic illness. Primary inflammation of the CNS may be monophasic in nature, or may represent the incident attack of a chronic disease (multiple sclerosis (MS), CNS vasculitis, neuromyelitis optica (NMO)). This chapter will focus on primary acquired inflammatory disorders of the CNS in children, specifically those in which the primary immune-mediated target is myelinated axons (demyelination), blood vessels (vasculitis), or astrocytic aquaporin-4 (NMO).

Inflammatory disorders of the CNS are increasingly being recognized in children. These disorders may have overlapping presenting symptoms, and may initially be difficult to distinguish from each other. However, because both the clinical course and treatment choices vary, accurate diagnosis is important. Clinical presentation includes focal or multifocal neurological deficits localizing to the brain, spinal cord, or optic nerves. Encephalopathy is a key clinical feature in children with acute disseminated encephalomyelitis (ADEM) [1]; children with primary angiitis of the CNS (PACNS) often manifest with psychiatric symptoms in addition to neurological impairment [2]. Classification, definitions, and diagnostic criteria are summarized in Table 30.1. Acute inflammatory demyelination is typically managed with corticosteroids [3]; plasma exchange or IV immunoglobulin therapy may be required for severe or life-threatening attacks or when clinical response to corticosteroids is minimal [4–6]. Immunomodulatory therapies currently used to treat children with MS include interferon-β1a, interferon-β1b, and glatiramer acetate [6,7]. Childhood NMO and PACNS have been managed with rituximab, azathioprine, mycophenolate mofetil, methotrexate, and cyclophosphamide to reduce active disease and improve short-term neurological outcome [8]. Considering that the onset of symptoms occurs at a time when primary brain development and maturation is still ongoing, early diagnosis and treatment initiation is pivotal to minimize the potentially deleterious impact of CNS inflammation.

With the exception of NMO, specific biomarkers for acute demyelination, MS, and childhood PACNS (cPACNS) are yet lacking. Therefore, the diagnosis of CNS inflammatory disorders involves a multi-disciplinary approach and consideration of clinical, neuroimaging, and laboratory findings. Owing to its high sensitivity for macroscopic tissue abnormalities, magnetic resonance imaging (MRI) is an important tool aiding clinicians in the diagnosis and monitoring of children with CNS inflammatory disorders.

This chapter discusses the clinical application of MRI in acute demyelinating syndromes, MS, NMO, and PACNS. The clinical and MRI features of neuro-Behçet's disease, systemic lupus erythematosus, and sarcoidosis are briefly reviewed. Advanced MRI techniques not yet routinely available for clinical use have been applied over the last decade to quantify *in vivo* the degree of brain inflammation, as well as the pathologic substrates of neurodegeneration in paediatric-onset MS. These key research findings are discussed in the latter portion of the chapter.

Acute demyelinating syndromes

The occurrence of monofocal or multifocal neurological deficits localized to the CNS in children with no prior history of demyelinating disease, in which the presumed aetiology is inflammatory demyelination, is defined as an acute demyelinating syndrome (ADS) [1]. The incidence of ADS has been reported in several population-based studies, and ranges between 0.5 and 1.56/100,000 children per year [9–12]. Paediatric-onset acute demyelination typically manifests as optic neuritis, transverse myelitis, a monofocal deficit extrinsic to the optic nerves and spinal cord, such as brainstem or cerebellar dysfunction, or a multifocal neurological deficit without encephalopathy. While monofocal presentations are more common in adolescents and adults, children more commonly present with multifocal symptoms [13]. ADEM is an acute demyelinating syndrome characterized by multifocal neurological deficits and encephalopathy (alteration in behaviour or consciousness) [1], and is most commonly a monophasic or transiently multiphasic illness.

Optic neuritis

Approximately 55% of children with optic neuritis (ON) have abnormal optic nerves (optic nerve swelling, abnormal T_2 signal, contrast-enhancement) visualized on optic nerve-focused MRI [14]. On fat-saturated, T_2-weighted fast spin-echo (FSE) or short-tau inversion recovery (STIR) orbital imaging, lesions appear as areas of intraneural hyperintensity at any point between the optic nerve head and optic chiasm. Relative to the unaffected nerve, thickening of the optic nerve may also be visible. The affected optic nerve may also enhance following fat-suppressed post-contrast T_1-weighted MRI. MRI features of acute ON are depicted in (Fig. 30.1a–c).

Table 30.1 Definitions and diagnostic criteria for CNS inflammatory disorders

	Definitions and criteria
Acute demyelinating syndromes	
Optic neuritis [94]	*One or more of:* ◆ Acute loss of vision with painful eye movement ◆ Decreased visual acuity ◆ Reduced colour vision perception ◆ Abnormal visual-evoked potentials *Plus:* ◆ Absence of CT or MRI evidence of optic nerve compression, infiltration or trauma
Transverse myelitis [95]	◆ Acute sensory, motor, or autonomic deficits attributable to the spinal cord ◆ Bilateral symmetric or asymmetric signs and/or symptoms ◆ Clearly defined sensory level ◆ Progression to maximal deficit between 4 hours and 21 days following symptom onset *Plus one of:* ◆ CSF pleocytosis ◆ Increased IgG index ◆ MRI gadolinium enhancement of spinal cord lesion *And:* ◆ Neuroimaging exclusion of cord compression
Acute disseminated encephalomyelitis [1]	◆ A first clinically determined inflammatory demyelinating event with multifocal neurological deficits ◆ Encephalopathy (i.e. behavioural change, alteration in consciousness, seizures) not explained by fever ◆ No clinical or MRI evidence of new disease emerges ≥3 months after onset ◆ Brain MRI is abnormal during the acute (first 3 months) phase
Monofocal demyelination [47]	◆ Acute onset of neurological deficits ◆ Deficits localize to a single CNS site ◆ Deficits extrinsic to optic nerve or spinal cord
Multifocal demyelination [47]	◆ Acute onset of multifocal neurological deficits ◆ Absence of encephalopathy
Multiple sclerosis [1,28]	◆ Less than 18 years of age at the time of first attack ◆ MS diagnosis may be made based on any of the following: • ≥2 non-encephalopathic, clinical demyelinating events, separated by >30 days and involving more than one region of the CNS • 1 non-encephalopathic episode typical of MS associated with MRI findings that meet 2010 McDonald DIS criteria [28], and in which serial MRI demonstrates DIT • 1 ADEM event followed by a non-encephalopathic attack ≥3 months after symptom onset associated with an MRI pattern consistent with 2010 McDonald DIS criteria [28] • Incident acute (non-ADEM) demyelinating event in which the MRI meets criteria for 2010 McDonald DIS and DIT [28] (applies only to children ≥12 years old)
Neuromyelitis optica [96]	◆ Optic neuritis ◆ Acute transverse myelitis *Plus two of:* ◆ Spinal cord lesion spanning ≥3 vertebral body segments ◆ Brain MRI acquired at onset does not meet criteria for MS ◆ Serum antibodies against aquaporin 4 water channel
Childhood primary angiitis of the CNS [97]	◆ Age less than 18 years at diagnosis ◆ An acquired neurological deficit ◆ Newly-developed psychiatric symptoms ◆ Exclusion of systemic vasculitis or any other condition in which angiographic or pathologic features of angiitis could be secondary *Plus:* Angiographic (conventional or MR) or histopathologic (biopsy) evidence of CNS angiitis

Abbreviations: CT, computed tomography; MRI, magnetic resonance imaging; CSF, cerebrospinal fluid; IgG, immunoglobulin G; DIS, dissemination in space; DIT, dissemination in time

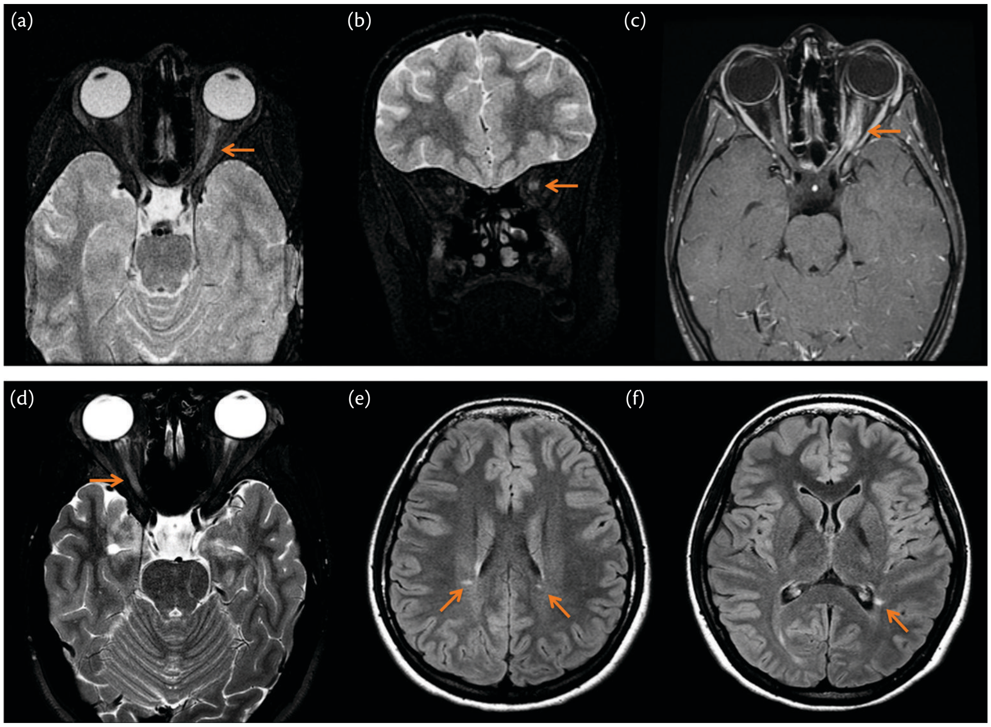

Fig. 30.1 (a) Axial and (b) coronal T_2-weighted MRI in a child with acute optic neuritis reveals swelling and hyperintense signal in the left optic nerve (arrows); (c) On contrast-enhanced fat-saturated T_1-weighted MRI of the orbit, the entire pre-chiasmatic portion of the optic nerve and nerve sheath enhances with blurring of the interface between optic nerve and orbital fat (arrow). (d) Axial T_2-weighted MRI of another child who presented with optic neuritis demonstrates expansion of the intra-orbital intracanalicular and pre-chiasmatic portions of the right optic nerve (arrow). (e,f) At the time of presentation with optic neuritis, multiple hyperintense lesions were present on FLAIR MRI in the periventricular and deep white matter regions, suggesting that this child is at high risk for a future MS diagnosis (arrows).

Isolated ON may represent the first attack of MS in 29% of children, according to a recent meta-analysis [15]. Brain MRI at the time of an incident attack of ON is important for evaluating the likelihood for a future MS diagnosis. Based on a recent meta-analysis of observational studies, MS risk is greater (odds ratio 28, $p < 0.001$, 95% CI 6.3–125.1) in children with at least one brain lesion at the time of presentation with ON, compared with children with normal MRI (Fig. 30.1d–e) [15].

Acute transverse myelitis

Isolated acute transverse myelitis (TM) with inflammation limited to the spinal cord typically occurs as a monophasic illness. TM may also occur in the context ADEM, as a component of a multifocal ADS (without encephalopathy), or in close temporal proximity to ON (prompting evaluation for NMO). Spinal cord involvement has been documented in approximately 12–20% of children presenting with an ADS [11,16,17], although a UK study reported a prevalence as high as 31% [18]. Compared with other acquired demyelinating syndromes, TM is often associated with severe impairment in the acute phase (i.e. patients may be non-ambulatory, require assisted ventilation, or require bladder catheterization) [19], and clinical outcome for severe TM is particularly poor [19,20]. When compared with other acute demyelinating syndromes, TM is less likely to represent a first attack of MS, with reports of only 13% of children subsequently being diagnosed with MS [10,16,20].

MRI plays a key role in excluding non-demyelinating aetiologies, such as spinal cord compression, ischaemia, or infection. T_2-weighted FSE MRI at the time of acute TM typically reveals spinal cord swelling and longitudinally-extensive TM—a T_2 lesion spanning ≥3 vertebral body segments (Fig. 30.2). Rarely, children have clinical features of acute spinal cord impairment without detection of a visible lesion on spinal MRI [19,20]. Small focal lesions (<3 vertebral body segments) are a common feature of spinal cord involvement in children with MS [16]. Longitudinally extensive transverse myelitis is more common in children with monophasic severe TM, in children with ADEM, and is the hallmark of spinal cord involvement in NMO. The presence of intralesional haemorrhage has been reported in children with longitudinally-extensive TM, as visualized on gradient-echo MRI, and is a poor prognostic sign [20]. Serial MRI of the spinal cord following TM often demonstrates atrophy of the affected spinal segments (Fig. 30.3).

In a study comparing children with monophasic TM with children diagnosed with MS who had spinal cord symptoms, 88% of children with monophasic TM had longitudinally-extensive lesions, while such lesions were present in only 17% of children with MS [20]. Conversely, focal lesions (less than three vertebral body segments) were more common in children with MS (75%) than those with TM (9%). In children with MS, spinal cord lesions are usually well-defined and preferentially involve the dorsolateral region of the spinal cord [16]; whereas, in children with TM, the entire transverse diameter is often involved in the region of maximal cord swelling [19,20].

Acute disseminated encephalomyelitis

According to the recently revised International Pediatric MS Study Group criteria, ADEM is defined as a multifocal neurological deficit

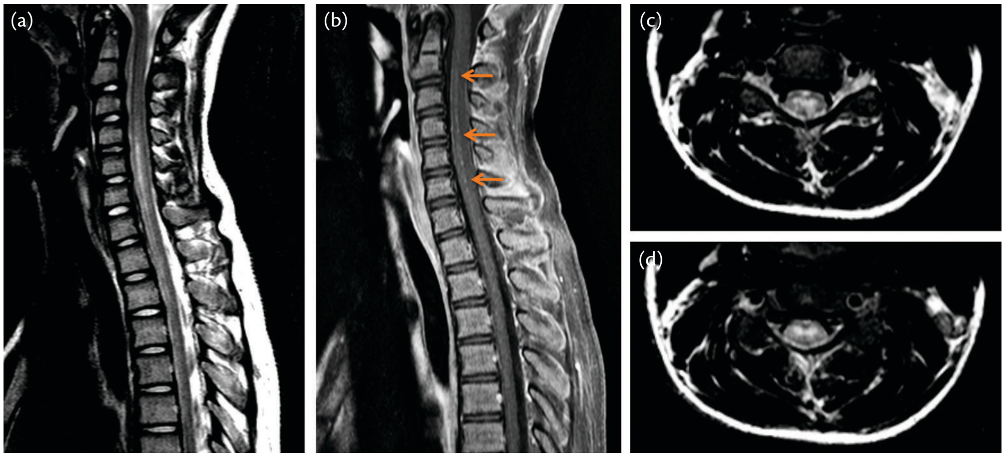

Fig. 30.2 (a) Spinal cord MRI of a child with acute idiopathic transverse myelitis reveals a longitudinally-extensive T_2-hyperintense lesion extending from C4–T5, which demonstrated a linear pattern of intralesional enhancement on post-contrast T_1-weighted MRI (arrows, b). Axial T_2-weighted images (c,d) showed the lesion to involve the central grey matter and anterior white matter portions of the spinal cord.

with encephalopathy [1]. ADEM is typically a monophasic illness, which requires prospective clinical and MRI evaluation to confirm the transient nature of the illness. A multiphasic course can occur, and the term 'multiphasic ADEM' is used to describe the occurrence of a second ADEM episode at least 3 months after the first, without any subsequent demyelinating events [1]. Relapses beyond the second ADEM event are likely to be indicative of a chronic disorder, such as MS or NMO [21,22]. The reported likelihood of a diagnosis of MS in children following a first presentation of ADEM varies from 2 to 18% [23–25]. Relapses consistent with MS typically occur within 2 years following the incident ADEM event [23,24].

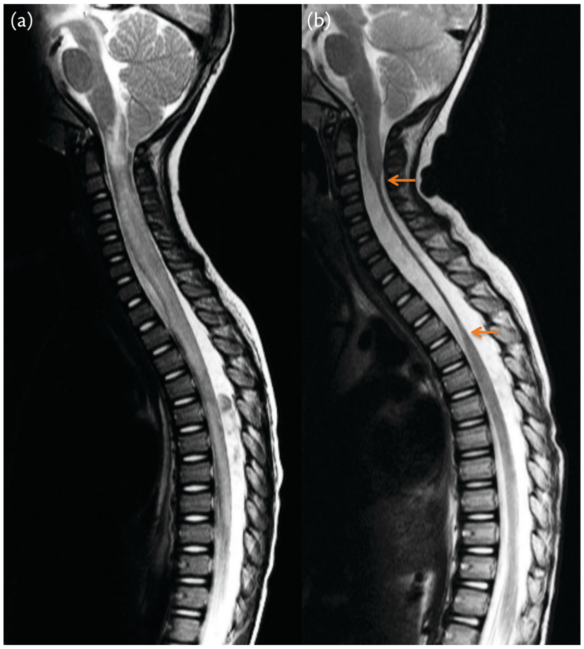

Fig. 30.3 A child with severe transverse myelitis involving the entire spinal cord, who remains quadriplegic. Shown here are T_2-weighted images of the cervicothoracic portion (a) where the lesion begins in the medulla and extends inferiorly; significant cord swelling is also present. (b) At 4 months after presentation, serial MRI demonstrates severe atrophy in the cervicothoracic spinal cord (arrow).

T_2-weighted or fluid attenuated inversion recovery (FLAIR) brain MRI of children with ADEM reveals multiple large (>1–2 cm), bilateral hyperintense lesions that have ill-defined lesion borders and involve the white matter, as well as the deep gray matter, with a predilection for the thalami (Fig. 30.4). Although ADEM is arguably the most inflammatory of all ADS phenotypes, in the authors' experience, gadolinium-enhancing lesions are less commonly seen than what might be expected [25]. One might propose that the degree of blood–brain barrier permeability is less or the permeability time may be longer in ADEM lesions, compared with acute MS lesions in which the blood–brain barrier is readily permeable to gadolinium. The presence of T_1-hypointense lesions (defined as hypointense to cortical gray matter on T_1-weighted MRI), and especially persisting T_1-hypointense lesions (i.e. black holes) are rare in ADEM [25,26]. 'Black holes' that persist on serial T_1-weighted images correlate with focal areas of irreversible neuroaxonal injury on histopathology [27]. On serial MRI, T_2 hyperintense lesions typically rapidly resolve with no new lesion formation and near complete resolution at 3–6 months following ADEM onset.

The ability to distinguish monophasic ADEM from a first attack of MS or NMO has important implications for treatment planning and clinical outcome. In the absence of a specific biomarker to distinguish monophasic inflammatory demyelination from recurrent chronic demyelinating disease, the utility of MRI to distinguish between monophasic ADEM and MS has been investigated. The International Pediatric MS Study Group criteria suggest that, in children with incident ADEM, the diagnosis of MS can be made if the MRI acquired at a second attack meets 2010 McDonald criteria for dissemination in space [1,28]. Based on a retrospective analysis of MRI scans from children with clinically-definite MS and monophasic ADEM, any two of the three following criteria were able to reliably distinguish a first attack of MS from ADEM:

1. Absence of diffuse bilateral pattern.
2. Presence of black holes.
3. Presence of ≥2 periventricular lesions [26,29].

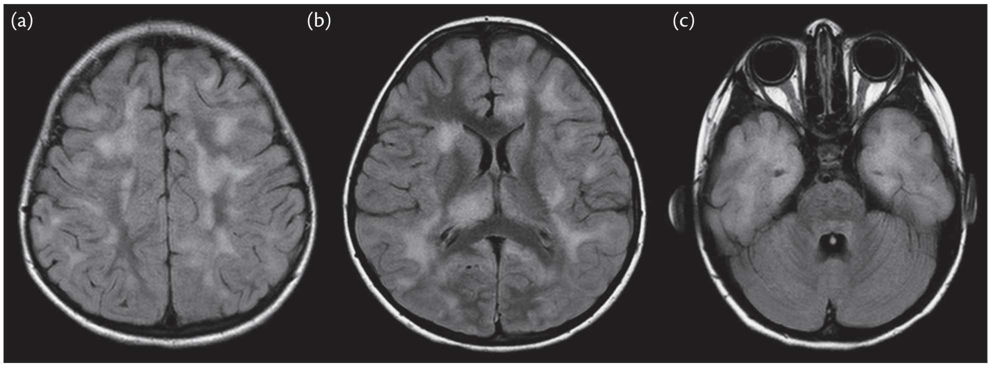

Fig. 30.4 (a-c) Axial FLAIR images of a child with ADEM demonstrate large supratentorial and infratentorial lesions with ill-defined borders throughout the brain parenchyma.

T_2-hyperintense thalamic lesions are associated with a decreased likelihood of MS diagnosis, and are commonly seen in children with monophasic ADEM [25]. T_1-hypointense lesions at the time of the initial ADEM illness are less common in children with monophasic ADEM than those with MS and are a stronger discriminatory feature than thalamic lesions. When T_1-hypointense lesions are present in children with ADEM, they typically resolve within 3 months of presentation, and therefore do not reflect areas of chronic tissue injury [25,26].

Other monofocal and multifocal acute demyelinating syndromes

Children with a monofocal neurological deficit other than ON or TM, such as an internuclear ophthalmoplegia localizing to the brainstem or a cerebellar deficit, may be at the highest risk of MS compared with other ADS phenotypes [25,30,31]. Similarly, multifocal neurological deficits without encephalopathy (e.g. a patient with acute ON who demonstrates brainstem or corticospinal tract abnormalities) are a typical manifestation in patients experiencing a first clinical attack of MS. Application of the 2010 McDonald criteria for MS diagnosis at the time of an initial attack has recently been validated in paediatric ADS, provided that the child does not meet criteria for ADEM [32,33].

Relapsing acute demyelinating syndromes that do not meet criteria for MS

Similar to the rare occurrence of multiphasic ADEM described previously, children presenting with ON or TM may experience recurrence of ON or TM symptoms. In a Canadian prospective cohort of children with ADS, 3 out of 284 had recurrent ON (or chronic relapsing inflammatory optic neuropathy (CRION)) and 2 out of 284 had recurrent TM [25]. In the absence of clinically-silent brain lesions on serial MRI and assuming that children do not meet criteria for NMO, these children are diagnosed with relapsing ADS. It is anticipated that many of these children will ultimately experience clinical features, which will confirm MS, NMO, vasculitis, or other aetiologies. Whether CRION is a distinct inflammatory disease remains to be determined.

Neuromyelitis optica

Neuromyelitis optica is an inflammatory disorder characterized by recurrent demyelination typically restricted to the optic nerve and spinal cord. The distinction between NMO and MS has been debated in the past. However, the NMO IgG biomarker [34] and unique clinical, laboratory, and MRI features lend supporting evidence to suggest NMO is a distinct disease. NMO is typically characterized by simultaneous or a rapid sequential occurrence of ON and TM, and the clinical course may be monophasic (i.e. one attack of ON and one attack of TM without further attacks in either location or elsewhere in the CNS) or relapsing. In children with NMO, a relapsing course has been reported in 53–100% of patients [21,35–37]. Clinical attacks are typically severe and characterized by poor recovery, leading to rapid accrual of disability [36,37].

MRI of children with NMO reveals lesion features similar to that discussed previously for acute ON and isolated acute TM (Fig. 30.5). Considering that in NMO the primary immune target is the astrocytic water channel aquaporin-4, brain lesions tend to be more commonly located in regions in which aquaporin-4 is richly expressed, including the brainstem (area postrema), diencephalon (hypothalamus), and peritrigonal region. Lesion involvement in these regions causes symptoms, such as hiccups, nausea or vomiting, hypersomnolence, narcolepsy, syndrome of inappropriate antidiuretic hormone secretion, or menstrual irregularities. In severe cases, respiratory failure, coma, or death may result [38]. T_2-hyperintense brain lesions occur in 50–100% of children with NMO [21,39], and may be large, ill-defined, and tumefactive in appearance, resembling lesions typical of ADEM (Fig. 30.5).

Multiple sclerosis

Paediatric-onset MS is increasingly being recognized and it is estimated that approximately 2.2–4.4% of all individuals with MS are diagnosed prior to age 18 years [40–44]. While the worldwide incidence of paediatric MS is as yet unknown, an American study recently reported an incidence rate of 0.51 per 100,000 per year [11]. North American and European studies have, however, reported incidence rates for the broader entity of acute CNS demyelination ranging between 0.9 and -1.56 per 100,000 children per year [9–12]. Onset of MS prior to age 10 years occurs in only 17% of all paediatric patients [45]. Gender ratio varies with age; prior to age 10 years, an equal number of boys and girls are affected, but after age 10, a female preponderance emerges, suggesting a possible hormonal or gender-defined influence on MS risk [13,45]. The immunobiology and risk factors, demographic and clinical characteristics, treatment, and physical and cognitive outcomes of

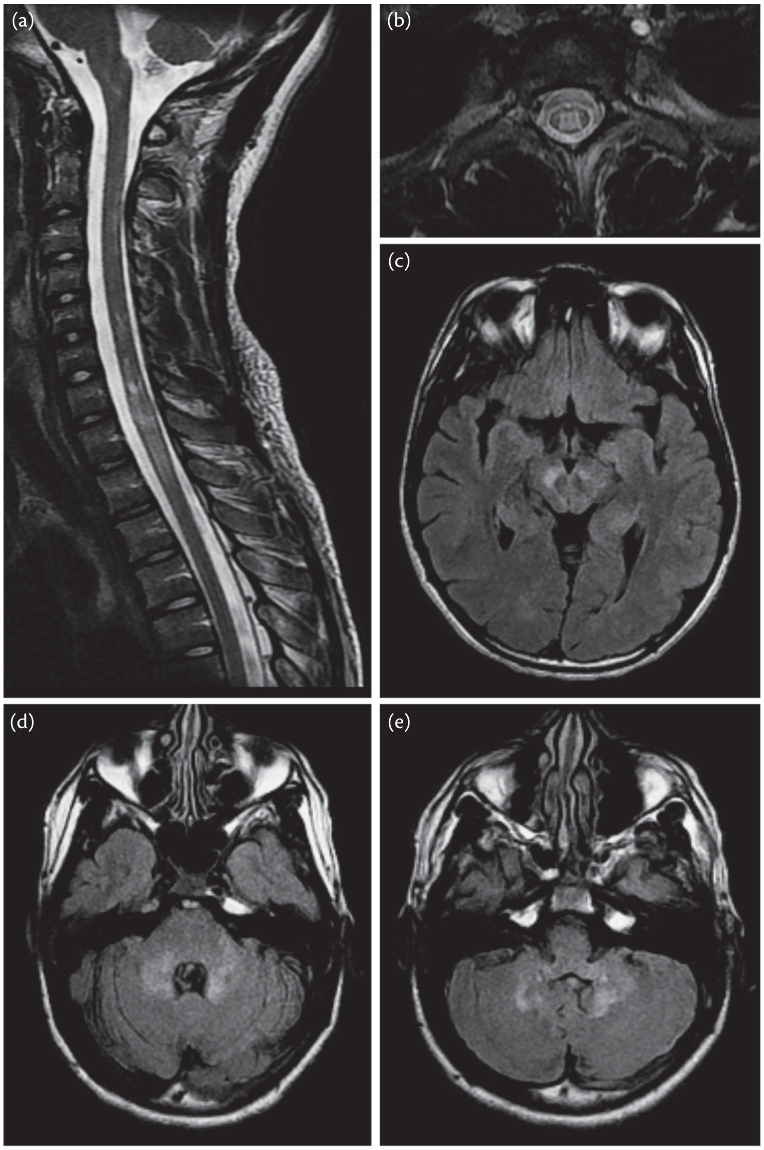

Fig. 30.5 MRI of the brain and spinal cord of a child with NMO at the time of first attack. (a) Sagittal and (b) axial T_2-weighted MRI demonstrates spinal cord oedema and a longitudinally-extensive lesion involving the cervicothoracic region. In the transverse plane, the lesion in centred in the central grey matter. (c–e) Axial FLAIR images of the brain demonstrate lesions located in regions typical for NMO, namely, the midbrain, cerebellar peduncles, cerebellum, and area postrema.

paediatric-onset MS have been extensively reviewed elsewhere [13, 46–48].

Typical brain lesion features on T_2-weighted MRI

MS lesions appear as focal ovoid areas of hyperintensity on T_2-weighted or FLAIR images, ranging in diameter from 3 mm (conventional definition for the minimal size of a lesion) to more than 1 cm (Fig. 30.6). MS lesions in both children and adults are typically located in the periventricular white matter; at the boundary between white matter and cortical gray matter (i.e. juxtacortical); and within the corpus callosum, brainstem, or cerebellum [25,49]. Supratentorial T_2 lesions have the highest probability of being located in the occipital periventricular white matter followed by frontal periventricular white matter, while cortical and deep gray matter lesions are less frequently detected (Fig. 30.7) [50]. One report has described T_2-weighted *hypo*-intensity within the deep gray matter structures, particularly the caudate head, of children with MS, and may suggest abnormal iron deposition [51]. The presence of tumefactive lesions (defined as lesions >2 cm in diameter) has been reported in children with ADS subsequently diagnosed with MS [52]. Given that the appearance of solitary tumefactive demyelination may resemble malignancy, biopsy may be required for accurate diagnosis in situations of a single tumefactive lesion [53].

Lesion features on T_1-weighted pre- and post-contrast MRI

Contrast-enhancement is indicative of increased blood–brain barrier permeability and corresponds to active immune cell transmigration into the CNS. As such, T_1-weighted gadolinium-enhanced MRI permits differentiation between active or newly-formed lesions and longer standing lesions. The presence of gadolinium-enhancing

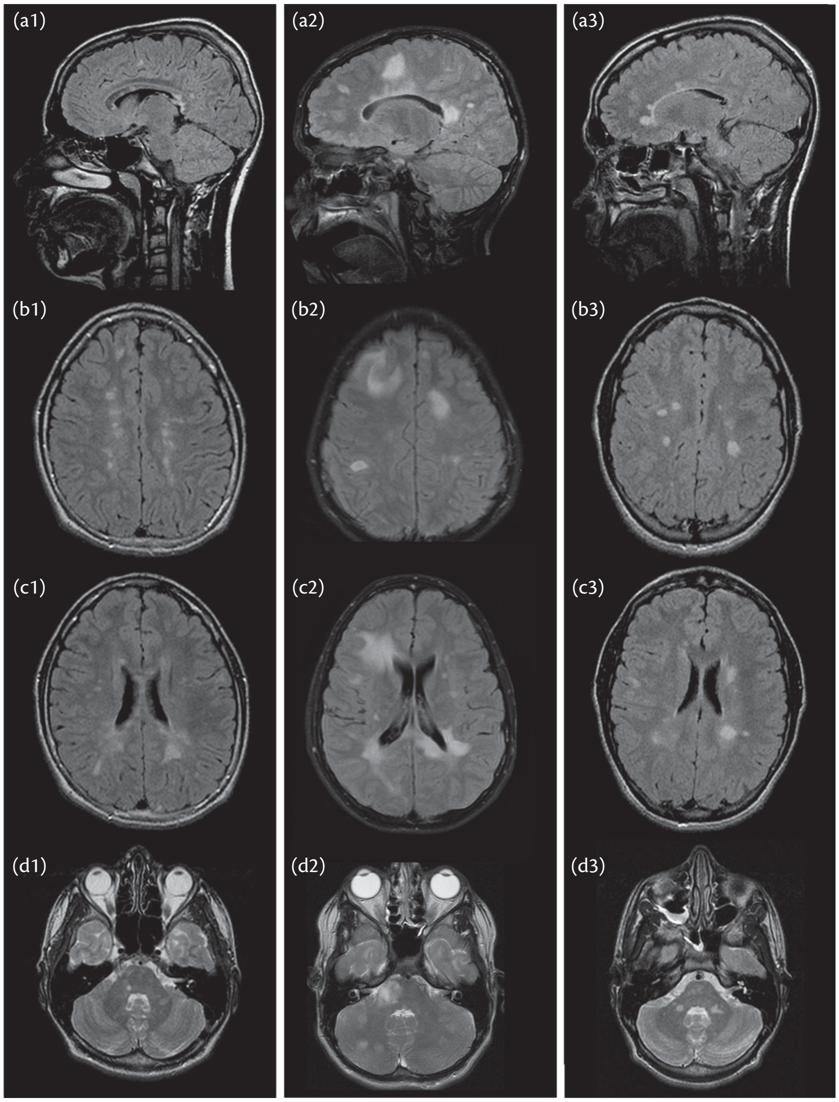

Fig. 30.6 Sagittal (row A) and axial (rows B and C) FLAIR and axial T_2-weighted (row D) images of children with MS. Images were acquired 4 months following onset (Column 1) and at the time of onset (Column 2) from two boys, both presenting with multifocal neurological deficits (without encephalopathy). Column 3 contains images acquired from a boy 6 months after presenting with brainstem symptoms.

Reproduced from Verhey LH, Shroff M, and Banwell B. (2013). Paediatric multiple sclerosis: pathobiological, clinical, and magnetic resonance imaging features. *Neuroimaging Clinics of North America*, **23**, 227–43. Copyright (2013), with permission from Elsevier.

lesions is highly predictive of future clinical relapse and was thus incorporated into the 2010 McDonald criteria as a key feature of MS [28]. Lesions with enhancement demonstrate either enhancement of the entire lesion, or more commonly a ring-like enhancement pattern (Fig. 30.8a–c). Prospective serial studies have shown that a newly-enhancing lesion remains enhancing for an average of three weeks [54,55], but the duration may be shorter in the context of methylprednisolone treatment or much longer in individual patients. Given that gadolinium-enhancing lesions capture subclinical activity with higher frequency than clinical relapses, gadolinium-enhancing lesion count is also used as an *in vivo* marker of inadequately suppressed inflammatory activity in treatment trials.

A subset of T_2 lesions appear hypointense on T_1-weighted MRI. T_1-hypointense lesions may initially enhance with gadolinium; 'black holes' are those T_1-hypointense lesions that persist on serial MRI. T_1-hypointense lesions are present in children with MS (Fig. 30.8d–f) [49], and are predictive of a subsequent MS diagnosis in children with ADS [25], suggesting that the neurodegenerative aspect of MS pathobiology occurs early in the disease course.

The conspicuity of T_1-hypointense lesions varies with MRI parameter settings. Black holes were initially defined as T_1-hypointense based on the contrast of spin echo images. Currently, gradient echo MRI is widely used given its advantages over spin echo (higher signal-to-noise ratio in a shorter scan time compared with spin echo and high tissue contrast necessary for performing brain volume analyses). There is a concern that, because of the intrinsic higher contrast of the gradient-echo MRI compared with spin echo sequences, gradient echo images may yield detection of a greater number of T_1-hypointense lesions, some of which may not represent regions of chronic tissue injury. To mitigate this potential bias, the TR on a high resolution, high tissue contrast gradient-echo T_1-weighted sequence

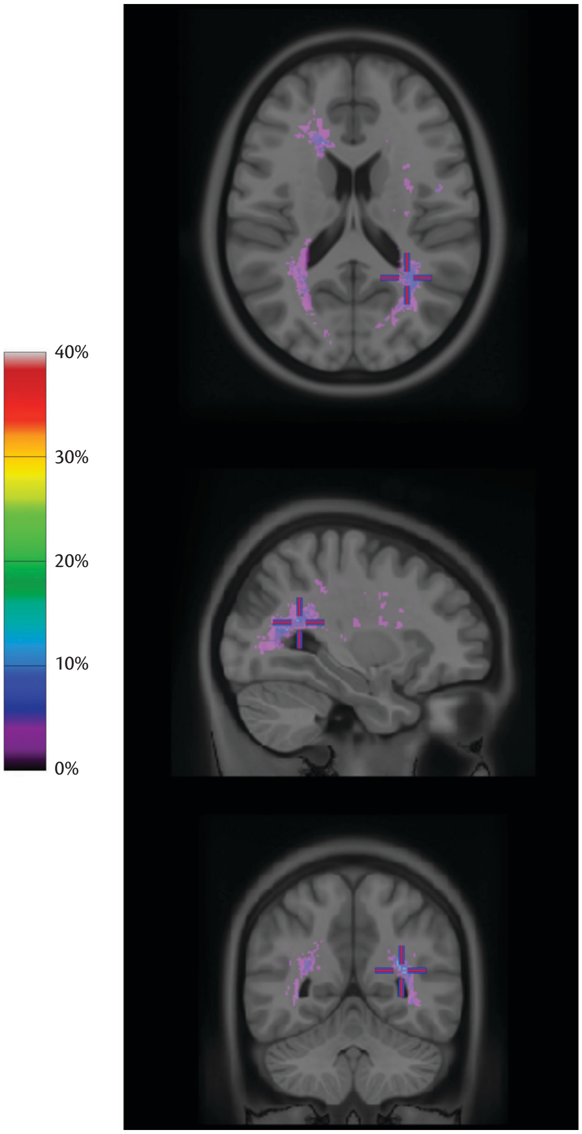

Fig. 30.7 T_2 lesion probability map of children with MS. The highest probability for supratentorial lesion accrual is in the occipital periventricular white matter followed by the frontal periventricular white matter.

Reproduced from Verhey LH, and Sled JG. (2013). Advanced magnetic resonance imaging in pediatric MS. *Neuroimaging Clinics of North America*, **23**, 337–54. Copyright (2013), with permission from Elsevier. Image provided courtesy of DL Collins, PhD, and B Aubert-Broche, PhD, McConnell Brain Imaging Center, Montreal Neurological Institute, McGill University, Montreal, Canada.

can be lengthened from a typical 20 to 30 ms. This provides a gradient echo T_1-weighted image with a muted contrast that is similar to spin-echo images, permitting evaluation of T_1 hypointensity according to the definition that was based on spin-echo images [56].

MRI features in pre-pubertal children

In children who present with a first attack of MS prior to age 10 years, MRI may show large confluent T_2 lesions with poorly defined borders [57]. In fact, the lesion features bear a resemblance to that seen in children with monophasic ADEM. On serial MRI, these large poorly defined lesions disappear, and over time, children develop a lesion pattern more typical of that seen in adolescents and adults with MS.

Spinal cord MRI lesion features

The frequency of clinically-silent spinal cord lesions in paediatric-onset MS is not known, but will be important in determining the added value of spinal cord MRI for paediatric MS diagnosis, given that the presence of clinically-silent spinal cord lesions is a component of the dissemination in space criteria of the recently revised McDonald criteria [28].

The features of spinal cord lesions in children with MS resemble that of adults. In a group of children with established MS who had spine MRI due to inter-current spinal cord symptoms or to aid in MS diagnosis, the median lesion count was one (range 1–6 lesions) with a predilection for the cervical region [16]. The same study found that lesions typically span less than three vertebral body segments in length, and involved only a portion of the transverse diameter with a preference for the posterior cord.

Routine spinal cord MRI in children is challenged by the length of time required to image both the brain and spinal cord, difficulty that children have in lying still for a prolonged duration of time without sedation or anaesthesia, and the poor imaging resolution as a result of a small spinal cord coupled with cardio-thoracic motion and cerebrospinal fluid flow pulsatility.

Role of MRI in MS diagnosis

Table 30.2 summarizes the MRI diagnostic criteria used in paediatric-onset MS, as well as MRI parameters predictive of MS in children with ADS.

Based on the recently revised International Pediatric MS Study Group consensus criteria [1], the 2010 McDonald criteria [28] are recommended for diagnosis of paediatric MS, with their cautionary application in younger children and with the exception that an initial attack meeting criteria for ADEM should not be evaluated using the 2010 criteria.

The 2010 McDonald criteria have been formally evaluated in children [30,32,33,58,59]. Compared with the 2001 and 2005 McDonald criteria, the 2010 dissemination in space (DIS) criteria are more sensitive [34,60]. For children older than 11 years of age at onset with non-ADEM ADS presentations, the sensitivity of the 2010 McDonald DIS and dissemination in time (DIT) criteria reported in an Austrian–German study was 84% [60], and 100% in a Canadian study [31]. In children with a non-ADEM ADS presentation who were less than 11 years of age, the sensitivity is lower (67%) [32]. In the Canadian cohort of 212 children with ADS, none of the 50 children with ADEM met clinical criteria for MS, but 10 met 2010 McDonald DIS and DIT criteria [32], reinforcing the 2010 McDonald Panel consensus that the criteria are not recommended for application in children with ADEM.

Comparison of MRI lesion features of adult- and paediatric-onset MS

Contrary to what may be expected, the assumed short duration of subclinical disease activity in children with MS does not limit the accrual of lesions, leading to a similar MRI disease burden when compared with adults [60,61]. In children with MS, T_2, and contrast-enhancing lesion volumes are similar to those of adult patients matched for disease duration, and the number of large T_2 lesions on initial MRI is higher in children compared with adults [61]. This finding suggests that lesion accrual does not require a lengthy subclinical disease duration. A greater frequency of contrast-enhancing

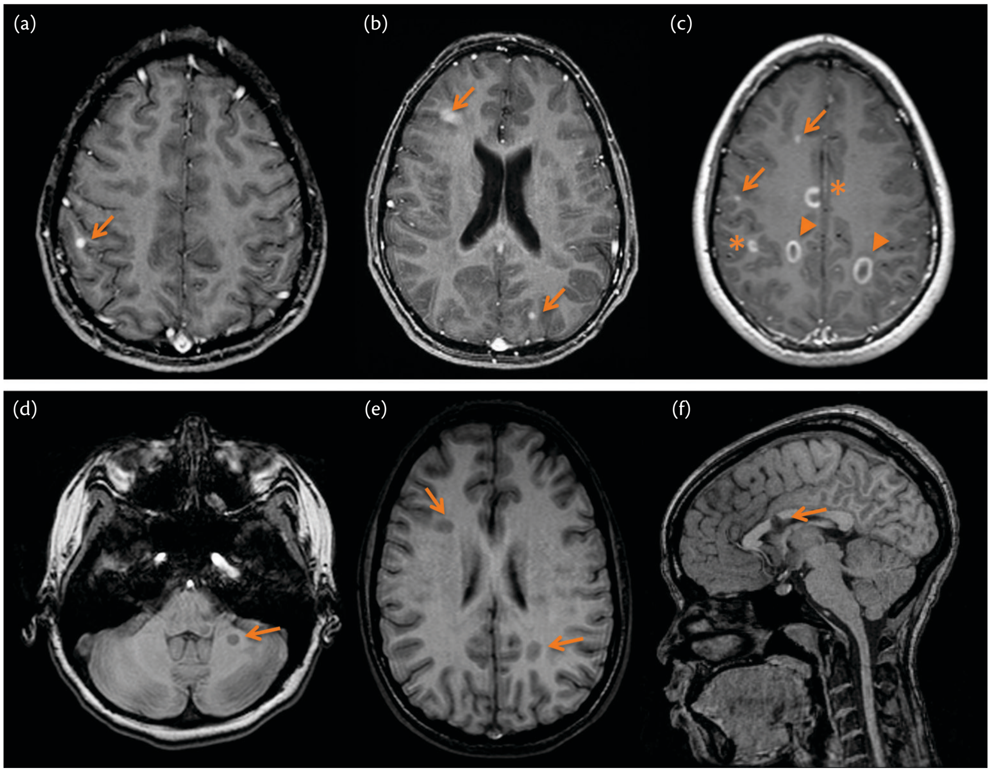

Fig. 30.8 (a–c) Axial post-gadolinium T_1-weighted images of two children with MS demonstrating the different patterns of lesions enhancement. Focal enhancing lesions are depicted by arrows in (a–c). Closed ring-like enhancing lesions are denoted by arrowheads in (c), and open ring-like enhancing lesions by asterisks. T_1-weighted images of three children with MS showing T_1 hypointense lesions (arrows) in the cerebellar (d) and cerebral (e) white matter, and in the corpus callosum (f).

Reproduced from Verhey LH, Shroff M, and Banwell B. (2013). Pediatric multiple sclerosis: pathobiological, clinical, and magnetic resonance imaging features. *Neuroimaging Clinics of North America*, **23**, 227–43. Copyright (2013), with permission from Elsevier.

lesions in children with MS compared with adults has been reported [61], suggesting that disease activity in the early phase may be higher in paediatric-, compared with adult-onset MS. However, the variable time from onset of clinical attack probably influences these findings. To properly assess whether children have a more active disease than adults, the frequency of contrast-enhancement in paediatric MS needs to be evaluated in the context of rigorous clinical trials, as has been done for adult-onset MS.

Primary angiitis of the central nervous system

There are three subtypes of childhood PACNS:

1. Non-progressive large-medium vessel cPACNS (angiography positive).
2. Progressive large-medium vessel cPACNS (angiography positive).
3. Small vessel cPACNS (angiography negative) (Figs 30.9 and 30.10) [62,63].

A recent review has been published elsewhere that extensively outlines the pathobiology, diagnosis, and clinical, laboratory, and conventional angiography features of primary CNS vasculitis [64].

Non-progressive cPACNS

MRI of children with non-progressive cPACNS (NP-cPACNS) typically demonstrates unilateral ischaemic lesions within the large vessel territories, with a predilection for the basal ganglia [65]. Vessel wall thickening and contrast enhancement due to inflammatory infiltrate in the vessel wall is present on gadolinium-enhanced magnetic resonance angiography (MRA) [66], and may persist for up to 6 weeks following diagnosis.

Progressive cPACNS

Parenchymal lesions in children with progressive cPACNS (P-cPACNS) are ischaemic or inflammatory in nature, and involve more than one vascular territory. In contrast to NP-cPACNS, lesions are located bilaterally and are asymmetric in children with P-cPACNS.[67] Vessel wall MRI is helpful in ascertaining with greater precision than is possible on MRA the specific region of the vessel segment affected. Contrast-enhancement may be present in segments of the affected vessel; it is yet unclear whether the intensity of enhancement is associated with the degree of inflammatory activity in the vessel wall. The yield of vessel wall imaging is highest when applied to large vessels, and is predicated on an understanding of which vessel may be affected, as determined on MRA.

Small vessel cPACNS

In isolated small vessel cPACNS (SV-cPACNS), MRA is normal. Differentiating SV-cPACNS from other inflammatory demyelinating disorders (such as ADEM or a first attack of MS) at the time of acute presentation remains a clinical challenge. Accurate and prompt diagnosis is important because, as mentioned at the outset of this chapter, the clinical course, prognosis, and treatment

Table 30.2 Diagnostic criteria and predictive parameters for paediatric-onset MS

	Paediatric-onset MS	**Adult-onset MS**
McDonald Criteria for MS diagnosis		
Polman et al. (2005) [98]		*DIS** Three of the following: 1. ≥9 T_2 lesions *or* ≥ 1 contrast enhancing lesion 2. ≥1 T_2 infratentorial lesion 3. ≥1 T_2 juxtacortical lesion 4. ≥3 T_2 periventricular lesions *DIT* One of the following: 1. ≥1 contrast-enhancing lesion at least 3 months after clinical onset 2. A *new* T_2 lesion at any time compared with a reference scan acquired at least 30 days after clinical onset
Polman et al. (2011) [28]	*DIS* Presence of ≥1 clinically silent T_2 lesion in at least two of the four following CNS regions: 1. Periventricular 2. Juxtacortical 3. Infratentorial 4. Spinal cord *DIT* One of the following: 1. A *new* T_2 or contrast-enhancing lesion on any serial scan with respect to a previous scan 2. Simultaneous presence of asymptomatic contrast-enhancing and non-enhancing lesions at any time	
MRI Criteria to distinguish paediatric MS from relapsing non-demyelinating disorders		
Callen et al. (2009) [49]	Two of the following: 1. ≥5 T_2 lesions 2. ≥2 T_2 periventricular lesions 3. ≥1 T_2 brainstem lesion	
MRI Criteria to distinguish first attack of paediatric MS from monophasic ADEM		
Callen et al. (2009) [26]	Two of the following: 1. Absence of a diffuse bilateral T_2 lesion pattern 2. Presence of black holes 3. ≥2 T_2 periventricular lesions	
MRI predictors of MS in children with ADS		
Mikaeloff et al. (2004) [99]	Two of the following: 1. T_2 lesions perpendicular to the long axis of the corpus callosum 2. Sole presence of well-defined T_2 lesions	
Verhey et al. (2011) [25]	Two of the following: 1. ≥1 T_2 periventricular lesion 2. ≥1 T_1-hypointense lesion	
Tantsis et al. (2013) [30]	Presence of one of the following: 1. Corpus callosal lesion(s) 2. Both poorly and well-defined lesions 3. Contrast-enhancing lesions	

*A contrast-enhancing spinal cord lesion is equivalent to an enhancing lesion in the brain; individual spinal cord lesions and brain lesions can together contribute to the requirement of ≥ 9 T_2 lesions.

Abbreviations: DIS, dissemination in space; DIT, dissemination in time; ADEM, acute disseminated encephalomyelitis.

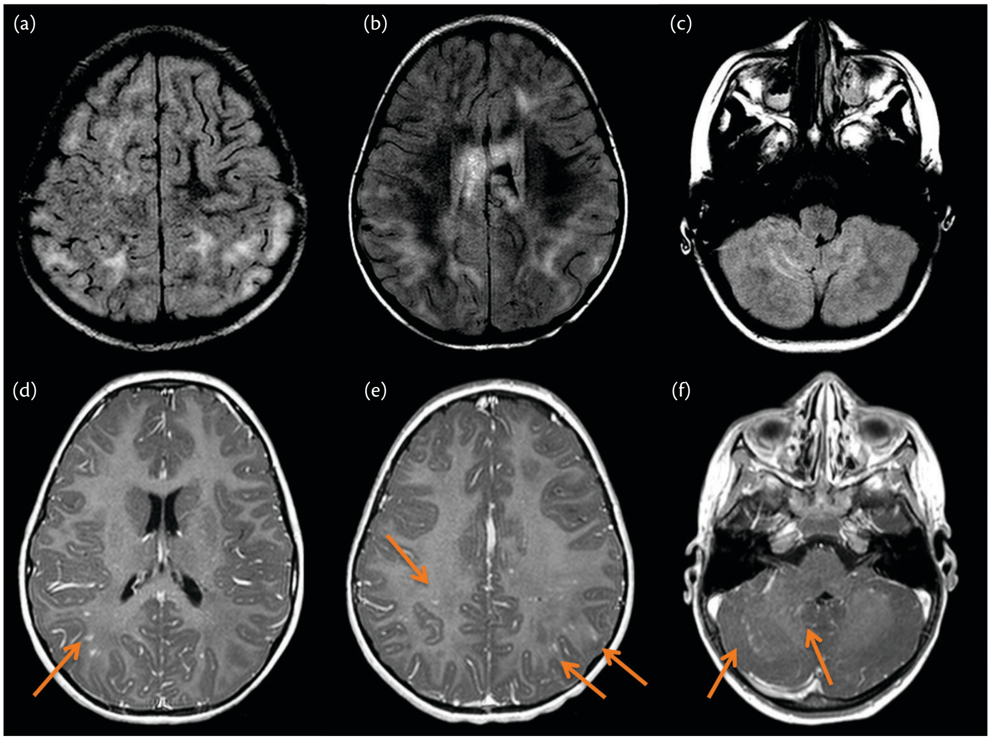

Fig. 30.9 MRI acquired at onset in a child diagnosed with SV-cPACNS. FLAIR images (a–c) reveal hyperintense lesions involving the periventricular and subcortical white matter throughout the brain parenchyma, including involvement of the body of the corpus callosum, inferior aspect of the cerebellar hemispheres and superior cerebellar peduncle. T_1-weighted post-contrast MRI (d–f) shows foci of enhancement in the region of the cerebellar tonsils, inferior right cerebellar hemisphere, and subcortical white matter of the occipital and parietal lobes bilaterally. Time of flight MRA of the main vessels was normal.

decisions differ between children with SV-cPACNS and inflammatory demyelination. Given that no absolute biomarker exists, diagnosis based on elective brain biopsy targeting MRI lesional tissue is essential.

MRI scans of children with SV-cPACNS are typically abnormal at the time of presentation [65]. Lesions are hyperintense on T_2-weighted or FLAIR images. Lesional contrast enhancement is rare. Leptomeningeal enhancement, though rare, is a relatively specific MRI finding of SV-cPACNS [65], as it is not present in other cPACNS subtypes or inflammatory demyelinating disease. Due to the ubiquitous presence of the small vessels within the brain and spinal cord parenchyma, essentially any pattern of lesion distribution is possible within the brain and spinal cord of children with SV-cPACNS, although a predilection for the juxtacortical white matter and cortical gray matter may be present [8].

Magnetic resonance imaging features of other central nervous system inflammatory disorders

Neuro-Behçet's disease

Neuro-Behcet's disease is exceptionally rare in children. The primary pathology is that of small vessel vasculitis, and thus clinical presentation includes cerebral venous thrombosis, intracranial hypertension and early onset of cognitive impairment [67,68]. Children more frequently have a solitary lesion in the initial phase, and only later do multifocal lesions form involving other regions of the neuroaxis [67]. On MRI of the brain and spinal cord, lesions are hypointense on T_1-weighted scans and hyperintense on T_2-weighted images. Lesional gadolinium enhancement may also be present. Spinal cord lesions are typically focal (involving ≤3 vertebral spinal segments), and may be associated with oedema [67]. Common sites of lesion involvement include the mesodiencephalic junction, cerebellar peduncles, pons, medulla, basal ganglia, internal capsule, cerebral hemispheres (with no increased proclivity for the periventricular region), and optic nerves.

Neurosarcoidosis

Neurosarcoidosis is also rare in children. Clinical features are variable and include encephalopathy, hypothalamic dysfunction, mass-like brain lesions, cranial neuropathies, and uveoparotid fever [69]. MRI features of neurosarcoidosis are variable. Lesional enhancement may be present and meningeal enhancement should always prompt consideration of neurosarcoidosis. T_2-weighted hyperintense periventricular lesions may resemble those of MS lesions. Diagnosis is aided by detection of angiotensin-converting enzyme in serum, by the presence of lymphadenopathy detected clinically or by chest imaging, and often requires tissue diagnosis.

CNS lupus

Children with system lupus erythematosus (SLE) who have CNS involvement typically present with psychiatric symptoms, although headache, cognitive impairment, cerebrovascular insult, seizures, chorea, or spinal cord involvement (lupus myelitis) also occur. Approximately 30% of children with SLE present with

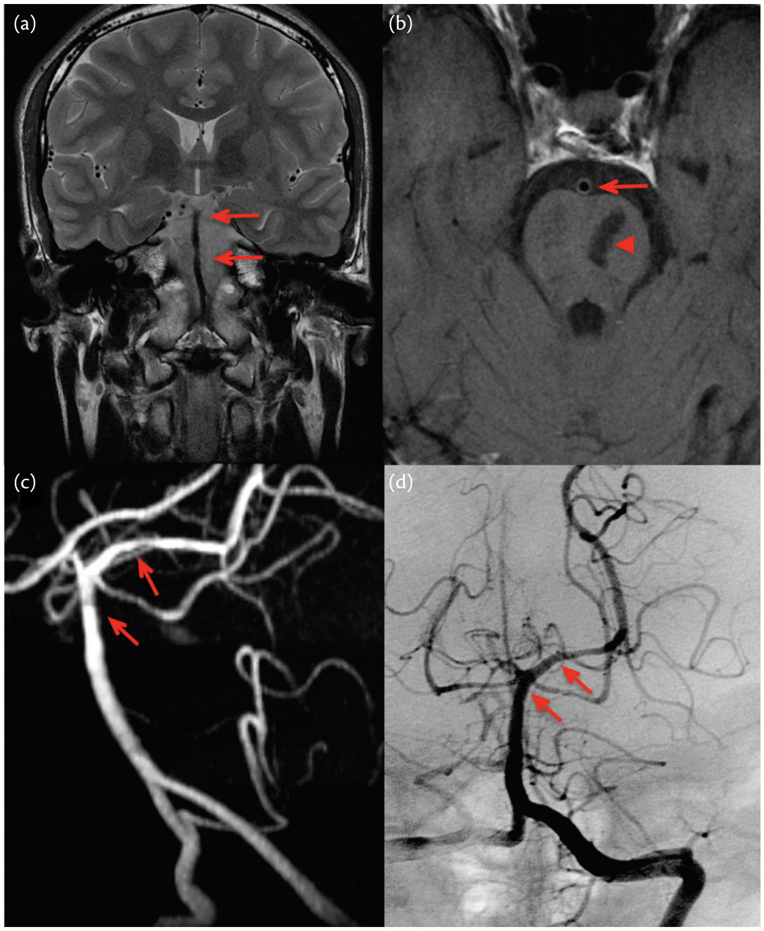

Fig. 30.10 Magnetic resonance images and digital subtraction angiography (DSA) of an adolescent boy with medium-large vessel cPACNS. (a) Coronal T_2-weighted FSE imaging shows irregular calibre and narrowing of the basilar artery between the arrows. (b) On axial T_1-weighted post-contrast imaging, a region of T_1-hypointensity (arrowhead) is present in the left pons representing an infarct. The wall of the basilar artery shows circumferential gadolinium enhancement (arrow). (c) Decreased calibre (arrows) is present in the basilar artery and posterior communicating artery on MRA. (d) DSA confirms the decreased vessel calibre in the basilar artery and posterior communicating artery (arrows) that were seen on MRA.

Images courtesy of Dr Manohar Shroff, Division of Pediatric Neuroradiology, Hospital for Sick Children, Toronto, Canada.

neuropsychiatric symptoms, only a fraction of whom will later develop other systemic symptoms [70]. MRI is normal in approximately 50% of children with clinical CNS lupus [70]. In those with an abnormal brain MRI, hyperintense T_2 lesions are present in the subcortical and periventricular white matter. Lesions may enhance on post-contrast T_1-weighted MRI.

Insights gained from magnetic resonance imaging research in paediatric-onset multiple sclerosis

The study of paediatric-onset MS provides a unique opportunity to explore the inciting features of MS pathobiology, given that the onset of disease symptoms occurs closely in time to the inciting events thought to be involved in disease initiation. To this end, MRI research in paediatric MS provides a unique opportunity to study early inflammatory and neurodegenerative processes of the disease *in vivo*.

Over the past decade, advanced MRI techniques have been applied in children and adolescents with MS with the goal of better understanding the pathological substrates of physical and cognitive impairment, that are not fully appreciable from studies correlating T_1 and T_2 lesion burden with clinical measures. At present, these advanced MRI techniques are not routinely available in the clinical setting, as they require standardized acquisition, robust image processing pipelines, and reference data from control populations.

In this final section, findings from studies applying cortical imaging techniques, volumetry, magnetization transfer (MT) and diffusion tensor (DT) MRI, ^{1}H-magnetic resonance spectroscopy (^{1}H-MRS), and functional MRI (fMRI) will be reviewed.

Cortical lesion detection in children with MS

Histopathological studies in adult MS have demonstrated that a substantial proportion of focal cerebral MS lesion load is located within cortex or at the juxtacortical margin [71,72]. Quantification of cortical disease in paediatric-onset MS will determine whether cortical lesions occur early in the disease, or as a later phenomenon, and will provide important insight on of the relative degree to which cognitive and physical impairments can be explained by cortical pathology.

To date, only one study has evaluated the frequency and type of cortical lesions in children with MS [73]. Compared with 66% of adult MS patients, only 8% of paediatric-onset patients had cortical lesions as detected on double inversion recovery images. While the number and volume of white matter lesions did not differ between children and adults with MS, mean cortical lesion count in paediatric MS patients was 0.1, compared with 2 lesions in adult patients. Additional studies are required to validate these findings. Future work should also evaluate cortical thickness to determine whether cortical thinning may be the more prominent feature, as opposed to or in conjunction with cortical lesion accrual, in children with MS.

Brain volumetry

Several cross-sectional studies have been conducted to evaluate global and regional brain volume changes in children with MS. When compared with healthy matched controls, children with MS have reduced gray matter volume in the thalami [60,74,75]. T_2 lesion load is associated with thalamic volume [50,74], suggesting that focal parenchymal white matter lesions may cause retrograde or anterograde transynaptic degeneration of neuronal connections that relay through the thalamus. Using deformation-based morphometry to evaluate the spatial distribution of brain volume loss in children with MS in a cross-sectional manner, one study further delineated the pathology of the thalamus, and reported significant volume reductions in the right and left thalami, specifically in the pulvinar bilaterally and right anterior nucleus; as well, splenium and globus pallidus volume was lower in paediatric-onset MS patients compared with healthy controls (Fig. 30.11) [50].

Compared with healthy individuals, global brain volume is significantly reduced in children with MS, and after correcting for global brain volume, an even greater reduction in thalamic volume has been observed [75]. Reduced skull size in children with MS compared with healthy controls has also been observed [75]. Given that skull size is largely driven by brain growth during the first 10 years following birth [76], these findings suggest that children with MS demonstrate a failure of age-expected growth. Whether this is indeed the case, and whether atrophy occurs in addition to this failure of brain and skull growth will require volumetric analyses of longitudinal datasets.

Studies correlating cognitive function with regional brain volume in children with MS support the notion that the neurodegenerative component of MS pathobiology is operative early in the disease and that immune-mediated damage of immature neural networks may have deleterious consequences on cognitive function. Thalamic volume and corpus callosal area are positively correlated with global intellectual function, mental processing speed, and confrontation naming [77,78]. With regards to memory performance in children with MS, hippocampal volume is positively correlated with word learning, and thalamic volume is modestly associated with visual recognition [78]. Impairment in executive function, as measured on the 'initiate', 'working memory', and 'plan/organize' scales of the Behaviour Rating Inventory of Executive Function, is associated with lower normalized brain volume, frontal lobe volume, and thalamic volume [79].

Magnetization transfer MRI

The application of MT MRI to evaluate microstructural tissue abnormalities in children with MS is limited to three studies [60,74,80]. In one study, no difference in average MT ratio (MTR) or histogram peak height was found in the normal appearing brain tissue or cervical spinal cord of children with MS compared with matched healthy controls [81]. In a follow-up study by the same authors, average MTR and histogram peak height were similar in both the normal appearing white matter (NAWM) and normal

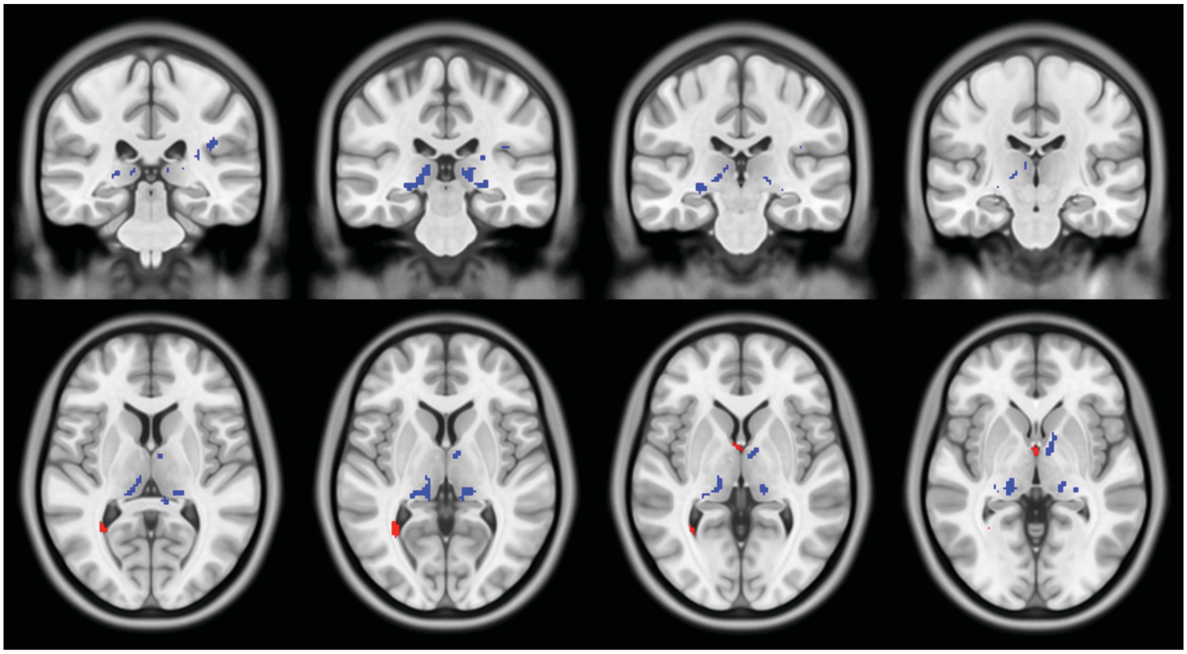

Fig. 30.11 Clusters of significant tissue loss (blue) and expansion (red) in children with MS compared with age- and sex-matched healthy controls ($p < 0.05$, corrected for multiple comparisons).

Reproduced from Verhey LH, and Sled JG. (2013). Advanced magnetic resonance imaging in pediatric MS. *Neuroimaging Clinics of North America*, **23**, 337–54. Copyright (2013), with permission from Elsevier. Image provided courtesy of DL Collins, PhD, and B Aubert-Broche, PhD, McConnell Brain Imaging Center, Montreal Neurological Institute, McGill University, Montreal, Canada.

appearing grey matter (NAGM) between children with MS compared with matched controls [80]. The final study compared MTR values between adult patients with paediatric-onset MS and adults with adult-onset disease; MTR was lower within lesions and within NAWM and NAGM of the adult patients with paediatric-onset disease suggesting that a longer disease duration may negatively impact tissue microstructure [60].

Diffusion tensor MRI

The earliest DTI studies in the context of paediatric-onset MS showed that mean diffusivity (MD) is higher and fractional anisotropy (FA) is lower in the NAWM of children with MS when compared with healthy individuals [80–82]. Compared with adults with a first attack of CNS demyelination, FA and MD of the NAWM, NAGM, or lesions in children with acute demyelination do not differ [82]. However, adults with relapsing-remitting MS have higher MD values within lesions and the NAGM compared with paediatric relapsing-remitting MS patients.

Using a tract-based approach to characterize pathway diffusion abnormalities, it has been shown that mean apparent diffusion coefficient (ADC) values are higher and FA values are lower within the lesional corpus callosum, posterior limb of the internal capsule, and long association fibres in children with MS compared with healthy individuals [83].

Correlations between DTI parameters and cognitive function can provide important information about the functional consequence of loss of microstructural integrity in children with MS. Processing speed is faster in children with higher lobar NAWM FA values, and this effect is particularly prominent in the right hemisphere [84]. Faster processing speed as assessed by the Symbol Digit Modalities Test is also correlated with higher FA and lower MD in the genu, whereas faster visual matching performance is associated with higher FA and lower MD in all corpus callosal regions [84]. Arithmetic ability is positively associated with corpus callosal, and right frontal and parietal lobe FA values [85].

Taken together, disruption of normal white matter structure occurs early in the MS disease course and has important functional consequences.

^{1}H-magnetic resonance spectroscopy

In NAWM of children with MS, the N-acetyl aspartate (NAA)/creatine (Cr) ratio is reduced compared with healthy children (Fig. 30.12), suggesting decreased neuroaxonal integrity due to decreased axonal density or atrophy. Lesional NAA and Cr resonances are decreased and choline (Cho) and myo-inositol resonances are increased in children with MS compared with healthy individuals [86]. ^{1}H-MRS of children with MS may reveal a citrulline peak in both NAWM and T_2 lesions [87], providing support for the hypothesis that citrullination of myelin basic protein may predispose the white matter to demyelination. The ^{1}H-MRS spectrum of children with monophasic ADEM may have a reduced myoinositol/Cr ratio [88], contrasting with an increased intralesional myoinositol/Cr ratio that has been reported in MS patients [89], suggesting that reduced myoinositol may represent a marker of ADEM.

Functional MRI

Paediatric-onset MS patients may have an increased capacity for brain network reorganization compared with adults with MS. In a

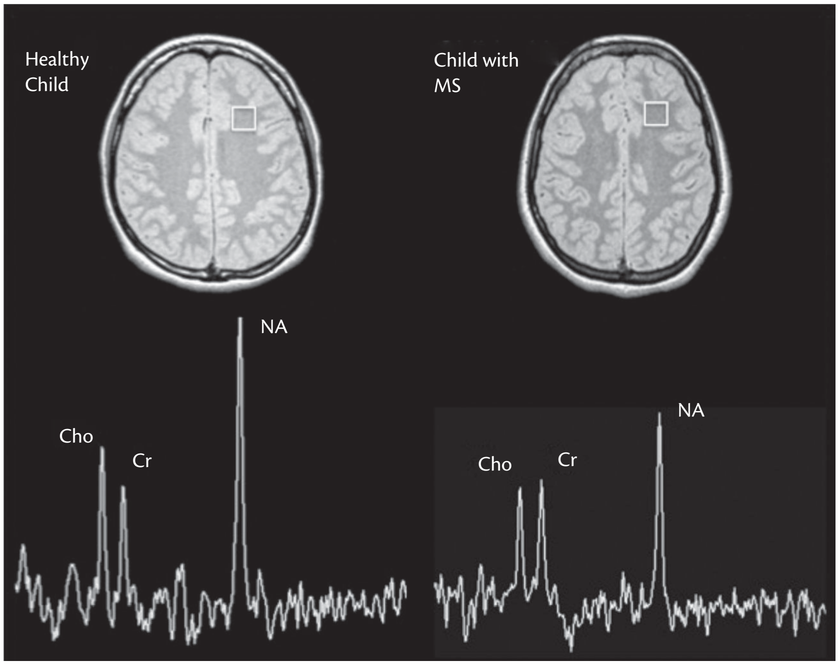

Fig. 30.12 ^{1}H-MRS resonances demonstrating a reduced NA/Cr ratio in the left frontal NAWM of child with MS compared with a healthy child. The NA peak includes methyl resonances from N-acetyl groups of NAA and NAAG. The Cr resonance includes creatine and phosphocreatine. The Cho peak includes methyl resonances of all choline-containing compounds (choline, phosphocholine, glycerphosphocholine, and betaine).

Reproduced from Verhey LH, and Sled JG. (2013). Advanced magnetic resonance imaging in pediatric MS. *Neuroimaging Clinics of North America*, **23**, 337–54. Copyright (2013), with permission from Elsevier. Image provided courtesy of S Narayanan, PhD, McConnell Brain Imaging Center, Montreal Neurological Institute, McGill University, Montreal, Canada.

study comparing the movement-associated pattern of cortical activations and motor network connectivity between children with MS and matched healthy individuals, increased activation was observed in the contralateral sensorimotor cortex, which was correlated with T_2 lesion volume [90]. Increased contralateral activation may suggest adaptation to network disruption in MS patients. When compared with controls, children with MS in the study demonstrated reduced network connectivity between the left primary sensorimotor cortex and left thalamus, left insula and left secondary sensorimotor cortex, supplementary motor area and left secondary sensorimotor cortex, left thalamus and left insula, and left thalamus and left secondary somatosensory cortex. The authors reporting these findings speculated that this suppressed connectivity may represent a functional reserve which may be upregulated when structural damage occurs in other brain regions [90].

That effective connectivity is similar between children with MS and matched healthy individuals suggests that cortical plasticity may be preserved in children with MS [91]. Effective intra- and inter-hemispheric motor network connectivity is up-regulated in adults with a first attack of CNS demyelination and more markedly so in adults with MS, compared with children with MS, and these connectivity changes are associated with corpus callosal and corticospinal tract microstructural changes as measured by MD and FA [91]. Incremental recruitment of networks suggests that plasticity may deplete over time, and after a critical threshold, manifest as physical or cognitive disability.

Magnetic resonance imaging surrogate endpoints of disease activity in paediatric multiple sclerosis treatment trials

Given the recent mandate from the European Medicines Agency, and the Food and Drug Administration in the United States, all newly-emerging therapies require a paediatric investigation plan. Therefore, paediatric MS treatment trials are currently being planned and will soon be launched, but data on appropriate trial endpoints and required sample sizes to inform on trial design are lacking (discussed in [7]). Longitudinal data on relapse rate, as well as new T_2 and contrast-enhancing lesion formation in children with MS are needed to evaluate the utility of these indices as primary and secondary endpoints in phase II and III treatment trials. Adequate sample sizes will only be achievable through multi-national collaboration. Standardization of MRI acquisition and reporting will be important to permit comparison of data across centres. To this end, a standardized MRI scoring tool[94] as well as an MRI acquisition protocol [56] for application in paediatric CNS demyelinating disorders have recently been proposed and require validation, as well as evaluation for clinical utility by other centres.

Conclusion

Paediatric primary CNS inflammation represents a spectrum of disorders in which outcome and the degree of neurological recovery are variable. Children may experience a monophasic illness and regain normal function or may be left with profound neurological impairment, or may experience an attack of acute CNS inflammation as a first episode of a chronic relapsing disease. MRI studies have now provided evidence of the utility of MS diagnostic criteria in the context of paediatric MS, have delineated MRI features that are highly predictive of future confirmation of MS, and have detailed 'red flags' that should alert the clinician to alternative diagnoses [93]. New MRI technologies are now informing on the impact of MS on regional and global brain tissue integrity and on age-expected brain growth. Such studies have yet to be done in children with other CNS inflammatory disorders, challenged by the rarity of such conditions.

References

1. Krupp LB, Tardieu M, Amato MP, et al. (2007). International Pediatric Multiple Sclerosis Study Group criteria for pediatric multiple sclerosis and immune-mediated central nervous system demyelinating disorders: revisions to the 2007 definitions. *Multiple Sclerosis*.
2. Cellucci T, and Benseler SM. (2010). Diagnosing central nervous system vasculitis in children. *Current Opinions in Pediatrics* 2010;22(6):731–8.
3. Dale RC, de Sousa C, Chong WK, et al. (2000). Acute disseminated encephalomyelitis, multiphasic disseminated encephalomyelitis and multiple sclerosis in children. *Brain*, **123**(Pt 12), 2407–22.
4. Hahn JS, Siegler DJ, Enzmann D. (1996). Intravenous gammaglobulin therapy in recurrent acute disseminated encephalomyelitis. *Neurology*, **46**(4), 1173–4.
5. Nishikawa M, Ichiyama T, Hayashi T, et al. (1999). Intravenous immunoglobulin therapy in acute disseminated encephalomyelitis. *Pediatric Neurology*, **21**(2), 583–6.
6. Banwell B, Bar-Or A, Giovannoni G, et al. (2011). Therapies for multiple sclerosis: considerations in the pediatric patient. *Nature Reviews in Neurology*, **7**, 109–22.
7. Chitnis T, Tenembaum S, Banwell B, et al. (2012). Consensus statement: evaluation of new and existing therapeutics for pediatric multiple sclerosis. *Multiple Sclerosis*, **18**(1), 116–27.
8. Hutchinson C, Elbers J, Halliday W et al. (2010). Treatment of small vessel primary CNS vasculitis in children: an open-label cohort study. *Lancet Neurology*, **9**(11), 1078–84.
9. Absoud M, Lim MJ, Chong WK, et al. (2013). Paediatric acquired demyelinating syndromes: incidence, clinical and magnetic resonance imaging features. *Multiple Sclerosis*, **19**(1), 76–86.
10. Ketelslegers IA, Catsman-Berrevoets CE, Neuteboom RF et al. (2012). Incidence of acquired demyelinating syndromes of the CNS in Dutch children: a nationwide study. *Journal of Neurology*, **259**(9), 1929–35.
11. Langer-Gould A, Zhang JL, Chung J, et al. (2011). Incidence of acquired CNS demyelinating syndromes in a multiethnic cohort of children. *Neurology*, **77**(12), 1143–8.
12. Banwell B, Kennedy J, Sadovnick D, et al. (2009). Incidence of acquired demyelination of the CNS in Canadian children. *Neurology*, **72**(3), 232–9.
13. Yeh EA, Chitnis T, Krupp L, et al. (2009). Pediatric multiple sclerosis. *Nature Reviews in Neurology*, **5**(11), 621–31.
14. Wilejto M, Shroff M, Buncic JR, et al. (2006). The clinical features, MRI findings, and outcome of optic neuritis in children. *Neurology*, **67**(2), 258–62.
15. Waldman AT, Stull LB, Galetta SL, et al. (2011). Pediatric optic neuritis and risk of multiple sclerosis: meta-analysis of observational studies. *Journal of AAPOS*, **15**(5), 441–6.
16. Verhey LH, Branson HM, Makhija M, et al. (2010). Magnetic resonance imaging features of the spinal cord in pediatric multiple sclerosis: a preliminary study. *Neuroradiology*, **52**(12), 1153–62.
17. Banwell BL. (2007). The long (-itudinally extensive) and the short of it: transverse myelitis in children. *Neurology*, **68**(18), 1447–9.
18. Absoud M, Lim MJ, Chong WK, et al. (2012). Paediatric acquired demyelinating syndromes: incidence, clinical and magnetic resonance imaging features. *Multiple Sclerosis*, **19**(1), 76–86.
19. Pidcock FS, Krishnan C, Crawford TO, et al. (2007). Acute transverse myelitis in childhood: center-based analysis of 47 cases. *Neurology*, **68**(18), 1474–80.

20. Thomas T, Branson HM, Verhey LH, et al. (2012). The demographic, clinical, and magnetic resonance imaging (MRI) features of transverse myelitis in children. *Journal of Child Neurology*, **27**(1), 11–21.
21. Lotze TE, Northrop JL, Hutton GJ, et al. (2008). Spectrum of pediatric neuromyelitis optica. *Pediatrics*, **122**(5), e1039–47.
22. Dundar NO, Anlar B, Guven A, et al. (2010). Relapsing acute disseminated encephalomyelitis in children: further evaluation of the diagnosis. *Journal of Child Neurology*, **25**(12), 1491–7.
23. Mikaeloff Y, Caridade G, Husson B, et al. (2007). Acute disseminated encephalomyelitis cohort study: prognostic factors for relapse. *European Journal of Paediatric Neurology*, **11**(2), 90–5.
24. Dale RC, and Pillai SC. (2007). Early relapse risk after a first CNS inflammatory demyelination episode: examining international consensus definitions. *Developmental Medicine & Child Neurology*, **49**(12), 887–93.
25. Verhey LH, Branson HM, Shroff MM, et al. (2011). MRI parameters for prediction of multiple sclerosis diagnosis in children with acute CNS demyelination: a prospective national cohort study. *Lancet Neurology*, **10**(12), 1065–73.
26. Callen DJ, Shroff MM, Branson HM, et al. (2008). Role of MRI in the differentiation of ADEM from MS in children. *Neurology*, **72**, 968–73.
27. van Walderveen MA, Kamphorst W, Scheltens P, et al. (1998). Histopathologic correlate of hypointense lesions on T1-weighted spin-echo MRI in multiple sclerosis. *Neurology*, **50**(5), 1282–8.
28. Polman CH, Reingold SC, Banwell B, et al. (2011). Diagnostic criteria for multiple sclerosis: 2010 revisions to the McDonald criteria. *Annals of Neurology*, **69**(2), 292–302.
29. Ketelslegers IA, Neuteboom RF, Boon M, et al. (2010). A comparison of MRI criteria for diagnosing pediatric ADEM and MS. *Neurology*, **74**(18), 1412–15.
30. Tantsis EM, Prelog K, Brilot F, et al. (2013) Risk of multiple sclerosis after a first demyelinating syndrome in an Australian Paediatric cohort: clinical, radiological features and application of the McDonald 2010 MRI criteria. *Multiple Sclerosis*, **19**(13): 1749–59
31. Mikaeloff Y, Suissa S, Vallee L, et al. (2004). First episode of acute CNS inflammatory demyelination in childhood: prognostic factors for multiple sclerosis and disability. *Journal of Pediatrics*, **144**(2), 246–52.
32. Sadaka Y, Verhey LH, Shroff MM, et al. (2012). 2010 McDonald criteria for diagnosing pediatric multiple sclerosis. *Annals of Neurology*, **72**(2), 211–23.
33. Sedani S, Lim MJ, Hemingway C, et al. (2012). Paediatric multiple sclerosis: examining utility of the McDonald 2010 criteria. *Multiple Sclerosis*, **18**(5), 679–82.
34. Lennon VA, Wingerchuk DM, Kryzer TJ, et al. (2004). A serum autoantibody marker of neuromyelitis optica: distinction from multiple sclerosis. *Lancet*, **364**(9451), 2106–12.
35. Huppke P, Bluthner M, Bauer O, et al. (2010). Neuromyelitis optica and NMO-IgG in European pediatric patients. *Neurology*, **75**(19), 1740–4.
36. Banwell B, Tenembaum S, Lennon VA, et al. (2008). Neuromyelitis optica-IgG in childhood inflammatory demyelinating CNS disorders. *Neurology*, **70**(5), 344–52.
37. McKeon A, Lennon VA, Lotze T, et al. (2008). CNS aquaporin-4 autoimmunity in children. *Neurology*, **71**(2), 93–100.
38. Makhani N, Bigi S, Banwell B, et al. (2013). Diagnosing neuromyelitis optica. *Neuroimaging Clinics of North America*, **23**(2), 279–91.
39. Collongues N, Marignier R, Zephir H, et al. (2010). Long-term follow-up of neuromyelitis optica with a pediatric onset. *Neurology*, **75**(12), 1084–8.
40. Simone IL, Carrara D, Tortorella C, et al. (2000). Early onset multiple sclerosis. *Neurological Science*, **21**(4, Suppl. 2), S861–3.
41. Boiko A, Vorobeychik G, Paty D, et al. (2002). Early onset multiple sclerosis: a longitudinal study. *Neurology*, **59**(7), 1006–10.
42. Deryck O, Ketelaer P, and Dubois B. (2006). Clinical characteristics and long term prognosis in early onset multiple sclerosis. *Journal of Neurology*, **253**(6), 720–3.
43. Renoux C, Vukusic S, Mikaeloff Y, et al. (2007). Natural history of multiple sclerosis with childhood onset. *New England Journal of Medicine*, **356**(25), 2603–13.
44. Chitnis T, Glanz B, Jaffin S, et al. (2009). Demographics of pediatric-onset multiple sclerosis in an MS center population from the Northeastern United States. *Multiple Sclerosis*, **15**(5), 627–31.
45. Banwell B, Krupp L, Kennedy J, et al. (2007). Clinical features and viral serologies in children with multiple sclerosis: a multinational observational study. *Lancet Neurology*, **6**(9), 773–81.
46. Verhey LH, Shroff M, and Banwell B. (2013). Pediatric multiple sclerosis: pathobiological, clinical, and magnetic resonance imaging features. *Neuroimaging Clinics of North America*, **23**(2), 227–43.
47. Banwell B, Bar-Or A, Arnold DL, et al. (2011). Clinical, environmental, and genetic determinants of multiple sclerosis in children with acute demyelination: a prospective national cohort study. *Lancet Neurology*, **10**(5), 436–45.
48. Chitnis T, Krupp L, Yeh A, et al. (2011). Pediatric multiple sclerosis. *Neurology Clinics*, **29**(2), 481–505.
49. Callen DJ, Shroff MM, Branson HM, et al. (2008). MRI in the diagnosis of pediatric multiple sclerosis. *Neurology*, **72**, 961–7.
50. Aubert-Broche B, Fonov V, Ghassemi R, et al. (2011). Regional brain atrophy in children with multiple sclerosis. *NeuroImage*, **58**(2), 409–15.
51. Ceccarelli A, Rocca MA, Perego E, et al. (2011). Deep grey matter T2 hypo-intensity in patients with paediatric multiple sclerosis. *Multiple Sclerosis*, **17**(6), 702–7.
52. Balassy C, Bernert G, Wober-Bingol C, et al. (2001). Long-term MRI observations of childhood-onset relapsing-remitting multiple sclerosis. *Neuropediatrics*, **32**(1), 28–37.
53. Lucchinetti CF, Gavrilova RH, Metz I, et al. (2008). Clinical and radiographic spectrum of pathologically confirmed tumefactive multiple sclerosis. *Brain*, **131**(Pt 7), 1759–75.
54. Cotton F, Weiner HL, Jolesz FA, et al. (2003). MRI contrast uptake in new lesions in relapsing-remitting MS followed at weekly intervals. *Neurology*, **60**(4), 640–6.
55. Katz D, Taubenberger JK, Cannella B, et al. (1993). Correlation between magnetic resonance imaging findings and lesion development in chronic, active multiple sclerosis. *Annals of Neurology*, **34**(5), 661–9.
56. Verhey LH, Narayanan S, and Banwell B. (2013). Standardized magnetic resonance imaging acquisition and reporting in pediatric multiple sclerosis. *Neuroimaging Clinics of North America*, **23**(2), 217–26.
57. Chabas D, Castillo-Trivino T, Mowry EM, et al. (2008). Vanishing MS T2-bright lesions before puberty: a distinct MRI phenotype? *Neurology*, **71**(14), 1090–3.
58. Bigi S, Marrie RA, Verhey L, et al. (2013). 2010 McDonald criteria in a pediatric cohort: is positivity at onset associated with a more aggressive multiple sclerosis course? *Multiple Sclerosis*, 19(10): 1359–62
59. Kornek B, Schmitl B, Vass K, et al. (2012). Evaluation of the 2010 McDonald multiple sclerosis criteria in children with a clinically isolated syndrome. *Multiple Sclerosis*, **18**(12), 1768–74.
60. Yeh EA, Weinstock-Guttman B, Ramanathan M, et al. (2009). Magnetic resonance imaging characteristics of children and adults with paediatric-onset multiple sclerosis. *Brain*, **132**(Pt 12), 3392–400.
61. Waubant E, Chabas D, Okuda DT, et al. (2009). Difference in disease burden and activity in pediatric patients on brain magnetic resonance imaging at time of multiple sclerosis onset vs adults. *Archives of Neurology*, **66**(8), 967–71.
62. Benseler S, and Schneider R. (2004). Central nervous system vasculitis in children. *Current Opinions in Rheumatology*, **16**(1), 43–50.
63. Benseler SM, Silverman E, Aviv RI, et al. (2006). Primary central nervous system vasculitis in children. *Arthritis & Rheumatology*, **54**(4), 1291–7.
64. Twilt M, and Benseler SM. (2012). The spectrum of CNS vasculitis in children and adults. *Nature Reviews in Rheumatology*, **8**(2), 97–107.
65. Aviv RI, Benseler SM, Silverman ED, et al. (2006). MR imaging and angiography of primary CNS vasculitis of childhood. *AJNR American Journal of Neuroradiology*, **27**(1), 192–9.
66. Kuker W, Gaertner S, Nagele T, et al. (2008). Vessel wall contrast enhancement: a diagnostic sign of cerebral vasculitis. *Cerebrovascular Disease*, **26**(1), 23–9.

67. Al-Araji A, and Kidd DP. (2009). Neuro-Behcet's disease: epidemiology, clinical characteristics, and management. *Lancet Neurology*, **8**(2), 192–204.
68. Mora P, Menozzi C, Orsoni JG, et al. (2013). Neuro-Behcet's disease in childhood: a focus on the neuro-ophthalmological features. *Orphanet Journal of Rare Diseases*, **8**, 18.
69. Baumann RJ, and Robertson WC, Jr (2003). Neurosarcoid presents differently in children than in adults. *Pediatrics*, **112**(6 Pt 1), e480–6.
70. Benseler SM, and Silverman ED. (2007). Systemic lupus erythematosus. *Rheumatic Disease Clinics of North America*, **33**(3), 471–98, vi.
71. Kidd D, Barkhof F, McConnell R, et al. (1999). Cortical lesions in multiple sclerosis. *Brain*, **122**(Pt 1), 17–26.
72. Geurts JJ, Pouwels PJ, Uitdehaag BM, et al. (2005). Intracortical lesions in multiple sclerosis: improved detection with 3D double inversion-recovery MR imaging. *Radiology*, **236**(1), 254–60.
73. Absinta M, Rocca MA, Moiola L, et al. (2011). Cortical lesions in children with multiple sclerosis. *Neurology*, **76**(10), 910–13.
74. Mesaros S, Rocca MA, Absinta M, et al. (2008). Evidence of thalamic gray matter loss in pediatric multiple sclerosis. *Neurology*, **70**(13, Pt 2), 1107–12.
75. Kerbrat A, Aubert-Broche B, Fonov V, et al. (2012). Reduced head and brain size for age and disproportionately smaller thalami in child-onset MS. *Neurology*, **78**(3), 194–201.
76. Giedd JN, Blumenthal J, Jeffries NO, et al. (1999). Brain development during childhood and adolescence: a longitudinal MRI study. *Nature Neuroscience*, **2**(10), 861–3.
77. Till C, Ghassemi R, Aubert-Broche B, et al. (2011). MRI correlates of cognitive impairment in childhood-onset multiple sclerosis. *Neuropsychology*, **25**(3), 319–32.
78. Fuentes A, Collins DL, Garcia-Lorenzo D, et al. (2012). Memory performance and normalized regional brain volumes in patients with pediatric-onset multiple sclerosis. *Journal of the International Neuropsychological Society*, **18**(3), 471–80.
79. Till C, Ho C, Dudani A, et al. (2012). Magnetic resonance imaging predictors of executive functioning in patients with pediatric-onset multiple sclerosis. *Archives of Clinical Neuropsychology*, **27**(5), 495–509.
80. Tortorella P, Rocca MA, Mezzapesa DM, et al. (2006). MRI quantification of gray and white matter damage in patients with early-onset multiple sclerosis. *Journal of Neurology*, **253**(7), 903–7.
81. Mezzapesa DM, Rocca MA, Falini A, et al. (2004). A preliminary diffusion tensor and magnetization transfer magnetic resonance imaging study of early-onset multiple sclerosis. *Archives of Neurology*, **61**(3), 366–8.
82. Absinta M, Rocca MA, Moiola L, et al. (2010). Brain macro- and microscopic damage in patients with paediatric MS. *Journal of Neurology, Neurosurgery & Psychiatry*, **81**(12), 1357–62.
83. Vishwas MS, Chitnis T, Pienaar R, et al. (2010). Tract-based analysis of callosal, projection, and association pathways in pediatric patients with multiple sclerosis: a preliminary study. *AJNR American Journal of Neuroradiology*, **31**(1), 121–8.
84. Bethune A, Tipu V, Sled JG, et al. (2011). Diffusion tensor imaging and cognitive speed in children with multiple sclerosis. *Journal of Neurological Sciences*, **309**(1–2), 68–74.
85. Till C, Deotto A, Tipu V, et al. (2011). White matter integrity and math performance in pediatric multiple sclerosis: a diffusion tensor imaging study. *Neuroreport*, **22**(18), 1005–9.
86. Bruhn H, Frahm J, Merboldt KD, et al. (1992). Multiple sclerosis in children: cerebral metabolic alterations monitored by localized proton magnetic resonance spectroscopy in vivo. *Annals of Neurology*, **32**(2), 140–50.
87. Oguz KK, Kurne A, Aksu AO, et al. (2009). Assessment of citrullinated myelin by 1H-MR spectroscopy in early-onset multiple sclerosis. *AJNR American Journal of Neuroradiology*, **30**(4), 716–21.
88. Ben SL, Miller E, Artzi M, et al. (2010). 1H-MRS for the diagnosis of acute disseminated encephalomyelitis: insight into the acute-disease stage. *Pediatric Radiology*, **40**(1), 106–13.
89. Brex PA, Parker GJ, Leary SM, et al. (2000). Lesion heterogeneity in multiple sclerosis: a study of the relations between appearances on T1 weighted images, T1 relaxation times, and metabolite concentrations. *Journal of Neurology, Neurosurgery & Psychiatry*, **68**(5), 627–32.
90. Rocca MA, Absinta M, Ghezzi A, et al. (2009). Is a preserved functional reserve a mechanism limiting clinical impairment in pediatric MS patients? *Human Brain Mapping*, **30**(9), 2844–51.
91. Rocca MA, Absinta M, Moiola L, et al. (2010). Functional and structural connectivity of the motor network in pediatric and adult-onset relapsing-remitting multiple sclerosis. *Radiology*, **254**(2), 541–50.
92. Verhey LH, Branson HM, Laughlin S, et al. (2013). Development of a standardized MRI scoring tool for CNS demyelination in children. *AJNR American Journal of Neuroradiology*, **34**(6), 1271–7.
93. O'Mahony J, Shroff M, and Banwell B. (2013). Mimics and rare presentations of pediatric demyelination. *Neuroimaging Clinics of North America*, **23**(2), 321–36.
94. Lucchinetti CF, Kiers L, O'Duffy A, et al. (1997). Risk factors for developing multiple sclerosis after childhood optic neuritis. *Neurology*, **49**(5), 1413–18.
95. Transverse Myelitis Consortium Working Group. (2002). Proposed diagnostic criteria and nosology of acute transverse myelitis. *Neurology*, **59**(4), 499–505.
96. Wingerchuk DM, Lennon VA, Pittock SJ, et al. (2006). Revised diagnostic criteria for neuromyelitis optica. *Neurology*, **66**(10), 1485–9.
97. Calabrese LH, Furlan AJ, Gragg LA, et al. (1992). Primary angiitis of the central nervous system: diagnostic criteria and clinical approach. *Cleveland Clinic Journal of Medicine*, **59**(3), 293–306.
98. Polman CH, Reingold SC, Edan G, et al. (2005). Diagnostic criteria for multiple sclerosis: 2005 revisions to the 'McDonald Criteria'. *Annals of Neurology*, **58**(6), 840–6.
99. Mikaeloff Y, Adamsbaum C, Husson B, et al. (2004). MRI prognostic factors for relapse after acute CNS inflammatory demyelination in childhood. *Brain*, **127**(Pt 9), 1942–7.

CHAPTER 31

Paediatrics

Congenital metabolic central nervous system disorders

Deborah L. Renaud

Introduction

Inherited metabolic disorders affect approximately 1 in 1000 to 1 in 3000 live births. The majority are autosomal recessive, although some conditions demonstrate X-linked, autosomal dominant or maternal (mitochondrial DNA) inheritance. The genetic defect results in the disruption of synthesis, breakdown or transport of metabolic substances. The clinical pictures are a reflection of the toxic effects of accumulated metabolites, deficiency of essential metabolites required for normal cell function or the secondary effects of these imbalances on essential metabolic pathways.

Neurometabolic disorders are inherited metabolic disorders affecting the central nervous system (CNS). Symptoms may present at any age. The CNS may be affected exclusively or be primarily affected with other organ systems demonstrating effects of the underlying inborn error of metabolism. CNS symptoms and signs may be non-specific and include developmental delay, abnormalities of tone, seizures, stroke-like episodes, extrapyramidal manifestations, leukoencephalopathy, and behavioural concerns. Non-neurological manifestations include dysmorphic features, ophthalmological, cardiac, hepatic, gastrointestinal, haematologic, skeletal, and skin abnormalities. In some conditions, a characteristic odour may be present. In general, small molecule disorders, including disorders of amino acid, organic acid, fatty acid, and carbohydrate metabolism, present with acute exacerbations, triggered by infections and illnesses, superimposed on chronic neurological symptoms. Large molecule/organelle disorders including mitochondrial, peroxisomal, and lysosomal disorders more commonly have a chronic neurological presentation with progressive decline in some conditions. Some inherited metabolic disorders do not primarily affect the CNS, but may contribute to secondary effects due to hypoglycaemia and other biochemical imbalances.

Magnetic resonance imaging (MRI) is the primary neuroimaging modality used for the evaluation of neurometabolic disorders. *In utero*, effects on brain development may result in brain malformation, including disorders of neuronal migration, abnormalities of the corpus callosum, and cerebellar hypoplasia/dysplasia. More commonly, neuroimaging abnormalities develop in the post-natal period and may have different appearances at different stages of the disease. Neuroimaging abnormalities associated with neurometabolic disorders may be mimicked by toxic, inflammatory, infectious, and autoimmune processes, as well as secondary effects of chemotherapy or radiation, making the diagnostic process challenging. Inherited leukoencephalopathies usually involve the white matter in a bilaterally symmetric, confluent fashion, whereas inflammatory and other causes tend to have more localized or multifocal involvement. The pattern of white matter involvement on MRI may be characteristic of the underlying inherited leukoencephalopathy and may involve the subcortical, periventricular and/or deep white matter. A changing pattern may be observed using serial MRI scans, which helps to distinguish demyelination (active destruction of previously acquired myelin consistent with a leukodystrophy), dysmyelination/hypomyelination (impaired formation of myelin) and delayed myelination from other forms of stable leukoencephalopathy [1–4]. An understanding of the normal evolution of MRI findings during myelin development is critical when assessing white matter changes in small children with suspected leukoencephalopathy [5]. Neurometabolic conditions, which involve energy metabolism in particular, may have significant involvement of the deep gray matter structures including the striatum (caudate and putamen) and the globus pallidus. Bilateral thalamic involvement may be indicative of a lysosomal storage disorder [6]. Acute cortical injury may be accompanied on MRI scan by sulcal effacement, cortical swelling, abnormal signal intensity, and regions of restricted diffusion. Frequently, both gray and white matter involvement is present. Cerebral atrophy is a common finding in the later stages of many neurometabolic disorders, but is particularly evident in neuronal ceroid lipofuscinosis. Cerebellar hypoplasia/dysplasia may be present at birth, associated with chronic non-progressive ataxia or cerebellar atrophy may be demonstrated in conditions with progressive ataxia including mitochondrial disorders, late-onset GM2-gangliosidosis and neuronal ceroid lipofuscinosis [7]. Brainstem involvement is most commonly seen in mitochondrial disorders. Computed tomography (CT) is helpful for detecting calcifications [8] and may also be indicated in emergent situations where MRI is not readily available. Proton magnetic resonance spectroscopy (^{1}H-MRS) is currently used to detect lactate, creatine, choline, N-acetyl aspartate (NAA) and other metabolites that may be specific for an individual neurometabolic disorder or evidence of underlying pathophysiologic disturbances. The role of ^{1}H-MRS in the evaluation of neurometabolic disorders is expected to expand as more metabolites and patterns for specific neurometabolic disorders are classified [9].

A comprehensive review of clinical and neuroimaging findings associated with neurometabolic disorders is beyond the scope of this chapter. Interested readers are referred to recent textbooks on these topics [10–12].

Disorders of organic acid metabolism

Glutaric aciduria type I (GA1) is due to a deficiency of glutaryl-CoA dehydrogenase (GCDH), resulting in the accumulation of glutaric acid and 3-hydroxyglutaric acid in the blood, urine, and cerebrospinal fluid (CSF). Macrocephaly is present within the first few weeks of life. Most untreated children present with an acute encephalopathic crisis between 3 and 24 months of age precipitated by infection or illness with dehydration. Abnormal tone is accompanied by decreased level of consciousness and seizures. Residual dystonia results from acute striatal injury. Intelligence is relatively preserved. Basal ganglia injury occurs in 85–94% of undiagnosed children with an acute encephalopathic crisis, but is decreased to 35% when children are prospectively treated due to early diagnosis [13,14]. Newborn screening for GA1 has improved neurological outcome. Treatment for GA1 consists of emergency treatment of episodes of acute encephalopathy with high energy fluids to prevent catabolism and maintain hydration, and maintenance therapy with a specialized low protein diet and carnitine supplementation [13–17]. Characteristic MRI findings of GA1 include widening of the Sylvian fissures, decreased opercularization of the insula, mild ventriculomegaly and expansion of CSF spaces anterior to the temporal lobes. Acute striatal necrosis presents with swelling and necrosis in the putamen initially, and spreading to the adjacent caudate nuclei and globus pallidus (Fig. 31.1).

White matter changes in the periventricular region may be seen. Acute subdural haematomas may be seen due to rupture of veins stretching across the widened CSF spaces with minor head trauma. This finding can be mistaken for non-accidental trauma [13,18,19].

L-2-hydroxyglutaric aciduria is due to deficiency of L-2-hydroxyglutarate dehydrogenase, a FAD-linked mitochondrial enzyme, which converts L-2 hydroxyglutarate to alpha-ketoglutarate.

A variable degree of developmental delay is followed by a slowly progressive neurodegenerative disorder with cognitive decline, ataxia, pyramidal, and extrapyramidal signs. Macrocephaly and seizures are common. An increased risk of brain tumours, including glioblastoma multiforme has been associated with L-2-hydroxglutaric aciduria. MRI findings are characteristic (Fig. 31.2) and consist of abnormal signal intensity in the subcortical white matter bilaterally with frontal predominance, with low signal on T_1-weighted images and increased signal on T_2-weighted images. Periventricular, cerebellar, and brain stem white matter is relatively spared. Characteristic involvement of the globus pallidus, caudate, and putamen bilaterally, as well as the dentate nucleus is present at all stages [20–24].

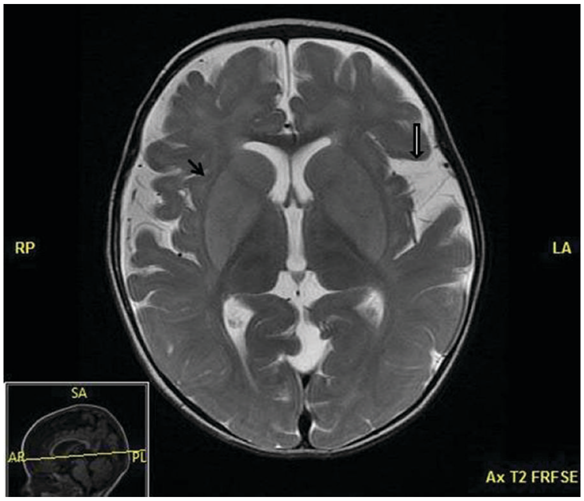

Fig. 31.1 MRI image of a patient with glutaric aciduria type I demonstrating widening of the Sylvian fissures (white arrow), expansion of CSF spaces anterior to the temporal lobes and abnormal signal intensity in the putamen, caudate nuclei and globus pallidi (black arrow).

Propionic acidaemia is due to a deficiency of propionyl CoA carboxylase, a biotin-dependent enzyme, which converts propionyl CoA to methylmalonyl CoA. Methylmalonyl-CoA mutase, a vitamin B12 (adenosylcobalamin)-dependent enzyme, converts L-methylmalonyl-CoA to succinyl-CoA, which enters the tricarboxylic acid cycle.

Methylmalonic acidaemia (MMA) may result from deficiency of methylmalonyl-CoA mutase (either complete [mut^0] or partial [mut^-]), defects in the synthesis of adenosylcobalamin (Cbl A, Cbl B), which produce a methylmalonic acidaemia alone, defects in the synthesis of both adenosylcobalamin and methylcobalamin (Cbl C, Cbl D) or defective lysosomal transport of cobalamin (Cbl F). Acute presentation in the neonatal period consists of severe metabolic acidosis with vomiting, progressive lethargy, hypotonia, and seizures. The chronic intermittent form presents with episodes of encephalopathy, vomiting, ketoacidosis, and dehydration, particularly in the setting of infection or protein ingestion. Chronic neurological features include developmental delay, hypotonia, and failure to thrive. The MRI scan may reveal bilateral basal ganglia involvement associated with dystonia clinically [10].

Disorders of creatine metabolism

Approximately 50% of the creatine required for adenosintriphosphate (ATP) generation is synthesized *de novo* with the remainder being supplied by the diet. Creatine is synthesized in two steps by the enzymes arginine: glycine amidinotransferase and guanidinoacetate methyltransferase. Creatine is actively transported across the blood–brain barrier by the X-linked creatine transporter. Three disorders of creatine metabolism have been described. The two synthesis enzyme defects are autosomal recessive conditions and the creatine transporter defect is X-linked affecting males more severely than females. Clinical symptoms include developmental delay especially expressive speech, autism, hypotonia, movement disorder, and seizures.

The MRI scan may show signal abnormalities within the globus pallidi. ^{1}H-MRS reveals absent or markedly decreased creatine peak (Fig. 31.3) [25]. Treatment with oral creatine monohydrate can improve the MRS creatine peak in synthesis defects, but does not significantly change the size of the creatine peak in X-linked creatine transporter deficiency.

Mitochondrial disorders

Mitochondrial disorders can result from mutations in mitochondrial DNA, and nuclear genes and may present with a wide range of neurological and non-neurological symptoms and signs. Neuroimaging in mitochondrial disease may show non-specific findings, such as cerebral and/or cerebellar atrophy, delayed

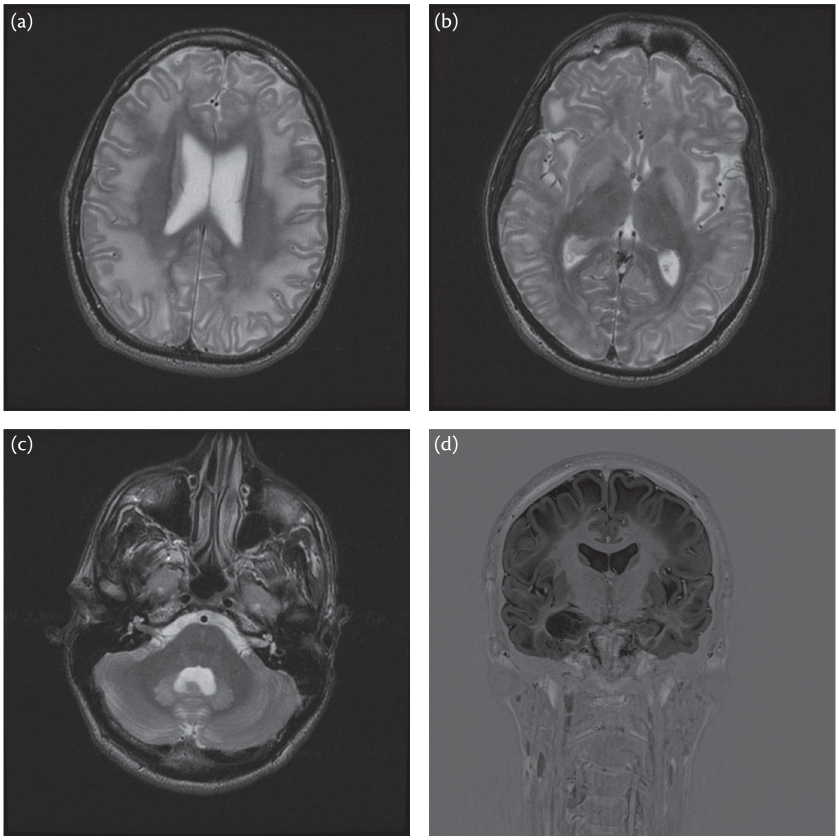

Fig. 31.2 MRI images of patient with L2-hydroxyglutaric aciduria. (a) T_2-weighted axial image demonstrating abnormal signal intensity in the subcortical white matter bilaterally. Periventricular white matter is relatively spared. T_2-weighted axial images demonstrating (b) involvement of the globus pallidus, caudate and putamen bilaterally as well as (c) the dentate nuclei. (d) Inversion recovery coronal image demonstrating present of glial tumour in right temporal lobe.

Reproduced from Renaud DL. (2012). Leukoencephalopathies associated with macrocephaly. *Seminars in Neurology*, **32**(1), 34–41. Copyright (2012), with permission from Thieme Medical Publishers.

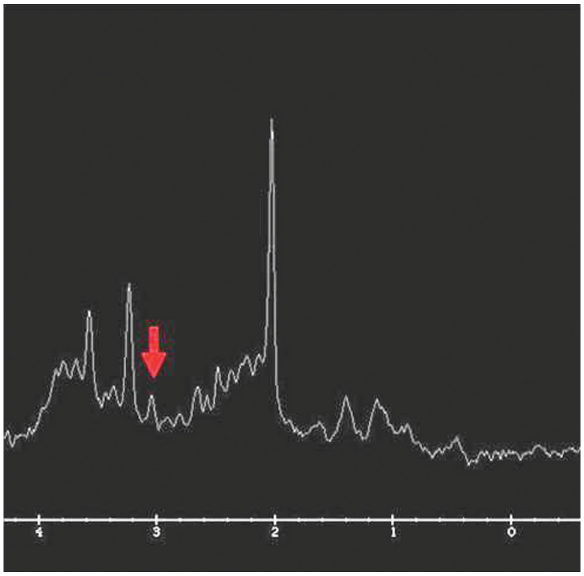

Fig. 31.3 MRS image from a patient with X-linked creatine transporter deficiency demonstrating a significantly decreased creatine peak (red arrow).

myelination, or may demonstrate characteristic MRI findings. Identical MRI findings may be caused by both mitochondrial DNA and nuclear gene defects, and the same genetic mutation can result in different clinical and neuroimaging phenotypes.

Leigh syndrome describes a clinical phenotype associated with progressive symmetric abnormalities in the basal ganglia, thalami, peri-aqueductal gray matter, tegmentum, red nuclei, and dentate nuclei. The mitochondrial DNA mutation most commonly associated with Leigh syndrome is 8993 T > C. Nuclear gene mutations involving subunits of the mitochondrial respiratory chain including NDUFS4 and SURF1 and pyruvate dehydrogenase deficiency can also present with Leigh syndrome [26,27].

Mitochondrial myopathy, encephalopathy, lactic acidosis, and stroke-like episodes (MELAS) presents with transient stroke-like lesions in the gray matter, which do not follow vascular territories. Although most commonly associated with the mitochondrial DNA mutation 3243 A > G (80%), other mitochondrial DNA, and nuclear gene defects have also been described. Diffuse white matter involvement is also seen in some patients [26–28].

Alpers syndrome is a severe hepatocerebral disease due primarily to mutations in POLG and Twinkle, resulting in mitochondrial DNA depletion. MRI findings include T_2 and FLAIR hyperintensities in the occipital cortices, basal ganglia, thalamim and deep cerebellar nuclei [26].

Leukoencephalopathy is a common finding in mitochondrial disorders with some patients having leukodystrophy with clinical deterioration. White matter abnormalities have been described in respiratory chain defects, mitochondrial depletion syndromes, POLG mutations, MELAS, Kearns–Sayre syndrome and leukoencephalopathy with brain stem and spinal cord involvement and lactate elevation (LBSL). Leukoencephalopathy associated with gastrointestinal dysmotility and peripheral neuropathy is characteristic of mitochondrial neuro-gastrointestinal encephalomyopathy (MNGIE) due to mutations in thymidine phosphorylase [26–28].

MRS may demonstrate the presence of a lactate peak, even in the absence of lactic acidosis in patients with Leigh syndrome, pyruvate dehydrogenase deficiency, respiratory chain defects, and MELAS (Fig. 31.4) [26,27].

Peroxisomal disorders

Peroxisomal biogenesis defects (PBD) result from defective import of PTS1 and PTS2 matrix enzymes, associated with mutations in *PEX* genes, encoding peroxins. As a result, peroxisomal enzymes are mislocalized to the cytoplasm leading to severe impairment of cholesterol synthesis, bile acid metabolism, oxidation of very long chain and branched chain fats, ether phospholipid synthesis, and phytanic acid and pipecolic acid metabolism. Four disorders historically considered to be distinct, Zellweger syndrome, neonatal adrenal leukodystrophy, infantile Refsum disease, and pipecolic acidaemia, are now known to form a spectrum of clinical severity. Classic Zellweger syndrome presents with characteristic dysmorphic facial features, renal cysts, liver dysfunction, and other malformations accompanied by severe neurological dysfunction with hypotonia and seizures. MRI findings include peri-sylvian polymicrogyria with thickened cortical mantle, decreased white matter volume, delayed myelination, bilateral ventricular dilatation, and germinolytic cysts. Neonatal adrenoleukodystrophy presents with an early onset of progressive leukodystrophy involving the cerebral and cerebellar whiter matter, which may be associated with peri-sylvian polymicrogyria. Milder forms of PBD may present with leukodystrophy in childhood, adolescence or adulthood which is characterized by cerebral demyelination sparing the U-fibres with central cerebellar white matter involvement [29,30].

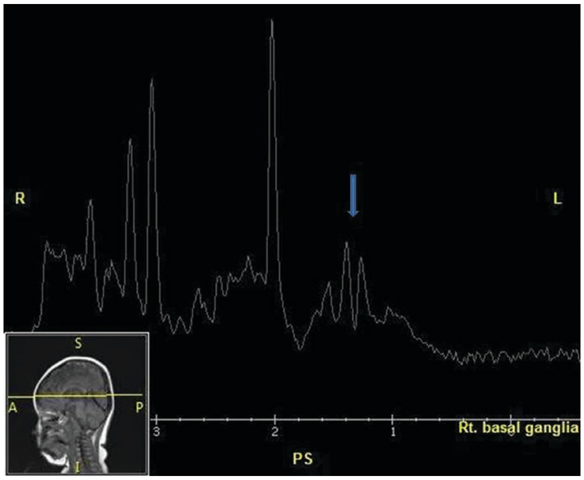

Fig. 31.4 MRS image from a patient with pyruvate dehydrogenase deficiency demonstrating the presence of a lactate peak (blue arrow).

Rhizomelic chondrodysplasia punctata (RCDP) type 1, characterized by abnormal facies, developmental delay, cataracts, abnormal calcifications of epiphyses, and severe proximal limb shortening, results from failure to import PTS2-associated enzymes due to mutations in the *PEX7* gene. RCDP type 2, DHAPAT deficiency, and RCDP type 3, alkyl DHAP synthase deficiency, have similar clinical features, but are isolated disorders of etherphospholipid biosynthesis resulting in plasmalogen deficiency with normal phytanic acid. MRI findings include delayed myelination and abnormal signal intensity, particularly in the parieto-occipital regions associated with progressive cerebellar atrophy [29].

X-linked adrenoleukodystrophy (X-ALD) is caused by mutations in the *ABCD1* gene, which encodes ALDP, an ATP-binding transporter located in the peroxisomal membrane. Childhood cerebral adrenoleukodystrophy (CCALD) accounts for 35% of cases. The adolescent and adult-onset cerebral phenotypes have similar features to the childhood cerebral disease, but a later age of onset. Multiple patterns of involvement on MRI have been described in the cerebral forms. Approximately 80% develop the posterior pattern with symmetric involvement of the parieto-occipital white matter, splenium of the corpus callosum, visual and auditory pathways, and occasionally the corticospinal tracts. The anterior pattern involves the frontal white matter, genu of the corpus callosum, and frontopontine tract in approximately 15%. Less common patterns include corticospinal tract or frontopontine projection fibres, cerebellar white matter and concomitant parieto-occipital, and frontal white matter involvement [31]. Contrast-enhancement of T_1-weighted images is restricted to the leading edge of the affected white matter and is predictive of clinical and MRI progression [32]. Fluid-attenuated inversion recovery (FLAIR) imaging is useful for distinguishing the central necrotic zone from the more peripheral zones within the affected white matter [33,34]. In boys with CCALD, MRS may reveal abnormalities in metabolite ratios within the affected white matter including decreased N-acetyl aspartate (NAA)/creatine and NAA/choline ratios and increased choline/creatine ratio in comparison with white matter from normal controls [35–37]. The three different pathological zones can be demonstrated with diffusion-weighted imaging with the burn-out central zone appearing hypointense, the intermediate inflammatory zone appearing moderately hyperintense and the most peripheral demyelinating zone appearing faintly hyperintense [38,39].

Approximately 40–45% of males develop adrenomyeloneuropathy (AMN) in the second to fourth decade, presenting with progressive spastic paraparesis and peripheral neuropathy. MRI may reveal spinal cord atrophy. Up to half of men with AMN may develop cerebral symptoms and at least 50% of female carriers develop symptoms of AMN after age 40 years. MRI scans for patients with the spinocerebellar variant demonstrate T_2 signal hyperintensity in the posterior limb of the internal capsule and cerebral peduncles with atrophy of the cerebellum (especially the vermis), brainstem and cervical spinal cord [40–42].

Lysosomal disorders

Metachromatic leukodystrophy is most commonly associated with deficiency of arylsulphatase A, although rare forms due to deficiency of the activator protein, saposin B, and multiple sulphatase deficiency can be seen. The late-infantile form is the most common, presenting with normal development until 1 or 2 years of age followed by progressive peripheral neuropathy, spasticity and cognitive decline. The juvenile form presents between 3 and 16 years of age, with behaviour and psychiatric changes followed by motor and cognitive decline. Adult-onset patients show a slow decline in intellectual abilities and gait accompanied by psychiatric changes. Peripheral neuropathy may be the presenting feature in the later onset forms [43] MRI findings consist of confluent, symmetrical T_2 hyperintensity in the periventricular white matter, which spares the subcortical U fibres. The progression of white matter changes is from the parieto-occipital to frontal regions in late-infantile cases (Fig. 31.5), and is frontal dominant in juvenile and adult-onset cases. Tigroid stripes extending radially consist of spared perivascular white matter and are characteristic of this condition. White matter changes in the corpus callosum, projection fibres and cerebellum are seen with severe disease. Cerebral atrophy is a late finding due to loss of white matter volume [43–46].

Krabbe disease, also known as globoid cell leukodystrophy, is associated with a deficiency of galactocerebrosidase (GALC). Accumulation of galactosylceramide and psychosine leads to extensive demyelination and gliosis, affecting both the central and peripheral nervous system white matter. The infantile form accounts for at least 85% of cases and presents at 2–5 months of age with irritability, arrest of development, and abnormal tone. Progressive regression of skills is associated with vision loss, seizures, and loss of tone leading to early death. Late-onset forms of Krabbe disease are associated with painful paraesthesias due to peripheral neuropathy, vision problems, and dementia. Early in the disease course, up to 25% of symptomatic infants may have normal MRI scans. White matter involvement can be extensive with diffusely increased T_2 signal involving the periventricular, deep and cerebellar white matter. Thickening of the optic nerves may be seen [47–49].

GM1 gangliosidosis results from deficiency of β-galactosidase associated with mutations in the *GLB1* gene. Lysosomal storage of GM1 ganglioside, glycoproteins, and glycosaminoglycans in the CNS results in three types of GM1 gangliosidosis. The infantile form (Type 1) has onset before 6 months of age with rapidly progressive hypotonia and neurological decline, and death by 2 years of age. Signs of storage including coarse facial features, gingival hypertrophy, corneal clouding, cherry-red spot, hepatosplenomegaly, and dysostosis multiplex may be present. The late infantile/juvenile (type 2) form presents between 7 months and 3 years of age with slowly progressive cognitive and motor decline. The adult-onset form presents primarily with a progressive extrapyramidal disorder between 3–30 years of age. Cardiomyopathy develops in about one-third of patients with any form [50]. MRI findings include abnormal signal in the globus pallidi and thalami bilaterally. White matter involvement can be diffuse, and includes both subcortical and periventricular regions, as well as the centrum semiovale, internal and external capsules [51].

GM2 gangliosidosis is associated with a deficiency of β-hexosaminidase A, resulting in GM2 ganglioside accumulation in the brain. Infantile-onset GM2 (Tay–Sachs disease) is characterized by macrocephaly, progressive weakness, and excessive startle starting at 3–6 months followed by loss of developmental skills, seizures, blindness, and spasticity leading to death by 4 years of age. Late-onset GM2 gangliosidosis (B1 variant) presents with slowly progressive dystonia and spinocerebellar degeneration. Sandhoff disease, which is associated with deficiency of both β-hexosaminidase A and B has similar clinical and imaging to Tay–Sachs disease. Early MRI signal changes in the thalami may be present in all forms. Infantile-onset forms have symmetric diffuse T_2 hyperintensity in the periventricular, lobar, and subcortical white matter. Late-onset forms of GM2 gangliosidosis present primarily with progressive cerebellar atrophy [52–54].

Neuronal ceroid lipofuscinosis describes a heterogeneous group of lysosomal storage disorders with variable ages of onset characterized by some combination of progressive cognitive decline, seizures, vision loss, and impaired motor function. Decreased T_2 signal intensity of the thalami is a consistent finding. Hyperintense

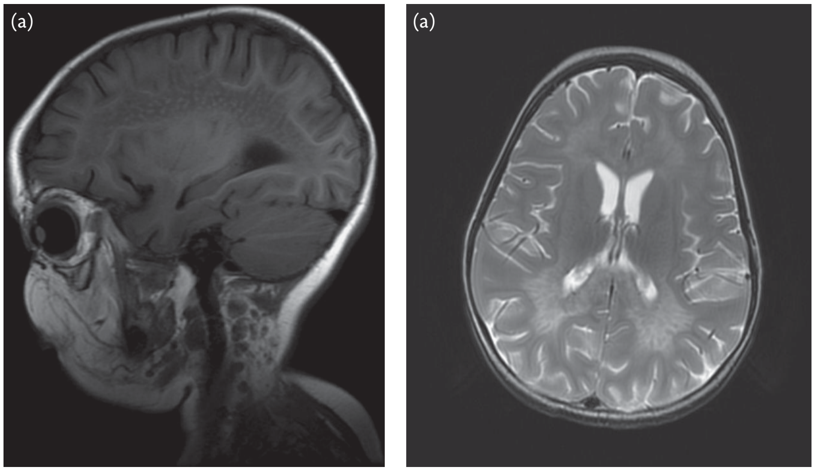

Fig. 31.5 MRI images of a patient with late-infantile metachromatic leukodystrophy. (a) T_1-weighted sagittal image and (b) T_2-weighted image demonstrating confluent, symmetrical abnormalities in the periventricular white matter with sparing of the subcortical U fibres, more prominent in the parieto-occipital regions with tigroid stripes, consisting of spared perivascular white matter, extend radially.

Reproduced from Renaud DL. (2012). Lysosomal disorders associated with leukoencephalopathy. Seminars in Neurology, **32**(1), 51–4. Copyright (2012), with permission from Thieme Medical Publishers.

periventricular white matter changes may be present and are associated with progressive generalized volume loss [6,55].

Fabry disease is an X-linked condition due to deficiency of α-galactosidase, presenting in males with angiokeratoma, painful acroparesthesias, nephropathy, and characteristic corneal and lenticular changes. White matter lesions, presumed to be microvascular in origin, are widespread and asymmetric similar in distribution to age-related white matter lesions. Strokes in both men and women with Fabry disease are more common in the posterior circulation than in the general population. The 'pulvinar sign', a T_1 hyperintensity in the bilateral posterior thalami, may appear with increasing age [56].

Mucopolysaccharidoses are a group of lysosomal storage disorders associated with the accumulation of mucopolysaccharides in the CNS, peripheral tissues or both. Symmetric T_2 signal hyperintensity in the periventricular white matter have been described in Hurler–Scheie (MPS I), Hunter syndrome (MPS II), and Sanfilippo syndrome (MPS III). Enlarged perivascular spaces are common findings in these conditions [57–60].

Mucolipidosis IV, due to mutations in MCOLN1 encoding mucolipin-1, is a neurodegenerative disorder with lysosomal storage. Hypoplasia of the corpus callosum is a common MRI finding associated with decreased T_2 signal in the basal ganglia and thalami. A variable degree of T_2 hyperintensity in the periventricular, deep and subcortical white matter may also be seen [61].

Fucosidosis is due to a deficiency of α-L-fucosidase, which results in the accumulation of fucose-containing oligosaccharides, glycolipids, and glycoproteins. Clinical features include slowly progressive cognitive and motor deterioration associated with visceromegaly and angiokeratoma. T_2-hypointensity in the globus pallidi and substantia nigra is characteristic. White matter changes are consistent with hypomyelination [4,62,63].

Salla disease, due to deficiency of the sialic acid transporter, SLC17A5, results in accumulation of free sialic acid (N-acetylneuraminic acid) in lysosomes in various tissues. MRI findings are consistent with hypomyelination, although normal myelin is present in the internal capsule and cerebellum. The corpus callosum is usually thin [1,4,64,65].

Other inherited leukoencephalopathies

Aicardi–Goutieres syndrome is an autosomal recessive condition characterized by an early encephalopathy followed by a stabilization of neurological symptoms. CSF analysis reveals chronic lymphocytosis, elevated interferon-alpha, and neopterin. At least five different genes have been described. Neuroimaging reveals a diffuse leukoencephalopathy associated with calcifications and cerebral atrophy [66–69].

Alexander disease is a primary disorder of astrocytes due to an autosomal dominant or de novo toxic gain of function mutation in the glial fibrillary acidic protein (*GFAP*) gene. The classical infantile form presents prior to 2 years of age with macrocephaly, developmental delay, and seizures followed by progressive spasticity, ataxia, bulbar signs, and hydrocephalus. The juvenile form presents between 2 and 13 years of age with developmental delay, and seizures with gradual deterioration or bulbar and pseudobulbar signs, ataxia, and spasticity similar to the adult form. MRI findings suggestive of Alexander disease include extensive cerebral white matter changes with frontal predominance, a periventricular rim with high signal on T_1-weighted images and low signal on T_2-weighted images, abnormalities of the basal ganglia and thalami, brain stem abnormalities, and contrast enhancement of particular gray and white matter structures (Fig. 31.6). The MRI findings in juvenile and adult-onset cases are more variable and, therefore, may not meet these criteria. White matter changes may be minimal and may be stable over many years despite disease progression. Scalloped garland-like signal enhancement on T_2 and FLAIR images lining the outer rim of the lateral ventricles may be present [70–74].

Canavan disease, due to a deficiency of aspartoacylase, results in increased levels of N-acetyl aspartic acid (NAA) in blood, urine, CSF, and brain. Children with Canavan disease develop macrocephaly in the first year of life associated with developmental delay followed by regression. Hypotonia evolves into spasticity associated with seizures, sleep disturbance, irritability, and optic atrophy. MRI scans may be normal initially followed by diffuse spongy degeneration of the white matter of the cerebral hemispheres, cerebellum, brainstem, internal and external capsules, subcortical U fibres, and

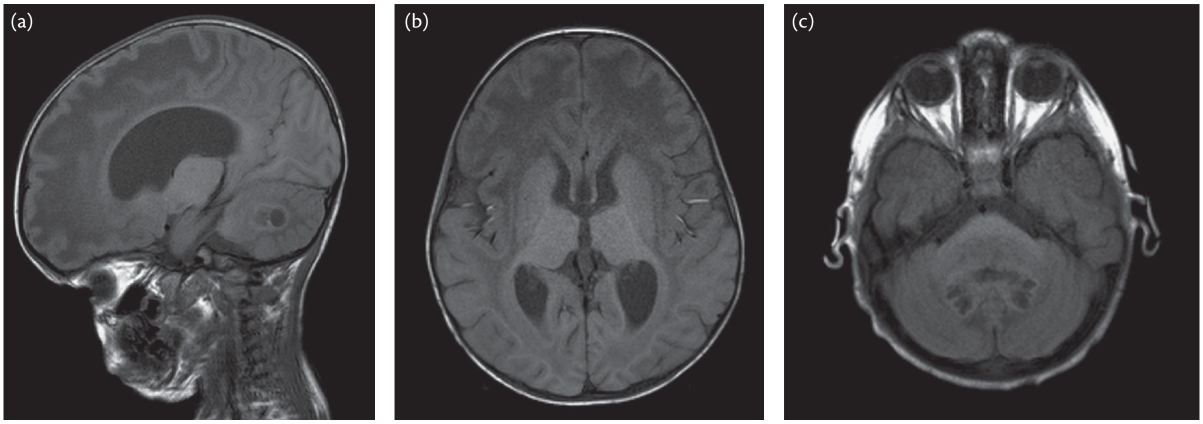

Fig. 31.6 MRI images of patient with infantile Alexander disease. (a) T_1-weighted sagittal image demonstrating extensive cerebral white matter changes with frontal predominance and cystic changes in the dentate nuclei of the cerebellum. (b,c) T_1-weighted axial images demonstrating extensive cerebral white matter changes with frontal predominance, a periventricular rim with high signal, abnormalities of the basal ganglia and thalami, and cystic changes in the dentate nuclei of the cerebellum.

Reproduced from Renaud DL. (2012). Leukoencephalopathies associated with macrocephaly. *Seminars in Neurology*, **32**(1), 34–41. Copyright (2012), with permission from Thieme Medical Publishers.

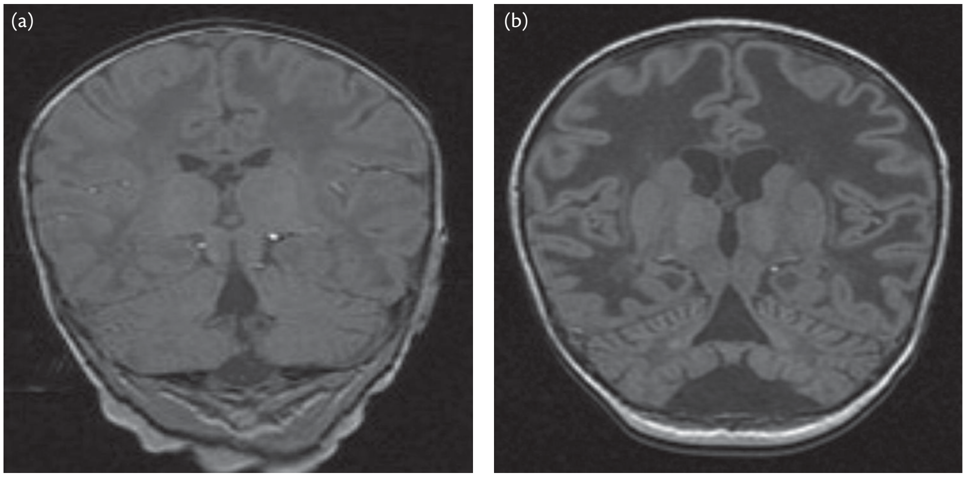

Fig. 31.7 Coronal MRI images of patient with leukoencephalopathy with vanishing white matter. (a) Diffuse symmetric cerebral white matter changes at 6 months of age. (b) Progressive cystic degeneration of the white matter results in replacement of the white matter by CSF at 11 months of age. Cerebellar atrophy has developed.

Reproduced from Renaud DL. (2012). Leukoencephalopathies associated with macrocephaly. *Seminars in Neurology*, **32**(1), 34–41. Copyright (2012), with permission from Thieme Medical Publishers.

spinal cord. Brain atrophy eventual develops. MR spectroscopy reveals a significantly elevated NAA peak [75–77].

Childhood ataxia with central hypomyelination/vanishing white matter disease (CACH/VWMD) is due to mutations in the genes encoding each of the five subunits of eukaryotic translation initiation factor eIF2B, which is responsible for regulation of protein synthesis in response to mild stressors. Children present with mild spasticity and ataxia with relatively spared cognition followed by episodic neurological deterioration initiated by minor infections, minor head trauma, or acute fright. Episodes present with unexplained coma, seizures, hypotonia, and irritability. Recovery from each episode is incomplete leading to a chronic progressive neurological decline. Female patients may have ovarian failure, which precedes or co-exists with neurological symptoms (also known as ovarioleukodystrophy). Adolescents and adults tend to have a milder and more protracted course. Cree encephalopathy has been shown to be a severe variant of VWMD. Characteristic MRI findings in the childhood form (Fig. 31.7) consist of diffuse symmetric cerebral white matter abnormalities, which spare the subcortical U fibres, corpus callosum, internal capsules, and anterior commissure. There is progressive cystic degeneration of the white matter with radial stripes extending from the ventricular wall to the subcortical region. Cortical gray matter is generally spared and cerebellar atrophy develops late [78–81].

Megalencephalic leukoencephalopathy with subcortical cysts (MLC) classically presents with macrocephaly in the first year of life with mild motor delay, and gradual onset of ataxia and spasticity. Seizures are common, but intelligence is relatively spared. Autosomal recessive mutations in the *MLC1* gene (80% of patients)

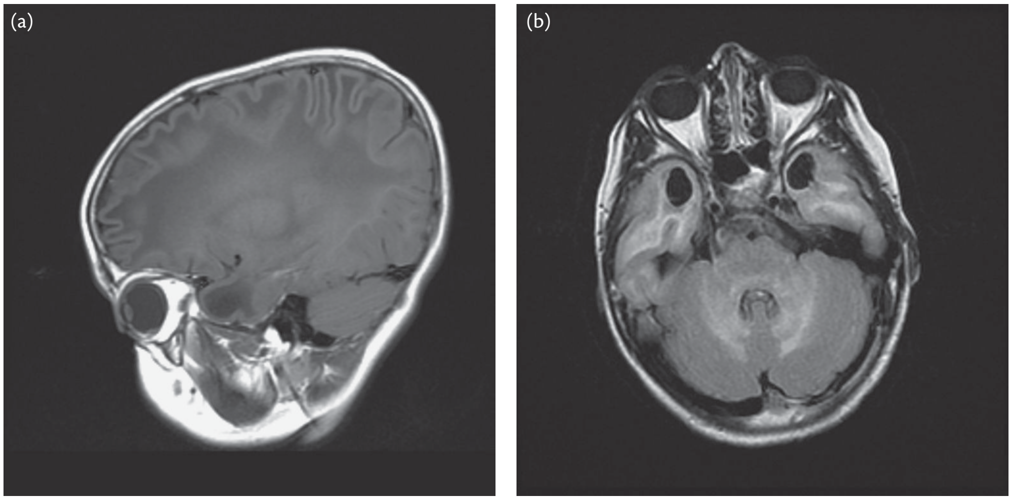

Fig. 31.8 MRI images of a patient with megalencephalic leukoencephalopathy with subcortical cysts. (a) Sagittal T_1-weighted, and (b) axial FLAIR images demonstrating diffuse subcortical and periventricular white matter abnormalities, and subcortical cysts located in the bilateral anterior temporal regions.

Reproduced from Renaud DL. (2012). Leukoencephalopathies associated with macrocephaly. *Seminars in Neurology*, **32**(1), 34–41. Copyright (2012), with permission from Thieme Medical Publishers.

and *HEPACAM* gene are present in patients with the classical form. A second improving clinical phenotype has been described in patients with an autosomal dominant (*de novo* or inherited from one parent) mutation in *HEPACAM*. MRI findings are characteristic, and consist of diffuse subcortical and periventricular white matter abnormalities associated with mild swelling of the cerebral white matter, and subcortical cysts located in the bilateral anterior temporal regions and sometimes also in the frontal or parieto-occipital regions (Fig. 31.8) [82–86].

Pelizaeus–Merzbacher disease (PMD) is an X-linked condition due to a mutation in *PLP1*, which encodes proteolipid protein, a major lipid component of the myelin sheath. Classical PMD presents with nystagmus, hypotonia, and developmental delay. Subsequently, ataxia develops and the hypotonia evolves into spasticity. A severe connatal form and a mild form of spastic paraplegia (SPG2) have also been described. MRI findings are consistent with diffuse hypomyelination involving the cerebral hemispheres, cerebellum and brain stem. An autosomal recessive PMD-like disease with mutations in GJC2 has been described with similar clinical and MRI findings to PMD [87].

References

1. Barker PB, and Horska A. (2004). Neuroimaging in leukodystrophies. *Journal of Child Neurology*, **19**(8), 559–70.
2. Schiffmann R, and van der Knaap MS. (2009). Invited article: an MRI-based approach to the diagnosis of white matter disorders. *Neurology*, **72**(8), 750–9.
3. Naidu S, Bibat G, and Lin D. (2011). Clinical approach to identification of leukoencephalopathies. In: Raymond G, Eichler F, Fatemi A, Naidu S (eds). *Leukodystrophies*. London: Mac Keith Press, pp. 209–27.
4. Steenweg ME, Vanderver A, Blaser S, et al. (2010). Magnetic resonance imaging pattern recognition in hypomyelinating disorders. *Brain*, **133**(10), 2971–82.
5. Welker KM, and Patton A. (2012). Assessment of normal myelination with magnetic resonance imaging. *Seminars in Neurology*, **32**(1), 15–28.
6. Autti T, Joensuu R, and Aberg L. (2007). Decreased T2 signal in the thalami may be a sign of lysosomal storage disease. *Neuroradiology*, **49**(7), 571–8.
7. Al-Maawali A, Blaser S, and Yoon G. (2012). Diagnostic approach to childhood-onset cerebellar atrophy: a 10-year retrospective study of 300 patients. *Journal of Child Neurology*, **27**(9), 1121–32.
8. Kiroglu Y, Calli C, Karabulut N, et al. (2010). Intracranial calcifications on CT. *Diagnostic and Interventional Radiology*, **16**(4), 263–9.
9. Cakmakci H, Pekcevik Y, Yis U, et al. (2010). Diagnostic value of proton MR spectroscopy and diffusion-weighted MR imaging in childhood inherited neurometabolic brain diseases and review of the literature. *European Journal of Radiology*, **74**(3), e161–71.
10. Barkovich AJ, and Patay Z. (2012). Metabolic, toxic and inflammatory brain disorders. In: Barkovich AJ, and Raybaud C (eds) *Pediatric neuroimaging*, 5th edn. Philadelphia: Lippincott Williams & Wilkins, pp. 81–239.
11. Saudubray JM, van den Berghe G, Walter JH (eds) (2012). *Inborn metabolic diseases: diagnosis and treatment*, 5th edn. New York: Springer.
12. Nyhan WL, Barshop BA, Al-Aqeel AI, (eds) (2012). *Atlas of inherited metabolic diseases*, 3rd edn. London: Hodder Arnold.
13. Strauss KA, Puffenberger EG, Robinson DL, et al. (2003). Type I glutaric aciduria, part 1: natural history of 77 patients. *American Journal of Medical Genetics Part C: Seminars in Medical Genetics*, **121C**(1), 38–52.
14. Kolker S, Greenberg CR, Lindner M, et al. (2004). Emergency treatment in glutaryl-CoA dehydrogenase deficiency. *Journal of Inherited Metabolic Diseases*, **27**(6), 893–902.
15. Goodman SI. (2004). Development of pathogenic concepts in glutaryl-CoA dehydrogenase deficiency: the challenge. *Journal of Inherited Metabolic Diseases*, **27**(6), 801–3.
16. Lindner M, Kolker S, Schulze A, et al. (2004). Neonatal screening for glutaryl-CoA dehydrogenase deficiency. *Journal of Inherited Metabolic Diseases*, **27**(6), 851–9.
17. Heringer J, Boy SP, Ensenauer R, et al. (2010). Use of guidelines improves the neurological outcome in glutaric aciduria type I. *Annals of Neurology*, **68**(5), 743–52.
18. Neumaier-Probst E, Harting I, Seitz A, et al. (2004). Neuroradiological findings in glutaric aciduria type I (glutaryl-CoA dehydrogenase deficiency). *Journal of Inherited Metabolic Diseases*, **27**(6), 869–76.
19. Twomey EL, Naughten ER, Donoghue VB, et al. (2003). Neuroimaging findings in glutaric aciduria type 1. *Pediatric Radiology*, **33**(12), 823–30.
20. Rzem R, Van Schaftingen E, and Veiga-da-Cunha M. (2006). The gene mutated in l-2-hydroxyglutaric aciduria encodes l-2-hydroxyglutarate dehydrogenase. *Biochimie*, **88**(1), 113–16.
21. Rzem R, Vincent MF, Van Schaftingen E, et al. (2007). L-2-hydroxyglutaric aciduria, a defect of metabolite repair. *Journal of Inherited Metabolic Diseases*, **30**(5), 681–9.
22. Barbot C, Fineza I, Diogo L, et al. (1997). L-2-Hydroxyglutaric aciduria: clinical, biochemical and magnetic resonance imaging in six Portuguese pediatric patients. *Brain Development*, **19**(4), 268–73.
23. Moroni I, D'Incerti L, Farina L, et al. (2000). Clinical, biochemical and neuroradiological findings in L-2-hydroxyglutaric aciduria. *Neurological Science*, **21**(2), 103–8.
24. D'Incerti L, Farina L, Moroni I, et al. (1998). L-2-hydroxyglutaric aciduria: MRI in seven cases. *Neuroradiology*, **40**(11), 727–33.
25. Barger AV, Campeau NG, Port JD, et al. (2009). MRS is the test of choice for detecting and monitoring disorders of creatine metabolism. *Pediatric Neurology*, **40**(5), 408–10.
26. Saneto RP, Friedman SD, and Shaw DW. (2008). Neuroimaging of mitochondrial disease. *Mitochondrion*, **8**(5–6), 396–413.
27. Friedman SD, Shaw DW, Ishak G, et al. (2010). The use of neuroimaging in the diagnosis of mitochondrial disease. *Developmental Disabilities Research Reviews*, **16**(2), 129–35.
28. Wong LJ. (2012). Mitochondrial syndromes with leukoencephalopathies. *Seminars in Neurology*, **32**(1), 55–61.
29. Poll-The BT, and Gartner J. (2012). Clinical diagnosis, biochemical findings and MRI spectrum of peroxisomal disorders. *Biochimica et Biophysica Acta*, 1822(9), 1421–9.
30. Poll-The BT, and Engelen M. (2012). Peroxisomal leukoencephalopathy. *Seminars in Neurology*, **32**(1), 42–50.
31. Loes DJ, Hite S, Moser H, et al. (1994). Adrenoleukodystrophy: a scoring method for brain MR observations. *AJNR American Journal of Neuroradiology*, **15**(9), 1761–6.
32. Melhem ER, Loes DJ, Georgiades CS, et al. (2000). X-linked adrenoleukodystrophy: the role of contrast-enhanced MR imaging in predicting disease progression. *AJNR American Journal of Neuroradiology*, **21**(5), 839–44.
33. Melhem ER, Gotwald TF, Itoh R, et al. (2001). T2 relaxation measurements in X-linked adrenoleukodystrophy performed using dual-echo fast fluid-attenuated inversion recovery MR imaging. *AJNR American Journal of Neuroradiology*, **22**(4), 773–6.
34. Sener RN. (2002). Atypical X-linked adrenoleukodystrophy: new MRI observations with FLAIR, magnetization transfer contrast, diffusion MRI, and proton spectroscopy. *Magnetic Resonance Imaging*, **20**(2), 215–19.
35. Tzika AA, Ball WS, Jr., Vigneron DB, et al. (1993). Childhood adrenoleukodystrophy: assessment with proton MR spectroscopy. *Radiology*, **189**(2), 467–80.
36. Rajanayagam V, Grad J, Krivit W, et al. (1996). Proton MR spectroscopy of childhood adrenoleukodystrophy. *AJNR American Journal of Neuroradiology*, **17**(6), 1013–24.
37. Rajanayagam V, Balthazor M, Shapiro EG, et al. (1997). Proton MR spectroscopy and neuropsychological testing in adrenoleukodystrophy. *AJNR American Journal of Neuroradiology*, **18**(10), 1909–14.

38. Ito R, Melhem ER, Mori S, et al. (2001). Diffusion tensor brain MR imaging in X-linked cerebral adrenoleukodystrophy. *Neurology*, **56**(4), 544–7.
39. Patay Z. (2005). Diffusion-weighted MR imaging in leukodystrophies. *European Radiology*, **15**(11), 2284–303.
40. Li JY, Hsu CC, and Tsai CR. (2010). Spinocerebellar variant of adrenoleukodystrophy with a novel ABCD1 gene mutation. *Journal of Neurological Sciences*, **290**(1–2), 163–5.
41. Mishra S, Modi M, Das CP, et al. (2006). Adrenoleukodystrophy manifesting as spinocerebellar degeneration. *Neurology India*, **54**(2), 195–6.
42. Vianello M, Manara R, Betterle C, et al. (2005). X-linked adrenoleukodystrophy with olivopontocerebellar atrophy. *European Journal of Neurology*, **12**(11), 912–14.
43. Gieselmann V, and Krugeloh-Mann I. (2011). Metachromatic leukodystrophy. In: Raymond G, Eichler F, Fatemi A, et al. (eds) *Leukodystrophies*. London: Mac Keith Press, pp. 130–55.
44. Cheon JE, Kim IO, Hwang YS, et al. (2002). Leukodystrophy in children: a pictorial review of MR imaging features. *Radiographics*, **22**(3), 461–76.
45. Eichler F, Grodd W, Grant E, et al. (2009). Metachromatic leukodystrophy: a scoring system for brain MR imaging observations. *AJNR American Journal of Neuroradiology*, **30**(10), 1893–7.
46. Groeschel S, Kehrer C, Engel C, et al. (2011). Metachromatic leukodystrophy: natural course of cerebral MRI changes in relation to clinical course. *Journal of Inherited Metabolic Disease*, **34**(5), 1095–102.
47. Wenger DA, Rafi MA, Luzi P, et al. (2000). Krabbe disease: genetic aspects and progress toward therapy. *Molecular Genetics and Metabolism*, **70**(1), 1–9.
48. Wenger DA. (2011). Krabbe disease (globoid cell leukodystrophy). In: Raymond G, Eichler F, Fatemi A, Naidu S (eds) *Leukodystrophies*. London: MacKeith Press, pp. 90–105.
49. Duffner PK, Barczykowski A, Jalal K, et al. (2011). Early infantile Krabbe disease: results of the World-Wide Krabbe Registry. *Pediatric Neurology*, **45**(3), 141–8.
50. Brunetti-Pierri N, and Scaglia F. (2008). GM1 gangliosidosis: review of clinical, molecular, and therapeutic aspects. *Molecular Genetics and Metabolism*, **94**(4), 391–6.
51. Gururaj A, Sztriha L, Hertecant J, et al. (2005). Magnetic resonance imaging findings and novel mutations in GM1 gangliosidosis. *Journal of Child Neurology*, **20**(1), 57–60.
52. Grosso S, Farnetani MA, Berardi R, et al. (2003). GM2 gangliosidosis variant B1 neuroradiological findings. *Journal of Neurology*, **250**(1), 17–21.
53. Inglese M, Nusbaum AO, Pastores GM, et al. (2005). MR imaging and proton spectroscopy of neuronal injury in late-onset GM2 gangliosidosis. *AJNR American Journal of Neuroradiology*, **26**(8), 2037–42.
54. Saouab R, Mahi M, Abilkacem R, et al. (2011). A case report of Sandhoff disease. *Clinical Neuroradiology*, **21**(2), 83–5.
55. Seitz D, Grodd W, Schwab A, et al. (1998). MR imaging and localized proton MR spectroscopy in late infantile neuronal ceroid lipofuscinosis. *AJNR American Journal of Neuroradiology*, **19**(7), 1373–7.
56. Viana-Baptista M. (2011). Stroke and Fabry disease. *Journal of Neurology*, **259**(6), 1019–28.
57. Matheus MG, Castillo M, Smith JK, et al. (2004). Brain MRI findings in patients with mucopolysaccharidosis types I and II and mild clinical presentation. *Neuroradiology*, **46**(8), 666–72.
58. Wang RY, Cambray-Forker EJ, Ohanian K, et al. (2009). Treatment reduces or stabilizes brain imaging abnormalities in patients with MPS I and II. *Molecular Genetics and Metabolism*, **98**(4), 406–11.
59. Kara S, Sherr EH, and Barkovich AJ. (2008). Dilated perivascular spaces: an informative radiologic finding in Sanfilippo syndrome type A. *Pediatric Neurology*, **38**(5), 363–6.
60. Manara R, Priante E, Grimaldi M, et al. (2011). Brain and spine MRI features of Hunter disease: frequency, natural evolution and response to therapy. *Journal of Inherited Metabolic Diseases*, **34**(3), 763–80.
61. Frei KP, Patronas NJ, Crutchfield KE, et al. (1998). Mucolipidosis type IV: characteristic MRI findings. *Neurology*, **51**(2), 565–9.
62. Willems PJ, Gatti R, Darby JK, et al. (1991). Fucosidosis revisited: a review of 77 patients. *American Journal of Medical Genetics*, **38**(1), 111–31.
63. Oner AY, Cansu A, Akpek S, et al. (2007). Fucosidosis: MRI and MRS findings. *Pediatric Radiology*, **37**(10), 1050–2.
64. Varho T, Jaaskelainen S, Tolonen U, et al. (2000). Central and peripheral nervous system dysfunction in the clinical variation of Salla disease. *Neurology*, **55**(1), 99–104.
65. Sonninen P, Autti T, Varho T, et al. (1999). Brain involvement in Salla disease. *AJNR American Journal of Neuroradiology*, **20**(3), 433–43.
66. Rice G, Patrick T, Parmar R, et al. (2007). Clinical and molecular phenotype of Aicardi–Goutieres syndrome. *American Journal of Human Genetics*, **81**(4), 713–25.
67. Orcesi S, La Piana R, and Fazzi E. (2009). Aicardi–Goutieres syndrome. *British Medical Bulletin*, **89**, 183–201.
68. Uggetti C, La Piana R, Orcesi S, et al. (2009). Aicardi–Goutieres syndrome: neuroradiologic findings and follow-up. *AJNR American Journal of Neuroradiology*, **30**(10), 1971–6.
69. Crow YJ, and Rehwinkel J. (2009). Aicardi–Goutieres syndrome and related phenotypes: linking nucleic acid metabolism with autoimmunity. *Human Molecular Genetics*, **18**(R2), R130–6.
70. Sawaishi Y. (2009). Review of Alexander disease: beyond the classical concept of leukodystrophy. *Brain Development*, **31**(7), 493–8.
71. Flint D, and Brenner M. (2011). Alexander disease. In: Raymond G, Eichler F, Fatemi A, Naidu S (eds) *Leukodystrophies*. London: MacKeith Press, pp. 106–29.
72. Balbi P, Salvini S, Fundaro C, et al. (2010). The clinical spectrum of late-onset Alexander disease: a systematic literature review. *Journal of Neurology*, **257**(12), 1955–62.
73. van der Knaap MS, Naidu S, Breiter SN, et al. (2001). Alexander disease: diagnosis with MR imaging. *AJNR American Journal of Neuroradiology*, **22**(3), 541–52.
74. van der Voorn JP, Pouwels PJ, Salomons GS, et al. (2009). Unraveling pathology in juvenile Alexander disease: serial quantitative MR imaging and spectroscopy of white matter. *Neuroradiology*, **51**(10), 669–75.
75. Matalon R, and Michals-Matalon K. (1999). Biochemistry and molecular biology of Canavan disease. *Neurochemistry Research*, **24**(4), 507–13.
76. Surendran S, Michals-Matalon K, Quast MJ, et al. (2003). Canavan disease: a monogenic trait with complex genomic interaction. *Molecular Genetics and Metabolism*, **80**(1–2), 74–80.
77. Michals K, and Matalon R. (2011). Canavan disease. In: Raymond G, Eichler F, Fatemi A, Naidu S (eds) *Leukodystrophies*. London: MacKeith Press, pp. 156–69.
78. van der Knaap MS, Barth PG, Gabreels FJ, et al. (1997). A new leukoencephalopathy with vanishing white matter. *Neurology*, **48**(4), 845–55.
79. van der Knaap MS, Leegwater PA, Konst AA, et al. (2002). Mutations in each of the five subunits of translation initiation factor eIF2B can cause leukoencephalopathy with vanishing white matter. *Annals of Neurology*, **51**(2), 264–70.
80. Bugiani M, Boor I, Powers JM, et al. (2010). Leukoencephalopathy with vanishing white matter: a review. *Journal of Neuropathology and Experimental Neurology*, **69**(10), 987–96.
81. Labauge P, Horzinski L, Ayrignac X, et al. (2009). Natural history of adult-onset eIF2B-related disorders: a multi-centric survey of 16 cases. *Brain*, **132**(Pt 8), 2161–9.
82. van der Knaap MS, Barth PG, Stroink H, et al. (1995). Leukoencephalopathy with swelling and a discrepantly mild clinical course in eight children. *Annals of Neurology*, **37**(3), 324–34.
83. van der Knaap MS, Valk J, Barth PG, et al. (1995). Leukoencephalopathy with swelling in children and adolescents: MRI patterns and differential diagnosis. *Neuroradiology*, **37**(8), 679–86.
84. Leegwater PA, Yuan BQ, van der Steen J, et al. (2001). Mutations of MLC1 (KIAA0027), encoding a putative membrane protein, cause

megalencephalic leukoencephalopathy with subcortical cysts. *American Journal of Human Genetics*, **68**(4), 831–8.

85. Lopez-Hernandez T, Ridder MC, Montolio M, et al. (2011). Mutant GlialCAM causes megalencephalic leukoencephalopathy with subcortical cysts, benign familial macrocephaly, and macrocephaly with retardation and autism. *American Journal of Human Genetics*, **88**(4), 422–32.
86. Lopez-Hernandez T, Sirisi S, Capdevila-Nortes X, et al. (2011). Molecular mechanisms of MLC1 and GLIALCAM mutations in megalencephalic leukoencephalopathy with subcortical cysts. *Human Molecular Genetics*, **20**(16), 3266–77.
87. Hobson GM, and Garbern JY. (2012). Pelizaeus–Merzbacher disease, Pelizaeus–Merzbacher-like disease 1, and related hypomyelinating disorders. *Seminars in Neurology*, **32**(1), 62–7.

CHAPTER 32

Central nervous system vasculitis

Giulio Zuccoli, Nicolò Pipitone,
Caterina Giannini, and Carlo Salvarani

Introduction

Vasculitis of the central nervous system (CNS) is a heterogenous group of disorders characterized by inflammatory changes in the walls of CNS vessels [1]. Such inflammatory changes may cause stenoses or occlusions leading to ischaemic damage, dilations and aneurysms leading to haemorrhages, or both [2]. CNS vasculitis can be idiopathic or secondary to a variety of causes, and be restricted to the CNS or be part of a systemic process. Idiopathic vasculitis limited to the CNS is often referred to as primary angiitis of the central nervous system (PACNS) or primary central nervous system vasculitis (PCNSV). This chapter focuses on the neuroimaging findings of PCNSV, and highlights their role in the diagnostic work-up and follow-up of patients with suspected or established disease.

Epidemiology

CNS vasculitis is a rare disorder. A retrospective review from the Mayo Clinic spanning a 17-year period identified 113 cases of CNS vasculitis, 73 of whom were classified as PCNSV. The average annual incidence rate of PCNSV has been estimated to be 2.4 cases per 1,000,000 person-years in the white United States population [3]. There is no clear gender preponderance, and the mean age at onset is 50 years [3,4]. However, PCNSV can affect any age group, including children [5].

Classification criteria

PCNSV is often classified according to the criteria proposed by Calabrese and Mallek, which include the history or presence of an acquired neurological deficit, histological or angiographic evidence of vasculitis, and the lack of evidence of a systemic vasculitis or other conditions to which the angiographic or pathologic features could be secondary [6]. However, these criteria perform poorly in discriminating PCNSV from the reversible cerebral vasoconstriction syndrome (RCVS), a frequent mimicker of PCNSV. Therefore, Birnbaum and Hellmann proposed a revised version of the Calabrese and Mallek criteria, according to which patients can receive a definite diagnosis of PCNSV if there is confirmation of vasculitis on analysis of a tissue biopsy specimen. Alternatively there can be a probable diagnosis of PCNSV, in the absence of tissue confirmation, if there are high-probability findings on an angiogram with abnormal findings on magnetic resonance imaging (MRI) and a cerebrospinal fluid (CSF) profile consistent with PCNSV [7].

Clinical manifestations

PCNSV can present with a vast array of focal and diffuse neurological manifestations. The onset is frequently insidious and the course is slowly progressive, but some patients have a remitting-relapsing course, while a few can present with rapidly progressive clinical manifestations. The commonest features are headache, altered cognition, hemiparesis, and neurological deficit including stroke [3,8]. Less common manifestations are aphasia, ataxia, diplopia, visual field defects, paraparesis, or quadriparesis, nausea or vomiting, dysarthria, and numbness [3]. Patients with small artery involvement (characterized by negative angiograms and positive biopsies) have, overall, a lesser disability and better survival rate compared with those with large artery involvement (characterized by multiple, severe stenoses at angiograms and diffuse ischaemic lesions on MRI) [3,9,10]. By definition, no constitutional or extra-neurological features should be present in patients with PCNSV [4]. In contrast, when the CNS is affected by a systemic vasculitis, there may be other symptoms and signs related to the systemic inflammatory process, and to the specific organ(s) involved.

Diagnostic work-up

Laboratory tests

Laboratory tests are usually normal in patients with PCNSV, although the erythrocyte sedimentation rate (ESR) can be mildly elevated [4]. Autoantibodies such as rheumatoid factor, antinuclear antibodies, and anti-neutrophil cytoplasmic antibodies are absent [11].

CSF analysis

CSF analysis is abnormal in 80–90% of patients with established PCNSV [3,4,11,12]. CSF changes are non-specific and include mildly increased protein concentration, leukocyte count, or both. Occasionally, oligoclonal bands can be found, while glucose levels are normal [3,11]. Adequate stains, cultures, and serological/molecular analysis investigations should be performed to rule out infections and tumours [13]. A normal CSF, together with a normal brain MRI' virtually rules out PCNSV [1].

Biopsy

Biopsy of the CNS remains the gold standard for diagnosis of PCNSV [12]. The most common histological pattern is of granulomatous vasculitis (58% of patients), followed by lymphocytic (28%), and necrotizing (14%) vasculitis [3]. β-amyloid vascular deposits are present in almost 50% of patients with granulomatous changes [14]. Biopsy is 62–78% sensitive for PCNSV and carries a negligible risk of serious complications when performed by an expert operator [3,12].

Neuroimaging findings in primary central nervous system vasculitis

Role of neuroimaging studies in the diagnosis of PCNSV

Computed tomography

Computed tomography (CT) demonstrates ischaemic lesions in about one-half of patients with PCNSV [3]. Bilateral lesions involving multiple vascular beds are suggestive, but by no means *per se* diagnostic, of vasculitis [15] [Fig. 32.4]. Compared with MRI, CT is less sensitive in detecting signs of ischaemia, related to vasculitis [3,16], and has largely been eclipsed by MRI in screening for suspected PCNSV.

MRI

Brain MRI is the investigation of choice in suspected PCNSV [Fig. 32.1–32.5]. The vast majority (>90%) of patients with PCNSV have an abnormal MRI of the CNS, and the negative predictive value of MRI is higher than that of angiography [3,15]. However, MRI findings are largely non-specific [15]. Infarctions are the commonest lesions, usually multiple in number and with a bilateral distribution [3]. In over half of cases, both the cortex and the subcortical white matter are involved [3]. The appearance of infarctions is quite variable—some are consistent with large artery or branch artery distributions, while others may occur in a small artery pattern [3]. Intracranial haemorrhages are far less common (<10% of cases); they are often associated with histological necrotizing changes, which are thought to predispose the affected arterial walls to weakening and subsequent rupture [3,17]. Petechial haemorrhages (microhaemorrhages) caused by small-artery breakdown are also rare, and are best appreciated on blood sensitive MRI sequences T_2*-weighted MR images [15,18]. The differential diagnosis of cerebral microhaemorrhages should include congophilic amyloid angiopathy (CoAA), and hypertensive cerebral angiopathy (HCA) [19]. Less common causes of microhaemorrhages are cerebral cavernous malformations

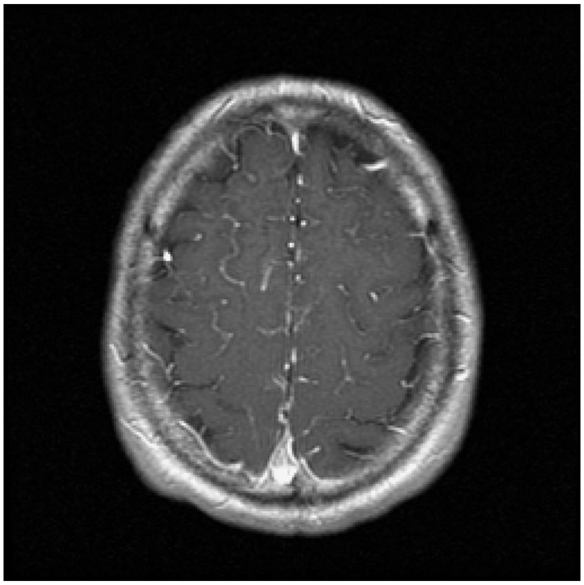

Fig. 32.1 Post-contrast MRI T_1-weighted image showing subtle leptomeningeal enhancement in a patient with PCNSV.

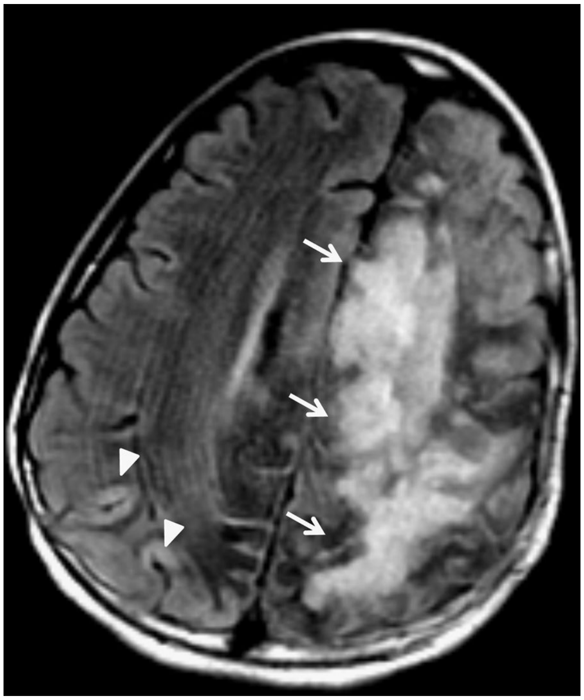

Fig. 32.2 FLAIR MRI image of a patient with PCNSV showing leptomeningeal disease with underlying infiltrative white matter disease.

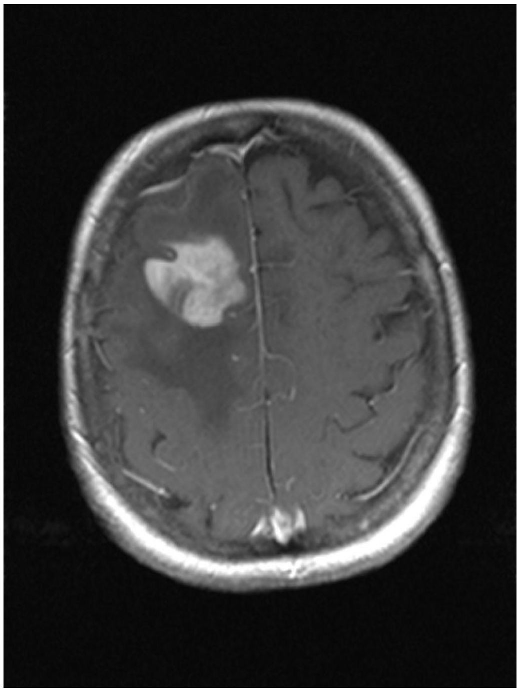

Fig. 32.3 Post-contrast MRI T_1-weighted image of a patient with PCNSV showing an enhancing parenchymal mass in the white matter of the right frontal lobe.

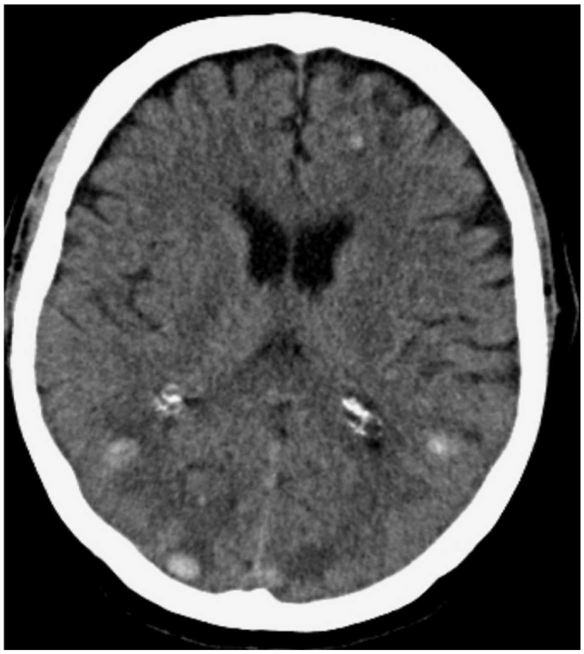

Fig. 32.4 CT of a patient with PCNSV showing multiple acute cortical and subcortical parenchymal haemorrhages.

(CCM); sporadic CCM cases present with single lesions, while individuals with multiple lesions have an autosomal dominant heritable form. Mutations in three *CCM* genes account for roughly 71% of Caucasian familial *CCM* cases. Thus, MRI features of multiple parenchymal microhaemorrhages on T_2*-weighted MR images should be tested for CCM genotypes (CCM1, CCM2 and CCM3), particularly in those patients presenting with seizures and headache [20]. According to Zabramski, one neuroimaging phenotype of cavernous malformation that can be indistinguishable from cerebral microhaemorrhages on T_2*-weighted gradient echo (T2*-GRE) MRI is type 4 cavernous malformation [21]. Microhaemorrhages have also been described in lymphoblastic leukaemia [22]. Rarely, brain microhaemorrhages are observed in micrometastasis from melanoma or renal cell carcinoma. Cerebral microhaemorrhages have been reported to occur in 25–70% of cases of cerebral autosomal dominant arteriopathy with subcortical infarcts and leukoencephalopathy (CADASIL), but have no typical distribution, while in CADASIL T_2 alterations demonstrate a quite typical distribution [23]. Multiple foci of blooming (marked low signal intensity) on susceptibility-weighted images (SWI) and more in general on T2*-GRE and/or SWI sequence may represent microbleeds from diffuse axonal injury (DAI). Particularly on SWI, these sequelae may last several years from the traumatic brain injury. Some patients display multiple foci that are hyperintense in T_2-weighted and fluid attenuated inversion recovery (FLAIR) sequences; such lesions have a low specificity for PCNSV, and should always be interpreted in conjunction with other imaging and clinical findings [13]. Multiple brain hyperintensities underlying gliosis from prior infarcts are frequently observed in hypertensive encephalopathy and hereditary cerebral small vessel diseases (SVDs) [24]. Most cerebral SVDs involve the small penetrating arteries originating from the large pial arteries at the skull base. They have a luminal dimension ranging from 0.05–0.4 to 1.4 mm. Infarcts in the regions irrigated by these small vessels are prone to occlusion-related hypoxic ischaemic injury being widely lacking distal collateralization. Bilateral, multifocal occlusions of these arteries cause lacunar infarctions and confluent white matter damage, defined as 'vascular leukoencephalopathy' or 'leuko-araiosis' (literally 'white matter rarefaction') [25]. Other non-specific MRI signs include multifocal hypointense lesions on T_1-weighted sequences and, in acute cases, restricted diffusion on diffusion-weighted imaging (DWI) [15]. DWI allows detection of cytotoxic oedema from CNS vasculitis-related stroke [26]. The hyperacute phase of infarction shows decreased apparent diffusion coefficient (ADC) map, which translates into normal to mildly high signal intensity on T_2-weighted images—the acute phase shows decreased ADC with hyperintensity on T_2-FLAIR images, while in the subacute phase, ADC values normalize, and in the chronic phase ADC values increase [26]. Typically, ADC continues to decrease reaching the maximum peak at 8–32 hours. Of note, ADC values remain markedly reduced for 3–5 days. At 1–4 weeks from the initial ischaemic event, ADC returns to baseline [27]. It should be noted that recent microhaemorrhages may demonstrate restricted diffusion; thus, DWI/ADC correlation with long and short repetition time (TR) sequences (T_1, T_2, FLAIR, T_2*) should always be obtained. Contrast enhancement is observed in approximately one-third of lesions of MRI, and often resolves following treatment [13,28]. Enhancement is also in small vessels diseases-related infarct due to the associated blood–brain barrier damage. Enhancement of Virchow–Robin perivascular spaces is uncommon, but fairly specific for vasculitis of the CNS [28], while 8% of patients with PCNSV have evidence of prominent leptomeningeal enhancement [29]. Patients with florid leptomeningeal enhancement often have negative angiograms and positive biopsies with a granulomatous pattern, consistent with small-vessel involvement [29]. When present, gadolinium-enhancement of the meninges should be considered a target for biopsy to confirm the diagnosis of PCNSV, given the lower incidence of neurological complications when compared to brain biopsy [13].

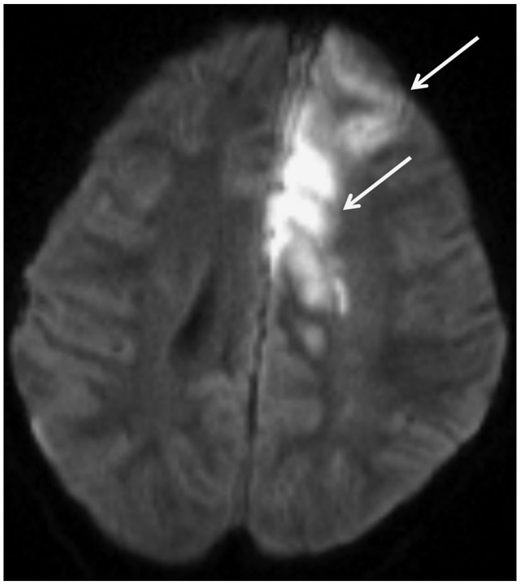

Fig. 32.5 DWI MRI image of a patient with PCNSV showing restricted diffusion consistent with cytotoxic oedema in the territory of the left anterior cerebral artery (arrows).

About 6% of patients with PCNSV present with a tumour-like single mass lesion; these patients have usually a more aggressive disease course and poorer outcomes [30].

Spinal cord lesions have been noted in 5% of patients with PCNSV. All patients with spinal involvement had also evidence of brain vasculitis [31].

The main limitation of MRI in PCNSV is its poor specificity. Recently, contrast enhancement of arterial walls on T_1 sequences using high-resolution MRI has been shown to be able to differentiate between vasculitis (where contrast-enhanced is present) from cerebral vasoconstriction syndromes (where contrast-enhanced is absent) [32]. This procedure may hold promise in increasing the specificity of MRI for diagnosing CNS vasculitis, although it may not discriminate PCNSV from other cerebral vasculitides [32].

Cerebral vascular imaging studies

Cerebral vascular imaging studies comprise digital subtraction angiography (DSA) and magnetic resonance angiography (MRA) (Fig. 32.6–32.7). Today, the routine protocol is mostly based on a large field-of-view contrast-enhanced MRA (CE-MRA) covering the entire course of the neck arteries as well as the circle of Willis. Whereas this is a good test for the detection of stenosis of the neck vessels caused by vasoconstriction, vessel wall inflammation, dissection, or cut-off, subtle occlusions within the circle of Willis may be not depicted given the low spatial and temporal resolution of CE-MRA imaging techniques. Hence, 3-dimensional (3D) time of flight (TOF) MR angiographic sequence should be obtained, since it offers higher spatial resolution particularly when a 3 T magnet is utilized [4]. Notably, the circle of Willis may not be adequately highlighted at 1.5 T 3D TOF. Both DSA and MRA can visualize large- and medium-sized intracranial arteries, but DSA is approximately 20% more sensitive than MRA in demonstrating vascular changes in PCSNV [3,12]. Another limitation of MRA is the overestimation of vascular stenosis, particularly at points of vessel branching [33]. On the other hand, the technical advantages provided by DSA, including its superior spatial resolution (0.2 mm), are partially offset by its higher risks including stroke (0.25% of cases) [15]. Therefore, it is reasonable to perform 3D-TOF MRA first in patients with suspected PCNSV, and undertake DSA only when MRA is not contributive. However, even DSA may be false-negative when the arteries involved are smaller than 500 μm in diameter [13]. Overall, the sensitivity of DSA for the clinical diagnosis of PCNSV varies between 40 and 90%, and is lower for PCNSV diagnosed according to histological criteria [3,8,34]. Therefore, DSA (and MRA) are not appropriate screening tests for suspected PCSNV. The specificity of DSA for PCNSV has also been estimated to be as low as 30% [8], although it can increase if the pre-test probability of PCSNV is high and if the angiographic changes are typical of vasculitis. Changes highly suggestive of vasculitis consist of diffuse segmental arterial wall narrowing followed by post-stenotic dilation in numerous cerebral arteries ('beading') in the absence of proximal vascular atherosclerosis or other recognized abnormalities [15]. In contrast, isolated abnormalities in several arteries or several abnormalities in a single artery are less consistent with PCNSV [12]. Additional vascular abnormalities that may be observed in PCNSV are the development of collaterals, delayed contrast enhancement and washout, and (rarely) true aneurysms [4].

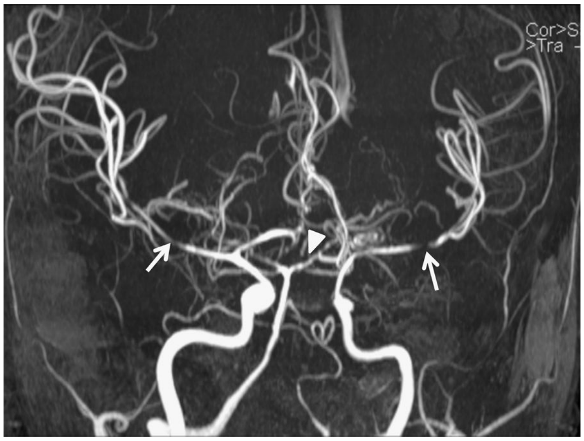

Fig. 32.6 Magnetic resonance angiography of a patient with PCNSV (images obtained on a 3 T scanner) showing a multisegmental stenosis involving the bilateral distal M1 segment of the middle cerebral artery and the left A1 segment of the anterior cerebral artery (arrows).

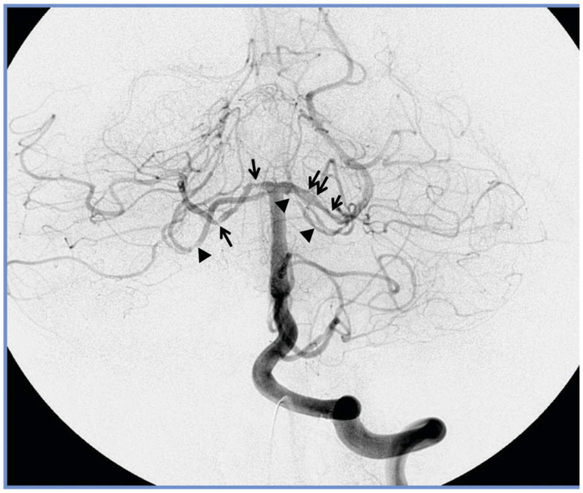

Fig. 32.7 Digital subtraction angiography of a patient with PCNSV. Multiple stenosis of the bilateral posterior cerebral arteries (arrows) and superior cerebellar arteries (black arrowheads). Please note fusiform enlargement of the P1 segment of left posterior cerebral artery (double arrow).

It is important to appreciate that none of the above changes is pathognomonic of PCNSV, and that the angiographic pattern seen in PCNSV can also be seen in some of its mimickers, particularly in the cerebral vasoconstriction syndromes [35]. Therefore, the correct interpretation of vascular imaging findings requires the integration of clinical and radiological information.

It is useful to compare MRA findings with MRI lesions. When the sites of infarctions on MRI correlate with angiographic abnormalities, this can be taken as further confirmation of CNS vasculitis causing ischaemic lesions [15]. However, vascular imaging studies, as a rule, show only a modest correlation with MRI. In a case series, about 65% of MRI lesions were also evident on MRA, while only 44% of MRA lesions were associated with MRI abnormal findings [36]. MRI lesions without MRA changes are probably due to small artery involvement, which is below the power of resolution of MRA; conversely, MRA lesions in the absence of abnormal MRI findings may be due to haemodynamically irrelevant arterial stenosis [36]. Severe, multiple changes on MRA with a normal or minimally-altered MRI should always raise the suspicion of cerebral vasoconstriction syndrome [4].

Cerebral perfusion studies

PCT and ASL: Although there are no reports available on perfusion imaging findings in PCNSV, perfusion deficits secondary to CNS vasculitis could be easily depicted by using perfusion computed tomography (PCT) and arterial spin-labelling (ASL) MRI that allow rapid qualitative and quantitative evaluation of cerebral perfusion by generating cerebral maps of blood flow [37]. Furthermore, vasculitis can occasionally present as mass-like (tumefactive) lesions, mimicking neoplasms on morphologic imaging. PCT and ASL can be used to exclude a neoplasm by demonstrating decreased blood volume in these lesions [38]. MRI ASL is a perfusion technique for quantitatively measuring cerebral blood flow (CBF) by utilizing arterial water as a freely diffusible tracer. To-date ASL represents the least invasive study to quantitatively and qualitatively evaluate brain perfusion, thus avoiding radiation exposure long-term related risk effects, particularly in younger patients, allowing non-invasive serial pre- and post-treatment analysis of brain perfusion [39,40].

Role of neuroimaging studies in the follow-up of patients of PCNSV

MRI changes parallel the clinical course of PCNSV [28]. In patients that have a favourable response to therapy, lesions disappear or decrease in size, number, or both; enhancement also resolves or becomes less widespread [28]. Conversely, clinical worsening is characterized by the appearance of new lesions, or increased signal and enhancement in existing ones [28]. Occasionally, cerebral haemorrhage may occur in relapsing patients [41]. Serial studies also demonstrate that angiographic changes improve or stabilize in patients with a clinical response to therapy [42]. These data support the use of imaging studies in monitoring patients with PCNSV.

Role of neuroimaging studies in the differential diagnosis of PCNSV

A large number of disorders can potentially mimic PCNSV (Table 32.1).

RCVS can present with severe ('thunderclap') headache and multiple stenoses on angiograms [Fig. 32.8]. However, unlike PCNSV, RCVS are characterized by a sudden onset followed by a monophasic course and there are often identifiable risk factors (exposure to vasoactive substances, onset in the post-partum period, and a history of migraine), CSF analysis is negative, and MRI is normal in 70% of cases [8,43]. In acute hemiplegic migraine (AHM) vasoconstriction of the proximal and distal anterior circulation arteries may be associated with transient ischaemic changes, as demonstrated by DWI/ADC sequences [44].

Numerous infective agents have been linked to vasculitis of the CNS, including *Mycobacterium* tuberculosis, syphilis, varicella-zoster virus (VZV), and HIV [1]. The pattern of lesions on imaging studies may sometimes be evocative of a specific type of vasculitis: for instance, tuberculosis often presents as meningitis with or without angiitis involving the arteries at the base of the cranium or as tuberculoma with adjacent focal angiitis, while syphilis typically causes infarctions in the middle cerebral artery distribution [1]. However, neither the morphology nor the distribution of lesions can reliably differentiate between different infectious vasculitides, or between infectious and non-infectious vasculitis. Therefore, if there is a suspicion of infectious vasculitis, CSF analysis with stains, culture, and serological or molecular biology tests is required to arrive at a precise diagnosis. If a biopsy is taken, a sample should also be analysed for evidence of infection.

Table 32.1 Main mimickers of primary central nervous system vasculitis

Non-inflammatory vascular diseases	
	RCVS (reversible cerebral vasoconstriction syndrome)
	Atherosclerosis
	Embolism
	Fibromuscular dysplasia
	Hypertensive vascular disease
	Hypercoagulation disorders
	Mitochondrial diseases (example: MELAS)
Hereditary small vessels angiopathies (example: CADASIL, CARASIL)	
	Moyamoya disease
	Radiation vasculopathy
	Susac syndrome
Demyelinating diseases	
	Multiple sclerosis
	ADEM (acute disseminated encephalomyelitis)
Primary systemic vasculitides	
	Adamantiades-Behçet disease
	ANCA-associated vasculitis
	Cogan syndrome
	Giant cell arteritis (very rarely)
	Hypersensitivity vasculitis
	Kawasaki disease
	Polyarteritis nodosa
Vasculitis associated with connective tissue diseases	
Infections	
Tumours and paraneoplastic vasculitis (example: angiotropic large cell lymphoma)	
Others	
Antiphospholipid syndrome	
Sarcoidosis-associated vasculitis	

Numerous primary systemic vasculitides can potentially affect the CNS (Table 32.1). Giant cell arteritis can cause headache like PCNSV, but involvement of intracranial arteries in giant cell arteritis is exceptional [45]. In contrast, CNS involvement can occur in a sizeable minority of patients with Adamantiades–Behçet disease, anti-neutrophil cytoplasmic antibodies (ANCA)-associated vasculitis, polyarteritis nodosa, Cogan syndrome, and hypersensitivity vasculitis [11,46].

Neurological symptoms are observed in 5–14% of patients with Adamantiades–Behçet disease (ABD) [47]. Neurological involvement in ABD may be subclassified into two major forms. In the parenchymal form, meningoencephalitis predominantly affecting the brainstem occurs, whereas the non-parenchymal form is characterized by thrombosis within the dural venous sinuses. The most prominent histopathological finding is the presence of perivascular infiltration of T lymphocytes and monocytes [48].

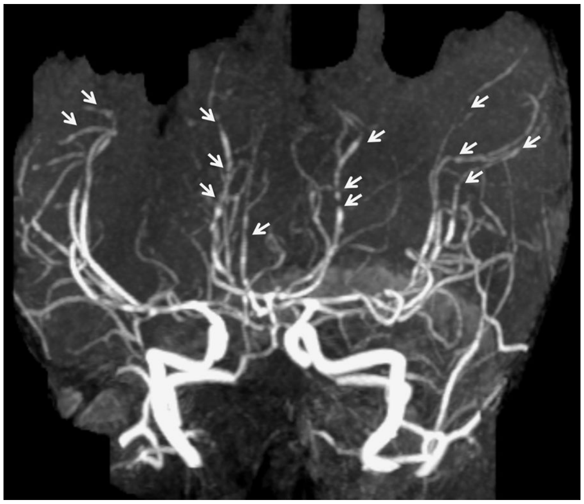

Fig. 32.8 3D-TOF magnetic resonance angiography showing multiple stenoses in a patient with the reversible cerebral vasoconstriction syndrome (arrows).

CNS symptoms are present in 7–11% of patients with granulomatous polyangiitis (previously known as Wegener's granulomatosis) [46,49] and 1–8% of patients with eosinophilic granulomatosis with polyangiitis (previously known as Churg–Strauss syndrome) [50,51]. In ANCA-associated vasculitis, CNS manifestations might be caused by vasculitis affecting the brain, but also by granulomata, uncontrolled hypertension, sepsis, and coagulation disorders. Radiographically-verified vasculitis of CNS is rare, and occurs in fewer than 2% of patients with granulomatosis with polyangiitis [49] and in only 4% of those with eosinophilic granulomatosis with polyangiitis [50].

Sometimes, vasculitis can be associated with a connective tissue disease [11]. In such cases, the clinical picture and the appropriate serological testing can guide to the correct diagnosis.

In addition to vasculitis proper, other vasculopathies can also mimic PCNSV. Cerebral autosomal dominant arteriopathy with subcortical infarcts and leuco-encephalopathy (CADASIL) is a hereditary disease of small cerebral arteries that affects middle-aged adults [52]. CADASIL typically presents with clinical manifestations reminiscent of PCNSV, including cerebral ischaemic events, cognitive impairment, and (usually migraine-type) headache. Brain MRI changes depend on the stage of the disease. Early alterations consist of STIR and T_2-weighted hyperintense punctiform or lacunar lesions predominantly involving the periventricular areas and the centrum semiovale. These lesions can subsequently spread—mostly in a symmetrical fashion—to the external capsule and the anterior part of the temporal lobes, as well as the basal ganglia and thalamus. Dilated perivascular spaces and microbleeds (on gradient echo images) can also occur. Later on, lacunar infarcts (hypointense on T_1-weighted sequences) and sometimes brain atrophy become appreciable [52,53].

Mitochondrial myopathy, encephalopathy, lactic acidosis, and stroke-like episodes (MELAS) is a multisystemic mitochondrial disease manifesting in children and young adults with recurrent episodes of strokes, seizures, headache, and cognitive deficit [54]. MRI shows infarctions mainly occurring in the occipital and parietal lobes, but the deep gray matter can also be affected (Fig. 32.9). The lesions depicted by MRI are not specific, but clues to the diagnosis are the lack of correlation between brain lesions and distinct arterial territories, as well as the tendency of brain lesions to migrate over time on serial MRI. Another feature that can arise the suspicion of MELAS is the presence of basal ganglial calcifications in young people [54].

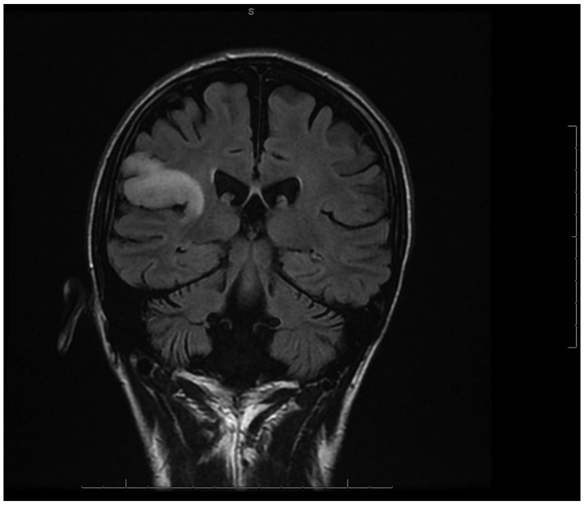

Fig. 32.9 MELAS: oedema mainly involving the cortex in the right frontoinsular lobe seen (coronal FLAIR images).

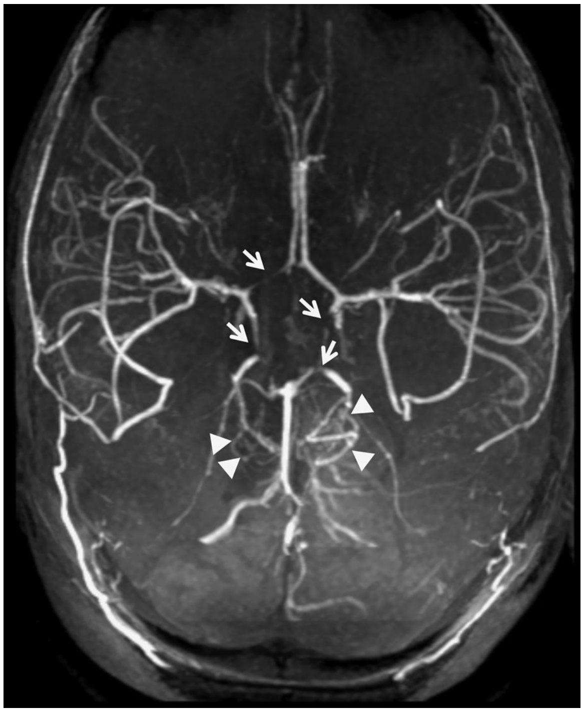

Fig. 32.10 Moyamoya syndrome: multilevel vascular stenoses on 3D TOF magnetic resonance angiography (arrows). Please note extensive asymmetric collateral circulation involving the posterior cerebral arteries (arrowheads).

Birnbaum J, and Hellmann DB. (2009). Primary angiitis of the central nervous system. *Archives of Neurology*, **66**, 704–9.

Hajj-Ali RA, Singhal AB, Benseler S, et al. (2011). Calabrese LH primary angiitis of the CNS. *Lancet Neurology*, **10**, 561–72.

Susac syndrome is a rare microangiopathy defined in its fully-fledged form by the triad of encephalopathy, branch retinal artery occlusions, and hearing loss [55]. MRI is the technique of choice to visualize brain lesions. Findings include small foci of high signal intensity on T_2-weighted or FLAIR sequences, often enhancing on T_1-weighted sequences, with preferential involvement of white over gray matter [56]. Leptomeningeal enhancement is present in one-third of cases. There is a typical predilection for the involvement of the central fibres of the corpus callosum with relative sparing of the periphery [55]. Cerebral angiography is invariably normal because Susac syndrome affects precapillary arterioles that are below the resolution of angiography [55].

Imaging studies rarely provide a strong diagnostic indication on their own [57]. However, sometimes the pattern observed on imaging can point to a specific diagnosis. An example is the progressive occlusion of the internal carotid arteries extending to the proximal anterior and middle arteries seen in Moyamoya disease (Fig. 32.10) [2].

Conclusion

Imaging studies play a key role in the screening, diagnosis, and monitoring of patients with CNS vasculitis. However, imaging findings need to be fully integrated with clinical and laboratory data to arrive at a confident diagnosis. Advances in neuroimaging will, in all likelihood, further increase the importance of imaging studies in patients with CNS vasculitis. A first line standard neuroimaging protocol in PCNS should include T2* or SWI, FLAIR, DWI/ADC, 3D-TOF MRA, and ASL imaging. When available, a 3 T magnet should be preferred given its higher spatial and temporal resolution to evaluate the intracranial arteries.

References

1. Zuber M, Blustajn J, Arquizan C, et al. (1999). Angiitis of the central nervous system. *Journal of Neuroradiology*, **26**, 101–17.
2. Garg A. (2011). Vascular brain pathologies. *Neuroimaging Clinics of North America*, **21**, 897–926, ix.
3. Salvarani C, Brown RD, Jr., Calamia KT, et al. (2007). Primary central nervous system vasculitis: analysis of 101 patients. *Annals of Neurology*, **62**, 442–51.
4. Neel A, and Pagnoux C. (2009). Primary angiitis of the central nervous system. *Clinical and Experimental Rheumatology*, **27**, S95–107.
5. Twilt M, and Benseler SM. (2012). The spectrum of CNS vasculitis in children and adults. *Nature Reviews Rheumatology*, **8**, 97–107.
6. Calabrese LH, and Mallek JA. (1988). Primary angiitis of the central nervous system. Report of 8 new cases, review of the literature, and proposal for diagnostic criteria. *Medicine (Baltimore)*, **67**, 20–39.
7. Birnbaum J, and Hellmann DB. (2009). Primary angiitis of the central nervous system. *Archives of Neurology*, **66**, 704–9.
8. Salvarani C, Brown RD, Jr, and Hunder GG. (2012). Adult primary central nervous system vasculitis: an update. *Current Opinions in Rheumatology*, **24**, 46–52.
9. Salvarani C, Brown RD, Jr., Calamia KT *et al.* (2011). Rapidly progressive primary central nervous system vasculitis. *Rheumatology (Oxford)*, **50**, 349–58.
10. Salvarani C, Brown RD, Jr., Calamia KT *et al.* (2008). Angiography-negative primary central nervous system vasculitis: a syndrome involving small cerebral vessels. *Medicine (Baltimore)*, **87**, 264–71.
11. Hajj-Ali RA. (2010). Primary angiitis of the central nervous system: differential diagnosis and treatment. *Best Practice & Research Clinical Rheumatology*, **24**, 413–26.
12. Salvarani C, Brown RD, Jr, and Hunder GG. (2012). Adult primary central nervous system vasculitis. *Lancet*, **380**, 767–77.
13. Hajj-Ali RA, Singhal AB, Benseler S, et al. (2011). Primary angiitis of the CNS. *Lancet Neurology*, **10**, 561–72.
14. Salvarani C, Brown RD, Jr, Calamia KT *et al.* (2008). Primary central nervous system vasculitis: comparison of patients with and without cerebral amyloid angiopathy. *Rheumatology (Oxford)*, **47**, 1671–7.
15. Zuccoli G, Pipitone N, Haldipur A, et al. (2011). Imaging findings in primary central nervous system vasculitis. *Clinical and Experimental Rheumatology*, **29**, S104–9.
16. Stone JH, Pomper MG, Roubenoff R, et al. (1994). Sensitivities of noninvasive tests for central nervous system vasculitis: a comparison of lumbar puncture, computed tomography, and magnetic resonance imaging. *Journal of Rheumatology*, **21**, 1277–82.
17. Salvarani C, Brown RD, Jr., Calamia KT *et al.* (2011). Primary central nervous system vasculitis presenting with intracranial hemorrhage. *Arthritis & Rheumatology*, **63**, 3598–606.
18. Ay H, Sahin G, Saatci I, et al. (2002). Primary angiitis of the central nervous system and silent cortical hemorrhages. *AJNR American Journal of Neuroradiology*, **23**, 1561–3.
19. Blitstein MK, and Tung GA. (2007). MRI of cerebral microhemorrhages. *AJR American Journal of Roentgenology*, **189**, 720–5.
20. Gault J, Sain S, Hu LJ, et al. (2006). Spectrum of genotype and clinical manifestations in cerebral cavernous malformations. *Neurosurgery*, **59**, 1278–84.
21. Zabramski JM, Wascher TM, Spetzler RF *et al.* (1994). The natural history of familial cavernous malformations: results of an ongoing study. *Journal of Neurosurgery*, **80**, 422–32.
22. Chan MS, Roebuck DJ, Yuen MP, et al. (2006). MR imaging of the brain in patients cured of acute lymphoblastic leukemia—the value of gradient echo imaging. *AJNR American Journal of Neuroradiology*, **27**, 548–52.
23. Sureka J, and Jakkani RK. (2012). Clinico-radiological spectrum of bilateral temporal lobe hyperintensity: a retrospective review. *British Journal of Radiology*, **85**, e782–92.
24. Federico A, Di D, I, Bianchi S, et al. (2012). Hereditary cerebral small vessel diseases: a review. *Journal of Neurological Science*, **322**, 25–30.
25. Ringelstein EB, and Nabavi DG. (2005). Cerebral small vessel diseases: cerebral microangiopathies. *Current Opinions in Neurology*, **18**, 179–88.
26. Moritani T, Hiwatashi A, Shrier DA, et al. (2004). CNS vasculitis and vasculopathy: efficacy and usefulness of diffusion-weighted echoplanar MR imaging. *Clinical Imaging*, **28**, 261–70.
27. Schaefer PW, Grant PE, and Gonzalez RG. (2000). Diffusion-weighted MR imaging of the brain. *Radiology*, **217**, 331–45.
28. Campi A, Benndorf G, Filippi M, et al. (2001). Primary angiitis of the central nervous system: serial MRI of brain and spinal cord. *Neuroradiology*, **43**, 599–607.
29. Salvarani C, Brown RD, Jr., Calamia KT *et al.* (2008). Primary central nervous system vasculitis with prominent leptomeningeal enhancement: a subset with a benign outcome. *Arthritis and Rheumatics*, **58**, 595–603.
30. Molloy ES, Singhal AB, and Calabrese LH. (2008). Tumour-like mass lesion: an under-recognised presentation of primary angiitis of the central nervous system. *Annals of Rheumatic Diseases*, **67**, 1732–5.
31. Salvarani C, Brown RD, Jr., Calamia KT *et al.* (2008). Primary CNS vasculitis with spinal cord involvement. *Neurology*, **70**, 2394–400.
32. Mandell DM, Matouk CC, Farb RI *et al.* (2012). Vessel wall MRI to differentiate between reversible cerebral vasoconstriction syndrome and central nervous system vasculitis: preliminary results. *Stroke*, **43**, 860–2.
33. Pipitone N, Versari A, and Salvarani C. (2008). Role of imaging studies in the diagnosis and follow-up of large-vessel vasculitis: an update. *Rheumatology (Oxford)*, **47**, 403–8.
34. Vollmer TL, Guarnaccia J, Harrington W, et al. (1993). Idiopathic granulomatous angiitis of the central nervous system. Diagnostic challenges. *Archives of Neurology*, **50**, 925–30.
35. Neel A, Auffray-Calvier E, Guillon B *et al.* (2012). Challenging the diagnosis of primary angiitis of the central nervous system: a single-center retrospective study. *Journal of Rheumatology*, **39**, 1026–34.

36. Pomper MG, Miller TJ, Stone JH, et al. (1999). CNS vasculitis in autoimmune disease: MR imaging findings and correlation with angiography. *AJNR American Journal of Neuroradiology*, **20**, 75–85.
37. Kose O, Simsek I, and Pay S. (2011). Mycophenolate sodium in the treatment of mucocutaneous Behcet's diseases. *International Journal of Dermatology*, **50**, 895–6.
38. Jain R. (2011). Perfusion CT imaging of brain tumors: an overview. *AJNR American Journal of Neuroradiology*, **32**, 1570–7.
39. Deibler AR, Pollock JM, Kraft RA, et al. (2008). Arterial spin-labeling in routine clinical practice, part 1: technique and artifacts. *AJNR American Journal of Neuroradiology*, **29**, 1228–34.
40. Deibler AR, Pollock JM, Kraft RA, et al. (2008). Arterial spin-labeling in routine clinical practice, part 2: hypoperfusion patterns. *AJNR American Journal of Neuroradiology*, **29**, 1235–41.
41. Pizzanelli C, Catarsi E, Pelliccia V, *et al.* (2011). Primary angiitis of the central nervous system: report of eight cases from a single Italian center. *Journal of Neurological Sciences*, **307**, 69–73.
42. Alhalabi M, and Moore PM. (1994). Serial angiography in isolated angiitis of the central nervous system. *Neurology*, **44**, 1221–6.
43. Ducros A. (2012). Reversible cerebral vasoconstriction syndrome. *Lancet Neurology*, **11**, 906–17.
44. Safier R, Cleves-Bayon C, Vaisleib I, et al. (2013). Magnetic resonance angiography evidence of vasospasm in children with suspected acute hemiplegic migraine. *Journal of Child Neurology*, **29**(6), 789–92.
45. Salvarani C, Giannini C, Miller DV, et al. (2006). Giant cell arteritis: Involvement of intracranial arteries. *Arthritis and Rheumatics*, **55**, 985–9.
46. Ghinoi A, Zuccoli G, Pipitone N, et al. (2010). Anti-neutrophil cytoplasmic antibody (ANCA)-associated vasculitis involving the central nervous system: case report and review of the literature. *Clinical and Experimental Rheumatology*, **28**, 759–66.
47. Al-Araji A, and Kidd DP. (2009). Neuro-Behcet's disease: epidemiology, clinical characteristics, and management. *Lancet Neurology*, **8**, 192–204.
48. Hirohata S. (2008). Histopathology of central nervous system lesions in Behcet's disease. *Journal of Neurological Sciences*, **267**, 41–7.
49. Nishino H, Rubino FA, DeRemee RA, et al. (1993). Neurological involvement in Wegener's granulomatosis: an analysis of 324 consecutive patients at the Mayo Clinic. *Annals of Neurology*, **33**, 4–9.
50. Sehgal M, Swanson JW, DeRemee RA, et al. (1995). Neurologic manifestations of Churg-Strauss syndrome. *Mayo Clinic Proceedings*, **70**, 337–41.
51. Guillevin L, Cohen P, Gayraud M, et al. (1999). Churg–Strauss syndrome. Clinical study and long-term follow-up of 96 patients. *Medicine (Baltimore)*, **78**, 26–37.
52. Chabriat H, Joutel A, Dichgans M, et al. (2009). Cadasil. *Lancet Neurology*, **8**, 643–53.
53. Chabriat H, Levy C, Taillia H *et al.* (1998). Patterns of MRI lesions in CADASIL. *Neurology*, **51**, 452–7.
54. Goodfellow JA, Dani K, Stewart W *et al.* (2012). Mitochondrial myopathy, encephalopathy, lactic acidosis and stroke-like episodes: an important cause of stroke in young people. *Postgraduate Medical Journal*, **88**, 326–34.
55. Susac JO. (2004). Susac's syndrome. *AJNR American Journal of Neuroradiology*, **25**, 351–2.
56. Gross M, and Eliashar R. (2005). Update on Susac's syndrome. *Current Opinions in Neurology*, **18**, 311–14.
57. Kim SS, Richman DP, Johnson WO, et al. (2013). Limited utility of current MRI criteria for distinguishing multiple sclerosis from common mimickers: primary and secondary CNS vasculitis, lupus and Sjogren's syndrome. *Multiple Sclerosis*, **20**(1), 57–63.

Index

Note: Main entries appear in their expanded form. A list of abbreviations appears on pp. ix–xii

^{1}H-MRS *see* magnetic resonance spectroscopy
4D CTA 3

A
5-aminolevulinic acid (5-ala) 147A
acquired immune deficiency syndrome *see* human immunodeficiency virus/acquired immune deficiency syndrome
acquisition energy window, SPECT 81
acute demyelinating syndrome (ADS) 370–4, 376, 377
acute disseminated encephalomyelitis (ADEM) 178–9
  children 370, 371, 372–4, 377
acute multiple sclerosis (Marburg Type) 178
Adamantiades–Behçet disease (ABD) 401–2
adrenomyeloneuropathy (AMN) 279, 390
agenesis of the corpus callosum (ACC) 367, 368
agyria 363
Aicardi–Goutieres syndrome 392
Aicardi syndrome 364
alanine 143
Albert Stroke Program Early CT Score (ASPECTS) 6–7
alcohol addiction 35
alcoholic cerebellar degeneration 307
alcohol intoxication 273
Alexander disease 392
alobar holoprosencephaly 361
Alpers syndrome 389–90
Alzheimer's disease (AD) 200, 208–23
  amyloid imaging 214–15, 233, 234, 240–1, 248
  atrophy patterns 225, 227–8
  cardiac imaging 241
  cerebral perfusion imaging 65
  cholinergic deficits 241
  diagnosis 208, 209
  differential diagnosis 227–8, 230–1, 233, 235, 239, 248
  DT MRI 216–17, 242
  fMRI 217–18, 243
  functional connectivity abnormalities 234
  functional imaging findings 213–14
  hippocampus subfields 215–16
  magnetization transfer 56
  microbleeds 202, 243
  MRI 241–2
  MRS 35, 216
  neurodegeneration 203
  parkinsonian features 246
  PET 95–6, 206
  SPECT 204, 205, 206
  structural imaging findings 208–13
amyloid imaging
  AD 214–15, 216, 218–19, 233, 234, 240–1, 248
  DLBD 240–1, 248
  FTLD 224, 233–4
  MCI 218–19
  PD 248–50
  PDD 241, 248
  prion diseases 270
amyotrophic lateral sclerosis (ALS) 279, 288, 289, 290, 291
  DT MRI 282, 283, 284
  fMRI 286–8
  MRI 279, 280
  MRS 283, 284, 285
  PET 285, 286
  spinal cord 288
  VBM and cortical thickness measures 279–82
antibody-mediated encephalopathies 274
anti-neutrophil cytoplasmic antibodies (ANCA)-associated vasculitis 401, 402
anxiety disorders 35
apparent diffusion coefficient (ADC)
  ataxias 303, 308
  CNS vasculitis 399, 401
  D-MRI 40, 44
  mimickers of CJD 272
  MS 383
  neoplasia 142, 148
  parenchymal infection 155
  prion diseases 264, 265, 267–8, 270
  spinal cord diseases 328, 330
  stroke 188, 189, 190, 192
arachnoid cyst 355–6
arachnoid mater 152
Arnold Chiari malformations 359–60
  type I 328, 359
  type II 360, 365
  type III 360, 366
arterial spin labelling (ASL) 61–3
  CNS vasculitis 401
  DLBD 240
  epilepsy 131
  MS 174
  TBI 340–1
  VCI 204, 206
Aspergillus infection 158
astrocytoma
  diagnostic and preoperative stage 140, 141, 142, 143, 144
  spinal 326, 327
asymptomatic carotid stenosis (ACS) 101–2
ataxia *see* cerebellar ataxias
ataxia oculomotor apraxia (AOA) 302, 303
ataxia telangiectasia (AT) 302, 303
atherosclerosis 100
attenuation
  PET 90–1, 92
  SPECT 83, 85
  ultrasound 97
atypical parkinsonisms 246, 253–8
autoimmune encephalopathies 272, 274
autosomal recessive spastic ataxia of Charlevois–Saguenay (ARSACS) 304

B
bacterial encephalitis 273–4
bacterial leptomeningitis 153, 154
bacterial parenchymal infection 155–6
Balo's concentric sclerosis (BCS) 178
Bartonella infection 271
behavioural variant of frontotemporal dementia (bvFTD) 224
  atrophy patterns 224–8
  functional connectivity abnormalities 234, 235
  genetic abnormalities 229
  international consensus criteria 225
  perfusion and metabolic brain alterations 232–3
  white matter microstructural damage 230–1
Behçet's disease 325
Bickerstaff's encephalitis 298
Binswanger's disease 204, 205
bipolar disorder 35
Blake's pouch cyst 355, 356
block design, fMRI 72
blood–brain barrier 108
blood oxygen level dependent (BOLD) 68, 69–70, 71, 72–3, 74
  ataxias 309
  epilepsy 131, 132
  FTLD 224
  functional connectivity analysis 75
  headache 120
  neoplasia 144
  spinal cord injury 321
  TBI 341–3

- bolus kinetics 107
- *Borrelia burgdorferi* myelitis 326
- brain development 44
- brain parenchyma 109–11
- brain tumour
  - cerebral perfusion imaging 65
  - DT-MRI 44, 46
  - MRS 34
  - *see also* neoplasia

C

- calcifications 5
- Canavan's disease 302, 392–3
- carbon monoxide poisoning 271–2
- cardiac imaging
  - DLBD 243
  - parkinsonisms 257
- cardiac scintigraphy 241
- carotid artery dissection 102, 103
- carotid artery distensibility (CAD) 100, 102
- carotid intima-media thickness (IMT) 100
- carotid plaques 100, 101
- carotid stenosis 100–2
- carotid system, ultrasound 99–103
- central nervous system (CNS)
  - D-MRI 40, 42
  - lupus 380–1
  - paediatric inflammatory disorders 370–86
    - acute demyelinating syndromes 370–4
    - definitions and diagnostic criteria 371
    - MRI 380–4
    - multiple sclerosis 374–8, 381–4
    - neuromyelitis optica 374
    - primary angiitis of CNS 378–80
  - vasculitis 325, 397–404
    - classification criteria 397
    - clinical manifestations 397
    - diagnostic work-up 397–8
    - epidemiology 397
    - neuroimaging findings 398–403
    - radiological mimicker of CJD 273
  - *see also* congenital metabolic central nervous system disorders; infections of nervous system
- cephaloceles 365–7
- CERASPECT 80
- cerebellar ataxias 295–314
  - acute 297–9
  - chronic 299–310
  - classification 296
  - MRI and MRS 295–6
  - SPECT and PET 296–7
- cerebellar hypoplasia, lissencephaly with 363
- cerebellar-vermian hypoplasia-dysplasia (CVH) 355, 357
- cerebellar vermis hypoplasia, oligophrenia, ataxia, ocular coloboma, hepatic fibrosis (COACH syndrome) 358
- cerebellitis 298
- cerebral amyloid angiopathy (CAA) 192, 193, 202
- cerebral autosomal dominant arteriopathy with subcortical infarcts and leukoencephalopathy (CADASIL) 193, 202, 203, 399, 402
- cerebral cavernous malformations (CCM) 398–9
- cerebral extradural (epidural) abscess 154
- cerebral perfusion imaging 59–67
  - clinical applications 65
  - CNS vasculitis 401
  - MR perfusion imaging 59–63
    - epilepsy 131
    - MS 174–5
    - stroke 195
  - nuclear medicine techniques 64–5
  - PCT 3, 5, 63–4
    - CNS vasculitis 401
    - intracranial haemorrhage 7–9
    - ischaemic stroke 7, 8
    - neoplasia 140–1
    - traumatic brain injury 10
  - TBI 339–41
  - ultrasound 107
- cerebral venous thrombosis 109
- cerebro-oculo-renal syndrome (CORS) 358
- cerebrotendineous xanthomatosis 304
- cerebrovascular disease (CVD)
  - management 193–6
  - *see also* stroke
- cervical spondylotic myelopathy 330
- cervical veins, ultrasound of 108–9
- Charcot–Marie–Tooth neuropathies 279
- chemical exchange saturation transfer (CEST) 56
- chemical shift 27, 28, 29
- chemical shift selective (CHESS) method for water suppression 31
- childhood ataxia with central hypomyelination (CACH) 393
- childhood primary angiitis of the central nervous system (cPACNS) 370, 371, 378–80, 381
- children *see* paediatrics
- choline (Cho)
  - ataxias 296, 303, 304, 305, 307, 309
  - BCS 178
  - CCALD 390
  - MND 283–4, 285
  - MRS 33, 34, 35
  - MS 173, 174, 383
  - neoplasia 143
  - TBI 336
- chronic lymphocytic inflammation with perivascular pontine enhancement responsive to steroids (CLIPPERS) 308
- chronic relapsing inflammatory optic neuropathy (CRION) 374
- Churg–Strauss syndrome 402
- classical cerebral childhood adrenoleukodystrophy (CCALD) 390
- cluster headache 117–18, 121
- cobblestone lissencephaly 363
- coded contrast harmonics (CCH) 107
- Cogan syndrome 401
- collimator 79, 80, 81
- collimator-detector response 83–4, 85, 86
- collimator-detector response function (CDRF) 84, 85
- collimator geometric response 83, 84
- coma 346, 347
- Coma Recovery Scale-Revised (CRS-R) 346, 347
- composite hindered and restricted model of diffusion (CHARMED) 44, 45, 47
- computed tomography (CT) 3–12
  - AD 208, 210
  - ataxias 297
  - carotid artery dissection 102
  - cerebral perfusion imaging 63–4
  - clinical applications 6–10
  - CNS vasculitis 398, 399
  - common features 5–6
  - comparison with MRI and SPECT/PET 4
  - congenital malformations of brain and skull
    - cephaloceles 366, 367
    - holoprosencephaly 361
    - schizencephaly 365
  - congenital metabolic CNS disorders 387
  - epilepsy 124
  - headache 117
  - hyperdensity 5, 6
  - hypodensity 5
  - image construction algorithms 3–4
  - imaging modalities 4–10
  - infections of nervous system 151
    - HIV/AIDS 163, 164
    - meningeal infection 152, 154
    - parenchymal infection 155, 156, 157, 158, 159
  - neoplasia 139–40
  - PD 250–2
  - perfusion 140–1
  - PET/CT 91, 92
  - radiation dose 3
  - single-slice vs multislice scanners 3
  - single-source vs dual-source 4
  - SPECT/CT 80, 87
  - spinal cord injury 315, 319
  - stroke 185, 196
    - haemorrhagic 191–2, 193
    - ischaemic 185–6, 187, 191
    - management 194, 195
  - TBI 335
  - technology 3
  - VCI 200, 201, 203, 205, 206
- computed tomography angiography (CTA) 3, 4–5
  - intracranial haemorrhage 7
  - stroke 7, 8, 191, 195
  - traumatic brain injury 10
- congenital malformations of brain and skull 354–69
  - Arnold Chiari malformations 359–60
  - brainstem 356
  - cephaloceles 365
  - cerebellum 354–5, 356–9
  - clinical and radiological feature 365–7
  - corpus callosum 367–8
  - holoprosencephaly and variants 360–2
  - nasal dermoids, intranasal cerebral heterotopia, and dermal sinus 367
  - neuronal migration and cortical organization disorders 363–5
  - posterior fossa 355–6
- congenital metabolic central nervous system disorders 387–96
  - creatine metabolism 388
  - leukoencephalopathies 392–4
  - lysosomal disorders 390–2
  - mitochondrial disorders 388–90
  - organic acid metabolism 388
  - peroxisomal disorders 390
- congophilic amyloid angiopathy (CoAA) 398
- consciousness
  - definition 346–7
  - disorders of (DOC) 346–53
    - active paradigms 348–9
    - clinical assessment 346–7
    - passive external stimulation 348
    - resting state 347–8

    structural MRI 347
    TMS and EEG 349–51
continuous arterial spin labelling (CASL) 62
contrast-enhanced computed tomography (CECT) 4–5
  HIV/AIDS 164
  intracranial haemorrhage 7, 8
  meningeal infection 152, 153, 154–5
  parenchymal infection 155, 156, 157, 158, 159
  tuberculosis 164, 165
contrast-enhanced magnetic resonance angiography (CE-MRA) 400
contrast-enhanced magnetic resonance imaging (CE-MRI)
  HIV/AIDS 164
  meningeal infection 152, 153–4
  parenchymal infection 155, 156, 157
  stroke 189, 192
  tuberculosis 164, 165
copper deficiency 330
cortical organization disorders 363–5
cortical spreading depression (CSD) 120
cortical thickness 119, 120
cortical thinning
  bvFTD 228
  MND 279–82, 289
  PD 251
corticobasal degeneration (CBD) 253
  atrophy patterns 229
  cardiac imaging 241
corticobasal syndrome (CBS) 246, 248, 253–4, 255, 256, 257
  genetic abnormalities 229
creatine (Cr)
  ADEM 383
  ataxias 296, 298, 299, 303, 304, 305, 306, 307, 308, 309
  BCS 178
  CCALD 390
  MND 283–5, 288
  MRS 33, 34–5
  MS 174, 383
  spinal cord diseases 330
  TBI 336
creatine metabolism disorders 388, 389
Creutzfeldt–Jakob disease (CJD) 263
  see also familial Creutzfeldt–Jakob disease; iatrogenic Creutzfeldt–Jakob disease; sporadic Creutzfeldt–Jakob disease; variant Creutzfeldt–Jakob disease
cross-talk, SPECT 84–6
Cryptococcus neoformans infection 158
cysticercosis 158–9
cytomegalovirus 164

D

Dandy–Walker continuum/complex 355–6, 357, 365
deep brain stimulation (DBS)
  headache 118
  ultrasound 110
degenerative spine disease 330
delayed coincidence window technique, PET 92
delayed gadolinium-enhanced magnetic resonance imaging (dGEMRIC) 14
dementia with Lewy-Bodies (DLBD) 239–45
  amyloid imaging 248
  atrophy patterns 228
  differential diagnosis 228
  MRI 241–3
  parkinsonian features 246
  PET 214, 239–41
  SPECT 205, 239–41
demyelinating diseases 323–5
depression 35
dermal sinus 367
diffuse axonal injury (DAI) 399
diffuse myelinoclastic sclerosis 178
diffusional kurtosis imaging (DKI) 47
  TBI 336, 339, 340
diffusion anisotropy 40
diffusion magnetic resonance imaging (D-MRI) 40–9
  clinical applications 44
  data acquisition 42–3
  data analysis 43
  epilepsy 130–1
diffusion tensor imaging (DTI)
  consciousness, disorders of 347, 348, 349
  neoplasia 143, 144, 145
  spinal cord injury 320
  VCI 204, 206
diffusion tensor magnetic resonance imaging (DT MRI) 40–1, 42, 47
  AD 216–17, 218, 231, 242
  ADEM 179
  ataxias 295, 303, 304, 305, 308, 309
  atypical parkinsonisms 257
  clinical applications 43–5
  data acquisition 42–3
  data analysis 43
  DLBD 242
  epilepsy 130
  FTLD 224, 230–1
  MCI 216–17
  MND 279, 282–3, 288, 289, 290
  MS 173, 174, 176, 178
    children 383
  MSA-P 251
  NMO 178
  PD 250, 251
  PSP 251
  spinal cord diseases 324, 326, 328, 330
  TBI 336, 337–9
diffusion tensor (DT) spectroscopy
  MS 177
diffusion-weighted magnetic imaging (DWI)
  ataxias 295, 297, 298, 299, 303, 309
  atypical parkinsonisms 257
  CCALD 390
  CNS vasculitis 399, 401
  HIV/AIDS 163, 164
  meningeal infection 152, 154
  mimickers of CJD 271, 272, 273, 274
  neoplasia 142–3, 148
  parenchymal infection 155, 157, 158
  prion diseases 263, 264–7, 268, 269, 270
  spinal cord injury 317, 320
  stroke 185, 187–9, 190, 192
    management 194, 195, 196
  TBI 336, 337, 339
digital subtraction angiography (DSA)
  CNS vasculitis 400
  comparison with CTA 4, 5, 7
  PACNS 381
disorders of consciousness *see* consciousness: disorders of
Doppler, Christian 98
Doppler imaging 98
double-inversion recovery (DIR) 169, 170–1, 177, 178
driven equilibrium single pulse observation of T_1 (DESPOT1) *see* variable flip angle spoiled gradient recalled method
driven equilibrium single pulse observation of T_2 (DESPOT2) *see* variable flip angle steady state free precession method
drug-induced ataxias 298, 307
drug-resistant epilepsy 132–3
dual-echo MRI 168
dual-isotope imaging 81, 84–5
dura mater 152
dynamic contrast-enhanced magnetic resonance imaging (DCE-MRI) 59–60
  MS 170
dynamic susceptibility contrast magnetic resonance imaging (DSC-MRI) 60–1

E

early onset cerebellar ataxia (EOCA) 302
Eastern equine encephalitis 157
Echinococcus infection 159
echo planar imaging (EPI) 14
  DSC-MRI 60
  DT-MRI 42
  fMRI 69, 70–1
  MRI 14–15, 19, 22
  MRS 31
echo planar imaging with signal targeting with alternative frequency (EPISTAR) 62
electroencephalography (EEG)
  consciousness, disorders of 349–51
  epilepsy 14, 96, 127, 128, 130, 131, 132
  prion diseases 264, 265
electrolyte disturbances, ataxias 298
emergence from minimally-conscious state (EMCS) 349
encephalitis 272
enterovirus 71:273
eosinophilic granulomatosis with polyangiitis 402
ependymitis 155
ependymomas, spinal 326
epidural haematomas (EDH) 9
epilepsy 124–38
  ataxias 307
  CT 124
  diffusion MRI 130–1
  fMRI 131–2
  magnetization transfer 56
  MRI 124–9
  MRS 129–30
  MT MRI 131
  perfusion MRI 131
  PET 96, 132
  quantitative relaxometry and water content mapping 14
  radiological mimicker of CJD 272, 274
  SPECT 132
episodic ataxia type 2 (EA-2) 306
ethylmalonic encephalopathy 272
event-related design, fMRI 72–3
experimental head pain 117–20
extradural (epidural) space 152

F

Fabry disease 392
false discovery rate (FDR) estimation 75
familial Creutzfeldt–Jakob disease (fCJD) 263, 269, 270, 271
family-wise error (FWE) correction 75
fastSPECT 80

fast spin echo (FSE) 14
fatal familial insomnia (FFI) 263, 269, 270–1
filtered back-projection (FBP)
  PET 93
  SPECT 82, 84
fingerprinting, MR 20–1
flavivirus infections 157
flow alternating inversion recovery (FAIR) 62
flow-mediated vasodilation (FMD) 100
fluid-attenuated inversion recovery (FLAIR)
  acute demyelinating syndromes 373, 374
  ataxias 298, 299, 300, 307, 308
  atypical parkinsonisms 255, 256
  CNS vasculitis 398, 399, 402, 403
  comparison with DT-MRI 45
  epilepsy 124, 127
  HIV/AIDS 161, 163
  holoprosencephaly 362
  leukoencephalopathies 392, 393
  meningeal infection 152, 154, 155
  mimickers of CJD 271, 272, 273, 274
  mitochondrial disorders 389–90
  molar tooth malformation 358
  MS 168
    children 375, 376
  neoplasia 139, 142
  neuromyelitis optica 375
  PACNS 380
  parenchymal infection 156
  peroxisomal disorders 390
  PD 250
  prion diseases 263, 264, 265, 267, 268, 269, 270
  stroke
    haemorrhagic 191, 192, 193, 194
    ischaemic 186, 188, 189, 190, 191
    management 195, 196
  TBI 335, 339
  VCI 201, 202, 203–4
focal cortical dysplasias 124, 125, 127–8, 129, 130, 131, 132, 364–5
fractional anisotropy (FA)
  AD 217, 218
  ataxias 295
  DLBD 242
  D-MRI 41, 42, 43–4, 45, 46
  epilepsy 130
  FTD 230, 231
  MND 282, 283, 284, 288, 290
  MS 173, 176, 324, 330
    children 383, 384
  PD 250
  spinal cord injury 320
  TBI 337, 338, 339, 340
fractional dimension (FD) 204
fragile X tremor ataxia syndrome 306–7
Friedreich ataxia 300, 302, 303
frontotemporal dementia (FTD) 206, 224, 225
  ALS 279, 281, 282, 285
  amyloid imaging 233
  differential diagnosis 214
  functional connectivity abnormalities 235
  genetic abnormalities 229, 232, 234–5
  neurodegeneration 203
  PET 96, 214, 286
  SPECT 204, 205
  see also behavioural variant of frontotemporal dementia; primary progressive aphasia
frontotemporal lobar degeneration (FTLD) 224–38
  amyloid imaging 233–4
  atrophy patterns 224–30
  functional connectivity abnormalities 234–5
  perfusion and metabolic brain alterations 232–3
  PET 214
  structural imaging findings 212
  TAR DNA-binding protein 43: 230
  white matter microstructural damage 230–2
fucosidosis 392
Fukuyama congenital muscular dystrophy 363
functional connectivity analysis 75–7
functional magnetic resonance imaging (fMRI) 68–78
  AD 217–18, 219, 243
  ataxias 295–6, 305, 309
  atypical parkinsonisms 257, 258
  BOLD effect 69–70
  clinical applications 77
  consciousness, disorders of 348, 349, 350
  data acquisition 70–1
  DLBD 243
  epilepsy 130, 131–2
  experimental design and data analysis 71–5
  FTLD 224, 234–5
  functional connectivity analysis 75–7
  headache 119, 120
  MCI 217, 218, 219
  MND 279, 286–8
  MS 175–6, 177, 178, 324
    children 383–4
  neoplasia 144–5
  NMO 178
  PD 251–2, 258
  SCI 321
  TBI 341–3
fungal leptomeningitis 154

G
galactosaemia type 1: 302
γ-aminobutyric acid (GABA)
  epilepsy 130
  MRS 33, 34, 35
gamma camera 79–80, 81
gangliosidosis 391
Gaussian random field (GRF) theory 75
Gerstmann–Straüssler–Scheinker disease (GSS) 263, 269–70
giant cell arteritis 401
glioblastoma 140, 142, 143, 148
glioma 142, 146, 147, 148
glucose
  MRS 33
  TBI 343
glutamate (Glu)
  epilepsy 130
  MRS 32, 33, 35
  MS 173
glutamic aciduria type I (GA1) 388
glutamine (Gln)
  MRS 33
  MS 173
glutathione (GSH)
  MRS 34
  MS 177
gluten ataxia 307
glycerophosphorylcholine (GPC) 33
GM1 gangliosidosis 391
GM2 gangliosidosis 391
granulomatous polyangiitis 402
graph theory 76
GRAPPA 71
group independent component analysis (ICA) 77
gyromagnetic ratio 27, 28

H
haemangioblastomas, spinal 326, 327
haemodynamic response function (HRF) 70, 72, 73, 74
haemorrhagic cerebrovascular disease 191–3
hand, foot, and mouth disease 273
headache 117–23
  experimental head pain 117
  future perspective 121
  migraine 118–20
  specificity of results 120–1
  tension-type 120
  trigeminal autonomic cephalagias 117–18
hemicrania continua 117, 118
hepatic encephalopathy 274
hepatic transplantation 279
hereditary spastic paraplegias (HSP) 279, 288, 289, 290
heroin abuse 330
herpes simplex encephalitis (HSE) 156–7, 273
herpes simplex virus (HSV) myelitis 325
heterotopia 363–4
high angular resolution diffusion imaging (HARDI) 45–7
Hirahyama disease 331–2
holoprosencephaly 360–2
human herpes virus 6 (HHV6) encephalitis 156
  radiological mimicker of CJD 273
human immunodeficiency virus/acquired immune deficiency syndrome (HIV/AIDS) 159–64
  radiological mimicker of CJD 271
  spinal symptoms 325–6
human T-lymphotrophic virus (HTLV-1) 326
Hunter syndrome 392
Huntington's disease 95
Hurler–Scheie syndrome 392
hydrocephalus 5, 6, 9
hyperammonemic encephalopathy 271
hypersensitivity vasculitis 401
hypertensive cerebral angiopathy (HCA) 398
hypertensive microangiopathy 192
hypocalcaemia 298
hypoglycaemic encephalopathy 271, 274
hypomagnesaemia 298
hyponatraemia 298
hypoxic encephalopathy 272–3

I
iatrogenic Creutzfeldt—Jakob disease (iCJD) 263, 269
idiopathic generalized epilepsy (IGE) 124, 128–9, 130, 132
ILOCA 309
image-selected *in vivo* spectroscopy (ISIS) 30
immune-mediated ataxia 307
immune reconstitution inflammatory syndrome (IRIS) 163
inborn error of metabolism, acute decompensation of 299, 300
independent component analysis (ICA) 76–7
infantile Refsum disease 390
infections of nervous system 151–67
  anatomy 151–2
  CNS vasculitis 401
  diagnostic work-up 151

  HIV/AIDS 159–64
  meningeal infection 152–5
  parenchymal infection 155–9
  spinal cord lesions 325–6
  tuberculosis 164–5
inferior fronto-occipital fasciculus (IFOF) 230, 231
inflammatory spinal cord diseases 323–5
influenza virus encephalitis 273
interhemispheric cystic meningeal dysplasia 367
interhemispheric meningeal lipomas 368
intracranial arteries, ultrasound of 106–8
intracranial haemorrhage (ICH) 191–3, 194
  CT 5, 7–9
intracranial pressure (ICP)
  lumbar puncture 151
  ultrasound 110–11
intracranial veins, ultrasound of 108–9, 110
intranasal cerebral heterotopia 367
inversion recovery steady-state free precession 20
ischaemic cerebrovascular disease 185–91
ischaemic myelopathy 328, 329
ischaemic stroke
  cerebral perfusion imaging 65
  CT 6–7, 8
  D-MRI 44
  management 194, 195
  ultrasound 103

J

Japanese encephalitis (JE) virus 157, 271
J-coupling 27, 29
J-difference editing 33–4
Joubert syndrome 301, 302, 358
juvenile myoclonic epilepsy 130

K

Kearns–Sayre syndrome 390
Klein–Nishina formula 83
Krabbe disease 279, 391
k-space
  fMRI 71
  MRI 68, 69
Kuru 263

L

L-2-hydroxyglutaric aciduria 388, 389
lactate
  ataxias 305
  BCS 178
  MRS 33, 35
  spinal cord diseases 330
  TBI 336
Larmor equation 27, 28, 31
Larmor frequency
  fMRI 71
  MRI 68
Leigh syndrome 300, 389, 390
lentiform nucleus 248
leptomeningeal glioneuronal heterotopias 364
leptomeningitis 152–4
leukoencephalopathies
  inherited 387, 392–4
  mitochondrial disorders 390
leukoencephalopathy with brain stem and spinal cord involvement and lactate elevation (LBSL) 390
Lewy, Friedrich 239
Lewy body (LB) 239
  see also dementia with Lewy-Bodies
limbic encephalopathies 274
lipids 33, 34
lissencephaly 363
lobar holoprosencephaly 361, 362
localization by adiabatic selective refocusing (LASER) 30
locked-in syndrome (LIS) 349, 351
Look–Locker (LL) 15–17, 20
lumbar puncture 151
Lyme's disease 153
lymphoma
  CT 5
  diagnostic and preoperative stage 142
  differential diagnosis 164
lysosomal disorders 390–2

M

macromolecules (MMs)
  MRI 50, 51
  MRS 33
  MTI 50
magnetic field homogeneity 31–2
magnetic resonance angiography (MRA)
  ataxias 295, 298
  CNS vasculitis 400–1, 402
  magnetization transfer 50
  PACNS 378
  stroke 191, 195, 196
magnetic resonance imaging (MRI) 13–26
  AD 208–10, 212, 215, 217, 218, 233, 241–2
  ADEM 178–9
  ataxias 295–6, 297, 298, 299–300, 301–2, 303, 304, 305, 306, 307, 308, 309
  atypical parkinsonisms 254–7
  basics 68–9
  carotid artery dissection 102
  cerebral perfusion imaging 59–63
    neoplasia 140–1, 148
  children with CNS inflammatory disorders 370, 380–1
    ADS 370–2, 373, 374
    MS 375–8, 379, 381–4
    neuromyelitis optica 374, 375
    PACNS 378, 380, 381
  CNS vasculitis 397, 398–401, 402, 403
  comparison with CT 4
  comparison with SPECT/PET 4
  congenital malformations of brain and skull
    Arnold Chiari malformations 359, 360
    cephaloceles 366, 367
    cerebellum 354
    corpus callosum 367, 368
    Dandy–Walker malformation 356, 357
    focal cortical dysplasia 364–5
    holoprosenephaly 362
    lissencephaly 363
    molar tooth malformation 358
    nasal dermoids, intranasal heterotopia, and dermal sinus 367
    periventricular nodular heterotopia 363
    polymicrogyria 364
    pontine tegmental cap dysplasia 358
    rhombencephalosynapsis 356, 358
    schizencephaly 365
    septo-optic dysplasia 362
  congenital metabolic CNS disorders 387
    leukoencephalopathies 392–3, 394
    lysosomal disorders 391, 392
    mitochondrial disorders 389–90
    organic acid metabolism 388, 389
    peroxisomal disorders 390
  consciousness, disorders of 347
  DLBD 240, 241–3
  epilepsy 124–9, 132, 133
  FTD 226–8, 233, 235
  FTLD 224, 229
  headache 117, 118, 119, 120, 121
  infections of nervous system 151
    HIV/AIDS 161, 163, 164
    meningeal infection 152, 155
    parenchymal infection 155, 156, 157, 158–9
    tuberculosis 165
  macromolecules 50, 51
  magnetization transfer 50–1, 55–6
  MCI 210, 212, 218
  methods 14–21
  mimickers of CJD 271, 273, 274
  MND 279, 288, 289
  MS 168, 169, 179
    acute (Marburg Type) 178
    diagnosis 168–70
    optic nerve 177
    prognosis 170
    treatment monitoring 177–8
    ultra-high field imaging 177
  multiple component relaxation 21
  neoplasia 139–40, 146, 148
  PD 250–2, 258
  prion diseases 263, 264–8, 269, 270–1
  SCI 315–17, 318, 321
  SPECT/MRI 87
  spinal cord diseases 323, 324, 325, 326, 327, 328, 329, 330, 331, 332
  stroke 185, 196
    haemorrhagic 192–3, 194
    ischaemic 186–9, 191
    management 194, 195, 196
  TBI 335, 336, 339
  VCI 200, 201, 202, 203–4, 206
  water content mapping 21–4
magnetic resonance spectroscopy (MRS) 27–39
  AD 216
  ADEM 179, 383
  advanced techniques 33–4
  Alzheimer's disease 35
  ataxias 295, 296, 298, 302, 303, 304, 305, 306, 307, 308
  BCS 178
  chemical shift 28
  clinical 32
  clinical applications 34–5
  congenital metabolic CNS disorders 387
    creatine metabolism 388, 389
    leukoencephalopathies 393
    mitochondrial disorders 390
    peroxisomal disorders 390
  DLBD 243
  epilepsy 129–30
  future 35–6
  imaging 30–1
  in vivo 27–8
  magnetic field homogeneity and shimming 31–2
  metabolites of interest 32–3
  methods 28
  MND 279, 285–6, 288
  MS 173–4, 177, 178, 383
  multiple sclerosis 34–5
  neoplasia 143
  neuropsychiatric disorders 35

magnetic resonance spectroscopy (*Cont.*)
  outer volume suppression 31
  Parkinson's disease 35
  quantification of spectra 29
  scalar coupling 29
  sequence imperfections and eddy currents 32
  single-voxel 30
  spinal cord diseases 327, 330
  TBI 336, 337
  tumours 34
  water suppression 31
magnetization transfer (MT) 50–8
  ADEM 179
  chemical exchange saturation transfer 56
  data analysis methods 54–5
  epilepsy 131
  interpretation 55–6
  measuring 50–4
  MS 173, 176, 178
    children 382–3
  NMO 178
  phenomenon 50
  in routine clinical imaging 50
  spinal cord diseases 323, 326, 330
  VCI 204
magnetization transfer ratio (MTR) 51, 52, 54, 55
  asymmetry analysis 56
  MS 173, 177, 324
    children 382–3
magnetoencephalography (MEG) 145
maple syrup urine disease 302
marginal zone heterotopias 364
mass effect, CT 5–6, 7
maximum a posteriori (MAP) reconstruction, SPECT 87
maximum likelihood expectation-maximization (ML-EM) algorithm 82
mean diffusivity (MD)
  AD 218
  ataxias 295
  D-MRI 41, 42, 44, 45, 46
  epilepsy 130
  MND 283
  MS 173, 174
    children 383, 384
  TBI 337, 339, 340
mechanical index (MI) 99
mega cisterna magna 355, 356, 357
megalencephalic leukoencephalopathy with subcortical cysts (MLC) 393–4
meningeal infection 152–5
meninges 151–2
meningioma 142, 143, 146, 148
meningoencephalitis 273
mesiotemporal sclerosis 125, 126
metabolic causes of spinal symptoms 329–30
metachromatic leukodystrophy 390–1
metastases 142, 146, 272
methylmalonic acidaemia (MMA) 388
methylmercury poisoning 307
microtubule-associated protein tau (MAPT)-associated frontotemporal lobar degeneration (FTLD) 228, 229
microvascular imaging (MVI) 107
migraine 117–18, 120–1
  photophobia 119–20
  white matter abnormalities 118
  with aura 118, 120
  without aura 118–19
mild cognitive impairment (MCI) 218
  amyloid imaging 214–15, 218–19
  diagnosis 208, 209
  DT MRI 216–17
  fMRI 217, 218, 219
  functional imaging findings 213–14
  hippocampus 216
  MRI 210
  MRS 216
  PD 248, 251, 252
  PET 218
  structural imaging findings 210–12
Miller–Dieker syndrome 363
Minamata disease 307
minimally-conscious state (MCS) 346, 347, 348, 349, 350, 351
mitochondrial disorders 387, 388–90
mitochondrial myopathy, encephalopathy, lactic acidosis, and stroke-like episodes (MELAS) 389, 390, 402
mitochondrial neuro-gastrointestinal encephalomyopathy (MNGIE) 390
mitochondropathies 302
model-based cross-talk compensation (MBCC) 86
modified Look–Locker inversion (MOLLI) 17
monofocal demyelination 371
moral tooth malformation 358–9
motor neuron disease (MND) 279–94
  atrophy patterns 226, 230
  DT MRI 282–3
  fMRI 286–8
  hereditary spastic paraplegia 288
  MRI 279
  MRS 283–5
  PET 286
  spinal cord 288
  VBM and cortical thickness measures 279–82
  white matter microstructural damage 230
movement disorders 246–62
  atypical parkinsonisms 253–8
  cardiac imaging 257
  PD 246–53, 257–8
Moyamoya syndrome 402, 403
mucolipidosis IV 392
mucopolysaccharidoses 392
Mucormycosis 157–8
multidrug resistant tuberculosis (MDR TB) 165
multi-echo gradient and spin echo (GRASE) 19–20
multifocal demyelination 371
multi-parameter mapping (MPM) 320
multiple coincidences, PET 90, 91
multiple component relaxometry (MCR) 21, 23
multiple sclerosis (MS) 168–84, 323–4
  children 371, 372, 373–8, 379, 381–4
  cross-sectional spinal cord area measurement 317, 318
  diagnostic criteria 168–9
  differential diagnosis 169–70
  D-MRI 44, 45
  DT MRI 173
  features 168
  fMRI 175–6
  magnetization transfer 54, 55
  migraine 118, 119
  MRI
    pathophysiology 170–3
    treatment monitoring 177–8
  MRS 29, 34–5, 173–4
  MT MRI 173
  optic nerve 177
  perfusion MRI 174–5
  PET 176
  prognosis 170
  quantitative relaxometry and water content mapping 13–14
  related disorders 178–9
  spinal cord 176
  ultra-high field imaging 177
multislice inversion time (TI)-cycled inversion recovery echo planar imaging (IR-EPI) 14–15
multi-system atrophy (MSA) 253
  cardiac imaging 241
multi-system atrophy cerebellar type (MSA-C) 308, 309–10
multi-system atrophy-parkinsonism (MSA-P) 246, 248, 253, 254–5, 257, 308
  DT MRI 251
Murray Valley encephalitis virus 271
muscle–eye–brain (MEB) disease 363
Mycobacterium tuberculosis 164, 326
myelin 55
myo-inositol
  AD 216
  ADEM 383
  ataxias 296, 303, 305
  DLBD 243
  MCI 216
  MND 285
  MRS 33, 34, 35
  MS 173, 174, 383
  neoplasia 143

N

N-acetyl aspartate (NAA)
  AD 216
  ADEM 179
  ataxias 296, 298, 299, 302, 303, 304, 305, 306, 307, 308, 309
  BCS 178
  CCALD 390
  DLBD 243
  epilepsy 130
  leukoencephalopathies 393
  MCI 216
  MND 283–5, 288, 289
  MRS 32, 34–5
  MS 173, 177, 324
    children 383
  neoplasia 143
  spinal cord diseases 330
  TBI 336, 337
nasal dermoids 367
neonatal adrenal leukodystrophy 390
neoplasia 139–50
  diagnostic and preoperative imaging 139–46
  intra-operative imaging 146–7
  post-operative and follow-up imaging 148
  spinal symptoms 326–7
  WHO classification 139
network-based statistic 77
neural tube defects (NTDs) 365
neuro-Behçet's disease 380
neuroborreliosis 153
neurodegenerative spine diseases 330–2
neurofilament inclusion body disease (NIBD) 272
NeuroFocus™ high-definition focusing emission tomographic scanner (HDFET) 80

neuromuscular ultrasound 111, 112
neuromyelitis optica (NMO) 169–70, 178, 324, 325
  children 371, 372, 373, 374, 375
neuronal ceroid lipofuscinosis 302, 391–2
neuronal migration disorders 363–5
neurosarcoid 274
neurosarcoidosis 324, 325, 380
neurosonology *see* ultrasound
neurosyphilis 164
  radiological mimicker of CJD 273–4
  spinal symptoms 326
Niemann–Pick type C 304
non-atherosclerotic disease 102
non-contrast head computed tomography (NCT) 4, 5
  intracranial haemorrhage 7, 9
  ischaemic stroke 6–7, 8
  traumatic brain injury 9, 10
non-convulsive status epilepticus (NCSE) 74
non-Hodgkin's lymphoma 273
non-progressive primary angiitis of the central nervous system (NP-PACNS) 378
nuclear medicine 64–5

O
oculo-facial-digital syndrome Type IV (OFD-IV syndrome) 358
oedema
  CT 5
  DT-MRI 44
  magnetization transfer 55
  neoplasia 142
oligodendroglioma 141, 145
optic neuritis
  children 370–2, 374
  D-MRI 44
  MS 173, 175, 177
  NMO 178
ordered-subsets expectation-maximization (OS-EM) algorithm, SPECT 82–3, 87
organic acid metabolism, disorders of 388
outer volume suppression (OVS), MRS 31, 32
ovarioleukodystrophy 393

P
pachygyria 363
pachymeningitis 153, 154–5
paediatrics
  ataxias 296, 297, 298, 299, 302
  CNS inflammatory disorders 370–86
    acute demyelinating syndromes 370–4
    definitions and diagnostic criteria 371
    MRI 380–4
    multiple sclerosis 374–8, 381–4
    neuromyelitis optica 374
    primary angiitis of CNS 378–80
  congenital metabolic CNS disorders 387–96
    creatine metabolism 388
    leukoencephalopathies 392–4
    lysosomal disorders 390–2
    mitochondrial disorders 388–90
    organic acid metabolism 388
    peroxisomal disorders 390
  neoplasia 143
  spinal cord diseases 327
  TBI 335–6, 339, 341, 343
panencephalopathic Creutzfeldt–Jakob disease 268
paraneoplastic cerebellar degeneration 307
paraneoplastic chorea 273
paraneoplastic encephalopathies 272, 274
paraneoplastic myelopathy 327
parasitic leptomeningitis 154, 155
parenchymal infection 155–9
Parkinson's disease (PD) 246–53, 257–8
  cardiac imaging 241
  cholinergic deficits 241
  CT and MRI 250–2
  dopaminergic system 239, 246–8
  magnetization transfer 56
  MRI 258
  MRS 35
  PET/SPECT 246–50, 257, 258, 286
  ultrasound 110
    transcranial sonography 252–3
Parkinson's disease cognitive-related network pattern (PDCP) 248
Parkinson's disease dementia (PDD) 239, 248
  amyloid imaging 241, 248
  brain atrophy 251
  cholinergic imaging 241
  MRI 250
Parkinson's disease-related covariance pattern (PDRP) 248
paroxysmal hemicrania 117, 118
partial volume compensation (PVC), SPECT 86
partial volume effects (PVEs), SPECT 84, 86
Pelizaeus–Merzbacher disease (PMD) 394
perfusion imaging *see* cerebral perfusion imaging
peri-Rolandic tumours 146
periventricular nodular heterotopia 363–4
peroxisomal biogenesis defects (PBD) 390
peroxisomal disorders 390
pharmacokinetic modelling, PET 94
phenylketonuria 302
phosphocreatine (PCr) 33
phosphorylcholine (phosphocholine, PCho) 33
photomultiplier tubes (PMTs), SPECT 79–80
photophobia 119–20
pia mater 151
Pick's disease 228, 229
pipecolic acidaemia 390
point-resolved spectroscopy (PRESS) 30
point spread function (PSF), PET 93
polioviruses 326
polyarteritis nodosa 401
polymicrogyria 364
pontine capillary telangiectasia 308
pontine tegmental cap dysplasia 356, 358
positron emission tomography (PET) 64–5, 90–6
  AD 208, 213–14, 215, 216, 218, 233
  ataxias 295, 296–7, 299, 303, 305, 306, 307, 309, 310
  atypical parkinsonisms 253–4
  comparison with CT and MRI 4
  comparison with SPECT 86
  consciousness, disorders of 347–8, 349
  data acquisition and image reconstruction 91–3
  data analysis 93–6
  DLBD 239–41
  epilepsy 132
  FTD 232, 233, 235, 236
  FTLD 224
  headache 118, 119, 120, 121
  MCI 213–14, 218
  MND 279, 285, 286
  MS 176
  PD 246–50, 258, 286
  principles 90–1
  prion diseases 269, 270, 271
  stroke 195
  TBI 340, 342, 343
  VCI 204, 205–6
posterior cortical atrophy (PCA), AD 212, 214, 215
posterior fossa, cystic malformations of the 355–6, 357
Pott disease 160–1, 165
primary angiitis of the central nervous system (PACNS) 370, 371, 378–80, 381
  see also central nervous system: vasculitis
primary central nervous system vasculitis (PCNSV) *see* central nervous system: vasculitis
primary lateral sclerosis (PLS) 279
  DT MRI 282
  MRS 284
  VBM and cortical thickness measures 280, 281, 282
primary progressive aphasia (PPA)
  AD 212–13, 214, 215
  atrophy patterns 227, 228–9
  diagnostic criteria 226
  FTLD 224
  functional connectivity abnormalities 234
  genetic abnormalities 229
  perfusion and metabolic brain alterations 233
  white matter microstructural damage 231–2
prion diseases (PrDs) 263–78
  differential diagnosis 271–4
  genetic 269–71
  iatrogenic CJD 269
  sporadic CJD 263–8
  variant CJD 268–9
progressive childhood primary angiitis of the central nervous system (P-cPACNS) 378
progressive multifocal leukoencephalopathy (PML) 161–3
progressive muscular atrophy (PMA) 279
  DT MRI 282, 283, 284
  MRS 284–5
progressive supranuclear palsy (PSP) 246, 248, 253, 254, 255, 256, 257, 258
  atrophy patterns 229
  cardiac imaging 241
  DT MRI 251
propionic acidaemia 388
proton density magnetic resonance imaging 13, 14, 21–4
  stroke 186
proton density mapping *see* water content mapping
proton magnetic resonance spectroscopy (^{1}H-MRS) *see* magnetic resonance spectroscopy
protoporphyrin IX (PPIX) 147
pseudo-continuous arterial spin labelling (PCASL) 62
pulsed arterial spin labelling (PASL) 62
pyogenic cerebral abscess 155–6

Q
quantification of relaxation times and proton density (QRAP) 20
quantitative magnetization transfer (QMT) 51, 53, 54, 55
quantitative relaxometry and water content mapping 13–14, 21
quantitative T_2^* mapping (QUTE) 22–3

R
radiation-induced myelopathy 327
random coincidences, PET 90, 91–2
random-effects model, fMRI 75
rapid acquisition with relaxation enhancement (RARE) 54
Rasmussen's encephalitis 273
reconstruction-based scatter compensation (RBSC) 85
region-of-interest (ROI)-based functional connectivity analysis 76
resting-state networks (RSN) 175
reversible cerebral vasoconstriction syndrome (RCVS) 397, 401, 402
rhizomelic chondrodysplasia punctata (RCDP) 390
rhombencephalitis 298–9
rhombencephalosynapsis 356–8
Richardson's syndrome 253, 256
robust estimation of tensors by outlier rejection (RESTORE) 43
Rocky Mountain Spotted Fever encephalitis 158
Rolandic cortex 265–7
Rotterdam Classification score 10

S
Salla disease 392
Sandhoff disease 391
Sanfilippo syndrome 392
sarcoidosis 324, 325
scatter
  PET 90, 91
    correction 92–3
  SPECT 83, 85
  ultrasound 97
Schilder's disease 178
schistosomiasis 326
schizencephaly 364, 365
schizophrenia
  MRS 35
  MT 56
scintillation crystals
  PET 91, 92
  SPECT 79
seed-based connectivity analysis 75–6, 77
seizures 272, 274
semi-LASER 30
semilobar holoprosencephaly 361
SENSE 71
septo-optic dysplasia 362
shimming, MRS 32
short-lasting unilateral neuralgiform headache attacks with conjunctival injection and tearing (SUNCT) 117, 118
siderosis of the CNS 307–8
similarity matrix, functional connectivity analysis 76
single photon emission computed tomography (SPECT) 65, 79–89
  AD 213, 214, 218, 233
  ataxias 295, 296, 298, 305, 306, 309–10
  atypical parkinsonisms 253–4, 257
  comparison with CT and MRI 4
  data acquisition protocols 81
  DLBD 239–41
  epilepsy 132
  FTD 232, 233, 235
  FTLD 224
  future perspectives 86–7
  headache 117
  image quality assessment and data analysis 86
  image reconstruction 81–6
  instrumentation 79–80
  MCI 213
  PD 246–50, 252, 257, 258
  prion diseases 269
  TBI 340
  VCI 204–5, 206
single-voxel magnetic resonance spectroscopy 30
Sjögren's syndrome (SS) 325
small vessel childhood primary angiitis of the central nervous system (SV-cPACNS) 378–80
small vessel diseases (SVDs) 399
SMASH 71
sonothrombolysis 107–8
specific binding potential (SBP) 86
spinal cord
  abscess 156
  ADEM 178
  CNS vasculitis 399
  compression (SCC) 326, 327, 330
  diseases 323–34
    degenerative and neurodegenerative diseases 330–2
    infectious diseases 325–6
    inflammatory/demyelinating diseases 323–5
    metabolic and toxic diseases 329–30
    neoplasm 326–7
    syringomyelia 328
    vascular disorders 328–9
  D-MRI 44
  injury (SCI) 315–22
    cross-sectional area measurement 317–19
    DWI 320
    future perspectives 320–1
    MRI 315–17
    VBM 319–20
    without radiographic abnormality (SCIWORA) 316
  MND 288
  MS 169, 176
    in children 377
spinal cord injury without radiographic abnormality (SCIWORA) 316
spinal extradural (epidural) abscess 154–5
spinal human immunodeficiency virus (spinal HIV) 163
spinal subdural abscess 155
spinal tuberculosis 160–1, 165
spine trauma 10
spinocerebellar ataxias
  SCA1 305, 309
  SCA2 301, 305, 309
  SCA3 305–6
  SCA6 306, 309
  SCA17 306
spirochete leptomeningitis 154–5
sporadic adult onset ataxia (SAOA) 308–9
sporadic Creutzfeldt–Jakob disease (sCJD) 263–8, 271, 274
SPRINT II 80
standardized uptake value (SUV), PET 93, 94–5
statistical parametric mapping (SPM) 86
stenogyria 360
stimulated echo acquisition mode (STEAM) 30, 31
stroke 185–99
  ataxias 297–8
  CNS vasculitis 399
  haemorrhagic CVD 191–3
  ischaemic *see* ischaemic stroke
  ischaemic cerebrovascular disease 185–91
  management 193–6
  microbleeds 202
  radiological mimicker of CJD 271, 272
  ultrasound 100, 101, 103, 107
subacute combined degeneration (SCD) 329–30, 331
subacute sclerosing panencephalitis (SSPE) 273
subarachnoid haemorrhage (SAH) 192–3, 194
  CT 7, 9
subarachnoid space 151
subcortical band heterotopia 364
subdural empyema 154
subdural haematomas (SDH) 9
subdural space 152
subjects with scans without evidence of dopaminergic deficit (SWEDD) 248, 253
Susac syndrome 403
susceptibility-weighted imaging (SWI)
  CNS vasculitis 399
  MS 174
  parenchymal infection 156, 158, 159
  stroke 190, 191, 193
  TBI 335–6
syntelencephaly 362
synthetic imaging, MRI 21, 22
syphilis 401
syringomyelia 328
systemic lupus erythematosus (SLE) 324–5
  childhood 380–1

T
T_1 magnetic resonance imaging 13–18, 20–1, 24, 139, 140, 142, 148
  AD 208, 218
  ataxias 295, 299–300, 301, 302
  atypical parkinsonisms 255
  children with CNS inflammatory disorders
    acute demyelinating syndromes 370–2, 373, 374
    CNS lupus 381
    MS 375–7, 378, 381
    neuro-Behçet's disease 380
  CNS vasculitis 398, 399, 400
  congenital malformations of brain and skull
    Arnold Chiari malformations 359
    corpus callosum 368
    Dandy–Walker malformation 356, 357
    periventricular nodular heterotopia 363
    polymicrogyria 364
    pontine tegmental cap dysplasia 358
  congenital metabolic CNS disorders
    leukoencephalopathies 392, 393
    lysosomal disorders 391, 392
    peroxisomal disorders 390
  DLBD 241
  epilepsy 124, 128
  FTLD 224, 227
  infections of nervous system
    HIV/AIDS 163, 164
    meningeal infection 152, 155
    parenchymal infection 156, 158, 159
    tuberculosis 164, 165
  MND 288, 289

  MS 168, 169
    optic nerve 177
    pathophysiology 170, 171
  neoplasia 141
  PACNS 380, 381
  PD 250
  spinal cord diseases 324, 325, 326, 327, 328, 329, 330, 331
  spinal cord injury 315, 316, 318
  stroke 187, 189, 191, 192, 271
  VCI 203, 204
  water content mapping 22, 23–4
T_1 mapping with partial inversion recovery (TAPIR) 23
T_2 magnetic resonance imaging (MRI) 13–14, 18–21, 24, 68
  ataxias 295, 297, 298, 299, 301, 304, 306, 307, 308, 309
  atypical parkinsonisms 254, 255, 256
  children with CNS inflammatory disorders
    acute demyelinating syndromes 370–2, 373, 374
    CNS lupus 381
    MS 375, 376, 377, 381, 382, 384
    neuro-Behçet's disease 380
    neuromyelitis optica 375
    neurosarcoidosis 380
  CNS vasculitis 399, 402, 403
  congenital malformations of brain and skull
    Arnold Chiari malformations 359, 360
    cephaloceles 366
    cerebellum 355
    corpus callosum 368
    Dandy–Walker malformation 356, 357
    molar tooth malformation 358
    periventricular nodular heterotopia 363
    polymicrogyria 364
    pontine tegmental cap dysplasia 358
    rhombencephalosynapsis 358
    schizencephaly 365
    septo-optic dysplasia 362
  congenital metabolic CNS disorders
    L-2-hydroxyglutaric aciduria 389
    leukoencephalopathies 392
    lysosomal disorders 391, 392
    mitochondrial disorders 389–90
    peroxisomal disorders 390
  DLBD 241
  epilepsy 124, 126, 127
  infections of nervous system
    HIV/AIDS 161, 163, 164
    meningeal infection 152, 154, 155
    parenchymal infection 155, 156, 157, 158, 159
    tuberculosis 164, 165
  MT 50, 51, 53, 54
  mimickers of CJD 271, 272, 273, 274
  MND 279, 288, 289
  MS 170, 177
  neoplasia 139, 140, 142, 148
  PACNS 380, 381
  PD 250
  prion diseases 263, 264, 268
  spinal cord diseases 324, 325, 326, 327, 328, 329, 330, 331, 332
  spinal cord injury 315, 316
  stroke 186, 187, 188, 190, 191, 192
  TBI 335
  VCI 201, 202, 203–4
T_2^* magnetic resonance imaging 13, 14, 68
  ataxias 298, 301, 303, 307, 308, 309
  CNS vasculitis 398, 399
  DLBD 243
  epilepsy 125
  fMRI 69, 70
  MS 177
  neoplasia 140, 141
  parenchymal infection 158
  PD 250
  perfusion 141
  stroke 190, 192, 193, 194
    management 194
  TBI 335, 336
  VCI 202, 203, 204
  water content mapping 22–3
Takayasu arteritis 102
taurine 143
Tay–Sachs disease 391
telemedicine 111
telestroke 111
tele-ultrasound 111–12
temporal arteritis 102
temporal lobe epilepsy (TLE) 124, 125–7, 130, 131, 132, 273
tension-type headache 120
tensor-based morphometry (TBM) 295, 300, 301, 303, 305
thermal index (TI) 99
thrombectomy 195
thrombolysis 194–5
thrombus 5
tick-borne encephalitis 157
time of flight (ToF) 93
toxic causes of spinal symptoms 329–30
toxin-induced ataxias 298, 307
toxoplasmosis 163–4
tracer kinetic modelling, PET 94
transbulbar sonography 110–11
transcranial magnetic stimulation (TMS)
  consciousness, disorders of 349–51
  neoplasia 145–6
transcranial sonography 104–6
  PD 252–3, 258
transducers, ultrasound 98
transforaminal insonation 105–6
transient ischaemic attack (TIA) 185, 195–6
transient symptoms with infarction (TSI) 195–6
transtemporal insonation 105
transverse myelitis (TM) 371, 372, 373, 374
traumatic brain injury (TBI) 335–45
  CT 9–10
  diffusion MRI 336–9
  fMRI 341–3
  MRS 336
  perfusion imaging 339–41
  PET 343
  SWI 335–6
trigeminal autonomic cephalalgias (TACs) 117–18, 120
true coincidences, PET 90, 91
tuberculoma 160, 165
tuberculosis 160, 164–5
  CNS vasculitis 401
  spinal symptoms 326
tuberculosis meningitis 160, 164
tuberculous cerebritis 165
tuberous sclerosis 131, 132
tumours
  spinal 326–7
  see also neoplasia
turbo spin echo (TSE) 14

U

ultra-high field magnetic resonance imaging
  AD 215
  MS 177
  PD 250
ultrasound 97–114
  brain parenchyma 109–11
  carotid system 99–103
  cervical and intracranial veins 108–9
  hazards 99
  intracranial arteries 106–8
  MS 174
  neoplasia 146–7
  neuromuscular 111
  PD 252–3, 258
  physical and technical principles 97–9
  tele-ultrasound 111–12
  transcranial insonation 104–6
  vertebral system 103–4
unresponsive wakefulness syndrome (UWS) 346–7, 348, 349, 350–1
urosepsis 273

V

vanishing white matter disease (VWMD) 393
variable flip angle spoiled gradient recalled method (DESPOT1) 17–18, 19, 20
variable flip angle steady state free precession method (DESPOT2) 18–19, 20
variable flip angle techniques, water content mapping 23–4
variant Creutzfeldt–Jakob disease (vCJD) 263, 264, 265, 268–9
vascular clot 5, 6
vascular cognitive impairment (VCI) 200–7
  ASL 204
  CT 203
  DTI 204
  hereditary forms of VaD 203
  lacunes 202
  large vessel disease 200
  microbleeds 202–3
  MRI 203–4
  neurodegeneration 203
  PET 204, 205–6
  small vessel disease 200–1
  SPECT 204–5
  white matter changes 201–2
vascular dementia (VaD) 200, 206, 213
  cerebral perfusion imaging 65
  differential diagnosis 214, 227
  hereditary forms 203
  lacunes 202
  large vessel disease 200
  microbleeds 202
  neurodegeneration 203
  PET 205–6
  small vessel disease 200–1
  SPECT 204, 205, 206
  white matter changes 201–2
vascular disease, HIV 163
vascular disorders, spinal symptoms 328–9
vasculitis, ultrasound 102
vegetative state 346
venous sinus thrombosis 5
ventriculitis 155
vertebral system, ultrasound of 103–4
viral encephalitis 156–7
viral leptomeningitis 153–4
Virchow–Robin spaces (VRS) 202, 203

vitamin B12 deficiency 330
vitamin C (aspartate) quantification 34
vitamin E deficiency 330
voltage-gated potassium channel complex (VGKCC) associated autoimmune encephalopathy 274
volumetry analysis, epilepsy 125–6
voxel-based morphometry (VBM)
  ataxias 295, 300–1, 305, 306, 309
  atypical parkinsonisms 257
  bvFTD 225, 226
  epilepsy 128
  headache 118, 119, 120
  MND 279–82, 288
  PD 251
  spinal cord injury 319–20
voxel-based quantification (VBQ) 319

W

Walker–Warburg syndrome (WWS) 363, 364
water content mapping 21–4
  see also quantitative relaxometry and water mapping
water suppression 31
Wegener's granulomatosis 402
Wernicke's encephalopathy 272, 299
West Nile virus (WNV) 157
Wilson's disease 272
World Health Organization (WHO), neoplasia classification 139

X

xenon computed tomography (Xe-CT) 63
  TBI 340
X-linked adrenoleukodystrophy (X-ALD) 390
X-linked ataxias 306–7
X-linked lissencephaly 363
X-rays 3

Z

Zellweger syndrome 364, 390
z-shimming 71
Z-spectrum
  CEST 56
  MT 52